ISSN 0386-5878
Technical Memorandum
of PWRI No.3692

PROCEEDINGS OF THE 15TH U.S.-JAPAN BRIDGE ENGINEERING WORKSHOP

NOVEMBER 9 AND 10, 1999

PUBLIC WORKS RESEARCH INSTITUTE
MINISTRY OF CONSTRUCTION

1, Asahi, Tsukuba-shi, Ibaraki-ken, 305-0804 Japan

Copyright © (2000) by P.W.R.I.

All rights reserved. No part of this book may be reproduced by any means, nor transmitted, nor translated into a machine language without the written permission of the Director General of P.W.R.I.

この報告書は、土木研究所長の承認を得て刊行したものである。したがって、本報告書の全部又は一部の転載、複製は、土木研究所長の文書による承認を得ずしてこれを行ってはならない。

Technical Memorandum
of PWRI No.3694

PROCEEDINGS OF THE 15TH U.S.-JAPAN BRIDGE ENGINEERING WORKSHOP

by

Kazuhiro Nishikawa

Synopsis:

The proceedings document the results of the 15th U.S.-Japan Bridge Engineering Workshop which was held at Tsukuba, Japan, on November 9 and 10 1999, under the auspices of the Panel on Wind and Seismic Effects, UJNR. The Workshop was organized by Task Committee J "Wind and Earthquake Engineering for Transportation Systems" (U.S. side chairman: Mr. J.D..Cooper, FHWA, Japan side chairmman: Mr. K. Nishikawa, PWRI) of the Panel.

Key Words: Earthquake Reports, Seismic Retrofit, Concrete, Maintenance, Advanced Materials, Wind, UJNR

FOREWORD

The 15th U.S.- Japan Bridge Engineering Workshop is a continuation of a series of technical interchanges between the United States and Japan on all topics related to bridge engineering. This series of Workshops have been conducted under the auspices of Task Committee J "Wind and Earthquake Engineering for Transportation Systems" of the U.S.-Japan panel on Wind and Seismic Effects, Which is one of 18 panels making up the United States - Japan Cooperative Program in Natural Resources(UJNR). The previous workshops are indicated in the table.

WORKSHOP	DATE	PLACE
First	February 20-22,1984	Tsukuba, *Japan*
Second	August 19-20,1985	San Francisco, CA, *United States*
Third	May 8-9,1987	Tsukuba, *Japan*
Forth	May 11-12,1988	San Diego, CA, *United States*
Fifth	May 9-10,1989	Tsukuba, *Japan*
Sixth	May 7-8,1990	Lake Tahoe, NV, *United States*
Seventh	May 8-9,1991	Tsukuba, *Japan*
Eighth	May11-12,1992	Chicago, IL, *United States*
Ninth	May 10-11,1993	Tsukuba, *Japan*
Tenth	May 10-11,1994	Lake Tahoe, NV, *United States*
Eleventh	May 30-31,1995	Tsukuba *Japan*
Twelfth	October 29-30,1996	Buffalo, NY, *United States*
Thirteenth	October 2-3,1997	Tsukuba, *Japan*
Fourteenth	November 3-4,1998	Pittsburgh, PA, *United States*
Fifteenth	November 9-10,1999	Tsukuba, *Japan*

The steering committee for the 15th U.S. - Japan Bridge Engineering Workshop consisted of Kazuhiro Nishikawa, James D. Cooper, Jiro Fukui, Masahiro Nishitani, Manos Maragakis and David Sanders. The principal funding for the workshop was provided by PWRI.

The workshop proper was held in the PWRI, Tsukuba. The participants of the Workshop reached the total of 87 persons (65 persons of Japan side and 22 of U.S. side).

The main topics of this workshop were 1) earthquake reports of Taiwan and Turkey Earthquake, 2) innovative seismic retrofit technology including the application of new materials and new structural systems, and 3) innovative bridge design concept; e.g., bridge types, materials, life cycle cost analysis. In the WorkShop, there were 48 presentations (24 papers of Japan side and 24 of U.S. side).

The study tour was held in three locations: Imabari - Onomichi, Kobe and Osaka City. The first leg of the study four was held in Shimanami-kaido(the west side route of the Honshu-Shikoku Bridges),going through the nine long-span bridges, such as the Kurushima Bridges and Tatara Bridge, from Imabari City to Onomichi City. The second leg of the study tour was held in the Akashi Kaikyo Bridge, Kobe City. Both study tours were organized by Honshu - Shikoku Bridge Authority. The third leg of the study tour, held in the Yumeshima - Maishima Movable Floating Bridge in Osaka City, was organized by Osaka City.



Participants of the Workshop

TABLE OF CONTENTS

FOREWORD

PAPERS

SESSION 1: OPENING SESSION 1

SESSION 2: EARTHQUAKE REPORTS 5
(1) The Kocaeli Earthquake Investigation Summary 7
(James D. Cooper, Hamid Ghasemi, Phillip Yen, Roy Imbsen, Saad El - Azazy)
(2) Damage to Transportation Facilities in the Recent August 17, 1999 Kocaeli Earthquake in Turkey..... 17
(Roy A. Imbsen)
(3) The Turkey Earthquake -- August 17,1999 Damage to the Transportation Infrastructure 29
(John B. Mander)
(4) Bridge Performance in the 921 Earthquake, CHI-CHI, TAIWAN 43
(Ian Buckle and Jenn-Shin Hwang)

SESSION 3: SEISMIC ISSUES (1) 55
(1) An Update on Analytical and Experimental Research on Bridge Restrainers..... 57
(Anastasios G. Vlassis, Emmanuel Manos Maragakis and Mehdi Saiid Saiidi)
(2) A Static Three-Dimensional Elastic-Plastic Analysis of Steel Frame Bridge Piers 73
(Motoaki Tanaka, Yuji Sato and Hideaki Kasabou)
(3) Cyclic Testing of Composite Concrete-Filled Circular Tubes and Foundation Detail..... 87
(Michel Bruneau and Julia Marson)
(4) Experimental Study on Strength and Ductility of One-Story and
Two-Story Rigid Frame Steel Piers of Highway Bridges 99
(Tatsumasa Takaku, Yuhshi Fukumoto, Tetsuhiko Aoki, Takashi Okamoto,
Tatsuo Kurokawa and Hiromitsu Morishita)
(5) Seismic Resistant Design of the Rio Tempisque Bridge 115
(Cris D. Subrizi)

SESSION 4: SEISMIC ISSUES (2) 131
(1) Liquefaction and Shear Wave Velocity Characteristics of Silty/Gravely Soils
- Implications for Bridge Foundations 133
(Sabanayagam Thevanayagam)
(2) Experimental Study on Seismic Behavior of Bridge Pile-to-Pile Cap Connections 149
(Yan Xiao, J.B. Mander, H.Wu and G. Martin)
(3) A Proposal of Aseismic Strengthening of Wall-type RC Bridge Pier,
with Minimum Impact on Its Foundation..... 163
(Kenji Ikeda, Hiroshi Mitamura, Norimitsu Kishi and Noriyoshi Murakami)
(4) Advanced Computational Methods in Bridge Engineering 175
(Jamshid Ghaboussi)
(5) Study on the Stability of the Akashi Kaikyo Bridge for Residual Displacement
of Tower Foundation by Large-Scale Earthquake 191
(Susumu Fukunaga)
(6) Micropiles for Seismic Retrofits..... 203
(James H. Long, Thomas E. Hunt and Boris W. Leoro)

SESSION 5: SEISMIC ISSUES (3) 217
(1) Assessing Oregon's Seismic Risk 219
(Martha Sartain, Richard Groff, Craig Shike and Mark Hirota)
(2) Developing Seismic Design Ground Motions for Super Long-Span Bridges..... 233
(Keiichi Tamura, Yoshihiro Nakao and Shojiro Kataoka)
(3) Seismic Vulnerability Study of Highway Systems: TEA-21 Research Project 247
(Gokhan Pekcan, W. Phillip Yen and Ian M. Friedland)

(4) The System of Real-time Earthquake Damage Estimation in Hanshin Expressway 259
(Kiyoshi Miyawaki, Taiichi Kagayama and Fuminobu Okunishi)
(5) The Newly Developed AASHTO Guide Specifications for Seismic Isolation Design 271
(H. Ghasemi)
(6) Guidelines for Testing Passive Energy Dissipation Devices 281
(Michael A. Riley, Fahim Sadek and Bijan Mohraz)

SESSION 6: CONCRETE 289
(1) Bending Behavior of Prestressed Concrete Girders Damaged by Salt Attack 291
(Yoshiki Tanaka, Hirotaka Kawano, Hiroshi Watanabe and Masahiro Suzuki)
(2) Performance of Reinforced Concrete Bridge Joints Subjected to Bi-Directional Loading 301
(Khalid M. Mosalam, Svetlana Khaykina and Clay Naito)
(3) Development of Electric Anticorrosion Methods for Newly Constructed Concrete Structures 317
(Masaru Terada and Seishi Meiarashi)
(4) Corrosion Control of Concrete Bridges 325
(Yash Paul Virmani)
(5) Durability and Structural Safety Evaluation
of RC Gerber's Bridge Servicing for More Than 60 Years 331
(Naoshige Nomura, Yoshihiro Tanaka and Takeyuki Yokooka)

SESSION 7: SEISMIC ISSUES (4) 343
(1) Draft Manual of Seismic Retrofit Design for Single-Type Reinforced Concrete Columns
Using Carbon Fiber Sheets 345
(Shigeki Unjoh, Toru Terayama and Junichi Hoshikuma)
(2) FRP Composites for Seismic Retrofitting of Non-Prismatic Reinforced Concrete Bridge Columns 355
(David H. Sanders, M. Saiidi Saiidi, Faramarz Gordaninejad,
Frank Martinovic and Brett McElhaney)
(3) Size Effect in Shear Behavior of Reinforced Concrete Piers Strengthened with Carbon Fiber Sheets 367
(Koji Osada, Yoshinori Igase, Takahiro Yamaguchi and Shoji Ikeda)
(4) Seismic Retrofit Methods of Cap Beam of Two-Column Bents 379
(Yukio Adachi, Shigeki Unjoh and Kazuhiro Nagaya)
(5) Application of Fiber Reinforced Polymers (FRP) for Seismic Retrofit of California Bridges 393
(Thomas E. Sardo)
(6) Seismic Behavior of Circular Hollow Columns without Inside Reinforcement 405
(Jun-ichi Hoshikuma and M. J. Nigel Priestley)

SESSION 8: ADVANCED MATERIALS 419
(1) Safety Factor and Calculation Method of FRP for Structural Material of Bridge 421
(Itaru Nishizaki, Takeshi Kishima and Seishi Meiarashi)
(2) Development, Testing and Deployment of FRP Structures 431
(Issam E. Harik and P. Alagusundaramoorthy)
(3) The Effect of Reinforcement for Bridge Superstructures with Carbon Fiber Sheets 447
(Kenji Suzukawa, Akeo Hattori, Akira Kobayashi and Tokitaro Hoshijima)
(4) FRP Composites for Bridge Engineering 461
(John B. Scalzi)

SESSION 9: WIND AND VIBRATION 465
(1) Flutter Characteristics of a Super Long-Span Bridge 467
(Hiroshi Sato, Shigeki Kusuhara and Nobuaki Furuya)
(2) Aerodynamic Stability of the Cable Stayed Bridge with New Type of Twin Girder 479
(Kensaku Hata, Masahiro Koike and Takumi Uno)
(3) Vibration Test of the Tatara Bridge 493
(Kazunori Yamaguchi)
(4) Damping Characteristics of Prestressed Concrete Cable-Stayed Bridges Based on Measured Data 501
(Shinichi Yamanobe, Yuji Niihara and Tesuo Takeda)

(5) Monitoring of Hakucho Suspension Bridge using Ambient Vibration 515
(Yozo Fujino, Masato Abe, Hajime Shibuya, Masato Yanagihara and Masashi Sato)

SESSION 10: CURRENT BRIDGE R&D 523
(1) AASHTO's Bridge Research Program 525
(David B. Beal)
(2) Design Concept of a Floating Swing Bridge in Osaka 535
(Tadaaki Maruyama, Yukio Kawamura, Masao Yubisui, and Hiroshi Tanaka.)
(3) International Scanning Tours Related to Bridge Technology 551
(David H. Densmore)
(4) Fretting Fatigue Characteristics in the Curved Layout of Large-Capacity Prestressing Strands 557
(Manabu Fujita, Keiji Umezu, Hideo Arai and Tamon Ueda)
(5) Use of an Alternate Shear Connector in a Beam-in-Slab Bridge System 573
(F.W. Klaiber and T. J. Wipf)
(6) Maintenance of Bridge and Reinforcement of Existing Deck Slabs 587
(Hiroshi Mitamura, Shizuo Kato, Shigeharu Onsen and Shigeyuki Matsui)

SESSION 11: CLOSING SESSION 599

APPENDICES
Workshop Program 603
List of Participants 613
Photos of Study Tour 629

SESSION 1: OPENING SESSION

SESSION 1: OPENING SESSION

Welcome Remarks: Tomomitsu Fujii (Director General, PWRI)

Remarks: James D.Cooper (Chairman for the U.S. Side)

Remarks: Kazuhiro Nishikawa (Chairman for the Japan Side)

SESSION 2: EARTHQUAKE REPORTS

(1) The Kocaeli Earthquake Investigation Summary
(James D. Cooper, Hamid Ghasemi, Phillip Yen, Roy Imbsen, Saad El - Azazy)

(2) Turkey Earthquake (presentation only)
(Micho Okahara)

(3) Damage to Transportation Facilities in the Recent August 17, 1999 Kocaeli Earthquake in Turkey
(Roy A. Imbsen)

(4) The Turkey Earthquake – August 17,1999 Damage to the Transportation Infrastructure
(John B. Mander)

(5) Taiwan Earthquake (presentation only)
(Shigeki Unjoh)

(6) Bridge Performance in the 921 Earthquake, CHI-CHI, TAIWAN
(Ian Buckle and Jenn-Shin Hwang)

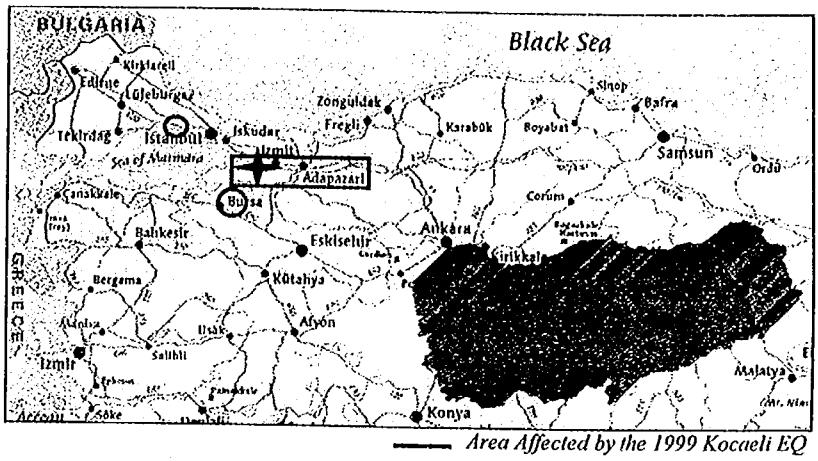
The Kocaeli Earthquake Investigation Summary

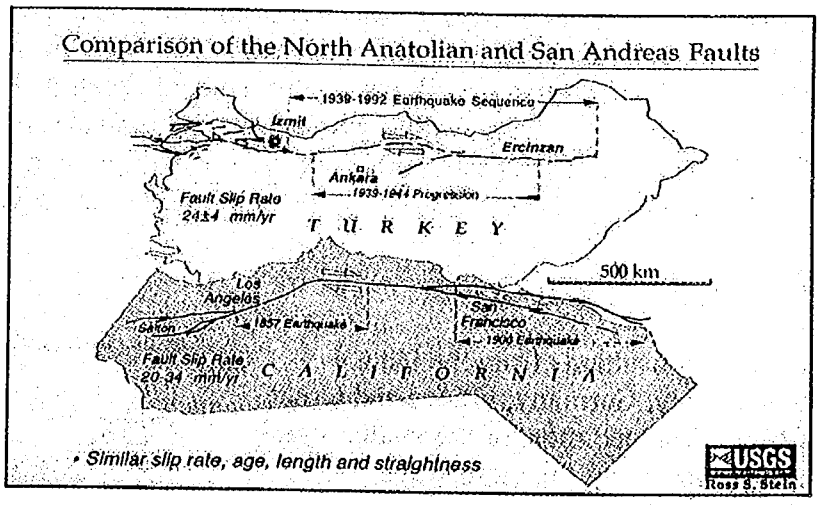
James D. Cooper[1], Hamid Ghasemi[2], Phillip Yen[3], Roy Imbsen[4], Saad El-Azazy[5]

Introduction

At 1:03 a.m. on August 17, 1999, a devastating 7.4 magnitude earthquake, which lasted 45 seconds, struck Turkey. The epicenter was located in the province of Kocaeli near the industrial city of Izmit. The earthquake resulted in at least 15,000 deaths and caused the collapse and destruction of thousands of buildings and other structures within approximately a 100 km radius centered on the city of Golcuk. Highway bridges however, performed relatively well in comparison to the performance of building stock. There were only two bridge collapses reported with minor to moderate damage to other bridges in the epicentral region.

The earthquake was caused by a rupture along a branch of the North Anatolian Fault Zone (NAFZ), along which destructive earthquakes have occurred frequently in this century. The NAFZ is of particular interest to the United States because it is virtually identical to the San Andreas Fault Zone in California. The NAFZ strike-slip fault is as active and is capable of generating earthquakes with equivalent magnitudes with about the same frequency of occurrence as the San Andreas. Since the devastating 7.8 magnitude 1939 Erzincan earthquake, which cost 16,000 lives, earthquakes have migrated along the NAFZ towards Istanbul. The August 17 earthquake occurred about 110 kilometers to the east of Istanbul and there is great concern by seismologists that the next earthquake will occur much closer to that densely populated city.





Courtesy of USGS

P.E., Technical Director, Bridge R&D, FHWA, Turner-Fairbank Highway Research Center, McLean, Virginia
Ph.D., Research Structural Engineer, FHWA, Turner-Fairbank Highway Research Center, McLean, Virginia
Ph.D., P.E., Research Structural Engineer, FHWA, Turner-Fairbank Highway Research Center, McLean, Virginia
P.E., D. Engr., President, IMBSEN & ASSOCIATES, INC., Sacramento, California
Ph.D., P.E., Senior Bridge Engineer, California Department of Transportation, Sacramento, California

The severe damage and destruction that occurred during the Kocaeli earthquake, coupled with the fact that the Turkish Road Directorate (KGM) has used the AASHTO Standard Specifications for Highway Bridges for bridge design, caused the KGM Director General to request technical assistance from the Federal Highway Administrator in assessing the performance and behavior of motorway bridges and structures. The FHWA Office of International Programs and the Office of Infrastructure requested that an FHWA investigative team be established and dispatched to Turkey to cooperate and work with Turkish road officials. Three FHWA bridge engineers, Mr. James Cooper, Dr. Hamid Ghasemi, and Dr. Phillip along with a Consultant from Sacramento, Dr. Roy Imbsen and a CALTRANS bridge engineer, Dr. Saad El-Azazy formed the FHWA team.

This paper will provide an overview of the cooperative effort between the FHWA team and their KGM counterparts in examining the Trans European Motorway (TEM) structures between Ankara and Istanbul.

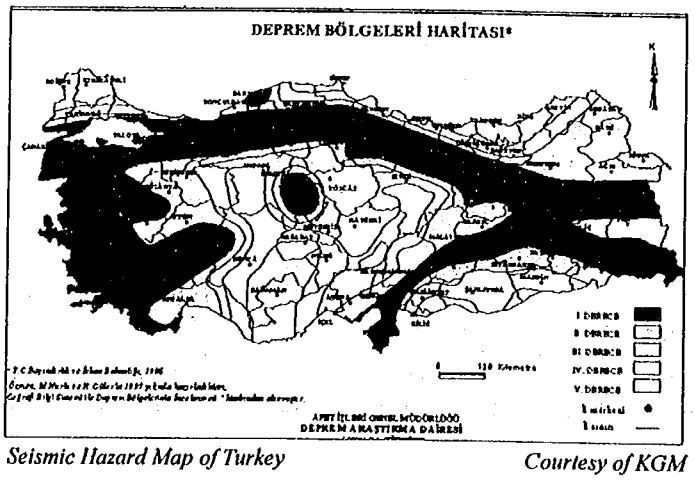
The Trans European Motorway

The Republic of Turkey with its 73 provinces and an estimated 65 million population provides a bridge between Europe and Asia. In order to achieve its economic development goals, Turkey spends a good third of all public investment on improving its transport infrastructure, by funding capital projects such as building roads and the expanding the rail network, especially in the western part of the country.

During the last 10 years, Turkey has built 1,500 km of motorway with the major portion of construction between Ankara and Istanbul, continuing to Europe, with remaining segments of construction in the west and south. There is also 800 km of motorway under construction from Ankara to the southern city of Adana, a 24 km strip near the town of Bolu, and additional construction in the north east and southwest. The TEM from Ankara to Istanbul is designated route # E80. This strip is built parallel to the NAFZ and includes a number of tunnels, viaducts, and many underpasses as well as overpasses. It represents the major through transportation route for the transport of goods and other commerce from Asia to Europe. The KGM is responsible for the services and maintenance of the entire motorway in Turkey.

Design Approach

Foreign consultants from the United States, Italy, Germany, France and Great Britain designed most of the viaducts and overpasses along the motorways. However, Turkish contractors performed most of the construction. It appears that a combination of the 1992 and 1983 AASHTO Standard Specifications for Highway Bridges and Euro Codes were applied for bridge design. However, on some occasions, when ductility of the

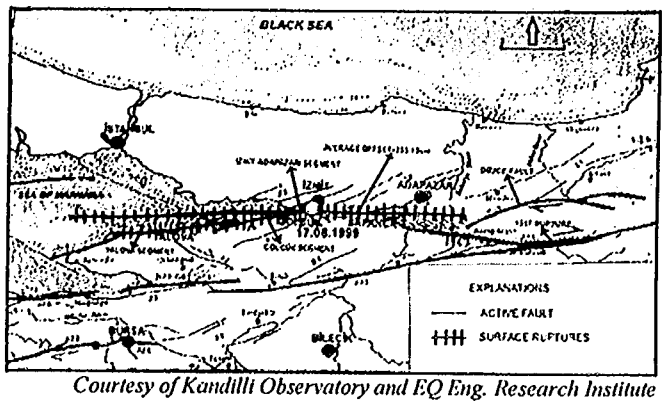


Seismic Hazard Map of Turkey *Courtesy of KGM*

columns was considered in the design process, the lap splices were located in the plastic hinge zones. Overall, an inherently improved seismic design approach was observed for newer bridges.

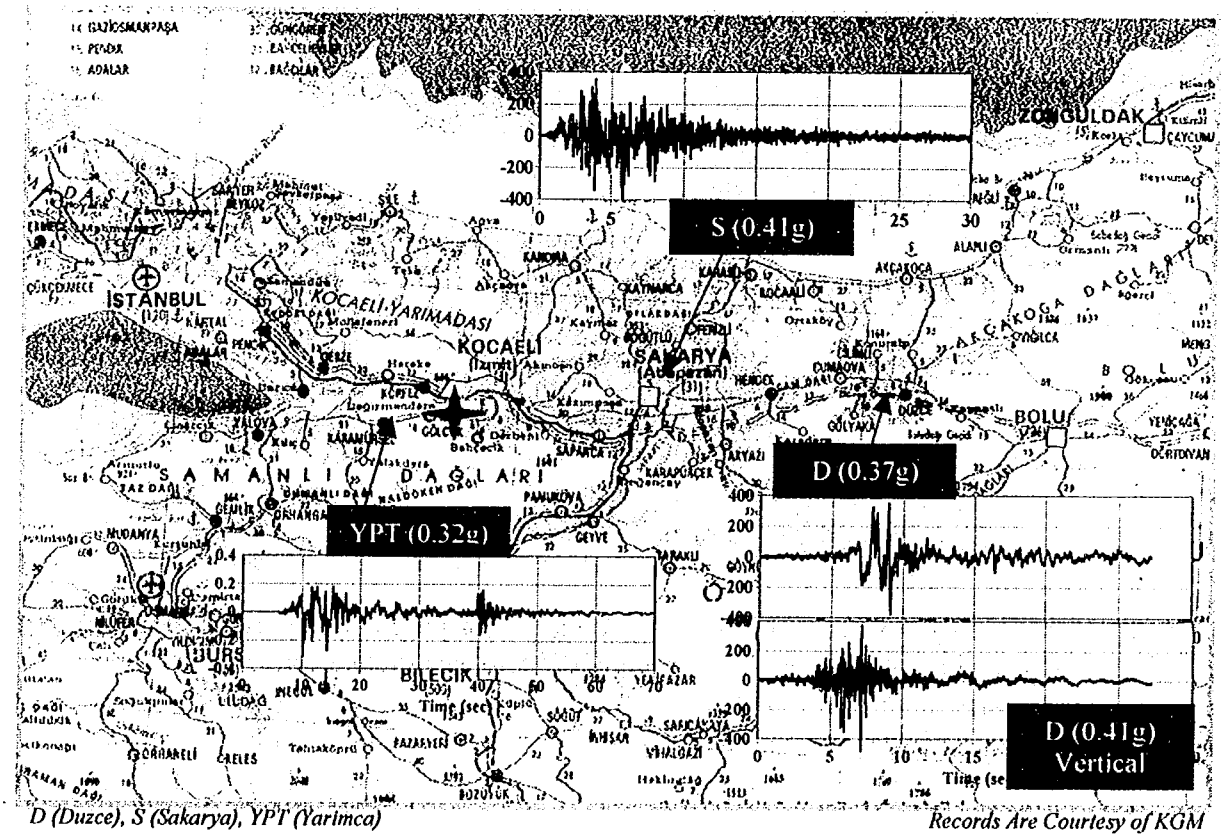
Geotechnical Issues

The Figure shows the surface fault ruptures during the Kocaeli earthquake that extended from Golcuk east to Adapazari and west into the Marmara Sea, where it was mapped using 1,500 km seismic profiles recorded on board the Turkish MTA Sismik-1 research vessel. There were many stations that recorded the ground motion during the earthquake, varying from 0.9g in Istanbul to 0.41g in Adapazari. At the epicenter, near Izmit, a ground acceleration of 0.22g was recorded.



Courtesy of Kandilli Observatory and EQ Eng. Research Institute

The near field or fling effects were evident in the records at Yarimca (YPT) station and at Duzce. The YPT station, 30 km west of the epicenter, recorded a double shock wave. According to the study at the Bogazici University, this is probably associated with an abrupt change in geology between Izmit and Sapanca Lake.

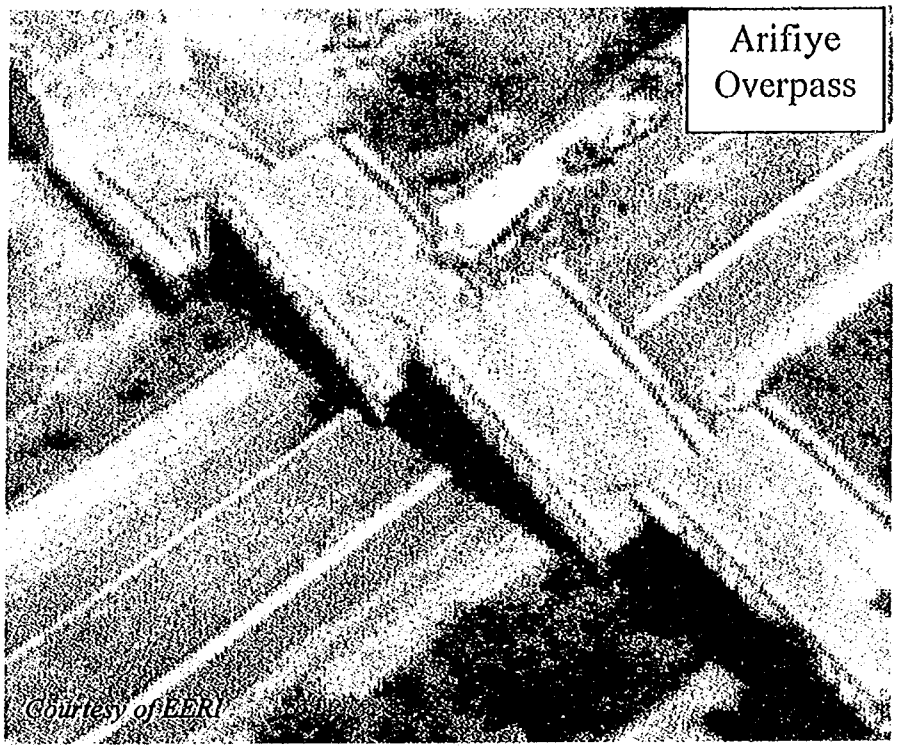


D (Duzce), S (Sakarya), YPT (Yarimca) *Records Are Courtesy of KGM*

Overall, much of the damage to buildings and bridges could be attributed to shallow structural foundations underlain by liquefied sediment and fault rupture adjacent to structures. However, the severity of the damage, in particular to buildings, could also be related to design issues and possibly to construction technique. It is important to note that in 1979 and again in 1997, a number of research studies concluded that risk of a large earthquake in the Izmit area was very likely.

Cooperation

During the Kocaeli earthquake, the extent of damage to bridges and buildings was observed from Duzce to the towns of Yalova and Hereke. The TEM segment, which runs 100 km between Duzce and Hereke, had suffered relatively minor damage, particularly when compared to the devastation and destruction of the building stock. The simply supported Arifiye overpass collapsed due to a fault rupture UNDER the bridge, while the Sakarya River Viaduct on the TEM suffered moderate damage when it slid off its bearings. There was additional minor to moderate damage to several other bridges. It is important to note that the KGM reacted quickly and had cleared the collapsed bridge and opened the TEM to traffic within three days of the event.



As a result of the damage to TEM bridges and a concern for public safety, the KGM Director General requested technical assistance from the FHWA to assess the performance and status of TEM bridges and structures. An FHWA investigative team was established and dispatched to Turkey on September 27 on a cooperative mission with their Turkish counterparts. On September 29, the team met with Director General Dincer Yigit and his technical staff to discuss details of the mission. Mr. Yigit requested that the team provide opinions on the seismic safety of structures on the Trans European Motorway (TEM) and recommend any seismic retrofitting

strategies that might be considered for increasing the seismic safety of the existing bridge network. Because of the destruction of so many buildings and structures, the Director General explained that the KGM desired to have an independent check on the performance of motorway structures during this earthquake and wanted to know how the KGM could improve the seismic resistance of the highway network. Specifically, the FHWA team, cooperating with their KGM counterparts, was asked to:

1. Assess the seismic safety of a major tunnel under construction in Bolu, a town about 125 kilometers west of Ankara, which experienced ground shaking estimated at 0.2 to 0.25g. The tunnel and two major viaducts are located on the last 24 km section of the TEM that is under construction in Turkey.

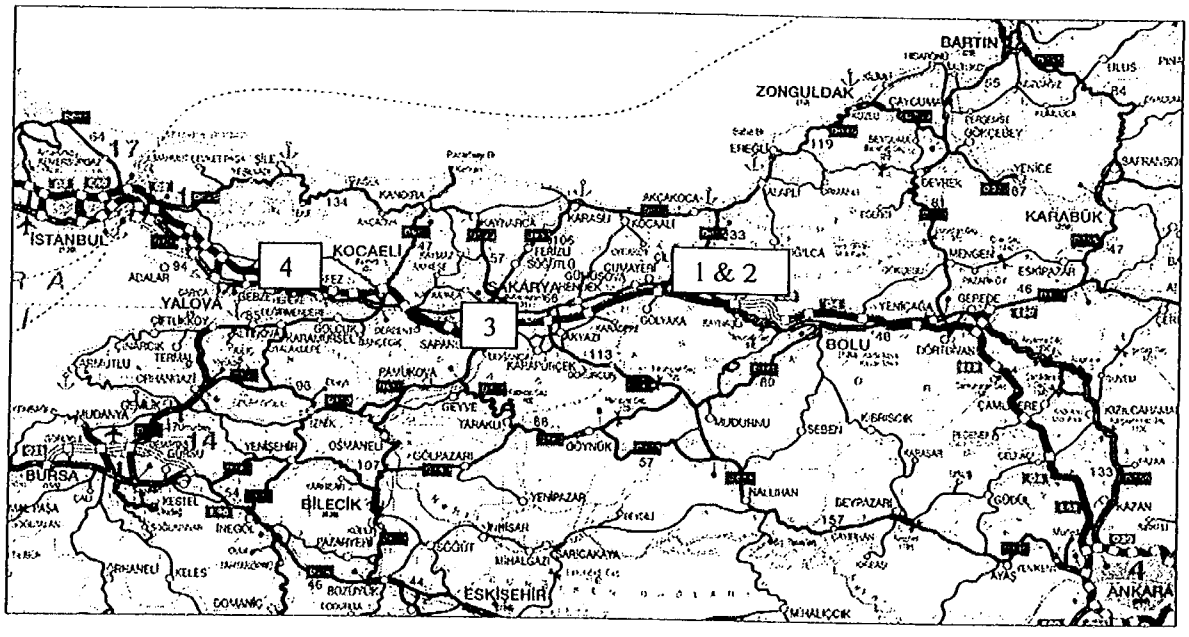
2. Assess the seismic safety of Viaduct #1 near the Bolu tunnel which is about 90 percent complete and Viaduct #2, also near the Bolu tunnel, where construction is just beginning.

3. Recommend how to repair the moderately damaged Sakarya River Viaduct located about 130 kilometers east of Istanbul, near the heart of the epicenter.

4. Assess the seismic safety of the undamaged Hereke Viaducts on the TEM, which experienced lower levels of seismic shaking without damage, and recommend retrofit measures.

5. Generally assess the seismic safety of all classes of bridges on the motorway, with emphasis on older motorway bridges in and around Istanbul.

The following figure shows the location of the sites1 to 4 on the TEM.



The FHWA team inspected over 20 bridges and tunnels. Two major briefings were presented at the KGM headquarters in Ankara prior to the team departure. The first was a major technical

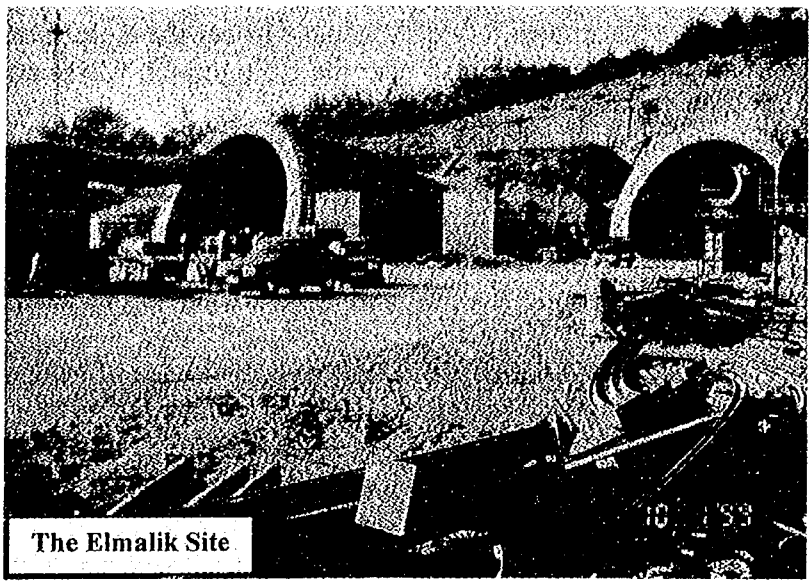
briefing to the Director of Motorway Bridges and his staff. The second was presented to the Director General where more general conclusions and recommendations were discussed. The team also presented lectures to 30 Turkish design engineers on seismic design and retrofit strategies in the U.S. On October 15, the FHWA team departed Turkey.

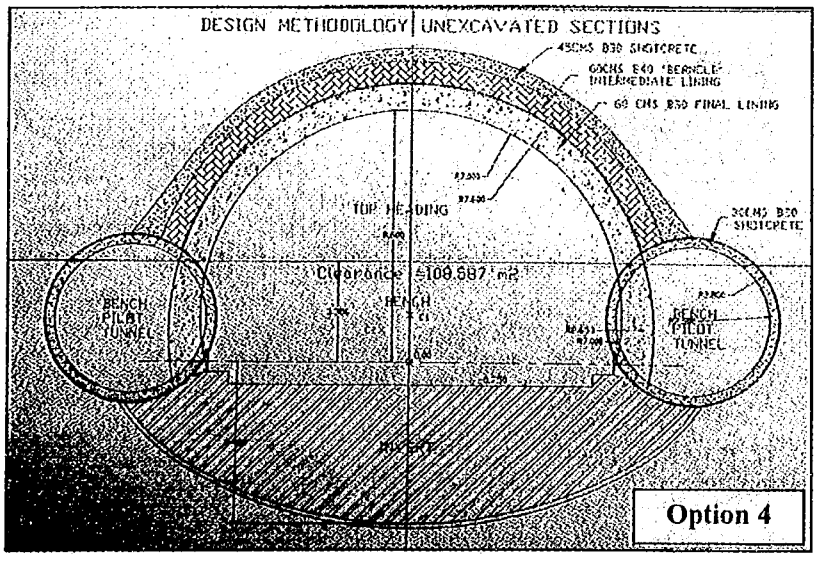
FHWA Team Observation

The following is a brief review of field observations related to items 1 through 4.

1- The Bolu Tunnel

The Bolu tunnel is located about 125 km east of the epicenter. Its total length is about 3.3 km of which 2 km has been completed. It has a width of 12 m, outer and inner heights of 15.3 m and 8.6 m respectively, and outside diameter of 17 m. From an engineering perspective, it is apparent that the Bolu tunnel represents the most difficult part of design and construction for the entire TEM due to a very complicated tectonic history and varied geological conditions. These complications are increased by the limitation of the exposure due to dense forest cover. In the past 60 years, there have been numerous earthquakes with magnitude 6.4 to 7.4 in the Bolu region, which has resulted in an extremely heterogeneous material varying from clays to competent rock.


The Elmalik Site



Option 4

The Bolu Tunnel openings are at the Elmalik site on the east side and at the Asarsuyu on the west side. The bore hole information, field observations and the study of regional geology, reveals that about 1.5 km from the Elmalik site there exists in a very soft clayey material and the remaining 1.7 km is located in weak to moderately competent rocks. It is also revealed that the rock portion of the tunnel is heavily deformed by vertical faults suggesting an

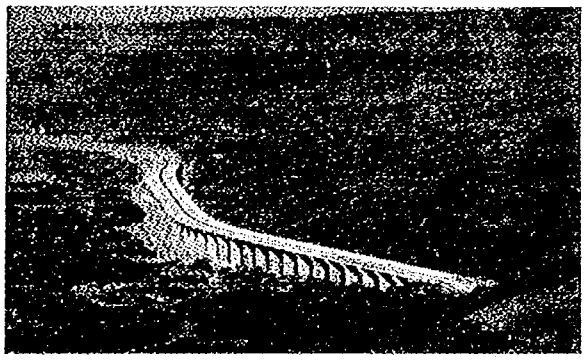
existence of a wide brittle shear zone. The tunnel may also be effected by the secondary faults called the Elmalik and the Asagi Bakacak, which connect the Duzce fault to the main NAF.

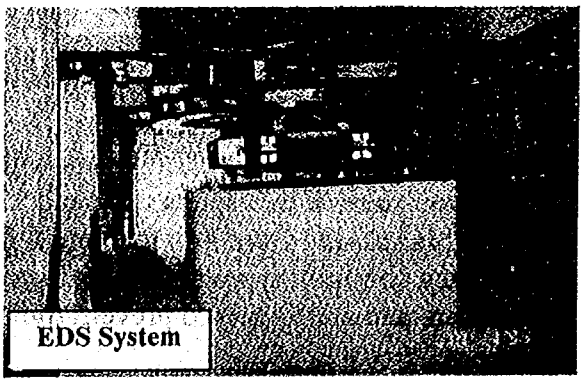
The Bolu tunnel design methodology is based on the New Austrian Tunneling Method (NATM). The tunnel consists of three layers (from outside inwards) of shotcrete, reinforced concrete and finally an unreinforced concrete layer. The complexity of the site forced the designers to consider 4 options for construction. Option 1 was to advance by blasting followed by shotcreting over rock. Option 2 was similar to option 1; however, a thicker shotcrete section was required. Due to the continuous deformation of the clay deposit at sections of the tunnel, a third option was considered. This option required 45 cm shotcrete, 60 cm intermediate reinforced concrete and finally a 60 cm of unreinforced concrete lining. Option 4 was planned for the worst condition since there was evidence of soil squeezing and also sinking of the tunnel due to extremely soft soil. In this option two bench pilot tunnels with a radius of 2.5 m were provided along the bottom side of the tunnel for rigidity and to stabilize the tunnel movement. The bench pilot tunnels were later filled with concrete. In bridge terms, these tunnels are similar to abutments in bridges (see Figure).

The seismic consideration for the tunnel was based on experience and judgement. The EPA of 0.4g was used in design, which corresponds to a return period of about 500 years. After the 1999 Kocaeli earthquake, an estimated ground shaking of about 0.2 to 0.25g was estimated at the site and the deformation rate in the clayey section of the tunnel increased from 3 mm/month to 5.5 mm/month. The deformation rate continues to be monitored although no plans are in progress to change liner design. There was no observed damage to the tunnel due to ground shaking with exception of a very shallow hairline cracks.

2- Viaduct 1

Viaduct 1 is also located about 125 km east of the epicenter. It consists of two parallel east-west sister bridges. The total number of spans in each direction is 30, which are simply-supported prestressed concrete box girders seated on elastomeric pot bearings. The maximum and minimum span lengths are 40 m and 29 m respectively. The bridge deck is continuous over a length of 3 to 4 spans. The piers are single, rectangular cast-in-place hollow core concrete columns with heights varying from 10 m to about 49 m. The pier foundation is supported by 1.8 m diameter friction piles. A shear key is provided between the adjacent boxes to inhibit transverse movement. The bridge also utilizes an Energy Dissipation System (EDS) which is installed on each pier cap to accommodate longitudinal thermal movements and to reduce any seismic forces through energy dissipation of the device during a





EDS System

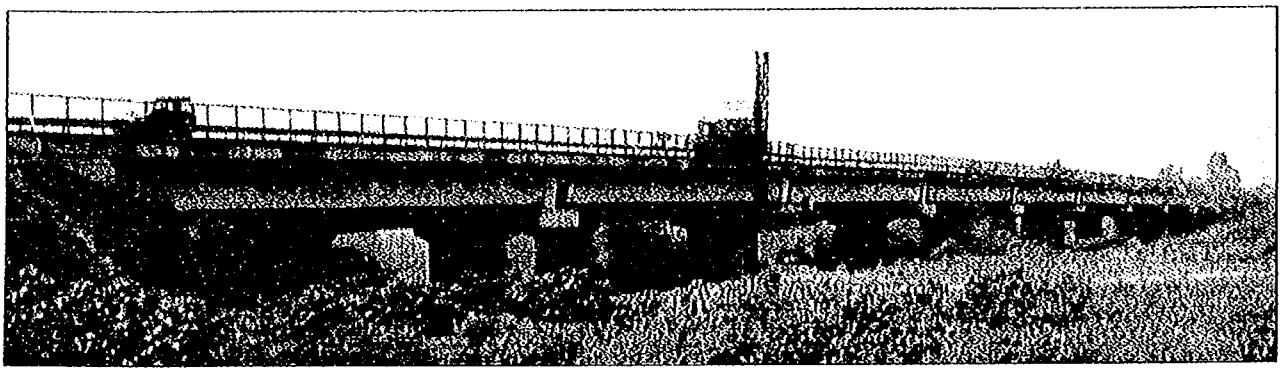
major event. Longitudinal cable restrainers are also provided for added protection at each expansion joint.

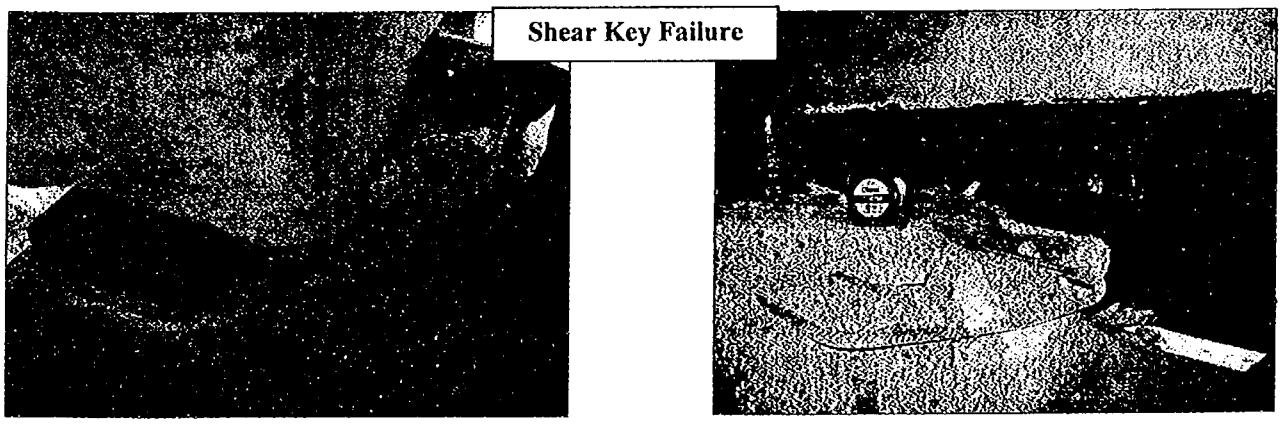
The viaduct was designed according to the 1992 AASHTO Standard Specifications for Highway Bridges and was coupled with the Euro code for the design of the EDS. The pier columns were detailed for ductile performance. However, the bridge was designed based on an elastic analysis and a force level equal to the yield force of the EDS. This provides additional seismic protection of the bridge through column hinging should a larger than expected earthquake occur.

During the Kocaeli earthquake, the EDS damping elements experienced movements of 45 to 80 mm. There was no damage observed to any bridge elements or the EDS.

3- Sakarya River Viaduct

The Sakarya River Viaduct is located less than 35 km east of the epicenter. It consists of two parallel east-west sister bridges which are founded on a soft clayey soil. The total number of spans in each direction is 10, all being simply-supported prestressed box concrete girders seated





on laminated elastomeric bearing pads with each span measuring 40 m. The superstructure deck is continuous over 2 to 3 spans. The piers are single rectangular cast-in-place concrete columns with heights varying from 4 m to about 6 m. The pier caps are inverted T-sections, which represents a common type of construction in Turkey. A shear key is set into the center of each box at piers and abutments to prevent transverse movement.

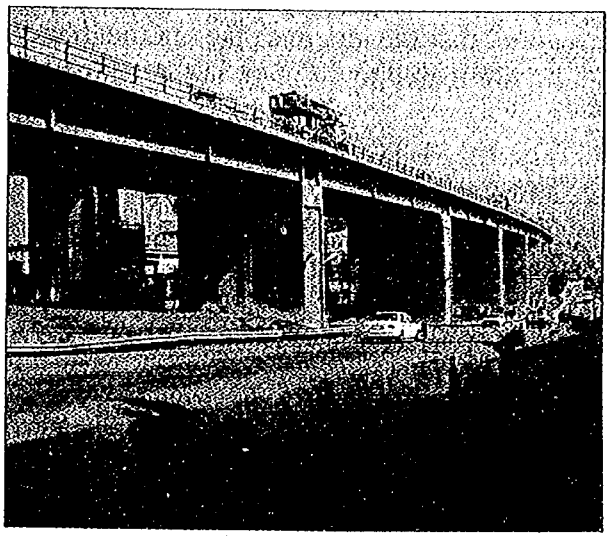
The viaduct was designed according to the seismic coefficient method of the1975 AASHTO Standard Specifications for Highway Bridges. During the earthquake, the viaduct experienced minor to moderate damage to the shear keys which resulted in the unseating of several spans from their bearings. This was much more severe for the westbound bridge and resulted in its closure. Perhaps this may be credited to the fact that the construction materials for the two sister bridges were not similar, according to KGM engineers.

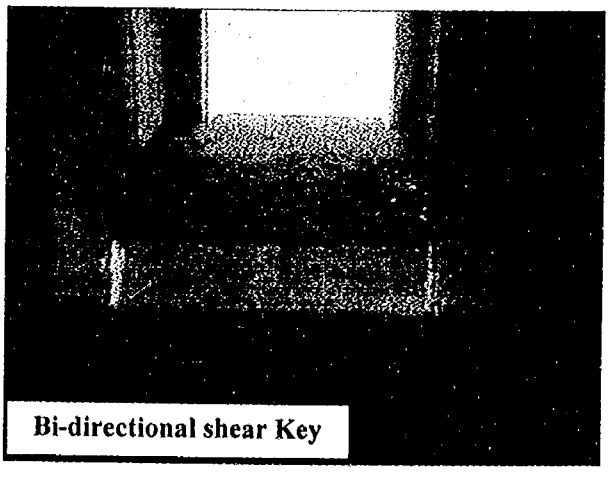
Also, the shear keys for both bridges were cast after the bridges were built and at different times by different contractors. Field observations revealed that the vertical reinforcement of shear keys for the westbound bridge were minimal, both in quantity and in length. However, the design plans showed that the detailing of the shear keys was considered sufficient according to current AASHTO Standards.

During the Kocaeli earthquake, there was also evidence of the collision of both superstructures (spaced 50 cm apart) due to sever shaking. The approach spans for both bridges had also settled roughly 5 cm.

4- Hereke Viaducts

The Hereke Viaducts are located less than 45 km west of the epicenter. They consist of two parallel east-west sister bridges with a total number of 19 spans in each direction. The superstructure is simply supported prestressed I beams seated on laminated elastomeric bearing pads with each span measuring 33 m. The piers are single, rectangular, cast-in-place concrete columns with heights varying from 8 m to about 16 m. Two bi-directional shear keys are provided at each pier cap between the girder ends to inhibit both transverse and longitudinal movements. A diaphragm is provided at the end of each span to tie the beams together and prevent possible collapse of the span in the transverse direction due to severe shaking. The bridge deck is continuous over 4 to 5 spans and it is appears that, at the expansion joints, there is insufficient seat width in the longitudinal direction.





Bi-directional shear Key

The viaduct was constructed in 1975 and its design was not according to AASHTO Standard Specifications for Highway Bridges. It appears that there was no damage observed due to Kocaeli earthquake.

Conclusions

- The FHWA team inspected more than 20 bridges and other facilities along the TEM. The soil condition at various sites was quite variable ranging from liquifiable to firm soil. This may have influenced ground response and damage distribution.

- One critical factor was the orientation of the fault parallel to the TEM and its nearness to the highway. That factor along with the high velocity impulses and large displacements caused two bridges to collapse and destroyed many buildings.

- Most of the bridge damage occurred when the reinforced concrete shear keys failed, permitting excessive transverse movement of the superstructure. The reinforcing cage in most keys was minimal, both in height and length.

- The use of diaphragms between the beam-ends was very beneficial in preventing the outside beams from falling off the support.

- The field observations revealed the need for a better design methodology for the approach slabs. At many bridges, their approach spans experienced significant settlement. It was also noted that the length of the approach span on many bridges in Turkey is quite short, about 1.5 m, compared to 3 to 5 m in the U.S.

- The AASHTO Standard Specifications for Highway Bridges has been applied to more recent TEM construction and in some cases mixed with the Euro Code to achieve seismic safety. The ductility of columns was considered and fully implemented in construction of a few bridges.

- In general, bridge performance on the TEM was acceptable during the Kocaeli earthquake.

DAMAGE TO TRANSPORTATION FACILITIES IN THE RECENT AUGUST 17, 1999 KOCAELI EARTHQUAKE IN TURKEY

Roy A. Imbsen[1]

Abstract

An earthquake having a magnitude MW 7.4 occurred in the western part of Turkey on August 17, 1999. Peak ground accelerations of approximately 0.4g were observed near the fault. These areas also experienced liquefaction and subsidence. This earthquake caused major damage to housing and industrial facilities; resulting in over 30,000 deaths and monetary losses of approximately 16 billion USD. The losses to the transportation system were minor compared to these losses. This paper describes transportation facilities' damage and outlines some recommendations which would minimize damage in a similar future earthquake.

Introduction

On August 17, 1999, an earthquake having a magnitude MW 7.4 struck the province of Kocaeli in Western Turkey at 3:02 a.m. local time. The epicenter was located southwest of the City of Izmit, less that 80 km southeast of Istanbul. The earthquake occurred on a branch of the North Anatolian Fault. This fault system is considered one of the most seismically active right-lateral strike-slip faults in the world. This segment of the North Anatolian fault was previously identified as having a high probability of producing a damaging earthquake (Toksoz, Shakal and Michael, 1979; Stein, Barka and Dieterich, 1997).

Surface faulting caused the collapse of the overpass at Artifye, as shown in Figure 1, and caused pavement damage at several locations to E80, Trans European Motorway (TEM), as shown in Figure 2. Although surface faulting caused major damage to buildings, industrial facilities and ports, the damage to transportation facilities was less significant.

A summary of the damages to transportation facilities is shown in Figure 3. The total estimated cost of this damage is approximately $200 million USD. Shown in Figure 4 is a summary of the measured maximum ground accelerations. The measured accelerations depicted on the map are somewhat less than might be anticipated from a magnitude 7.4 earthquake with a fault rupture length of 160 km. More recent information by Erdik suggests that four or five earthquakes occurred with magnitudes between 5.1 and 7.0, which explains the lower accelerations than those anticipated with a magnitude 7.4 earthquake. In part, this also explains why the amount of bridge damage suffered due to vibration effects was somewhat less than anticipated for a magnitude 7.4 earthquake. Damage to transportation facilities was restricted south-southeast of Sakarya (Adapazari), as shown on the map included in Figure 3. Also shown on the map in the effected area are the two main highways that run east-west parallel to the Anatolian Fault system. The TEM, E80, parallels the old main highway, E100, in the effected region. The TEM goes south to Ankara beyond the effected area and the old highway continues in the easterly direction.

[1] President, Imbsen & Associates, Inc., Sacramento, CA

Earthquake Damage Categories for Transportation Facilities

The levels of damage defined by Caltrans, as shown in Table 1, is used to rate the level of damage suffered to various transportation facilities, as described below. It should be noted that the types of bridges built in Turkey, particularly on the TEM, are somewhat different than those built in California and other parts of the world where transportation facilities have suffered significant damage in recent earthquakes.

Considering the relatively low level of damage to transportation facilities and the high magnitude of this earthquake, it may be concluded that the ground motion on the bridges for this earthquake was somewhat lower than anticipated, or that the bridges were designed in accordance with modern seismic design practices, and/or had some inherent seismic resistance. Although there are some unresolved issues or speculations on the low level of damage, it may be of some value to apply the damage categories used by Caltrans to these bridges.

Typical Bridge Types used on the TEM in Turkey

In Turkey, the majority of the TEM bridges are simply supported precast trough-shaped girders (see Figures 5 and 10) with maximum span lengths of approximately 40 meters. The precast girders are cast composite with the deck and are generally cast continuous over several spans. This articulation reduces the number of deck joints and provides added longitudinal and transverse restraint for the seismic motions.

Additionally, intermediate and end diaphragms are used to provide additional torsional and transverse rigidity to the superstructure. In some cases, the diaphragms are post-tensioned to provide additional transverse connectivity between the individual girders. Elastomeric bearings are placed on rather massive piers to support the individual simply-supported girders at the substructure-superstructure interface. Shear keys are used to provide longitudinal and/or transverse restraint at this interface. Shear keys' designs vary from bridge to bridge, providing what might be considered qualitatively adequate to inadequate restraint.

Damage to the Bridge at Artifye

The bridge at Artifye did collapse, as mentioned above, due to faulting. This bridge failure resulted in the deaths of 10 people in the bus that collided with the collapsing span. This bridge would be in a damage Category 4, as described in Table 1. The right lateral fault movement, as shown in the schematic included in Figure 5, increased the span length and pulled the spans tied together with the concrete deck toward the fault rupture. In so doing, it dragged the remaining three spans off of their seats, as shown in the Elevation View. Shown in the Plan View is an initial guess of the fault location at the bridge site. Actual trace of the faulting is depicted in Figure 6. The shear keys at the abutment in the span where the faulting occurred were undamaged, indicating that the abutment support was pulled away from the superstructure due to the increase in span length. The superstructure of this bridge is composed of four spans of the precast members, as described above, with a continuous deck extending from abutment to abutment.

Damage to the Reinforced Earth Embankment at Artifye

The reinforced earth embankment (REM) at the North Abutment suffered some minor damage, as shown in Figure 7. This is primarily due to soil compaction around a culvert which is beneath the embankment, as shown in Figure 8. The damage level of the REM would be Category 2 since it is unlikely that these repairs could be made as part of regular maintenance. This is the first test of a REM in an earthquake. Considering its close proximity to the fault, the REM performed well with minimal damage.

Damage to the Sakarya River Bridge

The Sakarya River Bridge, shown in Figures 9 and 10, suffered damage resulting in the closure of the westbound bridge. This bridge would be classified as Category 2, while the eastbound bridge would be Category 1 with minor damage; the eastbound bridge remained in service. However, the bridge should be repaired prior to a routine maintenance repair. The primary reason for the failures here are inadequate shear keys. The keys did not provide much resistance because they did not have much capacity and were only partially engaged with limited contact surface between the shear key and the girder.

Damage to the TEM Roadway

Damage to the E80 was caused by surface rupturing, settlement of engineered roadway fills and the settlement of bridge and culvert approaches (see Figure 3). The extent of damage to the engineered fills on the E80 Motorway extended some 50 km to the west and 50 km to the east of the Sakarya area. Settlements ranging from 100 mm to 500 mm were observed, as shown in Figure 6. This damage initially hampered the movement of emergency services equipment and supplies.

Repair of the damage was accomplished quickly in two stages. The first stage consisted of removing damaged portions of the pavement, grading and asphalt patching. This stage was completed within the first few days following the earthquake. A 50 km/hr speed restriction was imposed. The second stage included resurfacing a 50 km section of the motorway. This work was completed within 18 days following the earthquake and traffic is now operating normally, at a speed of 120 km/hr. Failure of the shear keys resulted in the relative bridge displacements, as shown in Figure 11.

Minor damage to other transportation facilities, as indicated in Figure 1, has had a minimal effect on traffic. Two long viaducts near Köreez and Düzce were undamaged. The undamaged viaduct near Düzce had been outfitted with energy dissipation devices. Initial inspections indicate that seismic movements were arrested by the energy dissipation devices.

Recommendations

The following short-term recommendations are based on the field observation and conversations held with Turkish Bridge Engineers:

- Inspect and retrofit all bridges that are designed with shear keys similar to those used on the Sakarya Viaduct.
- Implement a seismic design training program for Turkish Bridge Engineers.

- Designate post-earthquake investigation teams:
  - damage assessment; and,
  - emergency repair.
- Develop a cooperative exchange program with other developing countries that have similar seismic hazards and transportation needs.

The following recommendations are for the long-term and are specific to the TEM in Turkey. These recommendations could, however, be considered by other countries on the TEM with anticipated seismic activity.

- Develop a seismic design specification specifically for the Motorway which includes all the latest technology:
  - applicable to the types of bridges built on TEM; and,
  - uniform philosophy having consistent hazard and performance goals.
- Inventory all the Motorway facilities and evaluate their seismic resistance in accordance with the newly developed specifications.
- Develop retrofitting guidelines with a philosophy consistent with the developed specification for new construction on TEM.
- Conduct a preliminary screening of the existing inventory and prioritize retrofit needs.
- Evaluate seismic resistance in accordance with the newly developed guidelines.
- Perform retrofit detailed design.
- Develop a program to retrofit or include in a maintenance program, as resources become available.

Conclusions

The TEM in Turkey is a new transportation facility and is a vital part of the transportation network in Turkey and the surrounding countries in Europe and Asia, as indicated in Table 2. The system was festered in the recent Kocaeli earthquake and suffered only minor damage, as compared to other recent earthquakes. It is important to recognize that there is a substantial investment in this network and there is a large inventory of bridges which are vulnerable to damage in future earthquakes. A word of caution: the level of damage suffered in the Kocaeli should not be considered as a true test of the system's resistance to future earthquakes, because of the lower level of acceleration. Large earthquakes are anticipated in the Istanbul area where the population is more concentrated and there are fewer redundant routes. There are many older viaducts in this area which should be evaluated and upgraded with seismic retrofitting when needed.

Table 1: Earthquake Bridge Damage Level Categories (Caltrans*)

Category	Description	Functionality
No Damage "0"	No notable damage. Evidence of movement may be present.	No loss of functionality.
Minor Damage "1"	Some visible signs of damage. Repairs can be made under regularly scheduled maintenance program (except for deck joints).	Little or no loss of functionality.
Moderate Damage "2"	Visible and significant signs of damage. Repairs or stabilization likely to be completed under emergency traffic.	Some loss of functionality.
Major Damage "3"	Life safety is threatened under service loads: emergency repairs, stabilization, or replacement required.	Considerable to total loss of functionality.
Collapse "4"	Superstructure is off of supports or supports have failed.	Total loss of functionality.

*The California Department of Transportation

Table 2: International and Domestic Usage of Trans European Motorway

Shipping	Quantity (ton-km)	Percent of Total	Means
International	518.0	76.6	Highway
Domestic	139.8	20.7	Highway
	9.3	1.4	Railway
	8.4	1.2	Sea

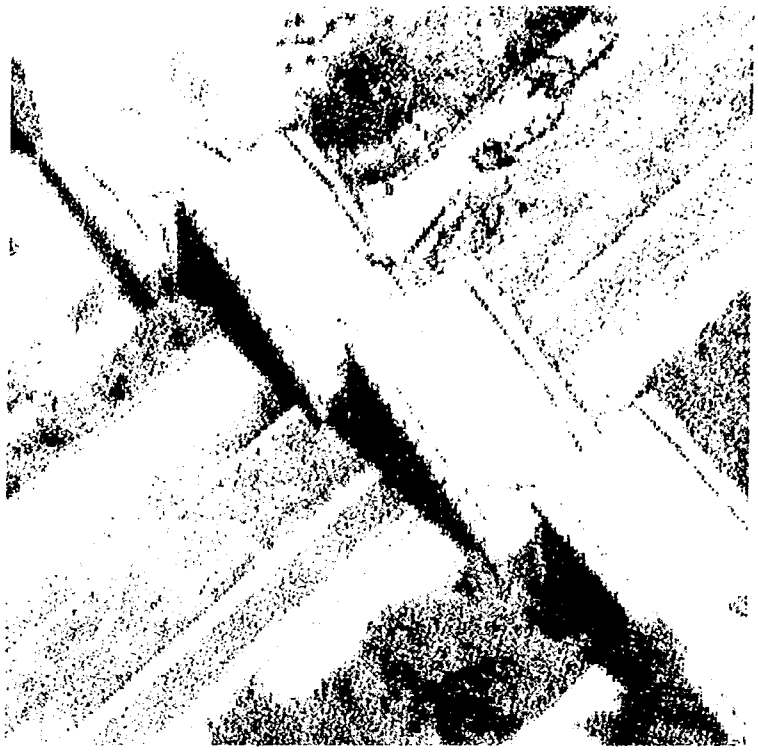


Figure 1: Bridge Collapse of Artifye due to Surface Faulting

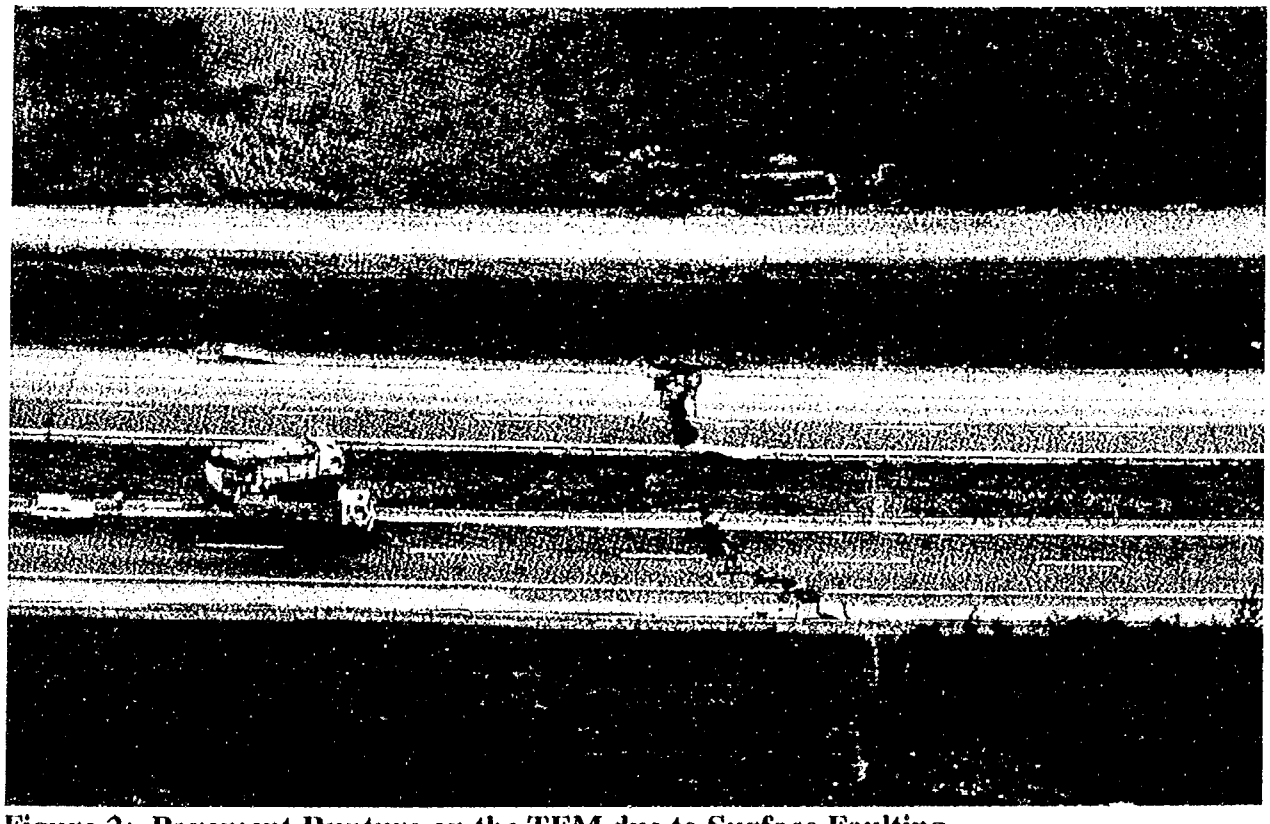


Figure 2: Pavement Rupture on the TEM due to Surface Faulting

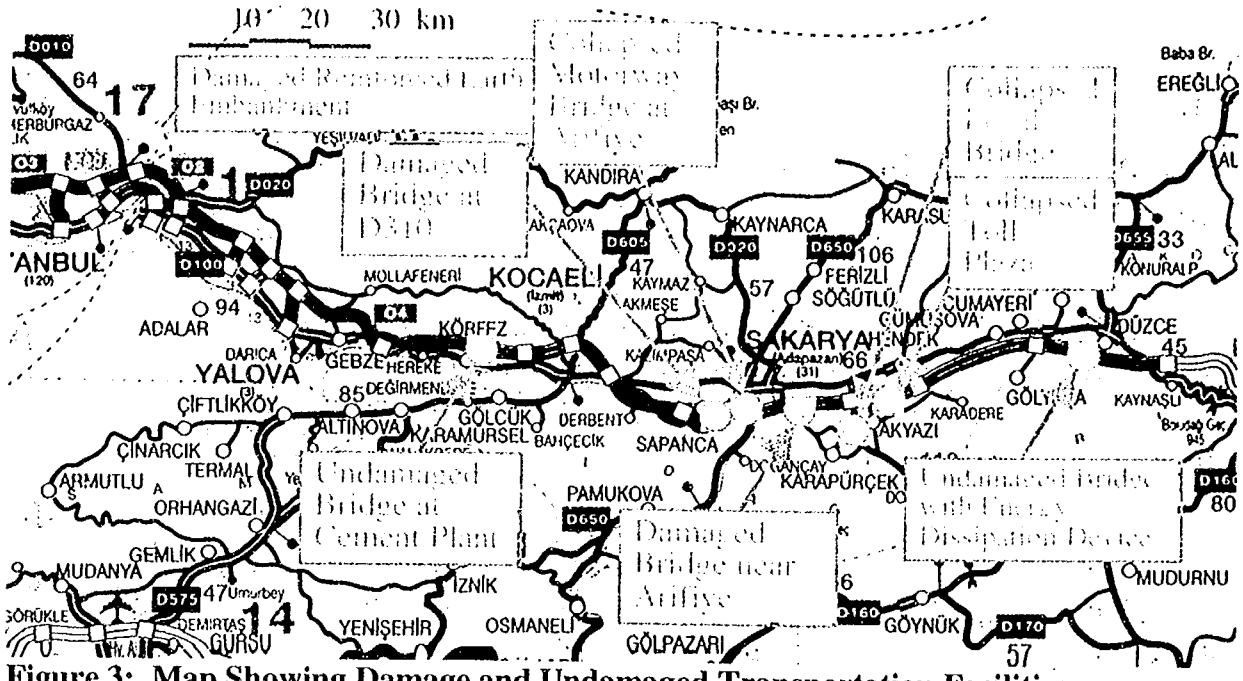


Figure 3: Map Showing Damage and Undamaged Transportation Facilities

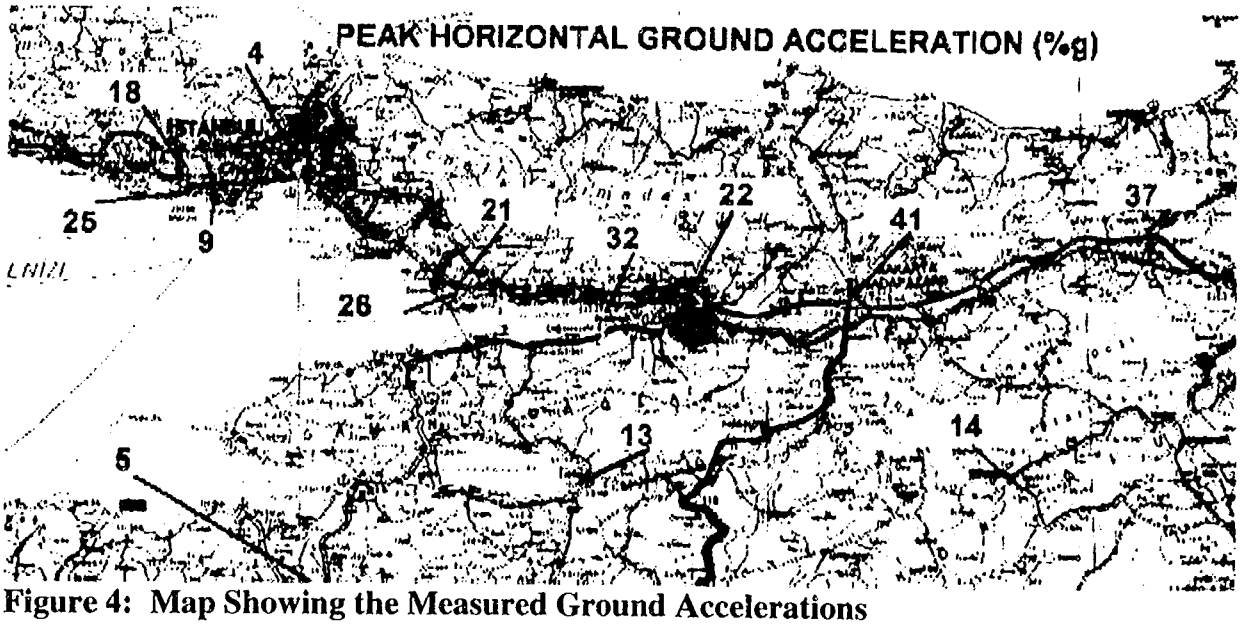


Figure 4: Map Showing the Measured Ground Accelerations

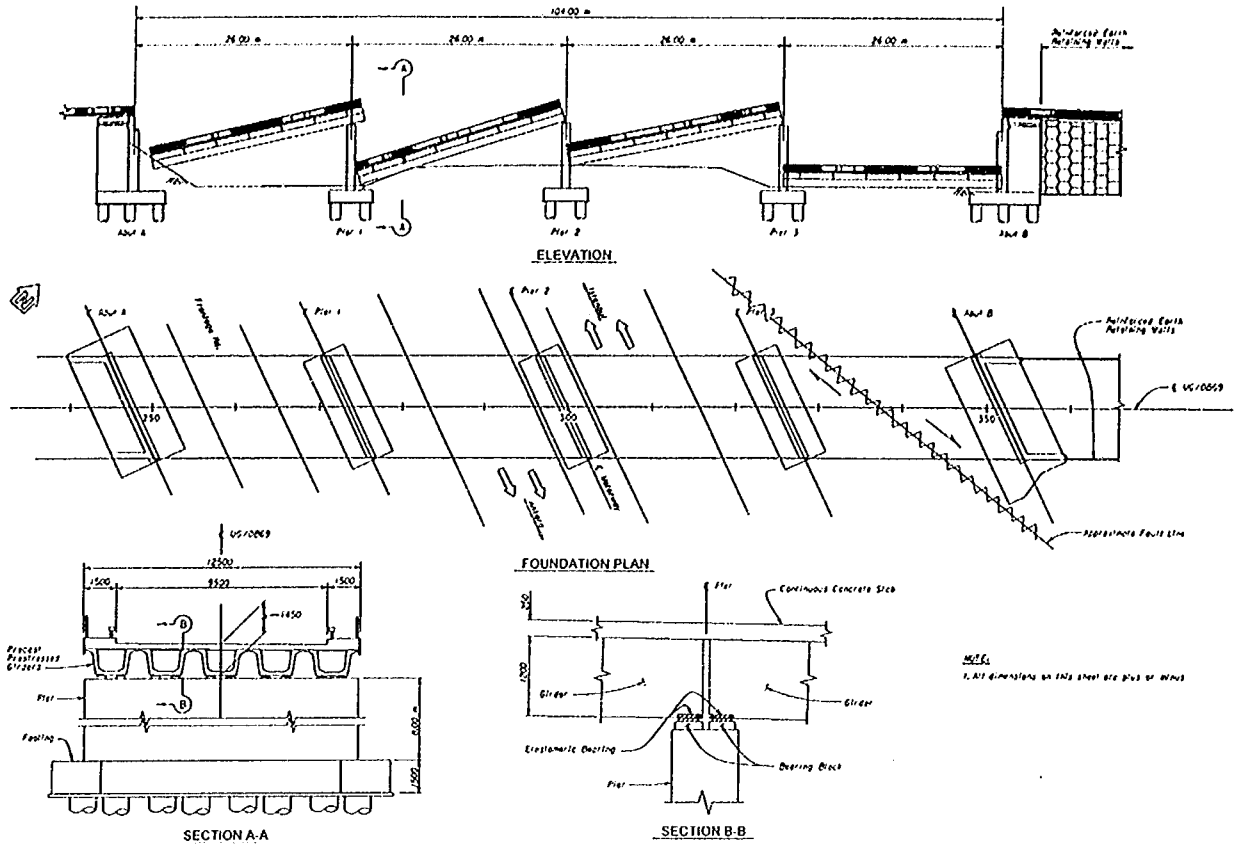


Figure 5: Schematic Showing the Collapsed Bridge of Artifye, Fault Movement and Elongated Span Length

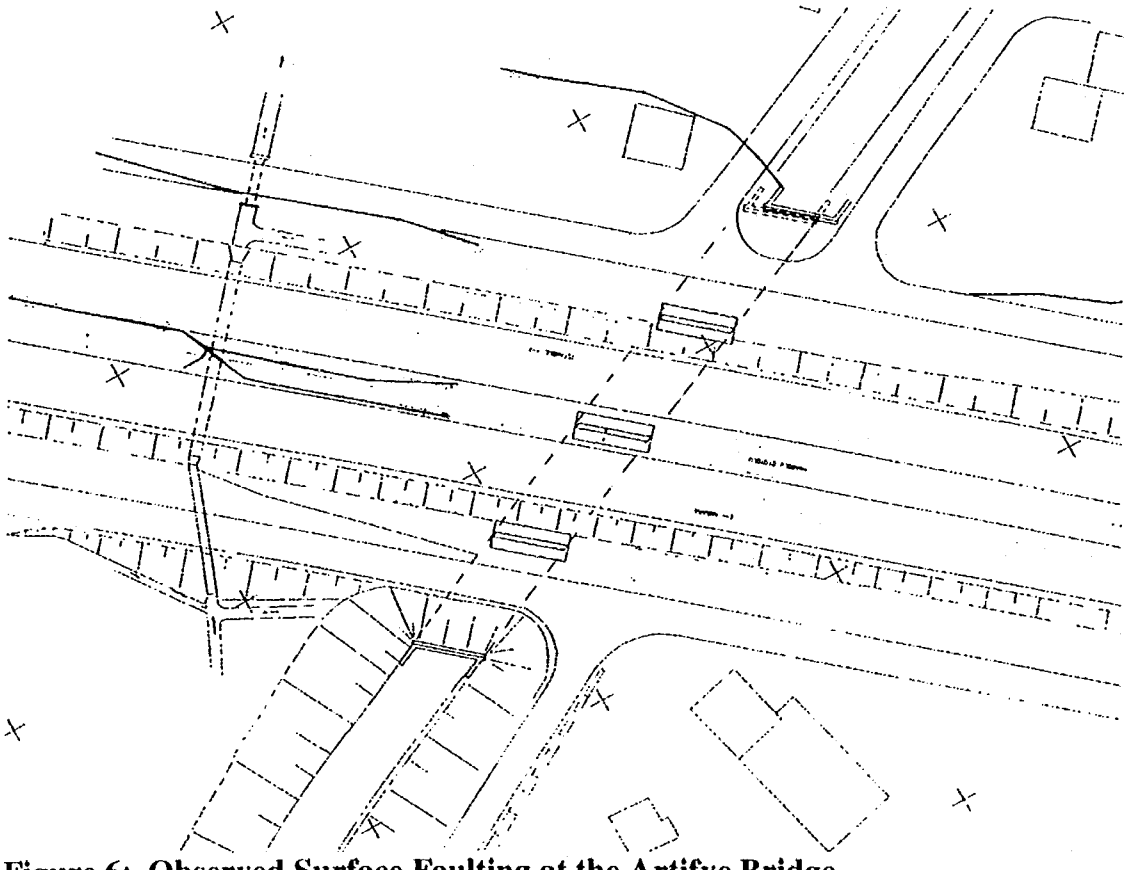


Figure 6: Observed Surface Faulting at the Artifye Bridge

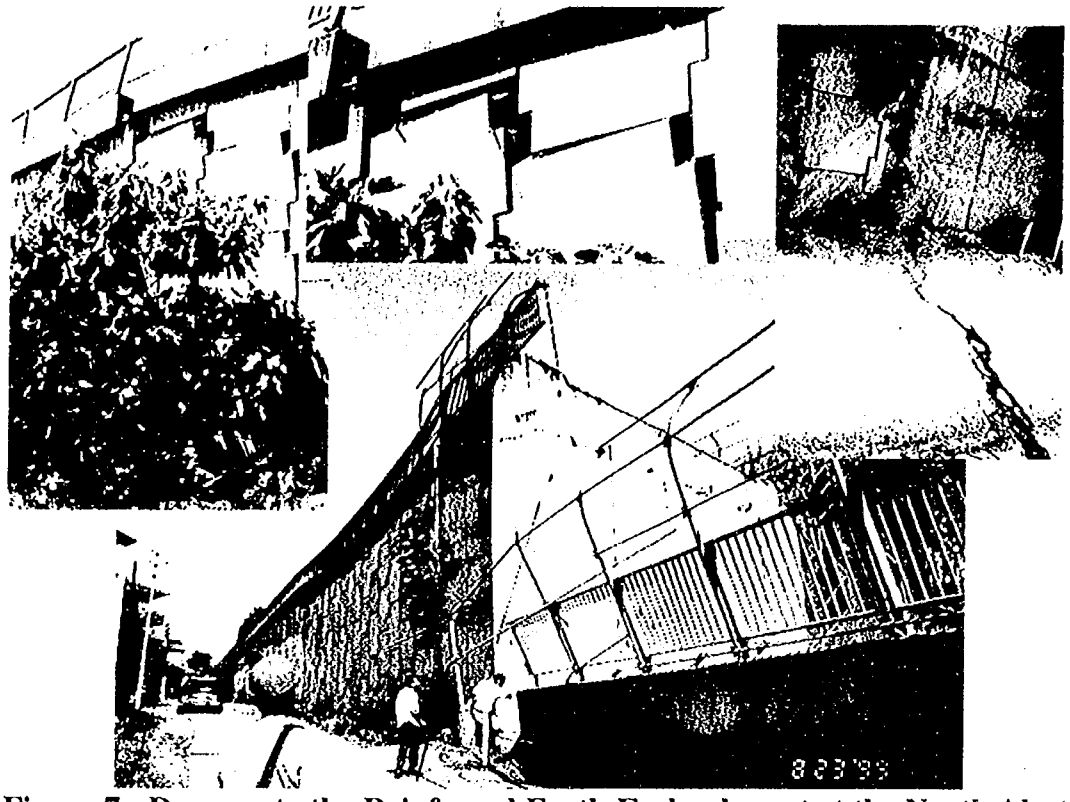


Figure 7: Damage to the Reinforced Earth Embankment at the North Abutment of the Bridge at Artifye

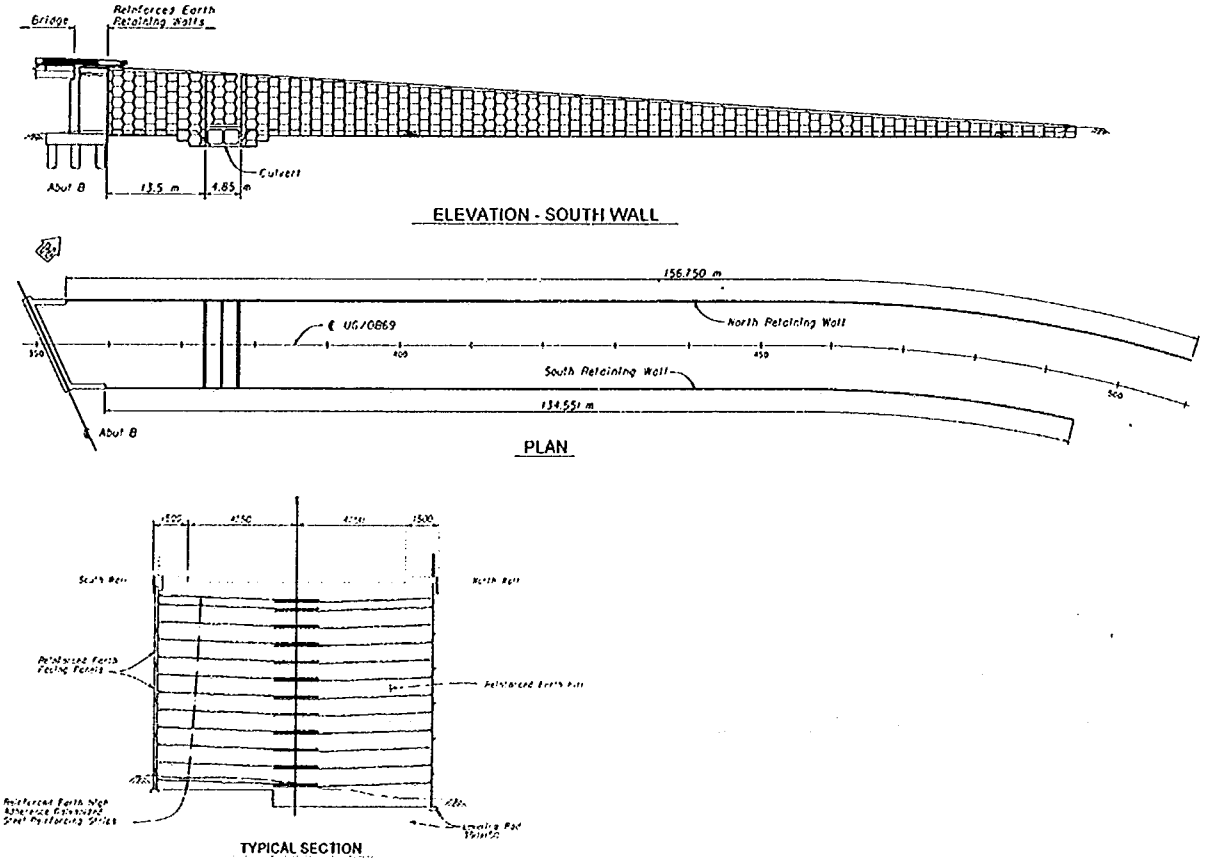
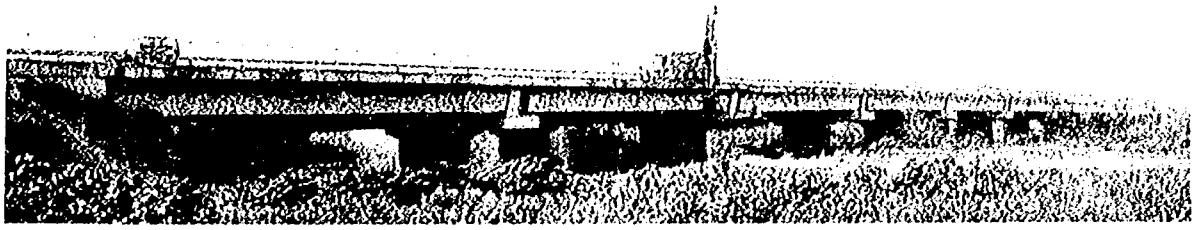


Figure 8: Sketch of the RE Embankment Elevation and Cross Section



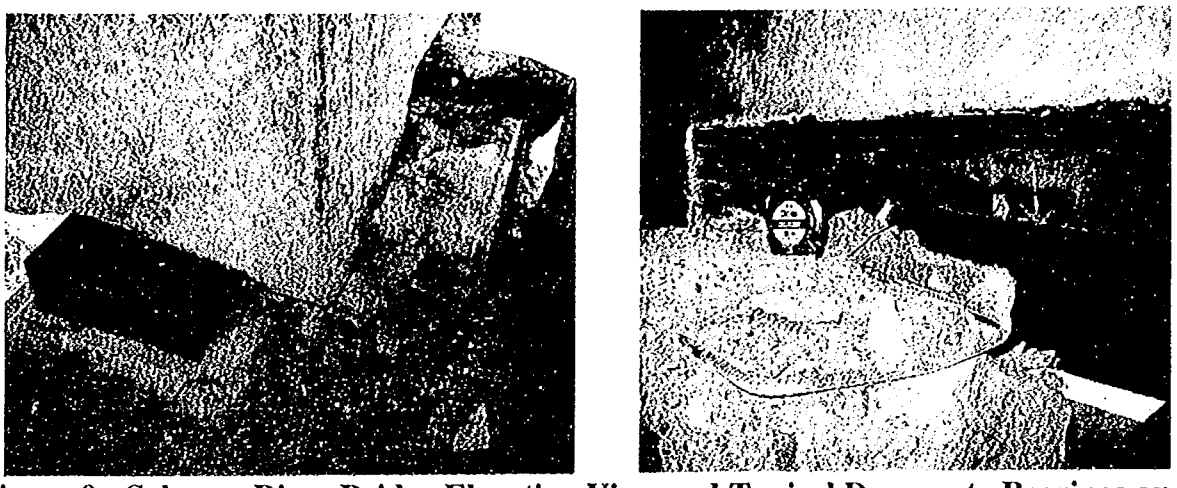


Figure 9: Sakarya River Bridge Elevation View and Typical Damage to Bearings and Shear Keys

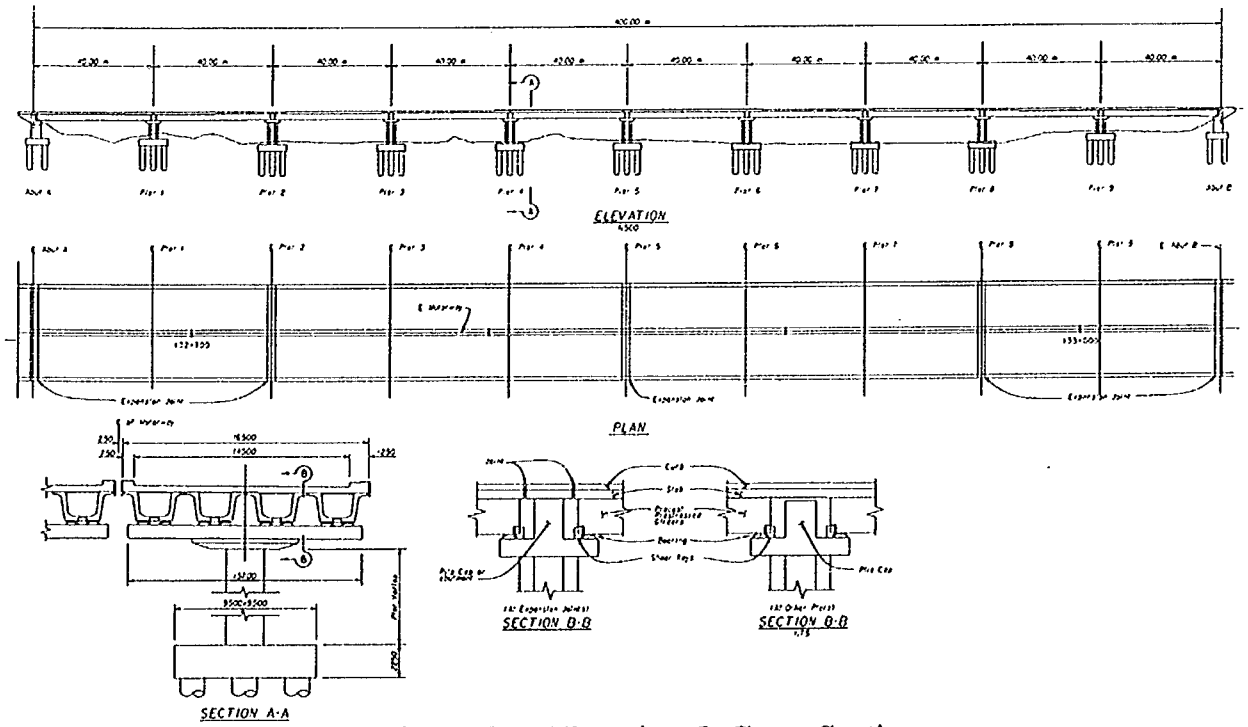


Figure 10: Sakarya River Bridge Plan, Elevation & Cross Section

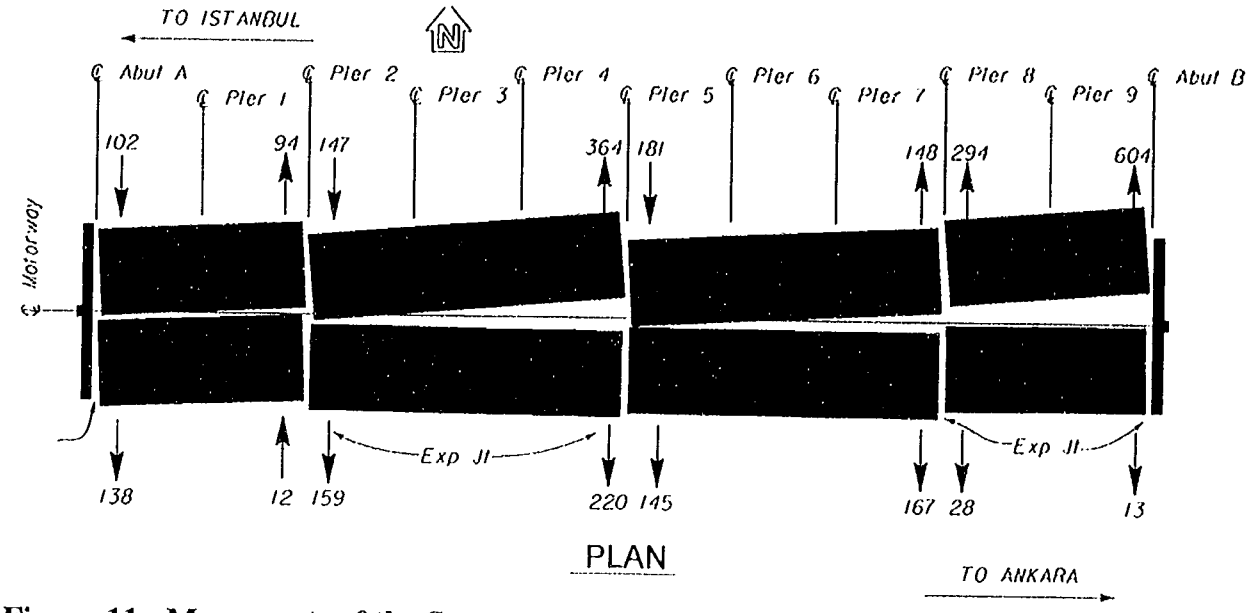


Figure 11: Movements of the Spans

THE TURKEY EARTHQUAKE – AUGUST 17, 1999
DAMAGE TO THE TRANSPORTAITON INFRASTRUCTURE

By

John B. Mander

Department of Civil, Structural and Environmental Engineering
State University of New York at Buffalo

1. INTRODUCTION

This paper discusses damage sustained by the transportation infrastructure as a result of the Kocaeli Earthquake in Turkey on August 17, 1999. Damage to both highway, railway and port facilities is described. Figure 1 shows a general map of the area. It will be noted that the prevailing traffic direction is generally east-west with secondary roads to outlying villages running in the north-south direction. Most of the damage was sustained along this east-west corridor. Perhaps this is not surprising as both the highway and railway systems run parallel to the fault rupture.

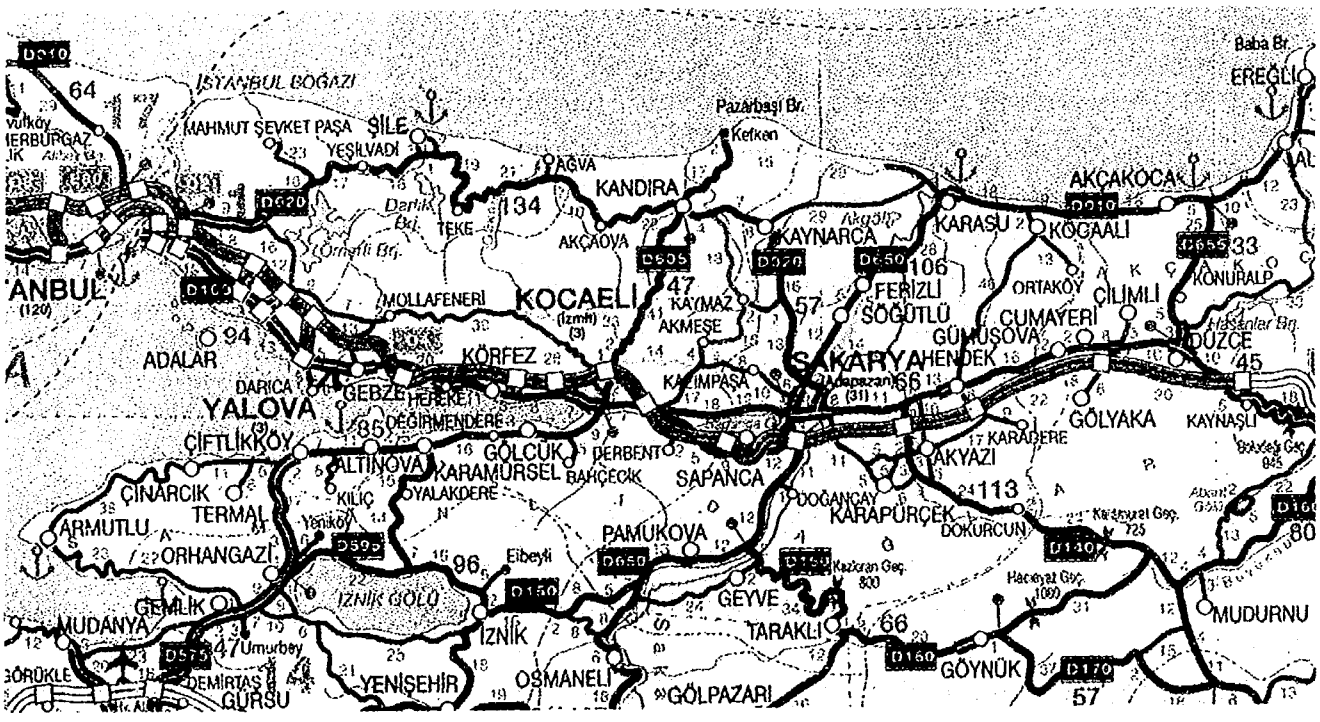


Fig. 1. Site map. Note earthquake damage extended from the city of Yalova in the west to Duzce in the east. Much of the human fatalities were located in a band from Yalova to Golcuk. Many of the soft soil sites were located in the Sakarya area (Adapazari).

2. DAMAGE TO THE HIGHWAY BRIDGES

This earthquake led to the collapse of only two bridges. It should be emphasized, however, that in both cases, the fault rupture passed directly beneath each bridge.

Collapse of the D650 E-80 Motorway Overpass

Figure 2 presents an aerial view of this overpass bridge that collapsed. This bridge structure consisted of bathtub style pre-cast concrete box beams with a cast in situ slab, each span being 26.0 m in length. The spans were simply supported for dead load, and as a result of the continuity provided by the deck, essentially continuous for live load. The piers were skewed 20°. During the earthquake, the fault rupture propagated between the third pier and the northern abutment, as seen in the top left-hand corner of figure 2. As the seat widths for the north span were insufficient to sustain the large (> 1.5 m) right-lateral offset movements, it unseated and fell from its support. In so falling, the fourth span, via deck continuity, also dragged the other three spans off their seats. Direct support to the soffit of the girders (south end of each girder) was lost—the deck slab possessed insufficient strength to carry the tributary weight of the span, and as a result, failed in shear. Consequently, as shown in figure 2, the south end of each span fell off its seat and came to rest on the ground. Unfortunately while falling off the seat, the third span (between piers 2 and 3) collapsed onto a passing bus killing ten people.

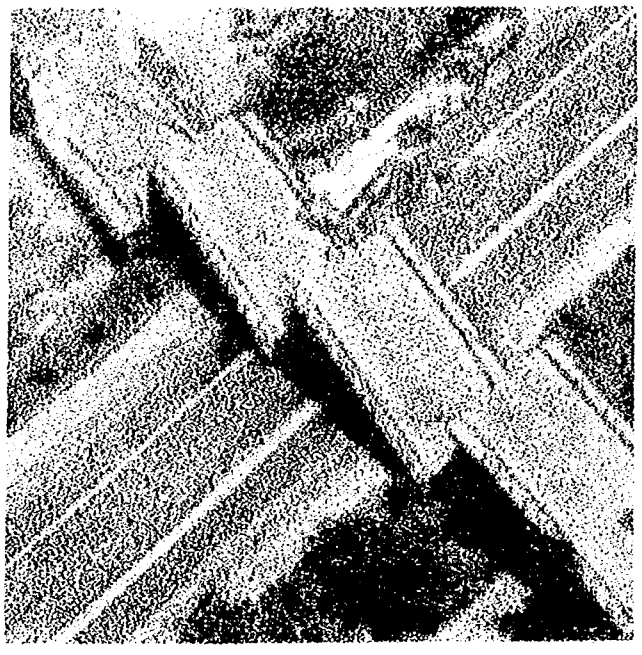


Fig. 2. Collapse of the Motorway overpass that carries the D650 road over the E80—the Trans European Motorway (TEM).

It is of interest to comment on the restoration of the highway as a result of the collapse of this bridge. Heavy earthmoving machinery was brought to this site soon after the earthquake occurred and the bridge was cleared away. This was undertaken with several hydraulic excavators each using concrete breaker attachments. Initially the central two spans were removed to enable the reopening of the E80 Motorway. Within four days of the earthquake,

practically all of the bridges had been demolished and the debris removed. Because the E80 Motorway is a toll road, vehicles that normally use this overpass were required to undertake a 3 km detour.

For this particular bridge, it is considered that little could have been done to avoid such a failure, other than dramatically increasing the seat width. This is because during the design process, it is not possible to assess whether a bridge will be directly within the zone of fault rupture. Moreover, the orientation as well as the magnitude of the movements can not be ascertained. About the only design improvement that should have been made in this structure would be to ensure full continuity is provided for dead loads as well as live loads. In this way, perhaps only one span would have collapsed with the fault passed directly beneath that span. As an alternative to providing continuity, cable restrainers that have the ability to restrain at least 50% of the weight of a span could be provided. This would stop the span from falling.

A Collapsed Local River Bridge Near Akyazi

Approximately 8 km east of the above-mentioned bridge was a bridge that collapsed into a river near the town of Akyazi. Little is known about the owner or details of this structure. The bridge was a three-span steel girder with concrete slab deck. The piers consisted of a relatively lightweight steel frame located on both banks of the river. Evidently the piers had insufficient axial capacity to sustain the ground shaking and permanent ground displacement as a result of the fault rupture. Both piers failed by what appears to be axial compression failure of the steel columns in the pier bents. It should be noted that near this facility the critical ground motions were in the order of at least 0.4g. Although only a minor road, the bridge provided the only access to two small villages. As a result of the bridge collapse, the people in those villages were inaccessible. It appears that failure of this bridge could have been prevented if the piers were of a more substantial nature and more capable of carrying the height vertical loads. Nevertheless, it is not surprising that the bridge failed as the fault rupture passed through the northern abutment.



Fig. 3. A local river crossing near the town of Akayazi.

Damage to the E80 Motorway Bridges over the Sakarya River

Figure 4 presents an elevation view of the twin highway bridges carrying the E80 Motorway across the Sakarya River. Both of these bridges are essentially identical and consist of ten 40.0 m spans. Each span is constructed from four pre-cast, prestressed (bathtub) girders with a reinforced concrete deck slab. The bathtub girders are seated on elastomoeric bearing pads with the deck slab continuous over every second support. In this way, the spans are designed to act as pairs with expansion joints located at every second pier (figure 5). Each girder is seated on two bearing pads and between each bearing pad is a shear key that is intended to inhibit transverse movement of the girders relative to the axis of the bridge. The bridge piers consist of rectangular sections that are quite stiff, as shown in figures 5 and 7.

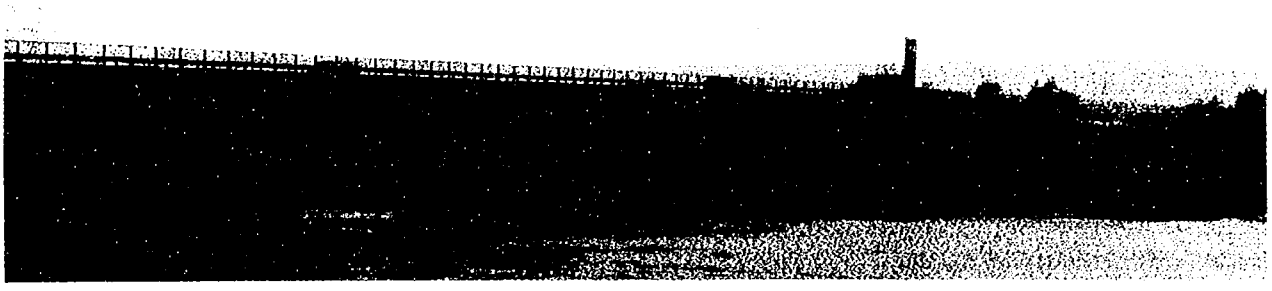


Fig. 4. A view looking south showing the side elevation of the twin E80 Motorway bridge over the Sakarya River.

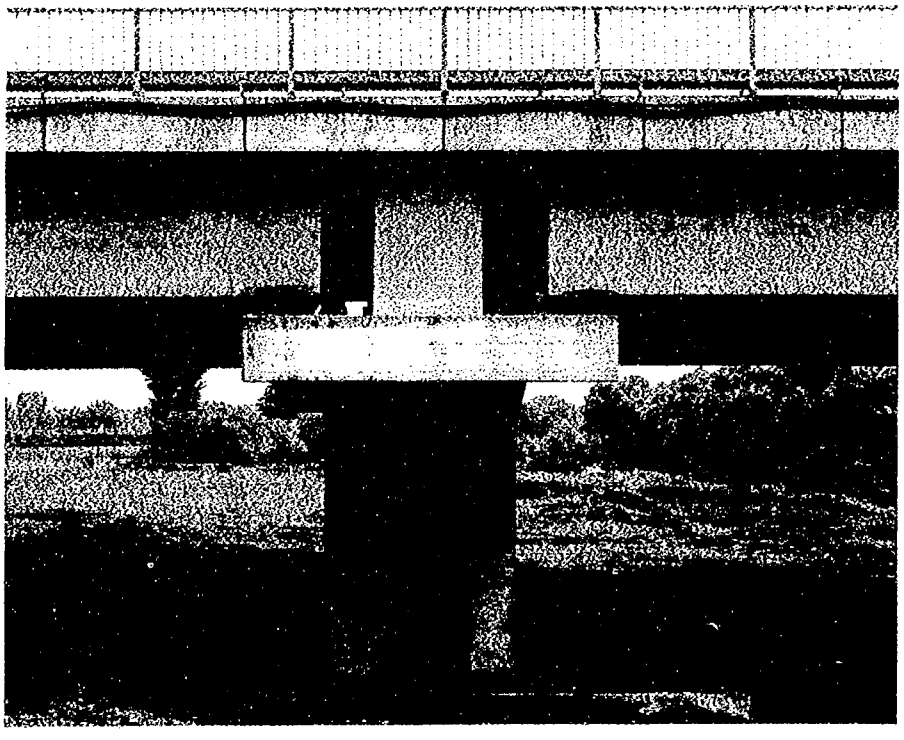


Fig. 5. A side elevation of one of the pier of the north-bound E80 Motorway bride over the Sakarya River. Note the concrete rubble located between the span ends and the diaphragm upstand.

As a result of the earthquake, a moderate degree of damage was sustained by these bridges, particularly the northern-most structure that carries the west-bound traffic. In several cases, the girders shifted off their seats by some 500 mm as shown in the abutment view of figure 6. The cause of this movement is a result failure of the shear keys. Site inspection showed that the dowel bars protruding above the pile cap had insufficient height and movement from the spans load to a failure in the cover concrete of shear keys. It appears that the construction of the shear keys was erratic because most of the shear key in the east-bound bridge survived with little damage.

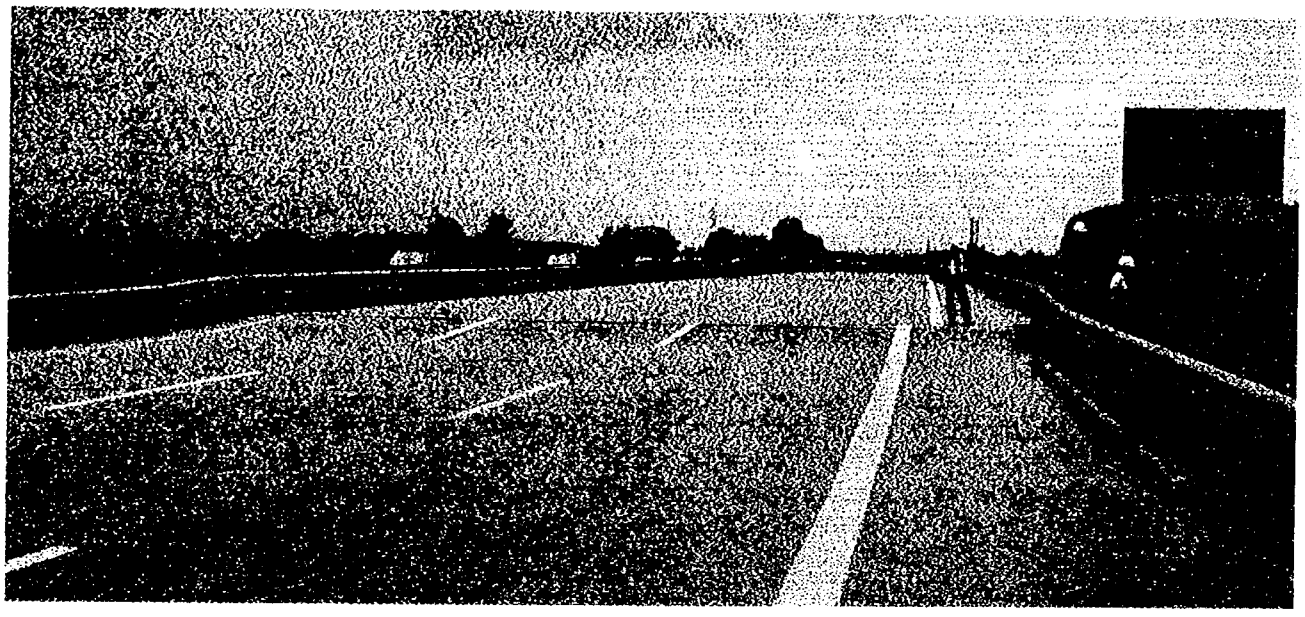


Fig. 6. The east abutment of the east-bound E80 Motorway bridge showing the 500 mm offset of the span with respect to the approach road.

Figure 7 shows a photographic view of the two bridges. On the east-bound bridge, the elastomeric bearing pads have started to "walk-out", but were still supporting the spans. However, for the west-bound bridge, the spans shifted their seating onto the shear key, many of the bearing pads being nonfunctional.

It is apparent that much of the damage to these bridges could have been avoided by providing more efficient and robust shear keys. Perhaps better still, much of the damage could have been entirely avoided if full continuity between the spans had been provided. Fortunately, the damage sustained by the east-bound bridge was insufficient to warrant closure. Immediately flowing the earthquake, the west-bound traffic was rerouted over the east-bound bridge. The west-bound bridge was considered to be sufficiently damaged to warrant closure to enable the spans to be reseated. However, due to the significant weight of these spans, this task could not be performed quickly.

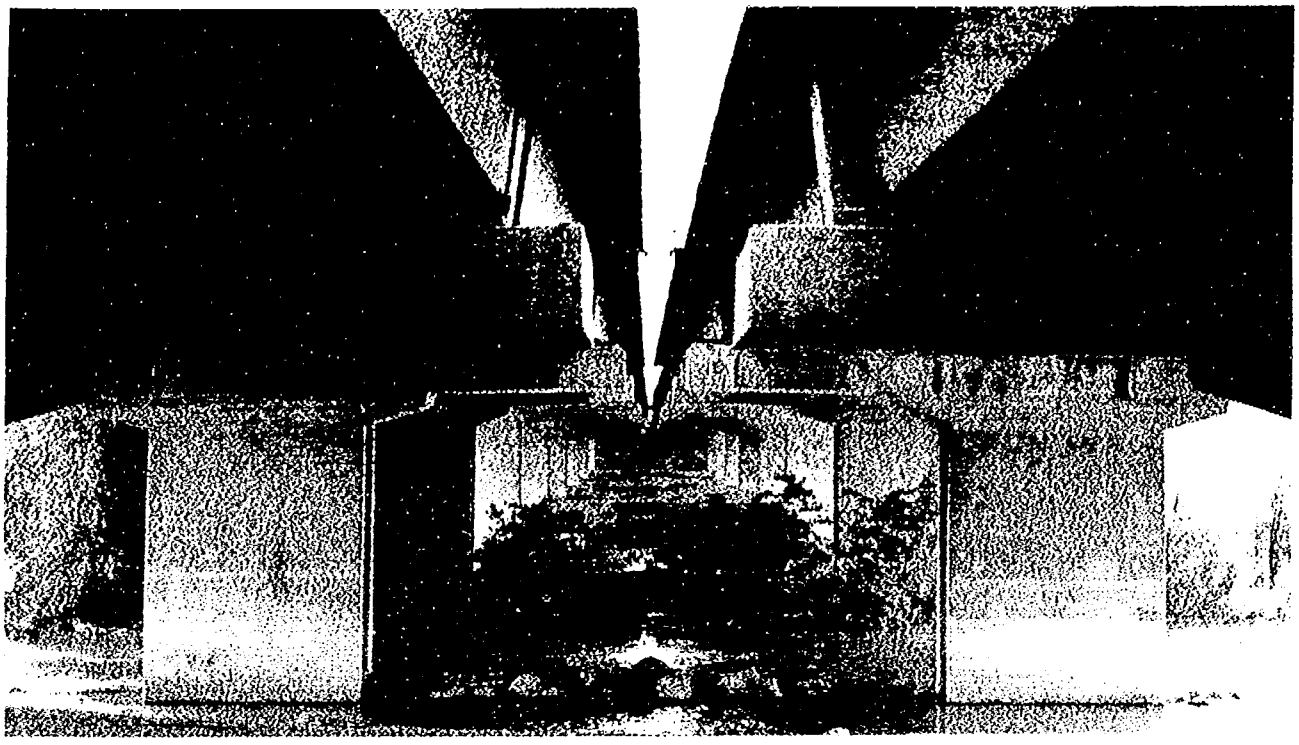


Fig. 7. A longitudinal view of the twin E80 bridges crossing the Sakarya River. The left bridge is the east-bound structure that showed minimal effect on the bearing seats, whereas the west-bound bridge (on the right) showed considerable damage to the shear keys and bearing seats. Note the dislodged bearing and the 500 mm right lateral offset of the girder directly above the right hand pier.

Damage to the D310 Overpass that Crosses the E80 Motorway

This bridge is typical of the overpasses that cross the E80 Motorway. It consists of five spans, each span having pre-cast, prestressed concrete beams with a cast in situ deck slab. There are expansion joints at each abutment and at the second pier (when viewed from the south abutment). The bridge was located 500 m within the fault rupture and oriented normal to the fault. It appears that fault-parallel ground shaking caused substantial movement of the deck segments resulting in some minor damage to the outside faces of the prestressed concrete girders. It is evident that the ground shaking caused a deck-pier mechanism to occur as shown in figure 8. In addition to this damage resulting from fault parallel shaking, there is some evidence of pier tilting due to foundational settlement of the above-mentioned second pier. It is not clear whether this pier tilting has resulted from fault-normal shaking or is an outcome of the deck pier mechanism. This feature requires further analysis.

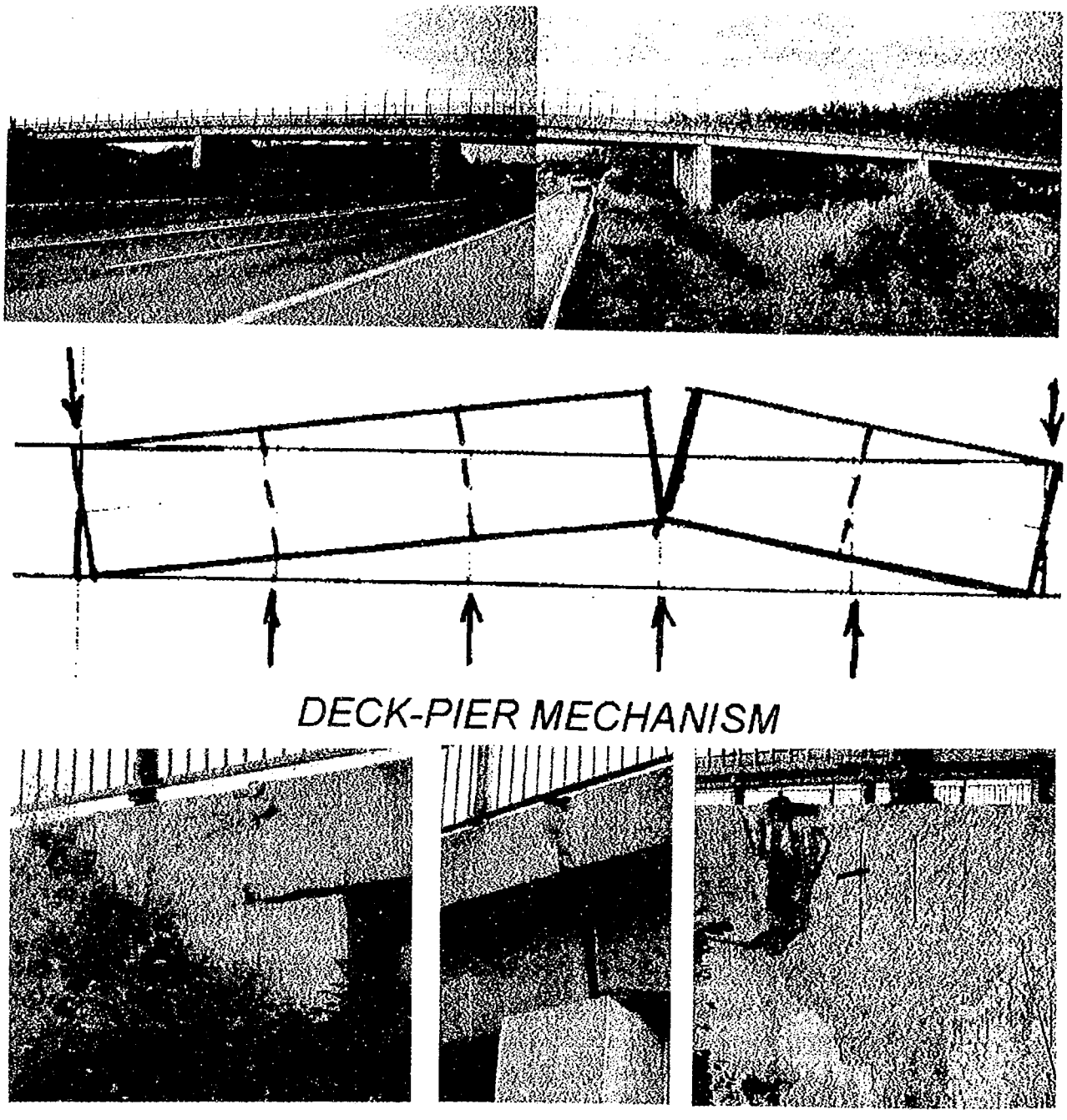


Fig. 8. The overpass carrying the D310 road across the E80 Motorway. The upper photograph shows a side elevation of the bridge looking eastward. In the center, a plan view sketch depicts the deck-pier mechanism that formed at the location of the joints that were located at the abutments and third pier. The lower photograph shows spalled concrete damage located at the deck at these joint connections.

Damage to Bridges on the D100 Highway

Some 2 km downstream, in a northerly direction from the above-mentioned twin bridge over the Sakarya River are another two bridges on the D100 highway. One of these bridges is quite old and carries the original two-lanes of this highway, while the other bridge, at the time of the earthquake, was under construction, with construction almost completed. Both of these bridges sustained a minor amount of damage. The older bridge is a reinforced concrete structure continuous over two spans, every second span being a drop-in span. Span supports alternate from fixed to free. Each of the free supports consists of a reinforced concrete bolster that sits on top of the pier that rocks under free thermal expansion. Inspection of this bridge revealed some damage at the support seats in the form of concrete crushing and spalling as shown in figure 9.



Fig. 9. The two bridges crossing the Sakarya River on the D100 Highway. The left hand bridge at the time of the earthquake was a new prestressed concrete bridge still under construction. The right hand bridge is the original reinforced concrete, two-lane highway bridge. The damage can be noticed on the new bridge were the fascia girder is misaligned near the top left hand corner of the photograph. Damage to the old bridge can be seen at the junction of the pier cap to span connection in the mid right portion of the photograph.

The new bridge, which is currently under construction, consists of closely-spaced pre-stressed concrete I-girders. These girders moved typically 50 mm on their bearing seats resulting on some misalignment of each of the spans. This is evident in figure 10. However, as traffic was not interrupted, the damage to both of these bridges could be regarded as "slight."

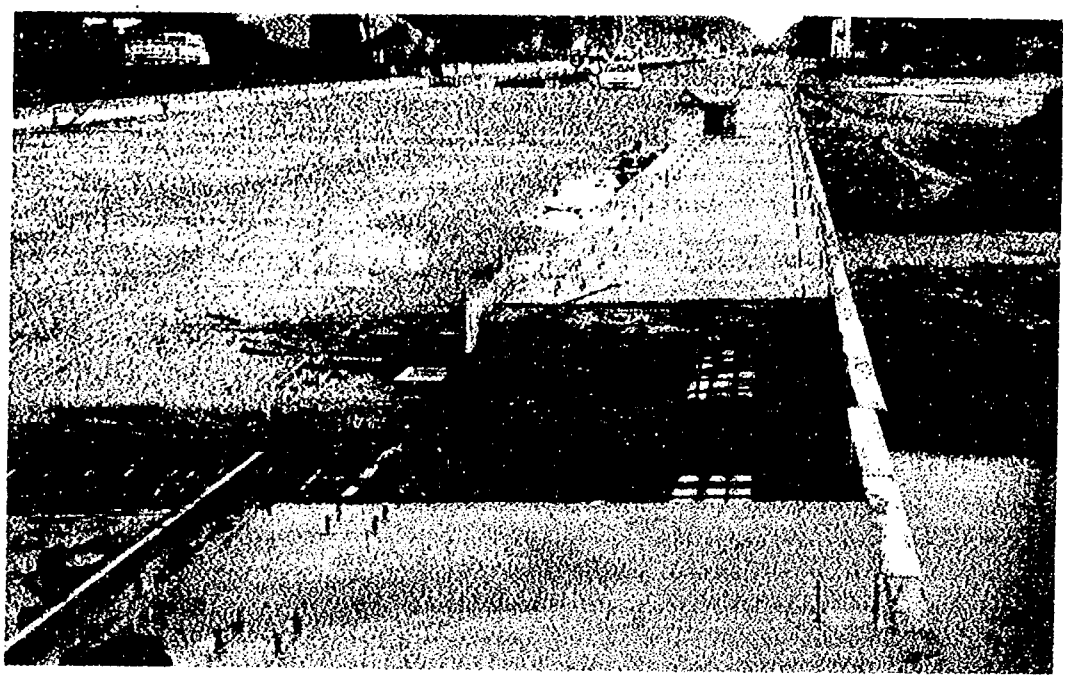


Fig. 10. The new two-lane bridge for the D100 Highway over the Sakarya River looking east. Notices the 50 mm offset of the fascia girders. The pouring of the construction joints was incomplete at the time of the earthquake.

3. DAMAGE TO ROADS

When traveling east, the E80 Motorway passes near the southern shores of Lake Sapanca. In this vicinity and some 30 km east, there was substantial damage to the roadway. Much of this was a result of the close proximity to the fault rupture. Indeed, in many instances the fault rupture traversed the road itself causing substantial damage to the pavement. There were numerous instances of damage to the road surface and a typical example is shown in figure 11. This damage led several vehicles careering off the road and also resulted in temporary closure of the Motorway. As shown in figure 12, the damage was quickly repaired and the Motorway brought back into service soon after the earthquake. Within one week, most of the surface damage was repaired and the Motorway operating at its usual 120 km/h speed limit.

Another major problem associated with E80 Motorway, particularly when it runs immediately adjacent to Lake Sapanca, was related to substantial settlements sustained by the embankments. Embankment settlements of 500 mm were commonplace. This resulted in two problems. First, the highway was left in a substantially wavy nature, and secondly, there were serious bump-onto-the-bridge problems at both culverts and single-span bridges, as shown in figure 13. Immediately following the earthquake and after the major highway debris had been cleared, asphalt was brought in and used to provide ramps onto and off the bridges at those locations where the bumps were very abrupt. Then within one week of the earthquake, major repairs were commenced. Where the bridges sat up high with respect to the surrounding roadway, the asphalt roadway was removed and the road was repaved and reprofiled to enable vehicles to travel at the regular full speed.

It is difficult to speculate whether this damage was a result of a bearing capacity failure, or settlement due to liquefaction, or a combination of the two. Although the surrounding soils appeared to be quite damp over to the crossing proximity at the lake, it is considered that the cause of failure was mostly due to the former rather than the latter. It is considered that liquefaction was unlikely as there was little evidence of sand boils in this vicinity.



Fig. 11. The distress to the pavement due to the fault rupture on the E80 Motorway.

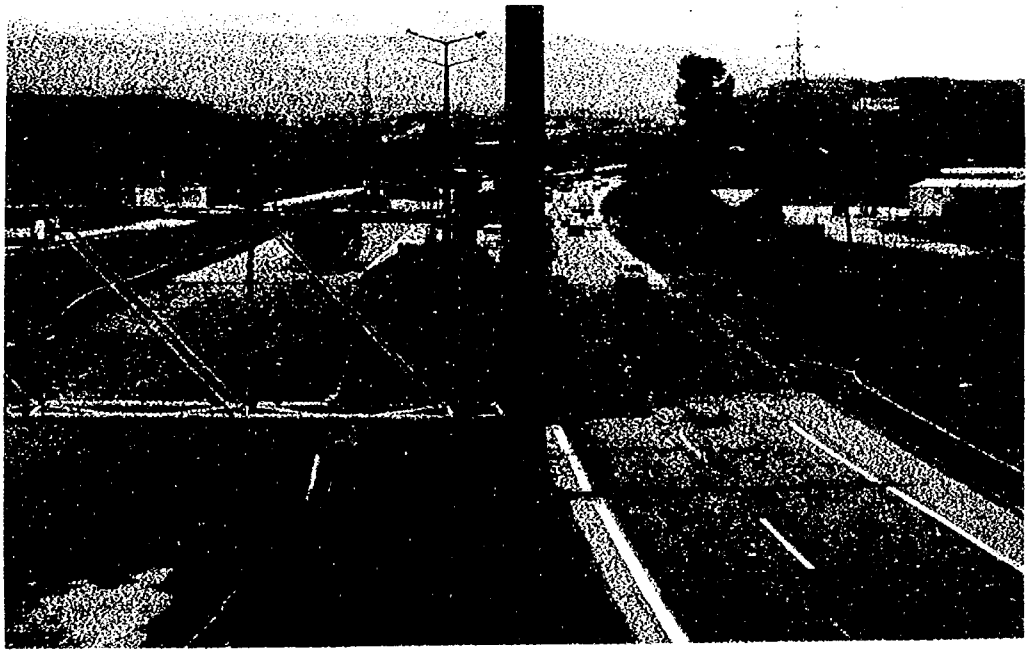


Fig. 12. A view of the E80 TEM taken from an overpass near Akyazi showing the restored roadway that had been severely damaged by the fault rupture.

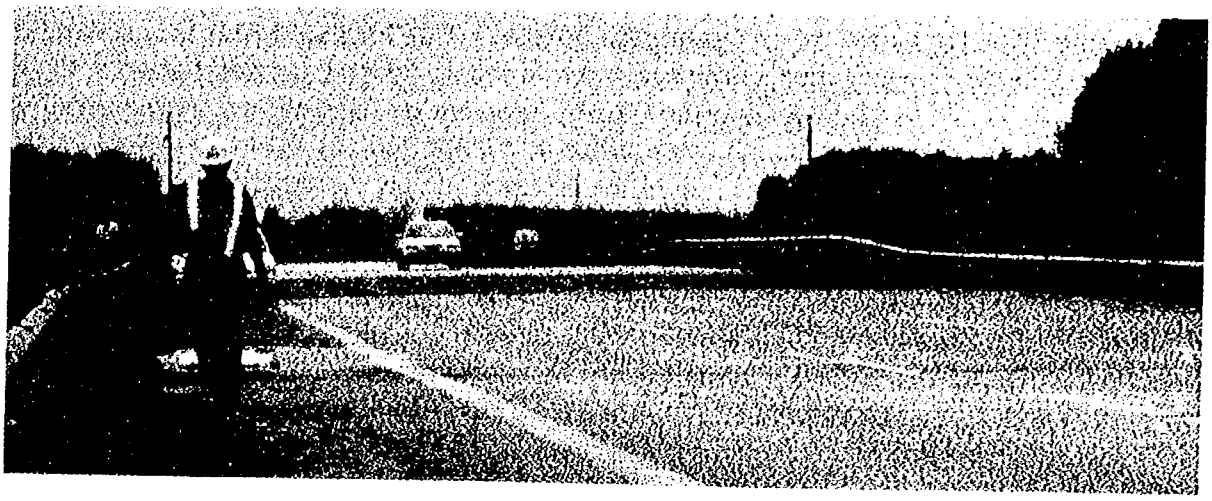


Fig. 13. One of the numerous bridges on the E80 TEM that is some 500 mm above the road surface. The severe shaking caused bearing capacity settlements of the road embankment leading to classic bump-onto-the-bridge problems.

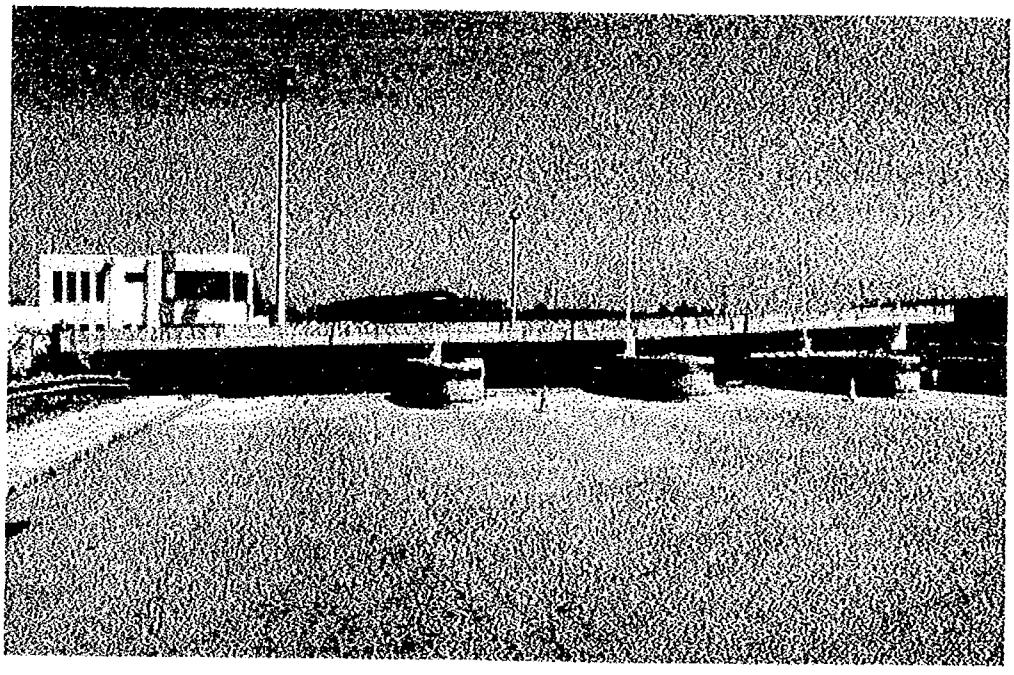


Fig. 14. Collapse of the toll plaza at an entrance to the E80 Trans European Motorway.

It is also of interest to mention the structural damage that lead to partial closure of the Trans European Motorway. A toll plaza at one of the entrances of the Motorway collapsed, as shown in figure 14, completely closing the entrance to the Motorway. This heavy reinforced concrete canopy structure was supported on small columns with inadequate detailing to sustain the large lateral sidesway. Following the earthquake, the collapsed structure was removed. Early reopening of this portion of the highway was essential to permit emergency access of response and recovery teams. Because of the demand for the use of this motorway, the government decreed that the payment of tolls would not be necessary due to the state of emergency.

4. Damage to Railways

Like the TEM Highway, the main railway system is dual track and runs in a general east-west direction. In the Sapanca area, it runs adjacent to the TEM E80. In this location, the fault rupture transverses both the highway and the railway with the damage shown by the aerial view in figure 15. From this photograph it is evident that the magnitude of the right lateral offset on the fault is about 1.5m—this is roughly equal tot he track gauge. Although the damage to the tracks is substantial as shown from the ground view in figure 16, repairs were implemented rather quickly. However, in one nearby branch line near Adapazari, an electric traction pole was brought down from the track requiring the restringing of the overhead traction wires. Such repairs to the electric traction system are generally more problematic than reopening the track itself, and until the traction system is operational, the use of diesel locomotives necessary. The railway system appeared to be fully operational within three days after the earthquake.

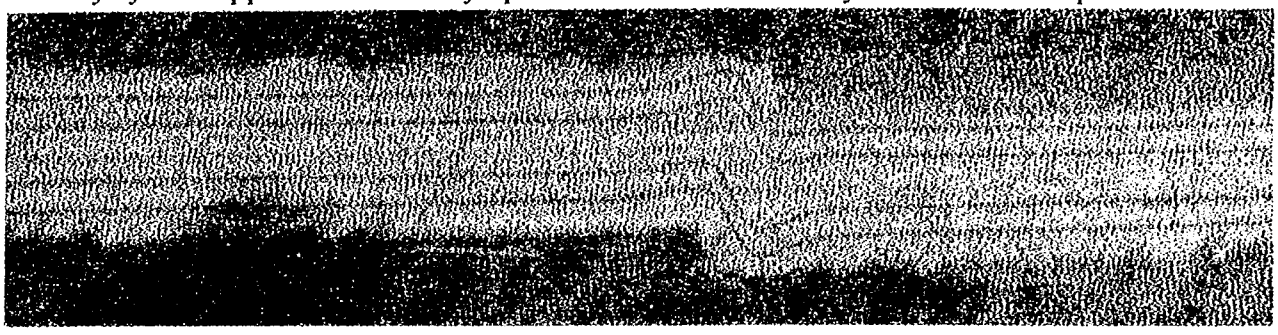


Fig. 15. An aerial view of the railway track buckling in the Sapanca area. Note there is a right lateral offset on the fault roughly equal to the track gauge of 1.5 m.

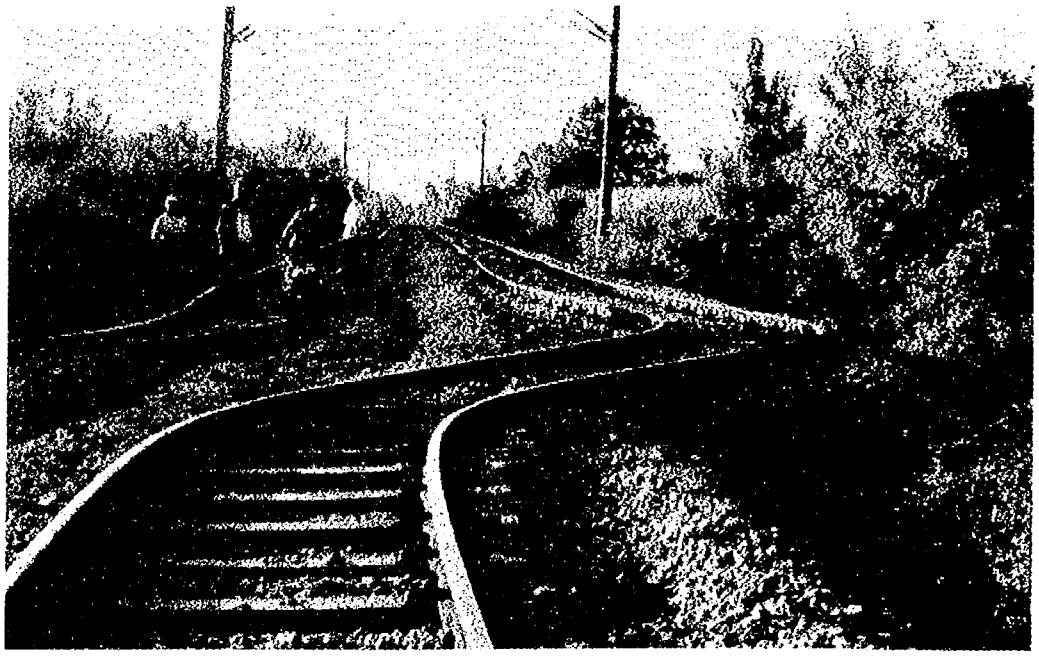


Fig. 16. A view of the fault passing through the railway embankment showing the substantial (2 m) right lateral offset.

5. Damage to Port Facilities

The eastern end of the Mamara Sea is a major port terminus. To the north of the bay there is a concentration of industrial facilities near Kocaeli (Izmit) port where cement, petrochemical plants and oil refineries abound. Considerable damage was reported to these facilities, but will not be discussed herein. To the south of the bay at Golcuk, is the main Turkish naval facility. The main fault rupture zone passed through this naval port including the dock and wharf facilities causing much damage to buildings and barracks as well. Figure 17 shows damage to the concrete quay wall due to the close proximity of the fault rupture. This quay wall, that was initially straight, has been both tilted and displaced approximately 1 m due to a combination of permanent ground displacement as well as shaking efforts. The extent of the damage resulting from the fault rupture is more clearly seen in figure 18. The wharf structure, which spanned between the land and the quay wall, collapsed in several places.

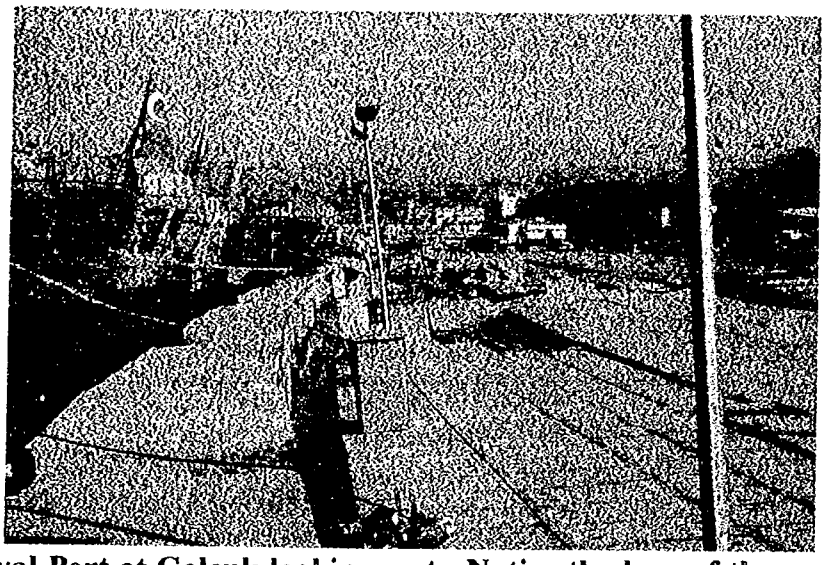


Fig. 17. The Naval Port at Golcuk looking east. Notice the bow of the quay wall resulting from near the fault rupture.

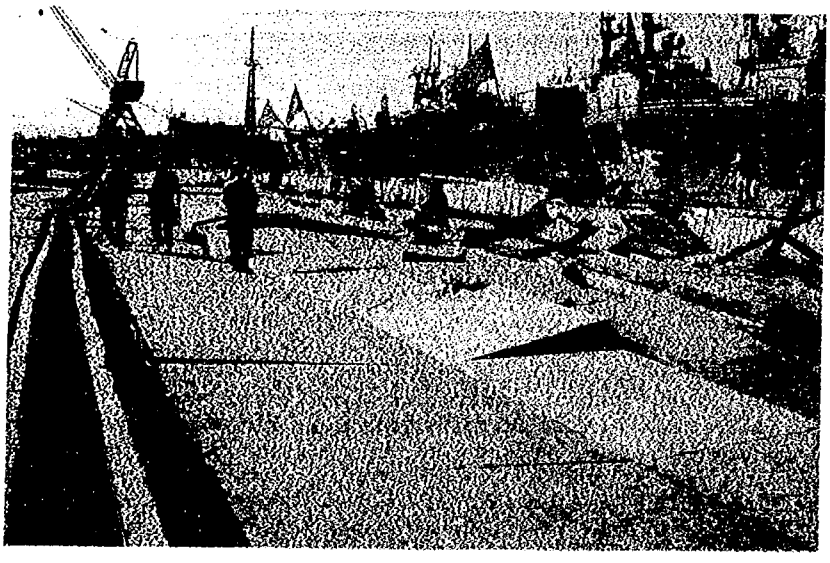


Fig. 18. Failure of the wharf structure at the naval port at Golcuk.

It is worth emphasizing the important role that the military are expected to play as part of civil defense following a natural disaster. Due to the collapse of the buildings on the naval compound as well as the failure of the wharf structures, many of the ships that were tied up (as seen in figures 17 and 18) had a full complement of men aboard that could not be gainfully employed on post-earthquake clean-up activities. Clearly such facilities are critical and essential to the response and recovery requirements of natural disasters.

6. Some Conclusions

This earthquake served to remind the profession of all lessons learned from previous events. Although few completely new lessons were learned from this earthquake, several points can be emphasized:

- Engineered structures, by and large, performed very well. This included the transportation structures as well as engineered buildings. This is in stark contrast with non-engineered structures such as domestic housing that performed quite badly and led to considerable loss of life and limb.

- In spite of the good performance of the transportation infrastructure, there is a need to classify and prioritize seismic retrofit needs for existing structural systems and facilities. Important structures should be held to a higher standard of performance. The traditional life-safety paradigm is insufficient for most public assets such as roads, highways, bridges and railways. There is a need to develop performance-based engineering standards that emphasize post-earthquake serviceability, damage avoidance (wherever possible) and rapid repairability if damage does indeed occur.

- The Turkey earthquake of August 17, 1999 demonstrated the importance of correctly characterizing soils and foundation problems. Structures and other facilities such as roads and highways on very soft soils did not perform particularly well. Moreover, non-engineered structures (housing and buildings) faired badly when located in soft-soil zones. It is clearly evident that well-engineered structures and facilities give due recognition to soft soils and site effects that can lead to large permanent ground displacements.

- This earthquake demonstrated the need for assesing the propensity for surface fault rupture. Inevitably wherever the surface fault rupture passed, mayhem and destruction was left in its trail. Admittedly, it is generally difficult to ascertain the precise location of a fault rupture, but wherever possible, this should be identified by microzonation mapping.

Acknowledgements

Financial support for travel was provided by the Federal Highway Administration (FHWA) via the Multidisciplinary Center for Earthquake Engineering (MCEER) headquartered at the University at Buffalo (SUNY). This funding enabled the author to travel to Turkey as part of the Earthquake Engineering Research Institute (EERI) Reconnaissance Team. This support is gratefully acknowledged.

BRIDGE PERFORMANCE IN THE 921 EARTHQUAKE, CHI-CHI, TAIWAN

Ian Buckle[1] and Jenn-Shin Hwang[2]

Abstract

Highway damage was widespread throughout Taichung and Nantou counties due to fault rupturing, crippled bridges, landslides and soil failures during the Chi-chi earthquake, Taiwan, on September 21, 1999. Approximately 10% of the bridge inventory experienced moderate-to-major damage and those structures most seriously affected range from 3 to 28-span structures, including simply supported and continuous superstructures, and long-span cable-stayed girders. Lessons learned include the importance of generous seat widths, and that ground failures precipitate structural failures. The punishing effect of near-field ground motions on both old and new bridges was also demonstrated, including the catastrophic consequences of fault rupture directly under or between bridge foundations. Observations of damage to ten of these bridges are briefly described in this paper. A brief discussion of lessons learned and recovery progress concludes the paper.

Introduction

Highway damage was widespread throughout Taichung and Nantou counties due to fault rupturing, collapsed or crippled bridges, landslides, soil settlement and slope failures. Ten days after the earthquake 45 kms of road remained closed, and another 400 kms were subject to delay and capacity restrictions (Figure 1).

Many hundreds of bridges are located in the Taichung and Nantou counties but most escaped serious damage and suffered only minor distress such as the settlement of approach fills behind abutment back-walls. But approximately 10% of the bridge inventory experienced moderate-to-major damage and those most seriously affected range from 3-span to 28-span structures, including simply supported reinforced concrete slab-and-girder superstructures, continuous steel plate–girders and long-span cable-stayed girders.

For example, Route 3 is a major north-south highway running the length of Taiwan from Taipei in the north to Pingtung in the south. There are approximately 65 bridges on this route as it passes through Taichung and Nantou counties. Five of these bridges suffered collapsed spans or were extensively damaged, such that the safety of the structure was in jeopardy, requiring closure pending demolition or significant repair. Another five bridges on county and city highways experienced similar distress, including one new cable-stayed bridge. Table 1 gives a summary of the pertinent data for these ten bridges. Figure 1 shows their approximate locations on Routes 3, 129 and 149, and their proximity to the epicenter at Chi-chi and the Chelungpu fault. It will be seen that all ten structures are within 10 km of the fault and most are within 5 km. Three are located directly on the fault itself. All are

1. Professor, Department of Civil Engineering, University of Nevada – Reno, Reno, NV 89557
2. Professor, Department of Construction Engineering, National Taiwan University of Science and Technology, Taipei

considered to be in the 'near field' and thus subjected to intense ground motions both horizontally (up to 1g) and vertically (up to 0,4g), and average fault dislocations of approximately 1.5m horizontally and 3m vertically.

Table 1. Partial list of bridges with significant[1] damage

Bridge ID	Bridge Name	Route No.	Date of Construction/ Widening	Type	Spans	Total Length (m)
1.	Tong-tou	149	1980	RC[2]	4 x 40 m	160
2.	Ming-tsu	3	1990	RC[2]	28 x 25 m	700
3.	Mao-luo-shi	3	1999	Steel/RC[3]	8-span segment	
4.	Wu-shi	3	1981/83	PC[4]	18 x 34.7 m	624
5.	E-jian	129	1972	RC[2]	24 x 11 m	264
6.	Tong-fong	3	1962/88	RC[2]	22 x 26 m	572
7.	Shi-wei	3	1994	PC[4]	3 x 25 m	75
8.	Ji-lu		1999	Cable-stayed	2 x 120 m	240
9.	Bei-feng[5]	located downstream of Shikhkang dam across Tachia Hsi				
10.	Chang-geng[5]	located upstream of Shikhkang dam across Tachia Hsi				

Notes:

1. Significant damage is defined as one or more collapsed spans, and/or extensive structural damage that jeopardizes the safety of the bridge requiring closure until repaired or replaced.
2. RC = Reinforced concrete superstructure
3. Steel/RC = Steel superstructure/reinforced concrete substructure
4. PC = Prestressed concrete superstructure
5. Details not available at this time (October 1999

Damage to these ten bridges included overturned bearings; shear failures in columns, pier walls, and caissons; joint failures in column-to-girder connections; loss of support for both normal and skewed simple and continuous girders; cable fracture; abutment back-wall failure; and foundation failures due to slope instabilities, liquefaction, and fault rupture. Brief descriptions of this damage are given in the following section. It is noted that the observations made in this paper, are the result of a reconnaissance visit to the Nantou and Taichung counties in the first week of October 1999, and that these observations are preliminary and subject to change as additional data becomes available in subsequent months.

Observations

All four simply supported spans of the *Tong-tou bridge* on Route 149, collapsed due to shear failures in the single column bents comprising the three river piers (Figure 2). These columns were supported on large diameter caissons, which extended well above the river bed thus shortening the overall height of the columns themselves. The columns appeared to have been shear critical but did not fail simultaneously. Instead one probably failed before the other leading to an asymmetrical collapse of spans 2 and 3 (one fell upstream and the other

downstream of the bridge centerline). In addition, the northern abutment suffered considerable structural damage that appears to have been due to large earth movements arising from either fault rupturing or ground failure behind the abutment, or both. Significant settlement of the approach pavement occurred (Figure 3).

Constructed in 1990, the *Ming-tsu bridge* on Route 3 comprises 28, 25 m spans for a total length of 700 m. Eight of these spans collapsed at the south end of the bridge (Figure 4). Although the superstructure comprised multiple spans of simply supported girders they had been made continuous by a cast-in-place reinforced concrete deck slab which was continuous over intermediate bents. Thus the bridge was a series of continuous segments, and at least two of these segments collapsed at the south end of the structure. At the time of our site visit, the northern-most segments had been demolished and only the southern segment remained 'standing'. Whereas liquefaction may have been responsible for pier tilting and collapse of the northern segments, the spans in the southern segment became unseated when the southern abutment failed. During strong longitudinal motion the superstructure impacted the back-wall of the south abutment, which was unable to arrest the motion. The wall and its back-fill failed and driven back about 0.5 m into the back-fill, followed by the superstructure (Figure 5). This longitudinal movement was sufficient to cause unseating of the adjacent spans comprising this segment.

The *Mao-luo-shi bridge* on Route 3 is a multiple-span viaduct comprising a set of continuous segments, each constructed from steel plate girders supported on concrete, single-column bents. In one 8-span segment (Figure 6), four of these bents are 'C –bents' where the column is eccentrically connected to the cross-girder. Although there were no collapsed spans in this viaduct, all of the eccentric connections showed distress, particularly in the column. Shear cracking was evident in the upper third of each column and increased in severity with increasing eccentricity (Figure 7). Despite the absence of gross deformations in the superstructure, the cross-girders have been temporarily shored and the bridge closed.

The *Wu-shi bridge* on Route 3 is in fact two bridges on a parallel alignment (Figure 8). Both are 18 spans long for a total length of 624 m. The first bridge was constructed in 1981 and the second one, two years later, in 1983. Both were of similar design (simple spans supported on wall-type piers) with one exception. The piers of the second bridge were not as wide as those of the first and in some cases (eg at Pier 3) the piers in the second bridge were one-half the width of the corresponding piers in the first bridge). Despite the fact that both bridges experienced similar ground motions, they failed in different ways. Ground failure occurred behind and under the northern abutment of both bridges, followed by soil deformation at the base of these wall-abutments of about 0.3 m towards the river. There was similar ground deformation under the first and second piers, but of lesser magnitude (perhaps 0.2 m). The two bridges accommodated this movement in different ways, as described below.

In addition to the ground failure, there was strong ground shaking transverse to both bridges, which caused massive shear failures in the first five piers and/or caissons of the second bridge (Figure 9). This did not happen in the first bridge, possibly due to the greater shear capacity of its wider columns. Instead, the first two spans of this bridge became unseated at Piers 1 and 2, due to the movement of these piers towards the river. Lesser soil deformations were experienced at the remaining piers and these were accommodated at the pier caps without unseating. But the shear keys at these caps were heavily damaged due to the transverse motion, and at Pier 2 they failed completely (Figure 10). As a consequence, although the superstructure was not unseated at this pier, it came to rest with a permanent

transverse offset and with the outside girder overhanging the pier cap. In the second bridge the longitudinal movement of the foundations under Piers 1 and 2 did not lead to span collapses. Instead this movement was accommodated within the plane of the massive shear cracks in both piers. Examination of these cracks showed longitudinal offsets of about 0.15 m (in addition to large vertical and transverse offsets), which was sufficient to allow the girders to remain on their seats.

Constructed in 1972, the *E-jian bridge* on Route 129 has 24, 11m spans providing a total length of 264 m. The superstructure comprises a pair of simply supported, reinforced concrete, double-T girders. Each pier is an unreinforced concrete wall on a spread footing. The structure was being widened at the time of the earthquake and new piers had been constructed, but at a different spacing than for the original bridge. During the earthquake, fault rupturing occurred under the north abutment with about 1.5 to 2 m of uplift. As a consequence twelve spans collapsed from the northern abutment to the center pier of the bridge (Figure 11). The remaining 12 spans to the south abutment remained standing with little apparent damage. Examination of the collapsed girders showed little distress and the field evidence suggests that collapse was due to large movements of the pier foundations towards the center of the river channel. At or near the abutment, where uplift occurred, these unreinforced piers were crushed, or snapped at mid height, but the remaining piers moved as rigid bodies towards the river or rotated with their footings due to slumping and flow of the uplifted material (Figure 12). In doing so, the piers were driven in under the adjacent 'downhill' span while unseating the adjacent 'uphill' span. Corresponding overhangs of the superstructure girders occurred, which at Pier 9 measured 3m. There is little evidence of residual displacements in the southern half of the bridge (which remains standing), and this appears to confirm the scenario that the collapses were due to gross movements of the northern foundations rather than unseating due to structural vibration. The extent of these movements appears to have been of the order of 5 m near the abutment, decreasing to about 3 m near the river channel.

The 22-span *Tong-fong bridge* on Route 3 was originally constructed in 1962 and widened in 1988. It is in fact three parallel bridges, each of total length 572 m. The spans are simply supported reinforced concrete girders resting on bearings at each pier cap. During the earthquake, the bearings at Piers 1 and 2 were dislodged due to strong transverse motion, and significant shear cracking and spalling occurred in Pier 5 of the downstream bridge. Within 13 days of the event, the bearings had been replaced with elastomeric bearings and the bridge reopened to traffic. Pier 5 was yet to be repaired.

The *Shi-wei bridge* on Route 3 was reconstructed in 1994 as a pair of 3-span bridges on single column bents. Each span is 25 m long and comprises five simply supported prestressed concrete girders and deck slab. Each is supported on elastomeric pads with shear keys for transverse restraint. Two spans in one bridge and one span in the second bridge collapsed when the second pier (column and caisson) in both bridges tilted away from the abutment by approximately 10 to 15 degrees (Figure 13). The tilting was most probably due to liquefaction over part of the depth of the caisson, but there was no obvious geotechnical evidence to confirm that liquefaction had indeed occurred. There was also no sign of abrasion on the vertical faces of either column to indicate sliding of the span down the face of the column. It therefore appears that titling happened first, followed by the 'free' fall of the end spans. The reason for the collapse of the middle span of the second bridge is not so clear, but it may have been due to the skewed nature of this span (Figure 14). Since the bridge is curved, there are angle changes between the straight girders in adjacent spans at common

piers and thus the middle span, of both bridges, has skewed supports. Such spans are known to exhibit excessive in-plane displacements due to rigid body rotations of the spans about a vertical axis during strong earthquakes. Unless generous seat widths are provided, collapse is likely. The fact that the middle span of the second bridge did not collapse may have been because it is on the 'inside' of the curve with shorter girders, and the displacements due to skew would not have been as large.

The *Ji-lu bridge* is a cable-stayed bridge across the Chu-shui Hsi, one of the largest rivers in Taiwan (Figure 15). Simply supported approach spans at both ends lead up to the two-span, single-tower structure that is approximately 240 m long. The concrete superstructure is symmetrically supported by 17 pairs of parallel cables from each side of the tower.

The structure was virtually complete at the time of the earthquake; only the guardrails and a section of the superstructure remained to be completed. A gap in the cantilevered section on the eastern side of the superstructure at the base of the tower had been created during erection to accommodate the construction crane. But although the crane had been dismantled, the gap had not been filled at the time of the earthquake.

Damage to the structure included a snapped cable, flexural and torsional cracking at the base of the tower and in the superstructure, and vertical and lateral pounding of the superstructure into the 'abutment' substructures (Figures 16, 17, and 18). These substructures provide the transition between the cable-stayed spans and the approach spans and consist of two-column bents with a cap beam. It is not clear why such a structure should suffer such distress, but the missing section of the superstructure girder (Figure 17) and the loss of one cable would lead to unbalanced loads and reduced stiffness in the superstructure, which in turn would generate asymmetric response and potentially large excursions of the girder in both torsion and in-plane flexure. Furthermore, the severity of the ground motions, particularly in the vertical direction, could have been responsible for the vertical pounding at the abutments, as evidenced by shear cracks in the abutment cap beams (Figure 18).

The *Bei-feng and Chang-geng bridges* are both located near the Shikhkang dam on the Tachia Hsi. They are long, multiple span, simply supported bridges similar to those described above. Both suffered collapsed spans due to fault rupture at or near their abutments.

Lessons learned

The following is a preliminary set of lessons to be learned from this earthquake:

- Fault rupture, directly under or between bridge foundations, is a catastrophic event and span collapse is inevitable if the dislocations are large.
- Near-field ground motions are intense and extremely punishing on bridge structures, particularly older bridges that have not been designed to modern codes.
- Long-span bridges are vulnerable in near-field sites, especially those still under construction.
- Ground failures precipitate structural failures.
- Engineered abutment back-walls and back-fills are essential to prevent span collapses even for continuous bridges.
- Generous seat widths are excellent insurance against unintended actions such as ground failure and rotation in skewed spans.
- Shear failures must be avoided in piers.

- Engineered shear keys are required to prevent spans falling transversely from pier caps.
- Load paths through column-to-girder joints must be specifically detailed, particularly for eccentric connections.

Recovery progress

Past earthquakes have shown that there at least three phases to recovery:

- Execution of urgent repairs and the construction of bypasses under emergency conditions (say the first 90 days).
- Replacement of crippled structures (say 3 to 12 months).
- Retrofit of existing bridges, and revision of design codes for new bridges, elsewhere in Taiwan (say 1 year onwards).

The first phase was well advanced in the Nantou and Taichung counties by the first week in October (2 weeks after the earthquake). By passes had been constructed (Figure 11), shoring erected (Figures 6 and 7), Bailey bridges installed, overturned bearings reinstated, and settled approach fills repaved. Only about 45 kms of highway remained closed at the beginning of October and these were mainly highways in the mountainous regions of the two counties where extensive landslides had yet to be cleared.

Progress in the second phase will be slower because it requires the design of replacement structures before the reasons for the damage are fully understood and agreed. Conservative designs are therefore expected in the interim, so as to minimize the risk of inadvertently constructing a new set of vulnerable structures. Seat widths are expected to be arbitrarily increased, shear keys strengthened for elastic response, shear and confining steel increased in columns, skew supports removed (or seat widths further increased to allow for skew), eccentric column to cross-girder connections eliminated, sacrificial spans installed in bridges that cross active faults, and site specific hazard analyses performed for critical bridges, including long-span bridges.

It is too early to estimate the implication of this experience on Taiwan's retrofitting program for existing bridges, and its design code for new bridges (Phase 3). However the lessons learned are expected to significantly affect both of these activities, not only in Taiwan, but also in seismically active regions through out the world.

Acknowledgements

This paper is the result of a reconnaissance visit to the sites of several damaged bridges in Nantou and Taichung counties, during the first week of October 1999. This visit was organized and coordinated by Dr George C. Lee, Director, Multidisciplinary Center for Earthquake Engineering Research at the University at Buffalo, New York, and Dr C-S Loh, Director, National Center for Research in Earthquake Engineering at the National Taiwan University of Science and Technology, Taipei. The authors also wish to acknowledge the generous assistance provided by the Highway Bureau of the Ministry of Transportation and Communications, to this reconnaissance effort. Specifically, the assistance of Mr James Yeh, Deputy Director General, and Mr Wei Wu, Deputy Chief Engineer for Central Taiwan, is gratefully acknowledged.

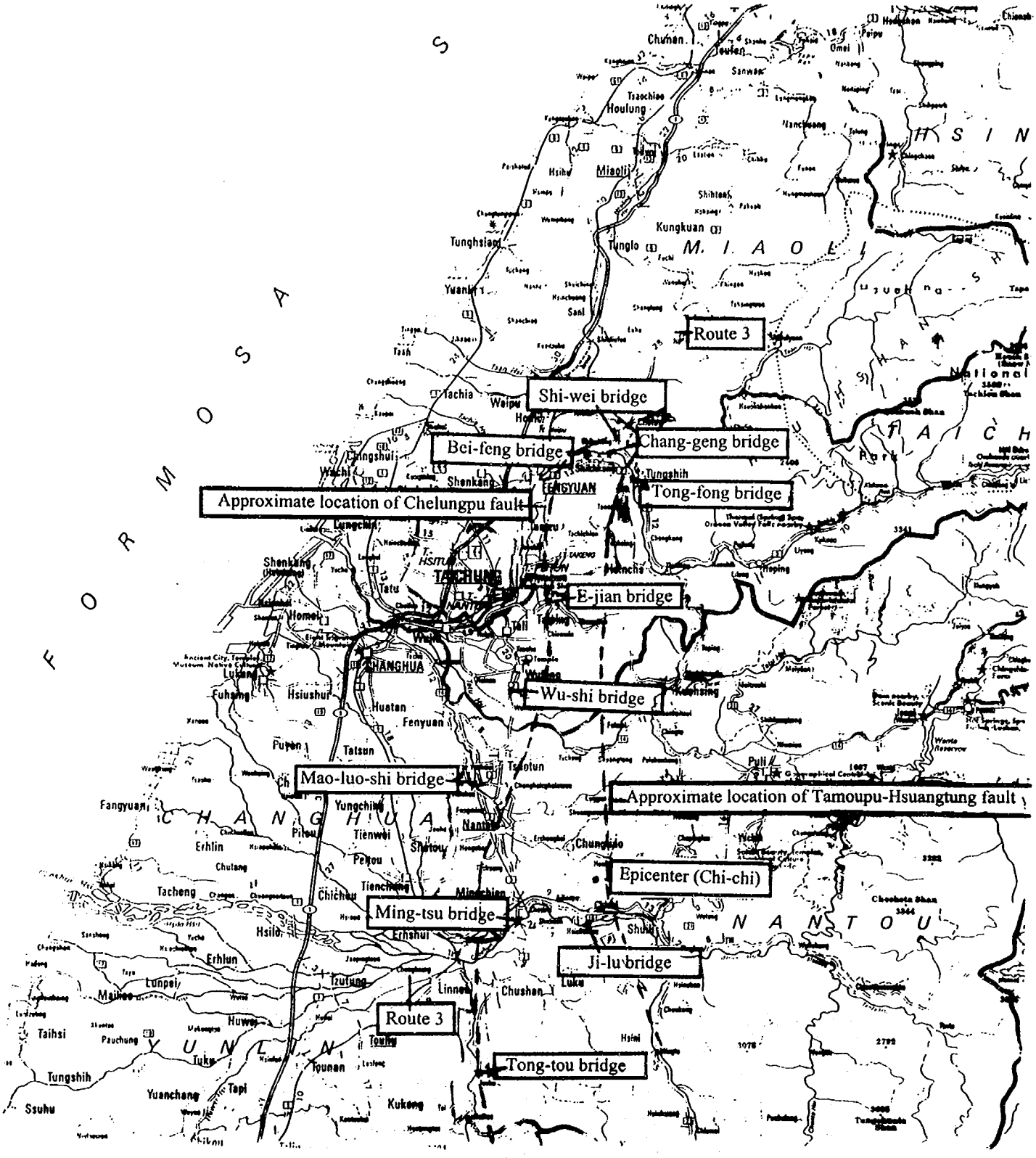


Figure 1: Bridges with significant damage in Taichung and Nantou counties.

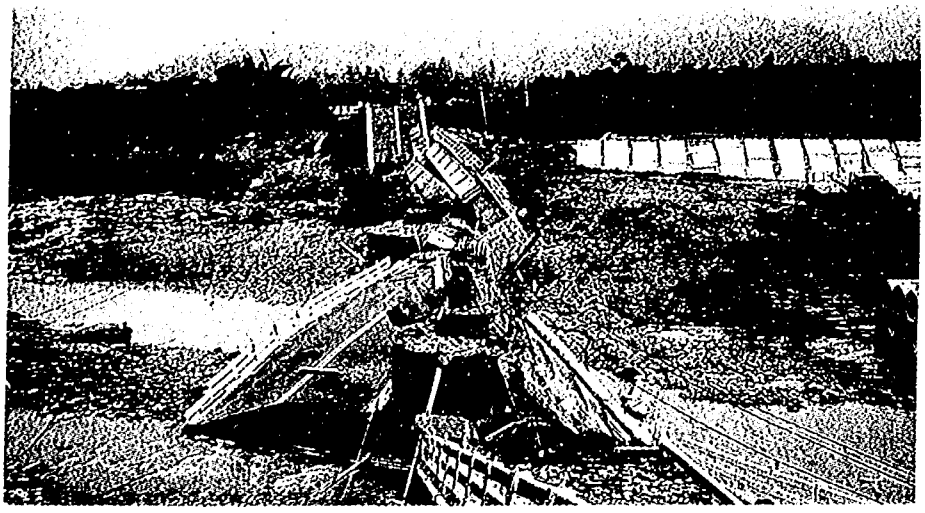


Figure 2: Collapse of the Tong-tou bridge due to shear-critical columns.

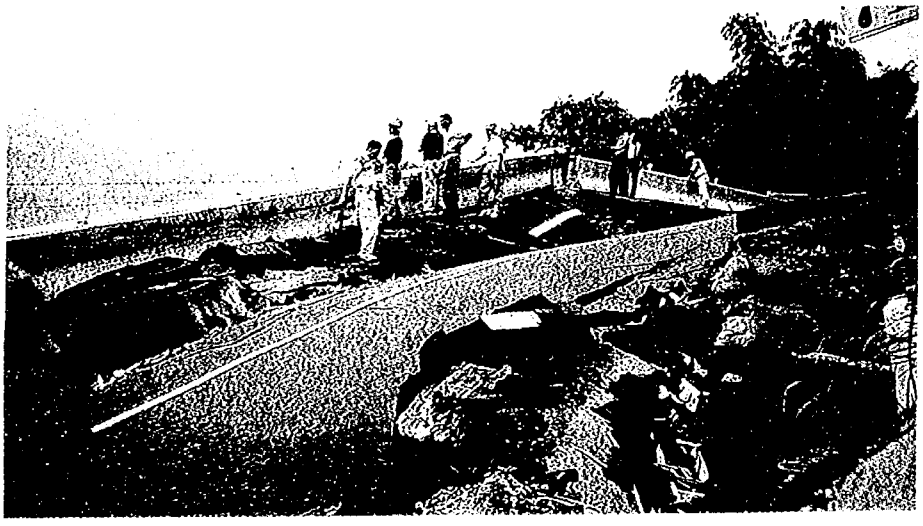


Figure 3: Failure of the approach-fill behind north abutment of Tong-tou bridge.



Figure 4: Ming-tsu bridge after removal of many of the collapsed spans.

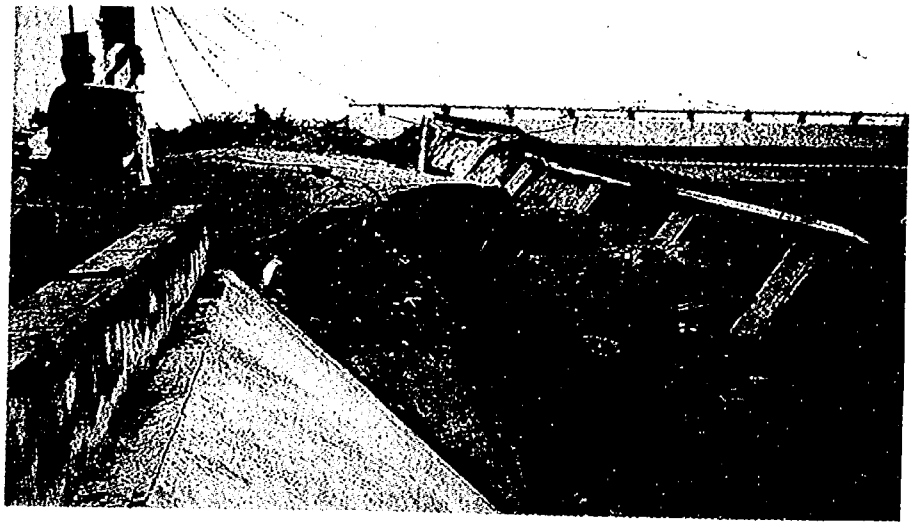


Figure 5: Failure of the back-wall and back-fill behind south abutment of the Ming-tsu bridge, leading to the unseating of adjacent spans.



Figure 6: Mao-luo-shi bridge, showing single-column concrete bents supporting continuous steel girders.



Figure 7: Typical distress in an eccentric, column-to-cap beam connection in the Mao-luo-shi bridge.

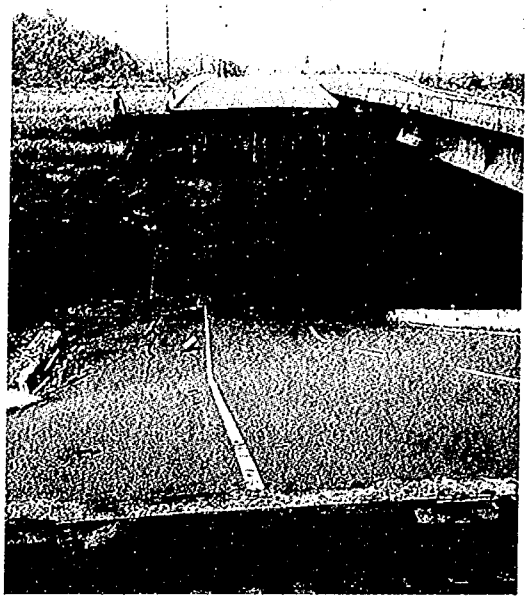


Figure 8: Collapsed span in the Wu-shi bridge (east).

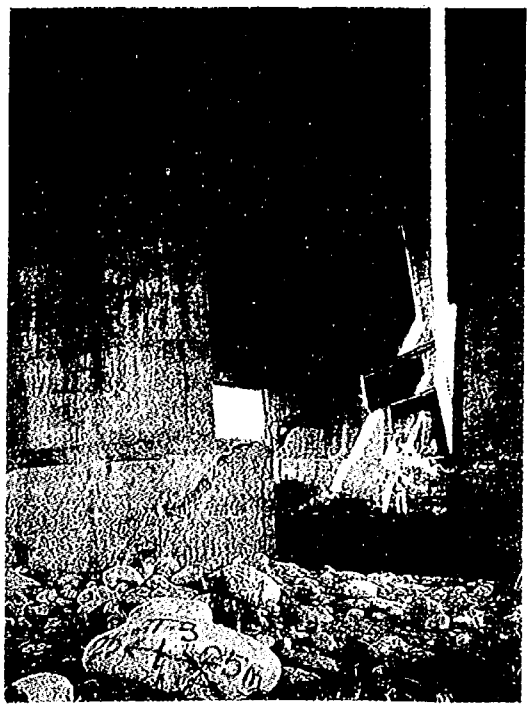


Figure 9: Shear failures in the columns and caissons of the Wu-shi bridge (west).

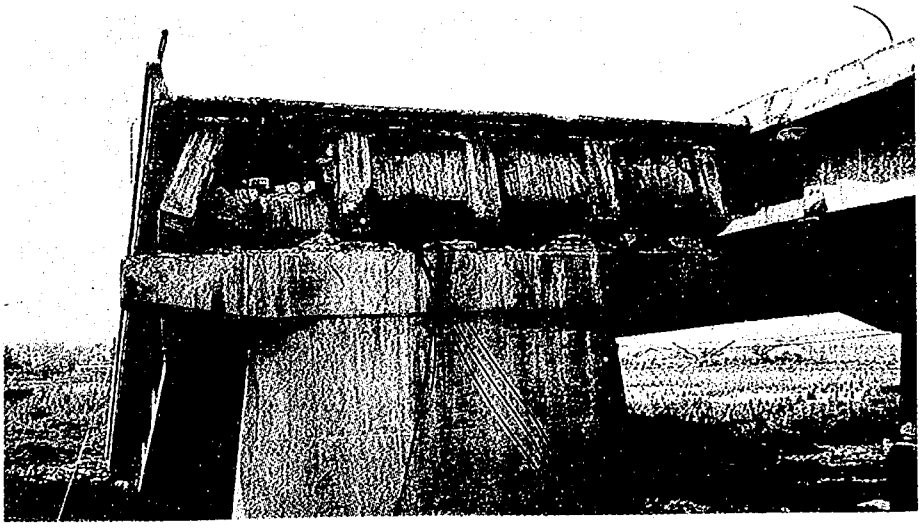


Figure 10: Diaphragm and shear key failures at Pier 2 of the Wu-shi bridge (east).



Figure 11: Collapsed spans of the E-jian bridge due to massive ground movements towards the river (left).



Figure 12. Tilting of Pier 10 of the E-jian bridge due to ground movements towards the river (left).

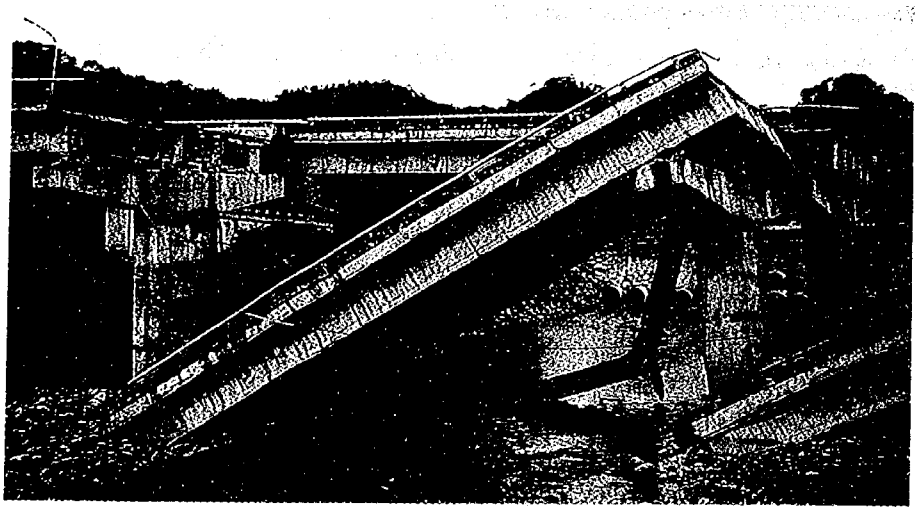


Figure 13. Collapse of the middle span of the Shi-wei bridge and tilting of Pier 2 (right); span to the right has also collapsed.

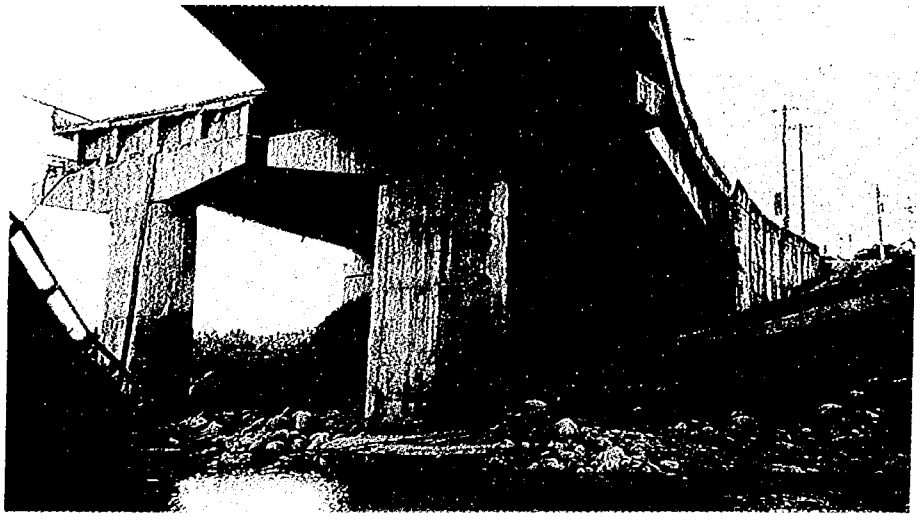


Figure 14: Shi-wei bridge showing curvature and skewed alignment of superstructure girders.

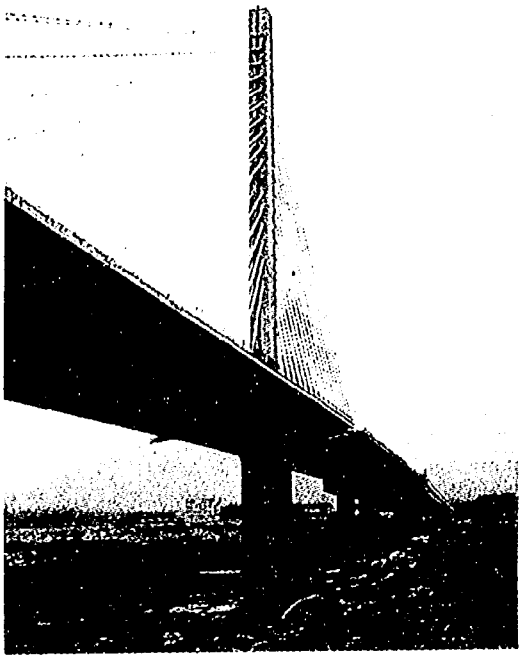


Figure 15: Ji-lu cable-stayed bridge; empty cable socket visible mid-height of the tower.

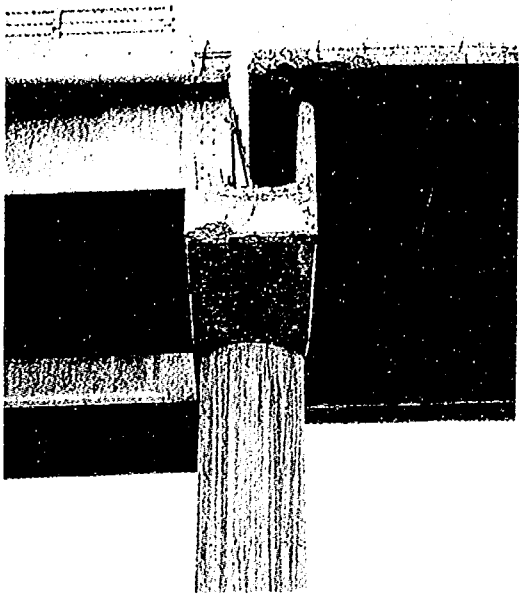


Figure 16: Damage at bent cap of south abutment, Ji-lu bridge; bent cap wall has been knocked off.



Figure 17: Damage to the soffit of the main girder near the pylon of the Ji-lu bridge; missing cantilevered section (right) had not been placed at time of earthquake.

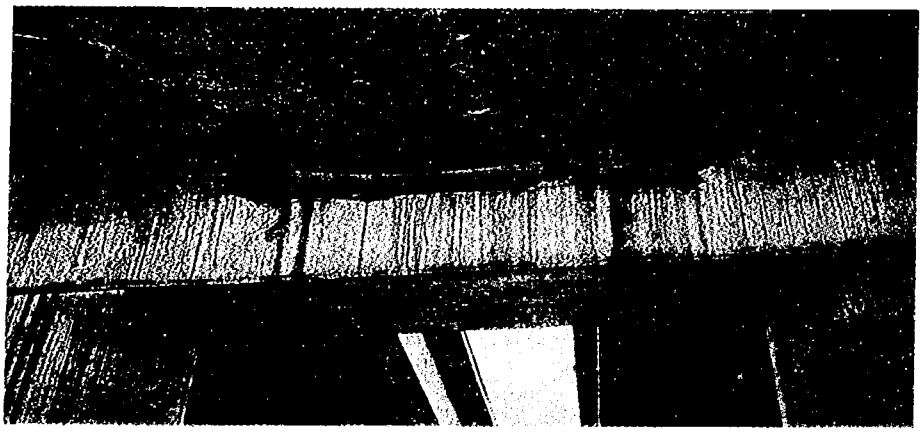


Figure 18: Pounding damage and shear cracks in the bent cap of the north abutment of the Ji-lu bridge.

SESSION 3: SEISMIC ISSUES (1)

(1) An Update on Analytical and Experimental Research on Bridge Restrainers
(Anastasios G. Vlassis, Emmanuel Manos Maragakis and Mehdi Saiid Saiidi)

(2) A Static Three Dimensional Elastic-Plastic Analysis of Steel Frame Bridge Piers
(Motoaki Tanaka, Yuji Sato and Hideaki Kasabou)

(3) Cyclic Testing of Composite Concrete-Filled Circular Tubes and Foundation Detail
(Michel Bruneau and Julia Marson)

(4) Experimental Study on Strength and Ductility of One-Story and
Two-Story Rigid Frame Steel Piers of Highway Bridges
(Tatsumasa Takaku, Yuhshi Fukumoto, Tetsuhiko Aoki, Takashi Okamoto,
Tatsuo Kurokawa and Hiromitsu Morishita)

(5) Seismic Resistant Design of the Rio Tempisque Bridge
(Cris D. Subrizi)

An Update on Analytical and Experimental Research on Bridge Restrainers

By Anastasios G. Vlassis[1], Emmanuel "Manos" Maragakis[2] and Mehdi "Saiid" Saiidi[3]

ABSTRACT: Bridge restrainers are used to inhibit relative displacements, prevent unseating and transfer longitudinal seismic forces between adjacent spans at in-span or simply supported hinges. They have proved to be very effective in earthquakes such as the 1987 Whittier Narrows, the 1989 Loma Prieta and the 1994 Northridge Earthquakes. Two procedures are currently used to design restrainers in the U.S.. At the same time, various analytical studies have investigated the dynamic performance of restrainers in both the cases of simply supported and in-span hinges and several new restrainer design methods have been developed. These studies have shown that although the currently used design methods are conservative in most cases, they neglect many parameters which are important for the response of hinges. Furthermore, new large scale experimental studies are in the development stage. These studies are expected to enhance our understanding of the complicated phenomenon of hinge response to earthquake excitations.

1. Introduction

During an earthquake, adjacent bridge segments can vibrate out-of-phase due to their different dynamic characteristics and variations in the ground motions. The out-of-phase motion results in two main problems. First, when the displacement between the bridge segments exceeds the range of support provided by the available seat width, the supported span can unseat. Many cases of bridge collapse that occurred in recent earthquakes were attributed to this phenomenon (Moehle, 1995, Saiidi et al., 1993). Second, when the distance between the frames decreases, eventually reaching zero, pounding occurs. The significant impact forces, which are developed, can result in local damage and crushing of concrete. Furthermore, impact can increase displacements in segments beyond what is typically assumed in design. Pounding of frames produces large impact forces that can increase hinge opening at simply supported spans or at in-span hinges, resulting in a greater possibility of unseating.

The 1971 San Fernando Earthquake in California showed that many highway bridges are vulnerable to collapse due to excessive longitudinal movements at expansion joints and supports (Jennings, 1971). In order to prevent unseating, the California Department of Transportation (CALTRANS) initiated a retrofit scheme, which consisted of tying bridge spans together with restrainers at their hinges. Since then, seismic restrainers have been extensively used in the U.S. mainly in California. Under the CALTRANS Phase I retrofit program approximately 1400 bridges were retrofitted using restrainers (Yashinsky et al., 1995).

A bridge restrainer is any type of device used to inhibit relative displacements, prevent unseating and transfer longitudinal seismic forces between adjacent bridge spans. Restrainers can be in the form of plates, rods or cables. The most common type of restrainer in the U.S. is the cable restrainer. Flexible restrainers used in California typically use high-strength steel cables anchored to the diaphragms or webs of concrete bridges (Fig. 1) or to the bottom flange of steel

1 Research Assistant, Dept. of Civil Engineering, University of Nevada, Reno, NV, 89557
2 Professor and Chair, Dept. of Civil Engineering, University of Nevada, Reno, NV, 89557
3 Professor, Dept. of Civil Engineering, University of Nevada, Reno, NV, 89557

2. Existing Restrainer Design Methods

Two procedures are currently used to design restrainers in the U.S.. CALTRANS and AASHTO (American Association of State Highway and Transportation Officials), each have methods to design restrainers for bridges with the potential to become unseated in an earthquake. The main features of these two methods are presented in the following paragraphs:

- *The CALTRANS Method*

CALTRANS uses an equivalent static procedure, which may be performed by hand, to determine the required number of restrainers to limit the hinge displacements to a prescribed value. The method can be applied to both simply supported spans and in-span hinges (CALTRANS, 1990). The general procedure is as follows:

1. Calculate the restrainer length based on the hinge dimensions, assume one restrainer, compute the maximum permissible restrainer deflection and limit deflection to the hinge seat width.
2. Compute the maximum longitudinal earthquake deflections on both sides of the superstructure joint under consideration. For curved bridges, compute the joint opening resulting from a lateral earthquake.
3. Compare the deflections from steps 1 and 2 and determine the governing case.
4. Determine the number of restrainers required.
5. Check the deflections of the restrained system and revise the restrainer and/or column assumptions if necessary. Repeat steps 1-5 if needed.

For in-span hinges, the procedure considers only the frame on either side of the intermediate hinge which has the smallest displacement. Restrainers are provided until the frame displacement is less than a prescribed value for a given design load. For simple spans on bearings, CALTRANS assumes that the bearings always fail in a strong earthquake. Further, the CALTRANS restrainer design method does not address skew specifically and the number of restrainers is not modified for skewed bridges.

- *The AASHTO Method*

Rather than specifying a detailed procedure, the AASHTO code defines a method to determine the longitudinal linkage force that a set of restrainers must withstand. The force is defined as the site acceleration coefficient times the weight of the lighter of the two adjoining spans or parts of the structure (AASHTO, 1996). Restrainers designed for a simply supported bridge would resist the force generated from the span weight. The AASHTO procedure is as follows:

1. Determine the longitudinal linkage force.
2. Determine the number of restrainers.

AASHTO requires that all bridges in seismic zones C and D must have restrainers and must satisfy seat width requirements, while bridges in zones A and B must satisfy seat width requirements only.

3. Analytical Studies

Several studies have investigated the seismic performance of restrainers and hinges in both the cases of simply supported spans and in-span hinges. These studies included skew and non-skew highway bridges with narrow and wide seats, subjected to uniform or non-uniform ground motions that were acting in several directions with respect to the bridge axis. Most of these bridges were modeled and analyzed using a variety of computer programs. Field performance reviews have also been conducted by some of the researchers.

In 1992 researchers at UNR (Saiidi et al., 1992) evaluated the effects of changing the cross-sectional area of the restrainers and the restrainer gap on the non-linear response of a representative bridge with several hinges. A four-frame bridge similar to the one described in the CALTRANS design method example was chosen. The difference between the two models was the type of the abutment on the right side of the bridge. The CALTRANS example had a seat-type abutment, while the UNR model had a diaphragm-type abutment. Furthermore, the CALTRANS example did not specify all of the dimensions and properties of the example bridge, which was the case with the UNR model. The bridge was modeled using NEABS-86 and subjected to the 1940 El Centro Earthquake, North-South component, the 1954 Eureka Earthquake, North-South component and the 1989 Loma Prieta Earthquake, East-West component. Only cable type restrainers were considered. Restrainer area was evaluated by changing the number of restrainers. Two different restrainer gaps of 19 mm and 0 mm were chosen to represent extreme temperature conditions. The parametric study indicated that the number of restrainers became more influential when the restrainer gap was reduced. A reduction in the number of cables generally increased the magnitude of restrainer stresses. To determine the most critical abutment forces it was necessary to analyze the bridge for both the extreme low and the extreme high ambient temperatures. Furthermore, abutment forces were sensitive to the ground motion. The study concluded that the extreme low ambient temperature should be considered to determine the critical restrainer stresses and that the maximum relative displacements may occur for the case of zero or non-zero restrainer gap depending on the number of restrainers. In addition, the current CALTRANS design procedure was shown to be inaccurate, since it did not produce results consistent with results of non-linear analysis. This was attributed to its lack of consideration of the restrainer gap and the non-linear behavior of other hinge elements.

Since restrainers are relatively simple systems with seemingly predictable behavior, very little research had been done on hinge restrainers prior to the 1989 Loma Prieta Earthquake. This earthquake gave researchers a good opportunity to study the response of in-span hinge restrainers that had been subjected to an actual earthquake (Saiidi et al., 1993). The primary objectives of this study conducted at UNR were: (1) to review the actual performance of bridge hinge restrainers during the earthquake, (2) to develop the analytical models of selected bridges and study their earthquake response, (3) to carry out a parametric study of these bridges in order to determine the effect of stronger earthquakes and the effect of changes on the restrainer gaps, and,

girders (Fig. 2). Japanese practice has also used a variety of restrainer types, including chains, rigid links and knee-joint links, which provide limited displacement before locking up (Priestley et al., 1992). Hinge restrainers are installed with a gap to allow for thermal movement of the bridge. In extreme cold conditions, this gap may be reduced to zero. At the same time the expansion joint gap increases, leaving a smaller seat width.

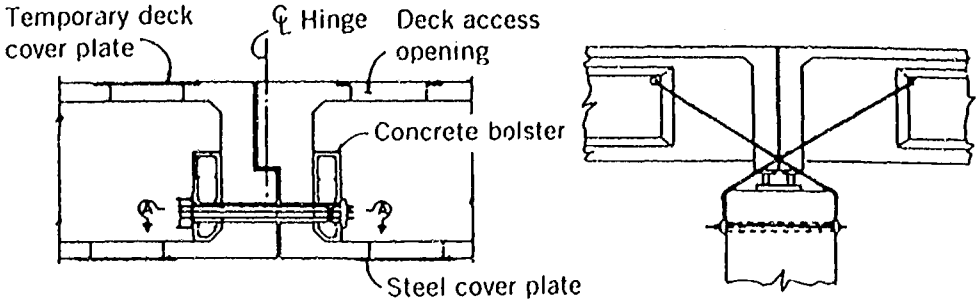
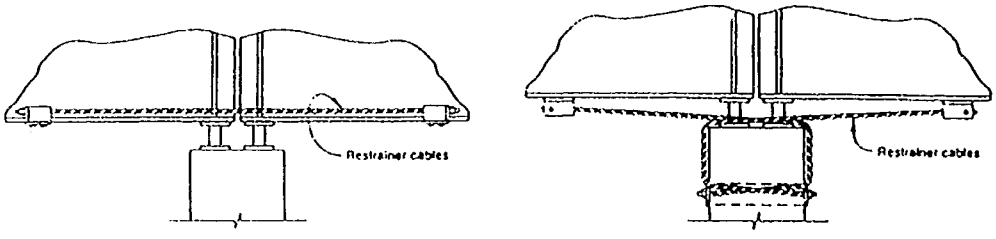


Fig. 1 Cable restrainers for concrete superstructure movement joints (a) Box-girder bridges, (b) I-girder bridges



(a) Straight Cables (b) Cables Looped over Bent-Cap

Fig. 2 Cable restrainers for steel superstructure movement joints

Recent earthquakes such as the 1987 Whittier Narrows Earthquake, the 1989 Loma Prieta Earthquake, the 1994 Northridge Earthquake and the 1995 Kobe Earthquake have provided a good opportunity to study the performance of bridge restrainers in bridges subjected to strong ground excitations. Reconnaissance reports following the 1989 Loma Prieta Earthquake found various cases where restrainers failed (Saiidi et al., 1993). During the 1994 Northridge Earthquake, several bridges which had been retrofitted with cable restrainers collapsed due to unseating at the hinges (Moehle, 1995). During the 1995 Kobe Earthquake, over 60% of all bridge structures in the Kobe area were damaged, costing approximately 10 billion U.S. dollars to repair (Comartin et al., 1995). In general modern bridges performed better than older ones. However, a major problem was excessive movement at the hinges due to bearing and restrainer failure.

The objective of this paper is to review the existing restrainer design methods, discuss the main results of the analytical studies and describe the already performed and upcoming experimental studies. Emphasis will be given to the description of the shake table test of in-span-hinge restrainers that is currently under development at the University of Nevada, Reno (UNR).

(4) to review current restrainer design procedures. The field study revealed that in the majority of the studied bridges restrainers were activated and, in most of the cases, performed well. It was also determined that restrainers should be analyzed as systems consisting of three components: (1) restrainer, (2) connecting hardware and diaphragms and (3) the superstructure adjacent to the hinge. Yielding of any of the components of this assembly depends on the available seat width of the bridge. In old bridges, which have narrow seat widths, yielding should not be allowed in any of the components of a restrainer assembly during a major earthquake because excessive movements would result in collapse. In new bridges, yielding is acceptable because seats are usually wide and cables can be easily replaced. The analytical study showed that restrainers indeed reduce hinge displacements and prevent collapse of the superstructure. Therefore, they should be used to maintain the overall integrity of the bridge structure even if analysis indicates that they are not needed. Furthermore, bridges with relatively soft frames and high ratio of number of hinges to number of spans may be more vulnerable to unseating. Restrainer forces were far more critical when the restrainer gap was reduced to zero. The conclusions also indicated that non-linear analysis should be used for restrainer design.

The damage and collapse of two-level viaducts in the Loma Prieta Earthquake prompted researchers at the University of California, Berkeley (UCB) to study their response (Singh and Fenves, 1994) using linear and non-linear finite element analysis. It was found that cable restrainers limited the out-of-phase motion between adjacent spans. The number of restrainers required by the CALTRANS method was found to be overconservative. It was also shown that relative displacements at hinges were larger when the input ground motions were non-uniform.

When the 1992 Landers and Big Bear Earthquakes occurred, the response of the Northwest Connector bridge in southern California was measured (Fenves and Desroches, 1994). Their study indicated that non-linear models were adequate for estimating the response of the bridge and were recommended over linear hinge models.

In 1994 researchers at the University of California, San Diego (UCSD) (Yang et al., 1994) conducted a parametric study of a two-frame bridge with an in-span hinge in order to investigate the influence of different bridge properties on the relative longitudinal displacements of hinges. The study considered the following parameters: (1) adjacent bridge frame stiffness, (2) restrainer stiffness, (3) earthquake intensity, and, (4) sliding friction and gap at the expansion joint. It was concluded that the CALTRANS design procedure is uncorsevative for cases where adjacent frames are out-of-phase and very conservative for cases where frames move in phase. This study also showed that both the expansion joint gap and the Coulomb friction between the bearing pads and the concrete surface had a small impact on the relative displacement between adjacent frames. Greater earthquake intensity increased frame displacements, as well as the maximum relative hinge displacement when the frames remained elastic. However, when non-linear behavior dominated the response, relative displacements did not change significantly with increasing earthquake intensity.

In order to evaluate the AASHTO and CALTRANS methods, researchers at the University of Washington (UW) (Trochalakis et al., 1995) modeled a two-frame bridge with an in-span hinge (Fig. 3). The non-linear response of the bridge was studied to determine the maximum opening experienced at the in-span hinge and the maximum relative displacements at the abutments. The following four parameters were found to be the most important in predicting the maximum relative hinge displacement: (1) restrainer stiffness, (2) restrainer gap, (3) frame period, and, (4)

frame stiffness ratio. Furthermore, the parametric study identified the following three variables as the most important in predicting the maximum relative abutment displacement: (1) abutment stiffness and strength, (2) sum of frame stiffnesses, and, (3) sum of frame weights. The AASHTO empirical seat width equation and the CALTRANS restrainer design method were compared with the results of non-linear time history analyses. The empirical seat width equation produced conservative results, even for very strong earthquakes. However, the AASHTO restrainer design procedure ignores variables that were shown to be very important in the parametric study. The CALTRANS method produced inconsistent results with a large amount of scatter. Using the results of the parametric study, the UW researchers developed a new restrainer design method based on the single-degree-of-freedom response of the two adjacent frames, using an equivalent stiffness representing the whole system. In this method, the mean response of both frames is determined and used in an empirical equation to determine the mean relative hinge displacement, which must be smaller than the available seat width.

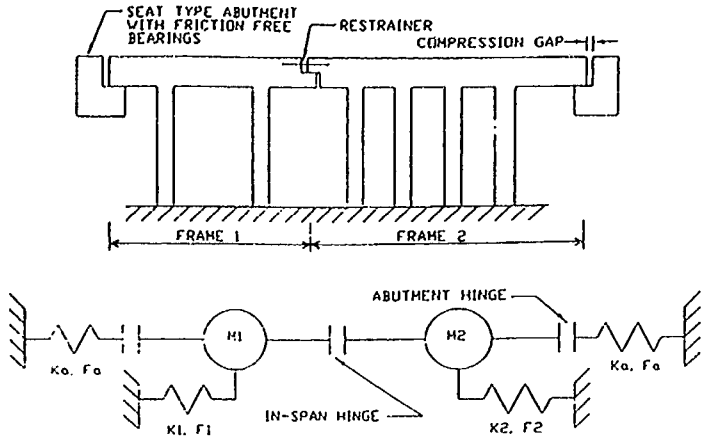


Fig. 3 Bridge Model Used for UW Parametric Study (Trochalakis et al., 1995)

In 1996 researchers at UCB also evaluated the CALTRANS and AASHTO restrainer design procedures and developed a new method for restrainers at in-span hinges (Fenves and Desroches, 1997). A non-linear numerical model was used to represent the longitudinal earthquake response of two frames connected at a hinge. The model included non-linear force-displacement relationships for the frames, while non-linear elements accounted for tension-only restrainers and Coulomb friction (Fig. 4). A parametric study showed that the hinge response is governed by the frame period ratio of the two frames adjacent to the hinge, the target ductility demand of the frames and the stiffness of the hinge restrainers. A multiple-step design procedure based on a linearized numerical method was developed. Parametric studies indicated that the procedure works well in limiting the relative hinge displacement for a wide range of parameters. The required number of restrainers decreases as the frame period ratio and the frame target ductility increase. A simplified single-step design procedure was also developed based on a non-dimensional value of the restrainer stiffness, which is determined by performing a large parametric study. Comparisons with current restrainer design procedures showed that the new

multiple-step and single-step procedures are more accurate than current procedures for designing hinge restrainers. The study also showed that pounding of frames and engaging of restrainers produce forces and displacements significantly different than what is typically assumed in design. Pounding typically increases the demand on stiffer frames and decreases the demand on the more flexible frames. Another conclusion drawn was that frames with higher ductility levels exhibit in-phase motion. Frames moving in-phase will experience smaller relative displacements and, thus, they will require fewer restrainers.

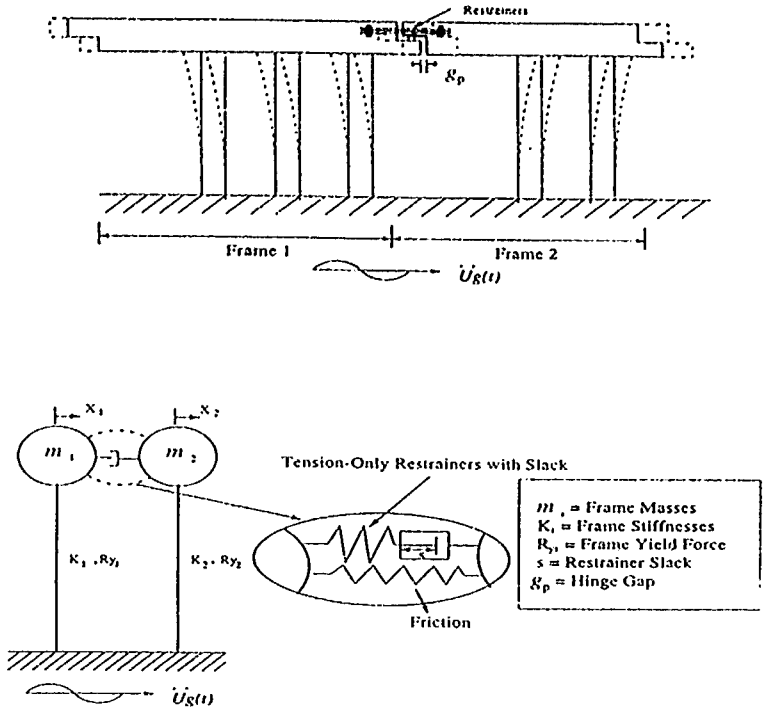


Fig. 4 Two Degree-of-Freedom Nonlinear Model for Longitudinal Response of Two Frames (Desroches et al., 1997)

A study to investigate unseating of simply supported spans was conducted by researchers at UW (Trochalakis et al., 1996). A set of 68 non-linear time history analyses was performed to determine the effects of varying six parameters including pier heights, abutment stiffness and strength, earthquake record and intensity, expansion joint gap, bearing stiffness and friction and restrainer stiffness. Restrainers were included in 16 analyses. The study concluded that bearing pad friction, earthquake record and intensity, as well as compression gap are the most significant parameters affecting the maximum relative displacement at a bearing support and that the maximum relative abutment displacement mainly depends on the bearing pad friction resistance and earthquake record and intensity. The study also found that restrainers were ineffective in reducing relative displacements of the simply supported bridges considered in the study. However, in this study restrainers were attached from span to span instead of span to bent cap, which is not a common restrainer configuration and is not typically used by CALTRANS.

In 1997 researchers at UW performed a study in order to examine the effects of spatially varying ground motions on the behavior of straight, two-frame bridges with unrestrained and restrained in-span hinges (Hudgings et al., 1997). The non-linear parametric study produced a 3600 case database of the maximum relative hinge displacement and maximum relative abutment displacement responses. Results from this study were used to develop a new comprehensive restrainer design method. It was found that the maximum relative hinge displacement of a two-frame bridge depends primarily on the frame stiffness ratio and restrainer stiffness, while the maximum relative abutment displacement is governed by the sum of the stiffnesses of both frames. The wave passage effect results in small increases in the maximum relative hinge displacements and has little impact on the maximum relative abutment displacements. The AASHTO minimum seat width equation proved to be conservative. Similarly, it was shown that the CATRANS restrainer design method does not predict the maximum relative hinge displacements accurately. Furthermore, both design procedures do not account for spatial variability of the input ground motions. The seismic bridge restrainer design method proposed by the UW researchers was able to produce rational, consistent and safe predictions of the maximum relative hinge displacements and also account for varying ground motions.

The most recent study on the performance of seismic restrainers was conducted by researchers at UNR in 1998 (Randall et al., 1998). The objectives of this study, which focused on bridges with simply supported spans, were: (1) to review the performance of longitudinal cable restrainers in past earthquakes, (2) to evaluate the adequacy of current restrainer design procedures, (3) to develop new restrainer design procedures that would prevent unseating, and, (4) to evaluate the adequacy of the new restrainer design procedures. Skew and non-skew, two- and five-span simply supported highway bridges with narrow and wide seats were modeled and studied (Fig. 5). Ground motions were applied in the longitudinal direction for non-skew bridges and in both the longitudinal and transverse directions for skew bridges. Abutments, superstructure, columns, foundations, restrainers, bearings and expansion joints were all included in models. Element behavior was assumed to be non-linear with the exception of the superstructure that was treated as elastic. Cable restrainers connecting spans to their seat in the longitudinal direction were the only type of restrainers considered. Three new design procedures were developed: (1) the Proposed method, (2) the W/2 method and (3) the Modified CALTRANS method. In addition to the development of these methods, which will be discussed in the following sections of the paper, it was shown that the bearing strength has a significant influence on the relative displacements at superstructure seats and should be considered in restrainer design. It was also shown that non-skew two- and five-span bridges do not need restrainers to prevent unseating if AASHTO seat width requirements are met. Finally, abutment restrainers were recommended unless wide abutment seats are provided.

4. New Restrainer Design Methods

As it was discussed in the previous sections of the paper, most of the analytical studies resulted in the development of new restrainer design methods for bridges with both in-span hinges and simply supported spans. These methods are summarized as follows:

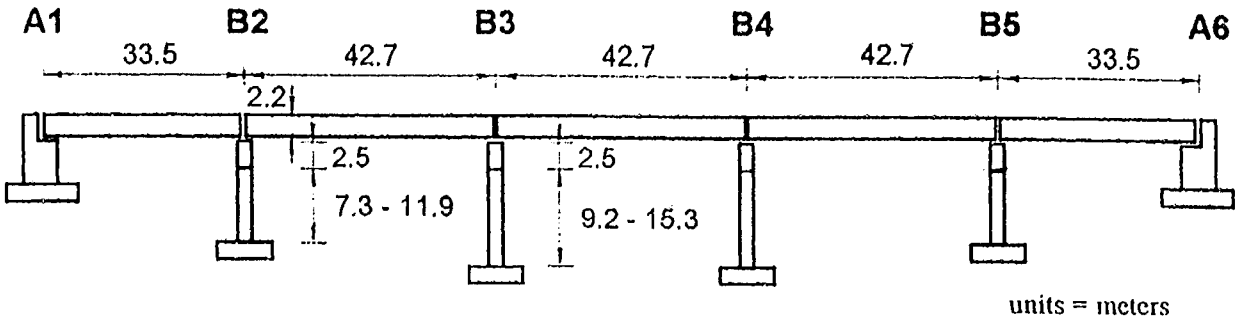


Fig. 5 Five-Span Bridge Elevation (Randall et al., 1998)

- ***University of California at Berkeley Restrainer Design Procedure***

In 1996 researchers at the University of California at Berkeley (UCB) developed a new multiple-step design procedure for restrainers at in-span hinges based on a linearized numerical method (Fenves and Desroches, 1997). The procedure accounts for the phasing between frames with a modal analysis. Yielding of frames was linearized by using a substitute structure method and optimization theory was used to obtain the restrainer stiffness. A simplified single-step restrainer design procedure for hinge restrainers was also developed based on a non-dimensional value of the restrainer stiffness, which was determined by performing a large parametric study.

- ***University of Washington Restrainer Design Methods***

Researchers at the University of Washington (UW) have also developed new restrainer design methods for both in-span hinges and simply supported spans (Trochalakis et al., 1995, Trochalakis et al., 1996 and Hudgings et al., 1997):

(1) Proposed Restrainer Design Method for In-Span Hinges

Using the results of a parametric study they conducted, the UW researchers developed a new restrainer design method based on the single-degree-of-freedom response of the two adjacent frames using an equivalent stiffness. The mean response of both frames is determined and used in an empirical equation to determine the mean relative hinge displacement, which must be smaller than the available seat width. The procedure incorporates many of the assumptions used in the CALTRANS method, but the new procedure relies on a different expression to estimate the maximum relative hinge displacement. Furthermore, it considers variables such as the restrainer gap and the frame period ratio that were ignored by the CALTRANS procedure but were shown to be very important in the parametric study that was carried out.

(2) Proposed Restrainer Design Method for Simply Supported Spans

In 1996 researchers at UW introduced this method for identifying simply supported bridges that are prone to span unseating. The new procedure is capable of predicting the maximum relative bearing displacement (MRBD) and the maximum relative abutment displacement (MRAD). These estimates can be compared with the available seat width to

determine whether retrofit is required. The method relies on an equivalent stiffness and a response spectrum to estimate the MRBD and the MRAD.

(3) Modified Restrainer Design Method for Spatially Varying Ground Motions

Three steps were added to the restrainer design method proposed by Trochalakis et al. for in-span hinges to account for the effect of spatially varying ground motions. A term describing the contribution of asynchronous ground motions was developed on the assumption that relative ground displacements induced pseudo-static relative frame displacements at the in-span hinge. Although the proposed iterative procedure is considerably more complicated than the AASHTO restrainer design method, the improved design efficiency can be considerable.

- ***University of Nevada, Reno Restrainer Design Methods***

The most recent restrainer design procedures were developed by researchers at the University of Nevada, Reno (UNR) in 1998 (Randall et al., 1998). The W/2, the Proposed and the Modified CALTRANS methods are hand analysis restrainer design methods for simply supported spans that were presented as alternatives to those specified by CALTANS and AASHTO:

(1) The W/2 Method

The objective of the W/2 method is not to prevent unseating but to prevent collapse. Hence, its main advantage is its simplicity. In this method restrainers on each side of the span must withstand one-half of the weight of the span they are restraining. The load to be resisted by the restrainers is treated as a static force even though the dropping of the span off the support would produce a dynamic force that is twice the static force. The W/2 method is an effective procedure for designing restrainers but its use should be limited to bridges that have wide seats and are not skew.

(2) *The Proposed Method*

The objective of this method is to limit longitudinal movement of adjacent bridge elements and to keep a bridge structure seated during strong earthquakes. It is similar to the existing CALTRANS method in that it uses response spectra to determine the force a restrainer set must withstand. However, it includes the effects of column, footing, abutment and bearing stiffness to determine an equivalent vibration period that is combined with response spectra to determine restrainer forces. Therefore, this method includes the effects of several elements of a bridge, while still keeping the procedure sufficiently simple so that an engineer may perform the analysis by hand. The Proposed method is recommended for use in all cases except for skew bridges with narrow seats when the substructure is very flexible.

(3) The Modified CALTRANS Method

The Modified CALTRANS method is a hybrid of CALTRANS and Proposed methods taking the best components of each. In this procedure, the connection between the span and bent must be evaluated first. If the connection has strength under seismic forces, a minimum number of restrainers is used. If the connection is insufficient, restrainers are designed according to the CALTRANS method. The Modified CALTRANS procedure is an effective method for designing restrainers to limit relative displacement at supports and prevent unseating and, therefore, it is recommended for use in all cases.

4. Experimental Studies

4.1 Full Scale Hinge Detail Static Test (University of California at Los Angeles, 1989)

In 1989 researchers at the University of California at Los Angeles (UCLA) (Selna et al., 1989) performed a full-scale structure experimental test in order to determine the strength, stiffness and cyclic load-deflection behavior of box-girder in-span hinge bridges, which had been retrofitted with longitudinal cable restrainers. The measured capacity of the retrofitted system was slightly greater than the design yield force of the restrainers. Furthermore, the failure occurred in the reinforced concrete hinge diaphragm due to deterioration resulting from combined bending and punching shear. The pullout failure near the middle of the diaphragm did not reduce substantially the vertical load carrying capacity of the hinge because the seat in the web or stem regions of the box-girder remained intact. However, if the horizontal displacement accompanying the failure exceeds the existing seat width, it can cause span collapse in hinges having narrow seats.

4.2 Shake Table Testing of In-Span Hinge Restrainers (University of Nevada, Reno, 1999)

- **Test Description**

A series of tests involving bridges with in-span hinges or simply supported spans, straight or skew retrofitted with restrainers are currently being developed at UNR. The first of these tests is related to straight bridges with in-span hinges retrofitted with cable restrainers. The primary goal of this test is to study the impact between adjacent spans at in-span hinges, the evaluation of the performance and effectiveness of the hinge restrainers under normal operating and failure conditions and the assessment of the performance of the shake table system when impact occurs. Since the impact between adjacent bridge segments causes high instantaneous forces and sudden changes of acceleration, phenomena such as out-of-phase motion and concrete pounding are also expected to occur. The specimen consists of two concrete blocks representing the adjacent parts of a reference bridge at an in-span hinge. The blocks were placed on one of the two shake tables available in the UNR laboratory and were supported by elastomeric bearings simulating the stiffness of the substructure (Fig. 6). The bearings have been designed such that their stiffness is equal to the scaled stiffness of the bent supporting the corresponding segment of the actual bridge. Lead plates were placed on each block as necessary to obtain the required mass values.

The final experimental design was based on a representative bridge, which was developed using the average dimensions of the following six typical existing CALTRANS bridges with in-span hinges: (1) Four Street Viaduct, (2) Rudgear Road Undercrossing, (3) South Walnut Creek Overhead, (4) Laurel Drive Undercrossing, (5) Tompkins Hill Road Overhead, and, (6) Danville Overhead. Most of them have been retrofitted with restrainers. The majority of this retrofit work involves installation of high-strength steel cables anchored to the diaphragms or webs at hinges and joints. Type C-1 restrainers were used in most of the cases. The elevation of the bridge model is shown in Fig. 7.

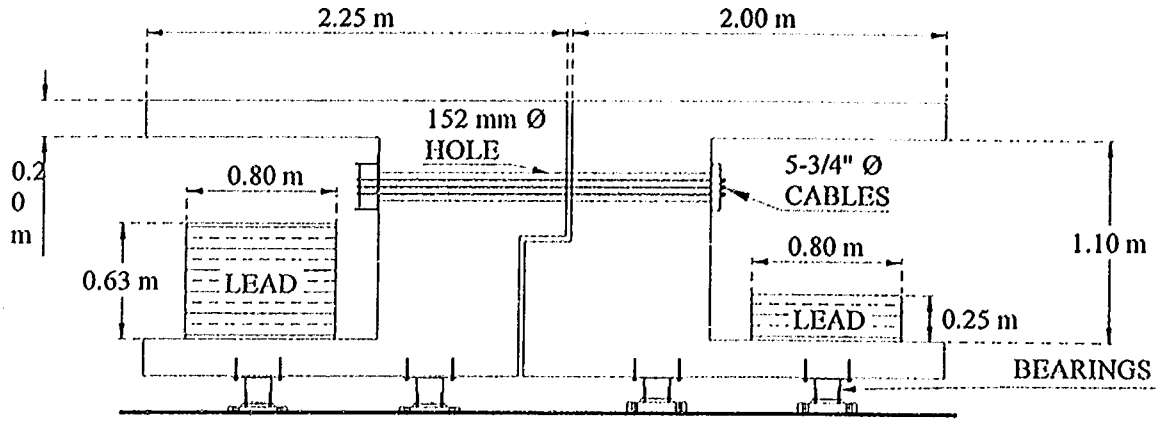


Fig. 6 In-Span Hinge Test Layout

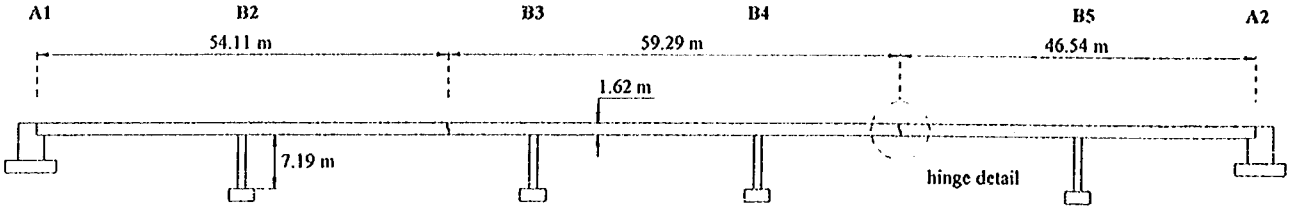


Fig. 7 In-span Hinge Average Bridge Elevation

In order to design the test specimen, the dynamic properties of the developed model bridge, including the superstructure mass and the substructure stiffness, had to be scaled down. Since dynamic response in the longitudinal direction only would be considered and skewness effects would be neglected, it was decided that the estimation of the mass of the superstructure could be based on 1/8 of the deck. Since the actual average bridge consisted of eight lanes, only one lane was considered. Further, in order to avoid in-phase motion and assure the impact of the two adjacent spans, only the heavier and the lighter of the bridge segments were considered. Finally, consideration had to be given not to exceed the capacity of the shake table (445 KN). Considering all these parameters, a scale factor of 1/4 was feasible, resulting in a total specimen weight of about 285 KN (64 kips).

Cable restrainers were used to connect the two blocks. The design of the restrainers was done according to the currently used CALTRANS restrainer design procedure (CALTRANS, 1994). The restrainers used were C-1 type with ¾" Φ cables. The restrainer gap was assumed to be 25 mm, which is a quite representative value according to the most commonly applied design procedures. A number of 20 cables (4 units of 5 cables each) 2.0 m long was estimated. It should be noted that this number corresponds to the actual unscaled bridge. To facilitate the fabrication of the specimen, it was decided not to scale down the area of each cable but the total number of restrainers based on the scale factor chosen for the entire model. Consequently, 1 unit of 5 cables was needed for the specimen. The restrainer system is shown in Fig. 6.

- **Analytical Model**

The personal computer software DRAIN 3DX was used in order to analyze the response of the specimen during a variety of earthquake excitations. The purpose of this analysis was to predict a range of values for the relative displacement at the hinge, to determine whether impact between the blocks will occur and estimate the restrainer forces. It was found that in the designed scaled specimen the restrainers will probably not fail under any of the earthquake records considered in the study. However, using a different combination of lead weights, and, thus, changing the masses of the two blocks, it was found that restrainer failure could occur. The specimen that would produce restrainer failure is the scaled model of a hinge with heavy spans supported by flexible bents. Based on these results, it was decided that a series of tests will be performed including the originally described specimen modeling the average representative bridge, and other specimens representative of structures in which restrainer failure is expected to occur. The instrumentation and final experimental set up are in progress at this moment.

5. Conclusions

The main scope of this paper was to demonstrate the main features of the currently used restrainer design methods and discuss the several new design procedures that have been recently developed. Further, a thorough review on the analytical and experimental studies investigating the dynamic performance of seismic restrainers in both the cases of simply supported spans and in-span hinges was presented. Emphasis was given to the upcoming shake table test of in-span-hinge restrainers that will be performed at UNR. By examining the fundamental results and conclusions of the individual studies presented in the paper, the following general conclusions can be drawn:

- The seismic response of in-span and simply supported span hinges is a highly non-linear phenomenon, including the interaction of several parameters such as the impact between the two spans, the restrainer and bearing non-linear stiffnesses, and the substructure stiffness, which includes the hysteretic bent and non-linear foundation effects.
- The current CALTRANS and AASHTO design methods do not account for several parameters that were shown to be very important in predicting the dynamic response of the hinges of the analytical studies. These parameters include the restrainer stiffness, the restrainer gap, the stiffness and period ratios of the adjacent frames, the bearing stiffness, the non-linear behavior of the bent, and the foundation effects. They also neglect both the abutment stiffness, which for shorter bridges could contribute significantly to limiting the hinge displacements, and the non-uniform excitation effects.
- The CALTRANS restrainer design method is an equivalent static analysis methodology. The method was proved to be uncorsevative when applied to bridges consisting of a combination of flexible and stiff frames, which are likely to experience out-of-phase motion during a strong earthquake. However, it is overconservative for cases of bridges with frames expected to respond in phase with each other.
- Since there have been no large scale experimental studies of in-span or simply supported span hinges with restrainers in the past, the upcoming shake table tests performed at UNR will provide a good opportunity to study the effectiveness of the restrainers, the overall

response of the hinges, the adequacy of current design methods, and the capability of the current analytical methods to predict the hinge response.

References

AASHTO (1996). "Standard Specifications for Highway Bridges," American Association of State Highway and Transportation Officials, Sixteenth Edition.

CALTRANS (1990). "Bridge Design Specifications Manual," California Department of Transportation.

CALTRANS (1994). "Memo to Designers, 20 – 3, 20 – 4," California Department of Transportation.

Comartin, C., Green, M., and Tubbesing, S. (1995) "The Hyogo – Ken Nanbu Earthquake," *Preliminary Reconnaissance Report*, Earthquake Engineering Research Institute, Oakland, CA., February.

Fenves, G., and Desroches, R. (1994)."Response of the Northwest Connector in the Landers and Big Bear Earthquakes," *Report No. UCB / EERC 94 – 12*, Earthquake Engineering Research Center, University of California, Berkeley, CA, December.

Fenves, G., and Desroches, R. (1997)."New Design and Analysis Procedures for Intermediate Hinges in Multiple Frame Bridges," *National Seismic Conference on Bridges and Highways*, Sacramento, CA, July, pp. 667 – 681.

Hudgings, T., Eberhard, M. O., and Stanton, J. F. (1997). "Design of Seismic Bridge Restrainers Considering Spatial Variation of Ground Motions," *Report No. SGEM 97 - 2*, Department of Civil Engineering, University of Washington, Seattle, WA, July.

Jennings, P. C. (1971). "Engineering Features of the San Fernando Earthquake of February 9, 1971," *Report No. EERL – 71 – 02*, Earthquake Engineering Research Laboratory, California Institute of Technology, Pasadena, CA, December.

Moehle, J. P. (1995). "Northridge Earthquake of January 17, 1994: Reconnaissance Report, - Volume 1 – Highway Bridges and Traffic Management," *Earthquake Spectra*, Vol. 11 (No. 3), pp. 287-372.

Priestley, M. J. N., Seible, F., and MacRae, G. (1992). "Design Guidelines for Assessment Retrofit and Repair of Bridges for Seismic Performance," *Structural Systems Research Project, Report No. SSRP – 92 / 01*, University of California, San Diego, CA, August, pp. 266.

Randall, M. J., Saiidi, M., Maragakis, E., and Isakovic, T. (1998). "Restrainer Design Procedures for Multi – Span Simply Supported Bridges," *Report No. NCEER 98/04*, Department of Civil Engineering, University of Nevada, Reno, NV, April.

Saiidi, M., Maragakis, E., and Feng, S. (1992). "An Evaluation of the Current CALTRANS Seismic Restrainer Design Method," *Report No. CCEER 92/08*, Department of Civil Engineering, University of Nevada, Reno, NV, October.

Saiidi, M., Maragakis, E., Abdel-Ghaffar, S., Feng, S., and O' Connor, D. (1993). "Response of Bridge Hinge Restrainers During Earthquakes – Field Performance, Analysis, and Design," *Report No. CCEER 93/06*, Center for Civil Engineering and Earthquake Research, University of Nevada, Reno, June.

Selna, L. G., Malvar, L., and Zelinski, R. (1989). "Bridge Retrofit Testing: Hinge Cable Restrainers," *Journal of Structural Engineering, ASCE*, Vol. 115 (No. 4), pp. 920-933.
Singh, S. and Fenves, G. L. (1994). "Earthquake Analysis and Response of Two – level Viaducts," *Report No. UCB / EERC 94 – 11*, Earthquake Engineering Research Center, University of California, Berkeley, CA, November.
Trochalakis, P., Eberhard, M. O., and Stanton, J. F. (1995). "Evaluation and Design of Seismic Restrainers for In-Span Hinges," *Report No. WA – RD 387.1*, Washington State Transportation Center, Seattle, WA, August.
Trochalakis, P., Eberhard, M. O., and Stanton, J. F. (1996). "Unseating of Simply Supported Spans During Earthquakes," *Report No. WA – RD 387.2*, Washington State Transportation Center, Seattle, WA, May.
Yang, Y. S., Priestley, M. J. N., and Ricles, J. (1994). "Longitudinal Seismic Response of Bridge Frames Connected By Restrainers," *Report No. UCSD / SSRP – 94 / 09*, Structural Systems Research Project, University of California, San Diego, La Jolla, September.
Yashinsky, M., Hipley, P., and Nguyen, Q., (1995). "The Performance of Bridge Seismic Retrofits During the Northridge Earthquake," Caltrans Office of Earthquake Engineering, June.

A Static Three - Dimensional Elastic - Plastic analysis of Steel Frame Bridge Piers

Motoaki TANAKA[1], Yuji SATO[1] and Hideaki KASABOU[2]

ABSTRACT

A simplified procedure of static and dynamic elastic-plastic analysis using beam element model is sought to be established to serve in the design of rigid-frame bridge piers. In order to derive the M-ϕ relation required for elastic-plastic analysis of the beam element model, a trial design was undertaken on a typical portal-form bridge pier with the lower part of the column filled with concrete, and this design was made the subject of static analysis based on a 3-dimensional finite element model, with the steel members represented by shell elements and the concrete filling by solid elements. The results of analysis substantiated the design concept that initial plastic buckling should take place in the region immediately above the concrete-filled support of the pier.

1. INTRODUCTION

The Southern Hyogo Prefecture Earthquake, 1995, inspired the initiation of numerous studies on the earthquake-resisting properties and design concepts of steel bridge piers. The studies have further extended to static and dynamic elastic-plastic analyses of self-supporting steel piers, including those that take account of local buckling[1),2)]. Nonetheless, there still remain problems awaiting solution in the domain of steel rigid-frame bridge piers and long-span bridges.

While many and various approaches are available for such analyses, ranging from treatment of an equivalent spring in single material-point system to detailed analyses for examining empirical phenomena, simplified analytical methods dispensing with unrealistic expenditure of time and cost are needed for practical applications that should usefully serve in design verification.

The present authors are seeking to establish a simplified procedure of static and dynamic analysis using beam element model, for the purpose of verifying the designs of rigid-frame bridge piers.

As a first step, a trial design was undertaken of a typical portal-form rigid-frame bridge pier based on a survey of existing examples, and additionally featuring a concrete-filled lower part of column. This design was then modeled in three

[1] Machinery & Structure Development Dept., Industrial Machine & Plant Development Center, Ishikawajima-Harima Heavy Industries Co., Ltd.

[2] Bridge Dept., Bridge Design Division, Ishikawajima-Harima Heavy Industries Co., Ltd.

dimensions for analysis by finite element method, representing the steel members by shell elements and the concrete filling by solid elements.

2. TRIAL DESIGN OF STEEL RIGID-FRAME BRIDGE PIER

2.1 Basic Concept Adopted in Trial Design

The steel rigid-frame bridge pier adopted for the trial design was of simple portal form, which is a most representative type of such pier. The frame height and spacing between columns was set at an average value derived from a literature search of existing simple rigid-frame bridge piers[3),4)], holding in view the eventual applications of the results to be obtained to the reinforcement of existing bridge piers for the purpose of enhancing their resistance to earthquake. For the members also, a commonly-adopted square cross section was adopted. Additionally, the lower part of the columns was filled with concrete.

Basically the dimensional parameters were chosen to conform with the 1990 edition (before the 1996 revision) of the Specifications for Highway Bridges[5),6)], which prescribes corner panels that are relatively thick, and hence more conducive to plastification in the lower part of column. In the present instance, the lower part of column being filled with concrete, the region of column close above the concrete filling would be considered most susceptible to plastification.

2.2 Key Specifications of the Trially Designed Rigid-Frame Bridge Pier

The tirally designed portal-form rigid-frame bridge pier is 12m high and 12m wide, with beam and columns of common 1.8m×1.8m box cross section. The columns are filled with concrete up to 3m from foot. The steel members are of SM490Y grade. The foregoing key specifications of the pier columns, together with some other values, are listed in Table 2-1.

Table 2-1 Principal specifications of trially designed rigid-frame bridge pier

ITEM	PARAMETER
Type	simple portal form rigid-frame
Column height	12m
Column spacing	12m
Column / beam cross section	1.8m×1.8m box form
steel grade	SM490Y
Height of concrete filling	3.0m

The bridge superstructure will impart its weight to the two supports with a force totaling 11,660kN(1,200tf). For deriving seismic load, a design horizontal seismic intensity of 0.33 was adopted.

Design calculation proceeded as schematized in Fig. 2-1, and the resulting cross-sections are as indicated in Fig. 2-2. The columns are not of uniform cross section from top to bottom, as it can be seen from the drawings of the parts designated SEC1 to SEC3. For SEC1 and SEC2, the web and flange have their panels and longitudinal ribs dimensioned as given in Table 2-2, which also indicates relevant parameters[7),8)].

Table 2-2 Key dimensions and parameters of trially designed rigid-frame bridge pier column sections (Dimensional unit: mm)

ITEM		SEC1		SEC2	
		Web	Flange	Web	Flange
Transverse rib interval	a	1850	1850	1850	1850
Panel width	b	1800	1740	1800	1764
Panel thickness	t	30	25	18	18
Number of panels	n	4	4	4	4
Longitudinal rib width	b_r	190	190	160	160
Longitudinal rib thickness	t_r	19	19	16	16
Longitudinal rib rigidity ratio	$\gamma_l / \gamma_{l.req}$	1.105	1.261	1.080	1.054
Longitudinal rib rigidity ratio	γ_l / γ^*	0.483	0.766	1.080	1.054
Parameters	R_R	0.328	0.380	0.546	0.535
	R_F	0.459	0.431	0.526	0.522
	λ_s	0.470	0.450	0.575	0.570

γ_l : Rigidity ratio of longitudinal ribs
$\gamma_{l.req}$: Requisite rigidity ratio of longitudinal ribs
γ^* : Minimum rigidity ratio of longitudinal ribs required from elastic buckling theory
R_R : Width / thickness ratio parameter of panel
R_F : Width / thickness ratio parameter of all ribs
λ_s : Short / long side length ratio parameter of ribs

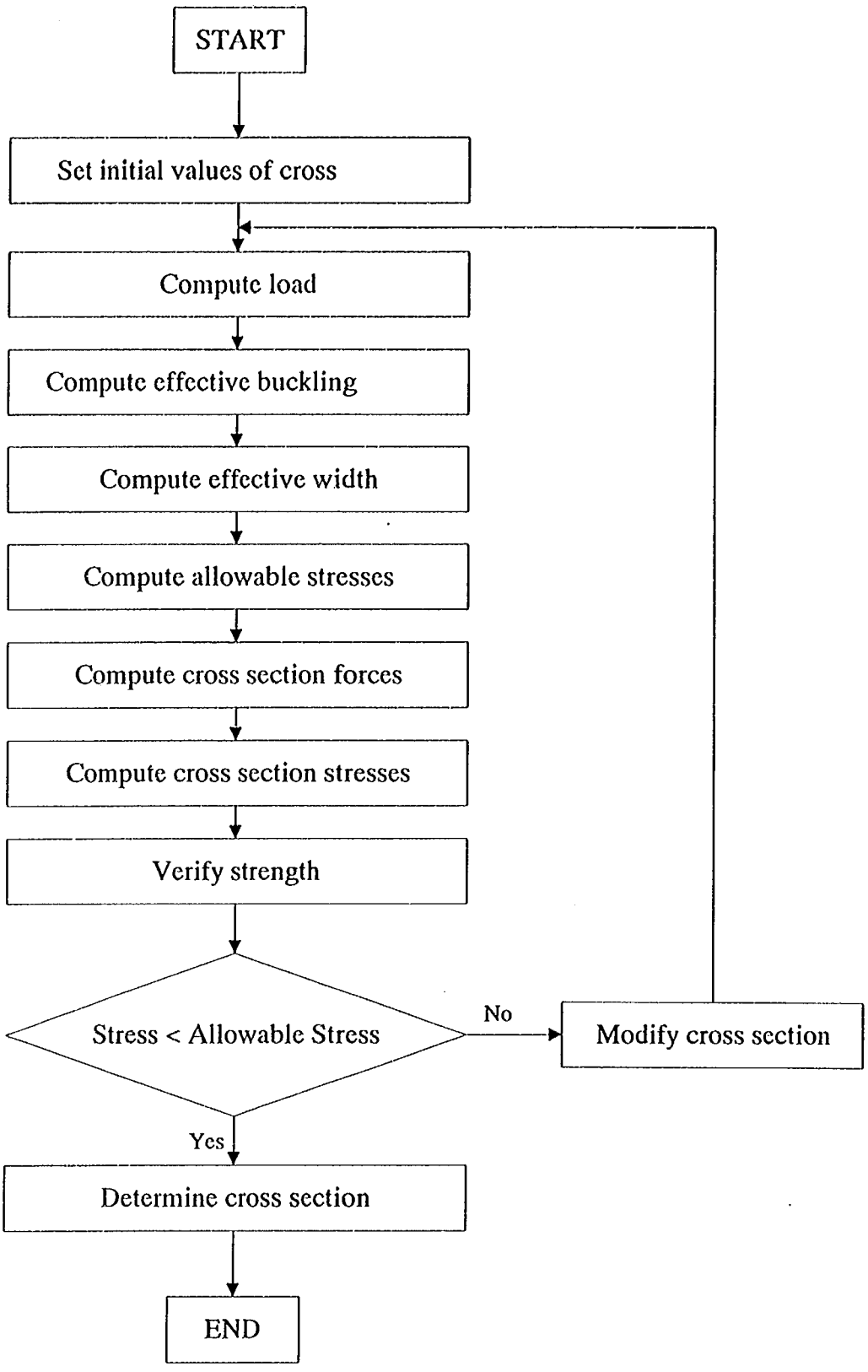


Fig. 2-1 Flow of trial design calculation

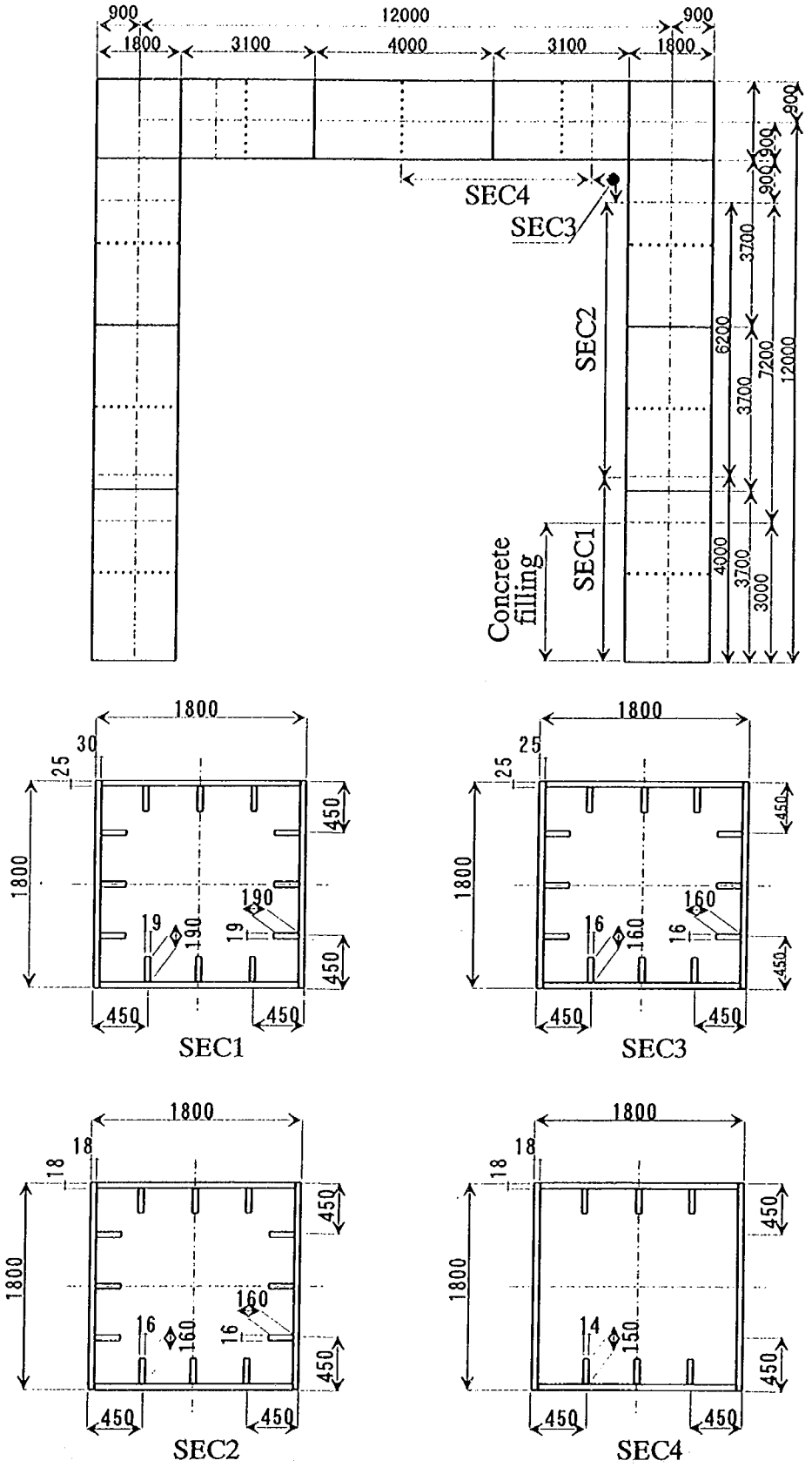


Fig. 2-2 Cross sections of trially designed rigid-frame bridge pier (Dimensional unit : mm)

3. METHOD OF ANALYSIS

3.1 Model

The trially-designed bridge pier was subjected to three-dimensional analysis of finite elastic-plastic displacements, using the general-purpose finite element analysis code ABAQUS. For economizing the cost of calculation, advantage was taken of system symmetry by adopting a model representing a half-module of the pier cut along a plane normal to bridge axis. The steel members were represented by shell elements, and the concrete filling by solid elements. The resulting finite element model is shown in Fig. 3-1, where it is seen that the portions likely to be susceptible to buckling are partitioned into finer elements. In the division into elements, simplicity was sought by adopting common nodal points for the steel members and solid concrete filling, i.e. without consideration given to stripping of concrete from steel surface.

3.2 Conditions of Analysis

Assuming the weight of pier to apply vertically, and the weight of superstructure [11,760kN (1,200tf)] to apply statically at the two beam supports, static analysis was performed to determine the force applying in the horizontal direction normal to bridge axis resulting from horizontal displacement at the two beam supports.

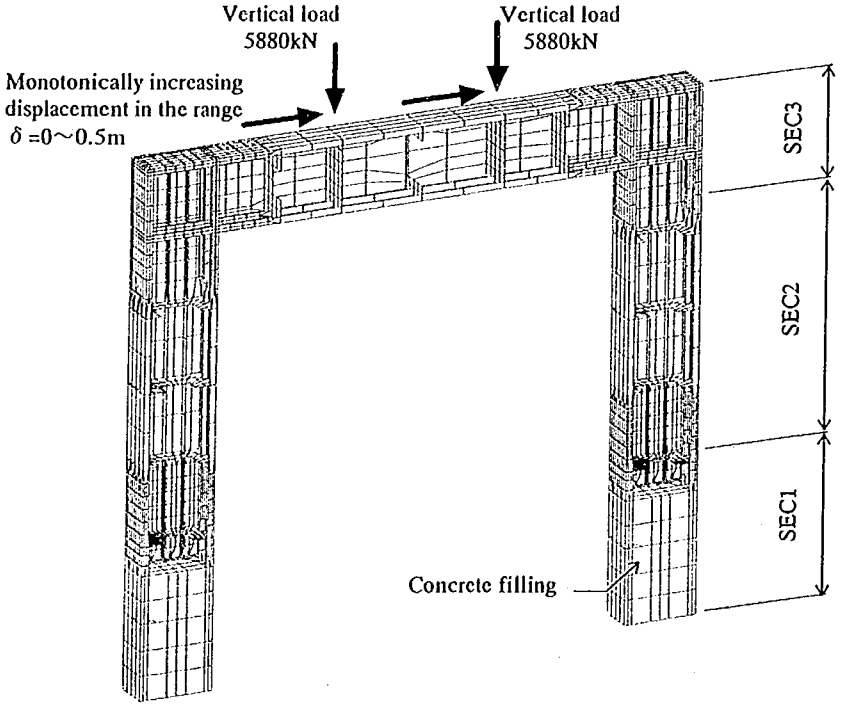


Fig. 3-1 Finite element model adopted for analyzing trially designed rigid-frame bridge pier (1/2 model)

Nonlinearity of the material properties and of the geometrical configuration was taken into account, the former nonlinearity being assumed to be as indicated in Fig. 3-2. For steel, the skeleton diagram adopted was of bilinear mobile hardening form, with secondary slope set at 1/100 of the primary slope, as indicated in diagram (a). For concrete, the skeleton curve[9] was drawn assuming little resistance against tensile stress, considering susceptibility of material to cracking. Against compressive stress, consideration was given to the constraining effect of the steel structure, which resulted in a linear relationship was maintained up to 10 times minimum design strength (σ_{ck}), beyond which complete elasticity was assumed against applied compressive stress, as indicated in diagram (b).

The adopted conditions of analysis and key parameters are indicated in Table 3-1.

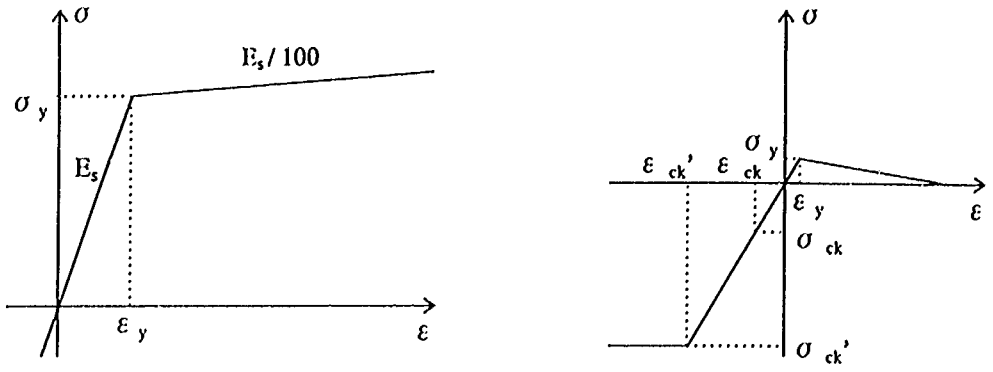
Table 3-1 Conditions adopted for analysis and other key values

ITEM	CONDITION OR VALUE ADOPTED	
Analysis code	ABAQUS	
Element considered	Steel	Shell element
	Concrete	Solid element
Nonlinearities considered	Material, geometry	
Material nonlinerities	Steel	Bilinear mobile hardening
	Concrete	Tension : cracking Compression : constraint of steel structure
Boundary conditions	Complete constraint at column bottom	
Loading conditions	Vertical	pier weight + Superstructure weight imparted at supports
	Horizontal	Monotonically increasing displacement up to δ =0.5m
Young's modulus	Steel	206GPa
	Concrete	23.0GPa
Poisson's ratio	Steel	0.3
	Concrete	0.15
Yield stress of steel	σ_y = 355MPa	
Concrete strength	σ_{ck} = 20.6MPa	
Work hardening ratio of steel	1 / 100	

4. RESULT OF ANALYSIS

4.1 Manner of Strain Propagation through Entire Pier

The manner in which strain propagates through the entire pier upon monotonic



(a) Steel
- Bilinear mobile hardening

(b) Concrete
- Against tension, cracking taken into account
- Against compression, elastic linear relation maintained up to $\sigma_{ck}' = 10\ \sigma_{ck}$ to account for constraint of steel structure

Fig. 3-2 Nonlinearity of material properties

loading in horizontal direction is reproduced in Fig. 4-1. The sequence of buckling strain generation in the columns is:

(a) On the right-hand column close above the concrete filling
(b) On the left-hand column close above the concrete filling
(c) On the right-hand column at the junction with horizontal beam.

The generation of initial buckling close above the concrete filling is as envisaged in design.

As easily imaginable, buckling strain upon monotonic loading is more prominent on the column whose lower part of the outer flange is subjected to compressive stress, i. e. the compression side column (right-hand side column in the drawing). The steel skeleton of the concrete-filled part of the column does not undergo buckling, which can be interpreted as simulating the actual case where no stripping takes place between concrete and steel surface.

Shown in Fig. 4-2 is the manner of stress evolution in the concrete-filled part of the right-hand column, in which buckling strain was the more prominent. Beyond around δ =0.076m (1.0 δ_y), the tensile stress applying on the tension side gradually lowers, accompanied by shifting of the neutral axis toward compression side. The region of lowing tensile stress can be considered to represent that of cracking, as considered in the modelization.

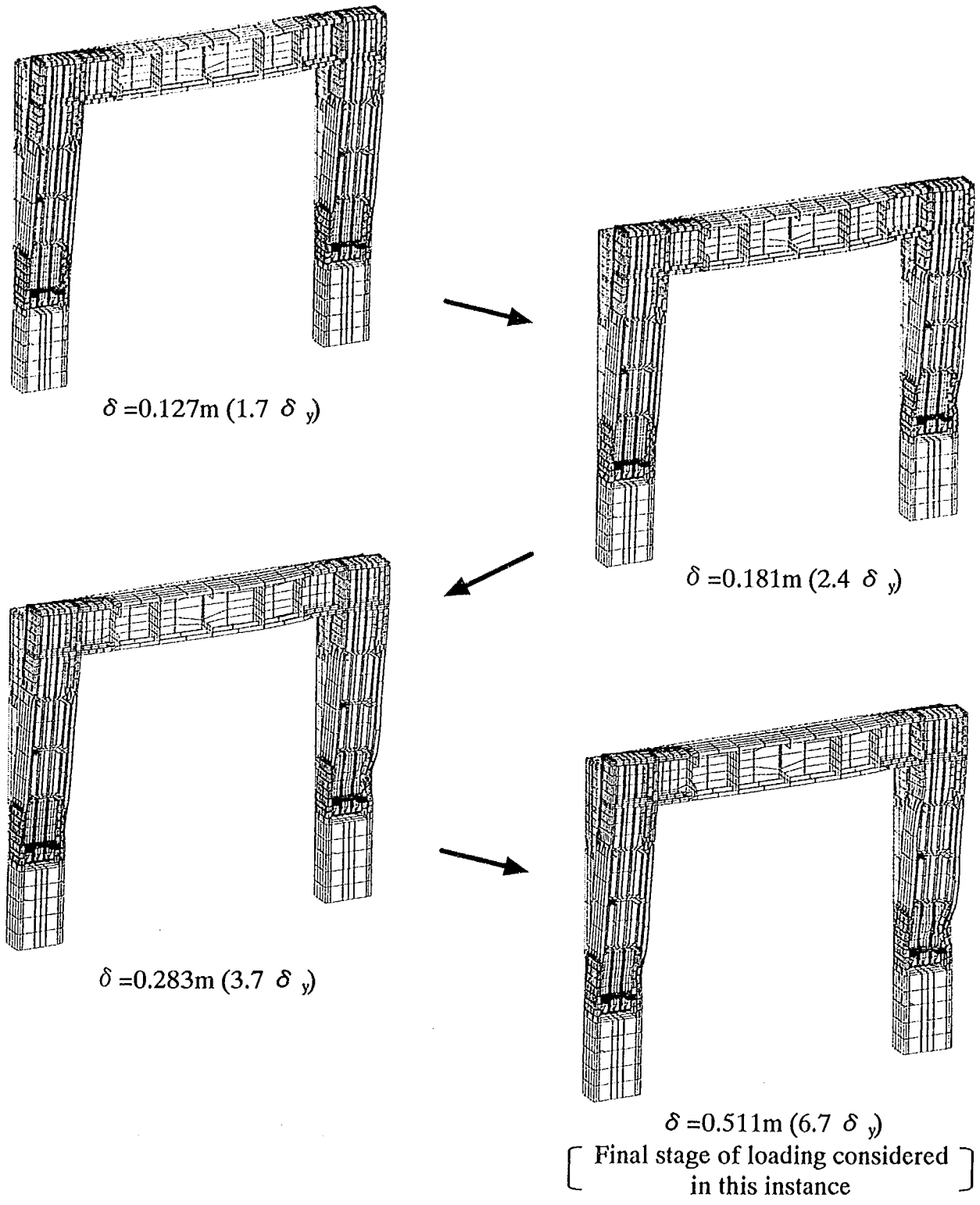


Fig. 4-1 Manner of strain propagation through entire pier upon loading in horizontal direction

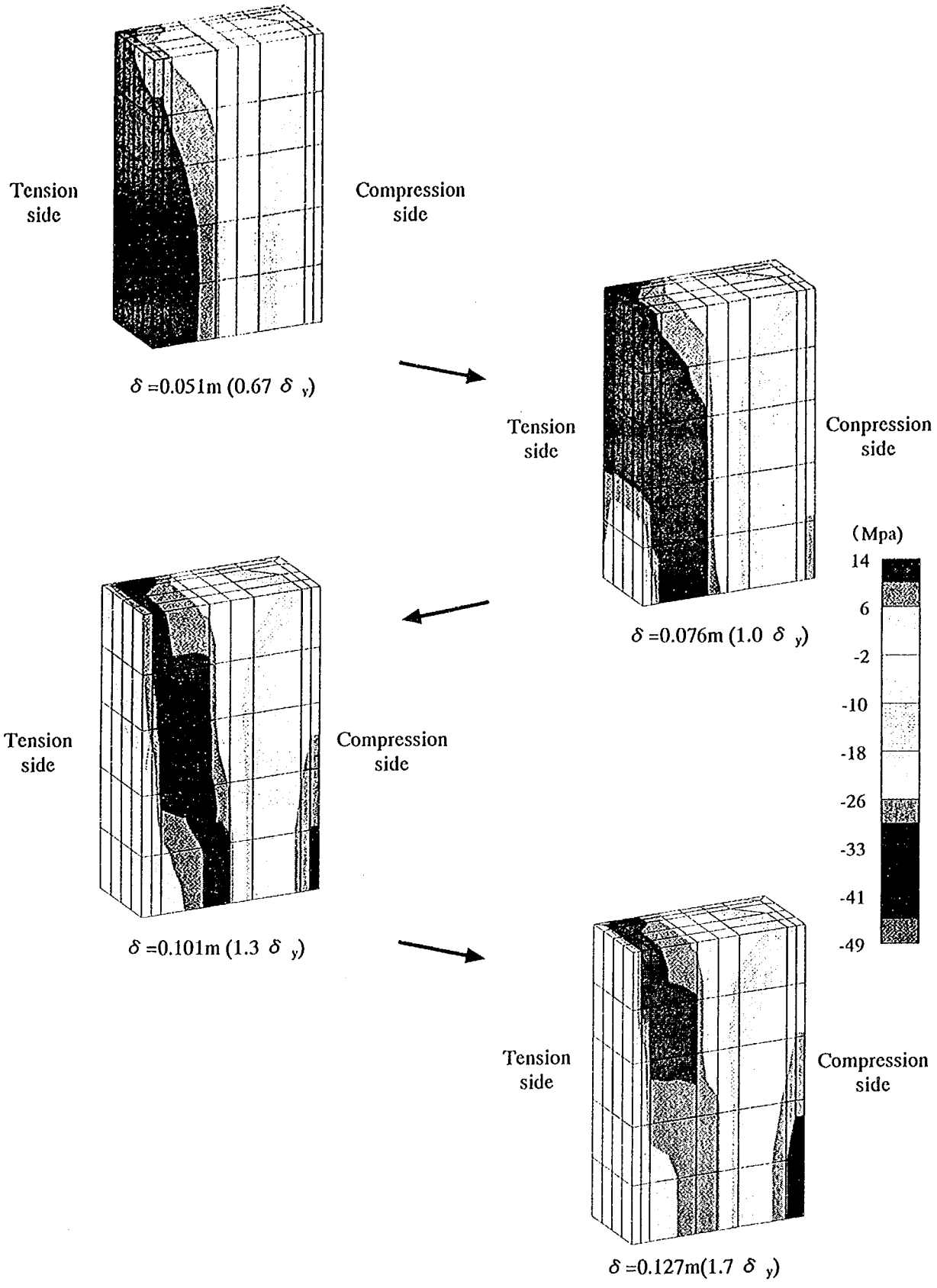


Fig. 4-2 Manner of stress evolution in concrete filling of right-hand column

4.2 Configuration at the Final Stage Considered in Analysis

Shown in Fig. 4-3 is an enlarged image of the right-hand side corner of the junction with horizontal beam at the final stage of loading considered in the present analysis, i.e. δ =0.511m (6.7 δ_y). Buckling is seen to have generated on the inner side flange immediately below the corner.

The region close above the concrete filling of the same column is shown similarly enlarged in Fig. 4-4, at the same final stage as the preceding Fig. 4-3. Close examination reveals the buckling to take place, not immediately above the concrete filling, but in the interval above, between the lower diaphragm and the reinforcing rib

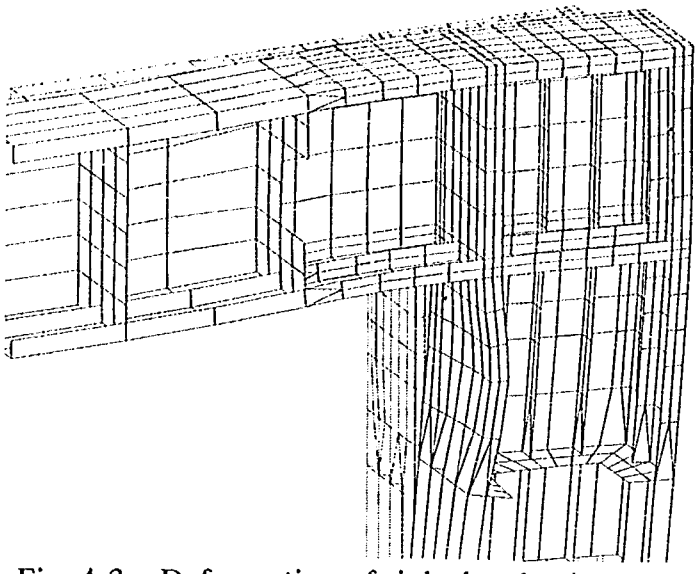


Fig. 4-3 Deformation of right-hand column below junction with beam, at final stage of loading, when δ =0.511m (6.7 δ_y)

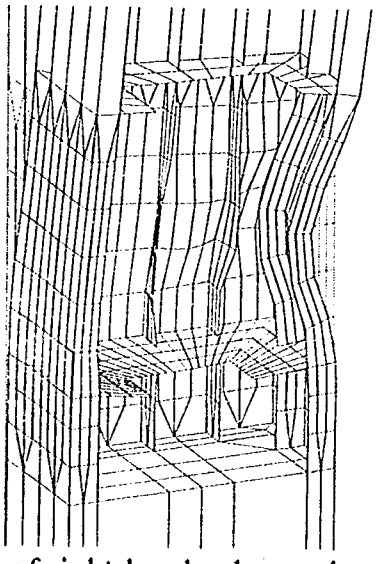


Fig. 4-4 Deformation of right-hand column close above concrete filling, at final stage of loading, when δ =0.511m (6.7 δ_y)

immediately above. The reason for the buckling not taking place in the interval immediately above the concrete filling is presumably the shortness of this interval, which enhanced the rigidity of this part.

The diagram further reveals the web to be deformed into wavy pattern, opening out the free end of longitudinal rib, which is indicative of buckling to the extent that will tilt the column. The longitudinal rib has been subjected to tensile stress exceeding yield strength.

4.3 P- δ curve

The P- δ curve, relating load to displacement, derived from analysis, is reproduced in Fig. 4-5, where the yield displacement has been timed to correspond to that at which the structural steel at the foot of the compression side column became stressed to yield point. The displacement at this point was δ_y=0.076m, when the load reached 20,160kN (2,057tf) and the horizontal displacement δ =0.282m.

In Fig. 4-6 is indicated the relation to horizontal displacement shown by the vertical membrane strain of the flange of the compression (outer) side column at the plane of symmetry (column center in direction normal to bridge axis), close above the concrete filling, where the buckling strain was the most prominent. It is seen that the strain on this outer side flange intensifies sharply from around horizontal displacement δ =0.1m. This displacement corresponds to that at which, in the P- δ curve of Fig. 4-5 yielding became prominent, indicating that the buckling strain of the part close above the concrete filling strongly affects the load-resisting performance of the entire pier.

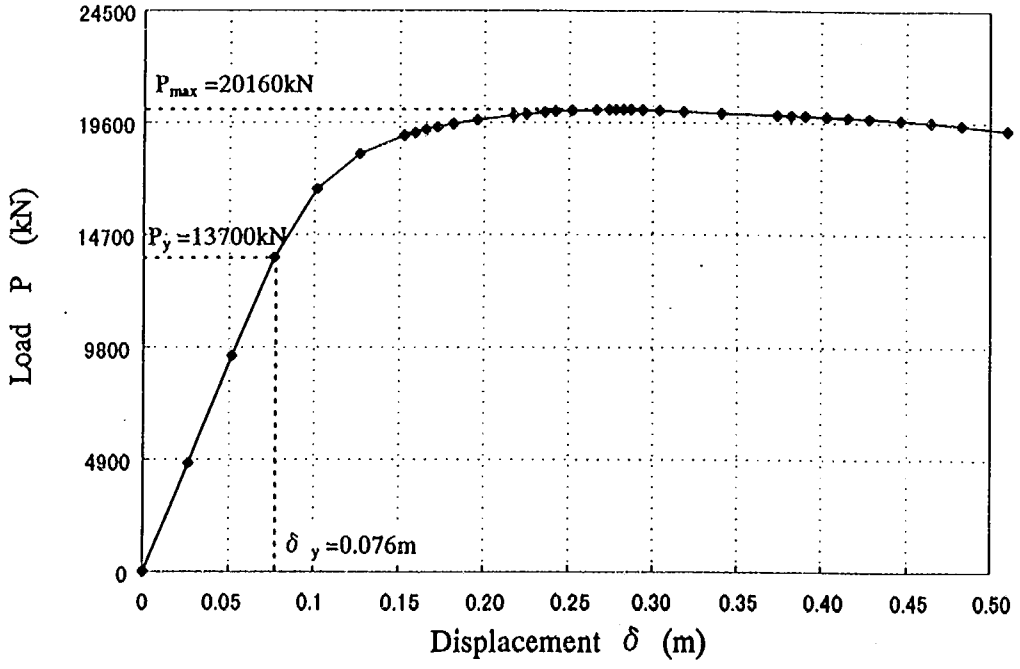


Fig. 4-5 Load vs. Displacement (P- δ) curve

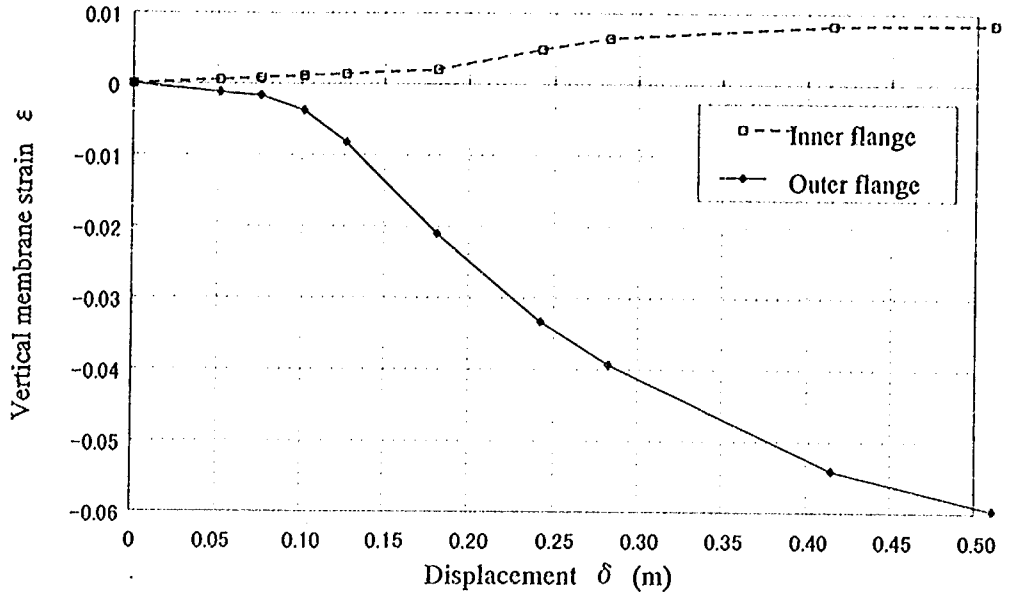


Fig. 4-6 Deformation vs. Displacement (ε - δ) curve of flange close above concrete filling

5. CONCLUDING REMAKS

The present authors are currently undertaking a study aimed at establishing a procedure of analysis based on beam element model, as a simplified means of static and dynamic elastic-plastic analysis to serve in the design of rigid-frame bridge piers. As a first step, for the purpose of deriving the M- ϕ relation required for elastic-plastic analysis of beam element model, a trial design was performed of a representative form of portal-form rigid-frame bridge pier with concrete-filled lower part of column. This rigid-frame bridge pier was made the subject of static analysis based on a 3-dimensional finite element model incorporating the concrete filling. The analysis revealed the following facts:

(1) Similarly to the actual case of no stripping between steel and concrete surfaces, the steel skeleton of the concrete-filled part of column proved not to undergo buckling.

(2) As envisaged in design, the sequence of generation of local buckling proved to be :
   (a) On the right-hand side column close above the concrete filling
   (b) On the left-hand side column close above the concrete filling
   (c) On the right-hand side column at the corner of junction with horizontal beam.

(3) In the steel piers of the rigid-frame bridge taken up in the present instance, buckling strain proved to be more prominent on the column whose lower part

of the outer flange is subjected to compressive stress, i.e. the compression side column.

(4) In the steel piers of the rigid-frame bridge taken up in the present instance, the displacement at yield point δ_y proved to equal 0.076m, when the load reaches 20,160kN (2,057tf), and the horizontal displacement δ =0.282m.

The results obtained above are to be utilized for further deriving the M-ϕ curves individually for each cross section, with which to perform static and dynamic elastic-plastic analysis, the results of which are to be compared with experimental data and other analytical results, with the aim of verifying the applicability of the present procedure.

REFERENCES

1) "Draft Guidelines for the Earthquake-Resistant design of Steel Bridges and New Techniques Applicable to Earthquake-Resistant Design", Japan Society of Civil Engineers - Committee on Steel Structures - Subcommittee on New Techniques of Steel Structures - Working Group on Earthquake-Resistant Design, July 1996
2) "Manual for Earthquake-Resistant Design of Steel Bridge Piers", Japan Association of Steel Bridge Construction, November 1998
3) Nakai et al.: "Survey of Steel Rigid-Frame Bridge Piers - Part 1", Bridge and Foundation Engineering, Vol. 16, No. 6, June 1982
4) Nakai et al.: "Survey of Steel Rigid-Frame Bridge Piers - Part 2", Bridge and Foundation Engineering, Vol. 16, No. 7, July 1982
5) "Specifications for Highway Bridges - Explanatory Supplement - Part V Seismic Design", Japan Road Association, February 1990
6) "Specifications for Highway Bridges - Explanatory Supplement - Part I General Part II Steel Bridges", Japan Road Association, February 1990
7) "Guidelines for Stability Design of Steel Structures", Japan Society of Civil Engineers, 1987
8) T. Usami: "High Ductility Steel Bridge Piers", Bridge and Foundation Engineering, Vol. 31, No. 6, June 1997
9) "Standard Specifications for Design and Construction of Concrete Structures - Part I Design", Japan Society of Civil Engineers, 1996

NOTE:

All the above publications are in the Japanese language.

CYCLIC TESTING OF COMPOSITE CONCRETE-FILLED CIRCULAR TUBES AND FOUNDATION DETAIL

Michel Bruneau[1] and Julia Marson[2]

Abstract

Four concrete-filled steel tubes were subjected to cyclic loading, with two of the columns having greater diameters than had been previously tested in North America. The steel tube of the test specimens had the following sizes: HSS 324 x 6.5, HSS 324 x 9.5, HSS 406 x 6.5, and HSS 406 x 9.5 (metric designation), and was filled with normal strength concrete. A foundation detail was designed to ensure that the full moment capacity of the composite column could be developed at its base without failure of the foundation. Each specimen developed its full moment capacity and exhibited excellent ductility up until drifts of 7%.

Introduction

According to the design philosophy prevailing in North America, bridges are designed to ensure that during an earthquake, their superstructure remains elastic while their substructure yields and behaves in a ductile manner. Currently in North America, nearly all new highway bridge substructures are constructed of reinforced concrete, even when bridges have a steel superstructure. Undeniably, the reinforced concrete industry has developed an expedient and inexpensive formwork method for those piers that currently gives them an economic advantage. However, in view of the growing worldwide emphasis on ductile detailing and sound earthquake resistance design, composite steel piers may be an economically viable concept worthy of consideration. Concrete-filled box-columns are popular in Japan, but direct import of the Japanese practice to North America is not likely; Japanese bridge engineers seem to favor rectangular pier cross-sections with many stiffeners, resulting in relatively expensive detailing. Furthermore, in Japan, concrete is typically only added for a few metres to enhance impact resistance of the pier in the event of a vehicle collision, and composite action is not considered (Kitada 1998).

Unstiffened circular tubes filled with concrete could be more viable in North America, and have other advantages over reinforced concrete piers. Among those: (a) The steel tube provide some confinement of the concrete and permits development of the full composite capacity of the column, with stable seismic energy dissipation; (b) All the concrete in the member contributes to strength and ductility of the member as concrete spalling does not occur; (c) The steel shell acts as the formwork for the concrete in a concrete-filled steel column; (d) Construction of the bridge may be accelerated if the steel shell alone can provide resistance to dead-load; (e) The steel components can be fabricated off site in a controlled environment; (f) The concrete core delays local buckling of the steel tube, and prevent its

---

[1] Professor and Deputy Director of Multidisciplinary Center for Earthquake Engineering Research, State University of New York at Buffalo, 105 Red Jacket Quadrangle, Buffalo, NY, 14261, (716) 645-3391x104, fax: (716) 645-3399.

[2] Harmer Podolak, 39 Robertson Road, Suite 221, Nepean, Ontario, Canada, K2H 8R2

inward buckling, also enhancing ductility of the composite columns; (g) Rebars are unnecessary in the concrete; (h) There is no need for stain protection on piers when the superstructure is of weathering steel (although some protection may be necessary at the base depending on the particular detailing used, it can be accomplished easier there), and; (i) The final aesthetics of a concrete-filled steel column are compatible with current bridge design practice.

The potential economical advantages of concrete-filled steel columns in tall buildings have long been recognized (Tarics 1972). In North America and Australia, concrete-filled steel columns have recently been used in some buildings (Bauer 1988, Engineering News-Record 1989, Webb and Peyton 1990), and much earlier in non-building applications, as pylons for hydroelectric lines in Switzerland (Preiswerk 1948, Vogeli 1948,1950) and as piles for railway bridges (Committee No. 30, 1954). A four level interchange was built in Almondsbury, UK and supported on concrete-filled steel piers (Kerensky and Dallard 1968). This suggests that filling a steel tube with concrete can be cost-effective, which, when coupled with their expected good strength and ductility, makes then desirable to provide seismic performance.

Literature Review

A literature review revealed that while a significant number of axial compression tests have been conducted, there has been far fewer flexural cyclic tests. From the results of seven researchers who have looked at forty-nine circular columns subjected to both axial and bending forces, only twelve columns have been subjected to cyclic loading. Furthermore, in these studies, the largest circular concrete-filled column subjected to cyclic loading had a diameter of 320 mm and a steel shell thickness of 6 mm. Most researchers welded the base of the steel tube to a thick steel plate (sometimes with thick base stiffeners) rather than providing a base connection representative of what could be encountered or constructed in the field. It also appears that the adequacy of the bond between the two materials during cyclic testing, and whether the concrete core becomes tri-axially confined by the steel tube, remain contentious unresolved issues.

Experimental Set-up

The test-set up shown in Figure 1 was used to apply a constant axial compressive load to the columns prior to application of the cyclic lateral load. The total column height from the top of the concrete foundation to the point of applied lateral load was 2.2 metres.

This study tested four concrete-filled steel tubes under cyclic loading, with two of the columns having greater diameters than had been previously tested in North America. The steel tube of the test specimens had the following sizes: HSS 324 x 6.5, HSS 324 x 9.5, HSS 406 x 6.5, and HSS 406 x 9.5 (metric designation), and was filled with normal strength concrete. Analytical work was performed to ensure that the test columns chosen would be representative of full-scale bridge piers found in North America. A foundation detail was designed to ensure that the full moment capacity of the composite column could be developed at its base without failure of the foundation. To achieve this, the steel tube was welded to a thick bottom plate, two C channels were placed against the steel tube and were welded longitudinally to the steel plate, and a smaller top plate with a hole in the middle was slipped down and welded to the top flanges of the two channels. This is schematically illustrated in

Figure 2. This assembly was designed to distribute the full plastic moment from the composite column to the ends of the channels, relying on the strength of the steel alone, and was then entirely encased in a concrete foundation.

Experimental Results

The four specimens were tested under a constant axial load and subjected to an increasing cyclic horizontal force applied at the top of the column. The columns were subjected to two or three cycles at each specified drift levels ranging from 0.25% to 7% drift. The resulting hysteretic curves are shown in Figure 3.

All four columns sustained drifts of 7% before failure occurred. Local buckling began to develop near the base of the columns during the cycles at 2% - 3% drift levels. These buckles grew during the following cycles. During the cycles at 7%, large transverse cracks opened near the buckles and caused a significant drop in moment carrying capacity of the column; this was defined as failure. The evolution of this local buckling is illustrated in Figure 4-6 for three of the four specimens tested. The foundation design was successful in allowing the composite column to reach its full moment carrying capacity during the tests.

Analysis of test results showed that, in all cases, the maximum moment location of the concrete-filled columns was below the top of the concrete foundation. Using information from the strain gauges positioned on the steel tube, the maximum moment appeared to occur at the most, 100 mm into the concrete foundation. The strain gauge results indicated that the steel sections used in the foundation were subjected to insignificant stresses, and that the concrete foundation likely provided most of the resistance. The P-Δ effects on the four tested specimens were significant, and show that these should be considered in analysis.

Subsequent analytical work lead to two new proposed design equations. These produce axial-flexure interaction equations in much better agreement with the existing data than the equations for circular concrete-filled steel tubes currently used by the Canadian CAN/CSA-S16.1-M94 standard, or American AISC LRFD 1994 Specifications. A computer program was also written to investigate the behavior of the four tested specimens. Many models were considered but with poor correlation with the data. Using an unconfined concrete model with high ductilility (caused by the confinement of the steel tube) and a bilinear stress-strain model for the steel tube, a good representation of the force-displacement envelope for the four specimens was obtained.

Recommendations for Future Research

The results from this study have been encouraging. However, these results also show that improvements can be made in the foundation design to make it both more effective and economical. More experimental study on concrete-filled steel tubes involving cyclic tests, with larger diameter specimens, and optimized foundation design, are recommended.

In particular, the foundation detail can be improved, particularly to reduce the size of the channels and transfer plates, if the design concept of the base assembly also relies on the concrete rather than on the steel alone. This can translate into smaller required base channels, itself an important improvement to the concept. Using the conservative design approach followed for these tests, the size of the channels that would be needed to accommodate large

diameter concrete-filled steel columns could become excessive, beyond the largest available rolled section sizes. A "leaner" foundation detail may also permit a simpler test set-up, and eliminate the need for local reinforcing in the concrete foundation under the actuator's reaction points. This will further simplify the foundation construction, as it will only consist of steel components fabricated off-site and placed in rectangular shoring that is filled with unreinforced concrete. Likewise, the amount of concrete cover above the top plate of the foundation in this study was dictated by the reinforcement needed in the foundation for cross-width transfer of the actuator's reaction points. New research could also seek to determine the required thickness of the concrete cover needed above the top of the steel base assembly. Since this concrete braces the top plate against buckling when pushed on by the concrete-filled steel tube, its failure could jeopardize the seismic performance of that detail, and due attention must be paid to this point. Future tests will also require that instrumentation be placed around the area of maximum moment in the tube to more accurately capture the moment gradient along the tube's base than what was done in this study.

More tests are also needed to fully understand the issues of bond and tri-axial effects. Full composite action of the steel tube and concrete core requires the development of shear at the interface between the two materials, either through friction, bond strength, or by artificial means such as shear studs. The specimens tested in this study clearly developed composite action, because their moment resistance exceeded that of the steel tube alone. However, after the tests, when a part of the steel tube was cut from the column, there was no evidence of bond between the concrete core and the steel tube. These two contradictory observations along with the discrepancy between previous researchers on this same topic illustrate a need for further research.

In some cases, tri-axial effects are seen in the concrete core. With low *D/t* and *L/D* ratios, the steel tube effectively confines the concrete core, increasing the strength of the concrete beyond its unconfined compressive resistance. However, as the size of the column increases, it is unclear whether concrete confinement will still be as effective. This study has shown that slightly larger specimens can still maintain concrete confinement. However, larger specimens must be tested to fully investigate the issue of concrete confinement.

Conclusions

In this study, four concrete-filled steel tubes were subjected to both an axial load and a cyclic bending moment. The diameter of these columns were 324 mm and 406 mm, with a D/t ratio ranging from 34 to 64. Based on the work conducted, it is concluded that:

- The ductility of all tested columns was good, all columns being able to reach drifts of 7% before a significant loss in moment capacity occurred as a result of cracks opening on the local buckles.
- The maximum flexural strength of all columns was reached at approximately 4% drift and was larger than the moment resistance of the steel tube alone.
- Strength deterioration after the maximum strength was reached was slow until fracture occurred during cycling at 7% drift.
- The favorable hysteretic curves produced from the tests showed good energy dissipation for all columns.
- The foundation detail worked well, ensuring that full moment resistance capacity of the concrete-filled steel column could be developed during testing.
- Data shows that the proposed foundation detail could be significantly optimized.

- No significant bond was seen between the steel tube and the concrete core after testing had been completed.
- New design equations have been developed for combined axial and bending moments, and correlate well with the results from this test and from tests by other researchers.
- A proposed new axial-flexure interaction equation for design is currently being considered for possible implementation in the next edition of the Canadian CSA-S16.1 standard (Limit State Design for Steel Structures), and the next edition of the AASHTO seismic provisions.

This study demonstrates that concrete-filled steel tubes can be a viable alternative to bridge piers in North America, up to the column sizes tested in this study. However, more knowledge will permit to significantly reduce the foundation sizes, to better understand details of the behavior, and to investigate whether larger columns would exhibit the same good behavior.

Acknowledgments

This research program was funded by the Natural Science and Engineering Research Council of Canada and the Structural Steel Education Foundation. This support is sincerely appreciated. However, the opinions expressed in this paper are those of the writers and do not reflect the views of the aforementioned sponsor or individuals.

References

Kerensky, O. and Dallard, N. "The Four-Level Interchange between M4 and M5 Motorways at Almodsbury," Proceedings, The Institution of Civil Engineers, Vol. 40 July, 1968. pp295-322.

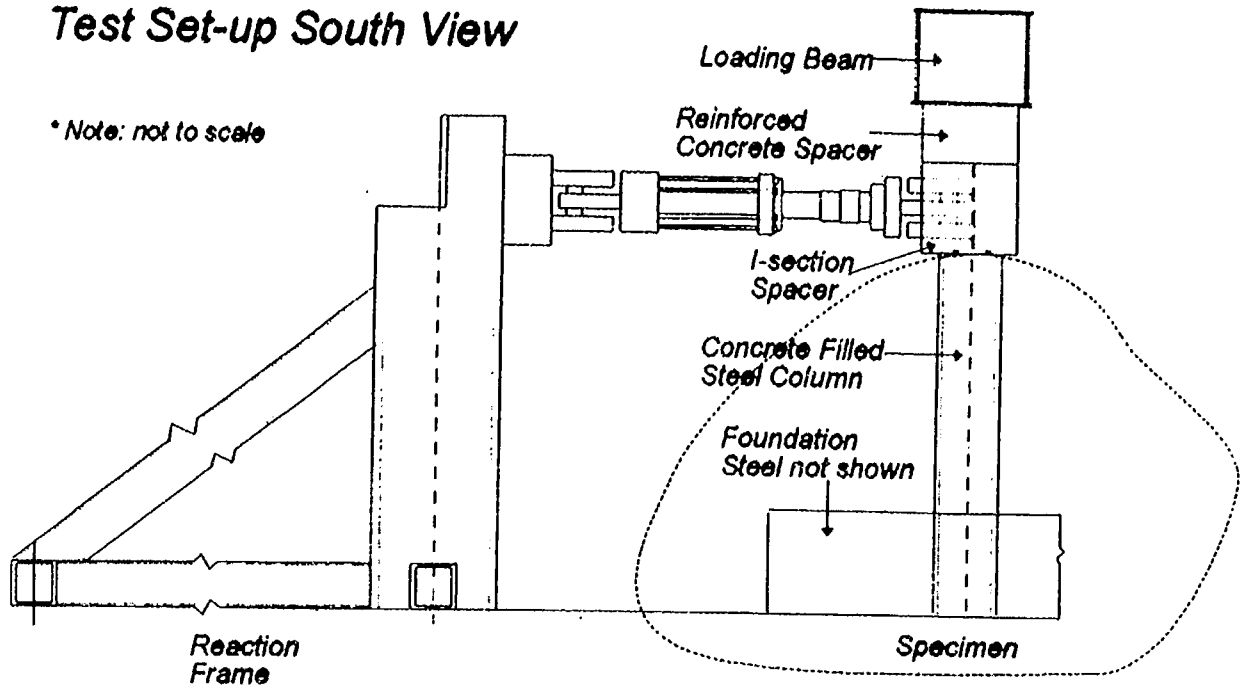
Kitada, T. "Ultimate Strength and Ductility of State-of-the-Art Concrete-Filled Steel Bridge Piers in Japan." Engineering Structures, Vol. 20, Nos. 4-6, pp 347-354. 1998.

Preiswerk, M.. "Application of New Methods of Construction on the High Mountain Transmission Line which crosses the Col du Nufenen" The International Conference on Large Electric Systems, 12th session, Vol.2 No. 220. 1948.

Tarics, A.G. "Concrete-Filled Steel Columns for Multistory Construction," Modern Steel Construction. Vol. 12, AISC 1972, pp 12-15.

Vogeli, R. "Steel Tube Pylons Filled with Concrete," The International Conference on Large Electric Systems, 12th session, Vol.2 No. 221. 1948.

Webb, J. and Peyton, J. "Composite Concrete Filled Steel Tube Columns" Proceedings, 2nd National Structures Conference, The Institution of Engineers, Australia, Adelaide, pp. 181-185. 1990.



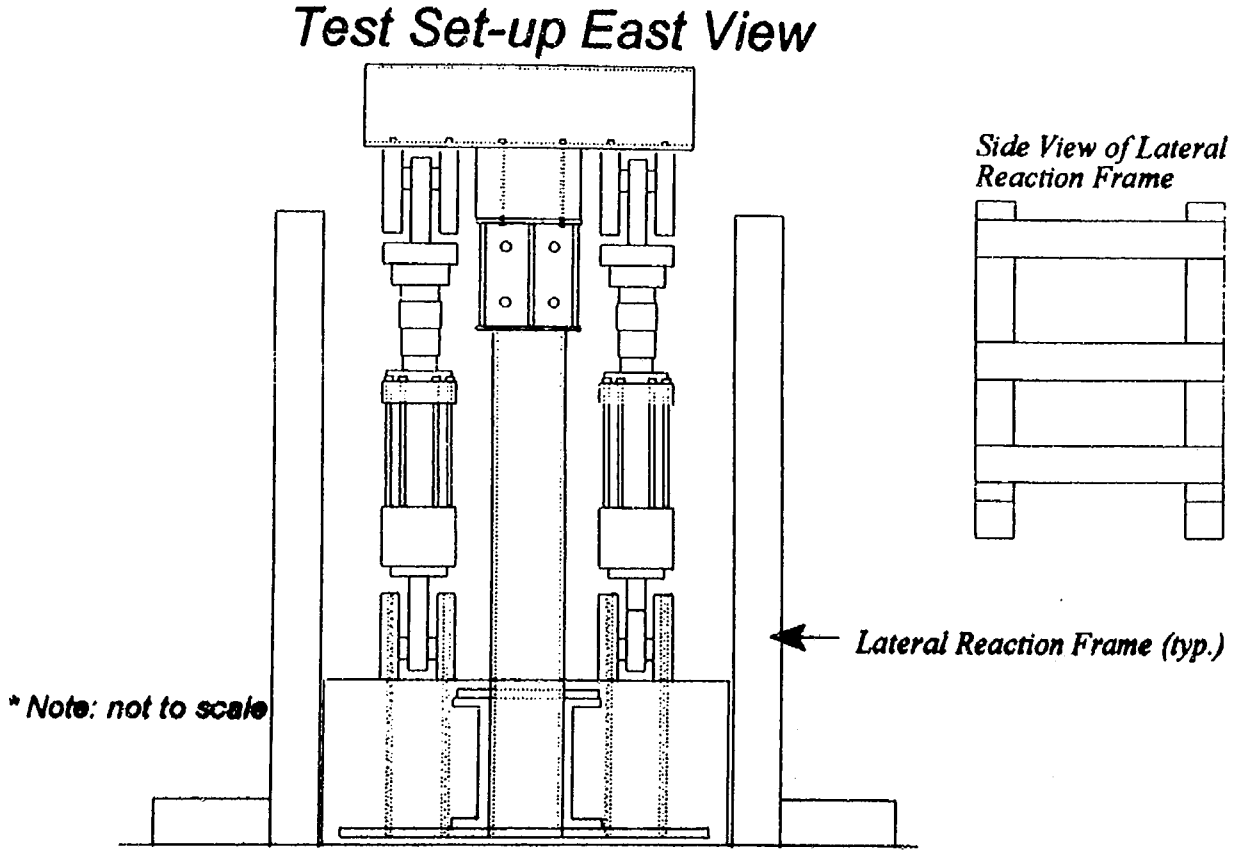


Figure 1: Test set-up - Height of Column above concrete is 2.2 metres.

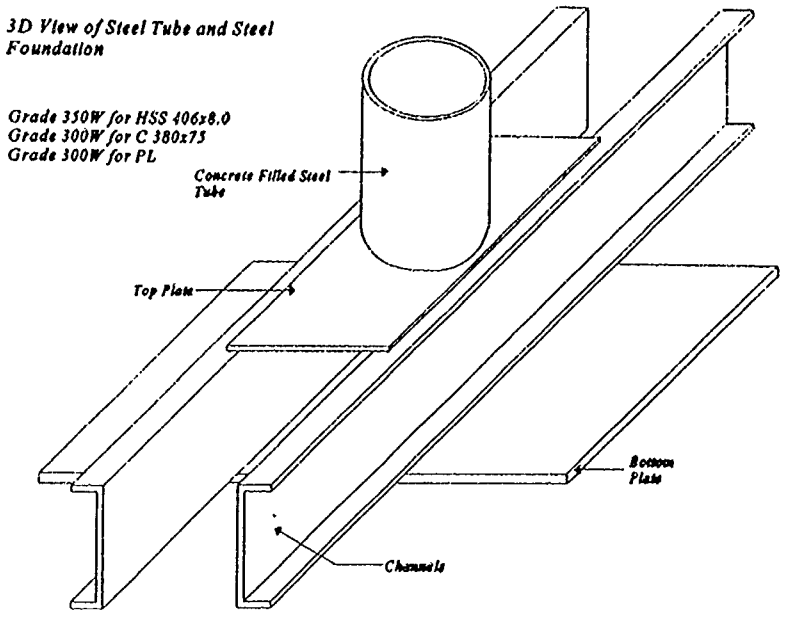


Figure 2: Schematic of Foundation Connection Detail.

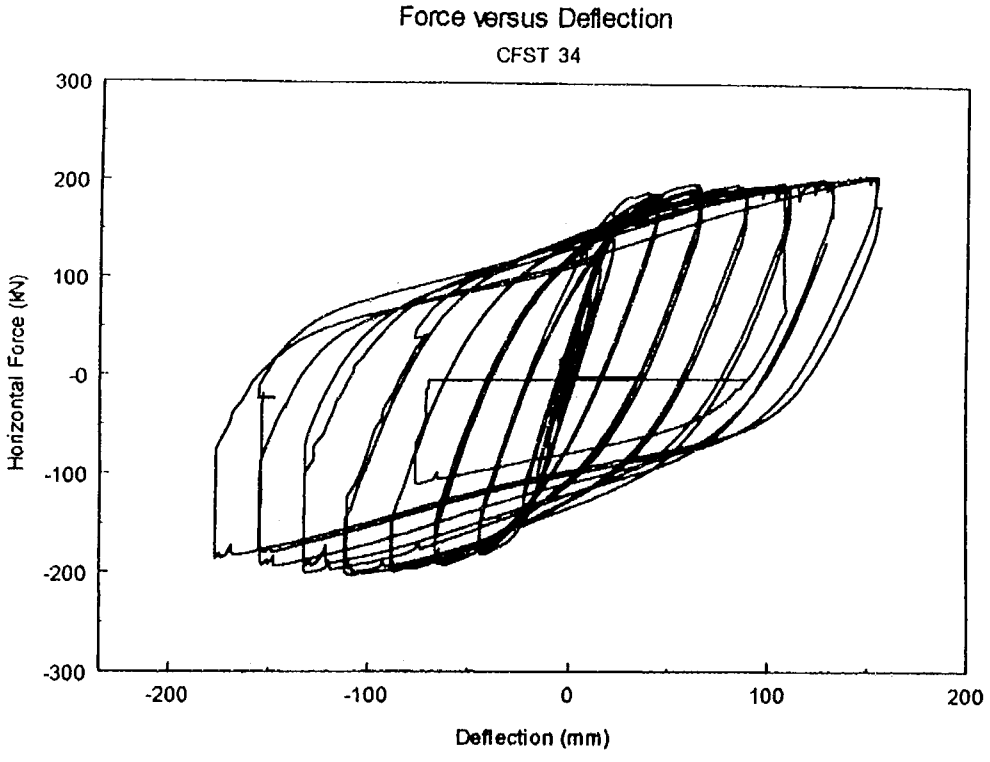


Figure 3 (cont.): Force-Displacement Hysteretic Curves for Tested Specimens

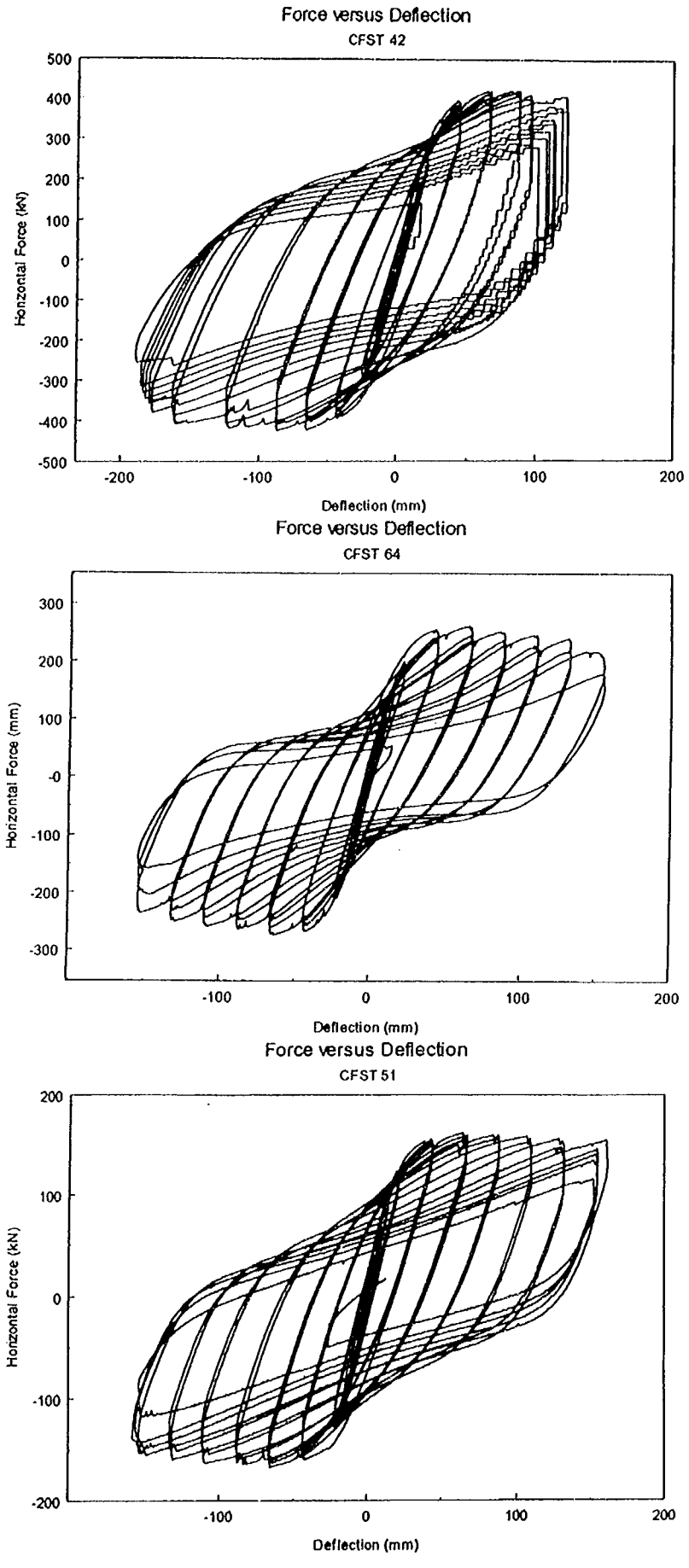


Figure 3 (cont.): Force-Displacement Hysteretic Curves for Tested Specimens

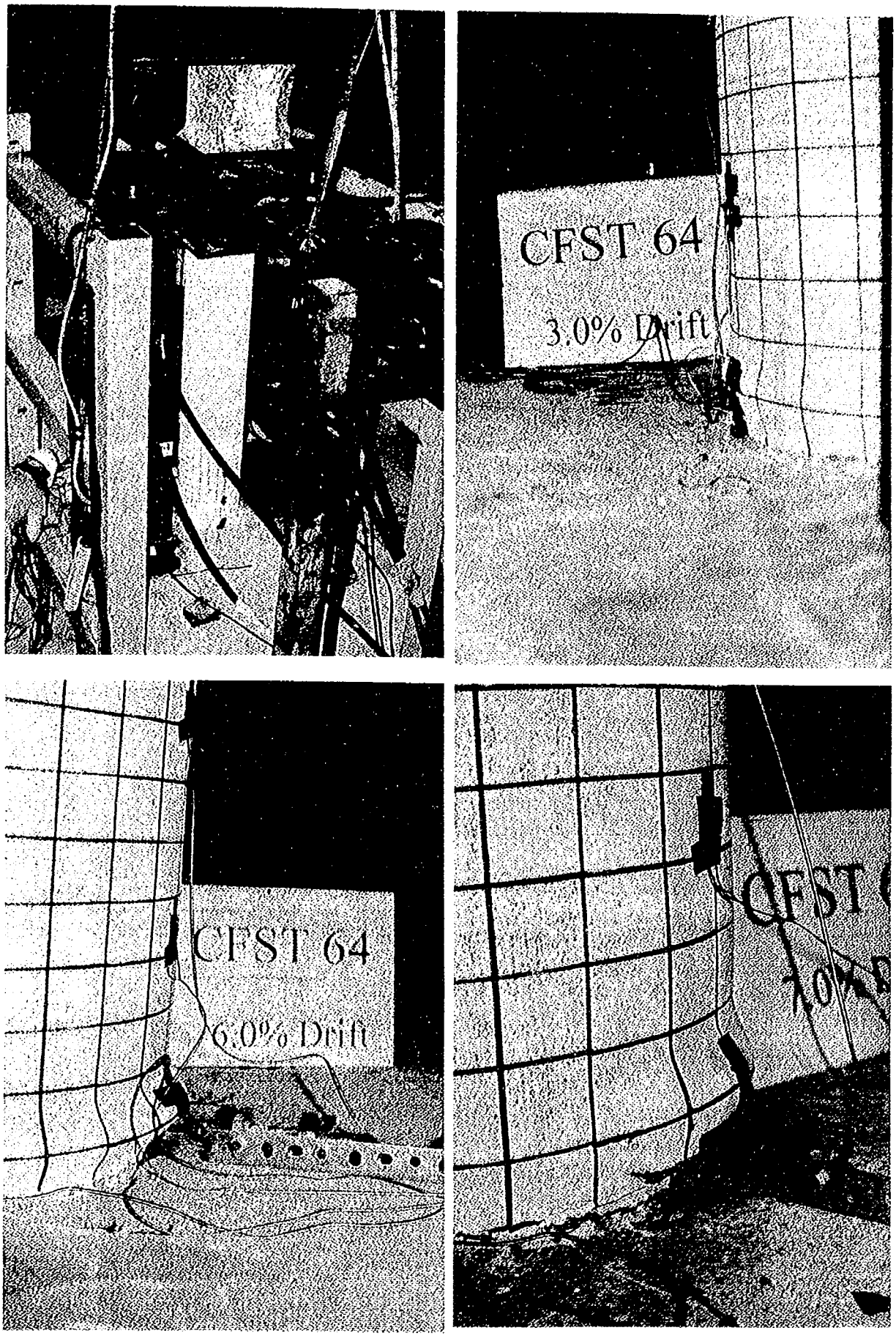


Figure 4: (a) Test set-up; (b-d) Local buckling at 3, 6, and 7% drift (with fracture at 7% drift).

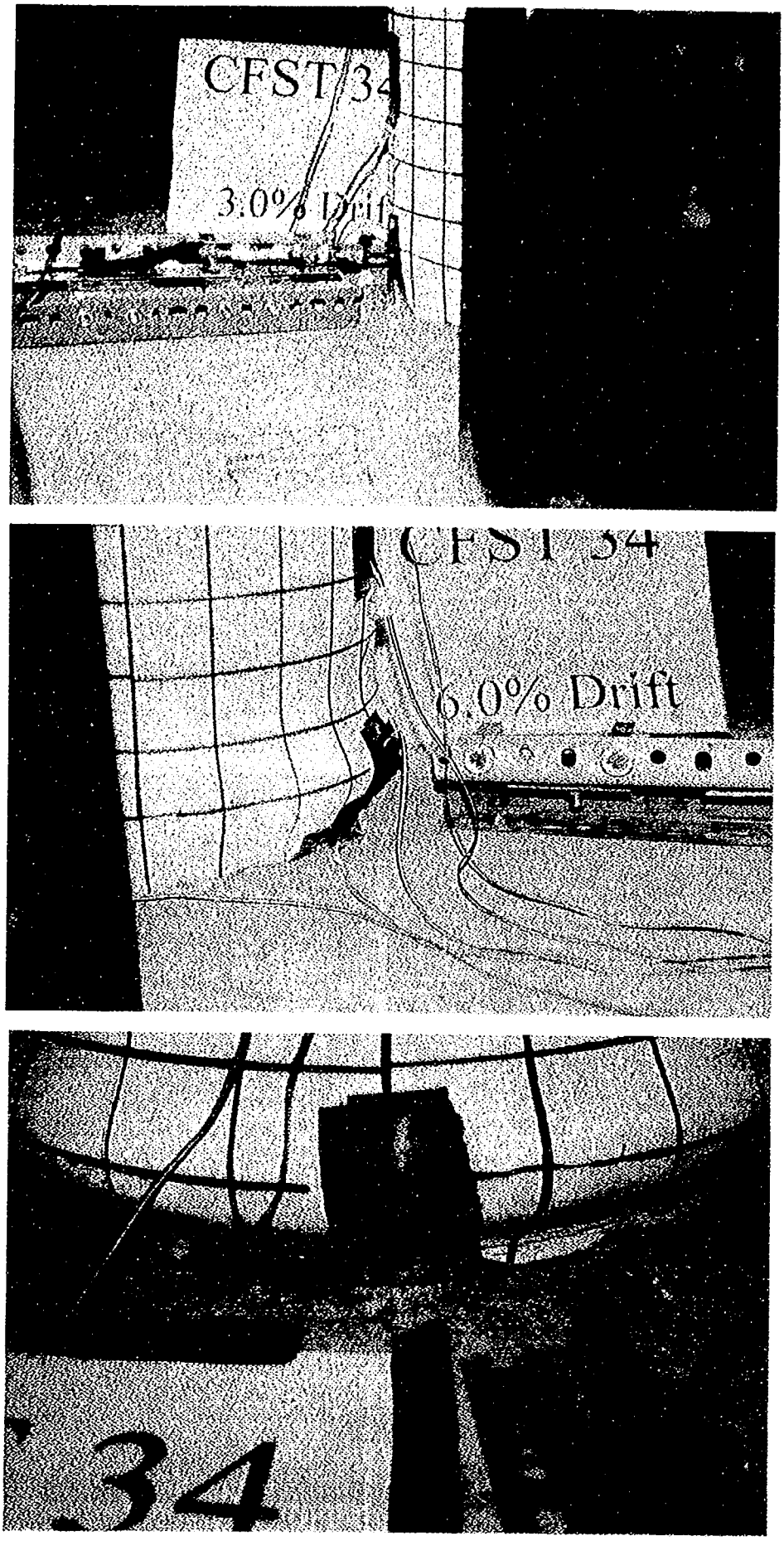
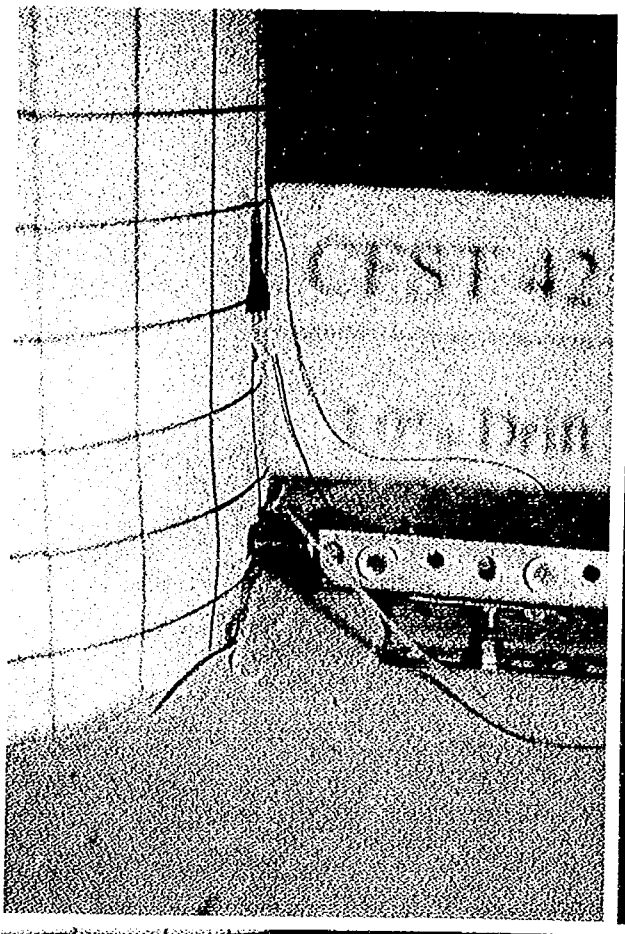
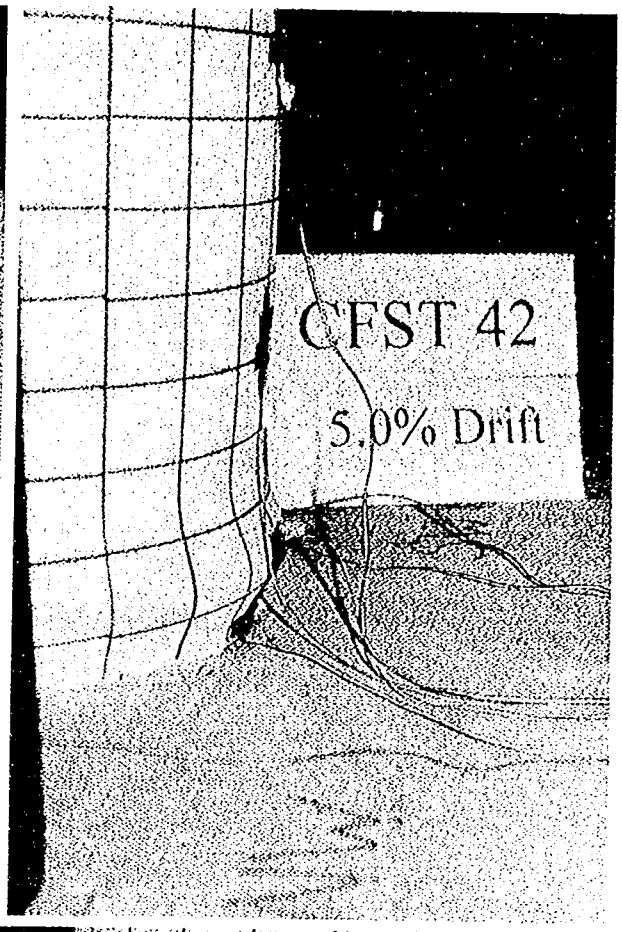
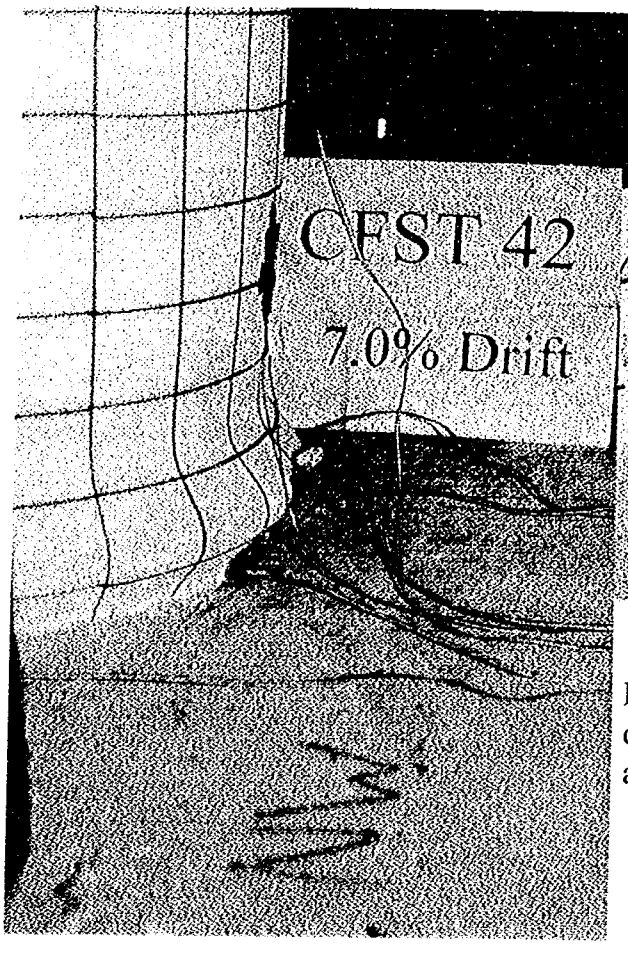


Figure 5: (a-c): Buckling at 3, 6, and 7% drift (with fracture at 7% drift).







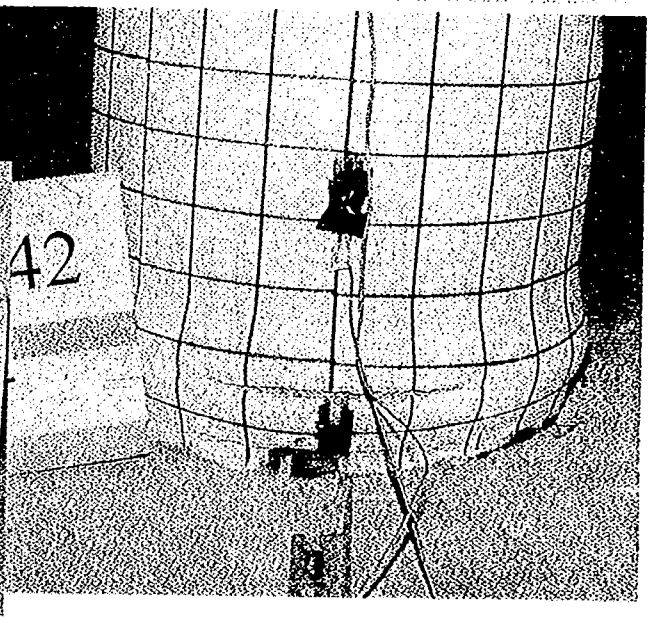


Figure 6 (a-c): Local buckling at 3, 5 and 7% drift (with fracture at 7% drift); (d) Specimen after 30 cycles.

EXPERIMENTAL STUDY ON STRENGTH AND DUCTILITY OF ONE-STORY AND TWO-STORY RIGID FRAME STEEL PIERS OF HIGHWAY BRIDGES

Tatsumasa Takaku[1], Yuhshi Fukumoto[2], Tetsuhiko Aoki [3],Takashi Okamoto[4],Tatsuo Kurokawa[5], Hiromitsu Morishita[6]

Abstract

This paper presents an experimental study on the strength and ductility of rigid-frame piers of highway bridges. Incremental cyclic loading tests were carried out to obtain the hysteresis load-deformation curves of the pier system

Two kinds of frames are used for experiments; 1) the one-story framed pier that was tested, and had a failure in the First phase Research Program in 1997, is used again after repairs, 2) an intermediate cross beam with the frame system changed to the two-story one is attached to the repaired frame. Low-yield strength steel is partly used for the center of the member in the cross beam.

The main results obtained from the study are as follows;

1. The repaired frame delivers similar strength and rigidity to the original one in the elastic range.
2. The two-story frame shows good strength and ductility due to the increased structural redundancy as compared to the one-story frame.
3. The hysteresis curves are well matched with the results obtained by the Finite Element Method (FEM).
4. Energy dissipation effect due to the early yielding of the low-yield web portion can be observed from the obtained hysteresis curves. However, more detailed analysis is needed to identify the effect quantitatively.

1. Introduction

In Japan, many steel piers are used in urban expressways. These steel piers, along with many other structures, suffered damages in the Hyogo-ken Nanbu Earthquake.

After the earthquake, many studies have been made for steel piers on such subjects as the "evaluation

---

1) Chief Engineer, Toko Consultants Co., Ltd., Tokyo, Japan

2) Professor, Department of Civil and Environmental Engineering, Fukuyama University, Fukuyama, Japan

3) Professor, Department of Civil Engineering, Aichi Institute of Technology, Nagoya, Japan

4) Chief Researcher, Applied Technology Research Center, NKK, Yokohama, Japan

5) Manager, Chiba Works,Matsuo Bridge Co., Ltd., Chiba,Japan

6) Manager, Takada Kikou Co., Ltd., Wakayama, Japan

of structure, strength, and ductility using a horizontal cyclic loading experiment", "evaluation of the behavior of structures during an earthquake using a hybrid earthquake response experiment (pseudo dynamic experiment)", "evaluation of the usability of finite element method-based elasto-plastic finite displacement analysis", and "analyses of restoring force models and their elasto-plastic responses", and various reports have been published on earthquake resistance characteristics of steel piers. In addition, studies on rigid frame piers have also been conducted.

This paper describes the result of following experiments: 1) an intermediate cross beam having shear links that employ low-yield strength steel for the web plate only was added to a one-story steel rigid frame pier to make a two-story rigid frame pier test model, 2) a cyclic loading test was conducted on the test model, and 3) the strength and ductility of the test model were analyzed.

2. Structural Behavior and Effects of an intermediate cross beam in Two-story Rigid Frame

Let us make a comparison of one-story and two-story rigid frames each having a column spacing (L) of 5.0m, a column height (h) of 5.8m, and uniform column and beam cross-section (Fig.1) using elastic frame analysis. Let us assume here that 15% of the axial compression yielding load of the column is applied at the center of the column cross-section as vertical load P, and horizontal load H is applied at the center of the beam cross-section. Here, Hy represents the horizontal load acting on the one-story rigid frame at the moment when the column base reaches its yielding stress under constant vertical load P and increasing horizontal load H, and δy represents the horizontal displacement that occurs at that moment at the horizontal loading point of the one-story rigid frame. The horizontal yielding load and horizontal yielding displacement of the two-story rigid frame, therefore, are represented as 1.45 Hy and $0.75\delta y$, respectively. This is the static effect of adding an intermediate cross beam to a one-story rigid frame. This indicates that the elasto-plastic behavior of the overall structural system can be controlled by adjusting the rigidity (elastic and elasto-plastic) of the intermediate cross beam.

At Fukuyama University, cyclic shear loading tests were conducted on plate girders to evaluate effects of the steel grade (mild steel and low-yield strength steel) and plate thickness of the web on the elasto-plastic behavior, and findings were obtained on failure modes, repetitive plastic deformation behavior, repetitive load capacity, and energy dissipation.

The findings of these tests include the following:

1) When load capacity is maintained at a constant level, the amount of energy dissipation increases in proportion with the magnitude of shearing deformation.
2) Load capacity and the amount of energy dissipation increase as the web becomes thicker, and the energy dissipation effect is higher in low-yield strength steel than in mild steel (See Fig.2).
3) Use of low-yield strength steel for the web will cause the strain hardening effect that expands the

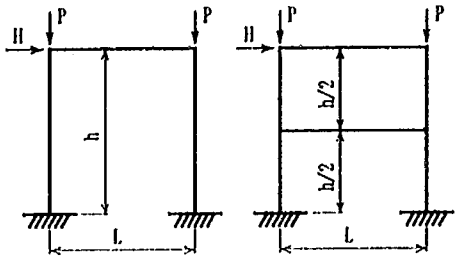
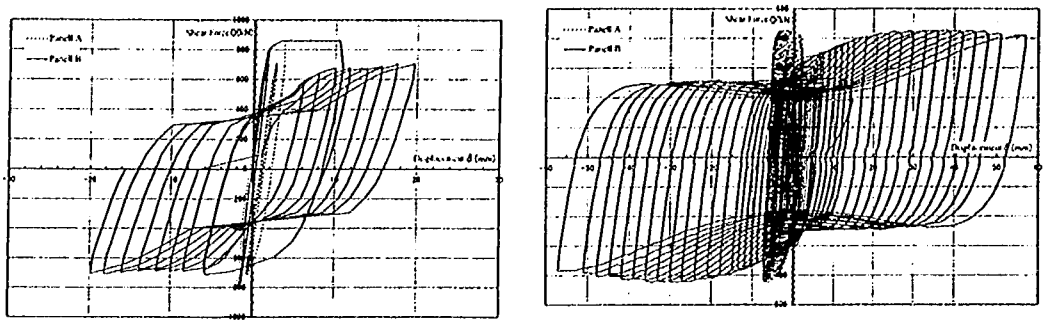


Fig. 1 Rigid Frame with an Intermediate Cross Beam



(a) Mild steel (SS400) (b) Low yield strength steel (NK-LY100)

Fig.2 Shear Force and Shear Displacement of Webs (Test Results, Ref.,3)

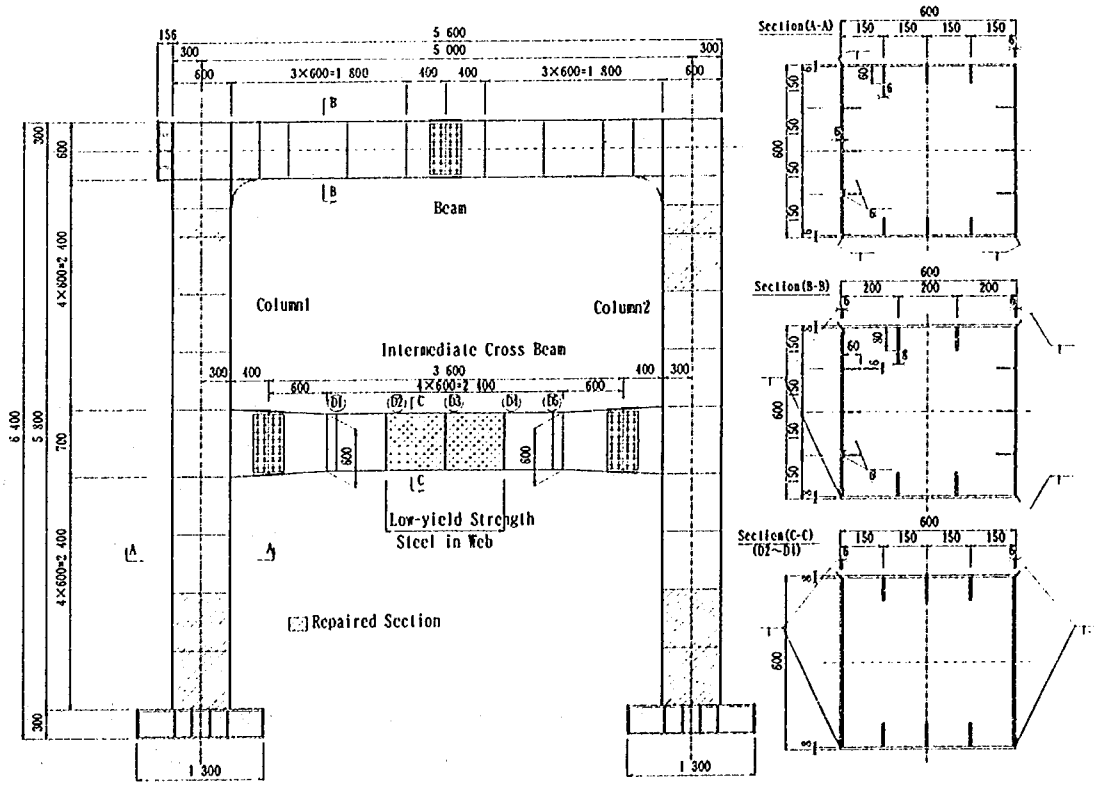


Fig. 3 Shape and Size of Test Model

plastic region, which lightens the local concentration of stress and thus the magnitude of local cracking and serious local deformation.

4) With regard to web failure mode, the shear yielding mode (thick web) is preferable to the shear buckling mode (thin web). As web panel boundary conditions, the rigidity of flange and that of web stiffener affect the final load capacity.
5) Shear type plastic links having significantly larger plastic deformation capability relative to bending and compressive deformation are effective as seismic resistance devices for structural systems.

Based on these findings, we planned an experiment on a two-story rigid frame pier that uses low-yield strength steel for the intermediate cross beam web.

3. Incremental Cyclic Loading Experiment on Steel Rigid Frame Pier

3.1 Outline of Experiment

(1) Test model

Fig.3 shows the shape and dimensions of the test model. Table 1 shows the specification of the test model.

The part of the test model that corresponds to the existing pier comprises two columns (Column 1, Column 2) and a beam that together form one-story rigid frame structure having a column spacing of 5.0m, a height of 5.8m, and a stiffened rectangular cross-section (beam and column) of 600mm x 600mm. For this part of the test model, we reused a test model that had been load tested to failure in the experiment of Reference (hereinafter referred to as "Experiment I") after cutting away the base sections and top joint sections of the columns in which serious cracks and out-of-plane deformation had developed (the hatched sections in Fig.3) and replacing them with steel members of the same material and same plate thickness.

For the intermediate cross beam, we made a new beam which has the same flange plate configuration as that of the existing beam and a beam cross-section that is basically the same as that of the existing beam (600mm x 600mm), with a cross-section of 700mm x 600mm given to the joint sections of the intermediate cross beam to accommodate the column diaphragm intervals of 700mm. The same web plate thickness as that of the existing beam (6mm) was used, but no stiffeners were used.

For the two web plate panels of the center section of the intermediate cross beam, low-yield strength steel plates having a thickness of 6mm were used as shear links. No stiffeners were used for this section either. For the low-yield strength steel material, the NKK low-yield strength steel NK-

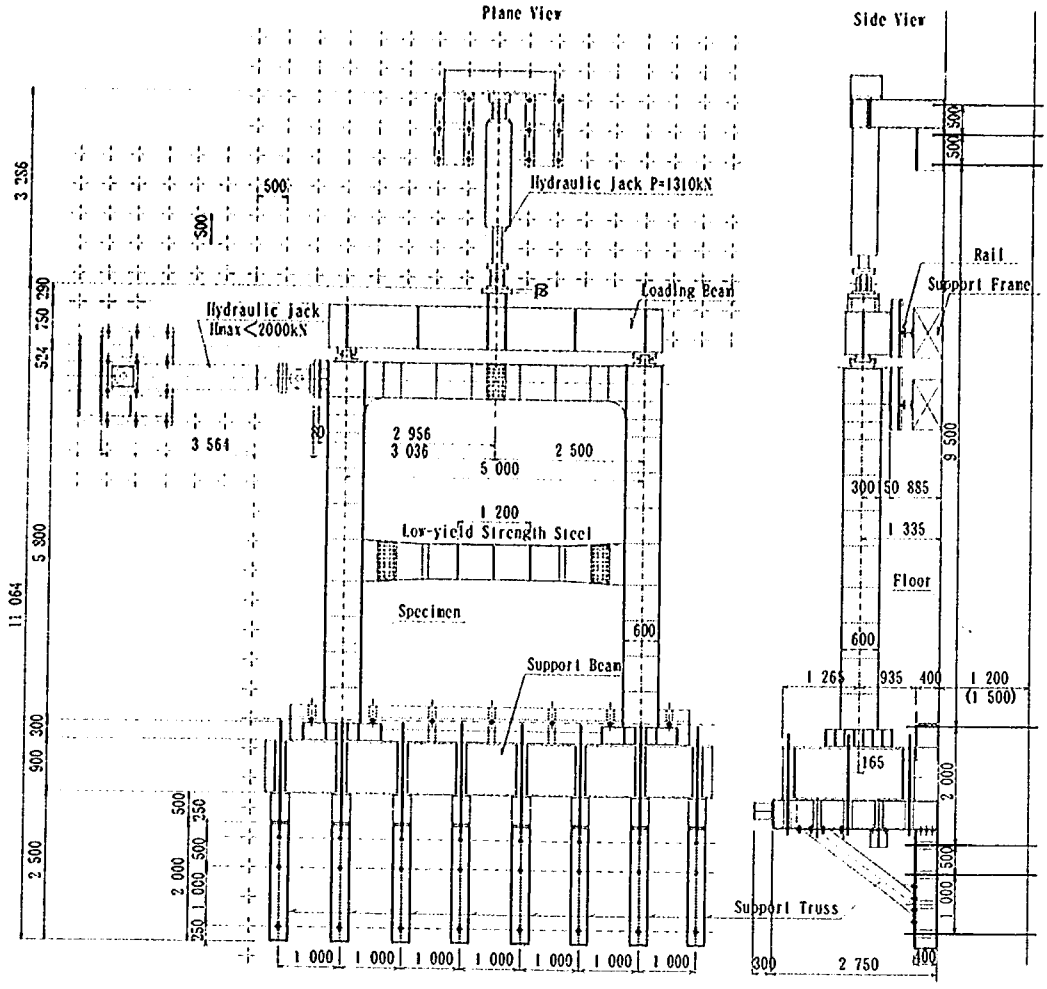


Fig. 4 Testing Rig

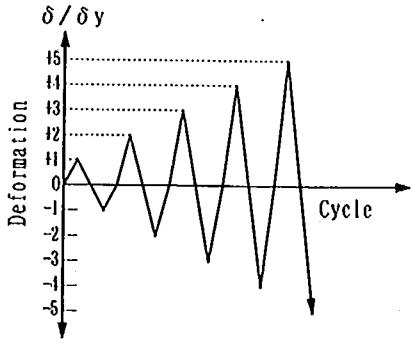


Fig. 5 Loading Cycle

LY100 (100N/mm^2 class) was used.

(2) Experiment Equipment

Experiment facility of the Seismic Experiment Center of Aichi Institute of Technology was used for the experiment. Fig.4 shows the experimental loading equipment and test model set ready for the experiment. The test model that had been disassembled into components for transportation was reassembled using high-tension bolts, placed horizontally on a support frame installed on the experiment floor, and fixed using PC steel bars.

As the test model was to be tested in the horizontally placed position, cradles made by combining linear rails were installed under the corner sections where the beam and columns join in order to eliminate out-of-plane displacement.

The constant axial load simulating the superstructure weight was applied using a loading beam and hydraulic jacks (maximum compression force = 2000kN). Movable supports were provided between the test model and loading beam to eliminate contribution of the rigidity of the loading beam to the test model beam. The horizontal load was applied by means of hydraulic jacks (maximum tensile force = 2000kN) mounted on a reaction force frame fixed on the experiment floor.

(3) Measurement of Strain and Displacement

Measurement of strain and displacement was made by means of strain and displacement gauges attached to the test model at several locations. The strain gauges were attached to the column base sections, the proximity of each joint section, and the intermediate cross beam. The displacement gauges were attached to the center of the beam on the side opposite to the loading point side to measure the horizontal displacement of the rigid frame structure as a whole and to the intermediate cross beam web plates and the diaphragms of the columns and beam to check the deformation mode of the test model. The displacement gauges for the intermediate cross beam web plates were deployed diagonally to measure the in-plane displacement of the panel.

(4) Loading Method

After the application of a constant axial force load simulating the superstructure weight (0.15Ny (1310kN): Ny = axial yielding force calculated from the specified yield point), a cyclic horizontal force was applied. The constant axial force load simulating the superstructure weight is normally determined based on the structural characteristics and design lateral seismic coefficient of the pier construction site, but in this experiment, 0.15Ny was used in consideration of the correlation of the experiment with the steel rigid frame pier test of Experiment I.

The horizontal loading was made by means of a displacement control method. As shown in Fig.5, reversed incremental cyclic loading was made with each cycle having a pair of amplitudes that are multiples of the horizontal yielding displacement δy. The loading speed applied for Experiment I was a 20mm/sec., which is relatively fast. For this experiment, a loading speed of approximately 2mm/sec. was used.

(5) Result of Material Test

Table 2 shows the result of a material test performed on the steel members used for the test model.

The "old members" were replaced with new members because of the severe damages given as a result of the loading made during Experiment I. It can be seen from Table 2 that both the yield point and tensile strength of the old members are higher than those of the "existing members". No breaking elongation data on the existing members were available, but the old members' elongation after fracture was smaller compared with that of the "new members". We presume that these changes are attributable to the strain history of the old members. Our experiment uses the existing members without any restoration work, but we consider that the effect of past loading on these members is negligible considering the fact that their strain history is not as severe as that of the old members.

(Notes) Table 2

1. Each figure shown in Table2 is the average of the test results of three test samples.
2. "Existing Member" indicates test samples taken from the original plate before making the test model in Experiment I.
3. "Old Member" indicates test samples taken from the test model after completion of Experiment I.
4. "New Member" indicates test samples taken from the original plate for making new members for this experiment.

(6) Horizontal Yield Displacement δy

The horizontal yielding displacement δy is the basic displacement quantum used in cyclic loading tests for two-story rigid frames. In this experiment, we defined this as the displacement at the moment when the flange of the compressive side column base section reaches its yielding stress.

The horizontal yielding load Py used in this experiment and the horizontal yielding displacement δy were 755kN and 24.0mm, respectively.

Table 1 Description of Test Model

	Column	Beam	Intermediate Beam	Shear Link
Section (mm)	600×600	600×600	600×600	600×600
Thickness (mm)	Flg : 6 Web : 6	Flg : 8 Web : 6	Flg : 8 Web : 6	Flg : 8 Web : 6
Number of Panels	4	Flg : 4 Web : 4	Flg : 4 Web : 1	Flg : 4 Web : 1
Steel Grade	SS400	SS400	SS400	SS400 NK-LY100
Yield Point ó y (N/mm^2)	292	t=8 : 306 t=6 : 292	t=8 : 294 t=6 : 283	t=8 : 294 t=6 : 121
Shear Yield Point ô y (N/mm^2)	—	—	163	70
Shear Buckling Stress ô cr	—	—	284	284
Rib Section (mm)	Flg : 60×6 Web : 60×6	Flg : 80×8 Web : 60×6	Flg : 80×8 Web : -	Flg : 80×8 Web : -
Width-Thickness Ratio R_R	0.49	Flg : 0.37 Web : 0.48	Flg : 0.37 Web : -	—
Width-Thickness Ratio R_F	0.38	Flg : 0.26 Web : 0.37	Flg : 0.26 Web : -	—
γ l/ γ lreq	2.256	Flg : 5.071 Web : 2.269	Flg : 5.071 Web : -	—
γ l/ γ *	1.703	Flg : 2.062 Web : 1.688	Flg : 2.062 Web : -	—
Area $A(cm^2)$	185.76	226.08	204.48	204.48
Moment of Inertia $I(cm^4)$	102,200	131,870	128,620	128,620

Table 2 Mechanical Properties of Steel Plates by Specimens Tests

Member	Steel Grade	Thickness (mm)	Position	Direction	Yield Point (N/mm2)	Tensile Strength (N/mm2)	Elongation (%)
Existing	SS400	6		Longitudinal	294	438	—
Existing	SS400	6		Transverse	292	442	—
Existing	SS400	8		Longitudinal	299	433	—
Existing	SS400	8		Transverse	312	450	—
Old	SS400	6	Flange	Longitudinal	302	445	34.8
Old	SS400	6	Web	Longitudinal	302	444	31.4
New	SS400	6		Longitudinal	283	421	41.2
New	SS400	8		Longitudinal	294	459	40.8
New	NK-LY100	6		Longitudinal	121	243	53.4
New	NK-LY100	6		Transverse	127	249	59.7

The horizontal yielding load Py1 used in Experiment I and the horizontal yielding displacement δ y1 were 547kN and 31.7mm, respectively.

3.2 Experiment Results

(1) Result of Confirmation Loading Test

As this experiment was to use a test model that had once been load tested to failure in Experiment I after performing some restoration work on it, it was necessary to confirm the effects of the restoration work prior to using the test model. For this purpose, we performed a loading test on the test model as a one-story rigid frame structure without attaching the intermediate cross beam.

Horizontal load was applied incrementally by means of displacement control as follows to the test model to which a constant axial force load simulating the superstructure weight (0.15Ny (1310kN)) had been applied in advance (yielding displacement δ ya = displacement at the moment when the strain value measured with the strain gauge attached to the column base section reaches the yielding strain): $0 \rightarrow +1\,\delta\,ya \rightarrow 0 \rightarrow -1\,\delta\,ya \rightarrow 0$.

Fig.6 shows the relationship between the horizontal load P and horizontal displacement δ recorded in the confirmation loading test. The maximum load used in the confirmation loading test and the displacement δ ya were 511kN and 32mm, respectively.

The figure shows that the result of the test is fairly consistent with that of Experiment I. This leads the conclusion that the restoration work made the test model to its original healthy state as before Experiment I with regards to the rigidity within the elastic range. This confirmation loading test and Experiment I are not same in terms of the loading equipment (reaction force truss was used in this test while Experiment I used reaction force wall), and of loading method (slow loading was used in this test while Experiment I used relatively fast loading). Nevertheless, we consider that these differences do not affect the test result significantly.

(2) Test Result of Two-story Rigid Frame

After completion of the confirmation loading test on the one-story rigid frame, the intermediate cross beam was attached to the one-story rigid frame and a loading experiment (hereinafter referred to as Experiment II) was performed on the two-story rigid frame. Table 3 shows the result of Experiment II.

Table 3 Summary of Experimental Loading Tests
(Experiment I and Experiment II)

	Yielding Load Py(kN)	Max Load Pmax(kN)	P97(kN)	P95(kN)	
Experiment I	547	1028	997	976	
Experiment II	755	1471	1427	1397	
	Yielding Displacement δ y(mm)	Displacement at Max Load δ m(mm)	δ 97(mm)	δ 95(mm)	δ u(mm)
Experiment I	31.7	95.3	117.9	125.6	191.8
Experiment II	24.0	89.0	108.1	121.1	205.0
	Ratio of Yielding Load				
	Pmax/Py	P97/Py	P95/Py		
Experiment I	1.88	1.82	1.78		
Experiment II	1.95	1.89	1.85		
	Ratio of Yielding Displacement				
	δ m/ δ y	δ 97/ δ y	δ 95/ δ y	δ u/ δ y	
Experiment I	3.01	3.72	3.96	6.05	
Experiment II	3.71	4.50	5.05	8.54	
	Ratio of Experiment I				
	Py/Py1	Pmax/Py1	P97/Py1	P95/Py1	
Experiment II	1.38	2.69	2.61	2.55	
	δ y/ δ y1	δ m/ δ y1	δ 97/ δ y1	δ 95/ δ y1	δ u/ δ y1
Experiment II	0.76	2.81	3.41	3.82	6.47

P97 : 97% of Pmax
P95 : 95% of Pmax
δ 97 : Horizontal Displacement at P97
δ 95 : Horizontal Displacement at P95
äm : Horizontal Displacement at Pmax
δ y : Horizontal Displacement at Py
δ u : Ultimate Horizontal Displacement at Py after Pmax

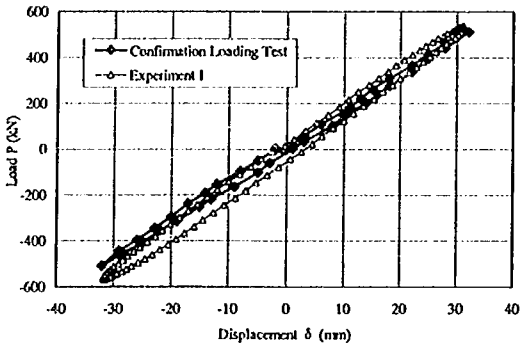


Fig. 6 Load-Deformation Curves by TEST1 (Original and after Repair)

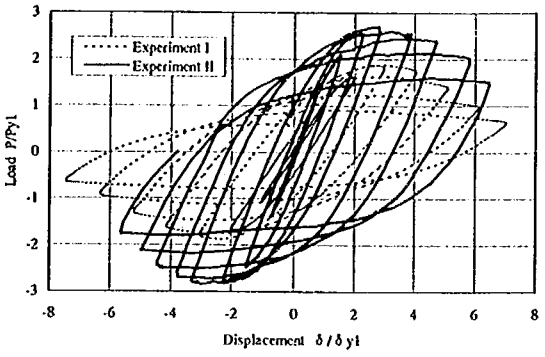


Fig.7 Normalized Horizontal Displacement

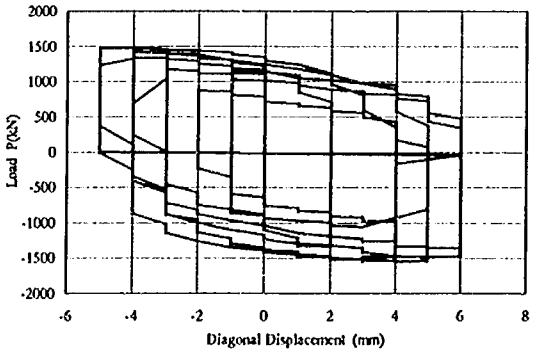


Fig.8 Load and Diagonal Displacement of Shear Links in Webs

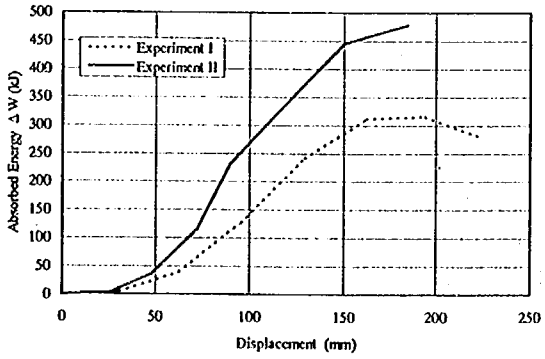


Fig.9 Relationship between Horizontal Displacement and Absorbed Energy

Fig.7 shows the relationship between the horizontal load P and horizontal displacement δ of Experiment II by normalizing to the horizontal yielding load Py1 and horizontal yielding displacement $\delta y1$ of Experiment I.

Fig.8 shows the relationship between the horizontal load and the diagonal displacement of the shear link section of the intermediate cross beam of Experiment II. It can be seen from the figure that the shear link section has sufficient energy dissipation capacity.

Fig.9 shows the energy dissipation level for each loading cycle of Experiment I and Experiment II. The energy dissipation levels were obtained by integrating the load-displacement curve. It can be seen from the figure that sufficient levels of energy dissipation capacity were maintained even after the load level had dropped below the maximum load. We consider that the fact that the energy dissipation levels are higher in Experiment II than those in Experiment I is attributable to; 1) the change of frame shape from one-story rigid frame to two-story rigid frame and 2) the use of low-yield strength steel for the shear link of the intermediate cross beam. As it was difficult to distinguish these two effects in this study, we decided to leave the confirmation of these effects to be pursued in our future studies.

4. Simulation of Experiment Results by Means of Analysis

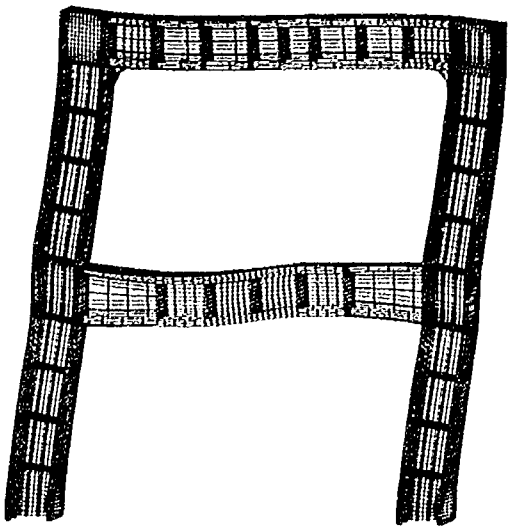
We performed simulation analysis of the results of the two-story rigid frame loading experiment by using the following analysis method in order to evaluate the legitimacy of using this type of two-story rigid frame:

4.1 Analysis by Finite Element Method

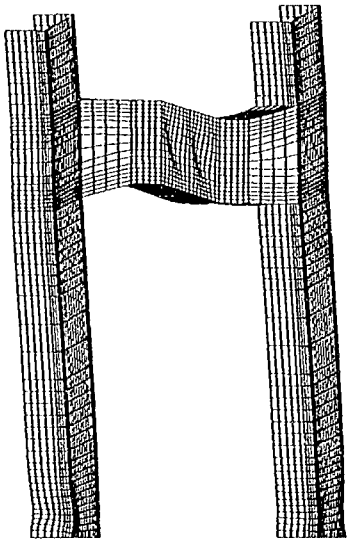
(1) Outline of Analysis

Among finite element methods, Elasto-plastic finite displacement analysis was chosen, and performed using the structure analysis program ADINA[29]. As the analysis object, we created an FEM analysis model that is a half model of the whole structure as a symmetry model with respect to the vertical plane containing the horizontal loading direction and that comprises 3-dimentional shells. For the finite element mesh decomposition, refer to the deformation diagrams shown in Figs.10 and 11. Arrangement was made in order to express the buckling modes at the meshes of the joint sections of the beam and columns and the column base section, where bucking may occur. In addition, the shear link sections of the intermediate cross beam web plate were divided into small fragments to enable the representation of shear buckling. The division of stiffeners in the plate width direction was also made in such a way that the effect of buckling could be evaluated.

In this analysis, four-joint shell elements were used. To express geometrical nonlinearity

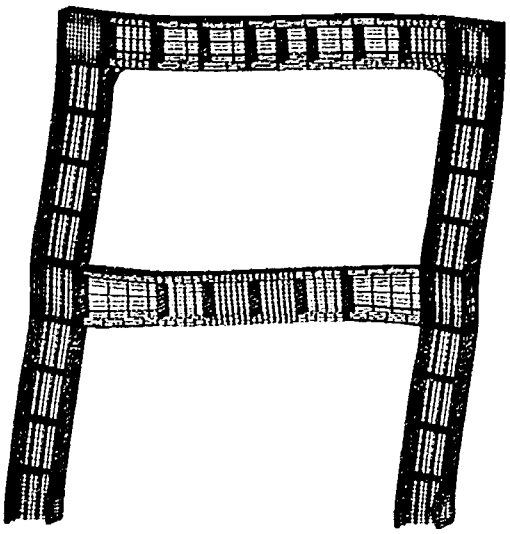


(a) General deformed shape

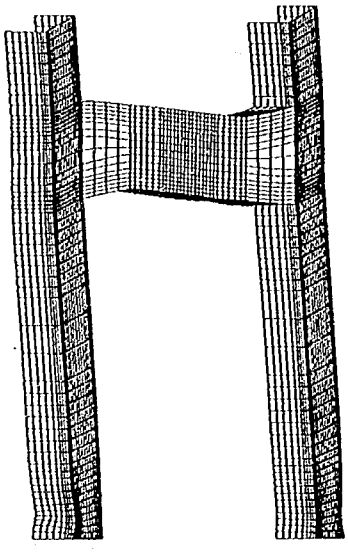


(b) Deformed intermediate cross beam

Fig. 10 Calculated Deformed Shapes by FEM (with NK-LY100, 2.5 δ y)



(a) General deformed shape



(b) Deformed intermediate cross beam

Fig. 11 Calculated Deformed Shapes by FEM (with SS400, 2.5 δ y)

such as local buckling, the Total Lagrangian formalization method was used. For the strain hardening rule, the kinematic hardening law that enables accurate representation of the stress-strain relationship was used. In addition, to achieve accurate compatibility with the characteristics of the materials used for the test model, multi-linear modeling was used in which the stress-strain relationship is matched at 7 points based on the result of a tensile test.

Horizontal loading was made by means of the same displacement control loading that had been used in the experiment, although simple one-directional incremental loading was employed in the analysis mainly because of analysis time saving while reversed cyclic incremental loading had been used in the experiment.

The analysis was performed for two different cases. That is, a case in which low-yield strength steel is used as in the experiment for the shear link section of the intermediate cross beam web plate and another in which the same SS400 that is used for the other members is used.

(2) Analysis Results

Figs. 10 and 11 show the deformation diagrams obtained from the finite element analysis. Fig. 10 shows the case where low-yield strength steel is used for the shear link section of the intermediate cross beam web plate. Fig.11 shows the case where SS400 is used for the shear link section of the intermediate cross beam web plate. In those figures, only deformation is expressed in 20 magnification.

In Fig.10, shear deformation is observed in the two web plate panels of the intermediate cross beam shear link section that are made of low-yield strength steel. It can also be seen from the figure that the intermediate cross beam as a whole is deformed into a polygonal line that bends at the two central panels. This deformation pattern is similar to that observed in the experiment, which means that this analysis is reasonably accurate.

In Fig.11, no shear deformation is observed in the web plate. In addition, the overall deformation of the intermediate cross beam shows the mild smooth curve pattern without local buckling. This means that the shear links made of low-yield strength steel are functioning effectively.

To further improve the accuracy of the simulation, it is necessary to perform analyses for the same reversed incremental cyclic loading that was used in the experiment to clarify the effectiveness of simulation method and the effects of using shear links.

5. Conclusion

In this study, an incremental cyclic loading test was performed on a two-story rigid frame pier test model that had been made by an existing one-story steel rigid frame pier with shear links employing low-yield strength steel for the web plates to evaluate the strength and ductility of the two-story rigid frame. The legitimacy of using this type of two-story rigid frames was also evaluated. The findings of this study are as follows:

1) To confirm the elastic behavior of the rigid frame, a loading test was performed on a test model that was once load tested to failure, and renewed by replacing the damaged sections of a one-story rigid frame with new ones. Then it was confirmed that the strength and rigidity had been restored to the elastic limit.

2) A reversed incremental cyclic loading test was performed on a two-story rigid frame test model that had been originally the one-story rigid frame test model mentioned above with an intermediate cross beam between the columns. In the test model, low-yield strength steel was applied for the web plates used as the shear links for the central section of the intermediate cross beam.
The results show a good improvement of the energy dissipation capacity of the structure.

3) The deformation mode obtained from a finite element analysis shows a good agreement with that obtained from the experiment. We also performed an analysis in which SS400 was used in place of the low-yield strength steel, and confirmed the good effects of using low-yield strength steel in terms of deformation mode.

4) In this study, we could not separate the structural model effects of modifying a one-story rigid frame into a two-story rigid frame from those of using shear links employing low-yield strength steel. We are going to pursue the confirmation of these effects in our future experiments and analyses.

Acknowledgement

This was a joint study conducted by the Japan Association of Steel Bridge Construction and Aichi Institute of Technology. We would like to express sincere appreciation to the people concerned at the Association and AIT for their cooperation.

References

1)Kazuhiro Nishiawa,Yasushi Josen,Minoru Takahashi,Tatumasa Takaku, Takashi Okamoto,Shingo Mizutani,Shigeru Ikeda and Yutaka Kawai;"Experimental Study on Failure and Collapse of Rigid-Frame Piers of Highway Bridges",Proceedings of The 14th U.S-Japan Bridge Engineering Workshop,PWRI,November,1998,Pittsburgh

2) ADINA,"A finite Element Program for Automatic Dynamic Incremental Nonlinear Analysis,ADINA R&D Inc.,Ver.6.16,1996.8

3) Fukumoto,Y.,Uenoya,M.,Nakamura,M.,Takaku,T.,"Ductility of Plate Girder Panels under Cyclic Shear ",Proceedings of the 6-th International Colloquium on Stability & Ductility of Steel Structures,Timisoara,Rumania,1999.9

SEISMIC RESISTANT DESIGN OF THE RIO TEMPISQUE BRIDGE

Cris D. Subrizi, P.E.[1]

Abstract

The purpose of this paper is to describe the project background, the design constraints and the evolution of the seismic design strategy. The bridge crosses the Tempisque River, which separates the Nicoya Peninsula from the Central American Isthmus, within the seismically active country of Costa Rica. A continuous steel plate girder superstructure, with a composite reinforced concrete deck, that is 764 meters long and 13.872 meters wide, was chosen. Seismic isolation of the superstructure from the substructure, using lead rubber bearings, was the selected seismic design strategy. The design featured a novel abutment design to accommodate the anticipated seismic displacements.

Introduction

A fixed crossing of the Tempisque had been promised many times and by many governments. A myriad of designs had been proposed, including a cable-stayed bridge with a restaurant on top. Several obstacles, however, prevented these bridge designs from being realized. The main obstacle was the environmental impact that the project had on the area. Like much of Costa Rica, the banks of the Tempisque are rich in unique flora and fauna. The Nicoya Peninsula, which would be the chief beneficiary of the development that would be enabled by the bridge, is also an internationally renowned environmentally sensitive area. Nevertheless, the need for a convenient transportation corridor remained.

Nicoya, in addition to its natural endowments, is also an important agricultural area. Its farmers presently rely on an auto-ferry in order to bring their goods across the Tempisque to the larger cities on the Isthmus, and eventually to the capital, San Jose. If the ferry is out of service they must drive costly distances to the north where the peninsula meets the Isthmus. See *figures 1 and 2*, for the location of the bridge site and the vehicular ferry that it will replace.

In the spring of 1998, after the completion of detailed environmental impact studies, by the Ministerio de Obras Publicas y Transporte (MOPT) de Costa Rica, the design team, Ingeniera Sismo Resistente/Parsons Brinckerhoff International (ISR/PBI) began their work.

ISR/PBI was contracted to investigate bridge alternatives for a conventional design bid construction scenario. Little work had been done to determine the engineering properties of the soil at the site even though the idea for the bridge was at least 25 years old. In order to develop the foundation design options, available soil data was supplemented with engineering judgement, since detailed soil investigations could not be undertaken until after the bridge type study phase. In addition to that, the seismic setting could not be well defined during this initial stage of work, since the seismic risk of Nicoya was in the process of being reevaluated. The team, however, worked from an envelope of seismic demands made available as the seismological investigations progressed.

[1] Lead Engineer, Major Bridge Service Center,
Parsons Brinckerhoff Quade & Douglas, Inc., 303 2nd St., Suite 700N, San Francisco, CA 94107

After the initial type study, the project was stalled over the next 2 years due to delays in the geotechnical investigations. When the project was eventually restarted the financial health of the MOPT had changed for the worse. The project scope would now be redirected to allow the possibility of a Tempisque River Bridge Concession. Bid documents were then modified to allow the design build option.

This reality persisted until the Taiwanese government announced in December 1998 that it would donate the bridge to the government of Costa Rica. Several months into the year 1999, the Taiwanese began adapting the design to suit their means and methods of construction. Their efforts were recently interrupted, due to the devastating Taiwan 921 earthquake.

When completed, this bridge will be the longest in Costa Rica as well as the first to employ the seismic isolation design strategy. The following sections serve to give a general overview of the evolution of the bridge design solution and its performance goals. We will begin by defining the site, in which the bridge will be located, its characteristics and the seismic risks.

Project and Site Constraints

- Design life to be 75 years
- Bridge must join existing approach roads and embankments
- Provide for an 68-m wide future commercial shipping lane
- Restricted Work Zone limits work with a 50-m wide band that is centered on the center-line of the bridge.

Site Geology

- Alluvial Deposits on Sedimentary Rock (Depths range = 0-m to 25-m)

Alluvial Deposits

- Loose to Very Loose Silty-Sands ($N < 5$, $0.2\text{-mm} < D50 < 0.3\text{-mm}$)
- Soft to Very Soft Clays ($N < 4$, $LL > 100$)

Sedimentary Rock

Where MR is a measure of rock quality used in the British Standard, BS8004, and RQD is the Rock Quality Designation:

- Poorly Cemented Sandstone and Cemented Black Shale (corresponds to MR approx. = 100 & RQD typically 0%)
- Uncemented Black Shale (corresponds to MR approx. = 75)

Summary of Geophysical Exploration

- Soil in alluvial deposit is very soft and cannot sustain load reliably
- Shear wave velocities indicate rock is hard
- Resistivities indicate high degree of rock fracture

Summary of Geotechnical Investigation

- Liquefaction is likely to occur in Silty-Sand layers within 10-m of the ground surface
- Unconfined compression results of 50 to 65 Mpa classify Rock as "Hard"(though at the low end of the geotechnical spectrum)

- Rock Mass Rating is "poor" to "very poor"

Site Geology (continued)

Conclusions drawn from Geotechnical Exploration and Investigation

The bridge foundation must be founded on or embedded in the rock layers. The soft soil layer will contribute little to load resistance but will act as a damping media. The question of how the foundation transfers lateral load to the rock, and the selection of the best foundation system to enable lateral load transfer, are the subject of the substructure type selection.

Seismic Setting

The western coast, including the Nicoya Peninsula, is in a region of subduction between the Caribbean, the Cocos and the Nazca Plates. In 1982 an intensive seismic cycle began that culminated in significant events in 1991 and 1992. Though, somewhat abated, this vigorous cycle of seismic activity is expected to persist. As a result of this activity the design earthquake demands in the Costa Rican seismic design code were revisited. Sufficient concern motivated site specific studies for this project. The design earthquake was defined as:

- Return Period = 261 years (Defined by MOPT)
- Peak ground accelerations, a_{max}
  0.45g :- soil
  0.32g :- rock

- Spatial Acceleration Distribution Factor, R = 0.80 (Ref. 1)
- Maximum Effective Ground Acceleration = R x a_{max}
  0.36g :-soil
  0.26g :- rock

The alluvial deposit, as suspected during the geotechnical exploration, was found to have a high liquefaction potential for the design earthquake.

Following, are sections that focus on the key components of the bridge and the design itself. These discussions are presented in an evolutionary context to illustrate the development of the design solution

Superstructure Type Selection

Steel, concrete, and composite steel/concrete superstructure types and their respective construction methods were investigated qualitatively and quantitatively. The two finalist bridge types, were a cast-in-situ post-tensioned concrete box girder, erected segmentally, by the balanced cantilever method, and a composite concrete and steel plate girder superstructure. For the plate girder option, span segments are to be erected over the piers. This is then followed by placement of the central span segments and finally the sequential in-situ casting of the composite concrete deck.

The steel alternative was ultimately selected based on first cost. See *figure 3,* for the general plan and elevation. Costa Rica, at the time of the type study, had a local market skew that favored steel. Quantitative life cycle cost analysis was not normal practice at the MOPT at the time. Their experience with the latest protective coatings for steel structures allayed

their concerns of long-term maintenance cost burdens, though, with maintenance in mind the MOPT requested that the number of expansion joints be minimized and that a maintenance manual be produced.

A favorable consequence of using steel was that it enabled the design team to minimize the weight of the superstructure, which in turn resulted in lower seismic-demands, and ultimately reduced the size of the substructure.

Substructure Type Selection

Typically bridge substructures are made up of piers that are supported on a specific type of foundation system, spread footing or a pile supported footing. The piers could be integrally connected into the superstructure or they could support bearings that would in turn support the superstructure.

Initially, the steel alternative was envisioned to be bearing supported and the concrete segmental alternative was initially to have integral connections, however, the resulting disparity in pier stiffness along the length of the bridge precluded either type of articulation. Though incomplete, the past soils investigations indicated that deep foundations were necessary, although additional investigations would be needed to determine the exact depth of penetration.

The site was characterized by loose alluvial deposits, which we determined to be prone to liquefaction, as well as experience pronounced local scour (approx. 11 meters). Once it was determined that the degree of lateral pile support attainable by the soil would be questionable at best, the design team turned its attention to larger and stiffer pile systems, that would provide significant lateral structural capacity.

Initially, plumb drilled shaft foundations were considered. They were familiar to contractors and the MOPT, so it was expected that an economic design could be realized. The structure shown in *figure 4*, is one of the configurations developed for the concrete alternative, while *figure 5* shows the typical section of a similar structural configuration for the steel alternate. Efforts to minimize the pile cap size with this plumb pile system continued to yield a pile cap with significant mass. That was because, increases in foundation stiffness yielded more piles and hence a larger pile-cap. We quickly realized that we were chasing our tails and ending up with a qualitative seismic response, as shown in *figure 6*, approximated best by the response modes of an idealized two-degree-of-freedom-system, with a significant secondary mass at the pile cap level. This was not considered desirable because it would only complicate the prediction of the overall seismic response of the bridge. It was also found that it was increasingly difficult to avoid plastic hinging in the piles. Waterline foundations were found to be the most cost-effective solution from a construction perspective however this scheme left open the possibility that a potential plastic hinge zone would experience the corrosive wet and dry cycles of a splash zone. A better design solution was needed.

Our attention was then focused on designing a foundation system that maximized stiffness and minimized substructure mass and was still economic to construct. Here experience as well as advances in construction technology teamed up to provide us with a viable solution. Several members of the design team have worked on offshore structures as well as some of the latest innovative bridge foundation engineering projects, such as the Jamuna River Bridge in Bangladesh. These projects took advantage of the fact that a

substructure with maximum stiffness and minimal weight penalty could be realized by using battered piles. The construction technology was successfully applied to bridge works at Jamuna where 2.5 meter and 3.15 meter diameter piles with a 1:6 batter were installed. It was noted that the success at Jamuna motivated the selection of the batter pile design concept for a crossing several hundred miles upstream. This fact only bolstered the idea for its use at Tempisque.

Taking this concept a bit further, it was decided that further weight reductions could be had if the footing, or pile cap, was eliminated all together, in effect, creating a large-scale pile bent. This approach required that proportioning of the piles for this system had to address the issues of local and global buckling. *Figure 7* depicts the batter pile substructure. The selected pile was an open-ended steel pipe pile, with an outside diameter of 1524 mm and wall thickness of 38.1 mm. The resulting slenderness ratio was less than 60 and the compactness of the section, D/t = 40, obviated local "Brazier" buckling during pile driving. A 4-pile group was planned, each with 1:8 batter and oriented 45 degrees with respect to the bridge centerline.

The lateral load resistance offered by the piles is a product of the batter itself and the flexural stiffness of the pile. The pile will penetrate into the rock layer to provide the prescribed lateral resistance. When the foundations are located in the alluvial deposit the pile will penetrate 4.5 meters into the rock. Where the alluvium has scoured away, the piles will penetrate 10 meters into the rock. The pile will be installed by assisted driving, where the "assistance" will be provided by a reverse circulating-drill that will advance from within the open-ended pile. The drilling will continue just (distance to be finalized during pile test program, but estimated at 305mm to 405mm) short of the specified tip. From there driving will continue until practical refusal is achieved.

The connection of the pile to the pile cap was detailed for ductile response in the case of an earthquake with a magnitude sufficient enough to repeatedly cause the superstructure to engage the seismic blocks. The ductility of the piles was estimated to range from 6 to 12, depending on the assumptions of the condition of the pile. This added reserve capacity could be provided with negligible additional construction expense.

As we had mentioned earlier, integral superstructure to substructure connections were found to have negligible benefits. The team realized that regularized response could only be achieved by using Isolation/Dissipation (I/D) devices to their full advantage. Remembering the stiffness relationship for elements acting in series, $1/K_{pier\ total} = 1/K_{pier} + 1/K_{I/D}$, shows that the batter pile substructure, allows the I/D devices to reside on a stiff base, that keeps the I/D device effective. *Figure 8* shows the qualitative response of the batter pile substructure.

Application of I/D Devices

Lead Rubber Bearings (LRB) were the chosen I/D device. The bearings were designed to meet the AASHTO Specification (Ref. 2). AASHTO requires the I/D device to have a reserve capacity to displace at least 1.5 x design displacement, should an earthquake of unforeseen greater magnitude occur. Discussions with the LRB unit designer, the OILES Corporation, revealed that the bearing had substantially greater displacement capacity. It was decided that this reserve capacity should be put to use. In the interest of isolating damage to areas where repair is relatively easy, the seismic gap was sized to allow the LRB to displace to its maximum stable displacement. The section on *Seismic Performance Levels* references these displacements.

Due to the varying pier stiffness and spans, three bearing types were selected. Note that all the bearings feature 4 lead cores. The breakdown was as follows:

- Abutments – 4 bearings with rubber thickness 130 mm & plan dimension 400 mm x 400 mm (total = 8)
- Typical Span Bents – 8 bearings per pier, with rubber thickness 130 mm & plan dimension 500 mm x 500 mm (total = 72)
- 86-m span bents – 8 bearings per pier, with rubber thickness 130 mm & plan dimension 550 mm x 550 mm (total =16)

In order to track the condition of the LRB as it ages the project specification calls for a spare LRB to be housed in an enclosure providing similar exposure conditions. This LRB will be loaded to a similar axial stress level as one of the LRB's that are in service. Every 5 years the spare LRB will be removed and tested by the manufacturer in order to track the changes in the LRB component properties due to aging. This data will aid the MOPT in developing their maintenance program.

It is anticipated that after the design seismic event, and for those greater in magnitude, the bearing will have to be realigned, See the *Seismic Performance Level* section. With that in mind the design provides a pair of external reaction blocks at the cantilever ends of the pier cap-beams, see *Figure 7.*

LRB displacement is provided for by a "seismic gap" between it and the shear key. The shear key will stop the bearing from displacing beyond the maximum stable displacement. Sections were added to the maintenance manual to describe the seismic gap's importance in order to insure that the clearance is maintained. LRB displacement must be accommodated by the joint system between the superstructure and the abutment. Current expansion joint technology successfully enables longitudinal displacements, however, when it comes to transverse displacements and torsional racking, their abilities are limited. Considering this reality, the following question was posed: can we shift the seismic displacement demands away from the modular expansion joint and still allow the LRB to move in all directions? The answer was to develop, what we call, the seismic joint.

Seismic Joint

The seismic joint is a floating slab that slides on top of the abutment "backwall". The "backwall" is an enclosed gallery with a roof that forms the sliding surface for the floating slab. When longitudinal movements are experienced the modular expansion joint will accommodate them up to its limit of safe displacement, then a stopper is engaged that impedes further deformation of the modular expansion joint but causes the floating slab to be engaged. The floating slab then pushes into the regularly graded gravel fill between the approach slab and the floating slab. See *Figure 9.*

Transverse movements are however, directly transferred, via a stopper, to the floating slab because the modular expansion joint has a low tolerance for that type of movement. The floating slab then shears the regularly graded gravel fill that is contained by sheet metal confining springs. These seismic induced deformations are expected to produce bumps and troughs in the gravel fill. See *Figure 10.*

To provide toughness for service loads, the regularly graded gravel fill will be reinforced with a Geo-Grid like material or galvanized wire mesh and topped with an

elastomeric asphalt layer. To drain the gravel bed we took advantage of the fact that the top of the gallery is slightly sloped towards the approach slab, as a result we could link the gravel drainage system to the approach slab drainage system.

Repairs to the seismic joint will entail clearing and replacement of the gravel fill as well as realignment of the floating slab. Transverse realignment of the floating slab will occur during transverse realignment of the bridge. Quick passage over the damaged joint can be achieved with steel bridging plates or expeditious temporary filling of troughs and compaction of bumps. Repairs were estimated to take less than 24 hours.

Seismic Performance Levels

Table –1, below summarizes the anticipated performance of the components of the structural system.

Table –1 Expected Damage after Various Level of Earthquakes

	Service Level	Safety Level	
Component	**Design EQ**	**Displacement 1.5 x Design EQ**	**Maximum Stable Displacement of I/D**
Approximate Lateral LRB displacements	105 mm	160 mm	325 mm
LRB Shear Strain	Approx. 0.8	Approx. 1.2	Approx. 2.5
Approximate Vertical LRB displacements	Negligible	Negligible	- 3 mm
Equivalent Risk	261 year return period	Approx. equivalent to 2000 year return period	Approx. equivalent to 5000 year return period
Superstructure	*No Damage*	*No Damage*	*Impact Damage due to impact against seismic blocks could cause buckling of lateral bracing*
Piles	*No Damage*	*No Damage*	*Inelastic Response due to impact against seismic blocks*
Seismic Blocks at Bents an Abutments	*No Damage*	*No Damage*	*Impact Damage*
Seismic Joint	*No Damage*	*Heaving and Settlement of Gravel*	*Significant Heaving and Settlement of Gravel*
Modular Expansion Joint	*No Damage*	*No Damage*	*Potential damage from racking resulting from superstructure elevation drop*
I/D device	*No Damage, but at least one inch offset expected*	*No Damage, at least one inch offset expected*	*No Damage, greater than one inch offset expected*

Seismic Analysis Strategy

Acknowledging that exact solutions to seismic design problems are not realistically achievable, the engineering team set about to bound the design solution. Our tools were limited to the dynamic response spectrum analysis. The available time-history data was insufficient and as a result Non-Linear Time-History analysis was not a practical alternative.

For the integral structural concept, the soil the pile/soil substructure stiffness had to be bounded in the dynamic analyses because the lateral support offered by the soil was highly variable due to its susceptibility to scour and liquefaction. The upper bound model captured

the stiffest soil/structure foundation system while the lower bound model captured the most flexible. The piles were modeled explicitly and extended to an estimated point of fixity. The point of fixity was derived from stand-alone soil structure interaction analyses. Due to its complexity, the damping added to the structural system from the weak soil was not quantified. The system damping considered was due only to the structures' modal response.

For the Isolated concept, the LRB's were modeled using their effective stiffness. The effective stiffness was derived from the candidate LRB's hysteresis loop. The model of the substructure below the LRB was bounded in the same way as it was for the integral structural solution. To capture the added damping provided by the LRB, a composite response spectrum (Ref. 2) was developed. For the selected LRB's and a target natural period of 2.0 seconds, the composite spectrum accounted for 5% damping for the structure modes (up to a period of 1.6 seconds) and 20% damping for the isolated modes (between 1.6 and 2.5 seconds).

The resulting natural period of the initially considered integral structural solution varied from 0.5 seconds to 0.7 seconds. With the resulting spectral accelerations ranging from 0.6g to 0.7g, where the peak spectral acceleration was 0.7 g.

In contrast the natural period of the isolated structure varied from 1.7 to 2.2 seconds with the resulting spectral accelerations ranging from 0.07g to 0.09g.

Corrosion Protection

To achieve the design life, the steel elements of the bridge are to be coated with the state of the art in coating materials, and the concrete is specified to contain corrosion inhibiting admixtures. Examples of these defense measures are listed in the table below.

Table – 2: Corrosion Protection Measures

Item	Coating
Superstructure	Zinc Primer/Intermediate Epoxy Coat/ Urethane Finish Coat
Reinforcing Bar	Fusion Bonded Epoxy(FBE) (purple in color)
Pile – above water/splash/salt spray zone	Epoxy Cladding w/ Urethane Finish
Pile – general	High Solids Epoxy

Conclusion

The design strategy presented attempts to meet the prescribed performance goals by defining the weak link in the structural system clearly. The weak link is the LRB. For the LRB to function the designers had to introduce sacrificial, secondary components, such as the seismic joint. The weak link and the sacrificial components were designed to absorb every day wear and tear without compromising their respective roles during a seismic event. Using I/D devices in this manner enabled an affordable design.

By taking advantage of the reserve capacity of the LRB and the flexural capacity of the piles, this structure is expected to safely handle the earthquake that is beyond our current expectation without adding an additional maintenance burden and cost. However, the true measure of success of this design approach, will only be possible once the structure has been constructed.

Project Status

The bridge construction, though presently delayed, is currently scheduled for a year 2002 completion.

Acknowledgments

The design was truly the product of a remarkable team effort of over 4 years. I would like to acknowledge my esteemed colleagues listed below as well as thank my wife for putting up with me during this project.

- Ing. Javier C. Cartin Phd., Principal, Ingenieria Sismo-Resistente (ISR) San Jose, Costa Rica
- Juan Murrillo P.E., Senior Vice President and Technical Director of Major Bridges, Parsons Brinckerhoff, San Francsico
- Ing. Eduardo M. Bonilla & Ing. Leon G. Mayer, ISR, San Jose, Costa Rica
- Kenneth Liu S.E and Gregory Benkovich P.E, Parsons Brinckerhoff, San Francsico
- David Williams, Phd. P.E., Special Foundation Consultant
- Herb Kubota, Eng.Yutaka Makiguchi & Allan Stewart of the Skellerup-Oiles Joint Venture
- Ing. Gerardo Acosta e Ing. Jose Chacon Laurita, Ministerio de Obras Publicas y Transporte (MOPT) de Costa Rica
- Ing. Tomas Del Carril

Project Reference Specifications

- AASHTO, Guide Specifications for Seismic Isolation Design,with revisions(1991)
- Codigo Sismico de Costa Rica (CSCR-86), by Colegio Federado de Ingenieros y Arquitectos de Costa Rica (1986)
- AASHTO, Standard Specifcation for Highway Bridges(16th ed.,1996)
- AASHTO, Guide Specfications for Design of Steel Bridges for Fatigue(1989)
- MOPT, Especificaciones Generales para la Construccion de Caminos, Carreteras y Puentes (CR-77)

References

1. Codigo Sismico de Costa Rica (CSCR-86), by Colegio Federado de Ingenieros y Arquitectos de Costa Rica (1986)
2. AASHTO, Guide Specifications for Seismic Isolation Design, with revisions(1991)

1. Figures

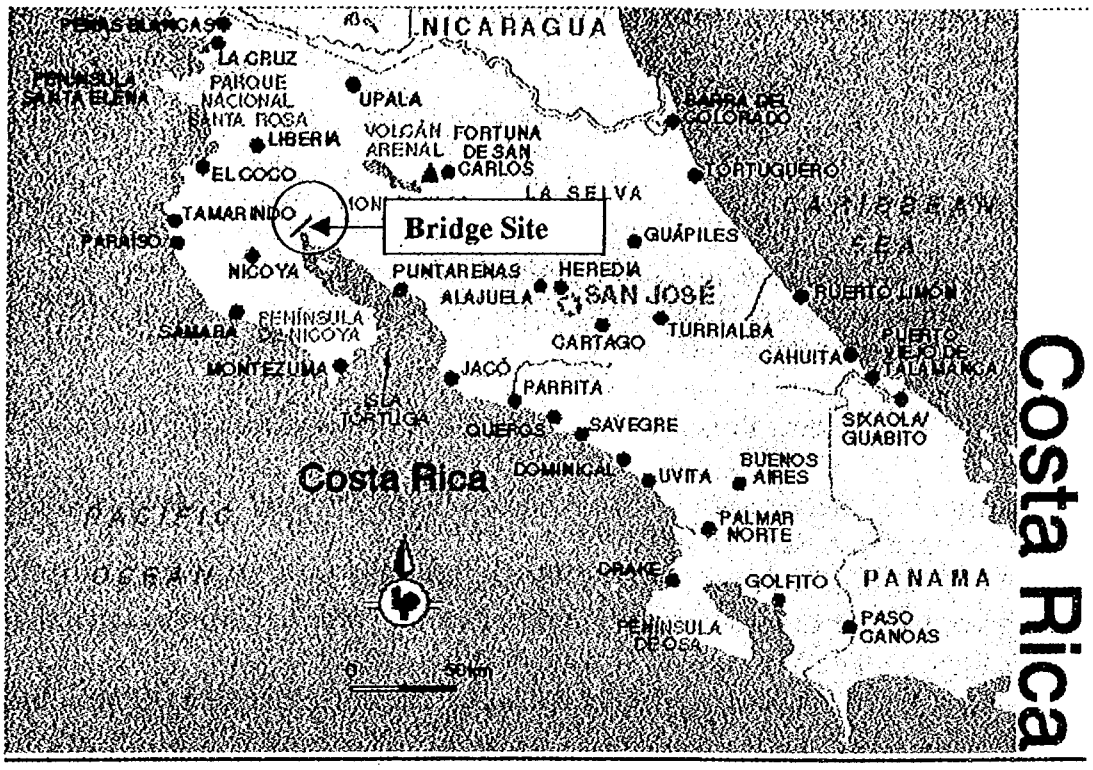


Fig. 1: Project Location (Map courtesy lonelyplanet.com)

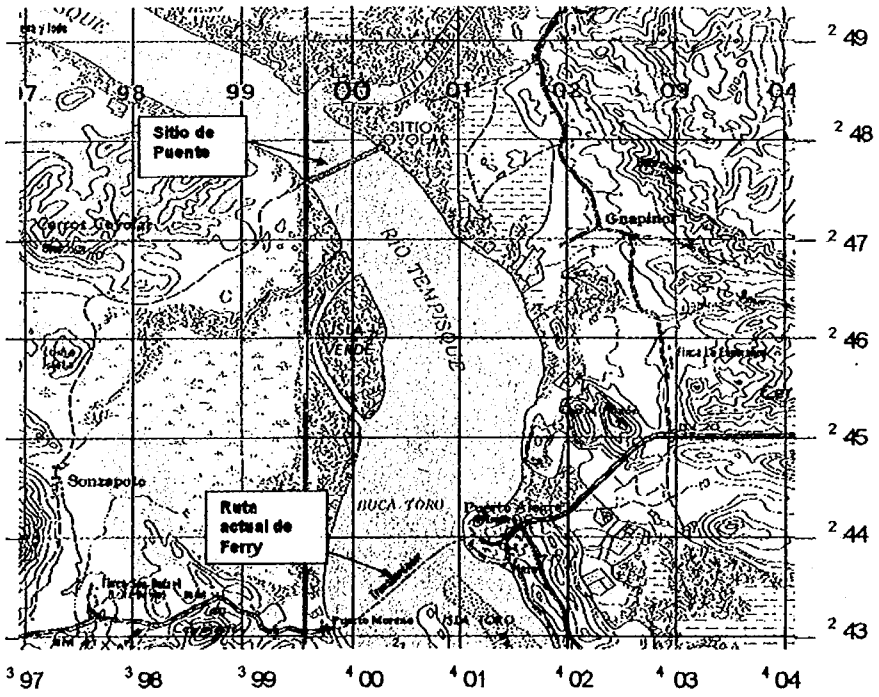


Fig. 2: Project Location shown in relation to Ferry

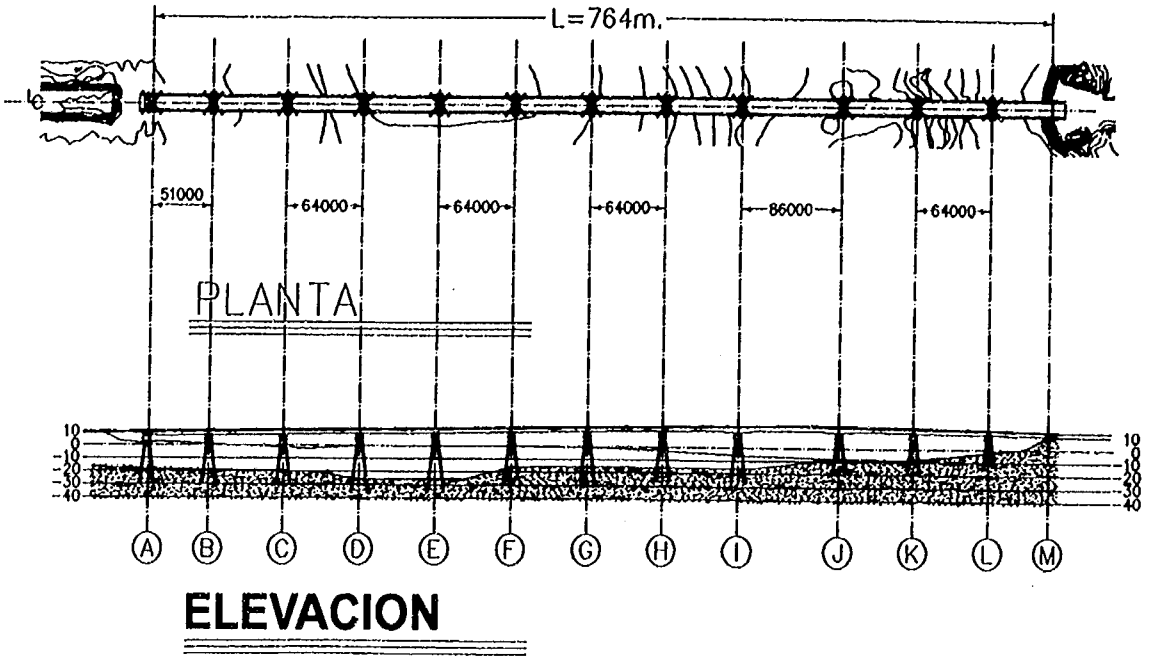


Fig. 3: Selected Alternative, Steel Superstructure with Batter Pile Bents

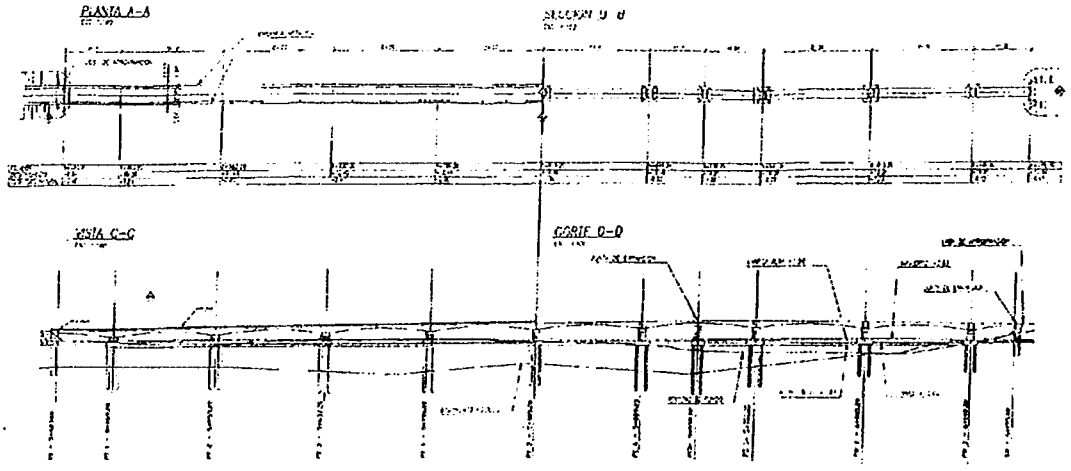


Fig. 4: Concrete Segmental Alternative with Plumb Piles

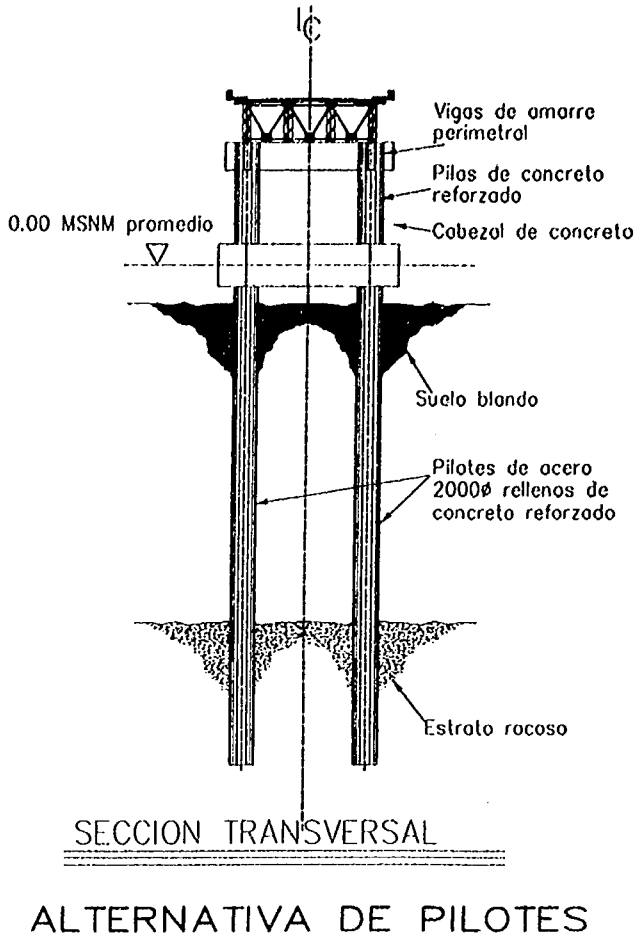


Fig. 5: Typical Section of Pier on Footing with Plumb Drilled Shafts

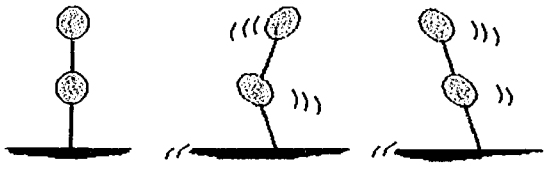


Fig. 6: Qualitative Seismic Response of Plumb Drilled Shaft Alternative

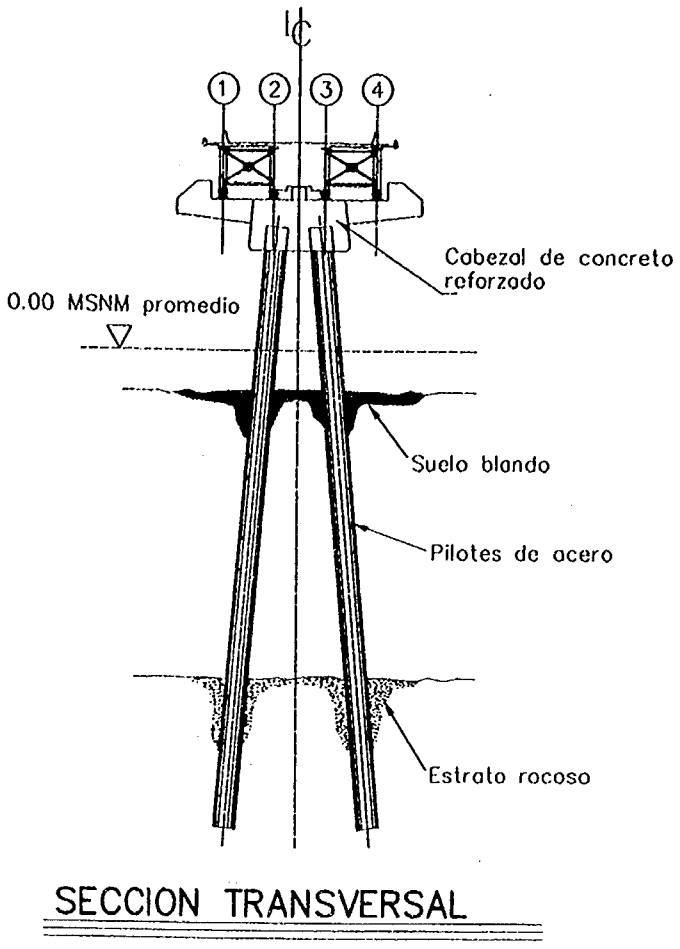


Fig. 7: Typical Section of Pile Bent

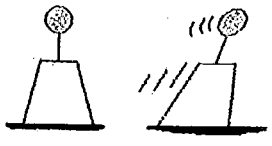
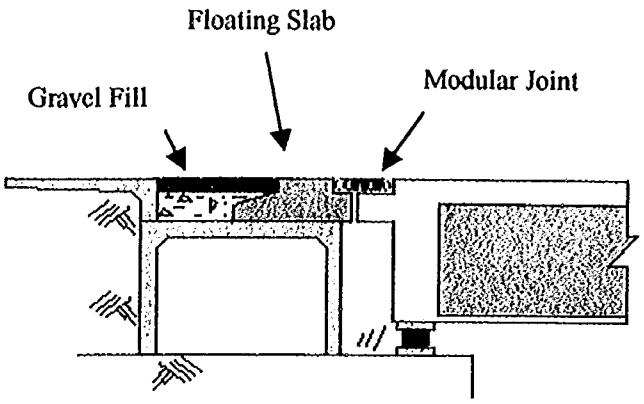
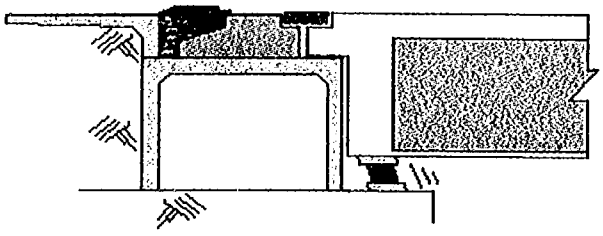


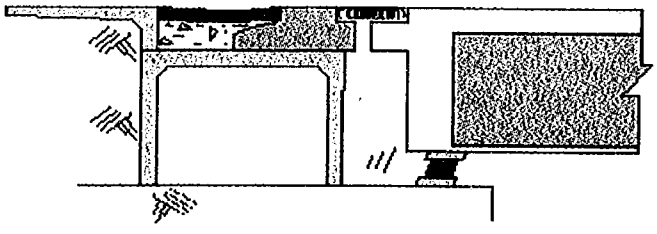
Fig. 8: Qualitative response of Pile Bent with I/D devices



Longitudinal section during normal bridge service

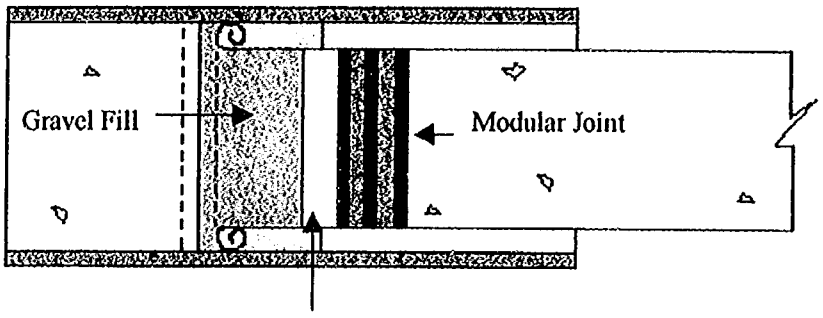


Longitudinal Seismic Response showing the bridge moving towards the abutment

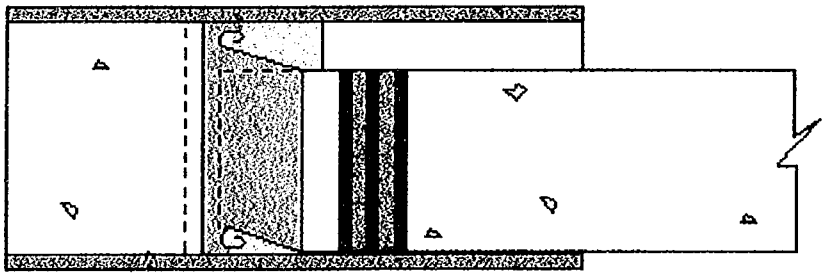


Longitudinal Seismic Response showing the bridge moving away from the abutment

Fig. 9: Longitudinal Response of Seismic Joint



Plan view of abutment showing bridge during normal service



Transverse Seismic Response showing bridge moving towards "cheek-walls"

Fig. 10: Transverse Response of Seismic Joint

SESSION 4: SEISMIC ISSUES (2)

(1)Liquefaction and Shear Wave Velocity Characteristics of Silty/Gravely Soils–Implications for Bridge Foundations
(Sabanayagam Thevanayagam)

(2) Experimental Study on Seismic Behavior of Bridge Pile-to-Pile Cap Connections
(Yan Xiao, J.B. Mander, H.Wu and G. Martin)

(3) A Proposal of Aseismic Strengthening of Wall-type RC Bridge Pier, with Minimum Impact on Its Foundation
(Kenji Ikeda, Hiroshi Mitamura, Norimitsu Kishi and Noriyoshi Murakami)

(4) Advanced Computational Methods in Bridge Engineering
(Jamshid Ghaboussi)

(5) Study on the Stability of the Akashi Kaikyo Bridge for Residual Displacement of Tower Foundation by Large-Scale Earthquake
(Susumu Fukunaga)

(6) Micropiles for Seismic Retrofits
(James H. Long, Thomas E. Hunt and Boris W. Leoro)

LIQUEFACTION AND SHEAR WAVE VELOCITY CHARACTERISTICS OF SILTY/GRAVELY SOILS - IMPLICATIONS FOR BRIDGE FOUNDATIONS

Sabanayagam Thevanayagam[1]

Abstract

Cyclic shear strength, post-liquefaction strength, and shear wave velocity v_s and damping characteristics are important parameters required for both static and dynamic response analyses of earth structures. Traditional indirect methods for estimation of these parameters based on void ratio, relative density, and mean effective stress have been successful for rather narrowly graded soils, but not for the most commonly found silty and gravelly soils. A simple array of two-sized particle system with large size disparity is presented to highlight the relative roles of intercoarser and interfiner grain contacts on mechanical response of such granular mixes. New parameters, namely intergranular void ratio e_c, interfine void ratio e_f, equivalent intergranular void ratio $(e_c)_{eq}$, and equivalent interfine void ratio $(e_f)_{eq}$ are introduced as indices of active intergrain contacts. They are related to v_s, cyclic strength, and post-liquefaction strength for silty and gravely soils.

Introduction

Dynamic stress-strain behavior, shear wave velocity (v_s) and damping characteristics of soils are important parameters required for dynamic response analysis, design, and performance evaluation of earth structures and both shallow and deep foundations associated with transportation facilities and bridges. Shear wave velocity characteristics influence attenuation characteristics and the level of ground accelerations anticipated as well as the shear stresses induced in the ground due to an input earthquake motion at the bedrock. When combined with monotonic and cyclic undrained stress-strain characteristics it foretells the expected performance of the ground in terms of its potential for liquefaction, ground settlement, displacement, sliding, etc in sandy soils. While often engineers resort to sophistication in analysis, the fact that the proper choice of the input soil parameters dictates the design/performance outcome much more than the sophistication in the analysis is not well ingrained. A few examples of the difficulties in estimating these parameters are presented followed by practical geotechnical insights to overcome these difficulties. It can help judicious design choices leading to successful foundation performances during earthquakes.

Soil Parameters: Several indirect methods have been developed, based on theoretical and laboratory studies on (clean) sands and/or field observations, to determine v_s (Duffy and Mindlin 1957, Hardin and Richart 1963, Hardin and Drenevich 1972, Seed et al. 1986, Goddard 1990, Lo Presti and Jamiolkowski 1999), liquefaction potential (Seed et al. 1983, Robertson et al. 1997, Andrews and Stokoe 1997), post-liquefaction strength (Seed 1987, Seed and Harder 1990), etc. which are required for such analyses. There are variations as well (Stark and Mesri 1992, Ishihara 1993, Baziar and Dobry 1995). These methods relate the above material characteristics to void ratio, relative density or some insitu parameters such as

[1] Associate Professor, Dept. of Civil, Struct. and Env. Eng., SUNY at Buffalo, Buffalo, NY 14260, USA; Email: theva@eng.buffalo.edu

SPT blow counts, CPT resistance which are considered to be related to relative density. For example, widely used relationship for v_s (m/s) is of the form:

$$v_s = v_{so}\left(\frac{\sigma'}{p_a}\right)^{\alpha} \quad where \quad v_{so} = Ap_a^{\alpha}(e_m - e) \quad or \quad v_{so} = Be^{-x} \qquad (1)$$

where A=9.1 for rounded grains and 6.2 for angular grains, α=0.25, e_m=2.17 for rounded grains and 2.97 for angular grains, σ'=mean normal stress (N/m^2); v_{so}= normalized shear wave velocity [v_s at $\sigma'=p_a$=atmospheric pressure=100,000 N/m^2]; x=1.3 for sands, all approximately. The underlying tenet has been that global void ratio e (or relative density) is an index of active contacts among the soil grains, and hence refers to the resistance they can offer.

While such relationships and methods have proven successful for rather clean sands their wide spread applicability to natural soils, which often contain silty and gravely sandy soils, have proven detrimental. Observations from recent earthquake case histories indicate that, despite rather broadly graded nature of grain size distribution and relatively high density (low void ratio), such soils are often fragile, do liquefy, and experience vertical settlement and lateral spreads (Seed et al. 1983, Seed and Harder 1990, JGS 1996) defying conventional wisdom. Experience gained from past studies on clean sands does not always directly translate to such broadly graded soils. Recognition of this has lead to several laboratory and field studies to evaluate the effects of increasing silt or gravel content on: (a) cyclic strength and liquefaction potential, (b) post-liquefaction strength, (c) shear wave velocity, etc.

Liquefaction Potential: Results from laboratory studies on clean sands mixed with non-plastic silts show that, at the same (global) void ratio, monotonic undrained (steady state) strength and cyclic strength of silty sand decreases with an increase in silt content (Chang 1990, Georgiannou et al. 1990, Vaid 1994, Koester 1994, Pitman et al. 1994, Singh 1994, Zlatovic and Ishihara 1995, 1997). An example is shown in Fig.1a for a soil prepared by mixing a sand with a silt (PI=4) at nearly constant global void ratio (e=0.558) and confining stress (104 kPa) but at different silt contents (0 to 60% by weight, M-0 to M-60). Fig.1b shows the number of cycles to reach initial liquefaction versus silt content for the same sand-silt mix, along with the data for two other sands mixed with the same silt. As observed in Figs.1a-b, beyond a certain transition range of silt content the trend in decrease of strength reverses and the strength increases with further increase in silt content. The transition silt content range is about 20 to 30%.

Undrained (steady state) Strength: Fig.2 shows the mean stress at steady state for another sand/silt mix at different silt contents (00,07,15,25,40,60, and 100%) obtained from undrained monotonic triaxial tests (Thevanayagam et al. 1999). The specimens were initially isotropically consolidated to 100 kPa confining stress. The steady state line for each mix falls below that of the (clean) sand (os00) progressively until reaching fines content range of 25 to 40%. A transition occurs in this range and the trend reverses thereafter.

Shear Wave Velocity: Experimental data for v_s for silty sands and gravely soils (e.g. Kokusho et al. 1995, Brignoli et al. 1997, Rollins et al. 1998) indicate that shear wave velocity for gravely soils [and silty soils] are often significantly smaller than the respective

values for 'pure' sand, silt, or gravel at the same e. An example is shown in Figs.3a-b. It shows the v_{so} data for Tone river sand (TRS) and three other gravely soils prepared by mixing TRS with 25, 50 and 75% gravel by weight.

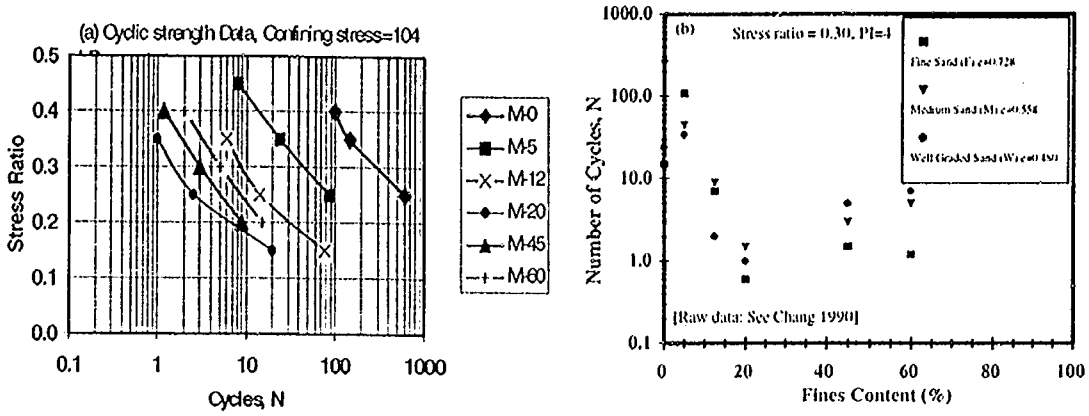


Fig.1 Influence of silt content on cyclic strength (a) Medium sand/silt, (b) Three sands/silt

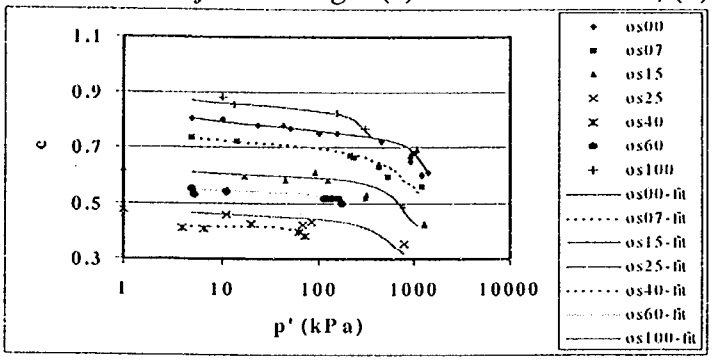


Fig.2 Influence of silt content on steady state

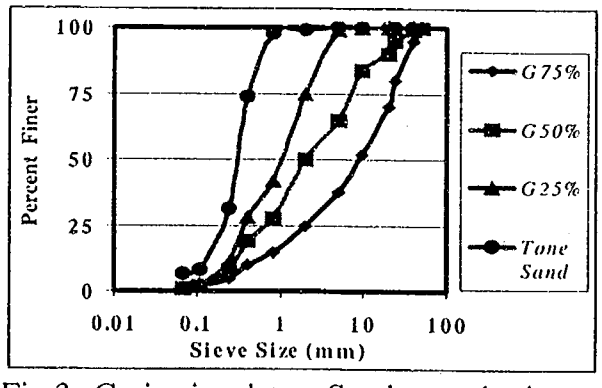


Fig.3a Grain size data – Sand-gravel mixes

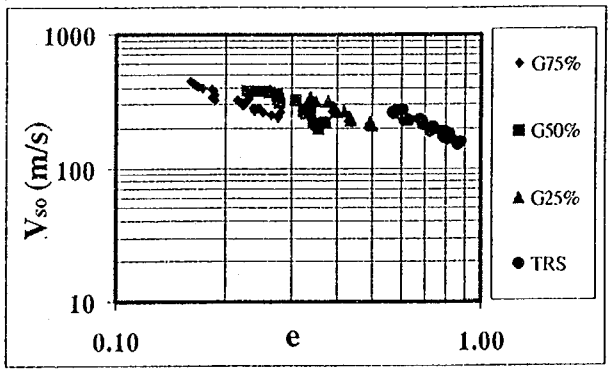


Fig.3b Influence of gravel content on V_{so}

The non-uniqueness of void ratio to correlate with the cyclic strength is clear. Low void ratio does not necessarily mean better mechanical properties. The physical meaning of the transition silt content is not clear. The conclusions in the literature on whether the presence of silt is beneficial or not is contentious. Similar concerns prevail regarding gravely soils (Evans and Zhou 1995). For the same reasons, questions also prevail among practicing engineers on broad applicability of the field SPT or CPT based correlations to all (new) sites.

Possible Reasons: Recently, it has been brought to the attention that physical nature of silty sands and gravely sands are entirely different from clean sand, silt or gravel (Thevanayagam 1998a-b, 1999a-d, Thevanayagam and Mohan 1998). As the void ratio and proportion of the coarser and finer grains content of these soils change the nature of their microstructure also changes. The relative participation of the particles of very different sizes in the *internal interparticle contact force chain* also changes. Due to particle size disparity and availability of pores larger than some particles, at low finer grains content (FC) some of the finer particles may remain inactive or move between pores without significantly affecting or contributing to the force chain. Yet they contribute to the global void ratio. Alternately when there is a sufficient amount of finer grains the coarser grains become dispersed contributing much less to the force chain than to the global void ratio. Global void ratio e ceases to be an index to represent the nature of *contact density* of active particles. The traditional use of e to compare and correlate with the behavior of soils containing different amounts of finer grains content ceases to be valid. The same holds for relative density. In general the stress-strain behavior, liquefaction potential, and v_{so} of granular mixes are affected by a critical combination of *intergranular and interfine contacts*. New *indices of active contacts* are needed to represent the nature of intergrain contacts in order to characterize the behavior of such soils.

Using a two-sized particle mix as a model, this paper highlights the nature of the microstructure of granular mixes. Based on this such granular mixes are classified into certain groups (Fig.4) depending on the relative frictional contributions at the intergranular and interfine grain contact level. Intergranular (e_c), interfine (e_f), equivalent intergranular $(e_c)_{eq}$, and equivalent interfine $(e_f)_{eq}$ void ratios (Fig.5) are introduced as primary indices of contact density for the various groups. Global void ratio is introduced as a secondary index. These new indices are related to v_s and undrained strength of young silty/gravely soils at different silt or gravel contents. Details are presented elsewhere (Thevanayagam 1999c-d, Thevanayagam et al. 1999). The underlying theme is that contact is the mechanism by which a granular medium responds to external excitations. The density of contacts may be expressed using the above indices.

Conceptual Microstructure

Consider a two-sized granular mix (Fig.4). The microstructure of this granular mix can be constituted by infinite different ways. Each one of them leads to a different internal force chain network among particles and hence each exhibits a different stress-strain response during shear. Among infinite variations, a few extreme limiting categories of microstructure and the relevant roles of coarser and finer grains are as follows.

Case-i: The first category (Fig.4a) is when the finer grains are fully confined within the void spaces between the coarser-grains with no contribution whatsoever in supporting the coarser grain skeleton. Finer grains are inactive (or secondary) in the transfer of inter particle forces. They may largely play the role of "filler" of intergranular voids. The mechanical behavior is affected primarily by the coarser grain contacts. During deformation the finer grains may move from one pore space to another without significantly contributing to the mechanical response of the soil. This requires that the finer grain particle size (d) is much

smaller than the pore size between the coarser grains and that the intergranular pore space is not completely filled with the finer grains. Typically this requires that the coarser grain size (D) is at least 6.5 times larger than the finer grain size, and that the finer grain content (FC) is less than a certain threshold value (FC_{th}). This category is called *case-i*. Even at low FC, if the size disparity R_d (=D/d) is not very large, the finer grains cannot freely move through the inter-coarser granular voids; They also tend to participate in the force chain and actively contribute to the stress-strain response.

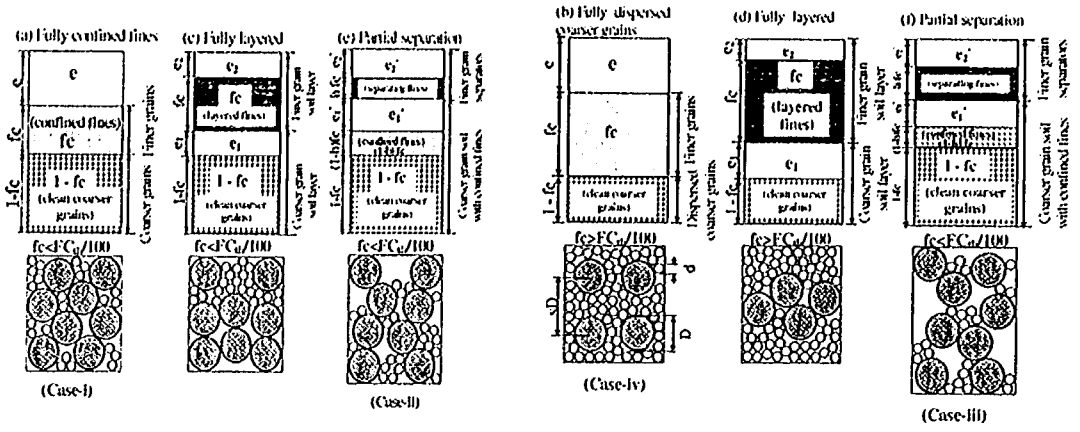


Fig.4 Microstructure and intergranular matrix phase diagram

Cases-ii and iii: Consider changing the microstructure shown in Fig.4a in two ways: (1) alter the position of some of the finer grains, or (2) add more finer grains. The consequences are significant. If one alters the position of some of the finer grains, while maintaining the finer grain content the same, the microstructure corresponding to the second and third categories shown in Figs.4e and f are obtained with a concurrent increase in global void ratio. Essentially, the microstructure in Figs.4e-f is made up of partial layering and partial separation of coarser grains by the finer grains along with confined finer grains within the voids between the coarser grains. Some of the finer grains become active participants in the internal force chain. These finer grains are termed the *'separating fines'* in Figs.4e and f. In Fig.4e, the finer grains may be supporting the coarser-grain skeleton that is otherwise unstable. They act as a load transfer vehicle between "some" of the coarse-grain particles in the soil-matrix while the remainder of the fines play the role of "filler" of voids. They may dominate the initial stress-strain behavior depending on the type of finer grains (plastic or non-plastic). In Fig.4f, the finer grains may play an active role of *"separator"* between a significant number of coarse-grain contacts and therefore begin to dominate the strength characteristics. Coarser grain skeleton is virtually unstable without the finer grains. These categories of microstructure are called case ii and iii, respectively. Case-ii is a transition between cases i and iii. Theoretically case-iii occurs at an intergranular void ratio exceeding the maximum void ratio ($e_{max,HC}$) achievable for the 'pure' host coarser grain soil.

Cases-iv-1 and iv-2: On the other hand if one increases the finer grains content sufficiently, one gets the fourth category (Fig.4b). It occurs naturally when sufficient finer grains are present making active contacts among themselves. The coarser grains begin to disperse in the finer grain matrix. Transition from Fig.4a to Fig.4b occurs when the finer grains content (FC) exceeds beyond the threshold fines content (FC_{th}). When $FC>FC_{th}$ the

finer grains begin to play a rather important role while the role of coarser grains begin to diminish. The fines may carry the contact and shear forces while the coarser grains may act as *reinforcing elements* embedded within the finer grain matrix. The effect of coarser grains cannot be completely neglected until they are separated sufficiently apart. This imposes a limiting fines content FC_l. There exists a transition zone between FC_{th} and FC_l before the behavior of the soil mix is entirely governed by the finer grains. This is called case-iv-2 whereas the case corresponding to $FC>FC_l$ is called case-iv-1. The size disparity constraint discussed before for cases i to iii needs not be satisfied.

The fifth category (Figs.4c-d) is when the coarser and finer grains constitute a fully layered system where the coarser grain layers have no fines contained in them and vice versa. This is called case-v. It is also possible to create a composite system that contains some of the cases i through v. The figures 4a, c, e and f are more relevant at low finer grains content. Figs.4b and d are relevant at high finer grains content.

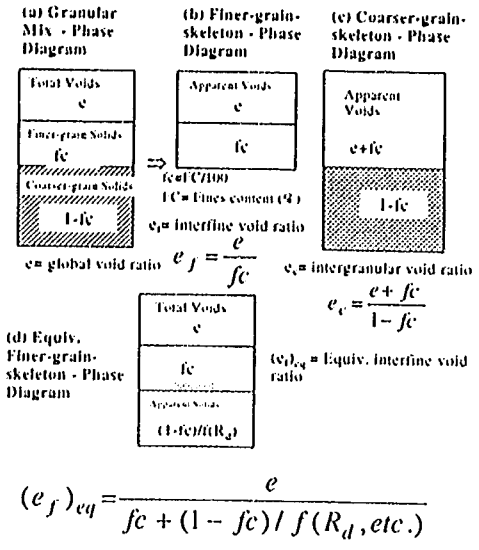
Intergranular Contact Indices

Case-i: Up to $FC=FC_{th}$ the finer grains can, but not necessarily, remain within the intergranular voids. Provided that the size disparity is large and the coarser granular skeleton is dense whether or not some of the finer grains fall between the coarser grain contacts or remain fully confined within the intergranular voids does not significantly affect the shear strength of the soil. Primarily the intergranular contacts between the coarser grains affect the mechanical behavior with secondary effects by the finer grains. Hence, neglecting the effects of fines, the *inter-coarser grain void ratio* e_c (Fig.5c) may be used as an index of active contacts. The magnitude of e_f (Fig.5b) may be used as an index to assess the secondary effects by the finer grains.

$$e_c=\frac{e+fc}{1-fc}; \qquad e_f=\frac{e}{fc}; \qquad fc=FC/100 \tag{2}$$

Cases-ii and iii: For these cases, still the inter-coarser grain contact plays a significant role. However, the influence of finer grains supporting the coarser grains must also be accounted for in devising an index of active contacts. The relevant contact index void ratio would be $(e_c)_{eq}$ (Figs.4e-f); 'b' refers to the finer grains contributing to active contacts. Although it may be possible to use e_c as an index of active contacts for these cases, it is expected the mechanical behavior of such mixes would be different and generally stronger than that of the host coarser grain soil at the same e_c.

$$(e_c)_{eq}=\frac{e+(1-b)fc}{1-(1-b)fc}; \qquad 0\le b\le 1 \tag{3}$$



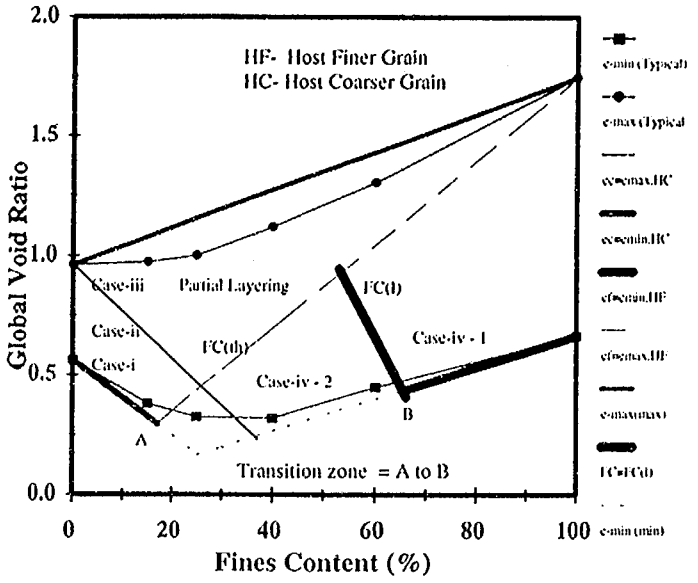


Fig.5 Intergranular contact indices

Fig.6 Intergranular matrix diagram – Mix classification

Case-iv: When $FC>FC_I$, for case-iv-1, neglecting the effects of dispersed coarser grains, the *interfine void ratio* e_f may be used as an index of active contacts. At $FC_{th}<FC<FC_I$, neither e, e_c, nor e_f can sufficiently represent the active contacts, alone, although all of them together can be used to deduce the mechanical response. Devising a primary index of active contacts in this range is useful, however.

For a granular mix in this range the global void ratio e overestimates the actual density of active contacts in the granular mix. This is so because the dispersed coarser grains in the mix do not contribute as many active contacts as if the soil was prepared at the same void ratio by substituting each coarser grain by an equal (solid) volume of finer grains. The reason is that solid volume of a dispersed coarser grain, which directly influences the global void ratio, grows in proportion to the power of three of size. Whereas its surface area, which influences the nature of contacts with the surrounding finer grains, grows in proportion to the power of only two. For equal solid volume, the substituted finer grains have a larger surface for contact than a dispersed coarser grain of equal (solid) volume embedded in the finer grain medium. The density of contacts in the mix is smaller than that in the finer grain soil at the same e. Hence e overestimates the active contacts in the mix.

The use of e_c as an index of active contacts is not valid since it ignores entirely the existence of interfiner grain contacts. It grossly underestimates the active contacts. Similarly, the interfine void ratio e_f also underestimates the active contacts, since it completely ignores the presence of the dispersed coarser grains. The latter do make contact with the surrounding finer grains and participate in the force chain. The effects of such contacts may not be negligible unless the spacing between the dispersed coarser grains is very large. The reinforcement effect by the coarser grains must also be introduced to obtain an *equivalent* interfine void ratio index $(e_f)_{eq}$ as the index of active contacts. The equation for e_f must be modified accordingly. Combining the above arguments, after simplifications, theoretically $(e_f)_{eq}$ (Fig.5d) is (Thevanayagam 1999c).

$$(e_f)_{eq}=\frac{e}{[fc+(1-fc)/R_d^m]};\qquad R_d=\frac{D}{d};\qquad 0<m<1;\qquad e_c>e_{max,HC} \tag{4}$$

Conceptually, Fig.6 shows the regions belonging to the four cases i through iv confined by various transition boundaries. The transition lines corresponding to the theoretical threshold and limiting finer grains contents (Thevanayagam 1999c) are given by:

$$FC_{th}\le\frac{100e_c}{1+e_c+e_{max,HF}}\%=\frac{100e}{e_{max,HF}}\%;\ FC_l\ge 100\left[1-\frac{\pi(1+e)}{6s^3}\right]\%=100\left[\frac{\frac{6s^3}{\pi}-1}{\frac{6s^3}{\pi}+e_f}\right]\%\ge FC_{th} \tag{5}$$

where $s=1+a(d/D)=1+a/R_d$ where a=10 (approximately). The various boundaries refer to the maximum and minimum void ratio profiles: $e=e_{max,HC}+(e_{max,HF}-e_{max,HC})fc$; $e_c=e_{max,HC}$; $e_f=e_{max,HF}$; $e_c=e_{min,HC}$; and $e_f=e_{min,HF}$ where $e_{max,HC}$ and $e_{max,HF}$=maximum void ratio of the host coarser and finer grains, respectively, beyond which they have no appreciable strength, $e_{min,HC}$ and $e_{min,HF}$ = minimum void ratio of the host coarser and finer grains, respectively.

The aforementioned contact indices and the location of a soil mix in Fig.6 can be used to predict the trends for stress-strain characteristics and v_s of silty or gravely soils *relative* to that of the host coarser grain soil or the host finer grain soil as reference.

Mechanical Behavior

Fig.7a shows a schematic diagram for *hypothetical* specimens satisfying the following specific constraints. (1) An increase in e at the same FC [specimens 1,2,3], (2) An increase in FC at the same e [4,2,5,6,7,13], (3) An increase in FC at the same e_c [8,1,9 or 3,10 or 14,2,15; $FC<FC_{th}$], or (4) An increase in coarser grain content at the same e_f [11,7,12; $FC>FC_{th}$]. For reasons discussed below the mechanical response parameters (v_s, and shear strength) for the four categories above is expected to be of the form shown in Fig.7b, although it refers only to cyclic strength.

Relative Trends -- Cyclic Strength: The anticipated trends in number of cycles (N) required to cause initial liquefaction at the same cyclic stress ratio are *schematically* shown in Fig.7b [N versus FC]. In (1) both intergranular and interfine void ratios increase with concurrent reduction in inter-coarser grain contacts. Therefore the soil becomes weaker. In (2) while e_c increases e_f decreases. Viz. the inter-coarser granular contacts decrease while the interfine contacts increase. Hence initially the soil is expected to weaken [4,2,5] followed by a transition in the vicinity of $e_f=e_{max,HF}$ ($FC=FC_{th}$). The soil becomes stronger beyond that [6,7,13]. In (3), the increase in a cushioning effect by the finer grains contained in the intergranular void spaces is manifested leading to a slight increase in strength [3,10, case-iii]. In (4) when the soil is at $FC_{th}<FC<FC_l$ [11,7,12] the reinforcement effect of the coarser grain 'inclusions' affect the stress- strain behavior. The specimen 11 is expected to be stronger than 7. Once FC exceeds FC_l the reinforcement effect is expected to be small. Primarily the interfine contacts and e_f are expected to affect the soil behavior [7,12].

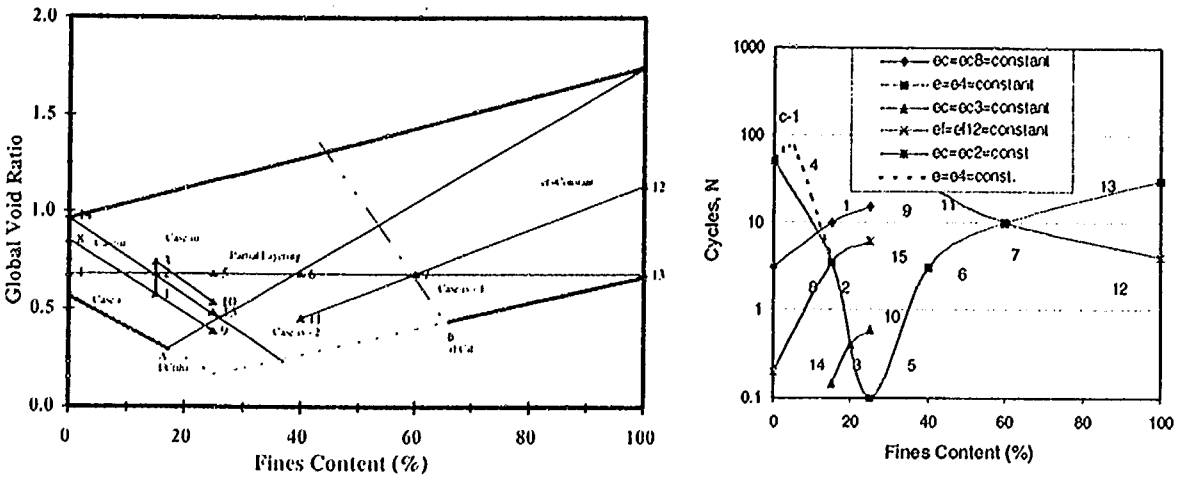


Fig.7 Relative trend in cyclic strength – Schematic

Shear wave velocity: Based on the above considerations, with due consideration for the dependence of v_s on the nature of contacts (Duffy and Mindlin 1957, Goddard 1990, Thevanayagam 1999d), v_s of granular mixes may be given by the following, reflecting its dependence on contact index e_{eq}:

$$v_s = v_{so}\left(\frac{\sigma'}{p_a}\right)^{\alpha} \quad ; \quad v_{so} = A p_a^{\alpha}\,(e_m - e_{eq}) \qquad \text{or} \quad v_{so} = B e_{eq}^{-x} \tag{6}$$

where $e_{eq}=(e_c)_{eq}$ for FC< FC_{th}; $e_{eq}=(e_i)_{eq}$ for FC>FC_{th}. Eq.6 may also be conveniently presented in terms of e by substituting the proposed expressions for e_{eq}:

$$v_{so} = A_{eq}\, p_a^{\alpha}\,((e_m)_{eq} - e) \tag{7a}$$

$$\text{or } v_{so} = B_{eq} e^{-x} \text{ for FC>}FC_{th} \text{ and } v_{so} = B(1-(1-b)fc)^{x}(e+(1-b)fc)^{-x} \text{ for FC< } FC_{th} \tag{7b}$$

where $A_{eq}=A/(1-(1-b)fc)$ and $(e_m)_{eq}=e_m(1-(1-b)fc)-(1-b)fc$ for FC<FC_{th}; $A_{eq}=A/[fc+(1-fc)/(R_d)^m]$ and $(e_m)_{eq}=e_m\,[fc+(1-fc)/(R_d)^m]$ for FC>FC_{th}; $B_{eq}=B[fc+(1-fc)/(R_d)^m]$ for for FC>FC_{th}. It is readily apparent that Eq.7 is similar to Eq.1 but with different coefficients depending on FC. The differences are manifestations of differences in contacts in granular mixes containing different proportions of coarser and finer grains. Direct use of Eq.1, without due consideration for the dependence of the coefficients in Eq.1 on FC can be misleading. Details are presented elsewhere (Thevanayagam 1999d).

Observations - Reinterpretations

A limited set of experimental data is available in support of the above conceptual framework. The following sections present one example each for cyclic strength, undrained steady state strength, and shear wave velocity.

Cyclic Strength: The data shown in Fig.1b is recalled again in Figs.9-10. Figs.8a-c show the intergranular matrix diagram for the three host sands [(1) Fine (F), (2) Medium (M), and (3) Well graded (W)] mixed with a low plasticity silt (PI=4) reported in Figs.1a-b. The

locations of the specimens are also shown. Each sand mix was tested at 0, 5, 12, 20, 45, and 60% silt content (FC). The specimens were prepared by moist tamping method and tested at nearly constant e=0.728 for F, e=0.558 for M, and e=0.480 for W, respectively. No data were available for $e_{max,HF}$ and $e_{min,HF}$ for the silt. FC_{th} was estimated assuming typical values of $e_{max,HF}$ =1.5 and $e_{min,HF}$ =0.6 for the silt. R_d (defined as D_{50}/d_{50}) for the soils F, M, and W were estimated to be about 15, 40, and 40 based on a typical value for d_{50} of silts.

An examination of Fig.8 and calculated index void ratios (shown in Fig.9) would readily reveal the cases each specimen belongs to and the expected behavior of each granular mix relative to one another. As the fines content increases, at the same e, e_c increases and e_f decreases. Initially e_f remains high indicating the lack of significant interfine contacts. With increase in FC the soil mixes move gradually from Case-i to Case-ii to Case-iii and then cross over to Case-iv-2. So is the behavior of the soils (Fig.9). Initially the strength decreases due to reduced intergranular contacts with increase in e_c with little or secondary contribution from the silt. As the soil moves beyond the threshold transition zone (FC_{th} at $e_f = e_{max,HF}$) and enters the zone for Case-iv-2 the influence of e_f becomes important with some reinforcement effect by the coarser grains. The $(e_f)_{eq}$ becomes the primary contact index void ratio. The trend reverses and the strength begins to increase with further increase in fines content.

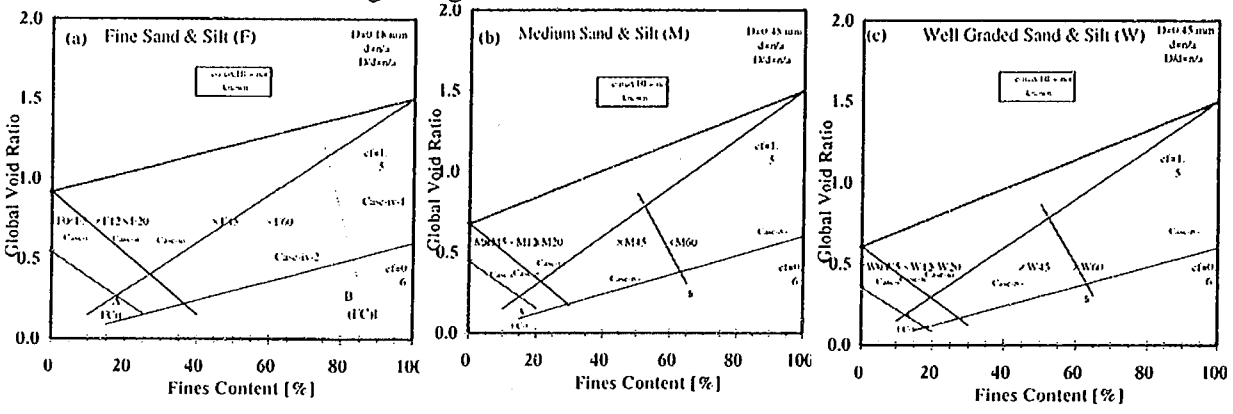


Fig.8 Intergranular matrix diagrams – Three Sand – Silt Mixes

Fig.10a shows the same data in a different format: Number of cycles to initial liquefaction versus e_c for Cases-i to iii [$FC<FC_{th}$]. For this case, a different cyclic strength profile is obtained for each mix depending on the parent sand type (F,M,W). Cyclic strength (N) is affected primarily by the parent sand type. e_c becomes the primary index of active contacts. The fines have a secondary role.

Fig.10b shows N versus e_f data for Case-iv ($FC>FC_{th}$). N data show significant dependency on e_f. The data for each fines content (45% and 60% separately) correlates well with e_f and fall in a (separate for 45% and 60%) narrow band regardless of the parent sand type. The separate narrow bands for the soils mixed with 45% fines and 60% fines are due to the differences in the degree of reinforcement effect. At the same e_f, the cyclic strength is higher for the soil with higher sands content. The reinforcement effect is higher at 45% fines content than at 60%. Fig.10c shows the same data, plotted against $(e_f)_{eq}$ [calculated assuming m=0.45). Interestingly the number of cycles required to cause liquefaction correlates with $(e_f)_{eq}$ for all three mixes. The reason for this is that all sands were mixed with the *same silt*.

Hence, once FC exceeds the threshold value, all soil mixes are affected by the same silt except for the minor differences due to the presence of different size coarser grains (F,M,W). Hence a single narrow band is obtained in Fig.10c.

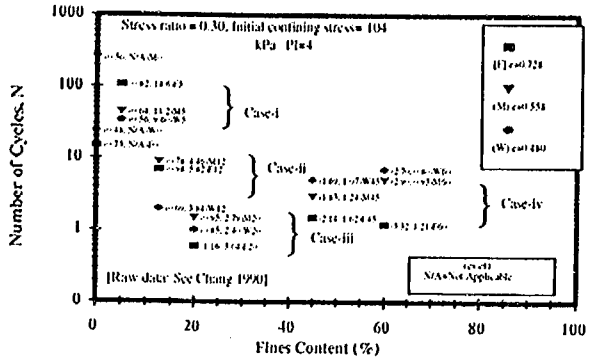


Fig.9 Effect of silt content on cyclic strength

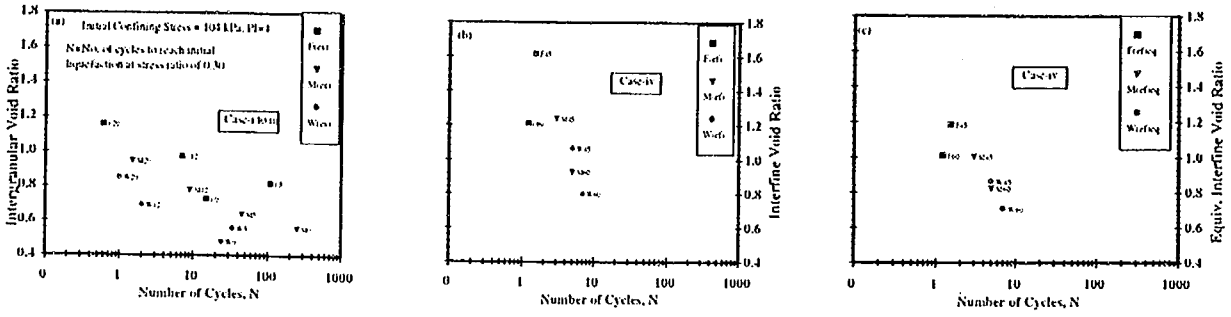


Fig.10 Influence of intergrain contacts on cyclic strength: (a) e_c, (b) e_f, and (c) $(e_f)_{eq}$

Undrained (steady state) Strength: Fig.11 shows the intergranular matrix diagram for the sand/silt mix reported before in Fig.2. Figs.12-13 show the same data plotted against $(e_c)_{eq}$ and $(e_f)_{eq}$, respectively, for up to silt content (FC) of 25% and beyond that. The values of 'b' and 'm' were 0.25 and 0.65, respectively. The data in each case fall in a narrow band surrounding the data for clean sand and silt, respectively. This is indicative of the primary role of inter coarser grain contacts at $FC<FC_{th}$ and interfiner grain contacts at $FC>FC_{th}$. The direct use of e to characterize steady state strength can be misleading (Fig.2). Further care is necessary due to possible dependence of undrained shear strength on confining stress (Thevanayagam 1998a).

Shear Wave Velocity: Fig.14 shows the intergranular matrix diagram for the sand/gravel mixes shown before in Figs.3a-b. In this case sand is the finer grain and gravel is the coarser grain. The gradation data (Fig.3a) was decomposed into gravel and sand and the respective D_{50} and d_{50} were determined (Table 1). FC_{th} was estimated for each specimen assuming $e_{max,HF}$=0.966 (TRS). FC exceeded FC_{th} for most specimens. They belong to case-iv-2. The relevant contact index void ratio $(e_f)_{eq}$ was calculated using assuming m=0.45. Fig.15 shows the same data shown in Fig.3b, but plotted against $(e_f)_{eq}$. v_{so} correlates well with $(e_f)_{eq}$. It also shows clearly that addition of gravel to sand did not contribute to the v_{so} as much as it did to e. Direct use of e to estimate v_{so} can be very unconservative. Indirect methods of estimating v_{so} may use

the relationships of the type Eqs.6-7. Further results are reported in Thevanayagam (1999d).

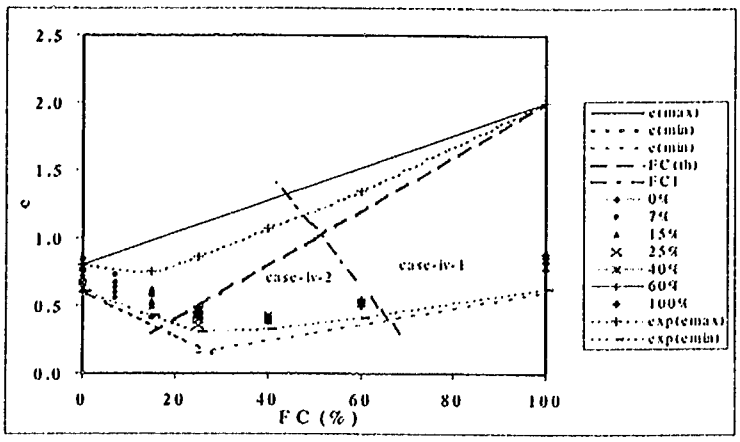


Fig.11: Intergranular matrix diagram

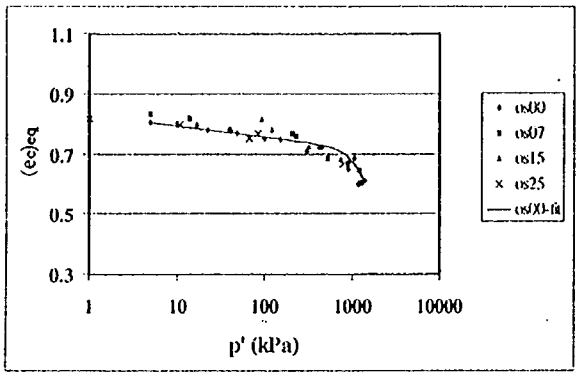


Fig.12: $(e_c)_{eq}$ vs p' –sand and silty sands

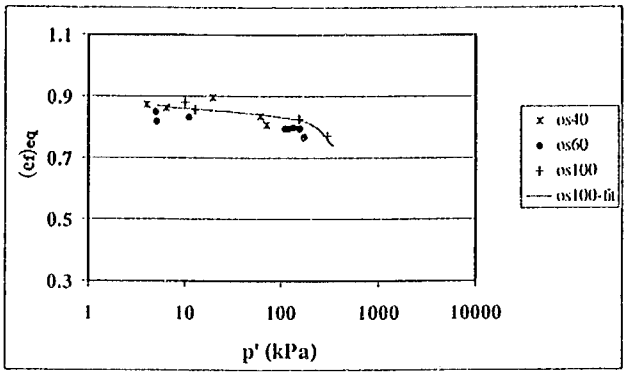


Fig.13: $(e_f)_{eq}$ vs p' – Sandy silts and silt

Table 1: Sand-gravel mix data

Soil	D_{50} *(mm)*	d_{50} *(mm)*	R_d	Range e	FC (%)	FC_{th} (%)	*Remarks*
Tone River Sand	---	0.34	---	0.55-0.90	100		Case-iv
G25 Gravel	3	0.7	4.3	0.33-0.50	75	35-52	Case-iv
G50 Gravel	7	0.7	10	0.22-0.37	50	24-38	Case-iv
G75 Gravel	15	0.6	25	0.16-0.28	25	17-29	Case-iv

Note: Data obtained from Fig.3a.

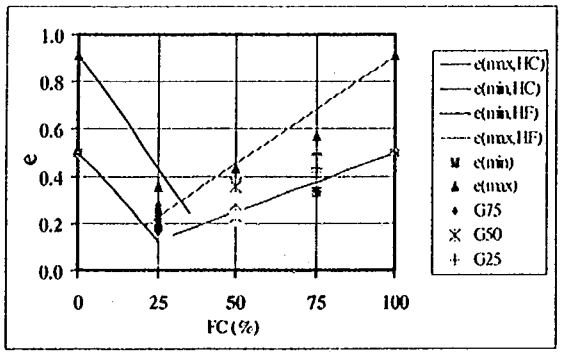


Fig.14 Intergranular matrix diagram-Sand-gravel Mix

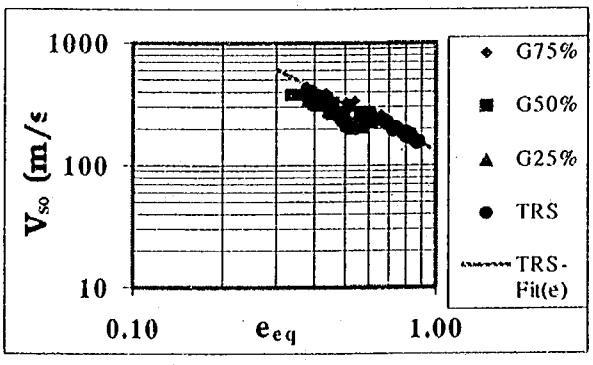


Fig.15: v_{so} versus $(e)_{eq}$ relations

Implications & Conclusions

The above analyses illustrate the differences in the relative contribution of coarser and finer grains in a soil to its mechanical response parameters. Indirect methods of estimating material parameters, even for preliminary design purposes, based on density or void ratio of a soil can yield often unconservative values for v_s, and shear strength. The reason for this is that void ratio or density of a soil is indeed an index of volume or mass density. Mechanical soil parameters are primarily affected by contact density (per grain).

A simple framework is presented to modify the relevant indirect methods to obtain more realistic input soil parameters. With this framework, one may deduce the behavior of granular mix soils at various finer grain contents and void ratios *relative* to the behavior of the host coarser grain soil or the finer grain soil as reference.

In general, (a) for soils containing low finer grains content less than a threshold value (FC_{th}), when compared at the same $(e_c)_{eq}$, the mechanical response is similar to that of the host coarser grain soil at the same void ratio, and (b) for soils containing large finer grains content, when compared at the same $(e_f)_{eq}$, the response is similar to that of the host finer grain soil at the same void ratio. Further work is needed to examine the applicability of these contact indices for different soils.

The above results indicate that the choice of soil parameters for dynamic analysis of earth structures, liquefaction potential evaluation, determination of post-liquefaction ground damage, foundation performance, etc. should consider a method that reflects the nature of active grain contacts. Insitu parameters such as SPT blow counts, CPT resistance, and field shear wave velocity do reflect this to some extent. But how well do they reflect this, on the face of the several uncertainties involved in the development of the empirical correlations of such parameters with soil parameters based on observed performances, remains the subject of an engineer's judgement. It is hoped that the geotechnical insights presented herein help engineers in judicious choice of soil parameters for foundation design involving young silty/gravely soils against seismic events.

Acknowledgments

Financial support by the USGS/NSF/MCEER for the various aspects of this ongoing research work is gratefully appreciated. Thanks are also due to J. Liang and T. Shenthan, SUNY at Buffalo, for their assistance in the laboratory triaxial tests on silty soils.

References

Andrus, R., and Stokoe, K. H. II (1997) "Liquefaction resistance based on shear wave velocity", NCEER Report, 97-0022, State University of New York at Buffalo, NY, 89-128.

Baziar, M.H. and Dobry, R. (1995), "Residual strength and large-deformation potential of loose silty sands", J. Geotech. Eng. Div., ASCE, 121(12), 896-906.

Brignoli, E., Fretti, C., Jamiolkowski, M. and Stokoe, K.H. II (1997) "Stiffness of gravelly soils to small strains", Proc. 14th Intl. Conf. SMFE, Germany, vol.1, 37-40.

Chang, N.Y. (1990) "Influence of fines content and plasticity on earthquake-induced soil liquefaction", Contract Rep., US Army WES, Vicksburg, MS Contract No. DACW3988-C-0078

Duffy, J. and Mindlin, R.D. (1957) "Stress-strain relations of a granular medium", Transactions, ASME, 585-593.

Evans, M. D. and Zhou, S. (1995) "Liquefaction behavior of sand-gravel composites", ASCE, J. Geotech. Eng., 121(3), 287-298.

Georgiannou, V.N, Hight, D.W and Burland, J.B (1990), "The undrained behaviour of clayey sands in triaxial compression and extension", Geotechnique, 40(3), 431-49.

Goddard, J. D. (1990) "Nonlinear elaasticity and pressure-dependent wave speeds in granular media", Proc. Royal Soc. London, A, 430, 105-131.

Hardin, B.O., and Richart, F. E. Jr. (1963). "Elastic wave velocities in granular soils" J. Soil Mech. and Found. Div., ASCE, 89(SM1), 33-65.

Hardin, B. O., and Drnevich, V. P. (1972). "Shear modulus and damping in soils: Measurements and parameter effects", *J. Soil Mech. Found. Div.*, ASCE, 98(6), 603-624.

Ishihara, K. (1997) "Terzaghi oration: Geotechnical aspects of 1995 Kobe earthquake", Proc. 14th Itnl. Conf. SMFE, vol.4, 2047-2073.

Ishihara, K. (1993), "Liquefaction and flow failure during earthquakes", Geotechnique, 43(3), 351-41.

JGS (1996) "Soils and Foundations - Special issue on geotechnical aspects of the January 17 1995 Hyogoken-Nambu Earthquake", Japanese Soc. Geotech. Eng.

Koester, J.P. (1994), "The influence of fines type and content on cyclic strength", ASCE Geotech. STP 44, 17-32.

Kokusho, T., Yoshida, Y. and Tanaka, Y. (1995) "Shear wave velocity in gravelly soils with different particle gradings", ASCE Geotech. STP 56, 92-106.

Kuerbis, R., Nagussey, D. and Vaid, Y.P. (1989), "Effect of gradation and fines content on the undrained response of sand", Proc. Conf. on Hyd. Fill Struc., ASCE Geotech. STP 21, 330-45.

Lo Presti, C.F. and Jamiolkowski, M. (1998) "SPT N-value and S-wave velocity for gravelly soils with different grain size distributions" Discussion, Soils and Foundation, 39(2), 138-140.

Mitchell, J. K. (1993) *Fundamentals of soil behavior*, 2nd ed. Wiley Interscience Publ.

Pitman, T.D., Robertson, P.K. and Sego, D.C. (1994), "Influence of fines on the collapse of loose sands", Can. Geotech. J., 31, 728-39

Robertson, P. K. and Wride, C. E. (1997) "Evaluation of cyclic liquefaction potential based on the CPT", Seis. Behavior of Ground & Geotech Struct., ed. P.S. Pinto, Balkema Publs., 269-278.

Rollins, K., Evans, M., Diehl, N. B., and Daily W.D. (1998) "Shear modulus and damping

relationships for gravels" J. Geotech. and Geoenv. Eng., 124(5), 396-405.
Seed, H.B., Wong, R.T., Idriss, I.M., and Tokimatsu, K. (1986). "Moduli and damping factors for dynamic analysis of cohesionless soils", J. Geot. Eng. Div., ASCE, 112(11), 1-17.
Seed, H. B., Idriss, I.M. and Arango, I. (1983) "Evaluation of liquefaction potential using field performance data", J. Geotech. Eng., ASCE, 109(3), 458-482
Seed, R. B. and Harder, L. F. Jr. (1990), "SPT-based analysis of cyclic pore pressure generation and undrained residual strength", Proc. Seed Memorial Symp., Berkeley, 2, 351-76
Seed, H.B. (1987), "Design problems in soil liquefaction", J. Geotech. Eng. Div., ASCE, 113(8), 827-45.
Singh, S. (1994), "Liquefaction characteristics of silts", ASCE Geotech. STP 44, 105-16.
Stark, T. D. and Mesri, G. (1992), "Undrained shear strength of liquefied sands for stability analysis", J. of Geotech. Eng., ASCE, 118(11), 1727-47.
Thevanayagam, S. (1998a) "Effect of fines and confining stress on steady state strength of silty sands," J. Geotech. & Geoenv. Engrg. Div., ASCE, 124(6), 479-491.
Thevanayagam, S. (1998b) "Role of intergrain contacts, friction, and interactions on undrained response of granular mixes", Proc. Intl. Workshop on *The Physics and Mechanics of Liquefaction*, Baltimore, ed. Lade, P. V., Balkema Publishiers.
Thevanayagam, S. (1999a) "Intergrain contact and shear modulus of non-plastic granular mixes", CD-ROM Proc. 13th ASCE Conf. on Eng. Mech., Eds. Jones, N. and Ghanem, R., Johns Hopkins Univ., Maryland, June 13-16, 1999.
Thevanayagam, S. (1999b) "Effect of fines and confining stress on steady state strength of silty sands," *Closure*, J. Geotech. & Geoenv. Engrg. Div., ASCE, 125(11), *in press*.
Thevanayagam, S. (1999c) "Relative roles of coarser and finer grains on undrained behavior of granular mixes", *in review*, J. Geotech. & Geoenv. Eng. Div., ASCE.
Thevanayagam, S. (1999d) "Contact indices - shear wave velocity - shear modulus for granular mixes" to be submitted, J. Geotech. & Geoenv. Engrg. Div., ASCE.
Thevanayagam, S. and Mohan, S. (1998) "Intergranular void ratio - steady state strength relations for silty sands" ASCE Geotech. STP 75, ed. P. Dakoulas et al., IIIrd Conf. on Geot. Earthq. Eng.
Thevanayagam, S. and Mohan, S. (1999) "Intergranular state variables and stress-strain behaviour of silty sands", Geotechnique, *in press*.
Thevanayagam, S., Liang, J., Mohan, S., and Shenthan, T. (1999) "Undrained fragility of clean sands, silty sands and sandy silts," *in review*, J. Geotech. & Geoenv. Engrg. Div., ASCE
Vaid, Y.P. (1994), "Liquefaction of silty soils", Proc. ASCE Conv., Geotech. Spec. Publ. 44, 1-16.
Zlatovic, S. and Ishihara, K. (1995). "On the influence of nonplastic fines on residual strength," Proc. IS-TOKYO'95, First Intl. Conf. Earthq. Geotech. Eng., Tokyo, eds. K. Ishihara, publs. A. A. Balkema, 239-244.
Zlatovic, S. and Ishihara, K. (1997). "Normalized behavior of very loose non-plastic soils: effects of fabric" Soils and Foundations, 37(4), 47-56.

Experimental Study on Seismic Behavior of Bridge Pile-to-Pile Cap Connections

Yan XIAO [1]; J.B. Mander [2]; H. Wu [3]; G. Martin [4]

Abstract

In order to investigate seismic behavior of bridge pile-to-pile cap connections, five full-scale H-shaped steel pile to pile-cap connection subassemblies representing a portion of a typical bridge pile foundation used in California were tested. Two of the full-scale subassembly specimens were subjected to vertical cyclic load simulating axial forces in pile due to footing overturning during an earthquake attack. Two others were loaded with cyclic later force and constant vertical load. One specimen was tested under proportionally varied vertical and horizontal forces. It was found that although designed as pin connection following the current design standard, the pile to pile-cap connection can sustain significant amount of moment. Test results also showed that the current standard anchorage details with two #25 (ASTM #8) V-shaped bars could not develop the full design ultimate tensile capacity.

Introduction

Significant research on seismic behavior and design of bridge structures has been conducted in various research programs, such as the retrofit program sponsored by California Transportation Department (Caltrans) and the Federal Highway Administration (FHWA) Highway Project at the National Center of Earthquake Engineering Research (NCEER). The primary research focus has been in two areas: pile foundation and bridge substructures. Research has shown that considerable loads from the superstructure must be transferred down though the substructure, the pile cap into the piles, and then finally the soils. This requires that considerable moment and shear be transferred through the pile cap. Existing pile-to-pile cap connections generally have inadequate details to develop their full moment capacity at the connection. It is unclear as to how moment and shear transfer and strength deterioration under cyclic loading will take place during large ground motion. Potential problems which were also noticed (Xiao et al. 1994-1999) but not yet addressed include the anchorage of pile in the pile cap which may not be adequate to develop the full design axial load of the pile.

---

1. Assistant Professor of Civil Engineering, University of Southern California
2. Associate Professor of Civil Engineering, State University of New York at Buffalo
3. Ph.D. Graduate Research Assistant, University of Southern California
4. Professor of Civil Engineering, University of Southern California

Under the sponsorship of FHWA-NCEER Highway Project, a joint research program has been conducted at the State University of New York at Buffalo (SUNY) and the University of Southern California (USC) to study the seismic behavior of bridge pile-to-pile cap with typical details representing current design standards. The tests conducted at SUNY were on pile-to-pile cap connections that is representative of construction in the eastern and central US, whereas the study at USC is on testing the pile-to-pile cap connections representative of construction in California, the major seismic area in the US. This paper summarizes the test results conducted at the University of Southern California.

Note that the SI units are used as the main units throughout the paper, with the corresponding English units provided in the parentheses. The sizes and grades of reinforcing bars are described based on so-called soft conversions (CRSI 1997).

Experimental Program

Full-scale Pile-to-Pile Cap Subassembly Specimens

As schematically shown in Fig.1, the specimens were designed to simulate a corner portion of a typical pile footing of an actual prototype bridge in California. The prototype bridge was originally selected from more than 100 California bridges constructed following the post-1971 design standards for a previous research program to study the bridge column to footing connection behavior (Xiao et al., 1994 - 1999). The 1982-built bridge is a 3-lane traffic single column bent bridge. The bridge has five single-column bents with steel HP friction pile footings and two abutments. Table-1 summarizes the details of the column footings in the prototype bridge.

The section properties of the 100T H-shaped pile (designated as HP14x89) are shown in Fig.2. The design service compressive capacity of the piles is 100 English ton (or 200kip =890kN), while the design ultimate capacity is 200 English ton (or 400kip=1779kN). Based on current Caltrans Bridge Design Specifications, the friction piles may be considered to resist an intermittent but not sustained uplift, with capacity equivalent to 40 percent of both the service and the ultimate compressive load capacity, or 50 percent of the ultimate compressive load for seismic design. Adequate pile anchorage, tensile strength, and skin friction must be provided. Fig.3 shows the typical details used widely in California for steel HP pile-to-pile cap connection. During a previous study, it was noticed that such detail might not be able to develop the required tensile capacity of the pile (Xiao et al., 1995).

Details of the pile-to-pile cap connection subassembly specimens are shown in Fig.4. Note that the specimens were configured in the upside down position compared to the prototype pile footing. Five full-scale H-shaped steel pile-to-pile cap connection subassemblies representing a portion of a typical bridge pile foundation used in California were tested. The experimental parameters include the pile orientation related to the horizontal loading direction, vertical and horizontal loading sequences, as summarized in Table-2. Two of the full-scale subassembly specimens were subjected to vertical cyclic load simulating axial forces in pile due to footing overturning during an earthquake attack. Two others were loaded with cyclic later

force and constant vertical load. One specimen was tested under proportionally varied vertical and horizontal forces.

Test Setup

The test setup used for cyclic vertical loading tests and cyclic horizontal loading tests under constant vertical load is shown in Fig.5(a). The specimen was tested in an upside down position with the pile cap portion post-tensioned to the strong reaction floor beam. The horizontal force was applied to the pile using an actuator with 1,334 kN (300 kip) capacity and push/pull stroke of 229mm (9in). The horizontal actuator was positioned at a distance of 1,067mm away from the pile cap surface, constituting a shear aspect ratio of 3.0 in the pile. The cyclic vertical loading system consisted a vertical actuator with 1,334 kN (300kip) capacity and lever arm system which can amplify the actuator force by 6 times. The vertical loading system was originally developed by the first author for testing of full-scale high-strength concrete columns (Xiao et al., 1998). In the case cyclic vertical loading test, the horizontal actuator was used as the lateral support to the free end of the HP pile. Similar test setup except configuring one of the actuator in an inclined position was used for the test of the pile-to-pile cap connection subassembly specimen under proportionally varied cyclic vertical and horizontal forces, as shown in Fig.5(b).

Instrumentation

Calibrated load cells were used to monitor the applied forces. The horizontal and vertical displacements at the application points of the forces were measured by 500mm stroke linear potentiometers. Four liner potentiometers were mounted to monitor the cap displacements in vertical and horizontal directions. Electrical-resistance strain gauges were mounted on the surfaces of the reinforcing bars at selected positions in pile cap. Strain gauges were also applied on the surface of the HP pile to monitor its strains near the connection.

Loading Program

For the vertical loading tests, the cyclic vertical force was applied following a sequence based on a peak force increment of 222kN. However, after the cap started to rock, the loading for tensile force was based on the uplift displacement control. For the other three tests where a horizontal load was involved, the loading cycle was applied corresponding to a displacement control sequence with a horizontal displacement increment of 0.25% drift ratio, Δ/H, until Δ/H=1% was reached. Two loading cycles were attempted for each of the drift ratios, Δ/H=1%, 1.5%, 2%, 3%, 4%, and 6%.

Experimental Results and Discussions

Cyclic Vertical Loading

The vertical load and displacement hysteretic relationships for the pile-to-pile cap connection subassembly specimens HP-S-V and HP-W-V are shown in Fig.6 (a) and (b), respectively. The difference between HP-S-V and HP-W-V was the orientation of the section principal axis related to the lateral support provided by the horizontal actuator at the free end of the pile provided by the horizontal actuator. The strong principal axis of the HP pile of specimen HP-S-V whereas the weak axis of HP-W-V was perpendicular to the axis of the horizontal

actuator, respectively. As shown in Fig.6, the responses of both specimens are similar. The pile-to-pile cap subassemblies developed significantly high stiffness and capacity in during the compressive loading, however, low stiffness and capacity under the tensile loading, due to the rocking response of the cap. The failure of both specimens was due to the rupture of the No.25, "V" shaped anchor bars at tensile forces much lower than the ultimate design tensile capacity of 890kN (200kip). Fig.7 shows the close up view of the rupture of the anchor bars.

Cyclic Horizontal Loading Under Constant vertical Load

The pile end moment versus lateral displacement drift ratio hysteretic relationships for the two specimens, HP-S-L and HP-W-L, which subjected to cyclic horizontal loading under constant vertical load are shown in Fig.8 (a) and (b), respectively. For specimen HP-S-L which subjected to a bending in its strong direction of the HP pile, the hysteretic response shown in Fig.8(a) is unsymmetric, due to the development of the rocking of the pile cap in the pull loading direction. The cracks on the pile cap were initiated near the end of the pile and fanned out towards the edges of the cap. At a drift ratio of 2% in the pushing loading direction, a crack suddenly penetrated through the front portion of the pile cap, which caused the reduction in the loading carrying capacity at the subsequent peak drift ratios. Fig.9 shows the crack pattern of the specimen. Rupture of one anchor bar occurred during the loading towards the second peak at drift ratio 4% in the pull loading direction.

Specimen HP-W-L developed stable hysteretic response shown in Fig.8(b). The hysteresis loops are relatively symmetric for the push and pull directions. No cap rocking was observed as the consequence of small moment demand in the week direction of the HP pile. Damage to the pile cap was relatively small with surface cracks localized near the pile end. Yield of the HP pile flanges near the pile end was identified by both strain gauge readings and the formation of the surface line patterns due to the falling of the oxidized skins. No anchor rupture was developed for this specimen.

Cyclic Horizontal and Vertical Loading

In the case of specimen HP-S-LV, a vertical load of 890kN (200kip) was applied first and maintained using the vertical loading system. The inclined actuator was then activated to generate the proportionally varied lateral and vertical cyclic loading. Fig.10 shows the pile end moment and the pile lateral drift ratio hysteretic relationship. The overall shape of the hysteresis loops for HP-S-HV is similar to that for specimen HP-S-L shown in Fig.8(a), however with lower capacity. The rupture of one anchor bar occurred during the pull loading towards the first peak at drift ratio 8%, and caused sudden degradation of the load carrying capacity.

Concluding Remarks

Testing of 5 full-scale pile-to-pile cap connection subassemblies revealed several problems in the current bridge footing design and practice. These issues include:

i. Despite a pin connection design, the connection can sustain a substantial moment. However, the capacity is unreliable due to the lack of a proper flexure design.

ii. The current design details used for the HP-pile connection anchor can not develop the ultimate design tensile capacity.

Future studies are suggested to evaluate the tensile and moment capacities of the connections with other pile types, such as prestressed, precast piles. Research is also urgently needed to improve the pile anchor design and to develop rational design guidelines for the pile-to-pile cap connections.

Acknowledgements

Research described in this paper has been funded by the NCEER Highway Project under FHWA contract DTFH61-92-C-00106. Comments and conclusions described in this paper are solely those of the authors and do not necessarily reflect the views of the funding agency.

References

Xiao, Y.; Priestley; M.J.N.; Seible, F.; and Hamada, N., (1994) "Seismic Assessment and Retrofit of Bridge Column Footings," *Structural Systems Research Project*, University of California at San Diego, Report No.SSRP-94/11, May, 167p.

Xiao, Y.; Priestley, M.J.N.; and Seible, F., "Experimental Evaluation of a Typical Bridge Column Footing Designed to Current Caltrans Standards," *Structural Systems Research Project,* Department of Applied Mechanics and Engineering Sciences, Report No. SSRP-95/08, March 1995, 39p.

Xiao, Y.; Priestley; M.J.N.; Seible, F., (1996) "Seismic Assessment and Retrofit of Bridge Column Footings," *ACI Structural Journal*, Vol.93, No.1, January-February, pp.79-94.

Xiao, Y.; Priestley, M.J.N.; and Seible, F., (1999) "Seismic Performance of Bridge Footings Designed to Current Standards," American Concrete Institute, *ACI Special Publications on Seismic Response of Concrete Bridges*, SP-187, Farmington Hills, Michigan, pp.131-157.

CRSI, (1997), "Using Soft Metric Reinforcing Bars in Non-Metric Construction Projects," Engineering Data Report, Concrete Reinforcing Steel Institute, No. 42, Schaumburg, Illinois.

Table-1 Details of prototype column footings

Bent	Column	Piles	Footing $L_f \times B_f \times T_f$ (m)	Footing Top Reinforcement	Footing Bottom Reinforcement	Footing Stirrups
Bent-2	2.13m Dia. 54#43 Bars	25-100T	7×7×1.75	19#32 Both Directions	37#32 Both Directions	200 #16 "J" Bars
Bent-3	2.13m Dia. 36#167 Bars	30-100T	8.5×7.6×1.92	26#32 Long. 25#32 Trans.	51#32 Long. 49#32 Trans.	310#16 "J" Bars
Bent-4	2.13m Dia. 64#167 & 30#36 Bars	30-100T	9.3×8.5×1.92	33#32 Long. 34#32 Trans.	65#32 Long. 67#32 Trans.	464#16 "J" Bars
Bent-5	1.68m Dia. 32#57 Bars	24-100T	7×6.4×1.92	7#25 Both Directions	45#25 Both Directions	336#16 "J" Bars
Bent-6	1.68m Dia. 22#36 & 22#57 Bars	20-100T	7×6.4×1.75	24#25 Both Directions	47#25 Both Directions	324#16 "J" Bars

Note: 1m=1000mm; 1mm=1/25.4inch.

Table-2 Testing Matrix

Model Specimens	Orientation of HP Pile	Loading Condition
HP-S-V	Strong dir.	Cyclic vertical loading only
HP-W-V	Weak Dir.	Cyclic vertical loading only
HP-S-L	Strong dir.	Cyclic lateral loading with constant vertical load
HP-W-L	Weak Dir.	Cyclic lateral loading with constant vertical load
HP-S-VL	Strong dir.	Proportionally varied cyclic lateral and vertical loading

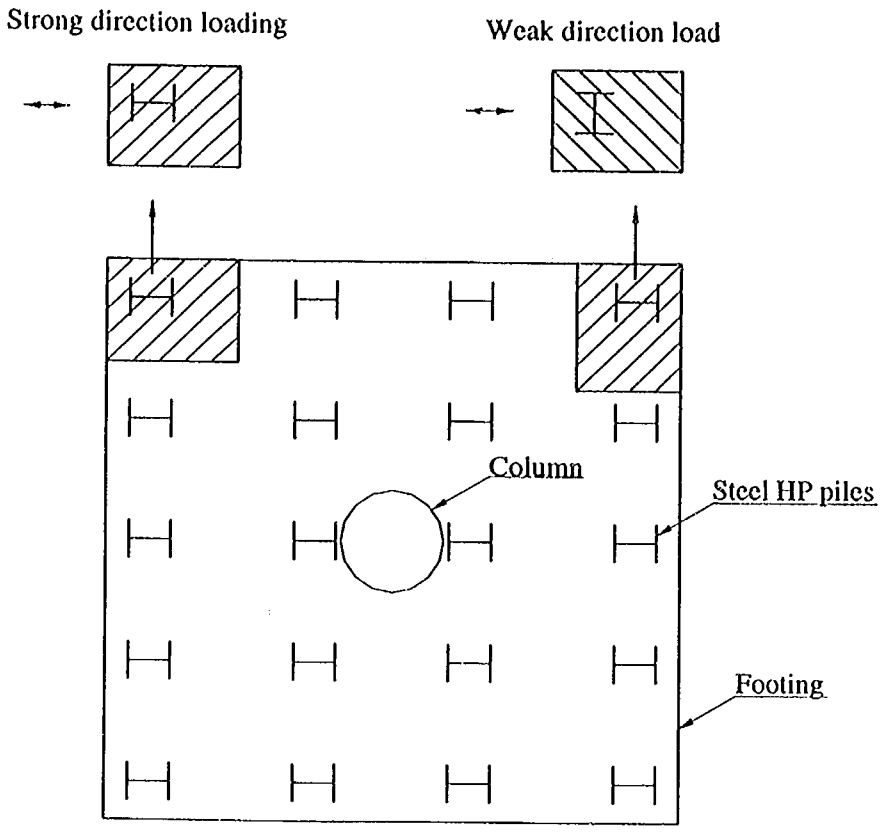
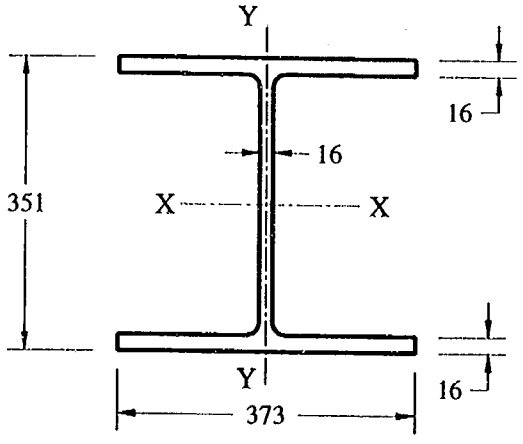


Fig.1 Prototype footing and connection modeling



Area A	Plastic Modulus	
	Z_X	Z_Y
mm^2 (in^2)	mm^3 (in^3)	mm^3 (in^3)
1.68×10^4 (26.1)	2.39×10^6 (146)	1.11×10^6 (67.7)
Elastic Properties		
Axis X-X		Axis Y-Y
I_{XX}	S_{XX}	I_{YY}	S_{YY}
mm^4 (in^4)	mm^3 (in^3)	mm^4 (in^4)	mm^3 (in^3)

Fig.2 HP-pile section details

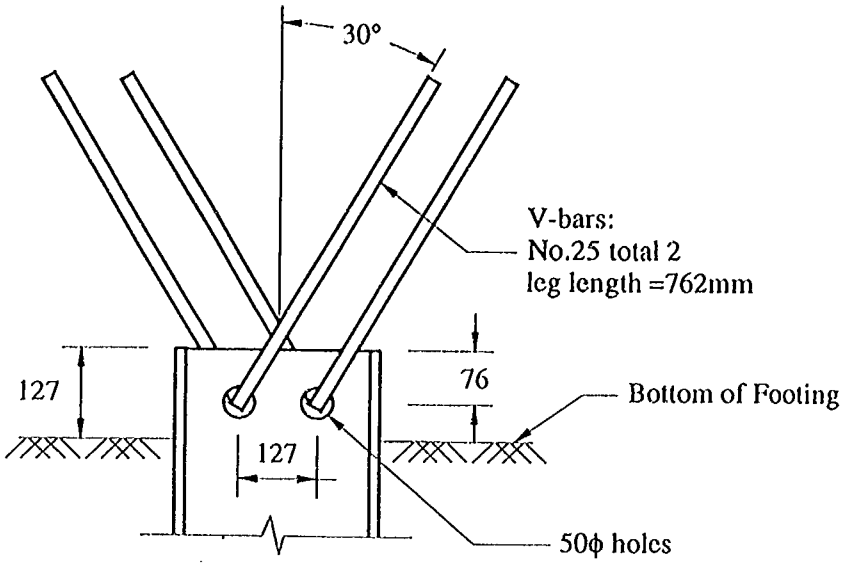
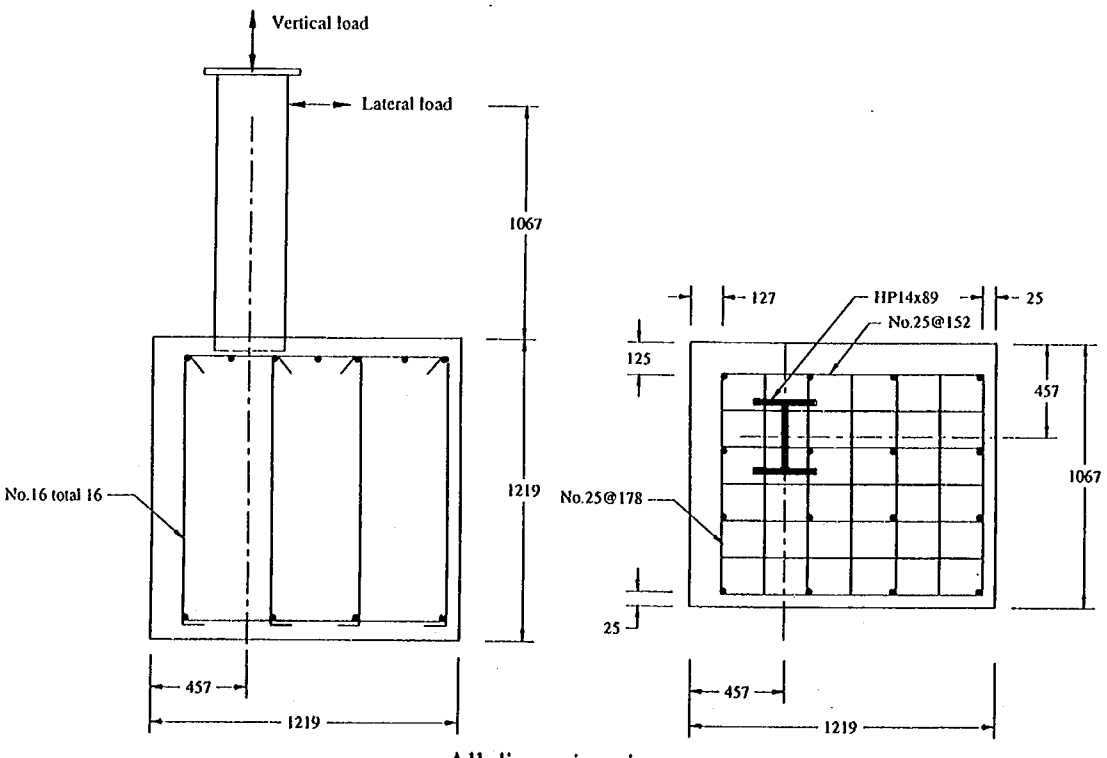
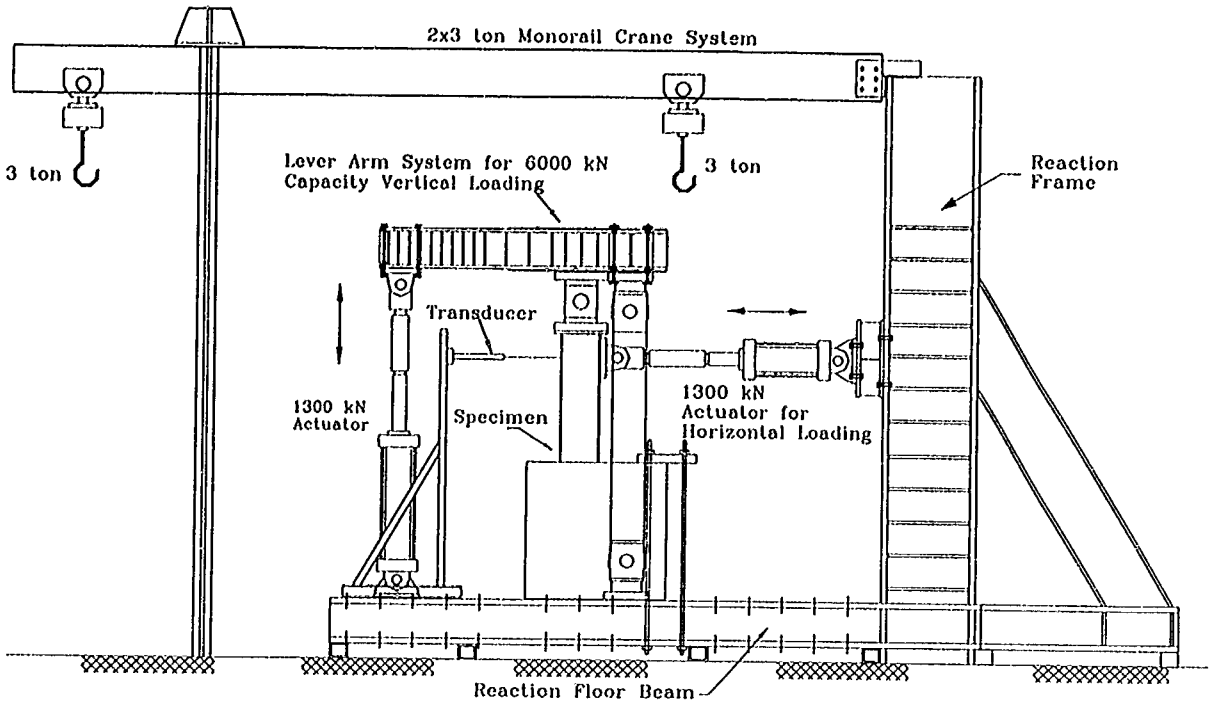


Fig. 3 Details of typical anchorage of HP-piles

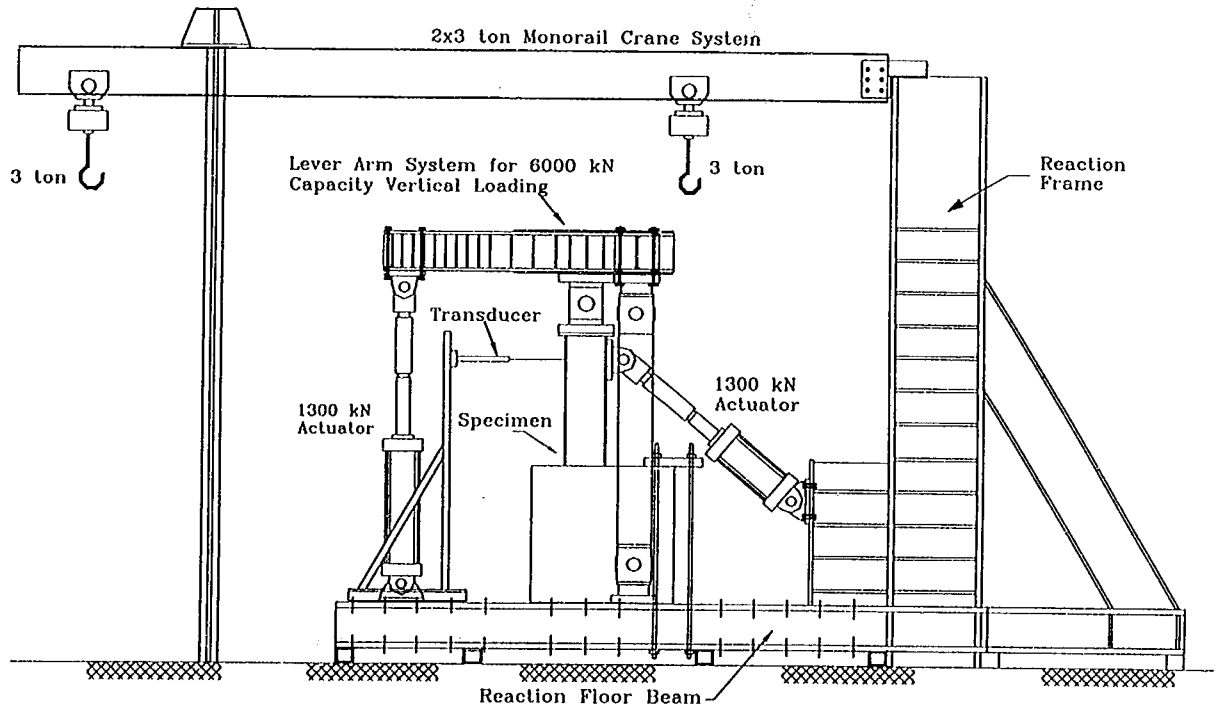


All dimensions in mm.

Fig. 4 Full-scale pile-to-cap subassembly model details

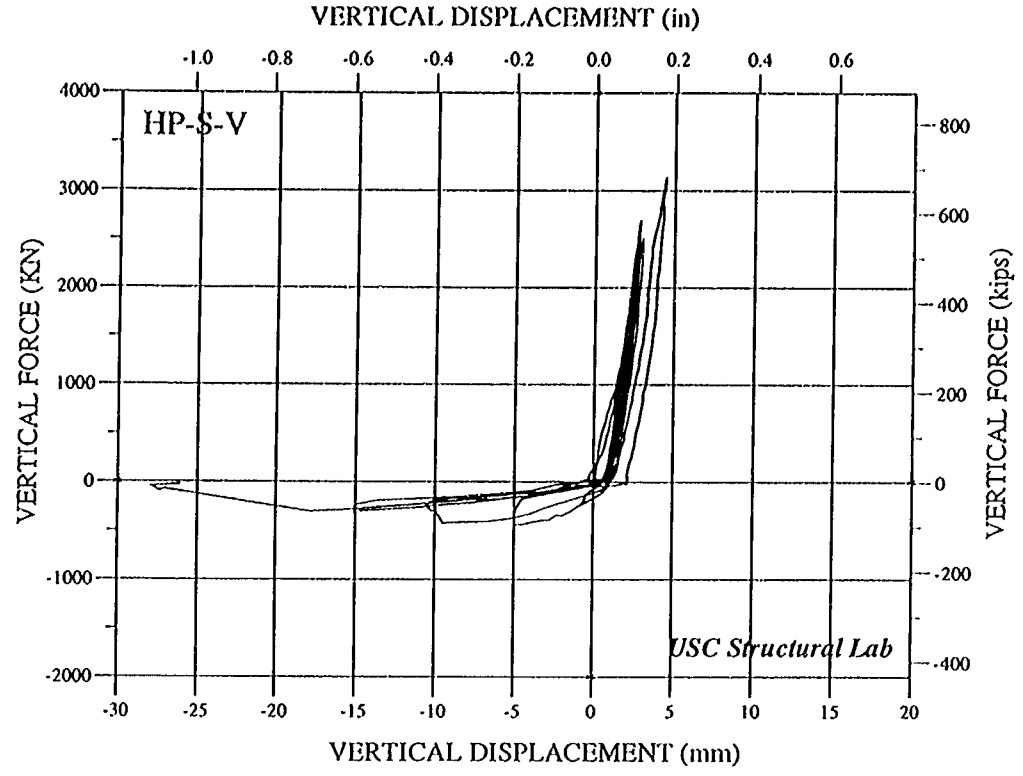


(a)

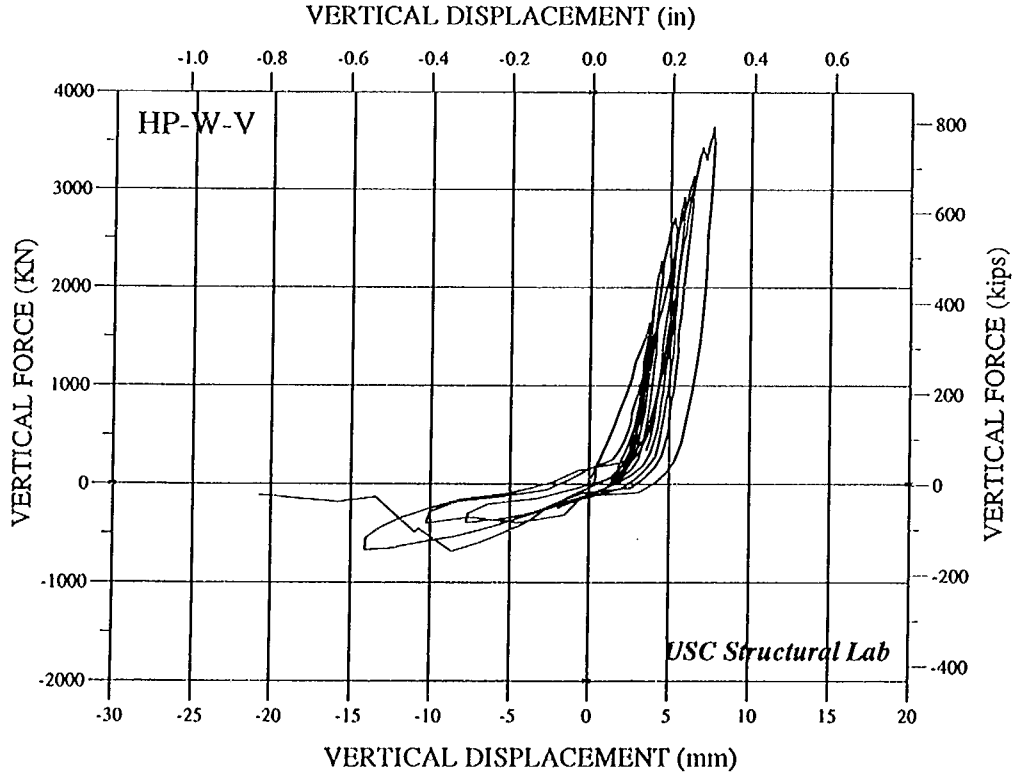


(b)

Fig. 5 Test Setups: (a) cyclic vertical loading tests and cyclic lateral loading under constant vertical load test; (b) proportionally varied cyclic vertical and lateral loading test

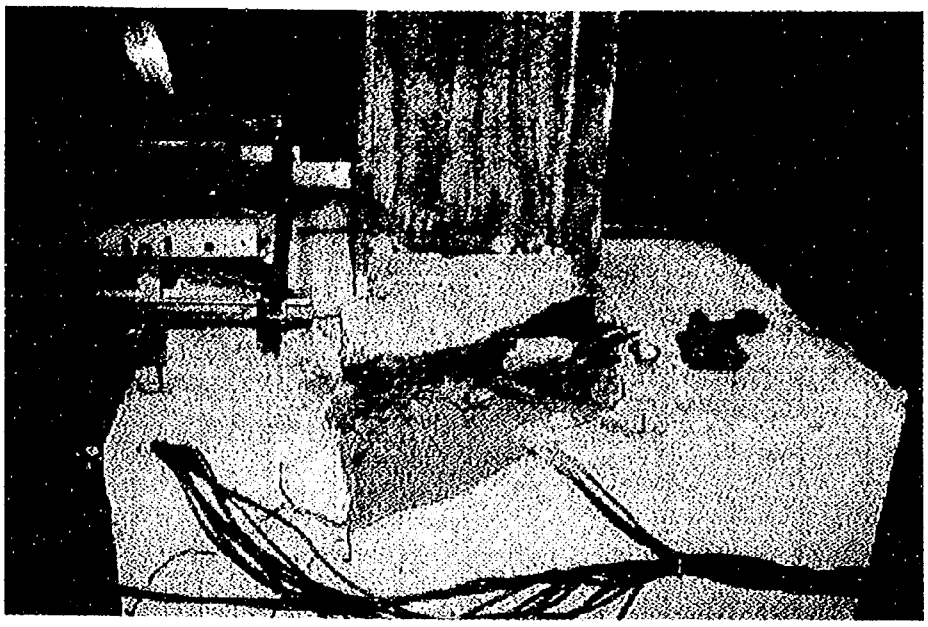


(a)

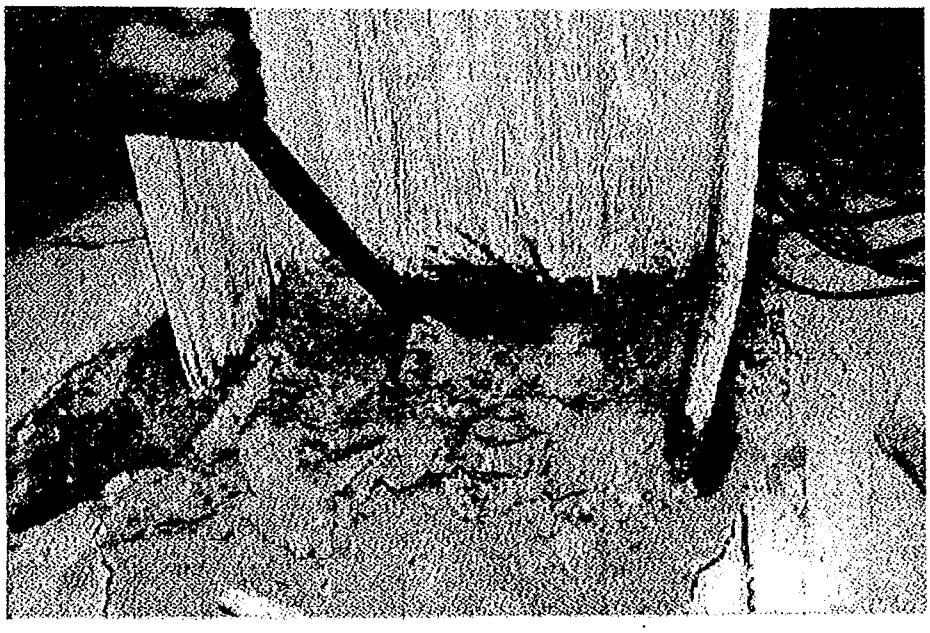


(b)

Fig. 6 Vertical force-displacement response: (a) model HP-S-V; (b) model HP-W-V

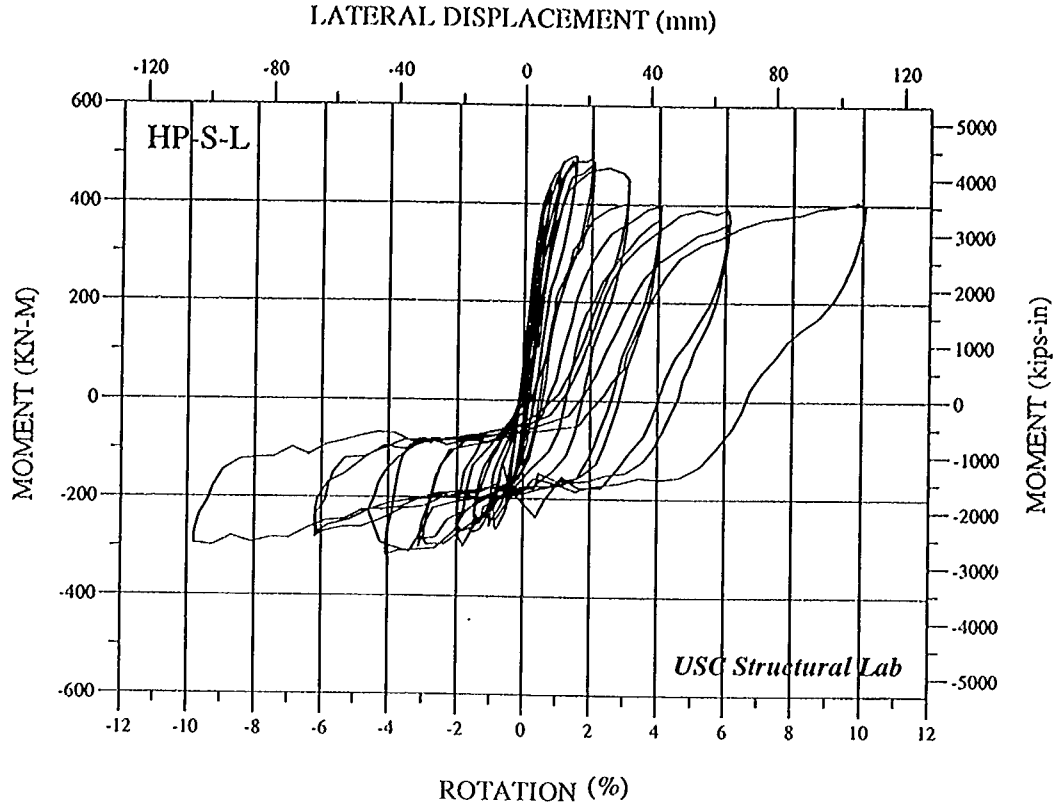


(a)

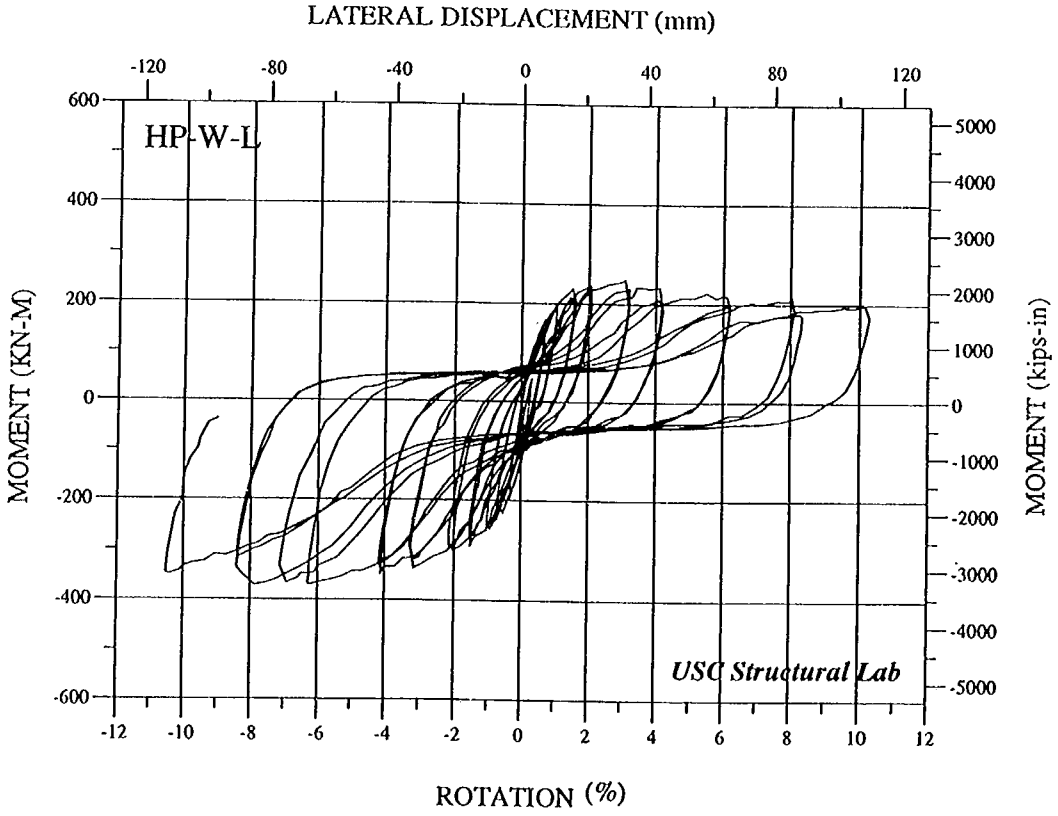


(b)

Fig.7 Observations of model pile-pile-cap connection under cyclic vertical loading: (a) crack pattern; (b) rupture of anchor bar.

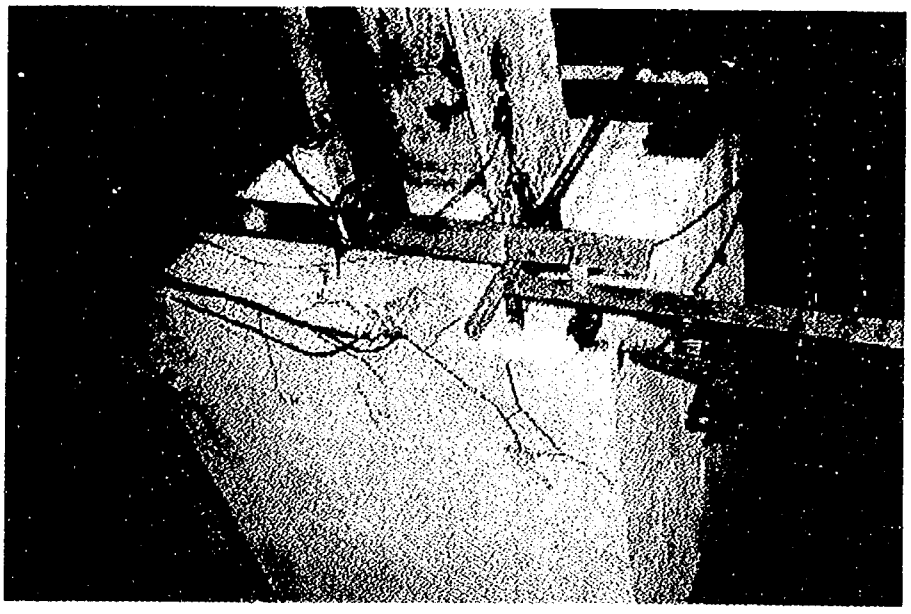


(a)



(b)

Fig. 8 Pile critical moment and rotation hysteresis response: (a) model HP-S-L; (b) model HP-W-L



(a)



(b)

Fig.9 Observations of model pile-pile-cap connection under cyclic lateral forces and constant vertical load: (a) crack pattern; (b) rupture of anchor bar.

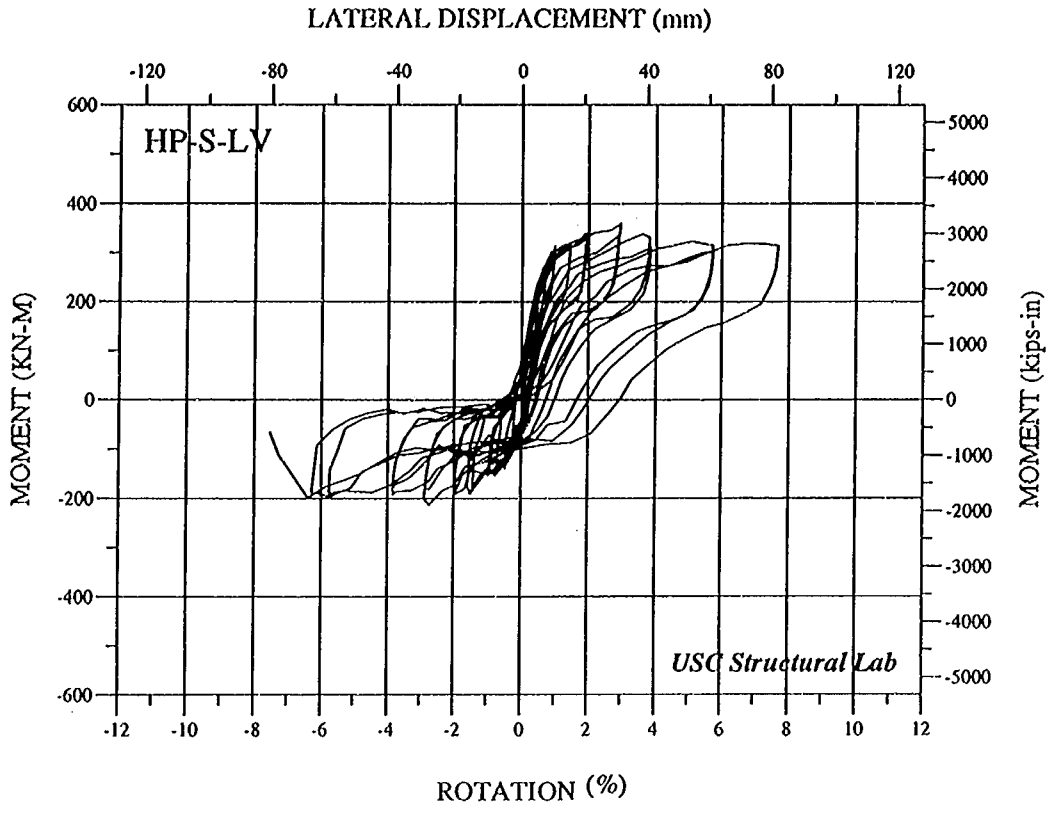


Fig. 10 Pile critical moment and rotation hysteresis responseof model HP-S-LV

A proposal of aseismic strengthening of wall-type RC Bridge Pier, with minimum impact on its foundation.

Kenji Ikeda[1], Hiroshi Mitamura[2], Norimitsu Kishi[3] and Noriyoshi Murakami[4]

Abstract

There are a number of aseismic strengthening methods for the existing conventional bridge piers such as flexural offset yield strength strengthening, toughness rate improvement and the combined method of these two. Whichever strengthening method is adopted, it is essential to consider the proof stress balance between the bridge pier and the foundation. Strengthening of the bridge pier possibly entails the need for aseismic strengthening of the foundation and repair of post-quake damage, which demands a considerable costs and labor. Thus, bridge pier strengthening should be such that any possible impact onto the foundation is minimized and that post-quake damage be not spread from the frame body of the pier to the foundation.

From the above viewpoints and based on the results, the including failure mode, of the rapid braking and vibration and other experiments using a full-scale bridge pier model, the Hokkaido Development Bureau has primarily been studying aseismic strengthening methods for the bridge pier that, with improved deformability and shear strength, are effective enough to prevent fatal damage at times of major earthquakes.

In this paper, a design analytical method is proposed that uses equivalent linearization which estimates equivalent stiffness from a trend found in nonlinear dynamic response analysis. In addition, based on the phase difference of material particles obtained from the analysis, bridge deck fall prevention and other systems were designed as part of our experiment on fatal damage prevention methods.

1: Office Manager, Structure Research, Civil Engineering Research Institute of Hokkaido Development Bureau
2: Office staffer, Structure Research, Civil Engineering Research Institute of Hokkaido Development Bureau
3: Professor, Construction System Engineering Division, Engineering Department, Muroran Institute of Technology,
4: General Manager, Sapporo Branch , Chodai Co. Ltd.

1. Introduction

Since January 1994 when the Hanshin-Awaji Earthquake struck, a lot of experiments and studies have been carried out on the basis of the damage sustained by a range of civil engineering structures. In 1995, the Specifications of highway bridges was revised and, with it, the need has arisen to reinforce the bridge piers designed and constructed prior to the release of the revised standards in order to prevent considerable damage when earthquakes of similar magnitude strike.

While strengthening of the existing bridge piers should be carried out with adequate consideration for the significance, executability and economy of the project, it will, in most cases, entail a range of difficulties to execute strengthening which meets various requirements, except in cases of bridge piers of specific design. In addition, depending on the strengthening method employed, not only major work may need to be done to the foundation but also considerable post-quake impact can be exerted on the foundation. In light of these implications, the authors concluded that the most rational strengthening method for wall-type bridge piers in every respect is to prevent fragility-originated destruction of a position of decrease reinforcing bar and improve toughness.

In this study, strengthening methods for wall-type bridge piers will be discussed and the resulting design approach examined, using a full-scale pier model which was devised to exclude any effect of scale as well as an experiment device which was also developed to recreate the closest possible conditions to those of the actual structure.

2. Outline of experiments

2. 1. Experiment methods

The experiment bridge device consists of a two-span H-beam continuous girder measuring 30.0m in length, 3.0m in width, 0.8m in girder height and 1058kN in gross weight, two abutments which support the girder, bearings, a bridge pier model and pedestals. Regarding the bearings, the middle of the test piece is supported by pins while the ends of the girder are supported by rollers to eliminate horizontal restraint.

Figure 1 shows a schematic diagram of the static phase of the experiment bridge device. On the experiment bridge pier model, 662kN of the tare of the two main girders representing the superstructure was applied as deadweight. Horizontal alternating load was applied horizontally to the pin support for the test piece, with vertical axial stress being exerted and using

compression/tension hydraulic jacks. Live load was measured by load cells, and horizontal displacement by wire displacement gauge.

Horizontal alternating load was repeatedly applied while gradually increasing displacement amplitude at 1 δ y, 2 δ y and 3 δ y, with the yield displacement of δ y and the yield load of Py. In this case, the yield of the main strengthening at the center of the wall was considered to have been achieved when the strain gauge on the main strengthening read 1,700 μ . Five alternation cycles were exerted at each displacement amplitude, and failure was considered to have been achieved when either the positive or negative live load dropped below Py for the first time.

Figure 2 is a schematic diagram of the rapid breaking/vibration experiment device. The bridge pier model and the superstructure were loaded on a traveling pedestal which then was supported by air bearings. The pedestal was allowed to travel by disengaging a latch which made the deadweight free fall. Rapid braking was achieved by reaction side wall, creating wave motion similar to seismic movement which was then input into the device. Styrofoam (hereafter referred to as "EPS material") installed at the front of the pedestal enabled the deceleration of the pedestal by its shock-absorbing effect. In addition, changing the thickness of the EPS material enabled the braking time and the maximum acceleration input to be adjusted. The experiment was carried out using this device and the methods described above, by applying rapid braking force to the pedestal as well as acceleration which corresponds to seismic movement on the bottom of the bridge pier.

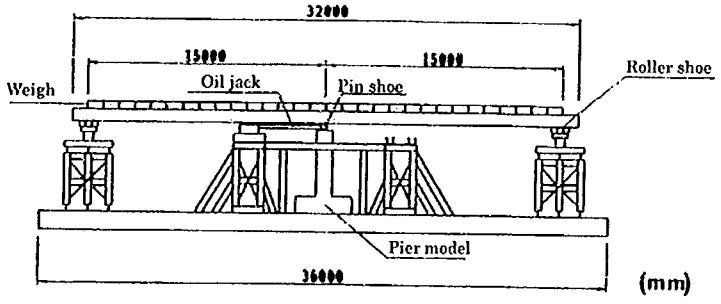


Figure 1 Schematic diagram of static experiment device

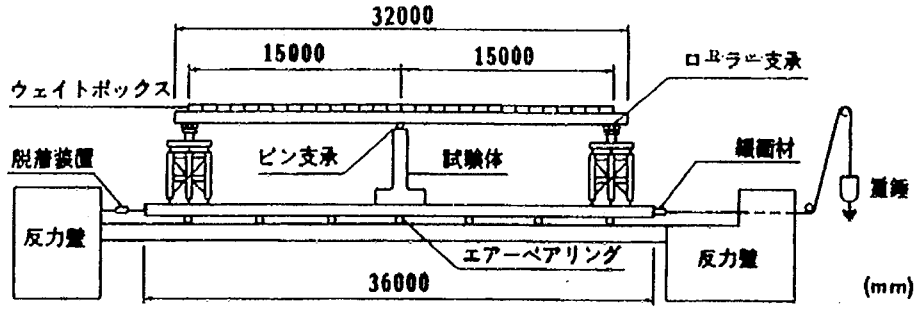


Figure 2 Rapid braking/vibration experiment device

2. 2. Test piece

Each of the test pieces, measuring 80cm in wall thickness, 250cm in wall width and 400cm in wall height, is decrease reinforcing bar at 150cm from the bottom, which was designed by the 1980th specifications of highway brides. Three test pieces were used: non-strengthening test piece A (ref. Figure 3), test piece B strengthening at the position of decrease reinforcing bar (ref. Figure 4) and test piece C strengthening across the whole height (ref. Figure 5). Both static horizontal alternating load and rapid braking/vibration were applied to each test piece, and the results were examined focusing on any effect the different strengthening methods might have on the improvement in toughness.

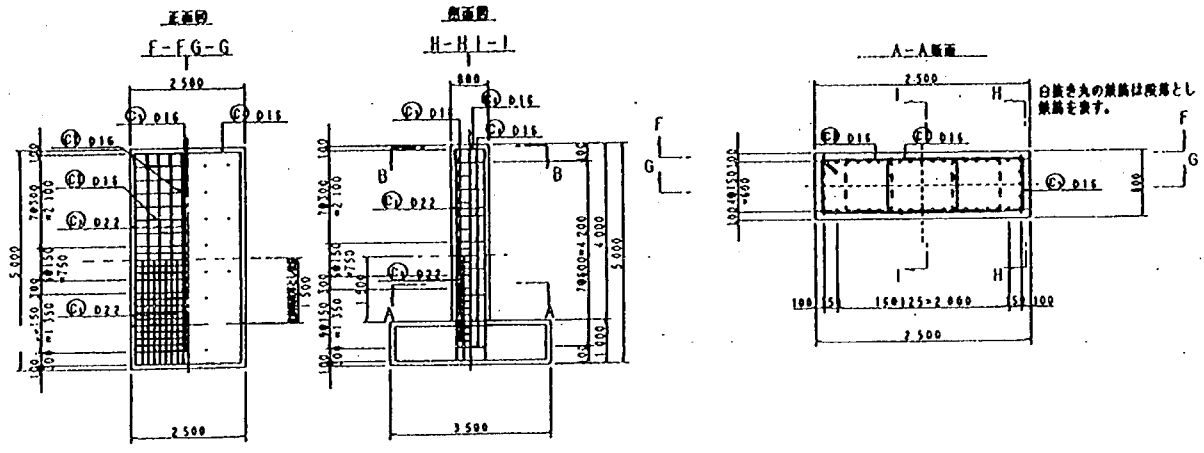


Figure 3 Dimensions and reinforcing steel distribution of non-reinforced (standard) test piece A

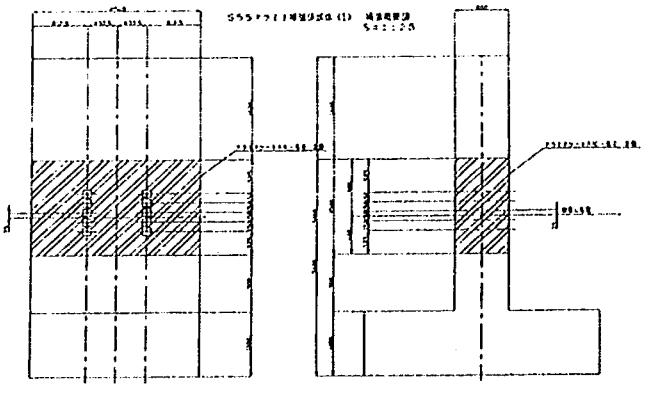


Figure 4 Schematic diagram of reinforced test model B

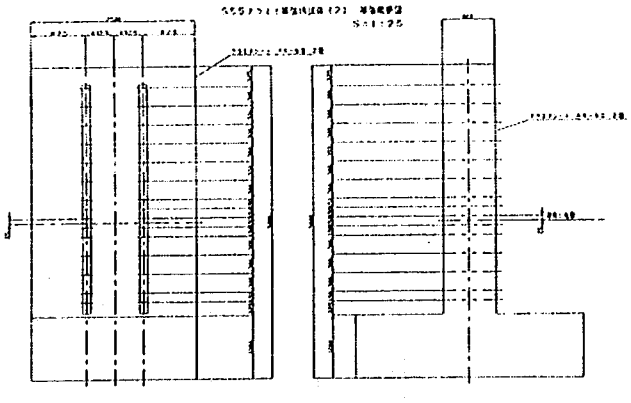


Figure 5 Schematic diagram of reinforced test model C

The test piece concrete, at the time of the experiment, had the compressive strength of 20.4MPa, the elastic modulus of 13.9Gpa and the Poisson's ratio of 0.112. The AFRP sheet used for strengthening of 415g/m^2, the thickness of 0.2866mm, the elastic modulus of 126.5GPa, the tensile strength of 2.48GPa and the breaking strain of 1.96%. All of the test piece main strengthening, hoop and confining strengthening had the grade of SD345, the tensile strength of 390MPa, the elastic modulus of 229GPa and the yield strain of 0.17%. The resisting bending moment of the test pieces at position of decrease reinforcing bar was Mu=1.29MNm based on the method of sectional division while the arm length (l) from the position of decrease reinforcing bar to the force application point was 2.65m. The test piece B was strengthening with two layers of a 30cm-wide AFRP sheet covering the width of 1.5m. The confining strengthening was arranged in two rows across the wall and five tiers vertically. The test piece C was strengthening with two layers of the AFRP sheet covering the whole height, with the confining strengthening arranged in two rows across the wall and 15 tiers closely together and vertically at the position of decrease reinforcing bar. The cross-sectional area of the confining strengthening for the test pieces B and C requires D19 or more. Considering the need for threading for nut attachment and taking into account the resulting reduction of the cross-sectional area, the confining strengthening of D22 was used. The confining strengthening, a square steel plate of 10cm on each side and 16mm thick, was attached via a washer. The bore hole for confining strengthening was filled with mortar after the strengthening installation to simulate the actual structure and prevent rust formation.

3. Experiment results and analysis

3. 1 Load-displacement relation

Table 1 shows the results of the experiment.
The non-reinforced test model A and the AFRP-reinforced test models B and C were compared. In improvement in yield displacement, test model B performed almost equally as test model A, while test model C was 26% better than test model A. With the ultimate displacement, test models B and C showed an improvement of approximately 10% and 60%, respectively, over the test model A. The ultimate load only improved by approximately 7% as the position of decrease reinforcing bar was not reinforced against bending. The ultimate plasticity rate of test models B and C improved 8% and 28%, respectively, over test model A.

Table 1 Experiment results

	displacement(mm)		Load (kN)						ultimate	ultimate ductility factor $\delta u/\delta y$
			Py			Pu				
	δy	δu	+	−	average	+	−	average		
Model A	20.7	116.0	399	-366	382	510	-521	515	$5\delta y$	5.60
Model B	21.0	126.8	344	-361	353	524	-510	517	$7\delta y$	6.04
Model C	26.1	186.3	452	-372	412	544	-567	556	$6\delta y$	7.14

Figures 6 to 8 show the P- δ relationship. Test model A showed a fall in yield strength from 5 δ y due to the failure of position of decrease reinforcing bar. Test model B showed a considerable full in yield strength from 7 δ y due to the aramid failure of position of decrease reinforcing bar. Test model C showed a slight fall in yield strength, while retaining a constant level of deformability. Calculated values calculated by the method of section and experimental values showed a reasonable correspondence except for test model B. However, test model B showed a correspondence between dynamic response values (dynamic load-displacement relation) obtained from the results of the rapid breaking/acceleration experiment and static load-displacement relation.

The load-displacement relation in Figure 9 shows a sharp drop in yield strength for test models A and B due to the failure of position of decrease reinforcing bar as described previously, as well as a rise in energy absorption for test model C.

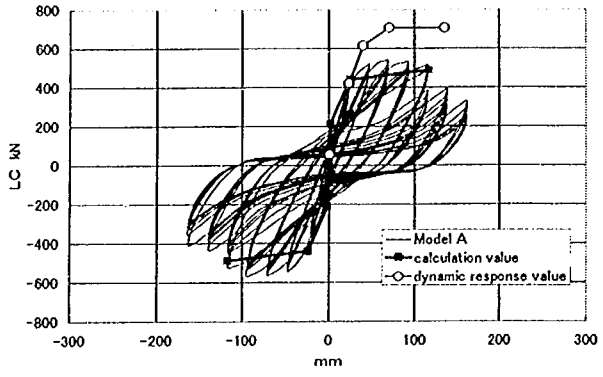


Figure 6 Model A

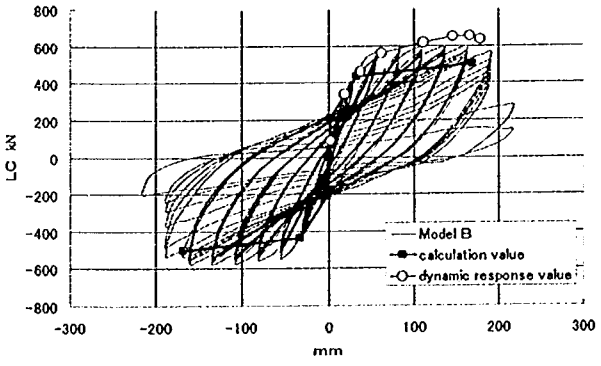


Figure 7 Model B

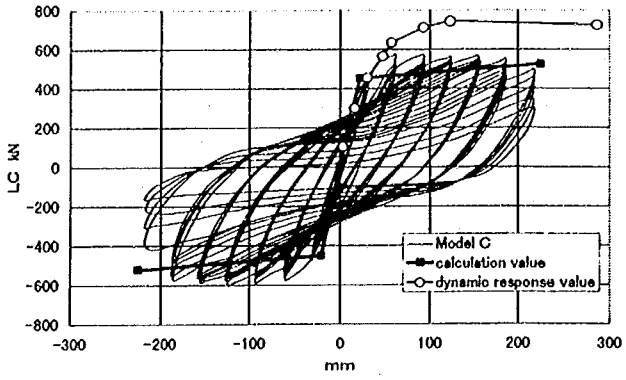


Figure 8 Model C

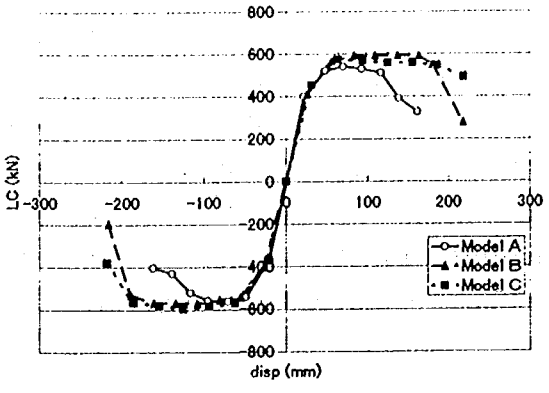


Figure 9 Load—Displacement relation curve

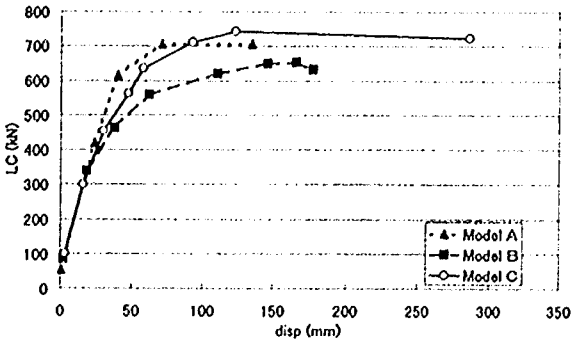
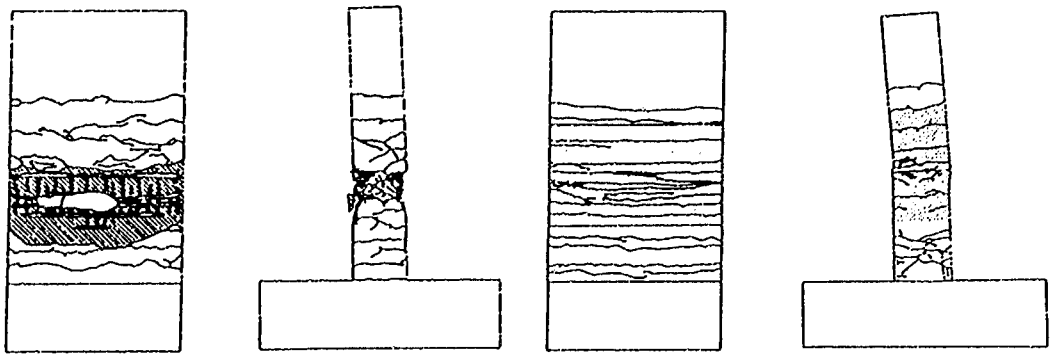


Figure 10 Dynamic Load-Displacement relation curve

3. 2 Failure mode

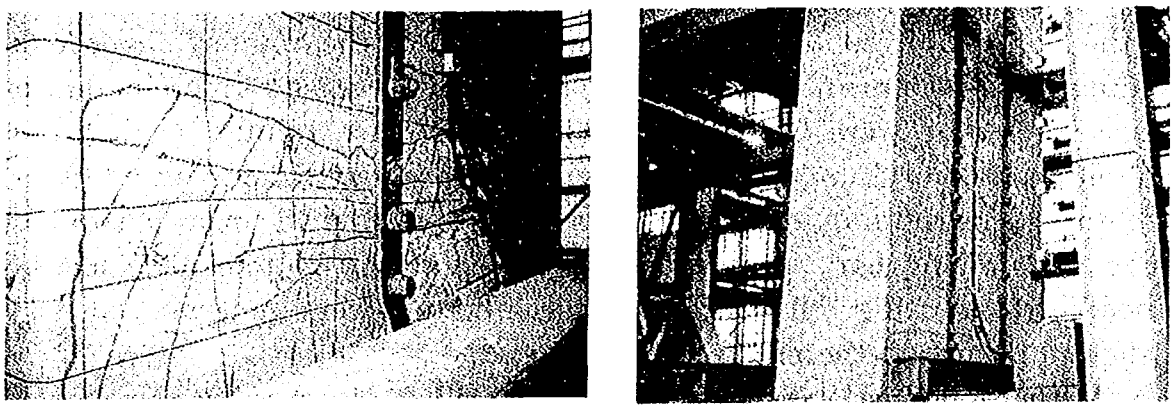
Figure 11 shows the failure mode of each test model's in the experiment. With the non-reinforced test model A, nearly all of the reinforcement rods extending up to the crown buckled near position of decrease reinforcing bar of which several rods were broken. Position of decrease reinforcing bar had flaked off position of decrease reinforcing bar extensively below. In addition, horizontal cracks running longitudinally started to incline 45° near position of decrease reinforcing bar. Flex cracking was near the bottom also, but no inclined shear cracking. All cracks near the bottom were generated at 1 δ y and showed no growth thereafter.

With reinforced test model B, threads (fiber glass) tying the aramid together broke at the ultimate phase of the experiment as described previously, allowing concrete to level deformation and, as a result, kinking the aramid up and down.This damage seems to have been extended by a small amount of covering bulging out between the kinking aramid. At this location, some reinforcement rods buckled. Longitudinal cracking in the reinforced section near position of decrease reinforcing bar was all horizontal flex cracking, while inclined shear cracking occurred in addition to flex cracking at the bottom that had not been reinforced by the AFRP sheet. With test model C that had been reinforced entirely, damage was concentrated on the bottom of the pier, and the AFRP sheet was lifted in a section from the bottom up approximately 50cm due to the bulging of the covering. While the binding of the AFRP sheet prevented the covering from flaking off, the main reinforcement at the bottom ultimately broke. Longitudinal cracking was all horizontal flex cracking at a vertical interval of approximately 50cm. No inclined shear cracking occured.
Consequently, AFRP-sheet reinforcement effectively reduced inclined cracking rate and damage to position of decrease reinforcing bar, both of which were experienced by test model A, and also substantially improved the toughness of test model C.



Front view　Side view　Front view　Side view

(a)Model A　(b)Model B



(c)Model C

Figure 11 failure mode in the experiment

3. 3 Toughness

Figure 12 shows the relationship between energy absorption and displacement amplitude for each test model. Energy absorption was evaluated using the average of the positive and negative values for the first loop of each displacement amplitude. The gradient of the energy absorption-displacement amplitude relation for reinforced test models B and C was clearly steeper than for test model A.The ultimate energy absorption was 63.7kJ for test model A, 97.5kJ for test model B and 139.6kJ for test model C, which indicates that reinforcement results in higher energy absorption, i.e. approximately 1.5 times for test model B and 2.5 times for test model C, without the need to increase yield strength.

Figure 13 shows the relationship between equivalent viscous damping constant and displacement amplitude for each test model. Equivalent viscous

damping constant was evaluated using the hysteresis loop for the first loop of each displacement amplitude.With non-reinforced test model A, the damping constant shows an almost linear increase until 5 δ y and then falls sharply at 6 δ y. However, with test model B, the damping constant did not fall and was ultimately maintained at approximately 18%. With test model C, the damping constant was stable at approximately 23% after 5 δ y, indicating a higher damping capacity than test models A and B at every amplitude.

Figure 14 shows the relationship between equivalent stiffness and displacement amplitude for each test model. The equivalent stiffness was evaluated using the load-displacement relation for the first loop of each displacement amplitude.With each test model, the equivalent stiffness had a tendency to decline as with the exponential function. At 1 δ y, the equivalent stiffness for the non-reinforced test model A is approximately 20% higher than for test models B and C. As the displacement amplitude increased, this gap narrowed: At 5 δ y, the value for test model B exceeded that for test model A and at 7 δ y, the value for test model C exceeded that for test model A, which indicates that reinforcement slows down the decline in equivalent stiffness at times of large displacement.

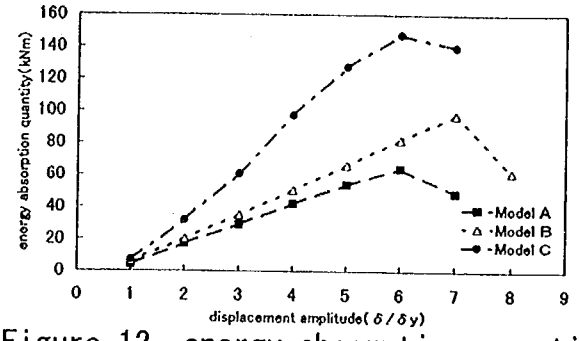


Figure 12 energy absorption quantity

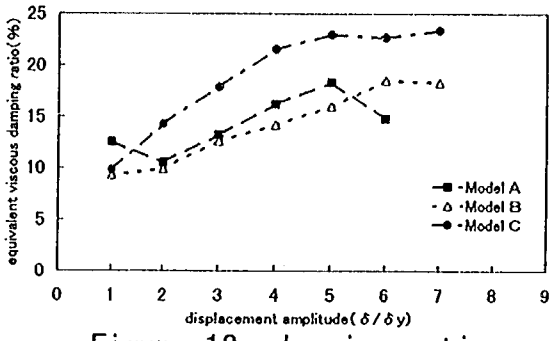


Figure 13 damping ratio

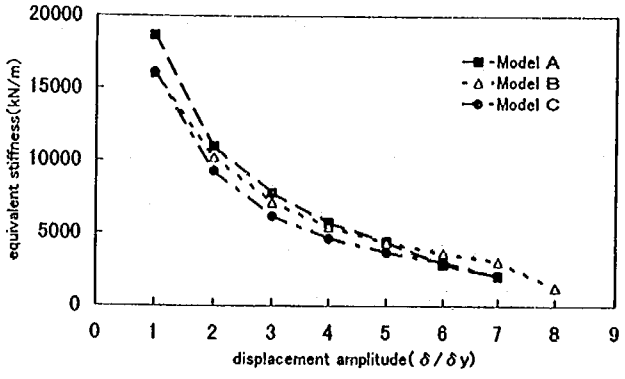


Figure 14 equivalent stiffness

4. Proposals of Design Principles

4.1 Basic policies for retrofitting

The following are the policies for retrofitting existing piers.

- As a mode of failure during earthquakes, the structure is designed so as to prevent brittle failure occurring from the point where reinforcement ratio of the pier changes, and to allow damage to occur from the base.
- The toughness is enhanced, and required yield strength of the pier base is declined.
- By approximating ultimate displacement, great relative displacement does not occur in each pier, so collapses of the pier that differs in the height of bridge seats and the girder drops at the girder end are prevented.
- The structure is designed not to cause shear failure.

4.2 Equivalent linearization method

Seismic retrofit of the pier to enhance the toughness retains ultimate horizontal strength of the pier during earthquakes by making a nonlinear dynamic analysis. According to the computational result that is within the range satisfying the maximum response displacement (the allowable displacement obtained from the ductility factor: $\partial a = \partial y + (\partial u - \partial y) / \alpha$) we gained a clear picture of the tendency.

By using the rigidity near the displacement ($\mu \cdot \delta y$) attained with the consideration given to the allowable ductility factor expressed by the load-displacement curves (**Figure16**), equivalent stiffness is to be set on a trial basis within the range where the ultimate horizontal strength is retained during earthquakes.

To take an example of a trial design model with the fixed and movable piers (**Figure 17**), in the verification method for seismic resistant capacity by the equivalent linearization method using the equivalent stiffness, the response values and maximum displacement of the base of the fixed pier are verified. As for the movable pier, verification of length girder seats on the pier by the relative displacement of the material particle of each system is made, and aseismic connectors are provided, where applicable.

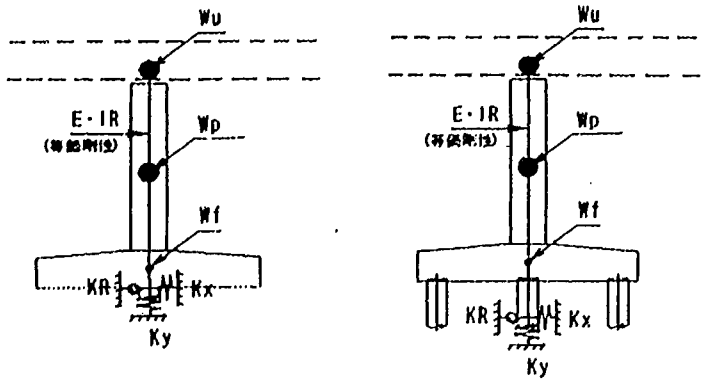


Figure 15: Model used for equivalent lincarization methods

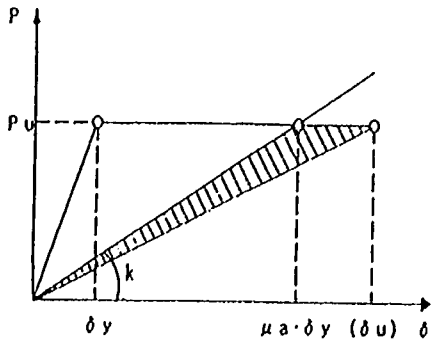


Figure 16: The range of equivalent stiffness in Trial design

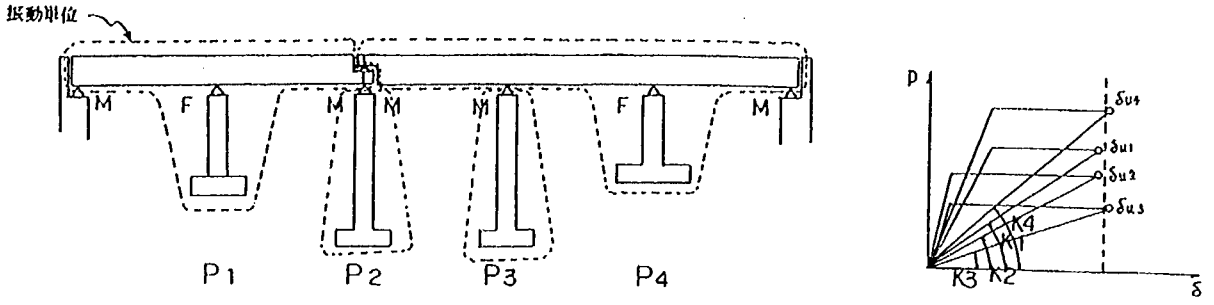


Figure 17: Examples of trial design

5. Summary

(1) The retrofitting method used jointly with the lateral restraining method by the winding of AFRP sheet and the through rein for cement is proposed for the RC wall-type pier having the point where the reinforcement ratio of the pier changes. We examined experimentally the effect of improvement of the capacity for the toughness.

(2) The experimental results showed that this retrofitting measure increases the energy absorption capacity by about 1.5 to 2.5 times, and that the loads can be maintained up to large displacement amplitude under the stable conditions. In addition, concerning the equivalent stiffness, as the displacement amplitude becomes greater, the difference becomes small and the decline in equivalent stiffness can be checked even at a time of finite deformation.

(3) This seismic retrofitting can be used jointly with the aseismic connector and other measures. Increased loads on the foundation work is relatively small, and it can be considered to be a well-balanced retrofitting method.

(4) It is possible to adopt a method to verify the seismic retrofitting of piers, employing the equivalent linearization method, for which the equivalent stiffness obtained from the tendency of the nonlinear dynamic analysis is used.

6. References

(1) The Effect of Improvement of Toughness Capacity of Full-Scale Wall-Type RC Piers by the Wrapping with AFRP Sheet
Masashi Sato, Hiroshi Mikami, Hiroshi Mitamura, Masaki Kinoshita
Proceedings of Annual Meeting, JCI, Vol.21, 1999

(2) A study of the Dynamic Behavior of Full-Scale Pier Model Using Rapid Braking Method
Tadashi Hasegawa, Masashi Sato, Hiroshi Mitamura, Kouichi Yoshida
JSCE. Proceedings of the 54th Annual Convention Scientific Lecture Meeting, September, 1999

(3) A Study of the Effect of Intermediate Reinforcing Bars of Small scale Pier Model under Rapid Braking Loads
Noriyoshi Murakami, Hidetoshi Osaka, Hiroshi Mitamura, Kouichi Yoshida
JSCE. Proceedings of the 54th Annual Convention Scientific Lecture Meeting, September, 1999

ADVANCED COMPUTATIONAL METHODS IN BRIDGE ENGINEERING

Jamshid Ghaboussi

Department of Civil and Environmental Engineering
University of Illinois at Urbana-Champaign
Urbana, Illinois 61801, USA

ABSTRACT

This paper describes the research on application of advanced computational methods in bridge engineering being conducted by the author and his co-workers at the Department of Civil and Environmental Engineering at the University of Illinois at Urbana-Champaign. Three areas of research will be described. The first area of research is in application of advanced computational mechanics in analysis of seismic response of long span bridges. This research addresses the especially difficult problem of seismic soil-structure interaction in long span bridges over soft soil conditions. This situation often exists in most major river-crossing bridges in the Mid-America. The second research area is the effect of simulation of construction on the modeling of the behavior of the long span bridges. The special case of cable stayed bridges will be discussed. The third area of research is the application of soft computing methods condition monitoring of railway bridges under normal traffic loading.

1. INTRODUCTION

Computational methods have been used in bridge engineering since the early days of development of computer methods of structural analysis and finite element method. Considerable advances have been made in development of methods of analysis for bridges, specially methods of dynamic analysis of seismic response of bridges. However, there are still some areas in the analysis of bridges that can benefit from additional development of more advanced computational methods. In this paper we will briefly describe the work of the author and his co-workers in development of advanced computational methods in bridge engineering.

The authors research work in bridge engineering has concentrated on two areas: seismic analysis of long span bridges, specially major river crossing bridges, and innovative methods for condition monitoring of railway bridges under normal traffic. In analysis of seismic response of long span bridges, the author and his co-workers have identified areas which have not been adequately studied, mainly due to the complexity of the problems and difficulty of modeling. Analysis of soil-structure interaction in long-span bridges was identified as one area, which needed additional research in studying the phenomena and in developing fully evaluated simplified methods of analysis.

Another area which could benefit from additional research is the determination of the existing state of internal forces in cable stayed bridges. The newly constructed bridges in Mid-America region tend to be cable stayed bridges. The dynamic characteristics of these bridges are strongly influenced by the state of internal forces in the cables and the bridge deck, and these internal forces are the result of construction sequence. The research work of the author in developing methods for computer simulation of the construction sequence in cable stayed bridges will be briefly discussed.

The third area of research, which will be briefly discussed in this paper is the condition monitoring of railway bridges. This is a new area of research, undertaken by the author and his co-workers. A new fiber optic system is being developed to provide a means for continuous condition monitoring of railway bridges under normal train traffic. This fiber optic system is specially designed to be easy to install on the existing bridges. Using advanced computational intelligence methods, a special method has been developed for performing the condition monitoring of the bridge every time a train passes over the bridge.

2. SOIL-STRUCTURE INTERACTION EFFECTS IN SEISMIC ANALYSIS OF LONG-SPAN BRIDGES

Major river crossing bridges in the Mid-America region are often constructed over deep alluvial layers of soft soils. As a result the soil-structure interaction effects become very important. Further advances in the methods of analysis are required in order to account for several aspects of soil-structure interaction in long span bridges. They include the determination of the appropriate ground motion, representation of the important effects of soil-structure interaction, effects of soil nonlinearity, and the effects of travelling and multiple support excitation combined with the soil-structure interaction effects. These are very complex problems. The current methods can not be used to directly model a complete soil-structure system with sufficient details to meaningfully represent the important effects of soil-structure interaction. It is for this reason that the soil-structure interaction effects in major river crossing bridges and other long span bridges have not been adequately studied.

The preferred foundation for the long span bridges on deep soft ground is floating pile foundation. Seismic behavior of pile groups in soft ground and their role in the soil-structure interaction is another important problem, which is very difficult to model and has not been adequately studied.

The author and his co-workers are currently conducting research soil-structure interaction for long span bridges, including the effects of pile foundations. Our research addresses two aspects of the problem. First, by developing very advanced and computationally intensive methods, we intend to study the phenomena itself. In these studies full three-dimensional nonlinear finite element models of the ground and the structure will be developed and subjected to travelling wave seismic motions. By using as realistic models as possible, we hope to determine the significance of the multiple support excitation and foundation-ground interaction on the seismic behavior of the supper-structure. The second purpose of our study is to develop fully evaluated simplified methods for modeling of the soil structure interaction.

2.1. Seismic Input Motions

Due to infrequent seismic event in Mid-America, actual strong motion records in the region are not available. Artificially generated earthquake records at a bedrock location reflecting the characteristics of the faults and the topography in the region are necessary for the evaluation. Complete sets of three orthogonal components of records are preferred, since in many cases it was observed that vertical components plays an important role in structural responses of large bridges. If a nonlinear three-dimensional finite element model is used for the site, the seismic wave at the bedrock will propagate through the soil domain and free field motions at each depth can be obtained. Methods using one-dimensional wave propagation theory and an equivalent linear shear modulus, such as SHAKE, cannot represent vertical motion and nonlinear behavior of the site and the effectiveness should be carefully examined

2.2. Effect of Travelling Waves

In most cases of evaluating the dynamic response of a single structure to earthquake excitations, it has been assumed that the ground motion is a function of time only, not a function of space. This assumption will give satisfactory results for structures occupying relatively small areas. For bridges with long span lengths, the effect of spatial variation of ground motion becomes more important, and thus the assumption could be inappropriate. Generally, to implement the feature of spatially varying ground motion to dynamic analysis of structures has been done by either deterministic or stochastic way. In deterministic ways of modeling it has been often assumed that a seismic wave propagates with constant velocity without changing its shape (e.g. Nazmy and Abdel-Ghaffar 1992; Leger et al. 1990). Traveling waves tend to reduce the maximum displacements, in that peak values of input seldom occur simultaneously for all supports because of the phase difference of the waves at each support. The reductions of the response do not always mean safer structures because they also introduce differential motions and result in the increase of internal forces. The amounts of the decrease of displacements and the increase of internal forces depend upon the geometry and stiffness of the structures and the seismic wave velocities. Even if these two effects can be seen clear for simple structures under harmonic excitations, the response is quite unpredictable and general tendency may not apply in complex situations such as long span bridges under earthquake loading, e.g. the maximum displacement can be significantly increased under certain circumstances like a specific wave velocity or angle of incidence (Nazmy and Abdel-Ghaffar 1992; Dusseau and Wen 1986). In real situations, however, ground motions at two distant points are not the same in general. Through the analysis of existing ground motion data, stochastic models of ground motions at spatially separated points can be constructed. In most cases, stochastic analyses have been performed in frequency domain, often in conjunction with response spectrum methods (e.g. Kiureghian and Neuenhofer 1992). The response spectrum method has the advantage of its computational effectiveness over a time domain analysis and it has been reported that it could yield satisfactory results (Dumanoglu and Severn 1990).

In most cases, it has been assumed that seismic waves travel along ground surface without consideration of soil-structure interaction. However, the interaction of

traveling waves through soil and the foundation of bridges may critically affect the behavior of the superstructure. As an example, vertically incident waves cause the phase difference of acceleration on the foundation, and it could result in rocking motion at the base of the bridge piers. For a more accurate differential motion at each support to be obtained, a three-dimensional FE analysis should be used where input motions travel along the bedrock and propagate through soil deposit, whether the FE model of the site is coupled with the superstructure model or not.

2.3. Soil-Structure Interaction

Most major river-crossing bridges in Mid-America are founded either on floating piles or caissons in deep alluvial soil deposit. Even though there have been extensive research conducted by researcher over the past several decades on the detailed modeling and behavior of pile foundations under dynamic loading, the foundations of bridges are often simplified with equivalent springs and dashpots. Geotechnical researchers, however, are mainly concerned with the study of the pile or pile group stiffness or behavior within piles, and they either ignore or overly simplify the oversimplify the superstructure. Therefore, it is important that we develop models, which include the superstructure and the foundation with the same level of detail. Currently, roughly three classes of methods are available to model dynamic behavior of pile foundations; finite element models, boundary element models and Winkler-type foundation models. Discussions on these methods are closely related to the topics of nonlinearity and coupling of two systems. Analytical methods are not suitable for irregular site conditions and complex structures.

Although they may require large computational times, FE analysis is considered to be the most accurate method for the combined system of the superstructure, the foundation and the soil deposit if proper boundary conditions are provided. Recently, a simplified quasi-3D nonlinear FE model (Finn et. al. 1996) and a full-scale 3D FE model using a plastic constitutive law of the soil medium (Cai et. al. 1995) were developed, and it was shown that nonlinearity and three dimensionality play an important role. For the most rigorous result to be obtained, wave passage effect of bedrock motions, as well as nonlinear soil behaviors, have to be taken into account.

The boundary element methods have advantages over the finite element method in that computational time can be significantly reduced and radiation of waves can be precisely reproduced. Even though several hybrid models have been reported (Guin et al. 1998), where FEM were used for structural components and BEM for soil domain, in general the BEM is not suitable for representing nonlinear behavior in soil medium. Therefore the effect of nonlinearity in soil deposit must be closely examined before a BEM is applied.

As another alternative to the FEM approach, Winkler-type foundation models easily allow the nonlinear behavior of soil medium (e.g. Nogami et al. 1992; Elassaly et al. 1995) and the time-domain analysis through frequency independent mass, springs and dashpots (Nogami et al. 1992). The accuracy of this approach critically depends upon proper representation of the pile-to-pile interaction and the effect of far-field motion.

A three-dimensional FE model including whole soil domain and the entire bridge spans will be quite large and it may not be appropriate for use in engineering practice. However, the existing simplified methods are based on approximations whose effect have

not been fully evaluated. In order to develop a more computationally effective method, it is necessary first to conduct a series of analyses using a coupled full-scale nonlinear FE model to obtain a reference case for the use in evaluating the other simplified methods.

2.4. Analysis of Cairo Bridge

Cairo Bridge over the Mississippi River in Southern Illinois was chosen for a case study in our research project. The bridge consists of approach spans and a main span, as shown in Figure 1. The soil deposit under the bridge is about 160m thick and consists of 5 layers of sand and clay. In order to examine the dynamic characteristics of the bridge, a three-dimensional finite element model was constructed using SAP2000, Figure 2. The modal characteristics of the bridge showed that there are two longitudinal modes around the period of 2.15sec and 47 modes above the period of 1.0 sec. It is also noteworthy that it has a significant number of modes associated with the torsion of approach spans and they may play an important role in the seismic behavior of the bridge

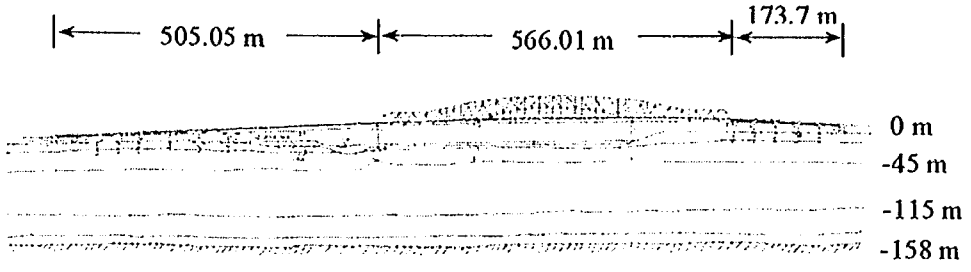


Figure 1. Description of the Cairo Bridge

Artificially generated acceleration time histories developed for the use in the New Madrid seismic zone (Hwang, 1998) were applied at the bedrock to obtain ground motions. Three types of models were used for time-domain analyses. In model A, the base of each pier is fixed and the model is completely linear. The base is still fixed in model B but nonlinear behavior in bearings and expansion joints were taken into account. In model C, in addition to nonlinear behavior, six spring elements were attached at the base of each pier to account for the foundation impedance. Absolute values of maximum displacements along the centerline of the deck were given for each model. The result shows that there exist significant differences between displacements from model A and C or B and C (Figure 4). This implies that the soil-structure interactions play a more influence in the longitudinal and transverse displacements than in the vertical displacements. Transverse displacements are observed to be so high that those can cause severe damage to the bearings. Significant torsion is present due to the difference between shear centers and mass centers of deck and truss sections. Additional results of this study are reported in (Nam, et. al. 1999, 2000; Kornkasem, et. al. 1999, 2000).

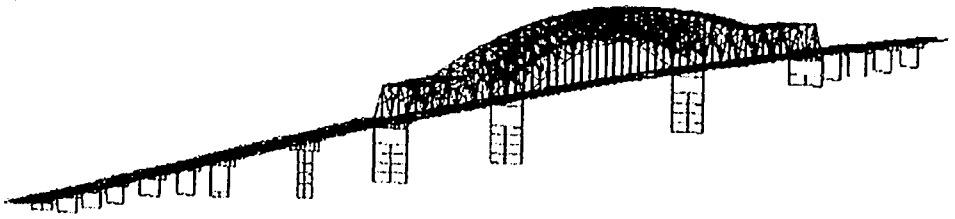


Figure 2. FE model of the bridge.

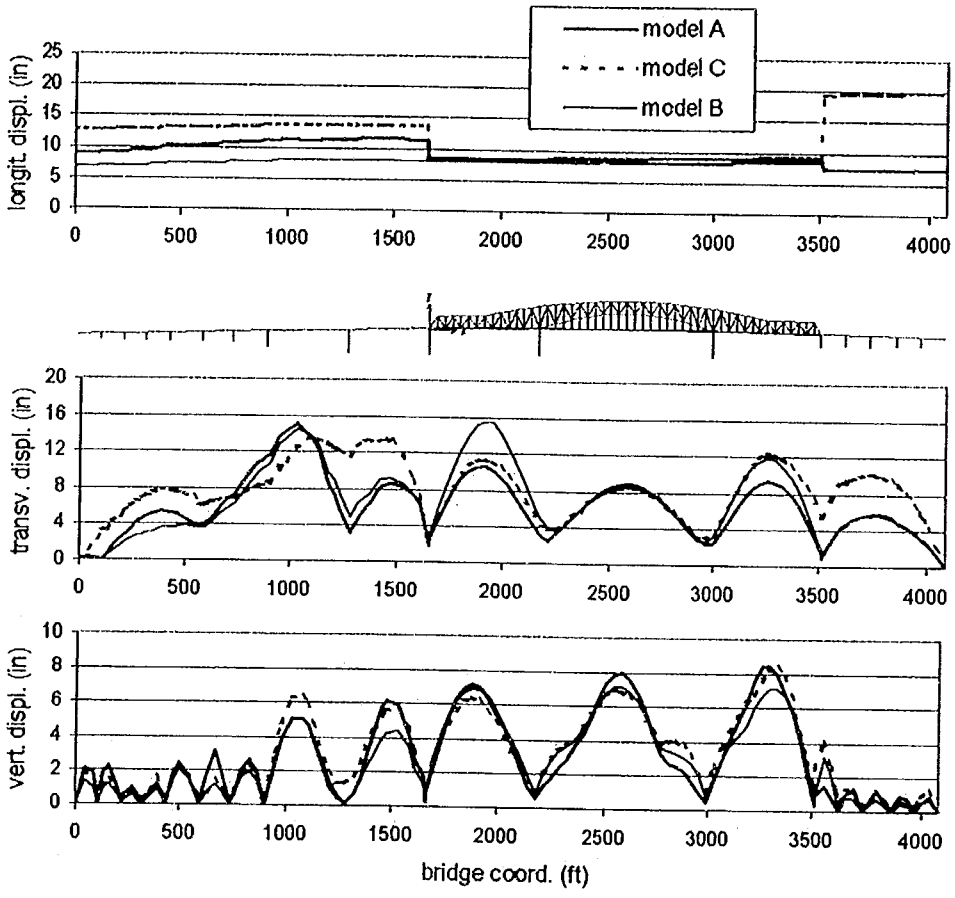


Figure 4. Max. displacements along the deck

3. SIMULATION OF CONSTRUCTION OF CABLE SUPPORTED BRIDGES

Fabrication and erection procedures are of primary importance in determining the state of stresses in cable stayed bridges. In general, the construction of the deck in cable stayed bridges progresses by the assembly of modular units, consisting of girder and deck segments with associated cables, on alternate sides of a supporting tower or pylon. During this process a sequence of partial structures arises. The bridge reaches its final form when the partial structures are joined at the mid-span or anchored to the piers. Temporary supports, counter weights, transient displacements and tensions in the cables

are all provided during construction in order to avoid overstressing of members of the partial structures and to attain the desired final configuration. The partial structures are more flexible than the completed structure and are subjected to construction loads, which are often different from those in the completed bridge.

The task of ensuring the attainment of specific internal forces and reference geometric configurations for a very flexible and highly redundant structure, such as a cable stayed bridge, is complex and involved. The complexity is the result of several factors such as the nonlinear behavior of the partial structures, their continuous structural changes and unforeseen erection variations. The recommended construction sequence is based on engineering analysis. Approximations in the engineering analysis lead to deviations from the predetermined geometry and cable forces. One of the major tasks of the contractor is to check the position control points of the partial structure so as to ensure that construction tolerances do not accumulate to the point where the bridge fails to achieve its desired final configuration. At every stage of construction, it is necessary to have information on the as built partial structure, in order to investigate the effects of possible modifications in construction procedures. The final construction stage determines the configuration of the completed bridge as well as the distribution of pre-stress in the bridge components, under the combined action of the dead load and pretension forces in the inclined cable stays. The high tension forces in the cable-stays also induce high compression forces in the towers and girders. Because high pretension forces exist in cable-stays before live loads are applied, the geometry and the pre-stress in cable stayed bridges are dependent on each other. They cannot be specified independently, as in many other types of steel or reinforced concrete bridges. The completed bridge must satisfy architectural as well as engineering design requirements. For these bridges, the interim and final stresses and deformations depend directly on the history and details of the construction process. Therefore, analysis of the actual construction sequence is an important first step in analysis of the bridge for other external loads, such as wind, earthquake and live loads.

Several investigators (Abdel-Ghaffer and Nazmy, 1987, 90; Farran, 1988; Fleming 1983; Podolny and Scalzi, 1976; Walther et. al., 1988) have referred to the importance of simulating construction process. However, the simulation of actual construction sequence is associated with a number of computational difficulties caused by geometric alteration problem. Some investigators (Behin 1990, 92) have recommended the using of approximate methods, such as backward analysis, in order to overcome these difficulties.

The author and his co-workers have developed a nonlinear finite element procedure for systematic construction sequence simulation of cable stayed bridges (Reddy, Ghaboussi and Hawkins, 1999). This methodology was primarily based on a method of analysis of construction sequences that was developed earlier by Ghaboussi and Pecknold, 1984. The objective of the simulation is to evaluate short-term and long-term influences of the construction sequence on the structural integrity of the cable stayed bridge. Short-term effects, as defined here, are those occurring during the construction process. The influence of changes during the construction on any subsequent loads is defined as long term effects. This method is applied to the specific example of the recently constructed Clark Bridge (Goodyear and Salamie, 1994: Hanson Engineers,

1991). Sufficient data was available on geometry control and cable forces for the Clark Bridge, so that the effects of the construction sequence could be thoroughly investigated.

4. DAMAGE DETECTION IN RAILWAY BRIDGES

The objective of the detection and identification of the structural damage is to construct the qualitative or quantitative description of the damage in a physical structural system from the measured response of the structure. In the past two decades, system identification techniques have been extensively applied to perform this task. Some studies have been proposed to detect and identify the structural damage directly through the measured response of structures.

There are three main questions in damage detection and identification: the existence, the location, and the extent of the damage. When condition monitoring is based on monitoring the changes in the structural response, then it is usually easier to detect the existence of the damage than determining the location and the extent of the damage.

The damage detection methods normally require some type of a controlled test and the measurement of the response during the tests. These tests may be static load tests or dynamic tests. It is very important to choose an appropriate type of measurement. The success of damage detection and identification highly depends on the sensitivity of the measurements to the type of the structural damage to be detected. As noted by Sanayei (1992), the location and accuracy of the measurements are other factors affecting the success of damage detection and identification. Bridge damage detection methods proposed in the literature are based on the measurements of either static or dynamic response.

Most of the damage detection and identification studies reported in the literature have used the dynamic measurements such as response time histories, frequency response functions, and modal data (natural frequencies, mode shapes). Monitoring of the changes in the natural frequencies appears to be the preferred method by most researchers. Although changes in the natural frequencies can easily determine the presence of structural damage, mode shapes are required for locating the damage. However, the incomplete mode shapes and the difficulty of pairing the corresponding mode shapes before and after the damage are practical limiting factors in the use of mode shapes to locate the structural damage in real structures.

The advantage of using the static response in damage detection as well as locating of the damage, recognized by Jenkins et al. (1997), is that the static response is more locally sensitive than the natural frequencies in structural damage detection.

System identification techniques have been increasingly applied in damage detection problems. First a mathematical or numerical model of a physical structural system is established to enable the analysis of the structural response. The basic strategy of most of the system identification methods is to minimize the difference between the measured and computed response of the structure. The state of the structure, including the existence and possibly the location of the damage, is determined in the process of minimization. There are two classes of methods in system identification techniques: parametric and non-parametric methods. Parametric methods involve estimation of parameters in the system model. If the unknown model parameters are chosen to represent physically meaningful quantities, the model is called a gray box model. On the other hand if the model parameters do not represent any physically meaningful quantities,

the model is called a black box model. The parameters in black box model are often chosen for the ease of measurement or for computational considerations.

A number of methods have been proposed for damage detection. A class of methods uses the optimization of some output quantity from a fixed model to detect and locate the structural damage (Hajela and Socіro 1990). Another class of methods, called model improvement methods, is used to modify the initial model so that it can represent the behavior of the current structure accurately, and in the process detect any structural damage. Some researchers have proposed a structural damage detection method by applying the eigensystem realization algorithm (Cobb and Liebst 1995), to directly extract the system parameters such as modal parameters and physical system parameters from the measured data. Methods based on modal analyses have also been used to locate and quantify the structural damage through the measured modal parameters (Chen and Garba 1988; Pandey and Biswas 1994,1995; Topole and Stubbs 1995a,b; Kim and Stubbs 1995a,b; Sheinman 1996; Stubbs and Kim 1996).

Some structural damage detection methods are based on the computational intelligence techniques, such as neural networks and genetic. Neural networks (Wu, Ghaboussi and Garrett 1992; Szewczyk and Hajela 1994; Barai and Pandey 1995,1997;) and genetic algorithms (Mares and Surace 1996; Chou and Ghaboussi 1997,1998) have been successfully used to locate and identify the structural damage in numerical simulations. One of the important characteristics of computational intelligence methods is their effectiveness and robustness in coping with uncertainty, insufficient information, and noise.

The detection and identification of structural damage from the measured response is influenced by several factors such as modeling error, measurement noise, and the number and location of the response measurements. Another important issue is the sufficiency of the measured data and whether the particular measurements are sensitive enough for all the possible structural damage. Some of these issues have been explored in the context of damage detection by dynamic signature analysis (Udwadia & Sharma 1978; Hjelmstad 1996; Juneja et al. 1997).

4.1. Condition Monitoring of Bridges under Normal Traffic

Most researchers have investigated methods of structural damage detection from its signature on the dynamic properties of the bridge such as natural frequencies and modes shapes. Other researchers look for damage signature in the pattern of deformations and displacements under static loads. In most cases, damage detection and condition monitoring of bridges requires control load tests, either static or dynamic. In static tests, a locomotive is used to load the bridge. In dynamic tests, the bridge is shaken at different frequencies. Controlled experiments of bridges are very costly and can only be justified at regular infrequent intervals.

The proposed methodology will permit continuous condition monitoring of a bridge under normal freight train traffic. The bridges can be permanently instrumented with a specially designed fiber optic monitoring system and remotely sensed. The system can be designed to perform both damage detection and long term condition monitoring.

Railway bridges can suffer damage and deterioration as a result of accidents, natural causes, such as earthquakes, strong wind, and flash floods, and normal wear and fatigue. Inspection at regular intervals is both costly and may miss damage occurring

between inspections. Continuous remote condition monitoring under normal train traffic loading is far less costly and can be as frequent as the train traffic, leading to highly economic method of increasing safety.

The proposed method will use the measured response of the bridge under the train traffic to perform the condition monitoring. Freight trains cause large measurable deformations and displacements in railway bridges. It is envisioned that the remotely sensed railway bridges have been permanently instrumented with a new specially designed and easy-to-install fiber optics sensing systems under development by the author and his co-workers. Passing of a train would trigger the recording system, which would collect the data and transmit to a central computer where the condition monitoring can be performed.

The recorded displacements and deformations of the bridge contain signatures of any defects and damage in the bridge. This is equivalent to performing a load test on the bridge, except that the exact value of the loads are not known, and they are basically time varying and maybe dynamic in nature. Ghaboussi and his co-workers have developed a smart soft computing method, which is capable of condition monitoring of railway bridges under normal service loads (Chou and Ghaboussi, 1997, 1998). The proposed methodology has been successful in computer simulations. An added benefit of the proposed methodology is its capability of determining the applied loads in the process of condition monitoring of the bridge.

4.2. Smart Soft Computing Method of Condition Monitoring

It is envisioned that the bridges will be permanently instrumented and remotely sensed. The condition monitoring will taken place at a central office by using the smart soft computing method developed by Ghaboussi and his co-workers (Chou and Ghaboussi, 1997, 1998). The methodology is soft computing version of system identification and is based on the premise that given sufficient information on the response of the bridge and some information about the bridge, the condition of the bridge and the loads acting on it can be determined.

The condition of the bridge is determined by matching the computed response of a model of the bridge as closely as possible to the large number of measurements. In order to develop a three dimensional numerical model of the bridge, data on the geometry of the bridge, section properties, connections, loads, and support conditions are needed. To make this model as realistic as possible, it is important that the data be as accurate as possible. Some of this data is assumed to be readily available, such as the geometry of the bridge and some section properties. The proposed smart soft computing method of condition monitoring determines the remaining part of the structural and loading data by minimizing the difference between the measured and computed response of the bridge. A specially developed Genetic Algorithm solves this minimization problem. Preliminary studies in numerical simulations have shown the method to be very effective in determination of the condition of the bridge as well as in determination of the loads acting on the bridge. The use of a large number of measurements makes the proposed method very robust and effective.

Genetic Algorithm is highly suitable for analysis of this type of difficult minimization problem since it does not require the gradients of cost function; only the function values are needed. However, Genetic Algorithm requires a large number of function evaluations. In some cases, several hundred thousand function evaluations are

needed. Cost function in this case is the error vector, and its evaluation requires a structural analysis, which is the most computationally costly part of the proposed methodology. In short, the condition monitoring of a railway bridge with the proposed methodology may require several hundred thousand structural analysis of the bridge. With the current very fast desktop computers this is not a serious impediment, nevertheless, it is a problem that needs to be addressed since each condition monitoring may take 20 to 30 hrs on even the fastest desktop computer. We have already addressed this problem and developed very efficient algorithms (Chou and Ghaboussi, 1997, 1998, Raich and Ghaboussi, 1998). These algorithms which are based on more approximate evaluation of the cost function (or fitness function), reduce the computational time for each condition monitoring to less than one hour on fast desktop computers.

An added attraction of the proposed soft computing method of condition monitoring is that it does not require any specific recorded quantities such as displacements, velocities, or strains. The proposed method can work equally well no matter what quantities of the response are recorded. In fact the recorded response does not have to be any physically identifiable function of the response of the bridge as long as the recordings are independent functions of the response of the bridge. In our fiber optic instrumentation, we have chosen to record average strains over 2-4 ft segments of the bottom cord and/or top cord of the bridge.

The question of what is a sufficiently large number of recorded measurements of the response for effective condition monitoring of bridges is very important. Currently, there are no rigorous guidelines for determining the minimum number of recordings. Our preliminary studies show that condition monitoring of the railway bridges with the proposed methodology requires a large number of recordings of the response the bridge. For an average truss or steel girder railway bridge approximately one hundred independent displacements and/or strains need to be measured. Our preliminary studies also seem to indicate that the error in condition monitoring is of the same order as the error in the response measurement.

The proposed fiber optic instrumentation system addresses both the quantity and accuracy of the required measured response of the bridge. The fibers will be arranged on a strip, which will be glued to the bottom cord of the bridge. Such a strip can easily contain one hundred fibers. We are planning to perform a small-scale laboratory experiment. In this experiment we will use a strip with 20 fibers. The fiber optics system also allows measurements with very high accuracy, far beyond the 10 micro-strain resolution determined to be sufficient for the proposed condition monitoring method.

A major extension of the basic methodology involves the determination of the condition of the joints and other critical regions of the structure, with the purpose of determining fatigue damage. Some preliminary work in this area has been done. The proposed method for condition monitoring of the joints and other critical regions is based on developing idealized models of these regions and on determining prescribed damage indices for these regions from the measured response by using the Autoprogressive Neural Network method, a method which has been developed and applied in related fields by Ghaboussi and his co-workers (Ghaboussi, Pecknold, Zhang and HajAli, 1998).

4.3. A New Fiber Optic Instrumentation System

The proposed condition monitoring system will be triggered when a train is approaching. The actual condition monitoring is performed when the train loads the bridge. The main requirement on the instrumentation system is that they generate a sufficient number of readings and that the fiber optic system be relatively simple to install and maintain. The proposed condition monitoring method requires a relatively large number of readings of the response of the bridge such that any possible damage will have some measurable effect in the response.

We propose to develop a fiber optics system, which is easy to install on the existing bridges and will generate a large number of readings. The instrumentation system consists of a large number of fiber optic sensors that are arranged into a strip. This strip is glued to the bottom cord of the bridge. The proposed system is suitable for steel truss, steel girder, and steel box girder bridges. In other types of bridges, the fiber optics strip can be glued to other appropriate locations. Each fiber optics sensor is only glued to the strip only over a length of the bottom cord of the bridge. Thus, each fiber optics sensor measures the average strain over the length that it is glued to the bridge. The glued segments of the fiber optics sensors will vary perhaps randomly and may overlap in some cases. The fiber optic strip may have more than a hundred sensors depending on the size of the bridge. All fiber optics loops in the strip will be attached to a terminal in which the average strains are recorded and transmitted to a control computer for processing.

ACKNOWLEDGEMENTS

This research was funded by grants from the Mid-America Earthquake Center and the National Science Foundation, Grant No. CMS-9908651. This support is gratefully acknowledged. Graduate students S.-I. Nam, S. Kornkasem, J.-H. Chou, N. Limsamphancharon, and former graduate student P. Reddy have worked on projects reported in this paper.

REFERENCES

AbdelGhaffer, Ahmed M. and Nazmy, Aly S., (1987) "Effects of three dimensionality and nonlinearity on the dynamic and seismic behavior of cable stayed bridges," Proc. 4th struct. congr., Bridges and Transmission Line Struct., ASCE, Orlando, Florida.

AbdelGhaffer, Ahmed M. and Nazmy, Aly S., (1990) "Three dimensional nonlinear static analysis of cable stayed bridges", Computers and Structures, V. 34, No. 2, pp 257-271.

Barai, S. V., and Pandey, P. C. (1997). Time-Delay Neural Networks in Damage Detection of Railway Bridges," Advances in Engineering Software, 28, 1-10.

Behin, Z., (1990) Erection Analysis of Cable Stayed Bridges, PhD Thesis, Department of Civil Engineering, University of Alberta.

Behin, Z., and Murray, D. W., (1992) ``A SubstructureFrontal Technique for Cantilever Erection

Analysis of CableStayed Bridges," Computers and Structures, Vol. 42, No. 3, pp. 145157.

Cai, Y. X., Gould, P. L. and Desai, C. S. (1995), "Investigation of 3-D nonlinear seismic performance of pile-supported structures", *Performance of Deep Foundations under Seismic Loading*, ASCE Geotech. Special Pub. No. 51, 17-31.

Chen J., and Garba, J. A. (1988). "On-Orbit Damage Assessment for Large Space Structures," AIAA Journal, 26(9), 1119-1126.

Chou, J. H., and Ghaboussi, J. (1997). "Structural Damage Detection and Identification Using Genetic Algorithm," Proceedings, Int. Conf. on Artificial Neural Networks in Engineering, St. Louis, U.S.A.

Chou, J. H., and Ghaboussi, J. (1998). "Studies in Bridge Damage Detection Using Genetic Algorithm," Proceedings, The 6th East Asia-Pacific Conf. on Structural Engineering & Construction, Taipei, Taiwan.

Cobb, R. G., and Liebst B. S. (1995). "Structural Damage Identification from Frequency Response Data," Proceedings of AIAA Guidance, Navigation and Control Conference, Baltimore, MD, U. S. A., 334-344.

Dumanoglu, A. A. and Severn, R. T. (1990), "Stochastic response of suspension bridges to earthquake forces", *Earthquake Eng. Struct. Dyn.*, **19**, 133-152.

Dusseau, R. A. and Wen, R. K. (1986), "Responses of a long span arch bridge to differential abutment motions", *Proc. 3rd U.S. Nat. Conf. Earthquake Eng.*, EERI, 2049-2060.

Elassaly, M., Ghali, A. and Elbadry, M. M. (1995), "Influence of soil conditions on the seismic behaviour of two cable-stayed bridges", *Canadian J. Civ. Eng.*, **22**, 1021-1040.

Farran, Hany J., (1988) "Computer Analysis and Design of Cable Stayed Bridge Structures Having Pre-stressed Post-tensioned Concrete Segmental Box girders (Volumes IIV), Report No. FHWA/CA/SD87/06, California Department of Transportation.

Finn, W. D. L., Thavaraj, T. and Wu, G. (1996), "Seismic Analysis of pile foundations: State-of-art", Proceedings 11th WCEE, paper no. 2073.

Finn, W. D. L. and Wu, G. (1996), "Nonlinear seismic analysis of pile foundations", Proceedings 11th WCEE, paper no. 1414.

Fleming, J. F., (1983) "Linear versus nonlinear behavior of cable stayed bridges; Wind & seismic effects," Proceedings 14th Joint Conf. U.S.Japan Cooperative Program on Natural Resources 343360,.

Ghaboussi, J. and Pecknold.D. (1984), "Incremental finite element analysis of geometrically altered structures," Int. Journal for Numerical Methods in Engineering, Vol. 20, pp. 20512064.

Ghaboussi, J., D. A. Pecknold, M. Zhang and R. HajAli, (1998). "Autoprogressive Training of Neural Network Constitutive Models" International Journal for Numerical Methods in Engineering, vol. 42, pp 105-126.

Goodyear, D. and Salamie, R., 1994) "Construction of Clarkcable stayed bridge at Alton, Illinois," Proceedings of the Structures Congress '94, ASCE, pp. 672676.

Guin, J. and Banerjee, P. K. (1998), "Coupled soil-pile-structure interaction analysis under Seismic excitation", *J. of Struct. Eng.*, ASCE, **124**, no 4, 434-444.

Hajela, P., and Soeiro, F. J. (1990). "Recent Developments in Damage Detection Based on System Identification Methods," Structural Optimization, 2, 1-10.

Hanson Engineers, (1991) "Structural Drawings of ClarkCable stayed bridge Steel Alternate", Hanson Engineers inc., Springfield, Illinois.

Hjelmstad, K. D. (1996). "On the Uniqueness of Modal Parameter Estimation," Journal of Sound and Vibration, 192(2), 2792-2801.

Hwang, H. M. (1998), *Artificial acceleration time histories*, Center for Earthquake Research and Information, University of Memphis.

Jenkins, C. H., Kjerengtroen, L., and Oestensen, H. (1997). "Sensitivity of Parameter Changes in Structural Damage Detection," Shock and Vibration, 4(1), 23-37.

Juneja, V., Haftka, R. T., and Cudney, H. H. (1997). "Damage Detection and Damage Detectability - Analysis and Experiments," Journal of Aerospace Engineering, ASCE, 10(4), 135-142.

Kim, J. T., and Stubbs, N. (1995a). "Damage Detection in Offshore Jacket Structures from Limited Modal Information," International Journal of Offshore and Polar Engineering, 5(1), 58-66.

Kim, J. T., and Stubbs, N. (1995b). "Model-Uncertainty Impact and Damage-Detection Accuracy in Plate Girder," Journal of Structural Engineering, ASCE, 121(10), 1409-1417.

Kiureghian, A. D. and Neuenhofer, A. (1992), "Response spectrum method for multiple-support seismic excitation", *Earthquake Eng. Struct. Dyn.*, **21**, 713-740.

Kornkasem, W., S-I Nam, D. A. Foutch, J. Ghaboussi and M. A. Ashheim, "Seismic Evaluation and Retrofit Analysis of a Truss-Arch Bridge in Southern Illinois", Proceedings, 5th National Conference on Lifeline Earthquake Engineering, Seattle, August 1999.

Kornkasem, W., S-I Nam, D. A. Foutch, J. Ghaboussi and M. A. Ashheim, "Seismic analysis of a truss bridge crossing Mississippi River", Proceedings, 12th World Conference on Earthquake Engineering, Auckland, New Zealand, Feb. 2000.

Leger, P., Ide, I. M. and Paultre, P. (1990), "Multiple support seismic analysis of large structures," *Compt. Struct.*, **36**, 1153-1158.

Nam, S-I, W. Kornkasem, J. Ghaboussi, D. A. Foutch and M. A. Ashheim, "Seismic Evaluation of Major River-Crossing Bridges", Proceedings, 5th National Conference on Lifeline Earthquake Engineering, Seattle, August 1999.

Nam, S-I, W. Kornkasem, J. Ghaboussi, D. A. Foutch and M. A. Ashheim, "Analysis of soil-structure interaction of major river crossing bridges", Proceedings, 12th World Conference on Earthquake Engineering, Auckland, New Zealand, Feb. 2000.

Nazmy, A. S. and Abdel-Ghaffar, A. M. (1992), "Effect of ground motion spatial variability on the response of cable-stayed bridges," *Earthquake Eng. Struct. Dyn.*, **21**, 1-20.

Nogami, T., Otani, J., Konagai, K. and Chen, H.-L. (1992), "Nonlinear soil-pile interaction model for dynamic lateral motion", *J. of Geotech. Eng.*, ASCE, **118**, no 1, 89-106.

Mares, C., and Surace, C. (1996). "An Application of Genetic Algorithms to Identify Damage in Elastic Structures," Journal of Sound and Vibration, 195(2), 195-215.

Pandey, A. K., and Biswas, M. (1994). "Damage Detection in Structures Using Changes in Flexibility," Journal of Sound and Vibration, 169(1), 3-17.

Pandey, A. K., and Biswas, M. (1995). "Damage Diagnosis of Truss Structures by Estimation of Flexibility Change," Modal Analysis: the International Journal of Analytical and Experimental Modal Analysis, 10(2), 104-117.

Raich, A. M. and Ghaboussi, J. (1977). "Implicit Representation in Genetic Algorithm Using Redundancy," International Journal of Evolutionary Computing, v. 5, n. 3.

Reddy, P., J. Ghaboussi and N. M. Hawkins, (1999) "Nonlinear Analysis and Simulation of Construction of Cable-Stayed Bridges", Journal of Bridge Engineering, ASCE, Vol 4, No. 4.

Sanayei, M. (1992). "Pre-Test Selection of Static Force and Displacement Measurement Locations for Damage Assessment," Proceedings of the 6th Specialty Conference on Probabilistic Mechanics and Structural and Geotechnical Reliability, ASCE, 567-570.

Sheinman (1996). "Damage Detection and Updating of Stiffness and Mass Matrices Using Mode Data," Computers and Structures, 59(1), 149-156.

Stubbs, N., and Kim, J. T. (1996). "Damage Localization in Structures without Baseline Modal Parameters," AIAA Journal, 34(8), 1644-1649.

Szewczyk, Z., and Hajela, P. (1994). "Damage Detection in Structures Based on Feature-Sensitive Neural Networks," Journal of Computing in Civil Engineering, ASCE, 8(2), 163-178.

Topole, K. G., and Stubbs, N. (1995a). "Non-Destructive Damage Evaluation of a Structure from Limited Modal Parameters," Earthquake Engineering and Structural Dynamics, 24, 1427-1436.

Topole, K. G., and Stubbs, N. (1995b). "Non-Destructive Damage Evaluation in Complex Structures from a Minimum of Modal Parameters," Modal Analysis: the International Journal of Analytical and Experimental Modal Analysis, 10(2), 95-103.

Udwadia, F. E., and Sharma, D. K. (1978). "Some Uniqueness Results Related to Building Structural Identification," SIAM Journal of Applied Mathematics, 34(1), 104-118.

Wu, X., Ghaboussi, J., and Garrett, J. H. (1992). "Use of Neural Networks in Detection of Structural Damage," Computers & Structures, 42(4), 649-659.

Study on the stability of the Akashi Kaikyo Bridge for residual displacement of tower foundation by large-scale earthquake

Susumu Fukunaga[1]

Abstract

Because the dynamic response of a foundation caused by a large-scale earthquake is very strong, it is anticipated that plastic deformation occurs in the ground around the foundation and hence the foundation may experience residual displacement. The residual displacement of the foundation has a large influence on the overall stability of the superstructure of the bridge. Therefore, a calculation method for residual displacement has been developed, which considers the deteriorated stiffness in the ground around the foundation caused by repetitious seismic motion. The calculated residual settlement was then compared with the measured settlement of the Akashi Kaikyo Bridge's tower foundation during the 1995 Hyogo-ken Nanbu earthquake, which confirmed the method to be roughly appropriate for use. Using this calculation method, the residual displacement caused by a large-scale earthquake was calculated for the Akashi Kaikyo Bridge's tower foundation and the stability of the Akashi Kaikyo Bridge was checked for a large-scale earthquake by using the calculated residual displacement of the foundation.

1. Introduction

As the input seismic motion from an inland direct strike type earthquake such as the 1995 Hyogo-ken Nanbu Earthquakes is very large, dynamic response of the foundation caused by the earthquake is also very large. It is not realistic to design the foundation to be elastic for such large dynamic response. Therefore, as the plastic deformation in the ground caused by the earthquake has to be allowed, it is necessary to calculate the plastic displacement of the foundation caused by the earthquake. In addition, it is also necessary to check the stability of the superstructure of the bridge for residual displacement of the foundation.

Therefore, the calculation method for residual settlement of a foundation was developed. This method utilizes the deteriorated stiffness in the ground caused by the repetitious seismic motions based on the result of soil tests. The validity of this calculation method was confirmed by comparing the calculated residual settlement and the measured residual settlement of the Akashi Kaikyo Bridge's tower foundation due to the 1995 Hyogo-ken Nanbu Earthquake.

In addition, this calculation method can be extended and a calculation method for horizontal and rotating residual displacement was developed. The horizontal and the rotating residual displacement of the foundation due to the 1995 Hyogo-ken Nanbu Earthquake was calculated. Moreover, as a long span bridge may be planned to cross faults, it is necessary that the displacement of the foundations by movement of the faults must be considered in long span bridge planning. The span

[1] Deputy Manager, Engineering Information Division Long-span Bridge Engineering Center, Honshu-Shikoku Bridge Authority

length of the Akashi Kaikyo Bridge was elongated by the fault movement by about 80cm. Therefore, it was necessary to consider the displacement of the foundation by the fault movement. The stability of the Akashi Kaikyo Bridge for a large-scale earthquake was examined by these amounts of displacement of the foundations.

Figure 1 shows the outline of the Akashi Kaikyo Bridge's geographical features and geological features. The 2P is founded on a weakly cemented gravel deposit (Akashi layer), while the 3P and the 1A are founded on sedimentary soft rock (Kobe layer) of early Neogene period. The 4A is founded on granite.

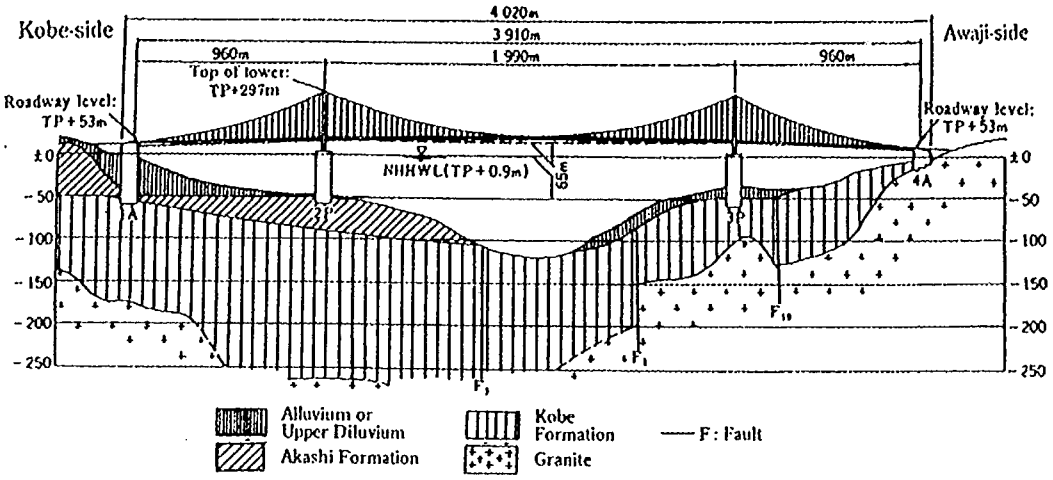


Figure 1. Geological profile at the Akashi Kaikyo Bridge

2. Analytic condition and analytic method for calculation of residual settlement of foundations

In the Akashi Kaikyo Bridge's tower foundation 2P, a residual settlement of about 20mm was measured after the 1995 Hyogo-ken Nanbu Earthquake. Then, the residual settlement due to the earthquake was calculated by considering the deteriorated stiffness in the ground caused by the repetitious seismic motions. The validity of the method was examined by comparing the calculated settlement with the measured settlement.

Figure 2 shows the ground model of the 2P tower foundation of the Akashi Kaikyo Bridge used for the analysis. In non-restrained ground, the modulus of deformation of the ground model (for dynamic analysis, the modulus of

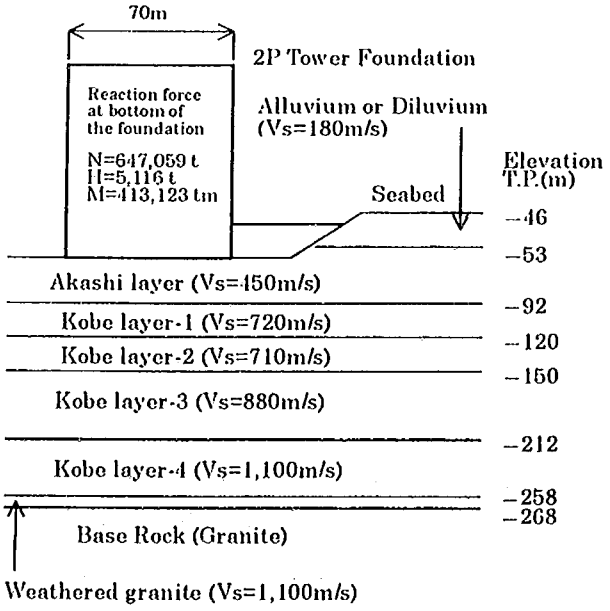


Figure 2. Geological model of 2P foundation of Akashi Kaikyo Bridge

deformation is the value at the slight strain level) is calculated by the elastic wave speed Vs measured at the in-situ before the construction of the foundation. Moreover, a larger modulus of deformation than that in non-restrained ground is used in the ground right under the foundation considering increased restraint pressure in the ground by the self-weight of the foundation. Figure 3 shows the relation between the restraint pressure and the modulus of deformation. In the analytic method, both static elastic FEM analysis and equivalent dynamic linear FEM analysis were used. For equivalent dynamic linear FEM analysis, both horizontal and vertical motions were input at the base ground (granite). The input seismic motions were converted from the records of the Kobe Marine Meteorological Observatory at the 1995 Hyogo-ken Nanbu Earthquake by the equivalent linear seismic response analysis of horizontally layered soil (SHAKE). Figure 4 shows the calculation method of the input seismic wave forms at the base ground of the ground model of the foundation. The ground deformation properties for repetitions of seismic loads are used for the calculation of deterioration of ground stiffness (hereafter called accumulative deterioration calculation). The ground deformation properties were determined by cyclic triaxial compression test under non drained conditions of the undisturbed sample of the Akashi layer. Figure 5 shows the flow chart of determining the ground deformation properties for repetitious of seismic loads and the procedure is explained below.

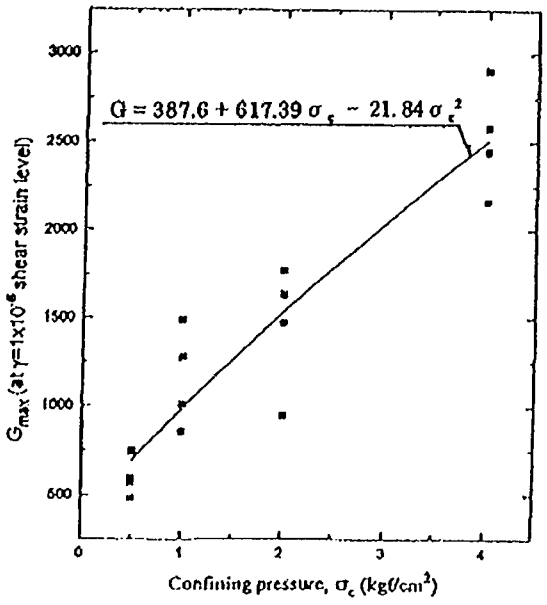


Figure 3. Relation between G and σ c (Akashi layer)

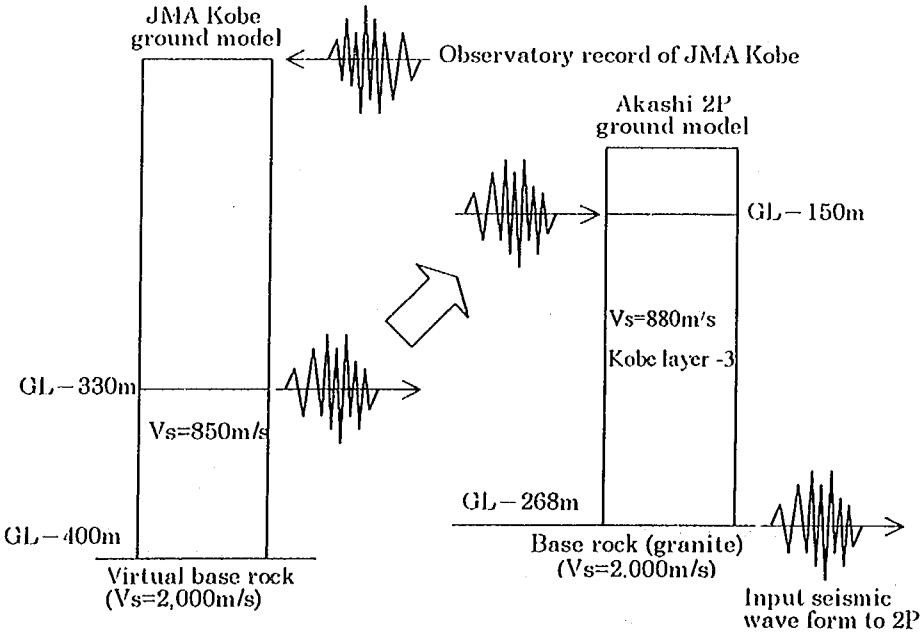


Figure 4. Calculation method of input seismic acceleration wave form

1) The relation between regulated dynamic shear stress ratio SR_d and generated strain in every repeated frequency of SR_d is calculated. And the numerical correlation formulas are determined in every repeated frequency of SR_d.

2) The numerical correlation formulas of both the factors of the numerical correlation formulas in 1) and the repeated frequency of SR_d are determined.

3) The numerical correlation formulas of regulated dynamic shear stress ratio SR_d, repeated frequency of SR_d and generated strain are determined based on the results of 1) and 2).

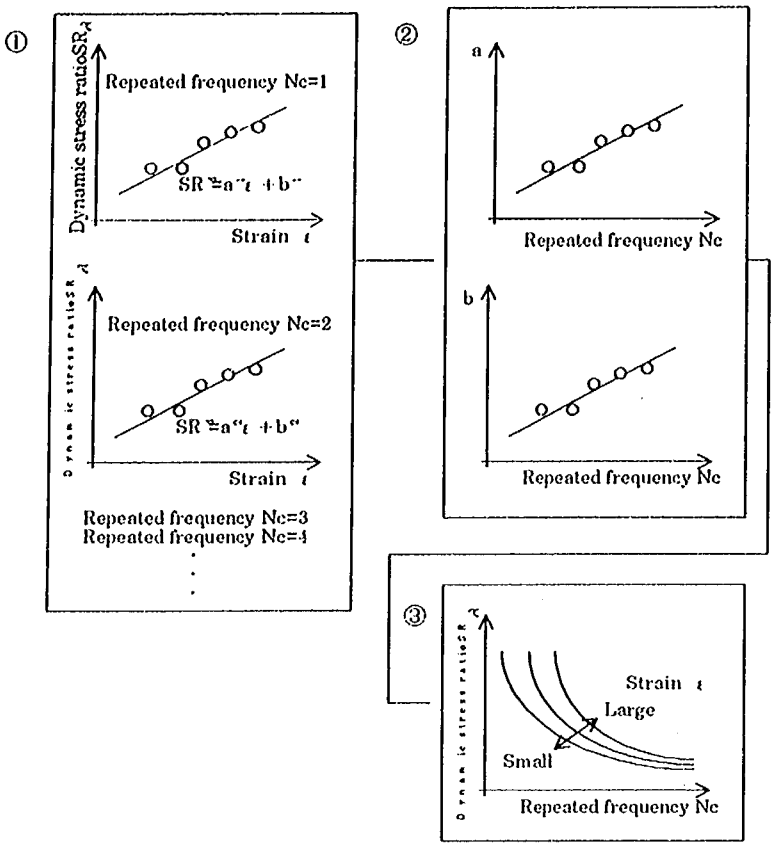


Figure 5. Flow chart for determining ground deformation properties

The dynamic shear stress ratio SR_d is regulated by the following formula based on the cyclic triaxial compression test of Akashi layer.

$$SR_d=(\sigma_1-\sigma_3)_d/2\sigma_{mc}'$$

σ_{mc}': Average effective principal stress

Figure 6 shows the ground deformation properties of the Akashi layer.

Moreover, the Vs calculated from shear modulus G obtained by laboratory test (cyclic compression test) is about 1/2 of the Vs measured by elastic wave exploration at in-situ position. Therefore the strain based on laboratory test was considered to be about 4 times of the actual strain, because of the effect of disturbance of the sample. The calculated strain decreases to 1/4.

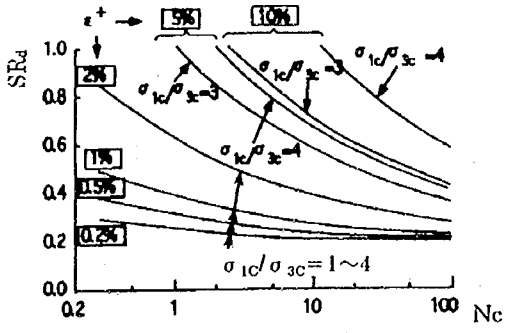


Figure 6. Ground deformation properties of the Akashi layer

The calculation flow of the foundation's settlement is shown in Figure 7 and the procedure is explained below. In this calculation flow, the accumulative deterioration calculation used to calculate the strain and the excess pore-water pressure was done only for the Akashi layer and not for the Kobe layer or deeper.

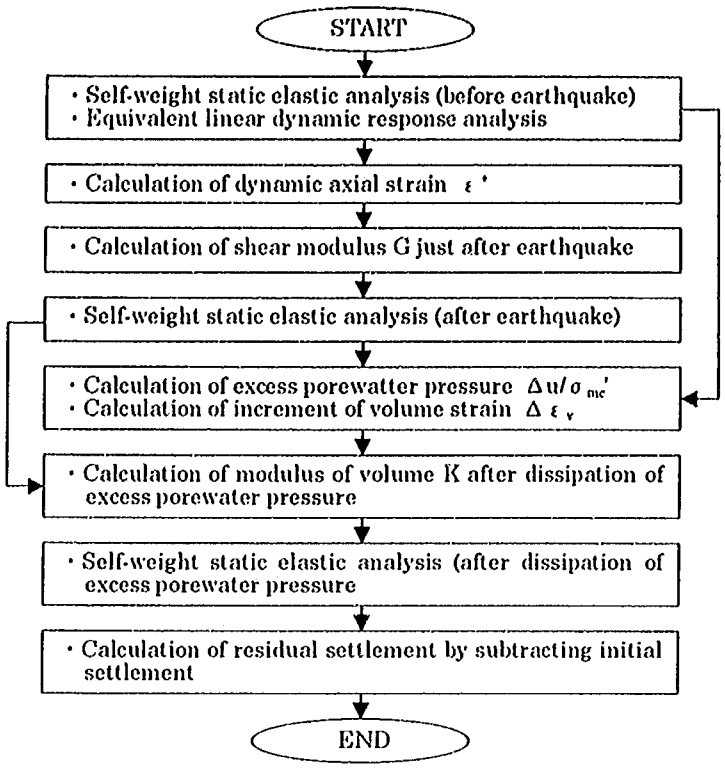


Figure 7. Calculation flow of foundation's residual settlement

1) The ground's stress and the foundation's settlement before the earthquake were calculated by self-weight static elastic analysis. In addition, the dynamic shear stress ratio generated in the ground by seismic motion was calculated by the equivalent linear dynamic response analysis.

2) Dynamic axial strain ε' which can be generated by seismic motion was calculated by the accumulative deterioration calculation based on the result of 1) and the ground deformation properties shown in Figure 6.

3) Dynamic axial strain was converted to dynamic shear strain and the maximum value of the converted dynamic shear strain assumed to remain the same value. But shear strain was thought to decrease to about 1/4 because of the effect of disturbance of the sample. The shear modulus G just after the earthquake was calculated based on this maximum shear strain and the shear stress before the earthquake calculated in 1).

4) The average effective principal stress and the foundation's settlement were calculated by self-weight static elastic analysis using the shear modulus G of the Akashi layer calculated in 3). The residual settlement just after the earthquake was calculated by subtracting the settlement before the earthquake calculated in 1) from the settlement calculated in this stage.

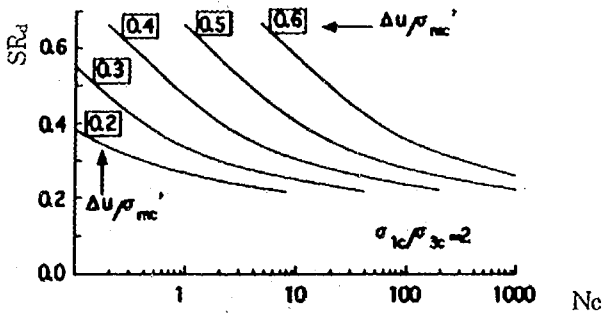


Figure 8. Properties of excess pore-water pressure

5) The excess pore-water pressure generated by seismic motion was calculated by the method in 2) based on the properties of the excess pore-water pressure ratio which was obtained by the cyclic triaxial

compression test (shown in Figure 8, but the properties are set based on every principal stress ratio σ_1/σ_{3c}). The average effective principal stress was calculated considering the increased excess pore-water pressure. The relation between the average effective principal stress and the volume strain ε_v was determined by using the amount of drained water during consolidation of the sample of the cyclic triaxial compression test. By using the relation the increment of the volume strain $\Delta\varepsilon_v$ was calculated based on dissipation of excess pore-water pressure.

6) Modulus of volume K after dissipation of excess pore-water pressure were calculated by using both the increment of the volume strain $\Delta\varepsilon_v$ calculated in 5) and the average effective principal stress after the earthquake calculated in 4).

7) The modulus of deformation of the Akashi layer was changed by using modulus of volume K calculated in 6) and the foundation's settlement was calculated by self-weight static elastic analysis after dissipation of excess pore-water pressure.

8) The residual settlement was calculated subtracting the settlement calculated in 1) from the settlement calculated in 7). Moreover, the residual settlement because of the dissipation of excess pore-water pressure was calculated subtracting the settlement calculated in 4) from the settlement calculated in 7).

3. Result of Residual settlement analysis of the foundation

Figure 9 shows the distribution of the maximum dynamic shear strain and Figure 10 shows the distribution of the excess pore-water pressure ratio. According to these Figures the maximum dynamic shear strain and the excess pore-water pressure ratio are small in a similar area of the vicinity right under the center part of the foundation. This is thought to be an influence of the increased restraint in the part where the foundation is set up. The part where the excess pore-water pressure ratio is small exists in a bulb-like area right under both end parts of the foundation. Because the excess pore-water pressure ratio before the earthquake was four or more in the area, this area is thought to become an area where the excess pore-water pressure ratio does not rise.

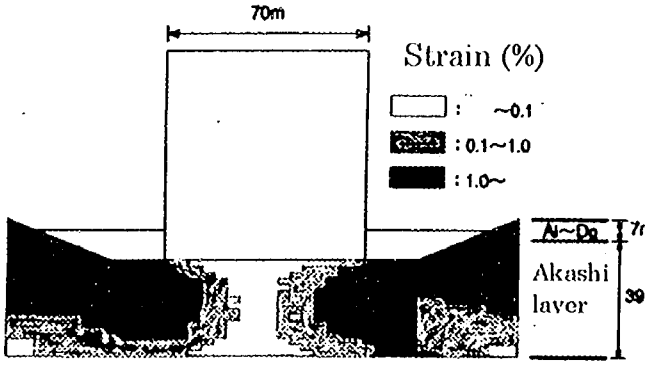


Figure 9. Distribution of maximum dynamic shear strain

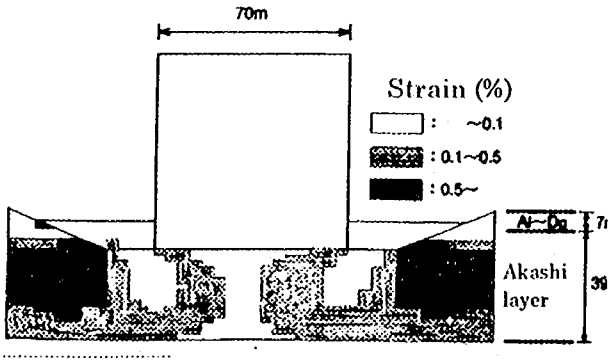


Figure 10. Distribution of excess pore-water pressure

Figure 11 shows the distribution of the amount of residual settlement of the direction of the depth along the centerline of the foundation. The Figure also shows the amount of measured residual settlement. Settlement of about 7.1cm was obtained as the analytical result. As the settlement generated by the dissipation of the excess pore-water pressure was about 23% (7.1 — 5.5=1.6 cm) of the sum of the settlement just after the earthquake, the influence of the dissipation of the increased excess pore-water pressure was small. Although the calculated settlement of about 7.1cm was larger than the measured settlement of about 2.0cm, it is thought that the calculation method of the residual settlement of the foundation is roughly appropriate.

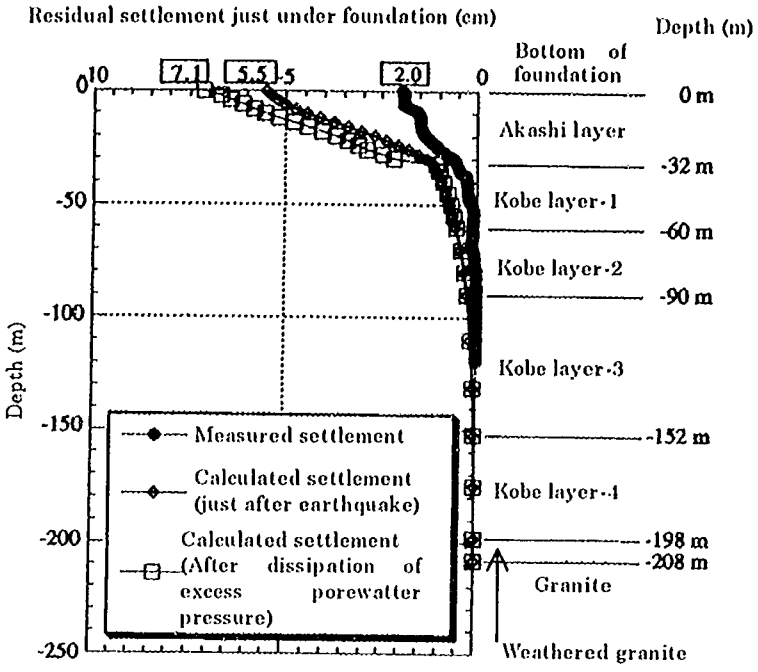


Figure 11. Distribution of residual settlement

Although the residual settlement after the earthquake was not measured at 3P, the residual settlement of 8.5 cm was calculated by the same method.

4. Analytic condition and analytic method for calculation of residual displacement of foundations

Although the allowable displacement of the foundation in the vertical direction of a long suspension bridge is very large (72-179cm for the tower's foundation of the Akashi Kaikyo Bridge), the vertical displacement of the foundation is accompanied by the horizontal and rotating displacements. Also these horizontal and rotating displacements of the foundation have an extremely large influence on the superstructure. Therefore, it was attempted to extend the above mentioned analysis method of the residual settlement and to develop an analytical method of the horizontal and rotating residual displacement.

The analysis was done for the tower's foundation 2P of the Akashi Kaikyo Bridge as well as the calculation of the residual settlement. The ground model and the input seismic motion were the same values with the calculation of the residual settlement (See Figure 2, 3, 4 and 6). Figure 12 shows the calculation flow and the procedure is explained below. In this calculation, as well as the calculation of the residual settlement, the accumulative deterioration calculation used to calculate the strain and the excess pore-water pressure was done only for the Akashi layer and not for the Kobe layer or deeper.

1) The ground's stress before the earthquake was calculated by self-weight static elastic analysis.
2) The dynamic shear stress ratio generated in the ground by seismic motion was calculated by the equivalent linear dynamic response analysis.
3) Dynamic axial strain ε' which can be generated by seismic motion was calculated by the accumulative deterioration calculation based on the result of 1) and the ground deformation properties shown in Figure 6.
4) Dynamic axial strain was converted to dynamic shear strain and the maximum value of the converted dynamic shear strain assumed to remain the same value. But shear strain was thought to decrease to about 1/4 because of the effect of disturbance of the sample. The time history value of the decreasing shear modulus G was calculated based on both the dynamic shear strain and the shear stress before the earthquake calculated in 1).

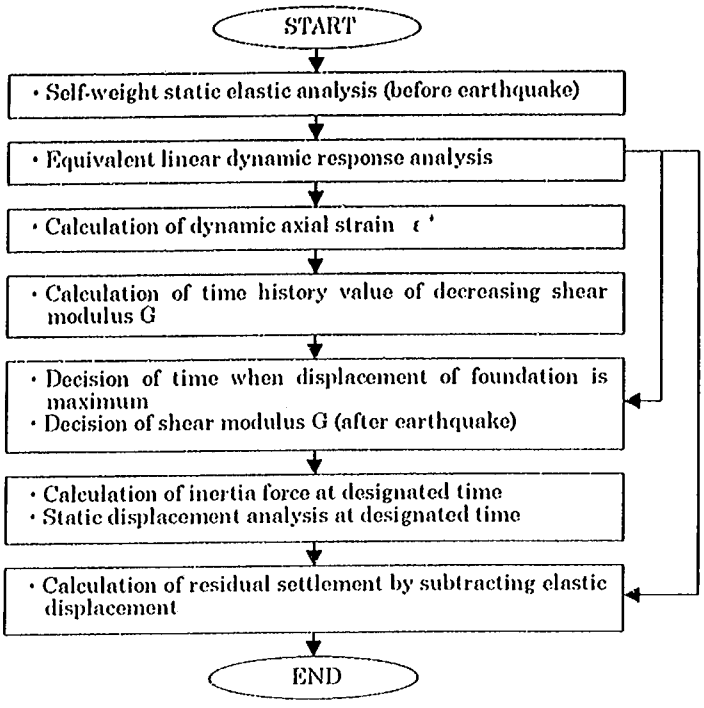


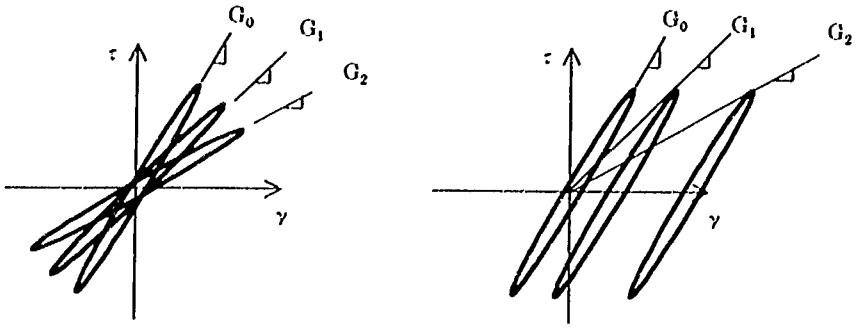
Figure 12. Calculation flow of foundation's residual displacement

5) The time when the displacement of the foundation is assumed to have the maximum value in the equivalent linear time history dynamic analysis was decided in 2). Shear modulus G at the time was decided by the time history values of shear modulus G calculated in 4).
6) Static displacement analysis of the foundation was done using the inertia force calculated by the acceleration acting on the foundation and shear modulus G at the time decided in 5). Thus the displacement of the foundation was calculated.
7) Assuming that the amount of displacement calculated by 6) is the sum of elastic displacement and plastic displacement, the residual displacement was calculated by subtracting the elastic displacement obtained by the equivalent linear dynamic analysis in 2) from the sum of the displacement.

As shown in Figure 12, the residual displacement is calculated by subtracting the displacement calculated by the dynamic FEM response analysis at the decided time from the displacement calculated by static FEM analysis based on accumulative deterioration calculation.

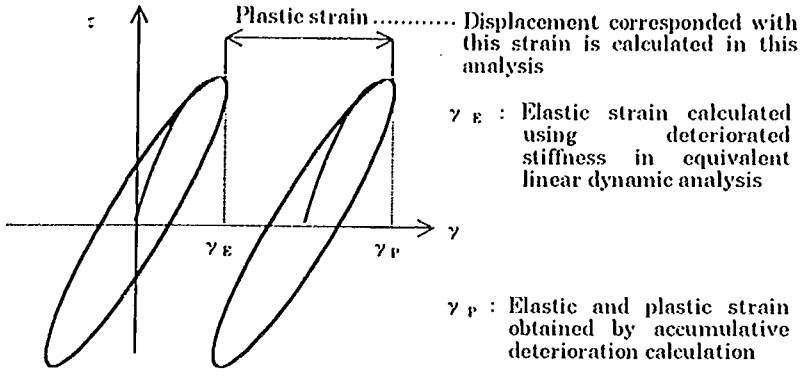
Figure 13 shows the explanation of stress-strain relation in this method. Although the convergent stiffness was used as the ground stiffness for the equivalent linear dynamic response analysis in (a), the relation between the stress and the strain is linear and the calculated strain is elastic strain. On the other hand, the relation between stress, strain and the repeated load frequency number was modeled to be able to calculate the sum of plastic and elastic strain in the static analysis based on the accumulative deterioration calculation in (b). Therefore, it is thought to be possible to calculate the

plastic strain by subtracting the elastic strain calculated by (a) from the sum of strain calculated by (b).



(a) Equivalent linear seismic response analysis

(b) Static analysis based on accumulative deterioration calculation



Displacement corresponded with this strain is calculated in this analysis

γ_E : Elastic strain calculated using deteriorated stiffness in equivalent linear dynamic analysis

γ_P : Elastic and plastic strain obtained by accumulative deterioration calculation

(c) Analysis of plastic strain

Figure 13. Stress – strain relation in this method

5. Result of residual displacement analysis of the foundation

The time when the foundation has maximum displacement is selected as the time when the movement of rocking of the foundation is large based on the result of the time history wave form of the rocking displacement of the foundation shown in Figure 14.

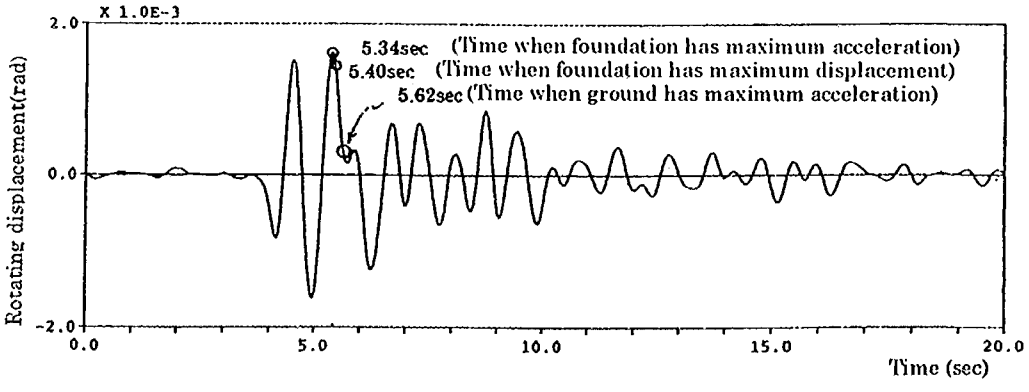


Figure 14. Time history wave form of rotating displacement of foundation

Figure 15 shows the time history of the deformation modulus of the ground calculated by the accumulative deterioration calculation. The dotted lines are the time when the maximum displacement of the foundation was calculated and the deformation modulus at the time is shown in the Figure 15. These deformation moduli shown in this Figure were used for the static FEM analysis.

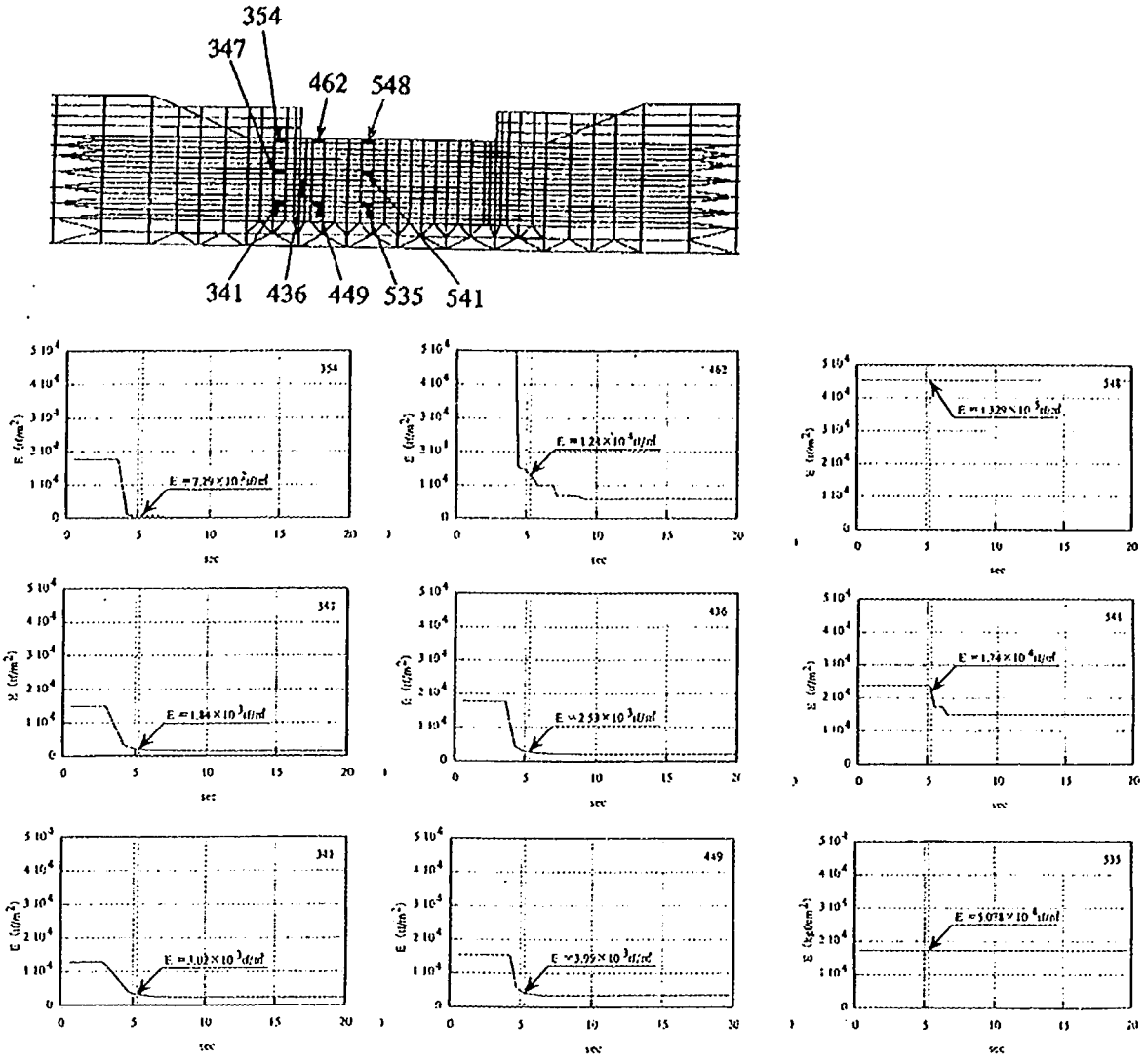
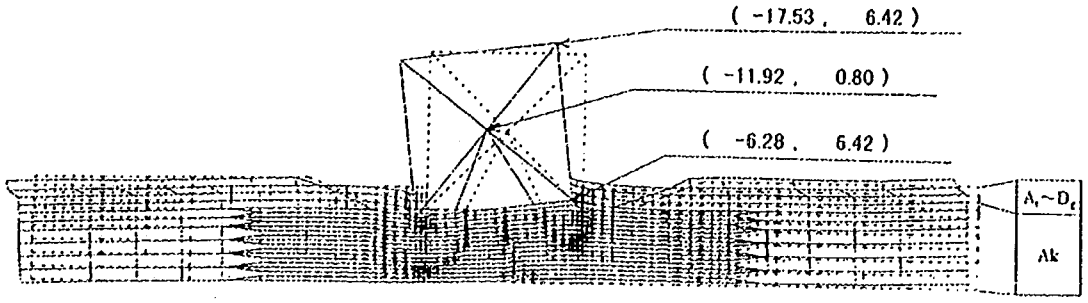


Figure 15. Time history of deformation modulus E calculated by accumulative deterioration

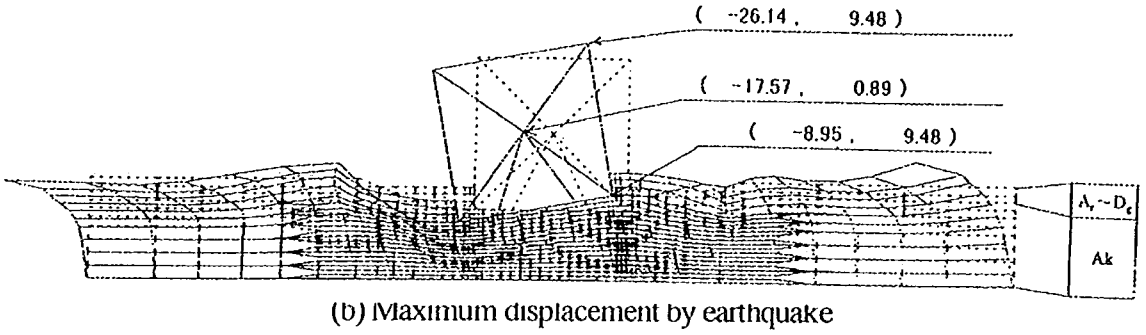
Figure 16 shows the displacement calculated by equivalent linear dynamic analysis(a), the maximum displacement calculated by the accumulative deterioration calculation(b) and the residual displacement calculated by this method((b)—(a)). The calculated residual displacements at the bottom of the foundation are as follows,

The residual horizontal displacement: 2.67cm

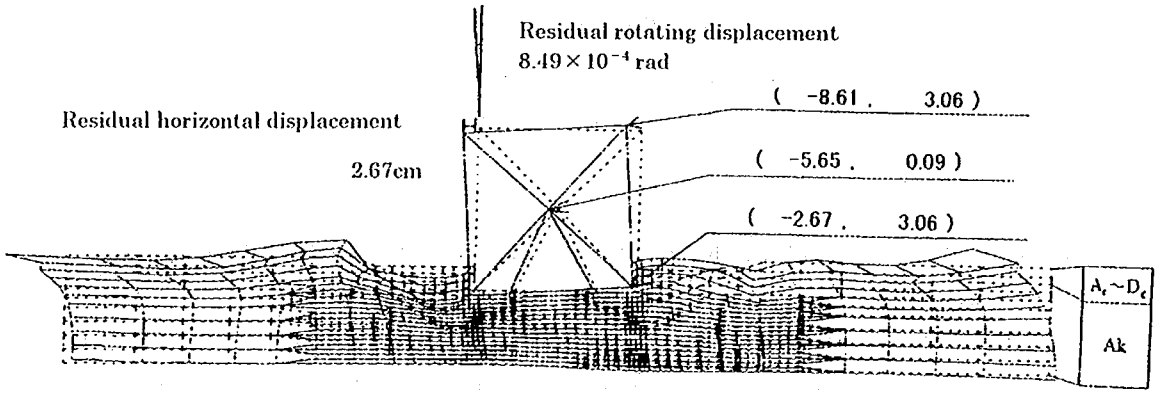
The residual rotating displacement: 8.49×10^{-4}rad.



(a) Result of equivalent linear dynamic response analysis



(b) Maximum displacement by earthquake



(c) Plastic displacement ((b)—(a))

Figure 16. Displacement of foundation in each stage

6. Stability check for the foundation

The stability of the superstructure of the Akashi Kaikyo Bridge was checked by using the above mentioned residual displacement of the foundation.

In this stability check, the large displacement of the foundation by the fault movement is also considered as well as the above mentioned residual displacement of the foundation. The large displacement of the foundation due to the fault movement were supposed to be 1 m, according to the case that the main span of the Akashi Kaikyo Bridge had been elongated about 80cm after the 1995 Hyogo-ken Nanbu Earthquake.

The stability was checked based on the following conditions.

- A large-scale earthquake such as an inland direct strike type earthquake (hereafter called an L2 earthquake) is supposed to occur one time during the service life of the bridge because the return period of this earthquake is very long, about 1,000 years or more.
- After the large-scale earthquake, an earthquake which occurs a few times during the service life of the bridge (hereafter called an L1 earthquake) is supposed to occur.

According to these conditions, the residual displacement of the foundation and fault movement by the L2 earthquake causes additional stress on the superstructure of the bridge. After an L2 earthquake, an L1 earthquake occurs and the dynamic stress by the L1 earthquake is added to the superstructure of the bridge.

The result of the stability check of the superstructure of the Akashi Kaikyo Bridge is shown below. The stability was checked for the bottom of the tower shaft because the bottom of the tower shaft is critical during an earthquake. The sum of the stress by the dead load σ_A, the stress by the residual displacement of the foundation caused by the L2 earthquake σ_{L2R} and the dynamic stress by the L1 earthquake σ_{L1} is less than the yield stress. Therefore the Akashi Kaikyo Bridge is thought to be able to retain stability, even if the displacement caused by the large-scale earthquake is considered.

$\sigma_A + \sigma_{L1} + \sigma_{L2R} = 4{,}254 < \sigma_y = 4{,}400$ kg/cm^2

Where, σ_A: Stress by the dead load (=2.470 kg/cm^2)

σ_{L1}: Dynamic stress by an L1 earthquake (=1,300 kg/cm^2)

σ_{L2R}: Stress by an L2 earthquake (=484 kg/cm^2)

σ_y: Yield stress of the steel plate of the tower shaft

7. Summaries

- The residual displacement of the foundation can be estimated to some accuracy by the accumulative deterioration calculation.
- The stability of the superstructure of the Akashi Kaikyo Bridge can be secured, even if the additional stress caused by both the residual displacement of the foundation and the fault displacement is considered.

8. References

1. K. Tada, H. Jin, M. Kitagawa, A. Nitta, R. Toriumi : "Effect of Southern Hyogo Earthquake on the Akashi Kaikyo Bridge", Structural Engineering International, March 1995, PP179-181

2. S. Saeki, T. Kurihara, R. Toriumi, M. Nishitani : "Effect of the Hyogo-ken Nanbu Earthquake on the Akashi Kaikyo Bridge" Second Italy-Japan Workshop on Seismic Design of Bridges, February 1997

MICROPILES FOR SEISMIC RETROFITS

James H. Long[1], Thomas E. Hunt[2], and Boris W. Leoro[3]

Abstract

Many structures around the world have been built on potentially liquefiable soil or were built before designs were required to account for seismic loads, leaving the foundations inadequate and/or connection of the foundation to the structure inadequate. Retrofitting is intended to increase the reliability of a foundation when subjected to seismic loads, and micropiles can offer a viable choice for retrofit. This is due in part to their ability to resist axial and lateral loads, but also due to their ability to be installed with minimal foundation disturbance in tight areas and in areas with low headroom. This paper discusses the use of micropiles as a seismic retrofit and provides a case in which micropiles were used as the primary retrofit of a seismically vulnerable foundation. Some aspects about the seismic behavior of micropiles are also discussed.

Introduction

Micropiles are defined as drilled piles that have diameters smaller than 300 mm (12 in.) and are composed of grout that is placed or injected under pressure, with some form of steel reinforcement to resist high tensile load. The load is primarily transferred from the steel reinforcement to the grout and then to the surrounding soil by friction. Due to the small diameter of the micropile, end bearing contribution is considered minimal. Development and use of the micropile is credited to Dr. Fernando Lizzi in the 1950's. He used micropiles to stabilize damaged historical buildings while working for Fondedile Construction in Italy

Micropiles have been used for retrofitting bridge foundations because of their capability to provide resistance to loads and their capability to be installed in difficult areas where space and headroom are limited. Micropiles can also develop large axial capacities in both tension and compression. Heavy steel casing can provide extra lateral stiffness and capacity if excessive lateral loads are anticipated. Micropiles may also be used when it is anticipated that liquefaction of the soil may occur beneath a foundation. Micropiles serve to transfer structural loads to lower, non-liquefiable soils if liquefaction occurs. If liquefaction results in ground movements or lateral spreading, micropiles may provide resistance to foundation translation.

Construction of Micropiles

The basic process for constructing micropiles is straightforward (Fig. 1). In most cases, a drill is placed inside of a thin-walled steel casing. Using water or slurry, soil cuttings are flushed up through the area between the drill and the casing as it advances. Subsequent

(1) Associate Professor of Civil Engineering, University of Illinois, Urbana, Illinois
(2) Graduate Research Assistant, University of Illinois, Urbana, Illinois
(3) Former Graduate Research Assistant, University of Illinois, Urbana, Illinois

sections can be continually attached until the casing reaches its desired depth. The drill is then withdrawn and reinforcement, usually a large diameter steel bar, is placed into the hole. A tremie pipe is used to deliver the grout to the hole, as the casing is removed via slow rotation- or jacking. After intermediate casing withdrawal, grout pressures can be applied to enhance friction between the soil and grout. If the design calls for a higher grout pressure than can be delivered by the original grouting process, post-grouting techniques may be implemented. This extra grout pressure results in increased frictional resistance and pile capacity (Littlejohn 1977).

One advantage of micropiles is that they can be installed in tight areas with low headroom. Because micropiles are installed in short sections that are rotated into the ground, large drilling or driving equipment that require headroom is unnecessary. Many projects where micropiles have been successful were limited by less than 6 meters of headroom and only a few meters of width.

Because they are drilled and grouted and have small diameters, micropiles minimize the disturbance of the existing footing during construction. Micropiles may be the only viable alternative if other structures are located near the foundation being retrofitted. Minimal vibration is associated with micropiling, which result in less settlements of adjacent structures and minimal volume change in the surrounding soil materials. Finally, micropiles can be installed in difficult soil conditions. Reports of their use in soils with boulders has been reported (FHWA, 1997).

Seismic Retrofit of the 1-57 Bridges Over Illinois Route 3

The 1-57 bridges over Route 3 are located about 6 km northwest of Cairo, Illinois, in southern Illinois. This location is near the New Madrid Seismic Zone, an area that has been designated by seismologists and earthquake engineers as the most hazardous zone in the eastern United States (Hwang, 1989). This retrofit was chosen as part of an ongoing seismic retrofitting program being conducted by the Illinois Department of Transportation (IDOT) and is described in greater detail by Gruendler, 1999.

The geotechnical evaluation performed for the site showed that liquefaction potential was great in the southern half of the bridges, due to loose silts and medium sands between the depths of 10 and 18 m. If liquefaction were to occur, the clayey upper layer could add more loads to the existing piles through down-drag forces. Therefore, the contribution of the existing pile capacity was not considered for the overall stability of the retrofitted structure.

If liquefaction did not occur at the site, there was still concern the existing piles were inadequate for resisting seismic loads. This concern included both the possibility of soil failure and the possibility of structural failure in the existing piles, as well as structural concerns at the connection between the pile and pile cap. Large overturning moments from the elevated structure imposed excessive tensile loads on the foundation piles. In addition, lateral loads were also a concern.

Underpinning was chosen as the retrofit procedure with options of using driven piles (pipe or H-piles) or drilled-in piles (micropiles). Driven piles are difficult to install where

headroom is limited, as in this case with a bridge deck above, and settlement of the existing bridge due to pile driving was likely. Accordingly, micropiles were selected because of their ability to be installed without significantly affecting although installation costs for micropiles were greater than for driven piles.

The micropiles were designed to carry the entire dead load of the bridge and seismic forces resulting from the design earthquake assuming liquefaction of the soil. Figure 2 shows details for the retrofit. Micropiles were installed around the perimeter of the existing pile-supported footing and a reinforced concrete overlay was used to structurally connect the micropiles with the existing foundation. The new pile cap extended 900 mm around the old footing and 600 mm above it.

Selected photographs at the site illustrate the bridge and its foundation retrofit (Fig. 3a). The elevated bridge deck, partly responsible for the large overturning moments, is seen in Fig. 3a. Fig. 3b shows drilling required for the structural connection to the footing. Holes were drilled and new reinforcement was epoxy-grouted into the footing. Fig. 3c shows the micropiles installed along the outside perimeter of the footing, and Fig. 3d illustrates the reinforcement in place and ready for the concrete overlay to be poured. The concrete overlay was placed on top of and around the existing footing.

Shown in Fig. 4 are details of a micropile and the results of an axial load test at the bridge retrofit site. The micropile extended through about 10 meters of clay into sand. Upon reaching the bottom elevation of about 80m, drilling ceased. The drilling rods were extracted and grout tremied into the micropile cavity. After filling the micropile with grout, a pressure varying from 0.7 to 1 MPa was applied while lifting the casing about 1.5 meters. Grout take was about 113 liters. The process of lifting casing and applying grout pressure was conducted a total of 5 times. Details for each grout section are given in Fig. 4. The 245 mm OD casing was left in place for only the upper 7 meters because it was not considered to add significant axial capacity, and a thick casing was necessary for resisting lateral seismic loads anticipated at the site. The resulting cross-section for the micropile is shown in the upper right hand corner of Fig. 4.

Load displacement behavior for the micropile is also shown in Fig. 4. The load test was conducted by applying a compression load first, and then releasing the compression load to zero. The load jacks were then rearranged to apply a tension load, and then the test was conducted. The light, dashed line represents the axial stiffness of the micropile column. About 1300 kN of compression were applied in the first half cycle of load resulting in 19mm of axial displacement. Upon loading the micropile to 1300 kN in tension, the micropile displaced to 24mm, illustrating a softening behavior and raising concern that either the tensile stiffness of the pile was significantly less than its compressive stiffness, or that the first half cycle of loading had softened the response of subsequent half cycle. No tests were conducted at the site in which more than one complete cycle of load (both compression and tension) were conducted.

Accordingly, the effects of cyclic loading on the behavior of micropiles is currently being investigated at the University of Illinois. Unfortunately, there is a dearth of information,

particularly full-scale test results, on the cyclic behavior of micropiles. The following sections discuss some aspects of behavior due to cyclic lateral and axial loads.

Lateral Loads

Methods to predict lateral load behavior of piles and drilled shafts form the basis of predicting behavior for micropiles. While several methods for predicting lateral response are available, a p-y approach (Reese, 1983) is commonly employed for critical foundations. These methods use p-y curves based on results of full-scale lateral load tests on piles and drilled shafts. However there are features of micropiles that differ from those of piles and drilled shafts, namely 1) the diameter of micropiles is typically smaller than those of piles and drilled shafts, and 2) the bending stiffness for micropiles can be very large compared to its diameter. Some p-y formulations base their predictions of lateral resistance provided by the soil on empirical factors that may be inappropriate for the combination of bending stiffness and diameter exhibited by micropiles. Lateral load tests are recommended for micropiles as a prudent measure for addressing these unknowns at a specific site. Lateral load tests could also provide an expanding knowledge base for developing more applicable prediction models for micropiles.

Models for predicting the behavior of a micropiles subjected to cyclic loading also use previous experience with full scale driven piling and drilled shafts. However, most recommendations for reducing the soil resistance to obtain cyclic p-y curves are based on the results of slow repetitive loading rather than seismic loading.

To describe the effects of cyclic loading on the behavior of a pile, this simplified soil pile model is used to illustrate how to soil and pile react to the application of lateral load at the head of a pile. The cyclic load applied at the head of the pile is assumed to impose equal and opposite horizontal loads to the pile head. Furthermore the loading is assumed to vary with time as shown in Fig. 5a.

The behavior of the pile is described for four phases during one cycle of load. The effect of each quarter-cycle of load is described and the influence of further cycles is mentioned.

During the first quarter-cycle, the magnitude of lateral load varies from a value of zero to a maximum horizontal load, H_{max}. As the load is applied, the head of the pile rotates and translates as shown in Fig. 5a-a. If the deflections along the pile large enough, a gap between the soil and pile wall will form along the back of the pile.

During the second quarter-cycle, the lateral load decreases from a value of H_{max} to zero, and the head of the pile returns to a position similar to its original configuration. As shown in Fig. 5a-b, the pile wall and soil may separate along the front the pile due to permanent deformations induced within the soil mass during the first quarter-cycle of loading. During the final portion of the second quarter cycle, the magnitude of load approaches zero and the pile returns to a configuration similar to its original shape, but displaced in the direction of the lateral load, H_{max}.

During the third quarter-cycle, the direction of the lateral load, H_{max}, and corresponding deflections of the pile head are reversed. As the magnitude of horizontal load increases from zero to H_{max}, the gap along the one face of the pile closes while a gap opens along the other face of the pile as shown in Fig. 5a-c.

The responses of the pile and soil during the fourth quarter-cycle are similar, but opposite in direction, to the responses described during the second quarter cycle. At the end of the fourth quarter cycle, with no load imposed on the head of the pile, gaps between the soil and pile may occur on both sides of the pile as shown in Fig. 5a-d.

As the cyclic load continues to be applied to the pile head, the behavior of the pile and soil will be similar to the behavior just described for the pile during cyclic loading (Fig. 5b). The cyclic load-displacement relationship becomes more S-shaped as cyclic loading continues, and the peak horizontal deformation at the head of the pile increases with each cycle of loading. Specific behavior will depend on characteristics of the cyclic load applied to the pile head, and characteristics of the soil surrounding the pile. Also, the behavior of the soil surrounding the pile depends largely on the characteristics of the stresses imposed.

Axial Loads

Micropiles can develop large axial loads in both compression and tension. It is this feature, along with construction and installation details, that makes them attractive as a method for seismic retrofit when additional axial capacity is a necessary component of the retrofit. The static axial capacity for a micropile can be controlled by either the soil/ground interface, or the steel/grout interface. The strength along the soil/ground interface depends on several factors such as 1) the construction technique used to install the micropile, 2) grout pressure used in the bond zone, and 3) soil properties, such as permeability, grain size, density, strength, and state of stress. The interface strength will also depend on the type of loading such as static or cyclic, and whether the cyclic load is in compression only, tension only, or both compression and tension.

For static loads, axial capacities can be predicted based on traditional methods (FHWA, 1997). However, load tests are prudent because the axial capacity is strongly dependent on details of construction and local soil conditions.

Much needs to be learned about the behavior of micropiles subjected to cyclic loads. Similar studies on piles and drilled shafts have shown that cyclic loading can have significant impact on axial stiffness and axial capacity (Karlsrud and Hagen, 1983; Turner and Kulhawy, 1987); however, similar information on micropiles is currently unavailable. Accordingly, current methodology draws from experience with piles subjected to cyclic axial loads.

A pile subjected to cyclic axial load may experience excessive displacement depending on the magnitude of cyclic load compared to its static capacity. Figure 6 is used to illustrate the effect of cyclic loading on axial pile capacity. Definitions for two-way cyclic loading are given in Fig. 6a where loading is taken to vary with time. Two-way cyclic loading is defined as a loading that applies both tension and compression (i.e. there must be a stress reversal). The half amplitude of load is defined as the cyclic component Q_{cyc}. One-way

loading is illustrated in Fig. 6b and is defined as a cyclic loading in which there is no stress reversal. The variation of load versus time is defined with an average load (Q_{avg}) and a cyclic component (Q_{cyc}). One-way loading will result for all values of $Q_{avg} > Q_{cyc}$. Two-way loading occurs when $Q_{avg} < Q_{cyc}$.

The Figs. 7a and 7b summarize results for cyclic loading. Figure 7a summarizes results of tests conducted by NGI for piles driven into clay (Karlsrud and Hagen, 1983). Curves are shown for combinations of cyclic and average load that resulted failure for 10, 100, and 1000 cycles of load. The plot is a arranged so that a 45 degree line from the origin forms the boundary between one-way and two-way loading. Loading is one-way below the 45 degree line and two-way above the line. The vertical axis corresponds to two-way cyclic loading in which compressive and tensile loads are equal.

The curves show that two-way cyclic loading with only 50 percent of the static capacity will result in failure of the pile within ten cycles. Thus, two-way cyclic loading can affect capacity greatly. For comparison, failure in 10 cycles of load for one-way cyclic loading requires the load to vary from zero to 90 percent of static capacity. Accordingly, load reversal can affect capacity significantly.

Few full-scale test results are available to produce graphs such as Fig. 7a for deep foundations. There have been a number of analytical and numerical studies to assess effects of cyclic loads. Chin and Poulos (1991) used small model pile tests to extend to larger size piles drilled and grouted into calcareous soils. The effects of two-way cyclic loading are shown to be significant. A better knowledge of the effect of cyclic loads on micropiles is necessary.

Results of a full-scale test on a micropile subjected to two-way cyclic axial loading is shown in Fig. 8. It is rare to conduct these load tests with many cycles of load, and in this case, only 2.5 cycles of load were applied. In spite of the few cycles, some behavior seen in piling are also exhibited here. Each cycle compression exhibits a softer load displacement relationship. Therefore, it is anticipated that two-way cyclic loading will reduce the capacity of micropiles even though little data are currently available to provide a quantitative measure of this reduction. Also note that as cycling continues, the load displacement curve become more S-shaped. The change in the slope of load displacement occurs when the load changes from compression to tension in the second cycle, and again, from tension to compression in the third cycle. One explanation for this change in slope could be either slippage developing along the soil/grout interface, or slippage occurring along the structure/grout interface.

Summary

Micropiles offer some significant advantages for seismic retrofitting. Micropiles can be used to minimize rocking in spread footings by taking the tensile and compressive loads. They can transfer loads through liquefiable layers of soil. They can be installed in tight areas or areas with limited headroom. Micropiles can also be installed in difficult soil conditions while minimizing disturbance of nearby footings or piles.

Knowledge is still being developed to define how these foundations behave when subjected to cyclic lateral and axial loads. This is an area where testing would be vital to our

understanding of micropile behavior because it models better the type of loading that an earthquake delivers. Presently, our knowledge of pile behavior coupled with scattered test data on micropiles forms the core of knowledge available on micropile behavior.

Acknowledgments

Work described in this paper was performed as a part of the Mid-America Earthquake Center at the University of Illinois. The center is sponsored by the National Science Foundation. Micropile data and bridge retrofit information was provided by the Illinois Department of Transportation, and cyclic load test information was provided by Mr. Joe Cavey of Hayward Baker, Inc. Their cooperation and assistance is gratefully acknowledged.

References

Chin, J.T. and Poulos, H.G. (I 99 1). "A t-z approach for cyclic loading analysis of single piles," Computers and Geotechniques, 289-320.

Federal Highway Administration (FHWA). (1997). "Drilled and grouted micropiles: state-of-practice review," FWWA-RD-96-016. July 1997.

Gruendler, J. J. (1999). "Seismic retrofitting of the 1-57 bridge over Illinois Route 3 in southern Illinois," Mid- America Highway Seismic Conference. St. Louis, Missouri, 1999.

Hwang, H. H. M., Clien, C. H. S. and Yu, G. (1989). "Bedrock accelerations in Memphis area due to large New Madrid earthquakes." Technical Report NCEER-89-0029.

Karlsrud, K. and T. Haugen (1983) "Cyclic Loading if Piles and Pile Anchors – Field Model Tests," Final Report, Norwegian Geotechnical Institute.

Littlejohn, G.S. and D.A. Bruce (1977) "Rock Anchors-state of the art," Foundation Publications Ltd., Brentwood, Essex, England.

Reese, L.C. (1983). Behavior of Piles and Pile Groups Under Lateral Load, Report submitted to Federal Highway Administration, Office of Research, Washington, D.C.

Turner, J. and F. Kulhawy (1987) "Experimental Analysis of Drilled Shaft Foundations Subjected to Repeated Axial Loads under Drained Conditions," Report submitted to EPRI, project 1493-4.

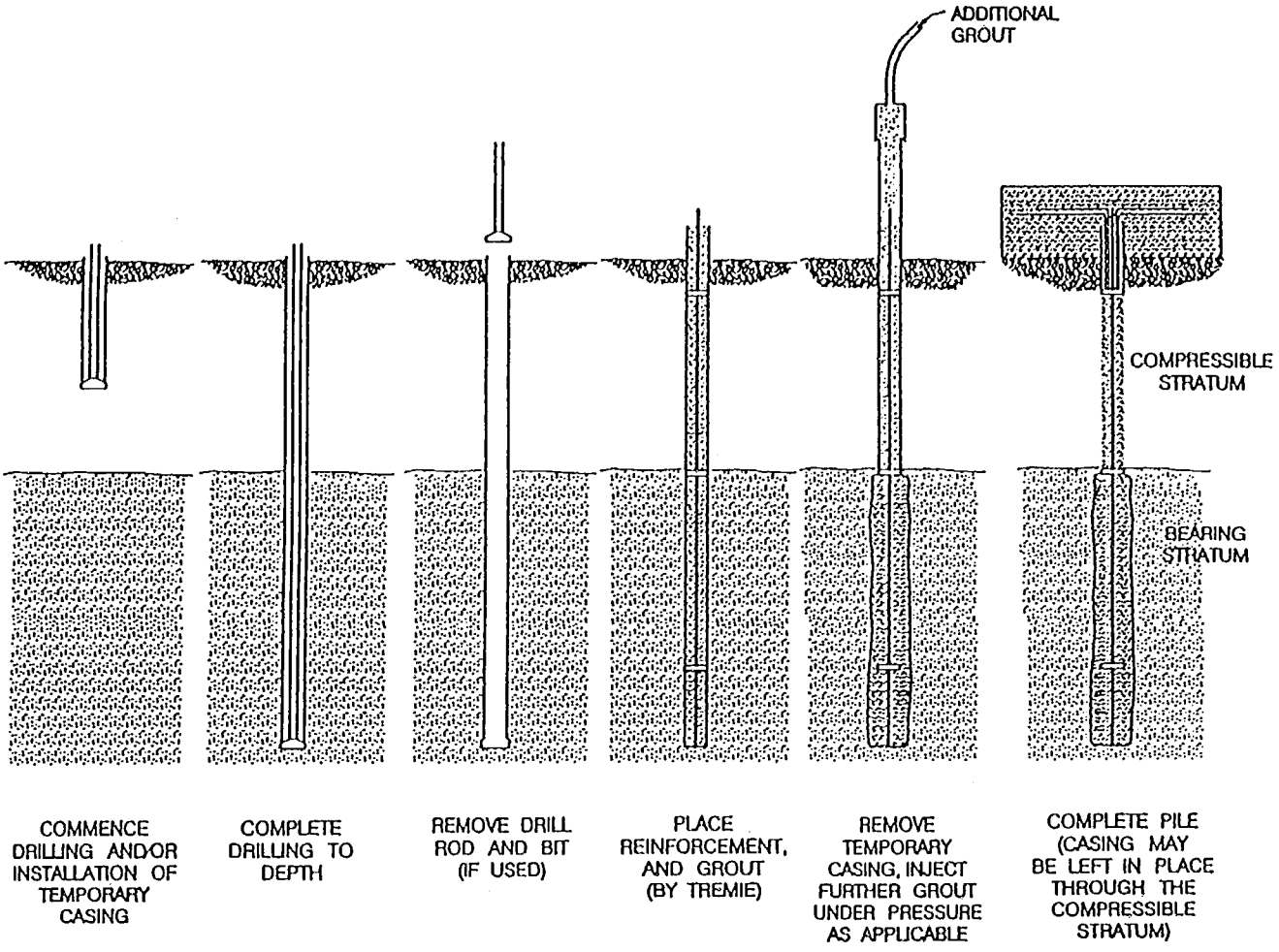
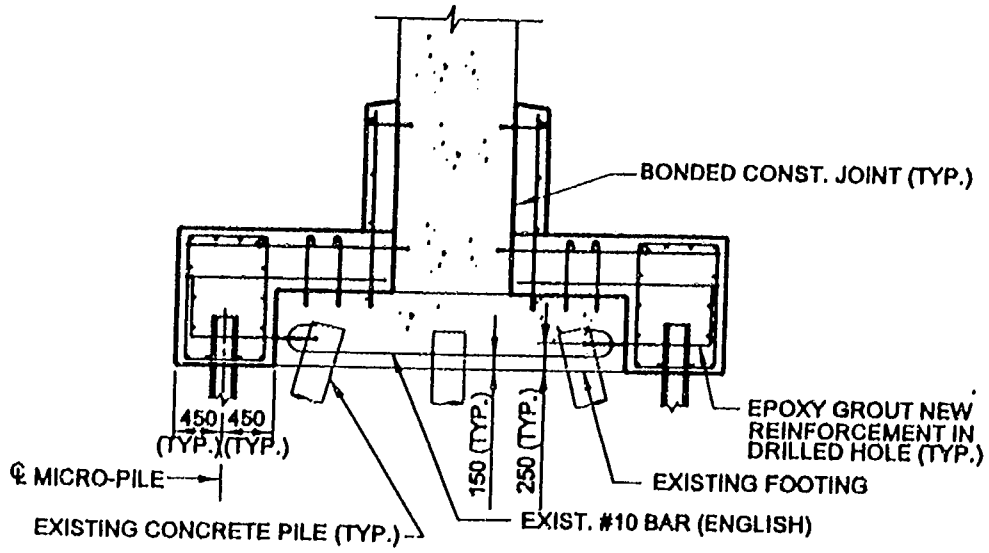
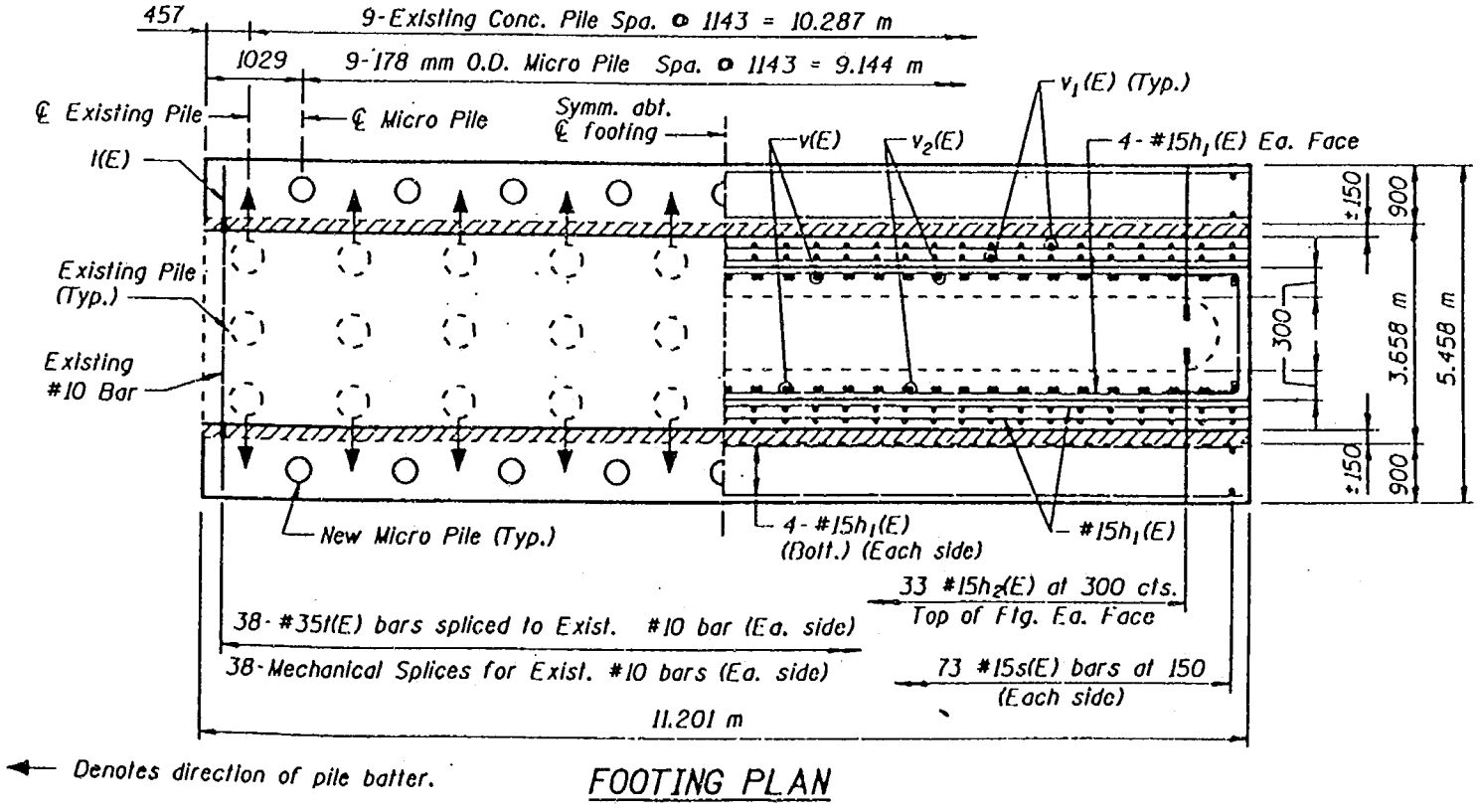


Figure 1. Installation technique for micropile (from ASCE, 1997)

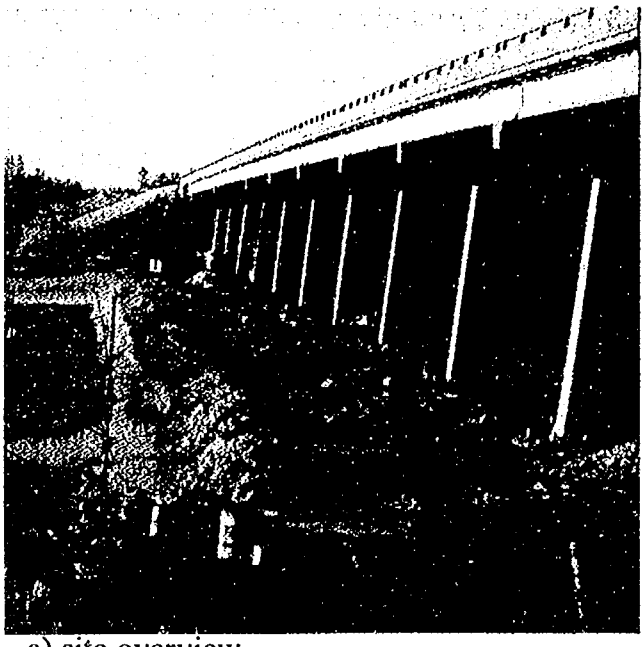


a) side view



b) top view

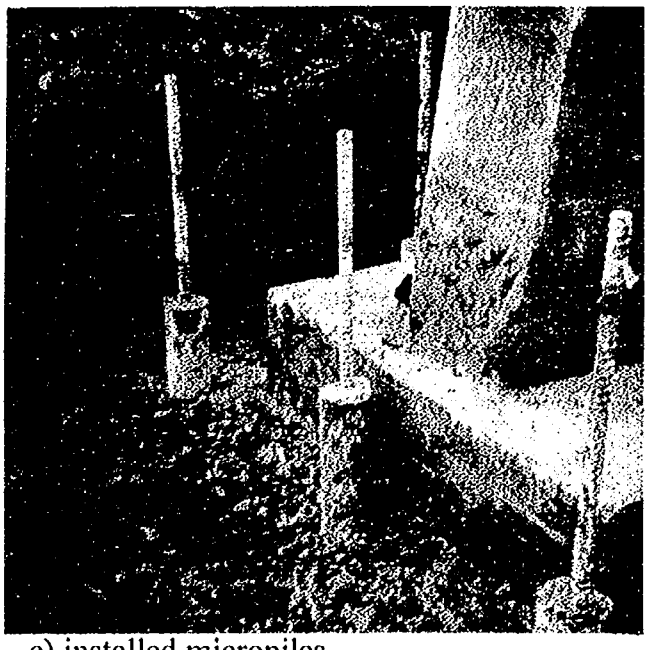
Figure 2. Micropile placement and reinforcement details for bridge foundations retrofit program (I57 over Rte 3).



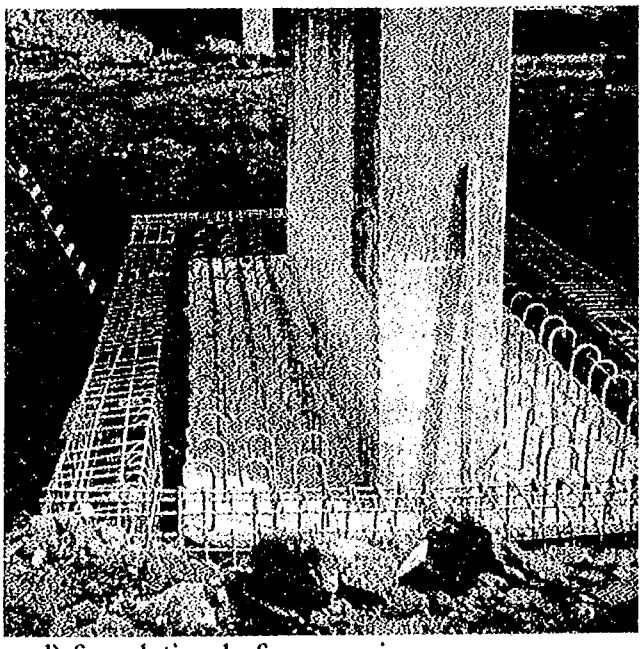
a) site overview



b) preparing old foundation



c) installed micropiles



d) foundation before pouring

Figure 3. Views of micropile retrofit.

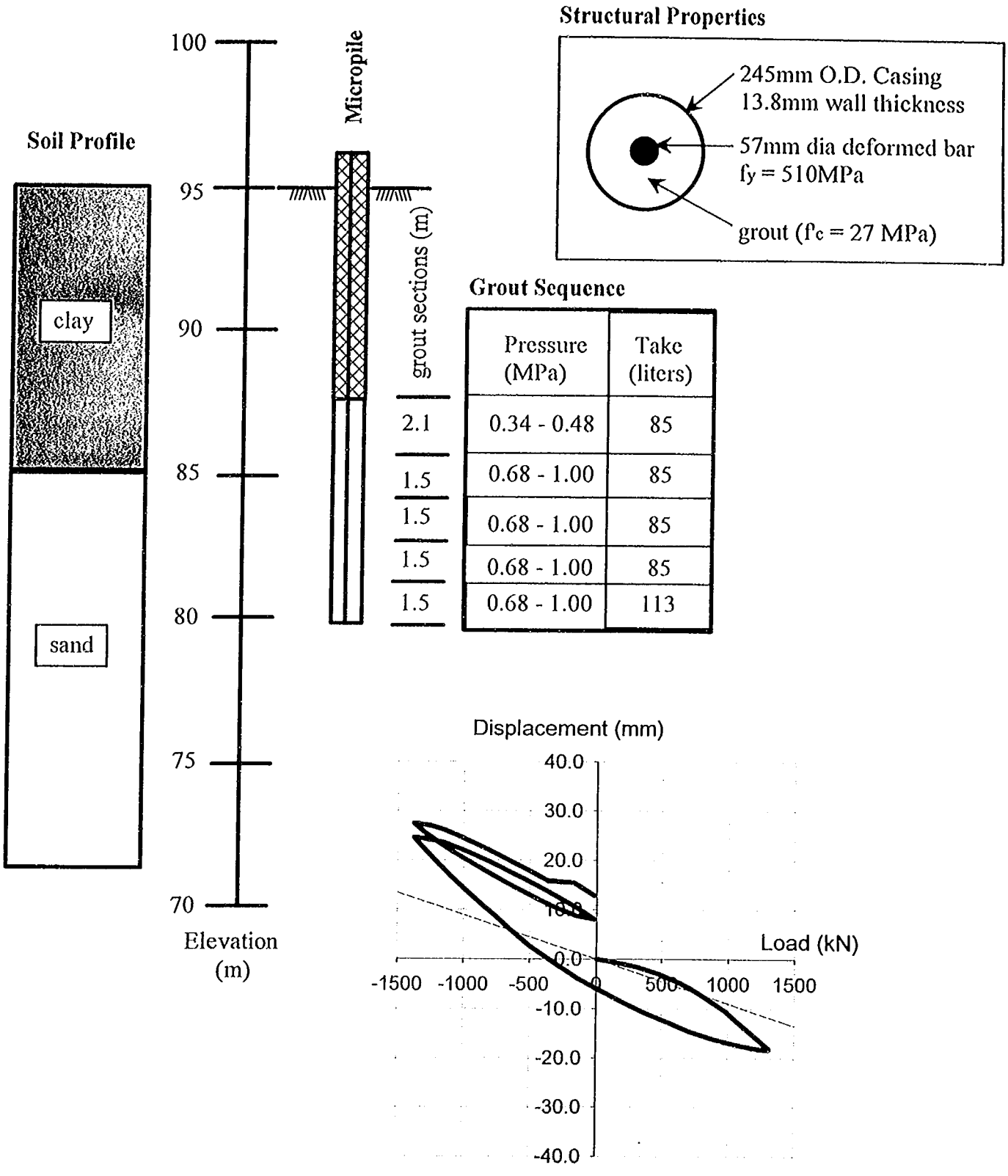
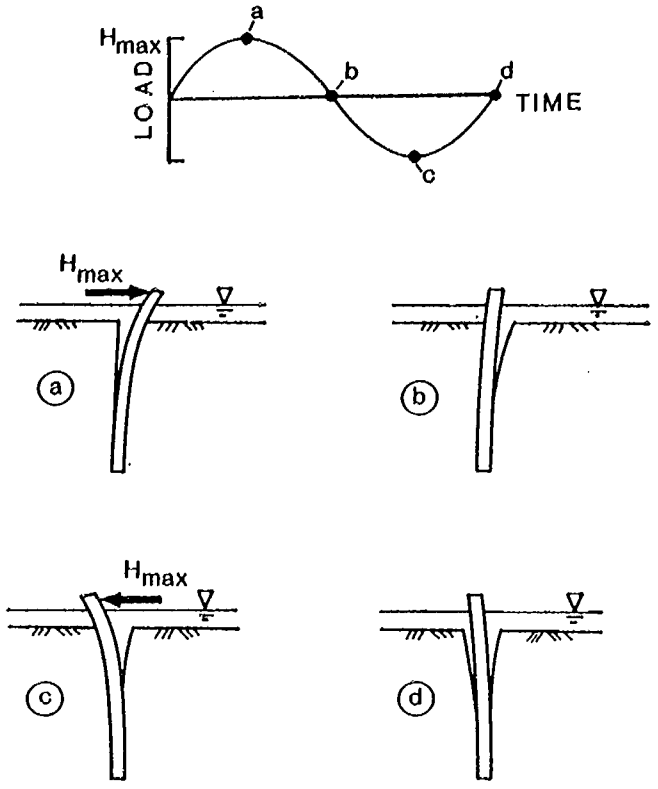
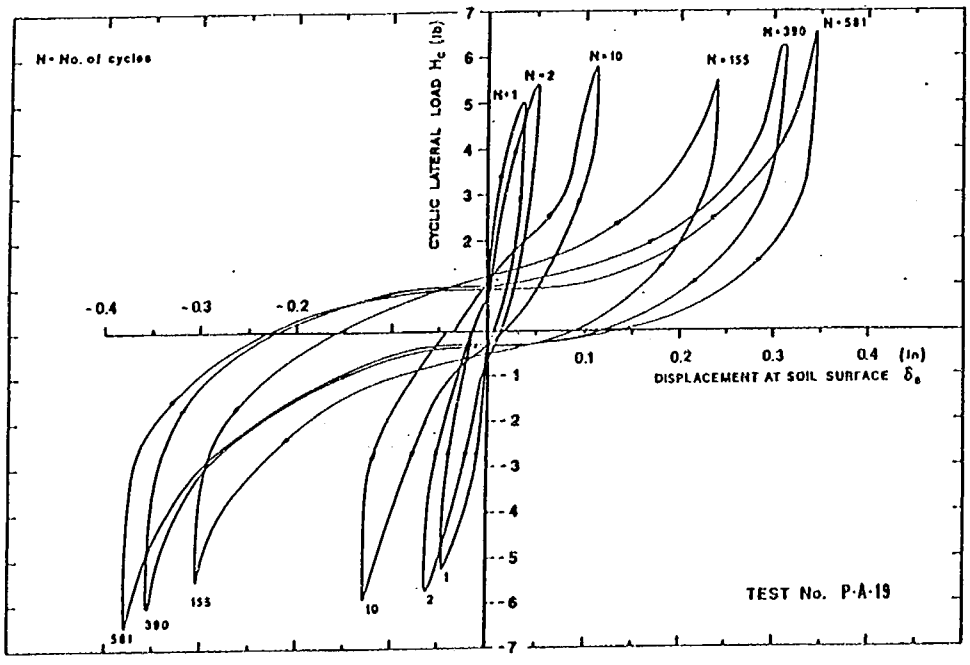


Figure 4. Construction information and load-displacement response for micropile

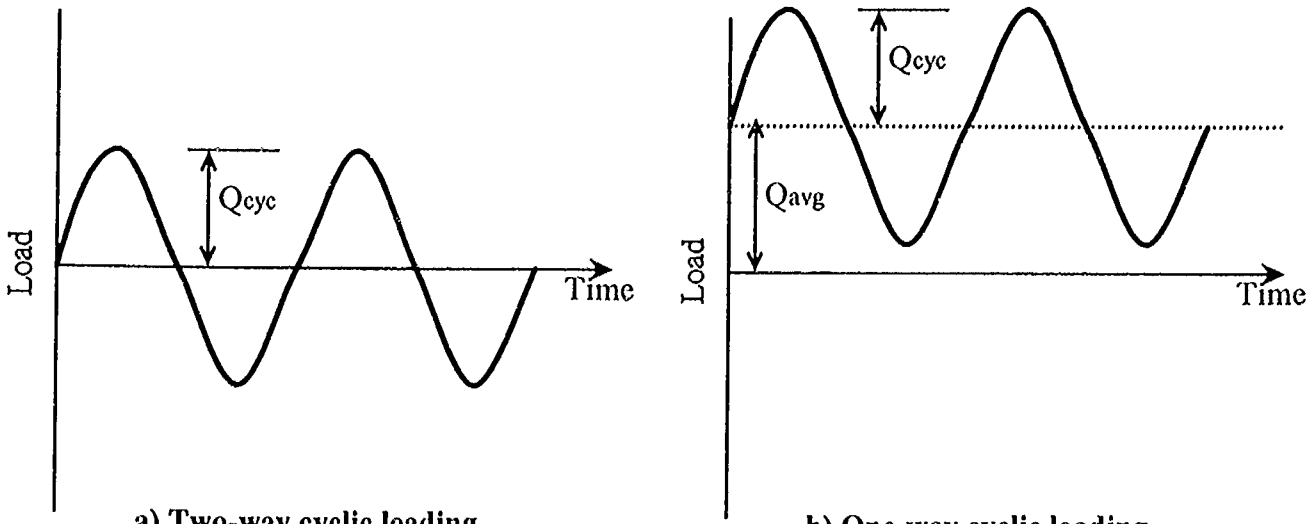


a) simplified response of pile due to cyclic lateral loading



b) pile head deflection versus load for several number of load cycles (from Valenzuela and Lee, 1978)

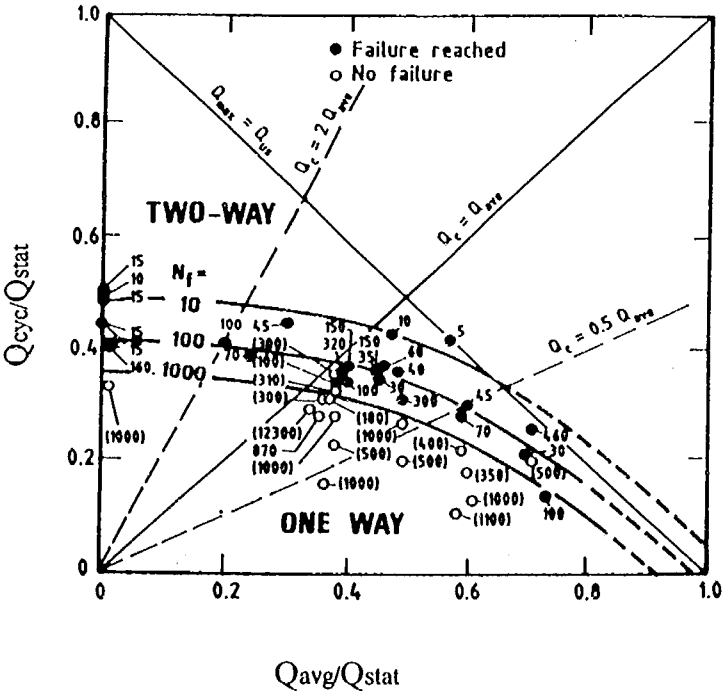
Figure 5. Effects of cyclic lateral loads on piles.



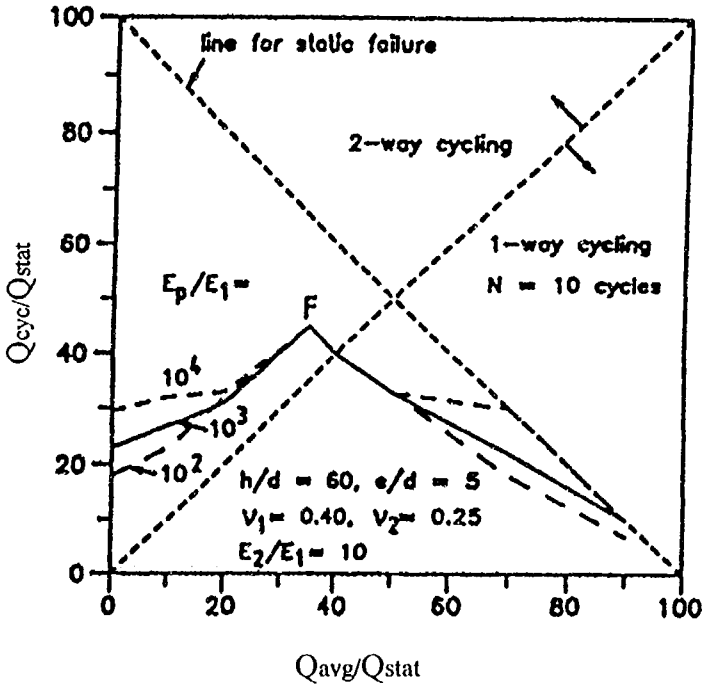
a) Two-way cyclic loading

b) One-way cyclic loading

Figure 6. Definition of cyclic load components



a) measured results for piles (Karlsrud and Haugen, 1983))



b) predicted results for drilled and grouted piles (Chin and Poulos, 1991)

Figure 7. Results of axial cyclic loading

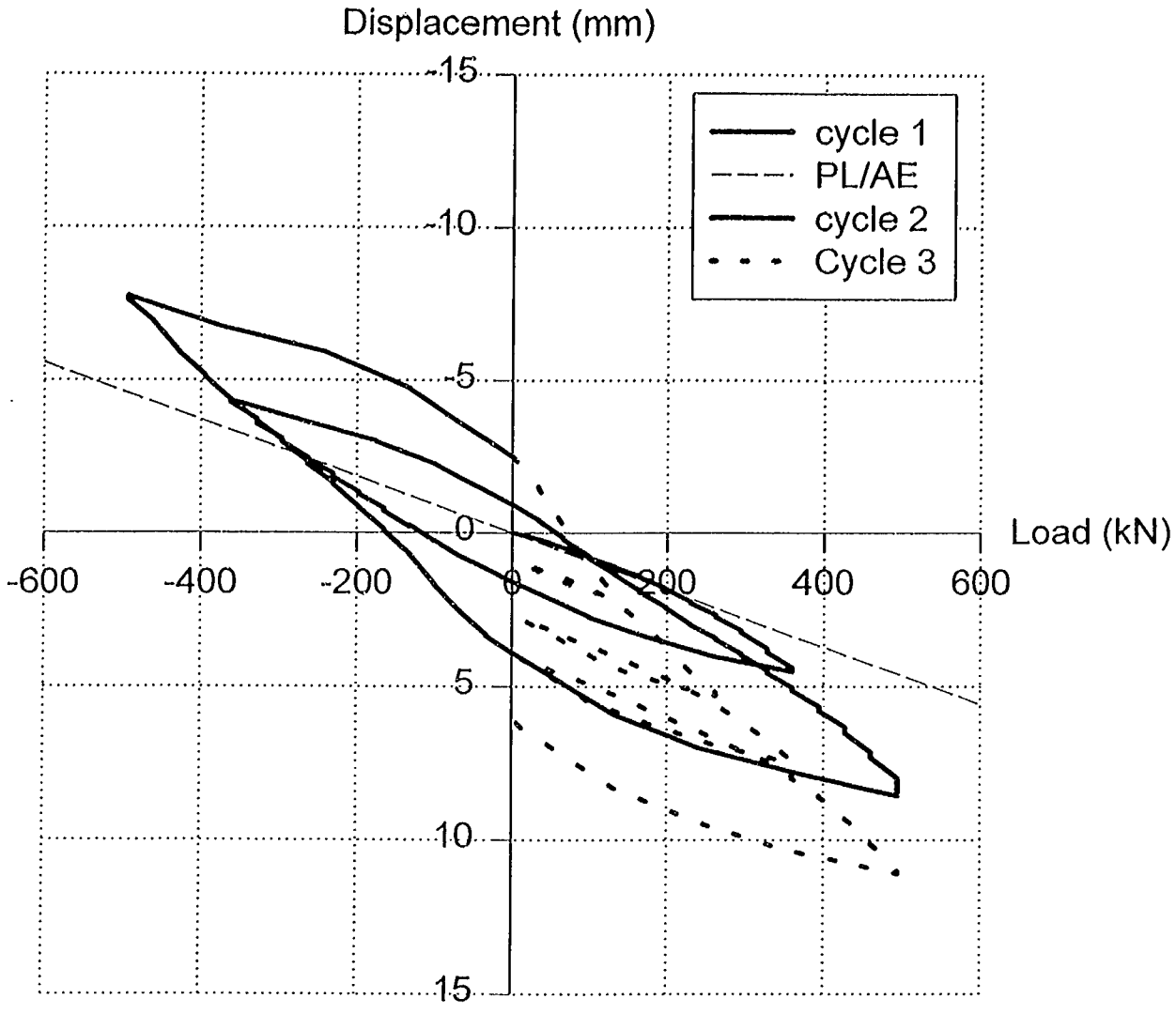


Figure 8. Load-displacement relationship for cycles of two-way cyclic axial load

SESSION 5: SEISMIC ISSUES (3)

(1) Assessing Oregon's Seismic Risk
(Martha Sartain, Richard Groff, Craig Shike and Mark Hirota)

(2) Developing Seismic Design Ground Motions for Super Long-Span Bridges
(Keiichi Tamura, Yoshihiro Nakao and Shojiro Kataoka)

(3) Seismic Vulnerability Study of Highway Systems: TEA-21 Research Project
(Gokhan Pekcan, W. Phillip Yen and Ian M. Friedland)

(4) The System of Real-time Earthquake Damage Estimation in Hanshin Expressway
(Kiyoshi Miyawaki, Taiichi Kagayama and Fuminobu Okunishi)

(5) The Newly Developed AASHTO Guide Specifications for Seismic Isolation Design
(H. Ghasemi)

(6) Guidelines for Testing Passive Energy Dissipation Devices
(Michael A. Riley, Fahim Sadek and Bijan Mohraz)

ASSESSING OREGON'S SEISMIC RISK

Martha Sartain[1]
Richard Groff, P.E.[2]
Craig Shike, P.E.[3]
Mark Hirota, P.E.[4]

Abstract

The State of Oregon has unique seismic risks associated with its location adjacent to the Cascadia Subduction Zone. The nature and probability of this risk are examined. Because this risk was only recently identified, most of the state's bridges are designed for little or no seismic loads, and thus require a comprehensive program of seismic retrofit. Divided into Phase 1 (superstructure) and Phase 2 (substructure), the retrofit needs have been identified with respect to structure vulnerability and criticality, and work has been proposed and prioritized to account for cost-effectiveness and lifeline classification.

[1] Bridge Management System Manager, Oregon Department of Transportation, Salem, OR
[2] Bridge Needs/Systems Engineer, Oregon Department of Transportation, Salem, OR
[3] Structural Design Engineer, Oregon Department of Transportation, Salem, OR
[4] State Bridge Engineer, Oregon Department of Transportation, Salem, OR

ASSESSING OREGON'S SEISMIC RISK

Seismic concern from historical evidence.

The state of Oregon is bordered by Washington to the north, California to the south and the Pacific Ocean to the west. Oregon's coastline is an eclectic collection of shear rock cliffs, flat sandy beaches, mountainous sand dunes and tidal marshlands.

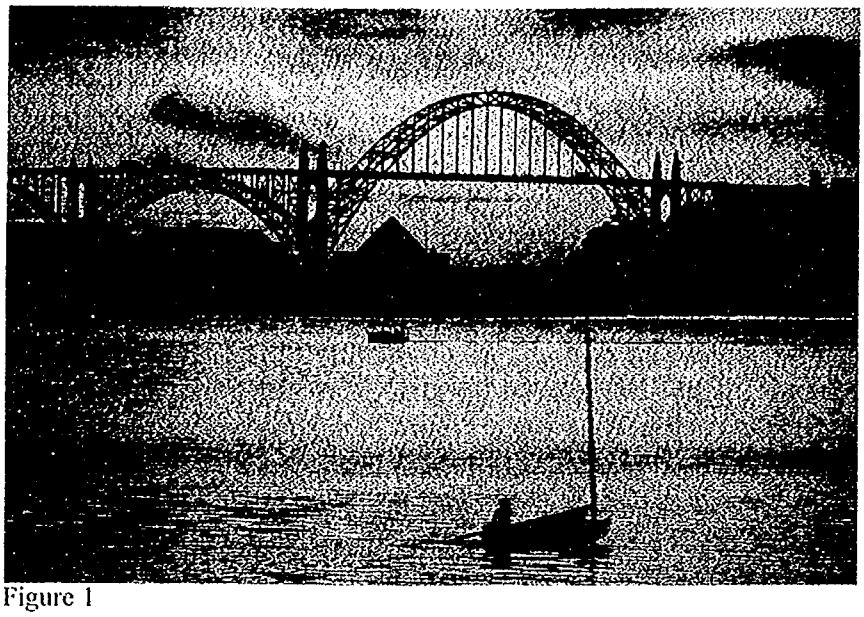


Figure 1

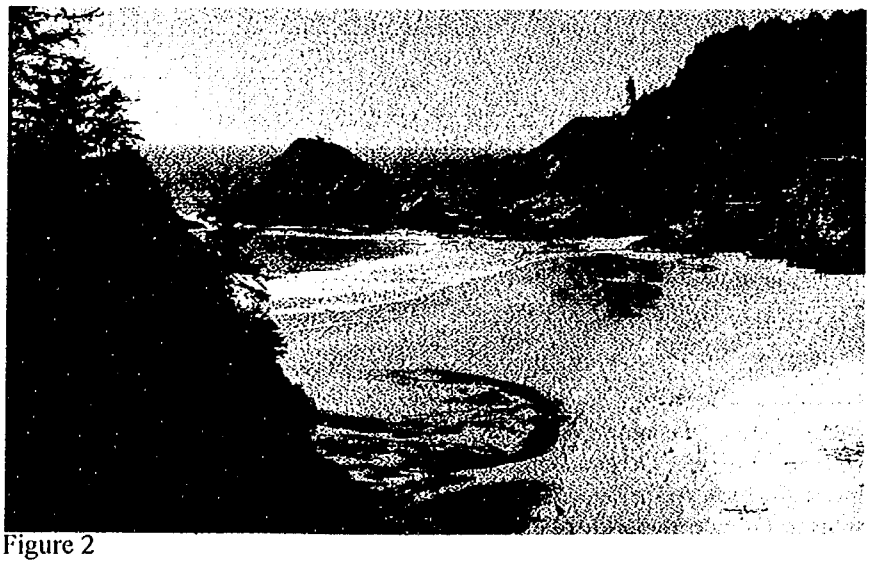


Figure 2

Its rugged beauty along the coastline and into the Cascade mountain range, can be attributed to the action of plate tectonics directly off of the coastline in the Pacific Ocean.

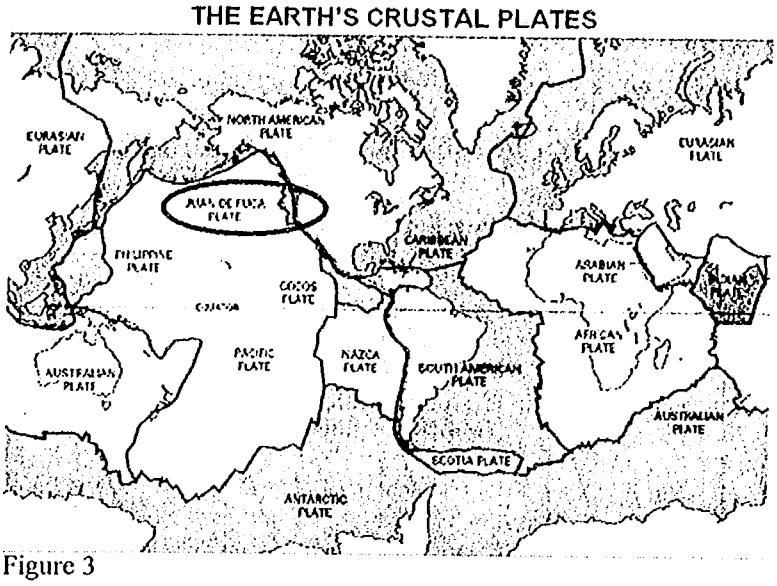


Figure 3

The movement of the Juan de Fuca Plate under the North American Plate creates the "Cascadia Subduction Zone". Subduction Zone earthquakes are greater in magnitude, affecting a much larger area than the crustal type earthquakes that are the common experience of California. The Cascadia Subduction Zone, along a 1600-km long plate boundary, is capable of generating a Magnitude 8 or 9 earthquake (Richter scale).

THE CASCADIA SUBDUCTION ZONE

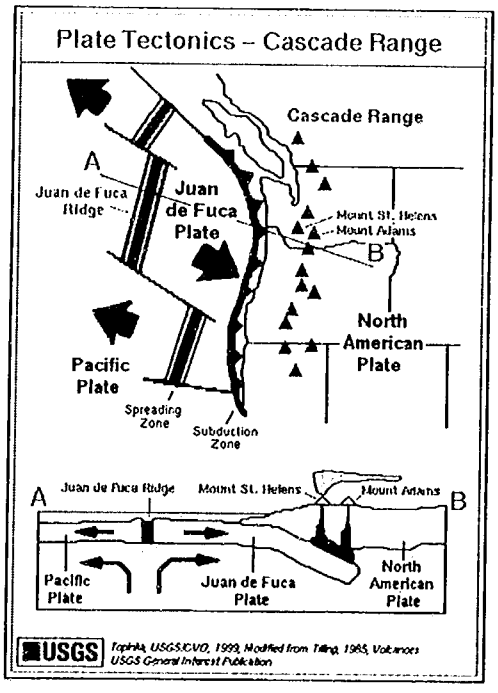


Figure 4

Numerous soil test holes have been evaluated along the coastline, in an effort to evaluate the magnitude and frequency of significant events. Tsunami sediment layers and carbon dating have been used to develop this approximate strain history.

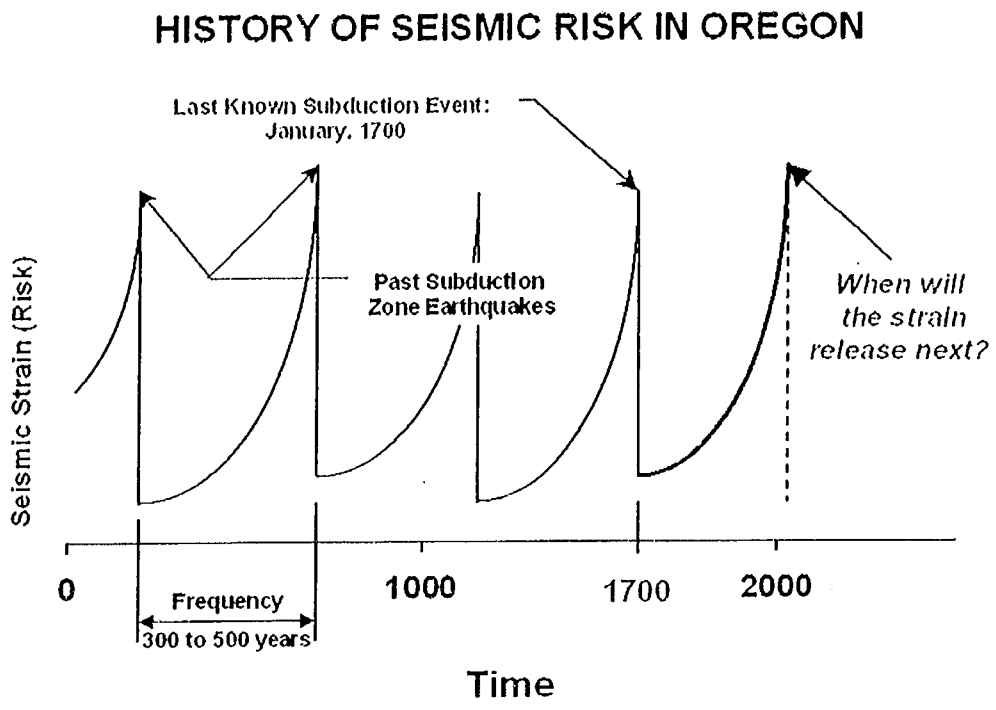


Figure 5

The sediment layers used to construct the history, correlate to a major tsunami event recorded in Japan, in January 27, 1700. It's been 300 years since the last Cascadia Subduction Zone Earthquake. Based on this historic and geologic evidence, a major subduction zone earthquake could occur at any time.

The impact of a subduction zone earthquake is different from the crustal earthquake in the fact that the potential magnitudes are higher. The area affected is much larger in the subduction zone event because the entire length of the plate boundary is involved. In the Oregon portion, this could affect approximately 70% of the state's 6500 bridges.

Design considerations

ODOT's designs have always met the basic AASHTO criteria. Designs prior to 1958 did not account for seismic loading, because the impact of Plate Tectonics was not yet fully understood. Designs between 1958 and 1974 included a seismic design force equal to 2-6% of the structure weight. Bridges designed during the time frame from 1975 to 1989 were designed for seismic forces of up to 12% of the structure weight. It was not until 1989, and the Loma Prieta earthquake in the San Francisco Bay area, that a more sophisticated structural analysis and ductile reinforcing details for seismic forces, became a part of mainstream bridge design in Oregon.

Due to the small number of recorded seismic events in Oregon, the available bedrock acceleration maps available prior to 1990 indicated lower seismic loads. In 1995, a consultant study assessed more realistic ground accelerations and developed site specific, probability-based bedrock acceleration contour maps to aid in seismic design. The 500-year peak ground acceleration map shown below was established as a rational design loading for most bridges. Generally the risk of seismic exposure increases westward along the entire length of the state. The peak ground acceleration ranges from 0.05g in the eastern regions of the state to 0.60g along the southern coastline.

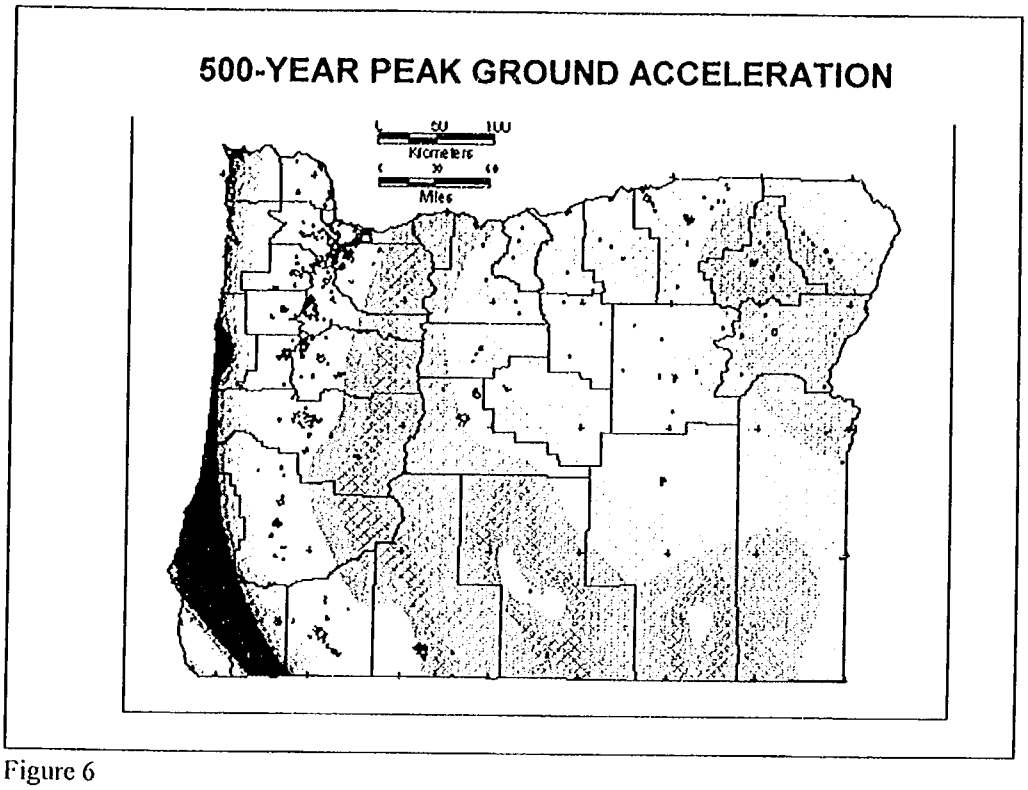
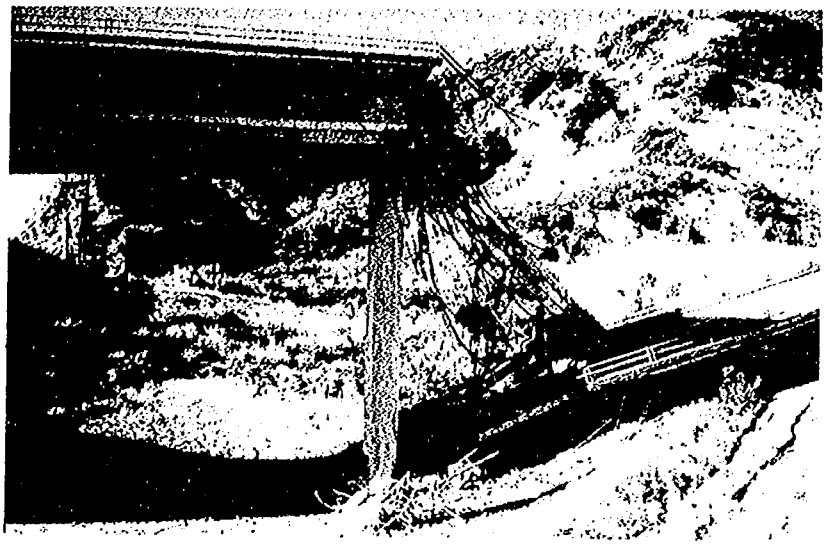


Figure 6

Oregon's state-owned bridge inventory contains about 2600 bridges, many of which are multi-span pre-cast/pre-stressed concrete beam bridges and cast-in-place post tensioned bridges. With these types of structures, two failure mechanisms have been identified from vulnerable detailing

The first failure mechanism would engage when the motion from the earthquake causes the bridge's superstructure to separate from the substructure. A typical bridge designed prior to extensive seismic detailing would not have an available beam seat greater than 300 mm for seismic movement in the longitudinal direction. Additionally, the beam seat would not have shear lugs designed to resist much, if any, transverse direction seismic force.

The following photo from the 1994 Northridge earthquake illustrates this type of failure.



Bridge 53-1964F Interstate 5/California State Route 14
Northridge, California earthquake, Jan. 17, 1994
Fallen span to west of shattered column
Copyright Credit Northridge Collection, Earthquake Engineering Research Center, University of California, Berkeley

Figure 7

When the superstructure spans collapse, this portion of the travel route immediately becomes unusable and inhibits emergency access. This type of damage can take several months to rebuild. If on a critical freight route, the loss to Oregon businesses would be many times the cost of the repair.

Typical seismic retrofit details to prevent this type of failure include longitudinal cable restraints and the addition of concrete or steel shear lugs for transverse force restraint. This type of seismic retrofit is referred to as a "Phase 1" seismic retrofit.

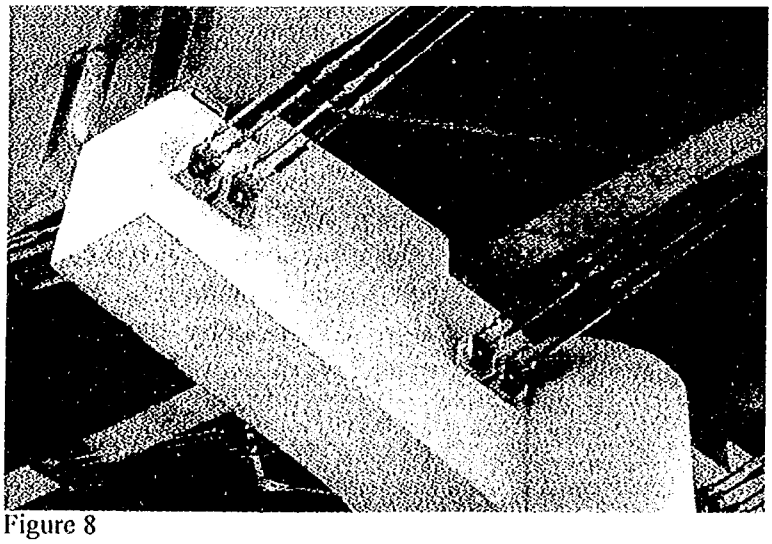


Figure 8

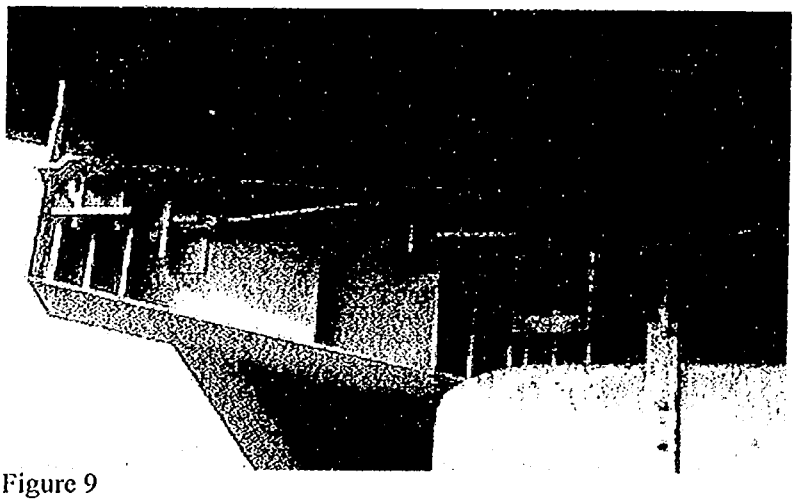


Figure 9

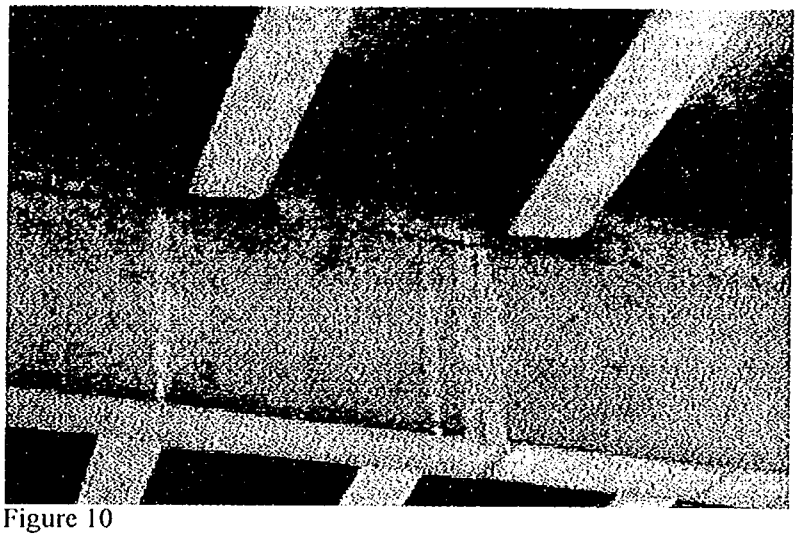


Figure 10

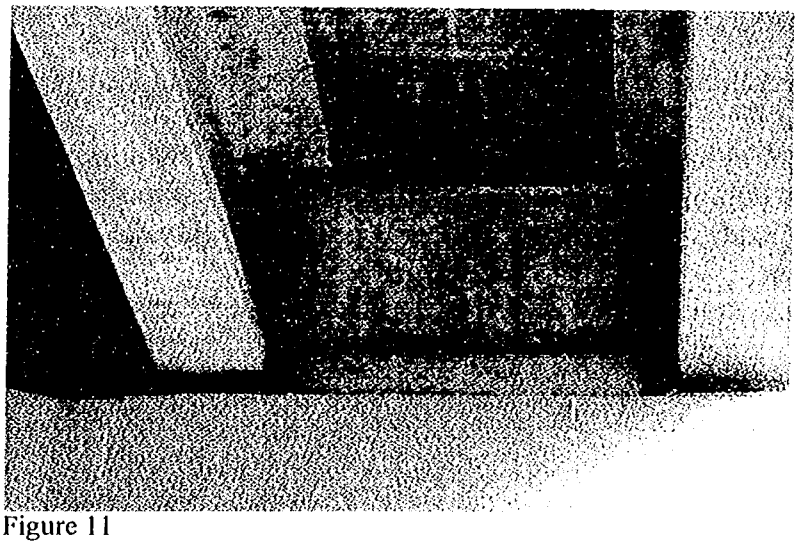
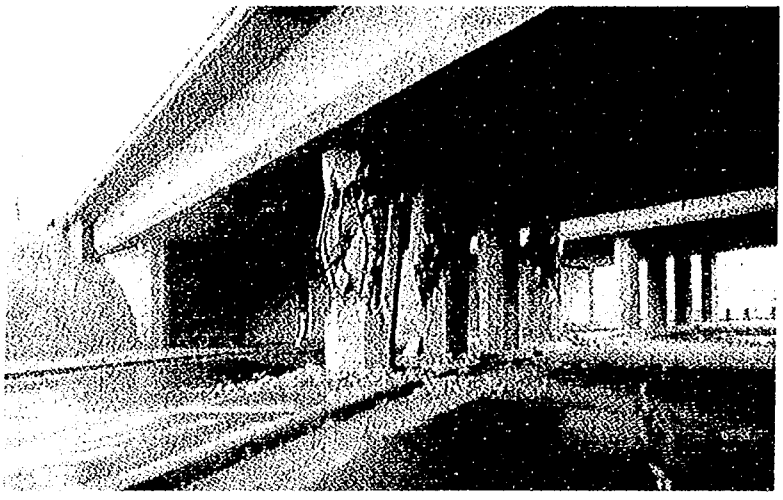


Figure 11

The second failure mechanism would engage when the motion from the earthquake which causes the bridge's substructure to collapse from the seismic force. Similar to the superstructure design shortcomings of earlier typical bridge design, substructures (columns in particular) were not designed to resist the intense forces experienced in a seismic event. Structures built before 1975 are particularly vulnerable due to their lack of seismic design detailing. These earlier designs typically contain multiple column redundancy, but do not contain adequate column confinement reinforcement and vertical bar splices and anchorage. The column's confinement reinforcement was typically #13 or #16 reinforcing hoops at 300 mm.

The following photo from the 1971 San Fernando earthquake illustrates the type of failure that is likely to occur with these earlier designs.



Freeway structures near interchange between I-5 and I-210
San Fernando, California earthquake, Feb. 9, 1971
Copyright Credit: Steinbrugge Collection,
Earthquake Engineering Research Center, University of California, Berkeley.
Figure 12

Substructure collapse or partial collapse requires careful engineering judgment regarding the compromise of structural integrity the remaining load carrying capacity. With each aftershock, the structural integrity can change along with the safety designation.

In addition to columns, the foundation of the bridge is also susceptible to seismic loads in excess of the design loads. Foundation failures may not be readily detectable with the damage hidden by overburden.

Substructure seismic retrofit is referred to as a "Phase 2" seismic retrofit and, for certain bridges, can exceed the replacement cost of the structure.

Due to insufficient funding, ODOT has not performed any Phase 2 seismic retrofit at this time. In the future, this type of work will involve footing strengthening and column jacketing to increase ductility.

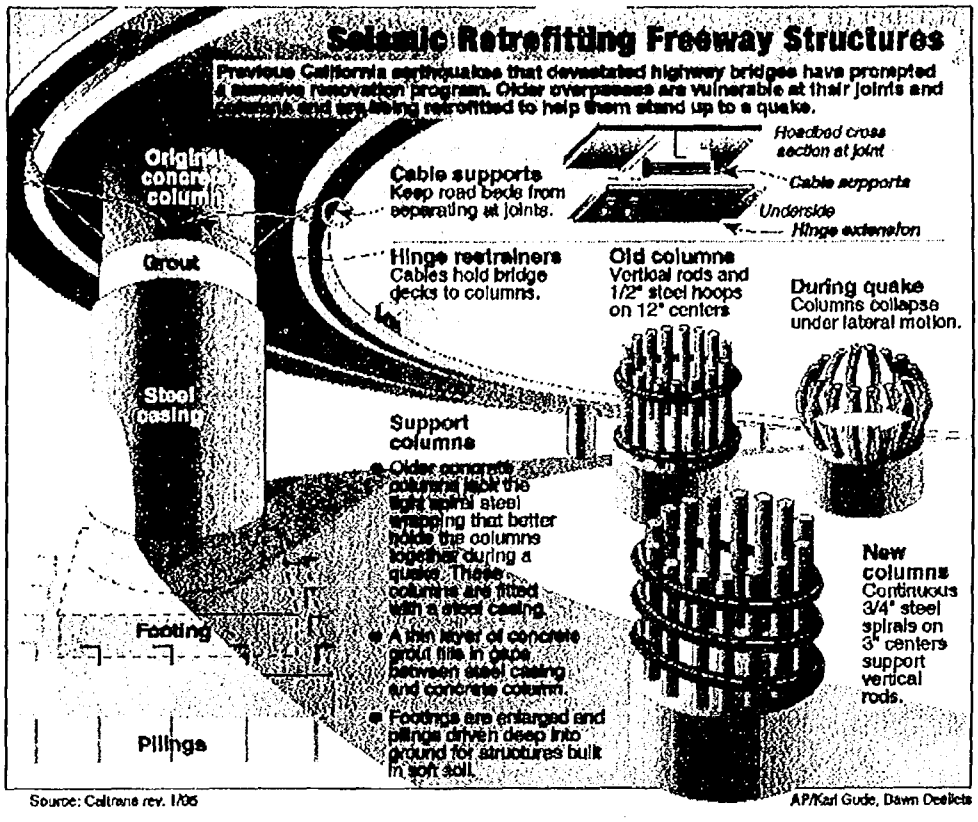
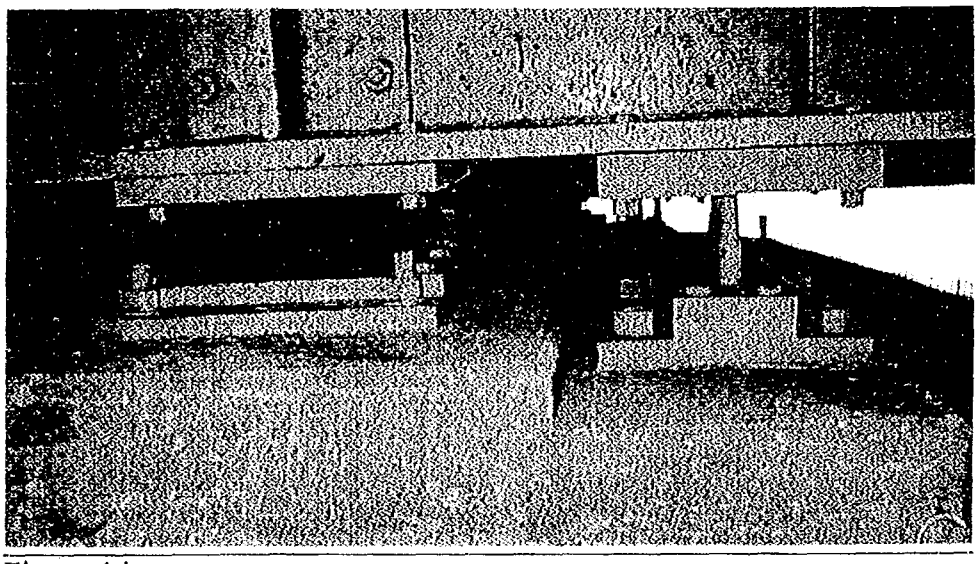


Figure 13

In rare cases, it has proven cost-effective to install seismic isolation bearings to absorb seismic energy without the need for substructure strengthening.


Figure 14

Seismic retrofit can greatly increase the resistance of bridges to earthquake damage. The degree of seismic resistance in a design is a trade-off of risk reduction vs. cost. ODOT's strategy is to do Phase I Retrofit before Phase 2 to quickly reduce risk to as many bridges as possible.

No amount of retrofit investment can assure absolutely no damage from a Subduction Zone Earthquake.

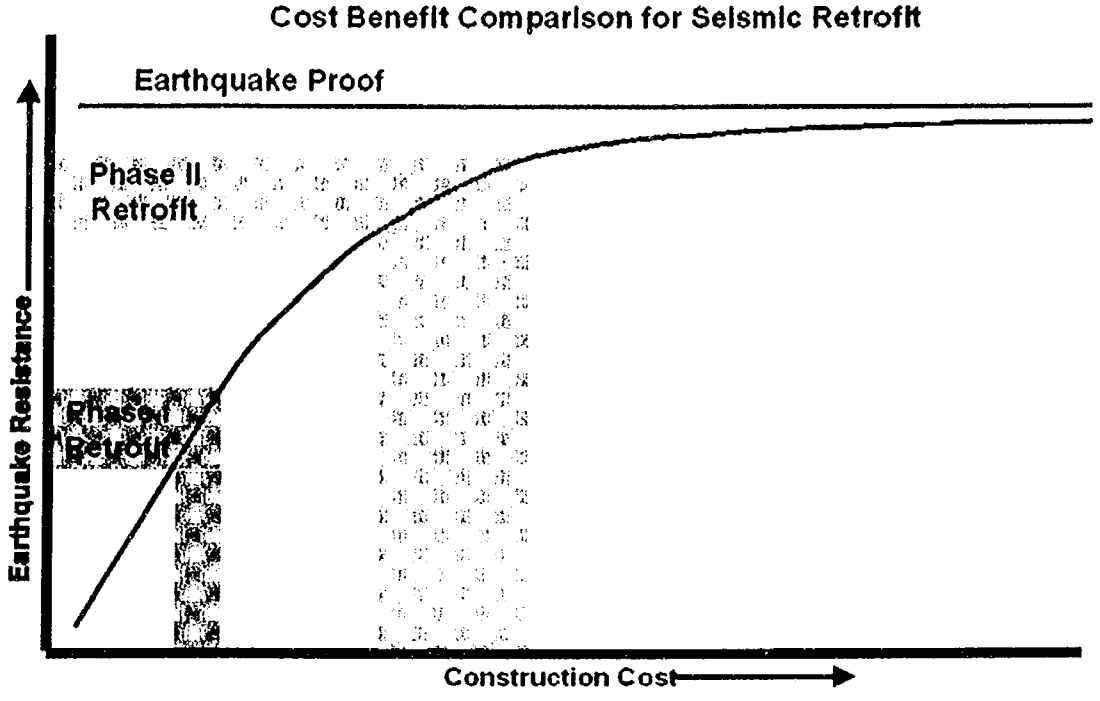


Figure 15

Route Priority Analysis

Lifeline routes were identified, using Emergency Response and Economic Recovery as criteria. Routes in the State have been categorized into four priority levels. They are as follows:

Priority 1: *Essential* for Emergency Response in the first 72 hours after the seismic event

Priority 2: *Desirable* for Emergency Response in the first 72 hours, or *Essential* for Economic Recovery in the months following the seismic event

Priority 3: Other Emergency Response Routes that are the only access serving relatively few people, and all NHS (National Highway System) Routes

Priority 4: Non-lifelines

Total Retrofit Need

Priority routes were matched up with peak ground acceleration levels to establish corridors for proposed bridge seismic retrofit. Lifeline routes are given the highest priority and matched to the lowest acceleration threshold.

For superstructure seismic retrofit, the numbers of bridges and the approximate cost of Phase 1 retrofitting are as follows:

- 145 bridges are on routes with a priority 1 and a peak ground acceleration of greater than 0.12g. The approximate cost is $40.6 million.
- 178 bridges are on routes with a priority 2 and a peak ground acceleration of greater than 0.12g. The approximate cost is $49.5 million.
- 30 bridges are on routes with a priority 3 and a peak ground acceleration of greater than 0.15g. The approximate cost is $9.3 million.
- 44 bridges are on routes with a non-lifeline and a peak ground acceleration of greater than 0.18g. The approximate cost is $4.2 million.

The Phase 1 seismic retrofit effort would include 397 bridges at a total of $103.6 million.

For Phase 2 substructure seismic retrofit, the numbers of bridges and the approximate cost are as follows:

- 345 bridges are on routes with a priority 1 and a peak ground acceleration of greater than 0.15g. The approximate cost is $177.5 million.

- 391 bridges are on routes with a priority 2 and a peak ground acceleration of greater than 0.18g. The approximate cost is $225.4 million.

- 22 bridges are on routes with a priority 3 and a peak ground acceleration of greater than 0.25g. The approximate cost is $10.7 million.

- No bridges are on routes that are not a lifeline.

The Phase 2 seismic retrofit effort would include 758 bridges at a total of $413.6 million.

In summary, Oregon has 1155 state-owned bridges (46% of the DOT's inventory) that require seismic retrofit, at a total cost of $517.2 million. If the Phase 1 and Phase 2 seismic retrofit were to be spread over a twenty year period, the approximate cost would be $26 million per year.

References

Figure 1: Photo by Richard L. Groff, P.E. , Oregon Dept. of Transportation.

Figure 2: Photo by Orrin Russie, Oregon Dept. of Transportation.

Figure 3: Kious, W. Jacquelyne & Tilling, Robert I., ***This Dynamic Earth: The Story of Plate Tectonics,*** U.S. Government Printing Office, Washington, DC, 1996, ISBN 0-16-048220-8. Online edition published by USGS.
URL: **http://pubs.usgs.gov/publications/text/slabs.html**

Figure 4: USGS Topinka, USGS/Cascades Volcano Observatory 1999, modified from Tilling, 1985, Volcanoes: USGS General Interest Publication, URL:
http://vulcan.wr.usgs.gov/Glossary/PlateTectonics/Maps/map_plate_tectonics_cascades.html

Figure 5: Conceptual diagram by Martha Sartain & Richard L. Groff, P.E., Oregon Dept. of Transportation.

Figure 6: State of Oregon Dept. of Geology & Mineral Industries, from GMS-100, Earthquake Hazard Maps for Oregon, edited by I.P.Madin & M.A.Mabey. based on ***Seismic Design Mapping State of Oregon***, prepared for Oregon Dept. of Transportation by Geomatrix Consultants, January 1995.
URL: **http://sarvis.dogami.state.or.us/store/gifs/eq5_2500.gif**

Figure 7: Bridge 53-1964F Interstate 5/California Route 14 Interchange, North Connector, 1994 Northridge, CA Earthquake (photographer Mark Ascheim), Northridge Collection, Earthquake Engineering Research Center, University of California, Berkeley.
URL: **http://www.eerc.berkeley.edu/cgi-bin/eqiis_detail?id=6972**

Figure 8: Bridge 08590C, Marquam Bridge Ramp. Photo by Dennis Carlson, P.E., Oregon Dept. of Transportation.

Figure 9: Bridge 08589B, Undercrossing Pacific Highway Connection No 3. Photo by Dennis Carlson, P.E., Oregon Dept. of Transportation.

Figure 10: Bridge 08590D, Northbound Marquam Bridge Ramp. Photo by Dennis Carlson, P.E., Oregon Dept. of Transportation.

Figure 11: Bridge 08590Y, Northbound Marquam Bridge Ramp Connection to Water Ave. Photo by Dennis Carlson, P.E., Oregon Dept. of Transportation.

Figure 12: Image No. S4382, Freeway structures near interchange between Interstates 5 and 210, 1971 San Fernando, CA Earthquake (photographer Karl V. Steinbrugge), Steinbrugge Collection, Earthquake Engineering Research Center, University of California, Berkeley. URL: **http://www.eerc.berkeley.edu/cgi-bin/eqiis_detail?id=4115**

Figure 13: Conceptual drawing from CalTrans Jan. 1995

Figure 14: Bridge 02444A, Hood River Bridge. Photo by Hormoz Seradj, P.E., Oregon Dept. of Transportation

Figure 15: Conceptual diagram by Martha Sartain & Richard L. Groff, P.E., Oregon Dept. of Transportation.

DEVELOPING SEISMIC DESIGN GROUND MOTIONS FOR SUPER LONG-SPAN BRIDGES

Keiichi Tamura[1], Yoshihiro Nakao[2] and Shojiro Kataoka[2]

ABSTRACT

Semi-empirical synthetic method of strong ground motion using a small event record as Green's function has recently been applied to establish seismic design ground motions. One of the advantages of this method is that seismic source mechanism can be incorporated into analysis. On the other hand, this method requires various earthquake source parameters, most of which are difficult to be determined accurately. We synthesize ground motion from the Kanto Earthquake by semi-empirical method, in which geometric source parameters are determined same as the case of 1923 Kanto Earthquake, while fault rupture mode and asperity are systematically changed. Based on the results of analysis, variation of ground motion resulting from uncertainty of source parameters is discussed.

INTRODUCTION

Feasibility of super long-span bridges crossing straits is being studied in Japan to meet the goal of constructing a multi-nuclei nation as set forth in the Comprehensive National Development Plan (National Land Agency, 1998). Some of these bridges will be located over or nearby the fault planes of past large earthquakes. For instance, the 1923 Kanto Earthquake (M_J=7.9, M_J is the Japan Meteorological Agency Magnitude) and 1944 Tonankai Earthquake (M_J=7.9) occurred in Tokyo Bay and Ise Bay regions, respectively, and two highway routes are being planned to cross the mouths of these two bays.

For establishing seismic design ground motions of large structures, seismic risk analysis and attenuation relation of ground motion have been widely used in Japan including the Trans-Tokyo Bay Highway Bridge (Public Works Research Institute, 1991) and Akashi Kaikyo Bridge (Honshu-Shikoku Bridge Authority, 1988). In the seismic risk analysis, an attenuation equation is usually incorporated to estimate ground motion intensity from an expected earthquake magnitude and distance. Although an attenuation equation is a simple and effective tool of engineering practice to predict ground motion, it should be noted that the applicability of this technique to the near field of large earthquake is limited, because it is an empirical formula and does not usually contain strong motion data obtained in the near fields of large earthquakes. Appling attenuation relation to the near field by substituting small value for distance may yield excessive ground motion for seismic design of structures.

The semi-empirical ground motion synthesizing method (e.g., Hartzell, 1978; Irikura, 1983), in which ground motion record from a small event is used as Green's function, has recently been applied to earthquake engineering. This method can incorporate complicated earthquake source mechanism into calculation, and has an advantage of estimating near field motions. On the other hand, this method requires various source parameters, and most of them are

[1] Head, Ground Vibration Division, Public Works Research Institute, Ministry of Construction, Japan
[2] Research Engineer, ditto

difficult to be determined accurately, especially for future earthquakes.

From an engineering point of view to establish seismic design ground motion, it is necessary to infer ground motion induced by a future earthquake. In this process, several static or geometric source parameters, such as fault location, fault size and dip angle, may be determined by assuming the similarity to past earthquakes, however it seems almost impossible to determine dynamic parameters, such as rupture mode and location of asperity, in advance.

In this paper we simulate ground motion at Tokyo Bay region, assuming the Kanto Earthquake, which will be most influential over this area. We employ geometric parameters of the 1923 Kanto Earthquake and change dynamic source parameters variously, and examine influence of uncertainty of source parameters on the synthesized ground motion, as a basis of developing design ground motions for a super long-span bridge crossing Tokyo Bay.

EARTHQUAKE SOURCE MODELING AND GREEN'S FUNCTION TECHNIQUE

To simulate ground motions from a large event, ground motion record from a small event such as foreshock or aftershock that occurred within the fault area of large event is used as Green's function, as schematically illustrated in Figure 1. The fault plane of the target event is divided into sub-faults so that their sizes coincide with the fault area of small event. The Green's functions are superimposed considering time delay due to fault rupture from the hypocenter to a sub-fault and wave traveling from each sub-fault to the estimation point. An advantage of using small event record as Green's function exists in that complicated path and site effects are incorporated automatically into ground motion estimation, which has large influence over the accuracy of simulating short period ground motions.

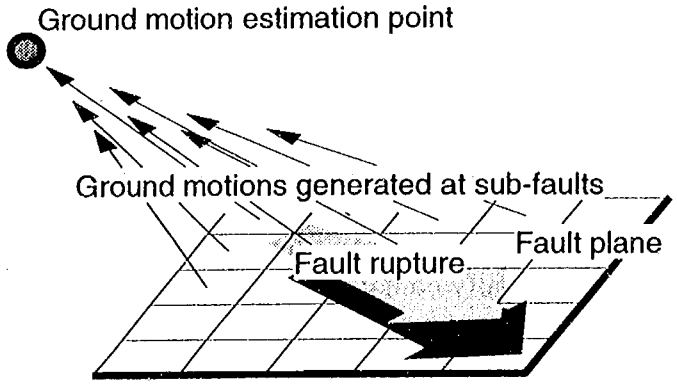


Figure 1 Semi-Empirical Method

Temporal and spatial variations of dislocation are considered here by introducing $T_{mn}(\omega)$ and ω_{mn}, respectively, and the Fourier transform of displacement from a large event $u(\omega)$ is expressed as

$$u(\omega)=\sum_{m=1}^{N}\sum_{n=1}^{N} T_{mn}(\omega)\omega_{mn}u_0(\omega)\exp(-i\omega\tau_{mn}) \qquad (1)$$

where,

T_{mn} : Function representing the difference in source time function between small and large events (Irikura, 1986)

ω_{mn} : Weight function representing spatial variation of dislocation

u_0 : Frequency component of ground motion from small event

τ_{mn} : Time delay due to fault rupture from hypocenter to sub-fault and wave traveling from sub-fault to estimation point.

N : Number of sub-faults

$$T_{mn}(\omega)=1+(N-1)\frac{\dfrac{\sin\dfrac{\omega\tau}{2}}{\dfrac{\omega\tau}{2}}}{\dfrac{\sin\dfrac{\omega\tau}{2(N-1)N_1}}{\dfrac{\omega\tau}{2(N-1)N_1}}}\cdot\exp\left[-i\left(\frac{\omega\tau}{2}-\frac{\omega\tau}{2(N-1)N_1}\right)\right] \tag{2}$$

τ : Rise time

N_1 : Coefficient to avoid the synthetically generated periodicity

The source time function after Irikura (1986) is used in the present study, which is shown in Figure 2.

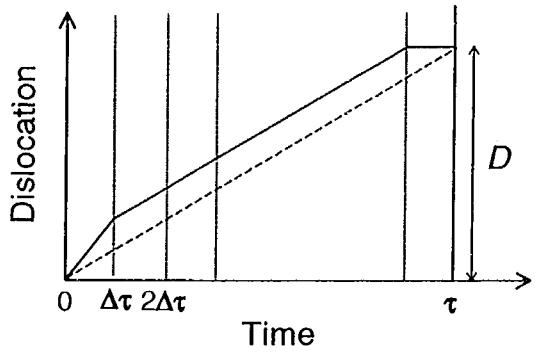


Figure 2 Source Time Function

VARIATION OF EARTHQUAKE SOURCE PARAMETERS

Target Event and Basic Source Parameters

We employ a source model of the 1923 Kanto Earthquake proposed by Wald and Somerville (1995). The major parameters of this model are listed in Table 1. Ground motion at Kannonzaki is synthesized in this study. We use a strong motion data from the 1987 Chiba-ken Toho-oki Earthquake (M_J=6.7) as a small event record, which was obtained on the siltstone at Kannonzaki. The fault plane of 1923 Kanto Earthquake, and locations of epicenters of the Kanto and Chiba-ken Toho-oki Earthquakes and Kannonzaki are presented in Figure 3. Figures 4 and 5 show acceleration waveform and acceleration response spectrum

(damping ratio h=0.05) of Kannonzaki record, respectively.

Table 1 Source Parameters

Fault Length	130 (km)
Fault Width	70 (km)
Strike	290 (deg)
Dip	25 (deg)
Seismic Moment	7.8×10^{27} (dyne·cm)
Rupture Velocity	3.0 (km/s)
Rise Time	5 (s)

Since the seismic moment of the Chiba-ken Toho-oki Earthquake is calculated as 7.05×10^{25} (dyne·cm) after Harvard University (1999), the fault plane of Kanto Earthquake is divided into 5×5 sub-faults in the following analysis, according to the seismic moment ratio between two earthquakes.

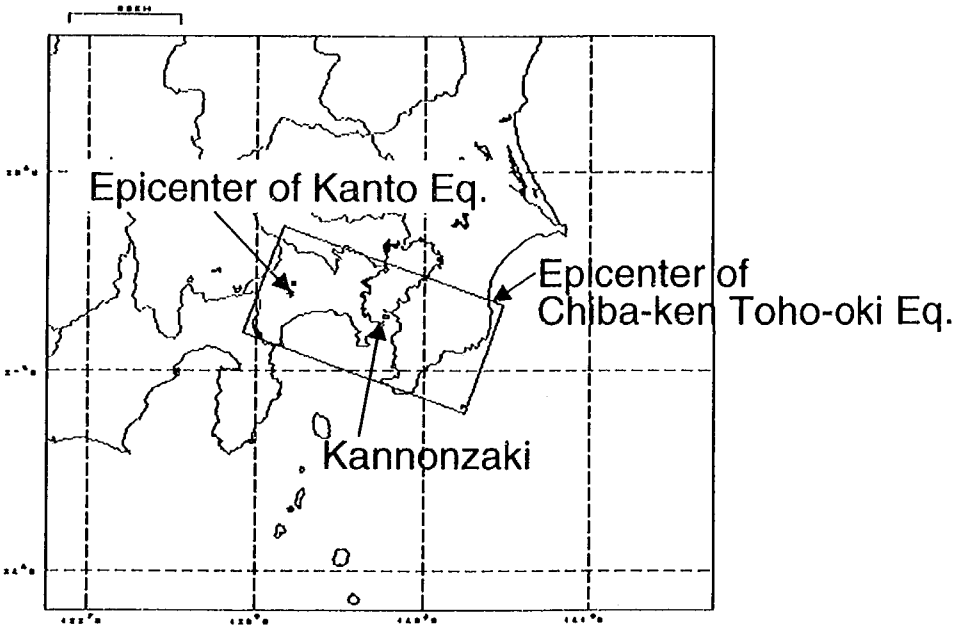


Figure 3 Fault Plane, Epicenters and Recording Site

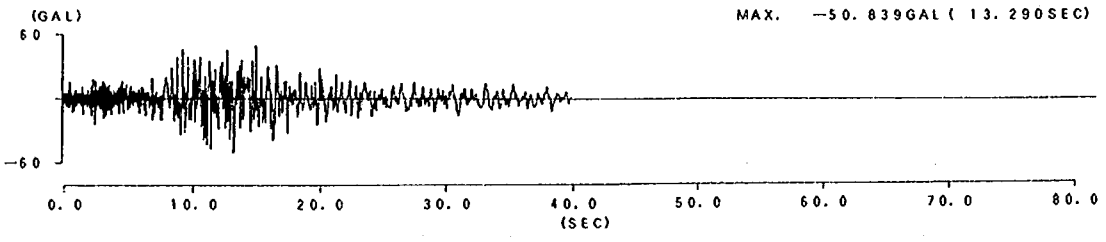


Figure 4 Kannonzaki Record from the 1987 Chiba-ken Toho-oki Earthquake (N-S Component)

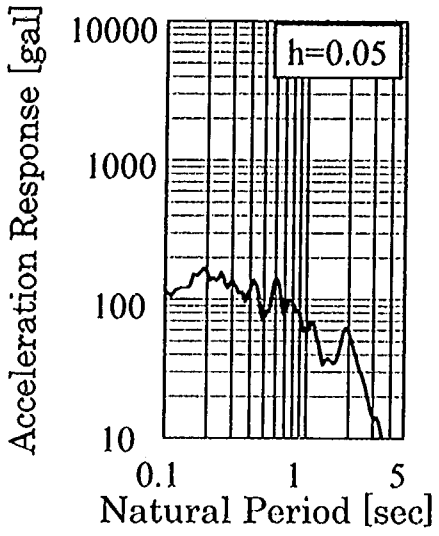
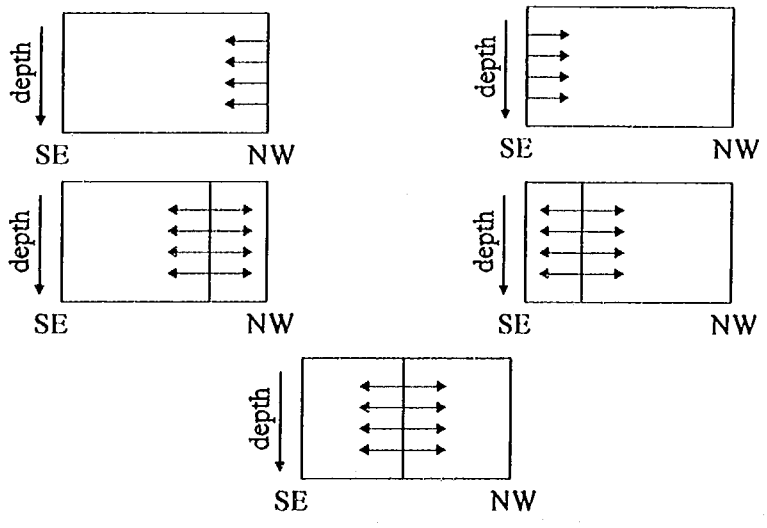


Figure 5 Acceleration Response Spectrum of Kannonzaki Record (h=0.05)

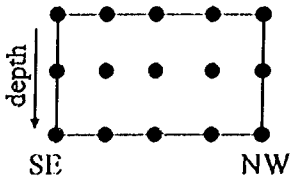
Source Parameters Changed

We systematically change fault rupture mode and location of asperity to examine their influence on the synthesized ground motion. We assume lateral rupture and radial rupture as illustrated in Figure 6, i.e., 5 cases for lateral rupture and 15 cases for radial rupture. According to Somerville et al. (1998), the area of asperity that has twice as large as average slip is 22% of total fault plane area, and we assign asperity for 6 sub-faults out of 25 sub-faults. Note that their result was derived from analysis of 15 intra-plate earthquakes, and further study may be necessary to apply it directly to the inter-plate Kanto Earthquake. We employ 2×3 and 3×2 asperities as shown in Figure 7. For each asperity shape, we assume 9 patterns of asperity distribution. Consequently, we set up (5+15)×(9+9)=360 cases for numerical simulation at this stage.



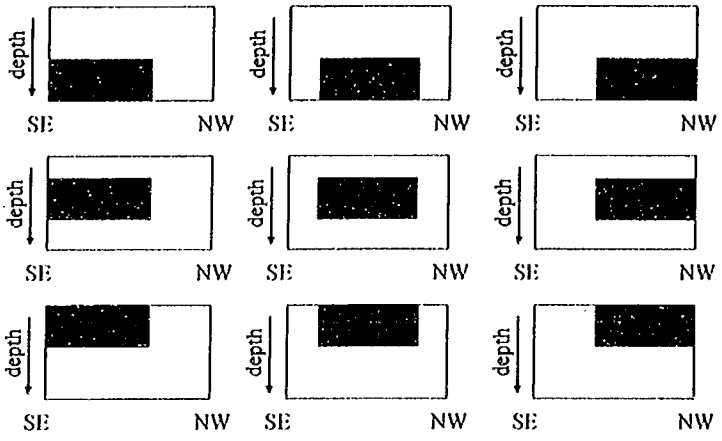
(a) Unilateral and Bilateral Rupture

Figure 6(1) Rupture Modes and Hypocenters of Radial Rupture

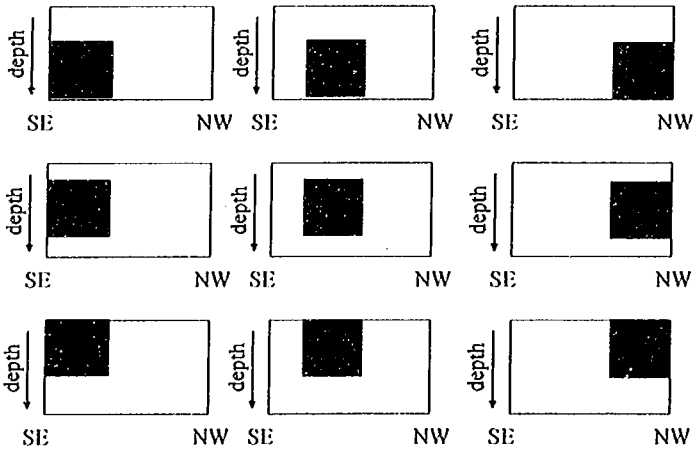


(b) Hypocenters of Radial Rupture

Figure 6(2) Rupture Modes and Hypocenters of Radial Rupture



(a) 2×3 Asperity



(b) 3×2 Asperity

Figure 7 Asperity Shape and Locations

In addition to the above-mentioned asperity models, we also employ the variable-slip rupture model of the 1923 Kanto Earthquake proposed by Wald and Somerville (1995) for reference. Note that slip vector is determined for each sub-fault in this model, however we use the slip amplitude and ignore slip angle in the present study. When we use this model, we assume bilateral rupture from the hypocenter that is indicated by a star in Figure 8, and other source

parameters are set as the same as shown in Table 1.

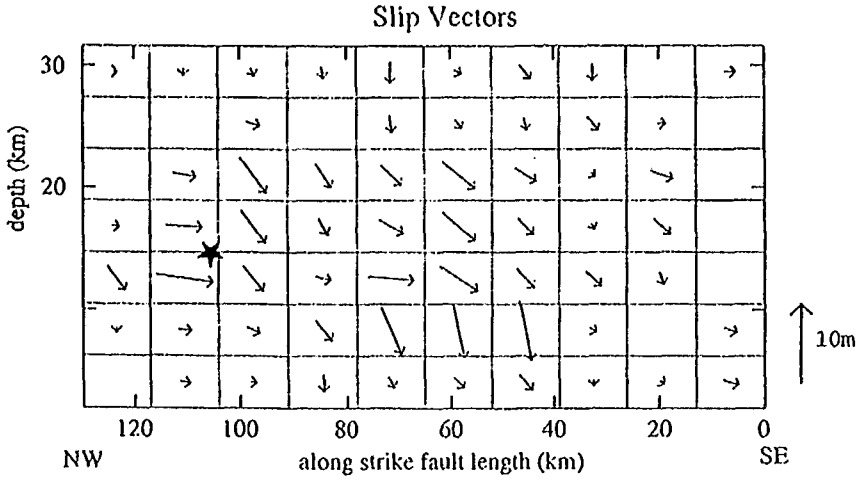
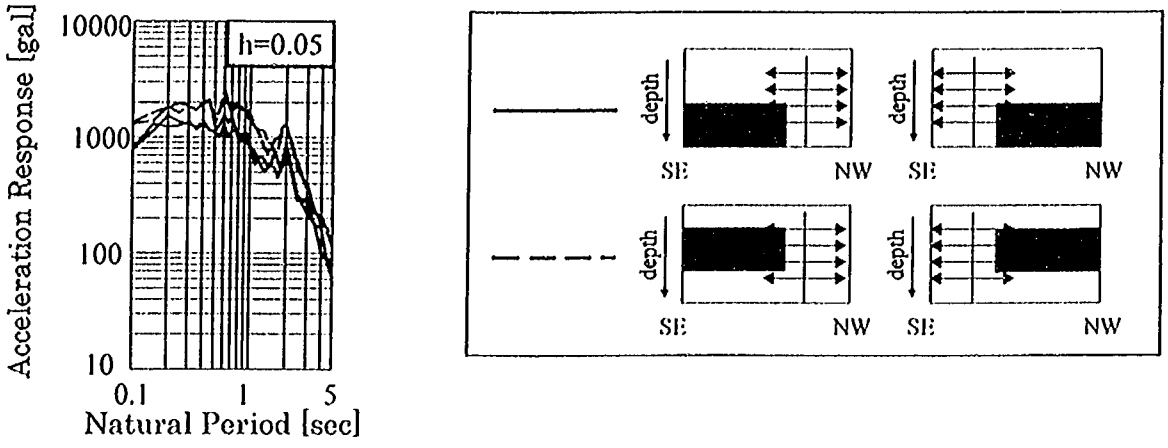


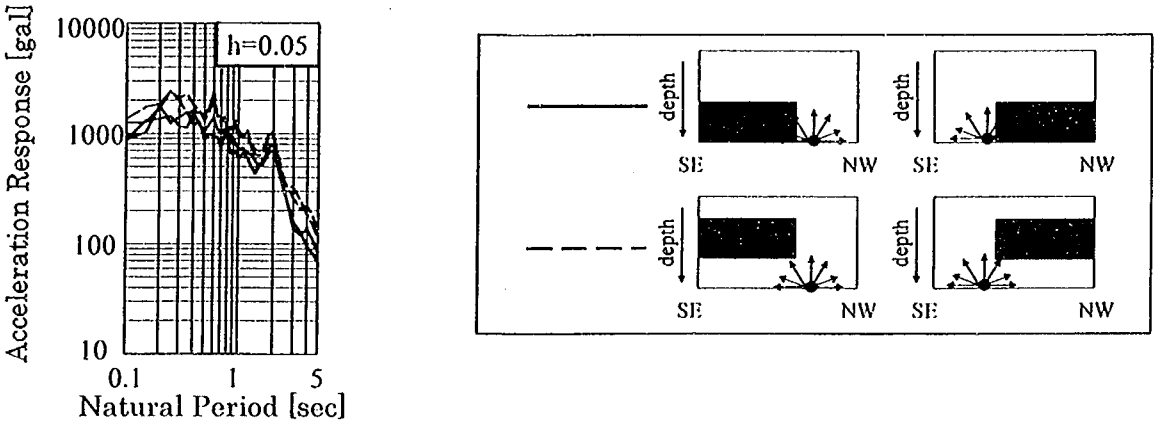
Figure 8 Variable-Slip Rupture Model of the 1923 Kanto Earthquake

Since the ground motion estimation point (Kannonzaki) is located over almost the center of fault plane as shown in Figure 3, some of assumed simulation cases may yield similar results when symmetric rupture mode and location of asperity is assigned. Besides this, we study influence of location of asperity on ground motion synthesis.

Figure 9(a) shows an example of the comparison of acceleration response spectra calculated for the Kanto Earthquake, in which combination of rupture start point and asperity is symmetrically changed for bilateral rupture. Figure 9(b) presents a case of radial rupture. It can be seen that the symmetric deployment of rupture start point and asperity yields similar ground motion.



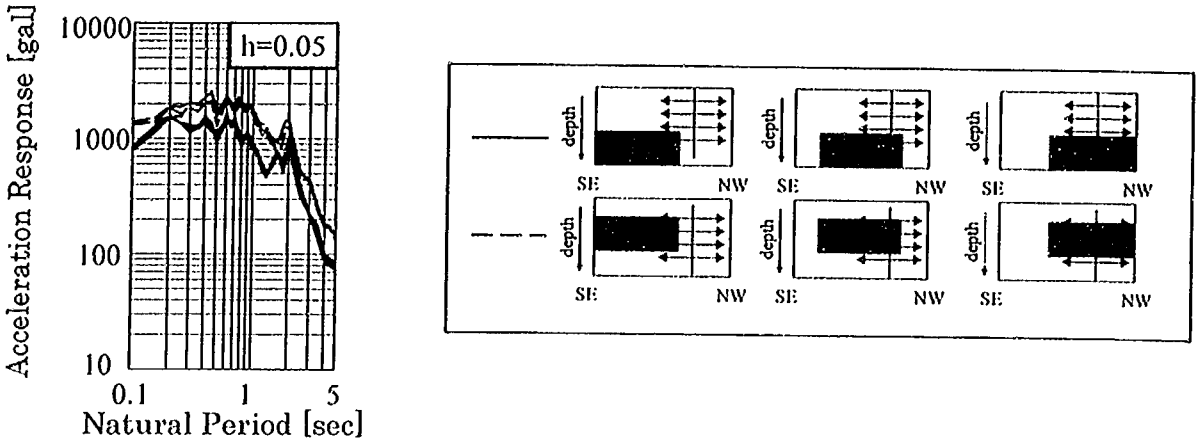
(a) Bilateral Rupture



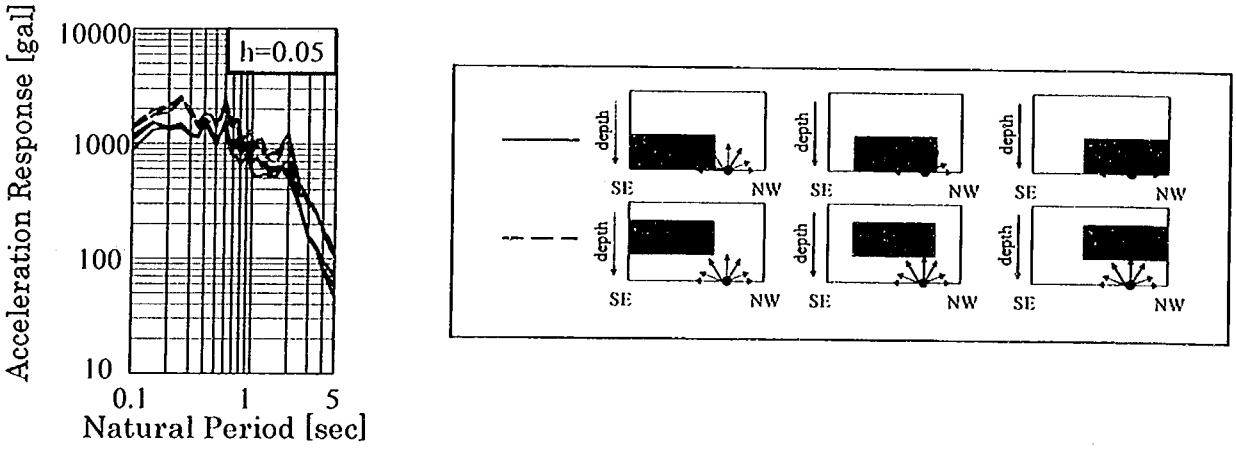
(b) Radial Rupture

Figure 9 Influence of Rupture Mode and Location of Asperity on Synthesized Ground Motion

Figure 10 compares results of lateral rupture cases, in which the horizontal location of 2×3 asperity is changed. This figure indicates that horizontal location of 2×3 asperity does not affect much calculation result. Figure 11 presents a result in which vertical location of 3×2 asperity is changed. Similar to Figure 10, acceleration response spectrum does not change much as vertical location of 3×2 asperity changes.

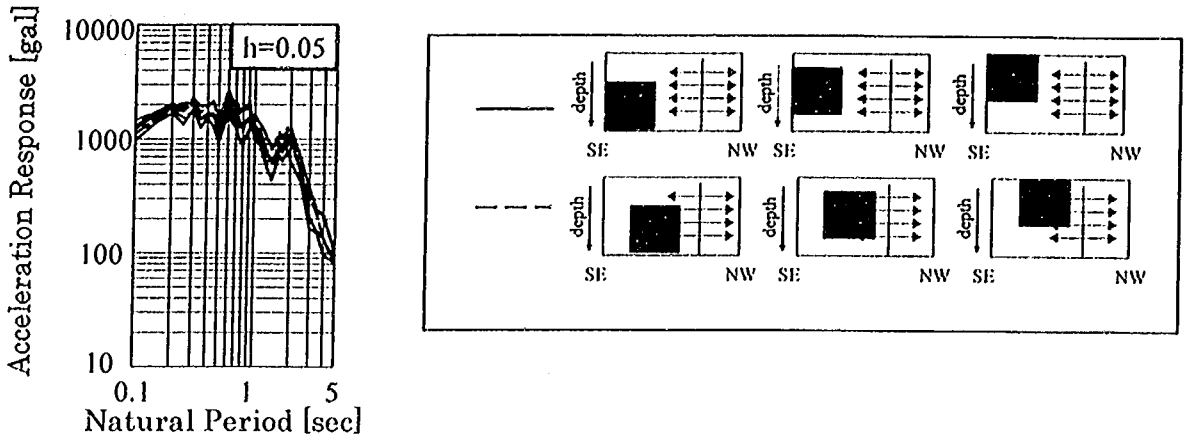


(a) Bilateral Rupture

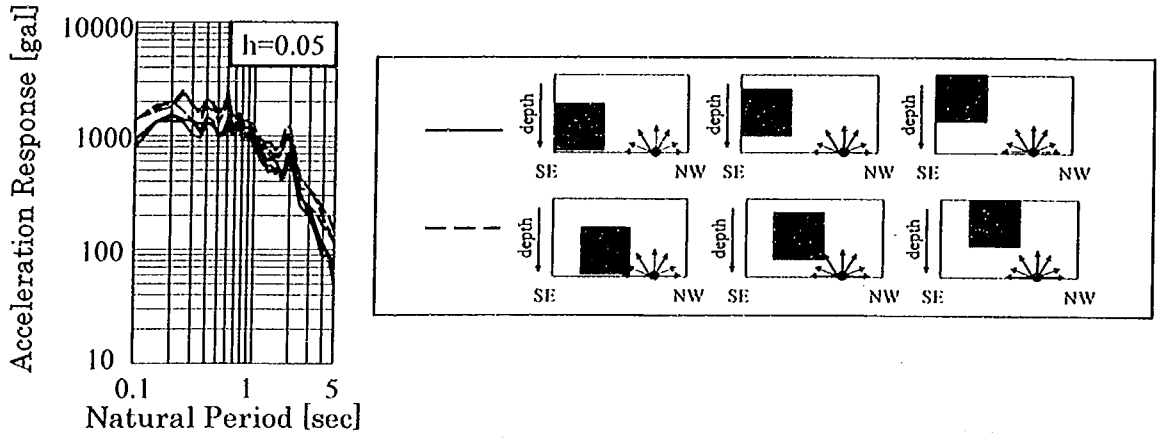


(b) Radial Rupture

Figure 10 Influence of Horizontal Location of Asperity on Synthesized Ground Motion (2×3 Asperity)



(a) Bilateral Rupture



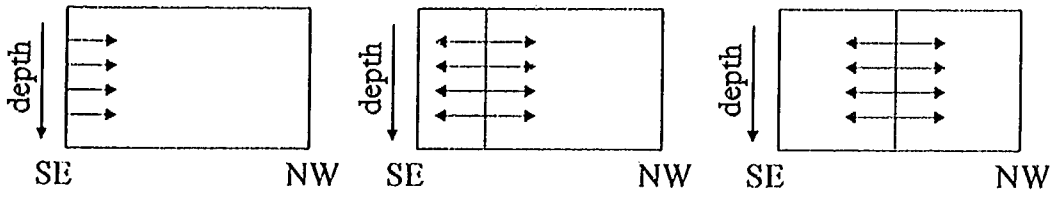
(b) Radial Rupture

Figure 11 Influence of Vertical Location of Asperity on Synthesized Ground Motion (3×2 Asperity)

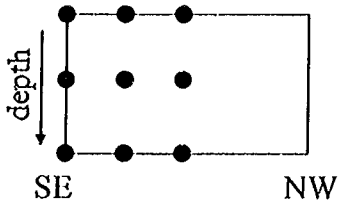
Considering the results shown in Figures 9 to 11, we reassign rupture mode and asperity locations as indicated in Figures 12 and 13. Then, numerical simulation cases are reduced to 124 cases (Table 2).

Table 2 Number of Reassigned Simulation Cases

Rupture starts from the center	(1+3) ×(3+4)=28 cases
Rupture does not start from the center	(2+6) ×(6+6)=96 cases
Total	124 cases

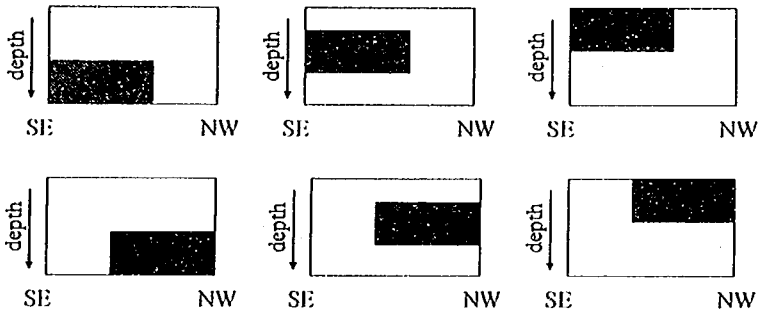


(a) Unilateral and Bilateral Rupture

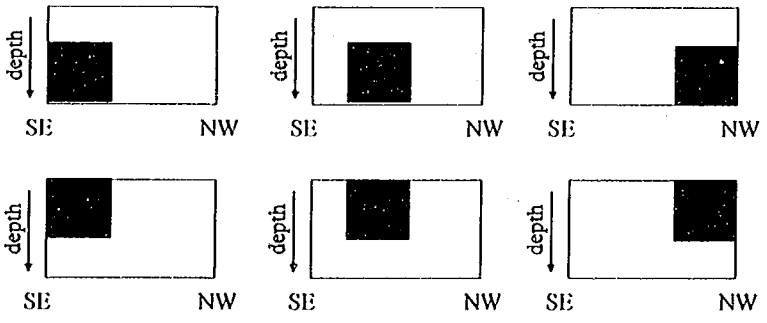


(b) Hypocenters of Radial Rupture

Figure 12 Reassigned Rupture Modes and Hypocenters of Radial Rupture



(a) 2×3 Asperity



(b) 3×2 Asperity

Figure 13 Reassigned Asperity Shape and Locations

VARIATION OF GROUND MOTION DUE TO UNCERTAINTY OF SOURCE PARAMETERS

Acceleration response spectra of the 124 cases are overlaid in Figure 14, where damping ratio is taken as h=0.05. Variation of spectral amplitude depends on natural period, and it ranges from 3 to 6 times. We should be attentive that this variation is inevitable when we infer ground motion for a future earthquake that has uncertain source parameters. Figure 15 shows acceleration response spectrum using the variable-slip rupture model that is shown in Figure 8. Comparing those two figures, result from the variable-slip rupture model gives almost upper limit of variation of synthesized ground motion.

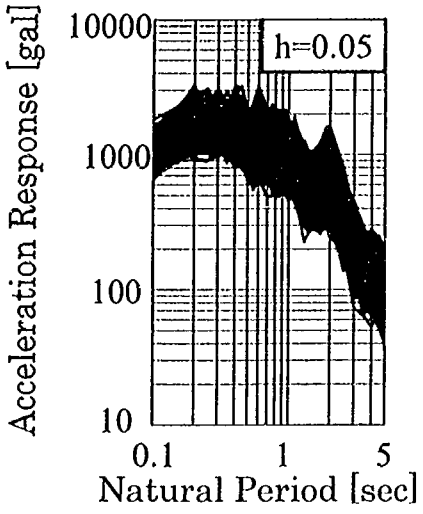


Figure 14 Acceleration Response Spectra of Synthesized Ground Motion

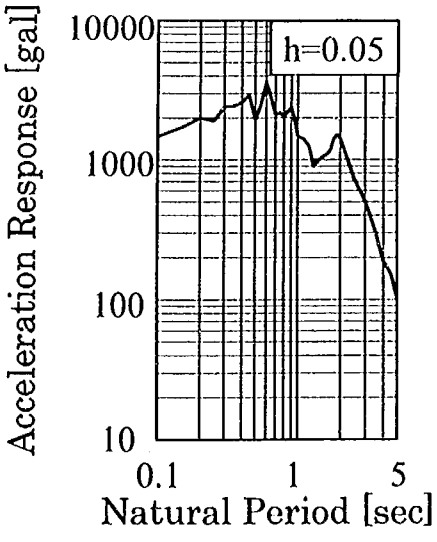


Figure 15 Acceleration Response Spectrum using the Variable-Slip Rupture Model

Figure 16 presents acceleration response spectra of typical strong ground motion data from the 1995 Hyogo-ken Nanbu Earthquake (M_J=7.1). They were recorded on the firm ground. Comparing Figure 14 to Figure 16, response spectra in Figure 14 have large spectral amplitude up to 2 seconds. This may be attributed to a fact the Kanto Earthquake has larger magnitude than the Hyogo-ken Nanbu Earthquake.

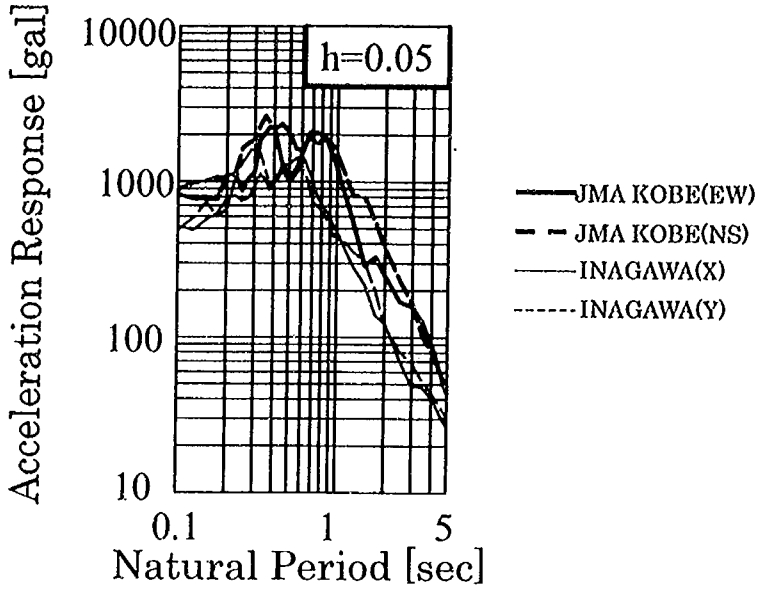


Figure 16 Acceleration Response Spectra of the Typical Strong Motion Records from the 1995 Hyogo-ken Nanbu Earthquake

CONCLUSIONS

Ground motion at the mouth of Tokyo Bay from the Kanto Earthquake was synthesized by semi-empirical technique using a small event record as Green's function. The geometric source parameters of the 1923 Kanto Earthquake were incorporated into this analysis, while the fault rupture mode and asperity were systematically changed to study their influence on synthesized ground motion. The following conclusions may be deduced from the present study.

1) Variation of fault rupture mode and asperity affects synthesized ground motion over wide period range, and the spectral amplitude of resultant synthesized ground motion changes 3 to 6 times due to this variation.

2) Synthesized ground motion for the Kanto Earthquake has large spectral amplitude up to 2 seconds.

3) The variable-slip rupture model yields almost upper limit of synthesized ground motions within the scope of present study.

REFERENCES

Hartzell, S. (1978). "Earthquake Aftershocks as Green's Functions", *Geophysical Research Letters*, Vol.5, No.1.

Harvard University (1999). *The Harvard CMT Catalog.*

Honshu-Shikoku Bridge Authority (1988). *Seismic Design Guideline of Akashi Kaikyo Bridge (Draft)* (in Japanese).

Irikura, K. (1983). "Semi-Empirical Estimation of Strong Ground Motions during Large Earthquakes", *Bulletin of Disaster Prevention Research Institute*, Kyoto University, Vol.33, No.298.

Irikura, K. (1986). "Prediction of Strong Acceleration Motions Using Empirical Green's Function", *Proc. of 7th Japan Earthquake Engineering Symposium.*

National Land Agency (1998). *The Grand Design for National Development in the 21st Century* (in Japanese).

Public Works Research Institute (1991). "Study on Structural Design of Trans-Tokyo Bay Highway", *Report of PWRI*, Vol. 184 (in Japanese).

Somerville, P. et al. (1998). "A Study on Empirical Modeling of Slip Distribution on Faults", *Proc. of 10th Japan Earthquake Engineering Symposium* (in Japanese).

Wald, D. and Somerville, P. (1995). "Variable-Slip Model of the Great 1923 Kanto, Japan Earthquake: Geodetic and Body-Waveform Analysis", *Bulletin of Seismological Society of America*, Vol.85, No.1.

SEISMIC VULNERABILITY STUDY OF HIGHWAY SYSTEMS: TEA-21 RESEARCH PROJECT

Gokhan Pekcan, Ph.D.
Acting Senior Program Officer, Multidisciplinary Center for Earthquake Engineering Research, State University of New York at Buffalo, 102 Red Jacket Quadrangle, Buffalo, New York 14261-0025

W. Phillip Yen, Ph.D.
Research Structural Engineer, Federal Highway Administration, HNR-10. Turner-Fairbank Highway Research Center, 6300 Georgetown Pike, VA 22101

Ian M. Friedland, P.E.
Associate Director for Development, Applied Technology Council, 555 Twin Dolphin Drive, Suite 550, Redwood City, California 94065 (formerly Assistant Director for Transportation Research, Multidisciplinary Center for Earthquake Engineering Research)

Ian G. Buckle, Ph.D.
Professor and Director of the Center for Civil Engineering Earthquake Research at the University of Nevada, Reno, Civil Engineering Department/ CCEER, Mail Stop 258, Reno, NV 89557-0152.

ABSTRACT

In the fall of 1998, the Multidisciplinary Center for Earthquake Engineering Research was awarded a 6-year, $10.8 million contract by the Federal Highway Administration of the U.S. Department of Transportation to conduct a series of studies related to the seismic performance of the U.S. national highway system. The research conducted under this contract is intended to provide improved tools for evaluating and assessing the social costs and impacts of earthquakes on highway systems and bridges, and to reduce the amount of damage that may occur to existing and future highway structures from a moderate-to-significant seismic event. This paper summarizes the motivation behind and objectives of the main group of tasks undertaken within the scope of this program: development of loss estimation methods for highway systems; preparation of a manual for the seismic design and retrofitting of long span bridges; development of earthquake protective systems and a systems design manual for bridges; and specialized ground motion, foundation, and geotechnical studies.

INTRODUCTION

A highway system is typically comprised of a network of urban expressways, surface streets, intersections, computerized signals, drainage systems, utility right-of-ways, and excavations and embankments, all of which can be impacted by earthquakes. Transportation networks must continue to function during and after the occurrence of a natural disaster such as an earthquake, so that lifelines can continue to provide emergency services and to minimize loss of life and economic distress. As evidenced in past earthquakes, highway transportation is often disrupted as a direct result of damage or collapse of highway system components. Of all the components of highway systems, bridges are usually considered to be the most vulnerable to earthquake induced damage and collapse. A survey of available statistics reveals that more than one-third of U.S. highway

bridges may be vulnerable to damage and/or failure due to earthquakes. In fact, more than 70 percent of the nation's 480,000 highway bridges were built prior to 1970, and can be regarded as vulnerable to moderate-to-major earthquake ground motions. Recent earthquakes, particularly the 1989 Loma Prieta, 1994 Northridge and 1995 Great Hanshin (Kobe) earthquake in Japan, have demonstrated the need, i) to find new and improved ways to design and construct bridges and highways which can withstand the force and displacement demands placed on them, ii) to cost-effectively retrofit existing seismically vulnerable structures, and iii) to develop tools and technologies which can adequately predict the economic and social impacts from damaging earthquakes, to assist in effective decision-making regarding operation, retrofit, and design strategies.

Recognizing the shortcomings evident in both existing highway bridges and current bridge design specifications, the Federal Highway Administration (FHWA) initiated a comprehensive seismic research program in cooperation with the Multidisciplinary Center for Earthquake Engineering Research (MCEER, formerly the National Center for Earthquake Engineering Research – NCEER), in 1992. That program included two contracts, one focused on existing highway construction and seismic vulnerability and the other on the development of improved methods and details for future bridge construction. Among the products of these studies are a set of manuals for seismic evaluation and retrofitting of conventional highway bridges and systems (MCEER, 1999a, 1999b, 1999c), and a series of recommendations for improving future seismic bridge design specifications (Rojahn et al., 1999).

Despite these gains in knowledge, there is still some distance to go before seismically-resistant highway systems are a reality. Some classes of bridges have yet to be studied in a systematic way; such as long span bridges, and structures on or crossing difficult sites continue to be problem. Some of these structures are very old and typically possess non-ductile structural details. Many are located on either unknown foundation types or incorporate lightly reinforced concrete substructures. In many cases, poor soil conditions exist, yet soil-foundation-structure interaction during an earthquake is a highly complex phenomenon and is still poorly understood. Hence, given the current state of knowledge, it is difficult, if not impossible, to quantify the seismic capacity and a highway bridge with much certainty. Therefore, unrestricted access to these "lifelines" cannot be assured at this time, which could have a major impact on emergency services following a damaging earthquake, and the resultant impediments to post-earthquake recovery.

Moreover, the high cost of retrofitting the Nation's bridges is a major disincentive to owner agencies who are faced with extensive upgrade programs. A more intelligent way of prioritizing a bridge inventory, and selecting bridges to be retrofitted, is required to ensure that scarce resources are utilized in the most cost-effective manner. For this purpose, a seismic risk assessment procedure has been developed by MCEER under one of the earlier FHWA contracts. To reach its full potential, however, the methodology must be extended to assess both direct and indirect costs of earthquake damage to highway systems and components such as tunnels, slopes, pavements, and retaining structures, and it must be validated and calibrated against actual earthquake experience-data. Concurrently, improved retrofit technologies are needed which are more efficient and reduce the overall cost to acceptable levels compared to standard strength-based retrofitting techniques.

To address these and other related needs, MCEER was awarded a 6-year, $10.8 million contract by the FHWA in the fall of 1998. This contract, which was authorized under the 1998 Transportation Equity Act for the 21st Century (TEA-21), will address research on the seismic vulnerability of the

U.S. national highway system. This new contract will draw on and extend the work that has been conducted under the two prior FHWA research projects being conducted by MCEER, and on work done by the California Department of Transportation (Caltrans) and others.

Seismic Vulnerability Of Highway Systems

The earlier FHWA contracts were primarily focused on the seismic design and retrofitting of typical highway bridges found throughout the United States. The TEA-21 contract focuses on several special issues considered as critical to the future of the Nation's highway transportation infrastructure. TEA-21 research addresses:

- Development of formal loss estimation methodologies for highway systems.
- Development of a seismic design and retrofitting manual for long span bridges, including long span trusses, suspension, and cable stayed bridges.
- Development of and improvements for "smart" or "intelligent" earthquake protective systems, including bearings and dampers, specialty materials like shape-memory alloys or viscous materials, and other passive and hybrid semi-active systems.
- Studies related to foundation design and soil behavior and response, including large pile group behavior, long period ground motions, and improvements in ground remediation technologies.

The project will also address a series of special studies, including: i) development of post-earthquake, non-destructive assessment technologies for retrofitted bridge components, ii) technical assistance and support for NCHRP[1] Project 12-49, which is developing a new seismic design specification for highway bridges, and iii) designing and implementing a seismic instrumentation network for a major cable-stayed bridge currently under construction across the Mississippi River between Cape Girardeau, Missouri and the State of Illinois.

The objective of this six-year research program is to study the seismic vulnerability of highway systems and components, and to develop cost-effective methods of retrofitting system components and facilitate the implementation of these methods in the field. The program has a national focus and addresses structure types and issues not currently being addressed in other research programs. Various experimental and analytical studies are expected to result in a number of manuals, guides, and design and retrofitting recommendations for evaluating and improving the seismic vulnerability of highway systems and components. Some of the new and improved knowledge and technologies may have applicability to other modes of transportation and opportunities for the transfer of this information to these other modes will be pursued.

The program is comprised of eight primary tasks as follows:

Task A - Project Administration

Task B - Loss Estimation Methods for Highway Systems

---

[1] National Cooperative Highway Research Program, a division of the Transportation Research Board

Task C - Seismic Design and Retrofit Manual for Long Span Bridges

Task D - Earthquake Protective Systems

Task E - Foundation and geotechnical Studies

Task F - Special Studies

Task G - Technology Exchange and Transfer

Task H - Project Reporting

The objective and focus of the research being conducted under Tasks B through G are summarized in what follows.

Loss Estimation Methods For Highway Systems

Loss estimation methods have moved to the forefront as earthquake hazard reduction tools. As a result of technological advances in data collection and management, relational data analysis, and software development, lost estimation methodologies can be utilized very efficiently. Much of this advancement in the highway field has been as a result of the seismic risk assessment (SRA) methodology developments under the FHWA-sponsored MCEER Highway Project. Acknowledging that the assessment of socioeconomic impacts caused by the failure and disruption of transportation systems was essentially absent until very recently, the current state of knowledge requires a continuing rapid advancement.

The role of loss estimation methods is three-fold. First, loss estimation methods can be used to estimate the seismic vulnerability of existing transportation systems, in particular highway networks. Second, based on this analysis, loss estimation methods can be used to project future benefits, in terms of reduced losses, from the execution of retrofit programs. Finally, loss estimation can be effectively applied in a post-earthquake environment, i.e., they can be used to help assess optimal recovery strategies allowing a comparison of relative benefits associated with each strategy or action.

The research being conducted by MCEER is focussed on the development and application of loss estimation methods for this broad range of purposes. The approach for integrating loss estimation methods into the current overall program is to build on what has been accomplished previously under the MCEER Highway Project, by enhancing that seismic system risk assessment models and expanding the types of losses that are considered (including indirect losses), incorporating new developments and data where appropriate, and ensuring the usability of the methodology so that it is presented as a flexible and user-friendly software tool with ample documentation. The importance of expanding the methodology to address other highway system components and transportation systems is also recognized. Consequently, the research plan for this task is envisioned to comprise three major subcomponents.

Subtask B1 - Loss Estimation Methodology Development, Additional Refinement of the on-going SRA Project; System Calibration and Validation.

Subtask B2 – Extend to Include Other Highway Structure Components

Subtask B3 – Extend to Include Other Types of Transportation Systems

Subtask B1 is comprised of five parts: i) validation, calibration, and refinement of the current SRA methodology; ii) development of direct and indirect loss modules; iii) calibration and validation of the complete system; iv) completion of the system software and documentation; and v) development of a demonstration and training workshop.

Under the earlier FHWA project, a major focus has been on bridge damage state modeling and traffic state analysis, with limited additional work in direct loss modeling and other highway elements. As part of Subtask B1-1, refinements in the current methodology will be made to address several limitations such as the applicability of models outside of the current demonstration city (Memphis, Tennessee), enhancements in network analysis uncertainties, and more rigorous treatment of site-specific assessments of certain seismic hazards. In order to extend the current SRA methodology to incorporate accurate assessment of direct and indirect economic losses, further model development will also take place in Subtask B1-2. To ensure the credibility of these new models, independent calibration and validation studies of the complete-integrated system, including the incorporation of other highway system components and transportation modes (under Subtasks B2 and B3), will be performed in Subtask B1-3 using data from a series of actual earthquakes.

To expand the current SRA methodology to other highway components, damage models will be developed for retaining structures, slopes, tunnels, culverts, approach fills, and pavements, under Subtask B2. Specific model development will include damage state fragility modeling, including uncertainty analysis, repair and restoration modeling, and traffic flow impact modeling based on different levels and types of damage. The goal of this task is to improve the overall modeling of damage and impacts to highway networks by including all key components.

The objective of Subtask B3 is to integrate freight and Urban Mass Transit (UMT) rail transportation systems models with the highway system models. Past experience in the U.S. and Japan has shown that these transportation alternatives can greatly facilitate emergency response and recovery operations after an earthquake and, hence, reduce overall economic losses due to earthquake damage. The end result of this integration will be a multi-modal land-transportation SRA methodology.

Finally, there is a tremendous opportunity to also facilitate cross-disciplinary research to improve particular loss estimation models. For example, the loss estimation methodology can be used to identify the relative importance of long span bridges with regard to overall system performance, as the necessary information (from Task C) will feed into the fragility and damage/loss modeling in this part of the program. In addition to the long span bridge task, the advanced bridge earthquake protective system task may provide important insights and information in the application of the methodology.

Seismic Design And Retrofit Manual For Long Span Bridges

In 1983, the FHWA published the "Seismic Retrofitting Guidelines for Highway Bridges," the first attempt at providing nationally-applicable guidance on screening, evaluating, and retrofitting seismically-vulnerable highway bridges. That report and its update (FHWA, 1995) were intended to address the vast majority of typical short-to-medium span structures found on the U.S. highway system. However, very limited information is available on a national basis concerning evaluating

the seismic vulnerability or retrofitting of long span bridges. As previously mentioned, because these structures are usually critically important to the region they serve, society expects higher levels of performance from them than for the more conventional highway structures. This part of the TEA-21 project will address this problem in a consistent manner, drawing on experience from recent earthquakes and the expertise of a team of skilled practitioners and researchers. Hence, the research for this task is comprised of three major components:

Subtask C1 - Design and Retrofit Manual Development

Subtask C2 – Supporting Ground Motion, Geotechnical and Foundation Studies

Subtask C3 – Supporting Structural Studies

For the purpose of this project, long span bridges have been defined as those structures where the main span exceeds 120 m and are classified into the following superstructure types:

- Steel Trusses - through trusses or deck trusses with articulation defined as simple span, cantilever, continuous, gerber or combination.
- Steel and Concrete Arches - through arches or deck arches with articulation defined as full arch, two hinged arch, or tied arch (single or multiple spans).
- Steel and Concrete Cable Stayed - single and double towers, or single and multi-planes of cables with varied articulation.
- Steel Suspension Spans - earth anchored or self anchored, typically with three spans of articulation.

In addition, most substructures for long span bridges can be classified into following types: spread footings, timber piles, concrete piles, steel piles, or caissons.

The "Seismic Design and Retrofitting Manual for Long Span Bridges" will be developed under Subtask C1. This manual will be complementary to but distinct from the 1995 Seismic Retrofitting Manual and its current revisions. Some of the issues to be covered in the proposed manual and to be provided by the supporting Subtasks C2 and C3 are discussed in the following.

Structural Issues

Long span bridges generally cross waterways at locations where there is little, if any, redundancy in the highway network. Therefore, operational demands on such bridges are considerably greater. This dictates that long span bridges should behave in a "mostly elastic" fashion and, thus, remain open following a major earthquake. The most prolific of all long span bridges in the U.S. is the truss-type of structure. Therefore, it is planned to primarily, but not exclusively, focus on the truss type of long span bridges in this research.

Establishing retrofitting measures for long span bridges is expected to be challenging. It is necessary to conduct experimental studies on critical subassemblages that are representative of typical long span bridge structures in order to gain an understanding of their expected performance and behavior under dynamic loading. Of particular importance are braced and unbraced sway

frames, bearing-pedestal seating systems, and the strength and ductility of bridge piers and foundations.

Subtask C3-1 is addressing issues related to braced piers in steel truss bridges and their substructure connection behavior. A series of analytical and experimental studies are being conducted to ascertain the most critical elements along with the need for retrofitting.

Ground Motion, Geotechnical, And Foundation Issues

There are a number of important considerations for long span bridges that must be addressed. These include the need for studies on improved evaluation of long period ground motion characteristics, developing methods for estimating liquefaction induced lateral spreading loads on caissons and pile supported piers, consideration of soil-foundation-structure interaction from large pile groups and caissons, and characterization of the site response at soft soil sites.

A comprehensive review and study of the factors that influence long period ground motions and their spatial variability that is important for long span bridges will be provided in Subtask C2-1. This task will result in guidelines for incorporating these factors explicitly in the estimation of seismic design ground motions, and to complement the deficient database of ground motion recordings close to large earthquakes with synthetic time histories.

Extremely large pile groups (involving hundreds of piles) are very common for long span bridges and group effects for such systems are believed to be extremely important. Limited pile group test data is available for 3x3 and 4x4 pile groups, which showed that elasticity pile-group theory over-predicts the group effects. Completely ignoring group effects can lead to very serious errors for very large pile groups, while relying on the elasticity approach has been found to be deficient even for small pile groups. In order to address this issue, Subtask C2-2 will establish practical approaches to determine the very large pile group effects by incorporating advances in constitutive modeling and 3-D finite element analysis.

EARTHQUAKE PROTECTIVE SYSTEMS

Earthquake protective systems (EPS) provide promise for reducing earthquake losses in highway systems. This family of technologies is continuing to grow at an increasing rate with potential for even greater improvement. Recognizing this fact, Task D is comprised of the following:

Subtask D1 - Current Practice and Performance Review

Subtask D2 - Intelligent Passive Systems (Passive and Adaptive Systems)

Subtask D3 - Manual for the Design and Retrofit of Bridges with Earthquake Protective Systems

The current state-of-practice will be reviewed in light of recent field experience and new developments in the modeling of highly-damped systems under Subtask D1. Subtask D2-1 will provide concurrently detailed reviews of state-of-the-art advanced technologies that may be applicable to the development of intelligent bridge bearings for highway bridge applications. These reviews are expected to lead to the development of a new generation of protective systems. The intent is to apply smart materials to the construction of intelligent passive systems (isolators and dissipaters) which will combine the reliability of passive devices with the real-time responsiveness

of active control. Other approaches for introducing "intelligence" into bridges will also be explored, such as the use of smart restrainers and adaptive structural forms.

Since, high damping is generally associated with EPS, the dynamic behavior of bridges with high damping will be investigated on the basis of 3-D nonlinear time history analyses, validated by large-scale model tests, under Subtask D2-2.

A major product from this task will be a manual for the design and retrofit of bridges with earthquake protective systems. The overall task will be coordinated with other tasks such as those concerned with ground motion and geotechnical hazards. In particular, there will be contributions to Tasks C and B (on long span bridges and loss estimation studies, respectively) where fragility functions are required for EPS-bridges.

Foundation And Geotechnical Studies

The research program under Task E includes studies on foundation retrofitting (Subtask E1) and soil retrofitting (Subtask E2). These studies are intended to augment and support research conducted on foundations and soils for long span bridges under Task C.

An earlier contract between MCEER and the FHWA addressed issues such as the improved assessment of seismic load demands on foundation elements, moment capacity of pile footing foundations, and pile-to-pile cap connection details and their movement and lateral capacity. In many cases, however, design approaches are still based on foundation displacement demands arising from bridge response. There is a lack of design guidance on the displacement capacity of various pile types and connection details. This issue is addressed in Subtask E1-1, which will result in seismic evaluation guidelines for assessing the rotational/ductility capacity of plastic hinges for piles within soil and for assessing the strength and inelastic rotational capacity of existing pile-to-cap connections. Recommendations for improving the ductility capability of new pile designs will be provided.

The vulnerability of bridges to earthquake induced liquefaction, lateral ground deformation (or spread) has also been clearly demonstrated in past earthquakes. Several liquefaction mitigation approaches using soil remediation have been studied in the past. However, further research is needed on the mitigation option related to foundation design or retrofit as current methods of soil improvement are very costly and time consuming to implement. The research to be undertaken in Subtask E1-2 will develop several models to simulate the interaction between soil in a lateral spread zone and pile or pile foundation elements and pile caps. General design guidelines on conditions suitable for structural retrofit, or a structural mitigation versus ground remediation option will be established under this task.

Most of the soft soil retrofit problems are generally associated with soil liquefaction, which clearly has been responsible for numerous bridge failures in past earthquakes. Recent research has identified a number of outstanding issues related to the use of ground densification approaches for soil remediation purposes. Accordingly, Subtask E2-1 will address part of this issue by developing an improved remediation technique and design method to mitigate liquefaction hazards in silty soils using stone columns.

Finally, the applicability of new alternative ground remediation techniques will be investigated under Task E. For example, deep soil mixing using cement or cement/lime mixtures as a

liquefaction mitigation method is receiving increased attention in the U.S. and Japan. This method has definite applications to bridge sites; therefore, research is coordinated to tailor the technology to bridge applications and to develop design guidelines for its use.

SPECIAL STUDIES

Task F of the project will address a series of special studies including:

Subtask F1 - Post-earthquake Nondestructive Assessment of Retrofitted Bridges

Subtask F2 - Cape Girardeau Cable-stayed Bridge Instrumentation

Subtask F3 - NCHRP Project 12-49 Supporting Studies

Subtask F4 - Earthquake Reconnaissance

Post-Earthquake Assessment Of Retrofitted Bridges

Following a strong earthquake, perhaps the most important question facing bridge engineers is whether or not a particular bridge has been damaged and to what extent. If there are visible signs of damage, is the bridge safe enough to allow continued traffic on it?

Damage is generally self-evident in the form of cracking and crushing of concrete columns, unseating of girders at the bearings and seats, and damage to foundations and abutment back-walls that is evident from pavement distress and bulging soil. However, if a bridge has been retrofitted with either cable-restrainers, column jackets, foundation improvements, or a combination thereof, the damage may not be as visible. In such cases, the engineer may need to resort to nondestructive evaluation (NDE) techniques as a means of damage detection and to assess the severity of damage.

This task will provide a comprehensive review and assessment of such techniques and will develop a manual for conducting post-earthquake evaluations using appropriate NDE methods and technologies.

Cape Girardeau Cable-stayed Bridge Instrumentation

The acquisition of structural response data during earthquakes is essential to confirm and develop methodologies for analysis, design, repair and retrofitting of bridges and other structures. To understand structural response to earthquake-induced ground shaking, it is necessary to obtain free-field ground motion data in the vicinity of a structure, acceleration and displacement data in and around the foundations to identify the soil-foundation interaction effects, and on the structure itself.

The new cable-stayed bridge currently under construction near Cape Girardeau, Missouri, provides an excellent opportunity to install a number of sensors in the free-field, within the foundation, and on various sub- and superstructure elements and subsystems within this long span Mississippi River crossing. Subtask F2 will provide a detailed seismic instrumentation design for the bridge, and will acquire all required equipment. The research team will then provide continued technical support to the bridge designer, construction contractor, and owners during installation of the system.

NCHRP Project 12-49 Technical Support

The AASHTO[2]-sponsored National Cooperative Highway Research Program (NCHRP) initiated NCHRP Project 12-49, "Comprehensive Specification for the Seismic Design of Bridges" in mid-1998. The project is intended to develop and incorporate new probability-based specifications into the AASHTO *LRFD Bridge Design Specifications*. The project is addressing improvements to the overall seismic design philosophy and performance criteria, seismic loads and site effects, analysis and modeling procedures, and design and detailing requirements. A joint venture of the Applied Technology Council (ATC) and MCEER is the primary contractor for the project.

Work under NCHRP Project 12-49 is intended to incorporate currently available research results and the state-of-practice, and does not include provisions for special analytical studies should they be needed to address important issues or gaps in knowledge. Therefore, under Subtask F3, support will is being provided to the research team conducting NCHRP Project 12-49. This support includes conducting a limited number of special studies identified as critical to the completion of the specifications by the ATC/MCEER Joint Venture. One such study was initiated under Subtask F3-1(a) to conduct a series of parameter studies necessary to address the development of design and detailing provisions for various bridge components, including columns, foundations and abutments. The parameter studies will also evaluate the cost impact of different design decisions in a variety of seismic zones of the U.S. A second subtask (F3-1(b)) is providing support for the design and conduct of a workshop to address various issues related to the development of performance criteria for geotechnical engineering and bridge foundation design.

Earthquake Reconnaissance

When damaging earthquakes occur, it is important to assemble and have on-site an earthquake reconnaissance team as soon after the earthquake as possible. There are many lessons that can be learned and technical information obtained from such an exercise by gathering and documenting data on the behavior and performance of soils, foundations, and structures. The MCEER Highway Project previously supported reconnaissance teams to document bridge and highway system performance and damage, often resulting in the initiation of special studies in order to develop an understanding of this performance and to improve analytical models and retrofit designs.

Consequently, Subtask F4 will provide for support of continued earthquake reconnaissance efforts, and the rapid compilation of reports documenting damaging events and dissemination of this information to the profession. In fact, in late summer of 1999, the project supported reconnaissance efforts in Turkey (August 17, 1999 Izmit (Kocaeli) Earthquake) and Taiwan.

TECHNOLOGY EXCHANGE AND TRANSFER

An important element of this project is the transfer of newly developed and improved technologies to the transportation engineering profession both in the U.S. and internationally. As a result, Task G will provide support for the development of workshops on various aspects of the program, and the planning and conduct of national and international conferences. The task will also provide support for outreach and coordination with AASHTO, and State and Federal transportation agencies.

---

[2] American Association of State Highway and Transportation Officials

Among the specific items under this task, a series of training courses will be developed to assist in the implementation and use of the "Seismic Retrofitting Manuals for Highway Systems" which are nearing completion under the prior FHWA contract with MCEER. This task will also provide for the planning and conduct of the 3rd National Seismic Conference on Bridges and Highways on behalf of the FHWA. Support will also be provided for the conduct of the 17th, 18th, and 19th UJNR U.S.-Japan Bridge Engineering Workshop.

It is anticipated that a number of demonstration projects will also be organized and conducted during latter years of the research program. These demonstration projects will assist in the implementation and transfer of new and improved technologies developed under this research program.

CONCLUSIONS

The FHWA-sponsored research program recently initiated by MCEER will address a number of important aspects related to the seismic vulnerability of highway systems. The overall research program includes six major task areas, which have been summarized in this paper. Further developments and achievements as a result of this project will be discussed in subsequent papers and presentations.

The results of this work are expected to have significant short- and long-term impacts on the performance and economics associated with the earthquake performance of highway systems, and it is expected that some of the advances made in this program will have direct application to other surface transportation modes. As the research is still in its early stages, initial results and products are not yet available.

REFERENCES

FHWA (1995), Seismic Retrofitting Manual for Highway Bridges, FHWA Publication No. FHWA-RD-94-052, May.

MCEER, (1999a), "Seismic Retrofitting Manuals for Highway Systems - Volume I: Seismic Risk Analysis of Highway Systems." (in progress)

MCEER, (1999a), "Seismic Retrofitting Manuals for Highway Systems - Volume II: Seismic Evaluation and Retrofitting Manual for Highway Bridges." (in progress)

MCEER, (1999c), "Seismic Retrofitting Manuals for Highway Systems - Volume III: Screening, Evaluation, and Retrofitting of Retaining Structures, Slopes, Tunnels, Culverts, and Pavements." (in progress)

Rojahn, C., Mayes, R., Anderson, D.G., Clark, J.H., D'Appolonia Engineering, Gloyd, S., and Nutt, R.V., (1999), "Impact Assessment of Selected MCEER Highway Project Research on the Seismic Design of Highway Structures," *Technical Report MCEER-99-0009*, Multidisciplinary Center for Earthquake Engineering Research, State University of New York at Buffalo.

The System of Real-time Earthquake Damage Estimation in Hanshin Expressway

Kiyoshi Miyawaki[1] , Taiichi Kagayama[2] and Fuminobu Okunishi[3]

Abstract

Since the occurrence of the Great Hanshin Earthquake in 1995, Hanshin Expressway Public Corporation (HEPC) has the necessary task of collecting information on seismic design and the maintenance of structures. Moreover, HEPC must work to improve the control systems of seismometer records for the purpose of establishing an initial activity system to inspect the structures and take emergent investigation immediately after an earthquake occurs.

Now HEPC is developing the system to approximately estimate the degree of damage of structures right after an earthquake in real time based on about 17 seismometers currently in use and seismometers that will be installed in the near future. The outline of this earthquake damage estimation system is described in this paper.

Introduction

The Hanshin Expressway Network has played a vital role for the Osaka and Kobe area, therefore the highway should be required to provide normal traffic service even after an earthquake as soon as possible. Presently, HEPC is developing an earthquake damage estimation system to approximately grasp the damage of structures. This system has been created for the purpose of supporting the initial activity to perform emergent investigation immediately after an earthquake.

Outline of this system is shown in Figure 1. The data recorded by strong-motion seismograph network in Hanshin Expressway are analyzed by this system in real time to estimate the degree of damage of road structures (piers). Since the purpose of this system is to support the initial activities right after an earthquake, it was decided to roughly divide each route into zones a few kilometers to several tens kilometers in length (each route to be divided into two or three zones) to estimate the damage in comparison with

1 Chief of maintenance design division, maintenance and facility design department. Hanshin Expressway Public Corporation, Osaka, Japan.

2 Chief Engineer of maintenance planning division, maintenance and facility design department. Hanshin Expressway Public Corporation.

3 Engineer of maintenance design division, maintenance and facility design department. Hanshin Expressway Public Corporation.

the seismic intensity at the typical points of each route (Figure 2). Furthermore, the location of active faults and the differences in ground characteristics were taken into consideration to divide each route into the zones.

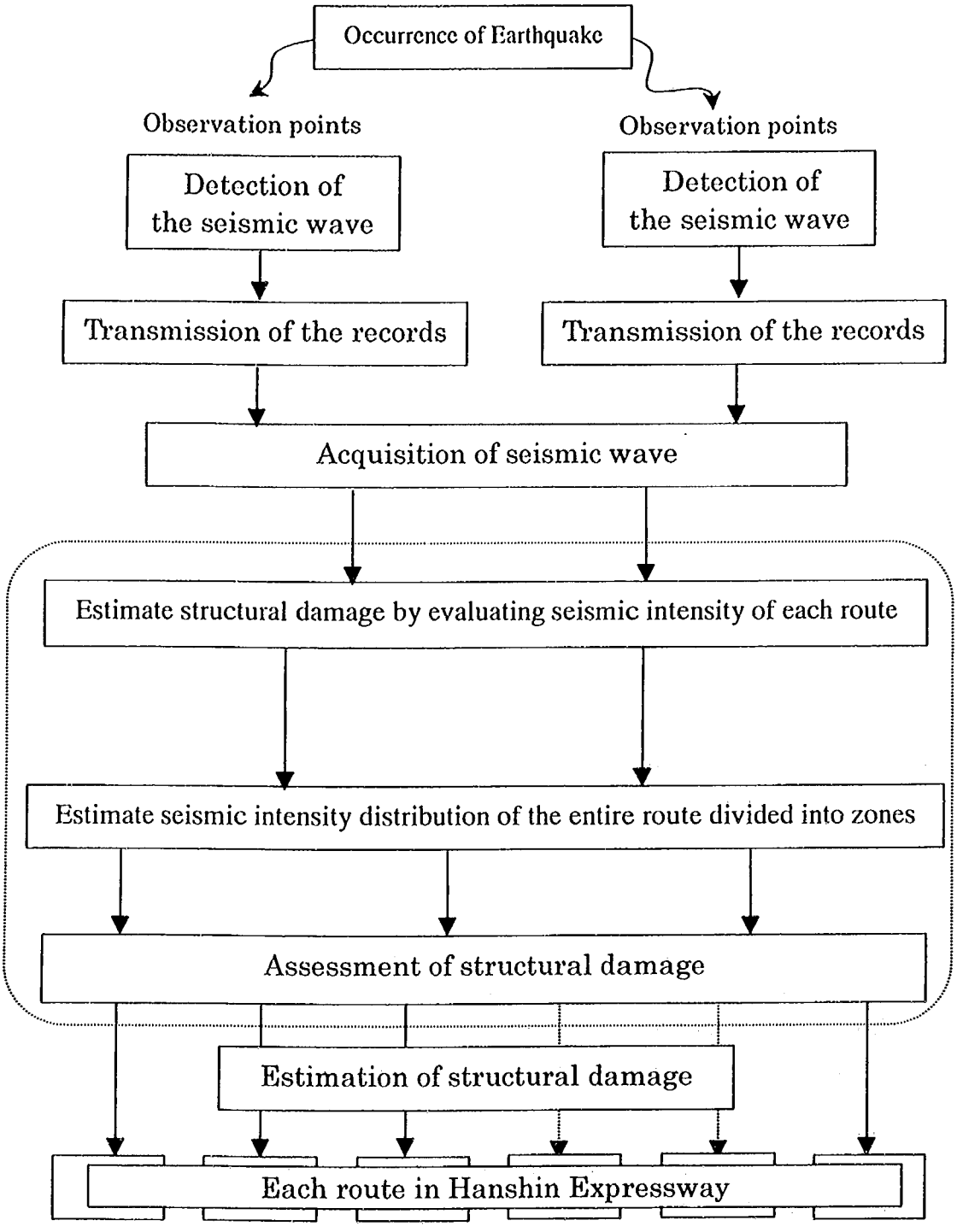


Figure-1 Flow of Real-time Earthquake Damage Estimation System

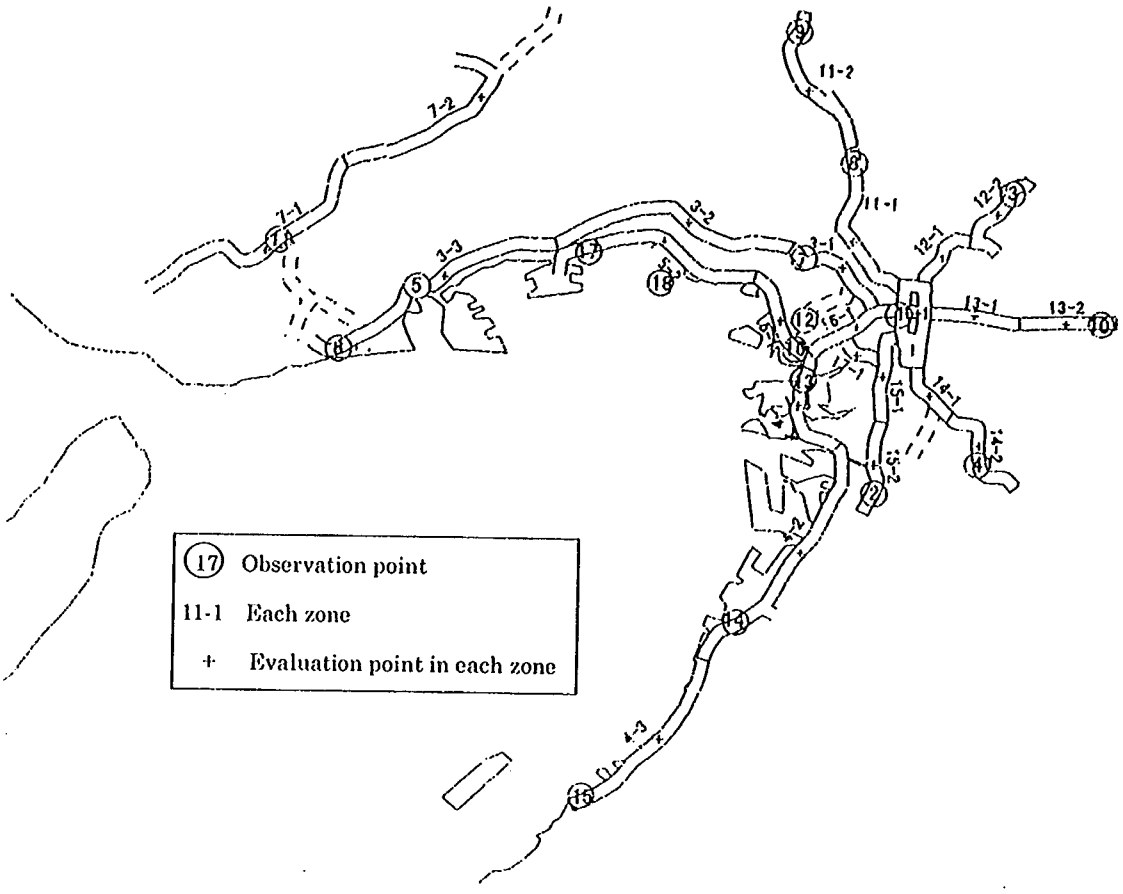


Figure-2 Divided zone to estimate damage

This damage estimation system consists of the following two main subsystems:

A. Subsystem to estimate structural damage by evaluating seismic intensity of each route.
B. Subsystem to estimate seismic intensity distribution of the entire route divided into zones.

These two subsystems are described the following.

A) Subsystem to estimate structural damage by evaluating seismic intensity of each route

Almost all the routes of the Hanshin Expressway are constructed as overhead piers and approximately 80% of these piers are RC structures. Therefore, we planned to perform seismic response analyses for a number of seismic motions based on database obtained by calculating RC pier capacity in advance to analytically determine the

relationship between the seismic intensity and the degree of damage (plasticity ratio) of RC piers

Seismic wave database (hereafter SWDB)

Prior to establishing this subsystem, total 32 seismic waves were collected from the past observation records to study the various cases of estimated seismic motion. We decided to prepare seismic waves of which amplitude was adjusted by ×0.5,×1.5 and× 2.0 by assuming the above 32 waves as standards to study a total of 128 waves (32×4).

Pier Database (hereafter PDB)

Technical specifications of the total 1425 piers after seismic retrofit performed in HEPC were used as the PDB. The histogram of natural periods, and yield magnitudes (*khy=Pa/W*) are shown in Figure 3. The natural periods of 97% are distributed in the range between 0.2 and 1.2 sec with a median value of T=0.69sec.

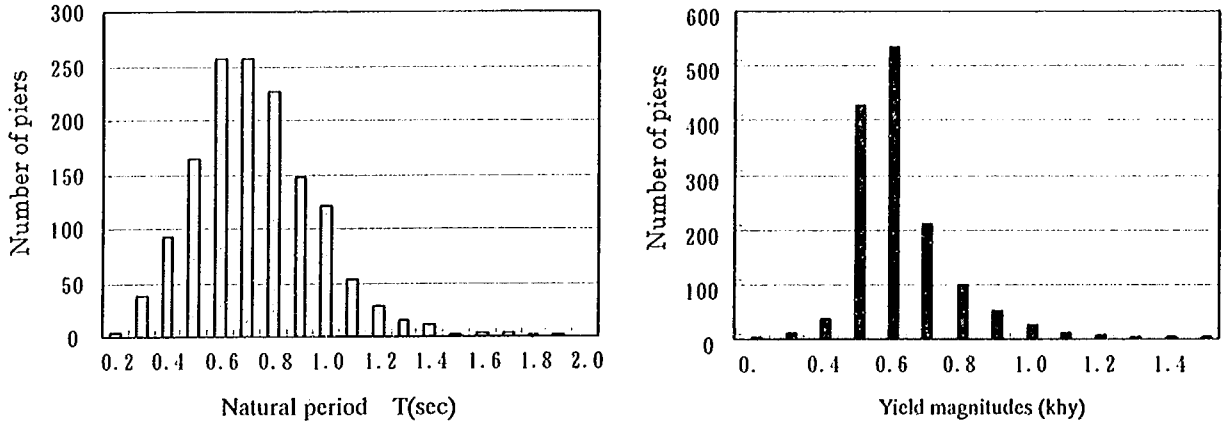


Figure-3 Pier Database

Response analyses

Since the degree of damage of structure is estimated by plasticity ratio of pier, it is necessary to determine response plasticity ratios of PDB (1425 piers) by a non-linear response analysis for SWDB (128 waves). However, since it takes a huge amount of time to perform non-linear time history response analyses for 128×1425 data, the response-plasticity ratios of structures are estimated by using the required yield magnitude spectrum. The required yield magnitude spectrum, based on one-degree-of-freedom non-linear time history analysis, enables us to estimate the response plasticity ratio from the yield

magnitude of structures and the natural period with relatively high accuracy. Therefore, the calculation of the required yield magnitude spectrum for 128 waves in advance immediately provides the response-plasticity ratio of piers using the technical values (yield magnitude k_{hy} and natural period T) of the piers.

Seismic intensity index

Several indexes for the seismic intensity correlation with damage of structures have been proposed. Typical indexes among those are the maximum acceleration, the maximum velocity, the *SI* value, the maximum response acceleration and so on. Firstly, these seismic intensities of SWDB are prepared is calculated and then the correlation between the calculation results and the response-plasticity ratio of each pier obtained in the above item is studied.

An example of the relationship between the seismic intensity and the response-plasticity ratio approximated by a quadratic parabola is shown in Figure 4. Each plot shows the average value of the response plasticity ratio for PDB of 1425 piers against SDB of 128 waves. And, the correlation between each seismic intensity index and the structural response plasticity ratio is shown in Table 1. Here it is found that SI' has the best correlation with the response-plasticity ratio.

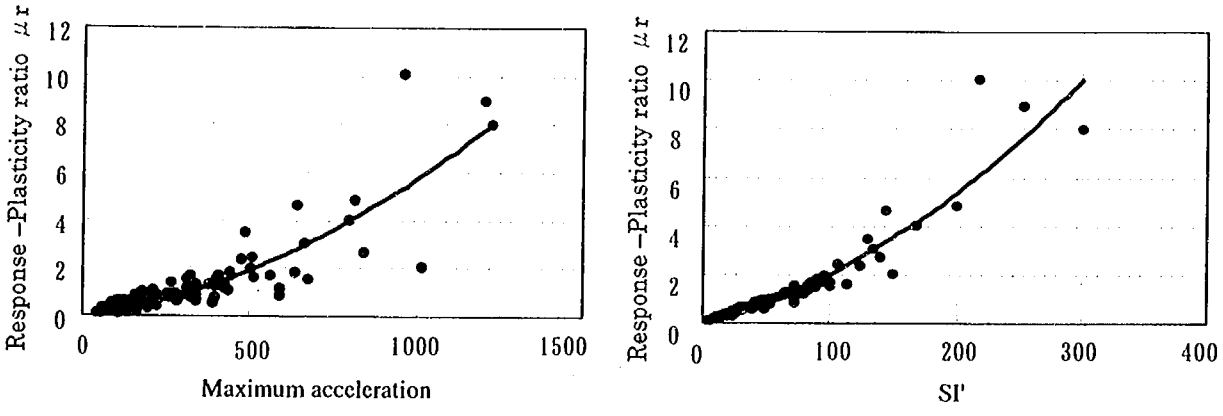


Figure-4 The relationship between the seismic intensity plasticity ratio

Table-1 The correlation between each seismic intensity index and the structural response plasticity

	Maximum acceleration	Maximum velocity	Maximum response acceleration	SI	SI'
Fluctuation coefficient	0.53	0.56	0.61	0.31	0.19

The spectrum intensity *SI* is shown by the following equation assuming that the natural periods of common structures are in the range between 0.1 and 2.5 (generally damping *h* of 20% is used):

$$SI = \int_{0.1}^{2.5} S_v(T,h)dT$$

When observing piers of the Hanshin Expressway, it is found that the natural periods concentrate in the range between 0.2 sec and 1.2 sec as shown in Figure 3. Therefore the spectrum intensity *SI'* is newly defined as the following equation:

$$SI' = \int_{0.2}^{1.2} S_v(T,h)dT$$

Seismic intensity and damage estimation method

In the above clause, it is found that the spectrum intensity *SI'* has the best correlation with the response plasticity ratio. Here the relation between *SI'* and the actual damage condition is studied.

Regarding general RC piers, the relation between the response-plasticity ratio and the damage condition is shown in Figure 5. Therefore, the relation between the degree of damage and the response-plasticity ratio is evaluated below :

0) Damage rank E

No damages

1) Damage rank D

The case in which the response acceleration of superstructure is 300 gal or more is provided with the rank D.

2) Damage rank C

The case in which the response plasticity μr is 1.0 or more is provided with the damage rank C as an index of the seismic intensity where the

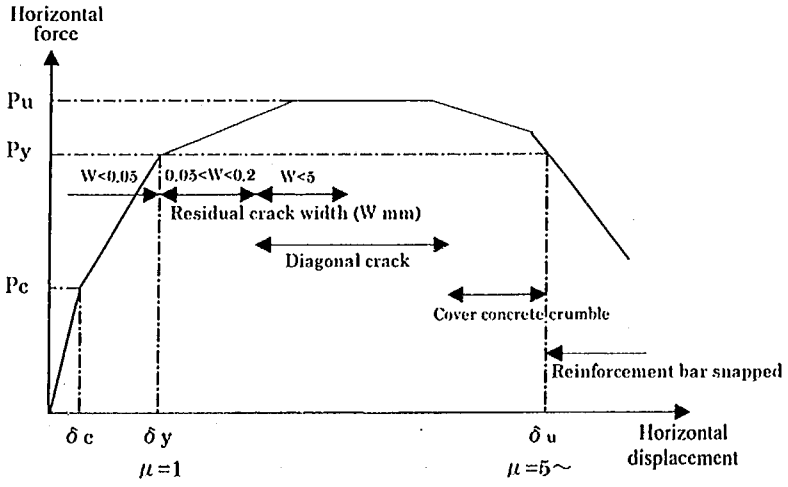


Figure-5 Relationship between the degree of damage and plasticity ratio

response of structures exceeds the yield strength to enter the plastic region. If the structure yields only a little, the structure can be restored to the normal condition with little or no repairs.

3) Damage rank B

When the response plasticity ratio μr exceeds 2 or 3, the residual cracks become larger and it is necessary to repair the cracks damaged by the earthquake. Therefore, the case in which μr exceeds 2 is provided with the damage rank B.

4) Damage rank A

The case in which the response plasticity ratio exceeds the ultimate plasticity ratio is provided with the damage rank A considering the degree of the damage that the structure reaches the ultimate condition.

The above evaluation ranks are summarized in Table 2.

Table-2 Relationship between the degree of damage and the response-plasticity ratio

Damage rank	Degree of the damage	Evaluation criterion
E	No damages	
D	Part of joints and bearing are damaged	Response acceleration >300gal
C	Middle damage	$\mu r>1.0$
B	Big damage (necessity of repair)	$\mu r>2$
A	Serious damage (necessity of repair and reinforce)	$\mu r>\mu u$

Now it is necessary to define the relationship between the response-plasticity ratio and the spectrum intensity SI' estimated in Table 2. Therefore, from the relation between the SI' values and the response-plasticity ratios obtained against PDB and SWDB:

(1) Perform response calculation of 1425 piers against a certain seismic wave by the required yield magnitude spectrum, sum up the number of piers subjected to the response of the damage rank A and higher, B and higher ··· and D and higher, and calculate the damage probability (=the number of piers subjected to the response of the damage rank X and higher/1425×100%) for each damage rank corresponding to the SI' value of the seismic wave.

(2) Plot the damage probability for each damage rank A through D against the SI' value of 128 seismic waves and evaluate the relationship between the spectrum intensity SI' and the damage rank.

Now the relationship between the SI' value and the damage probability of the damage rank C and higher is shown in Figure 6. It is found that the piers subjected to the damage rank C approximately appear from the SI'=30, and the piers of approximately 90% are subjected to the damage rank C when SI'=100.

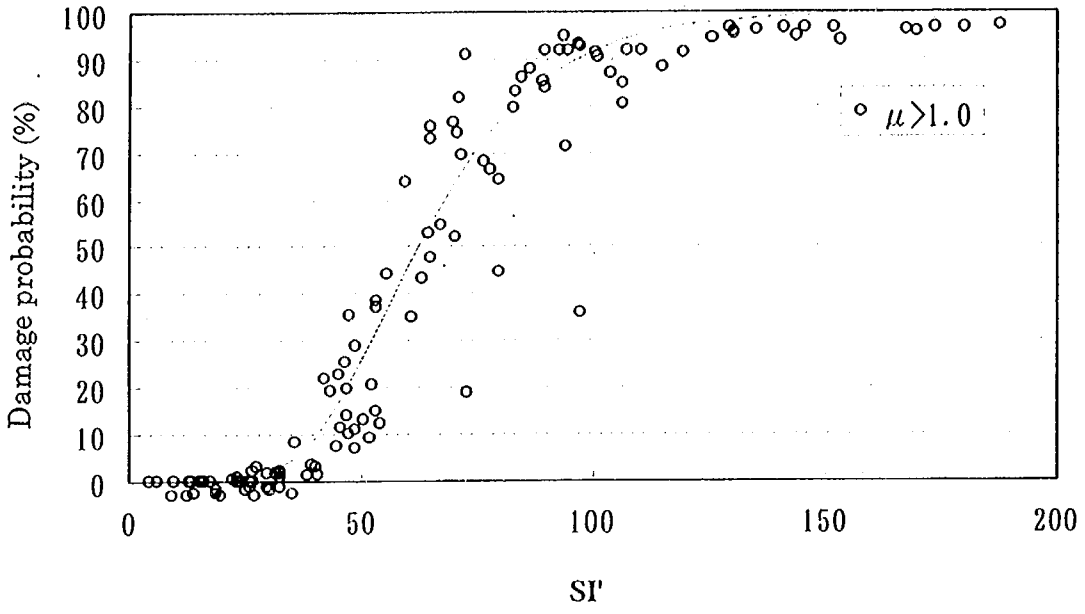


Figure-6 Relationship between SI' and damage probability on Damage Rank C

Table-3 Damage rank evaluation criteria

Damage rank		D	C	B	A
		acc>0.3	μ>1.0	μ>4.0	$\mu > \mu u$
SI'	Average	17.7	33.0	64.5	157.5
	Standard deviation	6.1	11.6	21.5	67.6
	SI' with non-exceeding probability of 95%	9.7	17.8	35.5	74.7

Each damage probability (cumulative hazard curve) for the damage rank A through D approximated by logarithmic normal distribution is also shown in Figure. 7. The application of Figure 7 enables us to estimate the percentage for each damage rank of piers in certain spectrum intensity *SI'*. The damage rank evaluation criteria, assuming SI' with non-exceeding probability of 95% for each damage rank as standard in this figure, are shown in Table 3.

The damage of structures can be estimated from the seismic intensity according to these evaluation criteria.

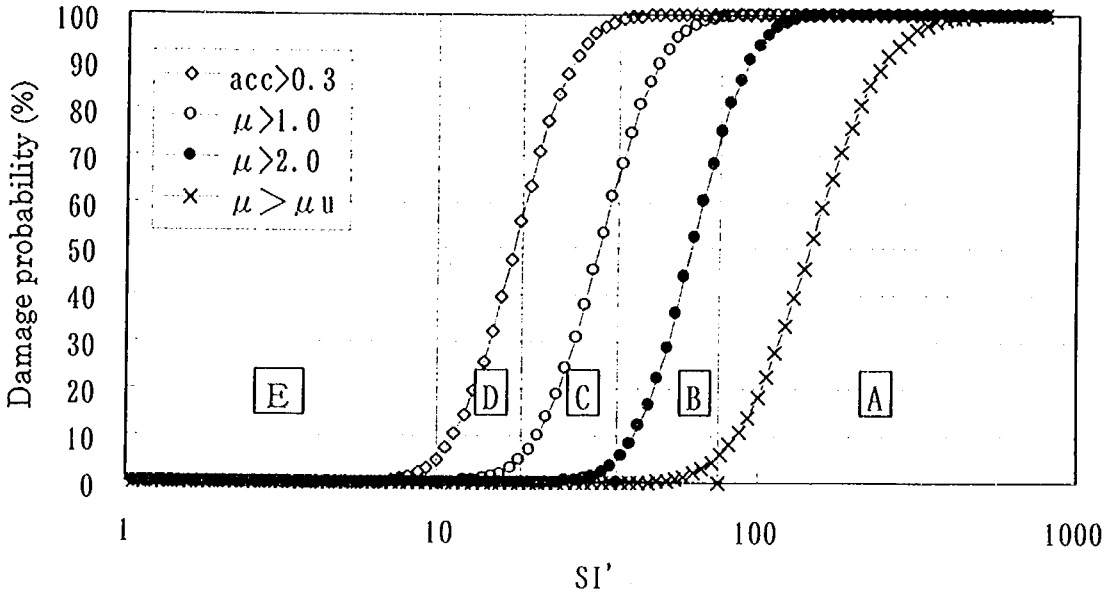


Figure-7 Relationship between SI' and damage probability

B) Subsystem to estimate seismic intensity distribution of the entire route divided into zones

So far, damage estimation methods for structures have been studied in case that the SI' values at the evaluation point are known. However, since the installation points (observation points) of the strong motion seismograph do not coincide with the evaluation points, it is necessary to calibrate SI' at the evaluation points from SI' at the ground surface of the observation points. Now these estimation methods are described in the following:

Seismic intensity estimation methods at evaluation point

When estimating SI' at the representative point of the zone (evaluation point) from

the observation point, it is desirable to perform interpolation on the bed rock surface where the local influence of surface layer is excluded. Therefore, the SI' at the evaluation point is estimated from SI' at the observation point according to the following procedure (Figure 8):

1) Conversion from SI' at the ground surface of the observation point to SI' at the bed rock surface of the observation point
2) Estimation of SI' at the bed rock surface of the evaluation point by the interpolation of SI' at the bed rock surface of the observation points
3) Conversion from SI' at the bed rock surface of the evaluation point to SI' at the ground surface of the evaluation point

In order to perform the above conversion and interpolation, it is necessary to develop:

a) Conversion method for SI' of the ground surface and SI' for the bed rock surface

b) Planar interpolation method on bed rock surface.

An outline of the estimation method of SI' value at the ground surface of the evaluation point is shown in this figure.

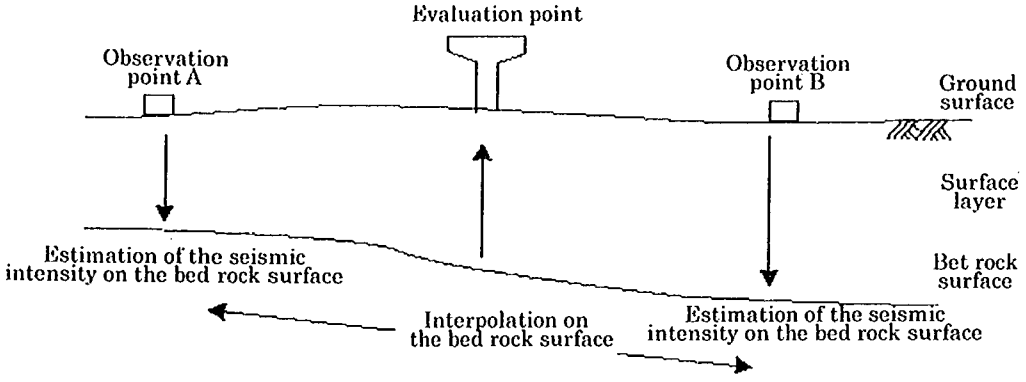


Figure-8 Outline of the estimation method of seismic intensity

a) Conversion method of SI' at ground surface and SI' at bed rock surface

When estimating SI' value of the bed rock surface from SI' value of the ground surface at the observation point, or estimating SI' value of the ground surface from the bed rock surface at the evaluation point, it is effective to perform the response analysis of the ground, such as an overlapping-reflection analysis. However, it is not reasonable to perform the response analysis of each point in real time because it takes too much time to calculate. Therefore, the ground-response analyses at relevant points are performed to 128 seismic waves (SWDB) in advance based on the soil-boring log at the observation and

evaluation points to express ground amplitude characteristics by approximate equations. Here, an example of the relationship of the bedrock - surface layer function at the observation points is shown in Figure 9.

The conversion function for the surface layer to the bedrock is shown in Figure 9 and the inverse conversion from the bedrock to the surface layer is performed in the similar manner.

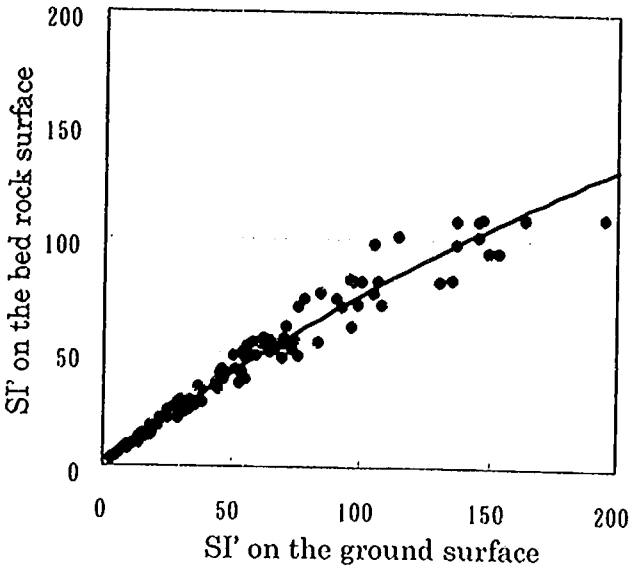


Figure-9 Relationship of the SI' on the bed rock surface layer

b) Planar interpolation method on bed rock surface

Since the evaluation points do not coincide with the observation points, SI' value on the bedrock surface at the evaluation point is estimated by interpolating SI' value on the bedrock surface at each observation point. The interpolation method shown in Figure 10 is now under consideration. In other words, the average of SI' value at all observation points is assumed as the SI' value at the evaluation point by weighing, based on the distance from the evaluation point. This weighing factor was assumed to exponentially decrease according to the distance.

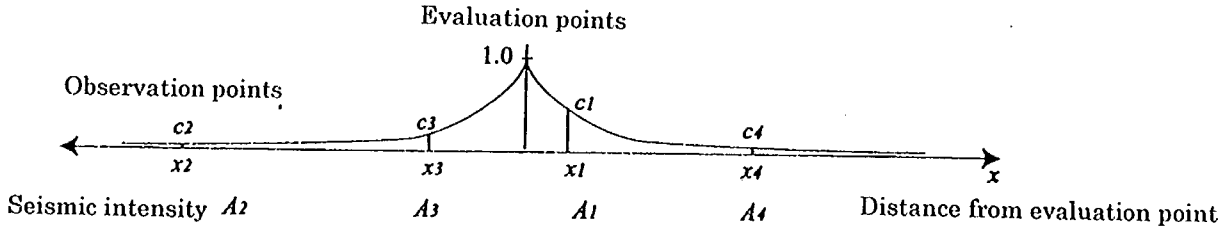


Figure-10 Interpolation method of seismic intensity

Conclusion

As described in this paper, the relationship between the seismic intensity (SI' value) and the degree of damage was clarified by summing up non-linear response with the required yield magnitude spectrum in cases entering the seismic wave database having 128 waves based on the RC pier database occupying more than 80% of Hanshin Expressway.

The method for estimating SI' value at the evaluation point for each zone, where the damage degree is evaluated, from SI' value at the observation point where a seismometer is installed was described. And it is clarified that "SI' value" that is newly defined has the best correlation with response-plasticity ration to the piers of Hanshin Expressway.

We plan to continue the study to further improve the estimation accuracy for the purpose of completing the earthquake damage estimation system.

Acknowledgment

The authors would like to acknowledge the members of the Technical Council of Hanshin Expressway Public Corporation.

Reference

1) Yutaka Nakamura: View of study: Study of general earthquake disaster prevention system, Journal of Civil Engineering Society,No.531.pp.331-340,1996

2) Shun'etsu Odagiri, Hideki Sugita and Masahiro Kaneko: Development of real time earthquake disaster prevention information system for public civil engineering facilities, Civil Engineering Information,39-9,pp.20-25,1997

3) Land Development Technical Research Center, Earthquake Disaster Restoration Technology Study Civil Engineering Committee: Report on restoration technology of structures damaged by earthquake, 1984

The Newly Developed AASHTO Guide Specifications For Seismic Isolation Design

Hamid Ghasemi, Ph.D.

The wide-spread use of seismic isolation strategy to combat earthquakes in the U.S. can be credited to a number of factors. 1) the development of the AASHTO Guide Specifications for Seismic Isolation Design in 1991, 2) HITEC's full-scale dynamic testing of a dozen seismic isolation and energy dissipation systems. (This was completed and twelve reports on their dynamic characteristics and longevity were published in 1999.), 3) a partnership among academic researchers, seismic design engineers and industrial entrepreneurs, and 4) the inherent logic and economy of the concept.

In 1997, the newly formed Seismic Committee T-3 was charged with the task of updating the guide specifications. The work was completed in 1999 and AASHTO published the new Guide Specifications for Seismic Isolation Design. In addition to numerous modifications, the new guide specification provides recommendations for design of sliding isolation bearings as well as elastomeric bearings.

This paper provides an overview of the new guide specifications.

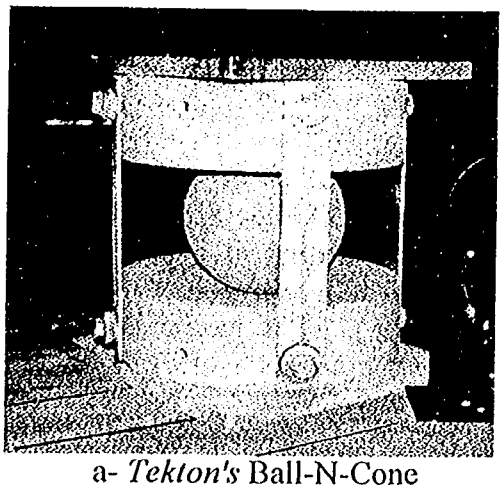
Introduction

The ductility-design philosophy is the mainframe of modern seismic design guidelines in the U.S. and most other countries. While this design philosophy provides safety against collapse, it tends to be costly due to the damage induced in plastic-hinge zones and severe lateral displacements after even a moderate earthquake. Therefore, in recent years design engineers have sought an alternative design philosophy that avoids or limits damage to bridge elements in order to maintain post-earthquake serviceability. One approach that has shown to be promising in limiting damage to bridge components due to moderate ground motions is the use of Seismic Isolation.

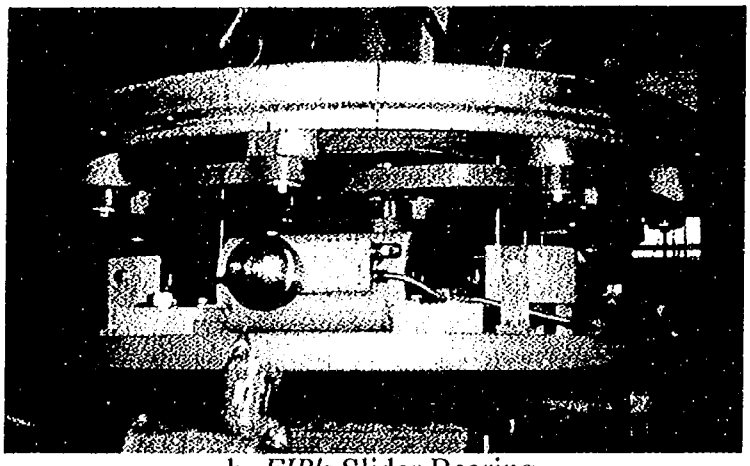
In recent years, the seismic isolation approach has reached a level of maturity in the U.S. Since 1985, when the California Department of Transportation (Caltrans) first used the seismic isolation approach as a retrofit measure for the Sierra Point Overpass, over 200 bridges have utilized this approach in the U.S. This can be credited to the development of numerous practical isolation systems and the 1999 AASHTO Guide Specifications for seismic isolation design.

Testing and Evaluation

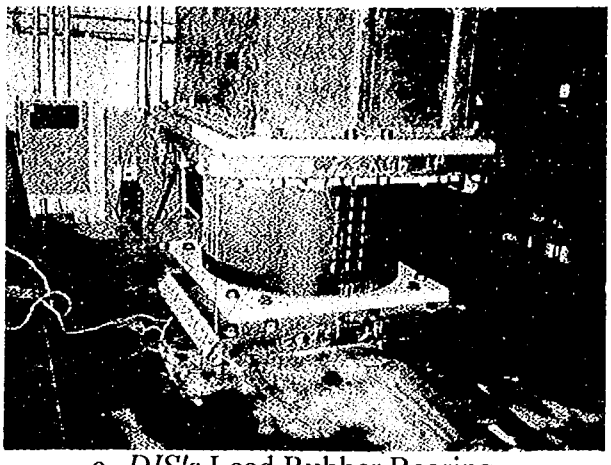
In 1994, an extensive testing and evaluation program of eight seismic isolation systems commenced. The program determined their dynamic characteristics, longevity, functionality in extreme environments, resistance to aging and creep, fatigue and wear and size effects. The program was established under a cooperative agreement among the Federal Highway Administration (FHWA), Caltrans, and the Highway Innovative Technology Evaluation Center (HITEC) who administered the program. Figure 1 shows some of the systems tested.



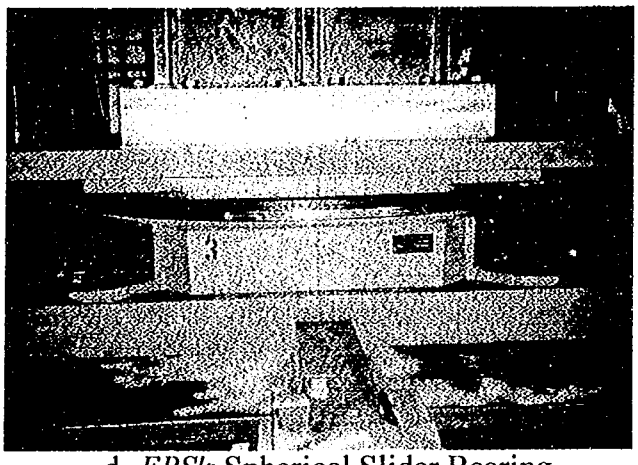
a- *Tekton's* Ball-N-Cone



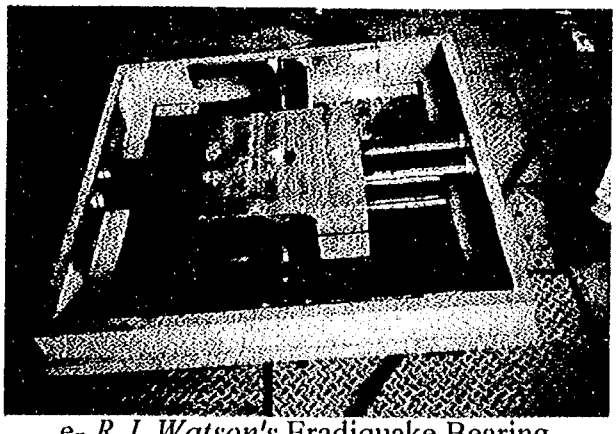
b- *FIP's* Slider Bearing



c- *DIS's* Lead Rubber Bearing



d- *EPS's* Spherical Slider Bearing



e- *R.J. Watson's* Eradiquake Bearing

Figure 1 - Five of the seismic isolation bearings submitted for testing

Updating the AASHTO Guide Specification

In 1995, the AASHTO Subcommittee on Bridges and Structures formed the T-3 Seismic Design Technical Committee with the task of modifying the 1991 Guide Specification for Seismic Isolation Design. The modification was needed because the old Guide Specification failed to incorporate systems other than elastomeric bearings. At the time of its development, elastomeric systems were the only readily available isolation bearings on the U.S. market. This made it difficult for systems other than elastomeric lead-rubber bearings to be competitive. There was also a lack of data on the dynamic characteristics and the longevity of the isolation systems then in use.

Committee T-3 formed a task group and developed the new specification by considering the current state-of-practice, results of completed and ongoing technical efforts, and research activities in the field of seismic isolation. The updated Guide Specification for Seismic Isolation Design was completed in May 1997 and was approved and published in February of 1999 by the AASHTO Subcommittee on Bridges and Structures. In addition to numerous, the new guide specification provides recommendations for design of sliding isolation bearings as well as elastomeric bearings.

The 1999 AASHTO Guide Specification for Seismic Isolation Design

The New Guide Specifications for Seismic Isolation Design made the following changes:

1. Numerous editorial changes and additions providing additional commentary and making the Guide Specification consistent with the Standard Specifications.

2. Changes in the methods of analysis and in particular in the Uniform Load Method. This method now accounts for substructure flexibility.

3. The requirement for sufficient lateral restoring force in the isolation system has been expanded to two requirements. The first is provided in order to accommodate imperfections in the installation of isolators, and the second to prevent the development of cumulative offset displacements and a reduction in stiffness due to column rotations.

4. The response modification factors (R-factors) have been reduced to values between 1.5 and 2.5. This implies that the ductility-based portion of the R-factor is unity or close to unity. The remainder of the factor accounts for material overstrength and structural redundancies inherent in most structures. The lower R-factors insure essentially elastic substructure response to the design-basis earthquake.

5. Criteria and procedures are provided for the design of sliding isolation bearings. The increasing use of sliding bearings since publication of the 1991 guide specifications made this addition necessary.

6. A procedure for determining bounding values of isolator properties for analysis and design is included. This procedure is based on the determination of system property modifications factors, termed the λ-factors, by which the nominal design values of isolator properties are

multiplied. The system property modification factors account for the effects of temperature, aging, wear/travel, contamination and other effects.

Response Modification Factor, R

In the ductility design approach, which mainly requires a nonlinear response of the substructure, the inelastic force for different components of the bridge is calculated by dividing the elastic forces by a response modification factor. In the new Guide Specification, the R-factors are taken as half of those given by the standard specifications. These R-factors are in the range of 1.5 to 2.5, of which the ductility-based portion is near unity and the remainder accounts for material overstrength and structural redundancies inherent in most structures. This increases the stiffness of the substructure.

Lower R-factors are required to ensure proper performance of the isolation system during the design-based earthquake. To demonstrate the concept, consider the case of an isolated bridge in which all piers and all isolator units have identical deformational characteristics. Moreover, consider isolator units with Q_d=0.06W and F_{max}=O.2W where W is the gravity load on the isolator units and F_{max} represents the statically equivalent seismic force on the substructure (calculated on the assumption of elastic substructure behavior). Also assume that the substructure is designed for an R-factor of 5, that is, the substructure is designed to have a strength of 0.04W. Actual strength, when accounting for material overstrength, is about 0.06W. Accordingly, inelastic action in the substructure will commence nearly instantaneously with inelastic deformation in the isolator units. Since typically the substructure has lower post-yield stiffness (essentially elastoplastic) than the isolator units above, deformation will occur first in the substructure with the isolator units rendered ineffective. The result would be excessive ductility demand in the substructure.

Methods of Analysis

The Guide Specifications permit four procedures for seismic isolation design. The first 3 procedures are Uniform Load Method (ULM), Single Mode Spectral Method, and Multimodal Spectral Method. The basic premise for these procedures is twofold. First, the energy dissipation of the isolation system can be expressed in terms of equivalent viscous damping; and second, the stiffness of the isolation system can be expressed as an effective linear stiffness K_{eff} (Figure 2). The advantage of a linear assumption is that it permits relatively simple analysis. According to the Guide Specification, the stiffness and damping of substructure should be considered in the ULM procedure.

The forth procedure is a linear time-history method. For isolation systems, where the effective damping expressed as a percentage of critical damping exceeds 30 percent of critical, the fourth procedure is performed utilizing the hysteresis curves of the isolation system.

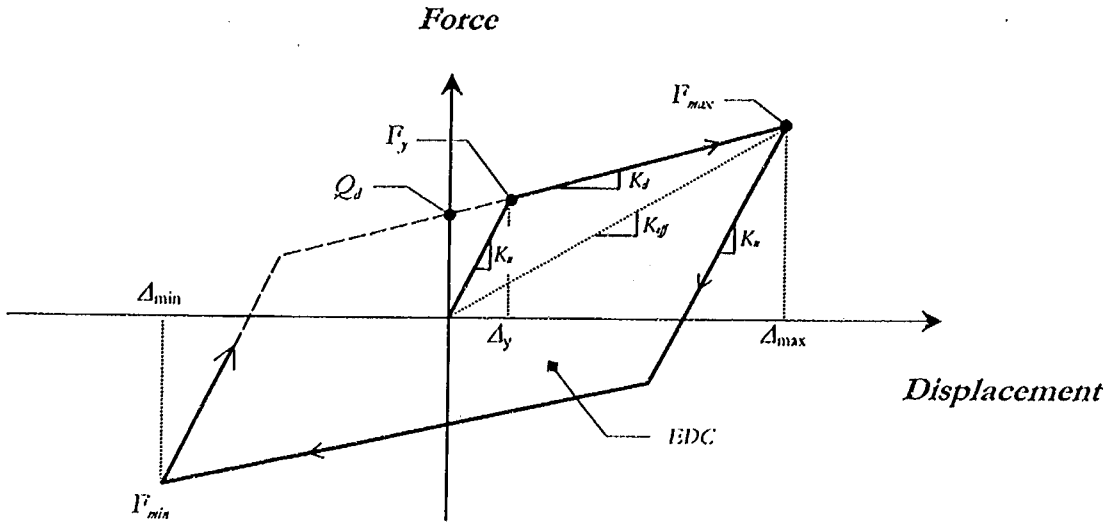


Fig. 2 - An idealized force-displacement (hysteretic) loop of an isolation bearing

EDC = Energy dissipation per cycle
(The area enclosed by the force-displacement curve = $4Q_d(\Delta_{max} - \Delta_y)$)
K_{eff} = Effective stiffness
β = Equivalent viscous damping of the system
K_u = Elastic (unloading) stiffness
K_d = Post-elastic stiffness
F_{max} = Maximum positive force during a single cycle of testing
F_y = Yield force
Δ_{max} = Maximum bearing displacement during a single cycle of testing
Δ_y = Bearing yield displacement
Q_d = Characteristic strength (Max. Lateral shear force at zero displacement ≈ 5 to 9 percent of the total gravity loads (DL+LL))

Upper and Lower Bound Analyses

One of the two most significant changes to the document is the requirement to consider long term environmental and temperature changes in the properties of the isolation system. An attempt has been made to account for the effects of long term aging, contamination, scragging, wear/travel and temperature effects.

An upper and lower bound analysis is required if the performance of the structure varies by more than 30 percent while the maximum and minimum values of the isolator properties are used. The purpose of this upper and lower bound analysis is to determine the maximum forces on the substructure elements and the maximum displacements of the isolation system (Figure 3).

The force deflection characteristics of a bilinear isolation system (Figure 2) have two important variables Q_d and K_d, both of which are affected by environmental and temperature effects. The area of the hysteresis loop or the energy dissipation per cycle (EDC); hence the damping-related

coefficient, β, is influenced primarily by Q_d. The effective stiffness, K_{eff}, is influenced by Q_d and K_d. The variation of K_{eff} alters the effective period, which influences the response. Thus, the Guide Specification requires that, in all design procedures for seismic isolation design, the analysis shall be conducted once with maximum probable properties and once with the minimum probable properties.

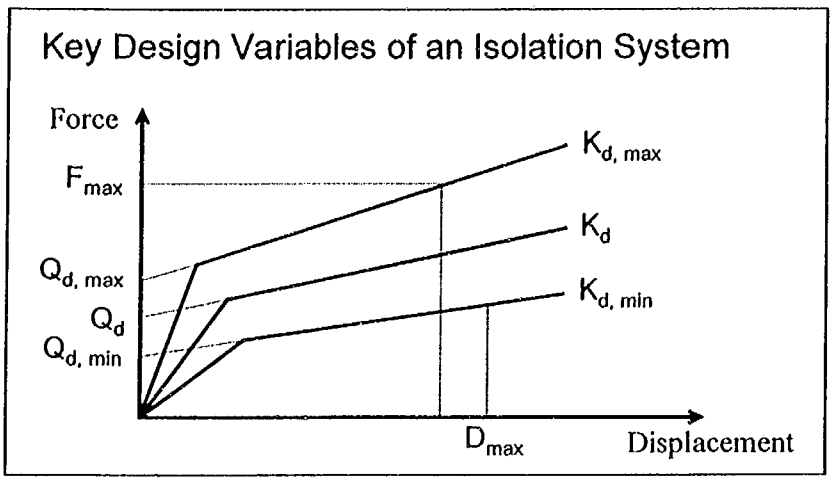


Figure 3 - Upper and lower bound analysis

System Property Modification Factors (λ)

Values of the probable maximum and minimum properties are based on a statistical analysis of relevant property variations. The Guide Specifications defined the ratios of the maximum and minimum properties to the nominal ones by a series of System Property Modification Factors, λ_{max} and λ_{min}. Different λ_{max} and λ_{min} values are associated with different aspects of specific isolation systems, such as wear, temperature, environmental effects, etc. In the absence of such information, provisional values defined in Appendix A of the Guide Specification will be used.

Sliding Isolation and Other Systems

Since developement of the 1991 Guide Specification, there has been a significant progress in the development and understanding of isolation system technologies other than elastomeric based. The new Guide Specification has two sections that cover sliding bearing design and construction, as well as a section on all other types of isolation systems.

The section on sliding bearings cover bearings that use PTFE and stainless steel as the primary sliding surface. The PTFE sections were modeled after the existing AASHTO LRFD specification and the NCHRP Report No. 10-20A. Although service contact stresses for PTFE are the same as those defined by the LRFD specification, they may be exceeded when the higher values are justified by tests on full-size bearings and by wear tests as for other sliding interfaces requirements.

Elastorneric Bearing Systems: λ-Factors

Elastomeric bearings are produced in a variety of compounds so that a vast number of experiments are needed to establish the relevant λ-factors.

For high damping rubber bearings, it is appropriate to establish λ-factors for the effective stiffness (or equivalently, effective shear modulus, G_{eff}) and the damping ratio (β). For lead-rubber bearings, it is appropriate to establish λ-factors for the rubber shear modulus (which affects the post-elastic stiffness) and the area of the hysteresis loop (which depends on the lead properties).

The aging factors depend significantly on the rubber compound, and recommended values in the absence of further test data are shown in Table 1. As a general rule, this factor is expected to be close to unity for low damping natural rubber (LDRB) and to be larger for high damping rubber (HDRB). The temperature factors are shown in Table 2.

TABLE 1: Aging λ-factors

	K_d	Q_d
Low Damping Natural Rubber	1.1	1.1
High Damping Rubber with Small Differences Between Scragged and Unscragged Properties	1.2	1.2
High Damping Rubber with Large Difference Between Scragged and Unscragged Properties(')	1.3	1.3
Lead	-	1.0
Neoprene	3.0	3.0

TABLE 2: Temperature λ-factors

Minimum Temperature for Design		K_d			Q_d		
°C	°F	HDRB(1)	HDRB (2)	LDRB (2)	HDRB(1)	HDRB(2)	LDRB (2)
21	70	1.0	1.0	1.0	1.0	1.0	1.0
0	32	1.3	1.3	1.3	1.2	1.1	1.1
-10	14	1.4	1.4	1.4	1.4	1.2	1.1
-30	-22	2.5	2.0	1.5	2.0	1.4	1.3

(1) Large difference between scragged and unscragged properties
(2) Small difference between scragged and unscragged properties
A large difference is one in which the unscragged properties are at least 25 percent more than the scragged ones. Values for natural low damping rubber in lead-rubber bearings are based on a Grade 3 elastomer.

Sliding Bearing Systems: λ-Factors

The aging factors are based on friction data for rough stainless steel plates with PTFE or other materials, and are shown in Table 3. It is assumed that the plate has uniform corrosion, which creates a rougher sliding surface. The temperature factors are shown in Table 4.

TABLE 3: Aging λ-factors

	Unlubricated PTFE		Lubricated PTFE		Bimetallic Interfaces	
Environment/ Condition	Sealed	Unsealed	Sealed	Unsealed	Sealed	Unsealed
Normal	1.1	1.2	1.3	1.4	2.0	2.2
Severe	1.2	1.5	1.4	1.8	2.2	2.5

- Values are for 30 year exposure of stainless steel. For chrome-plated carbon steel, multiply values by 3.0. This implies that corrosion increased shear force by 7.5 times.
- Unsealed conditions assumed to allow exposure to water and salt, thus promoting further corrosion.
- Severe environments include marine and industrial environments.
- Values for bimetallic interfaces apply for stainless steel-bronze interfaces.

TABLE 4: Temperature λ-factors

Minimum Temperature for Design		Unlubricated PTFE	Lubricated PTFE	Bimetallic Interfaces
°C	°F			
21	70	1.0	1.0	To be established by test
0	32	1.1	1.3	
-10	14	1.2	1.5	
-30	-22	1.5	3.0	

For bimetallic interfaces the factor is based on data for stainless steel and leaded bronze interfaces. Increases in friction due to stress effects have been observed in the absence of corrosion.

Testing Requirements

In General, there are three classes of test to be performed on any isolation system before installation. These are system characteristic tests, prototype tests, and production quality control tests.

I- System Characterization Tests

The overall stability and performance of any isolation system under different environmental condition should be established prior to its use. These tests substantiate the basic properties of the individual isolator units as well as the behavior of an isolation system. Therefore, these tests include both component tests of individual isolators and shake table tests of complete isolation system.

These tests are not project specific and need to be performed only once. They are normally conducted when a new isolation system is developed or when a substantially different version of an existing isolation system is evaluated. For system, with similar material and performance, there is no need to repeat the shake table tests.

II- Prototype Tests

These tests have been expanded to a total of seven tests. They are used to verify system performance under thermal loading, live load response, seismic performance, displacement dependent performance, survivability, and performance after earthquake. These tests are:

1. Thermal: Three fully reversed cycles of loads at a lateral displacement corresponding to the maximum thermal displacement.

2. Wind and Braking: Twenty fully reversed cycles between limits of plus and minus the maximum live load caused by wind or braking at a duration not less than 40 seconds. After the cyclic testing, the maximum load will be held for one minute.

3. Seismic: Three fully reversed cycles of loading at each of the following multiples of the total displacement: 1.0, 0.25, 0.50, 0.75, 1.0, and 1.25 in the sequence shown at a period equal to the isolation system.

4. Seismic: (15S*i*)/B cycles, not to exceed 25 but not less than 10 fully reversed cycles of loading at 1.0 times the design displacement. The test shall be started from a displacement equal to the offset displacement.

5. Wind and Braking: repeat test 2 to verify service load performance after a seismic event.

6. Performance Verification: Three fully reversed cycles of loading at the design displacement.

7. Supplemental Tests: Under special situation, more tests may be required to meet the project specific requirement. These tests may include stability, wear, and fatigue, and low temperature tests.

III- Production Quality Control Tests

Unlike isolators used in a building project, production quality control tests shall be conducted on every isolator bearing. Bearings used for bridge isolation projects are generally large and of limited number. A large variation between bearings can cause a great deal of difference in system performance. To ensure all bearings are within a certain performance range, quality control tests on every bearing are needed.

Conclusion

An updated AASHTO Guide Specification for Seismic Isolation Design has been developed by the T-3 Task Group. It reflects the influence of new isolator types, and by reducing the R-factors increases the substructure strength to better integrate the response of the structure and the isolator system. The effect of wear, temperature and environment effects on the isolator material is also considered by providing guidance in obtaining the λ-factors.

Although there are significant changes and improvements reflect the current state of knowledge development, it is far from perfect and will continue to be refined as with any code document. The contribution of all the member of the T-3 task group is gratefully acknowledged.

GUIDELINES FOR TESTING PASSIVE ENERGY DISSIPATION DEVICES

Michael A. Riley[1], Fahim Sadek[2], and Bijan Mohraz[3]

Abstract

Supplemental damping devices are effective for improving the dynamic response of structures by reducing their response to earthquake and wind excitations. Wide acceptance of these devices depends on good documentation of their performance, and on the availability of standards for evaluating and testing them. In response to this latter need, the National Institute of Standards and Technology initiated a research program to develop guidelines for testing passive, supplemental damping devices. The objective is to provide a standardized series of prototype and production tests, which are independent of both the device type and application. This paper provides an overview of the guidelines and describes their development.

Introduction

Extensive research and initial implementations have shown that passive energy dissipation devices can significantly improve the dynamic response of structures (Hanson, et al., 1993; Soong and Constantinou, 1994; Sadek, et al., 1996; and Soong and Dargush, 1997). These devices, which are also known as passive control devices, supplemental dampers, or passive dampers, can reduce structural responses due to wind, earthquake, and other dynamic loads. Such devices can absorb part of the energy induced in the structure, minimizing the energy dissipation demand on the primary structural members, and thus reducing the interstory drifts and minimizing non-structural damage. In addition, they can be designed to provide additional stiffness to the structure and to be easily replaced if they are damaged.

Research and development have led to a variety of passive energy dissipation devices. They use a range of materials and mechanisms, which operate on principles such as sliding friction, yielding of metals, deformation of viscoelastic materials, and fluid flow through orifices.

These devices are now used in the design of new structures and the rehabilitation of existing ones in Canada, Japan, Mexico, New Zealand, Europe, and the United States. Nevertheless, most of these devices are still designed and manufactured on a per-project basis. Design and test standards are necessary for their widespread use. Although some design and test guidelines already exist (NEHRP, 1997; Taylor and Constantinou, 1994), most are specific to certain types of structures, or have limited applications.

In response to the need for improved and comprehensive test standards, the Building and Fire Research Laboratory (BFRL) of the National Institute of Standards and Technology (NIST) has initiated a program to develop guidelines for testing supplemental damping devices. These guidelines, titled "Guidelines for Testing Passive Energy Dissipation

---

[1] Research Structural Engineer, National Institute of Standards and Technology, Gaithersburg, MD.
[2] Research Associate, Department of Mechanical Engineering, Southern Methodist University, on assignment to the National Institute of Standards and Technology, Gaithersburg, MD.
[3] Professor, Department of Mechanical Engineering, Southern Methodist University, Dallas, TX.

Devices" (Riley, et al., 1999), have been completed and are currently being reviewed. The guidelines recommend prototype and quality control tests for passive energy dissipation devices. In addition, they describe a series of basic property tests, which may be used as the basis for evaluating future devices as they are developed.

Types of Energy Dissipation Devices

For the purpose of the testing guidelines, energy dissipation devices can be categorized according to their mechanical behavior as rate dependent, rate independent, or others. A brief description of some types of common devices in each category and their properties is given below. These devices have been used in structures or laboratory experiments, and most are commercially available. This list of devices, however, is not complete, due to the large number of existing devices. In addition, the industry is rapidly evolving and it is anticipated that many additional devices will be developed in the future. The test guidelines described in this paper are intended to be applicable to all types of passive devices; not just those listed here.

Rate Independent Devices

Devices with force-displacement response characteristics that are primarily a function of the displacement amplitude are classified as rate independent devices. The behavior of these devices is independent of the relative velocity or the frequency of motion. They include friction and metallic devices.

Friction Devices

Friction devices use the friction between sliding surfaces to dissipate energy. They generally exhibit rigid-plastic behavior and their force response can be modeled by simple Coulomb friction, so the force-displacement curves of the devices are rectangular loops. These devices can be characterized by their displacement amplitude and slip-load.

Friction devices can dissipate large amounts of energy even at low velocities, while their peak forces are bounded even at large velocities. Unfortunately, their effective stiffness can be large when motions are small and their non-linear response complicates structural designs.

A variety of mechanisms can be used to create the friction forces, including sliding or twisting between simple metal surfaces. Using friction pads or wedges may enhance performance of the devices. One type of friction device combines friction pads with a spring mechanism, which gives the device a re-centering capability and slip forces that are proportional to the displacement. Friction devices are typically located in braces or at the intersection of cross braces.

Metallic Devices

Metallic yielding devices take advantage of the stable hysteretic force-displacement behavior of metals to absorb energy. These devices use flexural, shear, or extensional deformations in the metal's plastic range to provide the structure with increased stiffness and

energy dissipation capacity. They typically exhibit hysteretic force-displacement behavior, which can be approximated as bilinear or tri-linear.

These devices tend to be inexpensive to produce and their properties will remain stable over the long lives of buildings and bridges. Unfortunately, they often have a limited number of working cycles, which may require them to be replaced after large seismic events. Like friction devices, their non-linear response can complicate structural designs.

These devices can be installed in the bracing systems of building frames, or used between the structure and foundation of seismically isolated bridges and buildings to increase the damping in the isolation system.

Rate Dependent Devices

Rate dependent devices have force-displacement response characteristics that are a function of either the relative velocity between the ends of the device or the frequency of the motion. The response of the devices in this category, however, may be a function of the relative displacement as well. These devices include solid viscoelastic, fluid viscoelastic, and viscous fluid devices.

Fluid Viscous Devices

Fluid viscous devices are used extensively in a variety of structural and mechanical systems, to reduce responses to vibrations and shock. These devices dissipate energy by forcing a viscous fluid to flow through orifices. They can be designed and constructed to act as ideal viscous dampers, generating only damping forces, but they may exhibit some stiffness at high frequencies.

Fluid viscous devices can dissipate large amounts of energy, over a wide range of excitation frequencies. Since their force response is usually proportional to velocity, designing structures that use these devices is generally straightforward. The life span of these devices tends to be limited only by wear of their seals.

The devices are typically installed in the bracing systems of buildings or used in conjunction with the isolators in seismically isolated structures. They can be used effectively for buildings, bridges, and other structural systems.

Solid Viscoelastic Devices

Solid viscoelastic devices are constructed from constrained layers of acrylic polymers and designed such that they produce damping forces through shear deformations in the polymers. When deformed, the viscoelastic materials exhibit the combined features of an elastic solid and viscous liquid. The resulting response can be modeled using a Kelvin model, which consists of a spring and dashpot in parallel.

These devices have proven to be efficient and cost effective for reducing wind induced vibrations. Unfortunately, their effective stiffness and the damping forces are generally dependent on the excitation frequency and the operating temperature, including the temperature rise due to excitation. Because of this temperature dependence, these devices

Table 1: Test Categories.

Type of Test	Test Category	Notes
Quality Control Tests	Material Properties	Tests of materials and components.
	Production Unit	Tests of completed devices.
Prototype Tests	System Properties	Determination of response properties.
	Applied Loads	Validation of response to realistic loads.
	Reserve Capacities	Validation of response to extreme loads.
Basic Property Tests	Basic Properties	Tests for device development only.

may not be useful in structures, such as bridges, where the climate is not continuously controlled.

These devices are typically used in moment resisting frames, where they are installed in cross braces or in connections between floor trusses and columns.

Fluid Viscoelastic Devices

Fluid viscoelastic devices, such as viscous shear walls, operate by shearing viscoelastic fluids. Their behavior and response characteristics are similar to solid viscoelastic devices, except that the fluid viscoelastic dampers do not exhibit stiffness when static loads are applied. These devices can be modeled with Maxwell model, which consists of a spring and dashpot in series.

Other Types of Dampers

Other energy dissipation devices have been developed that cannot be classified as either rate dependent or independent. One such class of device is shape memory alloys, which undergo a reversible phase transformation and exhibit super-elastic behavior when deformed.

Overview of the guidelines

The guidelines include a series of test procedures and requirements for how the tests should be performed. The test procedures are grouped into five categories in two series, according to the nature and purpose of the tests. The test series are *quality control* tests and *prototype* tests. In addition, the guidelines describe a series of *basic property and response* tests, which are not required, but are intended as guidance for how to test newly developed device types. The test types and categories are listed in Table 1.

All of the tests in these guidelines are presented in a standard format, which includes the procedure and any applicable performance criteria. The performance criteria are intended to detect specimens that may not perform adequately in service.

Scope

The guidelines are intended to be comprehensive and to apply to all passive energy dissipators, all structural systems, and many types of dynamic loads. Therefore, the need to develop standards for a particular damper type or application is minimized. Although many of the proposed tests may be applicable to components of active, semi-active, or hybrid systems, the guidelines are not intended to be used for such devices.

The guidelines are not intended to recommend one energy dissipation system over another. They are intended only to validate that a particular device will perform properly in a given application.

Test Requirements

The guidelines include a set of general requirements that apply to all prototype and quality control tests. All tests should be conducted in accordance with these requirements; however, certain requirements may be waived if they are deemed unnecessary for a particular device or design. When necessary, additional special requirements are presented with the individual test specifications.

The general requirements define the necessary facilities and reported information. The necessary test apparatus, instrumentation, and data acquisition are described. The data that should be recorded, analyzed, and reported are also defined.

The requirements also describe how to define the device classification and capacity. To properly test a device, the required force, amplitude, and stroke capacities of the device need to be known. The design response may also be defined, to allow comparison between the actual and required response of the device.

Finally, the devices need to be categorized according to how their response varies to external influences. The devices should be categorized according to whether or not their response depends on the excitation frequency, the loading rate, stroke position, or device temperature. The devices should also be categorized according to how their response changes with continued use.

Test Series

As listed in Table 1, above, the guidelines contain three test series and six test categories. A graphical description of how the test series are related, and when each test series should be performed, is shown in Figure 1. The three test series - *quality control* tests, *prototype* tests, and *basic property and response* tests - are described in detail below.

Quality Control Tests

The quality control tests are intended to verify the as-built characteristics of the completed devices and should be performed on all units before installation. This test series includes two test categories, the *material property tests* and *production unit tests*.

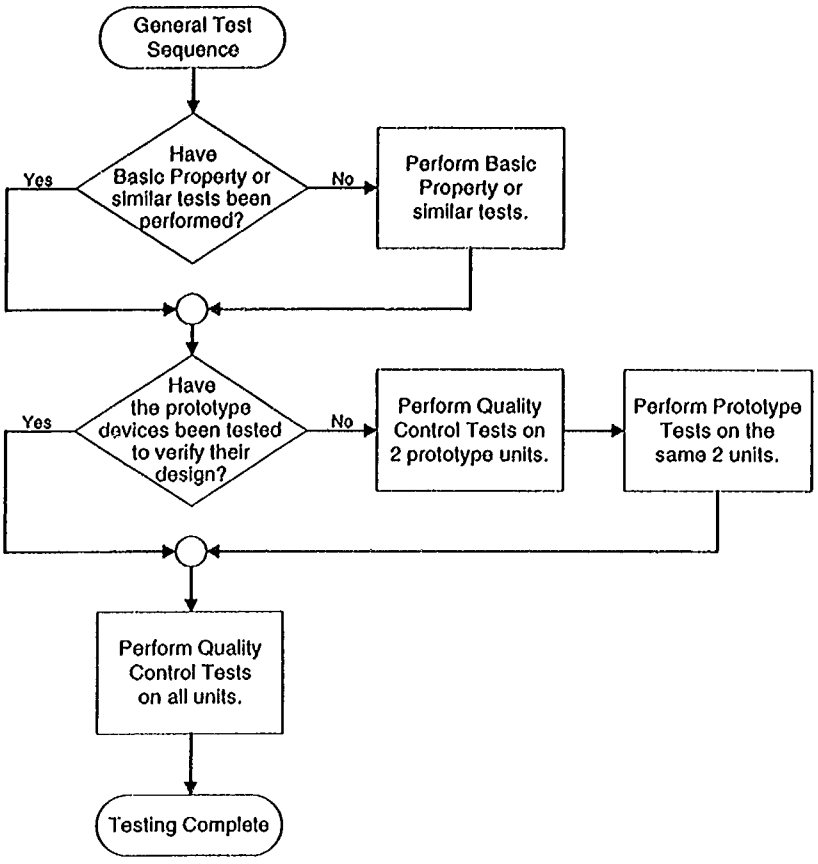


Figure 1: Test Sequence Defined in the Guidelines.

The material property test category includes tests of the materials used in the device and tests of each unit's sub-components. These tests are conducted to monitor the quality and consistency of the manufacturing process. They should be performed during fabrication of the devices and should meet the appropriate test standards. The details of these tests are not described in the guidelines; instead, appropriate tests should be performed for each type of device, as necessary.

The production unit test category consists of four tests, which are intended to verify the as-built properties of the devices. In general, only one of the four tests will need to be performed on a particular device, although in some cases a second test will be needed. All four tests investigate the stiffness and energy dissipation properties of the devices.

The response of the devices during the production unit tests is considered acceptable if the properties fall within a defined range of acceptable values.

Prototype Tests

The prototype tests are intended to verify the design properties of a specific device. This test series includes three test categories, the *system property tests*, *applied load tests*, and

reserve capacity tests. These tests should be performed on two specimens for each design and unique application.

The system property test category consists of four tests. The first test in this category is designed to determine the response properties of the device. This test is identical to the first production unit test, and needs to be performed only if the first production unit test was not performed. The remaining three tests are designed to determine how the properties change with changes in the loading conditions. These tests need to be performed only on devices whose response is dependent on the loading frequency, loading velocity, or device temperature.

The applied loads test category consists of three tests that are intended to validate the device's ability to withstand realistic loading. The first test verifies that the device can survive a lifetime of the expected loads. The second and third tests verify the device's ability to withstand seismic and wind loads. Only those tests that are applicable to a particular device and application need to be performed.

The reserve capacity test category consists of two tests that are intended to verify that the device can withstand loads that exceed the design values. The first test verifies that the device will perform properly when subjected to the maximum expected loading velocity. The second test verifies that the device has a reserve capacity for withstanding displacements and forces beyond the design values.

The device's response during the prototype tests is considered acceptable if the properties fall within a defined range of acceptable values, or if the variation of the properties may be accurately predicted by mathematical models of the device. In addition, the device should not be permanently damaged by the tests.

Basic Property and Response Tests

The basic property and response tests are included in an appendix to the guidelines. These tests are not required, but may be used to determine the characteristics of new devices or existing ones that are substantially modified. These test guidelines provide only guidance on how to perform these types of tests.

The basic property tests are intended to determine how the device will respond to a variety of loading conditions. These tests characterize the device properties and determine how the properties will vary with changes in loading frequency, load amplitude, temperature, and load history. These tests are intended to provide results that can be used to develop mathematical models of the device response. These tests are also intended to determine the device's usable life and resistance to damage, so as to verify that the devices will perform properly when installed in a bridge or building.

There are no acceptance criteria for the basic property tests, since these tests are intended only to determine how the device will perform in various, but general, conditions. The tests are not intended to verify how a device will perform in a particular application.

Development of the Guidelines

The proposed test guidelines have been developed with the assistance of a technical review committee, feedback from experts working in the area of passive energy dissipation, and a workshop to be sponsored by NIST. To develop confidence in the guidelines and to foster adoption of the proposed test procedures, the guidelines will be evaluated by conducting selected tests on typical supplemental damping devices. These tests will be performed on normal specimens and specimens with manufacturing flaws. The purpose of these tests will be to expose any inconsistencies, omissions of important data, or other unforeseen problems with the procedures, and validate the applicability of the test procedures.

Concluding Remarks

The guidelines for testing passive energy dissipation devices are intended to lead to more systematic evaluations of these devices. Properly used, these guidelines will ensure the quality of the installed devices and should expedite the development of new systems. Since they will be independent of the application and applicable to all passive energy dissipation devices, these guidelines should assist in the design and construction of structures with supplemental dampers. It is hoped that they will enhance the use of this promising technology.

References

Hanson, R. D., Aiken, I. D., Nims, D. K., Richter, P. J., and Bachman, R. E., (1993), "State-of-the-Art and State-of-the-Practice in Seismic Energy Dissipation," *Proc., ATC-17-1 Seminar on Seismic Isolation, Passive Energy Dissipation, and Active Control,* Applied Technology Council, Redwood City, CA., Vol. 2, pp.449-471.

NEHRP Guidelines for the Seismic Rehabilitation of Buildings, (1997), FEMA-273, Building Seismic Safety Council, Washington, D.C.

Riley, M. A., Sadek, F., and Mohraz, B. (1999), "Guidelines for Testing Passive Energy Dissipation Devices," *Report NISTIR xxxx,* National Institute of Standards and Technology, Gaithersburg, MD. (*Under Review*).

Sadek, F., Mohraz B., Taylor A. W., and Chung R. M., (1996), "Passive Energy Dissipation Devices for Seismic Applications," *Report NISTIR 5923,* National Institute of Standards and Technology, Gaithersburg, MD.

Soong, T. T., and Constantinou, M. C. (eds.), (1994), "*Passive and Active Structural Vibration Control in Civil Engineering,*" Springer-Verlag, Wien and New York.

Soong, T. T., and Dargush, G. F., (1997), "*Passive Energy Dissipation Systems in Structural Engineering,*" John Wiley and Sons, New York.

Taylor, D. P., and Constantinou, M. C., (1994) "*Test Methodology and Procedures for Fluid Viscous Dampers used in Structures to Dissipate Seismic Energy,*" Technical Report, Taylor Devices, Inc., Tonawanda, NY.

SESSION 6: CONCRETE

(1) Bending Behavior of Prestressed Concrete Girders Damaged by Salt Attack
(Yoshiki Tanaka, Hirotaka Kawano, Hiroshi Watanabe and Masahiro Suzuki)

(2) Performance of Reinforced Concrete Bridge Joints Subjected to Bi-Directional Loading
(Khalid M. Mosalam, Svetlana Khaykina and Clay Naito)

(3) Development of Electric Anticorrosion Methods for Newly Constructed Concrete Structures
(Masaru Terada and Seishi Meiarashi)

(4) Corrosion Control of Concrete Bridges
(Yash Paul Virmani)

(5) Durability and Structural Safety Evaluation of RC Gerber's Bridge Servicing for More Than 60 Years
(Naoshige Nomura, Yoshihiro Tanaka and Takeyuki Yokooka)

Bending Behavior of Prestressed Concrete Girders Damaged by Salt Attack

Yoshiki Tanaka[1], Hirotaka Kawano[2], Hiroshi Watanabe[3], Masahiro Suzuki[4]

ABSTRACT

This paper shows the results of tests and analysis on bending behavior of prestressed concrete girders damaged by salt attack. Reduction of ductility and moment capacity of the girders was observed. Reduction of steel elongation due to a little corrosion of remaining tendons as well as loss of cross-sectional area of tendons affected the bending behavior.

INTRODUCTION

There are many concrete bridges disturbed by corrosion problem at coastal area in Japan. The problems usually make highway management more difficult. It is important to evaluate remaining strength of existing concrete bridges damaged by salt attack for proper maintenance strategies such as repairing, strengthening or rebuilding. However, bending behavior of the damaged girder has not been clarified well so far.

There are some reports on bending behavior of retired prestressed concrete girders [1-3]. The reports described that calculations of ultimate strength and moment M - curvature Φ curve are almost reliable for practical estimation if real data of material characteristics can be obtained from girders. However, knowledge on bending behavior of retired prestressed concrete girders damaged by salt attack on site is not enough.

In 1997, a bridge was removed due to heavy corrosion of tendons. Then two retired prestressed concrete girders, in which some tendons showed serious loss of cross-sectional area by corrosion due to 26-year exposure under severe coastal environment, were provided for the test from the bridge.

To discuss the bending behavior, bending tests on two precast prestressed concrete girders (B-1, B-2) were carried out. Corrosion investigation and fundamental material tests were also performed after bending. Moreover, effects of epoxy resin concrete (Epoxy) used for repair on the bending behavior was discussed.

SPECIMENS

Design Specifications used for the Girders

The original configuration of the damaged girders on documents is shown in Fig. 1. B-1 was used for interior girder of the retired bridge that had 13 girders of same cross-section. B-2 was used for exterior girder of that. Design specifications for the girders are shown in Table 1.

---

1. Research Engineer, Concrete Division, Public Works Research Institute, Ministry of Construction, JAPAN
2. Head, ditto
3. Senior Research Engineer, ditto
4. Affiliated Researcher, ditto

Table 1 Design Specifications

Bridge Type	Precast Prestressed Concrete Bridge Composed of 13 Simple Beams
Design Strength of Concrete	49MPa
Type of Tendon	Strand, 7 Wires, Dia. 3mm SWPR7A(JIS G 3536)
Design Ultimate Strength of Tendon	1716MPa
Introduced Prestress	1177MPa
Effective Prestress	935MPa

Service Term : Dec. 1971 - Oct. 1997

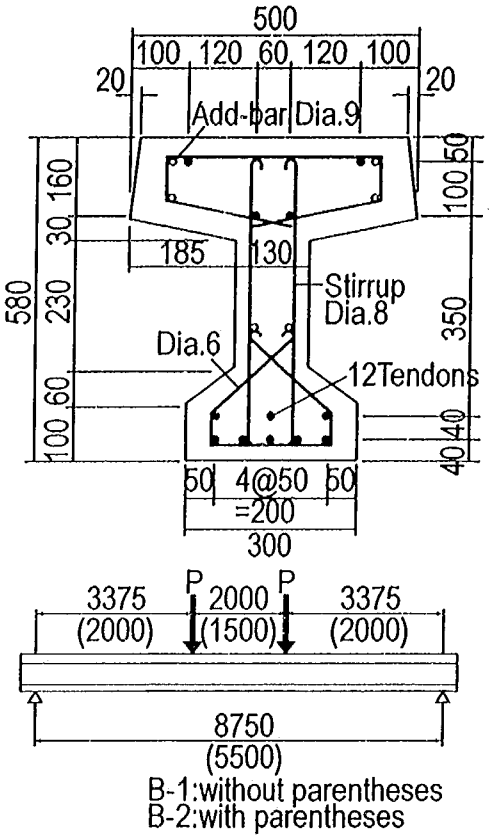


Fig. 1 Configulation of Specimens

Materials

All test pieces were obtained from the girders after bending tests.

1. Concrete

Five concrete cores were taken from top surface of upper flange near support points. The parts seemed to be little affected by loading. Average diameter of cores was 68.4mm. Height of them was 140mm for obtaining appropriate testing condition. Results of compressive strength tests are shown in Table 2. The average compressive strength and elastic modulus of concrete were 55.4 MPa, 30.5 GPa respectively.

2. Tendon

Five test pieces of tendon were carefully taken from upper flange near support points where seem to be little affected by loading and to be low concentration of chloride ion. Results of tensile tests are shown in Table 3.

Elongation of three tendon pieces out of five was less than specified elongation requirement of 3.5 %, although all tensile strength was more than specified strength. A little rust was found inside each strand unbraided after tensile failure. Maximum elongation of them was 5.1 % that satisfied specification, however that did not reach ordinarily observed elongation of 6.4 % when the bridge was built.

3. Epoxy

Epoxy used to be applied to retrofit the shape of cross section after dissection to remove concrete contaminated by chloride ion and rust of steel. It was not expected for Epoxy to strengthen the girders. However, it might be expected that there would be some strengthening effect on the bending behavior. Because Epoxy has much more tensile strength than ordinary concrete and it was usually used in tensile area of the girders. Bending tests were carried out to obtain tensile characteristics of Epoxy.

Four test pieces of Epoxy (approximately 40mm wide × 30mm height × 150mm long) could

Table 2 Result of Concrete Cores

Test Piece No.	Max. Strength (MPa)	Elastic Modulus (GPa)
1	50.6	30.0
2	54.0	32.8
3	55.4	32.1
4	58.8	29.4
5	58.4	28.3
Average	55.4	30.5

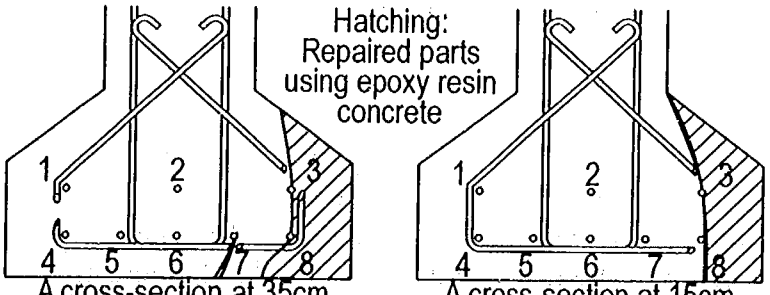
Table 3 Results of Tensile Tests for Tendon Strands

Test Piece No.	Ultimate Strength (MPa)	Elastic Modulus (GPa)	Elongation in 750mm (Percent)	Number of Ruptured Wires	Place of Rupture (cm)*
1	1820	181	1.84	1	0
2	1870	181	4.22	2	32
3	1890	192	5.12	7	0
4	1840	181	3.21	2	0
5	1820	182	1.53	1	0
Average	1850	183	3.18	2.6	—
Spec.	1720	(181)	>3.5	—	—

*) Distance from center of test piece

Table 4 Results of Bending Test for Epoxy

Test Piece No.	Ultimate Tensile Strength (MPa)	Elastic Modulus (GPa)
1	20.4	16.3
2	19.9	15.2
3	23.8	14.8
4	21.2	13.7
Average	21.4	15.0



A cross-section at 35cm from a loading point to end. Strand No.3, 8: No wire remained. Strand No.7: 1 wire remained. B-1

A cross-section at 15cm from a loading point to end. Strand No.3: 1 wire remained. Strand No.8: 3 wires remained. B-2

Fig. 2 Corrosion at Failed Cross-section

be taken from B-1 after test. All of them was sufficiently filled with aggregate and epoxy resin. Test pieces were simply supported and subjected to a point load. Then strain of lower surface on midspan was measured by a strain gauge for ordinary concrete with 30mm gauge length. Each test piece was set up to be downward the bottom surface that was also bottom of girder. The results are shown in Table 4. All of them were failed at midspan.

Corrosion

These girders had been once repaired at 13 year-old. Then shapes of the girders had been remade with Epoxy after rubbing off rust on rebar, then concrete surface including repaired parts had been painted. However, typical longitudinal cracks and spalling due to salt attack were found again on the side and bottom of the girders when the bridge was removed.

Corrosion states of rebar and tendons around failed cross-section of each girder were observed after bending tests as shown in Fig. 2. Three tendons of B-1 and two tendons of B-2 out of each eight tendons in lower frange showed severe corrosion, although other remaining tendons were seemed to be sound in appearance.

Acid-soluble chlorides around rebar or tendon were 2.0 - 3.4 kg/m^3 at upper flange, 2.6 - 9.7 kg/m^3 at web, 3.6 - 10.4 kg/m^3 at lower flange, respectively. Average cover depth measured were 26mm on top, 19mm on web, 37mm on bottom.

TEST PROCEDURE

Fig. 1 also shows loading scheme. Two point loads were applied to the girders supported simply. B-1 had original span of 8.75m. B-2 was cut to be span of 5.5m. Crack openings induced by loading were monitored by clip gauges, by which the extent of approximately 80 % of span were covered continuously after paint protection were peeled partially. To measure ultimate strain of concrete, strain gauges were attached on top surface around midspan. Inclinometers were set on the web near each loading point to determine the average curvature of midspan.

RESULTS OF BENDING TESTS

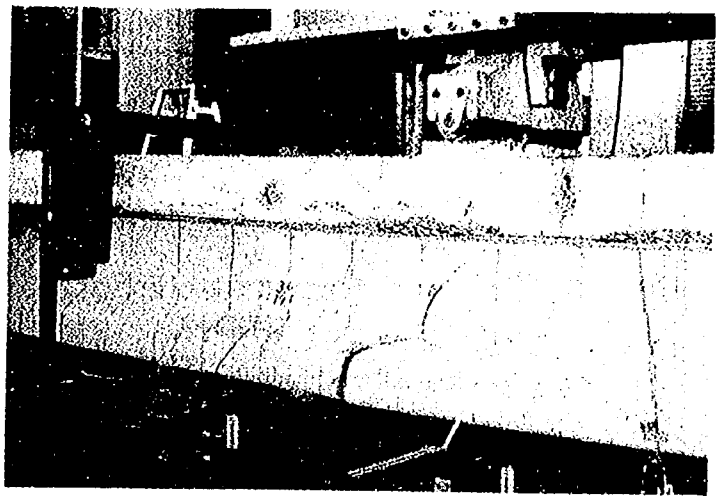
M-Φ Curve and Fracture

Ultimate states of both girders were conducted by rupture of some tendons as shown in Picture 1. Fig. 3 shows relationships between moment and average curvature obtained from inclinometers in extent of pure bending. Both girders showed same linear behavior until moment of approximately 160kN-m. The deference between B-1 and B-2 appeared after 160kN-m. The ultimate curvature of B-1 was much less than B-2.

Cracking

Crack pattern of B-1 is shown in Fig. 4. Bending Cracks took place around the repaired area in early stage of loading. In the further loading, bending crack spread in other area where no initial deterioration was observed. Average strain measured by clip gauges just before cracking at no initial deterioration area was 293 microstrain on B-1 and 308 microstrain on B-2, respectively. Fig. 5 shows behavior of strain by clip gauge around failure point. Broken line arrow in Fig. 5 was illustrated as example of estimating strain at crack opening when it would be reloaded. The strain of 230 microstrain was estimated at no deterioration area of B-1. The strain of 245 microstrain on B-2 was similar to B-1.

Visible cracking of Epoxy was observed at 119kN during B-1 tested. The behavior was also



Picture 1 State of Failure on B-1

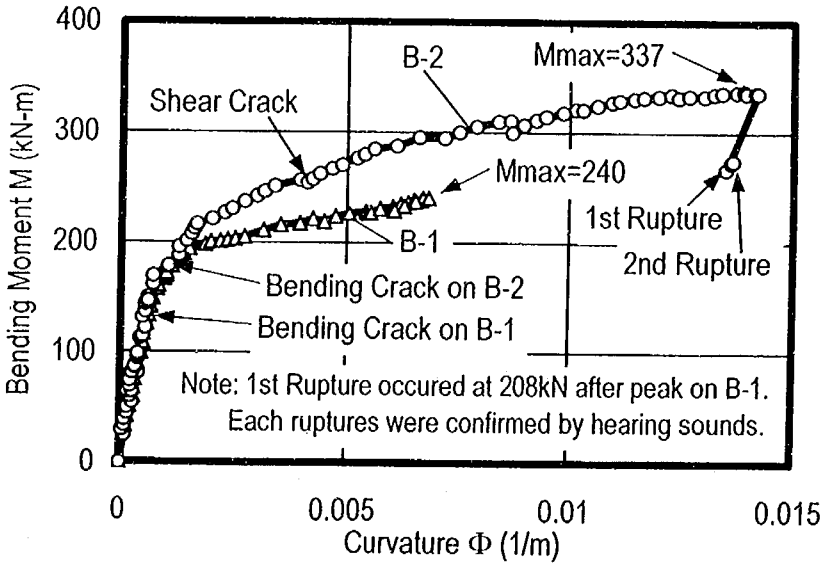


Fig. 3 M-Φ Curves from Bending Tests

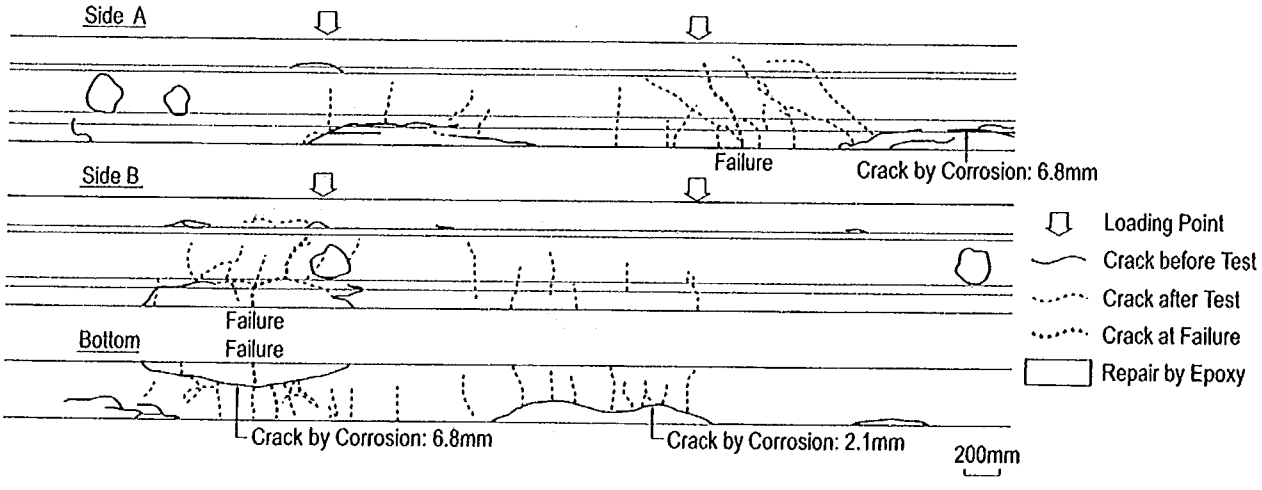


Fig.4 Crack Pattern on B-1

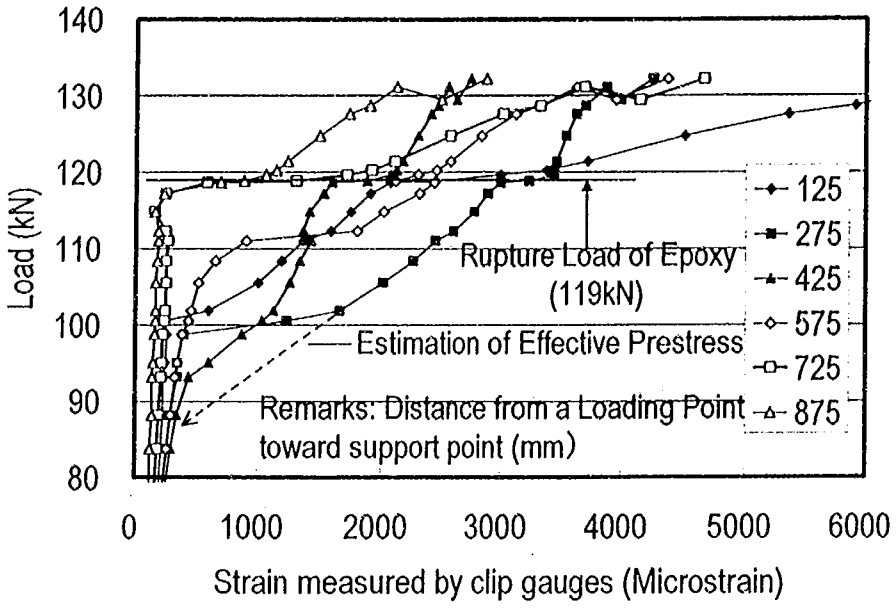


Fig.5 Effect of Epoxy on Crack Width

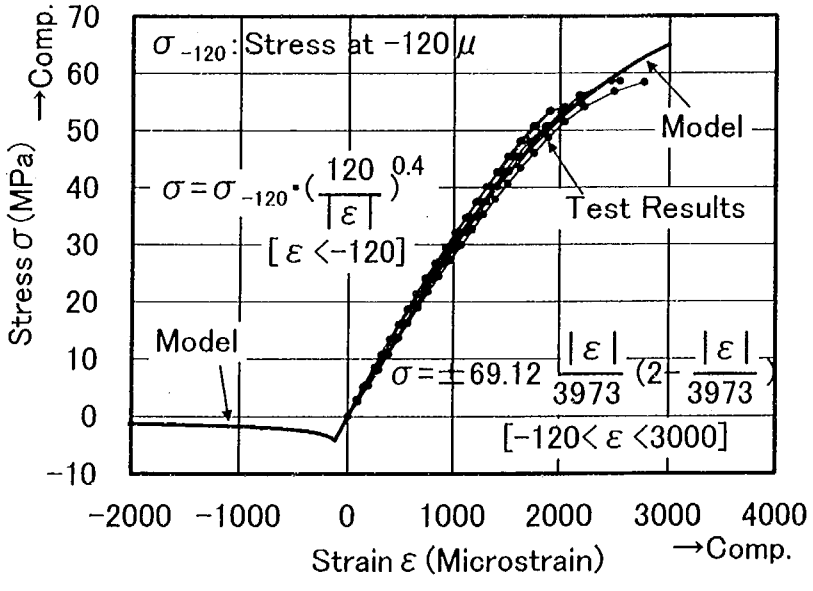


Fig.6 Stress-Strain Model for Concrete

Stress-Strain Models for Strands

State of Surface	Strain ε (Microstrain)	Stress (MPa)
Sound	0.0-0.008	192200ε
	0.008-0.016	1538+304(1-exp(-510(ε-0.008)))
	0.016-0.051	1837+1324(ε-0.016)
A little Corrosion	0.0-0.008	181400ε
	0.008-0.015	1451+374(1-exp(-510(ε-0.008)))

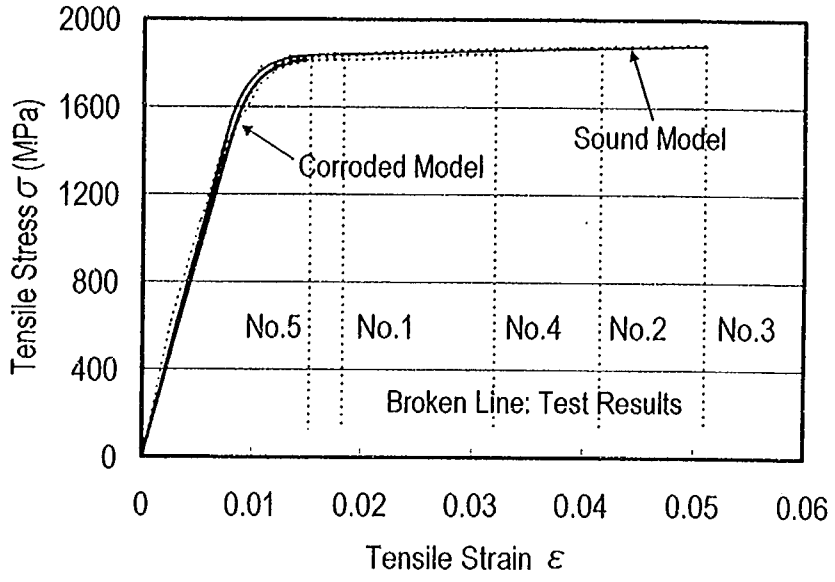


Fig.7 Stress-Strain Model for Tendon

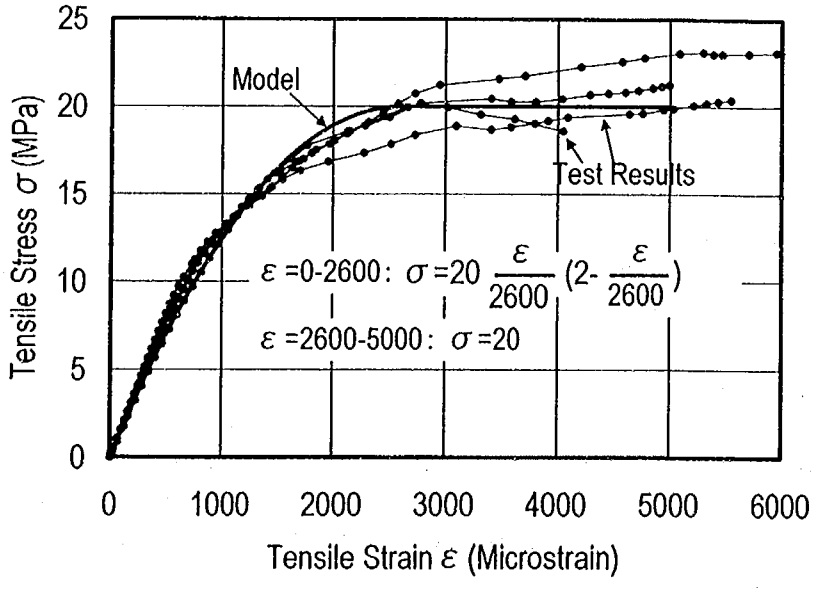


Fig.8 Stress-Strain Model for Epoxy

shown in Fig. 5. Only two cracks were illustrated at Epoxy part in Fig. 4, although many cracks of concrete occurred with relatively short pitch at the repaired area. Figs. 4 and 5 suggested that crack widths of concrete were kept small until cracking of Epoxy. Propagation of concrete cracking after then seemed to concentrate on a cracking at 125mm from loading point, which looks an extended crack of Epoxy.

Diagonal crack was observed in the ultimate state, as show in Picture 1. Then shear force of B-1 was estimated at 71kN. Calculated shear strength of 107kN was summed up with concrete contribution of 41kN, stirrups strength of 39kN and prestress contribution of 27kN considered with reduction due to corrosion. Capacity of shear strength, however, might be critical if stirrups would have lost their cross-section area. Actually, some stirrups at other area were remarkably lost by chloride while the state of the failure area is not still obvious.

METHOD OF ANALYSIS

Bending behaviors (M-Φ) with or without tendon corrosion were calculated at single cross section by Bernoulli's assumption to compare with test results. The stress-strain curves of concrete and tendon used in the analysis were determined from above mentioned material tests. The model by Okamura et al. [4] was used for tensile behavior of concrete. Then the factor c of 0.4 was used on the tensile model. Stress-strain models for each material are shown from Fig. 6 to Fig. 8.

The model for corroded tendon was based on the test result of tendon No.5, which showed the least elongation of 1.5 %. The model of non-corroded tendon was based on the result of No.3. The loss of cross-section area of tendon was also taken into account in the analysis with corrosion. It is assumed that bond between tendon and concrete were kept in all calculations because remained tendons had little lack of cross-section area.

Besides, it was attempted to calculate with considering of stiffness of Epoxy or ignoring stiffness of the repaired area.

DISCUSSION

Effects of Tendon Corrosion on M-Φ curve

Failure of both girders occurred by tendon rupture although this type of girders usually fails by crushing in extreme compressive fiber of concrete. Calculated M-Φ curves considered with and without corrosion as well as test results are shown in Fig. 9. Calculation shows that crushing of concrete was expected without corrosion and tendon rupture was expected with it. It was found that the results of analysis with considering corrosion agreed with test results. Fig. 9 also shows that calculated ultimate curvature with corrosion was less than a half of calculated ultimate curvature without corrosion. Besides ultimate strength was decreased by corrosion. It was found that ductility of prestressed concrete girders could be obviously decreased by elongation loss of tendon due to corrosion.

Generally, cracking at tensile surface of concrete makes slope of M-Φ curve declined. Results of the analysis show that a difference between B-1 and B-2 appeared after cracking, as shown in test results. A virgin cracking load almost depends on effective prestress and tensile strength of concrete. Tensile strength of concrete used for B-1 and B-2 seemed to be nearly the same. Thus, it is assumed that reduction of prestress due to loss of cross section area of corroded tendons brought the deference.

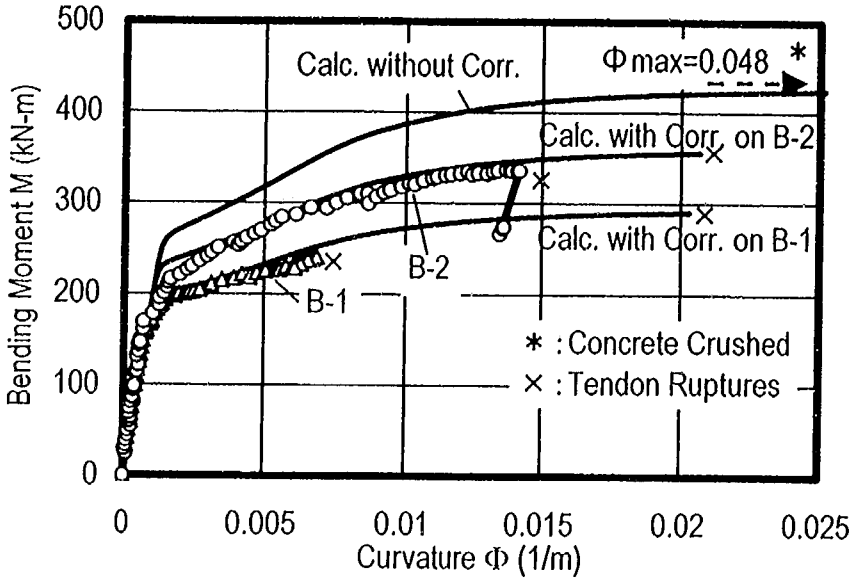


Fig. 9 Comparison between Tests and Analysis

Effect of Epoxy on M-Φ Curves

The Epoxy had tensile strength of 21.4 MPa, which is approximately 5 times of the concrete tensile strength. Its Young's modulus of 15.0 GPa was a half of the concrete cores. Fig. 10 shows the results of two analyses. An analysis considering tensile contribution of Epoxy shows ultimate strength higher than test result of B-1. In the other case, stiffness of repaired area was ignored. Test result of B-1 seems to be similar to the latter model rather than the Epoxy model. It was found that influence of Epoxy on M-Φ curve was little.

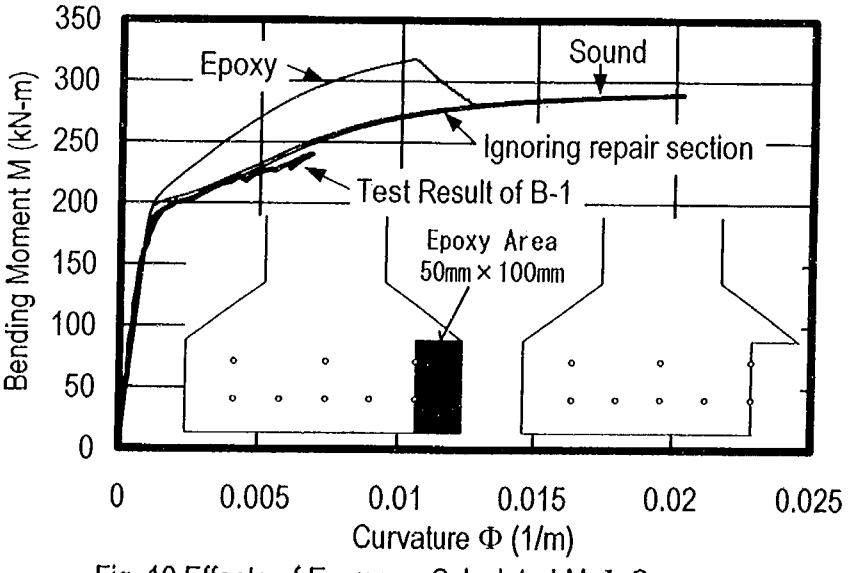


Fig. 10 Effects of Epoxy on Calculated M-Φ Curves

CONCLUSIONS

Based on the results of tests and analysis on bending behavior of precast prestressed concrete girders attacked by salt, the following conclusions can be described;

1. Reduction of ductility and moment capacity was observed on the damaged girders. Failure of the damaged girders was attributed to tendon rupture although this type of girders usually fails by crushing in extreme compressive fiber of concrete. It seemed to be caused by elongation loss of tendon due to corrosion. The results suggest that it is necessary to take into account reduction of elongation of remaining tendons as well as loss of tendon areas, to evaluate precisely bending behavior of the girders damaged by salt attack.
2. Repair of cross section using epoxy resin concrete could little influence to ultimate strength or ductility of the girders. Otherwise, the repair could a little effect to distribute cracking after initial cracking of concrete.

REFERENCES

1. Chandu V. Shenoy, Gregory C. Frantz: Structural Tests of 27-Year-Old Prestressed Concrete Bridge Beams, PCI Journal, Sep.-Oct., 1991, pp.80-90
2. Habib Tabatabai, Timothy J. Dickson: Structural Evaluation of a 34-Year-Old Precast Post-tentioned Concrete Girder, PCI Journal, Sep.-Oct., 1993, pp.50-63
3. J. Todd Halsey, Richard Miller: Destructive Testing of Two Forty-Year-Old Prestressed Concrete Bridge Beams, PCI Journal, Sep.-Oct., 1996, pp.84-93
4. H. Okamura, H. Maekawa: Nonlinear Analysis and Constitutive Models of Reinforced Concrete, The Gihodo Pub. Co. Japan, May 1991 (in English and Japanese)

PERFORMANCE OF REINFORCED CONCRETE BRIDGE JOINTS SUBJECTED TO BI-DIRECTIONAL LOADING

Khalid M. Mosalam[1], Svetlana Khaykina[2], and Clay Naito[3]

Abstract

This paper summarizes the recent findings of an experimental research program conducted at University of California at Berkeley on reinforced concrete beam-column bridge joints with integrated box-girder. The specimens are subjected to bi-directional cyclic lateral loading and constant axial load. The reinforcement detailing of the tested joints represent common practice in California and new design using headed reinforcing bars. The use of headed bars is intended to reduce congestion within the joint region and accordingly improve construction procedure of these critical regions of the bridge. As a future investigation, detailed three-dimentional finite element analysis will be utilized to analyze the tested specimens when subjected to different patterns of cyclic loading.

Introduction

An experimental and computational research program on reinforced concrete bridge joints is conducted at University of California, Berkeley. The test program involves several specimens of modern T-joints with integrated box-girders having various details including headed and traditional reinforcing bars. To complement the experimental program, computational studies using nonlinear two-dimensional and three-dimensional finite element analyses together with application of the lower-bound theorem of plasticity and linear programming for optimization of reinforcement are conducted. This paper provides a brief summary of findings from the most recent experimental phase of this research effort where testing of two beam-column connections with integrated box-girders is conducted.

The first two phases of the experimental study had focused on the behavior of beam-column T-joints under uni-directional lateral loading. The goal of the first phase (Group A) was to determine if the load transfer mechanism of the existing joint design agrees with any of the available models. Also this group (having two specimens with circular columns and two with square columns) provided means for verifying two-dimentional and three-dimentional finite element models for analytical investigation. Although Group A provided invaluable information on the behavior of current joint designs, it did not provide clear view of the mechanisms involved in governing the performance of beam-column connections. Therefore, joint design in the second phase (Group B) had been altered such that the specimens would allow more understanding of the role of different reinforcing bars in resisting joint demands. This was achieved by reducing the beam depth and increasing the quantity of longitudinal column reinforcement. In addition the amount of transverse reinforcement within the joint region was decreased and headed reinforcing bars were incorporated. This new design led to increase of the joint demands from shear and bond development. Preliminary results show that beam transverse reinforcement is more effective in joint confinement than column spiral reinforcement (Naito et al, 2000). The third phase (Group C), which is the main focus of this paper, was developed to investigate the effect of bi-directional loading on the joint behavior and the

[1] Assistant Professor, Department of Civil and Environmental Engineering, University of California, at Berkeley
[2] Graduate Student, Department of Civil and Environmental Engineering, University of California at Berkeley
[3] Doctoral Student, Department of Civil and Environmental Engineering, University of California at Berkeley

confinement of the joint from the box-girder in the direction of the longitudinal axis of the bridge. In order to compare the behavior of the joint under bi-directional loading with those tested uni-directionally, specimens C1 and C2 were designed to represent Groups A and B, respectively. Both specimens had identical box-girder design.

Specimens Design and Details

The structural configuration under investigation represents the interior joint subassembly of a three-column bridge bent with integral box-girder and pinned column to footing connections as shown in Figures 1 and 2. The test specimens consist of deck specimen assembly modeling the central joint region. The model includes the full column height, half the cap beam span on either side of the column, and approximately a quarter of the box-girder span on the other two sides of the column. In the sequel, the direction of the cap beam will be referred to as the transverse direction of the specimen and the direction of the box-girder will be referred to as the longitudinal direction of the specimen. The gross dimensions of the test specimens and their longitudinal and transverse beam reinforcement ratios are representative of the bridges constructed in California between 1982 and 1994. The length of the box-girder on one side of the cap beam was determined as the distance from the cap beam to the point of inflection along the longitudinal axis of the bridge due to gravity load. This approach for selecting the box-girder length was chosen to make modeling of the boundary conditions for the experimental setup easier. The laboratory space limited the scale of the test specimens to be 5/16.

As in Group B (Naito et al, 2000), shear demand was increased on the joint through increasing the column longitudinal reinforcing ratio and decreasing the beam depth from 2.13 % and 29 inches respectively in Group A to 3.11% and 20 inches respectively in Group C. Furthermore, specimen C1 has volume and configuration of the joint transverse reinforcement consistent with Caltrans Bridge Design Specifications (Caltrans, 1995) and is considered to be representative of Group A specimens. On the other hand, specimen C2 has reinforcement configuration representative of specimens in Group B. It should be noted that the volume of joint transverse reinforcement in Group C specimens was slightly higher than that of Group B specimens to ensure stronger joints.

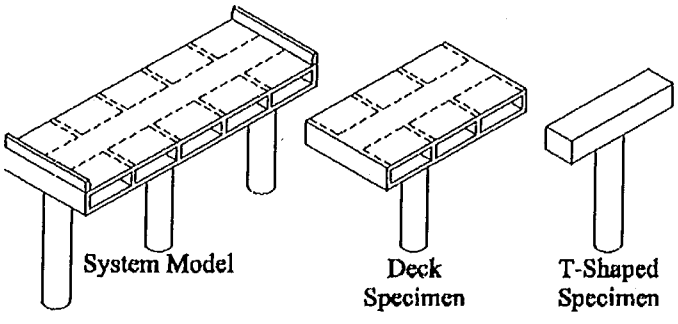


Figure 1: Specimens structural models

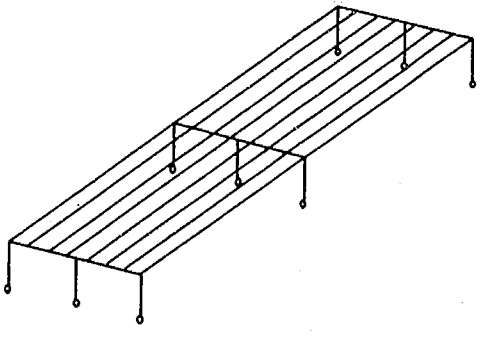


Figure 2: Bridge structural model

All specimens were evaluated considering the behavior of a bridge using the full bridge model shown in Figure 2 as well as the experimental sub-assembly structural model. Three load cases were considered for both the bridge model and the sub-assembly model in both transverse and longitudinal directions. These cases are, 1) Dead+Live+Impact, 2) Dead+Earthquake, and 3) Dead load applied to the system with hinged columns at the top (plastic analysis). Dead load was

calculated from the average box-girder and span dimensions based on database investigation of reinforced concrete bridges in California (Naito, 1999). Earthquake load was calculated using an Acceleration Response Spectra of ARS=2.0 and adjustment factor for ductility and risk assessment, Z=4.0 (Caltrans, 1995). As in Groups A and B, the controlling design criterion for the beam was that the beam flexural strength exceeds the ultimate column flexural strength computed using as-built details. This ensured that flexural yielding was isolated in the column. Specimen details are shown in Figures 3 through 6. Figures 3 and 4 show the reinforcement details of the beam and column cross sections and the box-girder. These details are common for both specimens C1 and C2. In Figure 5, the joint details of both specimens C1 and C2 are shown. Figures 6a and 6b represent close-up photos of the actual joint reinforcement before placing the concrete for specimens C1 and C2, respectively. It is clear that traditional reinforcement is used for specimen C1 as specified by Caltrans specifications. For specimen C2, use of headed bars is made where reinforcing bars in the joint regions are provided in the three orthogonal directions of the joint.

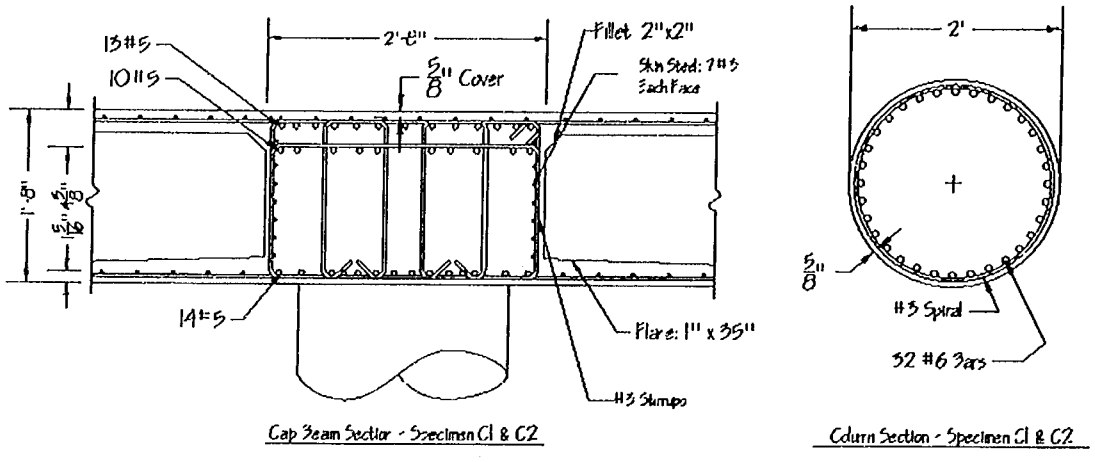


Figure 3: Details of specimens C1 and C2 for beam and column cross-sections

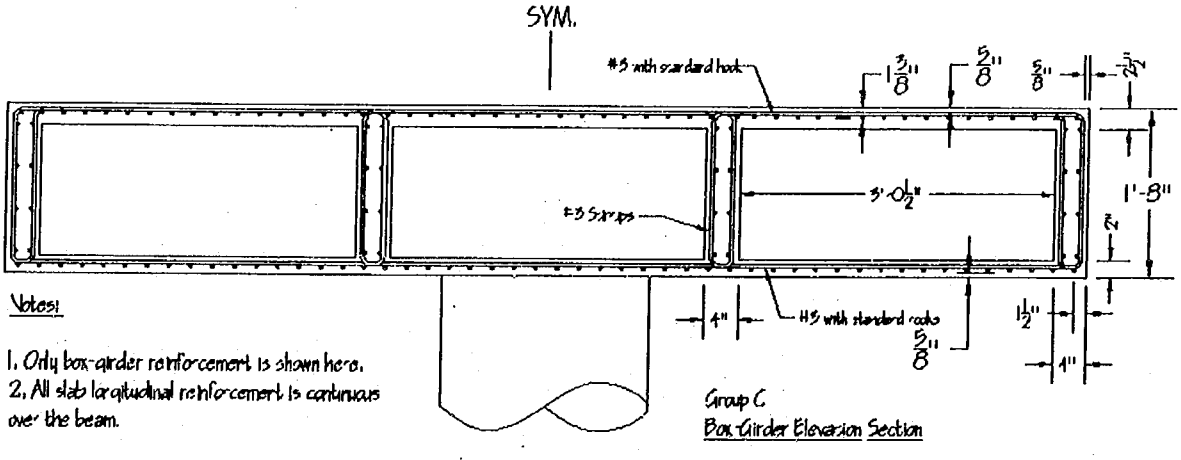


Figure 4: Details of specimens C1 and C2 for box-girder cross-section

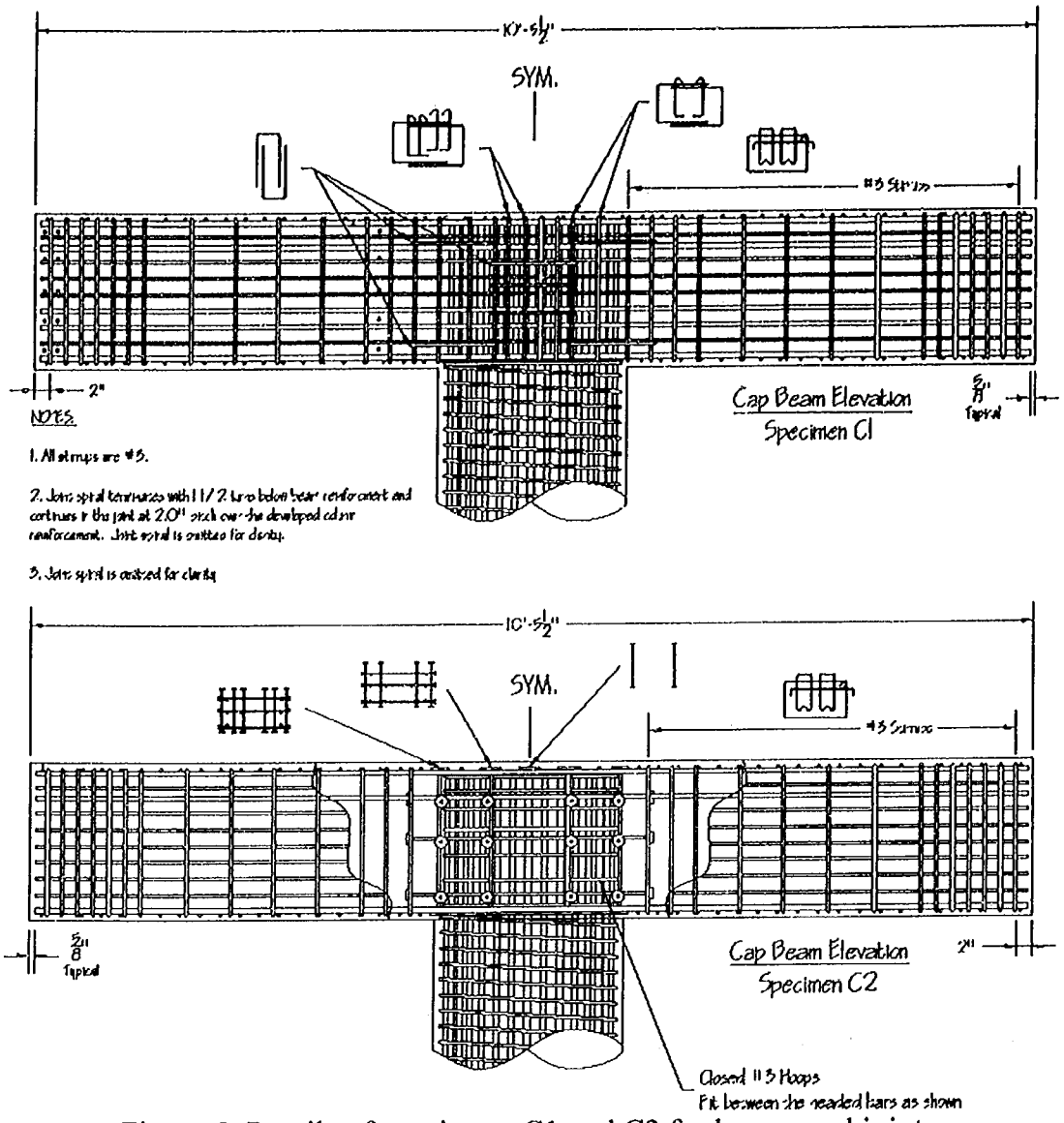


Figure 5: Details of specimens C1 and C2 for beams and joints

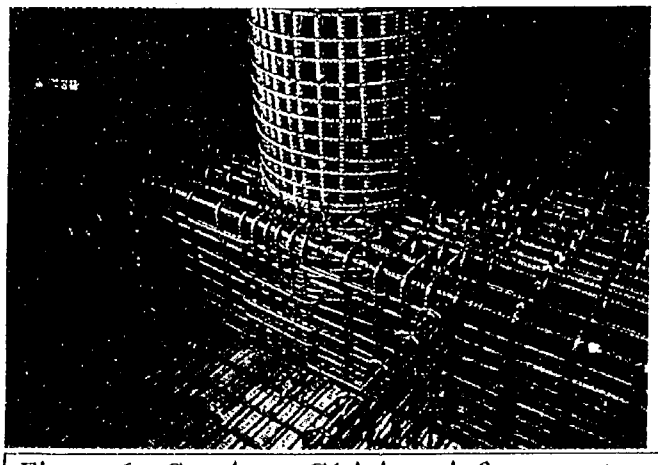


Figure 6a: Specimen C1 joint reinforcement detailing (current Caltrans design)

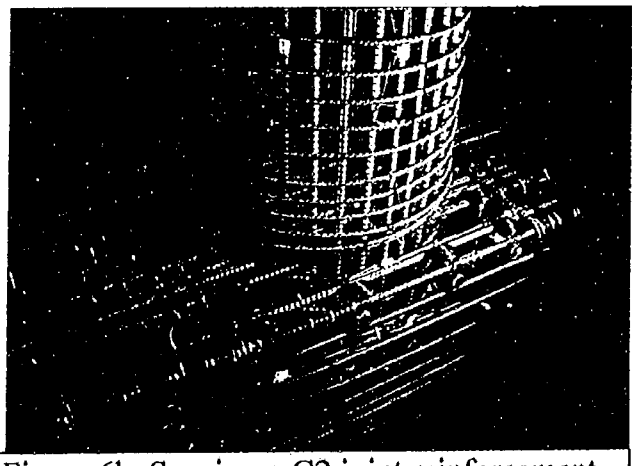


Figure 6b: Specimen C2 joint reinforcement detailing (design with headed bars)

The joint transverse reinforcement for specimen C1 was designed in accordance with Caltrans' Seismic Design Specifications (Caltrans, 1995), Figures 5 and 6a. These specifications require that, in addition to beam flexural and shear reinforcement, the following reinforcement be provided in the vicinity of the joint: 1) Vertical transverse reinforcement as 20% of the column longitudinal reinforcement, 2) Horizontal reinforcement as 10% of the column longitudinal reinforcement, and 3) Side face longitudinal reinforcement (skin reinforcement) as 10% of the tension reinforcement in the column. Accordingly, the resulting horizontal and vertical joint shear should be less than $12\sqrt{f'c}$ [psi] with the joint area defined by the beam width and column depth.

The design of the joint transverse reinforcement for specimen C2 was based upon proper bond of the column longitudinal reinforcement anchored in the beam and achieved through the use of headed transverse joint reinforcement and column hoops in the joint region. For this purpose, an idealized bond stress distribution along the embedded column bar was assumed based on results from Group A specimens. This distribution is composed of two distinct regions: 1) Region of average bond stress distribution along the bar of constant value of $6\sqrt{f'c}$ [psi] and 2) Region of high stress distribution generated by the active compressive force being applied to the bar from the beam. This region has triangular stress distribution of height equals the compression stress block and maximum additional stress of $34\sqrt{f'c}$ [psi] (i.e. total bond stress at extreme compression fibers of $40\sqrt{f'c}$ [psi] is assumed). To resist the forces associated with the reinforcing bars without bar pullout, the reinforcement is oriented in three orthogonal directions of the joint: parallel and perpendicular to the beam axis and parallel to the column axis, Figures 5 and 6b. A summary of the design parameters of specimens C1 and C2 are given in Tables 1 and 2.

Table 1: Specimen geometry – Test scale (5/16-scale) parameters [Dim. in inches]

Span between columns	115.0	Column diameter	24.0	Cap beam depth	20.0
Clear column height	82.0	Cap beam width	32.0	Soffit slab depth	2.0
Bridge clear span	210.5	Box-girder width	36.5	Deck slab depth	2.5
Web thickness	4.0				

Table 2: Specimen reinforcement details

Column	Beam
32#6 column bars	23#5 total negative reinforcement
#3 spiral at 2.0-in. in plastic hinge	14#5 positive reinforcement
#3 spiral at 3.5-in. outside of plastic hinge	Skin steel 7#3 each face
Plastic hinge length = Column diameter = 24.0-in.	#3 stirrups with 6 vl. and 3 hrz. legs at 5.5-in
Column reinforcement development length, $l_d = 28\ d_b = 21$-in	**Joint**
Box-Girder	Note: ρ_{vh} = Volumetric hrz. joint reinf. ratio
#3 with standard hook at 4.0-in transverse reinforcement	ρ_{vv} = Volumetric vl. joint reinf. ratio
#3 straight bars at 2.5-in longitudinal reinforcement	Specimen C1: $\rho_{vh} = 0.009$
Skin steel 8#3 each web	Specimen C1: $\rho_{vv} = 0.0059$
#3 web stirrups with 2 vertical legs at 4.0-in	Specimen C2: $\rho_{vh} = 0.0062$
	Specimen C2: $\rho_{vv} = 0.0053$

Material Properties

Material properties determined from quality control specimens for specimens C1 and C2 are shown in Tables 3 and 4. All tests were performed according to ASTM Standards, except tests for fracture energy, which used the European FMC-50 Draft Recommendation. The material data are intended for the development of the finite element models for further computational studies of the tested specimens.

Table 3: Concrete material properties

Member	Age at Test Date [days]	Modulus of Elasticity [ksi]	Compressive Strength [psi]	Modulus of Rupture [psi]	Splitting Tensile Strength [psi]	Fracture Energy [lb/in]
C1 deck slab	147	3113	4867	1010	397	1.0
C1 soffit slab, web, beam	134	3178	5041	1285	N.A.	1.36
C1 column	126	2823	4647	879	286.5	0.93
C2 deck slab	174	3068	4941	972	368	0.8
C2 soffit slab, web, beam	161	3218	4831	973	356	1.47
C2 column	153	2818	4283	955	344	1.05

N.A. – Not Available

Table 4: Reinforcing steel material properties

Bar Size	Reinforcement Usage	Grade	Yield Stress [ksi]		Ultimate Strength [ksi]	
			Mill Cert.	Lab. Test	Mill Cert.	Lab. Test
#3	Longitudinal	A615	74.5	76.9	110.9	121.2
#3	Transverse	A615	62.2	N.A.	100.9	108.3
#3	Headed	A615	N.A.	75.3	N.A.	119.7
#4	Headed	A706	N.A.	73.2	N.A.	101.3
#5	Longitudinal	A706	63	65.6	87.5	98.8
#6	Longitudinal	A706	72.5	73.6	103	110.9

N.A. – Not Available

Construction of Specimens

As discussed before the specimens were constructed using normal weight concrete and Grade A615 and A706 reinforcement (refer to previous section and Tables 3 and 4). The specimens were built and tested upside down to facilitate the construction and load application during testing. Figure 7 shows the sequence of construction of Group C specimens. This sequence consisted of the following three concrete lifts:

1) Construction of the deck slab
2) Construction of the cap beam, box-girder webs and the soffit slab
3) Construction of the column with the loading footing.

In this way, two cold construction joints at the interface between the column and the cap beam and at the interface between the webs and the deck slab were formed. It should be noted that similar construction sequence is commonly used in actual bridges but in the reversed order (Naito, 1999).

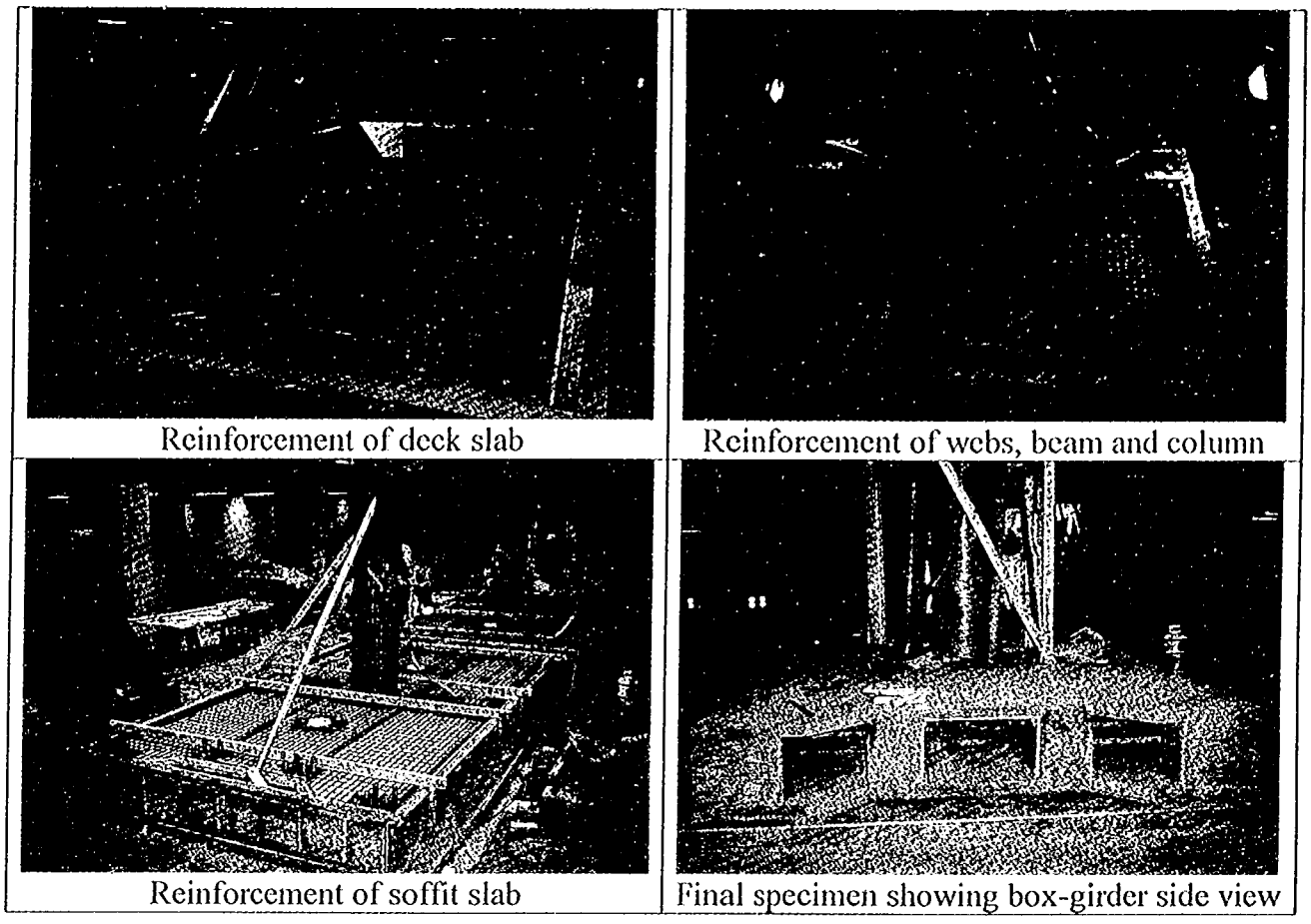


Figure 7: Construction sequence of Group C specimens

Test Setup and Loading Protocol

The specimens were tested upside down as shown in Figures 8 and 9. This testing arrangement facilitated the gravity and the lateral load application. The lateral resisting system consisted of strong frames reacting against the strong floor of the laboratory and three-dimensional (3-D) pins reacting against several small frames attached to the strong floor. The incorporation of the 3-D pins in the lateral resisting system allowed the specimens to rotate freely about the X and Y directions as was required from the analysis of the bridge model.

A constant dead load of about 4% of the column axial capacity was applied to the column and reacted against the strong floor in the laboratory. The magnitude of the dead load was chosen such that the moment in the vicinity of the specimen joint produced by this dead load alone was comparable to that produced by the distributed dead load on the bridge model (Figure 2). The specimens were laterally loaded at the column base in a quasi-static manner (loading rate ranged from 0.01 to 0.09 in/sec) under displacement control. The data was recorded during each loading cycle with approximately 820 points per cycle. Figures 10a and 10b show the loading procedure and the corresponding schedule for each specimen. One cycle was performed at each displacement level prior to yielding and two cycles were performed after yielding. Yield displacement was defined as the displacement corresponding to the first yield of the exterior longitudinal column reinforcement. This value was computed to be approximately 1.4 inches of column tip displacement producing

yielding in the column exterior longitudinal reinforcing bar at the column/cap beam interface. Pattern 2 of the loading procedure (Figure 10a) was applied after the 2nd cycle at each displacement level after yielding to investigate stiffness degradation of the specimen. The test setup is illustrated after the completion of the tests in Figures 11a and 11b for specimens C1 and C2, respectively.

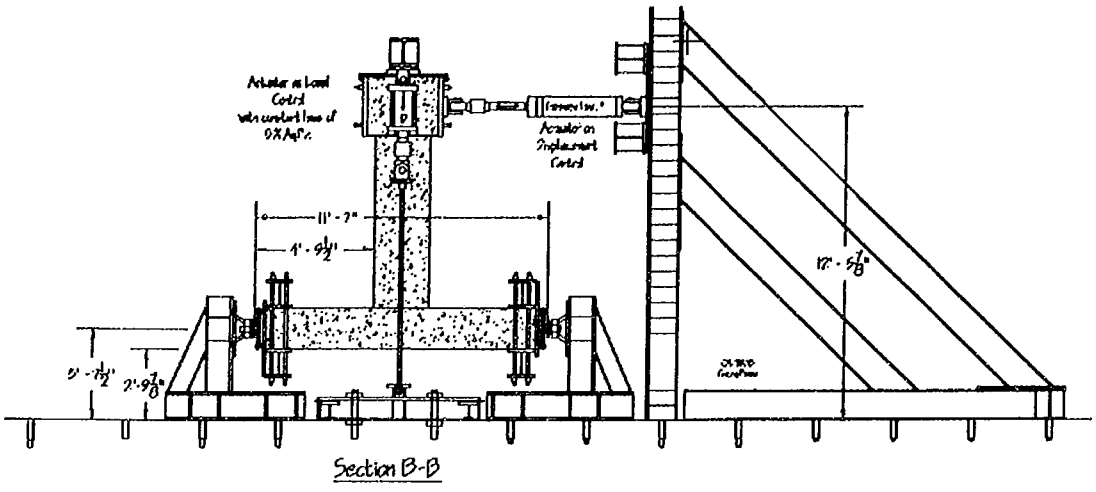


Figure 8: Elevation of test setup with pins [Sec. B-B location is indicated in Figure 9]

Test Results

In this section, results from testing specimens C1 and C2 are summarized. Figures 12a and 12b compare the sequence of joint damage for specimens C1 and C2, respectively. These different levels of damage are correlated with the observed displacement ductility (μ). The final damage states of the joint panels and the corresponding global damage of specimens C1 and C2 are illustrated in Figures 13a and 13b, respectively. Tables 5 and 6 give key observations and detailed information from testing these specimens. The loading protocol for specimen C2 is shown in Figures 14 and 15. It should be noted that the loading protocol for specimen C1 is similar to that of specimen C2. The obtained load-displacement relations in the transverse and longitudinal directions for specimen C1 are shown in Figures 16 and 17, respectively. Similar results are shown for specimen C2 in Figures 18, and 19. In Table 6, the peak displacement (δ_{max}) corresponds to the peak load and the ultimate displacement (δ_u) is the post-peak displacement which corresponds to an ultimate force equals to the yield force. The reported displacements in Tables 5 and 6 correspond to the displacements at the point of load application. This required some transformation of the command signals of displacements which were applied at a slightly lower level than the applied load because of the physical locations of the displacement transducers relative to the actuators applying the lateral loads.

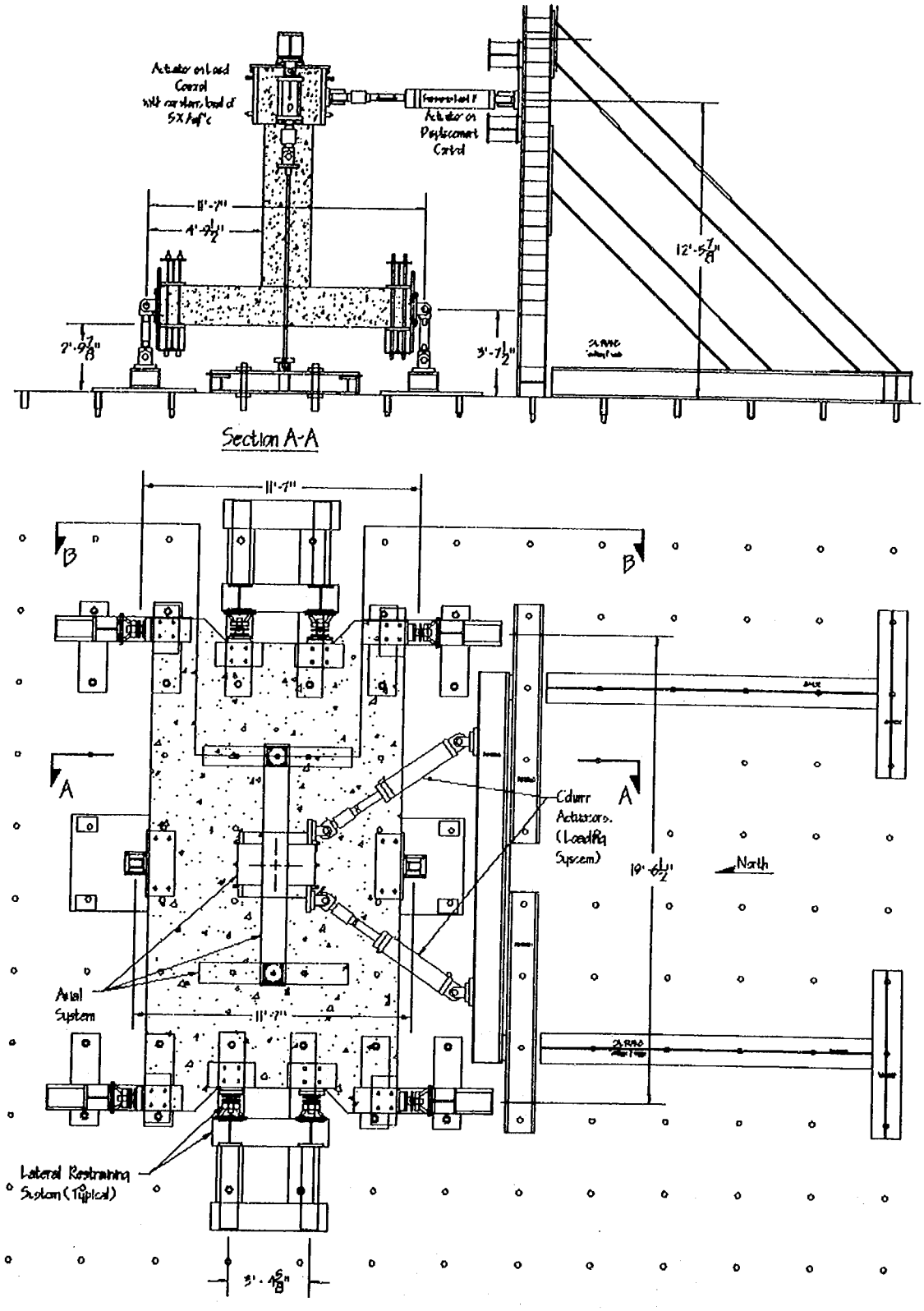


Figure 9: Elevation of test setup with struts (top) and plan view (bottom)

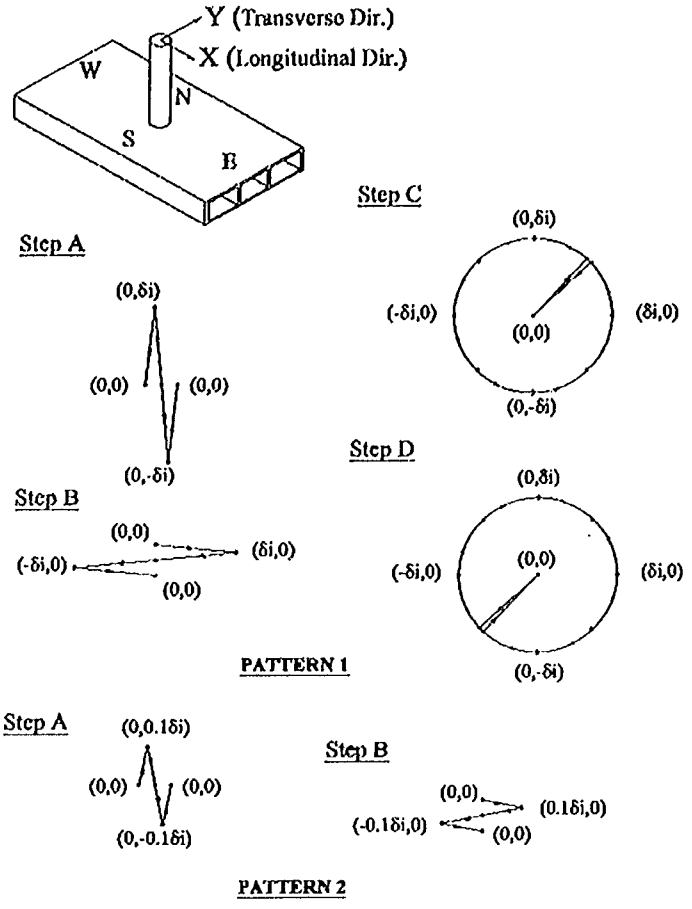


Figure 10a: Loading procedure

Specimen C1

Cycle Number (#)	Pattern Type	Displacement Ductility (#*Dy)	Peak Amplitude (inches)	Loading Rate (in/sec)
1	1	0.05	0.06	0.01
2	1	0.05	0.06	0.01
3	1	0.11	0.15	0.02
4	1	0.23	0.3	0.02
5	1	0.53	0.7	0.02
6	1	1.06	1.4	0.02
7	2*	0.5	0.66	0.02
8	1	2	2.64	0.02
9	1	2	2.64	0.02
10	2*	0.5	0.66	0.02
11	1	3	3.96	0.02
12	1	3	3.96	0.04
13	2*	0.5	0.66	0.02
14	1	5	6.6	0.06
15	1	5	6.6	0.06
16	2*	0.5	0.66	0.02
17	1	7	9.24	0.06
18	2*	0.5	0.66	0.02

Specimen C2

Cycle Number (#)	Pattern Type	Displacement Ductility (#*Dy)	Peak Amplitude (inches)	Loading Rate (in/sec)
1	1	0.12	0.15	0.02
2	1	0.23	0.30	0.02
3	1	0.54	0.70	0.02
4	1	1.08	1.40	0.02
5	2*	0.23	0.30	0.02
6	1	2.00	2.60	0.06
7	1	2.00	2.60	0.06
8	2*	0.50	0.65	0.02
9	1	3.00	3.90	0.06
10	1	3.00	3.90	0.06
11	2*	0.50	0.65	0.02
12	1	5.00	6.50	0.06
13	1	5.00	6.50	0.09
14	2*	0.50	0.65	0.02
15	1	6.00	7.80	0.09
16	2*	0.50	0.65	0.02

*Note: Prior to Pattern 2 cycles load is decreased to zero

Figure 10b: Loading schedule

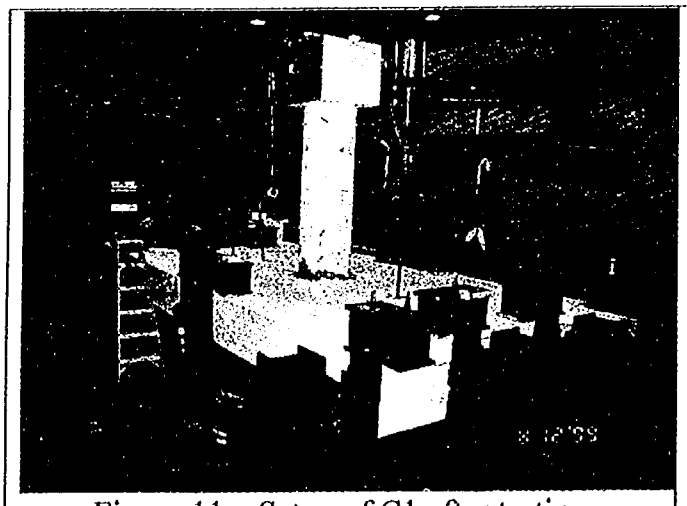


Figure 11a: Setup of C1 after testing

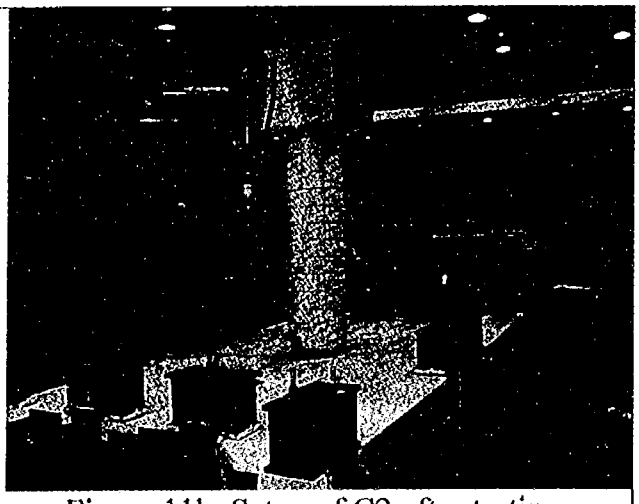
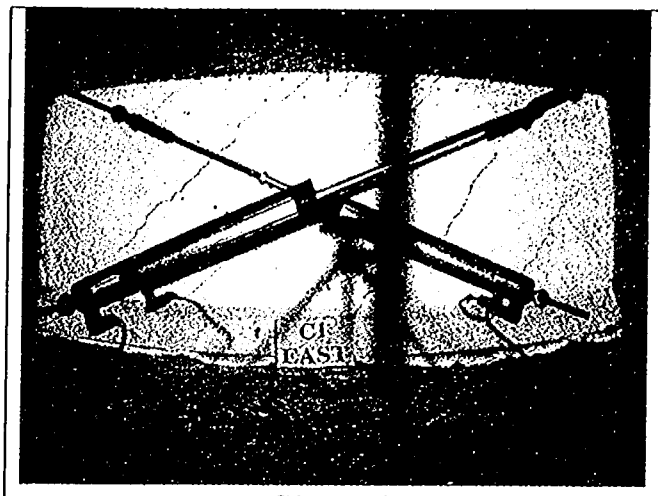
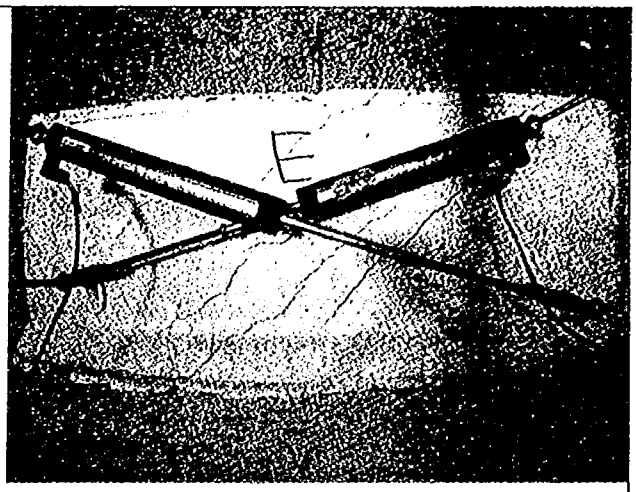


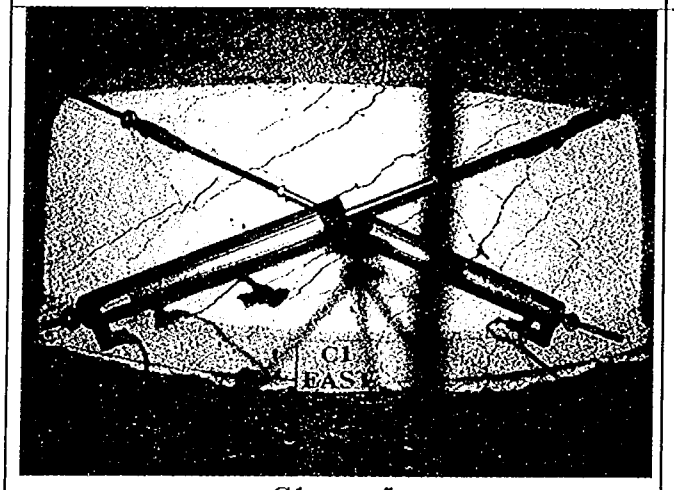
Figure 11b: Setup of C2 after testing



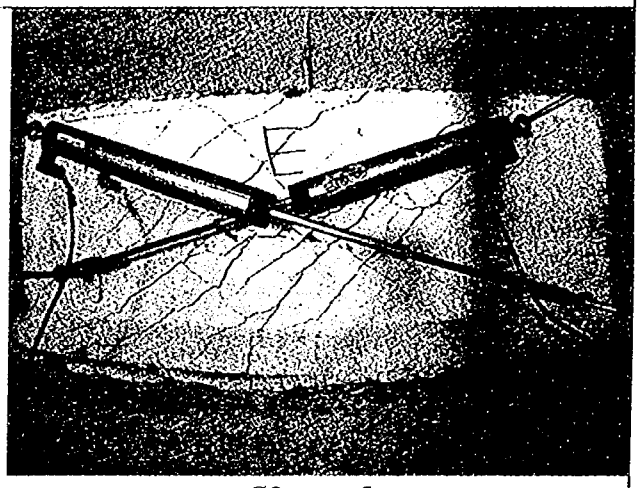
C1, $\mu = 3$



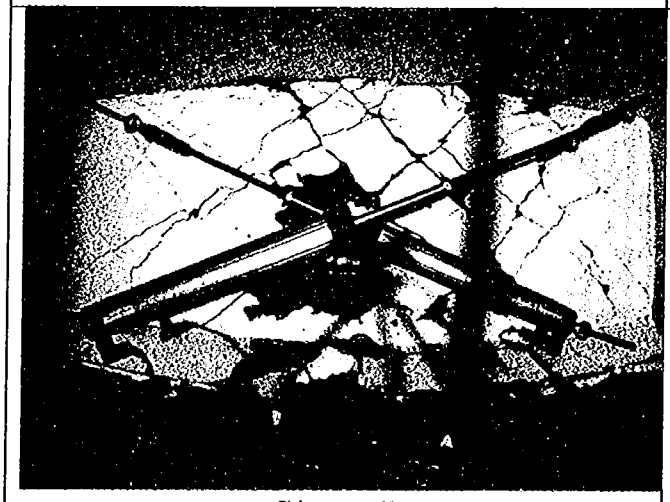
C2, $\mu = 3$



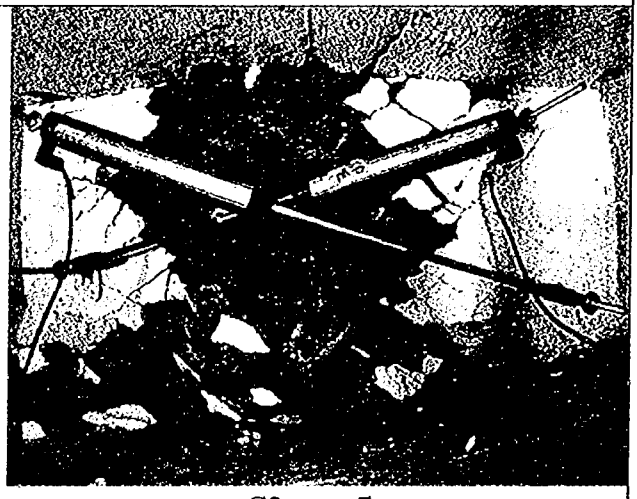
C1, $\mu = 5$



C2, $\mu = 5$



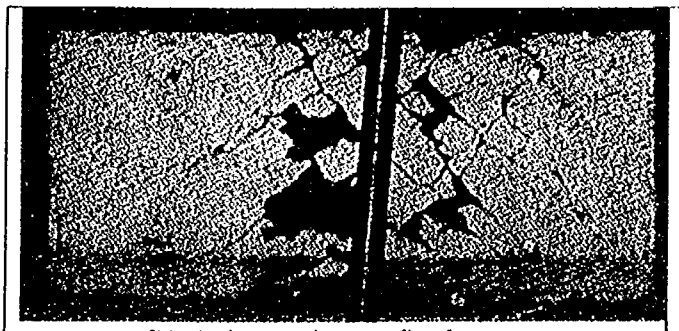
C1, $\mu = 7$



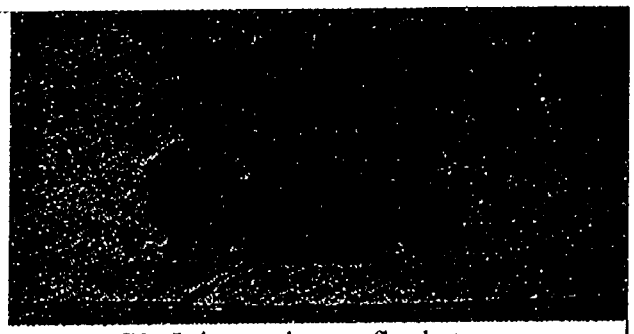
C2, $\mu = 7$

Figure 12a: Sequence of joint damage for specimen C1 at different ductility levels (μ)

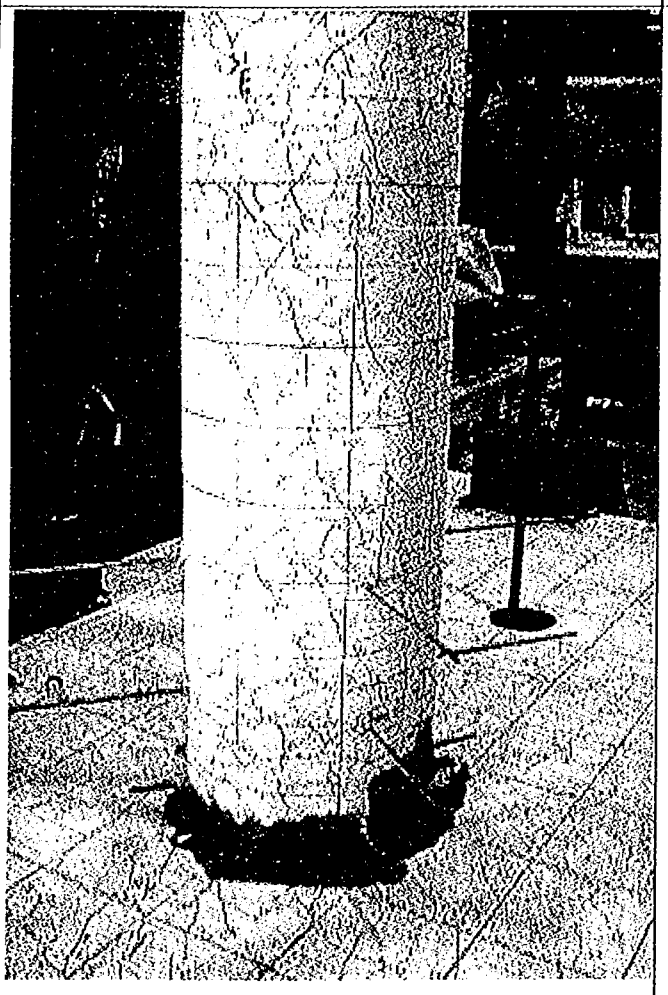
Figure 12b: Sequence of joint damage for specimen C2 at different ductility levels (μ)



C1, Joint region at final stage

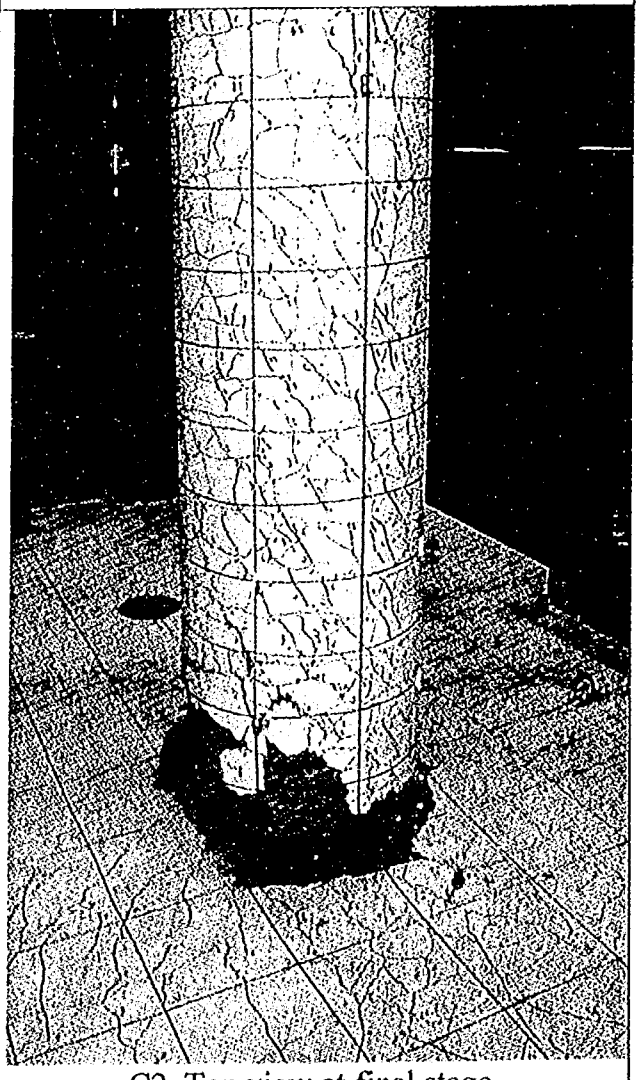


C2, Joint region at final stage



C1, Top view at final stage

Figure 13a: Specimen C1 at final stage of damage: joint panel (top), top view (bottom)



C2, Top view at final stage

Figure 13b: Specimen C2 at final stage of damage: joint panel (top), top view (bottom)

Table 5: Key test observations of specimens C1 and C2		
Event #	Column Tip Displacement (in.)	Event Description
Specimen C1		
1	0.30" – N – Cycle 1	Column cracking
2	0.70" – E – Cycle 1	Joint cracking
3	1.34" on 1.40" – S– Cycle 1	1st Yield of column N-S – North bar @ beam interface in column
4	1.368" on 2.64" – E – Cycle 1	Yield on column E-W – East bar @ beam interface in column *
5	4.35" on 3.96" – S – Cycle 1	Peak displacement N-S (Corresponding to peak force)
6	3.9" on 3.96" – W – Cycle 1	Peak displacement E-W (Corresponding to peak force)
Specimen C2		
1	0.15" – N – Cycle 1	Column cracking
2	0.70" – N – Cycle 1	Joint cracking & beam flexural cracking
3	1.42" on 1.4 " – S– Cycle 1	1st Yield of column N-S – North bar @ beam interface in column
4	1.37" on 2.6" – E – Cycle 1	Yield of column E-W – West bar @ beam interface in column**
5	6.25" on 6.5" – W – Cycle 1	Peak displacement E-W (Corresponding to peak force)
6	7.38" on 7.8" – S – Cycle 1	Peak displacement N-S (Corresponding to peak force)

* Yield in E-W direction is not the first yield of the bar. First yield occurred while moving North on 2.64" cycle.
**Yield in E-W direction is not the first yield of the bar. First yield occurred while moving South on 2.6" cycle.

Table 6: Detailed information of specimens C1 and C2		
Test Values	Transverse (N-S)	Longitudinal (E-W)
Specimen C1		
Yield force, P_y,	64.5 kips	53.62 kips
Peak force, P_{max}	96.0 kips	96.8 kips
Ultimate Force, P_{ult}	Yield force = 64.5 kips	53.62 kips
P_{max}/P_y	1.5	1.8
Yield displacement, δ_y	1.34 in.	1.37 in
Peak displacement, δ_{max}	4.35 in.	3.91 in.
Ultimate displacement, δ_u	8.28 in.	7.03 in.
Displacement ductility, δ_u/δ_y	6.18	5.13
Peak moment applied	9216 kip-in = 93.7 % of M_{ult}*	9293 kip-in = 94.5 % of M_{ult}*
Height of column spalling	~9 in.	~6 in.
Yield stiffness, $K_y = P_y/\delta_y$	48.0 kips/inch	39.1 kips/inch
Peak stiffness, $K_{max} = P_{max}/\delta_{max}$	22.1 kips/inch	24.8 kips/inch
Ultimate stiffness, $K_{ult} = P_{ult}/\delta_{ult}$	7.79 kips/inch	7.63 kips/inch
Specimen C2		
Yield force, P_y,	72.87 kips	45.07kips
Peak force, P_{max}	116.72 kips	91.67 kips
Ultimate Force, P_{ult}	Yield force = 72.87 kips	45.07kips
P_{max}/P_y	1.60	2.03
Yield displacement, δ_y	1.42 in.	1.37 in.
Peak displacement, δ_{max}	7.37 in.	6.25 in.
Ultimate displacement, δ_u	8.863 in.	7.70 in.
Displacement ductility, δ_u/δ_y	6.24	5.62
Peak moment applied	11205 kip-in = 113.9 % of M_{ult}*	8800 kip-in = 89.5 % of M_{ult}*
Height of column spalling	~ 9 in	~ 12 in.
Yield stiffness, $K_y = P_y/\delta_y$	51.30 kips/inch	32.90 kip/inch
Peak stiffness, $K_{max} = P_{max}/\delta_{max}$	15.84 kips/inch	14.67 kips/inch
Ultimate stiffness, $K_{ult} = P_{ult}/\delta_{ult}$	8.22 kips/inch	5.85 kips/inch

* Based on moment-curvature analysis of the as-built column cross-sections of the tested specimens.

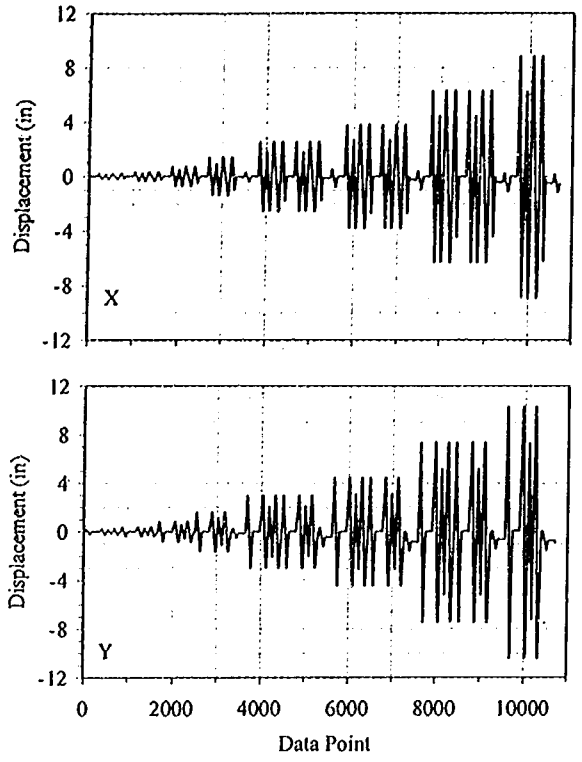


Figure 14: Displacement history, specimen C2

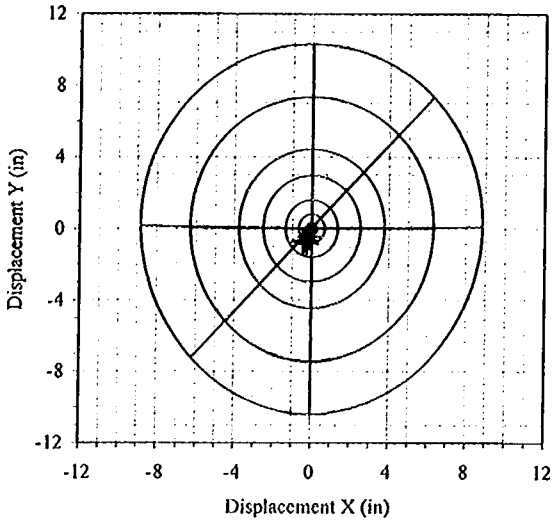


Figure 15: Displacement configuration, C2

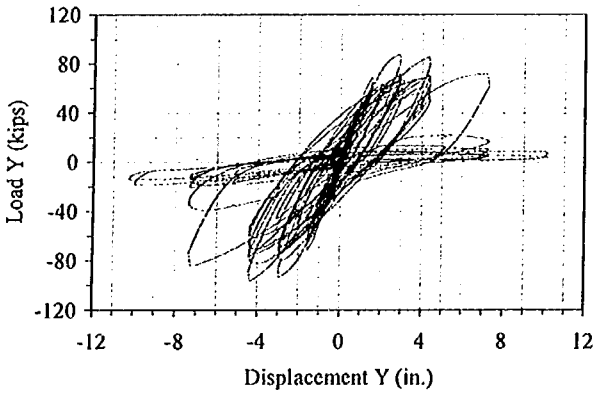


Figure 16: Load-displ. in trans. dir., C1 (N-S)

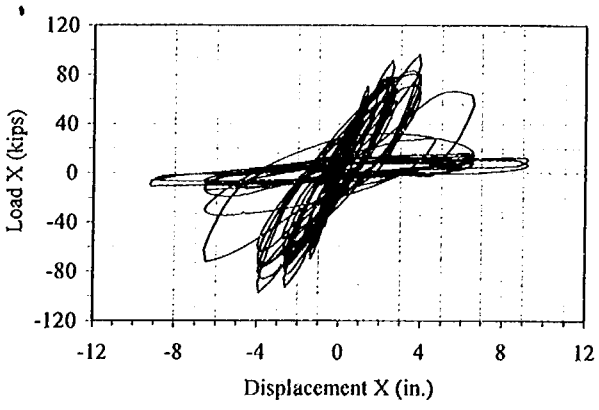


Figure 17: Load-displ. in long. dir., C1 (E-W)

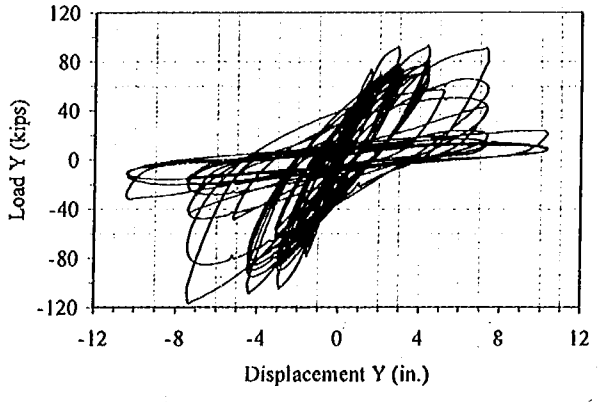


Figure 18: Load-displ. in trans. dir., C2 (N-S)

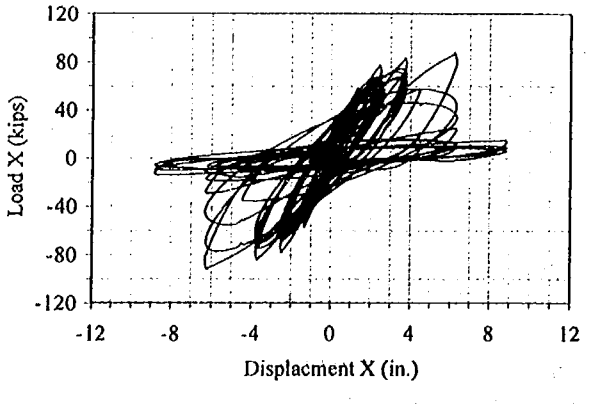


Figure 19: Load-displ. in long. dir., C2 (E-W)

Discussion of Test Results

In both specimens C1 and C2, pullout of the column longitudinal reinforcement controlled the ultimate response of the specimens. Column damage consisted of flexural and shear cracking and minor spalling all around the column in the vicinity of the column/cap beam interface. Unlike specimens of Group A, buckling or fracture of the column reinforcement did not occur. Overall system strength and stiffness were comparable for both specimens with higher yield load and displacement ductility in transverse direction than longitudinal direction. As expected, the beam/column joints showed less damage than specimens of Group B and more damage than specimens of Group A. It can be observed from the load-displacement relations (Figures 16 through 19) that loss of strength in specimen C1 occurred over a single cycle beyond the peak (brittle failure) whereas in specimen C2 the loss of strength was distributed over several cycles beyond the peak (gradual failure). From the external final damage states of the joint regions (Figures 13a and 13b), one observes that more concrete spalling occurred in specimen C2 (which is reinforced with headed bars) than that for specimen C1 (which is reinforced with traditional hairpins).

Concluding Remarks and Future Extensions

From the above test results and discussions, one may conclude the following:

1) The use of headed bars in the joint region instead of traditional reinforcement doesn't affect the response in the longitudinal direction of the bridge. On the contrary, significant improvement of the strength and stiffness is achieved in the transverse direction.
2) Although external damage (concrete spalling) of the joint region is more pronounced in the case of headed bars, it is evident that the joint suffered less internal damage in this case, i.e. had better confinement and less dilation. This is reflected in delaying the pullout of column bars.
3) It is recommended to investigate the use of headed bars as longitudinal column reinforcement to prevent their pullout.

Further investigation of the experimental data and development of computational models using three-dimensional finite elements are currently under development for in-depth understanding of these tested specimens. Some of the issues to be investigated analytically are the effect of different loading patterns and the role of post-tensioning.

Acknowledgments

This research was funded by California Department of Transportation and Headed Reinforcement Corporation. The authors acknowledge the assistance of the staff of the Structural Engineering lab. of UCB. Special thanks are due to Prof. Jack P. Moehle for his valuable input during this study.

References

California Department of Transportation (Caltrans), Division of Structures, California Bridge Design Specifications, December 1995.

Naito, C.J., Innovative Design and Performance of Reinforced Concrete Bridge Beam-Column Connections, PhD Dissertation, University of California, Berkeley, December 1999.

Naito, C.J., K.M. Mosalam, J.P. Moehle, Evaluation of Reinforced Concrete Bridge Joints, Proc. 12WCEE, January 2000.

Development of Electric Anticorrosion Methods for Newly Constructed Concrete Structures

Masaru Terada[*1]
Seishi Meiarashi[*2]

Summary

Electric anticorrosion methods have attracted attention as a countermeasure for deterioration due to salt damage, and there have been numerous reports on their effectiveness. However, the present electric anticorrosion methods focus on repair and strengthening of existing structures, without considering application to newly constructed structures. In this study, the authors conducted anticorrosion tests in an attempt to develop electric anticorrosion methods to be applied to newly constructed structures, with which electric current for anticorrosion is supplied when corrosion is detected.

Using PC columns and RC small-size specimens, on which electric anticorrosion materials had been installed during construction, electric anticorrosion tests were conducted to assess the workability and anticorrosion effect of five electric anticorrosion methods. When electric current was applied to the PC columns (170 days) and RC small-size specimens (140 days), no abnormality was observed on the reinforcing steels of any specimens, thus proving the effectiveness of these electric anticorrosion methods.

1. Introduction

Concrete structures constructed in marine environments may suffer damage due to salt air and salt-water splashes. The majority of deterioration of reinforced concrete structures is caused by corrosion of the reinforcing steels. Recently, electric anticorrosion methods have attracted attention as a countermeasure for deterioration due to salt damage, and there have been numerous reports on their effectiveness. Since the corrosion of reinforcing steels inside concrete due to salt damage is an electrochemical phenomenon, it is theoretically possible to use electrochemical methods for preventing such damage. However, the present electric anticorrosion methods focus on repair and strengthening of existing structures, without considering application to newly constructed structures. Thus, in an attempt to develop electric anticorrosion methods, with which electrodes are installed

---

*1 Research Engineer, Chemistry Division, Materials and Construction Department, Public Works Research Institute, Ministry of Construction

*2 Head, Chemistry Division, Materials and Construction Department, Public Works Research Institute, Ministry of Construction

when a structure is newly constructed to supply anticorrosion electric current when corrosion occurs, the authors assessed the workability and the effect of five anticorrosion methods.

2. Electric Anticorrosion Tests Using PC Columns

2.1 Methodology

Electric anticorrosion tests were conducted using five electric anticorrosion methods. The corrosion potential of reinforcing steels was measured using three reference electrodes that had been built into the specimens, the reduction of anode material by corrosion was measured upon detecting corrosion, and the weights before and after starting the tests were compared.

(1) Shape and types of the PC column specimens

PC columns of L5,300 mm × W700 mm × H350 mm (equivalent to those for the slab bridge JIS A 5313 AS-05) were prepared as specimens for the tests. Figure 1 shows the schematic illustration of the shape of a specimen.

(2) Concrete mix

Table 1 shows the specified mix of concrete. As for the conditions of the mix design, the design strength was 49.1 N/mm^2, and the strength at prestressing was 34.3 N/mm^2. The cement used was quick-high-strength Portland cement; the fine aggregate was river sand taken from Sakawa River (density in saturated surface-dry condition 2.63 g/cm^3, percentage water absorption 1.70%, and fineness modulus 2.89); the coarse aggregate was crushed stones taken from Hatsukari in Otsuki City (Gmax = 20 mm, density in saturated surface-dry condition 2.66 g/cm^3, percentage water absorption 1.30%, and fineness modulus 6.70); and a high-performance AE water reducing agent was used. To accelerate the initiation of rust, 10 kg/cm^3 of NaCl of Cl concentration was mixed into the specimens when produced. Three reference electrodes were built into the respective specimens to measure the electric potential of the reinforcing steels of the specimens.

(3) Place for exposure tests: The Construction Materials Research Facility located on the site of the Public Works Research Institute

(4) Electric anticorrosion methods: Five types of anode materials

1) Titanium grid method (TG)

Electrodes of ribbon-shaped titanium wires (20 mm wide and 0.6 mm thick) coated with a platinum oxide were fixed along stirrups on a mortar plate (L820 mm × W40 mm × H12 mm) by resin jigs; the respective electrodes were connected with each other by titanium plates; and then concrete was placed.

2) Panel anode method (TM)

A permanent form (t = 20 mm) with electrodes of titanium wires in meshes coated with a platinum oxide was prepared, onto which concrete was placed.

3) Titanium weld-spraying method (TS)

After making a specimen, the titanium material was arc-welded until the electric resistance of the electrode became 0.5 Ω (sq.) or less. Then, cobalt nitrate (catalyst solution) was applied to activate the electrode by anode electrolysis to make it a coated electrode.

4) Zinc aluminum pseudo alloy weld-spraying method (AS)

After making a specimen, a coated electrode was made by washing the concrete surface, applying a rough coating material, arc-welding a zinc aluminum pseudo alloy, and applying a sealing agent and a finish coat material.

5) Ribbon mesh method (RM)

Electrodes of ribbon-shaped titanium wires (13 mm wide and 0.6 mm thick) coated with a platinum oxide were fixed onto the reinforcing steels by resin jigs; the respective electrodes were connected with each other by titanium plates; and then concrete was placed.

2.2 Test Results

Measurements of the amount of corrosion of the anode and the corrosion electrodes of the respective specimens before the tests and up to the 170th day after applying electric current, showed that the corrosion electrodes of all the specimens to which electric anticorrosion treatment had been applied did not vary, and no rust was observed on the reinforcing steels. In addition, the weight reduction of anode materials due to corrosion was nearly zero, showing that no anode material suffered rust or deterioration. Figure 2 shows the density of electric current and the amount of depolarization after applying electric current. The amount of depolarization of all the specimens satisfied the value of 100 mV on the 170th day after applying electric current, which is the required criteria for the effect of anticorrosion (if depolarization exceeds 100 mV, electric anticorrosion is considered to have occurred); thus, all the five methods were proven to be effective. Electric current with a density of 4 ~ 8 mA/ m^2 had been applied to the respective specimens from the outset, but no reinforcing steels were corroded as of the 180th day after applying electric current. Thus, it is considered that the anticorrosion effect can be obtained even with a lower density of electric current.

3. Electric Anticorrosion Tests Using RC Small-side Specimens

3.1 Methodology

An acceleration test was conducted using a total of 7 specimens, i.e., 6 types of anode materials and one blank. After confirming the initiation of rust, electric anticorrosion tests were commenced. During monitoring, the specimens were overhauled to observe the state of corrosion of reinforcing steels.

(1) RC small-size specimen

35 mm of net covering with a reinforcing steel (SR24 ϕ 13 mm) measuring W200 mm $\times$ H200 mm $\times$ L400 mm (10 kg/m^3 of salt content (NaCl) was mixed into the specimen to accelerate rust initiation)

(2) Electric anticorrosion method

① titanium grid (TG) method; ② panel anode (TM) method; ③ zinc aluminum pseudo alloy weld-spraying (AS) method; ④ Titanium weld-spraying (TS) method; ⑤ ribbon mesh (RM) method; and ⑥ titanium rod (TR) method.

(3) Acceleration test

A cycle of "drying at 30℃ + spraying" was conducted for ten minutes once a week for 140 days.

3.2 Test results

Figure 3 shows the results of monitoring the corrosion electric potential. Although electric current with a density of 10 mV/ m^2 had been applied until the 80th day, the amount of depolarization of all the specimens was less than 100 mV. Accordingly, the density was increased to 20 mV/m^2 after the 80th day, by which the amount of depolarization of five electric anticorrosion methods (TG, TM, TS, RM, and TR) became 100 mV or over, thus showing the effect of anticorrosion. However, corrosion was not impeded for AS (zinc aluminum pseudo spraying method), for which the amount of depolarization was 100 mV or less. The authors intend to confirm further the effect of anticorrosion by applying electric current of higher density.

Table 2 shows the amount of reduction of the anode materials of the respective specimens due to corrosion and the ratio of corroded area of the reinforcing steels, which were measured before the electric anticorrosion tests and 140 days after applying electric current. Although corrosion progressed with the blank specimen, for which the corroded area had become double the initial value by the 140th day, all the remaining specimens showed no progress of corrosion, thus demonstrating the effectiveness of the electric anticorrosion methods. In addition, no weight reduction of the anode materials by corrosion was observed in any of the specimens after overhauling.

4. Future Plans

The authors plan to confirm further the anticorrosion effect by introducing a remote monitoring device, continue electric anticorrosion tests until stratified rust appears on the reinforcing steels to which no electric anticorrosion treatment has been applied, and conduct a comparative study on the electric anticorrosion methods to assess the durability of anode materials and the effect of anticorrosion.

Table 1 Specified Mix of Concrete

Water-cement ratio W/C (%)	Sand percentage S/a (%)	Quantity of materials per unit volume of concrete (kg/m^3)						Slump (cm)	Air content (%)
		Water W	Cement C	Fine aggregate S	Coarse aggregate G	Cl	AE Water-reducing agent		
37.1	39.0	156	420	710	1128	10	4.62	8.0 ±1.5	1.5 ±1.0

Table 2 Anode Corrosion of Specimens and Ratio of Corroded Area of Reinforcing Steels

Specimen	After applying electric current	0 day	140 days
TG	Reduction of anode material by corrosion (g)	0.0001	0.0001
	Ratio of corroded area of reinforcing steels (%)	14.8	15.6
TM	Reduction of anode material by corrosion (g)	0.0001	0.0001
	Ratio of corroded area of reinforcing steels (%)	11.6	13.5
AS	Reduction of anode material by corrosion (g)	0.0001	0.0001
	Ratio of corroded area of reinforcing steels (%)	16.8	18.9
TS	Reduction of anode material by corrosion (g)	0.0001	0.0001
	Ratio of corroded area of reinforcing steels (%)	19.3	21.3
RM	Reduction of anode material by corrosion (g)	0.0001	0.0001
	Ratio of corroded area of reinforcing steels (%)	20.6	29.1
TR	Reduction of anode material by corrosion (g)	0.0001	0.0001
	Ratio of corroded area of reinforcing steels (%)	19.7	21.5
Blank	Reduction of anode material by corrosion (g)	-	-
	Ratio of corroded area of reinforcing steels (%)	30.8	65.2

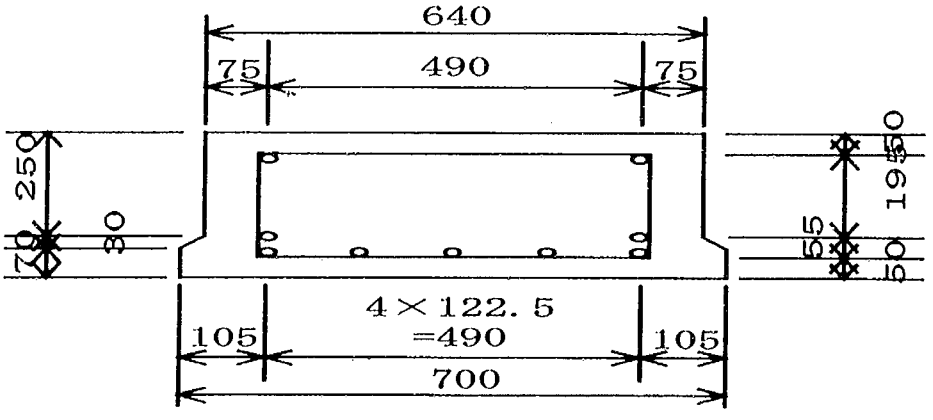


Figure 1 Shape of Specimen (cross section)
Unit: mm

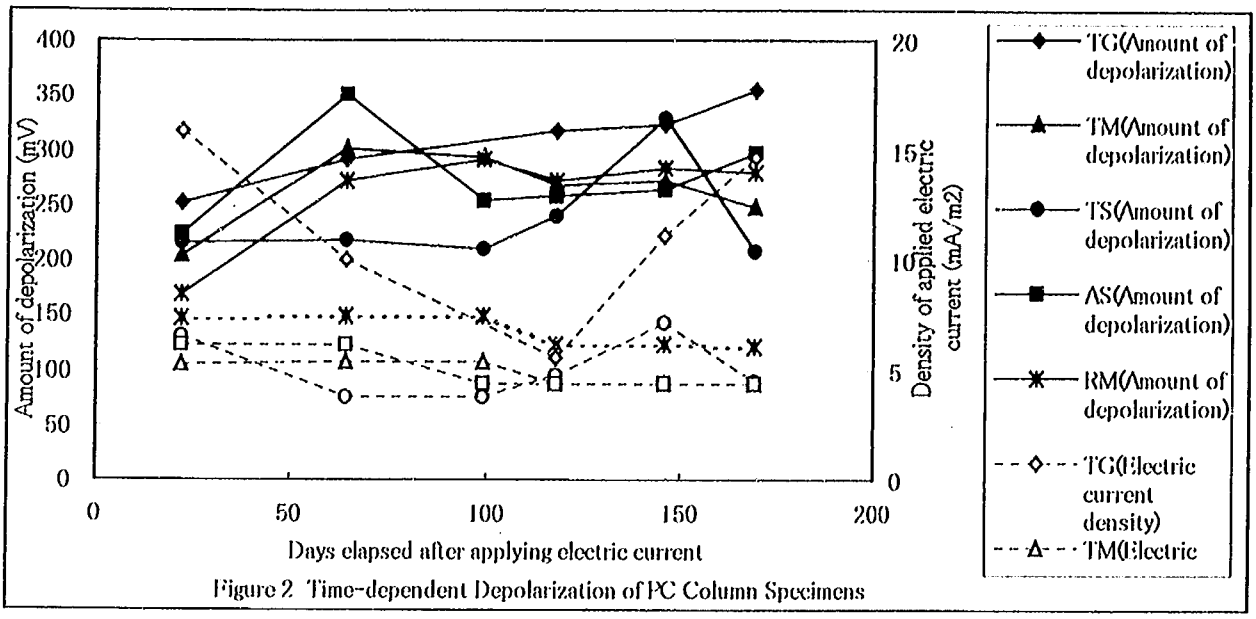


Figure 2 Time-dependent Depolarization of PC Column Specimens

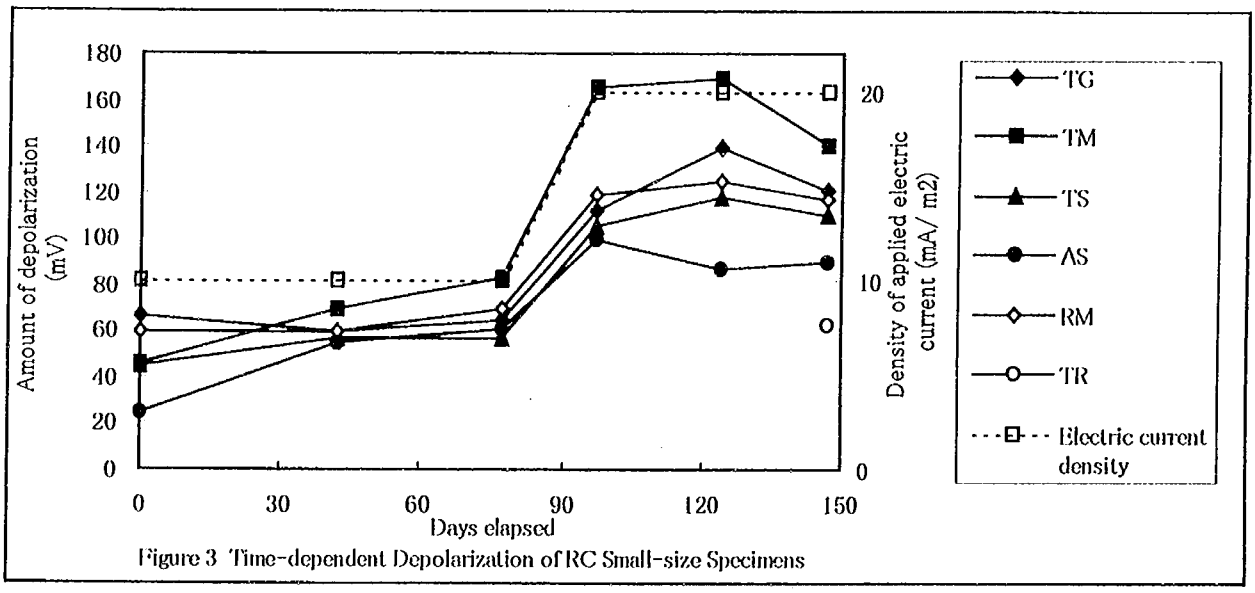


Figure 3 Time-dependent Depolarization of RC Small-size Specimens

Corrosion Control of Concrete Bridges

Yash Paul Virmani
Federal Highway Administration
6300 Georgetown Pike
McLean, VA 22101

Abstract

Premature corrosion of black reinforcing steel has caused many concrete bridges in the United States to deteriorate before their design life was attained. This brief paper summarizes the extent of the problem for both reinforced and prestressed concrete (R/C and PS/C) and solutions for their construction and rehabilitation with cost effective corrosion protection systems developed through intensive research and field validation studies.

Introduction: History and Problem

Concrete is a construction material that is relatively easy to work with. However, concrete is very weak in tension in comparison to its compressive strength. Because of the low tensile strength of concrete, reinforcing steel bars are placed in regions of tension in a concrete member. This combination of concrete and steel provides a relatively inexpensive and durable material that has become widely used in construction of roadways and bridges. Reinforced concrete bridges built with black steel have functioned reasonably well until the late 1960s, when premature concrete delamination and spalling, which used to be encountered only in coastal areas, became common in many of the reinforced concrete bridge decks in the "snow belt" and were beginning to require maintenance after being in service for as little as 5 years. The emergence of this type of concrete deterioration, which was first observed in marine structures and chemical manufacturing plants, coincided with the increased application of deicing salts (sodium and calcium chlorides) to roads and bridges during winter months in those states where ice and snow are a problem to implement a "bare pavement policy".

It was recognized by the mid 1970s that this problem is caused by the corrosion of the black reinforcing steel in the concrete which, in turns, is induced by the intrusion of even a small amount of chloride from the deicing salts into the concrete. It is difficult to estimate the cost of these corrosion-related damages to conventionally reinforced and prestressed concrete bridge components in the nation. According to a 1997 report, of the 581,862 bridges in and off the federal-aid system, about 101,518 bridges were rated as structurally deficient. Most of these bridges are not in danger of collapse, but they are likely to be load posted so that overweight trucks will be required to take a longer alternative route. The estimated cost to eliminate all backlog bridge deficiencies (including structurally and functionally) is approximately $78 billion, and it could increase to as much as $112 billions, depending on the number of years it takes to meet the objective. The average annual cost, through year 2,011, for just maintaining the overall bridge conditions, i.e., the total number and the distribution of structurally and functionally deficient bridges, is estimated to be $5.2 billions. While corrosion of the reinforcing steel is not the sole cause of all structural deficiencies, it is a significant contributor and has therefore becomes a matter of major concern.

The magnitude of this corrosion problem in the transportation infrastructure has increased

significantly in the last three decades and is likely to keep increasing. Even though the cost of maintaining bridge decks is becoming prohibitively expensive, the benefits provided by deicing salts are too great, however, that it's use is not likely to decrease in the future. In fact, the use of road deicing salts, which are extremely corrosive due to the disruptive effects of its chloride ions on protective films on metals, has actually increased in the first half of the 1990s—after a leveling off during the 1980s. Although an alternative effective and less corrosive deicing agent, calcium magnesium acetate (CMA), is available, its price is apparently not yet reasonable enough for winter maintenance engineers to use widely. Therefore, it can be expected that the road environment would likely remain corrosive, if not more, well into the future.

The application of prestressed concrete technology in building bridges is relatively recent. Therefore, the existing prestressed concrete members in bridges are still relatively young, and the corrosion and the concrete deterioration problems associated with this type of concrete members have only became evident in the early 1980s. Although prestressed concrete members were generally manufactured with concrete of relatively higher strength, time has shown that they are subject to the same adverse effects of reinforcement corrosion as reinforced concrete members are. Documented cases of prestressed strands breaking as a result of corrosion make this a most pressing problem. Since PS/C members rely on the tensile strength of the strands to resist loads, loss of even a few strands per member could prove catastrophic. In addition, because of the high stress the strands are subjected to accelerated corrosion effects. Even small corrosion pits could cause fracture of a strand, as compared to non-prestressed reinforcing steel that will literally rust away before breaking. Of the 581,862 bridges in the National Bridge Inventory, slightly more than 10 percent have prestressed concrete superstructures, all of which will eventually need some protective measures applied to them. In addition, many of the other structures not in the inventory have prestressed substructure members that will likewise need some degree of corrosion protection.

Corrosion Protection Systems for Construction of R/C and PS/C Bridges

The use of good construction design and procedures, adequate concrete cover depth, corrosion-inhibiting admixture, and low-permeability concrete alone will not abate the corrosion problem, because concrete has a tendency to crack inordinately. In fact, it has been observed lately that the new low permeability concrete or high-performance concrete (made from partial substitution of Portland cement with silica fume or fly ash) has an even more pronounced tendency than conventional concrete to crack—potentially trading a normally slow intrusion of chloride ions into the concrete (by the diffusion process) for a potentially faster gravity-assisted flow of salt-laden water. Even corrosion-inhibiting admixture for concrete would likely not be of use when the concrete cracked. This situation essentially leaves the reinforcing steel itself as the last line of defense against corrosion. For this very reason, the use of a barrier system on the reinforcing steel, such as epoxy coating or other organic or even other possible metallic coatings, is even more critical in abating this costly corrosion problem.

It is likely that there may never be any organic coating that can hold up to the extreme combination of constant wetting and high temperature and high humidity that reinforcing steel is exposed to in the marine environment in the state of Florida, especially in the splash zone, and that either steel bars coated with a sufficiently-stable metallic coating or a type of corrosion-resistant solid metal bars would have to be used in conjunction with the use of sound construction designs and concrete. However, there were very convincing reports of good corrosion resistance

performance shown by epoxy-coated steel bars in concrete bridge decks, where unlike in coastal bridges in the state of Florida, the concrete does not remain constantly wet and the other exposure condition is not as severe. And, just recently, good performance by epoxy-coated bars has been observed in 80 bridge decks surveyed in Pennsylvania and New York. It must also be mentioned that unfavorable performance by epoxy-coated bars has recently been claimed, albeit unconvincingly . In one latter case, the poor performing epoxy-coated rebars were located mostly in noise walls, where the quality of the concrete was known to be poor, and in concrete expansion dams (beside expansion joints), where it is suspected that the coated rebars may have been cleaned by abrasive blasting before pouring of the concrete.

The many successful performance of embedded epoxy-coated steel bars in places outside of Florida and possibly other similar locations, indicates that when used in exposure conditions that do not keep the concrete constantly wet, the epoxy coating will provide a good degree of protection to the steel bars and, thereby, delay the initiation of corrosion. The recent claims of poor performance of epoxy-coated rebars serve, at most, to indicate that the corrosion protection provided by ECR (more accurately, the old generation of ECR) is not permanent and also to raise the question: For how long does the use of ECR, in a particular exposure condition, delays the initiation of steel corrosion in the concrete? And, for a prospective user, the next question is: Is the savings in maintenance and traffic control costs resulting from this extra time worth the initial extra cost of using ECR instead of black steel bars? Unfortunately, accurate determination of the actual field performance of ECR in a particular state or region or exposure condition is extremely difficult, if not impossible, since many contributing factors are involved and have to be accounted for. Needless to say, the recent improvement of specifications for ECR by the industry and the tightening of requirements on proper storage and handling of ECR at construction sites will ensure good corrosion protection.

The recently completed research study on steel bars coated with new organic and metallic coatings and alternative solid metal bars has identified more corrosion-resistant and, hopefully, cost-effective alternative reinforcement for future use in concrete bridges.

For construction of new prestressed concrete bridge members, the use of a corrosion-inhibiting admixture in the concrete or the grout, in conjunction with use of good construction designs and practices, would provide some corrosion protection. However, studies on the long-term effectiveness of various commercial inhibitor admixtures are in progress.

Rehabilitation Methodology for R/C and PS/C Bridges

For existing chloride-contaminated concrete bridge decks, impressed-current cathodic protection—using titanium mesh anodes—provides the ultimate and permanent solution to stopping reinforcing steel corrosion in the structures, as long as associated rectifiers and electrical wiring are properly maintained. Electrochemical chloride extraction provides an alternative rehabilitation method for stopping steel corrosion in contaminated concrete, albeit less permanently. This alternative has the advantage of having no rectifier or wiring to maintain after the treatment.

These same corrosion protection methods are applicable for existing inland concrete substructures. However, in cathodic protection of such concrete members, the appropriate anodes to use include the arc- or flame-sprayed zinc coating and the water-based conductive paints. Although electrochemical chloride extraction is applicable to concrete substructures, it is more difficult to conduct this treatment efficiently on these bridge members than on bridge decks, because it is relatively difficult to set up the necessary treatment system on vertical concrete surfaces to keep

them wet during the entire treatment.

For various PS/C bridge members, either impressed-current or galvanic cathodic protection or both modes can be applied, depending on the types of the bridge members and their surrounding environments. However, before CP is applied to any of these PS/C members, it should be qualified. And, to ensure that no prestressed concrete member is overprotected, which may lead to hydrogen embrittlement of the high-strength prestressed steel strands, the use of electronic remote monitoring systems should be incorporated with any installed CP system.

For prestressed concrete bridge members, such as beams, box beams, etc., impressed-current cathodic protection—using arc-sprayed zinc or titanium as the anode—is the most suitable mode. However, when applying CP, measures must be taken to ensure that the drainage system on a bridge is always properly maintained, so that there would not be any uneven electrical resistivity across the concrete members that would lead to uneven distribution of protection current and subsequent overprotection of the wet areas. Otherwise, use of CP on such members has to be excluded.

For prestressed concrete piles in marine environment, either mode of CP can be applied—with the impressed-current mode allowing for control of the current density being applied on the prestressed steel strands. The use of the zinc-hydrogel and the arc-sprayed Al-Zn-In coating as a galvanic anode in this application appeared to be promising. However, the long-term durability of these galvanic anodes is still being evaluated.

Major Research Accomplishments

For New Construction

- The preferred primary corrosion-protection systems in many states has been fusion-bonded epoxy coated rebars (ECR), which have been used in approximately 20,000 reinforced concrete bridge decks. This rebar has performed very well in alleviating the problem of corrosion-induced deteriorations of concrete bridge decks. It is estimated that its use in the last 25 years has saved the taxpayers billions of dollars so far.

- To provide even longer service life to the concrete decks—75 years or longer—without any need to repair corrosion-induced concrete damage, a number of alloys and cladding have been developed for rebars. Most notable are solid stainless steel 316 rebars and stainless steel clad black bars, which have performed exceedingly well in accelerated screening corrosion tests. Both of these two new alternative reinforcing bars have the potential to provide an excellent corrosion protection system, albeit at a higher initial cost.

- The combined use of ECR and a corrosion inhibiting admixture, such as calcium nitrite, serves as a very good multiple corrosion protection system. However, the stability of this inhibitor is still under study. In addition, research efforts are under way to identify new inhibitors that are more effective than calcium nitrite.

- The combination of high temperature (38°C) and an intermediate level of humidity or moisture (75 percent) have been identified as environmental conditions that lead to high corrosion rates for steel in concrete. The use of a low water-cement ratio, incorporation of mineral admixture

and proper selection of cement type and aggregates contribute significantly to producing low-permeability durable concretes.

- For the protection of high-strength, seven-wire strands encased in ducts, mix designs for corrosion-resistant grout for filling the ducts have been developed. In addition, an accelerated corrosion test method has been developed for evaluating new grout mixes. These developments have become the basis of a new specification to be published by the Post-Tensioning Institute (PTI) by the end of 1999.

- Prompted by the sudden collapse of two post-tensioned bridges in the United Kingdom and one in Belgium, several different nondestructive inspection techniques were carefully evaluated to identify those that may be suitable for detecting voids in post-tensioned ducts. From these, the impact-echo technique was selected for improvement; then, it was successfully evaluated in the field. The equipment for this technique is now commercially available. A complementary magnetic-based, nondestructive technique for assessing section loss in the high strength steel strands in the ducts has been developed and field testing is underway. It is anticipated that when used in combination, the impact-echo and the magnetic-based techniques will allow complete inspection of post-tensioned systems, reducing the likelihood of any sudden collapse of post-tensioned bridges in the United States.

For Rehabilitation

- Cooperative research with industry and states in the development of durable anodes, monitoring devices, installation techniques, etc. has led to application of impressed-current cathodic protection systems on bridge decks as a routine rehabilitation technique.

- For cathodic protection of substructure members, especially those in a marine environment, two very promising galvanic anode systems have been developed. Initiatives in the industry and in some states, in cooperation with FHWA, have led to further developments and identification of additional anodes suitable for both impressed-current and galvanic cathodic protection of inland concrete substructures.

- Through extensive fundamental research and evaluation of cathodic protection systems that have been installed, significant advances have been made in the technology for cathodic protection of prestressed concrete components. Concerns about a loss of bond between the prestressing steel and concrete and possible hydrogen embrittlement (from overprotection of the prestressing steel) have been alleviated by the establishment of criteria for qualification of prestressed concrete bridge components for cathodic protection.

- Electrochemical chloride extraction is gaining acceptance by many State Highway Agencies due to the fact that no maintenance is required after completion of the process.

DURABILITY AND STRUCTURAL SAFETY EVALUATION OF RC GERBER'S BRIDGE SERVICING FOR MORE THAN 60 YEARS

Naoshige Nomura*1, Yoshihiro Tanaka*2 and Takeyuki Yokooka*3

Abstract

The Gerber's typed reinforced concrete bridge called Nasuno Bridge servicing for more than 60 years, has been investigated not only to examine the deterioration of concrete material and round bars but also to evaluate the structural safety of the Gerber's hinge member through the loading experiments and the finite element analyses. Through this investigation, valuable engineering information was obtained reasonably to maintain and strengthen the same type of the reinforced concrete bridges which were completed in the similar old ages in Japan. One of the remarkable points is that the material quality of concrete and the detail re-bar arrangement for the Gerber's hinge members are unveiled. It is also noted that the resisting shearing force of the Gerber's hinge members, although the diagonal cracks are appeared and the retrofit has been done by H-beams, demonstrated enough capacity.

1. Introduction

Nasuno Bridge on the national highway # 4 was completed in 1936. The bridge length and the width are 193.3 m and 7.5 m, respectively. The type of this bridge is so called "Gerber's type" which have been constructed more than 300 bridges in Japan. It is planned as shown in Photo. 1 that this bridge should be replaced because of the lack of traffic flow capacity, in May 1998 by new wider bridge.

The Road Management Technology Center organized the research working group of road bridge maintenance to carry out the material tests of bridge concrete and round bars as well as the structural experiments of the Gerber's hinge member according to the flow chart illustrated in Fig. 1. This paper will provide the basic information with respect to the bridge maintenance for the similar type of reinforced concrete bridge constructed in the years of 1930s in Japan.

2. Material Tests

2.1 Sampling spots for material tests and test items

The material physical and chemical tests were conducted for the core test specimen sampled from the slab, the main girder, the transverse girder and the piers of the 6th span (S_6) and the 7th span (S_7). The core test specimens are sampled one from in the air of the piers and other from in the underground of the piers. The material tests are composed of the in situ easy test and the detailed test using the core specimen. The material test procedure and the test items are illustrated in the Table 1. The sampling numbers of the concrete core specimen are 12 pieces from the suspended girders, 18 pieces from the supported girders and 5 pieces from the transverse girders.

2.2 Tests results

(1) Appearance check of concrete

Most of the crack width are less than 0.3 mm for all the main girder and the maximum crack width is observed 0.4 mm for the transverse girder. Furthermore, the extreme lack of the cover concrete or the evidence of corrosion of the round bars can seldom be found.

(2) Compressive strength and static elastic coefficient of concrete

The compressive strength of the concrete core specimens from Nasuno Bridge are scattering around 22.3 ~ 48.0 N/mm^2, the arithmetical average compressive strength becomes 36.7 N/mm^2 and the standard deviation is 5.67 N/mm^2.

The non-destructive compressive strength prediction test by Schmidt concrete test hammer was carried out in the vicinity of the sampling spots of concrete core specimens. The predicted values of compressive strength are calculated by the following formula which is recommended by Japan Society of Materials using the rebound hardness indicators (R_o) measured from Schmidt concrete test hammer.

$$F_c = 1.274R_o - 18.032 \qquad F_c : N/mm^2$$

The compressive strength test results obtained from the concrete core specimens and the predicted compressive strength measured by Schmidt concrete test hammer are compared in Fig. 2. Each compressive strength value by compressive testing machine and by Schmidt concrete test hammer is less mutually related; i.e. the coefficient of correlation is only 0.289. Although the compressive strength values from the concrete core specimens are showing from 25 to 45 N/mm^2, the predicted strength values by Schmidt concrete test hammer are upper bound around 30 N/mm^2. It should be noted that we have to be careful with the prediction for the old concrete strength by Schmidt concrete test hammer.

The compressive strength values of the concrete core specimens and the static elastic coefficients are illustrated in Fig. 3. The relationship between the compressive strength and the elastic coefficient which is recommended by "Concrete standard specification - design part" issued by Japan Society of Civil Engineering in 1996, is also compared with the tested data by compressive strength machine. It is observed that the static elastic coefficients from Nasuno Bridge concrete indicate a little bit lower than the recommended design value by JSCE.

(3) Estimation of concrete mix proportion

The concrete mix proportion of Nasuno Bridge is estimated according to the recommended method by Japan Cement Association. It is inspected that the coarse aggregate is composed of granite, sandstone, shale and tuff, however is not composed of limestone. Therefore, this prediction of concrete mix proportion must be accurate because of the lack of limestone.

The estimation result of the concrete mix proportion of Nasuno Bridge is indicated in Table 2. Another estimation of the concrete mix proportion based on "Concrete standard specification" issued by JSCE in 1931 is also listed in Table 2. At that old time, the concrete mix proportion is based on the mix proportion in volume; i.e. in general, proportional ratio of cement : fine aggregate : coarse aggregate was equal to 1 : 2 : 4. The listed mix proportion values are converted from this proportion in volume to proportion in weight. Compared with the estimated mix proportion values and the converted mix

proportion value, it is found that concrete mix proportion of Nasuno Bridge must be according to "Concrete standard specification" issued by JSCE in 1931.

The cement to water ratio obtained by the estimation of concrete mix proportion in Table 2, and the compressive strength of concrete core specimens are compared in Fig. 4. The relationship between the compressive strength and the cement to water ratio recommended by Japan Cement Association are also illustrated. From these comparisons, it should be noted that the quality of concrete strength in the yeas of 1930's is not inferior to that in nowadays.

(4) Resistance to freezing and thawing

The results of freezing and thawing test are illustrated in Table 3. After 30 cycles of freezing and thawing, the relative dynamic elastic coefficient decreased up to 20% in average; i.e. this means that this concrete is seriously poor for the resistance to freezing and thawing. One of the reason is that this concrete is non-AE concrete. It is said that the air entraining agent was applied to concrete for the first time in 1949 in Japan. Therefore, this concrete must be a sort of plain concrete. Through the appearance check, the severe deterioration of surface concrete was not observed. According to the risk distribution of frost damage in Japan by Hasegawa [1], the area of Nasuno Bridge is classified level-1 (small risk of frost damage). It should be noted that the severe maintenance check should be focused on the RC structures made of non-AE concrete in the years of 1930 ~ 1940's in cold regions.

(5) Carbonation thickness

The measured carbonation thickness from the concrete core specimens was 3.5 mm in minimum, 34.0 mm in maximum and 16.9 mm in average (standard deviation = 4.07 mm). The correlation between the carbonation thickness and compressive strength in core specimens is illustrated in Fig. 5. The correlation coefficient is 0.539. The carbonation thickness is predicted by Kishitani's formulation under the condition that the water cement ratio is 65 %, normal portland cement, no chemical admixture and river gravel. The carbonation thickness can be calculated 51 mm for the period of 60 years. Therefore, it is said that the carbonation thickness for the case of Nasuno Bridge is smaller compared with the general cases.

(6) Cover concrete thickness

Firstly the cover concrete thickness was measured at the main girder and piers by the reflection method of electromagnetic waves, then secondary the round bar location, diameter and cover concrete thickness were inspected by chipping the area of 200 mm x 200 mm. The cover concrete thickness measured by electromagnetic waves and by chipping method are compared in Fig. 6. It should be noted that the reflection method of electromagnetic waves is limited up to 60 mm cover concrete thickness.

(7) Tensile strength of round bars

The yield tensile stress and maximum tensile stress of the round bars are 282 N/mm^2 and 432 N/mm^2, respectively. It seems the round bars used in Nasuno Bridge must be the same type of SR235.

3. Structural Experiment

3.1 Cutting out specimens

The test specimens for the structural loading test were cut out of the main girder supported by the 10th pier (P10) as shown in Fig. 7. The main purpose of the structural loading experiment is to confirm the flexural and shearing strength of the hinge member which is in general easy to generate cracks. The main girders are consist of inside two main girders and outside two main girders. The outside girders are retrofitted by H-beams and are observed 0.1 mm wide cracks; on the other hand the inside girders seem to be no damages. The #1 test piece is cut from the inside girder and the #2 test piece is cut from the outside girder. The cutting method is that the main girders are cut by wire-saw and the slabs by wall-saw as shown in Photo. 2. From the observation of test pieces, it is found that the hinge member is fixed to slide; i.e. the round bars with diameter of 28 mm are X-crossing through the upper suspended girder and the lower supported girder which is called "Mesnager Hinge". Most of the cracks of the outside main girders seems to be caused by this Mesnager hinge.

3.2 Loading test

(1) Loading test arrangement

The test arrangement of bending moment and shearing loading for the hinge member is shown in Fig. 8. The test piece is up side down and is pressed at the center by the loading machine with the 9800 kN loading capacity. The loading force is supplied upwards on the hinge spot by the 1960kN capacity jack. The gap between the test piece and the loading machine is filled with the gypsum and cement mortal to uniformly transfer the reaction force to the loading machine and to the floor.

The measurement items of loading test are as follow ; the loading force is measured by the load cell, the deformation at each point of the test specimen is measured by the displacement gauges, the crack width of the hinge spot is measured by the contact-type strain gauge and the compressive strain of concrete surface is measured by the strain gauges.

(2) Experimental results

As a result of loading test, the loading force versus the displacement at the loading point is illustrated in Fig. 9 for the #1 test piece (no cracks in advance) and #2 test piece (cracks in advance). The crack pattern drawings for the #1 test piece and #2 test piece are illustrated in Fig. 10. The physical observation for the #1 test piece is as follow; the initial flexural crack is generated at the load of 235 kN, the initial shearing crack is caused at the load of 475 kN and finally the stress of the main tensile round bar yields at the load of 941 kN. On the other hand, for the #2 test piece, the initial flexural crack is at 353 kN, the initial shearing crack is at 588 kN, the yield stress of the main tensile round bar is at 931 kN. The final fracture mode is the flexural destruction due to the compressive damage of concrete for both test pieces.

The cracks propagation around the hinge spot are measured by the contact-type strain gauges using the 100 mm span mesh as shown in Fig. 11. The crack propagation of the #2 test piece is caused less load than what we predict in advance. This fact suggests that the advanced cracks must be locally caused by the confinement of Mesnager hinge due to the round bars, but must not be caused by the traffic live loads.

(3) Drawing for re-bar arrangement

No drawings for re-bar arrangement of Nasuno Bridge can be found, therefore all concrete of the test specimens was chipped out to remake the drawing for re-bar arrangement. Photo. 3 shows the re-bar arrangement for the hinge member after chipping. The restored to the original drawing for re-bar arrangement is illustrated in Fig. 12. Ten pieces round bars with 28 mm diameter are used as a main bar and the round bar with 9 mm diameter is used as a stirrup.

3.3 Analyses of structural strength

The non linear finite element analysis for the loading test using FEM code "DIANA" has been conducted applying the material information based on the results of the physical material tests and the renewed drawing for re-bar arrangement. The FEM mesh model and the boundary conditions are illustrated in Fig. 13. The numerical calculation results of the loading force versus the displacement at the loading point are compared with the test results in Fig. 9. The concrete constitutive model for compression side is that the stress increases up to the compression strength with second order strain till the strain becomes 0.2 %. The tension side is that the stress increases linearly up to the tensile strength, then the stress decreases linearly. The round bars are used for the reinforcement for this bridge, therefore the tension softening rate of concrete reduced by 70% compared with the usual deformed bars. From the comparison shown in Fig. 9, it is noted that the tension stiffening by FEM analysis is much clear than the actual phenomena.

As the #2 test specimen indicated the cracks in advance near the hinge spot, it is afraid weather if the shearing strength would reduce or not. According to the Yokomitchi's method [2], the shearing strength becomes 1225 kN. The cowbell's shearing strength formula based on "Concrete standard specification - design part" issued by Japan Society of Civil Engineering in 1996, shows that the shearing strength becomes 1245 kN. On the other hand, FEM analysis demonstrates that the diagonal re-bars for the hinge member still have enough strength even for the stress of the main re-bars being 100 N/mm2. In order to predict the maximum shearing strength by FEM analysis for the test specimen, the main re-bars are increased in the numerical model not to fail by the flexural mode, then the shearing strength becomes 1842 kN, which is about twice of the flexural strength.

4. Evaluation of Durability and Structural Safety

1) Concrete used in the year of 1930's, has not enough resistance to freezing and thawing because of the lack of the entraining air, therefore careful maintenance management and inspection should be conducted in the cold regions in Japan.
2) The maximum carbonation thickness for Nasuno Bridge servicing for 60 years, was about 30 mm. According to Kishitani's formula, the carbonation thickness for 100 years is predicted only 38.7 mm which is smaller than the averaged cover concrete thickness 50 mm.
3) Some cracks in the vicinity of Mesnager hinge of the #2 specimen are observed and then the retrofit by H-beams are carried out for this hinge member, therefore some misgivings for the reduction of the shearing strength are there in advance. However, both loading test and numerical calculation by FEM result in that the shearing strength

is good enough to the design load and the flexural strength has also good enough capacity.

4) The cracks in the hinge members may be caused by the confinement of the Mesnager hinge for the live load on the girder and for the expansion and shrinkage due to the temperature.
5) When some cracks are inspected in the Mesnager hinge of the Gerber's type bridge, we have to at first investigate the crack width, the crack pattern, the corrosion of re-bars and so on, then we need to predict the flexural bending moment strength and the shearing strength. Under those information, we have to judge the appropriate retrofit strategy.

5. Ending Remarks

We hope this report may be used for the maintenance, the inspection system as well as the retrofit for the similar type of Gerber bridge or the similar aged bridges. It is judged that the environment of Nasuno Bridge was good condition in terms of the ductility of the materials from the material tests. On the other hand, the structural safety was also good condition in terms of the flexural and shearing strength of the girders.

Reference

1) Hasegawa, H., 1975, "Proposal for prediction of concrete frost damage risk and corresponding critical water cement ratio", Journal of Cement Engineering XXIX, pp. 248-253.
2) Yokomichi, H., 1972, "Concrete bridge", Gihoudou, pp. 382-387.

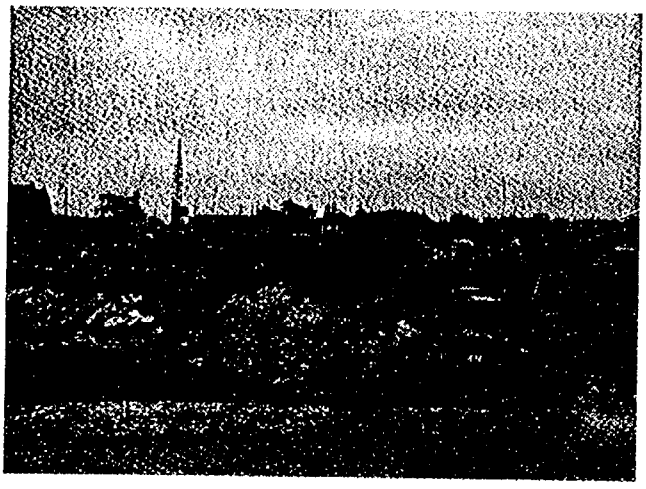


Photo. 1 Whole view of Nasuno Bridge



Photo. 2 Cutting out specimen

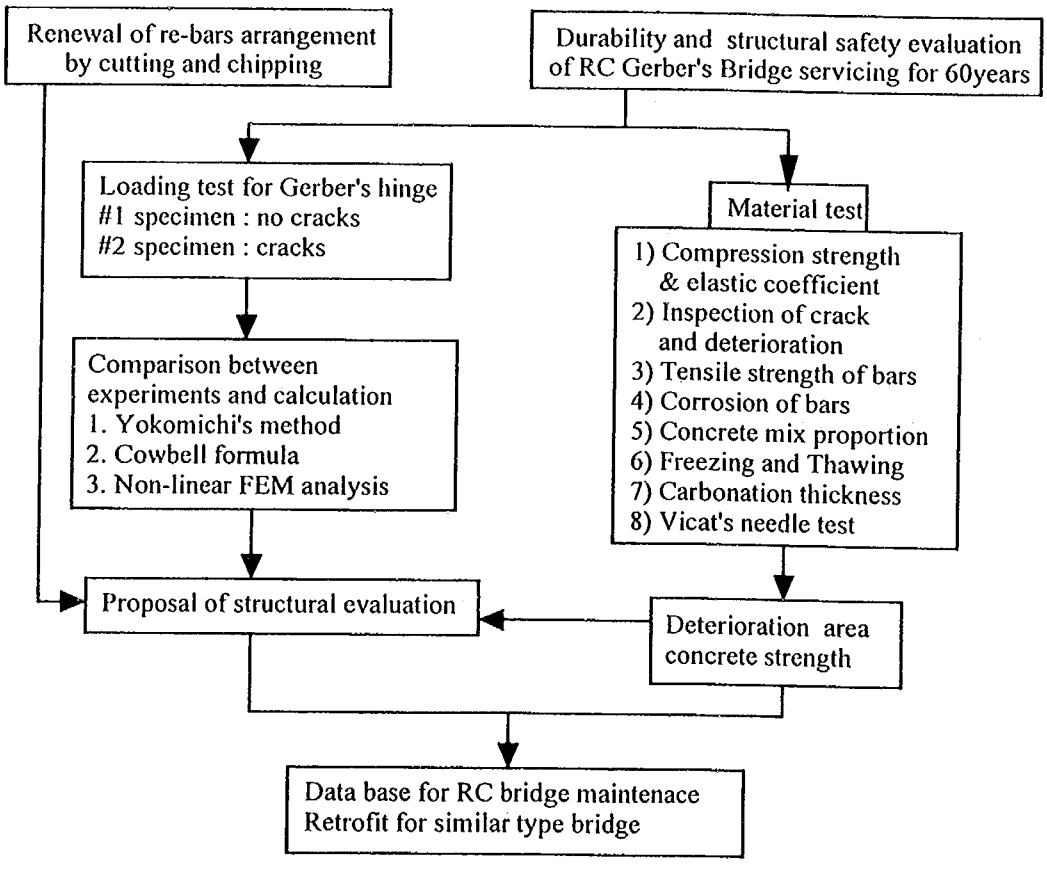


Fig 1. Study flow chart

Tabel 1 Inspection items and purpose

		inspection items	inspection purpose
in situ easy test	1)	appearance check of structures	rough inspection of deterioration pattern and grade of structures
	2)	compressive strength (non destructive)	data base of fundamental strength property
	3)	cover concrete thickness, re-bar location (non destractive)	data base of cover concrete thickness and re-bars location to evaluate the strucural safety
	4)	cover concrete thickness, location of re-bars (chipping)	
	5)	corroson of re-bars	data base of corrosion of re-bars to evaluate the structural safety
detailed test	6)	compressive strength (concrete core specimen)	data base of fundamental strength property
	7)	static elastic coefficient	
	8)	estimation of concrete proportion	data base of concrete proportion
	9)	resisntance of freezing and thawing	data base of freezing and thawing to evaluate the structural safety
	10)	carbonation of concrete	data base of deterioration pattern and grade of structures
	11)	tensile strength of re-bars	daba base of fundamental strength of re-bars

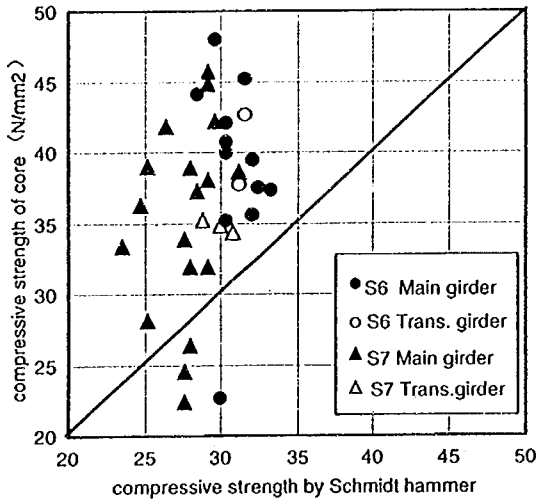


Fig. 2 Comparison between compressive strength from core and predicted that by Schmidt hammer

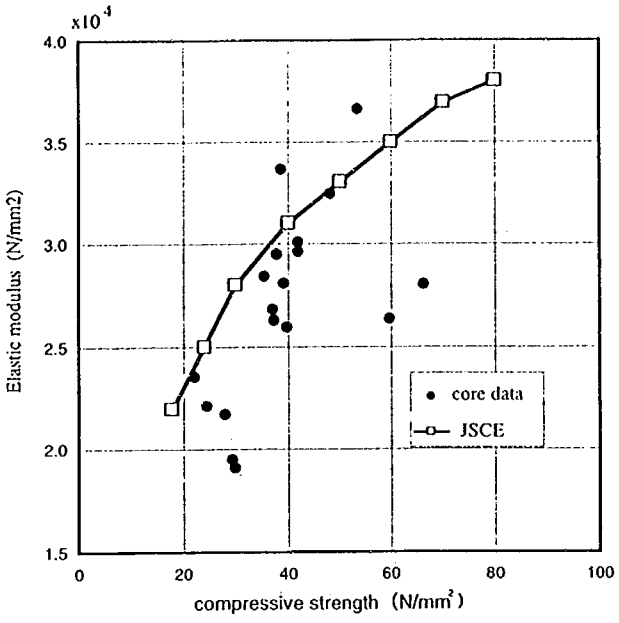


Fig. 3 Compressive strength from core and elastic modulus

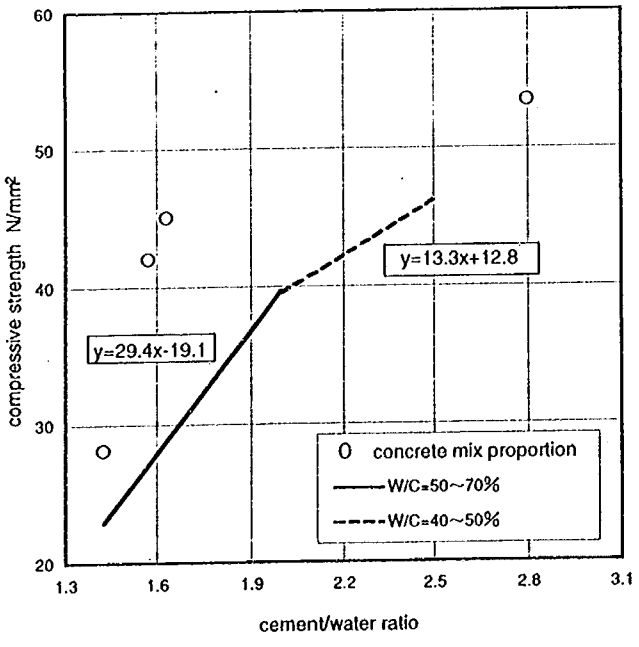


Fig. 4 Cement water ratio and compressive strength in core

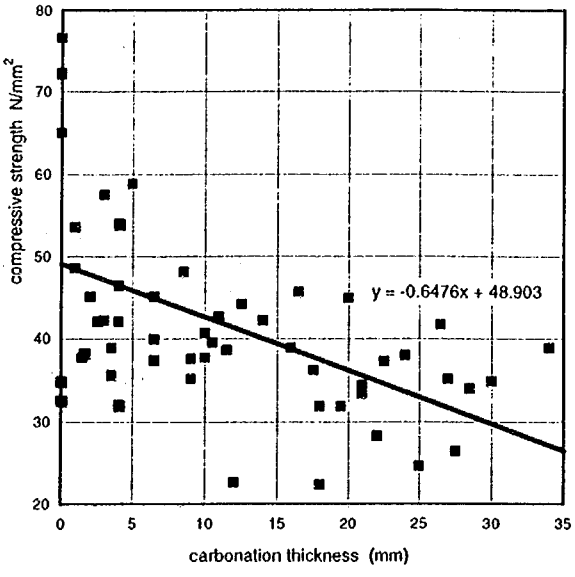


Fig. 5 Carbonation thickness and compressive strength in core

Table 2 Estimation of concrete proportion

sample name	cement (kgf/m3)	water (kgf/m3)	water cement ratio (%)	sand percentage (%)	weight of fine aggregate (kgf/m3)	weight of coarse aggregate (kgf/m3)	total unit weght	compressive strength (N/mm2)
S6-5	303	193	63.7	23	439	1476	2410	42
S7-5	309	217	70	33	597	1210	2333	28.1
P6-2	467	167	35.7	35	618	1124	2375	53.4
P6-8	330	203	61.3	28	509	1336	2378	45
1:2:4 *	300	180	60	34	655	1248	2383	-

*:based on "concrete standard specification" issued by JSCE in 1931

Table 3 Result of freezing and thawing test

number of cycle	sample number	mass (g)	variation of mass		first natural freq. (Hz)	relative elastic coefficient (%)	
			each sample	average		each sample	average
0	S6-13	9419	****	0	2086	***	100
	S6-14	9503	****		2045	***	
	S6-15	9506	****		2132	***	
30	S6-13	9487	0.722	0.707	516	6	20
	S6-14	9570	0.705		1416	48	
	S6-15	9572	0.694		569	7	

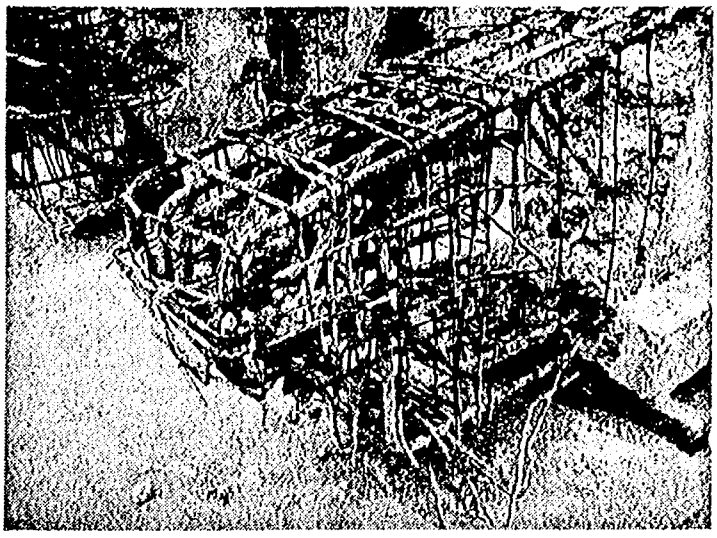


Photo. 3 Re-bar arrangement of Gerber's hinge

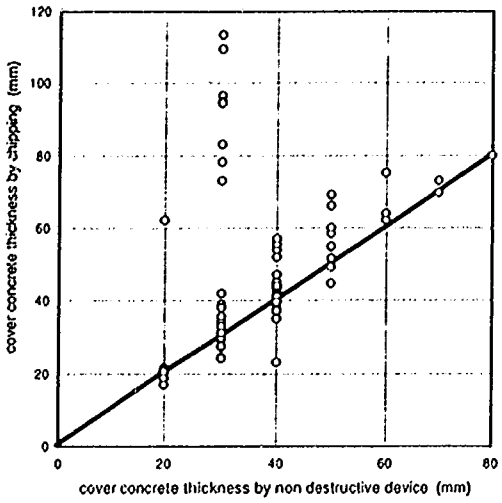


Fig. 6 Cover concrete thickness by non destructive device

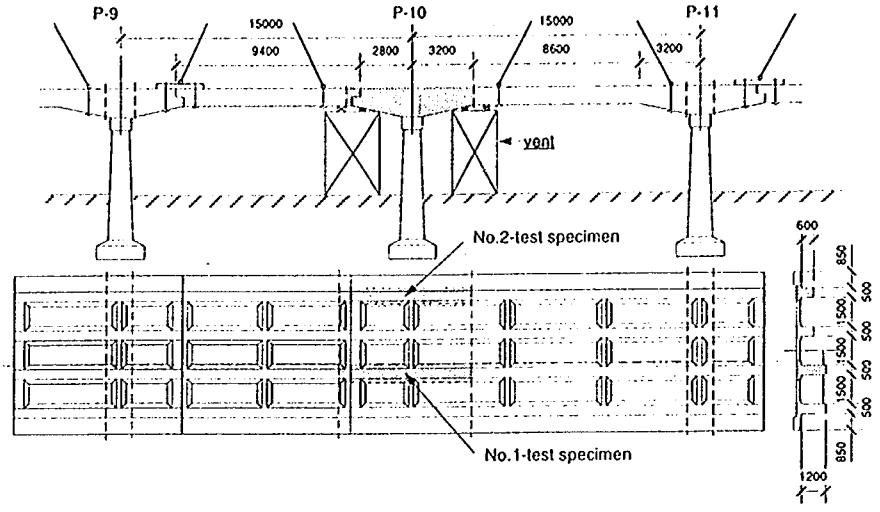


Fig. 7 Cutting out the test specimen (Pier 10)

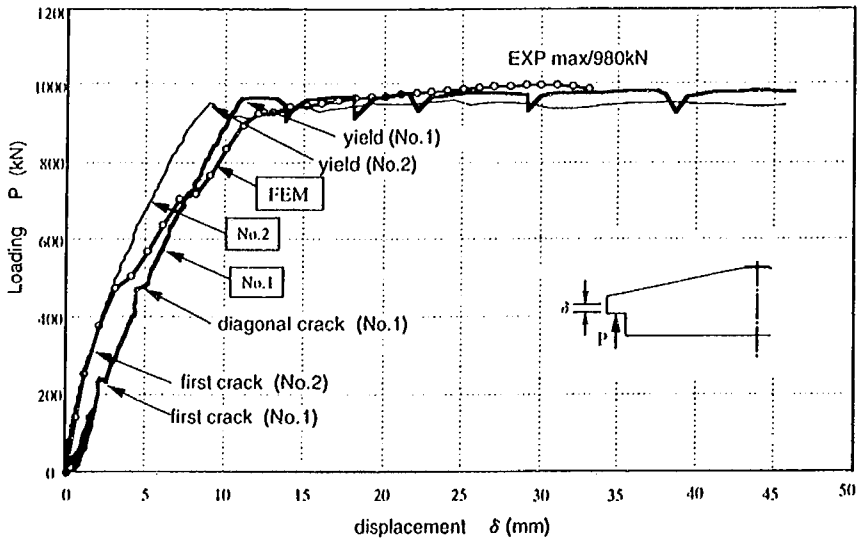


Fig. 9 Loading force and displacement

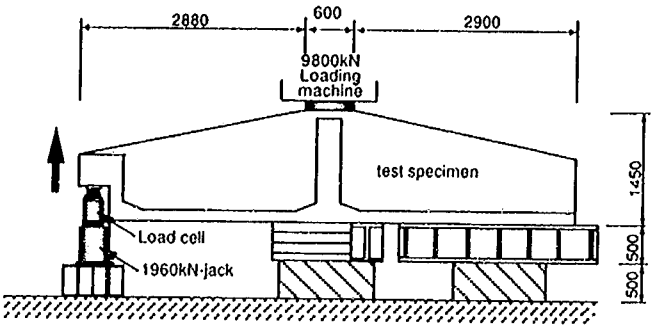


Fig. 8 Loading test arrangement

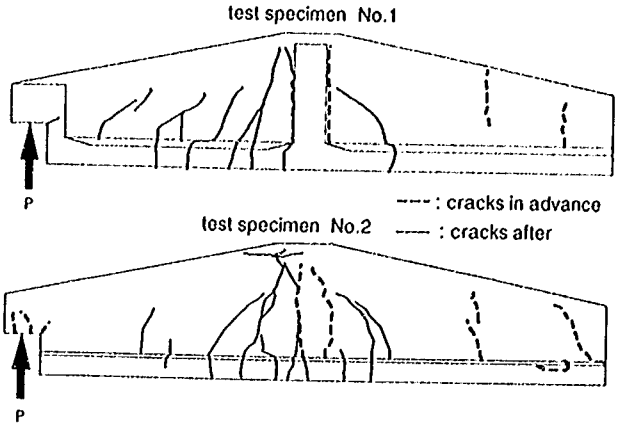


Fig. 10 Crack pattern

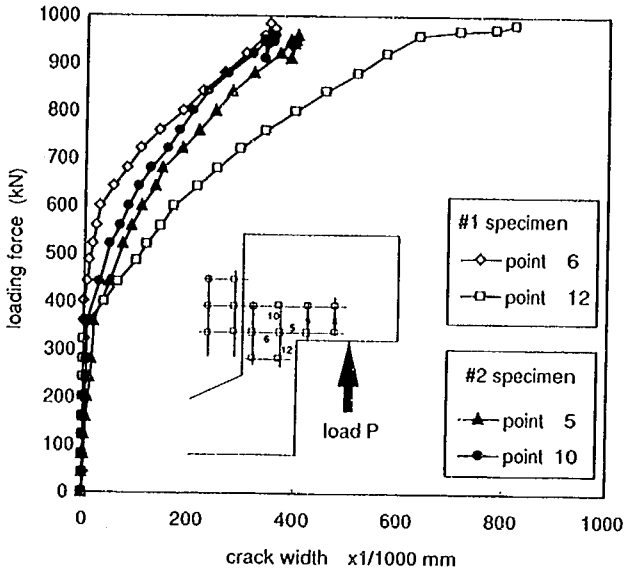


Fig. 11 Strain near Gerber's hinge by contact gauge

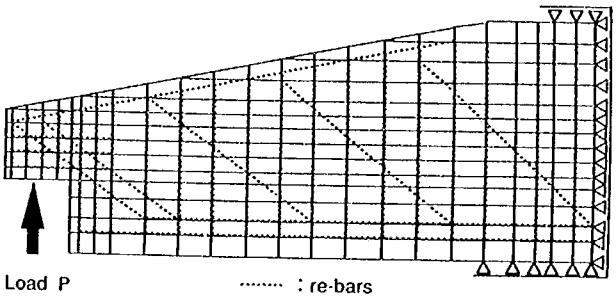


Fig.13 FEM mesh model

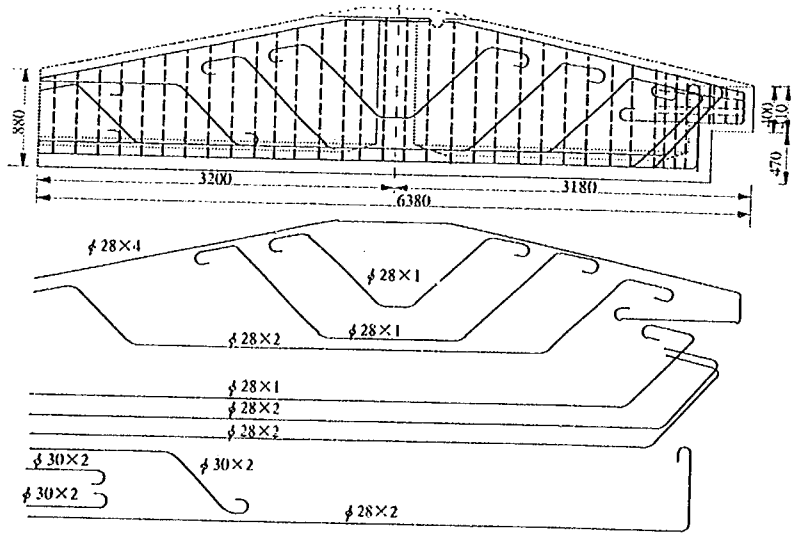


Fig. 12 Renewed re-bar arrangement of test specimen

SESSION 7: SEISMIC ISSUES (4)

(1) Draft Manual of Seismic Retrofit Design for Single-Type Reinforced Concrete Columns Using Carbon Fiber Sheets
(Shigeki Unjoh, Toru Terayama and Junichi Hoshikuma)

(2) FRP Composites for Seismic Retrofitting of Non-Prismatic Reinforced Concrete Bridge Columns
(David H. Sanders, M. Saiid Saiidi, Faramarz Gordaninejad, Frank Martinovic and Brett McElhaney)

(3) Size Effect in Shear Behavior of Reinforced Concrete Piers Strengthened with Carbon Fiber Sheets
(Koji Osada, Yoshinori Igase, Takahiro Yamaguchi and Shoji Ikeda)

(4) Seismic Retrofit Methods of Cap Beam of Two-Column Bents
(Yukio Adachi, Shigeki Unjoh and Kazuhiro Nagaya)

(5) Application of Fiber Reinforced Polymers (FRP) for Seismic Retrofit of California Bridges
(Thomas E. Sardo)

(6) Seismic Behavior of Circular Hollow Columns without Inside Reinforcement
(Jun-ichi Hoshikuma and M. J. Nigel Priestley)

DRAFT MANUAL OF SEISMIC RETROFIT DESIGN FOR SINGLE-TYPE REINFORCED CONCRETE COLUMNS USING CARBON FIBER SHEETS

Shigeki Unjoh[1] , Toru Terayama[2] , Jun-ichi Hoshikuma[3]

Abstract

It is essential to increase the shear strength and to increase ductility for the retrofit measures of existing reinforced concrete members to prevent brittle shear failure and to behave in a ductile manner. Steel jacketing and reinforced concrete jacketing methods are effective to increase the shear strength and the ductility. However, when the construction space and the use of construction machines are restricted, it is effective and very attractive to use light composite materials such as carbon fiber sheets.

This paper presents the outline of the "Draft Manual of Seismic Retrofit Design for Single-Type Reinforced Concrete Columns using Carbon Fiber Sheets." This draft manual was developed as an outcome of the Research Committee on Seismic Retrofit Methods using Carbon Fiber Sheets (Chairman: Professor Kazuhiko KAWASHIMA of Tokyo Institute of Technology)" which had been established at the Public Works Research Center from April 1996 to September 1998. The authors joined in the research committee and served in the working activities of the development of the draft manual.

1. Introduction

Based on the lessons learned from the destructive damage caused by the 1995 Hyogo-ken nanbu earthquake, the existing reinforced concrete structures have been retrofitted. In particular, it is essential to prevent the brittle shear failure. To transfer the failure mode to the ductile bending failure, it is important to appropriately increase the shear strength of members. The steel jacketing and reinforced concrete jacketing methods are commonly used to increase the shear strength and the ductility for single-type bridge columns. However, when the construction space is limited and the use of the construction machines is restricted, the steel jacketing and the concrete jacketing methods are difficult to be applied. Therefore, it is attractive to use the retrofit measures using light composite materials such as carbon fiber sheets that does not require such large construction machines and then that is not affected by the construction space.

---

1 Head, Earthquake Engineering Division, Public Works Research Institute, Tsukuba City

2 Deputy Manger, Kanagawa Construction Bureau, Metropolitan Expressway Public Cooperation, Yokohama City

3 Senior Research Engineer, Earthquake Engineering Division, Public Works Research Institute, Tsukuba City

The carbon fiber sheets have almost the same elastic modulus with steel reinforcing bars, and remains elastic up to the failure, and have about 10 times strength of the steel reinforcing bars. It is expected to apply such high performance materials to increase the seismic performance of existing reinforced concrete columns much effectively.

This paper presents the outline of the developed "Draft Manual of Seismic Retrofit Design for Single-Type Reinforced Concrete Columns using Carbon Fiber Sheets."

2. Activities in the Research Committee

Research committee on seismic retrofit methods using carbon fiber sheets was established to study the effectiveness of carbon fiber sheets on the retrofit of existing reinforced concrete structures and to develop the design guideline/manual. The committee was established in April 1996 at the Public Works Research Center (PWRC) sponsored by the Retrofit Research Group using Carbon Fiber Sheets which is a private institution related to the research on the application of carbon fiber sheets for seismic retrofit. The chairman of the research committee was Prof. Kazuhiko Kawashima, Tokyo Institute of Technology, and the members from the academic, private, governmental organizations joined.

The research committee had conducted comprehensive studies including the model tests as well as and correction of the test information conducted by the other organizations, analysis of tested data, evaluation studies of strength and ductility enhancement of jacketed reinforced concrete columns by the carbon fiber sheets. Final outcome was compiled in September 1998 as "Draft Manual of Seismic Retrofit Design for Single-Type Reinforced Concrete Columns using Carbon Fiber Sheets." The draft manual is just a research outcome based on the available information on the experimental and analytical data so far and is not mandatory design specification.

In the following, the developed design concept is introduced. In the general section of the draft manual, it is clearly explained that the manual should be improved with the increase of the tested data.

3 Outline of Draft Manual

3.1 Basic Concept and Applicability

The draft manual shows the design methods and design details when the retrofit of single-type reinforced concrete columns using carbon fiber sheets is made. The retrofit objectives are to increase shear strength, bending strength and ductility by jacketing the reinforced concrete columns. Basic design methods are according to the Design Specification for Highway Bridges, Part 5: Seismic Design. In the manual, it is recommended that since the scale effect on the enhancement of ductility is unknown, the evaluation methods, which were developed based on the scaled model test data, should carefully applied for the design of actual retrofit of columns with the size greater than about 3m.

It should be noted here that the carbon fiber sheets with the elastic modulas of

around $2.30 \times 10^5 N/mm^2$ and tensile strength in the range of 2,500 to $4,500 N/mm^2$ are used in the manual. The elastic modulus is almost the same as that of reinforcing bars and strength is about 10 times of that. Therefore, when the carbon fiber sheets with different mechanical characteristics from these, the retrofit effectiveness of the carbon fiber sheets should be studied experimentally. The elastic modulus and tensile strength is specified to get from the sample tests according to the JIS standard testing methodology.

3.2 Seismic Retrofit Design Concept

The retrofit methods using carbon fiber sheets is applied for the following cases.

1) Shear Strength Enhancement of Columns with Rectangular or Circular Sections
2) Ductility Enhancement of Columns with Circular Section
3) Strength Enhancement at Mid-Height Section with Termination of Longitudinal Re-bars

Therefore, the retrofit to enhance ductility characteristics of rectangular columns by carbon fiber sheets is not specified in the manual. This is because it is not significantly effective to use the jacketing methods with carbon fiber sheets for the increase of ductility of rectangular columns based on the model tests.

Basic design methods are according to the Seismic Design Specifications for Highway Bridges issued from the Japan Road Association. The draft manual specified as

1) Evaluation Methods of Ductility Enhancement with Retrofit by Carbon Fiber Sheets
2) Evaluation Methods of Shear Enhancement with Retrofit by Carbon Fiber Sheets
3) Design Details for Carbon Fiber Sheets

Fig.1 shows the design flow of the retrofit of single-type reinforced concrete column using carbon fiber jacketing. For the circular column, the enhancement of ductility by the carbon fiber sheet jacketing is considered but it is not considered for the rectangular columns based on the idea of safer judgement.

3.3 Evaluation of Ductility Enhancement

The ductility enhancement is evaluated by the stress-strain model of confined concrete by the carbon fiber sheets. The stress-strain model was developed in the research committee as:

$$\sigma c = \begin{cases} Ec \cdot \varepsilon c\{1-1/n(\varepsilon c/\varepsilon t)^{n-1} & (0<\varepsilon c<\varepsilon cc) \\ \sigma c - Edes(\varepsilon c - \varepsilon cc) & (\varepsilon cc<\varepsilon c<\varepsilon cu) \end{cases} \quad (1)$$

$$n = Ec \cdot \varepsilon cc / (Ec \cdot \varepsilon cc - \varepsilon cc) \quad (2)$$

$$\sigma cc/\sigma ck = 1.0 + \{A1 \cdot \rho cf \cdot \varepsilon cft \cdot Ecf/\sigma ck + A2 \cdot \rho s \cdot \sigma sy/\sigma ck\} \quad (3)$$

$$\varepsilon cc = 0.002 + \{B1 \cdot \rho cf \cdot \varepsilon cft \cdot Ecf/\sigma ck + B2 \cdot \rho s \cdot \sigma sy/\sigma ck\} \quad (4)$$

$$Edes = C1 \cdot \sigma ck^2 / (\rho cf \cdot \varepsilon cft \cdot Ecf + C2 \cdot \rho s \cdot \sigma sy) - C3 \cdot \sqrt{\rho cf \cdot Ecf} \quad (5)$$

$$\varepsilon cu = D1 + D2\{(\rho cf \cdot \sigma cf + \rho s \cdot \sigma sy)/\sigma ck\}^{3/4} \{\sigma cf/Ecf\}^{1/2} \quad (6)$$

$$\rho s = 4Ah/sd \quad (7)$$

$$\rho cf = 4N \cdot tcf/dcf \quad (8)$$

where

σc : compression stress in concrete (N/mm^2)

σcc : compression strength of confined concrete by carbon fiber sheets (N/mm^2)

σ ck : design compression strength of concrete (N/mm^2)
ε c : stress of concrete
ε cc : strain at peak compression strength
ε cu : ultimate strain of confined concrete by carbon fiber sheets
ε cft : strain developed in carbon fiver sheets at peak compression stress (can be 0.0015)
Ec : elastic modulus of concrete (N/mm^2)
Ecf : elastic modulus of carbon fiber sheet (N/mm^2)
Edes : gradient after peak stress (N/mm^2)
ρ s : volumetric ratio of confining steel bars
ρ cf : volumetric ratio of confining carbon fiver sheets
Ah : sectional area of confining steel bars
Acf : sectional area of confining carbon fiber sheets
N : number of sheets
tcf : thickness of 1 sheet of carbon fiber
s : space of confining steel bars
d : effective width of confining steel bars
dcf : effective width of carbon fiber sheets, radius in case of circular columns, and larger length of width in case of rectangular columns
σ sy : yielding stress (N/mm^2)
σ cf : tensile strength of carbon fiber sheets (design tensile strength)
Ai, Bi, Ci, Di : modification coefficients (for circular columns, A1=1.93, A2=3.80, B1=0.00939, B2=0.033, C1=0.658, C2=0.0588, C3=0.078, D1=0.00383, D2=0.1014)

The Eqs. (1) - (6) are obtained from the experimental study of the compression tests of 42 concrete cylinders with the size of diameter of 200mm and height of 600mm confined by carbon fiber sheets.

3.4 Evaluation of Shear Strength Enhancement

To expect the transfer of failure mode from brittle shear to ductile bending, the shear strength evaluation method was proposed as a conventional way as:

$$Ps = Sc + Ss + Scf \tag{9}$$

$$Sc = 10\, Cc \cdot Ce \cdot Cp \cdot \tau\, c \cdot b \cdot d \tag{10}$$

$$Ss = \frac{Aw \cdot \sigma\, sy \cdot d \cdot (\sin\theta + \cos\theta)}{10 \times 1.15a} \tag{11}$$

$$Scf = \frac{Acf \cdot Ecf \cdot \varepsilon\, cf \cdot d \cdot (\sin\theta' + \cos\theta')}{10 \times 1.15a'} \tag{12}$$

where

Ps : shear strength (kN)
Sc : contribution in shear strength by concrete (kN)
Ss : contribution in shear strength by tie rea-bars (kN)
Scf : contribution in shear strength by carbon fiber sheets (kN)
Aw : area of tie re-bar with space of a and angle of θ
Acf : area of carbon fiber sheet with space of a' and angle of θ'
Ecf : elastic modulus of carbon fiber sheets (N/mm^2)

ε cf : design strain of carbon fiber sheets (3,000 μ)
d : effective width of section (mm)

The important design factor to evaluate shear strength is design strain of carbon fiber sheets, ε cf. Based on the tests results in which the failure mode was changed from the shear to bending, it was evaluated that the design strain of the carbon fiber sheets was ranging from 1,700 μ to 3,400 μ. This is not large value considering the material strength characteristics itself. There is also discussions on the accuracy of the evaluation methods of concrete contribution, Sc, in the evaluation of tested data. In the manual, the design strain of 3,000 μ is tentatively proposed based on the tested data and design consideration of the prestressed concrete design and the application of high strength materials to the shear strength enhancement. This is because when the high strength is developed in the fibers the displacement also becomes large then the shear crack width becomes large. The development and increase of the crack width increases the progress of failure of concrete. Therefore, the design strain is proposed based on the tested data and the idea to limit the shear crack width in the concrete. But the carbon fiber sheets may be effective to decrease the development of beginning of cracking by the adhesion between concrete surface and fiber sheets as well as the decrease of the progress of the cracking. The design strain for carbon fiber sheets in the design of shear enhancement should be studied more in the future.

3.5 Retrofit of Mid-Height Section with Termination of Longitudinal Re-bars

During the Kobe earthquake, several bridges were collapsed by the failure at the mid-height section of reinforced concrete columns with the termination of longitudinal re-bars. Failure at the mid-height section may be transferred to the brittle shear failure at the section when the shear strength is not enough. To prevent failure at the section and to introduce ductile failure at the bottom of columns, it is essential to increase both bending and shear strength. Location where the failure is developed is evaluated by the following equations. The equation was obtained based on the tested data of model columns.

$$(M_{Ty0}/h_T)/(M_{By0}/h_B) > 1.2 \qquad (13)$$

In the design of increase of bending strength at the mid-height section, the design strength of carbon fiber sheets is assumed as 2/3 of the tensile strength.

3.6 Design Details

In the design details of the draft manual, the minimum anchorage and connection length of carbon fiber sheets and smoothing at the corner is specified. These are specified based on the tested data. The minimum anchorage and connection length between concrete and carbon fiber sheets is assumed as

$$Lcf = (\text{Tensile Strength} / \text{Adhesive Strength}) = \sigma cf \cdot n \cdot tcf / \tau cf \qquad (14)$$

where

Lcf : anchorage length or connection length (cm)
σ cf : tensile strength of carbon fiber sheets (N/mm^2)
n : number of sheets
tcf : thickness of 1 sheet of carbon fiber sheets

τ cf : adhesive stress (N/mm^2, assmed $0.44N/mm^2$)

The minimum anchorage and connection length between carbon fiber sheets is assumed as Lcf = 20cm in the manual. This is also based on the tensile model test.

To prevent stress concentration in the carbon fiber sheets, it is essential to make smooth at the corner of rectangular columns. In the manual, it is recommended to be about 5 cm or greater of radius. The tested data showed that the smoothing diameter is enough if it is greater than 1cm.

4. Conclusions

The "Draft Manual of Seismic Retrofit Design for Single-type Reinforced Concrete Columns using Carbon Fiber Sheets" which was developed in the Research Committee on Seismic Retrofit Methods using Carbon Fiber Sheets was briefly introduced. The applicability and design method to evaluate the shear and ductility enhancement and the strength at the mid-height section were introduced.

Acknowledgement

The authors sincerely thank to Prof. K. Kawahsima, Chairman of the Research Committee on Seismic Retrofit Methods using Carbon Fiber Sheets and all of the committee members as well as the Public Works Research Center who established the research committee and the Retrofit Research Group using Carbon Fiber Sheets who made a contract to established the research committee. Although the authors introduced the draft manual in this paper, the authors would like to emphasize that the draft manual was the outcome of the research committee.

References

1) Public Works Research Center : Report of the Research Committee on Seismic Retrofit Methods using Carbon Fiber Sheets, Sep. 1996
2) Public Works Research Center : Report of the Research Committee on Seismic Retrofit Methods using Carbon Fiber Sheets, Sep. 1998
3) Ministry of Construction : Design Specifications for Bridges damamed during the Hyogo-ken nanbu earthquake in 1995, Feb. 1995
4) Japan Road Association : References for the application of Design Specifications for Bridges Damaged during the Hyogo-ken nanbu earthquake in 1995, June 1995
5) Japan Road Association : References for the Seismic Retrofit of Highway Bridges, Aug. 1997
6) Hoshikuma, J., Kawashima, K., Nagaya, K. and Taylor A. : Stress-strain model for confined reinforced concrete in bridges piers, Journal of Structural Engineering, ASCE, Vol.123, No.5, pp.624-633, 1997
7) Hosotani, M., Kawashima, K. and Hoshikuma, J. : Effect of Confinement by Tie re-bars on the Stress-strain model for confined reinforced concrete column by the

carbon fiber sheets and the modelling, Proc. of JSCE, May, 1999
8) Hosotani, M. and Kawashima, K. : Effect of Confinement by Tie re-bars on the Stress-strain model for confined reinforced concrete column by the carbon fiber sheets and the modelling, Proc. of JSCE, No.592/V-39, pp..37-52, May 1998
9) Hosotani, M. and Kawashima, K. : Effect of Confinement by Tie re-bars on the Stress-strain model for confined reinforced concrete column by the carbon fiber sheets and the modelling, TIT Report, TIT/EERG98-3, Feb. 1998
10) Unjoh. S. and Terayama. T. : Design Methods of Shear Enhancement of Reinforced Concrete Columns by Carbon Fiber Sheets, Prof. of the 2nd Symposium on the Ductility Design Meethds for Bridges, JSCE, Dec. 1998
11) Japan Society of Civil Engineers : Concrete Design Standard, Seismic Design, 1996
12) Japan Road Association : Design Specifications for Highway Bridges, Part Ⅲ: Concere Bridges, Part V: Seismic Design, 1996
13) Architectural Institute of Japan : Ultimate Strength Seisnic Design Guidelines forft Reinforced Concrete Buildings, 1990
14) JH Japan Highway Public Cooperation Research Institute : Retrofit Manual (Draft) of Reinforced Concrete Columns by Carbon Fiber, Technical Memorandum of JHRC, No.615, Feb, 1995

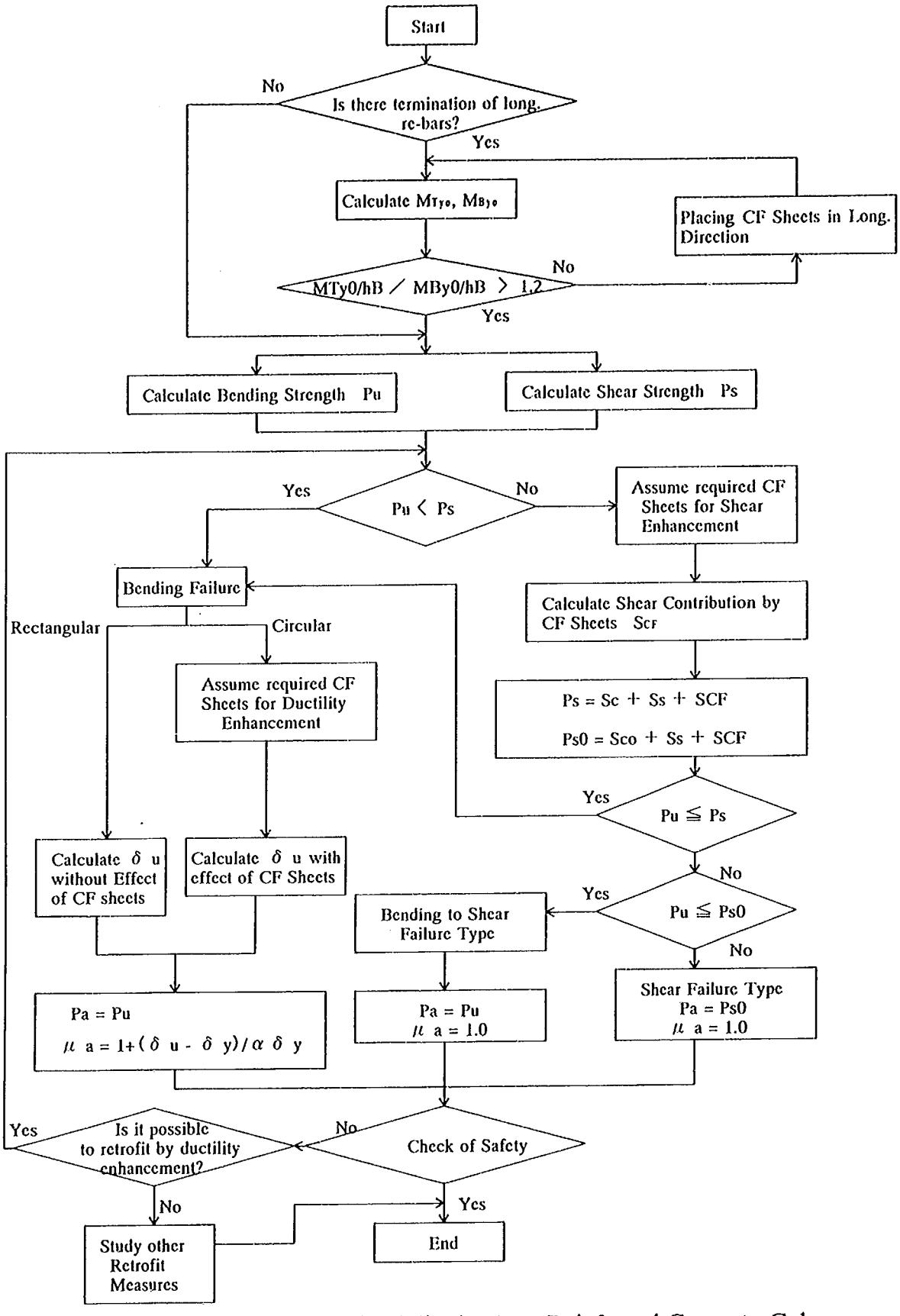


Fig. 1 Design Flow of Retrofit of Single-Type Reinforced Concrete Columns using Carbon Fiber Sheet Jacketing

APPENDIX

TABLE OF CONTENTS OF "DRAFT MANUAL OF SEISMIC RETROFIT DESIGN METHODS FOR SINGLE-TYPE REINFORCED CONCRETE COLUMNS USING CARBON FIBER SHEETS"

by

"Research Committee on Seismic Retrofit Methods using Carbon Fiber Sheets : Public Works Research Center, September 1998"

1. General
   1.1 Background of Draft Manual
   1.2 Scope of Draft Manual
   1.3 Definition of Terms

2. Materials
   2.1 Materials
   2.2 Design Strength of Materials
   2.3 Elastic Modulas of Materials

3. Basic Concept of Seismic Retrofit Design
   3.1 Basic Concept
   3.2 Seismic Retrofit Design

4. Lateral Capacity and Lateral Displacement at Yield and Ultimate

5. Shear capacity

6. Seismic Retrofit Design at the Termination of Main Reinforcement at Mid-height

7. Design Details
   7.1 Anchorage and Connection of Carbon Fiber Sheets
   7.2 Smoothing of the Corner of Rectangular Columns

References

FRP COMPOSITES FOR SEISMIC RETROFITTING OF NON-PRISMATIC REINFORCED CONCRETE BRIDGE COLUMNS

David H. Sanders[1], M. Saiid Saiidi[2], Faramarz Gordaninejad[3], Frank Martinovic[4] and Brett McElhaney[5]

Abstract

This paper describes the experimental part of a study on shake table response of reinforced concrete columns with structural flares. One as-built and two retrofitted 0.3-scale specimens are discussed. Two fiber-reinforced plastic (FRP) jackets, one with glass fibers and the other with carbon fibers were studied. The primary function of the retrofit was to improve the shear capacity of the columns. Both retrofit methods were found to be effective in changing the failure mode from flexure/shear to flexure and in improving the displacement ductility. The mechanical performance of the glass fiber and carbon fiber composites was nearly the same. The performances of the FRP jacketed columns are very close to that of the steel jacketed column. A comparison is made as part of this paper.

Introduction

The majority of the columns in the Mission Gothic Bridge in the Los Angeles area (see Fig. 1) were severely damaged or failed in shear during the 1994 Northridge earthquake [NIST, 1994]. These columns had architectural flares, which had been assumed to spall off during a strong earthquake and to allow for plastic hinging at the end of the column. During the earthquake, however, the flares enhanced the flexural capacity at the ends and shifted the plastic hinge to a point near the mid height of the columns. The reduction in the shear span led to nearly doubling the shear force and failure of the columns. A large number of recently constructed bridges in Nevada are supported on flared columns. Following the failure of the Mission Gothic Bridge, it was decided that an evaluation of these columns needed to be made and necessary corrective measures should be taken. This paper presents a summary of the use of advanced composites in enhancing the seismic performance of the columns.

Evaluation of Bridges

Four representative bridges constructed from the early 1980's to early 1990's were selected for the study. All these bridges were supported on columns that had structural flares (see Fig. 1). The flares in these columns were reinforced to provide at least a part of the required flexural capacity. The more recent columns were reinforced with a core steel cage with constant diameter that extended over the entire column height in addition to having a structural flare. The earlier columns did not have the core steel. Inelastic lateral load analysis of the piers revealed

[1] Professor, Dept. of Civil Engineering , University of Nevada, Reno
[2] Professor, Dept. of Civil Engineering , University of Nevada, Reno
[3] Professor, Dept. of Mechanical Engineering, University of Nevada, Reno
[4] Martin/Pelton Associates, Las Vegas, Nevada
[5] BJG and Associates, Reno, Nevada

that the columns with a core steel cage had sufficient ductility, whereas some of the columns without the core could experience shear failure at moderate levels of ductility [Wehbe and Saiidi, 1999]. Columns of Bridge 1250, a sixteen-span structure supported on nearly 100 columns were selected for further study. Cyclic testing of large-scale specimens revealed that only the columns with relatively large longitudinal steel ratio were susceptible to shear failure [Wehbe, et al., 1997]. Therefore, subsequent shake table tests were conducted on specimens that represented heavily-reinforced columns. Another conclusion of the cyclic tests was that the plastic hinge in columns with structural flares forms at some distance from the end, which is advantageous because it reduced the detailing demand at the connections. A continuous steel jacket retrofit was found to shift the plastic hinge closer to the connection. The tests showed that a steel jacket with an intermediate gap at a preassigned plastic hinge location is effective in controlling the column behavior (McElhaney et al).

Test Specimens

Three 0.3-scale specimens tested on one of the University of Nevada, Reno, shake tables are discussed in this paper. The first specimen, named FA, represented as-built columns, and the other two, named FRG and FRC, were retrofitted with glass fiber epoxy and carbon fiber epoxy composites, respectively. All the columns in Bridge 1250 were pinned at the base and flared over the upper 4.8 m. To simplify testing, the specimens modeled the columns in an upside down position with flares over the lower part of the column and the pinned connection at the top. Details of the specimens without retrofit are shown in Fig. 2. The footing in the specimens was over designed to ensure that damage is limited to the columns. The longitudinal bars were 13mm-diameter deformed bar and the transverse bars were 4.5mm-diameter smooth wire. Both the longitudinal and transverse steel ratios closely modeled the corresponding ratios in the prototype columns. The smoothness of the wire was addressed by increasing both the lap length and hook length in the reinforcement details. Lap lengths were increased from 36 bar diameters in the prototype to 45 in the test specimens. The section at the connection to the footing had a longitudinal reinforcement ratio of 1.8 percent. The reinforcement ratio then varied along the column height depending on bar terminations. The measured yield stress for the longitudinal and transverse bars was 462 and 417 MPa, respectively. The average measured steel yield stress in the columns of Bridge 1250 was 452 MPa. Normal weight concrete with a maximum aggregate size of 10mm was used. On the day of testing the concrete compressive strength were 37.6, 48.0, and 47.9 MPa, for FA, FRG, and FRC, respectively.

Composite Retrofit

Most of the space under Bridge 1250 is utilized as offices and garages for the Regional Transportation Commission of Reno. Walls and other facilities have been constructed around the bridge columns. It was important to identify the least intrusive method of retrofit for the columns to minimize reconstruction of the existing facilities. Because of their flexibility, fiber reinforced plastics (FRP's) can be installed in areas with limited working space. The use of unidirectional FRP's for seismic retrofit of prismatic columns has increased significantly in the past few years. However, no application of the composites on flared elements has been reported. What makes flared columns different with respect to FRP composite installation is that the fiber angle changes as the composite is wrapped around the column. Typically, in prismatic columns the fibers are perpendicular to the element axis so that they enhance confinement and shear

strength. Fibers that are not perpendicular to the column axis introduce a force component that is parallel to the axis. This force increases the flexural strength of the column, which is generally undesirable.

To minimize the angle change for the fibers, the composite jacket was formed by a series of butted straps. The wraps were not wound around the column, but rather were placed with pieces that covered 270 degrees around the column. This was done so that the inclination of the fibers did not become too vertical and begin to directly contribute to the vertical tensile strength of the column outside layers. Therefore, when the wrap was applied from the other side of the column, there was 90 degrees of overlap. This was done to provide sufficient development of the fibers in tension and prevent debonding. The width and the number of the straps were reduced in the zone at which the plastic hinge was to be formed. Figure 3 shows the details of the glass fiber composite jacket. The carbon fiber jacket was similar. The gap at the bottom was placed to avoid bearing of the jacket on the footing. The TYFO® S Fibrwrap® composite was used. The jacket thickness was designed using the provision of [USDOT, 1995] for shear enhancement. The glass fiber-epoxy wrap had an overall thickness of 3.48 mm (3 wraps), while the carbon wrap was 1.1 mm (2 wraps). Figure 4 shows the application of the composite strips. The objective of the retrofit was to improve the shear capacity. A factor of safety of two was used against shear failure. The concrete and steel contribution to the shear strength was accounted for using the provisions of [Caltrans, 1998]. The design tensile stress for the glass and carbon fiber epoxy composites was 124 and 393 MPa, respectively, as recommended in Ref. 5. In FRG, two wraps were installed in the plastic hinge area and three elsewhere. The plastic hinge area in FRC had one wrap with two wraps installed over the rest of the column. This was done to promote the hinge forming in the designated plastic hinge zone. The corners of the specimens were smoothed with a grinder before installation. During the installation process, a base coat of epoxy was placed. This was allowed to cure to a tacky state before the wraps were added.

Shake Table Testing

The as-built specimen was analyzed subjected to a large number of earthquake records using a nonlinear response history analysis program, RCShake, before an earthquake record for shake-table testing was selected [6]. The criteria considered included relevance of the record to the type of earthquakes expected in the region, ductility demand on the column, and the shake-table limitations. The Sylmar Hospital record obtained during the 1994 Northridge earthquake was selected. The measured peak ground acceleration for this record was 0.6g. The peak was adjusted in the course of the shake table tests to achieve different levels of ductility demand. The time axis of the record was compressed to account for the difference between the frequency of the test specimens and that of the prototype. Each specimen was subjected to successive earthquake runs with increasing peak amplitude using the shake-table facility at the University of Nevada, Reno (see Fig. 5). The photo shows the mass rig, which is what is used to apply the inertial force through a ridge link. The axial force is applied through rams that sit on top of the specimen. The first two inputs had peak amplitudes of 0.12g and 0.24g. The input peak acceleration in the third run was 0.45g, and was incremented by 0.15g in subsequent runs. Intermittent free vibration tests were conducted to measure the change in frequency and damping of the specimens as they were damaged. In all the tests, the columns were subjected to an axial load of 285 kN that represented the gravity load effect in the prototype. This load fluctuated during the tests, but the effect of the axial load variation was nine percent or less on the flexural

capacity of the columns [Martinovic, et al. 1999]. The actual recorded peak table acceleration varied from the target. The spectral analysis of the actual table motions, however, indicated that the spectral accelerations for all three specimens were nearly the same in the frequency range of interest [Martinovic, et al. 1999].

Test Results

As-Built and Steel Retrofit Specimens

Flexural and shear cracks became visible during the third earthquake run (0.75 times Sylmar) in Specimen FA. The peak lateral load of 254 kN occurred during the forth event (1.0 times Sylmar). As the amplitude of table acceleration increased, cracks became wider and concrete began to spall in the compression areas under bending. Spalling of the concrete was followed by an outward buckling of the longitudinal bars and rupture of some of the ties. During the last run with the peak table acceleration of 1 g (1.5 times Sylmar), several of the longitudinal bars ruptured due to low-cycle fatigue. Figure 6 shows FA at the end of the test. The maximum measured displacement was 137.9 mm corresponding to a displacement ductility of 5.4. The test data showed that many of the column ties yielded under the peak load and that the shear capacity of the column in the plastic hinge zone had been reached. The envelope of the measured load-displacement curves for FA is compared with those of the retrofitted specimens in subsequent sections. More details about the performance of the specimen are presented in [McElhaney, et al., 1999]. While not presented in detail in this paper, Fig. 6 shows the steel retrofitted specimen with the gap at failure.

Retrofitted Specimens

The response of the two retrofitted specimens was generally the same. Minor cracking of epoxy was observed during Run 2. In subsequent runs, more cracks were observed mostly at the junction of composite straps and in the plastic hinge zone, where a smaller number of composite wraps had been installed. No shear cracks were visible in the plastic hinge area. Following the tests, the composite jackets were removed in the plastic hinge area. Again, no shear cracks were observed. Both specimens failed in flexure due to the rupture of the longitudinal bars in the preassigned plastic hinge area. Figure 7 shows the specimens just before failure. Figure 8 show specimen FRG after catastrophic failure.

For specimen FRG, yielding of the longitudinal bars occurred during the second event (0.4 Sylmar) with cracks forming at the joints of the composite wrap. The maximum force of 341.1 kN was measured during event six (1.5 Sylmar). The peak table acceleration for the second to last event was 1.5g (2.5 Sylmar). This record had a peak load of 321.8 kN at a displacement of 162 mm. But permanent deformation of the specimen was 38 mm and cracks between the jacket segments had opened up to 3 mm. The maximum target acceleration in the final event was 1.75g and resulted in the complete flexural failure of the specimen. Figure 9 show the specimen after the jacket has been cut off. The plastic hinge region can be seen concentrated in the area that had a reduced number of wraps. The bond of the composite to concrete can be seen in the portion of the composite that has been removed from the specimen.

For specimen FRC, yielding of longitudinal bars and cracking at the composite wrap joints occurred during the second event (0.4 Sylmar). The maximum force was 323.7 kN at a

displacement of 77 mm (1.5 Sylmar). At this point, the specimen began to show extensive flexural cracking between the jacket segments. Specimen FRC developed plastic hinges at both 495 mm and 749 mm from the footing.

Effect of Retrofit

The objective of the retrofit was to increase the shear capacity of the columns. Even though the as-built column did not fail in a predominantly shear failure mode, yielding of the ties and wide shear cracks reduced the ductility capacity. It was, hence, anticipated that the retrofit would improve the ductility capacity in addition to increasing the shear strength. Figure 10 shows an example of a Sylmar motion. The motion shown is the 1.5 Sylmar for specimen FRC. Figure 11 shows the measured load-deflection envelopes for all four specimens. It can be seen that the FRP jackets affected the response in three ways: the initial stiffness, peak load, and ductility. The increase in the initial stiffness was mainly attributed to the contribution of the composite layer. Another possible reason is the application of a layer of epoxy on the column prior to the attachment of the FRP wraps to provide for a smooth surface. This layer of epoxy tends to close the micro cracks that are normally present due to concrete shrinkage and improve the initial stiffness. The increase in the peak load is also attributed to the jacket acting as a shell and resisting some flexural stresses in addition to the enhancing concrete confinement. The composite jacket does act as a flexural member even though the fibers are essentially in the transverse direction. The jacket contribution is due to a nominal number of fibers that run perpendicular to the main fibers to avoid fretting. Furthermore, the epoxy matrix has a reported tensile strength of 66 MPa, which would also provide some flexural strength. These contributions were quantified in [Martinovic, et al. 1999]. The third effect is the increase in the displacement ductility that is evident in the figure. To quantify the ductility increase, the load-displacement envelopes were idealized by elasto-plastic curves, taking the last data point shown for each specimen as the ultimate point. Note that the actual failure point was after the last point shown but it could not be accurately measured. It was found that the displacement ductilities were 5.4, 7.4, and 7.9 for specimens FA, FRG, and FRC, respectively, indicating an approximately 40 percent improvement in the displacement ductility capacity as a result of the retrofit. The difference between the response of FRG and FRC was minor and very close to that of the steel retrofitted specimen.

The effectiveness of the jacket in reducing the strains in the ties is shown in Fig. 12. It can be seen that the tie in FA yielded even under moderate levels of table motions. In contrast, the peak strain in the corresponding ties in the retrofitted specimens was only one-half of the yield strain. This trend was typical for the ties at or near the center of the plastic hinges. The improvement in the shear performance and the displacement ductility led to the conclusion that the FRP jackets were effective in accomplishing their objective. Extensive analytical studies of the specimens were also conducted [Martinovic, et al. 1999], but could not be included in this paper due to space limitation. The tie strains in FRC and FRG were nearly the same indicating that either jacket can be used for seismic retrofit.

Conclusions

1) The method of applying FRP composite wraps in the form of butted straps developed in this study was found to be an effective mean of constructing composite jackets for non-prismatic members.

2) The composite jackets accomplished their primary goal of enhancing the shear and displacement ductility capacity of the columns with structural flares. The jackets changed the mode of failure from flexure/shear to flexure.
3) The seismic performance of the glass-fiber epoxy jacket was very similar to that of the carbon-fiber epoxy composite. It should be noted that durability of the two composite types was not evaluated in this study. The performance was close to that of steel shell retrofit.

Acknowledgements

The study presented in this paper was funded by the Nevada Department of Transportation (NDOT). The support of Mr. Bill Crawford, Chief Bridge Engineer, and the staff engineers at the NDOT Bridge Division is appreciated. Thanks are also due Mr. John Drumm of the University of Nevada, Reno, for his assistance in the shake table tests. Messrs. Ed Fyfe and Scott Arnold of Fyfe and Associates are thanked for their timeliness and cooperation in installing the FRP wraps. This paper is an expanded version of a paper presented at the 12th World Congress on Earthquake Engineering.

References

1. California Department of Transportation (Caltrans), (1998) "Memo to Designers, 20-4," Engineering Service Center, Earthquake Engineering Branch, November 1998.
2. Laplace, P., (1999) "Shake Table Testing of Flexure Dominated Reinforced Concrete Bridge Columns," M.S.C.E. Thesis, Department of Civil Engineering, University of Nevada, Reno, August 1999.
3. Martinovic, F., M. Saiidi, D. Sanders, and F. Gordaninejad, (1999) "Dynamic Testing and Analysis of Nonprismatic Reinforced Concrete Bridge Columns Retrofitted with FRP Jackets," Report No. 99-xx CCEER (Under Review), Department of Civil Engineering, University of Nevada, Reno.
4. McElhaney, B., M. Saiidi, and D. Sanders, (1999) "Shake Table Testing of Flared Bridge Columns with Steel Jacket Retrofit," Report No. 99-xx CCEER (Under Review), Department of Civil Engineering, University of Nevada, Reno.
5. National Institute of Standards and Technology (NIST), (1994) "1994 Northridge Earthquake: Performance and Structures, Lifelines, and Fire Protection Systems," United States Department of Commerce, Special Publication 862, May 1994.
6. U.S. Department of Transportation (USDOT), "Seismic Retrofitting Manual for Highway Bridges, (1995) " Federal Highway Administration, Pub. No. FHWA-RD-94-052, May 1995.
7. Wehbe N., and M. Saiidi, (1999) "Effects of Confined Core on Seismic Vulnerability of Reinforced Concrete Column with Structural Flares," ACI Special Publication (SP-187), Seismic Response of Concrete Bridges, 1999.
8. Wehbe, N.I, M. Saiidi, and D. Sanders, (1997) "Effects of Confinement and Flares on the Seismic Performance of Reinforced Concrete Bridge Columns," Report No. 97-2, CCEER. Department of Civil Engineering, University of Nevada, Reno, September 1997.

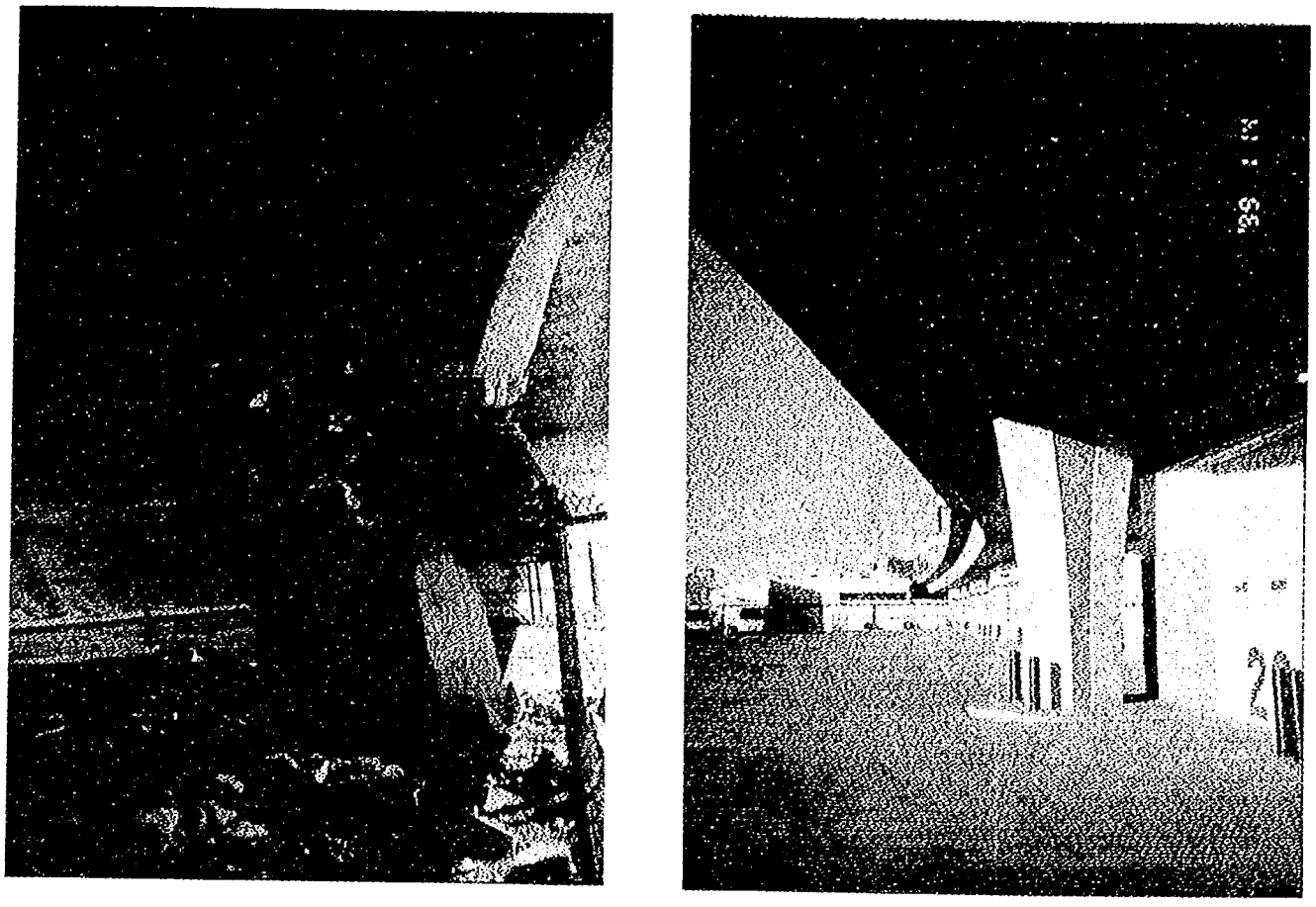


Figure 1: Flared Column Failure at Mission Gothic Bridge in Los Angeles and Existing Columns located in Reno, NV.

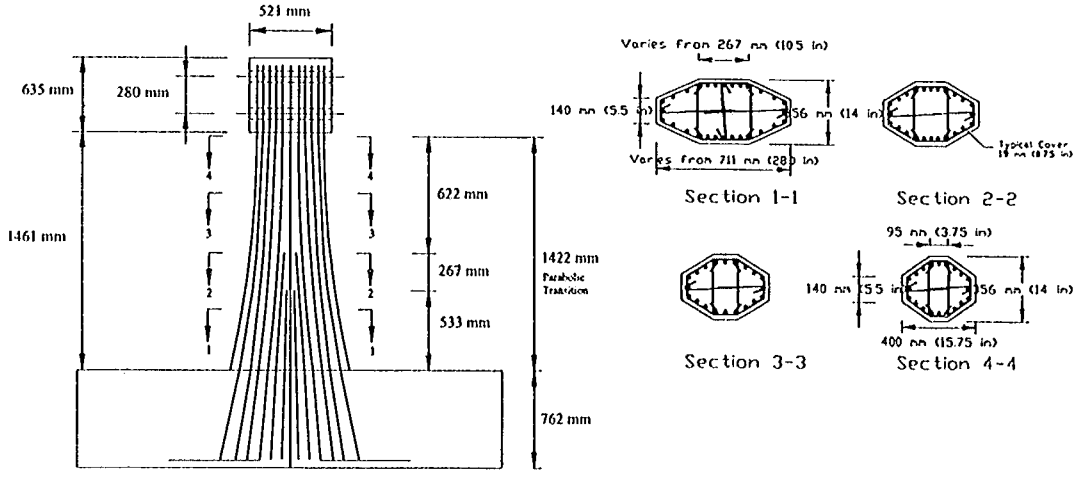


Figure 2: Elevation View of the As-Built Specimen

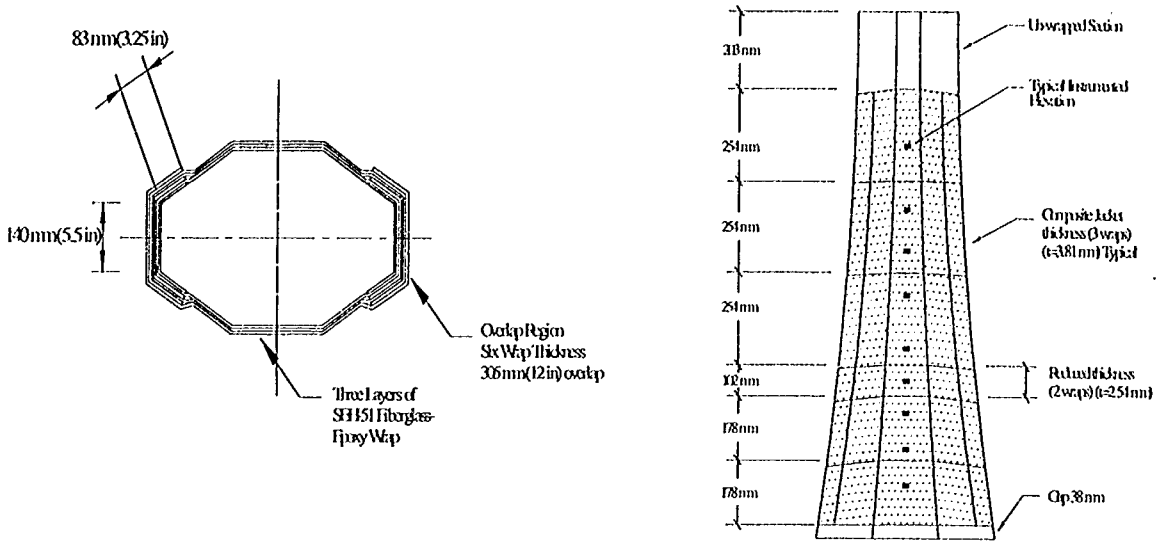


Figure 3: Details of Jacket in Specimen FRG

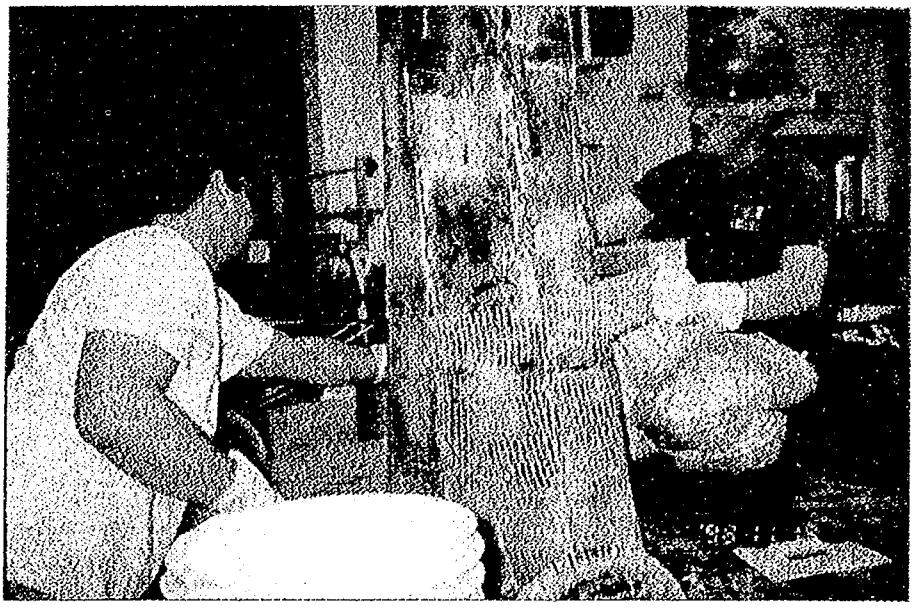


Figure 4: Application of Glass Fiber Sheet

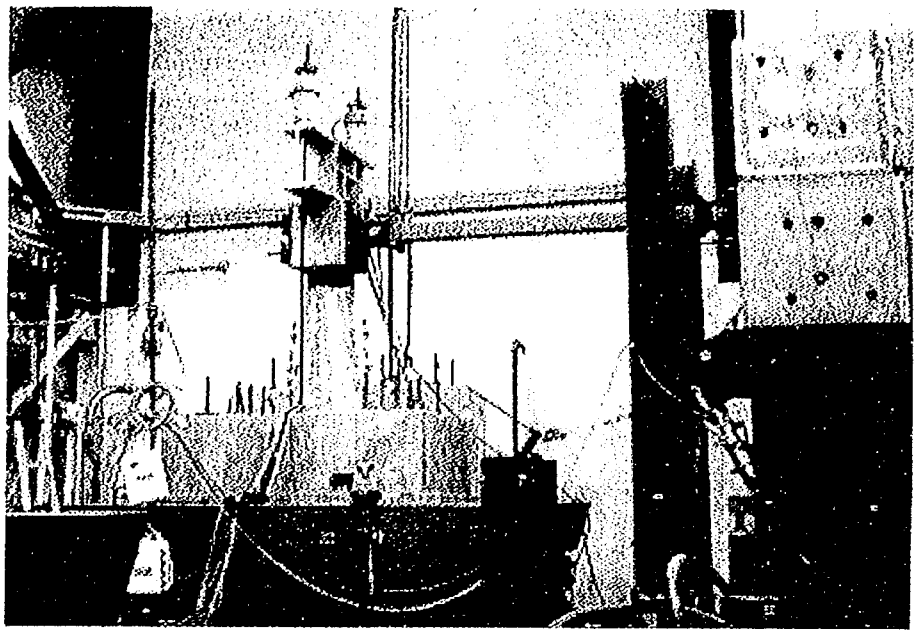


Figure 5: Shake Table with Mass Rig

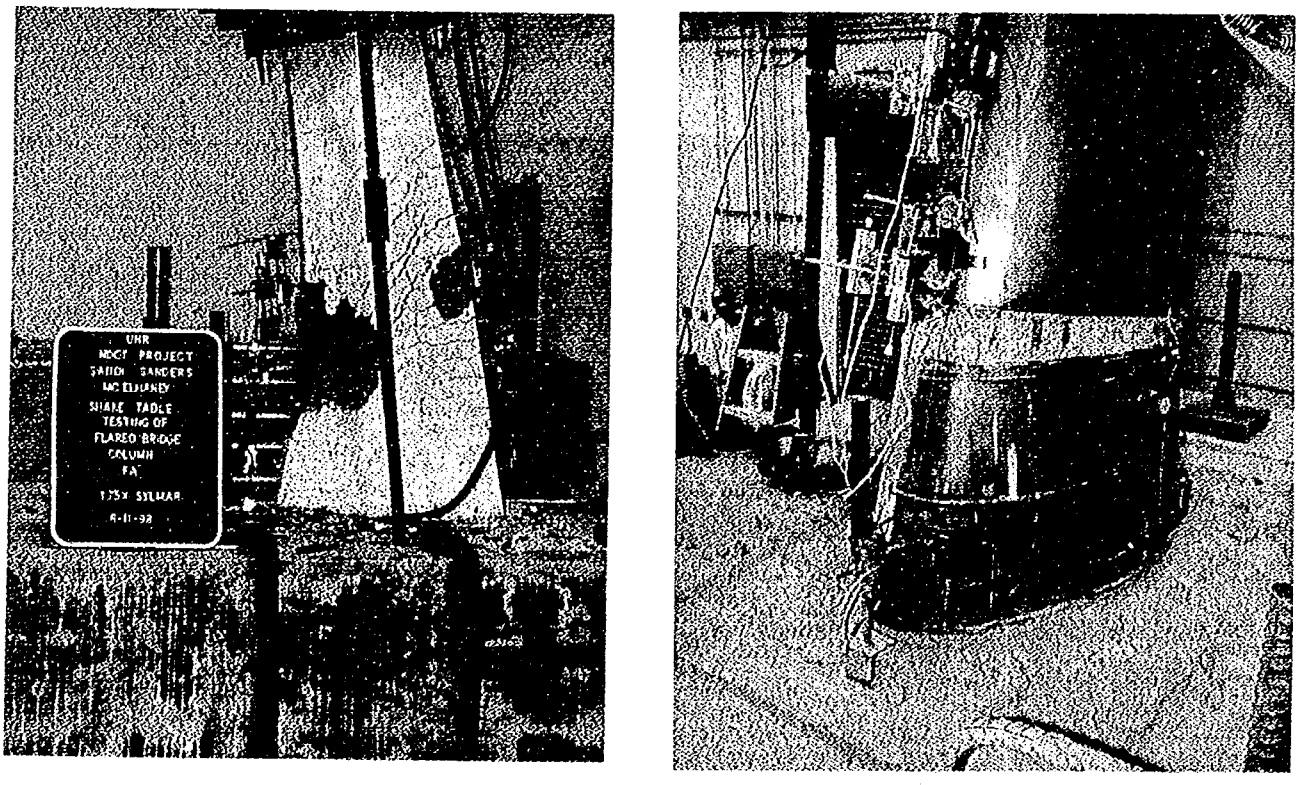


Figure 6: The Failure of Specimen FA and Specimen FR (Steel Jacket)

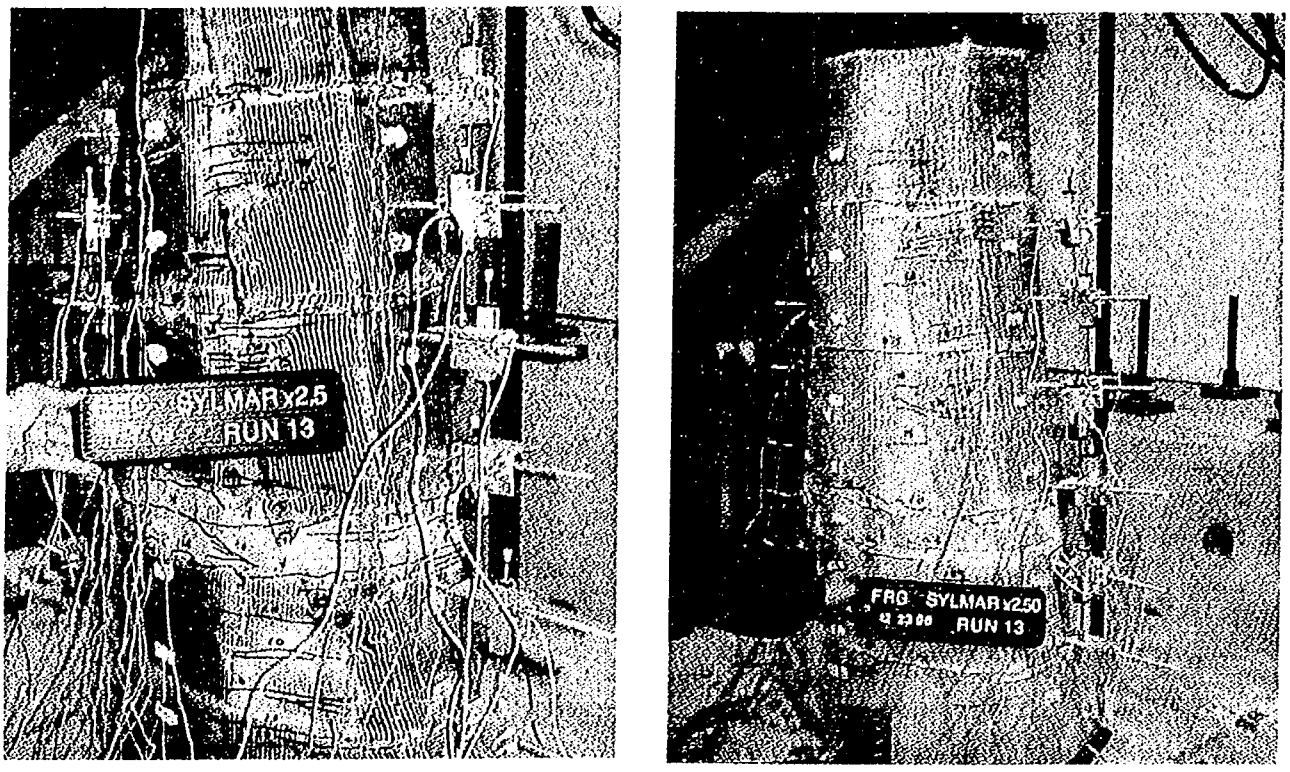


Figure 7: Specimens FRC and FRG near failure

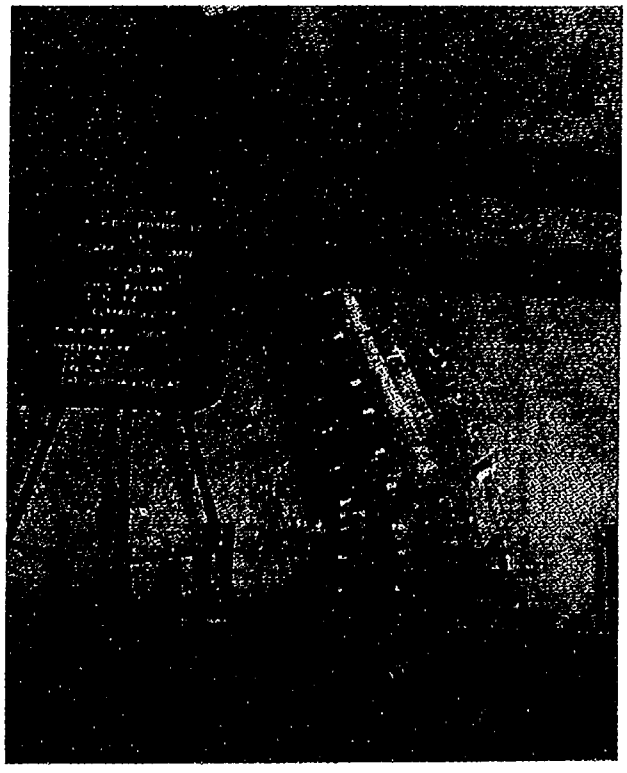


Figure 8: Specimen FRG at Failure

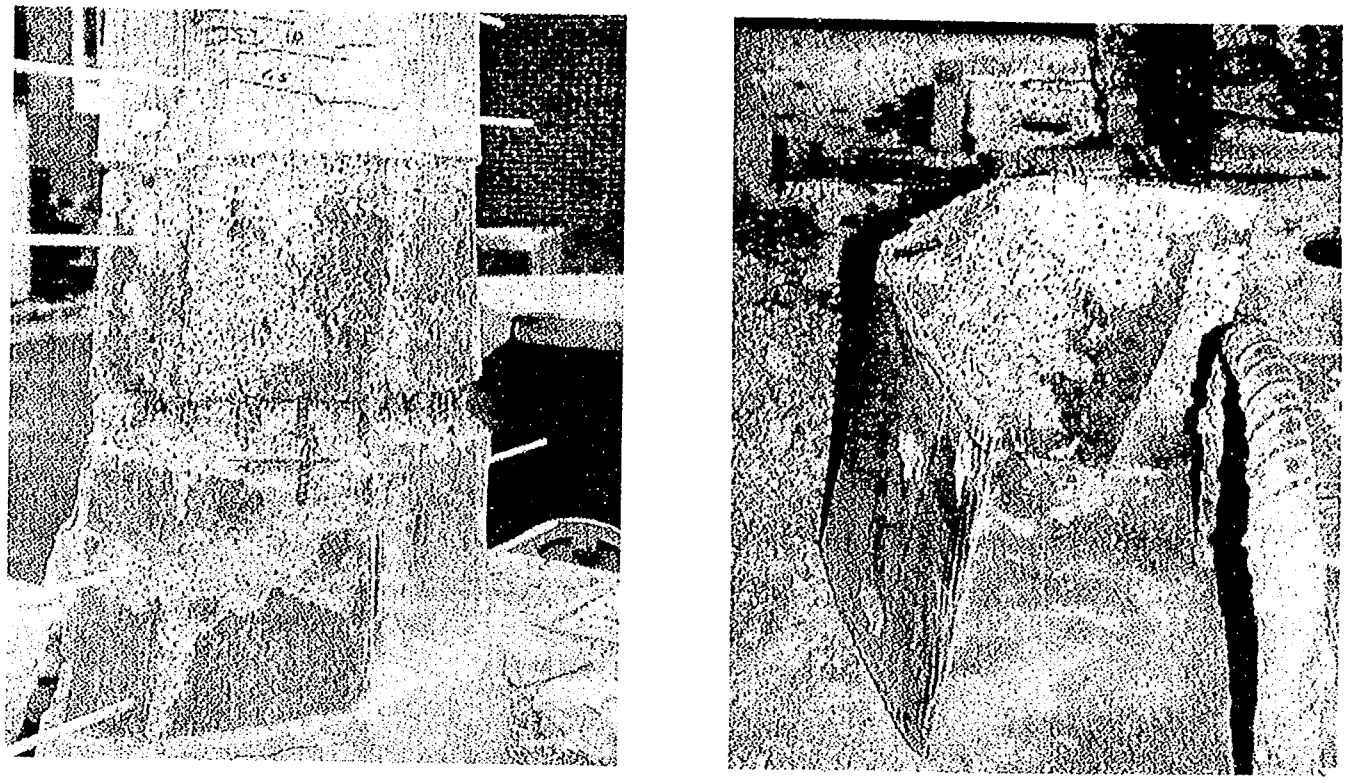


Figure 9: Post Failure Removal of Composite

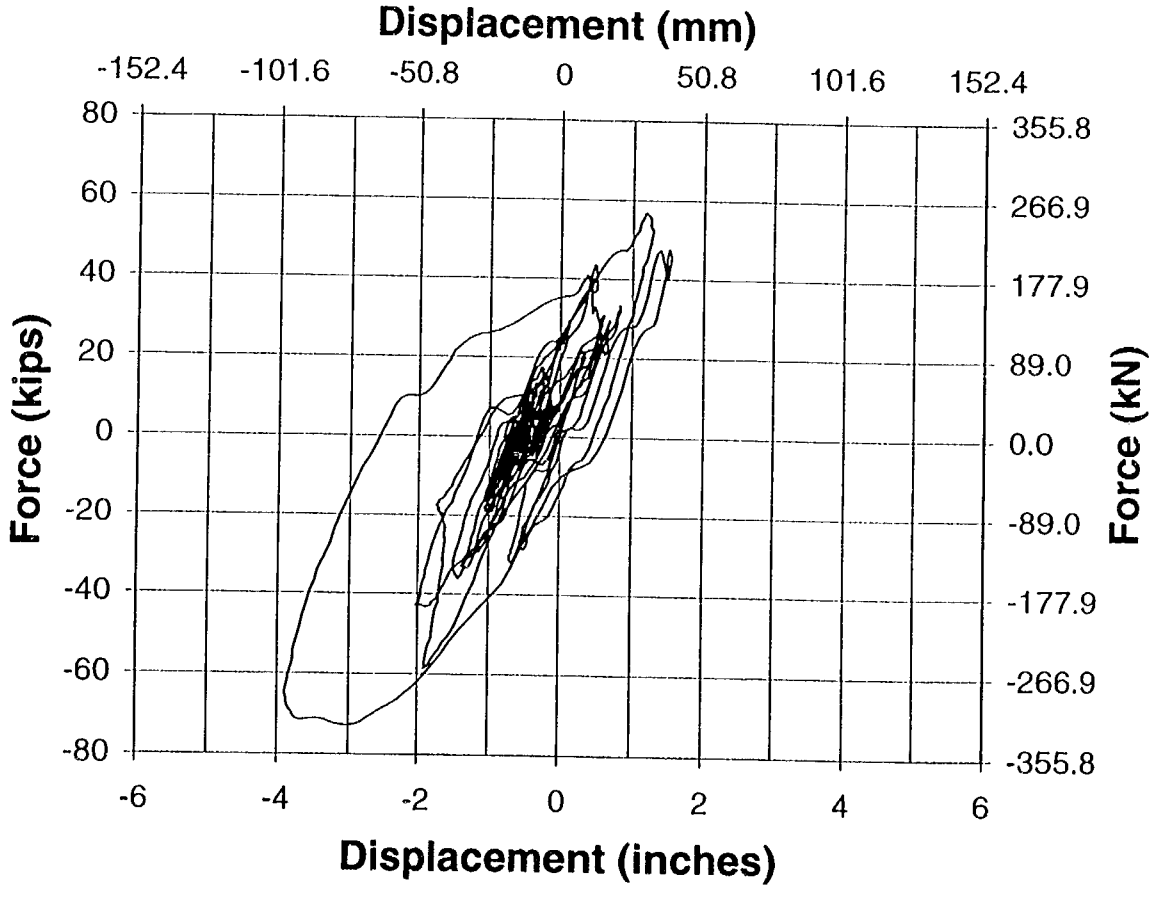


Figure 10: Motion for FRC at 1.5 Sylmar

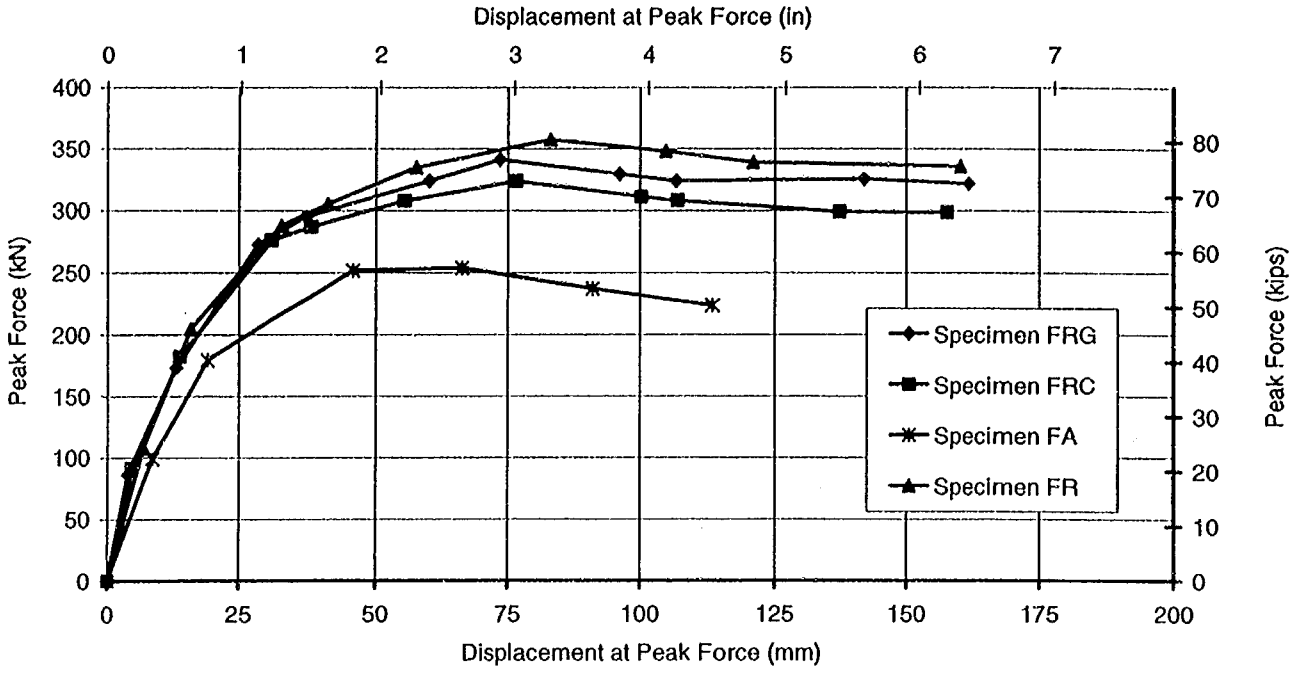


Figure 11: Load-Deflection Envelopes for All Specimens

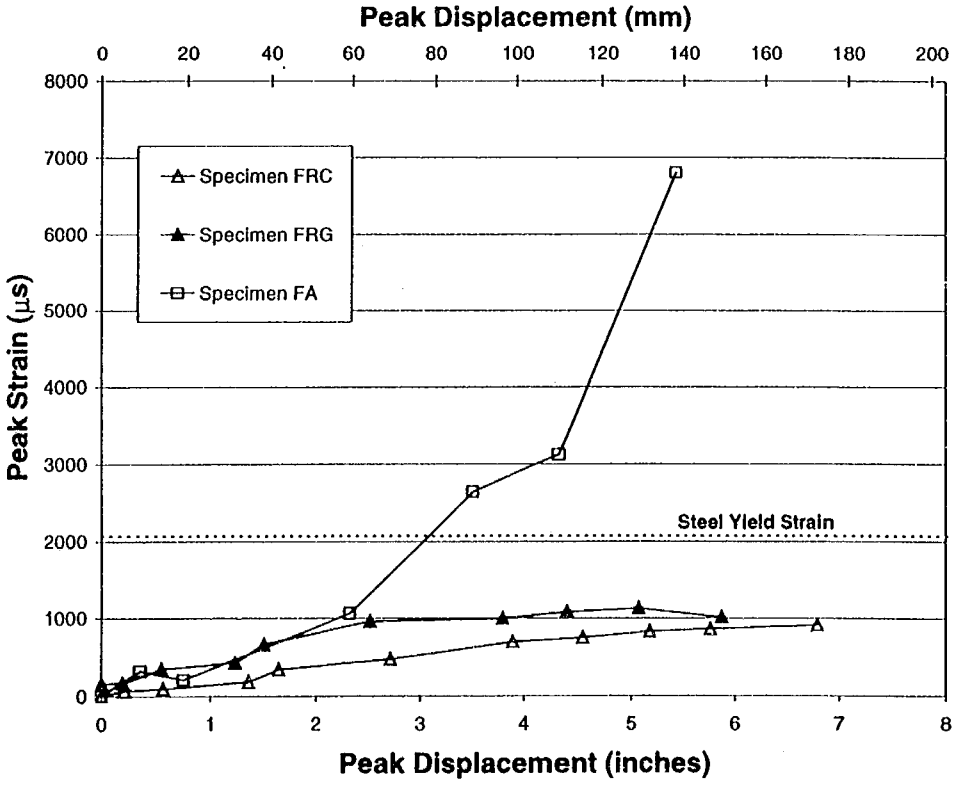


Figure 12: Tie Bar Strains in the Vicinity of the Plastic Hinge

Size Effect in Shear Behavior of Reinforced Concrete Piers Strengthened with Carbon Fiber Sheets

Koji Osada, Yoshinori Igase, Takahiro Yamaguchi and Shoji Ikeda

Abstract

In order to investigate the size effect in shear behavior of reinforced concrete piers strengthened with carbon fiber sheets, static reversed cyclic loading tests were carried out. In these tests 3 types of specimen, i.e., 1/4, 1/2 and 1/1 of prototype were used. Each specimen was carefully designed to have the same percentage of longitudinal and lateral reinforcing bars area, and similar figures of cross section, diameter and pitch of reinforcing bars, the maximum size of aggregate, and the amount of carbon fiber sheets. From the experimental results, it is to be concluded that the pier strengthened with carbon fiber sheets has no definite size effect in shear behavior as well as the pier without strengthening of carbon fiber sheets when the pier consists of the materials having similar figures.

1. Introduction

Studies of size effects on shear strength of reinforced concrete beams have been made by a large number of researchers[2)] and the test results have also been reflected in existing design standards[3)]. Few tests have, however, been carried out on the influence of size effects in the shear behavior of reinforced concrete members strengthened with carbon fiber sheets (hereinafter referred to as CFS). In addition, most of the tests conducted on size effects have so far focused on beams but few have been done for column specimens. In view of the above, this study aimed at examining the influence of size effects on the shear strength of reinforced concrete column specimens strengthened with CFS, under reversed cyclic loading tests. The specimens were carefully designed to have similar figure in three levels, ie, 1/4, 1/2 and 1/1 of prototipe strengthened with and without CFS were carried out

2. Specimens

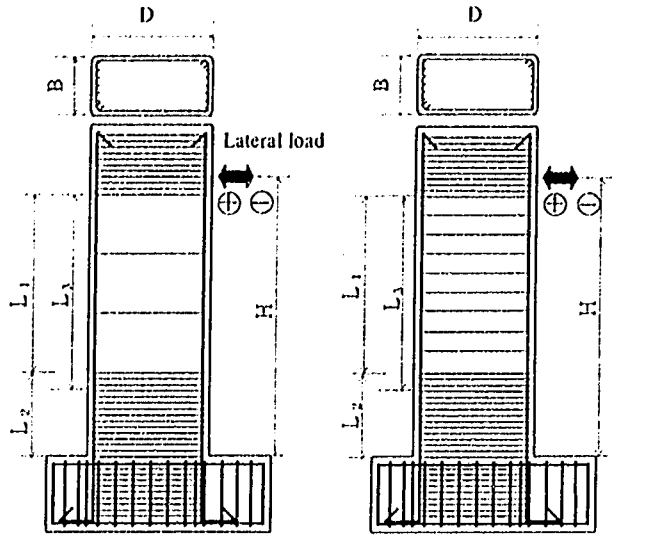
The shapes and types of specimens are shown in Figure 1 and Table 1, respectively. Mechanical properties of the materials used in the specimens are listed in

Engineer of Expressway Research Institute Japan Highway Public Corporation
Deputy Director Expressway Research Institute Japan Highway Public Corporation
Department of Civil Engineering Yokohama National University
Professor of Civil Engineering Yokohama National University

Tables 2 through 4. Characteristics of the cross section of specimens used in the test are described below.

(i) Size of specimens

Three different sizes of specimens were used, such as large, medium and small with G, B and S for their names, respectively. The height of cross section of large specimens was set at 1,400 mm, almost equivalent to the height of cross section of actual structures. The height of cross section of medium specimens was 700 mm, half that of large specimens. Small specimens had a sectional height of 350 mm, a quarter of that of the large specimens.



(a) Specimen with a low hoop ratio (b) Specimen with a high hoop ratio

H: Height from the column bottom to the loading point
B: Width of cross section, D: Height of cross section
L1: Shear span except high hoop ratio, L3: Strengthened with CFS portion
L2: High hoop ratio portion around the base

Figure 1 Shapes of specimens

The width of cross section was set at half the sectional height in view of the capacity of loading devices. The height from the column bottom to the loading point was set so as to achieve a shearing span ratio of 2.5.

(ii) Ratio of tension reinforcement

In this test, tension reinforcement ratio was designed to match that in actual piers on the assumption of piers consisting of independent two-column type that are most frequently found in expressway viaduct. As a result, tension reinforcement ratio was set at

Table 1 Types of specimens

No	Specimen name*1	Shape of cross section D×B	Effective depth d	Height H	Shear span except high hoop ratio L_1	High hoop ratio portion around the base L_2	Strengthened with CFS portion L_3	Tension reinforcement ratio (%)	Hoop ratio (%)	Area ratio of CFS (%)	Maximum aggregate size	Remarks
1	S-L-N	350×175	330	825	480	250	—	0.87	0.050	0	10mm	Non-strengthened
2	B-L-N	700×350	660	1650	1050	500	—	0.87	0.052	0	20mm	
3	G-L-N	1400×350	1320	3300	2100	1000	—	0.87	0.052	0	40mm	
4	S-H-N	350×175	330	825	477	250	—	0.87	0.151	0	10mm	
5	B-H-N	700×350	660	1650	1035	500	—	0.87	0.157	0	20mm	
6	S-L-CF	350×175	330	825	480	250	530	0.87	0.050	0.048	10mm	Strengthened with CFS
7	B-L-CF	700×350	660	1650	1050	500	1150	0.87	0.052	0.048	20mm	
8	G-L-CF	1400×350	1320	3300	2100	1000	2300	0.87	0.052	0.048	40mm	
9	S-H-CF	350×175	330	825	477	250	527	0.87	0.151	0.032	10mm	
10	B-H-CF	700×350	660	1650	1035	500	1135	0.87	0.157	0.032	20mm	
11	S-L-RCF	350×175	330	825	480	250	530	0.87	0.050	0.048*2	10mm	Post-loading Strengthened with CFS*3
12	B-L-RCF	700×350	660	1650	1050	500	1150	0.87	0.052	0.048*2	20mm	
13	G-L-RCF	1400×350	1320	3300	2100	1000	2300	0.87	0.052	0.071*2	40mm	
14	S-H-RCF	350×175	330	825	477	250	527	0.87	0.151	0.032*2	10mm	
15	B-H-RCF	700×350	660	1650	1035	500	1135	0.87	0.157	0.032*2	20mm	

*1: Naming of specimens (○-△-□)
○[Specimen size] △ [Hoop ratio] □ [Type of reinforcement]
S: Small specimen L: Low hoop ratio N: Non-reinforced
B: Large specimen H: High hoop ratio CF: CFS-reinforced
RCF: Post-loading CFS-reinforced

*2: The mount of CFS applied after pre-strengthening loading under non-reinforced condition

*3: With G-L-RCF, cracks were repaired by epoxy resin grouting, after pre-strengthening loading and then the specimen was strengthened with CFS. Specimens other than G-L-RCF were reinforced with CFS without repair of cracks after pre-strengthening loading.

0.87% for all the specimens. Since little has yet been known about the influence of longitudinal bars in web portion, however, no such reinforcement was used in the test to obtain explicit results.

Table 2 Mechanical properties of concrete

Specimen	Compressive strength (MPa)	Tensile strength (MPa)	Young's modulus (GPa)
S series*1	28.5	2.83	28.6
B series*2	29.2	2.76	23.7
G series*3	27.5	2.46	25.6

*1: Specimens with a section 350 x 175 listed in Table 1 (small specimens)
*2: Specimens with a section 700 x 350 listed in Table 1 (medium specimens)
*3: Specimens with a section 1400 x 700 listed in Table 1 (large specimens)

(iii) Hoop ratio

Specimens with L for their name had a low hoop ratio. The hoop ratio of these specimens was determined based on the ratio for piers with independent two-column type designed in or before 1980. Large, medium and small specimens were produced with a low hoop ratio. The ratio was 0.052% for large and medium specimens and 0.050% for small specimens.

Table 3 Mechanical properties of reinforcement

Type		Yield strength (MPa)	Tensile strength (MPa)	Young's modulus*1 (GPa)	Application
Size	Type				
D3	——	217	306	162	Hoop
D6	SD295A	362	538	177	Hoop
D10	SD295A	376	513	176	Longitudinal reinforcement
D13	SD345	358	515	191	Hoop
D19	SD345	399	556	184	Longitudinal reinforcement
D38	SD345	391	575	183	Longitudinal reinforcement

*1: Obtained using distortion value measured by a distortion gauge attached to reinforcement, and nominal cross section

Specimens with H for their name had a high hoop ratio. The hoop ratio of these specimens was set approximately at 0.15%, the minimum volume specified by the Standard Specifications for Design and Construction of Concrete Structures in 1980. Medium and small specimens were produced with a high hoop ratio an such a way that the ratio was 0.157% for medium specimens and 0.151% for small specimens.

Table 4 Mechanical properties of CFS

Fiber areal weight (g/m^2)	Fiber cross section*1 (mm)	Design thickness*2 (mm)	Tensile strength*3 (MPa)	Young's modulus*3 (GPa)	Application
50	0.444	0.028	3861	288	S-H-CF, B-H-CF S-H-RCF, B-H-RCF
75	0.444	0.042	3662	281	S-L-CF, B-L-CF G-L-CF, S-L-RCF B-L-RCF, G-L-RCF

*1 Obtained from standard values for density and weight of 12,000 fibers
*2 Fiber cross section is divided by the width of tensile bar, and multiplied by a ratio between the width of tensile bar and pitch
*3Results of test using 12.5 mm wide, 0.28 mm thick test pieces made by impregnation of resin

The hoop ratios in most of the piers designed in or before 1980 were somewhat between the low and high hoop ratios for the specimens used in the test.

(iv) Hoop ratio around the base of a column

In seismic retrofit of actual piers, ductility is increased appropriately at least for the height equivalent to the height of cross section from the column bottom. In the test, efforts were made to obtain explicit results by controlling shear failure due to reversed cyclic flexure exclusively in shear column without the influence of plastic zone. Hence the amount of hoop was increased for the height from the column bottom equivalent to approximately 3/4 of the height of cross section so that the hoop alone could bear the entire shear force.

(v) Aggregate size

In order to minimize the influence of aggregate on shear strength, maximum size

of aggregate was determined to have similar size for each size of specimens. The maximum aggregate size was 40 mm for large specimens, 20 mm for medium specimens and 10 mm for small specimens.

(vi) Amount of CFS

The amount of CFS was determined to have same area ratio for each hoop area ratio of specimens except G-L-RCF. For all the specimens strengthened with CFS except G-L-RCF, the amount of CFS was determined to have same combined amount of CFS and hoop for shear reinforcement and at a level slightly lower than bending strength of specimens. In the above process, amount of CFS was converted into reinforcement bar amount based on the tensile strength ratio. As a result, the area ratio was 0.048% for specimens with a low hoop ratio and 0.032% for those with a high hoop ratio. The amount of CFS in G-L-RCF was determined based on the test results for G-L-CF. Specifically, the effect of strengthening with CFS was assumed to perform until the maximum CFS strain reached 8,000 μ and design shear capacity of concrete was neglected. Under such conditions, amount of CFS was determined so that CFS, converted into reinforcement amount based on the tensile strength ratio. The area ratio of CFS in G-L-RCF was then set at 0.071%.

Layers of CFS were also set as equivalent as possible for each size of specimens. CFS strips were bonded to small specimens in one layer. They were bonded to medium and large specimens in two and four layers, respectively.

(vii) Specimens strengthened with CFS after loading

With the specimens of a name ending with RCF, certain loading was applied to cause shear cracks before strengthening with CFS. Then the specimens were strengthened with CFS. G-L-RCF was strengthened with CFS after repairing cracks of larger than 0.2mm width with epoxy resin referring the experimental results of B-L-RCF. With the specimens except G-L-RCF, loading was followed by strengthening with CFS without any repair of cracks with epoxy resin or other materials.

The displacement of the last stage as pre-strengthening applied to G-L-RCF specimen was –2/200rad. Because the G-L-N and G-L-RCF was same specimen, then pre-strengthening loading continued until the maximum strength to get load bearing behavior under a non-strengthened condition. The displacements of the last stage except G-L-RCF were determined based on the progress of shear cracks, strain of hoop and reduction in strength. Reversed cyclic displacement was applied for specimens with a low hoop ratio until a rotation angle reached -1/200 rad. For specimens with a high hoop ratio, reversed cyclic displacement was applied until a rotation angle reached -2/200 rad.

3. Test results

3.1 Loading method

For loading, an actuator was used and a lateral force or lateral displacement was applied as shown in Figure 1. While axial compressive forces act on actual bridges, no axial compressive forces were applied in the test because application of compressive forces against shear in actual bridges was considered on the safe side. The lateral displacement at loading point and the height from the column bottom to the loading point were represented by δ and H, respectively.

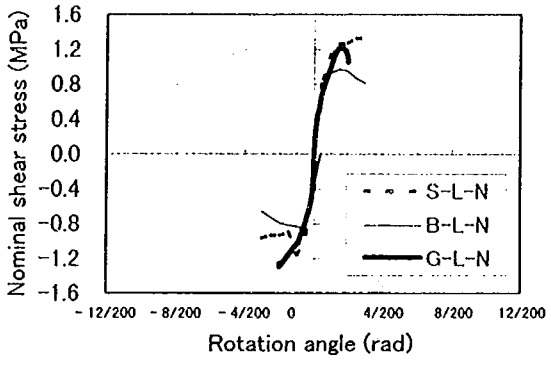
A positive load and negative load were applied once at each stage of displacements until the end of loading while increasing the rotation angle calculated by δ/H in increments of 1/200 rad. For control purposes, however, 1/10 mm or lower digits were rounded. As a result, the displacement at 1/200 rad was set at δ=4 mm for small specimens, 8 mm for medium specimens and 16 mm for large specimens. Displacement at a rotation angle of 1/200 rad was identical to the yield displacement of specimens of each size that experienced bending failure.

3.2 Load bearing behavior

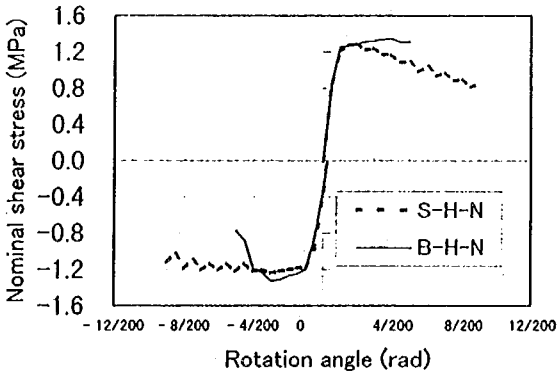
(1) Non-strengthened specimens

Envelopes for nominal shear stress-rotation angle for non-strengthened specimens are shown in Figure 2. Relationships between effective depth and the maximum of nominal shear stress are shown in Figure 3. Conditions in the final loading stage are shown in Photos 1 (a) through (e).

In S-L-N, a small specimen, B-L-N, a medium specimen, and G-L-N, a large specimen, that had a low hoop ratio, diagonal cracks occurred during loading at 1/200 rad. Hoops yielded in all the specimens during loading at -1/200 rad. The maximum crack width during loading at -1/200 rad was 0.6 mm for S-L-N, 1 mm for B-L-N and 3 mm for G-L-N. For G-L-N,



(a) Non-strengthened specimens with a low hoop ratio



(b) Non-strengthened specimens with a high hoop ratio

Figure 2 Envelopes for nominal shear stress-rotation angle

loading was terminated at -2/200 rad after the maximum strength was reached because it would be strengthened with CFS after loading into G-L-RCF and load would be applied again. The maximum crack width at the end of loading was 15 mm. Deformation behavior up to the ultimate state was quite similar either for S-L-N or B-L-N. Approximately at the time when the rotation angle reached 3/200 rad during loading, hooks started separating from hoops due to fracture of hoops or delamination of concrete cover.

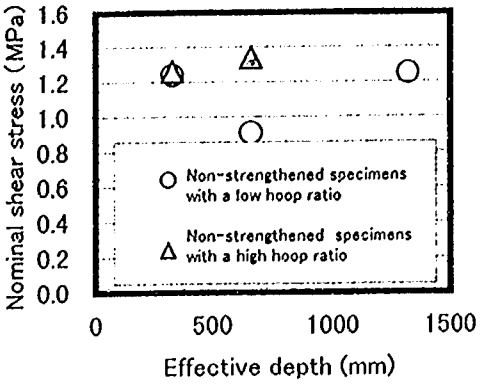
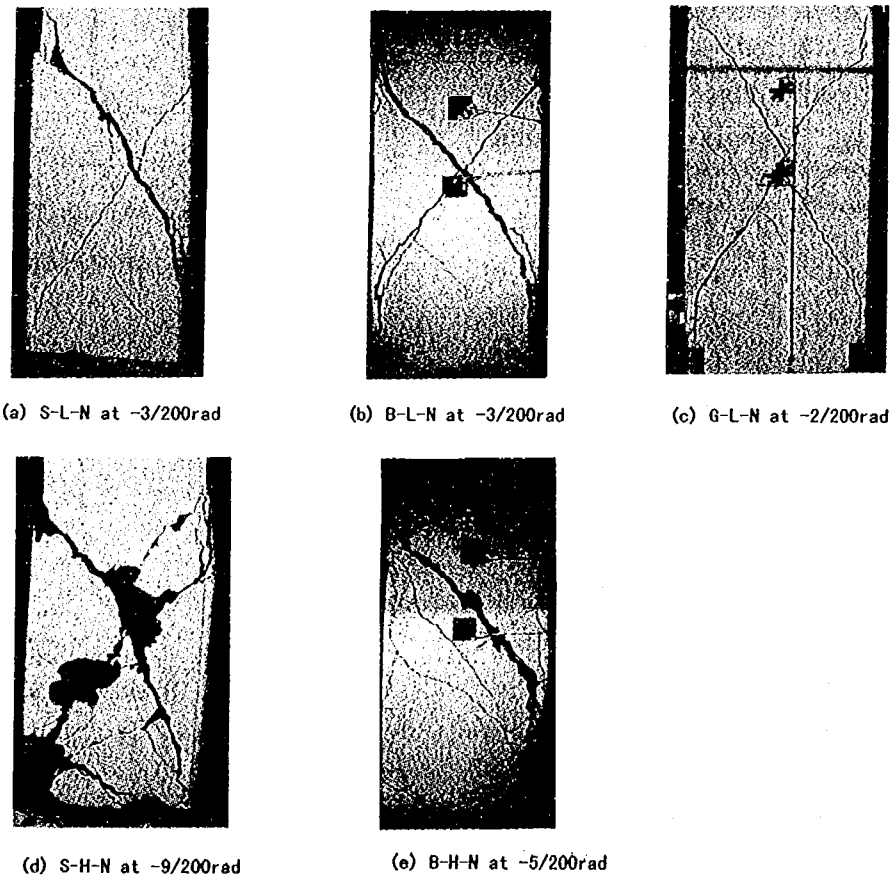


Figure 3 Relationships between maximum of nominal shear stress and effective depth

At the time of loading at -3/200 rad, strength was reduced substantially and the test was terminated. As shown in Figure 3, the maximum of nominal shear stress was somewhat small in medium specimens but was almost the same either in large or small specimens. In medium specimens, diagonal cracks occurred almost linearly. The maximum of nominal shear strength was small in medium specimens presumably because of dispersion of crack positions.



(a) S-L-N at -3/200rad (b) B-L-N at -3/200rad (c) G-L-N at -2/200rad

(d) S-H-N at -9/200rad (e) B-H-N at -5/200rad

Photograph 1 Conditions of non-strengthened specimens in the final loading stage

In S-H-N, a small specimen, and B-H-N, a medium specimen, with a high hoop ratio, diagonal cracks occurred during loading at 1/200 rad. At the time of loading at -1/200 rad, hoops experiencing the largest strain yielded. The crack width increased to as much as 0.45 mm in S-H-N and to 0.55 mm in B-H-N. S-H-N suffered no explicit reduction in strength due to loading but the strength lowered gradually. At the time of loading at -4/200 rad, shear failure progressed considerably. Then loading was terminated at -9/200 rad. In B-H-N, hoops fractured during loading at -5/200 rad. At the time of loading at -5/200, strength decreased substantially and loading was terminated.

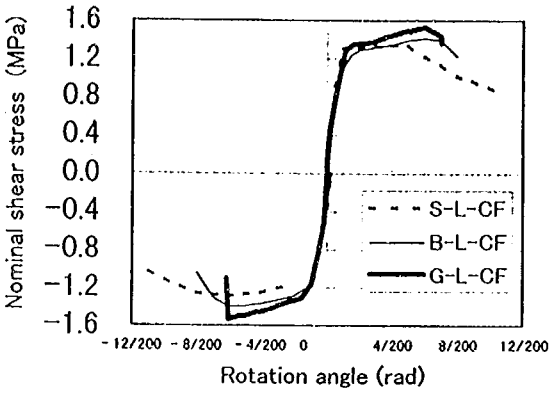
As shown in Figure 3, no definite difference could be seen in the maximum shear stress of the reinforced concrete column specimens having different size. Therefore, no definite size effect on the shear strength of reinforced concrete column seems to exist if the size of each portion including maximum size of aggregate of concrete is in similar figure.

(2) Strengthened with CFS specimens

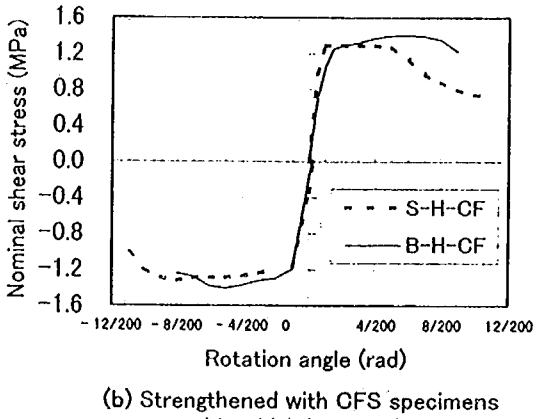
Envelopes for nominal shear stress-rotation angle for strengthened with CFS specimens are shown in Figure 4. Relationships between effective depth and maximum of nominal shear stress are shown in Figure 5. Conditions in the final loading stage are shown in Photos 2 (a) through (e).

With S-L-CF, a small specimen, and B-L-CF, a medium specimen, with a low hoop ratio, no noticeable shear failure occurred and no outstanding damage was caused in the portion strengthened with CFS except at the bottom end of CFS up to the final loading stage.

In G-L-CF, a large specimen, favorable deformation behavior was exhibited with no outstanding damage in the portion strengthened with CFS except at the bottom end of CFS up to the loading at -6/200 rad. During loading at 7/200 rad, however, CFS fractured in the lower portion strengthened with CFS and then shear



(a) Strengthened with CFS specimens with low hoop ratio



(b) Strengthened with CFS specimens with a high hoop ratio

Figure 4 Envelopes for nominal shear stress-rotation angle

failure progressed with the expansion of CFS fracture area. During loading at -7/200 rad, strength decreased so quickly that loading was terminated. CFS in specimen G-L-CF fractured probably for the following reason. Since reversed cyclic loading damaged internal concrete exclusively around cracks and thus the shear force to be borne by concrete lowered almost to none, CFS and hoops alone could no longer bear the shear force.

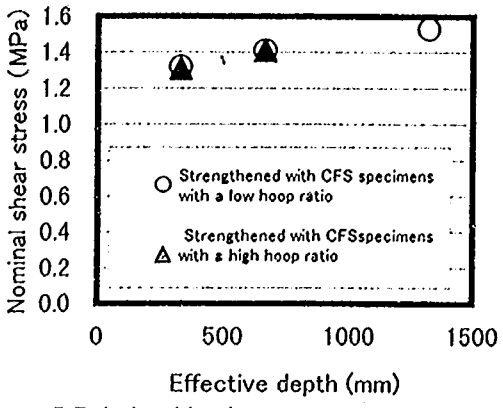
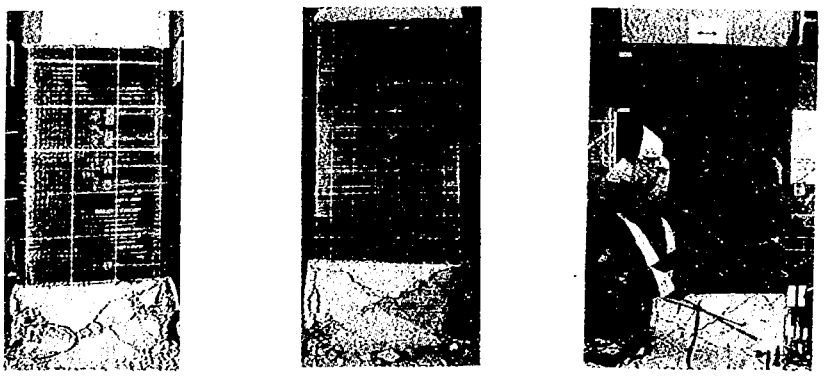


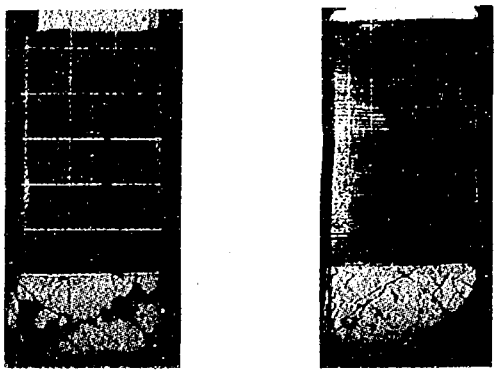
Figure 5 Relationships between maximum of nominal shear stress and effective depth

In S-L-CF, B-L-CF and G-L-CF, ultimate state was reached only after the maximum strength was obtained. No correlation was recognized between the size and the maximum of nominal shear stress as shown in Figure 5. Thus it was revealed that the size effects had no influence on shear strength. It was also illustrated that shear strengthening with CFS for reinforced concrete members with a low hoop ratio that had no longitudinal bars in web portion would cause damage to internal concrete to progress. That is, the shear force to be borne by concrete would decrease.

The load bearing behavior of S-H-CF, a small specimen, and B-H-CF, a medium



(a) S-L-CF at -11/200rad (b) B-L-CF at -8/200rad (c) G-L-CF at -7/200rad



(d) S-H-CF at -11/200rad (e) B-H-CF at +9/200rad

Photograph 2 Conditions of strengthened with CFS specimens in the final loading stage

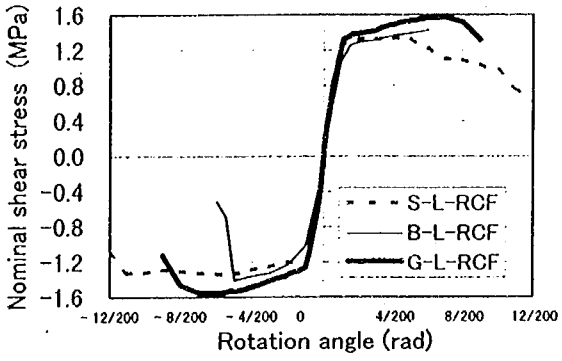
specimen, that had a high hoop ratio was almost similar to that of small and medium specimens with a low hoop ratio, respectively. CFS suffered no outstanding damage in the portion strengthened with CFS except at the bottom end of CFS until the final stage of loading. Bending failure of the base of a column gradually reduced the strength of the specimen and caused loading to be terminated. The maximum of nominal shear stress was almost the same either for small or medium specimens as shown in Figure 5. No influence of size effects was indicated.

(3) Specimens strengthened with CFS after loading

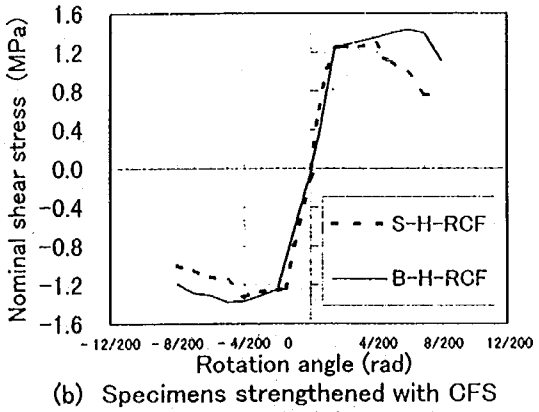
Envelopes for nominal shear stress-rotation angle for specimens strengthened with CFS after loading are shown in Figure 6. Relationships between effective depth and maximum of nominal shear stress are shown in Figure 7. Conditions in the final loading stage are shown in Photos 3 (a) through (e).

With S-L-RCF, a small specimen with a low hoop ratio, no outstanding damage occurred to CFS up to the final loading stage except at the bottom edge of the CFS. Bending failure at the base of a column gradually reduced strength and loading was finally discontinued.

In B-L-RCF, a medium specimen, no outstanding damage occurred up to loading at -5/200 rad. During loading at 6/200 rad, CFS fractured, shear failure progressed rapidly and internal concrete was greatly damaged. The maximum CFS strain measured at the time of CFS fracture was approximately 11,000μ. With the progress of shear failure, strength decreased considerably. Loading was terminated at -6/200 rad. CFS in specimen B-L-RCF fractured probably for the following reason. Since reversed cyclic loading damaged concrete exclusively around cracks that occurred after pre-strengthening loading, owing to a low



(a) Specimens strengthened with CFS after loading with a low hoop ratio



(b) Specimens strengthened with CFS after loading with a high hoop ratio

Figure 6 Envelopes for nominal shear stress-rotation angle

hoop ratio, CFS and hoops alone could no longer bear the shear force.

G-L-RCF was a large specimen with a low hoop ratio. And the cracks occurred pre-strengthening loading were repaired with epoxy resin. Then strengthened with adequate amount of CFS, i.e., design CFS strain of 8,000 μ and design shear capacity of concrete was neglected. G-L-RCF suffered no outstanding damage to CFS through the final stage of loading except at the base. Bending failure at the base gradually reduced strength and loading was finally discontinued.

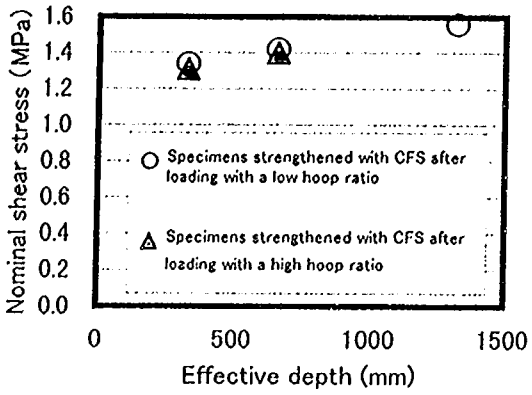
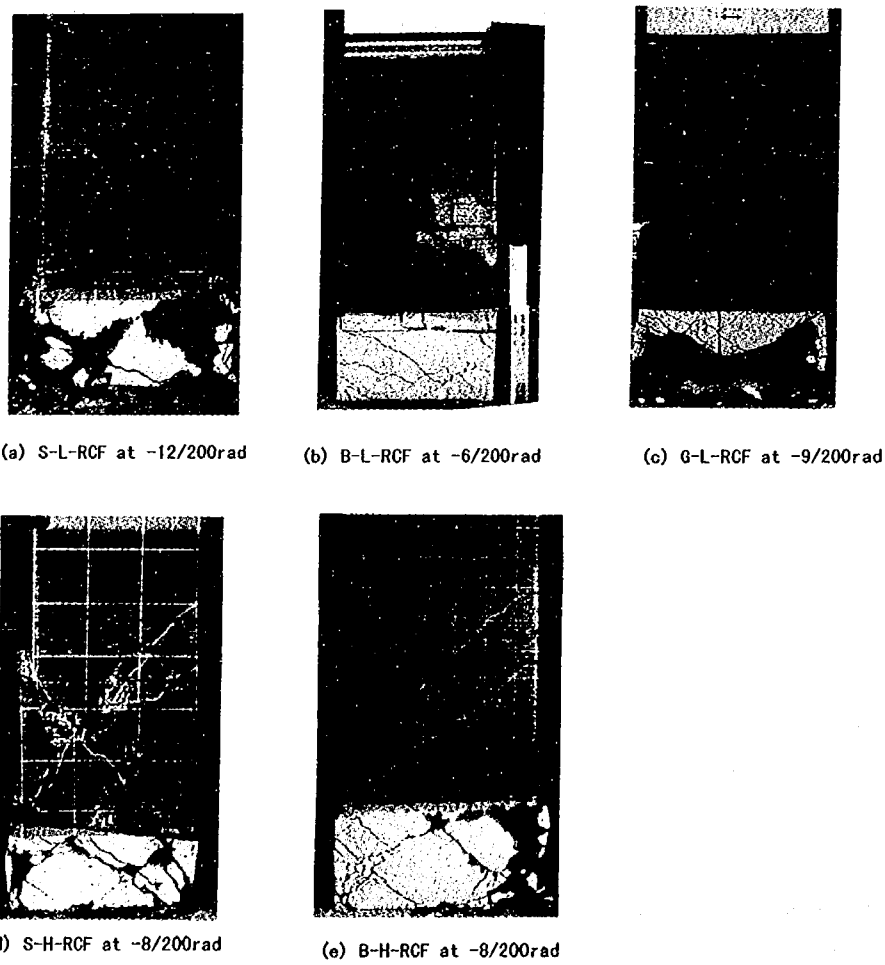


Figure 7 Relationships between maximum of nominal shear stress and effective depth

As shown in Figure 7, no correlation was recognized between the size and the maximum of nominal shear stress. Thus it was found that the size effects had no influence on shear strength.

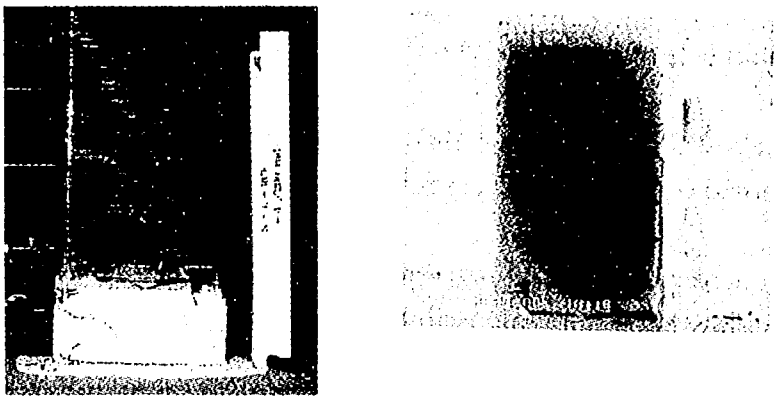
In S-H-RCF, a small specimen with a high hoop ratio, no outstanding damage



(a) S-L-RCF at -12/200rad (b) B-L-RCF at -6/200rad (c) G-L-RCF at -9/200rad

(d) S-H-RCF at -8/200rad (e) B-H-RCF at -8/200rad

Photograph 3 Conditions of specimen strengthened with CFS after loading in the final loading stage



(a) With an ordinary camera (b) With an infrared camera

Photograph 4 Condition of S-L-RCF at -4/200rad

occurred until loading at -4/200 rad. During loading at 5/200 rad, however, CFS fractured, shear failure progressed rapidly and strength decreased greatly. Then at -8/200 rad, loading was terminated. The maximum CFS strain measured in the meantime was approximately 12,000μ.. CFS fractured in specimen S-H-RCF for the following reason. When the amount of CFS is relatively small, no exfoliation between concrete and CFS is likely to occur with the increases of bond stress. Instead, CFS strain increases locally at cracks in concrete and eventually CFS is ruptured.

In B-H-RCF, a medium specimen with a high hoop ratio, no outstanding damage occurred to CFS up to the final stage of loading except at the bottom edge of the CFS. Bending failure at the base of a column gradually reduced strength and loading was terminated. The maximum of nominal shear stress was almost the same either for small or medium specimens as shown in Figure 7. Thus no influence of size effects was indicated.

(4) Results of observation of damage in CFS with an infrared camera

In this study, photographs were taken with an infrared camera in order to identify the progress of CFS delamination from concrete during loading referring to a document[4]. Photo 4 (a) is a photograph taken with an ordinary camera. Photo 4 (b) was taken with an infrared camera. Dark points in photo 4 (b) indicate positions of delamination. Dark images represented horizontally at constant intervals are cables. The photograph shows the progress of delamination around cracks stretching diagonally. Photographing showed that in reinforced concrete columns strengthened with CFS, local CFS strain was controlled by CFS exfoliation from concrete around cracks and that CFS remained non-fractured producing required reinforcing effects.

4. Conclusions

The conclusions obtained in this study are described below.

(1) No definite difference could be seen in the maximum shear stress of the reinforced

concrete column specimens having different size. Therefore, no definite size effect on the shear strength of reinforced concrete column seems to exist if the size of each portion including maximum size of aggregate of concrete is in similar figure.

(2) As same to above, it was shown that there is no influence of size effect on shear strength of reinforced concrete column specimens strengthened with CFS.

(3) Reinforced concrete columns strengthened with CFS without longitudinal bars in web portion and with a low hoop ratio, a possibility of gradual deteriorating in internal concrete was shown during reversed cyclic loading. No such tendency was observed for specimens with a high hoop ratio.

(4) Specimens, for which the amount of CFS was determined to have design CFS strain of 8,000μ and design shear capacity of concrete was neglected, exhibited favorable deformation behavior up to the final stage of loading even for the specimens with a low hoop ratio.

(5) When the amount of CFS is relatively small, no exfoliation between concrete and CFS is likely to occur with the increases of bond stress. Instead, CFS strain increases locally at cracks in concrete and eventually CFS is ruptured. No such tendency was, however, observed for specimens strengthened with adequate thickness of CFS due to the peeling of concrete just beneath the CFS. Thus, peeling of concrete surface bonded with CFS was clarified to be important to obtain the effect of strengthening with CFS in ductile manner.

(6) Monitoring by an infrared camera shows that in reinforced concrete columns strengthened with CFS, delamination of CFS from concrete at cracks as described above extended according to increase of crack width of concrete thus caused no immediate rupture of CFS.

References

1) Koji Osada, Takayuki Inoue, Takahiro Yamaguchi and Shoji Ikeda, Size Effect on Shear Behavior Strengthened with Carbon Fiber Sheets, Proceedings of the Japan Concrete Institute Vol. 21, No. 3, pp. 1411-1416, 1999

2) Z. P. Bazant and E.Becq-Giraudon: Size Effect in Shear Failure of Reinforced Concrete Beams, Proceedings FRAMCOS-3, pp. 2063-2074, October 1998

3) Japan Road Association: Descriptions on the Specifications for Highway Bridges, December 1996

4) Kenichi Sagara and Taketo Uomoto: Detection of Defects of RC Structures Reinforced with Carbon-Fiber Sheet, Proceedings of the Japan Concrete Institute Vol. 18, No. 1, pp. 1203-1208, 1996

SEISMIC RETROFIT METHODS OF CAP BEAM OF TWO COLUMN BENTS

Yukio ADACHI[1], Shigeki UNJOH[2], and Kazuhiro NAGAYA[3]

Abstract

Since the 1995 Hyogo-ken Nanbu earthquake, seismic retrofit works has been intensively carried out for especially bridge columns designed according to pre 1980 design specifications. Next targets for the retrofit of existing bridge piers are wall type piers and two column bents. The seismic retrofit of the two column bents should be made for not only column members but also cap beam members to enhance capacity as well as ductility. In particular, shear capacity enhancement for the cap beams is essentially important. In this paper, easy and reliable, but low cost and labor retrofit methods for the cap beams of the two column bents are discussed. Three series of retrofit methods, partial steel plate adhesion method, carbon fiber jacket method, and steel flat bar jacket method, were studied to make sure their shear enhancement effect by experiments. According to the experimental results of eight specimens, those methods are effective for shear capacity enhancement of reinforced concrete beam. The practical design method for evaluating shear capacity focusing on the effective height and the interval of reinforcements was discussed and proposed.

Introduction

Some of the two column bents of expressway bridges in Kobe urban area suffered shear damage to columns and shear cracks to cap beams due to 1995 Hyogo-ken Nanbu earthquake. The damages were considered to be resulted by the intensive earthquake force in transverse direction. Such damages had not been observed in the recent earthquakes Japan; therefore, the ductility design method for designing two column bents in the transverse direction had been quickly developed and was adopted to the national seismic design specifications in 1996[1]. At the same time, seismic retrofit design methods for two column bents were also developed for the practical design use[2]. The methods described were steel jacket method, concrete jacket method, and external tendon method. Those are well known retrofit methods and the effectiveness of those methods has been proved experimentally in the recent studies. Those methods are very familiar to the engineers in design but not so friendly to field practices for the retrofit in urban area. Because bearings on the top flange of the cap beam of the two column bent make the retrofit work more difficult.

The seismic retrofit of the two column bents should be made for not only columns but also cap beams to enhance flexural capacity as well as shear capacity. In particular, shear capacity enhancement for the cap beam is essentially important because of the following two

[1] Senior Research Engineer, Earthquake Engineering Div., Public Works Research Institute, MOC
[2] Head, Earthquake Engineering Div., Public Works Research Institute, MOC
[3] Research Engineer, Earthquake Engineering Div., Public Works Research Institute, MOC

reasons[3]. The ductility capacity of the cap beams is generally great enough because of very small axial force. The enhancement of the flexural capacity may result in the damage to beam-column joint. However, the bearings on the cap beam make the retrofit works very difficult and the height of the cap beam is generally high in urban area so the retrofit work is not so easy. Furthermore, low cost retrofit methods are also needed when considering the budget problems Therefore, easy and reliable, but low cost and labor seismic retrofit methods for shear capacity enhancement have been demanded.

Based on the mentioned back ground above, joint research project among the Public works research institute, Metropolitan expressway public corporation, and Hanshin expressway public corporation was launched in order to develop easy and reliable, but low cost and labor retrofit methods for the cap beams of the multi column bents and to develop shear enhancement evaluation method. In this project, the effectiveness of the following seismic retrofit methods, partial steel plate adhesion method, carbon fiber jacket method, and steel flat bar jacket method were experimentally evaluated and the design method for each retrofit measures were discussed.

Seismic damage of two column bents due to the 1995 Hyogo-ken Nanbu Earthquake [4]

The number of the seismic damage to two column bents was relatively not so many compared to that of the columns; however the damages themselves were very severe. The most representative damages were shown in Photo 1 and 2. Both photos show the damages to the two column bents of the urban expressway due to intensive in-plane direction seismic force. Photo 1 shows the whole view of the damaged two column bents. The cover concrete of the bottom of the right column spalled off and the spalled area was deeply spread from the ground level to the bottom of the column. The cover concrete of the top of the left column was also spalled off. The shear cracks were found at the cap beam. The damages were considered as flexure dominant damage. Photo 2 shows the typical shear damage found at another two column bent. It was considered that the damages were resulted by the insufficient shear reinforcement. According to the lessons from those damage, the shear capacity enhancement in order to avoid shear failure and the ductility enhancement to make ductile structure are most important for retrofit of existing two column bents.

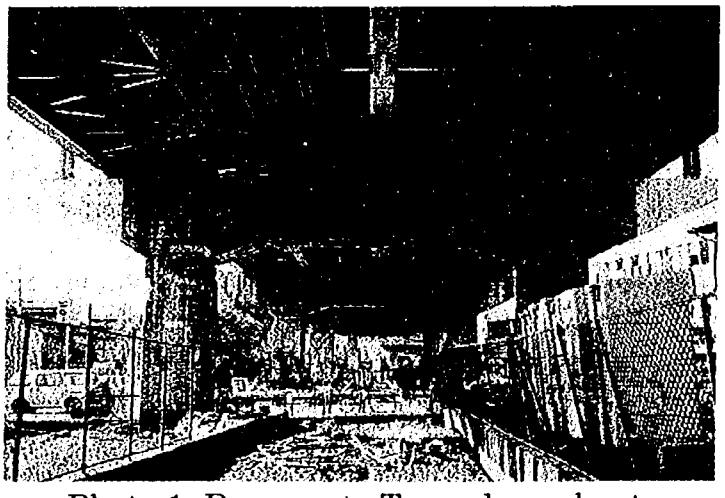


Photo 1. Damage to Two column bent (Hyogo-ken Nanbu Earthquake)

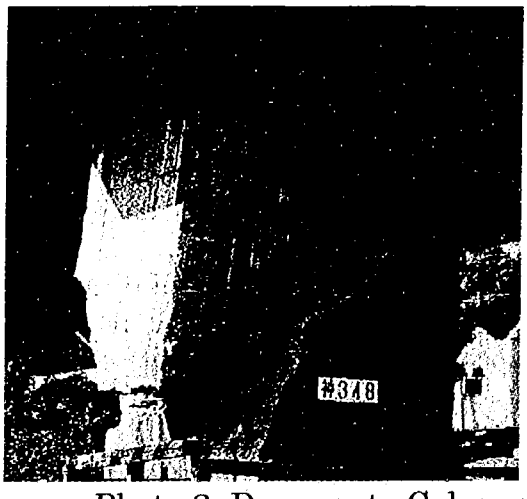


Photo 2. Damage to Column (Hyogo-ken Nanbu Earthquake)

Experiment

(1) Specimen

Figure 1 shows the un-retrofit specimen. The dimension and the steel reinforcement ratio were determined by considering the statistical result of the cap beams in urban area. The scale factor used for specimen design was chosen for 1/4. The dimensions of the cross section of the specimens were determined as 600×600 mm, the length from the loading point to the bottom of the specimen was 1,500mm. Therefore, shear san ratio was 2.5. 26 of deformed steel bars (SD295A) that had yield strength of 377N/mm^2 and the diameter of 22mm were employed for longitudinal reinforcements. The deformed steel bars (SD295A) that had yield strength of 365N/mm^2 and the diameter of 6mm were used for stirrups and the interval length was 500mm. The amount of the stirrups was very small in order to make shear failure dominant specimens. The experiment of this un-retrofit specimen was referred as Case0.[5]

Table 2 shows the retrofit methods to strengthen the shear capacity of Case0 specimen. Three series of retrofit techniques were experimentally evaluated in this study. The methods are partial steel plate adhesion method, carbon fiber jacket method, and steel flat bar jacket method. Case1 to Case4 are the cases for evaluating partial steel plate adhesion method. The popular method for widening seat width in Japan was to install steel fabricated seat width extension structure to the web of the cap beam. In this case, thick steel plate was anchored to the web so the

Table 1. Material Strength

			Case0	Case1	Case2	Case3	Case4	Case5	Case6	Case7	Case8
Concrete		(N/mm^2)	23.4	25.5	24.9	27.4	28.8	25	26.1	23.9	26.3
Longitudinal Bar (D13	Yield	(N/mm^2)	379	365							
Transverse Bar (D9)	Yield	(N/mm^2)	369	377							
Retrofit Member	Yield	(N/mm^2)	-	179	178	176	321	2,730*	320	324	321

*: Rapture Stress

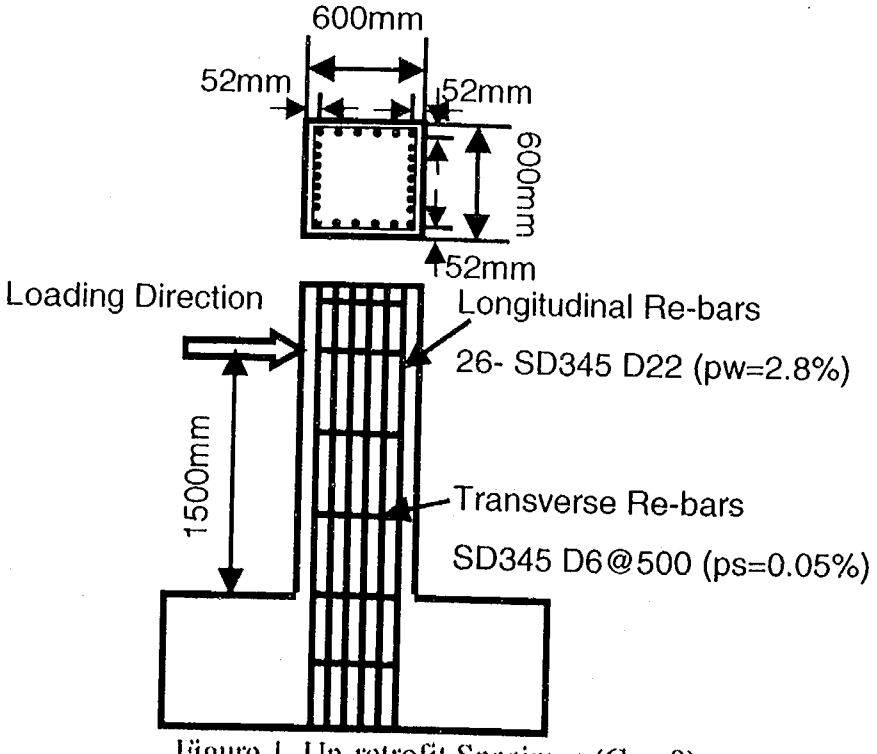
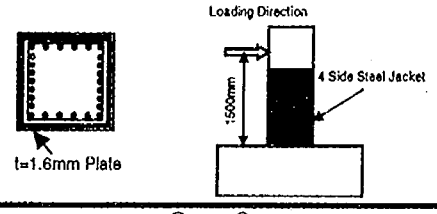
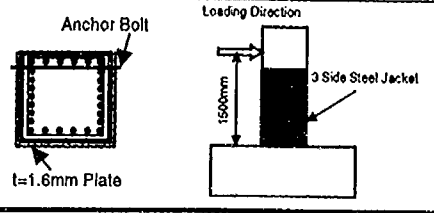
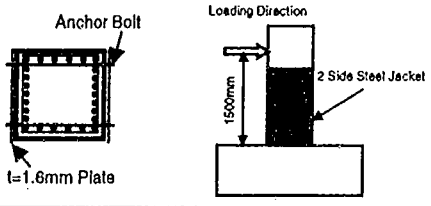
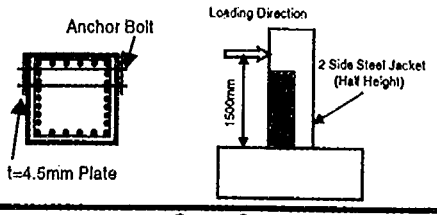
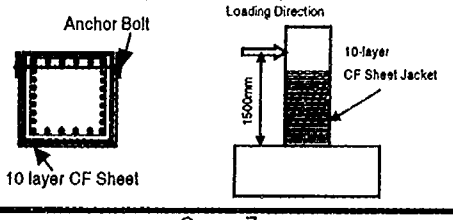
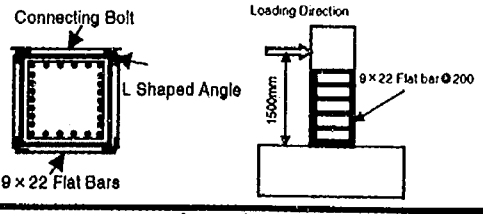
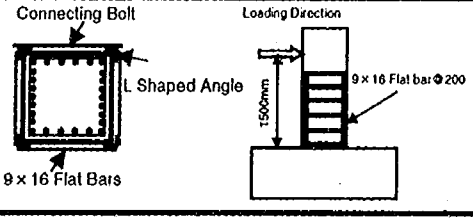
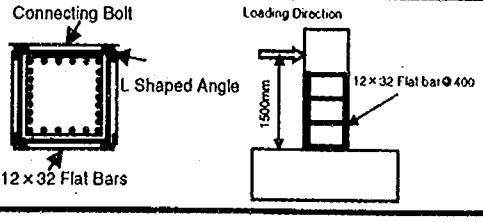


Figure 1. Un-retrofit Specimen (Case0)

anchored steel plate may strengthen the shear capacity of the beam. In order to make sure of this effect, this series of experiments were conducted.

As for Case1, SPCC steel plate was jacketed on the four side of the specimen. This was the reference specimen to recognize the reference retrofit effect and to obtain the force and displacement relationship. The thickness of the plate was 1.6mm and the yield strength of the plate was 179N/mm^2. The 10 mm gap between the plate and the concrete surface was grouted by shrinkage compensation mortar. As for Case2, the same thickness and strength SPCC steel plate was used for jacketing on 3 side of the specimen. Six in a row of M-16 bolts anchored the both side edge of the retrofit plate. The length from the edge to the bolts was 7.5cm. As for Case3, almost the same plate was used and jacketed on the both side of the specimen. And the both edge of the plate was anchored by bolts. The length between the two rows of the bolts was 45cm. As for the Case4, SS400 steel plate was used. The yield strength of this plate was 321N/mm^2. The plate was anchored by bolts like Case3. The length between the bolts was 15cm that was the 1/3 of that of the Case3. Therefore the plate with the thickness of 4.5mm was employed. If the truss analogy were applied for calculating the shear capacity, the amount of shear capacity

Table 2. Retrofit Method for Shear Enhancement of the Beam

Case 1	Case 2
4 Side Steel Jacket	3 Side Steel Jacket + Anchor Bolts
	
Case 3	**Case 4**
2 Side Steel Jacket + Anchor Bolts	2 Side Steel Jacket (Half Height) + Anchor Bolts
	
Case 5	**Case 6**
4 Side Steel Jacket	4 Side Flat Bar Jacket + L Shaped Angle
	
Case 7	**Case 8**
4 Side Flat Bar Jacket + L Shaped Angle	4 Side Flat Bar Jacket + L Shaped Angle
	

enhancement would be almost the same among four specimens described above.

The next method investigated was carbon fiber (CF) sheet jacket. In this case, the effectiveness of the three side jacketing techniques was experimentally studied. The peering of the edge of the CF sheet may have resulted in the loss of the strength so the anchor plate was used for firm bond between the sheet and the concrete. The 10 layers of the CF sheet were rapped up to the specimen. The number of the CF layer was determined by considering the effective tensile strain of the CF sheet that was limited to 3000μ. The effective height was assumed the length between the edge of the specimen and the anchor bolt for the sheet.

The last method investigated was steel flat bar jacket method. Case 6-8 were the experiment for the effectiveness of the externally installment of steel shear enhancement using steel flat bars. L shaped steel plate was placed on the four corners, and steel flat bars were welded to the L shaped steel plate on the three sides of the specimen and bolt connection was used to connect on the top flange side. For the field practice, the "cage" can fabricate in steel fabrication works. Therefore, only light field work will be needed. The amount of the steel reinforcement ratio of Case 6 and Case 8 were the same as that of Case 1. As for Case 6, 9×22 mm flat bar was used and the interval of each flat bars was determined to 200mm that was 1/3 of the section height of the specimen. As for Case 8, 12×32 mm flat bars that has twice the area of 9×22mm flat bar. The interval of each flat bars, however, was increased to twice. That was 2/3 of the section height. The amount of steel reinforcement ratio of Case 7 was the half of that of Case 6. The interval was set to 200mm and the size of the flat bar used was 9×22mm.

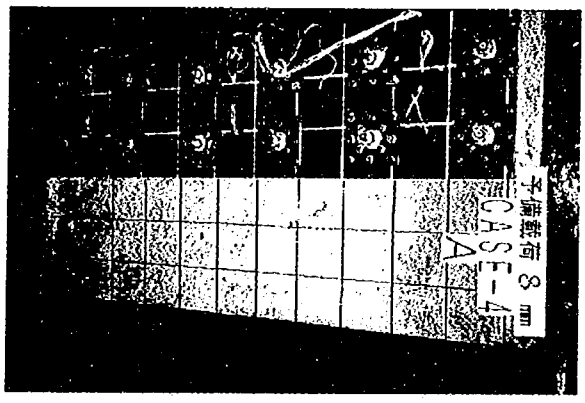


Photo 1. Partial Steel Plate Adhesion Method (Case 4)

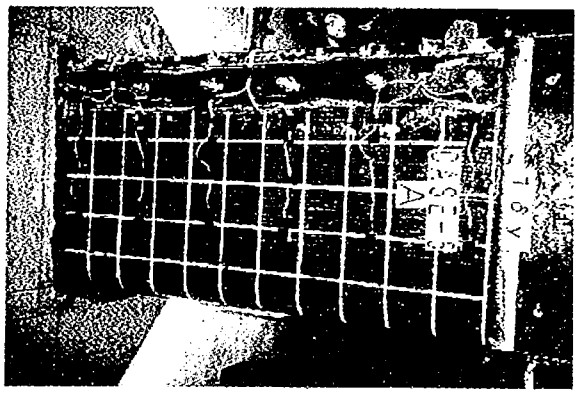


Photo 2. CF Sheet Jacket Method on 3 Sides (Case 5)

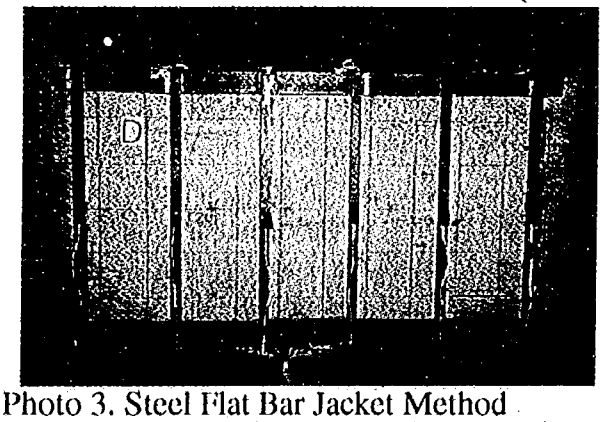


Photo 3. Steel Flat Bar Jacket Method (Case 6)

(2) Experiment procedure

The purpose of these experiments was to focus on shear enhancement effectiveness of each retrofit method. Generally, monotonic loading method was taken for evaluating shear capacity. But in this case, cyclic loading method was taken for evaluating shear capacity under reversal loading like earthquakes. The yield displacement that was defined as the displacement where the measured strain of the steel reinforcement of tension side experienced yield was taken as unit loading displacement. At the first loading, three cycles of loading was taken for 1 δ y loading step. Following loading steps, 2,$\cdots$,n δ y Loading steps, were taken similarly like 1 δ y Loading. As for Case 0, one cycle of loading was made until shear failure occurred by increasing loading displacement.

No axial force was applied because this was considered beam experiment.

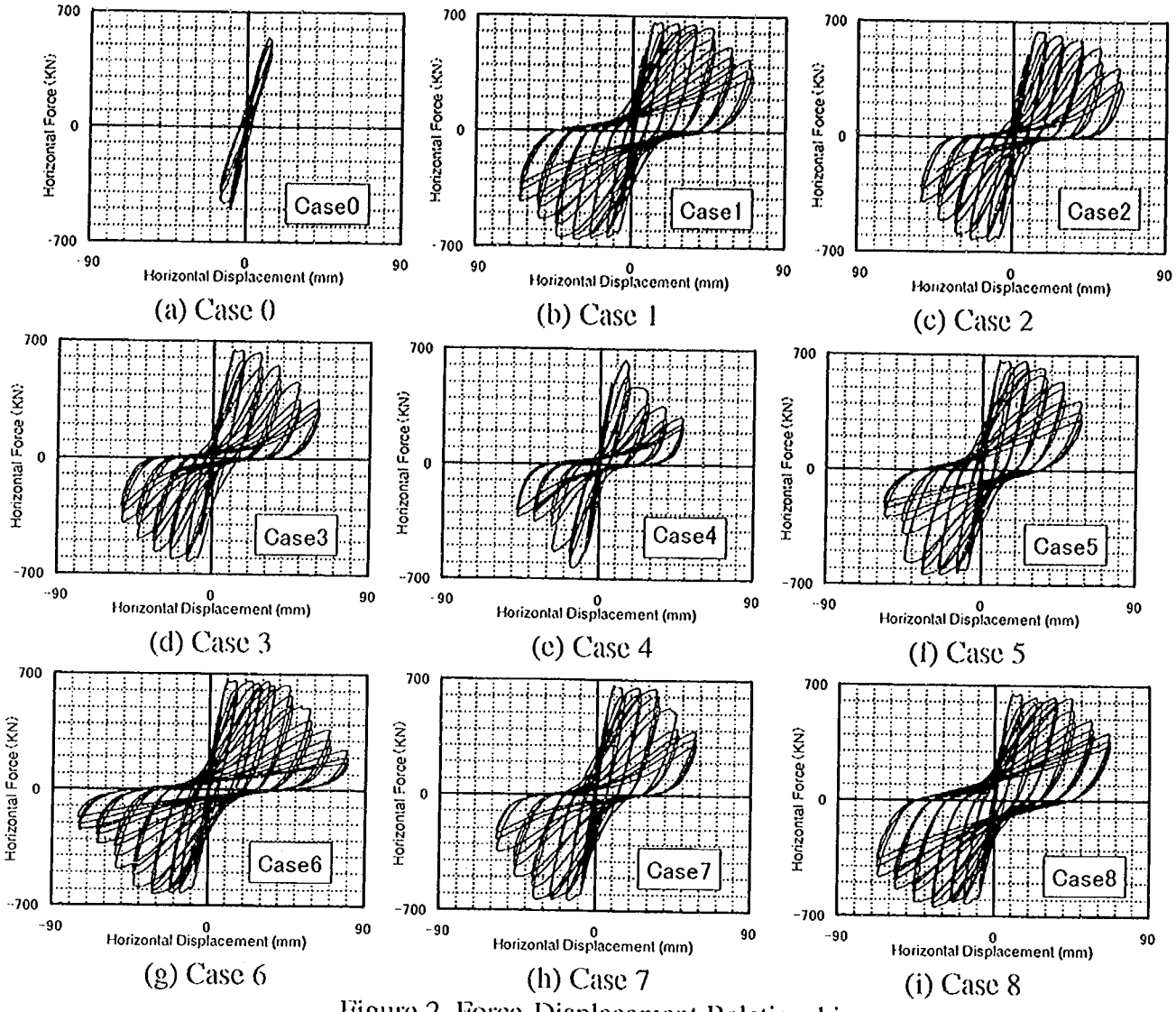
Experimental Results

(1) Force-displacement relationship and failure mode

The force-displacement relationship of each case was shown in Figure 2. As for Case 0 that was considered as the as-built specimen, shear cracks were found at the 0.7 δ y loading, then the specimen was experienced the yield but was broken by shear at the 1.5 δ y loading. The sudden drop of force-displacement envelope was found at the 1.5 δ y loading from Figure 2.(a).

As for Case 1 that was steel-jacketed on 4 sides, flexural cracks were found at the bottom of the specimen at the 2 δ y loading and the jacketed plate was slightly deformed. The deformation of the plate was progressed as the loading increased. At the 5 δ y loading, the horizontal restoring force was gradually decreased as the number of loading was increased. This drop was considered by flexure failure. According to the test result of Case1, it was observed that steel jacket method was effective for shear capacity enhancement. As for Case 2 that was steel jacketed on 3 side of the specimen, similar damage progress as that of Case 1 was observed. At the 4 δ y loading, the horizontal restoring force was gradually decreased. The longitudinal reinforcements of the no-jacketed side buckled at the 4 δ y loading and the side split failure was observed. Finally, the specimen was lost its strength by side split failure. As for Case3 that had two plates put on the both sides of the specimen and mechanically anchored by bolts to the specimen, side split failure was observed at the ultimate state like Case 2. However, steel jacket on 3 or 2 sides was effective for shear capacity enhancement until side split failure occurred. As for Case 4, the retrofit method was almost the same as that of Case 3. The different retrofit point was that the strengthened plate was three times thicker than that of Case 3 because the length between the two rows of the anchor bolts was one third of that of Case 3. The total length of the plate for height direction was half of that of Case 3. This specimen experienced the yield of the rebars so this retrofit method was effective for shear enhancement. However, at the 2 δ y loading, diagonal crack was observed at the first cycle of loading and the specimen was failed in shear. If the truss analogy could be applied to the Case 3 and 4, the effectiveness of shear capacity enhancement would have been the same. However, the same shear capacity enhancement effect was not obtained.

As for Case 5 that was jacketed by CF sheet on 3 sides, almost the same force-displacement behavior was observed and the specimen was broken by side split failure like



(a) Case 0 (b) Case 1 (c) Case 2

(d) Case 3 (e) Case 4 (f) Case 5

(g) Case 6 (h) Case 7 (i) Case 8

Figure 2. Force-Displacement Relationship

Case 2.

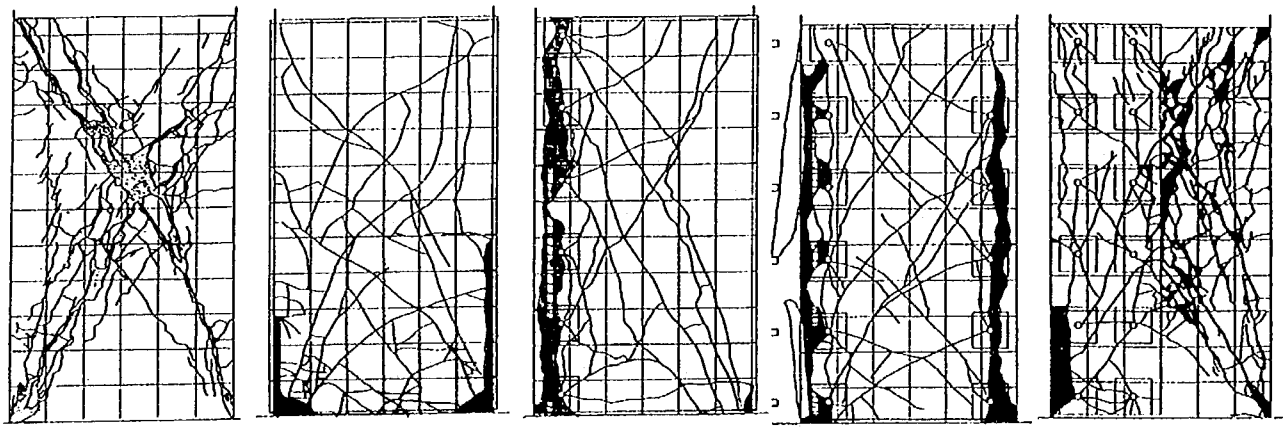
As for Case 6 that was jacketed by steel flat bars, almost the same force-displacement was observed like Case 1 so shear capacity enhancement effect was almost the same as steel plate jacket method on 4 sides. Minor shear cracks were found at the 3 δ y loading but those cracks did not grow so much. Finally, the specimen was lost its strength by flexure at the 5 δ y loading like Case 1. The same force-displacement behavior was found for Case 8. Minor shear cracks were found at the 2 δ y loading so the occurrence of shear cracks was relatively earlier but those cracks were not propagated so large like Case 6. As for Case 7 that was jacketed by steel flat bars but the amount of the reinforcement was half of that of Case 6, the specimen was lost its strength at the 3 δ y loading. The shear cracks were found at 2 δ y loading and those cracks were propagated as the number of loading was increased. Therefore, it was considered that the shear failure was dominated.

According to the experimental results described above, the shear enhancement effect was observed for any retrofit case. The amount of the shear strength enhancement of each case would have been almost the same except Case 7 only if the truss analogy could be applied. But

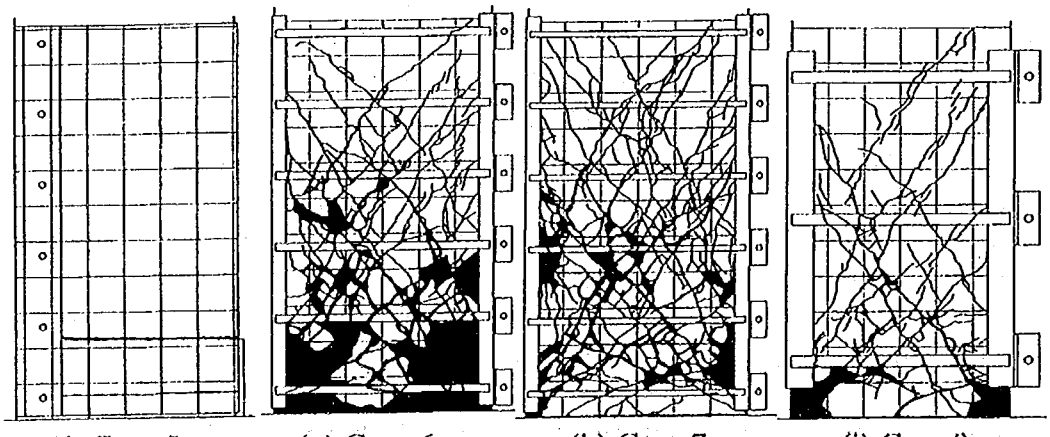
the shear enhancement effect of Case4 was apparently smaller than that of any other case.

(2) Failure mode

Figure 3 shows the sketch of the each specimen at the end of the experiment. The crack sketch was made after removal of the retrofit plates so the damage of the core concrete was shown. The Case1 specimen was broken by flexure but diagonal cracks were observed after removing of the retrofit plate. But the width of each crack was very small so the interlocking effect of coarse aggregates was considered not to be lost. The Case2 specimen was resulted in side split failure on the uncovered side by the retrofit plate. However, the side split on the covered side was not observed. Only minor diagonal cracks like that of the Case1 was observed at the surface of the surrounded concrete by the anchor bolts and the retrofit plate. This leaded to the conclusion that the shear enhancement effect was effective at the surrounded core concrete. The Case 3 specimen was also failed in side split failure. This case has two uncovered side so that side split failure was found on the both sides. The surrounded core concrete by anchor bolts and the plates on the both sides suffered minor cracks. The same consideration was made for the Case 3. The Case 4 specimen was failed in shear. The major diagonal crack was found and propagated at the uncovered concrete portion. The surrounded core concrete by the bolts and the plates, however, suffered minor cracks. This means the surrounded and un-surrounded core concrete worked differently for shear. Based on the above results, the shear capacity enhancement effect was worked only at the surrounded core concrete by retrofit plates or the anchor bolts. According to the consideration above, the effective height of shear enhancement

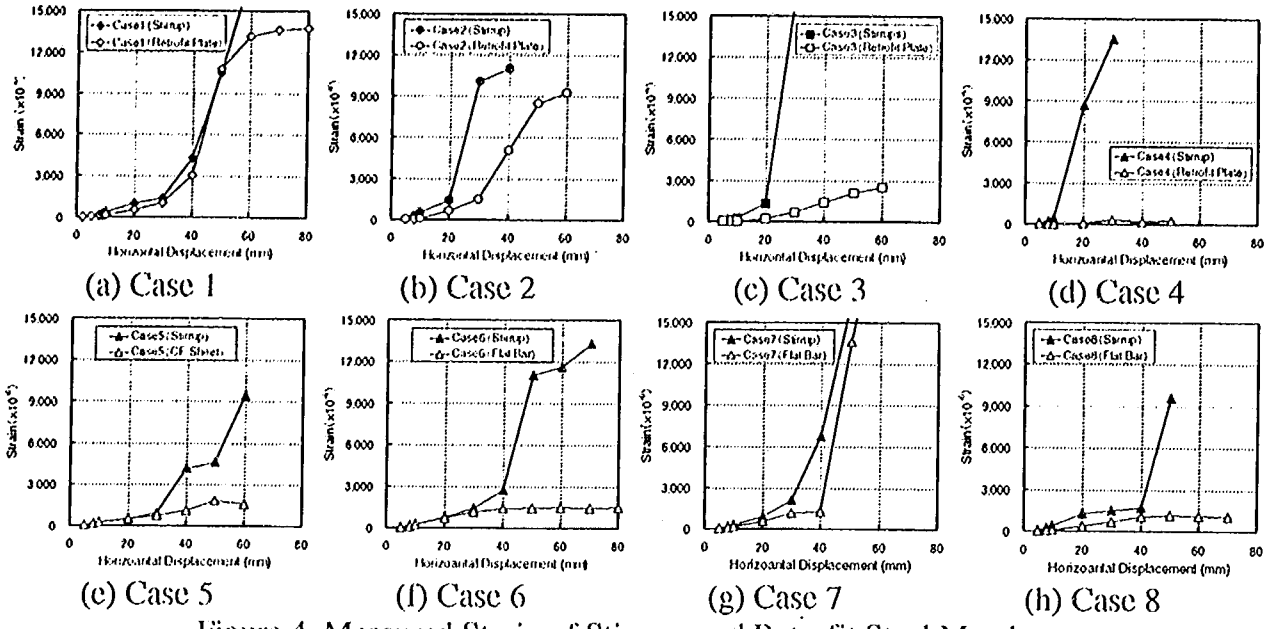


(a) Case 0 (b) Case 1 (c) Case 2 (d) Case 3 (e) Case 4



(f) Case 5 (g) Case 6 (h) Case 7 (i) Case 8

Figure 3. Crack Sketch



(a) Case 1 (b) Case 2 (c) Case 3 (d) Case 4

(e) Case 5 (f) Case 6 (g) Case 7 (h) Case 8

Figure 4. Measured Strain of Stirrups and Retrofit Steel Members

would be the whole height when jacketing steel plate on the 4 sides and the effective height would be the length between the two rows of the anchor bolts when anchoring steel plate on only two sides.

As for Case 5, only flexural cracks were observed on the surface of the concrete.

As for Case 6, 7 and 8, almost the same crack formulation was found. The diagonal cracks were found but the width of the cracks of Case 7 was greater than those of Case 6 and 8. So Case 6 and Case 7 were considered to be failed by flexure and Case 7 was considered to be failed by flexure.

(3) Measured strain of the stirrups and the retrofit plate in shear direction

Figure 4 shows the maximum strain observed at each loading of each case. The strain of the stirrups was measured at 500mm from the bottom of the specimen. The strain of the retrofit plate was measured at the nearest point of the measured stirrups.

As for Case 1, the strain of the retrofit plate and the stirrups increased almost the same manner as the number of the loading increased. This means the stirrups and the retrofit plate worked the same way for shear capacity enhancement. At the 4 δ y loading that corresponds to 40mm loading, the strain of the stirrups experienced the yield, and the strain increased sharply after the 5 δ y loading. According to the experienced strain level, shear damage was also progressed while the flexural damage was progressed. As for Case2, the strain of the stirrups and the retrofit plate increased almost the same way until the 3 δ y loading. The strain of the stirrups increased sharply after 3 δ y loading. The same strain increase was observed for Case 3, but the strain increase after 3 δ y was greater. The big jumps of the strain of the stirrups were considered to be related to the side split failure. The strain level of the retrofit plate observed was greater than that of obtained in Case 2. This means the shear enhancement effect was greater between the two methods. As for Case 4, the specimen was failed in shear at 2 δ y loading and the strain of the stirrups made a big jump at the same time. The strain level of the retrofit plate was very small enough to be neglected. This means the retrofit plate, when anchored at the middle height of the section, had no effect for shear capacity enhancement.

As for Case 5, the strain level of the CF sheet was under 3,000μ that was the almost the same strain level that can be considered in design for shear according to the previous study[6].

As for Case 6, 7 and 8, the measured strain of stirrups and retrofit plate increased the same way until 3-4 δ y loading. As for Case 6 and 8, the retrofit plate had yielded at 4-5 δ y loading but the strain level was almost stable from 3 to 5 δ y loading. This tendency was different from Case 1. As for Case 7, the strain level of stirrups and retrofit plate had great jump at 4 δ y loading where the specimen lost the horizontal resistant force.

(4) Shear resistance

Figure 5 shows the force-displacement envelop of the each loading of each Case and the sheared force resisted by concrete, stirrups, and retrofit plate were also shown in the same figure. The shear resistant force was calculated by the following equations based on the measured strain. The maximum strain used for the calculation was measured at the stirrups and retrofit members that were at 500mm from the bottom of the specimen or retrofit plate. The sudden drop of the envelop of cyclic loading was pointed out by showing "Failure Event" in Figure 5.

$$S_R{}^E = \frac{A_s{}^R \cdot \sigma_s{}^R(\varepsilon_s{}^R) \cdot d_R}{a} \tag{1}$$

$$S_S{}^E = \frac{A_s{}' \cdot \sigma_s{}'(\varepsilon_s{}') \cdot d}{a} \tag{2}$$

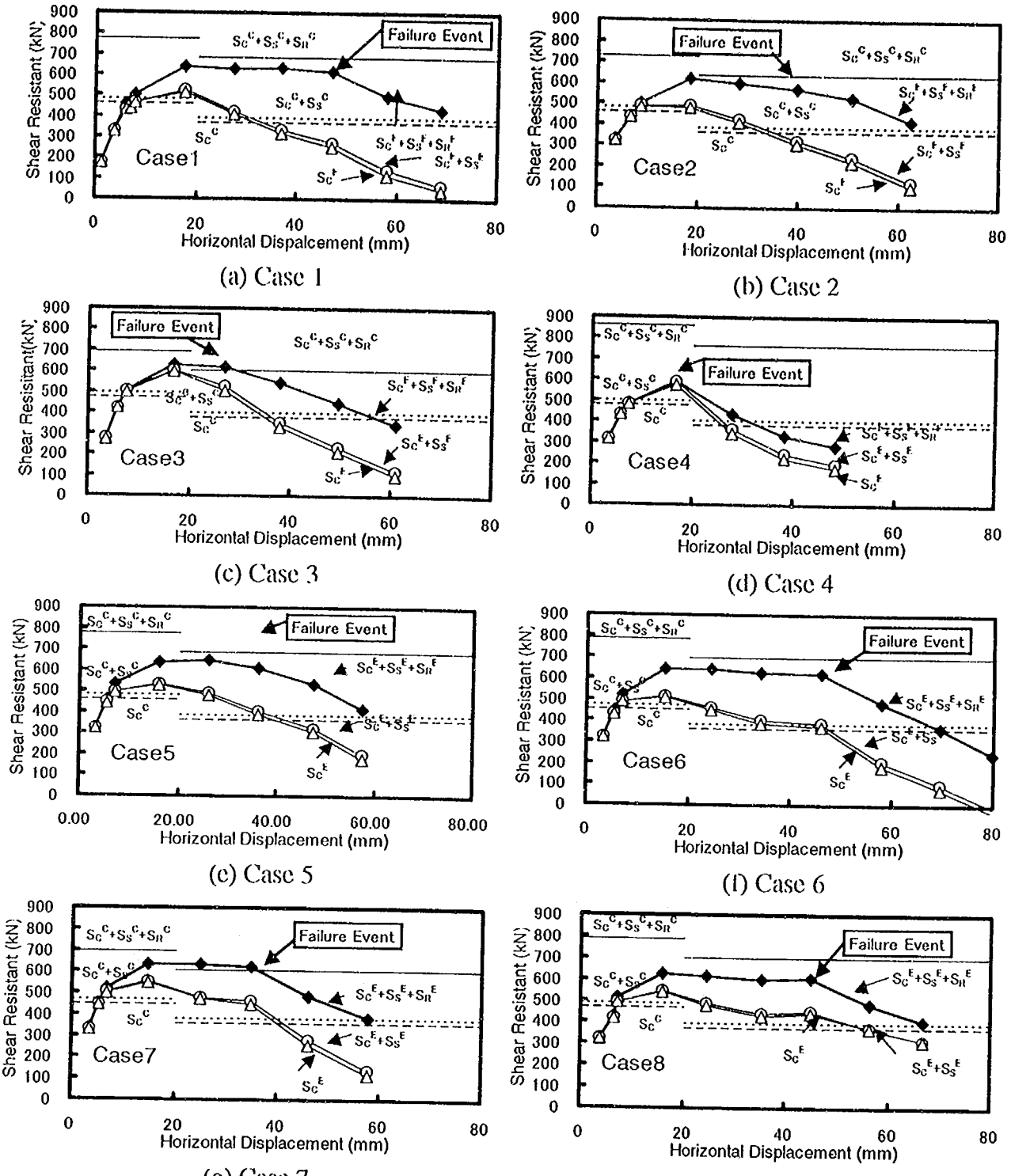
$$S_C{}^E = P - S_S - S_R \tag{3}$$

where, $S_R{}^E$: shear resistant force by the retrofit plate, $S_S{}^E$: shear resistant force by the stirrups, $S_C{}^E$: shear resistant force by the concrete, P : horizontal force, $A_s{}^R$: area of the retrofit plate in unit length " a ", $\sigma_s{}^R(\varepsilon_s{}^R)$: tensile stress in the retrofit plate at the strain of $\varepsilon_s{}^R$, d_R : shear effective height of the retrofit plate (=the length between the two rows of the anchor bolts), $A_s{}'$: the area of the stirrups, $\sigma_s{}'(\varepsilon_s{}')$: tensile stress in the stirrups at the stain of $\varepsilon_s{}'$, d : effective height of the un-rerofit specimen, a : the interval of stirrups

As shown in Figure 5, the shear resistant force carried by concrete was generally decreased as the loading cycle was increased. On the other hand, the shear resistant force carried by the retrofit members was increased. The shear resistant force carried by stirrups was almost stable. The shear resistant force carried by the retrofit plate was decreased from case1 to case 4. According to those results, it was concluded that the retrofit effect by steel plate was greatly depend on the jacket method and the location of the anchor. The same consideration can be made for Case 5-8.

Figure 5 also shows the shear capacity computed from the following equations. The computed shear capacity carried by retrofit plate and stirrups, $S_R{}^C$ and $S_S{}^E$, are calculated assuming the truss analogy. $S_C{}^C$ is assumed as the horizontal force carried by concrete that is calculated by $P - S_S$ using the result of Case 0 at 10mm loading displacement.

$$S_R{}^C = \frac{A_s{}^R \cdot \sigma_s{}^R(\varepsilon_y{}^R) \cdot d_R}{a} \tag{4}$$



(a) Case 1

(b) Case 2

(c) Case 3

(d) Case 4

(e) Case 5

(f) Case 6

(g) Case 7

(h) Case 8

Figure 5. Shear Force Carried by Concrete(S_c), Stirrups(S_s) and Retrofit Members(S_R)

$$S_S{}^C = \frac{A_s{}' \cdot \sigma_s{}'(\varepsilon_y{}') \cdot d}{a} \tag{5}$$

$$S_C{}^C = C_C \cdot \left(\sigma_c|_{Case(n)} / \sigma_c|_{Case0}\right)^{\frac{1}{3}} \cdot S_C{}^E|_{Case0(\delta=10mm)} \tag{6}$$

where, $S_R{}^C$: shear capacity carried by the retrofit member, $S_S{}^C$: shear capacity carried by the stirrups, $S_C{}^C$: shear capacity carried by the concrete, $\varepsilon_y{}^R$: yield strain of retrofit member, $\varepsilon_y{}'$: yield strain of stirrups, $S_C{}^E|_{Case0(\delta=10mm=1\delta y)}$: shear capacity carried by the concrete of the Case 1, $\sigma_c|_{Case(n)}$: concrete strength of Case (n), $\sigma_c|_{Case0}$: concrete strength of Case 0, C_C : modification factor for the effect of cyclic loading (In Figure 5, Cc was assumed 1.0 where $\delta < 2\delta y$, 0.8 where $\delta > 2\delta y$)

Comparing the sum of the shear capacity obtained by eq.(4)-(6) and the sum of the shear force computed by eq.(1)-(3), the failure mode can be judged. The cases except Case 4 and Case7, the computed shear capacity was always beyond the calculated shear force. Those cases were failed by flexure or side split failure so the comparison of the shear capacity and the shear force computed by the above method was effective for shear calculation.

As for Case 7, the shear capacity line and the force line crossed at the 4 δy that corresponded to the displacement where the restoring force began to decrease. This indicates that the accuracy of the shear capacity calculation using eq. (4)-(6) is good enough to estimate shear capacity for practical use. As for Case 4, the shear force carried by the retrofit plate was pretty small compared to the shear capacity computed by assuming the truss analogy. The truss analogy can be applied only when compression and tension cords makes "truss". But the bolt that anchored at the middle height of the concrete section did not have tension cord so it was considered no truss action could be made. Further experiment was needed for shear capacity enhancement effect when the retrofit plate was anchored at the middle height of the RC section.

Retrofit Design for Shear Capacity Enhancement

According to the experimental results, the following shear capacity calculation by retrofit members can be made for partial steel plate adhesion method, CF sheet jacket method, and steel flat bar jacket method.

$$S_R{}^C = \frac{A_s{}^R \cdot \sigma_y{}^R \cdot d_R}{a} \tag{7}$$

where, d_R : effective height

Effective height can be calculated as the whole section height when retrofit member was jacketed the RC section. but the effective height can be calculated as the length between the two rows of mechanical anchor bolts when the retrofit member attached at the both side of the specimen as shown in Figure 6.

a : the interval of retrofit members

The interval of the retrofit steel flat bars shall not be over 2/3 of the section height. The experiment results only covered this range.

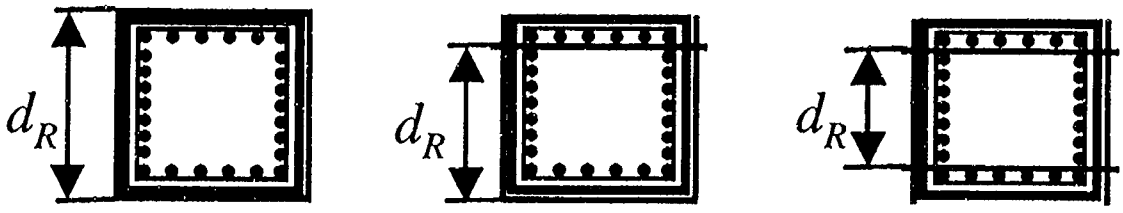


Figure 6. Effective height

The equation in the previous page can only be applied for jacket method. The equation can be applied when the steel plate was anchored at the both edge of the plate and the anchor bolts are placed near the longitudinal rebars. In this case, the effective height should be chosen the length between the two rows of the anchor bolts. But when those bolts are placed at the mid height of the section, shear calculation using eq. (7) over-estimates the capacity.

Conclusion

The shear enhancement effects of different retrofit methods were experimentally evaluated and the evaluation method of the shear enhancement effect for retrofit design was proposed in this paper. The main conclusions obtained in this study were listed as the followings.

a. The steel jacketing method is the good way to enhance shear capacity when proper steel plate used. The whole height of the section for the effective height for shear capacity computation yields the best estimate for shear enhancement effect.
b. Side split failure might be dominant where the stirrups are very few. Therefore, side split failure must be considered in design where the two side or 3 side retrofit method are chosen for shear enhancement.
c. The shear enhancement effect greatly depends on the jacket method and the location of the anchor bolts. The shear enhancement is effective where the RC beam is jacketed or the anchor bolts are installed near the longitudinal reinforcements. No shear enhancement effect was observed where the anchor bolts were installed middle height of the RC beam.
d. The carbon fiber sheet jacket method was would be the good way to enhance shear capacity and effective even though jacketing only on 3 sides of the RC member.
e. The flat bar jacket method is the good way to enhance shear capacity. The truss analogy can be applied to evaluate shear enhancement effect. The enhancement effect was not lost where the interval of installing the flat bars was placed 2/3 of the section height.

References

[1] Japan Road Association: "Japanese Design Specifications for Highway Bridges", December 1996
[2] Shigeki Unjoh, Toru Terayama, Yukio Adachi, Jun-ichi Hoshikuma: "Seismic Retrofit of Existing Highway Bridges in Japan, Cement, Concrete and Composite, (In Press)
[3] Toru Terayama, Shigeki Unjoh, Masuo Kondoh: "Dynamic Capacity and Strength of

Beam-Column Joint of Multi Column Bents", Proceedings of the first symposium of seismic bridge design using ductility design method, Tokyo, January 1998 (In Japanese)

[4] Toru Terayama and Shigeki Unjoh: "Seismic Evaluation and Retrofit of Existing Multi-Column Bents", Proceedings of the third US-Japan workshop on seismic retrofit of bridges, Osaka, December. 1996

[5] Toru Terayama, Shigeki Unjoh, Kazuhiro Nagaya: "Cyclic Loading Test of Reinforce Concrete Beam Retrofit by Carbon Fiber Sheet", Proc. of the 52nd annual meeting of the Japan society of civil engineers, Kobe, September 1998 (In Japanese)

[6] Shigeki Unjoh and Toru Terayama: "Design Methods for Shear Strength of RC members using Carbon Fiber Sheets", Proc of the 14th US-Japan Bridge Engineering Workshop, Pittsburgh, November 1998

APPLICATION OF FIBER REINFORCED POLYMERS (FRP) FOR SEISMIC RETROFIT OF CALIFORNIA BRIDGES.

Thomas E. Sardo, P.E.[1]

Abstract

Recently, Fiber Reinforced Polymers (FRP) have evolved into the mainstream of civil engineering. Although FRPs have been around for some time, these materials have primarily been used in aerospace and defense industries. Concrete, steel, masonry, asphalt, and wood have been the materials that civil engineers have become familiar for building our roads and bridges. When compared to these materials, the properties of FRPs are process dependent and therefore not as reproducible as, say, steel. It is for this reason that not only a standardized testing methodology be established, but also uniform procedures for manufacturing, design and construction for FRPs be established as well. Additionally, it is important for the construction industry to have standardized construction records and procedures.

Introduction

The advancements in the area of FRPs is exciting for the civil engineer when faced with the economic tasks of upgrading and/or seismic retrofitting existing bridges to withstand today's loading. The introduction of FRPs into California has been primarily for the use of seismic retrofitting of bridge columns. However, the use of FRPs is expanding to other applications from rehabilitating corroded and spalling concrete members and strengthening older bridges for current traffic volumes, to designing new members and structures made entirely from FRPs. When strengthening existing members, the low strength-to-weight ratio is advantageous to that of conventional materials. One must also consider the flexibility for a free form design to various geometric shapes and the ease at which they may be applied. FRPs also show great promise when considering existing roadway clearances both vertically and laterally. This becomes an important issue when one realizes the need for adding additional traffic lanes underneath and around existing bridges.

The California Department of Transportation (Caltrans), along with the aid of the Federal Highway Administration (FHWA) and private industry has expended much effort and expense to approve several different FRP casings for the enhancement of bridge columns against seismic attack. With the involvement of the Society for the Advancement of Materials and Process Engineering (SAMPE), Caltrans has been successful at not only developing pre-qualification requirements and standard specifications, but has also been successful at applying FRPs to existing bridges for seismic retrofitting.

Although FRPs have demonstrated themselves successful in many different applications, California's primary use for FRPs is to prevent collapse of bridge structures during a seismic event. Thus, the primary role of FRPs at Caltrans is to strengthen bridge columns to withstand current seismic forces. To date, Caltrans does not allow strengthening

[1]Bridge Engineer, California Department of Transportation, Office of Earthquake Engineering, MS 9, engineering Service Center, 1801 30th St., Sacramento, CA 95816

to other members other than columns using FRPs. However, Caltrans' continual advancements and research in the field of FRP composites will undoubtedly find California's bridges with many other FRP applications. This paper will attempt to summarize where the California Department of Transportation is in the development and implementation of using FRPs, and more importantly, how to simplify the design stage to be competitive with current accepted materials such as steel column casings.

Design Principles

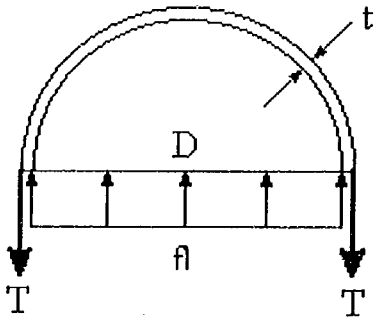
The use of FRPs in lieu of more conventional civil engineering materials (e.g. steel, concrete) has gained recognition for strengthening bridge columns and increasing load carrying capacity. However, to effectively compete with conventional materials in a production-oriented environment, the designer must be comfortable with the design principles and procedures. Furthermore, construction personnel must have an established manual for construction records and procedures to ensure proper installation. The California Department of Transportation has developed standard drawings for some basic bridge column applications for several pre-approved manufacturers of FRPs. Figure 1 shows Caltrans' standard plan for systems 1 and 2, an E-Glass wrap and an epoxy resin-prepreg carbon fiber jacket wrap, respectively. Figures 3 and 4 show a prefabricated vinylester E-glass and a prefabricated polyester E-glasscomposite shell, respectively. Recently, the approval of three more systems has been introduced for the seismic retrofit of California bridge columns. These newly approved systems are shown in Figure 5 and are all epoxy carbon fiber jackets. Nevertheless, if the design deviates from these standard drawings, the designer must have an established set of design criteria that can be followed.

The basic purpose of FRP column casings is to increase the ductility capacity of bridge columns. In addition, the intent is to enhance the shear capacity and increase the lateral confinement of the plastic hinge zone for bridge columns with poor transverse reinforcement details. Currently, Caltrans does not allow the use of FRPs in a potential plastic hinge zone where a lap splice exists, unless a pin or slipping is assumed in the analysis at the lap splice location. With further research and development, it is expected that this restriction will no longer be enforced and that FRP composite casings will be afforded the same opportunities as conventional civil engineering materials. Figure 5 shows the hysteretic behavior of a typical pre-1971 as-built bridge column from testing performed at the University of California, Irvine. As shown from Figure 6, the column wrapped with an FRP composite performed extremely well, increasing the ductility of the column significantly. It can be seen that a displacement ductility of up to10 is achievable. Although high ductility ratios have been attainable, it is Caltrans policy to limit the displacement ductility demand to 6 for circular columns and not more than 3 for rectangular columns. These ductility demand ratios have been reduced to provide a reasonable margin of safety to prohibit buckling and/or fracturing of the longitudinal bars and to limit demands to the connecting members.

Based on laboratory testing (Priestley, Seible et al., 1991), to effectively inhibit a lap splice failure, the radial dilating strain should be limited to 0.001 inside the plastic hinge zone with an associated confining stress of 300 psi (2 MPa). This limitation on the dilating strain has proven to inhibit lap splice failures. However, since current policy does not allow FRP casings to confine a lap splice, the radial dilating strain may be relaxed to a value of

0.004 with an associated confining stress of 300 psi (2 MPa) inside the plastic hinge zone for continuous reinforcement. Outside the plastic hinge zone, the radial dilating strain may be taken as 0.004 with an associated confining stress of 150 psi (1 MPa). As mentioned earlier, to effectively compete with steel column casings, the designer must have clear guidelines for the design of alternative materials. Therefore, the following simplified procedure has been adopted by Caltrans (Caltrans, 1999; Priestley, Seible et al., 1991).

For Equilibrium:



Where: T = hoop stress developed in the FRP casing
t = FRP casing thickness based on the composite dry fiber thickness
D = column diameter
f_l = confining stress developed on the column

From the free body diagram, it can be seen that for a hoop at a given spacing of "s", equilibrium dictates that:

$$\frac{2(T)}{s} = (f_l)(D)$$

Note that for a continuous casing, "s" may be taken as the area of the FRP composite jacket divided by its thickness, t. Furthermore, the hoop stress developed in the jacket, T, may be taken as the area of the jacket, A_j, multiplied by the yield stress of the jacket, f_{yj}. Moreover, since FRP composite materials typically exhibit elastic behavior and the radial dilating strain is limited to the values mentioned earlier, f_{yj} is defined as follows with a given reduction factor of 0.90:

$$f_{yj} = 0.90\,(E_j)\,(\varepsilon_j)$$

E_j and ε_j are the Young's Modulus and the strain of the jacket material, respectively. Upon substitution, it is easily shown that for a column retrofit inside the plastic hinge zone, requiring a confining pressure of 300 psi (2 MPa) with a limiting dilating strain of 0.004, as noted above, the required thickness is

$$t = \frac{4.17\text{x}10^{-4}\,(D)}{E_j} \quad \text{(inside the plastic hinge zone).}$$

It may also be shown that for a column retrofit outside the plastic hinge zone, the required thickness, with an appropriate transition, is shown to be

$$t = \frac{2.08 \times 10^{-4} (D)}{E_j} \quad \text{(outside the plastic hinge zone).}$$

As can be seen from Figures 1 – 4, an appropriate length to transition the number of required layers from inside the plastic hinge zone to outside the plastic hinge zone need not be taken greater than the column diameter, D. Therefore, the designer only needs the Young's Modulus for the system under consideration and the dry fiber thickness to calculate the required number of layers of FRP composite. This makes the analysis and application of FRP composites to seismic retrofit projects a very attractive and simple procedure for design engineers.

Applications

The advancements made in FRPs have been significant in civil engineering structures. Although California's primary goal is to apply FRPs to bridge columns, Caltrans is also attempting to apply FRPs to new bridges. The Kings Storm Water Channel bridge in Southern California is but one instance where FRPs may be applied to portions of a bridge using carbon shells.

As mentioned previously, there are several systems approved for the seismic retrofit of bridge columns. These systems have seen limited use throughout California. A brief description of some of these applications follows.

- Santa Monica Viaduct – Demonstration Project. This was a demonstration project, on the Santa Monica Viaduct in Southern California, in which 6 of the different approved manufacturers demonstrated the application of their products to bridge columns in the field.

- Route 2/5 Separation (Griffith Park). This structure was constructed in 1961 and is a continuous concrete box girder bridge located in Los Angeles, California. It has 11 spans and is 361 ft. (110 m) in length. The system applied was an epoxy E-glass system (by Hexcel-Fyfe) with both a passive and an active wrap. Two of the column jackets failed approximately one year after installation. It is important to note that the active wrap is no longer used as a viable system and that the two columns were repaired with a passive wrap. The bridge has seen moderate shaking during the 1994 Northridge Earthquake without any reports of damage.

- San Elijo Lagoon UC (R/L). This structure was constructed in 1963 and is a continuous concrete box girder bridge located in San Diego, California. It has 4 spans and is 104 ft. (31.7 m) in length. The system was applied by machine winding an epoxy resin-prepreg

carbon fiber (by XXSys) to the columns. This project was not without its own problems initially, but was later resolved by the end of the project.

- Arroyo Quemado. This structure was constructed in 1917 and is a multiple concrete arch bridge located in Santa Barbara, California on Route 101 and is approximately 341 ft. (103.9 m) in length. The spandrels were wrapped with epoxy E-glass fiber (by Hexcel-Fyfe).

- Arroyo Seco. This structure was constructed in 1953 and is a multiple concrete arch bridge located in Pasadena, California on Route 134. The spandrels were retrofitted with an epoxy resin-prepreg carbon fiber (by XXSys). This particular installation did have some problems in which the epoxy did not impregnate into the fibers consistently, fully, or adequately. However, further explanation is beyond the scope of this paper. Presently, the system is being removed and will soon be awarded to another pre-approved manufacturer for repair.

- Yolo Causeway. These structures were constructed in 1963 and are precast prestressed inverted "W" and "U" Girders founded on pile extensions located in Sacramento, California on Interstate 80. The former being 2880 ft. (878 m) in length while the latter is 8800 ft. (2682 m) in length. Whereas the other bridges were designated as sole source contracts, this particular job was awarded to CMI under a competitive bid contract. The system used for seismic retrofitting the numerous pile extensions was the prefabricated polyester E-glass jacket. CMI was the successful low bidder for the contract, under bidding other pre-approved FRP systems, as well as steel casings. The ease and speed at which the casings were applied proved that FRPs could be an economical alternative to conventional materials.

Conclusion

The design procedure adopted by Caltrans for determining the required FRP thickness is a simple one that will further encourage the production-oriented design engineer to utilize this relatively new material for civil engineering applications. With lessons learned from each field application, bridge engineers will become increasingly confident in using these materials. The use of FRPs for the seismic retrofitting of California's bridges has been tested successfully in labs and has been tested in moderate earthquakes in the field. The greatest challenge that awaits FRPs applied to California's bridges is the next Maximum Credible Earthquake. The use of FRP composites is worldwide and may prove to be an economical alternative to the accepted conventional materials for the 21st century.

References

Priestley, N., Seible, F. et al., "Seismic Assessment and Retrofit of Bridges", SSRP - 91/03, Structural Systems Research, University of California, San Diego, 1991.

California Department of Transportation, Caltrans Memo To Designers 20-4, April, 1999.

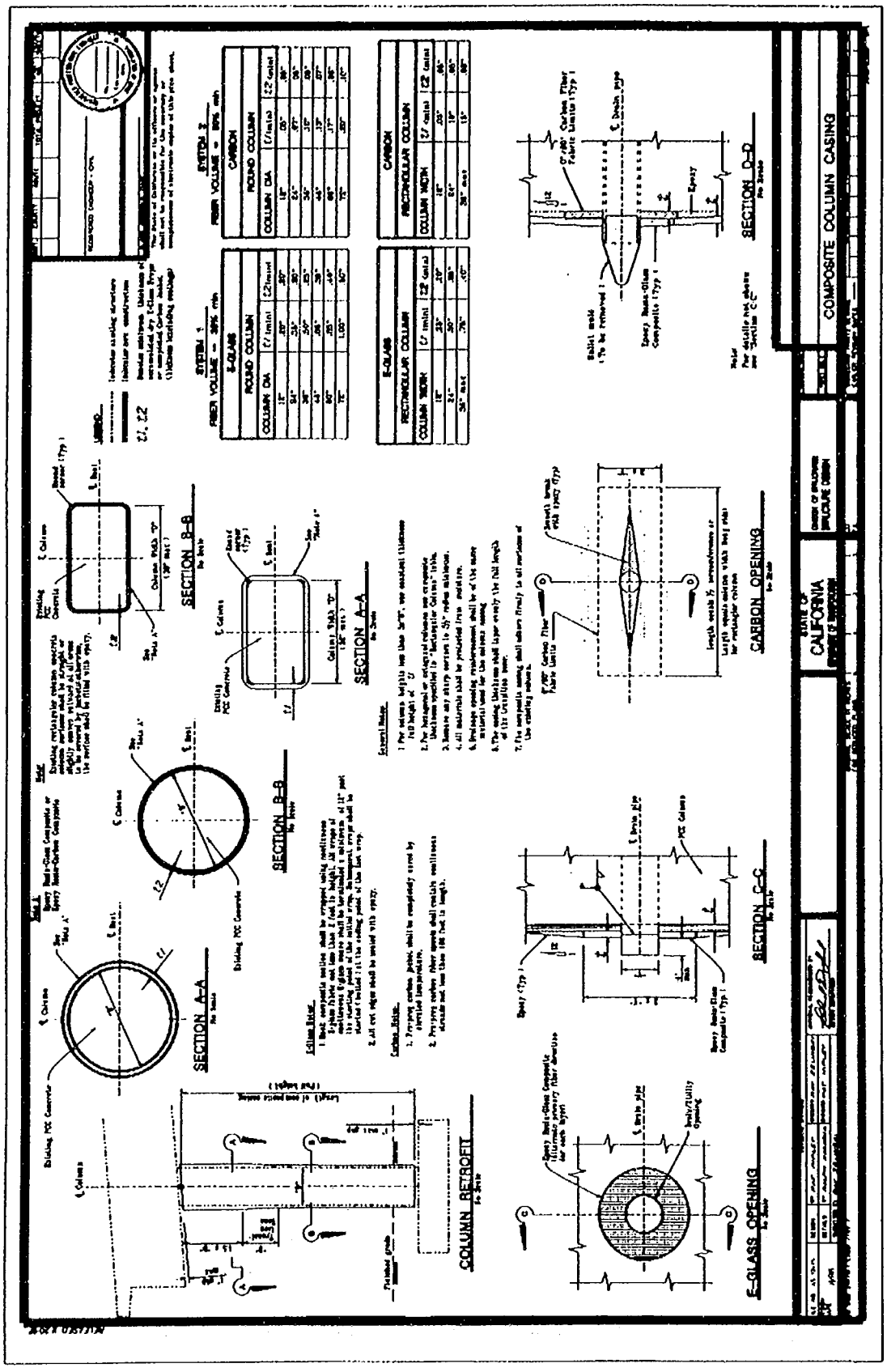


Figure 1. Systems 1 and 2 (Fyfe and Hexcel Corp., XXSys Technologies, Inc.)

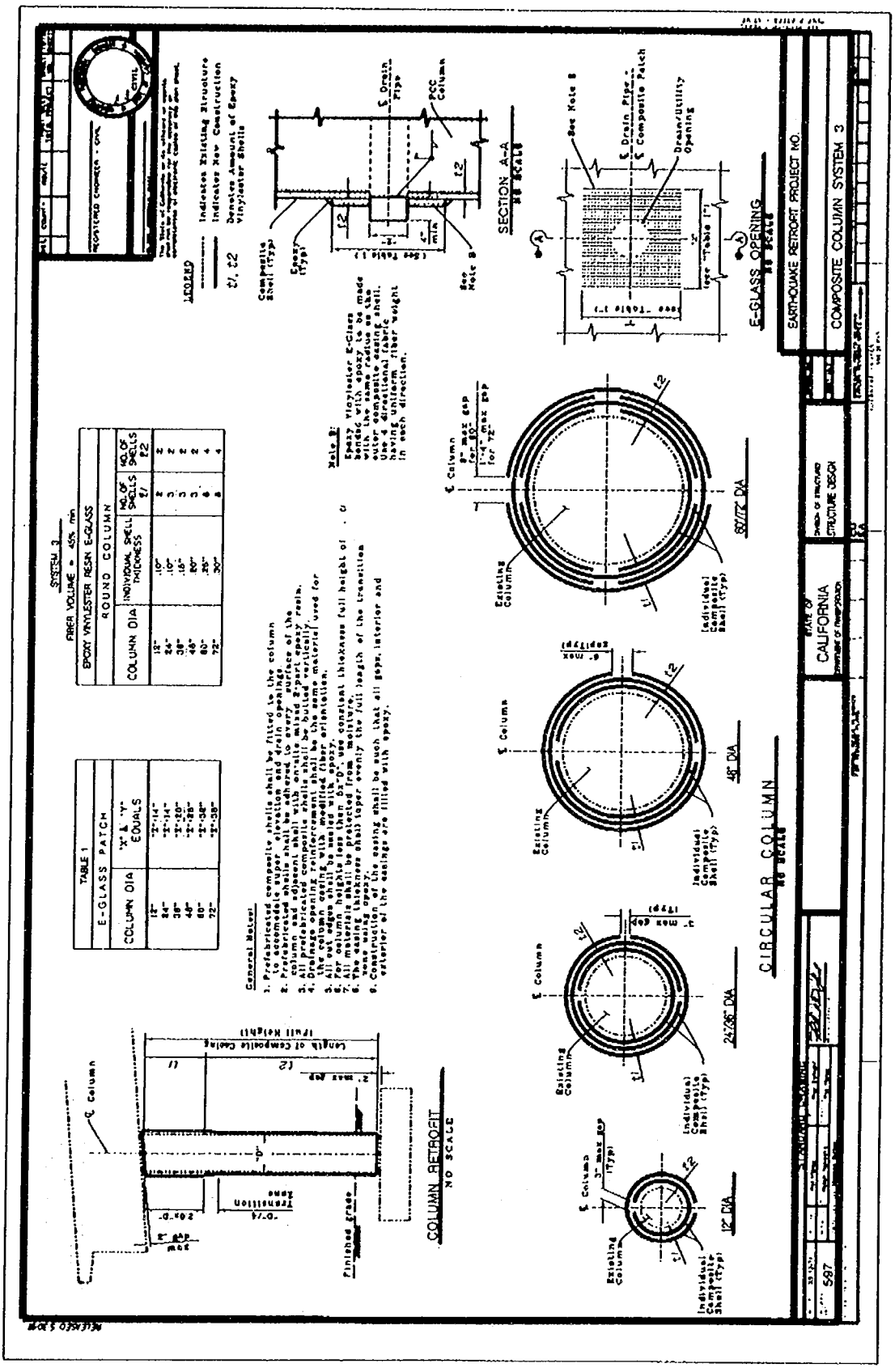


Figure 2. System 3 (Hardcore Composites, Ltd.)

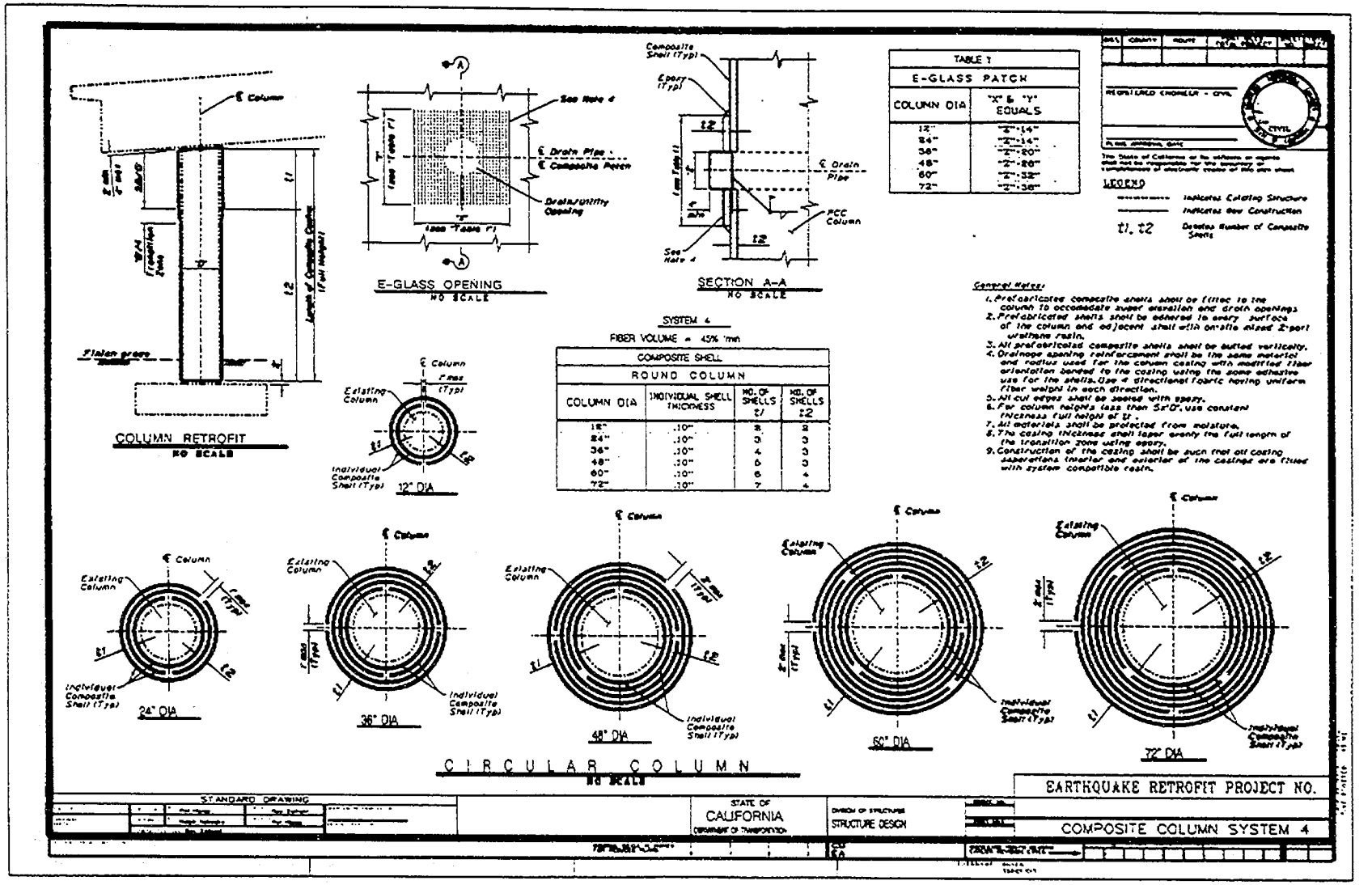


Figure 3. System 4 (CMI, Inc. – "SnapTite")

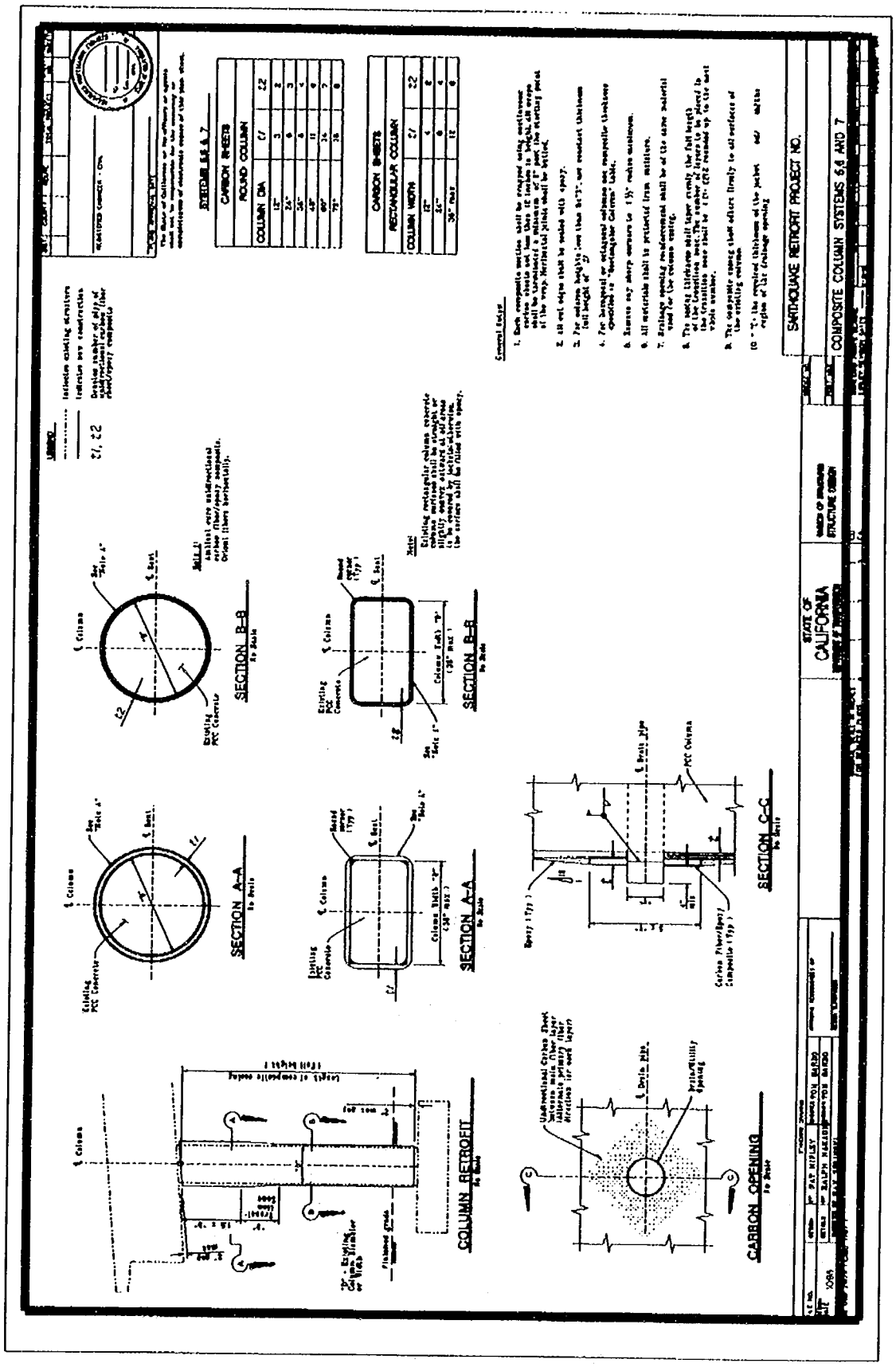


Figure 4. Systems 5, 6, and 7 (Mitsubishi Toray/ Replark, Master Builder MBRACE)

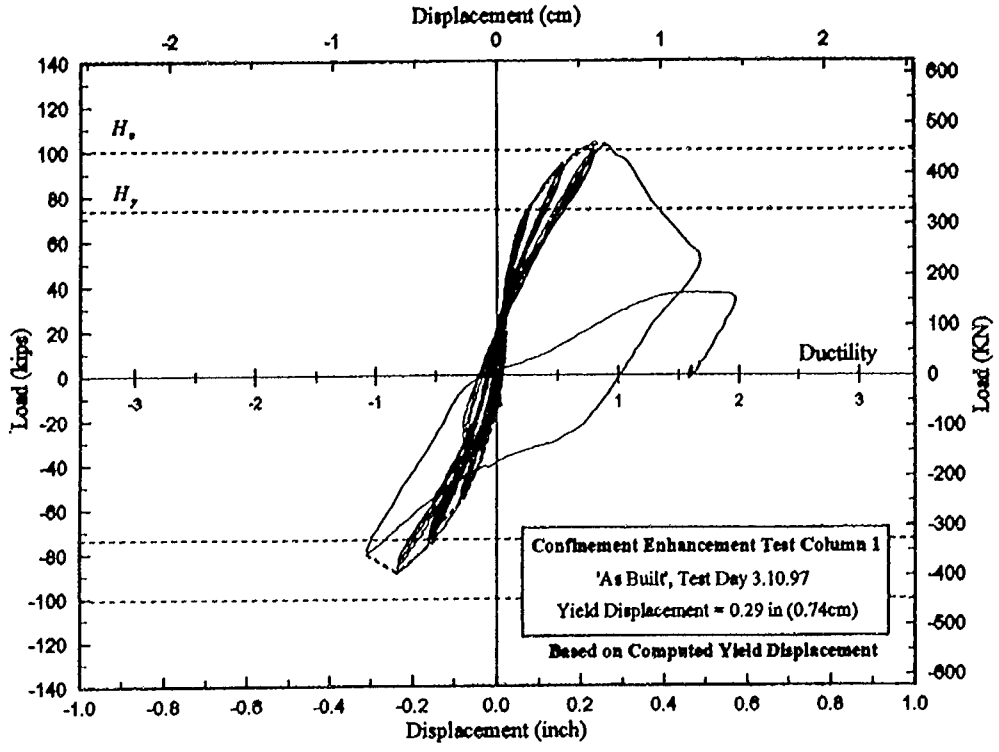


Figure 5. Pre-1971 As-Built Column Test Results

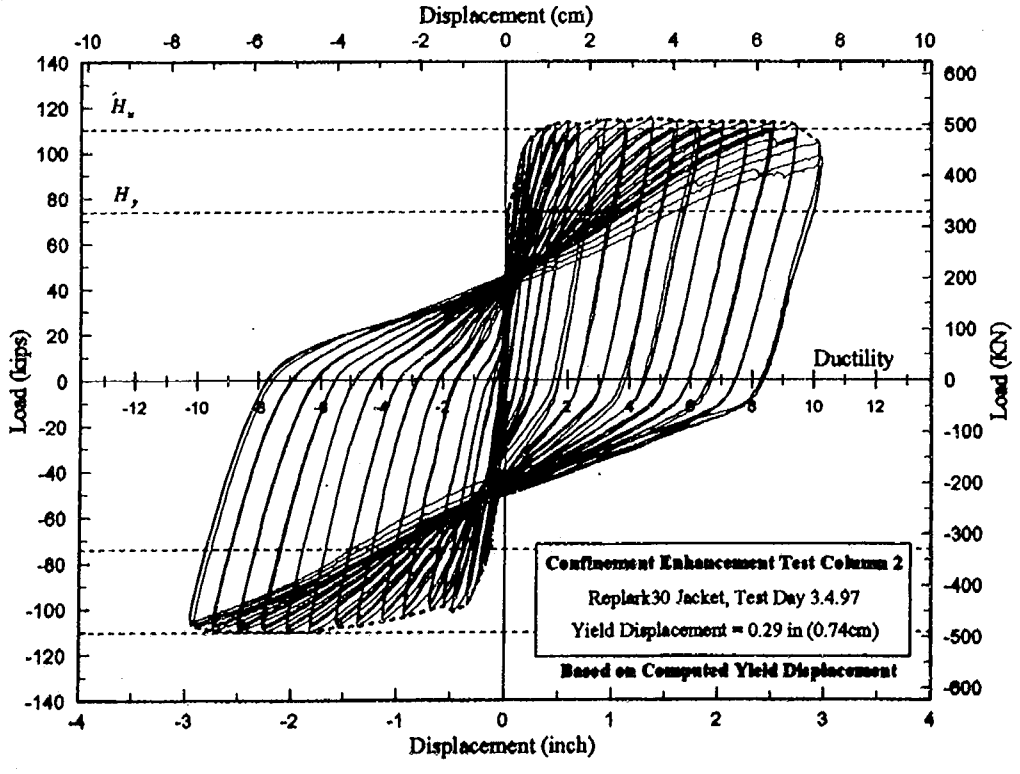


Figure 6. Retrofit of Pre-1971 As-Built Column Test Results

Metric Conversion Table:

English Units	SI Units
1 ft.	0.3048 m
1 in.	25.4 mm
1 lbm	0.45359 kg
1 psi	6894.8 Pa

SEISMIC BEHAVIOR OF CIRCULAR HOLLOW COLUMNS WITHOUT INSIDE REINFORCEMENT

Jun-ichi Hoshikuma[1] and M. J. Nigel Priestley[2]

1 Senior Research Engineer, Earthquake Engineering Division, Public Works Research Institute, Ministry of Construction

2 Professor, Division of Structural Engineering, University of California, San Diego

Abstract

The behavior of two flexure-dominant circular hollow reinforced concrete columns, with different longitudinal reinforcement ratios, under cyclic loading is investigated through a discussion of experimental studies. Test results showed that the columns were significantly failed when the inside concrete was crushed. It was also found that confinement-induced transverse strain at the plastic hinge region did not reach the yield strain before failure. These facts suggest that the limited lateral pressure is induced in the concrete shell and thus the inside face concrete is subjected to poor confinement even though sufficient transverse reinforcement is placed near the outside face of the hollow columns. Moment-curvature analyses were carried out for the test units, to evaluate the lateral force-displacement response. The stress-strain curve of the confined concrete was calculated with an assumption that the maximum effective lateral pressure occurred when the spiral strain reached a maximum useful confinement-induced strain of 0.001. As a result, the theoretical force-displacement relation showed a good agreement with the experimental response.

1. INTRODUCTION

A hollow concrete section has been often used for column design, particularly for very tall bridge columns in seismic areas including California, New Zealand, Japan and Italy et al., for reducing the mass and therefore minimizing the self-weight contribution to the inertial mode of vibration during an earthquake. The hollow columns also enable to reduce foundation dimensions and thus save the construction cost substantially. Therefore, these advantages have promoted the hollow columns instead of similar solid members. On the other hand, the seismic behavior of the hollow columns has been controversial due to a lack of understanding[1),2),3),4)].

The effect of the hollow section should be adequately assessed in the seismic design, because the structural response of the hollow column under seismic loading may be significantly different from that of solid column due to existence of a void section. However, there are several unknown areas which must be understood, that is, assessment of ductility capacity and shear strength, retrofit measures et al.

The research described in this report deals with the flexural ductility capacity of the hollow circular columns with one layer of longitudinal and transverse reinforcement placed

near the outside face of the section. In the circular hollow section, the spiral confinement-induced stress applies a radial pressure to the outside face of the core of the concrete wall and develops a circumferential compression stress, indicating that the concrete wall is subjected to biaxial compression. Judging from a simplified interaction diagram relating the confined strength ratio to the two orthogonal lateral confining stresses presented by Mander et al.[5], the confinement effect in the hollow section is significantly less than in the solid section which is subjected to triaxial compression. Such less confinement may cause the premature crush of the inside face concrete, even though sufficient transverse reinforcement is placed near the outside face of the hollow section.

In order to investigate the inelastic behavior of the hollow circular columns, cyclic loading tests were conducted for two large-scaled flexural columns with different longitudinal reinforcement ratios. Furthermore, the moment-curvature analyses were carried out for the test units. An analytical model was discussed for consideration of confinement loss due to existence of the void section. Analytical results were compared with the experimental response in terms of the strain and the lateral force-displacement relation.

2. DETAILS OF LOADING TESTS

2.1 Test Unit Dimensions

Two hollow circular columns with different longitudinal reinforcement ratio, called herein HF1 and HF2, were constructed and tested in this research. Dimensions of the columns are shown in Fig. 1. Since geometry of the section in actual hollow bridge columns constructed or planned by Caltrans is modeled as realistic as possible, and also prototypes are typically 3-6m diameter or sometimes more with longitudinal reinforcement of #18 bars, the scale ratio was targeted to 1:4 in this test program, which the scale effects would be minimal. It should be noted that the test unit below mid-height section was constructed by reinforced concrete with hollow section and a loading steel tube was connected to the column top for the extension of the height, which made on-site-construction at the Structural Components Laboratory, UCSD be speedy and efficient.

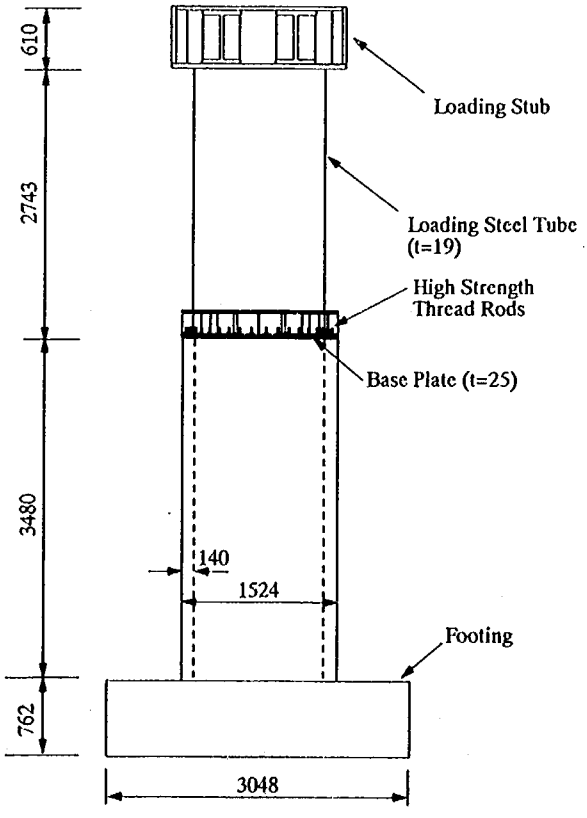


Fig. 1 Geometry of Test Unit

An outer diameter of the hollow section is 1524mm and an inner diameter is1244mm, resulting in 140mm wall thickness or the wall thickness ratio of 0.092. An elevation of hollow reinforced concrete section is 3480 mm which may be high enough to

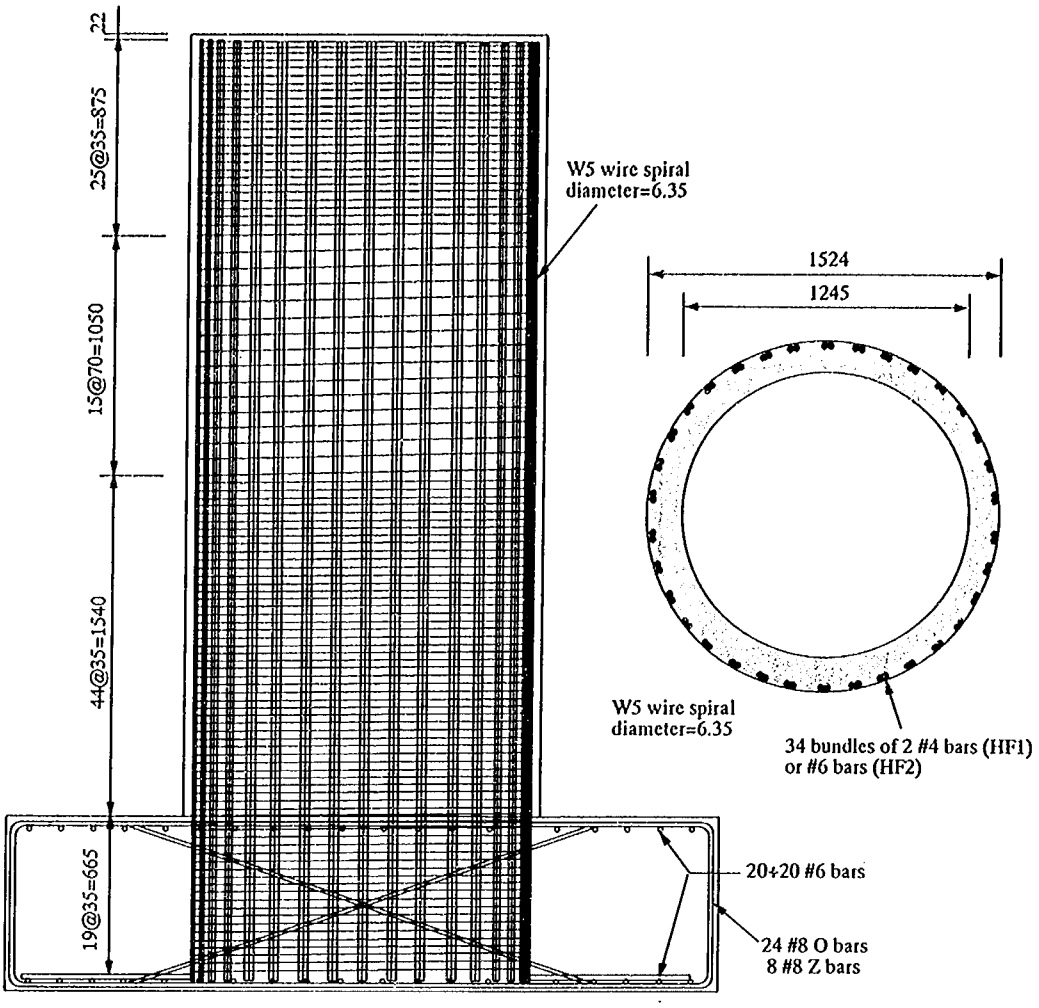


Fig. 2 Details of Reinforcement

observe the flexural behavior at the plastic hinge region. A total column height from the base to loading point is 6528mm, tested in single bending to give the aspect ratio of 4.28.

Details of steel arrangement are depicted in Fig. 2. The test column had 34 bundles of 2 #4 bars (HF1) or 2 #6 bars (HF2) in one layer distributed evenly with a constant cover of 19mm (HF1) or 16mm (HF2). The longitudinal reinforcement ratios to the net area of the concrete are 1.45% and 3.18%, respectively. The transverse reinforcement is a W5 wire (6.35mm diameter) placed with 35mm spiral pitch in the range of plastic end region[6] and column top region, and 70mm spiral pitch in the other region.

2.2 Test Setup

The overall test setup is illustrated in Fig. 3. The tests were carried out at the Structural Components Laboratory, UCSD. A vertical load was applied to the units through the use of four 46mm diameter dywidag high strength bars (Grade 150 (f_y =1030MPa)) and two rocker beam assemblies. A total vertical load of 2913kN (HF1) or 2997kN (HF2), corresponding to the axial load ratios (P / $f_c'A_g$) of nearly 0.13, was applied and maintained throughout the test.

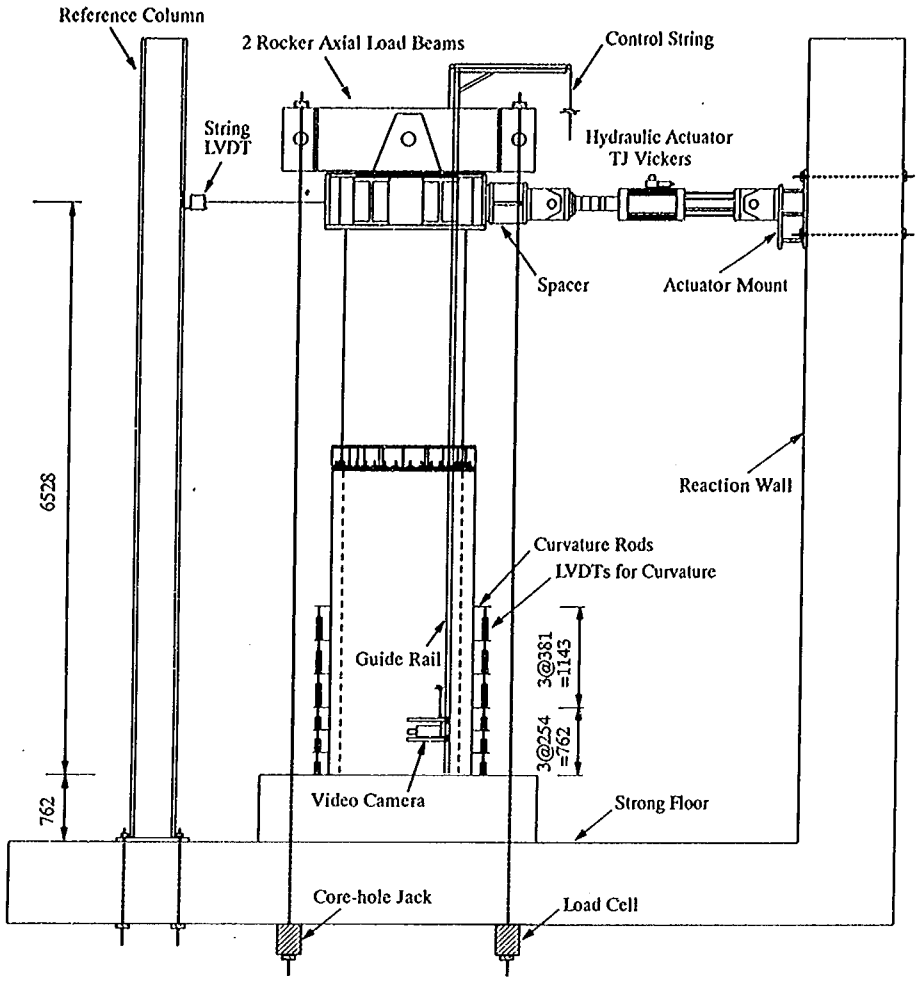


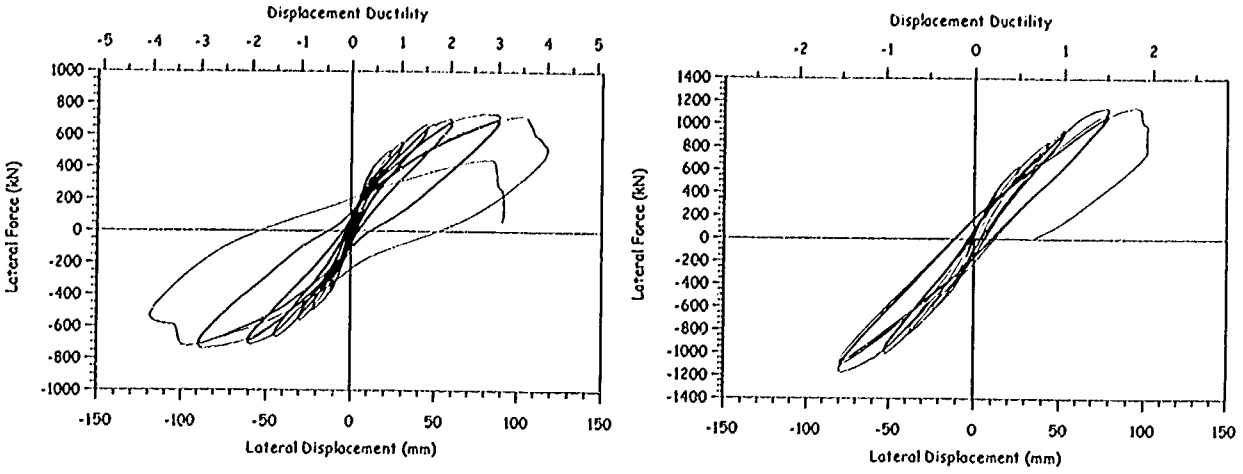
Fig. 3 Test Setup

The columns were loaded quasi-statically and subjected to cycles of force reversals under force control until theoretical first yield of the extreme longitudinal reinforcement, and subsequently cycles in displacement control to prescribed ductility levels. The test sequence consisted of single cycles at 25%, 50%, 75% and 100% of the first yield force and three cycles at ductility levels of 1.0, 1.5, 2.0, 3.0 and 4.0, respectively.

3. EXPERIMENTAL RESULTS

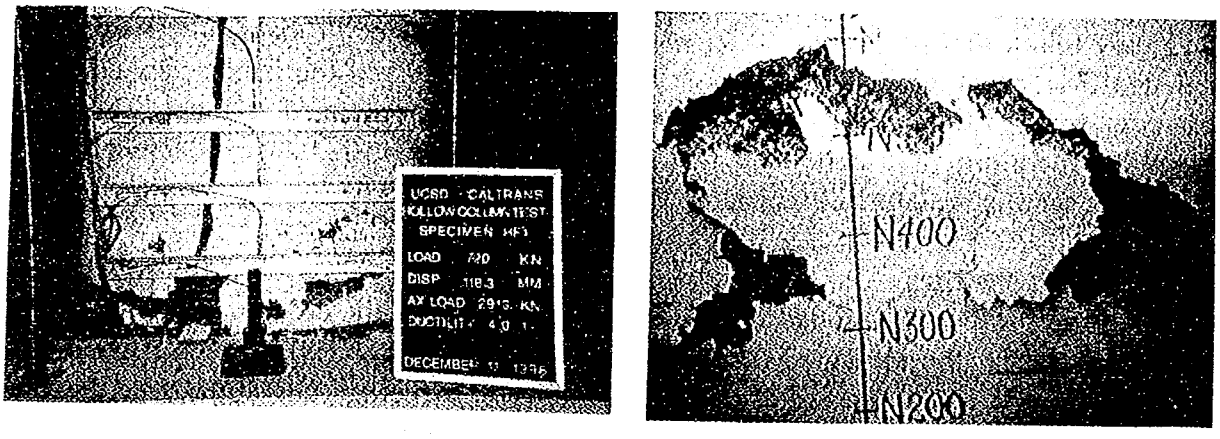
3.1 Hysteretic Responses

The overall response of lateral force and top displacement relation of the HF1 is depicted in Fig. 4(a). It is obviously found that the hysteretic response exhibits pinched loop shape, indicating that the column was subjected to high axial load. The experimental envelope of the hysteretic response exhibits a rounded shape or gradual stiffness degradation. The lateral force reached nearly peak value at the ductility 2.0 and significantly dropped at the ductility 3.5 in push direction, corresponding to the lateral displacement of 104mm where the inside face concrete was crushed as shown in Photo 1. For pull direction, deterioration of the lateral force was observed at the ductility of 3.3.



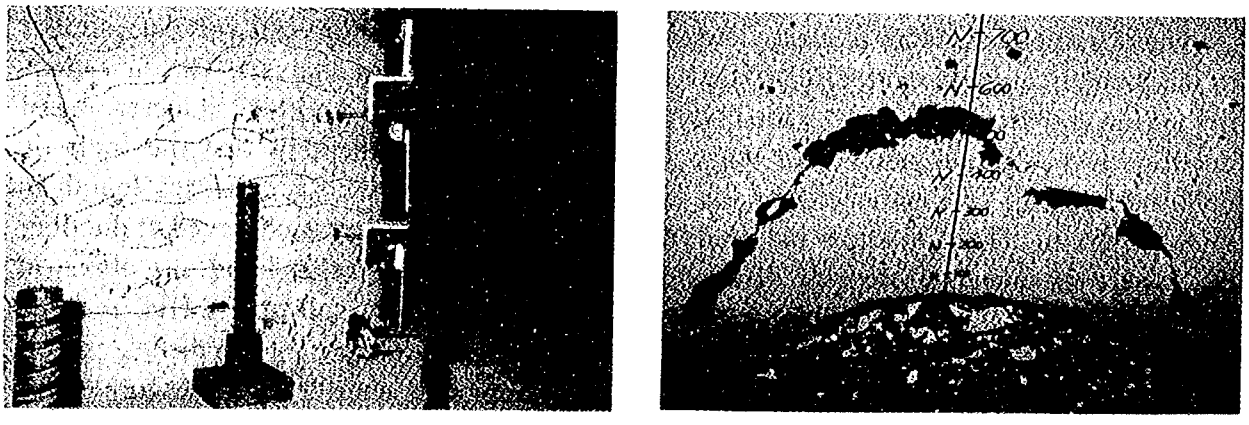
(a) HF1 Unit (b) HF2 Unit

Fig. 4 Lateral Force-Displacement Hysteretic Response



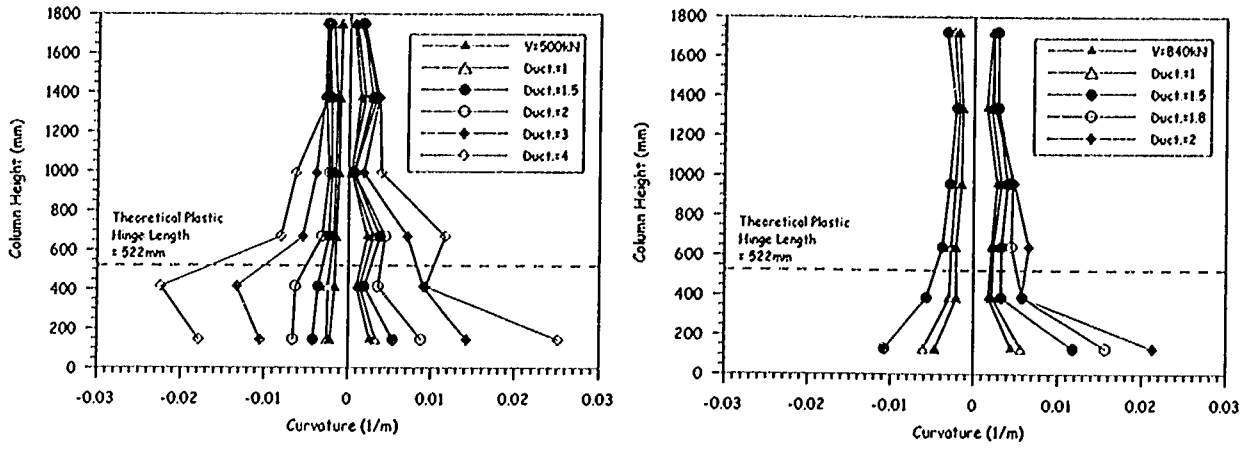
(a) Spalling-off of Cover Concrete (b) Crushing of Inside Face Concrete

Photo 1 Comparison of Damage Observed on Outside and Inside Face Concrete at Ductility of 4.0 (HF1)



(a) Onset of Spalling-off (b) Crushing of Inside Face Concrete

Photo 2 Comparison of Damage Observed on Outside and Inside Face Concrete at Ductility of 2.0 (HF2)



(a) HF1 Unit (b) HF2 Unit

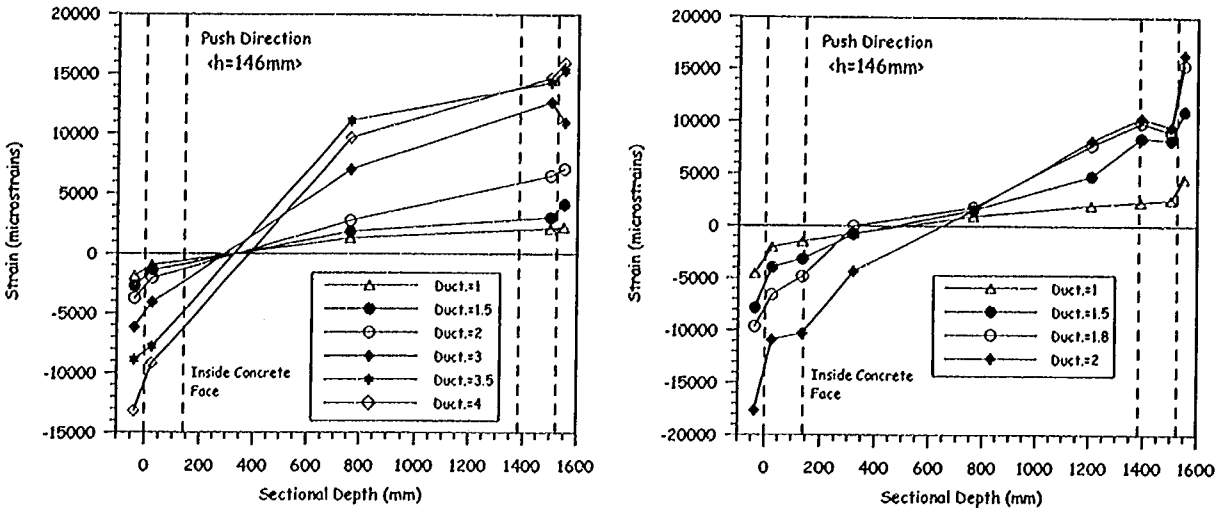
Fig. 5 Curvature Profiles

The lateral force-displacement hysteretic response of the HF2 is shown in Fig. 4(b). It is obviously found that the hysteretic response exhibits a non-ductile behavior as expected and significant degradation was noted at the ductility 2.0, when the inside face concrete was crushed even though the outside face concrete was not damaged seriously, shown in Photo 2. Therefore, it can be said that the failure of the inside face concrete would deteriorate the flexural ductility capacity.

3.2 Curvature Profiles

Curvature profiles are plotted in Fig. 5 for six sections of the column. Each curvature was calculated by the measured displacements of a pair of LVDTs. In each section, the curvature is reported at the center of the cell and is the average curvature over the cell height. It is noted that curvature at column bottom has been calculated taking into account of the strain penetration into the footing. The anticipated plastic hinge length based on $0.08L$ [6] (=522mm), where L is the column height and the rotation at the critical section resulting from strain penetration of the longitudinal reinforcement into the footing is excluded, is also noted in Fig. 5.

The observed curvature at ideal yield (ductility=1.0) in the bottom cell was very similar to the theoretical yield curvature (=0.003 1/m) based on a section analysis. The curvatures in the first and second cells from the bottom significantly increased with each increasing of ductility level as compared with those in the other cells, indicating that the inelastic deformation was concentrated over the first and second cells whose reference length in total is 540mm. The first major increase in curvatures of the HF1 was observed at ductility 3.0, where the onset of crushing of concrete was noted. On the other hand, the observed curvature at the maximum useful ductility of 1.8 in the bottom cell of the HF2 reached nearly 0.016 1/m which was not far from the ultimate curvature measured in the test unit of HF1, while it could be seen that the plastic hinge region is shorter than the anticipated plastic hinge length.



(a) HF1 Unit (b) HF2 Unit

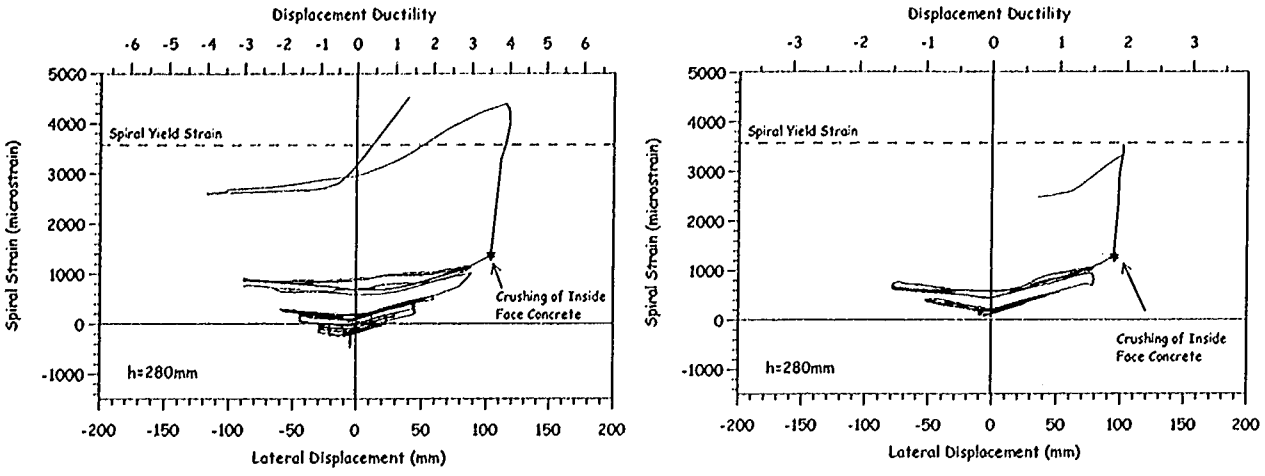
Fig. 6 Strain Profiles at Section of 146mm Height

3.3 Strain Profiles in Section

Fig. 6 shows the strain profiles in the plane section of 146mm height from the column base. The strains were directly calculated from vertical LVDTs and strain gauges attached on vertical reinforcements at the cardinal points. Because the vertical LDVTs give average longitudinal strains over the reference length, the average of two of longitudinal reinforcement strains measured in the reference length were plotted.

From Fig. 6(a), up to a displacement ductility of 2.0, sections remained plane obviously. The neutral axis depth at the ductility 2.0 is nearly 330mm, which is close to the theoretical position calculated by the moment-curvature analysis. Although the section does not remain plane at an interesting ductility level of 3.5, the strain of inside face concrete at the plastic hinge region seems to be less than 5000 microstrains, indicating that the compressive strain at crushing on the inside face of the test unit is at most 5000 microstrains, averaged over the experimental gauge length. At high levels of ductility, it is noted that strains indicated by strain gauges were less than those corresponding to the LVDTs. This is probably due to slip of reinforcing steel near the critical section with strain penetration into the base or up into the column.

It is also interesting in Fig. 6(b) that the compressive strain of near inside face concrete of the HF2 at the ductility 1.8 is close to 5000 microstrains, indicating that the inside face concrete was crushed when the compressive strain reached about 5000 microstrains at the column base. This test observation was exactly similar with the performance of the HF1. Although the compressive strain of the inside face concrete at crushing depends upon the wall thickness ratio and an amount of transverse steel, it could be suggested that the inside face compression strain of 0.005 represents an ultimate limit state for curvature ductility of the circular hollow section with the wall thickness ratio (t/D) of around 0.1 and a sufficient amount of transverse steel.



(a) HF1 Unit (b) HF2 Unit

Fig. 7 Confinement-induced Strain Hysteresis

3.4 Confinement-Induced Transverse Strain at Plastic Hinge

Fig. 7 shows the confinement-induced strain hysteresis response measured on the spiral. The spiral strain at a level of 280mm height (where is nearly mid-height of the theoretical plastic hinge length) has reached about 1380 microstrains at the maximum useful ductility 3.5 and the spiral has yielded immediately after crushing of the inside face concrete. Similar strain behavior was also observed on the spiral at levels of 140mm, 420mm and 560mm height where the inside face concrete spalled off as proved in Photo1. Therefore, it can be said that the maximum effective lateral pressure that occurs when the spirals are stressed to their yield strength was not induced to the concrete shell in the plastic hinge region before failure, and that yield strain was only induced by the buckling of the longitudinal bars, other than by concrete confinement. At the sections of 700mm and 840mm height, the strain responses showed almost elastic behavior and indicated peak strains (approximately 1000 microstrains) in a moment of crushing of the inside face concrete. A dramatic increase in strain after concrete failure was not noted at these sections since the longitudinal bars buckled up to 550mm height from the column base.

In the unit of HF2, the transverse strain at a level of 280mm height from the column base has reached 1315 microstrains at the ductility 1.8 and significantly increased immediately after crushing of inside face concrete. Such strain behavior is pretty similar to the test unit HF1. It should be noted that the dramatic increase in the transverse steel strain must be induced by no other than the concrete crush. Therefore, the full effective lateral pressure that may occur when the spirals are stressed to their yield strength was not induced in the concrete shell before failure of the inside face concrete. Based on the test results from the units of both HF1 and HF2, the strain of 0.001 would represent the effective confinement-induced strain in the hollow section.

4. ANALYTICAL STUDY OF INELASTIC HOLLOW COLUMN BEHAVIOR

4.1 Theoretical Background

The transverse steel placed near outside face in the plastic hinge region activates in tension when the section performs in a ductile manner in the inelastic range, and the resulting steel stress then applies the confinement pressure to the concrete core. It should be noted that the concrete wall in the circular hollow section is subjected to biaxial compression in such situation as illustrated in Fig. 8, since the confinement pressure arises in the only circumferential direction, other than in the radial direction. It is known that the biaxial compression applying to the core results in poorer confinement than the triaxial compression[5]. Accordingly, this confinement loss should be evaluated in the analytical consideration.

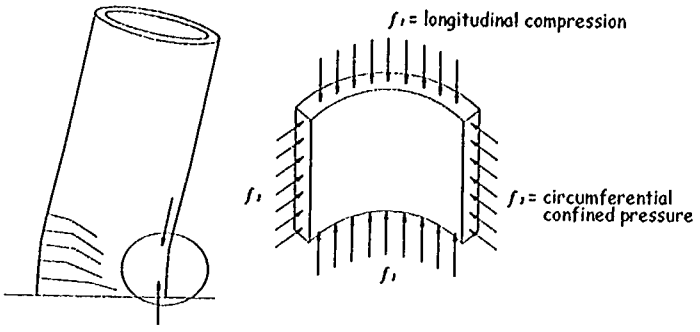


Fig. 8 Confinement in Circular Hollow Section

There are some applicable analytical approaches to predict the available flexural ductility of the reinforced concrete columns. In this research, the flexural response was estimated based on a conventional monotonic moment-curvature analysis because it is a simple and convenient approach and has been often employed in the earthquake engineering practice. The effect of the biaxial compression can be estimated through a stress-strain curve of the confined concrete proposed by Mander, Priestley and Park [1]. In the model, the confinement effect is represented by the confined strength ratio f_{cc}'/f_c', where f_{cc}' is a compressive strength of confined concrete and f_c' is a compressive strength of unconfined concrete. Fig. 9 shows a compression strength enhancement of confined sections related to two orthogonal confining stresses. For concrete confined in only one direction (biaxial compression), the left-hand curve noted in Fig. 9 can be used to get the confined strength. The circumferential confining stress f_{l2}' is written as

$$f_{l2}' = k_e \frac{f_h A_b}{t\, s} \qquad (1)$$

where, k_e = a confinement effectiveness coefficient relating the minimum area of the effectively confined core to the nominal core area; f_h = confinement-induced transverse steel stress; A_b = area of transverse steel; t' = concrete wall thickness inside the transverse steel; and s = spacing of transverse steel. An appropriate value of k_e for the hollow section may be 0.6 because it is recommended for wall sections[5]. As described in previous chapters, test results showed that the transverse steel strain induced by confinement was nearly 1000 microstrains averaged over the plastic hinge region before column failure, the confinement-induced transverse steel stress f_h is then calculated as (175000 MPa × 0.001) = 175 MPa. From Eq. (1),

$$f_{l2}' = 0.6 \times \frac{175 \times 32}{126 \times 35} = 0.76 MPa$$

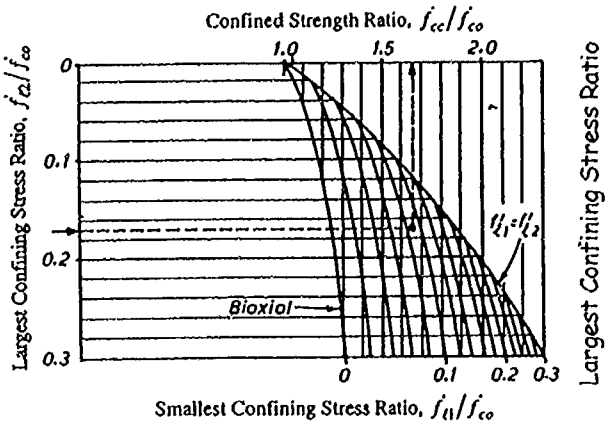


Fig. 9 Confinement Effect from Lateral Confining Pressure[5)]

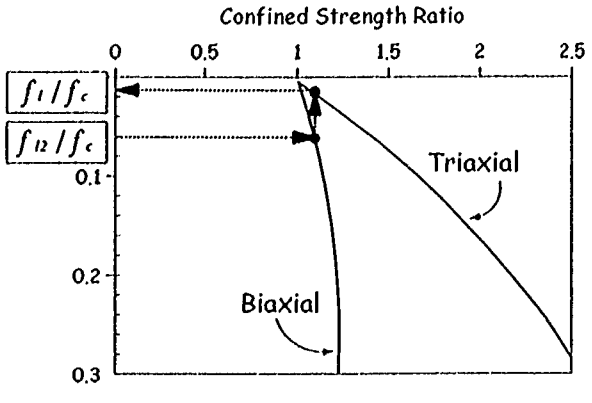


Fig. 10 Equivalent Confinement in Solid Circular Section

is the circumferential confining stress acting effectively to concrete wall. Using a confining stress ratio of $f_{l2}'/f_c' = 0.76 / 38 = 0.02$, the confined strength ratio can be read out from Fig. 9 as

$$\frac{f_{cc}'}{f_c'} \approx 1.04 \tag{2}$$

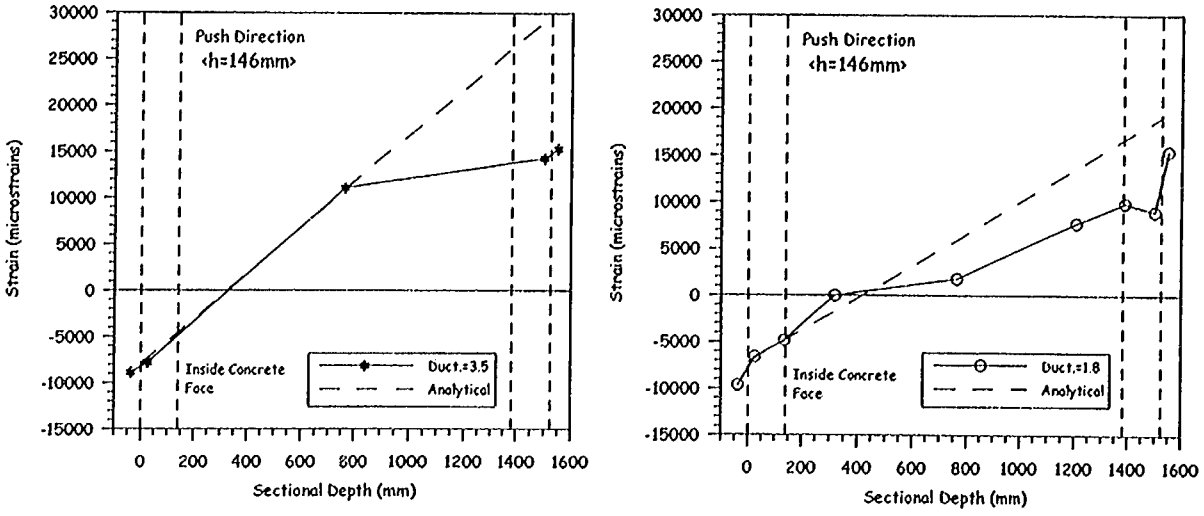
To simplify an analytical model, an equivalent solid circular section is assumed in terms of the confinement effect. The confined strength ratio in the solid circular section is given by

$$\frac{f_{cc}'}{f_c'} = 2.254\sqrt{1+\frac{7.94f_l'}{f_c'}} - \frac{2f_l'}{f_c'} - 1.254 \tag{3}$$

where f_l' is an effective lateral pressure[5)]. Equation (3) is solved for f_l' with Eq. (2) and then one obtains $f_l' = 0.22$ MPa, which indicates that the hollow section in the test unit is equivalent to the solid circular section with the confined core under the lateral pressure of 0.22 MPa. This procedure is illustrated in Fig. 10. It should be noted that the equivalent lateral pressure corresponds to nearly 30% of the maximum effective pressure that develops when the transverse steel is stressed to its yield strength. This significant confinement loss is obviously due to the existence of the void section, that is, the premature crushing of inside face concrete.

4.2 Moment-Curvature Analyses

Moment-curvature analyses for the critical sections of the test units were carried out based on stress-strain curves for concrete and reinforcement proposed by Mander et al.[5)]. Confinement effect and strain hardening of longitudinal reinforcement were taken into account through the stress-strain models, which is the same approach as the analyses for the solid circular sections. It should be noted that the lateral confinement pressure is assumed to be 0.22 MPa, as discussed in previous section, to determine the stress-strain curve of confined concrete.



(a) HF1 Unit (b) HF2 Unit

Fig. 11 Comparison of Strain Profiles at Critical Section with Theoretical Results

Experimental longitudinal strain profiles at the critical sections (h=146mm), measured at the maximum useful ductility, are compared with theoretical responses at ultimate in Fig. 11. The theoretical ultimate state is defined herein as the point when the extreme fiber compression strain reaches the ultimate strain of confined concrete or the inside face compression strain reaches 0.005, whichever comes first. As a consequence, analytical results showed that the ultimate state of the HF1 unit was determined by the extreme fiber compression strain, while that of the HF2 unit was determined by the inside face compression strain. Although experimental responses indicated that the plane sections no longer remain plane at the ultimate stage, neutral axis positions and strain profiles in the compression side are close well to theoretical results in both cases.

4.3 Theoretical Force-Displacement Responses

Theoretical force-displacement relations were evaluated from the moment-curvature responses of the sections, where curvature profiles were idealized as shown in Fig. 12. Accordingly, the theoretical structural displacement Δ was calculated from

$$\Delta = \int_0^L \phi h \, dh \tag{4}$$

where L is a column height and ϕ is the curvature. The plastic hinge length L_p was based on a standard equation[6] of

$$L_p = 0.08L + 0.022 f_y d_{bl} \tag{5}$$

where f_y and d_{bl} are yield strength (MPa) and diameter of longitudinal reinforcement, respectively. Equation (5) has been developed for solid columns originally, thus its applicability to the hollow columns may be controversial. However, as discussed in Chapters 3, the curvature profiles show that the plastic hinge length given by Eq. (5) seems

to provide a reasonable value. Although test data are not plenty enough to conclude the applicability of the standard equation of the plastic hinge length, Eq. (5) was employed temporarily in the analyses. A lateral displacement resulting from curvature in the loading steel tube was added on the elastic-plastic displacement due to the elastic curvature and the plastic rotation in the hollow section.

The measured envelopes of lateral force-displacement responses are compared with theoretical results in Fig. 13. Although the measured lateral force is slightly higher than the theoretical result, the experimental responses of the test units show a good agreement with the theoretical ones. It is also interesting in the analytical result of the HF2 unit that the inside face compression strain exceeded 5000 microstrains before the outside face strain reached the ultimate strain. This predicts that crushing of the inside face concrete occurs before failure of the outside face concrete, which coincided well with the test observation of the HF2 unit.

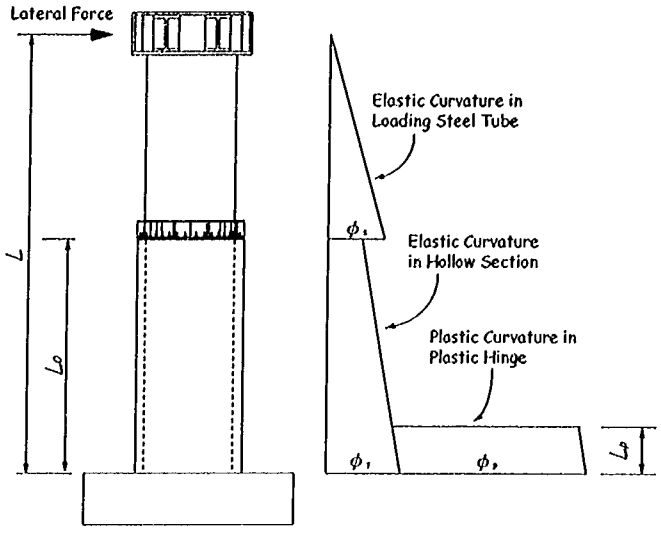
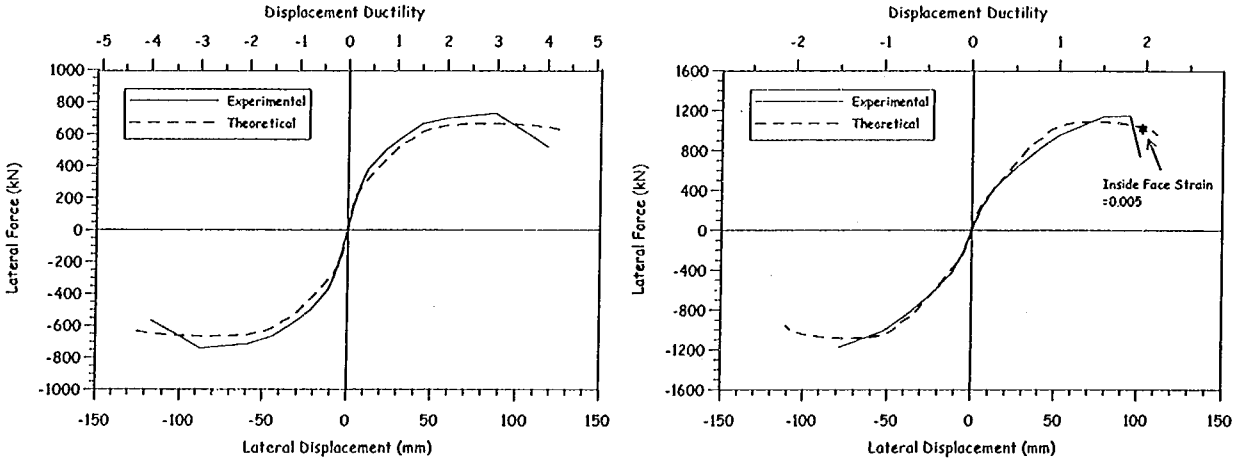


Fig. 12 Idealized Curvature Profiles



(a) HF1 Unit (b) HF2 Unit

Fig. 13 Comparison of Measured and Predicted Lateral Force-Displacement Envelops

5. CONCLUSIONS

Two flexural circular hollow columns with one layer of longitudinal and transverse reinforcement were tested under cyclic loading and the flexural performance was investigated based on the test results. The analytical approach methodology to predict the

flexural strength and the ductility capacity of the columns was also discussed in this report.

The inside face concrete compression strain is one of the most important parameters to control the ductility capacity of the hollow columns. High axial load, a thin wall or a high longitudinal steel ratio causes the neutral axis to pass through the void section with a deep clearance from the inside face, therefore the increase in the longitudinal compression strain at the inside face. Test results showed that the inside face concrete was crushed when the compression strain reached nearly 0.005 even though a sufficient amount of transverse steel was placed near outside face.

It should be also noted that the confinement-induced strain developed on the transverse steel seemed to be nearly 0.001 averaged over the anticipated plastic hinge length and did not exceed its yield strain before column failure. Concrete wall in the circular hollow section is subjected to the biaxial compression, which causes the significant confinement loss and then the premature crushing of inside face concrete. Therefore, the maximum effective lateral pressure should be calculated taking account of the confinement loss. The strain of 0.001 was proposed for the maximum useful transverse steel confinement-induced strain in the critical hollow section based on the test results.

The flexural strength and the ductility capacity of the circular hollow columns were evaluated with use of the conventional moment-curvature analysis for the equivalent solid circular section with the same confinement effectiveness, that is, the same confined strength ratio f_{cc}'/f_c'. Ultimate compression strain of concrete was defined at both outside and inside faces of the section, to estimate the response at ultimate limit state. It was noted that analytical results coincided well with experimental force-displacement behavior and the analytical approach presented herein could predict the available ductility of the circular hollow columns without inside longitudinal and transverse steel precisely.

Acknowledgement

This research described herein was funded by the California Department of Transportation (Caltrans) under contract of Caltrans/UCSD 1997-2001 project.
The authors greatly appreciate Giulio Ranzo and the technical staffs at the Charles Lee Powell Structures Laboratories for their help during construction and testing.

References

[1] Mander, J. B., Priestley, M. J. N., Park, R., "Behavior of Ductile Hollow Reinforced Concrete Columns," Bulletin of the New Zealand National Society for Earthquake Engineering, Vol. 16, No. 4, December 1983, pp. 273-290.

[2] Pinto, A. V., "Pseudodynamic and Shaking Table Tests on R.C. Bridges," ECOEST/ PREC8 Report, No. 5, November 1996.

[3] Zahn, F. A., Park, R., Priestley, M. J. N., "Flexural Strength and Ductility of Circular Hollow Reinforced Concrete Columns Without Confinement on Inside Face," ACI Structural Journal, Vol. 87, No. 2, March-April 1990, pp. 156-166.

[4] Kawashima, K., "Dynamic Strength and Ductility of Hollow Circular Reinforced Concrete Bridge Pier," Civil Engineering Journal, Vol. 34, No. 10, October 1992, pp. 34-39 (in Japanese).

[5] Mander, J. B., Priestley, M. J. N., Park, R., "Theoretical Stress-Strain Model for Confined Concrete," *Journal of the Structural Division*, ASCE, Vol. 114, No. 8, August 1988, pp. 1804-1826.

[6] Priestley, M. J. N., Seible F., Calvi G. M., "Seismic Design and Retrofit of Bridges," Wiley-Interscience.

SESSION 8: ADVANCED MATERIALS

(1) Safety Factor and Calculation Method of FRP for Structural Material of Bridge
(Itaru Nishizaki, Takeshi Kishima and Seishi Meiarashi)

(2) Development, Testing and Deployment of FRP Structures
(Issam E. Harik and P. Alagusundaramoorthy)

(3) The Effect of Reinforcement for Bridge Superstructures with Carbon Fiber Sheets
(Kenji Suzukawa, Akeo Hattori, Akira Kobayashi and Tokitaro Hoshijima)

(4) FRP Composites for Bridge Engineering
(John B. Scalzi)

Safety factor and calculation method of FRP for structural material of bridge

NISHIZAKI Itaru, KISHIMA Takeshi and MEIARASHI Seishi

Abstract

Safety factors of FRP for large water tank are well known as a part of design method based on reliability of the material. These concepts might be also available for FRP bridge design. The authors have been studying fatigue, creep and environmental deterioration properties of FRP, and considering safety factors of FRP for bridges. The authors show the example of calculation of the safety factors. The authors are also involved in the applicability of finite element method (FEM) for FRP structural materials, with comparing experiment result of a three-point bending test. The authors obtained the effectiveness of FEM based on the compatibility in experiment and calculation.

1. Introduction

Fiber Reinforced Plastic (FRP) has been recognized as one of the new structural materials. FRP has been already used for cables in pre-stressed concrete, reinforcement, ground anchors and others in construction industry area. However, it is very difficult to find the application example of FRP as main structural material as same as concrete and steel. In Japan, the foot bridge made by Public Works Research Institute is one of the rare example.

There are several advantages of FRP for bridges. For example, the coating cost will be reduced, as a result of protective performance. FRP has the property not only corrosion protection but also light weight, therefore this would drastically reduce the load to the substructures.

However, there are no specific criteria for the FRP safety factor for bridges. Safety factor of FRP cables has been already specified [1] for pre-stressed concrete as tendon, and there are safety factors [2],[3] for water tank. It is impossible to apply the same safety factors to bridge design, because conditions and reliability expected to bridges are different from these of water tank and FRP cables. In this paper, the authors proposed the general safety factors of pultruded FRP for structural material of bridge.

Many researches have been carried out on bridge design, focusing on steel bridge and RC/PC bridge. Though design method of steel and concrete bridge has been already established, that of FRP bridge has not yet. In the case of analyzing the performance of FRP member with multi-layer structural material, it is necessary to apply numerical method because of its anisotropy. In this paper, the authors also compared experiment result with FEM calculation result.

2. Study on safety factor of pultruded FRP

2.1 Materials and its main properties

Pultruded FRP has great freedom in its cross section figure, such as I-, H- and L-form. Adding to this, pultrusion is very good at producing long size of beam. Hence, the production by this method is suitable for the bridge material. The board part usually consists of three or five layer structure.(Figure-1) For outside layer, random direction fiber called Chopped Strand Mat (CSM) is

used. Middle layer is called "Roving layer" and uni-directional fiber is used. Some have clothe layer between CSM layer and Roving layer. CSM layer has no anisotropy, but Roving layer has high strength in only one direction. Pultruded FRP adjust strength and modulus of each direction with these layer combinations.

Figure-2 shows strain-load curve of tensile test on the direction of zero degree to pultrusion. Relation between strain and load is almost linear. It is difficult to set safety factor, because yield region does not exist. Figure-3 shows strain-load curve of tensile test on the direction of 90 degree to pultrusion. The gradient of the curvature becomes less when the strain increases more. This is because that an initial failure of layer structure occurs with deformation. The safety factor should be decided so that the design strain becomes less than the minimum initial failure strain.

2.2 Concept of safety factor

Concept of safety factor applied for FRP for construction structural materials is summarized as follows.

①Set safety factor within the range out of initial failure

②Set safety parameters on each deteriorating mode of FRP property, and combine these safety parameters.

There are four parameters concerned with above ②, reliability, dynamic load, static load and environmental deterioration.

(1) Safety parameter related to reliability

FRP has often used in plant and aircraft, and the considerations on safety factors in these areas have already been carried out. An example of FRP water tank is an application that could be an available reference. Table-1 shows the calculation method of FRP water tank. The factor related to the external forces are indicated in the other standard, hence it should set 1.0 in Table-1. Accordingly, external force for construction structural materials should be considered in the different way.

(2) Dynamic load

Table-2 shows the performance reduction ratio measured by the authors and other researchers. Information on pultruded materials was very few, therefore the authors also added their original test data.

In case of FRP bridges, they are lighter than steel bridges and a proportion of live load tends to bigger than dead load. It is necessary to set safety factor appropriately for fatigue property. Fatigue limit of 10^7times is 0.22–0.41 for GRRP and 0.4–0.8 for CFRP in literatures. Fatigue property is different from FRP types and loading condition, and it should be decided with considering in individual condition. Table-2 data shows that safety factor for fatigue is 2.5–5 for GFRP and 1.25–2.5 for GFRP.

(3) Static load

Creep failure does not become a problem in steel structure, but in case of GFRP, it is necessary to be considered because it was reported that 1000 hours failure stress is 0.25–0.7 by bending. However, FRP has relatively low elastic modulus and the critical state in designed based on not strength but deformation. It means that the ratio of design stress and approval stress automatically becomes larger than the safety factor and the fatigue could not become a critical failure mode. It is also necessary to determine safety factors corresponding to the expected service life.

(4) Environmental deterioration

Though FRP does not corrode, environmental deterioration should be considered, because there is different mechanism from steel and concrete. Sunshine is one of the main deterioration factors of FRP. In case of no coating, matrix resin will fall out and fiber will be bare on the surface. It is said that deterioration has few influences on FRP strength. The coating is necessary because it spoils the appearance and hurt skin. Water penetration into FRP is also a deterioration factor. This will influence strength reduction and a proper safety factor is required. Hence, the strength reduction by deterioration of FRP is different from individual environmental conditions. Table-2 shows the reduction ratio by environmental deterioration in the air. Bending strength may decrease approximately 0.8 of initial value in five years outside exposure test [4].

2.3 Definition example of safety factor

(1) Calculation example of safety factor

On the basis of above concept, the authors considered safety factor for foot bridges made of GFRP. Table-3 shows the result. In this example, each safety parameters were multiplied. However, the factors on dynamic load and static load should not be multiplied. The effects of dynamic load and static load have to calculate in the different way.

(2) Safety factor of FRP for general structure

Safety factor of FRP for general structure is also an available information for our research. "Pultruded FRP engineering manual (Reinforced plastic organization, 1996)" indicates safety factor as shown in Table -4. Table-5 shows safety factor that FRP manufacturer in USA recommend. These safety factors are empirical ones that include not only reliability but also a factor in the long term.

3. Calculation method for FRP member

3.1 Approach

FRP is a material with multi-layer structure as shown in Figure-1. In this paper, the authors try to apply FEM for analyzing the performance of FRP member. The authors compared the experiment value and the calculation result. The computer software, "ANSYS," is used for the FEM.

The FRP member is composed of three-layer materials, Mat/Roving/Mat. The elastic modulus is calculated as the following expression.

Roving: For 0°, $E = EROV \cdot Vf + ERES(1-Vf)$

For 90°, $1/E = Vf/EROV + (1-Vf)/ERES$

Mat: For 0°, $E = ECSM \cdot Vf + ERES(1-Vf)$

For 90°, $E = ECSM \cdot Vf + ERES(1-Vf)$

E: Elastic modulus for total layers EROV: Elastic modulus for Roving

ERES: Elastic modulus for Resin ESM: Elastic modulus for Mat

Vf: Fiber Inclusion Rate

3.2 Results

Figure-4 illustrates the FRP member used for the three point bending test. The test is conducted by loading on the top plate at the center of span, the length of which is 1500mm. The round pin is used at the loading point and the loading speed is 75mm/min. The displacement of the bottom plate at the center span is measured. Fig.5 shows the displacement of the bottom plate at the center span and the movement of the round pin at the loading point. The relation between load and displacement is approximately straight up to a failure point. The authors compare experiment displacement with calculation value one of the displacement of the bottom plate of the FRP member at the center of span, by considering FRP as a linear elasticity up to a break point based on a load-displacement curve. The "shell element type" for FEM is applied for numerical calculation, because the hollow member is considered as a shell structure. The material coefficients used for calculation are shown in Table-6.

The comparison between experiment displacement and calculated one are shown in Table-7. The both displacements are that of the member bottom plate at the center, in the case that 9.5kN is loaded. According to this table, the experiment and calculation are compatible. It appears to be effective to apply FEM for analyzing the performance of FRP.

4. Conclusion and future themes

In this study, the authors proposed that FRP should be used out of the range of early initial failure and set safety factor according to property deterioration factors. The authors also reported the approximate value of each safety parameters corresponding to individual deterioration mode. Improvement of accuracy of each parameters and study on safety factor for joint is necessary in near future.

According to the study on structural analysis, it appears to be effective to apply FEM for analyzing the performance FRP. It needs to use not only FEM, but the more simplified calculation method for effective analysis targeted at bridge design.

References

(1) "Manual for design and construction of continuous fiber reinforcing materials for concrete structures (draft)", Concrete Library No.88, JSCE (1996)

(2) "Calculation method of structural design for FRP water tank", Japan Reinforced Plastic Society (1996)

(3) "The technical manual for pultruded fiber reinforced plastics", Japan Reinforced Plastic Society (1996)

(4) "Manual for structural design of FRP", Japan Reinforced Plastic Society (1994)

(5) Sasaki and Nishizaki, "Fatigue and creep properties of pultruded FRP", not yet released

Table-1 Safety factor of FRP for water tank concept

Safety factor $F=F0\times L1\times\cdots Ln$

F0	Basic parameter	Material break strength	F0=1.3
		Material rigidity	F0=1.2
L1	Parameter on reliability of material properties (difference between test condition and real condition)		L1=1.1
L2	Application and importance (parameter against snow, wind, seismic load and others)		L2=1.0
L3	Indefiniteness of estimated external load (adopt authorized external force standard)		L3=1.0
L4	Precision in structural calculation		
	(precise method like FEM)		L4=1.0
	(Isotropic material mechanics)		L4=1.2
L5	Dispersion of material properties (calculate from mean value x of properties and standard deviation σ) (kp depends on reliability. In case of 99.9%, kp=3.09)		L5=1/[1-kp(σ /x)]

Table-2 Performance reduction ratio

	GFRP	CFRP	Steel materials (reference)
Fatigue – live load (10^7 times fatigue strength / static strength)	0.22-0.41 0.2-0.3 (bending)*	0.4-0.6 (double side) 0.6-0.8 (single side)	0.45-0.55 (tensile)
Creep – static load (1000 hours failure strength / static strength)	0.7 (tensile) 0.25 (bending) 0.64 (bending)*	0.9 (tensile) 0.7 (bending)	No problem at usual temperature
Deterioration strength caused by environmental degradation (Strength retention rate after exposure test)	0.8 (bending, five years) 0.9 (bending, two years)* 1.0 (coating, bending, two years)*	0.85 (tensile, shear, five years)	Corrosion should be considered.

* original data by the authors

Table-3 Example of calculation of safety factor

Conditions on reliability
Material rigidity : F0=1.2
Reliability of material properties : L1=1.1
Application and importance : L2=1.0
Indefiniteness of estimated external load : L3=1.0
Precision in structural calculation : L4=1.2 (Isotropic material mechanics)
Dispersion of material properties : L5=1.13 (based on test results)
Fatigue load condition : 1.0 (for foot bridge)
Static load condition : 1.6 (based on test results)
Environmental condition :1.1 (based on test results)
Safety factor = 1.2×1.1×1.0×1.0×1.2×1.13×1.6×1.1 = 3.2

Table-4 Example of safety factor of pultruded FRP for general use (Japan Reinforced Plastic Society)

Static short-term load (wind load, seismic load, etc.)	2-4
Static long-term load (connection, dead load, snow load, etc.)	3-6
Repeated load	6-12
Impact load	12-20
Environmental condition (safety factor is necessary individually for both temperature and chemicals)	

Table-5 Example of safety factor of FRP manufacturers (Design manual of MMFG, U.S.A.)

Bending members, Beam	2.5
Compressive members, Column	3.0
Shear	3.0
Connected part	4.0
Elastic modulus	1.0

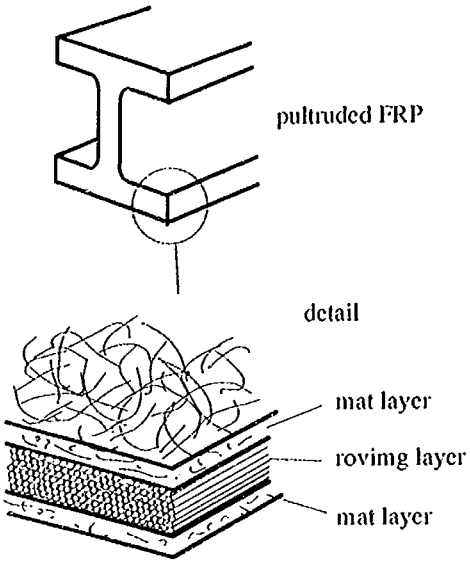


Figure 1 Structure of pultruded FRP

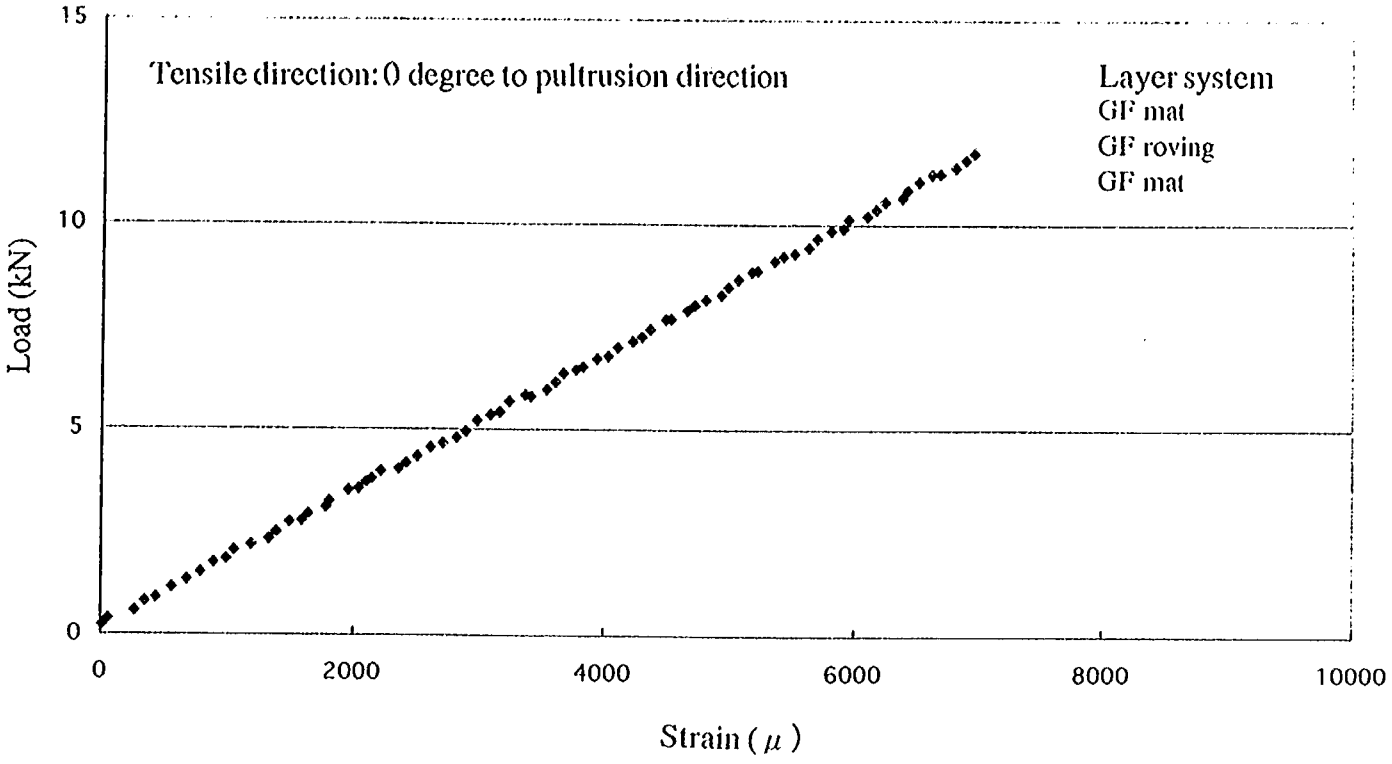


Figure 2 Example of tensile test of pultruded FRP

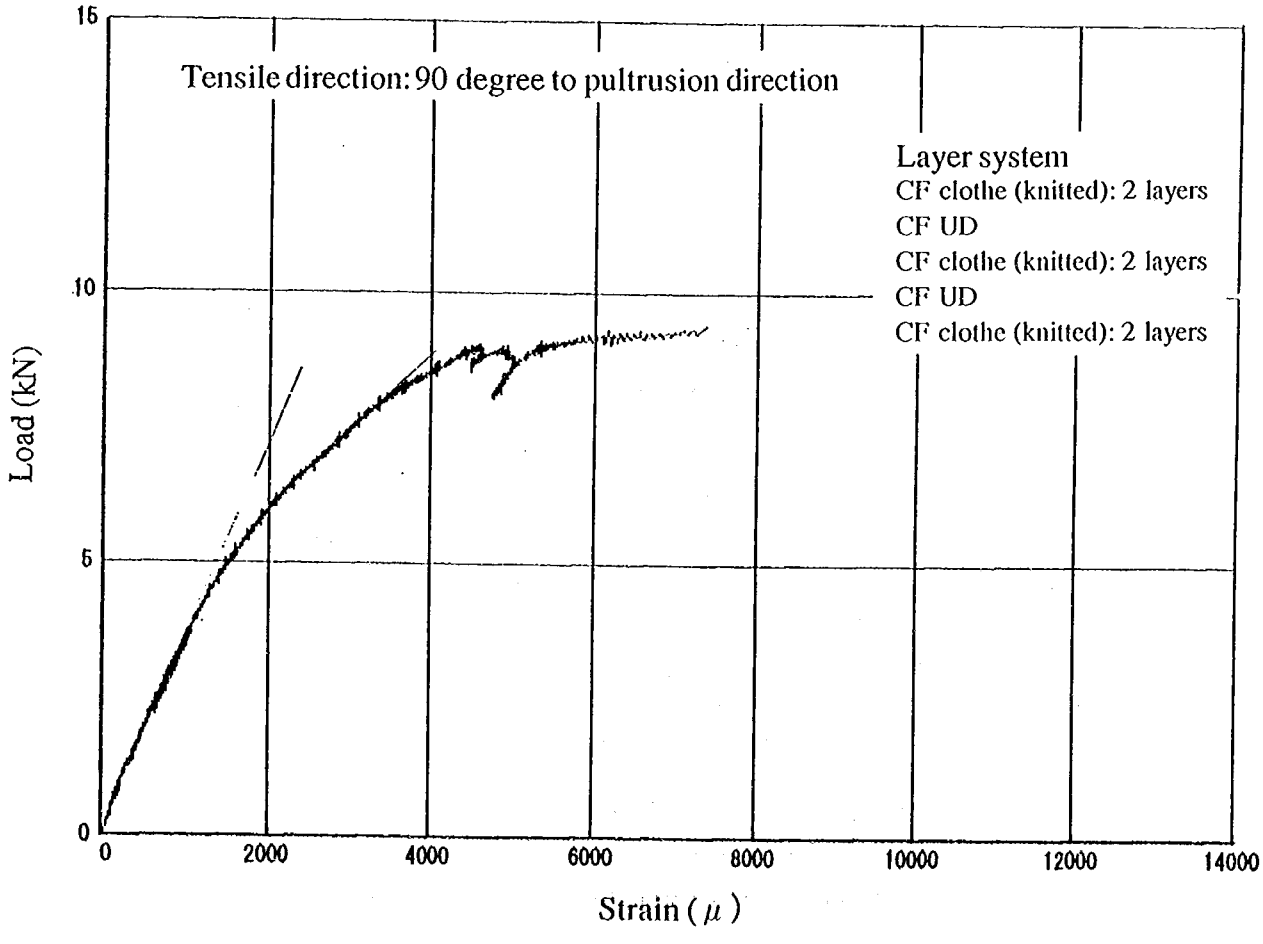


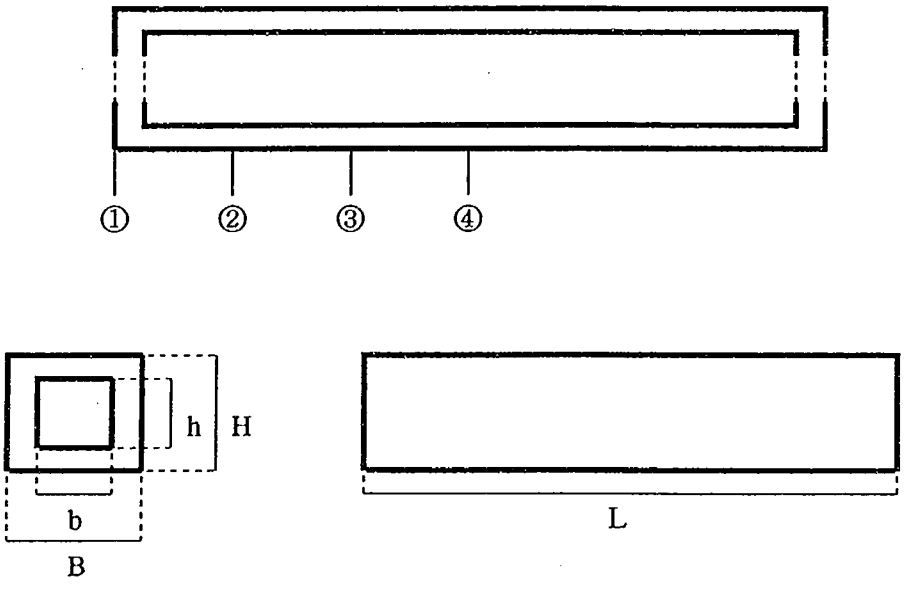
Figure 3 Example of tensile test of pultruded FRP

Table-6 Material Coefficients

	Elastic Modulus (0°)	Elastic Modulus (90°)	Poison's Ratio	Thickness (mm)
Mat Layer	18.7GPa	18.7GPa	0.32	0.693
Roving Layer	48.2GPa	9.18GPa	0.25	2.464
Mat Layer	18.7GPa	18.7GPa	0.32	0.693

Table-7 Comparison between Experiment and Calculation

	①	②	③	④
calculation	- 72.8mm	- 72.6mm	- 72.5mm	- 72.4mm
experiment	- 67.6mm			



B=H=50mm, b=h=42.3mm L=1700mm

Fig.4 Details of FRP Member

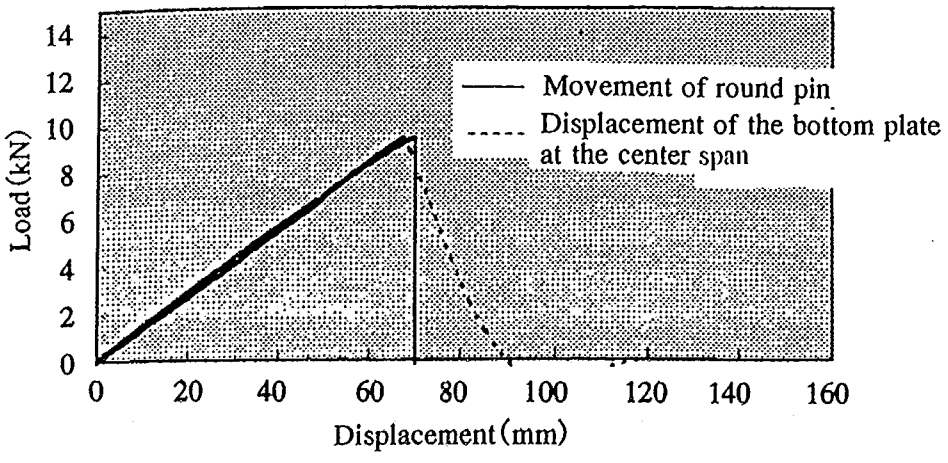


Fig.5 Relation between Experiment and Calculation

DEVELOPMENT, TESTING AND DEPLOYMENT OF FRP STRUCTURES

Issam E. Harik[1] and P.Alagusundaramoorthy[2]

Abstract

The paper summarizes the details of tests conducted on fiber reinforced polymer (FRP) structural components for infrastructure applications. Test methods are presented for FRP rebars, pultruded FRP structural members, concrete bridge deck panels reinforced with GFRP rebars, bridge barrier wall specimens and FRP reinforced concrete deck panels. The field application of FRP components in three bridges is also reported.

Introduction

The use of fiber reinforced polymer (FRP) structural systems for infrastructure applications offers, in certain applications, both economical and structural advantages, and improved performance. As FRP structural components are relatively new materials for construction, their material characteristics and structural performances are being evaluated at a number of research organizations. Standard testing procedures for a number of FRP structural components have recently been or are being developed by a number of international committees. This paper highlights the details of tests conducted on FRP components and test methodologies adopted at the University of Kentucky since 1994. The field application and monitoring of FRP components in three bridges is also reported.

Laboratory Testing of FRP Bars, Tendons, Cloth and Sheets

Several test methods have been developed for tensile testing of GFRP and CFRP bars (e.g. Nanni 1993, GangaRao and Faza 1991, and Castro and Carino 1998), carbon cloth and sheets/plates (e.g. Oral Buyukozturk and Brain Hearing 1998, Phalguni Mukhopadhyaya, Narayan Swamy and Cyril Lynsdale 1998 and Saadatmanesh and Malek 1998). Testing on a large number of these components, and structural elements reinforced or strengthened with these components have been conducted at the University of Kentucky are shown in Figs. 1, 2, 3, 4 & 5.

---

[1] Professor of Civil Engineering, and Head, Structures Section, Kentucky Transportation Center, 371 Oliver H. Raymond Building, Lexington, Kentucky 40506-0281.
[2] Visiting Professor, Kentucky Transportation Center, 382 Oliver H. Raymond Building, Lexington, Kentucky 40506-0281.



Figure 1. Steel Pipe Halves Epoxied to the GFRP Rebars during Tensile Tests

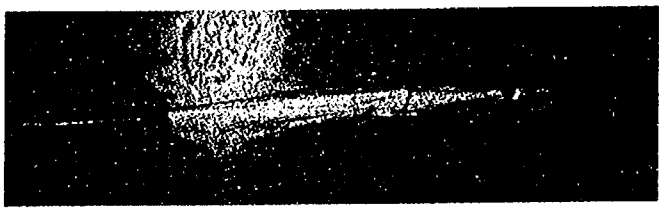


Figure 2. GFRP Tensile Specimen after Failure

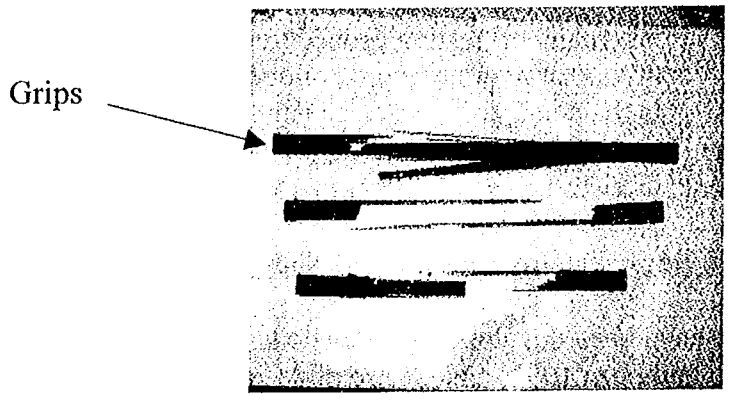


Figure 3. Carbon Cloth Specimen after Failure

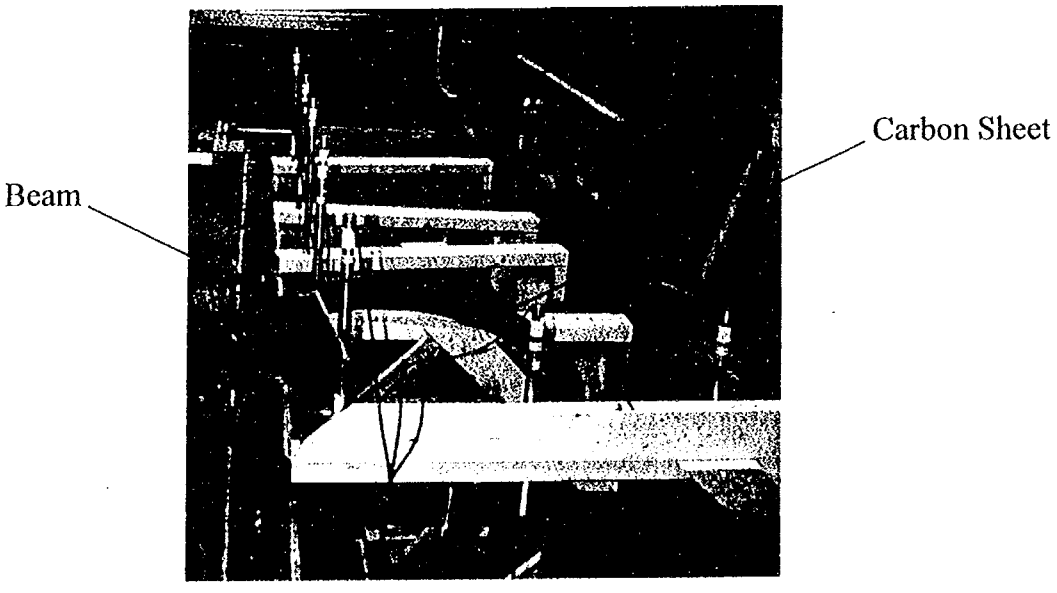


Figure 4. Concrete Beam Reinforced with Carbon Sheets

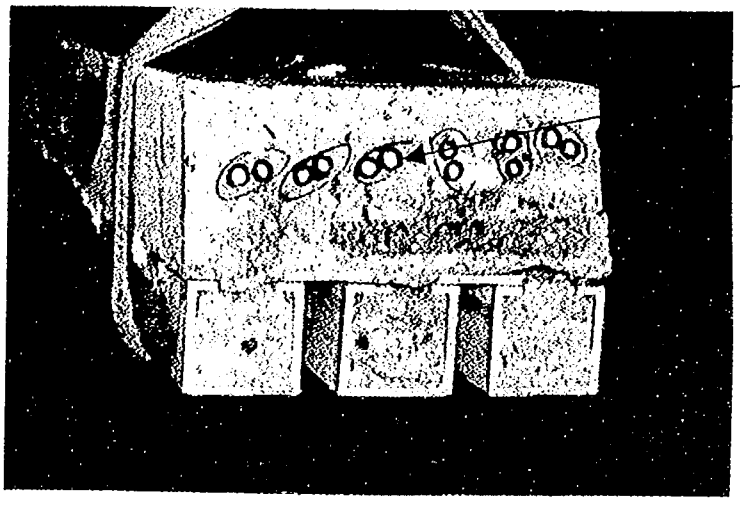


Figure 5. Pultruded Box Beam-Concrete Deck Assembly

The following two subsections describe the test methods developed at the University of Kentucky for gripping CFRP rebars and tendons, and for conducting compression tests on GFRP rebars.

Tension Tests of Carbon Rebars and Tendons

A gripping mechanism, developed at the West Virginia University's Constructed Facilities Center for GFRP rebars, was modified for the CFRP bars and tendons in order to prevent slippage at the grips. A steel pipe with a length of 250 mm was threaded on the inside and cut lengthwise into two pieces. The carbon rebars were also threaded (or sand blasted) on both ends for the same length of the steel pipes halves. The inner surface of the pipe halves was cleaned to remove rust and other debris, wiped with mineral spirits to remove residue, coated with a generic two part metal epoxy and then clamped at the ends of the CFRP bar or tendon until the epoxy was fully cured. The total length of the rebar specimens tested was approximately 1500 mm. The completed grips at one side of test specimens are shown in Fig. 6.

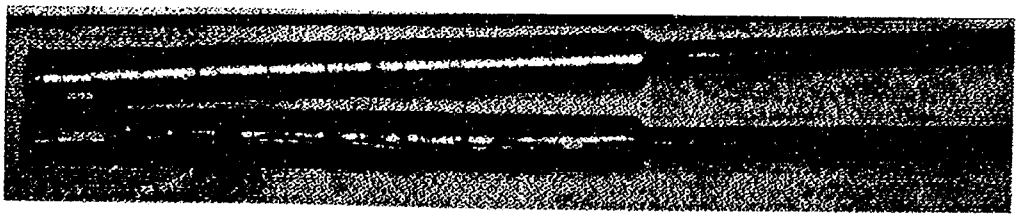


Figure 6. Split Steel Pipe Grips for Tensile Testing of Carbon rebars

Foil type strain gages were attached and the specimens were tested using hydraulic testing machine with wedge type grips. Over 250 carbon rebars/tendons have been tested by this method at the University of Kentucky for five manufacturers and for variety of resin types, fiber content and types of fibers. The ultimate stress of the CFRP rebars/tendons

ranged from 100,000 psi to 470,000 psi. The modulus of elasticity varied between $12x10^6$ psi and $22x10^6$ psi.

Compression Tests on GFRP Rebars

Generally, GFRP rebars located in the compression zone of a reinforced concrete member, are disregarded in the analysis/design, because of the low modulus of elasticity. However, when comparing experimental results with detailed theoretical calculations, the compressive material property of GFRP rebars is required for accurate analysis. The equipment used to test the GFRP rebars in tension could not be used to test the specimens in compression without any modification. The testing apparatus as shown in Fig. 7 was developed in order to conduct the tests (David Holman Deitz, 1998).

The ends of the specimen were gripped into the threaded rods as shown (Fig. 8). Specimens were tested with unbraced lengths ranging from 50 mm to 380 mm. To prepare the GFRP rebar test specimens, the surface deformations were removed in a small area using a belt sander providing a smooth surface to fix strain gages. Diameter of the rebar in the section where the deformations removed was measured using digital calipers to account for the small section loss during sanding. Since the moment applied by the hydraulic testing machine during the test was significant, strain gages were placed radially at the center of the specimens (Fig. 8) to allow for the separation of axial and flexural strains from the test data. Three distinct failure modes such as crushing, buckling and combination of crushing and buckling were observed during the tests and the crushing and buckling failure modes are shown in Figs. 9 & 10 respectively. Crushing failure was found in the tests of the shorter specimens ranging in unbraced length from 50 mm to 110 mm. The longer specimens with unbraced lengths from 210 mm to 380 mm were failed in buckling mode.

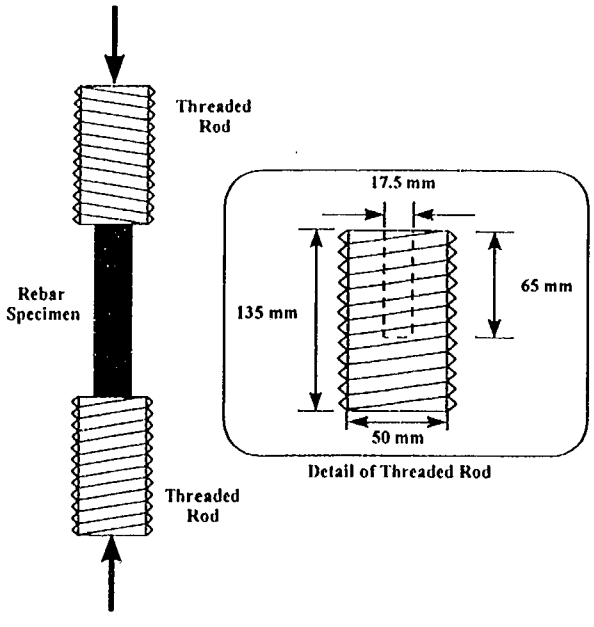


Figure 7. Apparatus used During the Tests of GFRP Rebars in Compression

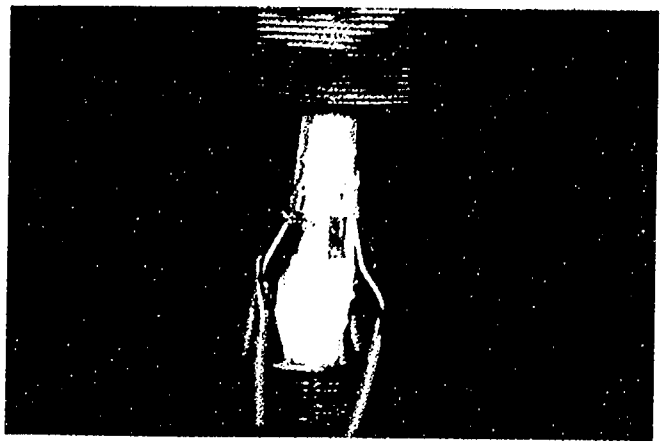


Figure 8. Position of Strain Gages on GFRP Rebar

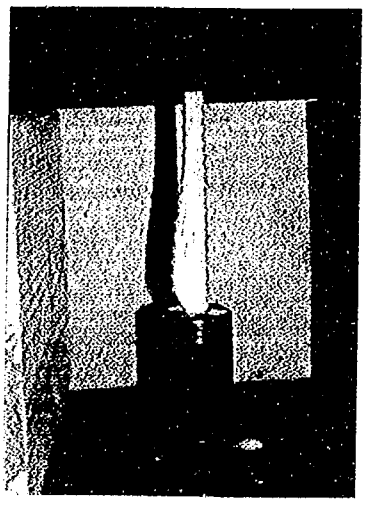


Figure 9. Crushing Failure Mode

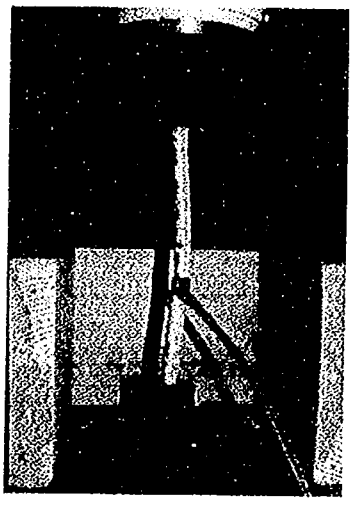


Figure 10. Buckling Failure Mode

Specimens with unbraced lengths ranging from 110 mm to 210 mm would fail in either mode. In some cases buckling failure would occur and then under continued loading a crushing type failure would occur for the same specimen. For GFRP rebars in the compression zone of reinforced concrete members, they can be assumed to be fully braced, and the test results show that the modulus of elasticity in compression is equal to the modulus of elasticity in tension, while the ultimate compressive stress is 50% of the ultimate tensile stress.

Laboratory Testing of Pultruded Glass/Carbon Hybrid I-Beam

Laboratory testing was conducted on a 61cm deep hybrid FRP I-beam in order to quantify the increased stiffness due to the inclusion of high strength/stiffness carbon fibers in to the flanges of the beam as shown in Fig. 11. The carbon fibers in the beam were pulled as individual tows, and amounted to 30% of the flange area. The beams were produced by

Strongwell, and the typical non-hybrid beams (series 625) have an effective modulus of elasticity of 17.3 Gpa ($2.5x10^6$ psi). Three beam specimens of length 7.62 m, 7.92 m, and 9.12 m were tested (Szak, Robson, Harik & Brailsford, 1999). A four point bending test was conducted with the load points as shown in Fig. 12. The modulus of elasticity for the hybrid section was determined to be 39.3 Gpa ($5.7x10^6$ psi) or 128% higher than the non-hybrid section.

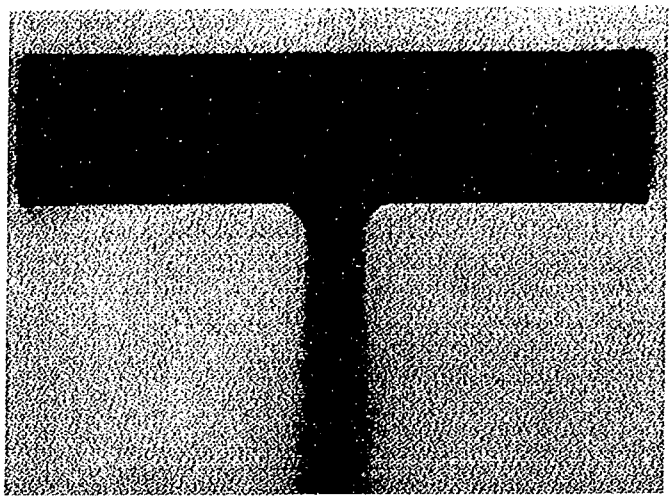


Figure 11. Cross-Section of the Hybrid Composite Beam

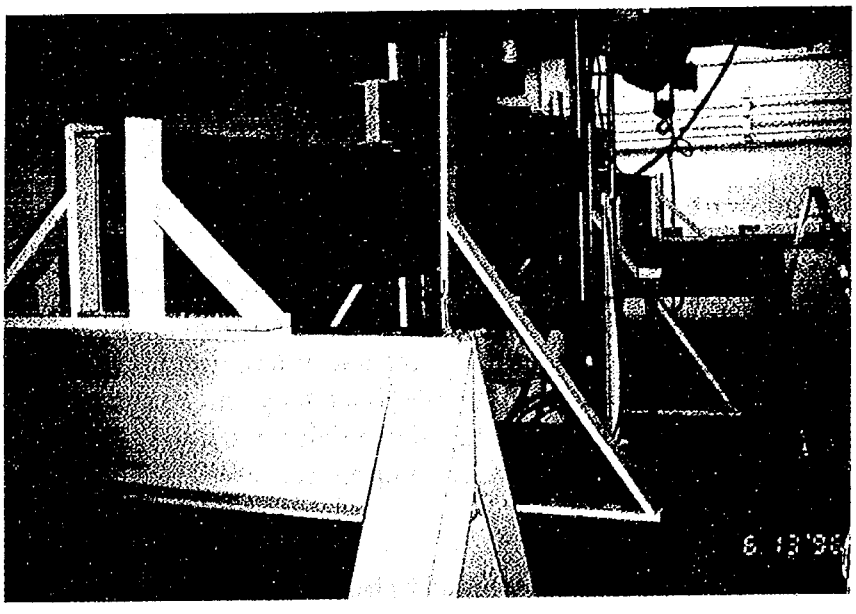


Figure 12. Four Point Loading Setup

Laboratory Testing of Bridge Deck Panels

Reinforced Concrete Panels

The cross section of a bridge deck is shown in Fig. 13. Typically, bridge decks are designed to transfer loads to main support girders in a direction transverse to the traffic flow, and to resist forces caused by barrier wall impacts. In the event of a barrier wall impact, a portion of the deck would be subjected to a tensile-flexural load combination. Twelve concrete deck panels were cast and tested to evaluate the behavior of bridge decks in the transverse direction reinforced with different combinations of glass fiber reinforced polymer (GFRP) and epoxy coated steel (ECS) rebars (David Holman Deitz, 1998).

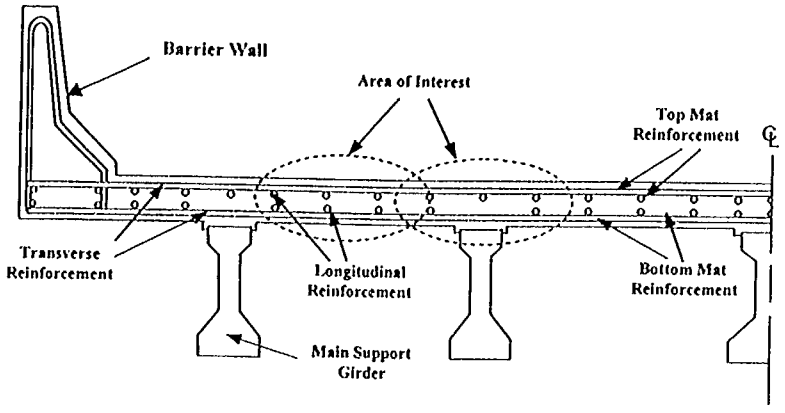


Figure 13. Bridge Deck Cross Section Showing Regions of Interest

Three different reinforcing schemes were considered in the study as shown in Fig. 14. The span length was an average Kentucky main support girder spacing (2740 mm). The instrumentation and the test setup are shown in Fig. 15. Two failure modes were observed and are shown in Figs. 16 and 17. All of the deck panels had similar crack patterns and spacing until near ultimate load levels were achieved.

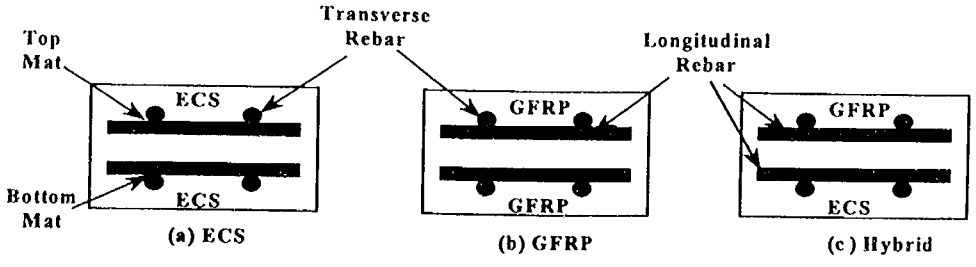


Figure 14. Deck Panel Cross Sections

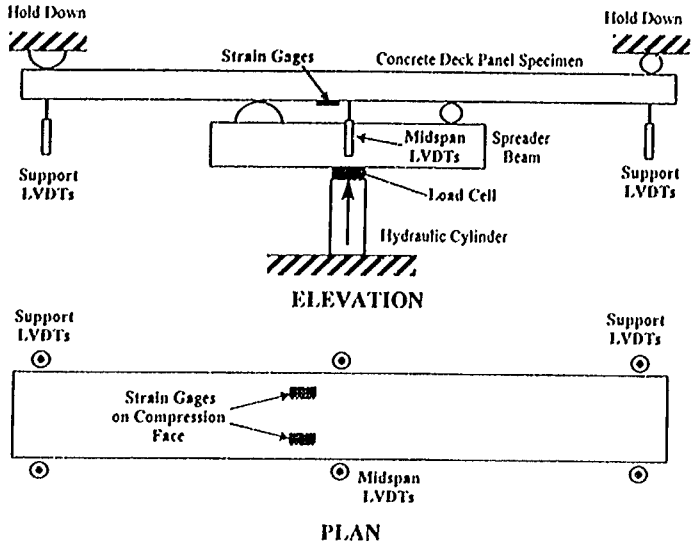


Figure 15. Deck Panel Load Setup and Instrumentation

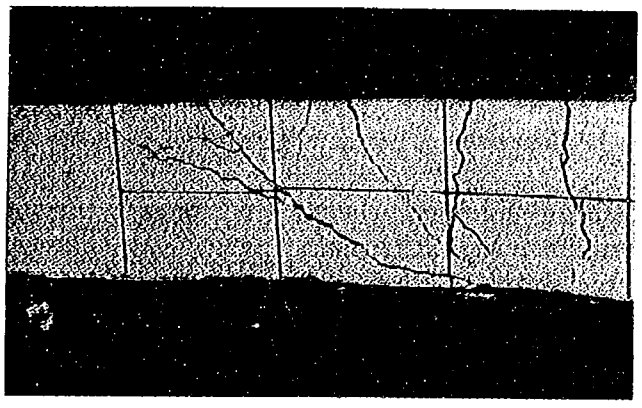


Figure 16. Shear – Diagonal Tension Failure of Deck Panels with GFRP Tensile Reinforcement

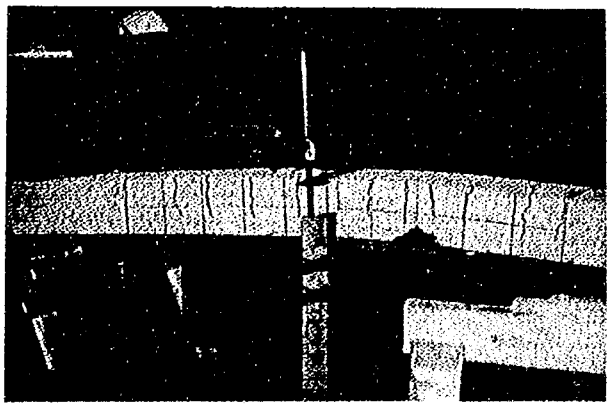
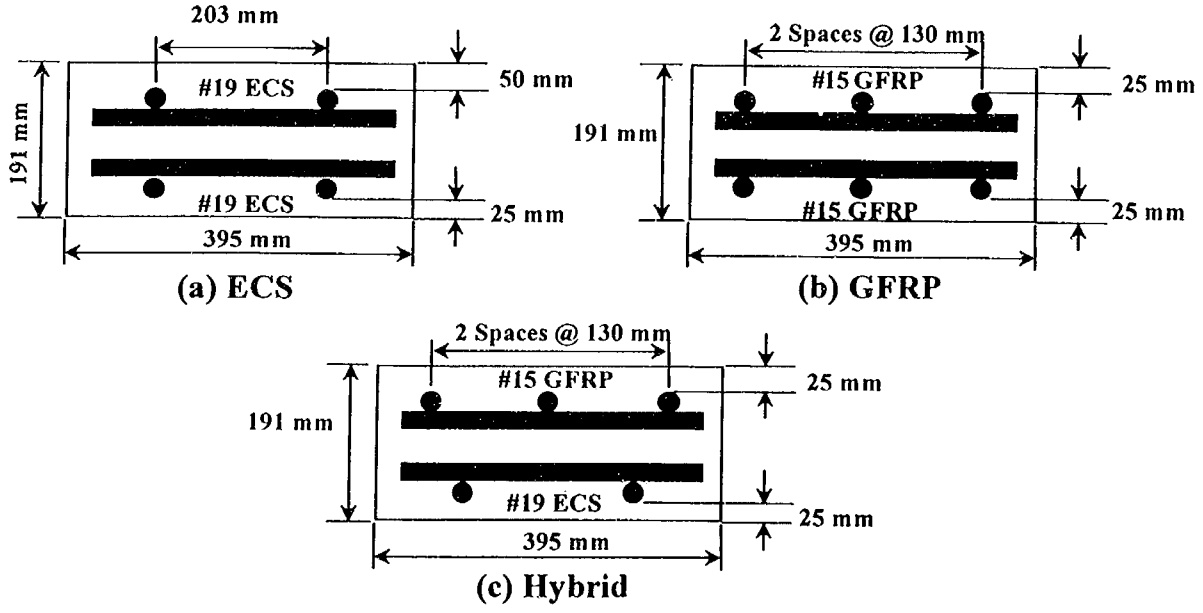


Figure 17. Flexural Failure of Deck Panels with ECS Tensile Reinforcement

The deck panels with epoxy coated steel on the tension side exhibited ductility and provided adequate warning through apparent yielding prior to the final compressive failure of the concrete. The deck panels with GFRP reinforcement on the tension side failed between the active load point and support in a region of high shear and flexure.

The behavior of deck overhang during a vehicle-barrier wall impact was evaluated by testing nine reinforced concrete barrier wall specimens with three different combinations of rebars (David Holman Deitz, 1998). The geometry of the barrier wall specimens was taken from the plans of the US-460 bridge over Roger's Creek, in Bourbon County Kentucky. The objectives of this study included the comparative stiffness, ultimate strength and failure modes of the barrier wall specimens. The decks of the barrier wall specimens were reinforced with the three different combinations of rebars shown in Fig. 18. The barrier walls were tested in a normal vertical position with the instrumentation as shown in Fig. 19. Three different failure modes observed during the tests are shown in Figs. 20. Results from the tests showed that all of the specimens exhibited the same behavior up until cracking of the deck. Based on the experimental results, all three proposed reinforcing schemes, e.g. ECS, GFRP, and Hybrid, can be recommended for use in actual bridge decks since they provided adequate resistance in case of a barrier wall impact. Each reinforcing scheme met the AASHTO specifications for barrier wall resistance and provided adequate warning of failure with ductile behavior.



GFRP Transverse Reinforcement #15

ECS Transverse Reinforcement #16

Figure 18. Cross Section of Barrier Wall Specimen Deck

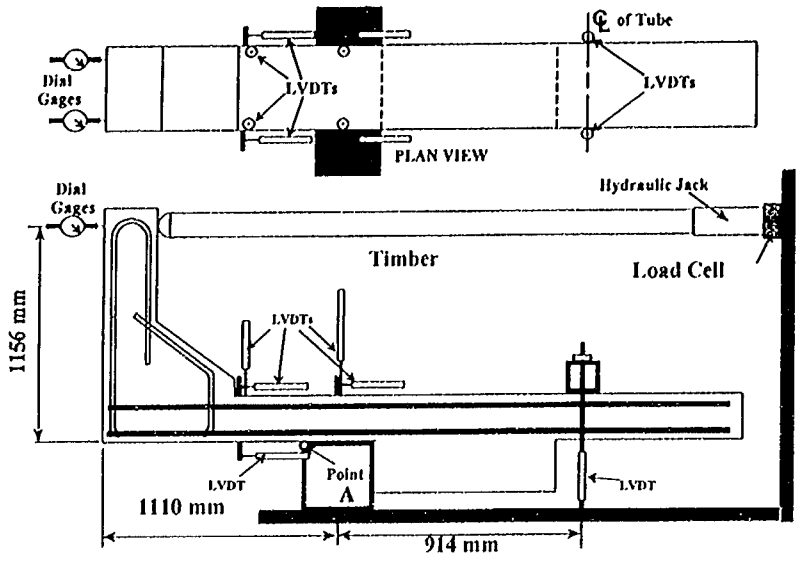
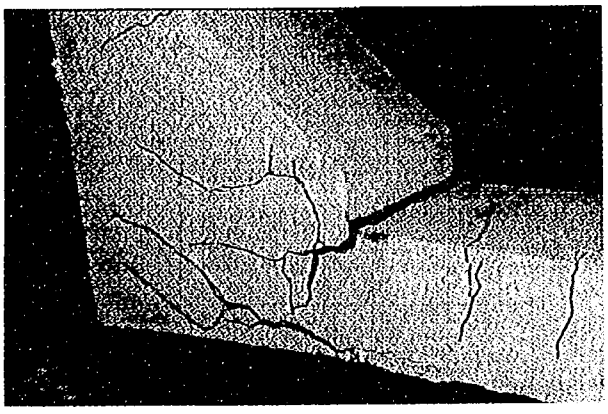
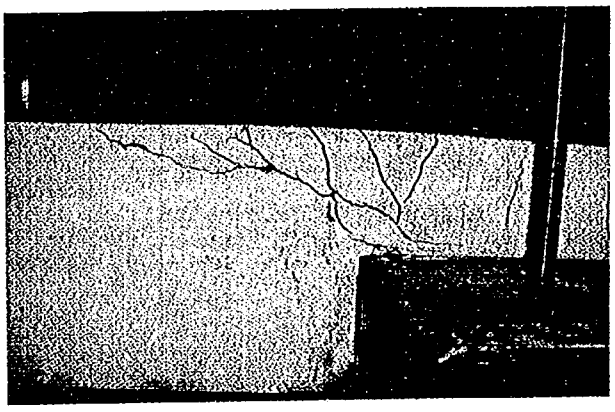


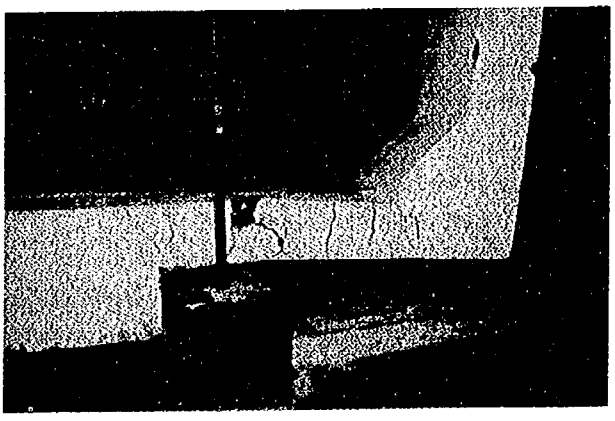
Figure 19. Illustration of Instrumentation Locations



(a). Anchorage Failure



(b). Shear-Tension-Bond Failure



(c) Flexural-Tension Failure

Figure 20. Crack Patterns

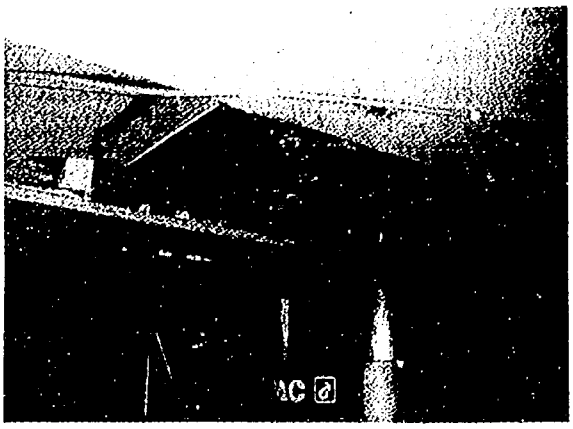
FRP Bridge Deck Panels

The design of FRP composite bridge decks is generally stiffness driven since it is mainly controlled by deflection limits. Experiments were conducted on four individual sets of FRP deck panels supplied by the following manufacturers: Creative Pultrusions, Composite Deck Suppliers, Infrastructure Composites International, and Hardcore Composites. For baseline comparison, a set of steel reinforced concrete panels was tested. The objective of this experimental study was to compare the deflection of FRP composite deck panels under the service and factored loads, and to determine the factor of safety against collapse. Each set consisted of three single span panels with effective span lengths of 2438mm, 3048mm and 3658 mm, and a double span panel with an effective span length of 2743mm on each span. The breadth of all panels was 914 mm. The depth of the panels varied from 185 mm to 234 mm. All the single span panels were tested under three-point loading and the double span panels under five point loading (Fig.21). Out-of-plane deflections at three points along the mid-section and at quarter span from both supports were measured using Linear Variable Deflection Transducers (LVDT). Electrical resistance strain gages and reusable strain gages were used to measure the strains across the mid-section of the panel.

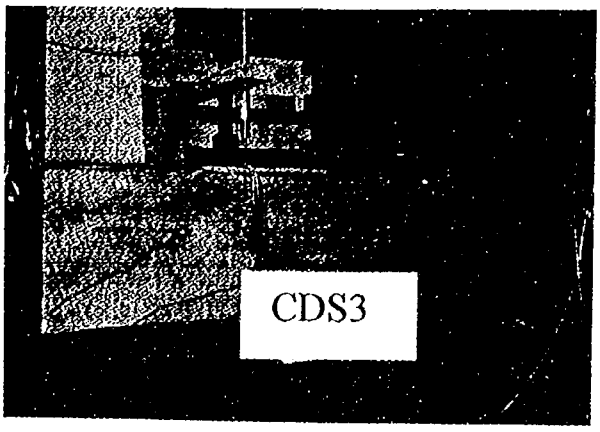


Figure 21. Test Setup

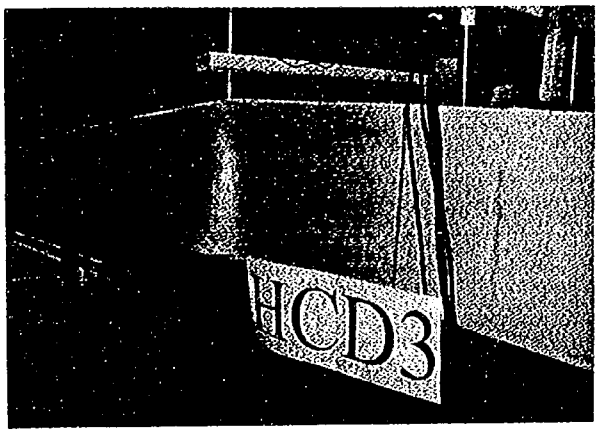
Four types of failure modes such as punching failure, flexure-shear failure, buckling failure and buckling and delamination failure observed during the tests were shown in Fig. 22. The factor of safety (= Load at Failure / 26000 lb) was calculated for all FRP composite panels and compared with steel reinforced concrete panels. The factor of safety for FRP deck panels varied from 3.0 to 8.2.



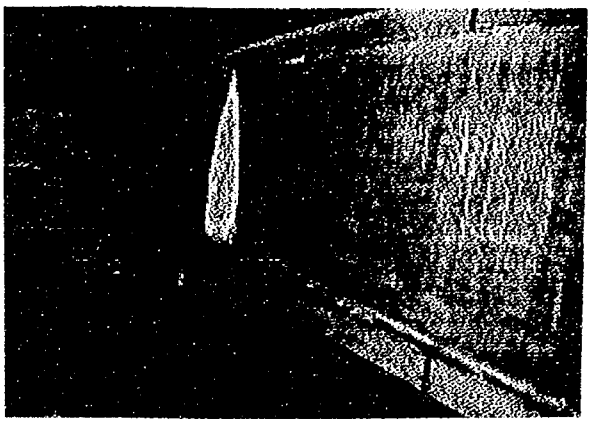
(i) Punching Failure



(ii) Flexure-Shear Failure



(iii) Buckling Failure



(iv) Buckling and Delamination

Figure 22. Failure Patterns

FIELD APPLICATIONS

Clear Creek Bridge

A pultruded FRP composite I-girder pedestrian bridge (Fig. 23) was constructed in 1996 over the Clear Creek in the Daniel Boone National Forest near Cave Run Lake in Bath County, Kentucky, USA (Szak, Robson, Harik & Brailsford, 1999). The main load carrying members for the bridge are two 61 cm deep hybrid composite I – girders. These girders were made of glass fibers in web and flanges with embedded carbon fibers in flanges (dark horizontal lines in Fig.11). The beam was manufactured by STRONGWELL in Bristol, Virginia. The addition of the carbon fibers in the flanges produced a 128 % increase in the rigidity of the beam, and since the design was controlled by deflection limitations, the number of girders was reduced from four to two. Many new features were incorporated in the construction of this bridge. These features include (i) the use of a hybrid carbon/glass fiber

reinforced polymer (FRP) I-beam section; (ii) the use of fiberglass sucker rods as supports for a bridge; and (iii) the use of spliced composite I-girders in a bridge.

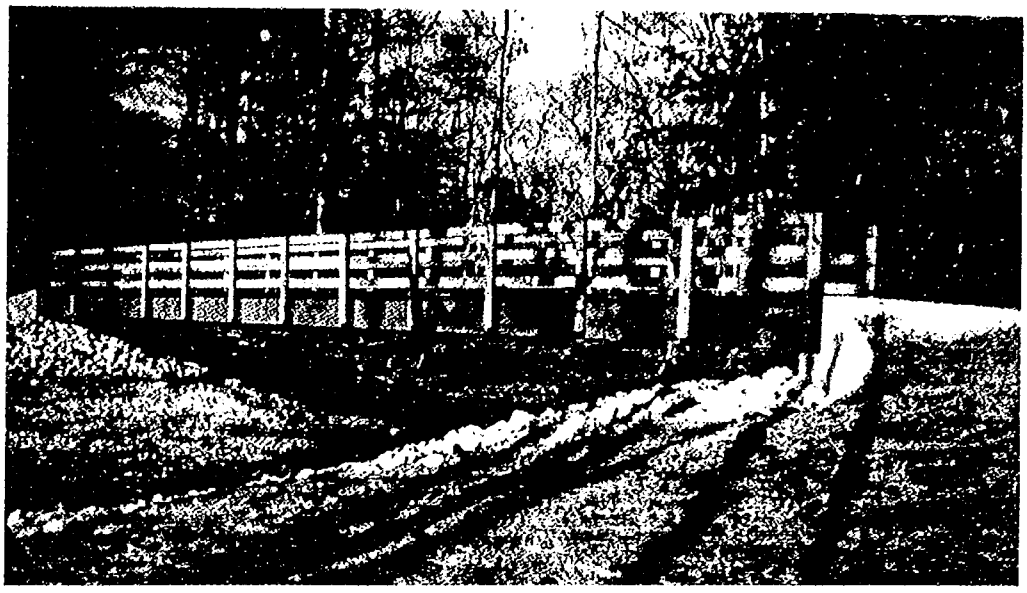


Figure 23. Clear Creek Bridge in the Daniel Boone National Forest

Roger's Creek Bridge Deck

A bridge deck 11.2 m long and 11.0 m wide was constructed in 1997 across Roger's Creek in Bourbon County, Kentucky with GFRP rebars in a region of the top reinforcing mat as shown in Fig. 24 (David Holman Deitz, 1998).

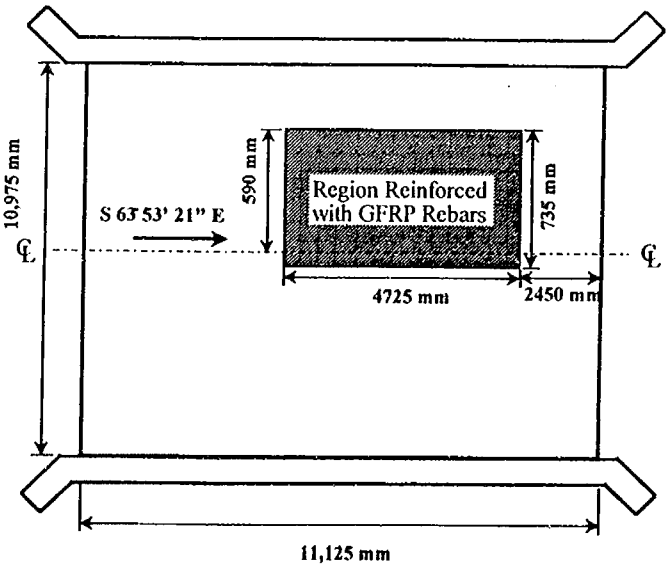


Figure 24. Plan View of Bridge Deck Showing Location of the GFRP Rebars

The remainder of the top mat was reinforced with epoxy coated steel (ECS) bars. Fig. 25 shows a photograph of the bridge deck reinforcement. The lighter area of the mat close to the center of the bridge, highlighted with dots, is the GFRP rebar area. The bridge is being monitored on a monthly basis to evaluate crack formation, crack width and propagation between the GFRP reinforced area and the ECS reinforced area.

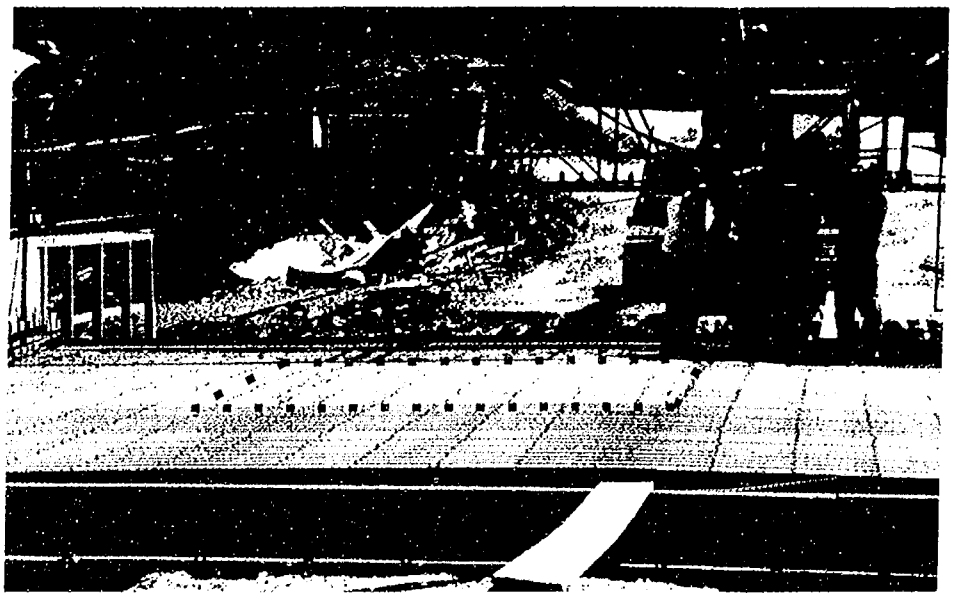


Figure 25. Bridge Deck Prior to Concrete Placement

Swinging Bridge

A pedestrian swinging bridge 128 m long and 0.92 m wide was constructed in April 1999 over the Big Sandy River in Johnson County, Kentucky (Fig. 26).



Figure 26. The Swinging Bridge

The superstructure in the suspension bridge is made from pultruded GFRP components. The deck is composed of an open grid resting transverse box section, which in turn rest on longitudinal box sections.

Acknowledgements

The work reported in this article is a summary of research conducted at the University of Kentucky on numerous research projects. The following persons worked on these research projects: Sean Anderson, Dan Blakeman, Dr. Biswajit Chattopadhyay, Emily Delaney, Dr. David Deitz, Chen Denglin, Dan Eaton, Dr. Jeff Griffin, Dr. Vijay Gupta, Chris Hill, Meg Hopkins, Mario Johnson, Tyler Julliard, Professor Anibal Manzelli, Dr. Vasudevan Krishnappa Naidu, Dr. Chelliah Madasamy, Louis Mattingly, David Ritchie, Dr. Brad Robson, Laura Schweri, Robin Siddiqui, Dr. Duraiswamy Subbana Gounder, Pete Szak, Tim Taylor, Dr. Michael Whitney, Everett Wilson, Louis Mattingly, Anthony Kordenbrock

References

1. AASHTO. 1996. " *Standard Specifications for Highway Bridges*," Washington, DC.
2. AASHTO. 1998. " *LRFD Bridge Design Specifications*," Washington, DC.
3. Castro, P., and Carino, N. 1998. "Tensile and Nondestructive Testing FRP Bars," *Journal of Composites for Construction*, 2 (1).
4. David Holman Deitz. 1998. "*GFRP Reinforced Concrete Bridge Decks*," Ph.D. Thesis, University of Kentucky, Lexington, USA.
5. GangaRao, H. & Faza, S. 1991. "Bending and Bond Behavior and Design of Concrete Beams Reinforced with Fiber Reinforced Plastic Rebars," Technical Report Submitted to the FHWA, WVDOH, International Grating, Inc., and Vega Technologies, Inc. West Virginia Constructed Facilities Center, Morgantown, WV.
6. Nanni, A. 1993. "Flexural Behavior and Design of RC Members using FRP Reinforcement," *ASCE, Journal of Structural Engineering*, 119(11).
7. Oral Buyukozturk and Brian Hearing . 1998. "Failure Behaviour of Precracked Concrete Beams Retrofitted with FRP," *ASCE, Journal of Composites for Construction*, 2 (3): 138-144.
8. Phalguni Mukhopadhyaya, Narayan Swamy and Cyril Lynsdale .1998. " Optimizing Structural Response of Beams Strengthened with GFRP Plates," *ASCE, Journal of Composites for Construction*, 2 (2): 87-95.
9. Saadatmanesh, H. and Malek, A.M. 1998. "Design Guidelines for Flexural Strengthening of RC Beams with FRP Plates," *ASCE, Journal of Composites for Construction*, 2 (4): 158-164.
10. Szak, P.J., Robson, B.N., Harik, I.E. and Brailsford, B. 1999. "The Clear Creek Hybrid Composite I-Girder Pedestrian Bridge," *ASCE, Journal of composites for construction*, 3 (2): 101-104.

THE EFFECT OF REINFORCEMENT FOR BRIDGE SUPERSTRUCTURES WITH CARBON FIBER SHEETS

Kenji Suzukawa[1], Akeo Hattori1, Akira Kobayashi[2] and Tokitaro Hoshijima[3]

Abstract

Since 1996, the Public Works Research Institute of Japan's Ministry of Construction and the Carbon Fiber Repair and Reinforcement Research Association, have been conducting joint studies to determine the effect of reinforcement for bridge superstructures with carbon fiber sheets and to establish rational design of their repair and reinforcement.

This paper contains the results of such studies especially on the static and dynamic ultimate strengths of concrete members reinforced with carbon fiber sheets.

1. Introduction

Today approximately 130,000 road bridges (bridge length 15 meters or longer) are in use in Japan. The control and proper maintenance of such a huge number of bridges is an important task. The constantly increasing traffic volume, and administrative changes such as the deregulation on the authorized gross vehicle weight in the Cabinet Order on Vehicle Restriction (introduced in 1993), present growing concerns due to faster deterioration of bridges. These situations inevitably call for establishing effective methods of repair and reinforcement.

Carbon fiber sheet bonding is the technique to bond resin-impregnated carbon fiber sheet or fabric onto the surface of concrete members for the purpose of increasing flexural strength, shear strength, and fatigue strength, thereby reinforcing the members effectively. The other advantages of this method include excellent workability, lighter weight and less susceptibility to deterioration due to corrosion. Consequently, the carbon fiber sheet bonding is applied to repairing and reinforcing of the concrete members in the bridge superstructures. Being a relatively new technique, however, further studies are yet needed to determine reinforcing effects, the scope of application, and design and construction procedures for the carbon fiber sheet bonding.

Introduced in this paper are some of the results of various tests in the three-year joint studies initiated in 1996 by the Public Works Research Institute of Japan's Ministry of Construction and the Carbon Fiber Repair and Reinforcement Research Association (CFRRA, see Table 1.1), with the goal of determining the above and establishing design and application methods. The first report of the joint studies was published a year ago (Ref. 1) regarding material characteristics (tensile, joint, and bond strength) of the carbon fiber sheet, flexural reinforcement of the reinforced concrete girders and reinforcement of the reinforced concrete deck slabs with regard to the amount of carbon fiber sheet reinforcement.

---

[1] Manager, Toray Industries, Inc.
[2] General Manager, Nippon Steel Composite Co.,Ltd.
[3] General Manager, Mitsubishi Chemical Corporation

This paper reports the results of later tests regarding the flexural reinforcement of prestressed concrete girders, shear reinforcement of reinforced concrete girders, and reinforcing effects of reinforced concrete deck slabs by wheel running machines under actual load .

Table 1.1 Organization of Joint Research

Bridge Division, Structure and Bridge Department, Public Works Research Institute, Ministry of Construction		Kazuhiro Nishikawa, Kenichi Uchida, Shinji Matsuo, et al.
Carbon Fiber Repair and Reinforcement Research Association (CFRRA)	Slab reinforcement sub working group	Kimimata Uji, Akira Kobayashi, et al.
	Girder reinforcement sub working group	Masajiro Koga, Akeo Hattori, et al.

2. Effect of Reinforcement of Bending Capacity of PC Girders

2.1 Background

The allowable stress design method for PC members where cracks are not allowed is often undesirable for economic reasons, as it requires a large number of carbon fiber sheets to be laminated. However, RC girder flexural test results have revealed favorable effects such as less deflection, crack distribution, less stress in steel reinforcement after cracking, and improved fracture resistance bending moment (Ref. 1). This means economical reinforcement is possible if cracks are allowed in PC members.

In the joint studies, experiments were conducted on the PC T-shaped girders used in posttensioning type T-girder designed with L-20 load representing a typical scale for PC bridges. Specimens having the cross-section about 1/2 the PC girder of the applicable bridge was prepared and carbon fiber sheets were attached over them. The specimens were put under fatigue tests by repeated loading and destructive tests by static loading to determine improvement in the deflection control and bending resistance.

2.2 Test Details

Figure 2.1 shows the reinforcement arrangement and dimension of the test specimen. Fatigue tests were conducted using two types of specimens; PC-1 specimen without reinforcement and PC-2 specimen of a girder reinforced underneath with four layers of carbon fiber sheeting having a modulus of elasticity 390 kN/mm^2, tensile strength 2,940 N/mm^2, and fiber weight 300 g/m^2. The lower and upper limit loads for the fatigue test varied in two levels, as shown in Table 2.1, from the stress at the bottom surface of the cross-section of 4.5 to 0.0 N/mm^2 (loading level 1) to 4.5 to -3.5 N/mm^2 (loading level 2) in reference to the PC girder design stress for the applicable bridges. The specimens were subjected to 2,000,000 cycles in each level for a total of 4,000,000 cycles. The loading levels were determined by first causing bending cracks in them and then calculating the compressive stress due to prestressing immediately before the test based on the cracking load and the tensile strength of concrete.

In the case of the reinforced PC-2 specimen, carbon fiber sheet was placed over it after cracking under a load equivalent to the dead load. The load was left acting on the specimen for a week until the epoxy resin hardened completely, and the fatigue test was conducted at that time. The unreinforced PC-1 specimen was also subjected to a fatigue

test after it was left under a load equivalent to the dead load. The loading rate was 1-3 Hz and the static deflection of the specimens and strain of the tensile reinforcing bar were measured from time to time. The static loading test was conducted after the 4,000,000-cycle fatigue test to determine the deformation performance and bending resistance of the specimens.

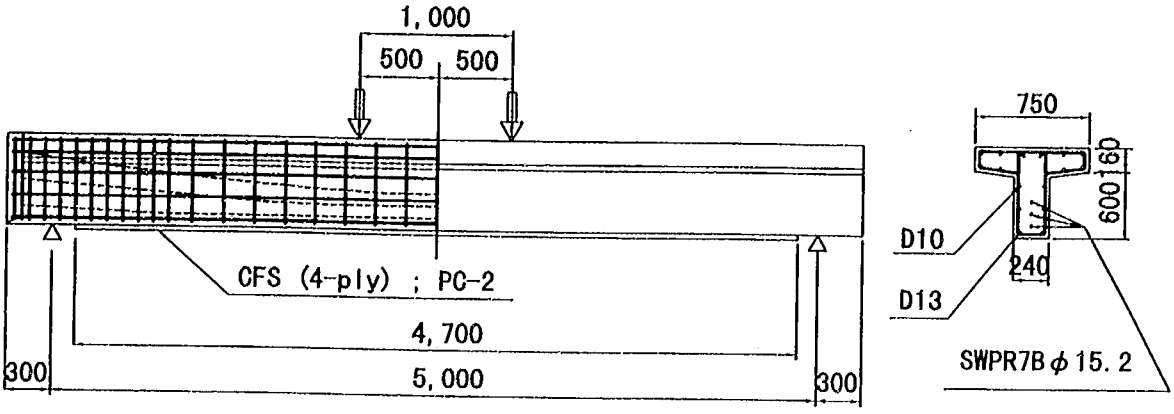


Fig.2.1 Dimension and Reinforcement Arrangement of the PC Girder

Table 2.1 Limit Load in the Fatigue Test

No.	CFS ply	Loading Level 1		Loading Level 2	
		Stress at bottom fiber of the concrete N/mm² Lower / Upper	Load, kN Lower / Upper	Stress at bottom fiber of the concrete N/mm² Lower / Upper	Load, kN Lower / Upper
PC-1	---	4.5 / 0.0	10 / 88	4.5 / -3.5	10 / 172
PC-2	4	4.5 / 0.0	34 / 113	4.5 / -3.5	34 / 191

CFS: Carbon Fiber Sheet

2.3 Results and Discussion

(1) Fatigue Test

Figure 2.2 shows changes in the deflection due to the live load, which is the difference between the upper and lower limit loads in the fatigue test. No significant difference was observed between PC-1 and PC-2 in loading level 1 where the entire cross section of the girder was thought to function effectively because of prestressing. In loading level 2 test that followed, however, deflection in the unreinforced PC-1 due to the live load increased rapidly after about 10 loading cycles, and it tended to increase further gradually with the progress of loading. On the other hand, the initial live load deflection of the reinforced PC-2 was maintained at both loading levels until the end of the fatigue test. It was also verified that the carbon fiber sheet reinforcement prevented the member stiffness from decreasing after repeated loading in which a -3.5 N/mm² stress acted on the bottom surface of the concrete. The amount of reduced deflection due to carbon fiber sheeting at the end of the 4,000,000 cycles was about 25% live load equivalent and around 12% in total deflection compared to the deflection in the unreinforced specimen.

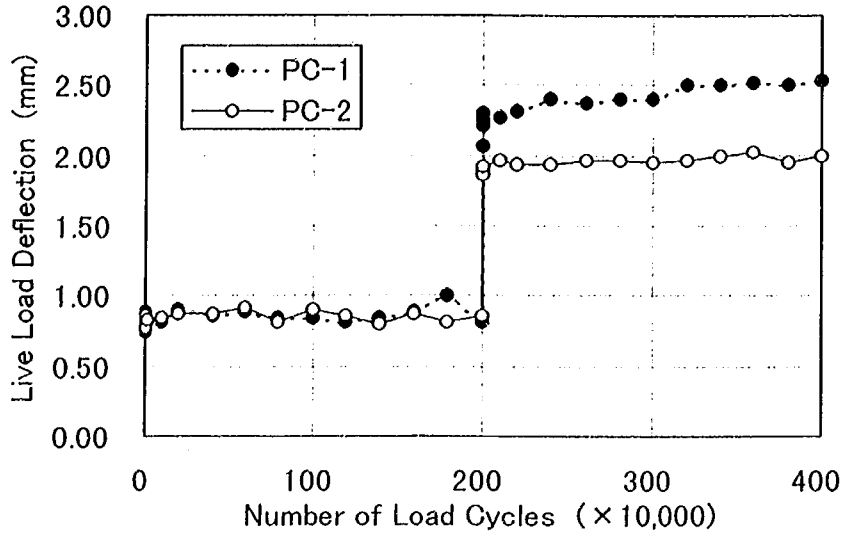


Fig.2.2 Relationship between Deflection due to Live Load and Load Cycles

(2) Behavior during Static Test after Fatigue Test

Figure 2.3 shows the relationship between load and deflection during the static load test. The unreinforced PC-1 indicated a decrease in the flexural stiffness starting from a load lower than the cracking load 172 kN that was applied before the test. The decreasing tendency grew stronger after the tensile reinforcement bar yielded and the concrete began to crush in the compressive side at the load of 427 kN. The load did not increase much after that until the specimen fractured at the rapture of the prestressing steel.

The relationship between load and deflection of the reinforced PC-2 nearly remained linear after the pre-reinforcement cracking load 191 kN. New cracks were found at the center of the specimen at 235 kN after which a decrease of flexural stiffness was observed although the amount of decrease was smaller than in the unreinforced specimen. The yield load of the tensile bar was 372 kN, 46% higher than the unreinforced specimen. The load kept on increasing after the tensile bar yielded until the carbon fiber sheet encountered a bond fracture and the sheet was separated completely. The load at the time of bond fracture was 538 kN and the maximum flexural resistance increased 24% compared to PC-1. The amount of mid-span strain of the carbon fiber sheet was approximately 5500 μ .

Figure 2.4 shows the strain of the reinforcement at the center of cross-section of each specimen. It shows the amount of strain after the cracking load is reduced significantly by reinforcement. The relationship between load and strain of the reinforcement bar of the PC-1 tends to deviate from the initial slope before reaching the cracking load 172 kN after which the curve basically remained linear. The bar yielded at 255 kN. The relationship between load and strain of the reinforcement bar of the PC-2 followed the initial slope past the cracking load 191 kN. The amount of strain increased rapidly after 235 kN most likely because new flexural cracks occurred near the mid-span strain measurement point and the tensile force originally carried by the underbeam concrete was carried by the reinforcement bar and the carbon fiber sheet. The carbon fiber sheet maintained an elastic load and strain relationship, similar to that of the reinforcement bar, until the bar yielded (372 kN), after which point the strain increased elastically as the increased load was carried by the sheet.

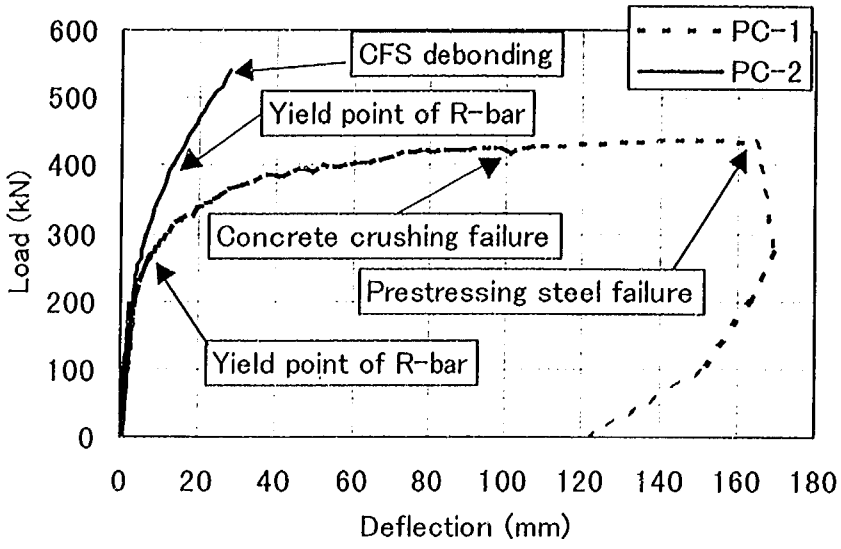


Fig.2.3 Relationship between Static Load and Deflection at the center of Girders

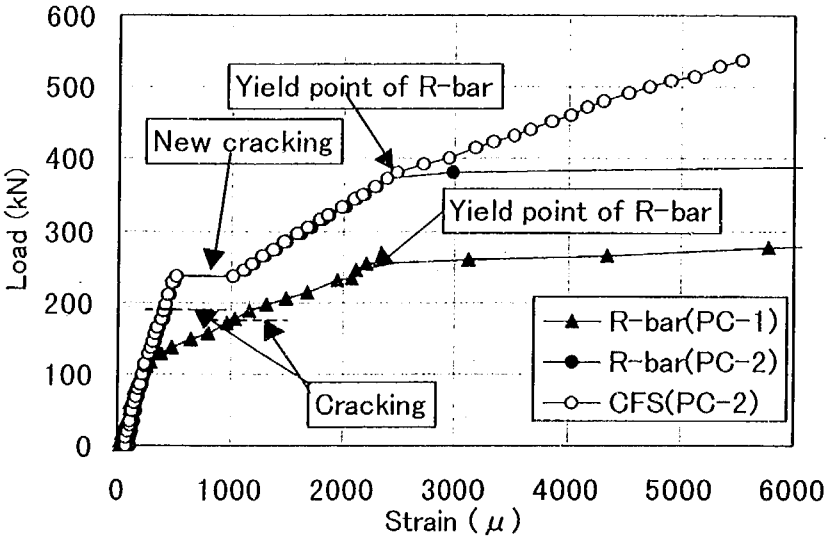


Fig.2.4 Relationship between Static Load and Reinforcement Strain at the center of Girders

3. Effect of Reinforcement of Shear Capacity of RC Girders

3.1 Background

Based on the experimental results of carbon fiber sheet closed wrapped around a columnar member, various studies were conducted to establish a method to evaluate seismic reinforcement against shear of reinforced concrete members. Accordingly, necessary steps are being taken to apply carbon fiber sheet bonding to columnar members. However, there are only a few cases of evaluating the behavior and reinforcement effect of attaching carbon fiber sheeting in U-shape or other styles onto the girder web and bottom for the purpose of shear reinforcement.

In our experiment, carbon fiber sheeting was bonded in a U-shape application onto the shear span of a real-sized RC T-shaped girder specimen to verify the shear

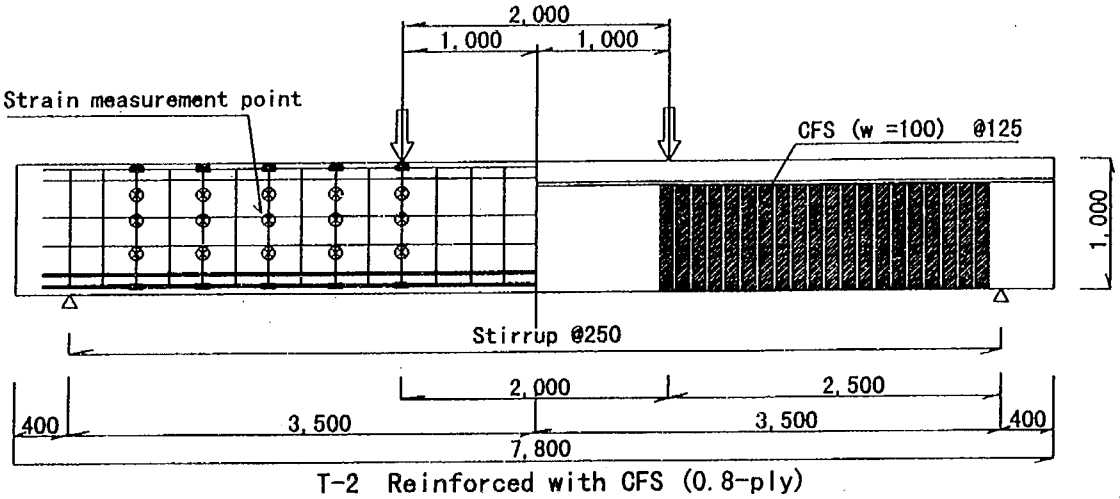
reinforcement effect. Since it was feared that the carbon fiber sheeting in a U-application might debond in the ultimate mode, the carbon fiber sheeting was anchored at ends to determine the effect on shear reinforcement.

3.2 Test Details

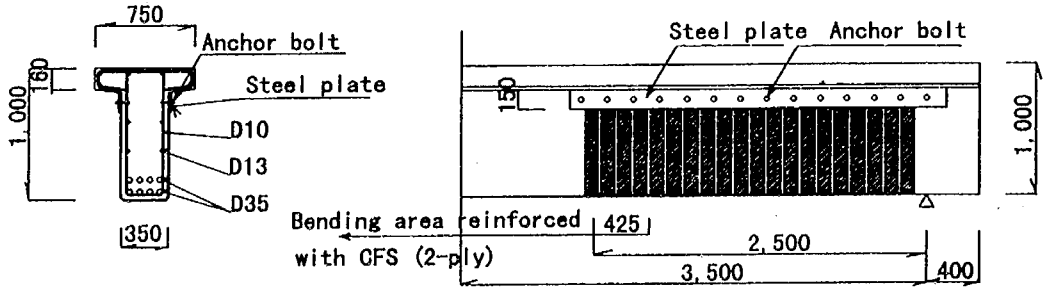
Table 3.1 shows the specimens used and Figure 3.1 shows their dimensions and reinforcement arrangements. The girder height was set to the height of a real-sized bridge girder so that the carbon fiber sheet bonding was reflected correctly. A shear span-depth ratio of 2.5 was chosen.

Table 3.1 Specimens

No.	Shear Reinforcement of CFS (200g/m^2), ply	Bending Reinforcement of CFS (300g/m^2), ply	Mechanical Anchorage
T-1	unreinforced	unreinforced	--------
T-2	0.8	unreinforced	--------
T-3	0.8	2.0	used
T-4	1.6	2.0	used



T-2 Reinforced with CFS (0.8-ply)



T-3 Reinforced with CFS(0.8-ply) and mechanical anchorage
T-4 Reinforced with CFS(1.6-ply) and mechanical anchorage

Fig.3.1 Dimensions and Reinforcement Arrangements of the RC Girders

T-1 is an unreinforced specimen and T-2 ~ T-4 are T-1 specimens with reinforcement. Carbon fiber sheeting was attached to the girder web and bottom of the T-2 specimen. T-3 and T-4 were prepared in the same way as T-2 but the sheeting was fixed

mechanically to concrete at the upper end of the web using steel plates and anchor bolts.

The test was conducted using carbon fiber sheeting having a modulus of elasticity 240 kN/mm^2 and tensile strength 3,430 N/mm^2. For the purpose of observing cracking and its progress during loading, the carbon fiber sheeting was applied in exactly the same manner on all specimens with the sheet width of 100 mm and center-to-center distance of 125 mm leaving a gap of 25 mm. Tests were conducted using the minimum amounts of carbon fiber sheet reinforcement. T-2 and T-3 used only a sheet of carbon fiber with the specific weight of 200 g/m^2 (lowest value for general use) to 0.8 layers (= 100/125). T-4 had 1.6 layers of carbon fiber sheet reinforcement (twice the T-3 reinforcement).

In the case of T-3 and T-4, it was expected that the ultimate shear resistance would increase because of the mechanical anchorage. Since flexural failure might occur first, flexural reinforcement was applied using two layers of carbon fiber sheeting (300 g/m^2) over the area of 425 mm from the net flexural section in the girder bottom to the inner span shear section.

3.3 Results and Discussion

Table 3.2 shows the test results. The unreinforced T-1 specimen reached shear failure at 1,330 kN. Debonding was observed in the reinforced T-2 specimen at 1,270 kN along the upper edge of the carbon fiber sheet. Diagonal crack occurred followed by progressive debonding between the carbon fiber sheet and the concrete starting with the smallest carbon fiber sheet bond area above the crack. The carbon fiber sheeting peeled at 1,480 kN and the specimen ultimately reached shear failure. The axial reinforcement bar of T-3 yielded at 1,570 kN and, at 1,780 kN, a sound was heard likely due to a local debonding of the carbon fiber sheeting for flexural reinforcement. After reaching the peak load of 1,830 kN, T-3 reached the ultimate mode when the carbon fiber sheeting for flexural reinforcement peeled at 1,720 kN. Similarly, the axial reinforcement bar of T-4 yielded at 1,570 kN. After reaching the peak load of 1,860 kN, T-4 reached the ultimate mode when the carbon fiber sheeting for flexural reinforcement peeled at 1,650 kN.

Table 3.2 Test Results

No.	Compressive Strength of Concrete, N/mm^2	Diagonal Cracking Load kN	Stirrup Yield Load kN	Maximum Load kN	Fracture Mode
T-1	27.8	442 (1.00)	710 (1.00)	1332 (1.00)	Shear failure
T-2	23.0	538 (1.22)	1039 (1.46)	1482 (1.11)	Shear failure after CFS of shear section peeled
T-3	27.1	574 (1.30)	1130 (1.59)	1833 (1.38)	Bending failure after CFS of flexural section peeled
T-4	27.3	623 (1.41)	1249 (1.76)	1859 (1.40)	Bending failure after CFS of flexural section peeled

The diagonal cracking load was determined for each specimen in reference to the crack progress observation chart, stirrup strain records, and measured tensile strength of

each specimen concrete. The increase ratio of diagonal cracking load of the reinforced T-2~T-4 specimens to that of the unreinforced T-1 was 22% (T-2), 30% (T-3) and 41% (T-4). The effect of mechanical anchorage upon the increase in the diagonal cracking load was estimated to be around 8% (the difference between 22% load increase on T-2 without anchorage and 30% on T-3 using the same amount of reinforcement as T-2 plus mechanical anchorage).

As shown in Table 3.2, the stirrup yield load was also increased by 46% (T-2), 59% (T-3), and 76% (T-4). In terms of the amount of carbon fiber sheet reinforcement, the load increase was 46 to 59% for the 0.8-layer reinforced T-2 and T-3 specimens and 76% for the 1.6-layer reinforced T-4 specimen. This indicates that a drastic gain in reinforcement effect can be obtained by extra reinforcement and that a greater gain results as the amount of reinforcement increases. The effect of mechanical anchorage upon increase in the stirrup yield load was 46% for T-2, and 59% for T-3 with the same amount of reinforcement as T-2 plus mechanical anchorage. We may say a 13% increase in the stirrup yield load was ensured by the mechanical anchorage.

Figure 3.2 shows the relationship between the estimated acting tensile force and load determined from the strain of carbon fiber sheet and stirrup at the point nearest to the diagonal crack and where the largest strain was observed (see Figure 3.1). The statements (1) through (4) below may be derived from this figure. In order to clarify the difference from the tensile force carried by the carbon fiber sheeting, the value of 1,867 μ was used for the sake of convenience when the stirrup strain exceeded the yield point 1,867 μ significantly and the load kept increasing.

(1) The carbon fiber sheeting barely carried the shearing force and the stirrup carried only a small portion of the tensile force up to the diagonal cracking load.
(2) The stirrup carried the shearing force as the load kept increasing immediately after diagonal cracking while the carbon fiber sheeting was somewhat slow in carrying the force.
(3) The carbon fiber tended to begin carrying more shearing force as the stirrup began carrying less force slightly before the stirrup yielded. The carbon fiber tended to keep carrying more shearing force in proportion to the increase in loading after the stirrup yielded. This tendency was linear and likely to continue until the specimen itself reached a shear failure as long as it was effectively anchored by a mechanical means.
(4) The rate of increase of the tensile force acting upon both the stirrup and the carbon fiber sheeting was evidently less when more shear reinforcement was used. We may assume that the shearing force sharing tendency of the carbon fiber sheeting after the stirrup yield can be increased significantly by increasing the amount of reinforcement as long as mechanical anchorage is used.

Now, while the fracture mode varied among the specimens, the increase ratio of maximum load was 11% (T-2), 38% (T-3), and 40% (T-4). Since it was observed during the test that the debonding of the carbon fiber sheeting progressed from near the crack with the progress of the diagonal crack, we may say the effect of the shear reinforcement by the carbon fiber sheet bonding on the increase in maximum load is contributable primarily to the mechanical anchorage that prevents complete peeling of the sheet rather than to the carbon fiber sheeting itself.

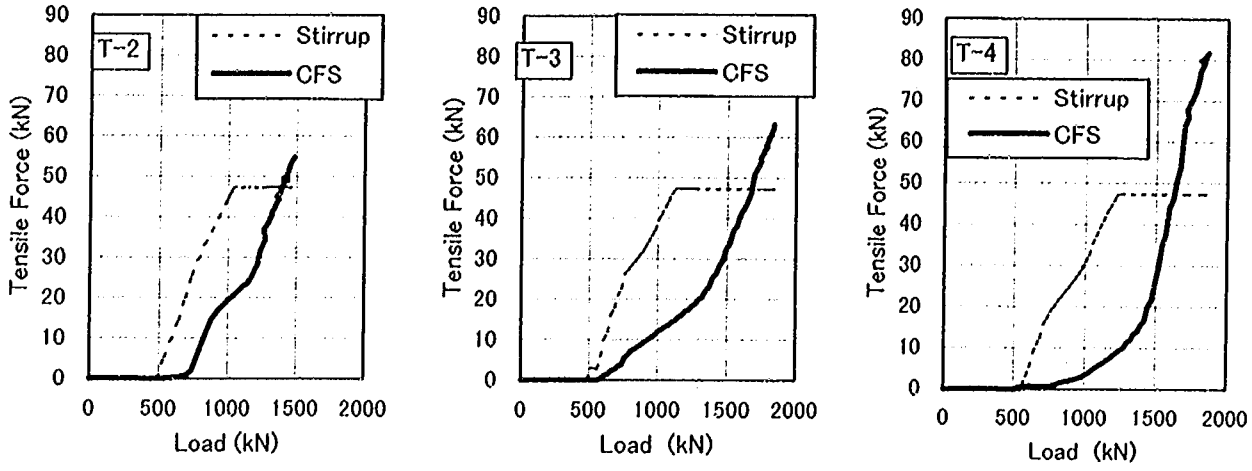


Fig.3.2 Estimated Tensile Force Carried by Carbon Fiber Sheet and Stirrup

4. Fatigue Durability of RC Slabs

4.1 Background

Wheel load running tests by stepped incrementing loading (hereinafter referred to as "stepped loading") have been conducted for the purpose of identifying the fatigue durability by bonding carbon fiber sheet to damaged RC slabs designed according to the 1964 Specifications for design of high way bridges (Ref. 2). A significant increase in fatigue durability has been verified on RC slabs designed to the old specifications but reinforced by carbon fiber sheet bonding. This is attributed, among other factors, to the cracking at the bottom of the slab being suppressed by the carbon fiber sheet.

The stepped loading is considered ideal for direct comparison of fatigue durability among various slabs. However, in the carbon fiber sheet bonding and other methods in which the bond performance between concrete and carbon fiber sheet plays an important role, it is thought that the debonding between concrete and carbon fiber sheet was promoted because a relatively larger load than a realistic load was applied just before the failure in the stepped loading tests.

This section of the paper concerns wheel load running tests by constant application of lower load (hereinafter referred to as "constant loading") conducted for the purpose of identifying fatigue durability of slabs reinforced by carbon fiber sheet bonding in simulation of actual load on bridges.

4.2 Test Details

Table 4.1 shows the specimens that were used in the test. RC slabs designed in accordance with the 1964 Specifications (hereinafter referred to as "S-1964") were used as the reference specimen. The S-1964 are known for lacking in necessary distributing reinforcement that caused damages.

Carbon fiber sheet reinforcement being applied to the S-1964 will require four layers of carbon fiber sheet (tensile strength 3400 N/mm^2, modulus of elasticity 230 kN/mm^2, fiber weight 300 g/m^2) each along the main reinforcement and along distributing

reinforcement assuming the bar stress of 140 N/mm^2 or less. Based on the results of past wheel load running tests by stepped loading, however, only two layers were used each along the main reinforcement and along distributing reinforcement (Refs. 1, 2). For the purpose of the test, a comparison of fatigue durability was made between the S-1964 and the RC slab designed in accordance with the present Specifications (hereinafter referred to as "S-1996") to determine the effect of reinforcement.

Table 4.1 Dimensions and bar arrangement of the slabs

No.	CFS ply main r-bar x dist. r-bar	Dimension of Slab W x L x t (cm)	Main Reinforcing Bar Upper column : Compressive Lower column: Tensile			Distribution Reinforcing Bar Upper column : Compressive Lower column: Tensile		
			Nominal diameter	Depth (cm)	Spacing (cm)	Nominal diameter	Depth (cm)	Spacing (cm)
S-1964	2 x 2	28x45x19 (span 250)	D16	3.00	30.00	D10	4.30	30.00
			D16	16.00	15.00	D13	14.55	30.00
S-1996	---	28x45x25 (span 250)	D16	4.00	15.00	D13	5.45	12.50
			D19	21.00	15.00	D16	19.25	12.50

Loading tests were conducted using a wheel load running machines. The specimens were held by simple support 2.5m apart and 500 x 200mm blocks were laid in a row over them to construct a rail so that an iron wheel (500mm wide) could move back and forth over the distance of $\pm$1.5m.

Prior to the test, the specimens were damaged (damage level II, Ref. 3) using the wheel load running machines to determine the reinforced fatigue durability of damaged RC slabs. Figure 4.1 shows cracks at the bottom of the pre-reinforced S-1964 in damage level II condition. After carbon fiber sheet bonding, the specimens were left for 7 days of no-load curing before wheel load running tests.

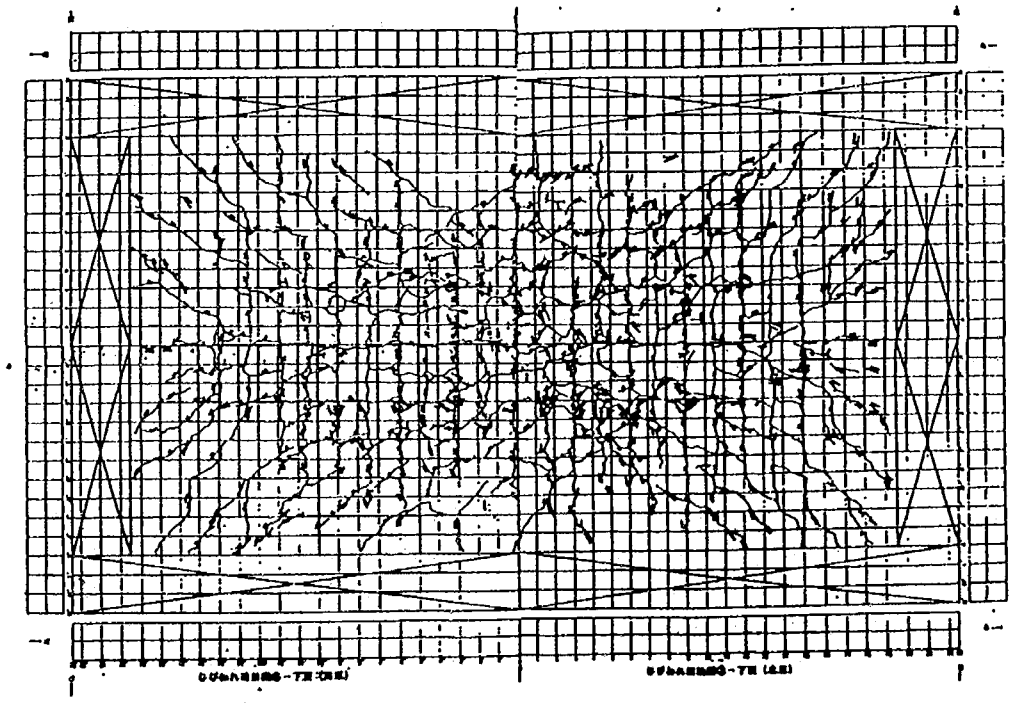


Fig.4.1 Crack Map of Level 2 Damaged Slab (S-1964)

Figure 4.2 shows the result (Ref. 1) of past wheel load running tests by stepped loading and the method of loading. During this past test, the S-1996 failed at stepped load 275 kN (255,649 cycles). The reinforced S-1964 failed at stepped load 255 kN (200,626 cycles) after bond failed between concrete and the carbon fiber sheeting at stepped load 235 kN. Based on these results, the load for testing the carbon fiber sheet bonded slab, S-1964, was decided as following:

The cycle number at the time of failure of the S-1996 under stepped loading was converted as a constant load (the 12.76th power of the S-N line gradient of the RC slabs) in reference to the past study (Ref. 4). As the result of conversion, the constant load for the reinforced S-1964 was decided to be 196 kN considering the bond failing load between concrete and carbon fiber sheet and the number of days spent for testing. This is equivalent to 2,880,000 cycles before failure for the S-1996 when converted at a constant load of 196 kN.

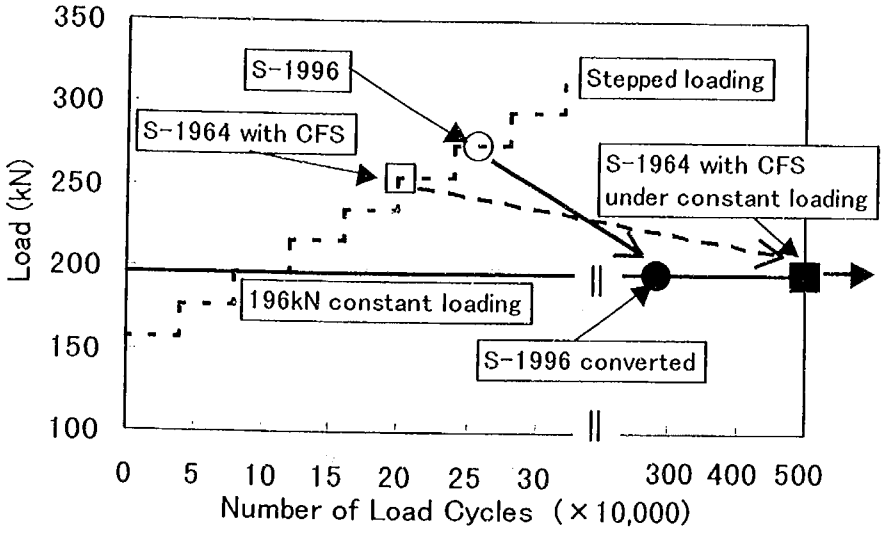


Fig.4.2 Past Test Results and Loading Program

4.3 Results and Discussion

Figure 4.3 shows the relationship between the test cycles after carbon fiber reinforcement and the live load deflection at the slab (S-1964) center and the live load strain of the main tensile reinforcement. The live load deflection increased slowly without any drastic change until loading ended at 5,000,000 cycles. The live load deflection tended to increase slightly after 1,750,000 load cycles, which nearly coincides with the 1,800,000 cycles at which point debonding between concrete and the carbon fiber sheet was observed in a hitting inspection. The live load strain also was basically stable without a noticeable change although it tended to decrease slightly.

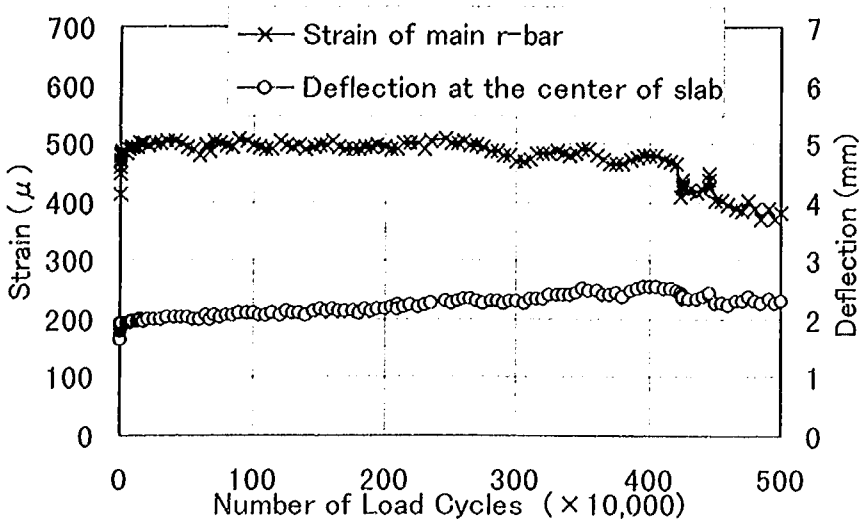


Fig.4.3 Relationship between Cycles and Live Load Deflection and Strain at the center of reinforced Slab (S-1964)

Ultimate fracture was not observed at the end of 5,000,000 load cycles. Partial debonding between concrete and the carbon fiber sheet was seen near the slab center at about 1,800,000 cycles and the carbon fiber sheet was debonding at many places after the loading test (see Figure 4.4). A close examination of the sections cut out after the loading test revealed diagonal crack in the central section along the main reinforcement.

The same specimen (S-1964) showed bond failure between concrete and carbon fiber sheet over a large area just before fracture (200,626 cycles at 255 kN) in the stepped loading test. In contrast, only small bond failure increased gradually in the constant loading test.

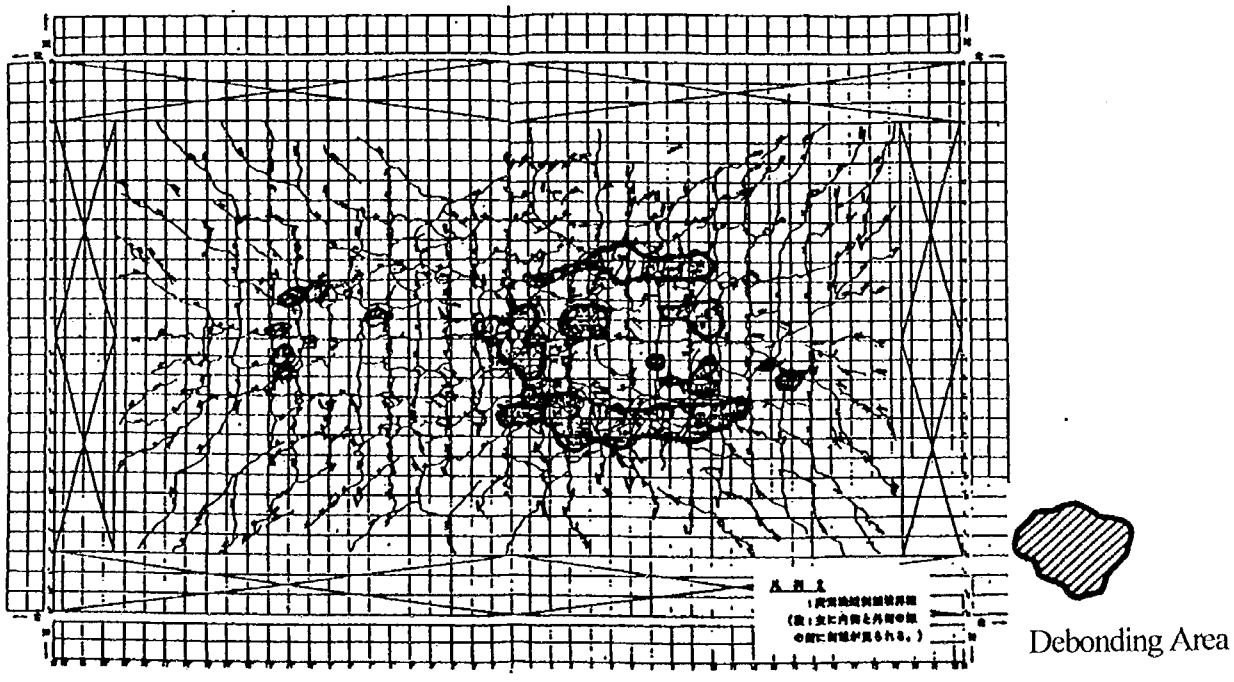


Fig.4.4 Crack Map of the Slab after Fatigue Test (S-1964)

5. Conclusions

(1) The increase in the live load deflection at fatigue subjected to cracking load was suppressed in the PC girders by flexural reinforcement provided by carbon fiber sheet. The static test after the fatigue test also revealed an increase in both the reinforcement bar yield load and the maximum flexural resistance. This endorsed the effect of the reinforcement when crack was permitted.

(2) In the shear reinforcement by the carbon fiber sheet bonding, the reinforcement itself provided the reinforcing effect against the diagonal cracking load. The mechanical anchorage at the edges of the carbon fiber sheet tends to further increase this reinforcing effect. An increase in the amount of carbon fiber sheeting and the use of mechanical anchorage tend to increase the reinforcing effect against the stirrup yield load. Mechanical anchorage is necessary in order to produce reinforcing effect against the maximum load.

(3) It was verified in the test that the RC slabs, designed and fabricated under old standards and damaged prior to reinforcement by carbon fiber sheet bonding, had basically the same fatigue resistance as that of the slabs per S-1996 as converted by a constant loading test. It was also verified that the carbon fiber sheet bonding provides sufficient reinforcement for existing, damaged RC slabs. The tests were conducted using carbon fiber sheet reinforcement in the less number of layers than those designed based on the allowable stress of the reinforcement bars. But the test results indicated that the reinforcement provided sufficient fatigue resistance

Acknowledgements

The authors wish to thank Mr. Nishikawa, Mr. Uchida and Mr. Matsuo, et al. in the bridge division Public Work Research Institute for their helpful advice; the authors also would like to express their appreciation to Dr. Koga and Dr. Uji, et al. in the CFRRA.

References

(1) Akira Kobayashi, et. al.; Study on The Reinforcement of Bridge Superstructures by Carbon Fiber Sheet Bonding, the Proc. of 14th U.S.-Japan Bridge Workshop, Pittsburgh, November. 1998

(2) Shinji Matsuo, Kazuhiro Nishikawa, Kenichi Uchida; A Study on Fatigue Durability of Existing RC slabs Strengthened by Carbon Fiber Sheets Bonding Method, the Proc. of 1st Symposium on Decks of High-way Bridges of Japan society of civil engineering, November.1998,(in Japanese)

(3) Ministry of Construction; Bridge Inspection Instruction (draft)", Technical report No2651, Public Work Research Institute, 7.1988, (in Japanese)

(4) Shigeyuki Matsui, et. al., Fatigue Test of RC Deck of High-way Bridges used during 23 years, the Proc. of the 48th Annuals of Japan Society of Civil Engineering,1986 (in Japanese)

FRP COMPOSITES FOR BRIDGE ENGINEERING

John B. Scalzi[1]

Abstract

FRP composites have mechanical properties which may be beneficial and advantageous for design of bridges. The application of these advanced fiber reinforced polymers {FRP} are currently being used for demonstration projects for repair / retrofit / rehabilitation of existing bridges and a few new installations. The future applications of these materials / products will depend upon the development of the appropriate standards and performance criteria. The need for research is emphasized for the development of the necessary standards. Only with proper standards will the FRP composites become another material available for the construction of bridges.

Introduction

The advent of FRP composites as a constructional material has stimulated a great deal of interest from researchers and bridge engineers. The material may have great potential for use in bridge engineering. Much research has been performed and many demonstration bridges have been constructed. The future applications for the FRP composites becomes an important concern for design engineers.

The reason for concern is the fact that the construction industry operates on the specific need for ASTM standards for all products to be used in the construction project. This requirement is necessary to comply with the bid process for awarding bridge contracts.

Current Practice

A bridge designer must rely on the minimum engineering properties of materials as defined by ASTM standards. He must also know that the product is the same regardless of the supplier and there must be at least three suppliers to comply with the bidding process. This practice is of long standing in the construction arena.

All construction materials must be ASTM approved standards. At the present time there are no such standards for the FRP materials / products. Consequently, these materials / products will not be generally acceptable to the design engineers. Special demonstration cases may be required to illustrate a specific application.

---

[1] Program Director, National Science Foundation, Arlington, Virginia.

Research Needs

Current academic research is investigating the structural behavior of various FRP composite products for the design of bridges. These studies are focusing on the total performance of the product with less consideration to the composition of the material constituents. Without a detailed description of the product the results of the research will be limited in use. The results will not be sufficient to compare with other similar type research results or be capable of replication by other researchers. Therefore, each project will be considered as one of a kind lacking comparison with other research results.

It is insufficient to simply state the ultimate tensile strength and modulus of elasticity to describe the product. Other factors should be included such as: type of fiber and matrix, ratio of fiber to matrix, density, manufacturing process, effect of accidental damage to the product, creep, relaxation, fire, temperature effects, environmental effects and other pertinent data for design of bridges. This type of data is required for design purposes and for condition assessment of the material and product in future years.

Researchers may be well advised to coordinate their research activities more closely in order to develop the type of data required to establish standards and criteria for general applications. It is the practice in construction that the designs will be facilitated and simplified by using well-defined components that are ASTM standards with established minimum engineering properties.

Current research and demonstration projects should document fully the composition of the product and how it was produced for future assessment. Without this information it may be impossible in future years to compare performance of different products. Such important features as ductility, fatigue and other pertinent data will be difficult to assess.

There is a great need for coordinated research activities between researchers from different countries in order to avoid duplication and to build upon each other's research results. There is an urgent need for continuous monitoring of bridge behavior to obtain data on details for design such as: durability, fatigue, environmental effects, etc. There is always the need to provide assurance to owners of bridges, data to amend specifications, codes, and design procedures.

Although there are many bridges that have been repaired/retrofitted it is acknowledged that these are demonstration projects to illustrate the potential use of FRP composite products for bridge engineering. The time has come to develop material / product standards, testing methods, quality assurance and minimum engineering values for design. These standards are required if FRP composite products are to be considered for construction projects.

Standard for Fibers

A research program similar to that which the steel and concrete industries performed to produce their products is required for the FRP composite products. Research data and field applications have demonstrated the feasibility of the products for infrastructure applications. Standards must now be established for general applications.

The research needed involves performing a sufficient number of tests to provide data to establish minimum engineering values for design consideration. For the product to be sufficiently defined, the test specimens should be supplied by several different producers fabricated with the identical process. Catalysts may vary. These standards may then be used for quality assurance for future products. Fibers and matrix should be the most economical to produce in order to be competitive in the construction market.
The standards will serve as benchmarks for other combinations and manufacturing processes.

The type of data to be obtained should include consideration of: wet and dry conditions, maximum strain, tensile strength, modulus of elasticity, creep, fatigue, relaxation, temperature effects, fire resistance, durability, notch effects, etc.

Resin

Resins to be used are those which are most likely to be competitive and provide the required engineering properties for bridge design. The resins should be tested in the same manner as the fibers with respect to the desired data.

Laminates

Because laminates are currently being used for repair/retrofit of existing structures, they should become standardized for general acceptance for use by design engineers. The objective of the standard is to establish guaranteed minimum values for design.

Tests to be conducted are similar to those for fibers, resins and laminates. Sufficient number of tests should be performed to establish meaningful values. Most economical combinations of fiber and matrix should be investigated. Method of manufacture should be the same or proved to be equivalent. Directions of fibers should be investigated for the various angles important for design purposes. All types of conditions should be investigated. The results of the tests will establish minimum engineering values for design to be included in the ASTM standard

Applications

At the present time tests are required for each application in order to prove the product worthy of the use to which it is being applied. Repair methods using adhesives should be competitive and economical and provide the required strength and environmental protection desired by the design. Bridge decks consisting entirely of FRP products must be tested for each application. The products should be described in sufficient detail to assure structural integrity for

future applications. In essence this description is a standard. The individual components should be ASTM standards. As an assemblage the deck must satisfy specified performance requirements, which as yet, are not available.

Summary

FRP composites have engineering properties that appear to be beneficial for application to bridge construction. Currently they are being used for repair/retrofit of existing deteriorating bridges of steel and concrete. A few short span bridges have been constructed entirely of FRP composite products. These are considered demonstration projects indicating the feasibility of the FRP products for infrastructure uses. Research activities are required to establish ASTM standards. Cooperation between nations would be very desirable to hasten the adoption of standards for FRP composite materials for bridge construction.

SESSION 9: WIND AND VIBRATION

(1) Flutter Characteristics of a Super Long-Span Bridge
(Hiroshi Sato, Shigeki Kusuhara and Nobuaki Furuya)

(2) Aerodynamic Stability of the Cable Stayed Bridge with New Type of Twin Girder
(Kensaku Hata, Masahiro Koike and Takumi Uno)

(3)Vibration Test of the Tatara Bridge
(Kazunori Yamaguchi)

(4) Damping Characteristics of Prestressed Concrete Cable-Stayed Bridges Based on Measured Data
(Shinichi Yamanobe, Yuji Niihara and Tesuo Takeda)

(5) Monitoring of Hakucho Suspension Bridge using Ambient Vibration
(Yozo Fujino, Masato Abe, Hajime Shibuya, Masato Yanagihara and Masashi Sato)

FLUTTER CHARACTERISTICS OF A SUPER LONG-SPAN BRIDGE

Hiroshi Sato[1], Shigeki Kusuhara[2] and Nobuaki Furuya[3]

ABSTRACT

Aerodynamic stability is one of the most important themes in the design of super long-span bridge. In order to improve the aerodynamic stability, various researches were conducted and it was confirmed that slotted box girder with some devices shows the good aerodynamic stability. In this paper, the results of flutter analysis (2-dimensional and 3-dimensional) for a super long-span bridge, whose main span is 2.8km, are described and compared with the results of a full model wind-tunnel study.

1. INTRODUCTION

There are some ideas of strait crossing road projects in Japan. In these projects, super long-span bridges larger than Akashi Kaikyo Bridge may be needed. In order to realize a super long-span bridge, aerodynamic stability is one of the most important themes. Furthermore, it is also required to reduce construction cost. Therefore, Public Works Research Institute and Honshu-Shikoku Bridge Authority have been conducting cooperative study on super structure of super long-span bridges that have aerodynamic stability and economical efficiency.

Slotted box girder, which has center-barrier and guide-vane, was found to have good aerodynamic characteristics. We applied the slotted box girder to a super long-span bridge whose main span is 2.8km, and confirmed its safety to flutter. In this paper, the measured unsteady aerodynamic forces and the results of 2-dimensional flutter analysis are described first. Then, the result of full bridge model wind-tunnel test and 3-dimensional flutter analysis are shown.

---

1 Head, Structure Division, Public Works Research Institute, Ministry of Construction, Japan

2 Senior Research Engineer, ditto

3 Manager, Engineering Management Division, Long-span Bridge Engineering Center, Honshu-Shikoku Bridge Authority, Japan

2. BASIC FLUTTER CHARACTERISTICS OF SLOTTED BOX GIRDER

From the previous paper[1], it was found that the flutter characteristics of slotted box girder are improved by installing center barrier and guide vane. Then, we proposed stiffening girder whose cross section is shown in Fig. 1. This box girder has 4-lanes, whose 2-lanes are on the grating installed on the slot in consideration of economical efficiency. We measured unsteady aerodynamic forces using the section model of this box girder whose scale was 1/85.

In super long-span bridges, torsional rigidity may decrease and torsional deformation may become large. Therefore, angle of attack for measurement of unsteady aerodynamic forces was every degree in the range to 0 to -12 degrees. The defined coordinate system is shown in Fig.2. The conditions of measurement are shown in Table 1. Coefficients of the unsteady aerodynamic forces were defined as follows:

$$L=\pi\rho\{B^2[L_{ZR}\omega^2 z + L_{ZI}\omega z'] + B^3[L_{\theta R}\omega^2\theta + L_{\theta I}\omega\theta']\} \quad (1)$$

$$M=\pi\rho\{B^3[M_{ZR}\omega^2 z + M_{ZI}\omega z'] + B^4[M_{\theta R}\omega^2\theta + M_{\theta I}\omega\theta']\} \quad (2)$$

where, L: lift, M: aerodynamic moment, z: vertical displacement, θ: torsional displacement, ω:circular frequency, ( )':d( )/dt, L_{xx} or M_{xx}: coefficients of unsteady aerodynamic forces (z: caused by vertical vibration, θ:caused by torsional vibration, R:in phase with displacement, I:in phase with velocity)

The measured coefficients are shown in Fig.3. These figures show that the value of a coefficient is influenced of angle of attack. Especially, $M_{\theta I}$, which influences flutter characteristic greatly, became positive when the angle of attack was -7 to -9 degrees.

Then, 2-dimensional flutter analysis was performed with measured coefficient of unsteady aerodynamic forces. Analysis conditions are shown in Table 2. The result of analysis is shown in Fig.4. This figure shows that flutter characteristic is getting worse when the angle of attack was about -7 degree where $M_{\theta I}$ becomes positive. The triangle mark (△) of Fig.4 is a result of a spring-supported test. Analytical values agree fairly well with the experimental value. Therefore, it was decided that the measured coefficient is applicable for flutter analysis.

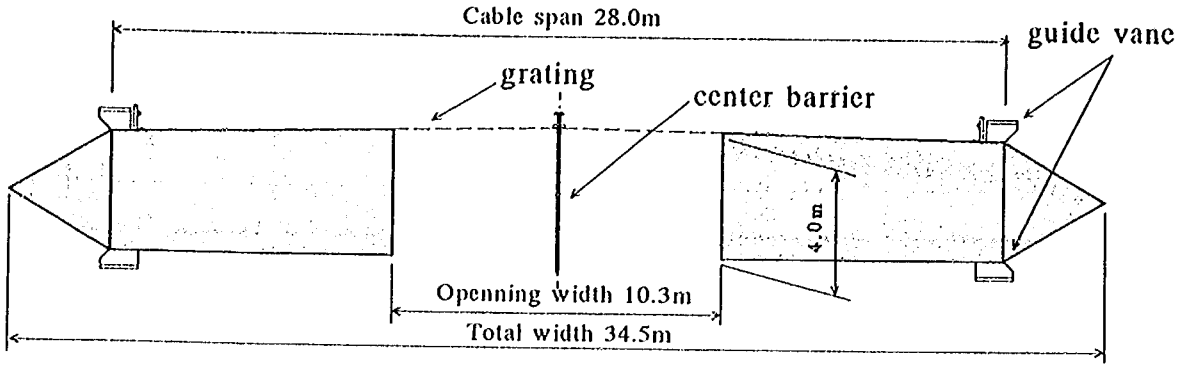


Fig. 1 Slotted box girder

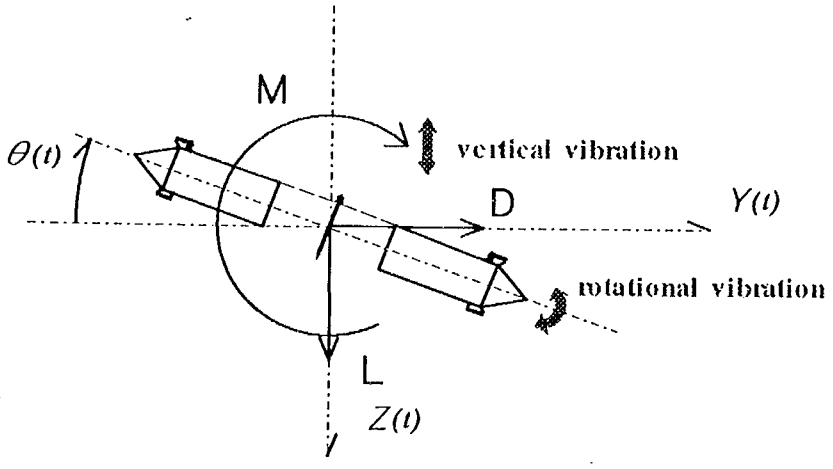


Fig. 2 Coordinate system for unsteady aerodynamic forces

Table 1 Condition of measurement

Wind velocity	8m/s or 14m/s	
Amplitude of vibration	Vertical	±4mm
	Torsional	±1deg.
Frequency	0.5Hz - 3.5Hz	

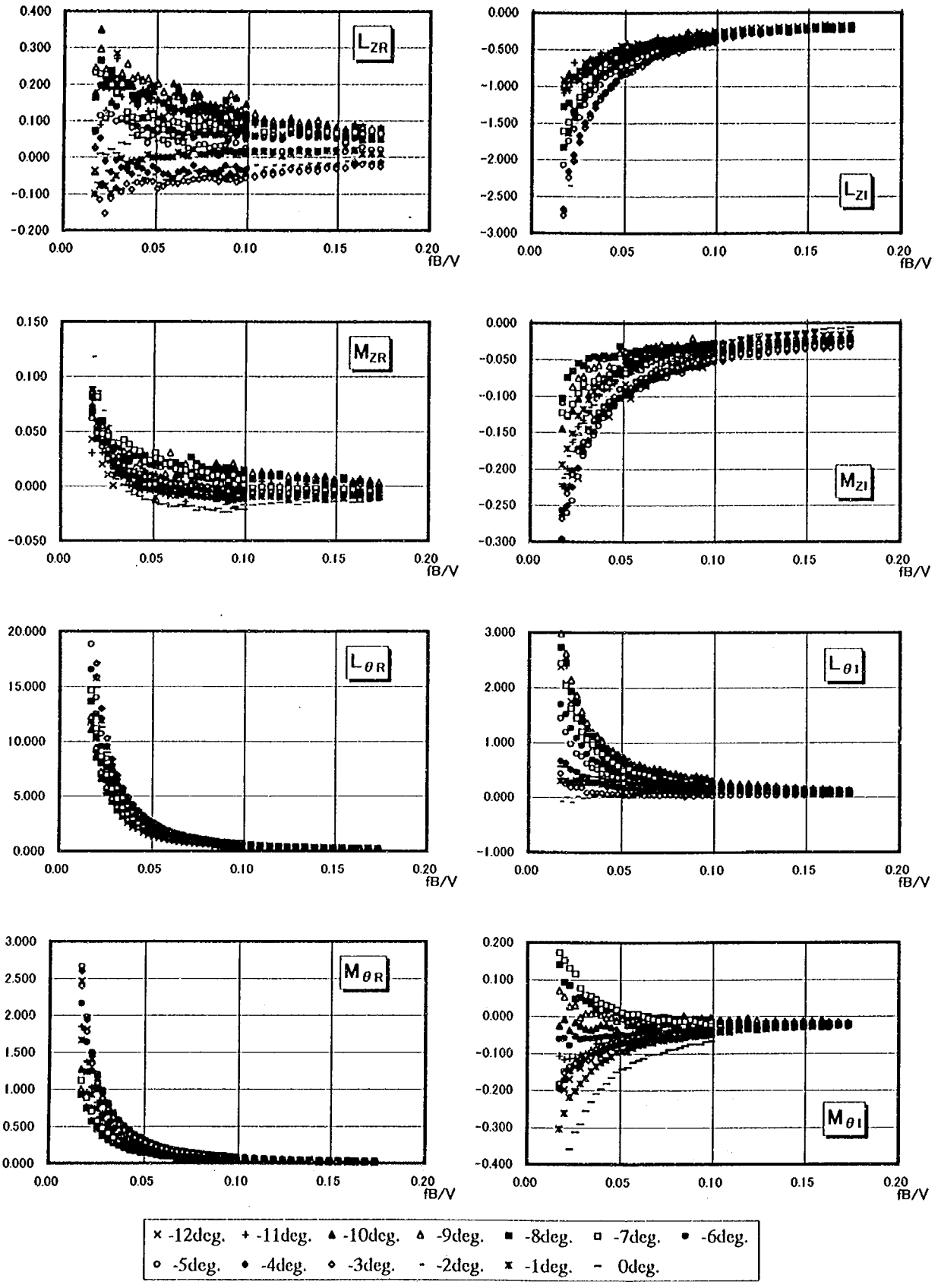


Fig.3 Coefficient of unsteady aerodynamic forces

Table 2 Analysis condition

Mass of dead load		m	0.215kg/m
Polar moment of inertia		I_p	0.00246kg·m²/m
Girder size	Width	(B)	0.276m
	Depth	(D)	0.032m
Frequency	Vertical	f_z	0.674Hz
	Torsional	f_θ	1.312Hz
	Ratio	f_θ/f_z	1.96

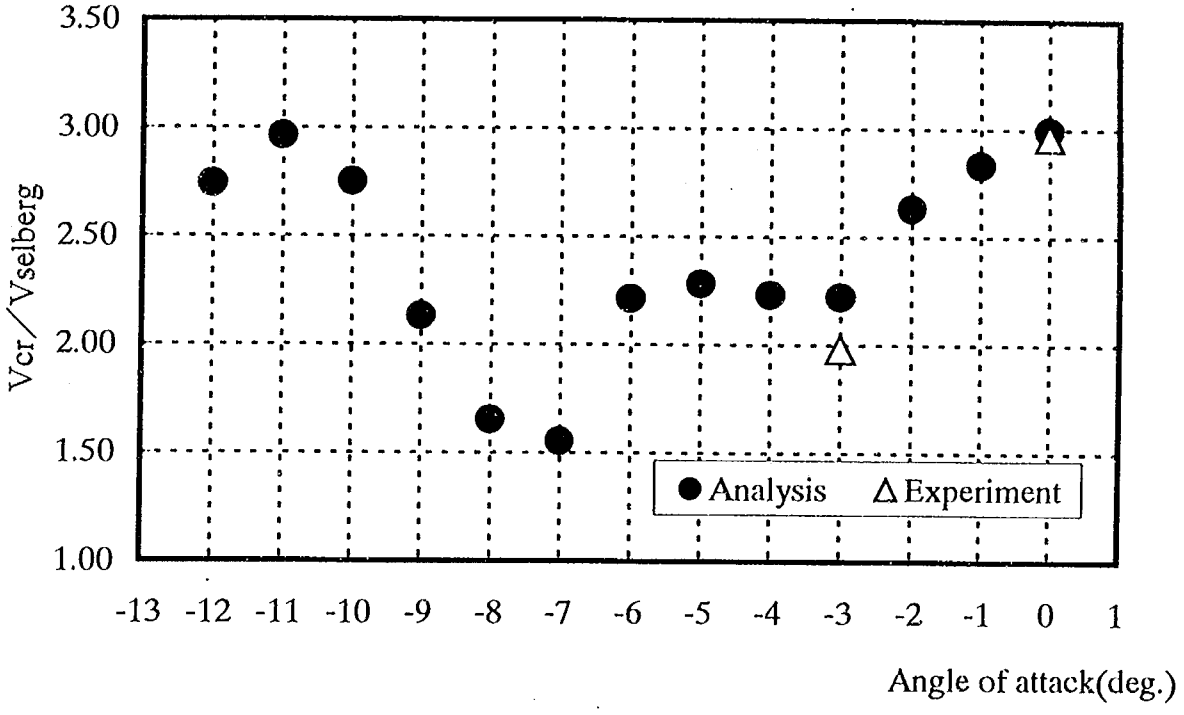


Fig.4 The result of 2-dimensional flutter analysis

3. FULL BRIDGE MODEL TEST

Full bridge model test was performed in smooth flow, to confirm flutter stability of a super long-span bridge that has the slotted box girder. We assumed a generic super long-span suspension bridge whose main span length is 2.8km and total length is 5.0km (Fig.5). Structural dimensions of the full scale bridge and the model are shown in Table 3, and the scale ratio of the model was 1/125. Because we did not want to change the aerodynamic characteristic of slotted box girder, we did not put the stiffness bar into the part of slot. Therefore, we used two aluminum bars whose vertical bending stiffness was almost similar to that of each box. Although the horizontal bending stiffness per box was smaller than the requirement value, we adjusted the stiffness by horizontal beams which connected the stiffness bar at the hanger rope position, and the overall stiffness was made to match the required values.

Static deformation by wind load is shown in Fig.6. The center of main span shows large horizontal deformation (leeward side) and large torsional deformation (head down) with the increase in wind velocity.

Logarithmic decrement in each wind velocity is shown in Fig.7. Logarithmic decrement increased gradually with the increase in wind velocity, and began decreasing from wind velocity of about 6m/s. After that, logarithmic decrement decreased, and changed to negative value at 8.8m/s, and flutter started. The scale ratio of wind velocity was the square root of the scale ratio of length. Therefore, this critical wind velocity was equivalent to about 100m/s on a full scale. However, because the model did not match completely with required dimensions, actual critical wind velocity for flutter needs some modification.

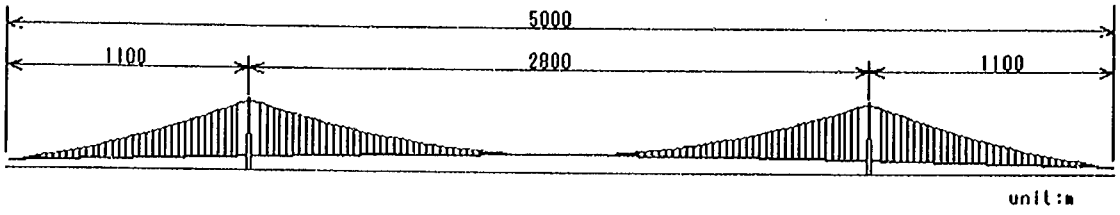


Fig.5 The Model of super long-span bridge

Table 3 Structure dimensions of super long-span bridge

			Real scale	Required value (a)	Full bridge model (b)	(b)/(a)
Scale			–	1/125	1/125	–
Mass of Dead load		m	28.41t/m	1.818kg/m	2.100kg/m	1.156
Polar moment of inertia		I_P	388t·m²/m	0.00159kg·m²/m	0.00246kg·m²/m	1.547
Girder size	Width	B	34.5m	0.276m	0.276m	1.000
	Depth	D	4.0m	0.032m	0.032m	1.000
Stiffness	Vertical	EI_V	1.707kNm²/box	9.384Nm²/box	12.277Nm²/box	1.308
	Holizontal	EI_H	3.107kNm²/box	48.828Nm²/box	12.277Nm²/box	0.251
	Torsional	GJ	1.090kNm²/box	6.906Nm²/box	6.853Nm²/box	0.992
Natural frequency	Vertical	1st	0.0621Hz	0.693Hz	0.674Hz	0.973
		2nd	0.0990Hz	1.111Hz	1.106Hz	0.995
		[1st]	0.0610Hz	0.683Hz	0.703Hz	1.029
		[2nd]	0.0831Hz	1.499Hz	1.494Hz	0.997
	Torsional	1st	0.1256Hz	1.369Hz	1.321Hz	0.965
		[1st]	0.1466Hz	1.600Hz	1.597Hz	0.998
	Holizontal	1st	0.0316Hz	0.352Hz	0.352Hz	1.000
		[1st]	0.0550Hz	0.502Hz	0.491Hz	0.978

[ ] means asymmetry mode

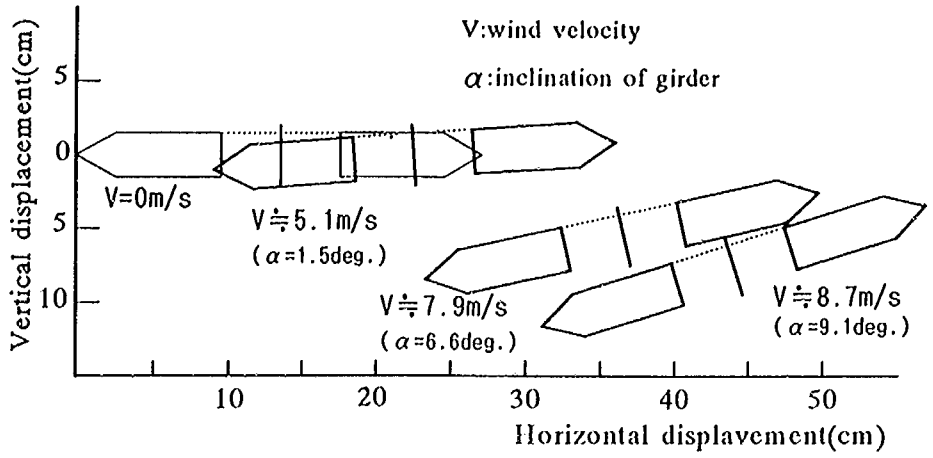


Fig.6 Deformation of girder

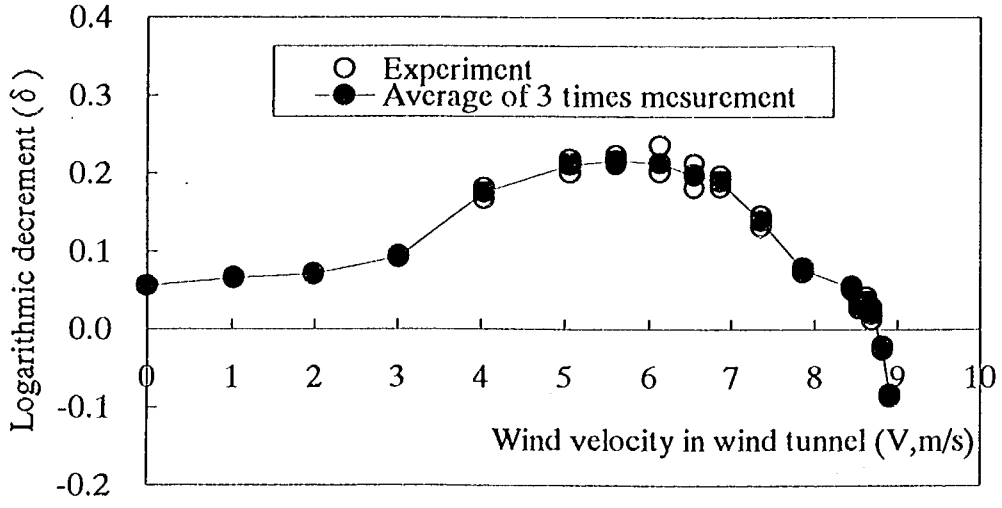


Fig.7 Apparent damping – wind velocity (Test result)

4. 3-DIMENTIONAL FLUTTER ANALYSIS

3-dimentional flutter analysis for the full bridge model was performed by using the coefficient of unsteady aerodynamic forces obtained by section model test. Dimensions of analysis were almost same as those of the model as is shown in Table 4. Model of analysis is shown in Fig.8.

Although analysis value is a little smaller than experiment value in torsional deformation, the analytical results on static deformation by the wind agree well with the experimental results (Fig.9). We performed flutter analysis on the conditions shown in Table 5. The analysis program was the same as that was used for Akashi Kaikyo Bridge. In the analysis, vibrational modes in still air were used, and the effects of static deformation were considered.

The result of analysis is shown in Fig.10. The analysis results of all modes were plotted by square mark (□), because we could not identify the logarithmic decrement for each mode. The result of 3-dimentional flutter analysis was 7.8m/s. It was a little smaller than an experiment result (●;8.8m/s).

From this, it was confirmed that flutter analysis was applicable to a super long-span bridge which main span is approximately 3km. However, when the super long-span bridge deformed by the wind load, vibrational modes might change. Therefore, we are going to perform analysis using the vibrational modes in wind.

Table 4 Dimensions of analysis for super long-span bridge

			Full bridge model(a)	Analysis model(b)	(b)/(a)
Mass of Dead load		m	2.100kg/m	2.100kg/m	1.000
Polar moment of inertia		I_p	0.00246kg·m²/m	0.00246kg·m²/m	1.000
Girder size	Width	(B)	0.276m	0.276m	1.000
	Depth	(D)	0.032m	0.032m	1.000
Natural frequency	Vertical	1st	0.674Hz	0.669Hz	0.993
		[1st]	0.703Hz	0.681Hz	0.969
	Torsional	1st	1.321Hz	1.310Hz	0.992
		[1st]	1.597Hz	1.736Hz	1.087
	Holizontal	1st	0.344Hz	0.345Hz	1.003
		[1st]	0.491Hz	0.487Hz	0.992

[ ] means asymmetry mode

Table 5 The conditions of flutter analysis

Item	Analysis condition
Analytical method	Mode conbination method. Using lower 50 modes.
Air density	0.12 kg/m³
Structural damping	All modes δ =0.02
Coefficient of aero-dynamic forces	Main girder Vertical / Torsional / Horizontal Lift: ○ / ○ / △ Moment: ○ / ○ / △ Drag: ○ / ○ / △ ○;Unsteadey aerodynamic forces △;Quasi-steady aerodynamic forces Cable Quasi-steady drag force and lift force (C_D=0.7) Tower Not considered

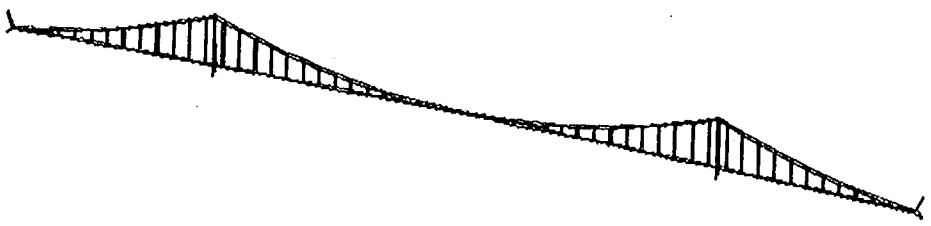


Fig.8 Analysis model for super long-span bridge

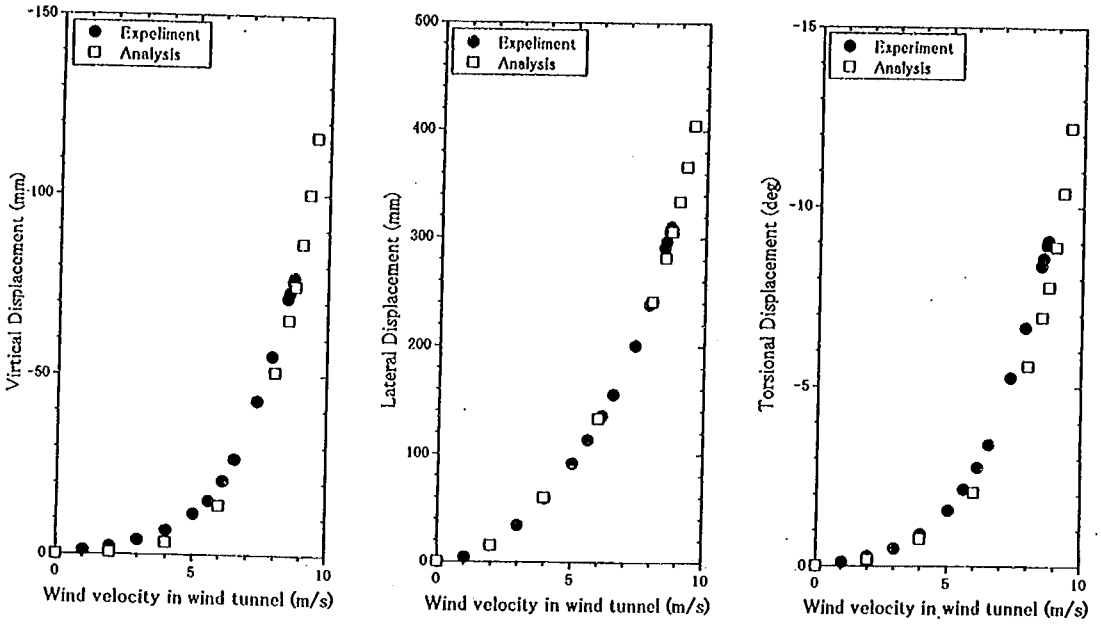


Fig. 9 Deformation of analysis model and experiment

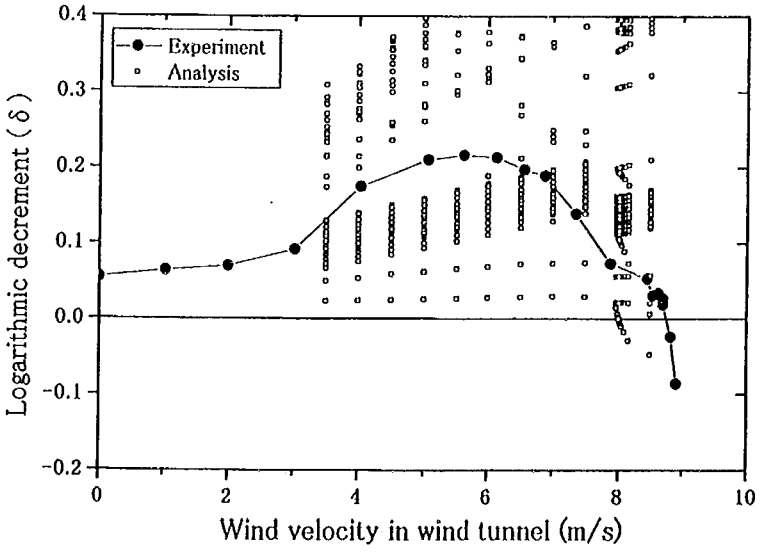


Fig.10 Apparent damping – wind velocity (Analysis result and test result)

5. CONCLUSIONS

1) We proposed a super long-span bridge with slotted box girder, which has center-barrier and guide-vane. It has good aerodynamic stability. And it is very economical, because 2-lanes are on the grating installed on the slot.

2) Flutter characteristic was greatly influenced by angle of attack. Therefore, in the flutter analysis of super long-span bridges, which deform remarkably, the effect of angle of attack should be considered appropriately.

3) It is possible to use 3-dimensional flutter analysis for the prediction of the flutter characteristic of super long-span bridges.

Hereafter, we are planning to perform the following researches on the super long-span bridge with slotted box girder using Large Boundary Layer Wind Tunnel Laboratory.

a) aerodynamic characteristic in turbulent flow.

b) aerodynamic stability of the main tower.

c) aerodynamic stability at the erection stage.

REFERENCES

1) H. Sato, S. Kusuhara, K. Ogi and H. Matsufuji, "Aerodynamic characteristics of super long-span bridges with slotted box girder", Proceedings of the 10th International Conference on Wind Engineering, 1999.6, pp.1049-1054

Aerodynamic Stability of the Cable Stayed Bridge with New Type of Twin Girder

Kensaku HATA[1], Masahiro KOIKE[2], and Takumi UNO[3]

Abstract

Hanshin Expressway Public Corporation is now considering to use some new type of girders, such as two box girders with steel deck, steel pipe girders, and two steel box girders with pre-stressed concrete deck, for a new cable stayed bridge with a center span of about 600m. These girders are developed to reduce the cost of construction of the bridges, because, recently, it becomes very important to reduce the cost of construction of the infrastructure in Japan.

To examine the aerodynamic stability of these girders, investigation including wind tunnel test was conducted. The aerostatic force coefficient and unsteady aerodynamic force coefficient were measured with wind tunnel test, and flutter analysis to estimate the critical flutter wind velocity was conducted with unsteady aerodynamic force coefficient.

The results of the wind tunnel tests and flutter analysis are reported.

1. Introduction

Hanshin Expressway Public Corporation (H.E.P.C.) is planning to construct a cable-stayed bridge with a center span of about 600m, and conducting design and investigation for this bridge.

Recently, it has become very important in Japan to reduce the construction cost of the infrastructure. So, it is required that this cable-stayed bridge with a long span should be constructed cheaper than before.

H.E.P.C. has developed some new type of girders, such as two box girders with steel deck, steel pipe girders, and two steel box girders with pre-stressed concrete deck, for this cable-stayed bridge, and it will be possible to reduce the construction cost of the bridge with these types of girders.

H.E.P.C. has conducted investigation for the feasibility of these new types of girders, and the aerodynamic stability was one of most important issues in this investigation.

The aerodynamic stability of these types of girders was confirmed as following.

First, wind tunnel tests were conducted to measure the aerostatic force coefficient and unsteady aerodynamic force coefficient. Then, flutter analysis to estimate the critical flutter wind velocity was conducted with unsteady aerodynamic force coefficient.

In this report, the outline of these new types of girder, and the result of the wind tunnel tests and flutter analysis are reported.

---

[1] Deputy Manager of the Design Division, Hanshin Expressway Public Corporation

[2] Manager of the Design Division, ditto

[3] Engineer, Survey Division of the Second Kobe Construction Department, ditto

2. Outline of the New Cable-Stayed Bridge and New Types of Girders.

Fig. 1 shows the general plan of this cable-stayed bridge. This bridge has a center span of 610 meters and carries 6 lane highway. H.E.P.C. has conducted design and investigation for this bridge, but Japanese government has not ordered to construct this bridge yet.

Three new types of girder are proposed to reduce the construction cost of this bridge, and those are two box girders with steel deck (Fig. 2), steel pipe girders (Fig. 3), and two steel box girders with pre-stressed concrete deck (Fig.4).

The two box girder with steel deck plan is almost same as the conventional two box girder used many cable-stayed bridges. However, the detail of the anchor block for the cable at girder and that of the steel deck are different. The main towers are not steel structures, but reinforced concrete is used for the main towers.

The steel pipe girder plan is a composite structure. The ordinary steel pipes are used for the main girder, and the pre-stressed concrete panel is used for the deck. The cost for the steel pipe is much cheaper than the ordinary steel structure, and it is possible to reduce the construction cost of the bridge with this type of girder. The pipe girders and pre-stressed concrete deck slab are connected with dowel as a composite girder. The main towers are concrete structure same as the twin box girder plan.

The two steel box girders with pre-stressed concrete deck plan is also a composite structure. Two box girders with simplified cross section are placed at the end of the girder, and the cables are anchored directly to these girders. Pre-stressed concrete panels are used for the deck. The box girders and pre-stressed concrete deck slab are connected with dowel as a composite girder. The main towers are concrete structure same as the above-mentioned plan.

3. Aerostatic Force Coefficient of Each Section

3.1. General

Aerostatic force coefficient, drag force coefficient, lift coefficient, and pitching moment coefficient, of the each cross section was measured with wind tunnel tests.

The aerostatic force coefficient was measured with smooth flow. Two kinds of wind velocity were used for this smooth flow to confirm the effect of Reynolds number. The angle of attack was varied from –10 degrees to 10 degrees.

3.2. Aerostatic force coefficient for the two box girders with steel deck

Fig. 5 shows the aerostatic force coefficient for the two box girders with steel deck.

The drag coefficient at the angle of attack of 0 degree is 0.78. The drag coefficient significantly decreases when the angle of attack decreases. The value of the drag coefficient is relatively low compared to that for the truss girder or that for the box girder with bluff cross section. This means that this two box cross section is an advantageous cross section for the static wind load.

The lift coefficient at the angle of attack of 0 degree has negative value, and this means that the downward wind force will be loaded to the girder.

The gradient of both lift coefficient and pitching moment coefficient to the angle of attack is positive. This shows that the instability of 1st mode of bending and torsion may not occur to this two box girder cross section.

The aerostatic coefficient with two kinds of flow of different velocity is almost same, and this means there is no effect of Reynolds number.

3.3. Aerostatic force coefficient for the pipe girders

Fig. 6 shows the aerostatic force coefficient for the pipe girders cross section.

The drag coefficient at the angle of attack of 0 degree is about 1.3, and larger than that of the two box girders. This means that pipe girders cross section is disadvantageous for the static wind load compared to the two steel box girders with steel deck.

The lift coefficient at the angle of attack of 0 degree has negative value, and this means that the downward wind force will be loaded to the girder.

The gradient of pitching moment coefficient to the angle of attack is positive for the angle of attack of 0 degree or less. However, the gradient becomes negative for the angle of attack larger than 0 degree. This shows that the instability of 1st mode of torsion, namely torsional flutter, may occur against wind of high velocity, and the aerodynamic stability should be carefully examined.

The aerostatic coefficient with two kinds of flow of different velocity is almost same, and this means there is no effect of Reynolds number.

3.4. Aerostatic force coefficient for the two steel box girders with pre-stressed concrete deck

Fig. 7 shows the aerostatic force coefficient for the two steel box girders with pre-stressed concrete deck.

The drag coefficient at the angle of attack of 0 degree is about 1.4, and larger than that of the two box girders with steel deck and of pipe girders cross section. This means that two steel box girders with pre-stressed concrete deck cross section is disadvantageous for the static wind load compared to the two steel box girders with steel deck and pipe girders.

The lift coefficient at the angle of attack of 0 degree has negative value, and this means that the downward wind force will be loaded to the girder.

The gradient of pitching moment coefficient to the angle of attack is positive for the angle of attack of 0 degree or less. However, the gradient becomes negative for the angle of attack larger than 6 degrees. This shows that the instability of 1st mode of torsion, namely torsional flutter, may occur against the wind of high velocity, and the aerodynamic stability should be carefully checked.

The aerostatic coefficient with two kinds of flow of different velocity is almost same, and this means there is no effect of Reynolds number.

4. Aerodynamic Stability of Each Section

4.1. General

The aerodynamic stability of the each cross section was investigated with flutter analysis based on the modal analysis in frequency domain.

The measurement of the unsteady aerodynamic force coefficient for each crass section is conducted with wind tunnel test, and the flutter analysis conducted for each cross section.

4.2. Flutter Analysis

The procedure of the flutter analysis is summarized as following.

The governing equation of motion for bending and torsion can be expressed as following.

$$m\ddot{\eta} + C_\eta \dot{\eta} + k_\eta \eta = \frac{1}{2}\rho (2b) U^2 \left\{ kH_1^* \frac{\dot{\eta}}{U} + kH_2^* \frac{b\dot{\phi}}{U} + k^2 H_3^* \phi + k^2 H_4^* \frac{\eta}{b} \right\}$$

$$I\ddot{\phi} + C_\phi \dot{\phi} + k_\phi \phi = \frac{1}{2}\rho (2b^2) U^2 \left\{ kA_1^* \frac{\dot{\eta}}{U} + kA_2^* \frac{b\dot{\phi}}{U} + k^2 A_3^* \phi + k^2 A_4^* \frac{\eta}{b} \right\}$$

where, $C_\eta (C_\phi)$: Bending (Torsion) coefficient of viscosity for unit length,

$k_\eta (k_\phi)$: Bending (Torsion) stiffness constant for unit length,

$m(I)$: Mass (Moment of inertia) for unit length, and

$A_{1\text{-}4}^*, H_{1\text{-}4}^*$: Unsteady aerodynamic force coefficient.

These equations can be expressed in matrix notation.

$$[M]\{\ddot{Z}\} + [C]\{\dot{Z}\} + [K]\{Z\} = [A]\{\dot{Z}\} + [B]\{Z\}$$

where,

$$[M] = \begin{bmatrix} m & 0 \\ 0 & I \end{bmatrix} \quad [C] = \begin{bmatrix} C_\eta & 0 \\ 0 & C_\phi \end{bmatrix} \quad [K] = \begin{bmatrix} k_\eta & 0 \\ 0 & k_\phi \end{bmatrix} \quad \{Z\} = \begin{Bmatrix} \eta \\ \phi \end{Bmatrix}$$

$$[A] = \begin{bmatrix} \rho b^2 \omega H_1^* & \rho b^3 \omega H_2^* \\ \rho b^3 \omega A_1^* & \rho b^4 \omega A_2^* \end{bmatrix} \quad [B] = \begin{bmatrix} \rho b^2 \omega^2 H_4^* & \rho b^3 \omega^2 H_3^* \\ \rho b^3 \omega^2 A_4^* & \rho b^4 \omega^2 A_3^* \end{bmatrix}$$

Substituting the motion vector of free vibration {Z} to this equation.

$$\{Z\} = \begin{pmatrix} \eta_0 \\ \phi_0 \end{pmatrix} e^{\lambda t} = \{Z_0\} e^{\lambda t}$$

The eigenvalue problem can be derived as following.

$$[A]\{Y\} = \lambda [M]\{Y\}$$

where,

$$[A] = \begin{bmatrix} -[C^*] & -[K^*] \\ [M] & [0] \end{bmatrix} \quad [M] = \begin{bmatrix} [M] & [0] \\ [0] & [M] \end{bmatrix} \quad \{Y\} = \begin{Bmatrix} \lambda [Z] \\ [Z] \end{Bmatrix}$$

$$[C^*] = [C] - [A] \qquad [K^*] = [K] - [B]$$

Solving this eigenvalue problem, the conjugate complex number as follows can be derived.

$$\lambda_j=(\zeta_j \pm i)\omega_j \quad (j=1, 2)$$

where, ζ_j : Damping coefficient for mode j (δ_j : Logarithmic decrement ($\delta_j=-2\pi\zeta_j$))
ω_j : Circular frequency for mode j

The stability of the system can be decided as following.

For one mode j $\delta_j \leqq 0$ ($\zeta_j \geqq 0$) : unstable, or
For all the mode $\delta_j > 0$ ($\zeta_j < 0$) : stable.

The analysis is conducted as following. First, the range of the wind velocity and the increment of the wind velocity are assumed. Then, the wind velocity and vibration mode are determined. The frequency is assumed for this mode, and reduced frequency is obtained. With this reduced frequency, the unsteady aerodynamic force coefficient is determined based on the result of the wind tunnel tests. Then, the eigenvalue problem is solved to obtain eigenvalue. The frequency is obtained from this eigenvalue, and is compared to the assumed frequency. If the difference between obtained and assumed frequency large, the assumed frequency is replaced with obtained value and eigenvalue is calculated again. This procedure is repeated until the frequency converges. When the frequency converges, the damping can be obtained from the eigenvalue. This procedure is repeated for each mode. Then the same calculation is conducted for the next step of wind velocity. If the damping becomes negative for one wind velocity, it is considered that the flutter occurs at this wind velocity.

4.3. Aerodynamic stability of the two box girders with steel deck

The result of the flutter analysis for the two box girders with steel deck is shown in Fig.8.

Fig. 8 shows the relationship between wind velocity and damping. Also, the relationship between wind velocity and frequency is shown in Fig.8. As shown in Fig. 8, the torsional flutter occurs at high wind velocity. However, the decrease of aerodynamic damping is mild, because the unsteady aerodynamic force coefficient is small compared to that of the flat plate.

When the angle of attack increases, the critical flutter wind velocity decreases. However, the critical flutter wind velocity is high, and it can be concluded that this two box girders with steel deck cross section is an aerodynamically stable cross section.

The wind tunnel test with spring supported model was also conducted to estimate the critical flutter wind velocity. The result of the flutter analysis and that of the wind tunnel test were compared and the both show the good agreement.

4.4. Aerodynamic stability of the pipe girders

The result of the flutter analysis for the pipe girders cross section is shown in Fig.9.

Fig. 9 shows the relationship between wind velocity and damping, and the relationship between wind velocity and frequency. As shown in Fig. 9, the torsional flutter occurs at high wind

velocity at the all angle of attack. But, the critical flutter wind velocity is relatively high compared to that of the flat plate.

4.5. Aerodynamic stability of the two steel box girders with pre-stressed concrete deck

The result of the flutter analysis for the two box girders with pre-stressed concrete deck cross section is shown in Fig. 10.

Fig. 10 shows the relationship between wind velocity and damping. Also, the relationship between wind velocity and frequency is shown in Fig.10. As shown in Fig. 10, the torsional flutter occurs at high wind velocity at the angle of 0 degree, but this wind velocity is higher than the design wind velocity. The analysis was conducted only for the wind of angle of attack 0 degree. The analysis against the wind with angle of attack would be conducted in the future.

5. Conclusion

To reduce the construction cost of the new cable-stayed bridge that H.E.P.C. is planning, new type of girders was developed and the aerodynamic stability of these girders were investigated with wind tunnel tests and flutter analysis. The proposed girders are two box girders with steel deck, steel pipe girders, and two steel box girders with pre-stressed concrete deck.

First, with wind tunnel tests, the aerostatic force coefficient and unsteady aerodynamic force coefficient were measured. Then, flutter analysis to estimate the critical flutter wind velocity was conducted with unsteady aerodynamic force coefficient.

It was concluded that the critical flutter wind velocity of each cross section is higher than the design wind velocity and each cross section is aerodynamically stable.

Acknowledgement

The wind tunnel tests and flutter analysis were conducted by Dr. Matsumoto, Professor of Kyoto University and the researchers at his research lavatory.

The authors wish to express their sincere appreciation to Dr. Matsumoto and his colleagues for their assistance and advice.

References

1) Bridge and Wind Engineering Laboratory, "Research on the Aerodynamic Stability of the Cable-Stayed Bridge on which the Cost Reduction is considered", March 1998, (in Japanese)
2) Bridge and Wind Engineering Laboratory, "Research on the Aerodynamic Stability of the Cable-Stayed Bridge against the Turbulent Flow", March 1999, (in Japanese)
3) Hanshin Expressway Public Corporation, "Investigation of the Conceptual Plan for the New Long Span Bridges", March 1998, (in Japanese)

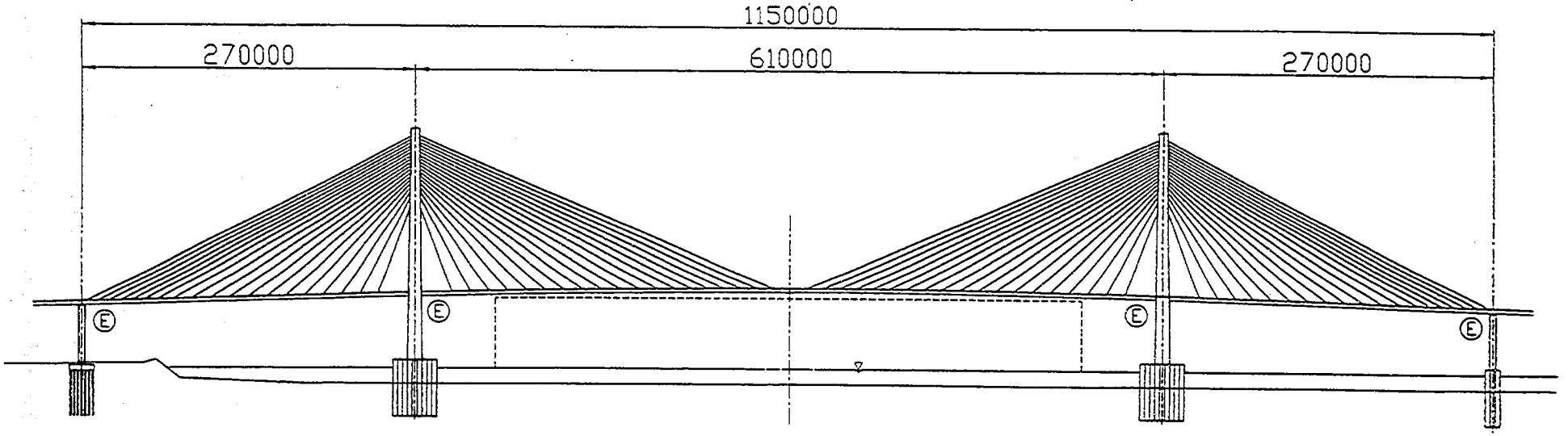


Fig. 1 General Plan of the Proposed Cable-Stayed Bridge

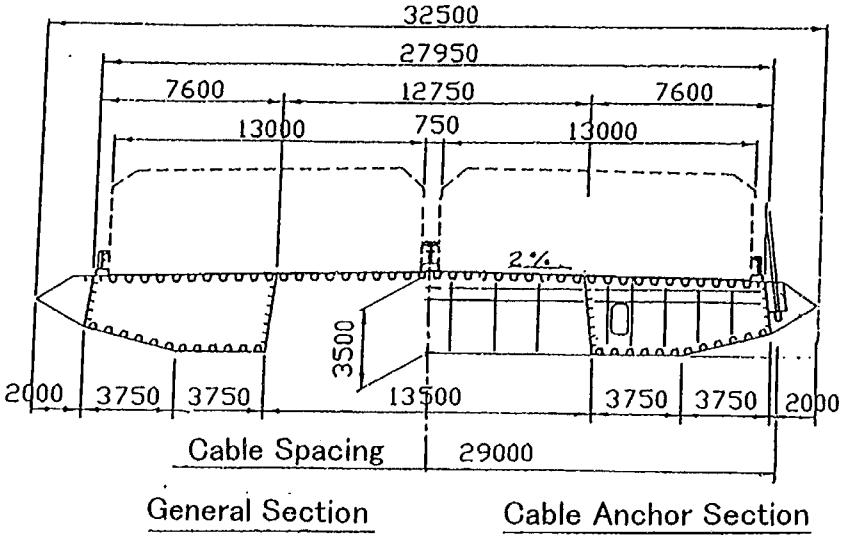


Fig. 2 Two Box Girders with Steel Deck Cross Section

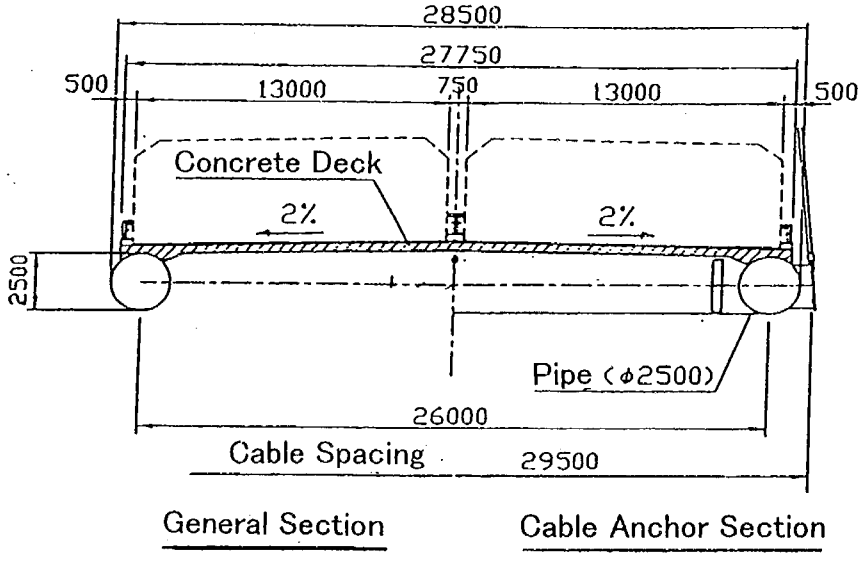


Fig. 3 Steel Pipe Girders Cross Section

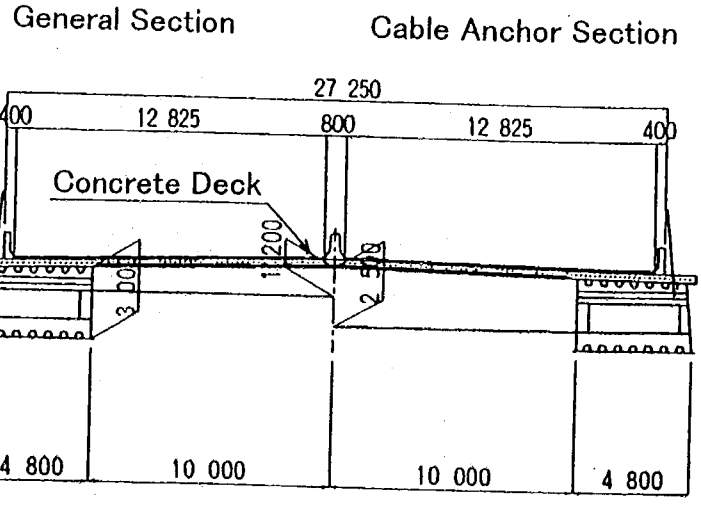
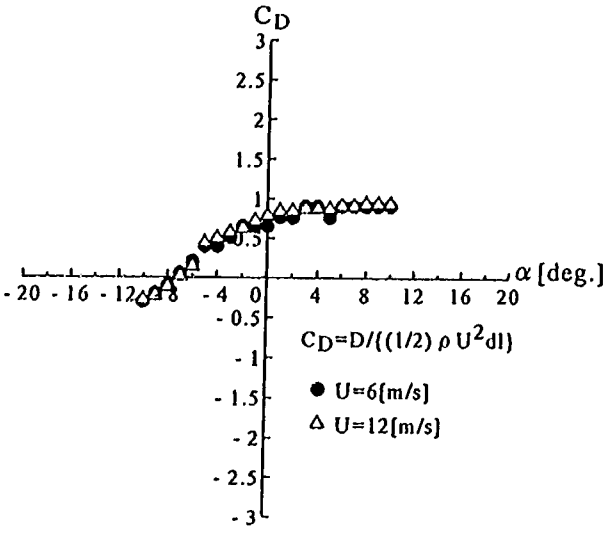
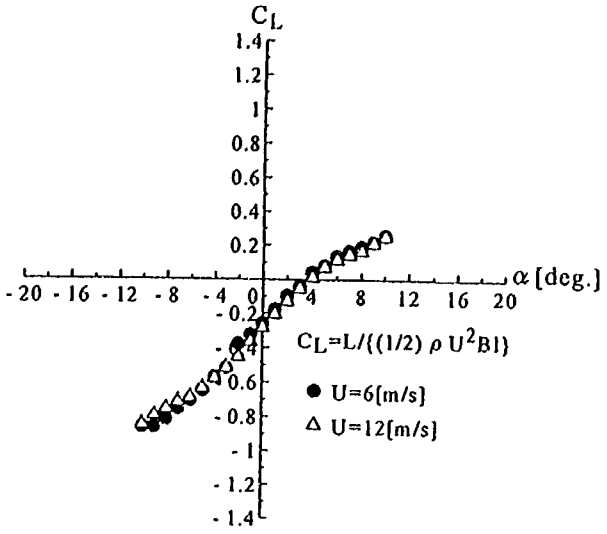


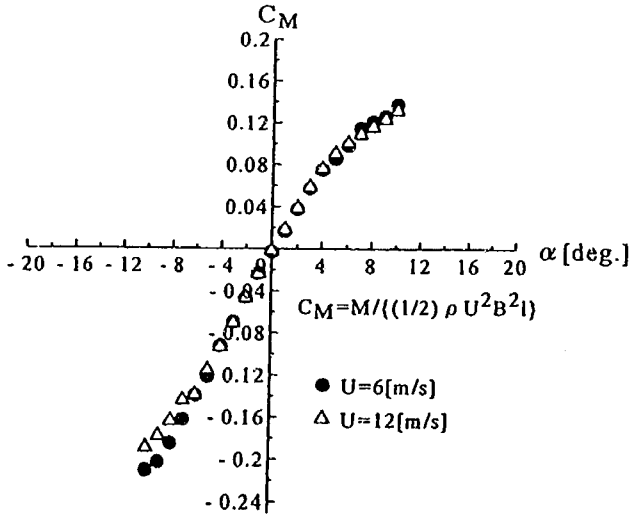
Fig. 4 Two Steel Box Girders with Pre-Stressed Concrete Deck Cross Section

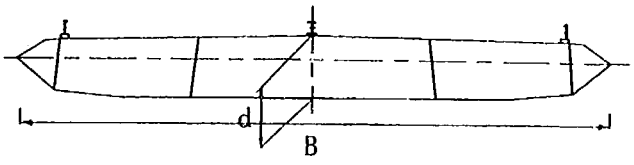


Drag Coefficient C_D
(in Smooth Flow)



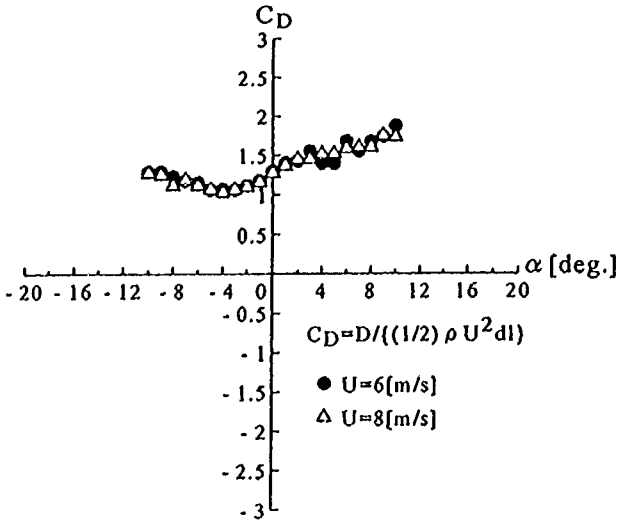
Lift Coefficient C_L
(in Smooth Flow)



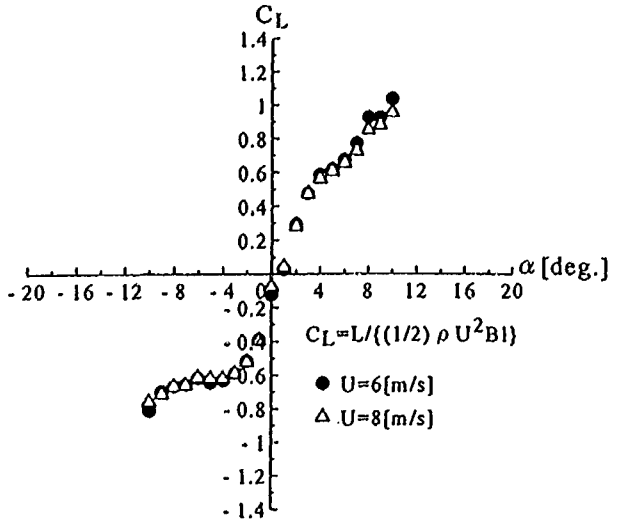


Pitching Moment Coefficient C_M
(in Smooth Flow)

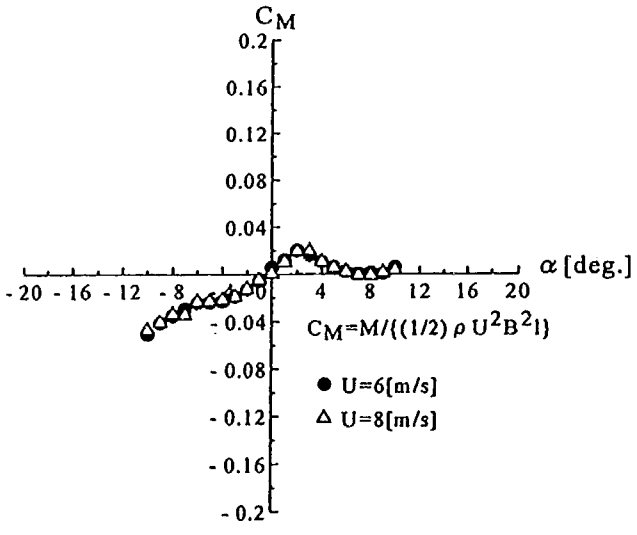
Fig. 5 Aerostatic Force Coefficient for the Two Box Girders with Steel Deck



Drag Coefficient C_D
(in Smooth Flow)



Lift Coefficient C_L
(in Smooth Flow)



Pitching Moment Coefficient C_M
(in Smooth Flow)

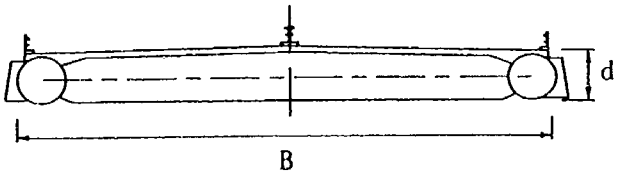


Fig. 6 Aerostatic Force Coefficient for the Pipe Girders Cross Section

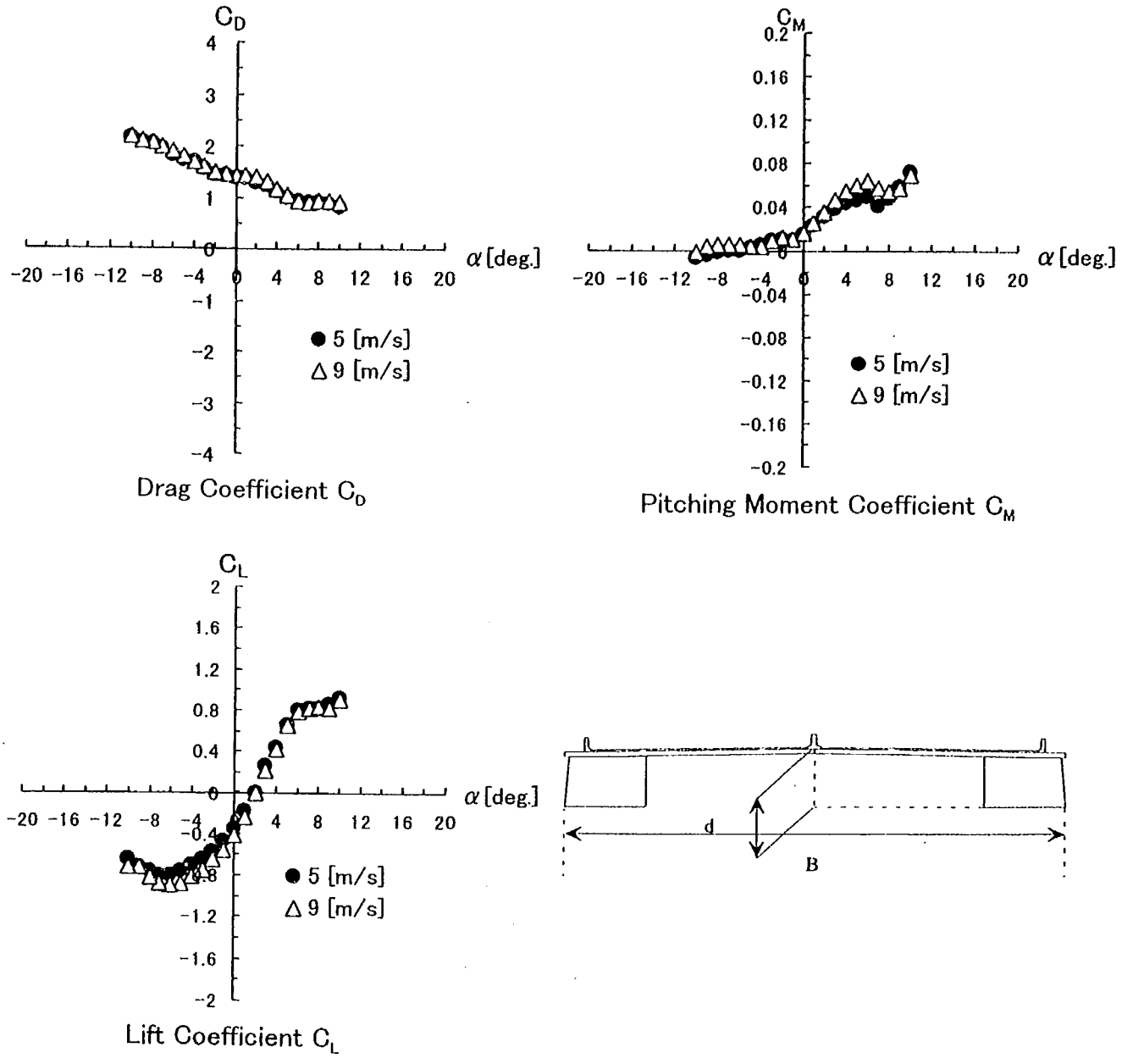
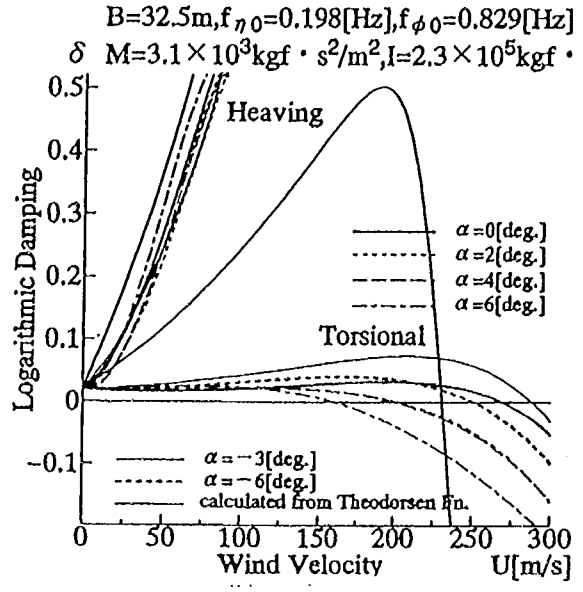


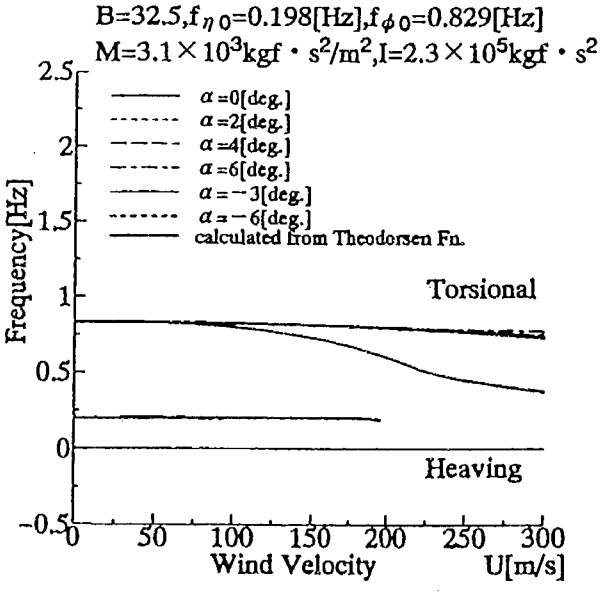
Fig. 7 Aerostatic Force Coefficient for the Two Box Girders with Concrete Deck



Flutter onset wind velocity

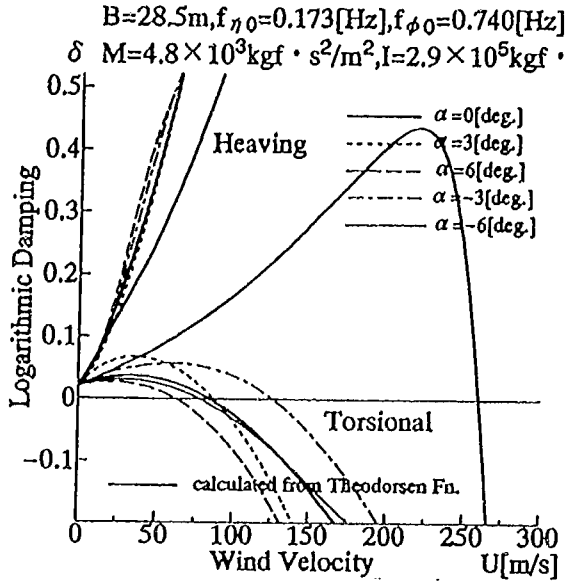
α[deg.]	Vcr[m/s]
0	269
2	202
4	200
6	160
−3	288
−6	251
Theodorsen	231

(a) V-δ diagram



(b) V-f diagram

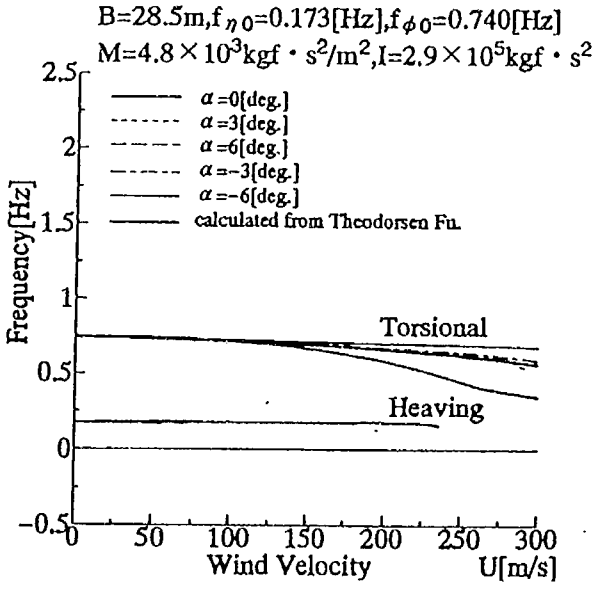
Fig. 8 Result of Flutter Analysis for Two Box Girders with Steel Deck



Flutter onset wind velocity

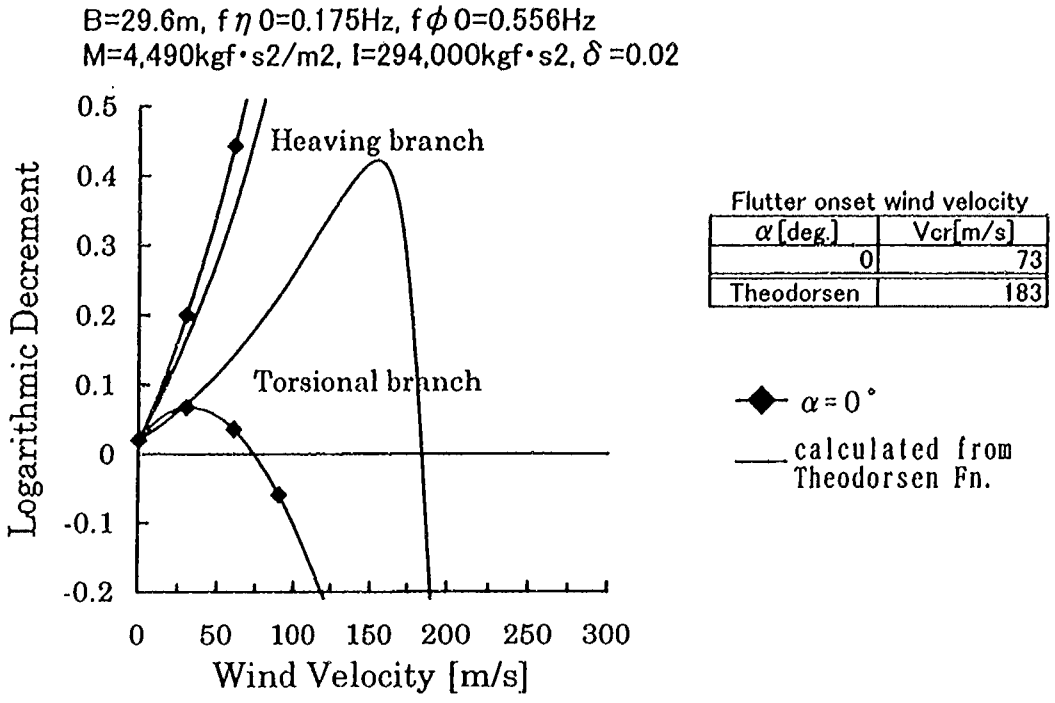
α[deg.]	Vcr[m/s]
0	84
3	87
6	62
-3	126
-6	78
Theodorsen	231

(a) V-δ diagram

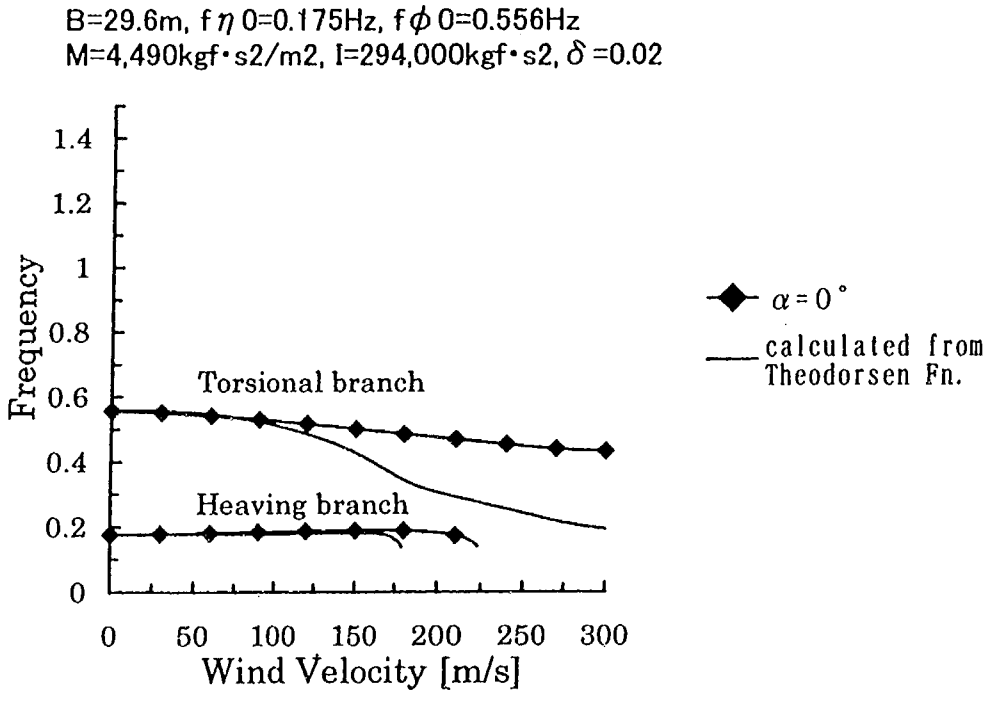


(b) V-f diagram

Fig. 9 Result of Flutter Analysis for Pipe Girders Cross Section



(a) V-δ diagram



(b) V-f diagram

Fig. 10 Result of Flutter Analysis for Two Box Girders with Concret Deck

Vibration Test of the Tatara Bridge

Kazunori Yamaguchi[1]

Abstract

Tatara bridge is located at the middle of the Onomichi-Imabari Route, the most westerly route among the three routes of the Honshu-Shikoku Bridge project. It is a Cable -- stayed Bridge connecting Ikuchijima Island and Ohmisima Island , with and a center span length of 890 meters. It is the world's longest bridge as a cable-stayed bridge.

The Tatara bridge is a hybrid structure having prestressed concrete girders in end spans, between the intermediate and end piers and has 2.7m web depth girders of mono-box, 220m height towers with reversed Y shape and 21 layers of multi-fan cables, having the maximum length cables of 460m.

Vibration test was carried out for checking assumption of aerodynamic design and aseismic design. It was the first test vibrating transverse direction of such a long cable-stayed bridge and newly knowledge of vibration characteristics of long span cable-stayed bridge obtained. This report informs the test results.

1. Introduction

The field vibration test had been performed from November to December 1998 when the construction of pavement almost completed. The exciters were used and vibrated the girder in the vertical directions to investigate three vertical bending and two torsinal vibration modes, and in the horizontal directions to investigate three bending vibration modes in the normal direction of the bridge axis. The horizontal vibration in large amplitude is the first trial on such a long-span bridge.

The aims of field vibration tests are to confirm the dynamic properties of important vibration modes by comparing with the results of analyses, especially structural damping, and to verify the vibration design of this bridge, furthermore, to make these observed data useful for the future design of the long-span cable-stayed bridge by investigating the phenomena of a coupled vibration consisting of girder and cables and the causes of structural damping.

2. Testing procedure

The exciters used in the field test were newly developed especially for the excitation in such a long period of this bridge. The specifications are shown in **Table-1**. These are a pair of large exciters and enable to work in both vertical and horizontal directions. The exciting direction is changed by using each steel frames supporting motors and weights, respectively corresponding to the tests for the vertical and horizontal

[1] Deputy Manager of Construction Division Mukaishima Operation Office,
3rd Operation Bureau, Honshu-Shikoku Bridge Authority

vibrations

In the vertical vibration test, two exciters were placed at both ends of the cross section of the bridge and they were operated in the same phase and the opposite phase to excite vertical bending and torsional vibration modes respectively. In the horizontal test, two exciters were operated in the same phase.

The exciters were installed at the point in distance of three eighth of the mid-span from the end of girder in the longitudinal direction. The location of transducers are shown in **Fig.-1**. The servo-type accelerometers were used in order to measure vibrations of girder, tower and cables. Two sensors were installed on the principal cables shown in **Fig.-1**, and accelerations in both vertical (in-plane of cable) and horizontal (out-of-plane cable) were respectively measured. These sensors were properly replaced to cables that swayed greatly during field test. As regards all bearings, the strain gauge type displacement meters were installed and slip of bearings in the horizontal direction were measured. Furthermore, the wind direction and wind speed were measured with Ace Vane type anemometer, and outside temperature was measured for reference. The situation of field vibration test is shown in **Photo.-1**.

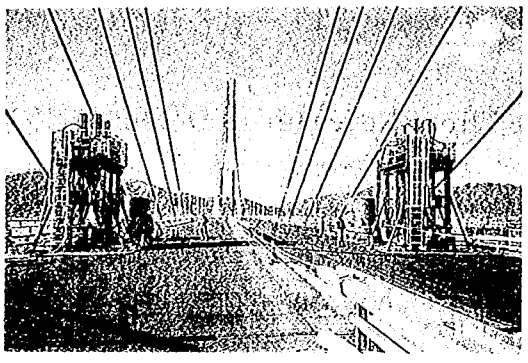


Photo.-1 *Situation of field vibration test*

Table-1 *Specification of the exciter*

exciting direction	vertical or horizontal
total weight	about 37 ton·f (with sliding mass)
sliding mass	20 ton·f
mass stroke	±100 cm
operation system	in-phase or out-of-phase
driving motor	AC servo motor (55KWX2set)
brake device	disk brakes
electric source	generator (200KVAX2set)

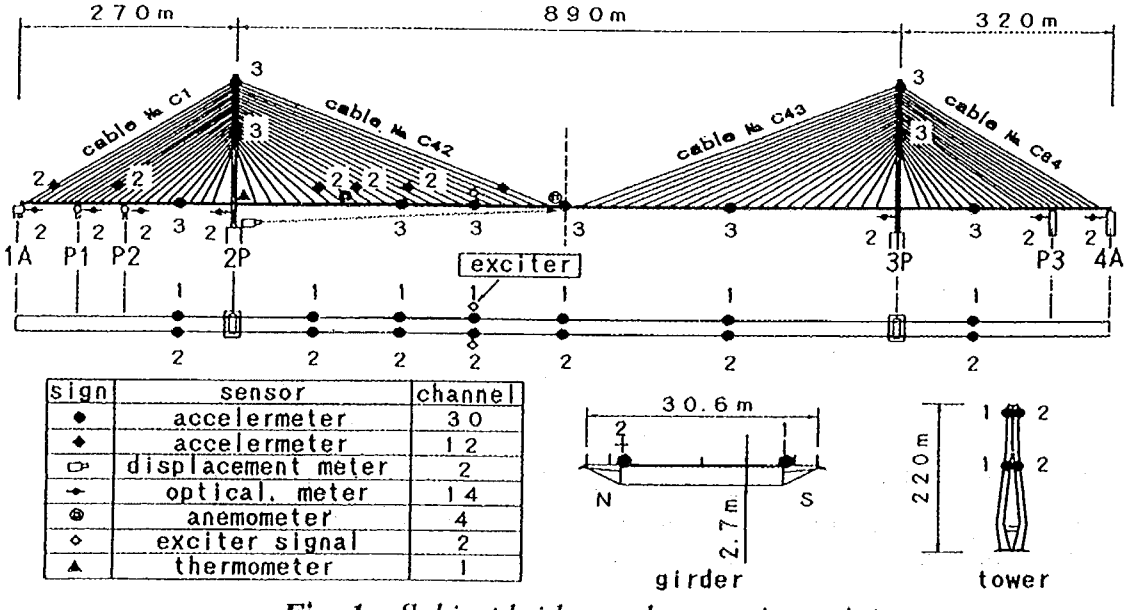


Fig.-1 *Subject bridge and measuring points*

3. Theoretical analysis

Previously theoretical analysis were carried out to compare with field test results. The natural vibration analysis was performed using three dimensional frame model of a whole structure system shown in **Fig.-2**. The cable models had 50 nodal points with mass that were linked by spring elements each other, and cable sag was taken into account. As the above cable models, coupled system consisting of girder and cable, have too many nodal points and analysis must be performed using large dimensional matrix, it is difficult to analyze directly using a whole structure system model. Therefore, the mass condensation method [1] and the partial structural combined method [2] were used as the efficient and accuracy analysis method.



Fig.-2 Analytical model

4. Test results and discussion

(1)Natural frequency and vibration mode

Examples of amplitude response curves are shown in **Fig.-3**. These indicate the amplitude-excitation frequency relations and phase-excitation frequency corresponding to the vertical and horizontal excitations. In the lower frequency range, there are single peaks, respectively corresponding to the 1st symm. vertical bending and 1st symm. horizontal bending mode, however, the shapes of curves in the higher frequency range are complicated. There are several peaks in the amplitude response curve of each modes and similarly on the phase response curves. The cause would be considered as coupled vibration between girder and cable. As the minimum frequency of cables is 0.25 Hz on the top cable and another cables have higher frequency, the coupled vibration is tend to be excited in higher frequency range than 0.25 Hz. Such phenomena of coupled vibration appeared in the sine excitation test.

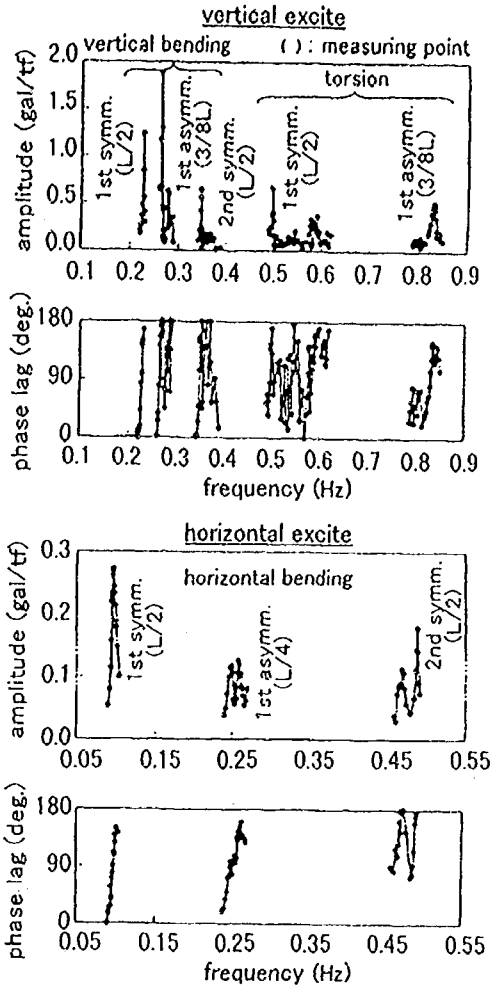


Fig.-3 Amplitude and phase response curve

In this paper, the peak frequency and amplitude distribution, on which the maximum response of girder was obtained, were selected respectively as the natural frequency and the mode shape of each modes out of many data. The comparisons of natural frequency and mode shapes between test results and analysis results are shown in

Table-2 and **Fig.-4**. As the results, there is a less difference than 10% on the natural frequency and only a few differences on the mode shapes.

(2)Structural damping

Structural damping in logarithmic decrement was calculated with free vibration data corresponding to each modes obtained by suddenly stopping excitation in the resonant condition. Examples of free vibration data are shown in **Fig.-5** and it indicates that the damping changes according to the change of amplitude of the girder and damping tends to increase proportional to the amplitude of girder. The structural damping at each modes was calculated by two methods which are shown in **Table-2**. It is important that the structural damping change greatly according to each vibration directions.

Table-2 Test results

		frequency (Hz)		logarithmic decrement ①	logarithmic decrement ②	max. amp. (cm)
		measured	calculated			
vertical bending	1st symm.	0.226	0.223	0.024	-	30.5
	1st asymm.	0.263	0.262	0.018	0.019	22.6
	2nd symm.	0.348	0.345	0.007	0.012	9.5
torsion	1st symm.	0.497	0.498	0.017	0.010	4.8
	1st asymm	0.831	0.822	0.051	0.020	1.6
horizontal bending	1st symm.	0.097	0.094	0.132	-	9.4
	1st asymm.	0.248	0.249	0.213	0.037	4.0
	2nd symm	0.470	0.494	0.173	0.020	1.1

① the structural damping was calculated as the average damping in the range from the maximum amplitude to the amplitude reduce to 70% of the maximum one.

② The structural damping was calculated in the small amplitude that is excluded superposition of the another mode.

Regarding to the vertical bending and torsional vibration modes in the vertical excitation, the damping is δ (logarithmic decrement ①)=0.01 ~ 0.05, and on the horizontal bending vibration mode in the horizontal excitation δ (logarithmic decrement ①)=0.10~0.20, that are much larger than ones of vertical vibration. As the reason, it is considered that the attachments such as fairings(**Fig.-6**) installed at the ends of the cross section of girder have influence of these phenomena. There are several attachments such as fairings for wind resistance and handrails at the ends of the cross section. These are separated at regular interval 10 meters in the longitudinal of the girder not to propagate stress, and linked to each members with loose-tightened bolts. On the horizontal vibration, it is predicted that as the amplitude become larger, the more bolts would slip and the friction force would have more influences of the damping. In order to verify this prediction, the slip of bolts were measured with displacement meters installed on the joint of fairings at the mid-point of the mid-span. As the results, it was confirmed that the above prediction

might be right.

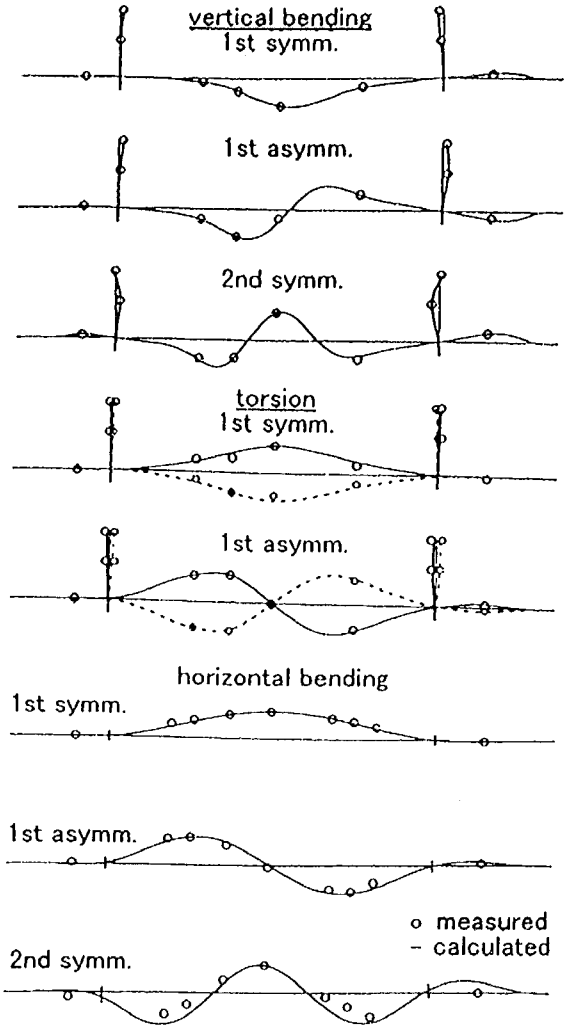


Fig.-4 Comparison of mode shapes

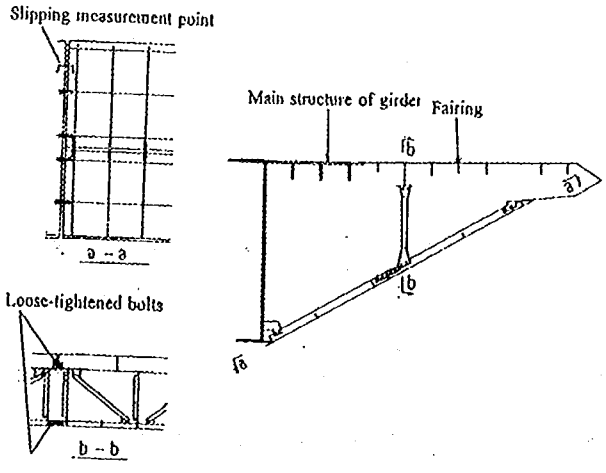


Fig.-6 Structure of fairing

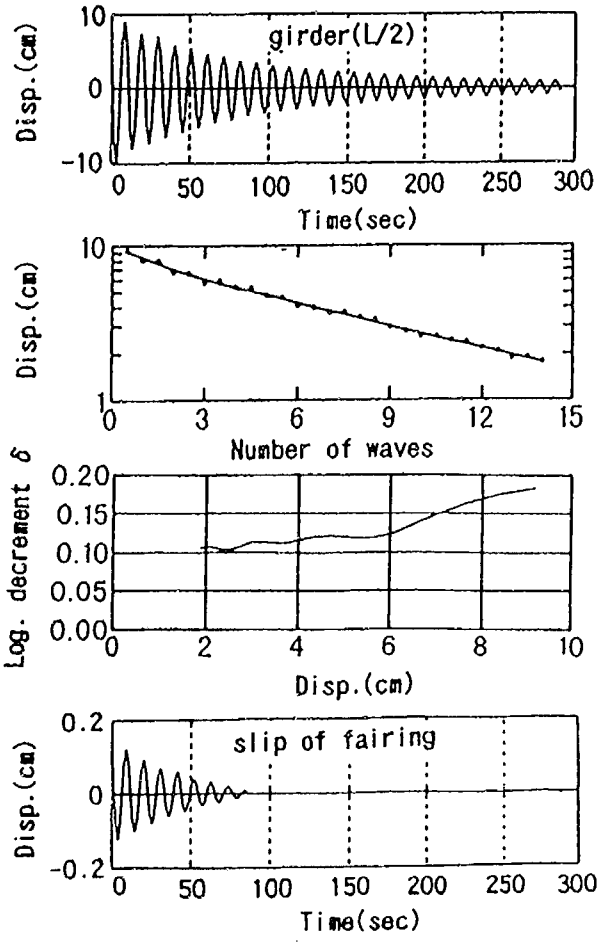


Fig.-5 Free vibration and structural damping

(3)Cable vibration

This chapter reports about the phenomena of coupled vibration between girder and cables obtained in the field vibrationtest.

a)Linear coupled vibration

There happened several coupled vibrations between girder and cable on numbers of vibration modes mentioned in 4.(1). General coupled vibrations were excited when the excitation frequency of the girder became near one of cable. In this case, this

phenomenon is considered as the linear coupled vibration. The mode in this phenomenon is almost same as one of the result of natural vibration analysis mentioned in 3.

Fig.-7 shows displacement of free vibration and its' Fourier amplitude of 1st symm. torsional vibration mode. As peak of Fourier amplitude of girder and cable correspond to each other, it is considered coupled vibration. Time history of cables' displacement is complex due to superpose another mode.

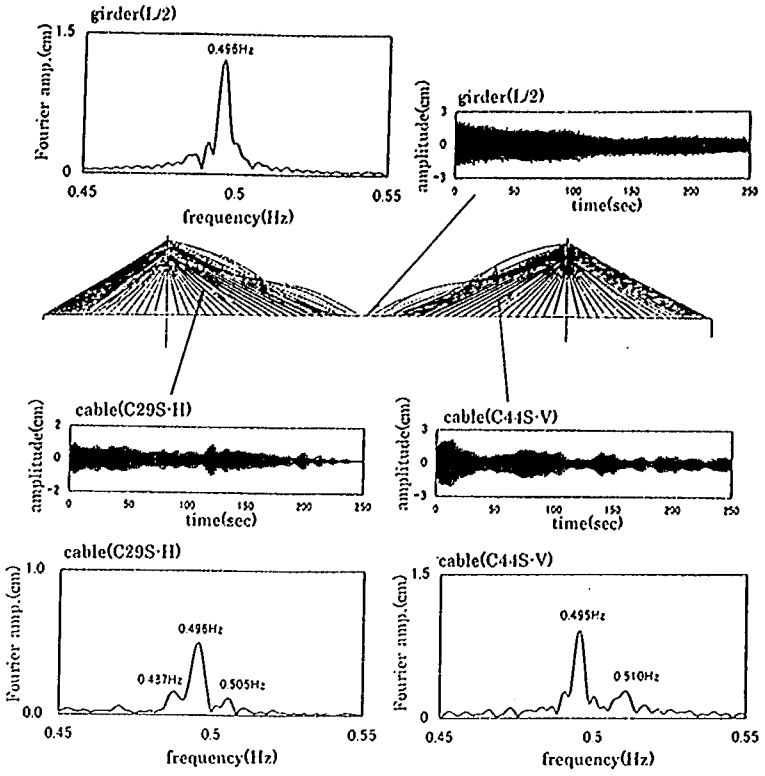


Fig.-7 Coupled vibration of girder and cable

b)Non-linear coupled vibration (parametric excitation)

On the other hand, non-linear coupled vibration was excited, when the frequency of the cable was nearly equal to half of the excitation frequency of the girder. This is considered as the non-linear coupled vibration excited due to fluctuation of cable tension. This phenomenon had been confirmed in another field vibration test [3].

The non-linear coupled vibration was excited at resonance of 1st asymm. tosional vibration mode in this test. C53 cable suddenly began to oscillate in half frequency of exciting frequency during the girder was being excited. The comparison of the amplitude between girder and cable is shown in **Fig.-8**. After non-linear coupled vibration was excited, exciters were stopped due to a sudden increase of the cable amplitude. The 1st asymm. torsional vibration mode would be excited only in case that an asymm. wind blow in the normal direction of the bridge axis in a stormy condition, therefore it is considered that non-linear coupled vibration would be rarely excited. However,

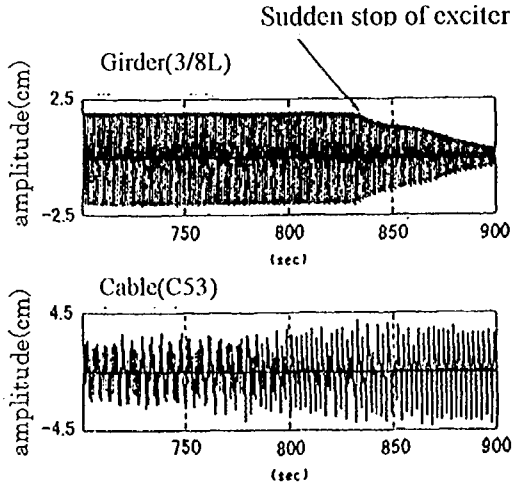


Fig.-8 Non-linear coupled vibration

the confirmation of the possibility that such a vibration will be excited including reinvestigation of data in wind tunnel test will be carried out quantitatively.

5. Summary

The results of field vibration test are summarized as follows;

① The frequencies in filed tests and ones in analyses are almost same on the important 8 modes taken into account, furthermore, each mode are very similar.

② There are several peaks in the amplitude response curve of girder's each mode over longest cable's 1st frequency 0.25 Hz interacted by cable vibration.

③ The structural damping on the vertical bending and torsional modes are relatively small by comparing with the test results of another long-span cable-stayed bridges, however these satisfy the design value δ=0.02. While it is considered that this bridge system is stable against the divergence type flutter which was examined to occur at high wind speed in the wind tunnel test.

④ The structural damping on the horizontal bending mode is large and this cause is presumed that bolts installed on the fairings and so on would slip according to the horizontal girder vibration. It is considered that this phenomenon reduces the amplitude of gust response in the transverse direction.

⑤ Linear coupled vibration between girder and cable was excited in the condition that the frequency of the cable vibration was equal to exciting frequency of the girder. On the other hand, non-linear coupled vibration (parametric excitation) was excited at resonance of 1st asymm. torsional vibration mode and at that time the frequency of the cable has become the one second of exciting frequency of the girder. It is considered that non-linear coupled vibration would be rarely excited, however, the confirmation of this phenomenon will be performed.

Analyzing of structural damping and interacted vibration of cable – girder is carrying out till now. And several interesting vibration characteristics about long span cable stayed bridge are clearing from these results. The new results would be presented in the near future.

ACKNOWLEDGEMENTS

The authors would like to thank Professor YAMAGUCHI Hiroki, Department of Construction Engineering, Saitama University in carrying out the experiment.

REFFERENCE

1)K. Morishita et al. : Non-linear Seismic Response Analysis of Long Span Bridge, *Proc. of 2nd World Conference of Structural Control*, June-July 1998.

2)K. Washizu et al. : *Handbook of Finite Element Method II, Application Part*, Baifukan, pp.5-7,1983(in Japanese).

3)I. Okauchi et al. : Field Vibration Test of a Long-Span Cable-Stayed Bridge Using Large Exciters, *Journal of Struct. Engrg., JSCE*, Vol.14, No.1, pp.83s-93s, April 1997.

DAMPING CHARACTERISTICS OF PRESTRESSED CONCRETE CABLE-STAYED BRIDGES BASED ON MEASURED DATA

Shin-ichi YAMANOBE, Yuji NIIHARA and Tesuo TAKEDA

Abstract

In dynamic design of cable-stayed bridges, the evaluation of structural damping is important. As theoretical evaluation is difficult, however, it is usual to measure the damping ratio through vibration tests. The accumulated test data on PC cable-stayed bridges has been insufficient. In this study, the damping type, measurement method and evaluation in seismic design are firstly reviewed, and the measured data from vibration tests are analyzed for recent PC cable-stayed bridges. The relation between damping ratio and natural frequency is studied, and the damping ratios of PC and steel cable-stayed bridges are compared. In addition, the damping characteristics during cantilever erection are investigated.

1. Introduction

Recently, the number of PC cable-stayed bridges has significantly increased. The bridge style is one of those oriented towards large bridges, and concrete is used as the main material. The Ikara bridge with a central span of 260m, which is the longest in Japan, and the 2-span Shin-inagawa bridge with a maximum span of 199m have been successively constructed, and the realizable span length has become close to that of steel cable-stayed bridges.

As PC cable-stayed bridges tend to be large, it has become more important to assure the safety of the bridge against earthquakes and wind loading. In the case of PC cable-stayed bridges, dynamic analysis has been applied to the design as it shows complicated behavior during earthquakes. Since the Hyogoken-Nanbu earthquake, "Specifications for Highway Bridges Part V: Seismic Design" has been revised, and the function of dynamic analysis in seismic design has been clearly indicated. Therefore, the dynamic analysis of PC cable-stayed bridges has become more and more important.

In designs based on dynamic analysis, the evaluation of structural damping is very important. Generally, structural damping is evaluated in the form of its modal damping ratio in dynamic design and field vibration tests, although damping characteristics depend on the structural members. Some theoretical studies have been challenged recently as observed in the study of Yamaguchi et al.[1]. Because theoretical evaluation of modal damping is difficult, however, the modal damping ratio is often measured through such field vibration tests at bridges in actual use. Up to now, many vibration tests have been performed and the measured data accumulated. However, many of them have not been performed systematically, and only the studies conducted by Kawashima et al.[2], Yamaguchi et al.[3] and Davenport et al.[4] have been statistically summarized. In the above studies, data for steel cable-stayed bridges has been mainly used although those for PC ones has also been included. Since the previous studies, the measured damping data for PC cable-stayed bridges has increased, but the

[1]Senior Research Engineer, Civil Engineering Department, Kajima Technical Research Institute, Japan
[2]Research Engineer, Civil Engineering Department, ditto
[3]Senior Manager, Planning and Administration Office, ditto

Table 1 Type of vibration damping of structure.

Type of damping		Outline and features
Damping of material itself	Internal damping (Energy loss due to material itself)	This is energy loss due to nonlinearity, and is known as hysteresis damping when plasticity-induced damping is included. This kind of damping depends on vibration amplitude, but is almost independent of frequency.
Damping of structure system	Structural damping (Energy loss inside structure)	This is energy loss due to friction at bearings and joints, and depends on vibration amplitude. This kind of damping is almost independent of frequency.
	Dissipation damping (Dissipation of energy to outside of structure)	This is due to energy dissipation from the foundations to the surrounding subsoil and air resistance. This kind of damping depends on frequency, and is affected by the interaction between the foundations and soil.

damping characteristics have not been fully clarified as PC cable-stayed bridges are relatively new. In Japan with its high seismic activity, seismic evaluations will be more and more important in order to construct larger PC cable-stayed bridges, and thus an understanding of their damping characteristics is absolutely indispensable.

In this study, the measurements from past vibration tests on damping characteristics of PC cable-stayed bridges are reviewed, and the damping behavior is studied in comparison with steel cable-stayed bridges. Firstly, kinds of damping, measuring methods and the evaluation in seismic design are briefly reviewed. Then the damping characteristics are statistically analyzed for the PC cable-stayed bridges for which vibration tests have been conducted, and the relationship with vibration mode and natural frequency is discussed. In this study, 15 PC cable-stayed bridges and 17 steel ones are investigated.

2. Damping Measuring Methods

(1) Damping source and evaluation method in seismic design

As shown in **Table 2**, the damping of structures can be divided into the following three types according to their mechanism: a) internal damping (or hysteresis damping), which is caused by the material itself; b) structural damping, which is by energy absorption inside the structure; and c) dissipation damping, which is from the dissipation of energy away from the structure. Internal damping consists of the following two parts: a) hysteresis damping caused by energy absorption due to a hysteresis loop of the stress-strain curve when plastic deformation occurs; and b) viscous damping of material, which exists even when behavior is linear. In the case of concrete, it is known that a hysteresis loop could be observed at extremely small levels of stress. Therefore it is generally accepted that hysteresis damping is the main component of internal damping, especially in the seismic design of concrete structures. Besides the above types of damping, there are also other types of damping, e.g., aerodynamic damping due to wind, system damping in cable-stayed bridges due to energy transferal between cables and girders, and so on. The measured damping in vibration tests is a combination of the various aforementioned damping, and is often evaluated in the form of modal damping. It is very difficult to separate damping according to its mechanism. In seismic designs, damping is evaluated in the following way.

In the seismic design of highway bridges, the damping ratio is set for each member as indicated in **Table 2**, and then the modal damping is computed as strain energy proportional damping, according to the method shown in Specifications for Highway Bridges, Part V: Seismic Design[5]. For the superstructure of concrete bridges (main girders and main tower in PC cable-stayed bridges), the

Table 2 Reference value of damping ratio in "Specifications for Highway Bridges, Part V: Seismic Design".

Structural member	Linear case		Non-linear case	
	Steel structure	Concrete structure	Steel structure	Concrete structure
Superstructure	0.02~0.03	0.03~0.05	0.02~0.03	0.03~0.05
Rubber bearing	0.02		0.02	
Isolator	Equivalent damping ratio		Equivalent damping ratio	
Substructure	0.03~0.05	0.05~0.1	0.1~0.2	0.12~0.2
Foundation structure	0.1~0.3		0.2~0.4	

Table 3 Damping measuring method for bridge structure.

Vibrating the bridge artificially	Forced vibration method	Vibration is induced by exciter, and resonant curve is obtained. Damping ratio is computed using Half-Power method and modal circle curve fitting method.
	Free vibration method	Sudden stopping of exciter
		Manual vibrations
		Movement of vehicles
		Vertical motion of weight by crane
		Use of quick release jack
Naturally-induced Vibrations	Vibrations caused by Earthquakes and wind	System identification method, Random Decrement method
	Microtremor measuring method	Computed from Fourier spectra

damping ratio is often set as h=0.03 in seismic designs. Therefore, the computed damping ratio for the predominant vibration mode of superstructures using strain energy proportional damping is around 0.03 in most cases. The damping ratio of rubber bearings shown in **Table 2** is the equivalent damping ratio of linear rubber bearings, and any damping due to friction at moveable supports is not explicitly taken into account in the general design.

In the case of PC cable-stayed bridges, most measured damping ratios in field vibration tests for the predominant vibration mode of superstructures are smaller than those used in seismic design. However, as the vibration amplitude during earthquakes is large and internal damping and damping due to friction at the supports are added, the total damping is supposed to be around 0.03.

(2) Damping measurement methods

There are many kinds of methods to measure the damping of bridges. The methods used in the study are shown in **Table 3**, and can be divided into two categories, i.e., vibrating bridges using an exciter and observing damping during earthquakes or wind loading. In the latter case, the measured data are affected by the data processing method. When the microtremor measuring method is adopted, the measuring duration should be long and the measurements should be performed several times, and it is suggested that an averaging technique be used. The former type is more accurate, and can be divided into forced vibration tests and free vibration tests.

When the forced vibration test method is used, a vibration exciter is employed, and the exciting frequency is changed. The structure's response is observed, and the damping ratio is obtained from a resonant curve using the half-power method or modal circle curve fitting method. In the case of large PC cable-stayed bridges, a powerful exciter is required as the bridge is very heavy. In addition, a highly accurate vibration frequency setting is needed because the resonant curve is very sharp due to the small damping. However, the minimum frequency interval of exciters used for PC cable-stayed bridges is often around 0.01Hz, and it is difficult to assure sufficient measuring points around the peak when the half-power method is adopted.

On the other hand, in the case of free vibration tests, initial displacement is applied to the

structure, and the damping ratio is computed from the observed waves of free vibration. In order to induce the initial displacement, the following ways are well adopted: a) sudden stopping of an exciter; b) movement of people or vehicles; c) vertical moving of a weight by crane; and d) quick releasing. The damping ratio could be directly observed and high accuracy could be achieved in this method, if it could result in a large initial displacement and a clear damping wave with no oscillating disturbance could be obtained.

3. Damping Characteristics of PC Cable-stayed Bridges

In this section, PC cable-stayed bridges where damping characteristics have been studied through vibration tests and other methods are selected as investigation objectives, and the measurement obtained through a literature survey are statistically summarized. 15 bridges where damping characteristics were investigated are shown in **Table 4**.

There is both data computed using the half-power method from resonant curves and data obtained from free vibration waves. As was mentioned before, the latter data is more accurate, and therefore the damping ratios obtained from free vibration waves are given priority, and the observed data from resonant curve or microtremor measurements is only used when data from free vibration tests is not available. In addition, middle values are employed for some bridges when a range of damping ratios are indicated.

The damping characteristics of PC cable-stayed bridges are discussed in the following ways. Firstly, the maximum span length is used as a parameter and the overall tendency is studied in (1). Then, a detailed investigation concerning the vertical bending mode is performed in (2) and (3), as the corresponding data is relatively sufficient. In the next section, a comparison between PC and steel cable-stayed bridges is performed. Finally, the damping characteristics during cantilever erection, which is a special structural type, are investigated.

(1) Relation between the damping ratio and maximum span length

Among the PC cable-stayed bridges investigated in this study, most are 2 or 3-span ones although the number of spans varies from 1 to 5. **Fig. 1** shows the lower orders of vertical bending vibration modes for 2 and 3-span bridges. In the case of 3-span bridges where the main girder can move in the longitudinal direction, the lowest mode is a swinging pole vibration mode of the main girder in the longitudinal direction. However, this type of vibrations was not induced because the capacity of the exciter at low frequencies was

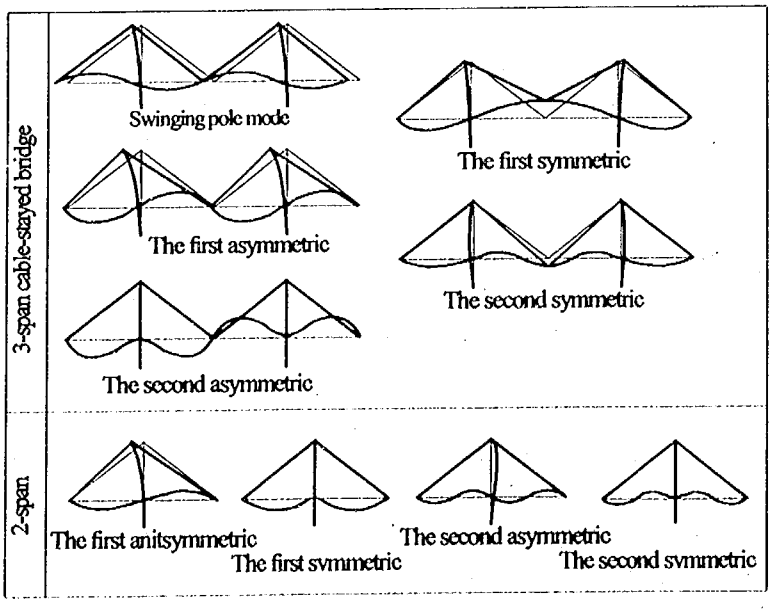


Fig. 1 Vibration modes of cable-stayed bridges.

Table 4 PC cable-stayed bridges where vibration tests have been performed.

Bridge name	Type	Span length / Width of girder (m)	Type of cable arrangement and number of stays / girder type
Ikara bridge	5-span continuous	44+120+260+120+44 / 11.0	Semi-harp type, double plane, 16 stays / Inversed-trapezoidal 2 boxes
Tokachi bridge	3-span continuous	125+251+125 32.8	Semi-harp type, double plane, 16 stays / Inversed-trapezoidal 4 boxes
Yobuko bridge		121+250+121 10.9	Semi-harp type, double plane, 17 stays / Inversed-trapezoidal 2 boxes
Utagenka Bridge		61.05+170+61.05 14.9	Fan type, double plane, 12 stays / Separating 2 boxes
Twinharp bridge		69.4+140+69.4 27.0	Harp type, single plane, 9 stays / 3 boxes
Shin-ayabe bridge		51.5+110+77.5 10.75	Fan type, double plane, 5 stays / Inversed-trapezoidal single box
Omotogawa bridge		46.65+85+46.65 7.0	Harp type, double plane, 5 stays / Single box
Shin-inagawa bridge	2-span continuous	198.7+198.7 20.7	Fan type, double plane, 14 stays / Inversed-trapezoidal 3 boxes
Shimamaruyama bridge		113.4+113.4 11.5	Semi-harp type, double plane, 9 stays / Inversed-trapezoidal single box
Fukiagehama-sunset bridge		94.3+94.3 6.8	Semi-fan type, double plane, 10 stays / Inversed-trapezoidal single box
Koshiki-Daimyojin Bridge		84.4+84.4	Semi-fan type, double plane, 7 stays
Seiwun bridge		53.5+53.5 5.4	Harp type, double plane, 4 stays / Edge girder
Bungo bridge		37.45+37.45 16.8	Harp type, double plane, 3 stays / PC hollow slab
Matsugayama bridge	one-sided single span	96.6 4.2	Fan type, double plane, 4 stays / PC girder
Yasuragi bridge		63.9 3.8	Fan type, double plane, 4 stays / PC girder

insufficient. The damping ratio for the swinging pole mode was not observes in all bridges investigated in this study.

The relation between the damping ratio and the maximum span length of PC cable-stayed bridge is shown in **Fig. 2**. All the measured damping ratios after completion of construction are plotted, and averaging of data for each bridge is not conducted. From **Fig. 2**, the following approximate formula could be found representing the relation between the damping ratio h and maximum span length L[m].

for all data: $h = 0.0757L^{-0.482}$ (1)

for vertical bending vibrations: $h = 0.0484L^{-0.388}$ (2)

for vibrations in the transverse direction: $h = 1.248L^{-0.968}$ (3)

for torsional vibrations: $h = 0.223L^{-0.824}$ (4)

As the maximum span length increases, the damping ratio decreases for all vibration modes. It can also been seen that the damping ratio for the torsional mode is the smallest of the three types.

In addition, the damping ratios obtained by Kawashima et al.[2] from the data of 13 bridges (steel bridges: 10, PC bridges: 3) are also shown on the same figure by dotted lines. The values from equations (1)-(4) are smaller than those obtained by Kawashima et al. In the formulas, the data used mainly consisted of the damping ratios for steel cable-stayed bridges. As described in the next section, very large measured damping ratios of steel cable-stayed bridges with truss girder are also included.

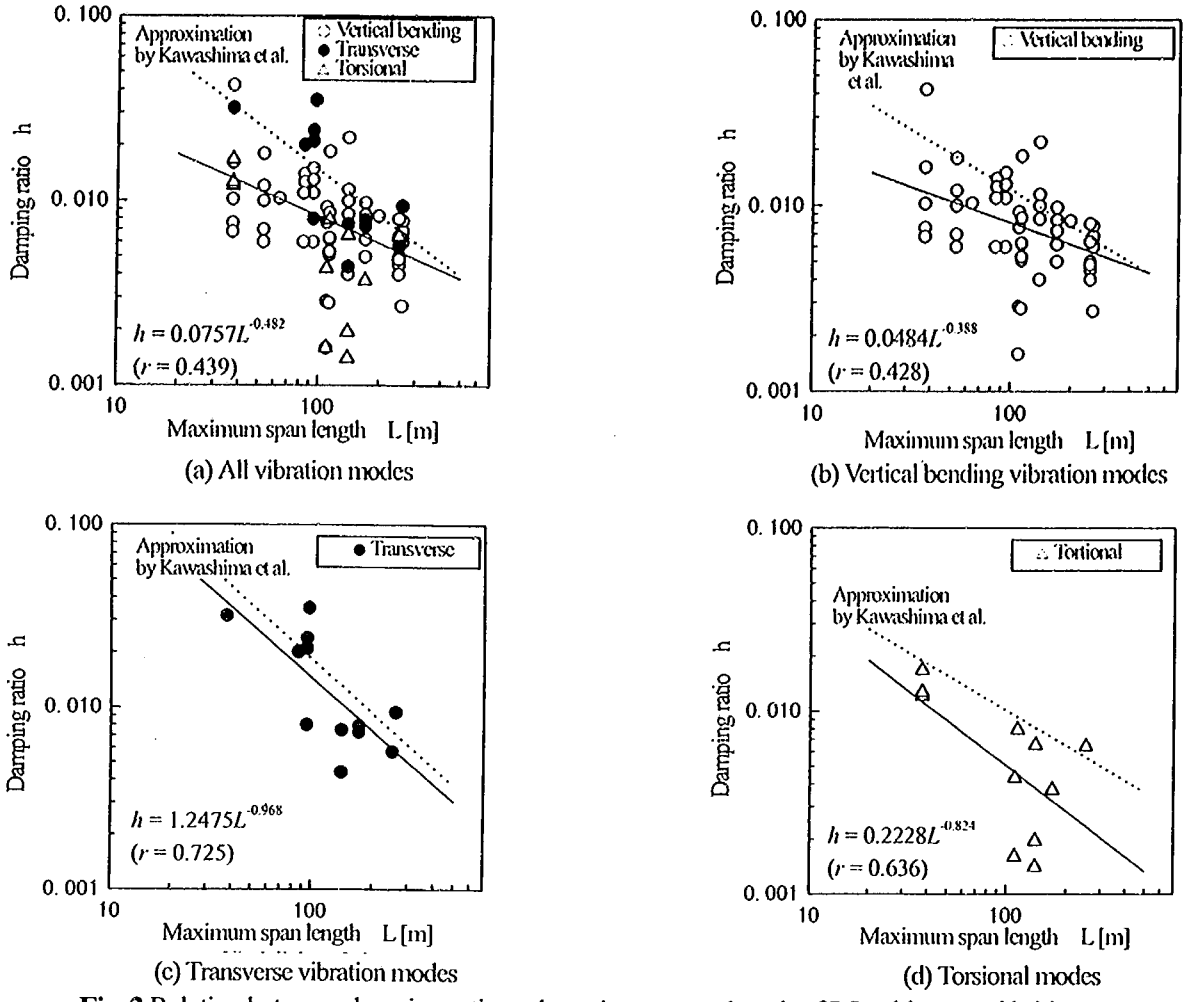


Fig. 2 Relation between damping ratio and maximum span length of PC cable-stayed bridges.

(2) Damping characteristics of the vertical bending mode

As for the transverse mode and torsional mode, there are few measurement. In addition, such data is from bridges with different types of structures, and it is judged that an analysis of the two modes is difficult. On the other hand, more data was obtained for the vertical bending mode than those of the other two modes, and therefore further investigation is performed.

Except for single-span bridges, the 2 and 3-span PC cable-stayed bridges are selected for the study of damping characteristics. Only the lower modes as shown in **Fig. 1**, which are important in the design, are studied.

The main factors affecting the damping ratio are as follows.

a) Structural type (span arrangement, cable layout, system for supporting the main girder)

b) Vibration mode and frequency

(vertical bending mode, transverse mode, torsional mode, frequency)

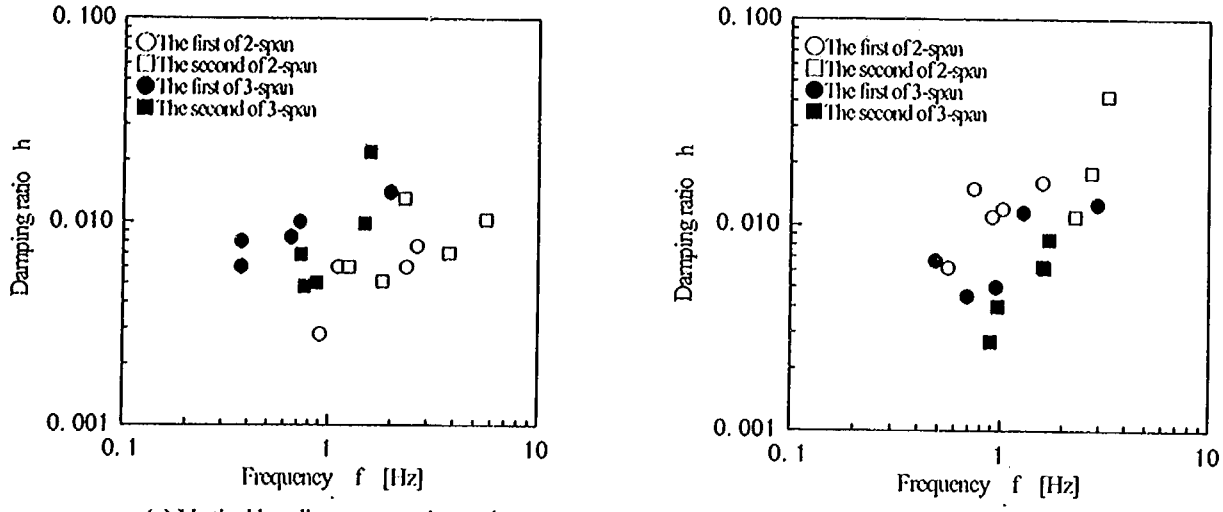
c) Test and measuring methods (resonant curve method, free vibration method)

d) Vibration amplitude

d) Test conditions (with or without wind during test, temperature during test)

Among these factors, (c), (d) and (e) may cause large variations, and it is considered that an analysis on (a) and (b) could result in meaningful results for design.

It is considered that the cable layout has almost no effect on the damping of vertical bending



(a) Vertical bending symmetric modes (b) Vertical bending asymmetric modes

Fig. 3 Comparison of damping ratios of 2-span and 3-span bridges for vertical bending modes.

mode, therefore this factor is not considered in the study. The data for single-plane types, of which there were few, are compared with those for double-plane types, and no notable differences are observed.

As for the supporting system for the main girder, bridges with rigid connections are all 2-span ones, and therefore the data for 2-span bridges and that for 3-span bridges are separated from the start. In the case of the Ikara bridge which has 5 spans, its data are used in the analysis of 3-span bridges as it has two main towers. In the same way, data from the Shinayabe bridge which has 3 spans is adopted in the analysis of 2-span bridges because it has only one main tower. In addition, in the case where data for both 2 and 3-span bridges is analyzed, it is appropriate to use fundamental frequencies other than the maximum span length in order to evaluate the relation to the vibration mode. In the following discussion, the fundamental frequency is used as the parameter. The reasons are as follows. Dissipation damping from foundations to the subsoil depends on the frequency and tends to be larger as the frequency increases. The damping of cable-stayed bridges includes dissipation damping although its effect may not be very significant. In addition, the frequency dependence of damping is generally assumed in dynamic analysis using Rayleigh type or stiffness-proportional type damping. Therefore, the analyzed results using frequency as a parameter may easily be reflected in the dynamic analysis.

Fig. 3(a) and (b) indicate the analyzed results arranged for symmetric and asymmetric vertical bending modes, respectively. Data for cases where symmetric and asymmetric modes could not be separated are not included. In both modes, the damping ratio increases as the frequency increases. In the cases with symmetric modes, the damping ratios for 3-span bridges are larger than those for 2-span bridges. In the cases with asymmetric modes, the damping ratio for the second mode of the 3-span bridges is the smallest.

Considering the shape of the vibration modes, vertical bending modes could be divided into the following two types: a) vibration modes without bending deformation of the main tower (the first and second symmetric modes of 2-span bridges, and the second asymmetric mode of 3-span bridges); and b) vibration modes with bending deformation of the main tower (the first and second asymmetric modes of 2-span bridges, the first and second symmetric modes of 3-span bridges, and the first asymmetric mode of 3-span bridges). However, in the case of 3-span bridges, the ratio

between the length of the side span and central span is not exactly 1:2 in most bridges, and the bending deformation of the main tower did not vanish completely.

Fig. 4 shows the analyzed results arranged for the vibration modes with and without bending deformation of the main tower. The tendencies in both modes are quite similar, and the damping ratio for those modes with bending deformation of the main tower is larger than those without it. In the case without bending deformation of the main tower, the relation between damping ratio and frequency could be expressed using the following approximate formula.

$$h = 0.0042 f^{0.597} \quad (5)$$

In the same way, an approximate formula for the mode with bending deformation of the main tower could be found as follows. Compared with the above mode, the damping ratio for the mode with bending deformation of main tower is almost twice as large.

$$h = 0.0094 f^{0.579} \quad (6)$$

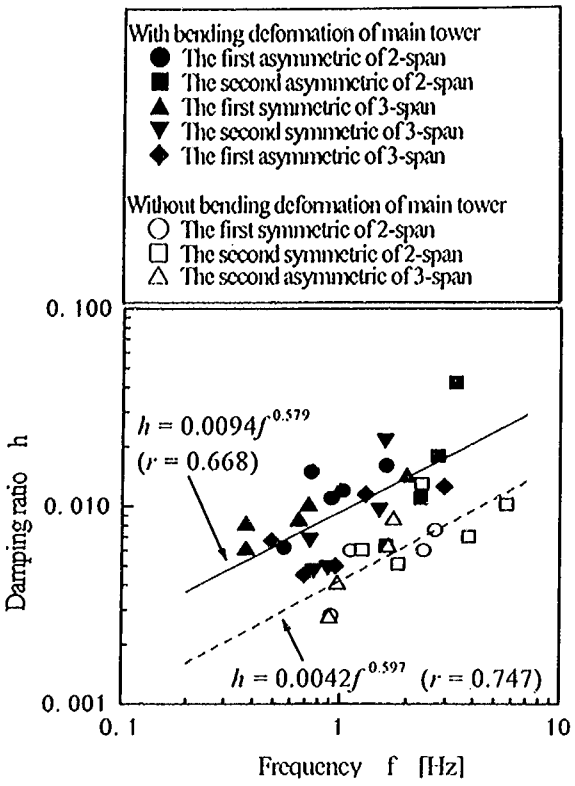


Fig. 4 Comparison of damping ratios for vertical bending modes with focus on bending deformation of the main tower.

In the previous studies[3], the relation between the damping ratio and other factors for PC cable-stayed bridges has not been established. Through this study, it is confirmed that an incremental change in frequency leads to an incremental change in the damping ratio. The reasons could be considered as follows. In previous studies on PC cable-stayed bridges, 18 sets of data for vertical bending modes and 3 sets of data for torsional modes were available. In this study, 55 sets of data from 13 bridges for vertical bending modes, and 11 sets of data from 6 bridges for torsional modes are used. A clear relation could be observed because there is sufficient data.

The reasons why the damping ratio in the modes with bending deformation of the main tower is larger than those without it could be interpreted as follows.

In the PC cable-stayed bridges, the main tower is a RC structure, which is different from that of the main girder. Generally, the axial stress of the main tower is around several tens of kgf/cm^2 (several MPa) and vibration tests could be conducted right after completion of construction, when there should be no cracks in the main tower. Therefore, it is impossible for the damping ratio of the main tower to become larger than that of the PC main girder. In addition, as discussed in a later section, the tendency for the damping ratio of the mode with bending deformation of the main tower to be large could also be observed in cases of steel cable-stayed bridges. Therefore, large damping of the main tower cannot be considered as the reason for the large damping ratio in the mode with bending deformation of the main tower.

On the other hand, the mode with bending deformation of main tower is considered together

with the rotational deformation (rocking) of the foundation. It has been demonstrated that the rotational deformation significantly affects the radiation damping from the foundation[6]. In the mode with bending deformation of the main tower, radiation damping due to rotation of the foundation is added to that caused by energy dissipation in the main girder, cables and main tower, which leads to a larger damping ratio.

Additionally, in the mode with bending deformation of the main tower, sliding occurs at all supports together with rotational deformation. It has been confirmed that the friction at the supports has a large effect on the damping ratio[7),8),9)]. Among the data obtained from vibration tests of PC cable-stayed bridges in this study, the displacement of supports is unclear in almost all cases. However, it can be said that the friction at the supports affects the damping ratio obtained through vibration tests to a certain degree.

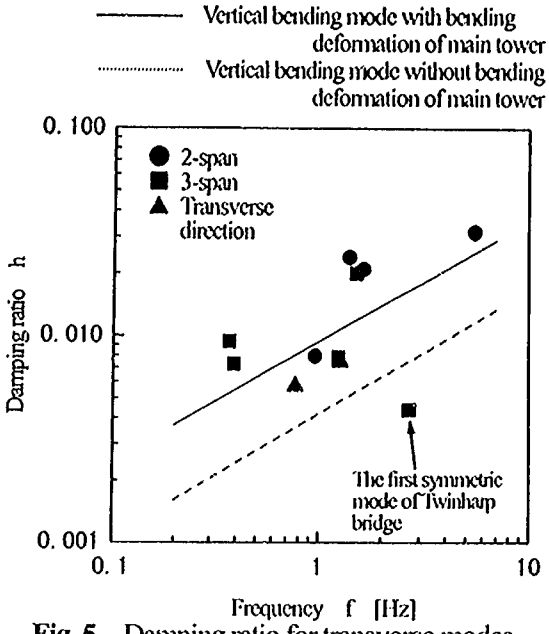


Fig. 5 Damping ratio for transverse modes.

At this stage, it is difficult to identify which factor has the larger effect, out of radiation damping from the foundations and friction at the supports. However, it can be understood that both factors have a significant effect on the damping ratio, which leads to a larger damping ratio in the mode with bending deformation of the main tower. In addition, the reason for smaller damping in the torsional mode than those in other modes as shown in eq. (4) is interpreted as being because the torsional mode mainly consists of vibrations of the main girder and cables, and there is no bending deformation of the main tower.

(3) Damping ratio of the transverse vibration mode

Based on the above discussion results, the data for transverse vibrations is analyzed in this section.

Firstly, the measured damping ratios for transverse vibrations are compared with those from the approximate formulas for vertical bending modes with and without bending deformation of the main tower, as shown in **Fig. 5**. Although the data for transverse vibrations is significantly scattered, it can be observed that the damping ratio increases as the frequency increases, and is close to that of the approximate formula for the mode with bending deformation of the main tower. However, the damping ratio is relatively small for the first symmetric mode of the Twinharp bridge in the transverse direction. It has been reported that in the first symmetric mode of the Twinharp bridge in the transverse direction, only the main girder of the central span showed significant deformation while the main tower showed almost no deformation[10)]. As there is no rotational deformation of the foundations, it can be understood that the damping ratio is small compared with the others.

Next, the damping ratio for single-column towers in the transverse direction is discussed. As the damping that is added for transverse vibrations is small in the case of single-column towers, the earthquake resistance in the transverse direction is very important, and thus the evaluation of damping is an important key point. In this study, the PC cable-stayed bridges with single-column main towers are the Tokachi and Twinharp bridges.

Table 5 Steel cable-stayed bridges where vibration tests have been performed.

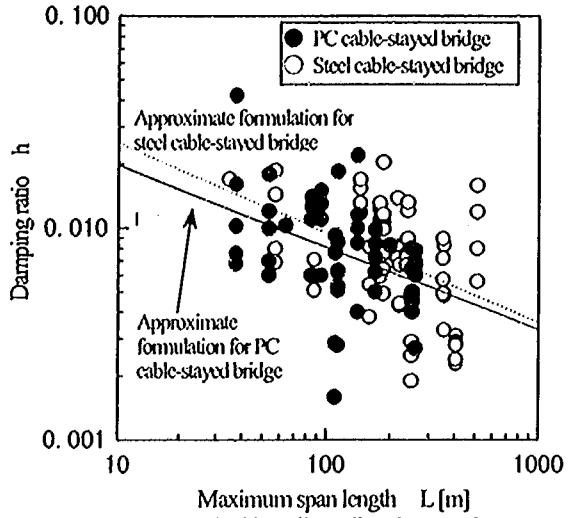
Bridge name	Type	Span length / Width of girder (m)	Type of cable arrangement and number of stays / girder type
Onomichi bridge	3-span continuous	85+215+85 10.2	Radiation type, double plane, 2 stays / Two main girders of I shape
Toyosato bridge		80.5+216+80.5	Fan type, single plane, 2 stays / Steel slab with box girder
Arakawa bridge		60.3+160+60.3 17.9	Harp type, single plane, 2 stays / Two girders of I shape and one box girder
Kamome bridge		100+240+100 20.1	Multi-type, single plane, 10 stays / Steel slab with inversed-trapezoidal box
Suchiro bridge		110+250+110 18.5	Fan type, single plane, 2 stays / Inversed-trapezoid one box girder
Tsurumi Tsubasa bridge		255+510+250 38.0	Multi-fan type, single plane, 17 stays / Flat box girder
Sugawara Jhohok		119+238+119 26.5	Fan type, single plane, 11 stays / Steel slab with inversed-trapezoidal box
Yamatogawa bridge		149+355+149 30.0	Harp type, single plane, 4 stays / Box girder
Meiko-Nishi Bridge		175+405+175 16	Fan type, double plane, 12 stays / Flat hexagonal box
Katsushika Harp bridge		40.5+134+220 +60.5 / 25.7	Multi-fan type, single plane, 17+7 stays / Inversed-trapezoid 3 box
Tenpozan bridge		170+350+120 39.25	Fan type, double plane, 9 stays / Flat hexagonal box
Suigo bridge	2-span continuous	178.85+111.6 20.5	Harp type, single plane, 3 stays / Steel slab with inversed- trapezoidal box
Aratsu bridge		185+115+45 21	Fan type, single plane, 13 stays / Steel slab with inversed-trapezoidal box
Yukitsuri bridge		44.4+57 3.5	Fan type, double plane, 5 stays / Flat hexagonal box
Kawasaki bridge		87.5+40.65 3	Fan type, double plane, 6+4 stays / Flat hexagonal box
Shinyo Country Club Sidewalk bridge		11+34.6 2.5	Radiation type, double plane, 1+2 stays / 3 boxes
Gasyou bridge	2-span uncontinuous	144+46+144 10.5	Fan type, double plane, 3 stays / Steel slab with 2 boxes

In the Tokachi bridge, vibrations were induced manually, and the measured damping ratio is 0.0057. At the Twinharp bridge, the damping ratio is 0.0075, which is computed from the resonant curve. However, it has been suggested that the damping ratio obtained from the resonant curve might to be slightly exaggerated[10]. Taking the above into account, it can be said that the damping ratio for transverse vibrations of single-column towers is around 0.006~0.007.

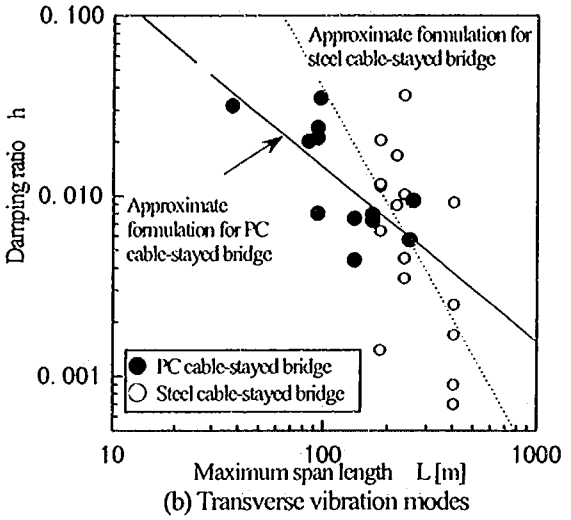
This data is smaller than predicted using the approximate formula eq. (6) for the mode with bending deformation of the main tower. This is because the main girder has almost no deformation in the transverse vibration mode of the single-column main tower. As described above, the tendency of the damping ratio in the transverse direction could be explained by considering the condition of bending deformation of the main tower in the vibration mode.

4. Comparison of damping characteristics between PC and steel cable-stayed bridges

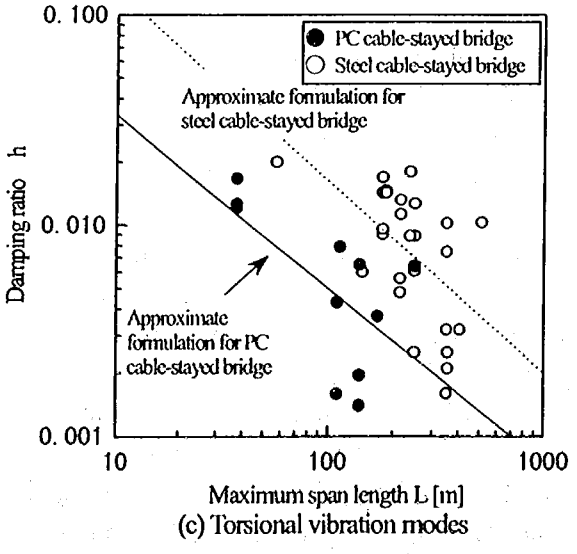
As for steel cable-stayed bridges, the data for 17 bridges shown in **Table 5** were obtained through a literature survey. As already pointed out by previous research, the damping ratios of bridges with steel truss girder are larger than those with steel box girder. In comparison of the damping of PC and steel cable-stayed bridges, only data for bridges with steel box girder was used.



(a) Vertical bending vibration modes



(b) Transverse vibration modes



(c) Torsional vibration modes

Fig. 8 Comparison of damping ratios of PC and Steel box girder cable-stayed bridges

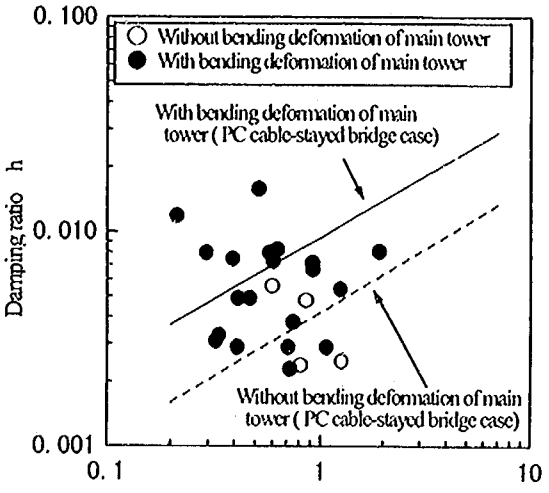


Fig. 9 Damping ratio of steel box girder cable-stayed bridges for vertical bending modes.

Fig. 8 shows a comparison between the damping ratios of PC and steel cable-stayed bridges. The maximum span length of PC cable-stayed bridges is shorter than those of steel ones, and it may be difficult to make direct comparisons. However, it can be said that the damping of PC cable-stayed bridges, which mainly consist of concrete materials, is not always larger than that of steel ones with steel box girder. With vertical bending vibrations and transverse vibrations, the damping ratios for the two types of bridges are almost the same. In terms of torsional vibrations, the damping of PC cable-stayed bridges tends to be rather smaller.

Fig. 9 shows the results corresponding to the vibration modes with and without bending deformation of the main tower, as in the case of PC cable-stayed bridges. Among the steel cable-stayed bridges on which vibration tests were conducted, there is no bridge with a symmetric continuous 2-span, and the amount of data for the vibration modes without bending deformation of the main tower is small. However, it can be observed from the figure that in the case of steel cable-stayed bridges, the damping ratio for the mode with bending deformation of the main tower is also larger than that without bending deformation of the main tower. The approximate

Table 6 Frequency and damping ratio during cantilever erection.

Bridge name	Frequency (Hz)	Damping ratio
Ikara bridge	0.130	0.0076~0.0078
Shin-inagawa bridge	0.116	0.0084

formulas eq. (5) and (6) of the damping ratios for the modes with and without bending deformation of the main tower in the case of PC cable-stayed bridges are shown in the same figure. It can be seen that they agree well with to the data for steel cable-stayed bridges.

The damping of PC cable-stayed bridges which mainly consist of concrete materials is not larger than that of steel ones with box girder. The reasons can be considered as follows.

Firstly, as described before, the damping due to friction at the supports and energy radiation from the foundations dominates the damping ratio, and therefore the effect of hysteresis damping, which depends on the type of materials, is insignificant. Secondly, PC cable-stayed bridges are very heavy, and large amplitude vibration tests are difficult to conduct. In the case of steel cable-stayed bridges like the Tsurumi Tsubasa bridge, vibration tests were conducted with such large amplitude that frictional damping occurred at the supports. Therefore, vibration amplitude is different in the two types of bridges. Compared to PC cable-stayed bridges, the effects of damping due to friction at the supports might be larger in steel cable-stayed bridges.

At this stage, it can not be concluded from the available measurement of vibration tests that damping of PC cable-stayed bridges is larger than that of steel ones with box girder.

5. Damping characteristics of PC cable-stayed bridges during cantilever erection

PC cable-stayed bridges are unstable during cantilever erection. The construction time is short compared to the service time after completion, and thus there have been few studies on seismic behavior during construction. In the case of PC cable-stayed bridges, however, a much larger bridge may be constructed which requires a longer construction time, and thus seismic investigations during construction may become very necessary. In addition, gust responses are induced by wind turbulence easily, and wind resistance should be assured.

As for the vertical bending vibration mode during cantilever erection, the damping ratio was observed at the Ikara and Shin-inagawa bridges[11),12)]. The vibration amplitudes in both cases reached a certain level, and thus the data is very reliable. **Table 6** shows the measured results. Although the amount of data is insufficient and further accumulation of data is necessary, the following can be confirmed from the data.

During cantilever erection of PC cable-stayed bridges, there is no damping due to friction at the supports, and damping due to hysteresis damping of the concrete material and energy dissipation from the foundations dominates the damping behavior in the Ikara and Shin-inagawa bridges. From the measurements, it can be concluded that the damping ratio during cantilever erection is around 0.008, which is close to that of the bridge after completion of construction. When construction is complete, however, during earthquakes of the level assumed in the design, the vibration amplitude increases and damping due to friction at the supports may become large. Conversely, concerning the cantilever erection, even in cases with supports at the main tower, like 3-span bridges, the main girder is temporarily fixed to the top of the pier, and there is no frictional damping at the supports.

The measured damping ratio during cantilever erection is larger than that derived from approximate formula eq. (6) for the relation between the damping ratio and frequency for the mode

with bending deformation of the main tower. This is because the rotational deformation during cantilever erection is larger than that of the completed bridge. In addition, the temporary member, especially for the main tower, is supposed to increase damping.

6. Conclusions

In order to clarify the damping characteristics of PC cable-stayed bridges, the measured damping data from vibration tests at 15 bridges are analyzed according to vibration mode and frequency, and damping characteristics are discussed. Concerning the damping characteristics of PC cable-stayed bridges, the following new findings are obtained.

(1) The damping ratio of PC cable-stayed bridges decreases as the maximum span length becomes larger. An approximate formula for each vibration mode has been established. The damping ratio of the torsional mode is smaller than those of the vertical bending and transverse modes.
(2) As for the vertical bending vibration mode, the measurements are analyzed according to whether the vibration mode is with or without bending deformation of the main tower, and an approximate formula between the damping ratio and frequency has been established. The tendencies of frequency dependence are similar in the two modes, and the damping ratio in the mode with bending deformation of the main tower is about twice as large as that in the mode without bending deformation of the main tower. In the mode with bending deformation of the main tower, energy dissipation from the foundations is large, and damping due to friction at the supports caused by sliding deformation occurs. These are considered to lead to the large damping ratio in the mode.
(3) Concerning the damping ratio for transverse vibrations, as the amount of data is small and the scattering of data is significant, no clear tendency could be observed. However, it was confirmed that higher frequencies lead to larger damping ratios, which are close to those for the vertical bending vibration mode with bending deformation of the main tower.
(4) It can be confirmed that the damping ratio for the first transverse vibration mode of single column towers, which may undergo large seismic forces during earthquakes, is around 0.006～0.007, although there is little data.
(5) Although PC cable-stayed bridges mainly consist of concrete materials, its damping ratio is not larger than that of steel cable-stayed bridges with box girder. The reasons can be considered as follows. Energy dissipation from the foundations and friction at the supports has a large effect on the damping ratio. In addition, PC bridges are very heavy, and the amplitude of vibration tests on PC bridges is small compared with that on steel bridges.
(6) As for cases of cantilever erection, there are only measurements from Ikara and Shin-inagawa bridges. However, the amplitudes of vibration tests at both bridges are sufficently large, and the data reliability is high. The damping ratio is around 0.008, which is close to that of completed bridges. However, damping due to friction at the supports does not occur and thus the damping ratio will not increase as the amplitude increases. This tendency is different from that in completed bridges.

References

1) Yamaguchi H., Takano H., Ogasahara M., Shimosato T., Kato M. and Kato H.: Energy-based damping of cable-stayed bridges and its application to Tsurumi Tsubasa Bridge, Proc. JSCE, No. 543/I-36, pp.217-227, July, 1996.(in Japanese)

2) Kawashima K., Unjoh S. and Goda Y.: A seismic design procedure of cable-stayed bridges, Part 1. Dynamic characteristics of cable-stayed bridges based on field vibration test results, Report of Public Works Research Institute, No.2388, June, 1986. (in Japanese)
3) Yamaguchi H., Ito M., Sakamoto K. and Adikari R.: Damping database of cable-stayed bridges and its analysis, Journal of Constructional Steel, Vol.1, July, 1993. (in Japanese)
4) Davenport A., Larose G.: The structural damping of long-span bridges. An interpretation of observations, Canada-Japan Workshop on Bridge Aerodynamics, Ottawa, pp.111-118, September, 1989.
5) Japan Road Association: Specifications for Highway Bridges, Part V: Seismic design, December, 1996. (in Japanese)
6) Kawashima K., Unjoh S. and Tsunomoto M.: Damping characteristics of cable-stayed bridges associated with energy dissipation from foundation, Civil Engineering Journal, Vol.32, No.9, pp.33-39, 1990. (in Japanese)
7) Kawashima K. and Unjoh S.: Damping characteristics of cable-stayed bridges associated with energy dissipation at movable supports, Proc. of JSCE, No.404/I-11, pp.145-152, April, 1989.
8) Nagai K., Egusa T. and Sasaki N.: Damping characteristics of long span box girder bridge, Journal of Civil Engineering Structure and Material, No.3, pp.79-87, January, 1988. (in Japanese)
9) Yoneda M.: Some considerations on damping characteristics of bridge structures due to Coulomb friction force at movable supports, Proc. of JSCE, No.492/VI-23, pp.137-145, June, 1994. (in Japanese)
10) Mukae K., Fujita M., Honma H. and Kondo S.: Vibration test on PC cable-stayed bridge having the stays of single plane anchored at the single shaft pylons, Technical Reports of Research Laboratory of Sumitomo Construction Co., Ltd., pp.71-79, 1992. (in Japanese)
11) Niihara Y., Takeda T., Oshio M. and Nakano R.: Vibration control of PC cable-stayed bridge during cantilever erection by AMD, Proc. of the 5th Symposium on Developments in Prestressed Concrete, pp.75-78, October,1995. (in Japanese)
12) Enomoto S., Okuda H., Niihara Y. and Yamauchi T.: Vibration characteristics of Shin-inagawa bridge under cantilever construction obtained by wind observation, Proc. of the 8th Symposium on Developments in Prestressed Concrete, October, pp.721-726, 1998. (in Japanese)

Monitoring of Hakucho Suspension Bridge using Ambient Vibration

Yozo FUJINO[1], Masato ABE[1], Hajime Shibuya[2], Masato Yanagihara[2], and Masashi Sato[2]

1) Department of Civil Engineering, University of Tokyo, Tokyo, Japan
2) Hokkaido Bureau of Development, Hokkaido, Japan

ABSTRACT

Feasibility of health monitoring of a long span suspension bridge by ambient vibration measurement is studied. At the first half of paper, measurement installation is presented and identification scheme is constructed. Then the developed method is applied to analyze continuously monitored ambient vibration measurement at a 720[m] span suspension bridge. The results indicates that ambient vibration measurement can provide reliable information on dynamic properties of the structure, which shows the potential to be applied to health monitoring.

INTRODUCTION

Monitoring of civil structures using vibration measurement has been attracting wide interest[1]. Vibration response itself can be used to examine performance of structures and possibly be used to evaluate structural state by inversely solving the structural parameters based on the measurement. Especially, information on dynamic properties is extremely important for long span bridges which are extremely flexible and can become unstable due to dynamic wind effects. Ambient vibration measurement is one of the most practical and convenient vibration measurement methods for large civil structures, because no specific excitation device is required and can be measured even under service conditions. Ambient sources such as wind and ground motion tend to have broad band frequency components which is suitable to identify multiple vibration modes. However, monitoring through vibration measurement is known to have several difficulties. For instance, reliable measurement and identification of higher vibration modes are usually difficult due to measurement noise and limitation of density of measurement points, although information of higher modes is essential to identify local defects with sufficient resolution.

In this paper, continuously monitored ambient vibration measurement at "Hakucho Bridge" located at windy and seismically active area in northern part of Japan are investiated.

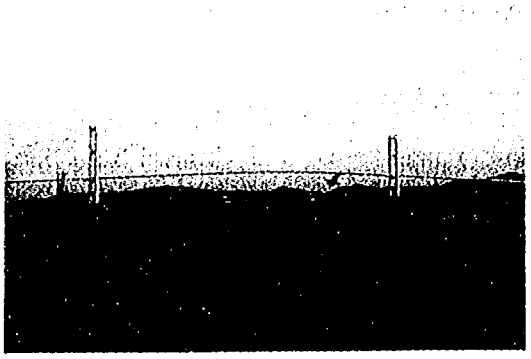


Figure 1. Hakucho Bridge

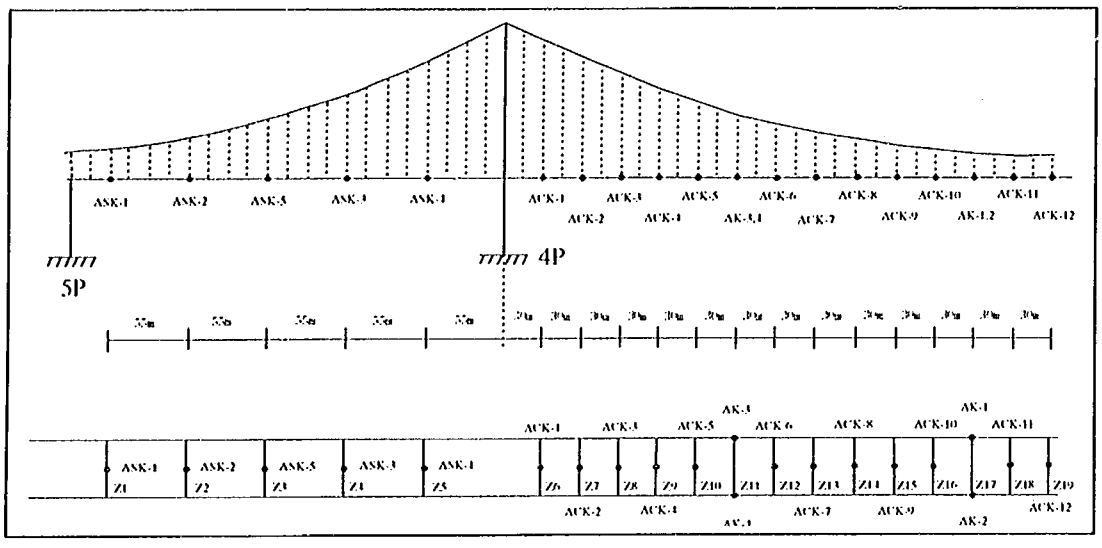


Figure 2. Measurement installation

Hakucho Bridge is a 720[m] span suspension bridge with steel box girder. Until now, measured data are available for ranges of wind and temperature conditions, while no major seismic event has taken place at the site.

The bridge has been monitored by densely distributed ambient vibration measurement system with 19 measurement points. The purpose is to understand the actual dynamic behavior and loading conditions, and to develop a framework for health monitoring using ambient vibration measurement. This paper shows construction of data processing and identification scheme for ambient vibration based monitoring and its applicability to the health monitoring of this bridge.

OUTLINE OF THE BRIDGE AND MEASUREMENT

The outline of the bridge is shown in Figure 1, which is located at the entrance of Muroran Gulf in Hokkaido Prefecture.

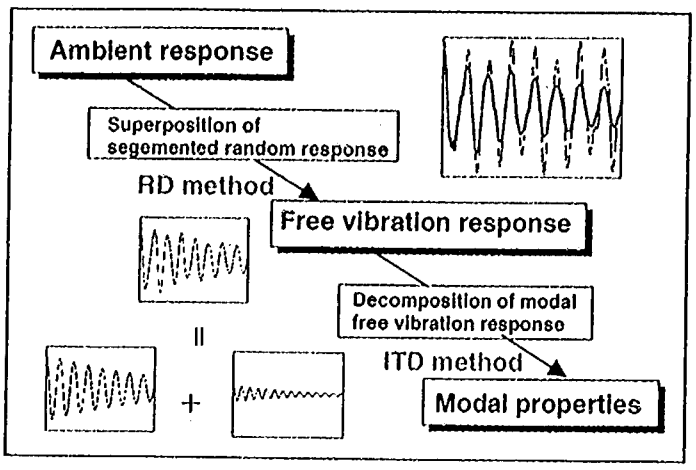


Figure 3. Outline of the identification scheme

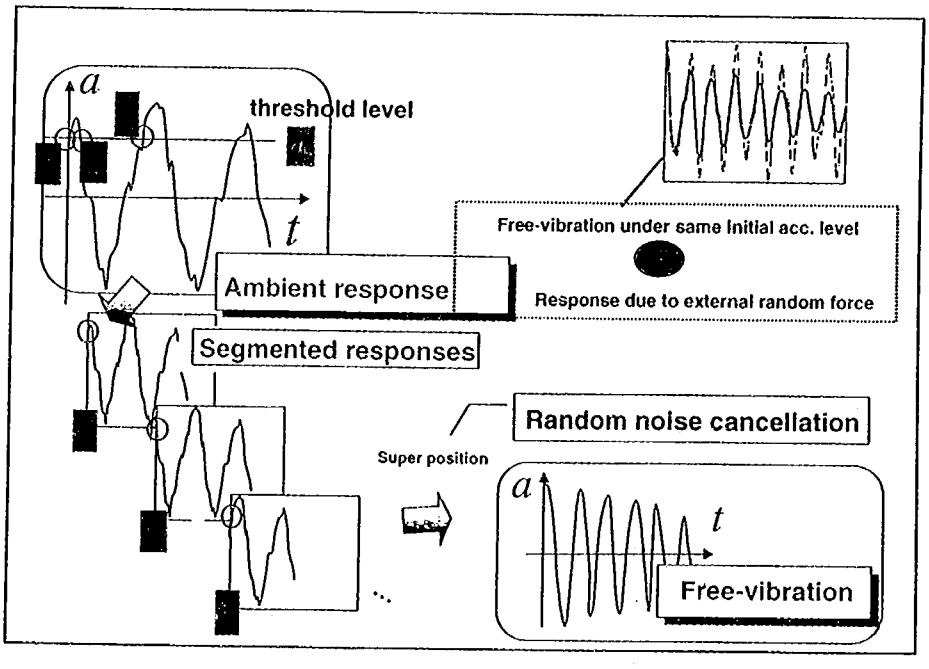


Figure 4. Outline of the random decrement method

The dominant wind direction is the transverse direction of the bridge. The bridge was completed in 1998, and extensive measurement was conducted prior to its opening, which provides initial state of structural performance. The towers and girders are made of welded steel boxes. The total length is 1380[m], with center span of 720[m] and each side span of 330[m]. Each span is discontinuous and the center span is simply supported at the attachment to the tower.

Nineteen stations of accelerometers are installed to measure vertical motion of the girder. Station locations are shown in Figure 2. Because of these densely distributed measurement stations, reliable identification up to higher vibration modes are expected. Anemometer is installed at the center of the span to measure wind velocity and direction. In this study, continuously measured ambient vibration data

over 100 hours in June 1998 is analyzed. It encompasses various excitation conditions, i.e., wind velocity/direction, temperature, e.t.c.

IDENTIFICATION OF DYNAMIC PROPERTIES

Outline of the identification scheme is shown in Figure 3. The scheme is the integration of the data processing part using random decrement method to cancel random components in measurement and the identification part using free vibration response. In this section, outline of each part is presented.

Processing of random response

Because excitation source cannot be identified and measurement of the input force is not available for ambient vibration, statistical treatment of measured response data is required to obtain reliable results. Assuming that the excitation is stationary white noise process, random decrement method, which eliminates random component by stacking of time history of response, is employed herein[2]. Time history after occurrence of response value a_0 can be linearly decomposed into (i) free response part with initial condition a_0, and (ii) forced oscillation part. When the excitation is random white noise process, the second part is expected to be cancelled by stacking many time responses which starts from a_0. The data is stacked 5000 times and a_0 is taken as 0.8 of root mean square response in the following calculation. The measurement for a_0 is selected at center span for identification of symmetric modes and quarter span for anti-symmetric modes. Outline of the method is shown in the Figure 4. Figure 5 shows identified free response from actual measurement data. It can be seen that time history of free response is successfully constructed after 5000 stacking by this method.

Identification of dynamic properties

Ibrahim's time domain method [3] is employed for identification of natural frequencies, mode shapes and modal damping ratios. The free vibration response obtained in the previous sub-section is expanded into linear combination of free response of each mode, i.e.,

$$x(t)=\sum_{r=1}^{2N}\exp[s_r t]\{\Psi_r\} \tag{1}$$

where x(t) is the time history of response, N is the number of degrees of freedom, and $\{\Psi_r\}$ is the mode shape of r-th mode. Because non-classically damped system is considered and complex conjugate eigenvalues are treated as distinct, the summation is up to $2N$ instead of N. The r-th eigenvalue s_r can be expressed as,

$$s_r=-\zeta_r\omega_r+i\omega_r\sqrt{1-\zeta_r^2} \tag{2}$$

where ω_r and ζ_r are natural frequencies and damping ratios of the r-th mode. Equation (1) can be expressed in terms of matrix form by discretizing the response x at time steps t_j (j=1,2,...,L) as,

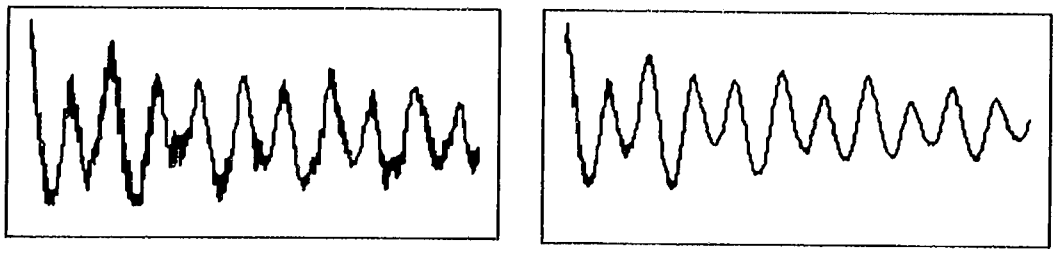


Figure 5. Sample time history after stacking, left: stacked 50 times, right: stacked 5000 times

$$[x]=[\Psi][\Lambda] \tag{3}$$

where $[x]=[x_i(t_j)]$, $[\Psi]=[\Psi_{ij}]$, and $[\Lambda]=[\exp(s_i t_j)]$. The dimension of each matrix is, $[x]$: n x L, $[\Psi]$: n x $2N$, and $[\Lambda]$: $2N$ x L, where n is the number of measurement points, and L is the total number of time steps.

The response with delay time of Δt is expressed as

$$\hat{x}(t)=x(t+\Delta t), \tag{4}$$

which can again be discretized to,

$$[\hat{x}]=[\hat{\Psi}][\Lambda], \tag{5}$$

where each raw of $[\hat{\Psi}]$ is defined as,

$$\{\hat{\Psi}_r\}=\exp(s_r\Delta t)\{\Psi_r\}. \tag{6}$$

An n x n square matrix $[A]$ to transform from the original time history to the lagged time history is defined as,

$$[A][\Psi]=[\hat{\Psi}]. \tag{7}$$

Using this relationship, the modal properties can be obtained by solving the following eigenvalue problem:

$$[A]\{\Psi_r\}=\exp(s_r\Delta t)\{\Psi_r\}. \tag{8}$$

The matrix $[A]$ is derived by the following procedure. First, pre-multiplying both sides of equation (3) by $[A]$, one obtains,

$$[A][x]=[A][\Psi][\Lambda] \tag{9}$$

which yields,

$$[A][x]=[\hat{x}] \tag{10}$$

Post-multiplying equation (9) by pseudo-inverse of $[x]$: $[x]^+=[x]'\left([x][x]'\right)$, $[A]$ can be obtained as,

$$[A]=[\hat{x}][x]^+=[\hat{x}][x]'\left([x][x]'\right)^{-1}. \tag{11}$$

Because all the modes are identified simultaneously by solving the eigenvalue problem of equation(8), this method can easily be applied to not only single mode structures, but also to multi mode structures with closely spaced natural frequencies, such as cable supported bridges.

Table 1 shows the comparison of identified frequency by the proposed method using ambient vibration measurement, with forced vibration test results and finite element prediction. All three are in good agreement, which validates the accuracy of the proposed identification technique. Figure 6 shows an example of identified mode shape of the fifth vertical bending mode.

TABLE I. IDENTIFIED FREQUENCIES

Vibration Mode			Natural frequency [Hz]		
			Forced	Ambient	Analysis
Girder vertical mode	Symmetric	1	0.129	**0.131**	0.123
		2	0.218	**0.223**	0.217
		3	0.435	**0.440**	0.436
		4	0.719	**0.724**	0.720
	Anti-symmetric	1	0.149	**0.152**	0.149
		2	0.317	**0.318**	0.320
		3	0.568	**0.571**	0.567
		4	0.906	**0.902**	0.893
Girder torsional mode	Symmetric	1	0.487	**0.494**	0.472
		2	1.164	**1.160**	1.128
		3	1.866	**1.860**	1.852
	Anti-symmetric	1	0.772	**0.778**	0.761
		2	1.502	**1.530**	1.490
Girder lateral mode	Symmetric	1	0.099	**0.093**	0.101
		2	0.560	**0.566**	0.541
Tower in-plane mode		1	0.599	**0.598**	0.624

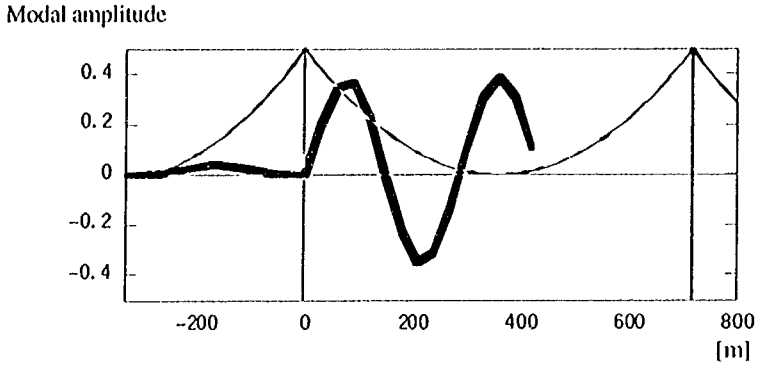


Figure 6. Identified fifth bending mode.

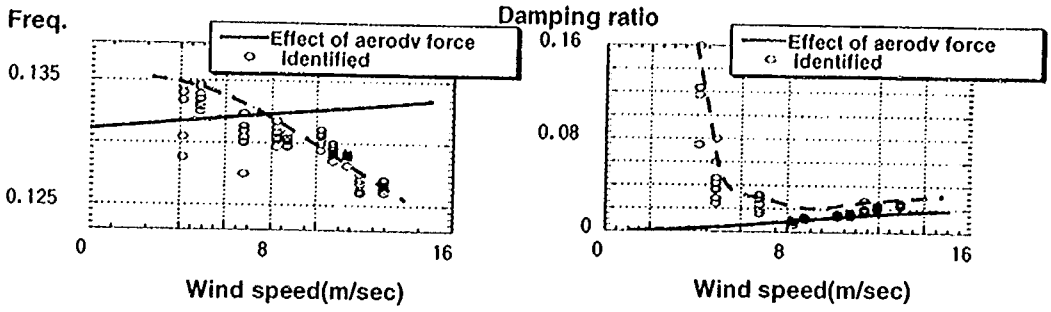
VARIATION OF DYNAMIC PROPERTIES UNDER VARIOUS WIND VELOCITY CONDITIONS

The proposed scheme is applied to analyze the actual ambient vibration measurement of the bridge under various wind loading conditions[4]. The ambient vibration data in June 1998 is analyzed. The maximum wind velocity observed was 14.9[m/sec]. The measured data are categorized into 10 classes by wind velocity in the transverse direction of the bridge as shown in Table 2, and the identification method presented in the previous section is applied for each class of record. The time history data used for identification are stacked 5000 times. Ten time histories are sampled randomly from each rank of records.

Figure 7a) shows the variation of the identified natural frequency for the first bending mode with respect to wind velocity.

TABLE II. CLASS OF WIND VELOCITY USED IN THIS STUDY

Class	1	2	3	4	5	6	7	8	9	10
Wind velocity [m/sec]	4.1	4.9	6.8	8.2	8.7	10.2	10.7	11.4	11.9	12.9
RMS of acceleration [cm/sec^2]	0.02	0.02	0.09	0.21	0.37	0.78	1.26	1.84	2.46	4.45



a) natural frequency b) modal damping

Figure 7. Effect of wind velocity on modal properties of the first vertical bending mode

The natural frequency is observed to reduce as wind velocity becomes higher. However, it is expected to increase for stronger wind according to prediction by the self-exciting aerodynamic force which was obtained wind tunnel experiment conducted prior to construction. The identified damping ratios are shown in Figure 7b). Here, the results match with prediction by wind tunnel results when wind velocity is higher than 8[m/sec]. For lower wind velocity, the identified damping ratios are significantly higher than prediction. The cause of this discrepancy in natural frequency and damping ratio appears to be the effect of stick-slip behavior of Coulomb friction element, where it sticks for lower wind velocity and slips with certain friction force for higher wind velocity. The modal amplitudes near the tower are found to become smaller for lower wind velocity, which indicates sliding and friction at bearing supports and/or expansion joints of the center span are the main cause of this behavior. Although these secondary connection elements are usually idealized as friction less pin connection in the analysis, their precise modeling is required for monitoring and evaluations of structural performance. Inverse analysis is currently underway to quantitatively investigate this behavior.

The results presented in Figure 7 indicate that this data processing and identification methods are applicable to track variation of natural frequencies and damping ratios due to variation of wind velocity and friction force at bearings and/or joints. Therefore, ambient vibration measurement can provide reliable information of dynamic properties, which has the potential to be applied to health monitoring.

CONCLUSIONS

Feasibility of health monitoring of a long span suspension bridge by ambient vibration measurement is studied using actual measurement data. To utilize ambient vibration measurement data, an identification scheme which makes use of cancellation of randomness in data by stacking is employed. The proposed method is shown to be applicable to identify modal properties from ambient vibration with high accuracy. It is also shown that the variation of natural frequencies and modal damping ratios due to change in wind velocity can be tracked by the current measurement installation and identification scheme. The results indicates that ambient vibration measurement can provide reliable information of dynamic properties, which has the potential to be applied to health monitoring.

REFERENCES

1. Abé, M. 1998. "Structural monitoring using vibration measurement – current practice and future -," *Artificial Intelligence in Structural Engineering*, Ian Smith, ed, Lecture Notes in Artificial Intelligence 1454, Springer, pp.1-18.
2. Cole, H.A., jr. 1973. "On-line Failure Detection and Damping Measurement of Aerospace Structures by Random Decrement Signatures," NASA CR-2205.
3. Ibraham, S.R., et.al. 1977. "A Method for the Direct Identification of Vibration Parameters From the Free Response," *Shock and Vibration Bullet*in Vol.47.
4. Kajimura, T. 1999. "Construction of Structural Monitoring Method for Ambient Vibration Testing," *B.S. Thesis*, Department of Civil Engineering, The University of Tokyo (in Japanese).

SESSION 10: CURRENT BRIDGE R&D

(1) AASHTO's Bridge Research Program

(David B. Beal)

(2) Design Concept of a Floating Swing Bridge in Osaka

(Tadaaki Maruyama, Yukio Kawamura, Masao Yubisui, and Hiroshi Tanaka.)

(3) International Scanning Tours Related to Bridge Technology

(David H. Densmore)

(4) Fretting Fatigue Characteristics in the Curved Layout of Large-Capacity Prestressing Strands

(Manabu Fujita, Keiji Umezu, Hideo Arai and Tamon Ueda)

(5) Use of an Alternate Shear Connector in a Beam-in-Slab Bridge System

(F.W. Klaiber and T. J. Wipf)

(6) Maintenance of Bridge and Reinforcement of Existing Deck Slabs

(Hiroshi Mitamura, Shizuo Kato, Shigeharu Onsen and Shigeyuki Matsui)

AASHTO's BRIDGE RESEARCH PROGRAM

David B. Beal, P.E.[1]

Abstract
The American Association of State Highway and Transportation Officials has sponsored the National Cooperative Highway Research Program since 1962. The Transportation Research Board, a unit of the National Academies, manages this program. This paper describes the operation of this applied research program, provides details on the recent products of the bridge research activities, and provides an overview of the current bridge research program.

[1] Senior Program Officer, National Cooperative Highway Research Program, Transportation Research Board, Washington, D.C.

Introduction

The National Cooperative Highway Research Program (NCHRP) was created in 1962 to conduct research on highway planning, design, construction, operation, and maintenance. This program is managed by the Transportation Research Board (TRB) and sponsored by the American Association of State Highway and Transportation Officials (AASHTO), in cooperation with the Federal Highway Administration (FHWA).

Each state's Department of Transportation (DOT) is a member of AASHTO. The states voluntarily support NCHRP with funds drawn from their Federal-Aid Highway apportionment. The funds available for research contracts in recent years and the funds allocated to bridge research are shown below. The 7-year average annual funding for bridge research is $2.5 million, or approximately 17% of the total funding.

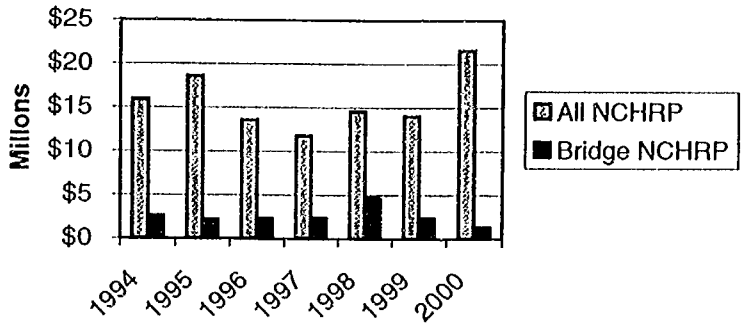


Figure 1, NCHRP Funding.

Since the beginning of the program, there have been 156 bridge-related research projects funded at $40,300,000. The first "bridge" project, started in 1965, was titled "Deformation of Steel Beams Related to Permitted Highway Bridge Overloads" and was funded at $50,000. This project's objective was to study the magnitude and effect of permanent deformations in simple-span composite and non-composite highway bridges.

The development of the annual program starts with the solicitation of research problem suggestions from the state DOTs and from the FHWA. NCHRP and FHWA staff review these first-stage research problem statements, and recommendations for further action on the statement are provided to the originator. The statement may be resubmitted as written, revised in accordance with the staff comments, or withdrawn.

All second-stage research statements are distributed to AASHTO's Standing Committee on Research (SCOR). SCOR comprises 16 representatives, a chair and vice chair. The committee meets annually to select problems for the NCHRP program and to allocate problem funding. The recommendations of SCOR must be approved by at least two-thirds of the DOTs in order for a proposed research project to be supported by NCHRP.

Each approved problem is assigned to an ad hoc panel of experts. Although the majority of the panel members are from state DOTs, panels also consist of academics, consultants and federal representatives. Each panel prepares a research project statement, which is used to solicit research proposals, selects the research contractor, monitors research in progress, provides technical guidance, and reviews reports for acceptability and for accomplishment of the research plan.

Research findings are published in the *NCHRP Reports* series and in the *NCHRP Synthesis of Highway Practice* series. The reporting format is designed specifically to accommodate the transportation administrator and the practicing engineer. In addition, to provide the earliest possible awareness of research findings, *NCHRP Research Results Digests* and *NCHRP Legal Research Digests* are issued as warranted. Copies of all published reports are issued to the chief administrative officer of each highway and transportation department.

The NCHRP program is a goal-oriented applied research program. With bridge related issues the program has been particularly successful with producing research results that are implemented by the states. The primary role of the states in selecting the problems to be studied, defining the research objectives, selecting the research contractor, and monitoring the research effort is considered to be a fundamental reason for this success.

Recent Products of the Bridge Research Program

Four examples of recently completed NCHRP projects that resulted in implemented AASHTO documents are given. The first of these examples is NCHRP Project 12-33, "Development of a Comprehensive Bridge Specification and Commentary." In 1986 a group of state bridge engineers sent a letter to the Chair of the AASHTO Highway Subcommittee on Bridges and Structures (HSCOBS) expressing concern that the AASHTO standard specifications were outdated. Based on this letter and subsequent discussions and presentations, an NCHRP pilot study was initiated to develop a comprehensive outline for an updated AASHTO bridge specification. After a thorough review of the findings of that study, HSCOBS decided to develop a probability-based limit states specification with commentary. NCHRP Project 12-33 was initiated to prepare the new specification. The product of this project is the "LRFD Bridge Design Specification," published in 1994 (1).

The specification development process extended over 5 years and involved more than 50 consultants (2). Four drafts of the specification were prepared. Approximately 250 engineers reviewed the various drafts, and it is estimated that more than 12,000 individual comments were received. Two series of trial designs were a key feature of the code development process. In addition to broadening the base of practicing engineers familiar with the new specifications, the trial designs exposed areas where further development of load models and resistance formulations were needed. Major changes introduced by the new specifications are:

- Introduction of a new philosophy of safety – LRFD
- Identification of four limit states
- Development of new load factors

- Determination of the relationship between the chosen reliability level, the load and resistance factors, and load models through the process of calibration
- The development of improved load models necessary to achieve adequate calibration, including a new live load model
- Revision of techniques for analyzing and calculating load distribution
- Combined presentation of plain, reinforced, and prestressed concrete
- Introduction of limit state-based provisions for foundation design and soil mechanics
- Expanded coverage of hydraulics and scour
- Revision of earthquake provisions to make the method of analysis a function of the importance of the structure
- Inclusion of large portions of the Guide Specification for Segmental Concrete Bridge Design
- Inclusion of large portions of the FHWA specification for ship collision
- Introduction of the isotropic deck design process
- Development of parallel commentary

The evolution of the load and resistance factor design code has continued under NCHRP Project 12-42, LRFD Bridge Design Specification Support, and the second edition of the specifications was published in 1998.

A second example of recent NCHRP projects resulting in implemented AASHTO documents is the specifications for the design of movable bridges, which were developed under NCHRP Project 12-44 and adopted by AASHTO in 1999. The structural portions of these specifications are in an LRFD format. Although the intention was to extend the LRFD design methodology to electrical, mechanical, and hydraulic specification provisions, this effort was only partially successful. For mechanical and hydraulic design, the current standard design practices and associated design equations were transformed into LRFD-like methodologies to maximize consistency with LRFD. The electrical design, however, was found to be totally unique and non-transformable in terms of LRFD.

Additional load cases beyond those required in the AASHTO LRFD Bridge Design Specifications need to be investigated for movable bridges. For example, load cases for structure in the open position, including the dynamic effects resulting from the acceleration of the span due to stopping or starting are required. Also requiring investigation are situations where the bridge is closed and the counterweight is supported independently of the bridge, as may be appropriate for certain maintenance or rehabilitation conditions, and where the structure is available for traffic. Because this is a temporary condition, the load factors required are similar to those applicable to permit loads in the fixed bridge specifications.

A third example of NCHRP projects resulting in AASHTO documents is Project 12-38, under which the specifications for the design of horizontally curved steel girders in a load factor format were completely revised (4). This work was adopted by AASHTO as a guide specification in 1999. In addition to the specifications, detailed design examples for I girder and box girder bridges were prepared.

Notable features of the new specifications include a constructibility limit state and provisions to control concrete deck cracking. The erection and construction of curved-girder bridges is generally more complex than those of straight-girder spans. The constructibility limit state considers deflection, stability, and steel and concrete strength. One scheme to construct the bridge must be shown on the design plans.

The researchers determined that the high torsional shears in curved-girder concrete decks - compared with straight, right, girders - required the inclusion of a serviceability provision. These provisions require that longitudinal reinforcement be included wherever the computed tensile deck stresses during sequential deck placement or due to overload may cause cracking. The researchers also proposed that these requirements be extended to skew bridges.

The final example of AASHTO documents resulting from NCHRP projects is the specifications for the design of structural supports for highway signs, luminaires, and traffic signals, which were developed in Project 17-10 (5). These specifications were adopted by AASHTO in 1999. A major impediment to the implementation of these specifications was the change to a wind load map based on a 3-sec gust. The wind speeds from the new map, coupled with an approximate gust factor, resulted in wind loads inconsistent with experience both in coastal areas and in the interior of the country. The new gust factor is an average value that results in the same wind load as the previous specification. This average value inadequately models local conditions.

Because of the large local changes in design loads, adoption of the new specifications was delayed for a year for HSCOBS review. The issue was resolved through the introduction of a specification clause permitting the use of the old wind map and gust factors at the discretion of the design engineer. Additional significant changes introduced by the new specifications are:

- Change the basis of wind pressure calculations from fastest-mile wind speed to 3-sec gust, including updating the wind speed map
- Change the increase in allowable stress for groups II and III load combinations from 40 to 33 percent
- Add a new section on fatigue design criteria for steel and aluminum cantilevered structures
- Add a new section on wood design
- Add a new section on fiber-reinforced composite design
- Update the allowable stress equations for multi-sided tubular steel sections
- Correct the combined stress ratio equation for non-pole type members
- Provide a revised equation for the coefficient for amplification, C_A
- Add an appendix on anchorage of cast-in-place headed anchor bolts
- Implement a format similar to that of the AASHTO LRFD Bridge Design Specifications, including an SI version of the specifications.

Table 1 provides a list of NCHRP bridge products delivered in recent years.

Table 1 – NCHRP Products for the AASHTO Highway Subcommittee on Bridges and Structures.

NCHRP Project	Product	Status
10-20A	Bearing **Selection Guide** and recommended **Specifications** for design and construction of high-load, multi-rotational bridge bearings.	Adopted by SCOBS in May 1996. Contact: David Beal, 202/334-3228.
10-35	Fatigue **specifications** for welded and mechanical splices in reinforcing steel.	Adopted by SCOBS in May 1996. Contact: David Beal, 202/334-3228.
10-43	Inspection, evaluation, and maintenance **manual** for moveable bridges.	Adopted by SCOBS in 1997. Contact: David Beal, 202/334-3228.
10-46	Recommended **practices** for corrosion evaluation of new and existing steel pile structures in nonmarine applications.	Published as *AASHTO Provisional Standard PP36-97*. Contact: David Beal, 202/334-3228.
12-28(2)C	Conversion of BRIDGIT bridge management **software** to Windows.	Release 3.0 distributed in July 1998. Bridgit is now an AASHTOWare project. Contact: David Beal, 202/334-3228.
12-33	LRFD bridge design **specifications**.	Adopted by AASHTO in 1993. Contact: David Beal, 202/334-3228.
12-44	Recommended **specifications** for the design and construction of moveable highway bridges.	Adopted by AASHTO in May 1999. Contact: David Beal, 202/334-3228.
17-10	Revised **specifications** for the design of structural supports for highway signs, luminaries, and traffic signals.	Adopted by ASHTO in May 1999. Contact: David Beal, 202/334-3228.
20-7(45)	Revised seismic design **provisions** (Division I-A) of the AASHTO *Standard Specifications for Highway Bridges.*	Adopted by SCOBS in June 1994. Contact: David Beal, 202/334-3228.
20-7(46)	AASHTO **Guidelines** for bridge management systems.	Adopted by AASHTO. Contact: David Beal, 202/334-3228.
20-7(69)	LRFD bridge construction **specifications**.	Adopted by AASHTO in 1995. Contact: David Beal, 202/334-3228.
22-8	Metric version of guide **specifications** for bridge rail selection.	Included by reference in *AASHTO Bridge Specifications* in 1993. Completed. Contact: Timothy Hess, 202/334-2049.

Current Program

Table 2 lists the currently active NCHRP bridge research program. These 39 projects are funded at $12,000,000. LRFD and scour dominate the research themes of this program.

The AASHTO Highway Subcommittee on Bridges and Structures has committed to the load and resistance factor design approach. At their meeting in May of this year, they voted to suspend all maintenance of the traditional specification. Although the use of the standard

Table 2 – Current NCHRP Bridge Research Program.

Project Number	Title
04-26	Thermoplastic Drainage Pipe, Design and Testing
04-27	Application of Advanced Composites to Highway Infrastructure: Strategic Plan
10-37A(01)	Extended Exposure and Monitoring of Epoxy-Coated Reinforced Concrete Test Slabs
10-37C	Repair and Rehabilitation of Bridge Components Containing Epoxy-Coated Reinforcement
10-38(02)	Fatigue-Resistant Design of Cantilevered Signal, Sign, and Light Supports
10-51	Performance-Related Specifications for Elastomeric Bridge Bearings
10-52	Performance Tests for Modular Bridge Joints
10-55	Fiber Reinforced Polymer Composites for Concrete Bridge Deck Reinforcement
10-57	Structural Safety Appraisal Guidelines For Suspension Bridge Cables
12-39	Design Specifications for Debris Forces on Highway Bridges
12-42	LRFD Bridge Design Specifications Support
12-43	Life-Cycle Cost Analysis for Bridges
12-45	Recommended Specifications for Large-Span Culverts
12-46	Manual for Condition Evaluation and Load Rating of Highway Bridges Using Load and Resistance Factor Philosophy
12-47	Redundancy in Highway Bridge Substructures
12-48	Design of Highway Bridges for Extreme Events
12-49	Comprehensive Specification for the Seismic Design of Bridges
12-50	Bridge Software Validation Guidelines and Examples
12-51	Effect of Truck Weight on Bridge Network Costs
12-52	LRFD Specifications for Horizontally Curved Steel Girder Highway Bridges
12-53	Connection Between Simple-Span Precast Concrete Girders Made Continuous
12-54	Integral Connections of Modern Steel Bridge Structures
17-10(02)	Structural Supports for Highway Signs, Luminaires, and Traffic Signals
18-06	Service Life of Corrosion-Damaged Reinforced Concrete Bridge Superstructure Elements
18-07	Prestress Losses in Pretensioned High-Strength Concrete Bridge Girders
20-07/Task 107	Shear Design Guidelines for Skewed Multi-Beam Bridges
20-07/Task 121	Strategic Plan for Bridge Engineering Research
20-07/Task 97	Bridge Performance Measures
21-06	Corrosion in the Soil Environment: Soil Resistivity and pH Measurements
21-07	Development of Portable Scour Monitoring Equipment
21-08	Assessment of Innovative Load Testing of Deep Foundations
24-07(02)	Countermeasures to Protect Bridge Piers from Scour
24-09	Static and Dynamic Lateral Loading of Pile Groups
24-10	Thermally Sprayed Metallic Coatings to Protect Steel Pilings
24-13	Evaluation of Metal Tensioned Systems in Geotechnical Applications
24-14	Scour at Contracted Bridge Sites
24-15	Bridge Scour in Cohesive Materials
24-16	Methodology for Predicting Channel Migration
24-17	LRFD Deep Foundation Design

specification is still allowed, its use will become indefensible as the art and science of bridge engineering evolves. Because of this commitment, research to enhance the load and resistance factor specifications is encouraged. Three examples of this emphasis are given.

Project 12-42, mentioned previously, is a general support contract. It is a loosely structured project that provides on-demand assistance to the many technical committees of HSCOBS with interpreting and enhancing the specification. The visible products of this project, which has been active since 1995, are the annual interim changes to the specification. The second edition of the LRFD Bridge Design Specifications, published in 1998, is a direct result of the work funded under this project.

Project 12-52, *Comprehensive Specifications for the Seismic Design of Bridges* is a major undertaking that is expected to result in a substantive enhancement in seismic design requirements. Because this will be a national specification, a major consideration is the development of requirements that ensure the performance of structures in seismically active regions of the United States while not imposing unrealistic cost burdens on regions with lesser seismic activity. The effort on this project has only recently started, but consideration is being given to providing performance criteria for two design ground motions. The first of these criteria requires that all structures resist without service interruption a seismic event with a 50% probability of exceedance in 75 years. The higher level event has a 3% probability of occurrence in 75 years. All structures must resist this event without collapse, but only certain bridges, selected by the individual states, are required to remain in service. These tentative performance criteria are shown in Table 3.

Table 3 – Recommended Seismic Performance Criteria

	Performance Level		
Probability of Exceedance for Design Ground Motion (Approximate Return Period)	**Life Safety**	**Functional**	**Fully Operational**
Frequent Earthquake Service 50% in 75 years *R Factor* (Approx. 100 Year) *Damage*	Immediate *R = 1.0* *Minimal*	Immediate *R = 0.80* *Minimal to none*	Immediate *R = 0.67* *None*
Rare Earthquake Service 3% in 75 years *R Factor* (Approx. 2500 Year) *Damage*	Significant Disruption *R = 6 to 8* *Significant*	Limited *R = 3 to 6* *Repairable*	Immediate *R = 2* *Minimal*

The foundations portions of the LRFD specifications have come under increasing criticism from geotechnical engineers. Although this specialty area was consulted during the development of the specifications, it is clear now that the communication between bridge designers and geotechnical engineers was inadequate. The objective of project 24-17, *LRFD Deep Foundation Design,* is to recommend revisions to the driven pile and drilled shaft portions of the foundations section of the AASHTO *LRFD Bridge Design Specifications* that reflect current best practice in geotechnical design and construction. In addition, the research is expected to provide a detailed procedure for calibrating deep foundation resistance factors. Additional funding has been requested to provide a complete revision of the foundation section of the specification.

Scour is the other major theme of the NCHRP bridge research program. The five active projects are funded at approximately $1,500,000, which is a modest amount, considering that scour accounts for nearly 60% of bridge failures in the United States. The NCHRP effort focuses on the monitoring and retrofitting of existing structures (Projects 21-07 and 24-07(2)), and understanding and predicting scour behavior (Projects 24-14, 24-14 and 24-16).

Project 24-14, *Scour at Contracted Bridge Sites,* is typical of the effort to understand scour mechanisms. Current scour-prediction equations overestimate scour depths around abutments and in contracted openings. Excessive scour-depth prediction results in construction of unnecessarily deep foundations or installation of unnecessary countermeasures or both. Methodologies for predicting scour around abutments are based on laboratory-derived equations and cover only a narrow range of the wide variation of field conditions that commonly occur. Development of realistic scour-prediction equations must be based, at least in part, on field data. The use of field data is vital to understanding scour processes. The objective of this project is to develop quantitative guidelines for applying scour-prediction methodology at contracted bridge sites for a wide range of common field situations.

Conclusion

The National Cooperative Highway Research Program has provided the highway transportation community in the United States with implementable research products since 1962. AASHTO's satisfaction with the productivity of this program is clearly demonstrated by member states' annual agreement to contribute funds.

References

1. AASHTO LRFD Bridge Design Specifications, Washington, D.C. (1994).
2. *NCHRP Research Results Digest Number 198,* "Development of Comprehensive Bridge Specifications and Commentary," Transportation Research Board, Washington, D.C. (1998).
3. Modjeski and Masters, Inc., AASHTO LRFD Movable Bridge Design Specifications, Final Report on NCHRP Project 12-44 (unpublished).
4. Hall, D.H., Grubb, M.A., and Yoo, C.Y., *NCHRP Report 424,* "Improved Design Specifications for Horizontally Curved Steel Girder Highway Bridges," Transportation Research Board, Washington, D.C. (1999).
5. Fouad, F. H., Calvert, E.A., and Nunez, E., *NCHRP Report 411,* "Structural Supports for Highway Signs, Luminaires, and Traffic Signals," Transportation Research Board, Washington, D.C. (1998).

DESIGN CONCEPT OF A FLOATING SWING BRIDGE IN OSAKA

Tadaaki Maruyama[1], Yukio Kawamura[1], Masao Yubisui[1] and Hiroshi Tanaka[2]

ABSTRACT

The world's first swing and floating bridge is under construction in the Port of Osaka. It will be completed in the year of 2000 to connect two reclaimed islands. The bridge rests on the two hollow steel pontoons and is supported horizontally by rubber fenders and dolphins. Investigated herein are many important engineering issues such as the dynamic response to the wave, wind, earthquake and vehicle loads. The bridge can be regarded as a high-tech bridge on the advanced technology opening vistas onto 21st century.

1. INTRODUCTION

The Greater Osaka Region with a population of 16 million constitutes one of the largest production, inhabitation and consumption centers in Japan.

Osaka municipal government is promoting the project called "Tech Port Osaka" to develop the waterfront districts near the Port of Osaka to serve as the new center of Osaka City.

The project covers the construction of the three reclaimed islands, which have not only the harbor, residential and commercial area but also have parks and sport stadiums.

Under these circumstances, it has been decided to start the construction of the Yumeshima-Maishima Bridge (provisional name) connecting Yumeshima and Maishima reclaimed islands across North Waterway (Figure 1). The width of the North Waterway is about 400m. This sub-waterway is to play the part of the main waterway nearby in the case of some unforeseen accidents or events there ([1],[2],[3]).

To satisfy the above-mentioned purpose, the type of the bridge is selected as an arched skew floating highway bridge with total length of 940m and width of 38.8m for six traffic lanes with doubled-rib arch(Figure 2).

It stands on the two pontoons, which can swing around the pivot axis near an end of the girder. After the completion, the bridge will contribute to accelerate the development of especially Yumeshima Island and play an important role as a traffic access to the waterfront districts.

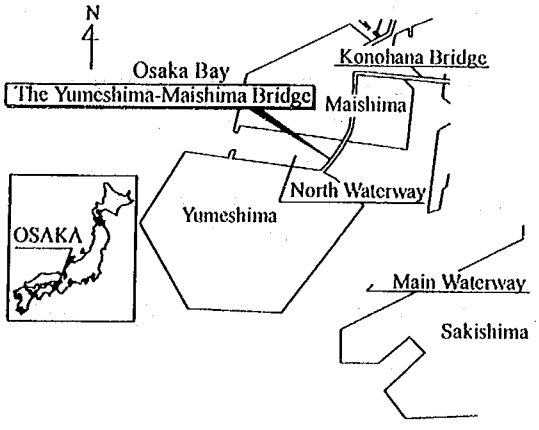


Figure 1: Reclaimed islands of Maishima and Yumeshima

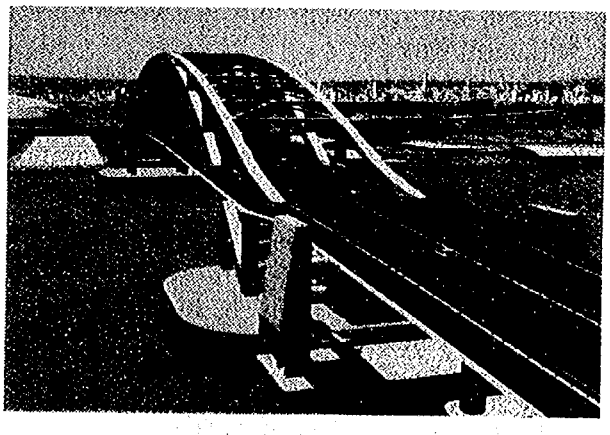


Figure 2: The Yumeshima-Maishima Bridge

1 Public Works Bureau, Osaka Municipal Government
2 Structures Design Dept., Hitachi Zosen Corporation

2. SELECTION OF BRIDGE TYPE

The ordinary fixed bridges or movable with foundations fixed to seabed, such as swing bridge, bascule bridge, rolling bridge or transporter bridge were investigated and assessed ([4]). It is concluded from the comparative study that those ordinary bridges would be difficult or economically infeasible; instead, a bridge with two pontoon foundations of the swing type (Figure 3) was proposed to be adopted as the first of this kind in the world.

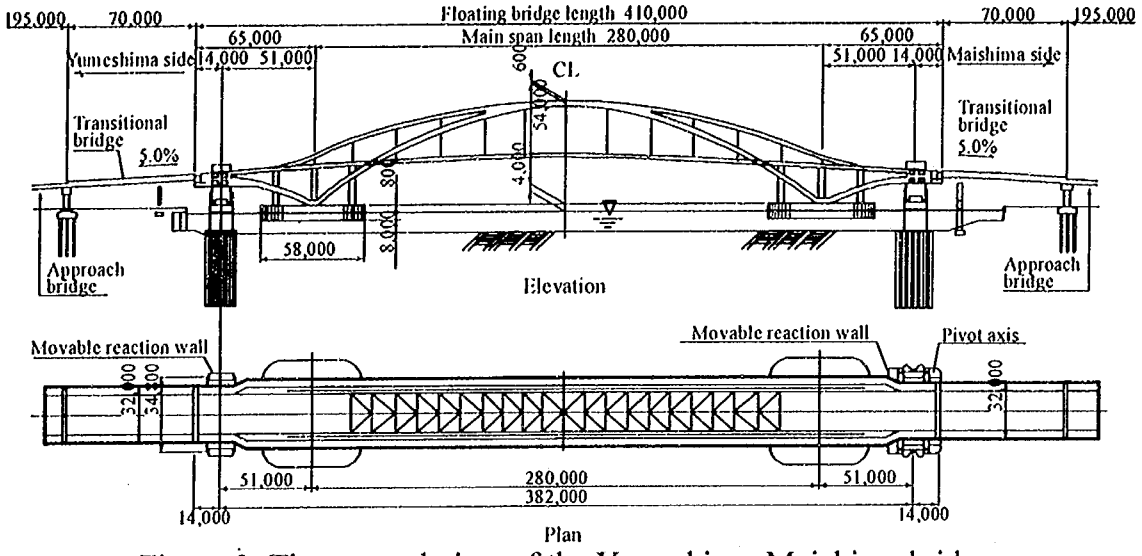


Figure 3: The general view of the Yumeshima-Maishima bridge

3. CHARACTERISTICS OF THE BRIDGE

The characteristics of Yumeshima-Maishima Bridge are as follows ([1]-[5]):

(1) The type of the bridge is doubled-rib arch with 38.8m width and it accommodates six traffic lanes. The bridge rests on two hollow steel pontoons vertically and rubber fenders support it horizontally. The two pontoons can swing around a pivot axis near the Maishima end (Figure 3).

(2) The mooring system consists of dolphins, movable reaction walls and rubber fenders.

(3) The structure is designed to be strong and stable enough to withstand typhoon-level wind and waves.

(4) The swinging operation begins when a pivot axis is inserted and the transitional side bridges are jacked up. Then the reaction walls are released from their mooring function and rotated, and the bridge is swung about the pivot axis by tugboats.

(5) Concerning the erection, the superstructure, with pontoons, are being assembled at a dock. The complete bridge section will be towed to the site and joined to the mooring systems. So the construction is very timesaving.

(6) Many experiments have been performed to assure the safety and comfortability of the bridge.

4. TECHNICAL PROBLEMS

"Specification for Highway Bridge" is con-ventionally used when bridges are designed in Japan. However it is not sufficient because it does not cover the design of floating bridges.

Therefore many technical problems mentioned later were solved by establishing the design

methods and by deciding the design safeties etc. These were referred to the Technical Committee of Movable Floating Bridge (Chairman: Prof. of Kyoto University, Eiichi Watanabe).

The technical development was proceeded as shown in the flow chart of Figure 4.

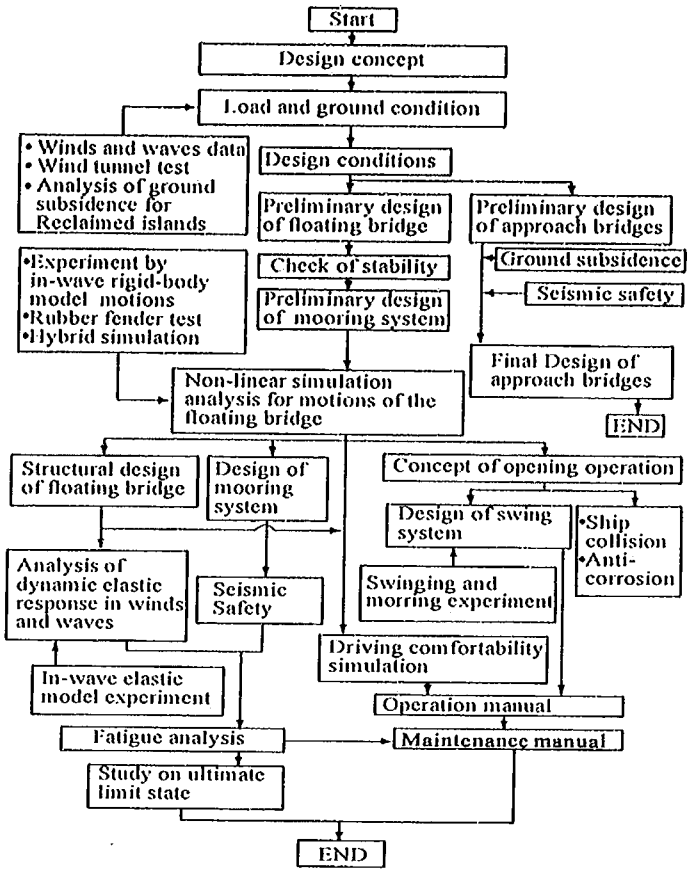


Figure 4: Flow chart for design of Yumeshima-Maishima Bridge

The followings are the main technical problems.

(1) Design conditions must be determined more strictly than fixed bridges because floating bridges are much more vulnerable to wind and wave loads than fixed bridges.

(2) The motion of the floating bridge caused by the winds and waves should be accurately simulated so that its result can be reflected in the design.

(3) The driving comfortability and riding comfort of vehicles have to be maintained against not only motions of the floating bridge but also the change of longitudinal gradient of the transitional side bridges caused by the tidal change.

(4) The floating bridge is moored to the mooring dolphins by means of rubber fenders. The characteristics of the fender must be clarified by the experiments and the result should be considered in the design.

(5) The structural effect to the floating bridge by the ground subsidence at the site had to be evaluated.

(6) Generally speaking floating bridges are considered to be not affected by earthquakes. However the seismic safety had to be verified and the displacements caused by

earthquakes needed to be considered in the design.

(7) Since the bridge is movable, then not only the operation manuals for the opening and closing but also maintenance manuals are necessary to be made for the healthy operation.

5. DESIGN CONDITIONS

The design specifications and dimensions are shown in Table 1. The followings are their details ([1]-[5]):

5.1 Winds

Design wind velocity (i.e., V_{10}: wind velocity at the height of 10m) is determined by the analysis based on the observed wind velocity at the Hokko Yacht Harbor from 1987 to 1995 which is the nearest observatory from the bridge site. The observation period is rather short comparing with the life time (i.e., one hundred years) then observed data at Osaka District Meteorological Observatory from 1931 to 1995 were also used making the correlation between them by using Petrukas-Aagaard method. Thus one hundred-year recurrence wind velocity is determined as 42m/sec for designing bridge structures and mooring dolphins. The wind velocity for regulations on transportation and that for swing operation are determined as less than 20m/sec and less than 15m/sec, respectively.

Table 1: Design specifications and dimensions

Bridge type	Movable floating bridge (Swing type)				
Road standard	Grade 4, Type 1				
Live load	B live load	Wind load	V_{10}=42m/s		
		Waves	$H_{1/3}$=1.4m, $T_{1/3}$ =5.7~7.7s		
Bridge length	410m				
Effective width	31.2m (6-lanes roadway with 2-side walks)				
Spans	65.7m+280.0m+65.7m				
Waterway width	Usual use	135.0m	Emergency	200.0m	
Under clearance		DL+26.0m		———	
Super elevation	2% straight line				
Longitudinal gradient	5% both grades (V.C.L140m)				
Pavement thickness	Roadway/80mm Walkway/40mm				
Earthquake load	Level I	by "Specification for Highway Bridge"			
	Level II	Plate boundary and fault type earthquakes			
Approximate steel weight (Unit in tons)	Pontoon	6,600			
	Floating bridge	18,200			
	Mooring structure	8,200			
	Total	33,000			

5.2 Waves

Design wave height of one hundred year recurrence is determined based upon the estimation analysis of 40 years observed strong wind data and model tests in the water tank(Table 2)

Bretschneider-Mitsuyasu type is employed as the wave spectrum for the numerical simulations.

Table 2: Wave conditions for design

	Wind Wave			Swell			Wind Condition for Combination (m/sec)
	Significant Wave Height $H_{1/3}$ (m)		Period	Significant Wave Height $H_{1/3}$ (m)		Period	
	Yumeshima Side	Maishima Side	$T_{1/3}$ (sec)	Yumeshima Side	Maishima Side	$T_{1/3}$ (sec)	
During Typhoon	1.0	1.4	5.7~7.7	0.2	0.3	17.0	V_{10}= 42
	1.0	1.4	5.7~7.7	0.1	0.1	11.0	
During Service	0.4	0.5	3.5	0.1	0.1	11.0	V_{10}= 10
	-	-	-	0.1	0.1	11.0	-
Under Trafic Regulation due to Wind	0.8	1.0	5.7	0.1	0.1	11.0	V_{10}= 20
During Opening Operation	0.8	0.8	5.0	-	-	-	V_{10}= 15
During Opening	0.8	0.8	5.0	-	-	-	V_{10}= 15

5.3 Earthquake

"Expected earthquake" was used for the seismic design in consideration of the effects of the active faults, the nature of soil and the topography. In other words, two types of expected earthquake such as Type I and II, which are referred to as a plate boundary and fault type earthquakes, were basically considered. The actual observed seismic data at Kobe Port Island –83m were also used.

5.4 Other Loads

Other design loads such as ship collision load, reaction force on the support beams and the pivot pin during the swing operation and fender reaction forces from mooring dolphins were considered.

5.5 Load Combinations, Allowable Stress and Safety Factors

When we establish a new design specification for new type bridges, it is ideal if we can make an assumption of the failure mode and can determine the safety factor using stochastic theory. However these were too difficult to be realized since it needs many academic works and verifications.

Then we applied many kinds of specifications so that they might correspond to what we need. Otherwise we referred to the safety evaluation method proposed by JSCE ([6]).

Against each combination, the allowable stresses and safety factors are determined as shown in Table 3.

Incidentally as for the design of bearing shoes, expansions and the top width of mooring beams, displacements at these parts are large then they play significant roles when we determine their configurations.

Table 3: Load combinations and increment factors of allowable stress for bridge, pontoon and pivot axis

Loads	Combination	Increment factor
Standard	D + U + L + I	1.00
Temperature	D + U + L + I + T	1.15
Storm	D + U + W + WP	1.20
Earthquake	D + U + EQ	1.50
During swinging	D + U + W + WP + DR	1.25
Bridge open position	D + U + W + WP	1.25
Erection	D + U + W + WP + ER	1.25

Where, Dead load (D) Wave load (MP)
Live load (L) Temperature (T)
Impact (I) Seismic load (EQ)
Buayncy (U) Ineartia load (DR)
Wind load (W) Erection load(ER)

6. STABILITY OF FLOATING STRUCTURE

The stability of the floating structure is one of the important aspects because it rests on two pontoons and its mass center is rather high to maintain 26m sailing clearance. The dynamic stability by winds and wave was checked by the analysis and experiments, which will be discussed later. In this chapter, the design way of static stability will be shown according to the conventional specification ([4]).

The static stability of the floating structure is good enough when the vertical distance (i.e., TGM) between the center of mass and meta-center is positive: the initial restoring force works to stabilize the structure as shown in Figure 5. When the magnitude of numerical values is the larger, the stability becomes the more stable.

The results of the static stability calculations for the three cases are shown in Table 4 where S1: without live load; S2: partially loaded live load based on the influence line; S3: full loaded live load. The floating bridge is very stable since its magnitude of numerical values is larger than that of ships or marine structures.

The following formula was conventionally applied to check the dynamic stability in Japan :

$$\text{Area}(A+B) \geqq 1.4 \times \text{Area}(B+C) \quad (1)$$

Where Area A, B and C are shown in Figure 6, the specification requires that the magnitude of the restoring force must be 1.4 times larger than that of the slope moment. The dimensions of the pontoon were decided to satisfy the above formula. The ratio of these magnitudes (DSR) is shown in Table 4 when the size of the pontoon is 58m x 58m x 8m. The items for dynamic stability are as follows :

D1: wind load (V_{10}=42m/sec) without live load
D2: partially loaded live load based on the influence line and wind load (V_{10}=20m/sec)
D3: full loaded live load and wind load (V_{10}=20m/sec)

Incidentally double-hull structure is applied to the pontoon against leakage of water or a ship collision forces.

Table 4: Results of hydrostatic and dynamic stabilities

	Case S1&D1	Case S2&D2	Case S3&D3	Remark
Average draught d(m)	4.80	5.08	5.30	
Volume of drainage (t)	31 445	32 287	34 700	
Height of center of mass KG(m)	26.38	26.58	26.72	
Transverse metacentic height TGM(m)	30.09	27.03	24.92	TGM>0
Transverse inclined angle θ (deg)	0.00	1.14	0.25	
DSR = (A+B)/(B+C)	1.44	4.97	4.50	DSR≧1.4

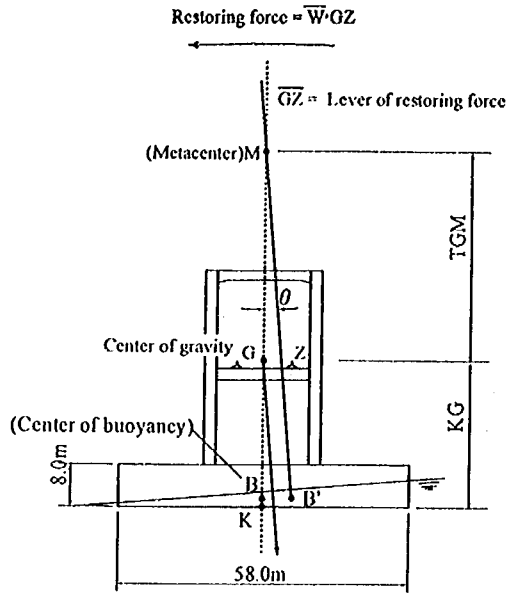


Figure 5: Stability check of floating bridges

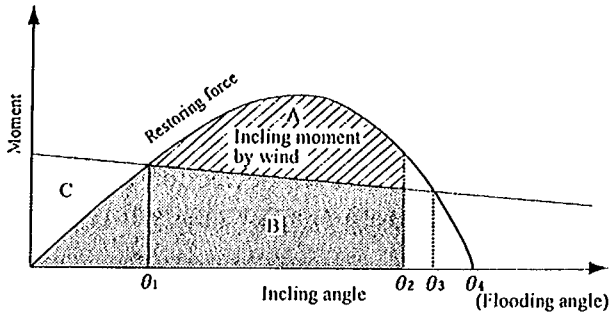


Figure 6: Check of dynamic stability

7. MOORING SYSTEM

The mooring system is necessary to resist to such forces as winds, waves and earthquake (i.e., the lateral force). On the contrary the buoyancy of seawater at the pontoons resists the dead and live loads of the floating bridge (i.e., the vertical force).

The followings are three types of mooring systems investigated for the design of the floating bridge (see [4]):

(1) Anchor chain mooring
(2) Submergible mooring
(3) Rubber fender mooring

Anchor chain mooring is the most popular and simple however it needs twenty anchors chains with the radius about 150mm in this case. It was determined unfeasible for these reasons:

(1) the quick removal of the chains is difficult before the swinging.
(2) fixed anchors at seabed must be very large then the ground improvement is uneconomically necessary.
(3) displacement by the dynamic force is about 3m and it is very harmful to the transportation.

Submergible mooring prohibits the bridge movement by winds or waves however it is vulnerable to earthquake. We allowed some slip of the pontoon by earthquake however we

did not allow it by winds or waves in the feasible designing. As a result, this method needs the construction of a very large substructure on the muddy seabed of this district and it also needs much time to drain water in the pontoon before swinging. So the plan of submergible mooring was abandoned.

Rubber fender mooring can reduce the movement of the floating bridge to small limit and is relatively economical. It is commonly applied for ship berthing using its energy absorption. It has also been used for mooring devices of large floating structures such as floating oil reservoirs and floating terminals. The development of rubber fenders of high and reliable performance has realized these applications. The following two methods were intensively studied. One was reaction wall method and the other was link damper method. The configurations are shown in Figures 7 and 8 respectively. The characteristics of these methods are shown in Table 5. The wall reaction method is applied for the easiness in swinging operation and for the small motions in transportation service.

Cell type fender is used for the rubber fender mooring. The characteristic of load-deflection exhibits the non-linearity and a large hysteresis as shown in Figure 9.

Tests to evaluate the performance of the rubber fender were carried out in the laboratory. They were carried out to find the effect against the reaction force on such factors as loading speed, temperature, fatigue and creep. From the test results, the following specifications were established:

(1) The maximum reaction force obtained by the computer simulation should be multiplied by the factor of 1.5 to design reaction walls for unknown factors of the analysis.
(2) The deviation of load-deflection is considered for the design.
(3) The fender strain against steady force due to winds and waves is to be less than 10% in the design.
(4) The maximum fender strain considering all kind of loads (δa) must be less than 38%.

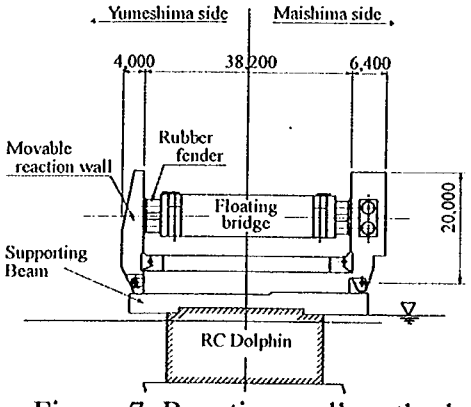


Figure 7: Reaction wall method

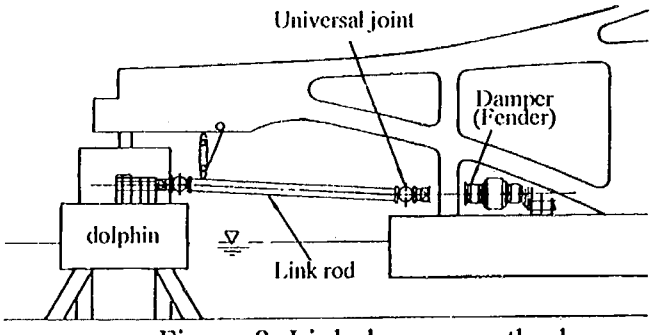


Figure 8: Link damper method

Table 5: Reaction wall and link damper method

Methods / Items	Reaction wall method (Figure 7)	Link damper method (Figure 8)
Motion of bridge body	Small	Not small
Swinging operation	Easy	Time-consuming
Technical problems	•Large structure to rotate •Rotation and fixing of reaction wall	•Link mechanism •Removement of rod before swinging
Dolphin/foundation	Large	Small

8. SWING PROCEDURE

The swing procedure of figure 10 will be executed to allow large vessels to pass through sub-waterway in an emergency. The swing operation is as follows([2]):

(1) The swinging operation begins when a pivot axis is inserted and the transitional side bridges are jacked up.
(2) Then the reaction walls are released from their mooring function and rotated.
(3) The bridge is swung about the pivot axis by tugboats.
(4) After rotation is completed, the bridge is temporarily moored in the open position.
(5) Reversing the process reconnects the floating bridge section to the original position.

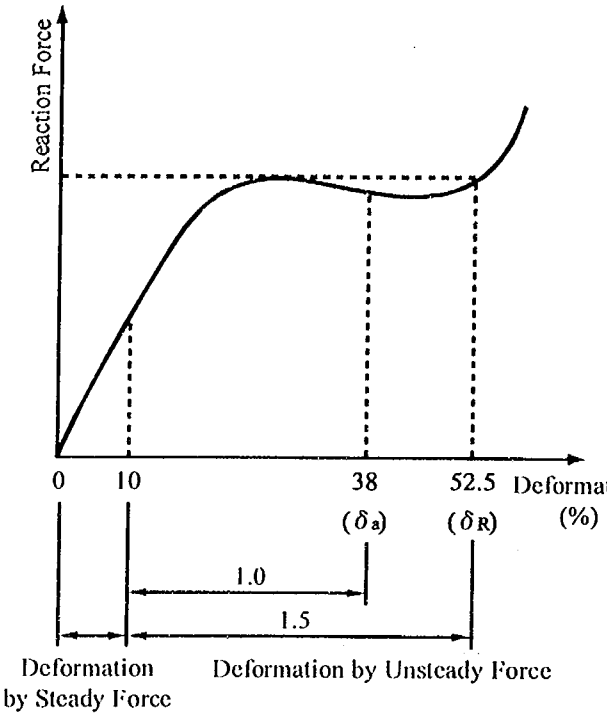
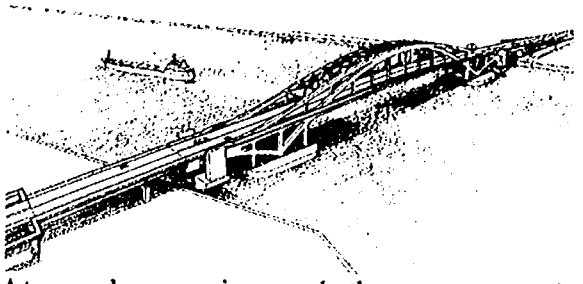
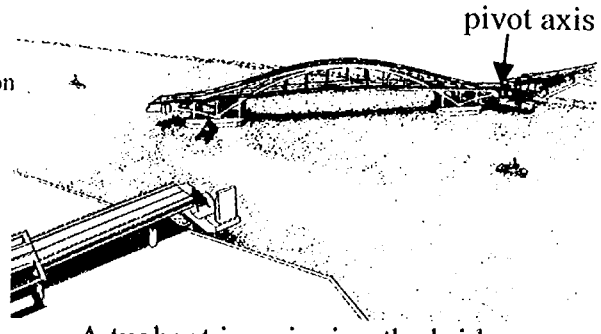


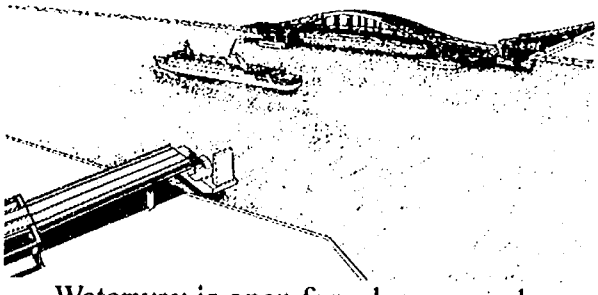
Figure 9: Relationship between reaction force and deformaitn of rubber fender



At regular service and the waterway is closed to large vessels.



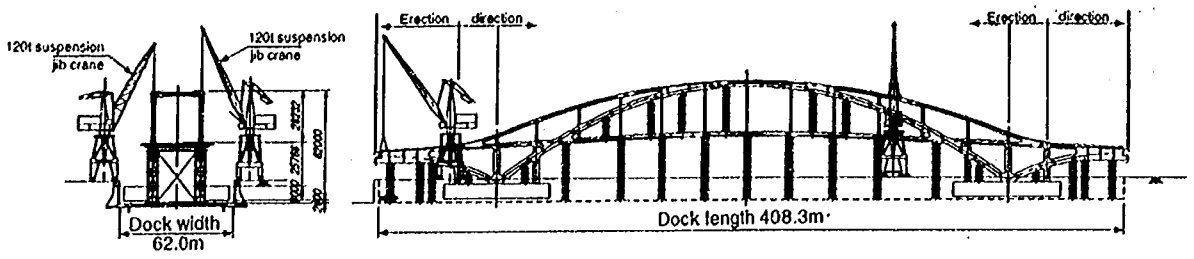
A tugboat is swinging the bridge.



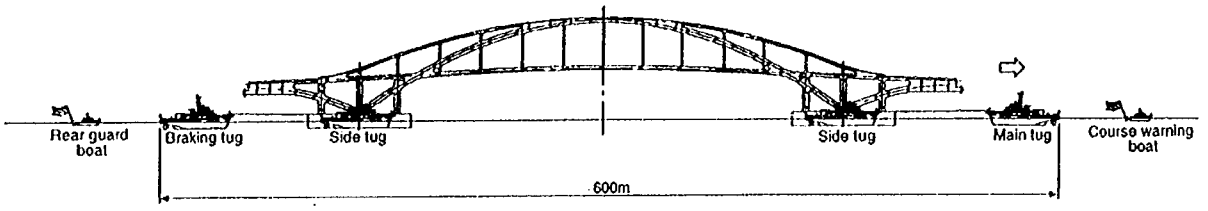
Waterway is open for a large vessel.

Figure 10: Swinging Procedure

(STEP 1) Erection is done in a dock by the temporary supporting method, using two 120t suspension jib cranes.



(STEP 2) The bridge is towed to the installation position by a formation of 8 tugboats in the 3,600 horsepower class.



(STEP 3) The floating bridge is connected to the mooring equipment via tug winch operation.

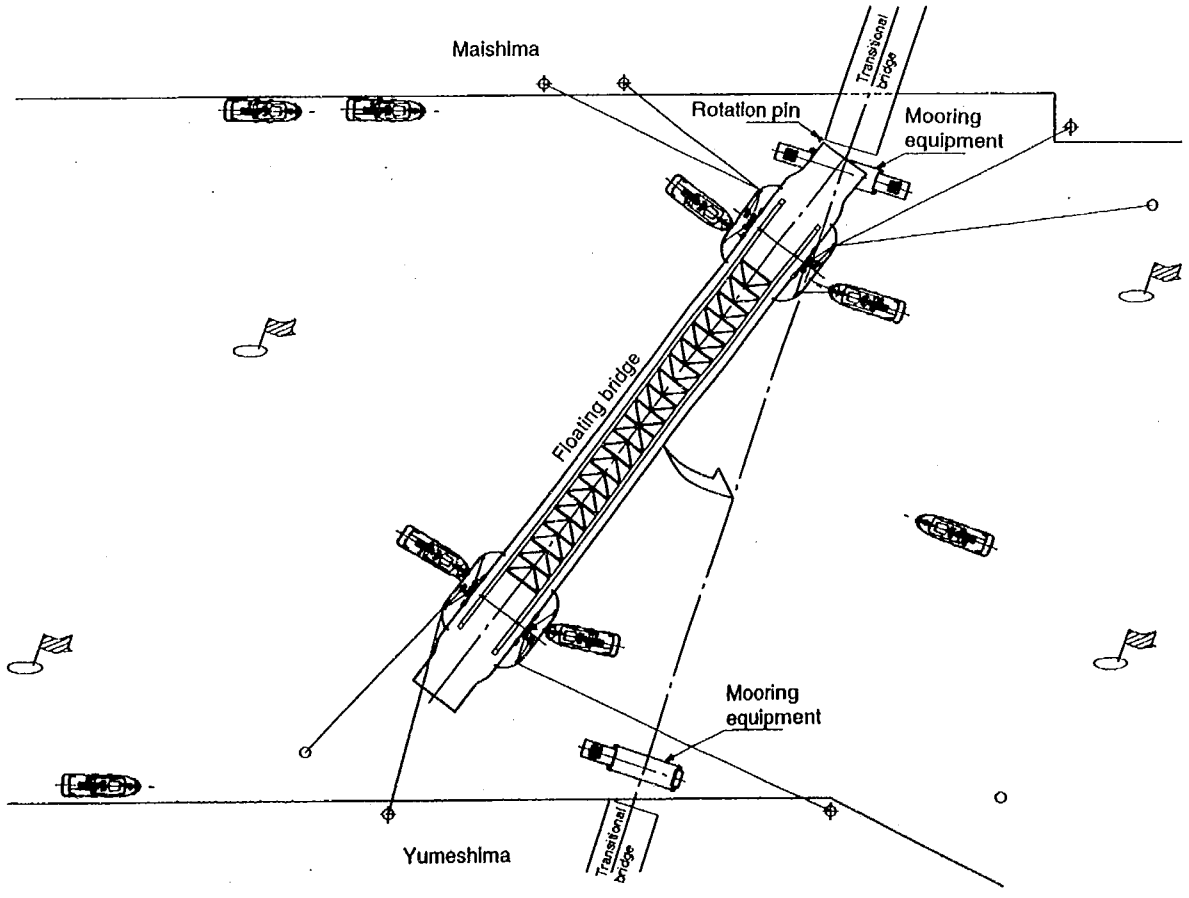


Figure 11: Erection Steps

9. ERECTION

The erection method has been chosen based on the use of a dock-yard. The erection steps are shown in Figure 11 as follows([4]):

(1) The super-structure with pontoons is now being assembled in Sakai-Dock-Yard of Hitachi Zosen Corp., which is about 10 km away from the bridge construction site.
(2) Separately, mooring piers are constructed at Yumeshima-Maishima site.
(3) After the completion of piers, whole floating bridge will be towed to the site and be installed to the mooring system via tug-winch operation.
(4) After some site assembling, the bridge will be completed in the year of 2000.

10. EXPERIMENTS

Many experiments have been performed to assure the safety and comfortability of this bridge. Main subjects of the experiments included ([7],[8],[9]) :

(1) Rigid-body motions of floating bridge model (scale: 1:80), examined in a large-scale water tank with the size of 50m x 40m and compared with its computer simulations (Figure 12)
(2) Behavior of the structure under wave loads, examined by an elastic model (scale: 1:40); the effect of flexibility was found to be minimal (Figure 13).
(3) Behavior during the swing operation and temporary mooring examined using the rigid model (Figure 14).
(4) Behavior of mooring fender were clarified (Figure 15).

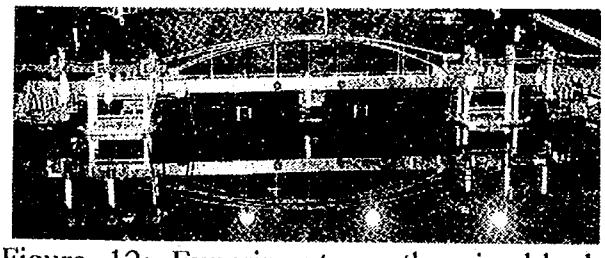


Figure 12: Experiment on the riged-body model motions in a large-scaled water-tank

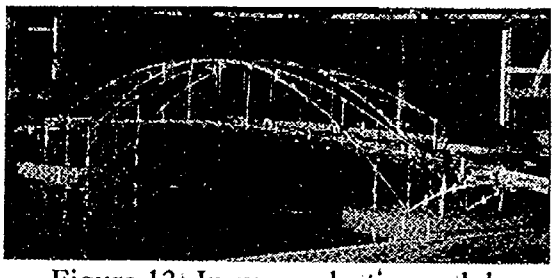


Figure 13: In-wave elastic model experiment (Scale: 1/40)

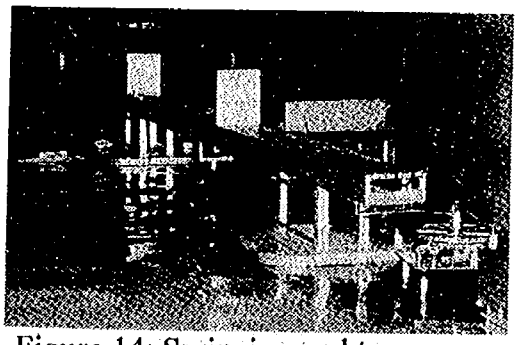


Figure 14: Swinging and temporary mooring experiment

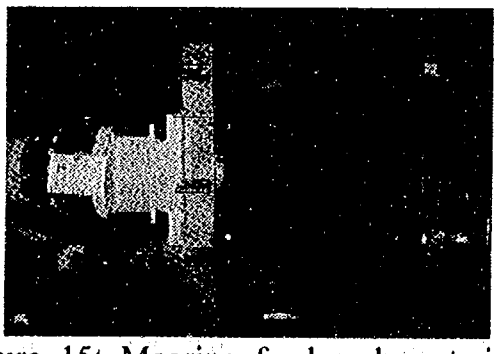


Figure 15: Mooring fender characteristic test

(5) The six steady-state force coefficients, measured by wind tunnel testing, which resulted in changes to the configuration of the girder to reduce drag force by 22% from winds (Figure 16).

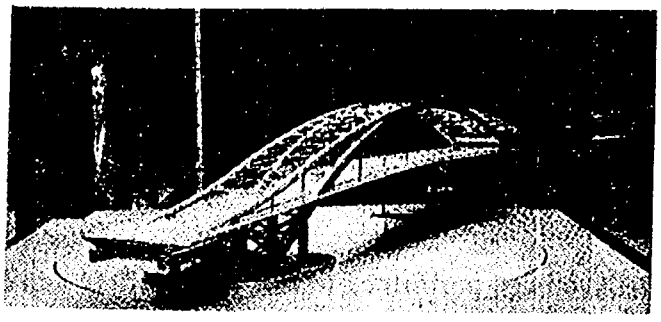


Figure 16: Wind tunnel test

11. HYBRID SIMULATION METHOD

Since in the above-mentioned experiments, an accurate modeling of rubber fenders is difficult, the equivalent spring or other instruments were used. However these models could not simulate the shearing deformation and so on. The proto-type shows the change of hysteresis of the load-deformation after repeated loading.

Oda, et al. developed a new method; Hybrid Simulation Method (i.e., HSM) which is composed of a PC, tri-axis compression test equipment and the small-scaled rubber fenders as shown conceptually in Figure 17 ([10]).

HSM deals with the two dimensional dynamic motion of the floating bridge with rubber fender mooring systems. The external forces applied here are winds and waves, which act to the bridge from the offing. Those external forces will be computed in advance and stored in the memories of the PC as the table of external forces. When the simulation starts, the tri-axis compression test equipment will be run according to the external forces in the table. It will make the rubber fenders compressed and fender's reaction forces will be measured. After converting the data from analog to digital, the dynamic equation of the floating bridge will be solved by the total forces such as waves, winds and the reaction forces in Eq. (2).

$$M\cdot\begin{pmatrix}\ddot{y}\\ \ddot{z}\\ \ddot{\theta}\end{pmatrix}+N\cdot\begin{pmatrix}\dot{y}\\ \dot{z}\\ \dot{\theta}\end{pmatrix}+K\cdot\begin{pmatrix}y\\ z\\ \theta\end{pmatrix}=\begin{pmatrix}F_y\\ F_z\\ F_\theta\end{pmatrix} \qquad (2)$$

where respectively M, N and K refer to mass, damping and stiffness matrices; y, z and θ refer to sway, heave and roll displacements.

The coefficients of added-mass and wave damping depends on the magnitude of frequency. To take account of it, assumptive frequency for each mode is given at first and the dynamic equation is solved. The new frequency will be given by statistical method from the time history. After some repetition converged solution will be given.

The ordinary-type numerical simulation method (i.e., OSM) is used for the design. Comparative studies were conducted and the followings are the main results.

(1) The movement of the rubber fender can be predicted in HSM and no abnormal movements of fenders were observed.

(2) The rubber fender became somewhat soft in three hours elapse. However the time dependent effects were negligibly small.

(3) The fender movement by OSM and HSM are almost the same as shown in Figure 18. Then the non-linear characteristic of the rubber fender by OSM is reasonable.
(4) The shear deformation of the rubber fender was found small. Therefore the effect of the shear deformation can be discarded.
(5) The use of OSM for the design of this bridge has been verified.

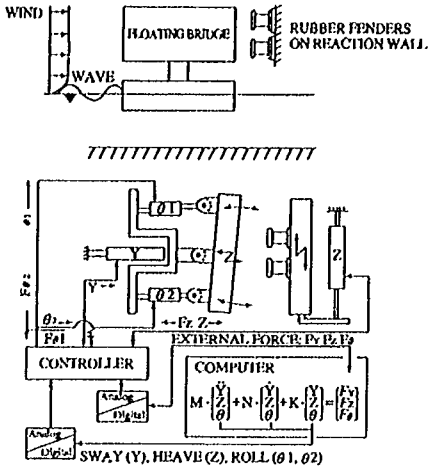


Figure 17: Computational scheme of the hybrid type numerical simulation method (HSM)

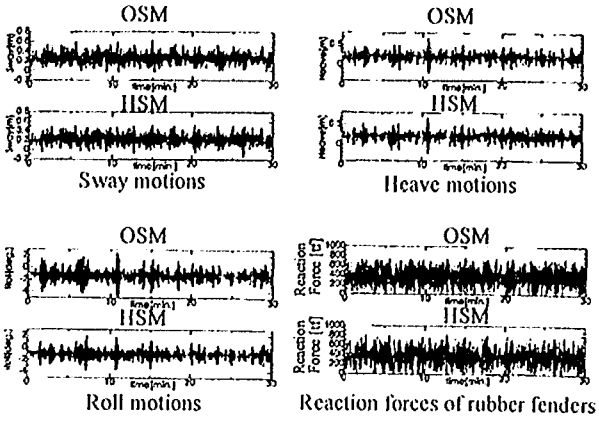


Figure 18: Output comparisons between OSM and NSM

12. DRIVING COMFORTABILITY SIMULATION

The movement of this bridge is complex for it is floating in the sea moored softly by rubber fenders and their restrictions are relatively weak. The following subjects were studied from the viewpoint of driving comfortability ([5]):

(1) The longitudinal gradient of transitional side bridges changes due to tidal change.
(2) The super elevation and longitudinal gradient of the floating bridge change due to waves and winds.
(3) The same situation happens by the live load.

There is no rule in the specification concerning driving comfortability under the present conditions. We carried out the driving comfortability simulation. In addition, we took passengers' questionnaires concerning the riding comfort when the bus passed main bridges in Osaka City. We evaluated the driving comfortability by the relationship between the simulation and the answers to questionnaires.

12.1 Method of simulation

The analytical model includes the floating bridge and transitional side ones and the frame model is supported by springs at the positions of pontoons. Three analytical cases corresponding to tidal levels (i.e., HWL, MSL and LWL) were examined. The live load model in Figure 19 is loaded on both up and down lines as the so called L-live load: width: 10.5m; length: 205m. A special attention was paid to the top car of L-load (i.e., observed car in Figure 18) and the two-axis spring model (Figure 20) was installed. Acceleration here was chosen as the evaluation item.

12.2 Criteria for riding comfort

To evaluate riding comfort, we ran a large bus through long span bridges and viaducts in Osaka City at speed 30~60 km/h. The acceleration of vibration was measured in the bus.

Thirty-six passengers on the bus answered the questionnaires and the correlation between the values of riding comfort and the magnitudes of acceleration were obtained. The riding comfort was evaluated in five grades as shown in Table 6.

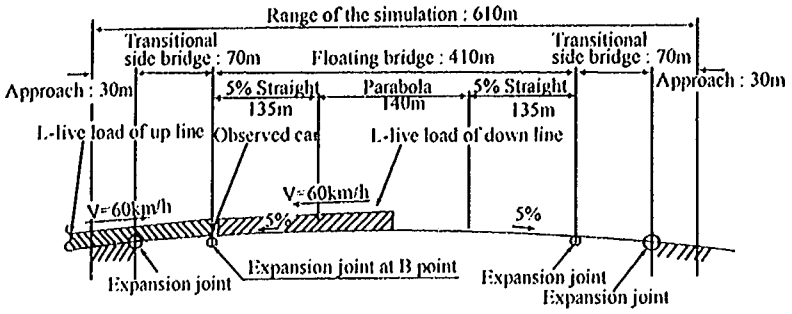


Figure 19: Model for driving comfortability simulation

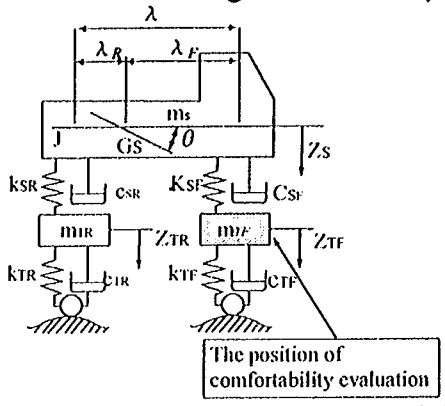


Figure 20: Two-axis spring model

Table 6: Grades of riding comfort

1: not feel some vibration
2: feel vibration but alright
3: feel some vibration
4: feel somewhat large vibration and feel some discomfort
5: feel large vibration and feel discomfort & uneasiness

12.3 Evaluation of driving comfortabilty

Figure 21 and 22 show the correlations between the riding comfort index and averaged acceleration and correlations between the riding comfort and the maximum acceleration respectively.

The driving comfortability simulation brought the results that the average acceleration ranged from 0.19g to 0.33g and maximum acceleration ranged from 0.36g to 0.76g. ([5]).

It was concluded that even if we had the worst driving comfortabilty comfort on the floating bridge, we might feel the some vibration however we would not feel discomfort on the bridge. It is just short period on the expansion joint that we feel the worst riding driving comfortabilty.

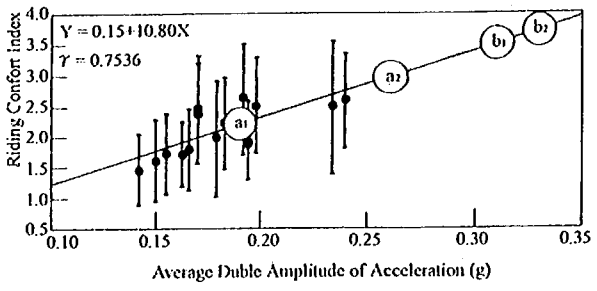


Figure 21: Relationship between average double amplitude of acceleration and riding comfort index

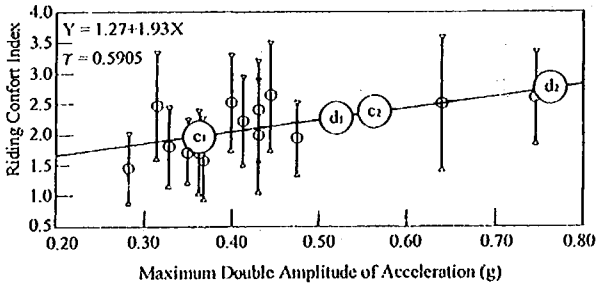


Figure 22: Relationship between maximum double amplitude of acceleration and riding comfort index

13. CONCLUSIONS

The Yumeshima-Maishima Bridge, which is the world's first floating and swing bridge, is now under construction in Osaka Japan (Figure 23).

It will be completed in the year of 2000 and the construction will surely contribute to the development of waterfront districts around the Port of Osaka.

New technological developments and findings were obtained through the comprehensive research works including experiments and discussions. These are the results of cooperation among universities, Osaka Municipal Government, the Ministry of Transport, heavy industrial companies, fabricators, design consultant companies and a fender manufacturing company. Many experts examined the results carefully at the Technical Committee on Movable Floating Bridge (Chairman: Prof. E. Watanabe) from 1990 to the present time. The Committee will continue until some time after the completion of the bridge.

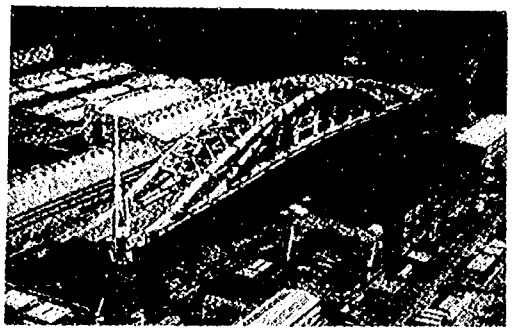


Figure 23: Scene of assembling of the Yumeshima-Maishima Bride at Sakai-Dock-Yard (September 1999)

Authors hope that this paper will be utilized for the construction of similar floating bridges constructed near future.

References

[1] Maruyama, T., Watanabe, E., Utsunomiya, T. and Tanaka, H., "A New Movable Floating Arch Bridge in Osaka Harbor," *Proc. of the Sixth East Asia-Pacific Conference on Structural Engineering & Construction*, EASEC 6, Taipei, Taiwan, pp. 429-434, January14-16, 1998

[2] Watanabe, E., Maruyama, T., Kawamura, Y. and Tanaka, H., "A New Movable Floating Bridge Project in Osaka City," *Proc. of the IABSE Symposium*, Kobe, Japan, pp. 155-160, September, 1998

[3] Ueda, S., Maruyama, T., Tanaka, H., Nagata, S., Ikegami, I., Kobayashi, M. and Yamase, S., "Construction of Movable Floating Road Bridge at Yumeshima-Maishima Osaka City," Proc. of UJNR MFP, 23rd meeting, MD, USA, October, 1998

[4] Maruyama, T., Kawamura, Y., Tsuda, T., Kishimoto, T., Tanaka, H. and Yasuda, Y., " Plan and Design of Yumeshima-Maishima Bridge (1) –Movable Floating Bridge–," *Bridge and Foundation*, Vol.32, No.2, 1998 (*in Japanese*)

[5] Maruyama, T., Kawamura, Y., Tsuda, T., Takeda, S., Nakaji, E., Oka, S. and Tsuchiya, M., " Plan and Design of Yumeshima-Maishima Bridge (2) –Movable Floating Bridge–," *Bridge and Foundation*, Vol.32, No.3, 1998 (*in Japanese*)

[6] Shiraishi, N., Evaluation of Life-Time Lisk for Structures, Structure Engineering Series 2, JSCE, December, 1988

[7] Nagata, S., Fujita, T., Yoshida, H., Tanaka, H., Maruyama, T. and Ueda, S., "Motion of a Movable Floating Bridge in Wave," *Proc. of VLFS '99*, Hawaii, USA, September,1999

[8] Ueda, S., Maruyama, T., Ikegami, K., Seto, H., Kumamoto, N. and Inoue, K., "Experimental Study on the Elastic Response of a Movable Floating Bridge in Waves," *Proc. of VLFS '99*, Hawaii, USA, September,1999

[9] Kobayashi, M., Hineno, M., Shimada, K., Hyodo T., Kawamoto, A., Ueda, S. and Maruyama, T., "Model Experiments on Swinging of a Movable Floating Bridge in Waves," *Proc. of VLFS '99*, Hawaii, USA, September,1999

[10] Oda, K., Maruyama, T., Tanaka, H., Nagata, S. and Yamase, S., "Hybrid Simulation for A New Movable Floating Bridge," *Proc. of the Sixth East Asia-Pacific Conference on Structural Engineering & Construction*, EASEC 6, Taipei, Taiwan, pp. 435-440, January14-16, 1998

INTERNATIONAL SCANNING TOURS RELATED TO BRIDGE TECHNOLOGY

David H. Densmore[1]

Abstract

The International Scanning Program evaluates foreign technologies and innovations that could significantly benefit highway transportation systems. The program looks for the best and most appropriate technology, management practices, and research that can be cost-effectively incorporated into highway programs. This approach allows for an exchange in technology with other countries, and for highway agencies to put advanced technology into practice much more efficiently without expending scarce funds to recreate advances already developed by other countries. This presentation calls attention to a few of the most significant of the recommendations. The reports written for the scanning tours contain many other observations and recommendations. For additional information and copies of the reports, contact the FHWA International Programs Office or go to the web site at "www.international.fhwa.dot.gov".

Introduction

The International Technology Scanning Program is a cooperative program involving the key partners of the Federal Highway Administration (FHWA) and the American Association of State Highway and Transportation Officials (AASHTO). The program involves a team of technical specialists traveling to other countries to access and evaluate foreign technologies and innovations that could significantly benefit highway transportation systems. It looks for the best and most appropriate technology, management practices, and research that can be cost-effectively adopted into highway programs. This approach allows for advanced technology to be adapted and put into practice much more efficiently without spending scarce research funds to recreate advances already developed by other countries.

Completed Bridge Scans

This presentation will highlight the results of bridge related scanning reviews. These scans took place during 1995 through 1999 and final reports have been prepared for all but the Steel Bridge Fabrication Scan.

- European Bridge Structures – 1995
- Asian Bridge Structures – 1997
- Advanced Composites – 1996
- Bridge Maintenance Coatings – 1995
- Northumberland Strait Crossing – 1995
- Bridge Scour Countermeasures – 1998
- Steel Bridge Fabrication – 1999

---

[1] Director of Bridge Technology, Federal Highway Administration, Washington, DC

Although the reports contain many observations and recommendations, the presentation will highlight only a few which are believed to have the greatest potential for implementation. In some cases significant implementation has already been accomplished . The purpose is to call attention to a few of the most significant or most implementable of the recommendations. For additional information and to get copies of the full scan reports contact the FHWA International Programs Office or go to their web site at "www.international.fhwa.dot.gov". The telephone number in the U.S. is (202) 366-0111 and fax (202) 366-9626.

European Bridge Scan -- Design for Durability

The European Bridge Structures Scan occurred in June of 1995 and included Denmark, Germany, Switzerland, France, and the United Kingdom. One of the most significant observations from the European scan was that concrete mixes are designed with prime considerations given to durability -- not strength. Although this may be changing in recent years, concrete bridges in the U.S. and other countries have been generally designed for strength with durability as the secondary consideration. The recommendation of the panel of technical specialists is to continue ongoing high-performance concrete research and implementation initiatives and further investigate the European practices designed to emphasize durability. As a result of this and other ongoing initiatives many highway agencies have implemented high performance concrete (HPC) projects. The benefits of HPC are enhanced durability and economy. Perhaps even more important, to achieve HPC, we are reminded of the wet-curing and other fundamentals of quality concrete. It is important to teach the importance of designing for durability at the university level. The panel also recommended the funding of curriculum development to enhance university teaching of design for durability. It was also encouraged that the design for concrete durability be among the criteria for evaluating engineering design curricula for university accreditation.

Corrugated Steel Webs

Another observation was that the Europeans have used corrugated steel webs, with both steel and concrete flanges. In the case of steel flanges, the perceived advantage is thinner unstiffened webs. In the case of prestressed concrete flanges, prestressing is not lost to the web, because the corrugated web resists little compression. At the time of the scan, tests were underway to quantify the fatigue resistance of corrugated steel web details as no specification existed. The panel of technical specialists encouraged the continued ongoing research on high performance materials and investigate the use of corrugated steel webs with both steel and prestressed concrete flanges, with consideration to fatigue resistance, constructability, and economic viability. There is at least one project under development with the cooperation of the federal government, the bridge owner, and industry for examining this concept.

Bridge Deck Waterproofing

The European emphasis on bridge-deck waterproofing systems was one of the significant observations. Systems vary by country, but all countries visited used elaborate bridge deck waterproofing systems. The Europeans estimated the life of the membrane systems at 20 years.

Because of the contrasts of this practice, the panel encouraged research-funding agencies to develop or undertake a study to evaluate the performance and cost effectiveness of domestic and European deck waterproofing systems and their application to current practice. Perhaps of most importance is to compare the elaborate deck strategies used in Europe with current practice. The issue of bridge deck protection strategies deserves more attention. One very elaborate system being applied in Denmark is a multi-layered system consisting of an epoxy-with-sand prime coat applied to a sand blasted concrete deck; two polymer-modified bitumen sheets, fully bonded to the concrete; a 20 mm-thick drain layer of open-graded asphalt concrete; a 40 mm-thick binder course of modified asphalt concrete; and 40 mm-thick wearing course of asphalt concrete.

Asian Bridge Scan -- Computerized Assembly and Testing System

The Asian Bridge Structures scan took place in September of 1997 and visited Japan, South Korea and Taiwan. One bridge corporation has developed a computerized assembly and testing system (CATS) to simulate erection of complicated structures and to eliminate the need for shop assembly of bridges. CATS uses photogrametry methods with four cameras to take 3D pictures of each element. The members are then shop assembled in simulation on the computer screen using software developed for that purpose.

Although this system would have significant initial cost, the scanning technical specialists recommended that CATS be studied further and research be considered to develop a system that can be used in the U.S. The system has great potential to reduce labor cost of shop fit-up.

Dimpled Pipe Used on Stay Cables

Vibrations of stay cables can be a serious problem under certain weather conditions and a phenomena that is getting increased attention. Wind-rain vibration is one that both dramatic to see and a serious problem. It was observed that on the Tatara Bridge in Japan, the cables were encased in a black polyethylene pipe with a dimpled outer surface to reduce vibrations caused by wind and rain. Information that was received about the pipe is being made available to the bridge engineering community. This innovation needs to be followed closely as it has the potential of being a low cost solution to the cable vibration.

Advanced Composites Scan in Europe and Japan -- Structural Rehabilitation

The Advanced Composites Scan to Europe and Japan took place in October of 1996. Composites in Europe and Japan were found to be used primarily in structural rehabilitation, both for strengthening of existing structures and for seismic retrofit. In both cases several commercial systems have been developed in the countries visited, including materials, design, and application methods and specifications. One example shows laminate strips being applied to the underside of a bridge deck over the Rhine River between Switzerland and Austria. Advantages of the composite strips for strengthening is the light weight of the laminates, their ease of handling and installation without heavy equipment, and their simple application in overhead situations. The technologies encountered are of potential interest for the rehabilitation. **Recommendation**—Design guidelines need to be developed and based on well-defined

performance criteria. A balance is needed between basic and applied research and programs that include full participation of the industry and engineering and construction industries. Bridge strengthening systems have considerable relevance because of the large number of deficient bridges in the U.S. inventory. Design guidelines need to be developed and based on well-defined performance criteria. It is important that a balance be maintained between basic and applied research and programs that include full participation of the industry and engineering and construction industries. It will be especially important that future projects to demonstrate this technology include provisions for long term documentation and monitoring.

Industry Cooperation

Probably the most significant finding of the scanning team was the close collaboration among the construction industry, the composite materials and manufacturing industry, the civil engineering design community, the academic community, and government agencies. The partnership works together to educate the civil engineering profession in composite technology, and in implementing demonstration projects.

Scour Countermeasures in Europe -- Riprap and Filters

The Scour Countermeasures Scan to the United Kingdom, the Netherlands, Switzerland and Germany took place in October 1998. The panel of specialists observed that the use of stone riprap in combination with geotextiles is by far the most common scour and stream instability countermeasure in all the countries visited. Its availability, economy, ease of installation, and flexibility are considered highly desirable characteristics. As a result, considerable effort has been devoted to techniques for determining size, gradation, layer thickness and horizontal extent, filters, and placement techniques including equipment. Riprap is considered an effective and permanent countermeasure against channel instability and scour, including local scour at bridge piers. The panel's preliminary recommendation is that design and installation techniques for riprap be based on the information from Europe and not be considered a temporary solution at piers as is the case in the US. The panel also recommends that there be an evaluation of innovative techniques for placing appropriate filters under riprap and other countermeasures, including geotextile containers and fascine mattresses.

Steel Bridge Fabrication -- Computer Integrated Manufacturing

The Steel Bridge Fabrication Scan visited Japan, Italy, Germany, and the United Kingdom in May and June 1999. The panel observed that all of the fabricators visited had computer-aided drawing (CAD) and computer-aided manufacturing (CAM) software. These systems also included three-dimensional bridge modeling that was used to verify assembly field erection location and elevation checks. Shop detail drawings are unnecessary in the modern automated shop. The dimensional checks can identify necessary deviations on the design drawings for review by the owner. The accuracy of the fabricated pieces reduces the need for shop assembly and allows virtual assembly based on the 3-D modeling program. The recommendation was that development of a Computer Integrated Manufacturing (CIM) Software package should be given high priority assisted by the technology from Japan and the U.K. A pilot project using digital

fabrication shop documents in lieu of shop drawings was also recommended. It was also recommended to explore the feasibility and carry out a pilot project, using digital geometric measurements on fabricated components for virtual assembly.

Welding

The prevalent shop and field welding was observed as being done with the gas-shielded process using solid, metal-cored, and flux-cored wire electrodes. The benefits included high production, lower rejection rates, and low hydrogen weld deposits. Gas shielded welding is often prohibited on U.S. bridge projects. Also, the need for preheat has been eliminated with the use of steels with low carbon content and the use of low hydrogen and a high heat input process. A new high speed rotating arc technique developed in Japan provided enhanced weld tracking for robotic fillet welds. Advantages include deeper penetration and fewer passes.

The recommendation of the panel was that a workshop for owners and fabricators on the merits of gas-shielded welding and other new methods of welding should be developed. It was also recommended that the U.S. explore the use of the high speed rotating arc technique for fillet welding.

Conclusion

The International Technical Scanning Program will be a continuing program which the FHWA will carry out with it primary partner, AASHTO. A bridge scan currently being conducted is to look at the durability of concrete segmental bridges in Europe. The intent of this scan is to evaluate the European inventory and performance of concrete segmental bridges, which have a longer in-service history than in the U.S. Additional scanning tour subjects will be solicited from all technical sources, and are expected to cover a broad range of transportation subjects including bridge technology.

The International Scanning Program, the U.S. believes, provides a valuable experience, not only for what the technical specialists can learn from other countries' transportation technology and innovation, but also from the professional working relationship that have developed. Through these relationships, there can be a positive exchange in ideas that will be of important benefit to all of our international partners. This presentation was meant as a short introduction to the many worthwhile observations and recommendations, and it is hoped, will lead to an interest in acquiring the scanning report and trying to put into practice, the technological advances of other world leaders. The scanning reports are all available from the FHWA International Programs Office, 400 Seventh Street, SW, Washington, DC 20590, or by communicating with Ms. HanaM Maier (202) 366-6003; E-mail address: HanaM.Maier@fhwa.dot.gov.

Acknowledgment

The work of Mr. James Siebels, Chief Bridge Engineer, of the consulting firm of CH2M Hill is acknowledged for his gathering, assembling and preparing the information used in this presentation.

FRETTING FATIGUE CHARACTERISTICS IN THE CURVED LAYOUT OF LARGE-CAPACITY PRESTRESSING STRANDS

Manabu Fujita[1], Kenji Umezu[2], Hideo Arai[3] and Tamon Ueda[4]

Abstract

Fatigue tests were carried out on the fretting of prestressing strands S15.2 given a small radius of curvature, in external tendons of a prestressed concrete bridge. It was confirmed that fracture locations consentrate at outside-wires of prestressing strands, and fretting mark and crack were found at the point of fracture origins, by the fretting associated with high bearing stress and relative slipping at the contact points between prestresing strands causes the fractures of strands. It was learned that the lifetime under these conditions is shorter than the usual fatigue lifetime in which fretting effects are negligible, and the fretting effects cannot be negligible in the fatigue design of prestressing strands with small radius of curvature. From the test results, we propose a design fatigue strength formula of prestresing strands that takes fretting in small radius of curvature into account.

1.Introduction

Methods for layout of tendons for prestressing the main girder concrete in prestressed concrete bridges include internal-tendon methods in which tendons are laid out inside the girder members, and external-tendon methods, with the tendons laid out outside. In external-tendon methods, the tendons are deviated, and in order to reduce the dimensions of the deviator at which the layout shape is maintained, the radius of curvature of tendons is generally set at from one-third to one-half the radius of curvature for internal-tendon layout.

Under conditions in which the radius of curvature of tendons is reduced, there are concerns of a decline in fatigue strength due to fretting. Fretting is a wear phenomenon occurring at two surfaces in contact under relative motion with minute amplitudes[1]. Figure 1 is a conceptual diagram of fretting fatigue in prestressing strands. When prestressing strands are bundled to form tendons, the steel material overlaps in multiple stages at deflected portion, and lateral pressure acts due to deviation from the external-side steel toward the internal-side steel material. In this case, there is point contact between strands, and so stress due to lateral pressure is concentrated at the points of contact. In this state, axial-direction stress

---

[1] Chief Reserch Engineer, Institute of Technology & Development, Sumitomo Constraction Co., Ltd., M.E., Japan

[2] Chief Reserch Engineer, Institute of Technology & Development, Sumitomo Constraction Co., Ltd., Japan

[3] Prestressed Concrete Works Design Department, Sumitomo Constraction Co., Ltd., Japan

[4] Associate Professor, Division of Structural and Geotechnical Engineering , Hokkaido University, Dr. Eng., Japan

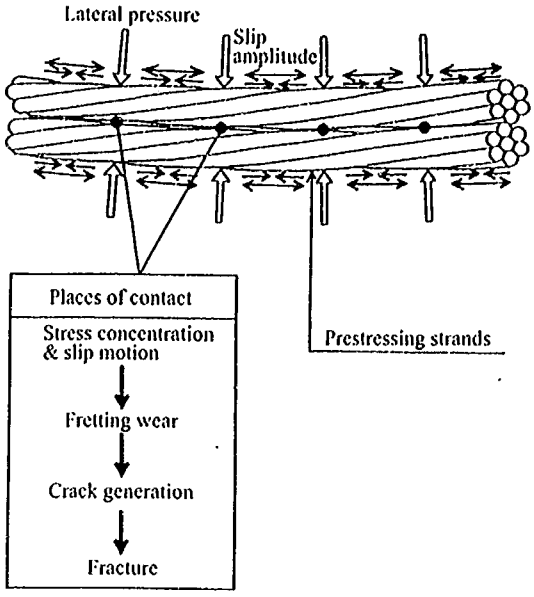


Fig. 1. Concept of fretting fatigue of prestressing strands

fluctuations occur in the steel material, and when this is accompanied by minute relative slipping between prestressing strands or bare wires, wear and cracking occur at points of contact. If this progresses further, it may culminate in fracture. This series of phenomena is known as fretting fatigue.

Research on fretting fatigue characteristics of prestressing strands is limited to only a few cases overseas, nor have many studies appeared in Japan as yet. Hence the authors conducted fatigue tests in order to investigate fracture states and fatigue lifetimes. Specimens used in tests were large-capacity 19S15.2 specimens, on the assumption of external tendons for use in actual bridges. The deviation structures included those modeled with deflected portion on the girder-side face.

In this paper, we report the knowledge obtained in this study, and also propose a design formula for fretting fatigue strength which takes into account fretting fatigue under conditions of a small radius of curvature for large-capacity prestressing strands.

2. Fatigue Tests of Large-Capacity Prestressing Strands

(1) Summary of Tests

a) Testing equipment and specimens

The testing equipment is shown in Fig. 2. The concrete block mounted directly beneath the actuator is a model of a deviator within a box girder. The external tendon layout shape within the deviator block is a straight -line layout at the center (length 1 m), and arc-shaped layouts on both sides (radius of curvature 3 m). A radius of curvature of 3 m is widely used in the deviator of 19S15 external tendons in actual bridges [3] . In consideration of the fact that the deviation angle of external tendons within the box girders of actual bridges is generally between 3° and 10°, the deviation angle per arc layout was set at the intermediate value of 7°.

Table 1. Chemical composition and mechanical properties of prestressing strands

Description	JIS G 3502 piano wire, SWRS82B					
Chemical composition	C	Si	Mn	P	S	Cu
%	0.82	0.21	0.68	0.0144	0.014	0.051
Standard value	—	—	—	≦0.025	≦0.025	≦0.20

Mechanical properties	Yield stress (N/mm^2)	Tensile stress (N/mm^2)	Elongation (%)	Eastic constant (N/mm^2)
	1710	1880	6.9	191400
Standard value	≧1570	≧1860	3.5	—

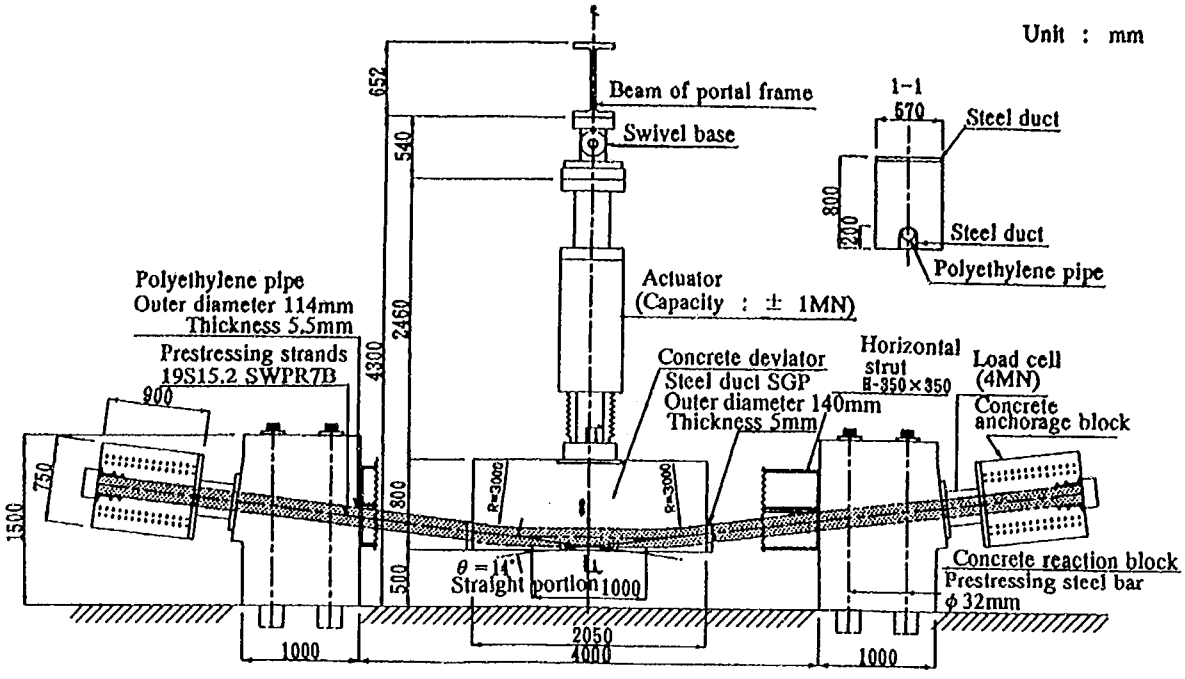


Fig. 2. Specimen testing setup

Tendon specimens were to-scale models of large-capacity external tendons used in prestressed concrete bridges, and employed the following components.

Steel material : 19S15.2 prestressing strands, SWPR7B. Here 19S15.2 means a bundle of nineteen S15.2 strands.

Cross-sectional area = 2673.3 mm^2 (from test records)

The total number of wires of 19S15.2 is 133 (=7x19).

Protective duct : high-density PE (polyethylene) pipe (external diameter 114 mm, wall thickness 5.5 mm).

Interior of protective duct : As a rule, specimens were packed with grout (ordinary Portland cement, water-cement ratio = 45%, with a melamine non-bleeding type admixture)

At the deviator area of the test setup, the steel duct and the prestressing steel protective duct are in contact; the configuration is shown in Fig. 3. In order to prevent folding of the tendon, the ends of the steel duct are bent over.

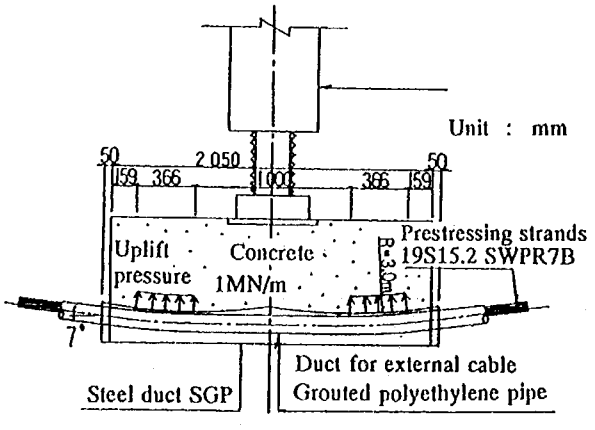


Fig. 3. Deviator construction

Tendon specimens were stressed to 60% of their tensile strength by single-side tensioning

Though there was some difference in friction losses during tensioning, by means of pull-in during anchoring immediately after tensioning , tensioning force of tensioned end and fixed end could be

made nearly equal.

After tensioning and anchoring, cement grout was injected from the anchorage on one end until it was discharged from the anchorage on the other end, to pack the interior of the specimen protective duct. The grout was cured for approximately one week, and after development of a compression strength of 20 N/mm or higher, fatigue tests (repeated loading) were begun.

b) Loading conditions

In fatigue tests, by applying a fixed displacement amplitude in the vertical direction to the deviator block by means of the actuator, axial-direction strain fluctuations were induced in the tendon specimen, to impart a stress amplitude. This loading method is similar to the method used by J.E. Breen and coworkers in fretting fatigue tests[4].

Because the free length (the length of straight -line layout segments in air) of the external tendons in bridges occupies a larger proportion of the total length than the length in deviator, and because in this member axial stiffness is superior to bending stiffness, axial-direction strain fluctuations in free lengths due to live loads are uniform within the tendon cross-section. In these fatigue tests, the total deviation angle was increased to 14° by providing arc layouts in two places within the deviator, and so only a small vertical deviator amplitude of 4 to 20 mm was needed to induce the desired stress amplitude in the tendon specimen between anchorages (8600 mm); by this means, the behavior of external tendons in actual bridges was reproduced.

Further, in these fatigue tests there exists an area, at the boundary between the arc layout within the deviator and the straight -line layout segment on the outside, an area in which the layout shape of the external tendon changes from arc-shape to straight, and this area feels the influence of bending fatigue during amplitude cycles. The external tendons in actual bridges are movable with respect to girders, and so there is slipping within the deviator under fatigue loading, and there is an area in which the layout shape changes from arc-shape to straight. Hence this behavior in these experiments does not depart from the behavior of actual bridges.

Actuator displacement was controlled such that the stress amplitude of prestressing strands was maintained at the preset value even as fracture of prestressing strands progressed.

The loading conditions used in these tests appear in Table 2. M-1 through M-4 are specimens which assume an external tendon at the deviator. High-density PE pipe was used as the protective duct, and use the stress amplitude as a parameter.

The lower-limit stress intensity for the steel material of specimens in all fatigue tests was unified at 1120 N/mm^2, or 60% of the tensile strength.

Table 2. Repeated loading conditions

Specimen No.	Prestressing material stress (N/mm^2)			Actuator vertical displacement amplitude	Frequency	Oscillation velocity
	Amplitude σ_r	Lower limit σ_{min}	Upper limit σ_{max}	δ (mm)	n (Hz)	v* (mm/sec)
M-1	120	1120	1240	20.0	0.40	25
M-2	80	1120	1200	12.6	0.54	21
M-3	50	1120	1170	8.8	0.70	19
M-4	20	1120	1140	3.8	1.80	21

*$v=\delta\pi n$

Table 3. Quantities for measurement and equipment used

Quantity	Equipment
Tendon tension	Load cells placed between anchorage and reaction block, strain gauges mounted on prestressing strands
Tendon vertical force	Actuator
Deviator vertical displacement	Actuator, Deviator vertical displacement
Wire fracture	Accelerometers (±5 G), load cells

The frequency was set such that the vertical loading rate at the center of the actuator amplitude was close for all specimens (Table 2), at 19 to 25 mm/sec.

c) Parameters for study in tests

1)Fatigue lifetime of prestressing steel

Tests have been conducted[4] in which the fatigue lifetime is taken to occur at fracture of 2% of all wires (testing standard for stayed-cable in U.S. PTI standards[5]) and at fracture of 5% of all wires. In these tests, the points of initial fracture (the first fracture of a wire), 2% fracture (fracture of three wires), and 5% fracture (fracture of seven wires) were measured.

2) Mechanical performance of prestressing strands after fatigue tests

Following fatigue tests, the setup was disassembled, and the prestressing strands recovered and subjected to static tensile tests, to determine whether the requisite mechanical properties (strength, elongation) were satisfied. By this means, prestressing strands containing cracks due to fretting were identified.

d) Instrumentation system

Table 3 lists the quantities measured and equipment used.

In fatigue testing, it is important that material fracture occurring during tests be detected accurately. In these tests, sensing of the fracture of wires in prestressing strands relied on accelerometers to measure vibrations occurring at fracture, and dynamic measurements of changes in tension by a load cell. The system appears in Fig. 4; this system, which connects waveform sampling equipment to a personal computer and is provided with a function for triggering by accelerometers installed on the tendon specimen, was developed specifically for these tests.

When a wire fractures, shock waves reach accelerometers mounted at six locations on the specimen, in order of proximity to the fracture. An example of waveforms sensed by an accelerometer appears in Fig. 5; the waveform rising edge appears earliest for accelerometer no. 4, installed close to the arc area on the tensioned side of the deviator, and the acceleration at this device is also large. Hence in this case, we infer that a wire fracture occurred in the vicinity of accelerometer no. 4. In this way, during fatigue testing fracture locations were inferred by comparing the simultaneous waveforms from the accelerometers at six locations. The results of inferences, including both positions and number of

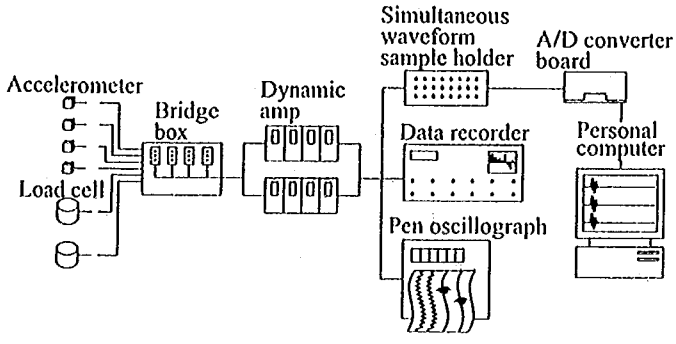


Fig. 4. Fracture sensing system

Table 4. Results of fatigue tests

Specimen no	Stress amplitude σr (N/mm²)	Repeated load cycles			Number of Load cycles when stopped	Days of fatigue testing	No. of fractures in deviator during fatigue testing
		Initial fracture (1 wire)	2% fracture (3 wires)	5% fracture (7 wires)			
M-1	120	259,000	281,000	351,000	385,000	12	22
M-2	80	786,000	817,000	888,000	980,000	21	13
M-3	50	1,157,000	1,227,000	2,027,000	3,000,000	50	13
M-4	20	no fractures	no fractures	no fractures	10,000,000	65	0

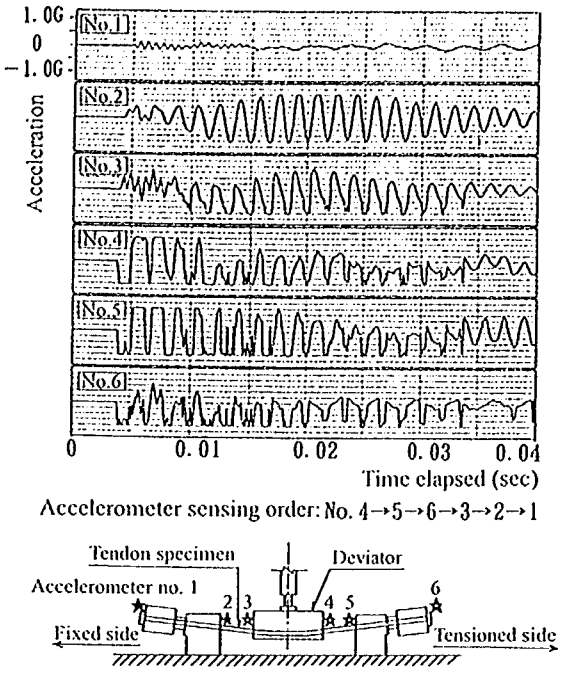


Fig. 5. Example of waveforms sensed by accelerometers

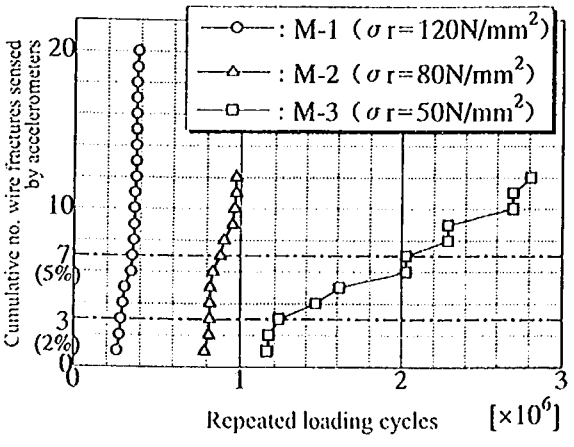


Fig. 6. Trends in wire fracture occurrence with repeated loading

fractures, were correlated with studies of disassembled tendons conducted after the tests, and it was confirmed that this method enabled accurate fracture detection.

(2) Test Results

The results of fatigue tests for each specimen appear in Table 4. Figures for number of cycles are shown rounded down to the nearest 1000.

a) Trends in fracture occurrence

Figure 6 shows cumulative results for the number of wire fractures detected by accelerometers corresponding to the number of loading repetitions. The larger the stress amplitude for a specimen, the shorter was the interval between fractures under repeated loading. In other words, when stress amplitudes in large-capacity prestressing strands are large, there is a tendency for fractures due to fretting fatigue to occur simultaneously, but when stress amplitudes are small there is some degree of lifetime remaining after some wires fracture and before others fracture.

b) Fracture properties

After fatigue testing, specimens were disassembled and studied. Fractures occurred in units of wires comprising prestressing strands. The distribution of locations of wire fractures in the deviator appears in Fig. 7. Here "fixed end" and "tensioned end" at the

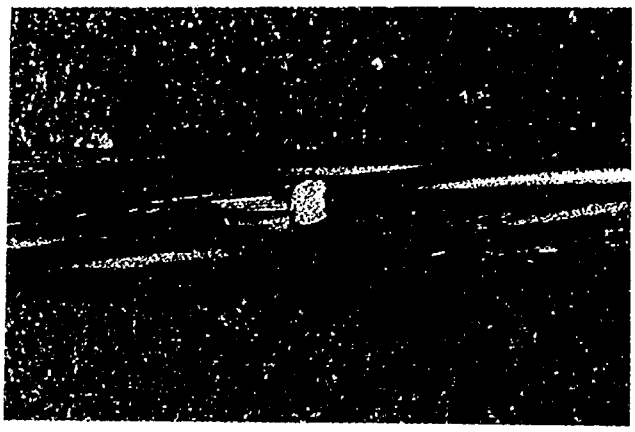


Photo 1. Fracture location in prestressing strand

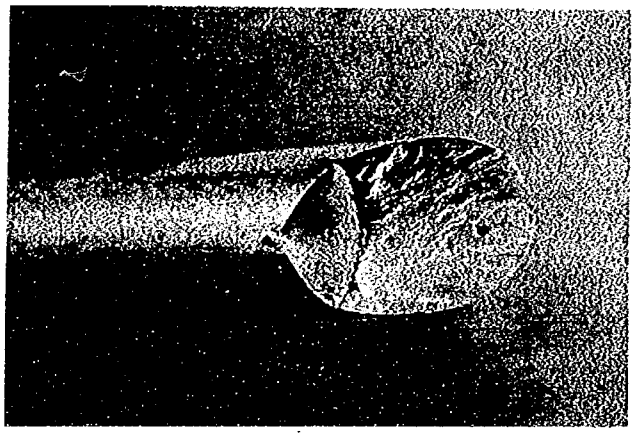


Photo 2. Wire fracture surface

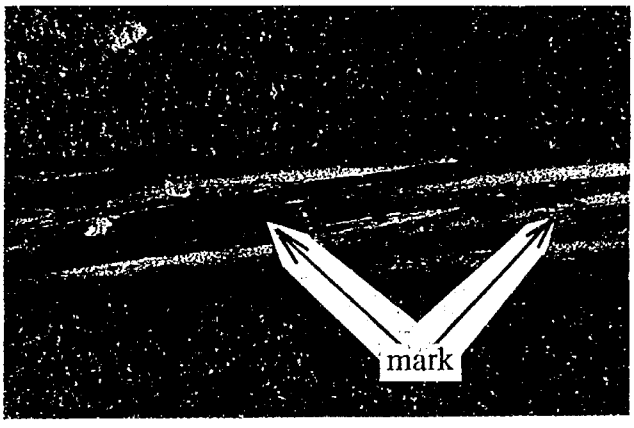


Photo 3. Fretting marks

arc area indicate the direction of single-side tensioning when the prestressing strands are fixed in the testing equipment.

Specimens were cut at the center of the straight -line layout segment in the deviator in order to investigate the state of prestressing strand layout in the tendon cross-section. Diagrams of tendon cross-sections appear in Fig. 7. There are prestressing strands in the cross-sectional diagrams which are not in mutual contact; this is because the section was cut in a straight -line layout area. At arc areas, strands are expected to be in contact in layers.

A prestressing strand fracture point is shown in Photo 1, a wire fracture end in Photo 2, and fretting marks in Photo 3. In Photo 3, there are oxide abrasion particles (rust) due to fretting corrosion on the surface of the fretting marks. As shown in the conceptual diagram for vertically neighboring prestressing strands in Fig. 1, at this contact plane there is an intersection of twist directions, and so point contact occurs. As a result fretting marks appear at intervals equal to the interval of wires (35 mm) in the prestressing strand axial direction, as seen in Photo 3.

Table 5 indicates the states of all fractured wires. For convenience, wire fracture surfaces are classified into two shapes according to the proportion of the cross-section occupied by the crack (Fig. 8). Fracture origins were classified as either on the inner side or the outer side of the prestressing strand, as in Fig. 9.

Observed fracture properties were as follows.

1) At the ends or within fretting marks indicating contact with other steel members were the origins of cracks, and cracks propagated nearly perpendicular to the wire axis direction (cf. Photo 2). Subsequently the fracture surface is surmised to have propagated in a direction diagonal to the wire axis, culminating in fracture.
2) Nearly all of the fracture origins in prestressing strands were on the outside, but some were on the inside.

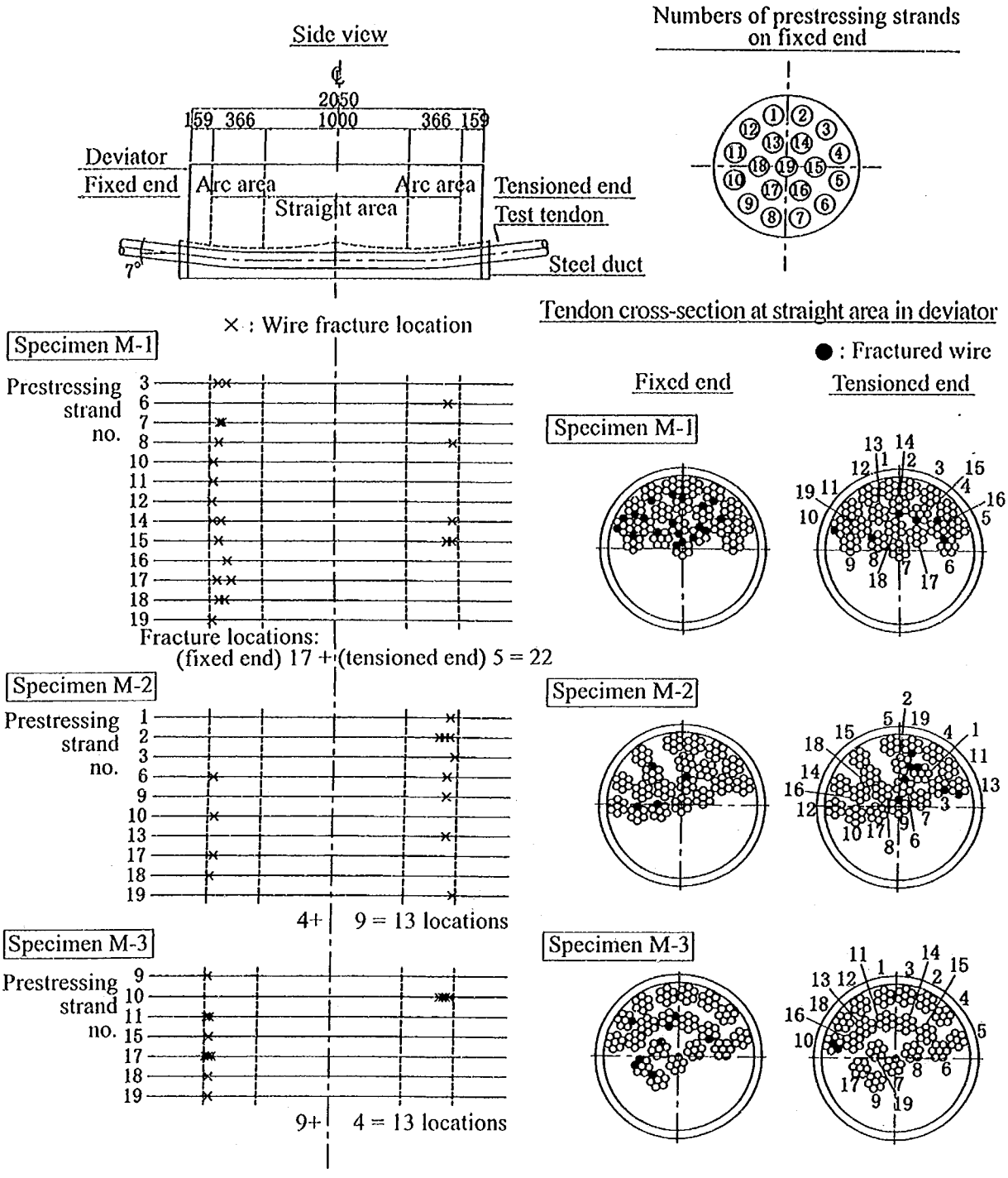
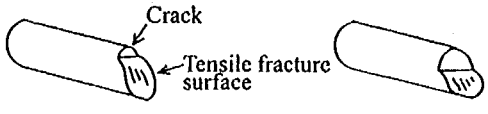


Fig. 7. Wire fracture areas in prestressing strands

Table 5. Wire fracture surface properties

Specimen no.	Arc area	Prestressing strand no.	Fracture position	Shape of fracture surface	Fracture origin	Fretting rust?
M-1	Fixed side 17 places	3	760	A	Outside	Yes
			810			
22 fractures		7	770			
			770			
		8	810			
		10	840			
		11	830			
		12	845			
		14	790			
			825			
		15	800			
		16	745			
		17	720			
			820			
		18	770			
			800			
		19	850			
	Tensioned side 5 places	6	785			
		8	810			
		14	815			
		15	780			
			815			
M-2	Fixed side 4 places	6	820	B	Outside	Yes
		10	805			
13 fractures		17	820	A		
		18	835	B		
	Tensioned side 9 places	1	800			
		2	735			
			775			
			810			
		3	850			
		6	790	A		
		9	775	B		
		13	780	A		
		19	860			
M-3	Fixed side 9 places	9	850	A	Outside	Yes
		11	850			
13 fractures			855	B		
		15	825	A		
		17	830	B		
			860		Inside	Yes (somewhat numerous)
			865	A	Outside	Yes
		18	830	B		
		19	825			
	Tensioned side 4 places	10	780	A		
			810			
			845			
			790	B	Outside	Yes (somewhat numerous)

*Fracture positions are distances from the deviator center



A: Crack cross-sectional area less than 1/3 of wire cross-section

B: Crack cross-sectional area 1/3 or more of wire cross-section

Fig. 8. Classification of fatigue fracture surfaces

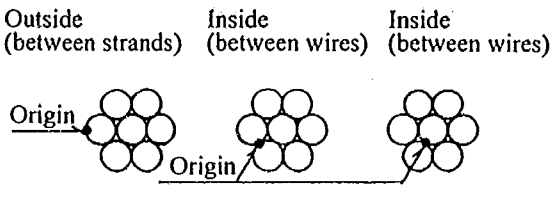


Fig. 9. Fracture origins

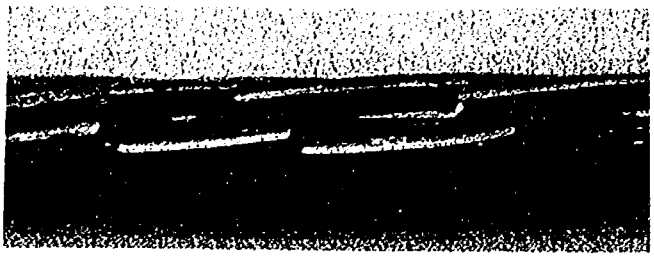


Photo 4. Prestressing strand with core wire fractured

Fractures with origins on the outside are due to cracks resulting from fretting of the prestressing strand; fractures originating on the inside result from fretting between wires within the prestressing strand. In the specimens M-1 and M-2, all fracture origins were on the outside. In specimen M-3, of the 14 fractures, two had origins on the inside.

Whereas there is point contact between prestressing strands in the bending layout areas of prestressing strands, the contact between wires is macroscopic. From this we infer that the lateral stress intensity per unit area at contact surfaces is greater for pairs of prestressing strands, with their smaller contact areas, than for pairs of wires; and the harsh fretting environment suggests a short fatigue lifetime.

Prestressing strands in which fracture origins were observed on the inside included no. 10 and 17 of M-3 (cf. Table 5). In both cases multiple wires in close proximity had fractured within a single prestressing strand, at an interval of 65 mm in no. 10 and 35 mm in no. 17. Of these, fractures in no. 10, in which there was fracture of the core wire, are shown in Photo 4. Observations revealed that wire fracture due to fretting between prestressing strands occurred first, with a strong possibility that fretting and further fracture occurred at places of point contact of the fractur surface with other unfractured wires. Hence this is thought to be fretting fatigue fracture induced by linear contact between wires. M-3 was subjected to three million loading cycles, a large number, and this is believed to have induced this mode of fracture.

3) Examination of the external appearance of wires in the specimens M-1, M-2 and M-3 occasionally revealed cracks thought to be due to fretting fatigue in prestressing strands which did not develop into fractures.

c) Discussion of the distribution of fracture locations

Wire fractures in the deviator were concentrated near arc ends, as shown in Fig. 7. This may be attributed to the following two causes.

1)Relative slippage

In external tendons employing prestressing strands in which layout shapes are straight and bent, there is a slight difference in the extensions passing through the inside of the arc and those passing through the outside. Hence when uniform elongation occurs in the axial direction, strain occurring in the inner prestressing strands and in the outer strands will be different. As a result of this, minute slippage occurs between prestressing strands.

Figure 10 shows the distribution in the amount of relative slippage between neighboring inner and outer prestressing strands, when friction in the layout interval (for example, friction between tendon and steel duct, or between prestressing strands) is ignored. In the arc area, slippage is greater in moving toward the ends, and clearly fretting fatigue will occur more readily at the arc ends.

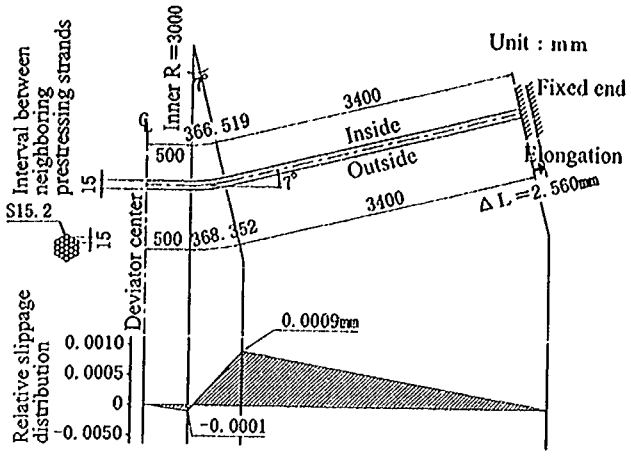


Fig. 10. Distribution of relative slippage

2) Changes in layout shape

The amplitude of the elevation angle of the free length of the tendon specimen was 0.3° for specimen M-1 and 0.06° for M-4. Consequently within amplitude cycles there is a part in which, at the arc end, the external tendon layout shape changes from straight to arced, and at this part the influence of bending fatigue also acts to make fatigue conditions still more severe. However, this area of change extends for an axial-direction length of 16 mm in M-1 and 3 mm in M-4; even outside these areas of change, there are numerous fracture locations. Hence within the range of the fracture lifetime of prestressing strands due to fretting fatigue, the effect of bending fatigue is not thought to be dominant.

d) Relative slippage

As indicated in Fig. 10, when the stress amplitude is 120 N/mm^2, the calculated relative slip between neighboring prestressing strands, when friction losses in the layout interval are ignored, is at most only a very small 0.0009 mm. In reality there is friction, and so slippage will be smaller still. This indicates that fretting fatigue can occur even for such infinitesimal slip amounts.

e) Tensile tests

Static tensile tests were conducted for unfractured prestressing strands taken from among the strands recovered by disassembly after fatigue tests. As a result, it was found that free-length prestressing strands exhibit tensile strength comparable to sound parent material, with no decline in tensile strength.

On the other hand, prestressing strands from the deviator area in specimens M-1, M-2 and M-3 fractured at lower loads than the tensile strength. The fractures appeared to differ from the "contraction fracture" (ductile fracture) seen in sound prestressing strands in tensile tests; as Photo 5 indicates, these fractures originated in cracks in directions perpendicular to the wire axis, characteristic of fatigue. Photo 6 is a photo of juxtaposed wire ends showing such a fractured state after tensile testing. The length of the fretting mark in the wire axis direction was 4 mm, but the origin of the crack was not at an end, but in the middle of the fretting mark.

In this way, cracks which are difficult to detect visually but which, if fatigue tests are continued, result in fractures appeared in prestressing strands in the deviator area. Hence in the stage in which fracture has occurred in some prestressing strands, it is highly likely that cracks have also appeared in the wires of other strands. On the basis of this, and in consideration of the need to guarantee the required performance as tension members, it is thought that as the fatigue lifetime of prestressing strands laid out with a small radius of curvature, 2% fracture or 5% fracture, representing the initial fracture stage, is reasonable.

In light of the occasional observation of wires with fracture states and cracks similar to those resulting from tensile tests, we may make the following inferences regarding the progress of the fracture surface due to fretting fatigue under repeated loading.

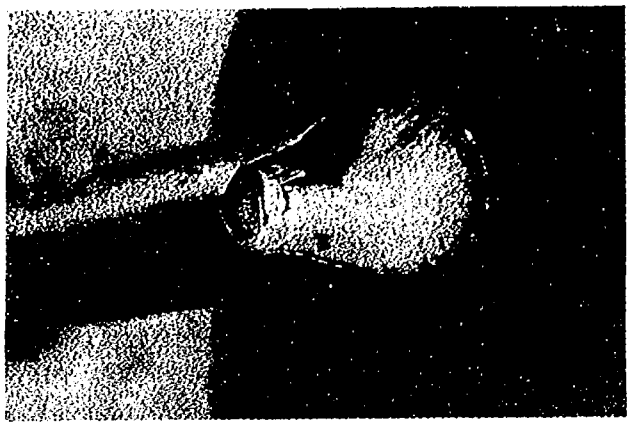


Photo 5. Fracture surface originating in fatigue crack in tensile tests.

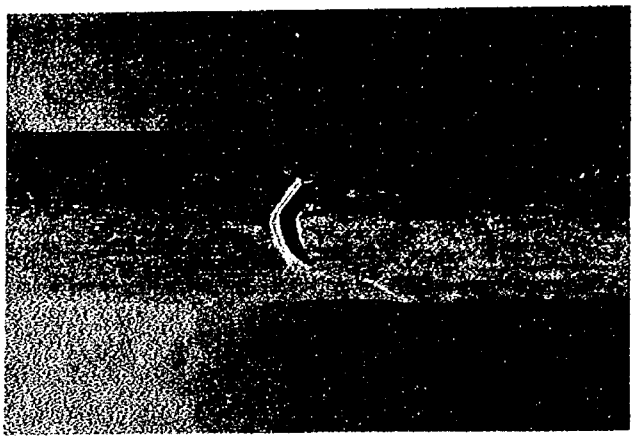


Photo 6. Wire photographed with ends joined.

Wire cracks due to fretting fatigue propagate gradually after appearance. As a crack develops in a wire, the cross-section bearing the tensile stress decreases, and when the remaining wire cross-section can no longer bear the tensile stress, fracture occurs. Oblique tensile fracture surfaces appear at this instant; the fracture surface is created instantaneously during fatigue testing.

f) Zero-fracture test results

In specimen M-4 ($\sigma r = 20$ N/mm^2), there were no fractures in prestressing strands during ten million repeated loading cycles.

On conducting tensile tests for all prestressing strands in the deviator area taken from a disassembled tendon, all underwent contraction fracture with tensile strengths comparable to that of the parent material. In other words, there were no cracks or strength degradation due to fretting fatigue. By this means it was confirmed that 19S15.2 packed with grout at a stress amplitude of 20 N/mm^2 has a sufficiently long fatigue lifetime.

2.S-N Curve for Large-Capacity Prestressing Strands

(1) S-N Regression Lines

Fatigue lifetimes (number of cycles to fracture), obtained as the results of fatigue testing, are plotted in Fig. 11 for the 19S15.2 specimens M-1 through M-4. The specimen which had not undergone fractures at the conclusion of repeated loading is marked with a horizontal arrow (→).

A regression line for log S vs. log N for the initial fractures in the 19S15.2 specimens M-1, M-2 and M-3 is also shown in the figure. The y-intercept, slope, and correlation coefficient for the regression equation (1) appear in Table 6.

$$S = \frac{10^{\alpha}}{N^{\kappa}} (N/mm^2) \qquad (1)$$

S : Prestressing strand stress amplitude
N : Repeated loading cycles
α : y-intercept
κ : Slope

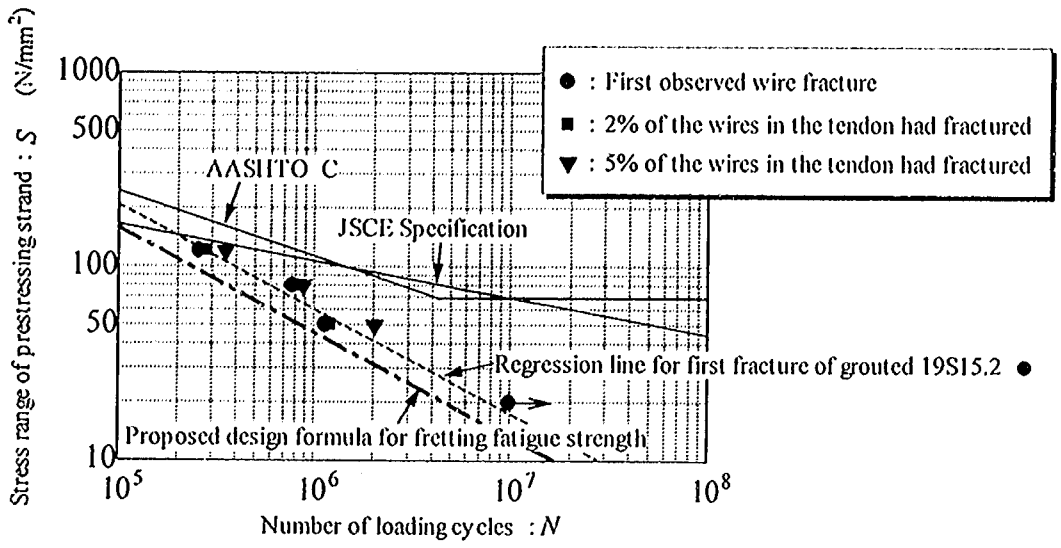


Fig. 11. S-N plot of fretting fatigue test results for 19S15.2 prestressing strands

(2) Comparison with Texas University Fatigue Testing Results

Fatigue testing of prestressing steel members focusing on fretting fatigue has been conducted by J.E. Breen et al (Texas University, VSL International) [4][6]. The specimens of reference[4] employ as the tension member 12S12.7 prestressing strands; the protective duct is galvanized steel duct (inner diameter 75 mm); and cement grout packing is used. The method used to apply stress amplitudes to the specimen tendons is the same as that used in this study, with a deviator block to induce tendon deviation cycled through a displacement amplitude by hydraulic equipment. A stress amplitude of 170 N/mm^2 was applied to the prestressing strand specimens. Three specimen were tested, with prestressing strands smoothly and properly laid out (radius of curvature 3 m) at the deviator, and with two types of twist angle applied at the ends. Based on these results, Breen and coworkers recommended that fatigue design of inner- or outer-tendon post-tensioned concrete girder conform to the Category C curve applied to "redundant load path structures" by AASHTO (American Association of State Highway and Transportation Officials)[7] (cf. Fig. 11). Here AASHTO S-N lines are indicated for categories of steel bridge design corresponding to the smoothness of steel member surfaces, flange dimensions and welding conditions; categories from A to F are provided, where fatigue strengths are greatest for A and weakest for F.

J.E. Breen et al report that initial fracture in fatigue tests of the specimen with smooth layout occurred at 470,380 cycles.

In the fatigue tests conducted by the authors for large-capacity prestressing strands, the fatigue strength corresponding to initial fracture at 470,000 cycles is 90 N/mm^2 on the S-N regression line, so that fatigue strengths in the authors' tests are lower. The following are two differences in the testing conditions used in these studies.

1) Whereas the specimens used by Breen et al were 12S12.7, those used by the authors were 19S15.2. The latter has a greater number of prestressing strands, so that there are more overlapping layers in deflected

Table 6. Regression line for initial fracture in 19S15.2 (grouted)

y-intercept α	Slope κ	Correlation coefficient r
4.999	0.536	0.95

areas, and to this extent lateral pressure is increased, creating more severe conditions for fretting fatigue.

2) The lower-limit stresses applied to tendon specimens in the tests of Breen et al appear to have been lower than the lower-limit stresses in the tests of the authors (60% of the tensile strength), judging from the minimum loading value of the hydraulic equipment at the fatigue testing amplitude. It may therefore be conjectured that lifetimes were extended beyond those seen in the fatigue tests conducted by the authors.

The difference in fatigue strengths obtained in tests by Breen et al and those measured in fatigue tests by the authors are inferred to be due to the above factors.

4. Proposal of a Design Formula for Fretting Fatigue Strength of Large-Capacity Prestressing Strands

As is clear from Fig. 11, if the design fatigue strength formula for prestressing strands stipulated by the standard specifications for concrete[2] of the Japan Society of Civil Engineers (JSCE) is applied to prestressing strands with small radii of curvature, the error is on the dangerous side. Hence we propose eq. (2) as a design formula for fatigue strength which takes into account fretting fatigue in prestressing strands. Equation (2) is obtained from the first-fracture fatigue lifetime for 19S15.2 large-capacity prestressing strand specimens, with the probability of falling below test values at 5%. Specifically, for the regression line for the results of these tests, this formula is obtained as double the standard error[8] in the S-axis direction.

$$f_{prd} = \frac{10^{\alpha}}{N^{\kappa}} (N/mm^2) \qquad (2)$$

Here α=4.9 and k=0.54.

The prestressing strand fatigue testing method and specimen conditions used in proposing this formula are summarized below.

Method : A stress amplitude is applied to prestressing strands to induce an axial-direction strain fluctuation by applying a fixed displacement amplitude to a deviator block (deviation angle 14°) in the direction perpendicular to the layout direction of the tendon specimen.

Conditions : 1) Prestressing strands are 19S15.2B.
2) Lower-limit stress intensity is 0.6 times tensile strength.
3) Radius of curvature is 3.0 m.
4) Interior of protective duct is packed with grout.

5. Conclusion

The conclusions obtained in this research are summarized below.

(1) In fatigue tests of 19S15.2 prestressing strands, fracture was confirmed at bending layout areas of radius 3.0 m. The origins of wire fractures were observed to include fretting marks and cracks. The combination of the high bearing pressure due to point contact between prestressing strands and the minute relative slip accompanying stress amplitudes resulted in fretting-induced fatigue damage, which was the principle cause leading to wire fractures in prestressing strands.

(2) Wire fracture origins were nearly all due to fretting between prestressing strands, but fractures

originating in fretting between wires comprising a prestressing strand were also observed. However, fatigue lifetime due to fretting was shorter for fretting between prestressing strands than for fretting between wires.

(3) It was confirmed that fatigue strength accompanying fretting is lower than fatigue strength in an environment in air in which the occurrence of fretting is negligible. It is thought that in fatigue design of prestressing strands with a small radius-of-curvature layout, as in the case of external tendons, the decline in fatigue strength due to fretting must be taken into account.

(4) A design formula (eq. (2)) for fatigue strength was proposed which takes into account fretting in large-capacity prestressing strands with small radius-of-curvature layouts.

(5) Upon subjecting 19S15.2 tendons having a deviator with a bending layout radius of curvature of 3.0 m and with the protective duct interior packed with grout to ten million repeated loading cycles at a stress amplitude of 20 N/mm^2, no fractures occurred in prestressing strands due to fretting fatigue, nor was there any degradation of mechanical performance whatsoever. Hence the prestressing strands of these specifications were confirmed to have a fatigue lifetime of ten million cycles or more at a stress amplitude of 20 N/mm^2.

Acknowledgments

The authors want to express their deep appreciation to Sumitomo Electric Industries, Ltd. for their valuable cooperation in this investigation.

References

[1] See for example R.B. Waterhouse: Fretting Corrosion, Pergamon Press, 1972

[2] Japan Society of Civil Engineers: Standard Specification for Design and Construction of Concrete Structures, Part1 Design, pp. 35-36, March 1996.

[3] Express Highway Research Foundation of Japan: Research Report on Cases of New Structures for Prestressed Concrete Bridges (Study on effectiveness and application of external tendons), p. 30, March 1993.

[4]Gregor P. Wollmann, Karen Ryals, John E. Breen and Michael E. Kreger: Fretting Fatigue of External Tendons in Segmental Bridge Deviators, Workship - Behaviour of External Prestressing in Structure, AFPC, pp.131-140, June 1993.

[5]Post-Tensioning Insttute Committee on Cable-Stayed Bridges: Recommendations for Stay Cable Design, Testing and Installtion, pp21-22, August 1993

[6]Gregor P. Wollmann, David L. Yates, John E. Breen and Michael E.Kreger: Fretting Fatigue in Post-tensioned Concrete Beams, ACI Structural Journal, Vol.93, No.2, pp172-179, March 1996.

[7]American Association of State Highway and Transportation Officals, Inc.: Standard Spesifications for Highway Bridges, Fourteenth Edition, pp. 112-117, 1989

[8] H. Ikeda: Statistical Methods I, pp. 100-112, Shinyou-sha, 1976.

USE OF AN ALTERNATE SHEAR CONNECTOR IN A BEAM-IN-SLAB BRIDGE SYSTEM

F. W. Klaiber[1] and T. J. Wipf[1]

Abstract

In Iowa there are over 20,000 bridges on the secondary system. The majority of these bridges are the responsibility of the local county engineers who with limited budgets, frequently design and construct short span bridges with their own labor forces. The primary objective of the research presented in this paper is to perform laboratory testing on an alternative that counties can design and construct. This project involves testing and modifying a system of steel beams with concrete fill between them. This system has been used by several Iowa counties on low water stream crossings for more than 20 years. There is no reinforcing steel in this system or connection between the steel beams and the concrete. With the proposed modification which uses an alternate shear connector (ASC) for composite action, less materials will be required and longer spans will be possible.

Introduction

This paper will provide an overview on the use of an alternate shear connector (ASC) for obtaining composite action. The ASC was conceived as a means of using an existing bridge alternative on longer span bridges. The existing alternative is referred to as a beam-in-slab-bridge (BISB).

In Iowa there are a significant number of BISBs on low volume roads. As shown in Fig. 1, the structure uses a series of steel W sections spanning between abutments. The majority of bridges constructed to date have used W10 and W12 sections on 2 ft (0.61 m) centers. Steel straps are welded to the bottom flanges to hold the steel beams in place while the concrete is placed; there is no reinforcing in this system or physical connection between the steel beams and the concrete. Plywood, placed between adjacent beams on the top surface of the bottom flanges, is used for form work. The width of the forms is made a few inches less than the beam spacing so that the concrete is in contact with the bottom flange when placed. Thus, even after the form work deteriorates there will be adequate bearing between the steel and the concrete. These structures have been used for spans varying from 20 ft (6.10 m) to 40 ft (12.19 m) with and without guardrails.

Upon reviewing this system, the authors determined that by making two modifications to the beam-in-slab system (adding composite action and reducing the weight of the structure), it would be possible to increase the strength of the system and use the system on longer spans. Also, if the top flanges of the beams were removed from the riding surface, the

[1]Professor, Department of Civil and Construction Engineering, Iowa State University, Ames, IA.

skid resistance of the bridge surface could be improved. In the BISB system, there is sufficient concrete to carry compressive forces without the contribution of the top flange of the steel beams. The two modifications investigated were: 1) developing composite action between the concrete and steel and 2) reduction of concrete slab.

Leonhardt, et al. [1987] have shown that by punching holes in the web of the steel sections, composite action between the concrete and steel can be developed. Concrete dowels are formed when concrete fills the holes. These concrete dowels resist the horizontal shear at the steel-concrete interface and prevent vertical separation of the two materials. Transverse reinforcement in some of the holes is required to confine the concrete to the steel. This type of shear connector has also been investigated by Roberts and Heywood [1994] and is similar to Perfobond strips shown in Fig. 2 that were tested by Oguejiofor and Hosain [1992]. Concrete on the tension side of the BISB (see Figure 1) is obviously providing minimal strength contribution and thus is essentially only adding to the dead load of the system. By replacing the plywood forms with sections of arched formwork (corrugated metal pipe or plastic pipe) as shown in Figure 3, the amount of concrete on the tension side could be significantly reduced. Pipe formwork of the appropriate diameter will provide the desired slab thickness (dimension 'h' in Figure 3). Coring holes through the web of the steel beam with steel reinforcement through several of the holes (i.e. the ASC) will make it possible to obtain composite action. Incorporating these modifications to the beam-in-slab system would make it possible to use this system on significantly longer spans with reduced cost. Even with these modifications, the simplicity of the beam-in-slab system permits it to be constructed by county work forces.

This investigation consists of several tasks to address the desired modifications:

- Static push-out tests for determining the strength of various types of ASC between concrete and steel.
- Cyclic load tests of the ASC for determining their fatigue characteristics and slip behavior.
- Use of ASC's in composite beam tests for strength and behavior data.

In the following sections, the first two tasks will be briefly described. As the composite beam tests are still in progress, limited information on these tests is included.

Static push-out tests

Dimensions of the push-out specimens are shown in Figure 4. As shown, each specimen consisted of a stiffened steel plate 3/8 in. (10 mm) x 20 in. (510 mm) x 15 in. (380 mm) and two concrete slabs: 8 1/4 in. (210 mm) x 21 in. (535 mm) x 20 in. (510 mm). In each specimen, the steel plate and reinforced concrete slabs were positioned so that the contact area was 17 in. (430 mm) x 2 1/2 in. (65 mm) in each slab for a total contact area of 85 in^2 (54,840 mm^2). Load was applied to the steel and transmitted into the concrete slabs

through shear; voids at the bottom of the steel plates (see Figure 4) prevented transfer of force by bearing.

Previous research has shown that the surface bond between the steel and concrete does not change the specimen's ultimate strength (Seiss, et al., 1952). Thus, although the steel plates were thoroughly cleaned prior to casting the concrete, no attempt was made to destroy the natural bond between the concrete and steel.

Eleven series of push-out tests have been completed. Variables investigated include hole diameter, hole spacing, hole alignment, addition of reinforcement through a hole, reinforcement size, and cored vs. torched holes. The configuration of holes in the steel plate, presence of reinforcement, etc. in 10 of the 11 series is illustrated in Figure 5. Series 7 involved plain steel plates and thus has not been included in this figure. In reviewing Figure 5, one notes there are three series without reinforcement (Series 1, 2, and 3) and two series with torched holes (Series 8 and 9). There were 3 specimens in each series except for Series 1 in which there were 6 specimens; thus, a total of 36 push-out tests were completed.

Slip and separation between the steel plates and concrete slabs were measured on all push-out specimens. The instrumentation for all specimens consisted of seven direct current differential transformers (DCDTs). Two of the DCDTs were positioned to measure slip between the concrete slabs and steel plates, four to measure separation at two elevations along the slab, and one for detecting lateral deflection of the stiffened plate. The two slip readings obtained were averaged to produce the average slip per connector. The load per connector is half the total load applied to the specimen. Separation between the concrete and steel was very small and thus could be neglected. Out-of-plane movement of the stiffener plate was also determined to be very small.

Typical load-slip data for some of the series tested are presented in Figures 6 and 7. Shown in Figure 6 is the load-slip data from Series 1 and 10; both these series have 1 1/4 in. (30 mm) holes on 3 in. (75 mm) centers. The only difference is Series 10 also has a #4 reinforcing bar. Comparing the two curves in this figure one notes the increase in strength resulting from the added reinforcement. The effect of torching holes vs. coring holes in the steel is illustrated in Figure 7. As indicated, poor quality torched holes have slightly less strength, however, carefully torched holes have essentially the same strength as cored holes.

From the results of the tests, it was determined that the strength of the ASC was influenced by five variables: concrete compressive strength, the friction between the steel plate and the concrete, the concrete dowel formed by concrete, the reinforcing bar placed through the shear hole, and the transverse slab reinforcing. From the results of the push out tests, it was determined that hole spacing was not an important influence on the strength of the connection if the spacing was at least 1.6 times the hole diameter. Therefore, spacing of the shear holes was not included in the design equation that was developed; the design equation is only valid for hole spacings greater than 1.6 times the shear hole diameter.

By reviewing beam sizes that might be used for bridge stringers, it was determined that the smallest web thickness that might be encountered in the field would be approximately 3/8 in. (10 mm) which is the plate thickness used in the push-out specimens. Therefore, steel plate thickness also was not included as a variable; the expression developed will thus result in conservative strength values for web thicknesses greater than 3/8 in. (10 mm).

Fitting a curve to the experimental data resulted in the following equation which may be used to predict the shear strength of the ASC:

$$q = 0.62\ A_s\sqrt{f'_c} + .35A_r f_{yr} + n\left(.35A_{tr}\ f_{ytr} + 19A_{cd}\sqrt{f'_c}\right) \qquad (1)$$

where

A_{cd} = Shear area of each concrete dowel, in^2.
A_r = Area of reinforcing bar through shear holes, in^2 per five holes.
A_s = Total area of steel in contact with the concrete, in^2.
A_{tr} = Area of transverse reinforcement per hole divided by two, in^2.
f'_c = Concrete compressive cylinder strength, psi.
f_{ytr} = Yield strength of the transverse reinforcement, psi.
f_{yr} = Yield strength of reinforcing bar, psi.
n = Number of concrete dowels.
q = Shear strength of ASC, lbs.

Since the concrete dowels are subjected to double shear, the term A_{cd}, the total shear area, would be twice the area of the shear hole. Likewise, the steel is in contact with the concrete on both sides; thus, A_s is two times the cross-sectional area of the steel in contact with the concrete.

An analysis was conducted to determine the contribution of each of the four terms in Equation 1. Based on this sensitivity analysis, it was determined that the shear hole area, the amount of transverse reinforcement, the number of shear holes, and the concrete compressive strength are the primary factors that influence the shear strength of the ASC. Since Equation 1 was obtained from the testing of a limited number (36) of specimens and it does provide ultimate strength, appropriate conservative factors of safety will need to be applied if it is used in design.

Fatigue Strength of the ASC

In this portion of the investigation it was desired to determine the fatigue strength and slip behavior of the ASC when subjected to cyclic loading. Push out specimens (shown in Figure 4) were fabricated and tested to failure. Three different series of specimens were tested. Series SH1 was the same as Series 10 illustrated in Figure 5i. Series SH2 was the same as Series 5 illustrated in Figure 5e except a #4 reinforcing bar was used instead of a #3

reinforcing bar that is illustrated. Series SH3 was the same as Series 1 presented in Figure 5a, except a #4 reinforcing bar was inserted in the middle hole. As is apparent when comparing these three series, the variables investigated were hole alignment (Series SH1 vs Series SH2) and the influence of the placement of reinforcing bars through the shear holes (Series SH1 vs. SH3). Hole diameter (1 1/4 in. (30 mm)) was kept constant; also all series had a #4 reinforcing bar through the center hole. A total of 27 push out specimens were tested; six statically to determine the ultimate static strength and 21 subjected to cyclic loading at load levels that were various percentages of the ultimate static strength.

Using the data from the cyclic tests and a linear regression analysis, which provided the best fit, S-N curves for the three series were developed. These three curves are shown in Figure 8. An inspection of these curves indicates that there is minimal strength gained when the shear hole alignment was staggered. Placing reinforcing bars through full diameter holes (Series SH3) is more effective than placing reinforcing bars in half-circle holes (Series SH1).

Design Implications

For simple span bridges which have stringers on 4.5 ft (1.37 m) centers, span lengths ranging from 30 to 80 ft (9.14 to 24.38 m), and are subjected to H20 AASHTO truck loading; the maximum horizontal shear was determined to vary from 34.51 kips (153 kN) to 35.31 kips (157 kN).

For a concrete compressive strength of 3,000 psi (20.68 MPa), the ultimate static strength of the three series of connectors investigated (SH1, SH2, and SH3) was determined to be 70.1 kips (311 kN), 69.5 kips (309 kN), and 66.5 kips (296 kN), respectively. To relate the typical design conditions to the fatigue test results, the largest horizontal shear previously determined (35.31 kips (157 kN)) was expressed as a percentage of the ultimate static strength, (i.e., SH1: 50.4%, SH2: 51% and SH3: 53%).

From the regression analysis model, at 500,000 loading cycles (the AASHTO design criteria for low volume roads), the fatigue strength of the ASC was determined to be 69% of the ultimate static strength. This implies that the fatigue strength of the ASC is approximately 16% greater than the horizontal shear in the typical single span bridge previously described.

Since only 27 specimens were tested in this portion of the investigation, the results should be considered preliminary and only provide general trends on the fatigue strength and slip behavior. Several more series of specimens need to be tested to obtain more definite strengths and behavior relationships.

Use of ASC in Composite Beams

To obtain additional strength and behavior information on the ASC, three full-scale composite beam specimens (two static and one fatigue) and two full-scale two-beam specimens representing potential bridge systems were constructed. The ASC was used in all

five specimens. As was previously noted, this portion of the investigation is still in progress, thus only information on the two beam specimens (Specimens 4 and 5) is presented in this paper. Both of these specimens were 34 ft (10.36 m) in length.

Specimen 4, as shown in Figure 9 consisted of two W21 x 62's with their top flanges embedded in an 8 in. (205 mm) concrete slab. As may be seen in this figure, the only reinforcement in the slab was #5 bars placed every 15 in. (380 mm) through the 1 1/4 in. (30 mm) diameter holes which were torched in both beams. The reinforcing system in Specimen 4 is based on the Canadian steel-free deck research (Bakht, et al., 1998). A steel-free deck obtains its strength through an arching type behavior of the concrete slab with the beams acting as the supports and the reinforcing steel providing the lateral restraint (tension ties). The transverse reinforcement in Specimen 4 has a dual purpose; it acts as a tension tie between the beams, and it contributes to the strength of the ASC. Also illustrated in Figure 9 is the additional reinforcement at both ends of the specimens which is necessary for developing arching action near the transverse free edge. To obtain proper development of the transverse steel it was necessary to provide the hooks illustrated.

Specimen 5 shown in Figure 10 consisted of two W21 x 62's fully embedded in a concrete arch system which spans between the beams. This specimen is more directly related to the modified BISB (shown in Figure 3) in that it incorporates removing some of the concrete on the tension side of the specimen and using the ASC for composite action between the steel beams and concrete.

Summary and Conclusions

Based on the limited number of specimens tested in this investigation, the following observations and conclusions can be made:

1.) The strength of the ASC was determined to be primarily a function of shear hole area, amount of transverse reinforcement, number of shear holes, and the concrete compressive strength. A relationship (Equation 1) was developed for predicting the strength of the ASC.

2.) The ASC was determined to have adequate fatigue strength for use on low volume roads which are typically designed for 500,000 cycles of loading.

3.) As previously indicated, testing of the ASC in composite beams is currently in progress. Specimens tested to date have reached their ultimate capacity without any distress in the ASC.

4.) Modifications can be made to the existing BISB system that will result in more efficient use of the materials and make it possible to use the system in situations requiring longer span lengths. These modifications will not effect the ease of construction of the bridge system.

Acknowledgments

The research presented in this paper was funded by the Highway Research Board and the Highway Division, Iowa DOT, Ames, Iowa. The authors wish to thank numerous Iowa county engineers for their support, cooperation, and counsel and the several civil engineering graduate and undergraduate students who worked on this investigation. The opinions, findings, and conclusions expressed herein are those of the authors and not necessarily those of the Iowa DOT or the Iowa Highway Research Board.

References

Bakht, B., Mufti, A. A., and Jaeger, L. G. (1998). "Design Provisions for Steel-free Deck Slabs", Developments in Short and Medium Span Bridges '98. Limit States and LRFD Codes.

Leonhardt, E. F., Andra, H. P., Harre, W. (1987). "New Improved Shear Connector with High Fatigue Strength for Composite Structure", (Neues vorteilhaftes Verbundmittel fur stahlverbund - Tragwerke mit hoher Danerfestigkeit"), Beton-Und Stahlbetoubau, Vol. 12, pp. 325-331.

Oguejiofor, E. C., and Hosain, M. J. (1992). "Behavior of Perfobond Rib Shear Connectors in Composite Beams: Full Size Tests", Canadian Journal of Civil Engineering, Vol. 19, No. 2, pp. 224-235.

Roberts, W. S., and Heywood, R. J. (1994). "An Innovation to Increase the Competitiveness of Short Span Steel Concrete Composite Bridges", Proc., Developments in Short and Medium Span Bridge Engineering '94, Halifax, Nova Scotia, Canada, pp. 1161-1171.

Seiss, C. P., N. M. Newmark, I. M. Viest. (1952). "Small Scale Tests of Shear Connectors and Composite T-Beams", Studies of Slab and Beam Highway Bridges, Part III. University of Illinois Bulletin, Vol. 49, No. 45, Bulletin Series No. 396.

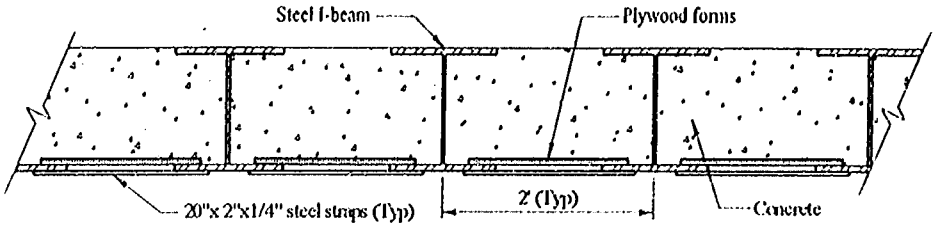


Figure 1. Beam-in-slab bridge system (1 in. = 25.4 mm).

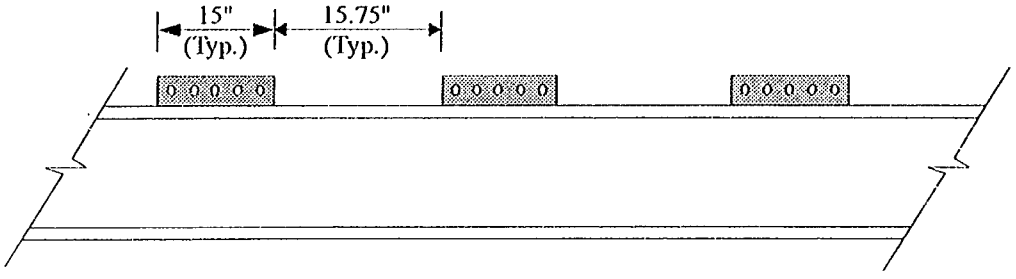


Figure 2. Perfobond ribs on top flange of steel beam (1 in. = 25.4 mm).

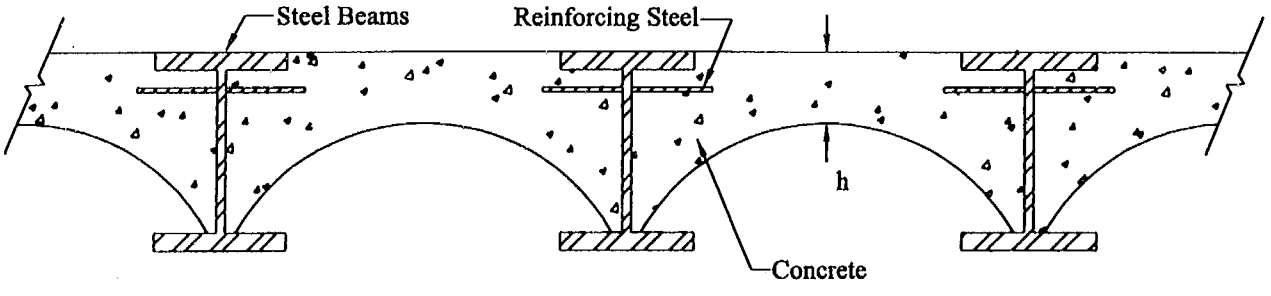


Figure 3. Modified beam-in-slab system (1 in. = 25.4 mm).

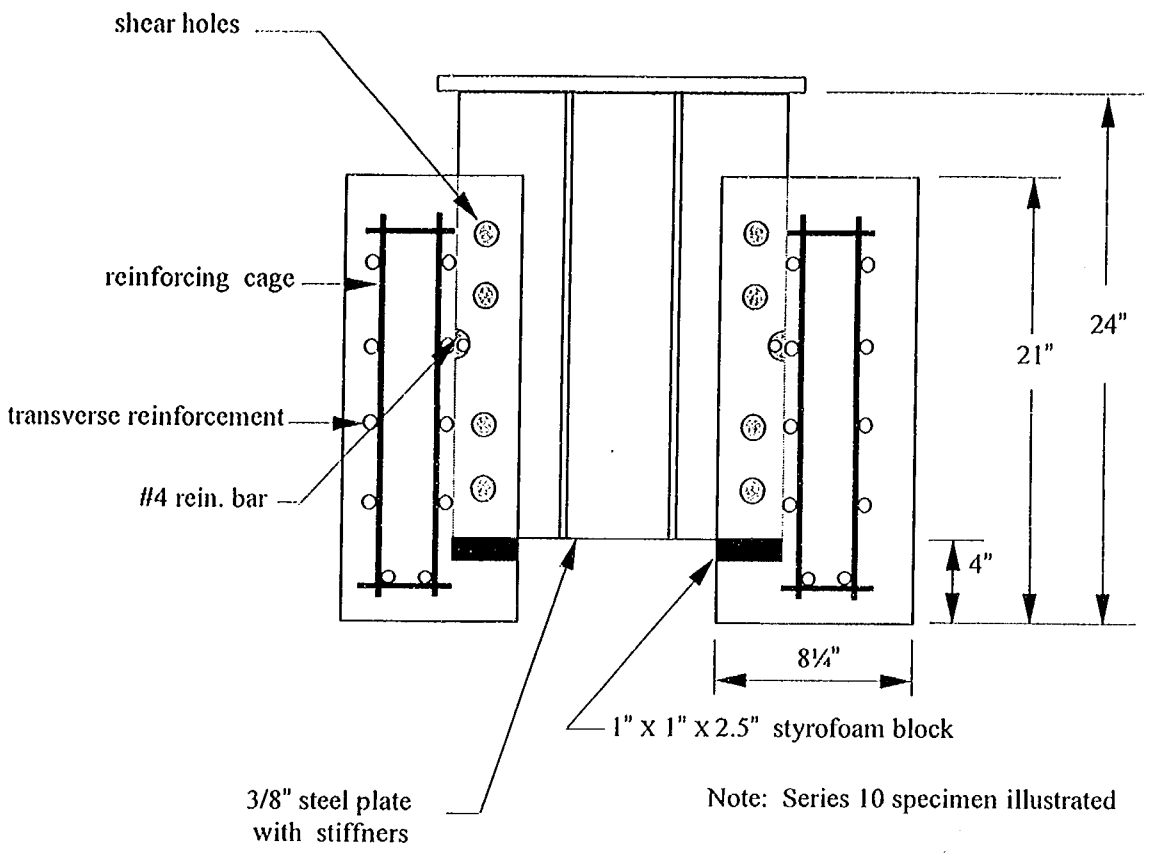
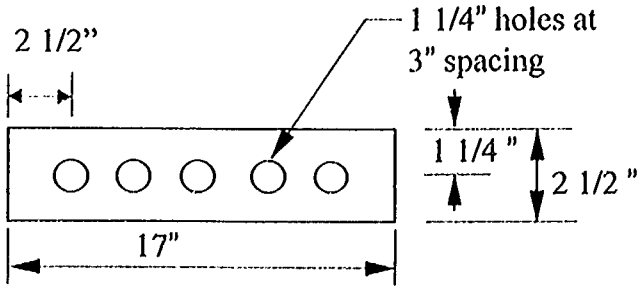
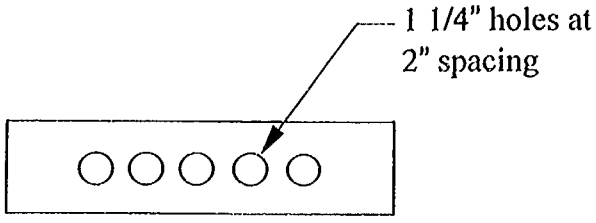


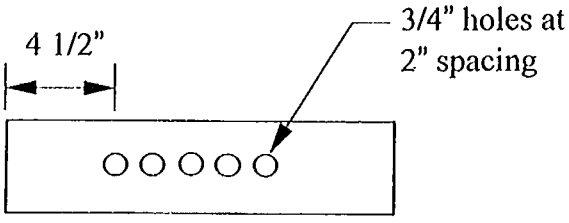
Figure 4. Details of push-out specimen (1 in. = 25.4 mm).



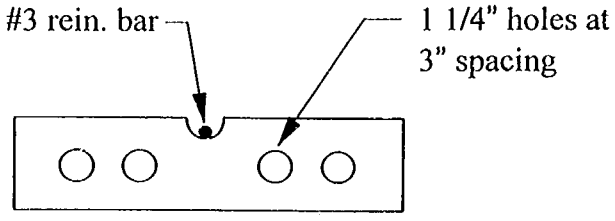
a.) Series 1



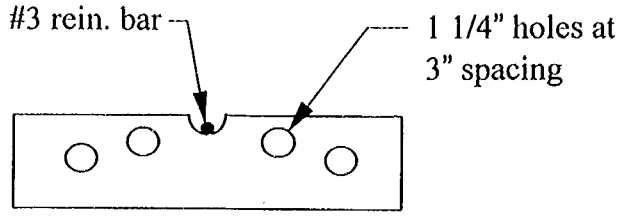
b.) Series 2



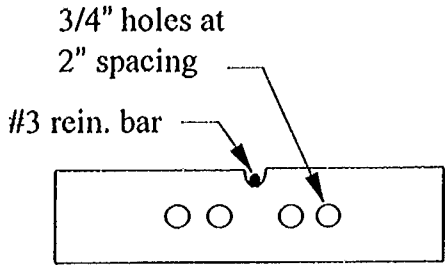
c.) Series 3



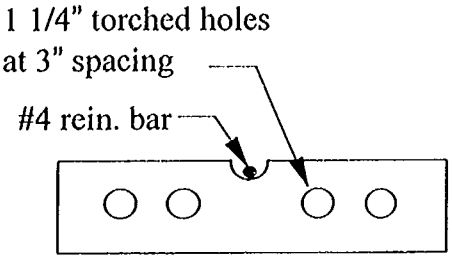
d.) Series 4



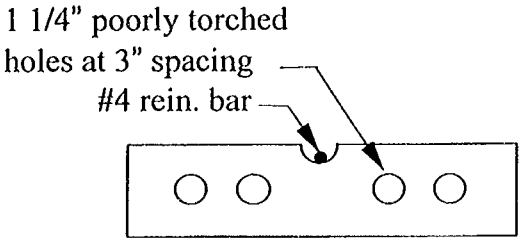
e.) Series 5



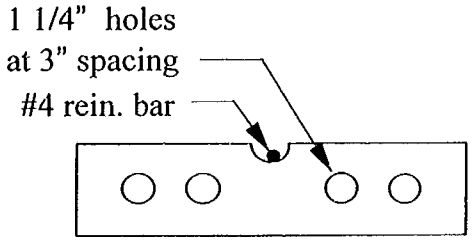
f.) Series 6



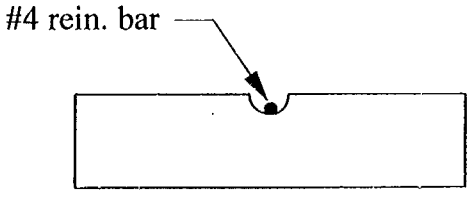
g.) Series 8



h.) Series 9



i.) Series 10



j.) Series 11

Figure 5. Details of hole arrangements used in push-out tests (1 in. = 25.4 mm).

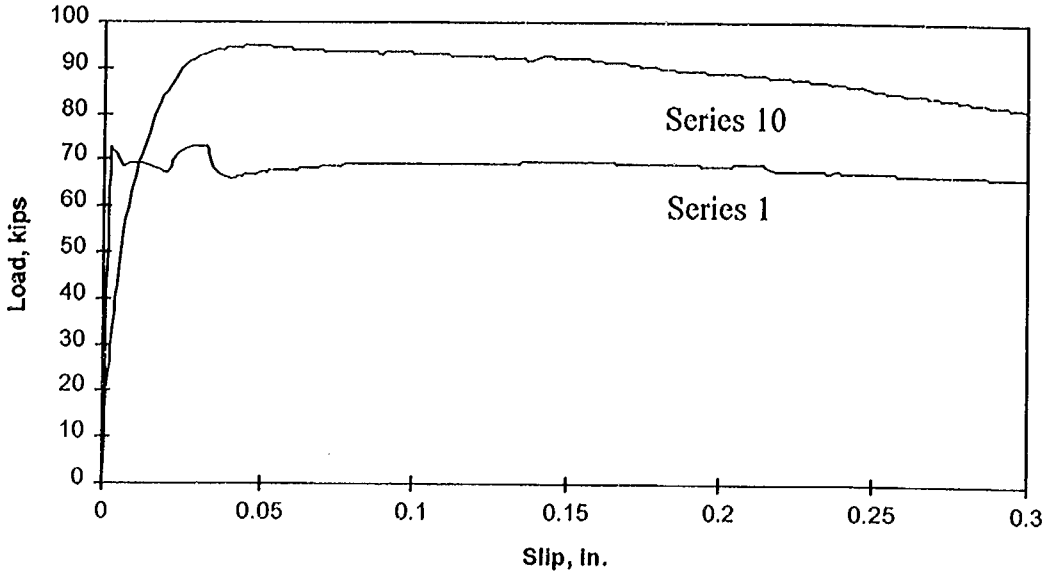


Figure. 6. Load-slip curves for Series 1 and 10
(1 in. = 25.4 mm; 1 kip = 4.45 kN).

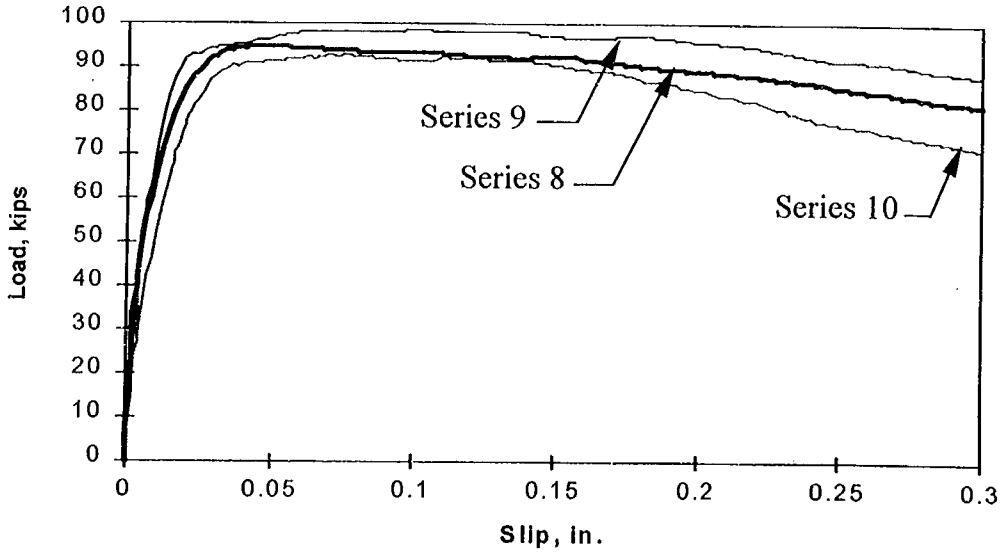


Figure 7. Load-slip curves for Series 8, 9, and 10
(1 in. = 25.4 mm; 1 kip = 4.45 kN).

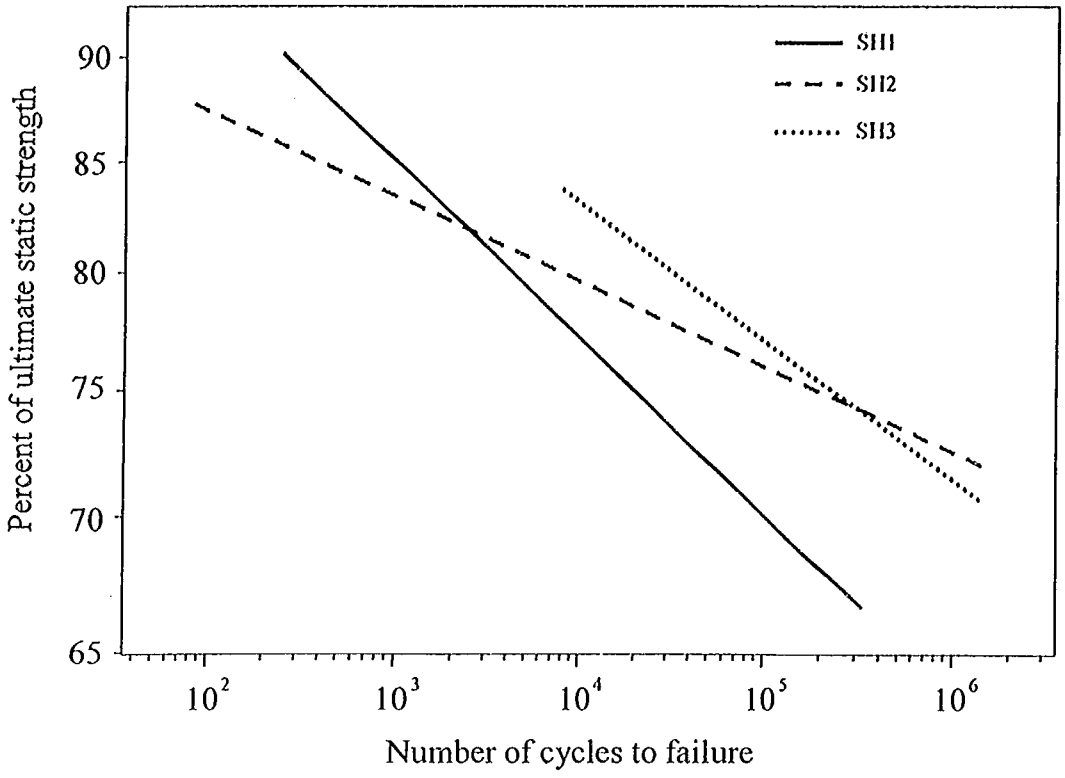
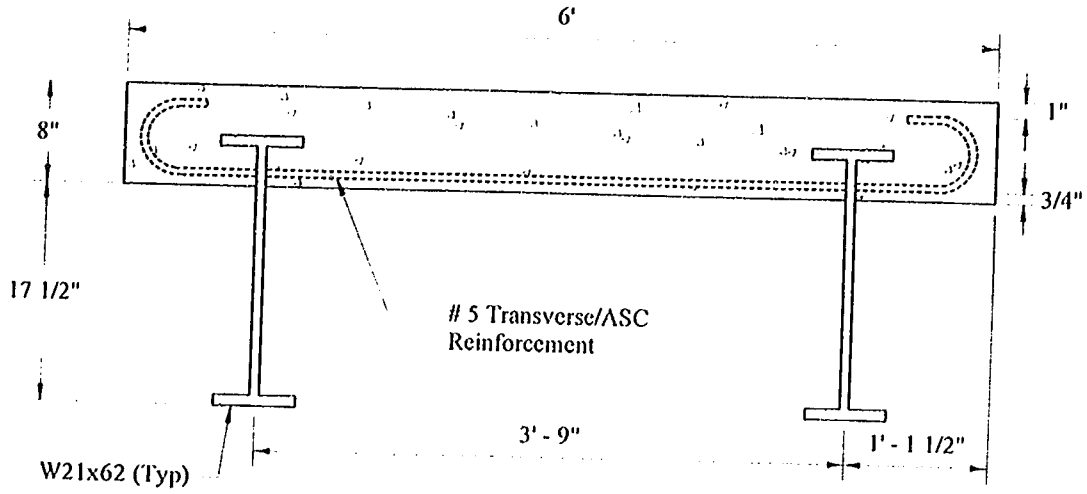
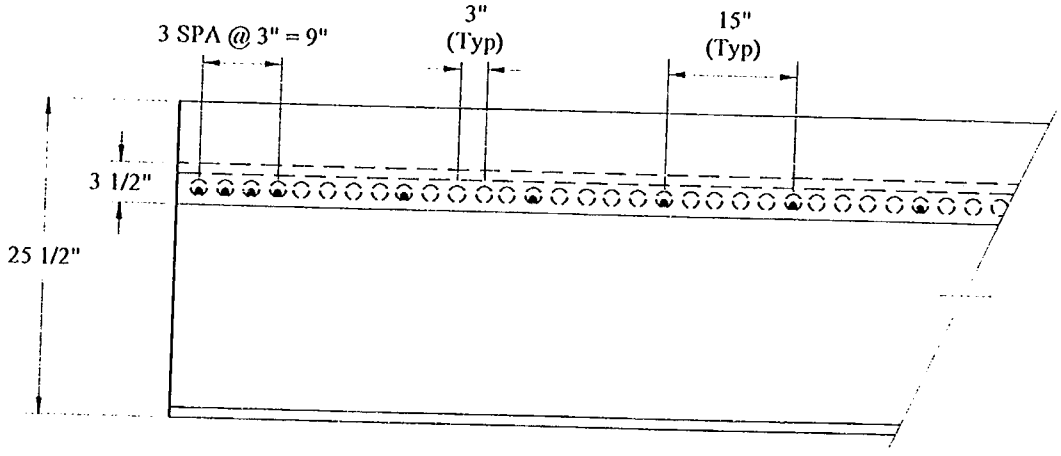


Figure 8. Composite S-N curves.

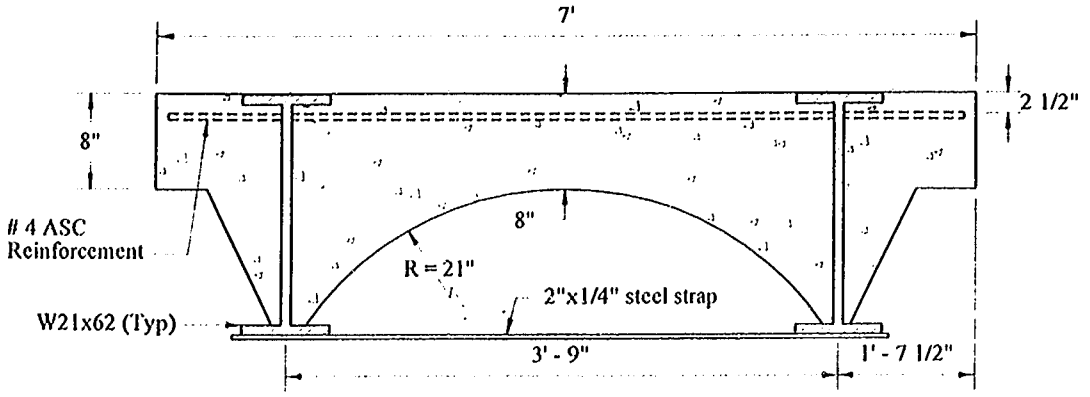


a. Cross-section view

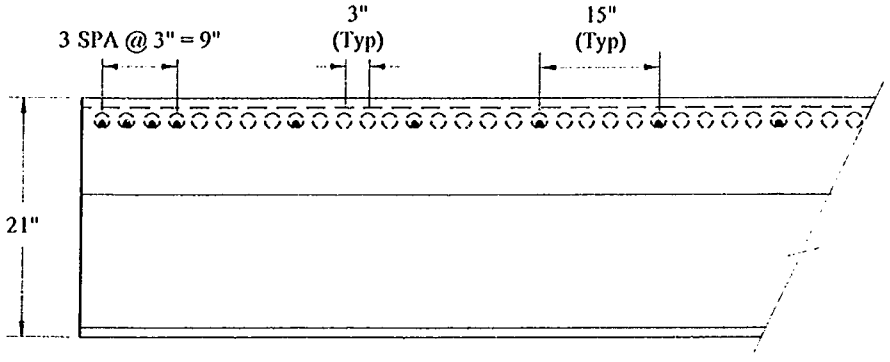


b. Side view

Figure 9. Details of Specimen 4 (1 in. = 25.4 mm; 1 ft = 305 mm).



a. Cross-section view



b. Side view

Figure 10. Details of Specimen 5 (1 in. = 25.4 mm; 1 ft = 305 mm).

MAINTENANCE OF BRIDGE AND REINFORCEMENT OF EXISTING DECK SLABS

Hiroshi Mitamura[1], Shizuo Kato[2], Shigeharu Onsen[3] and Shigeyuki Matsui[4]

Abstract

Inspection and bridge maintenance plays an important role in the safety and operation of an efficient transport system. Maintenance cost of bridges will be lowered and life cycles extended depending on suitable and early maintenance.

Hokkaido Development Bureau (HDB) is supporting about 3,000 bridges. HDB has been making guidelines for maintenance of bridges including inspection diagnosis repairs and accumulation of maintenance information for efficient operation of bridges. We aim at the next points.

1.Reason of damage
2.Effect of structure by damage
3.Repair and reinforcement

This paper will introduce these concepts and explain the reinforcement of existing deck slabs by the Steel Compsite Sandwich Method.

1. The Bridge Diagnosis

1-1 Introduction

In our country, road maintenance has proceeded actively in the days after the war, and many bridges have been built in the advanced economic growth period of 60's and 70's. Recently, the decaying of these bridges is causing troubles, and bridge maintenance is an urgent critical subject to contend with increase in the demand for traffic and to secure safe and smooth traffic.

At present, HDB manages about 3,000 bridges and works for securing of the safe and smooth traffic by the regular inspection. But then, The Bridge Diagnosis has made for the following points to carry out more effective maintenance.

1. To comprehend the function of the members which compose bridge.
2. To make clear the point which damage is easy to cause.
3. To turn over the damage which discovered by the inspection to the maintenance service responsibly.
4. To attempt to accumulate maintenance information and to use them effectively.

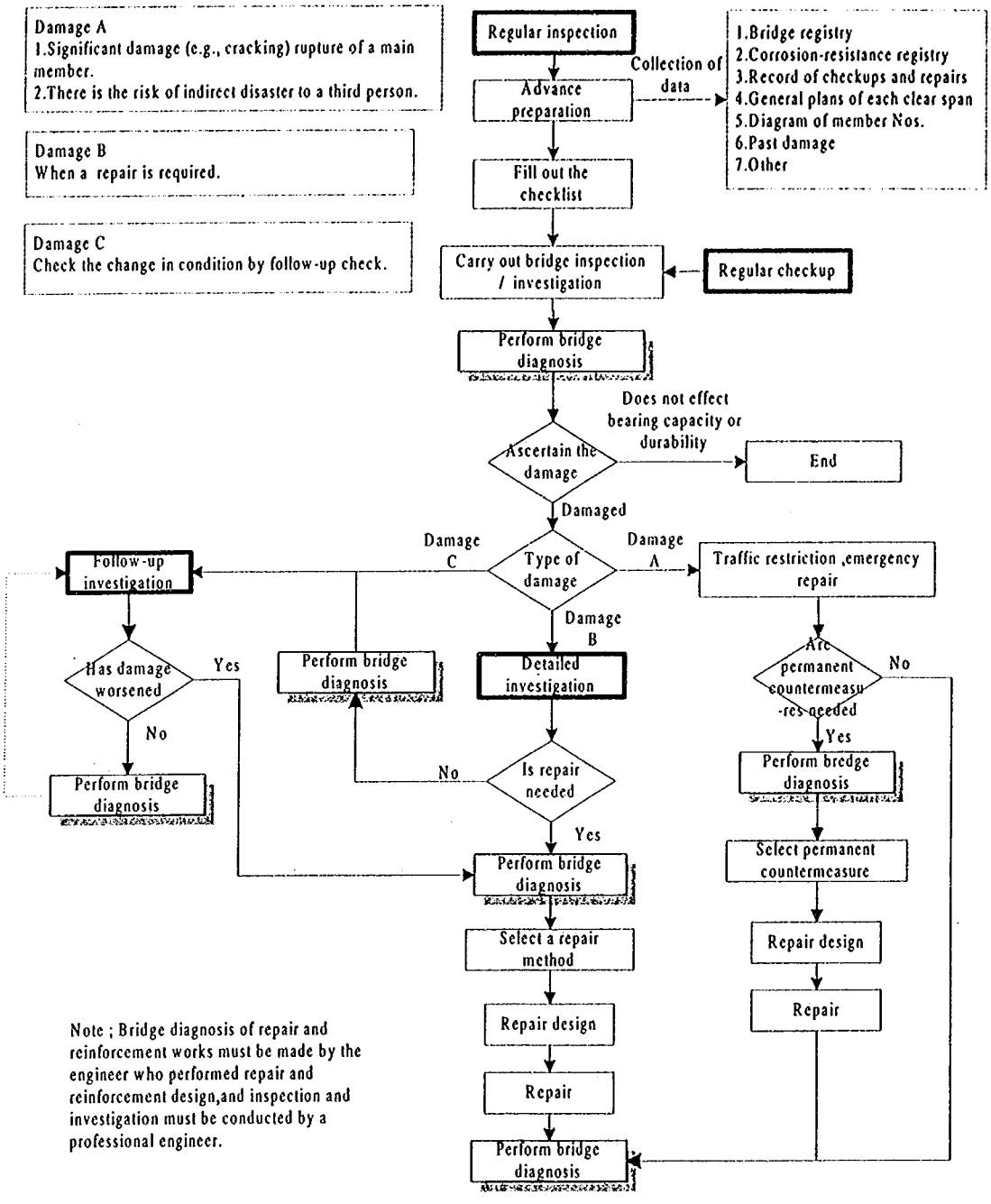
The following chapters describe the profile of the Bridge Diagnosis.

---

1)Civil Engineering Research Institute, Hokkaido Development Bureau
2)Bridge Engineering Department, Hokkaido Engineering consultants, Japan
3)Head of Engineering Division, Sho-Bond Corporation
4) Professor, Civil Engineering, Osaka University

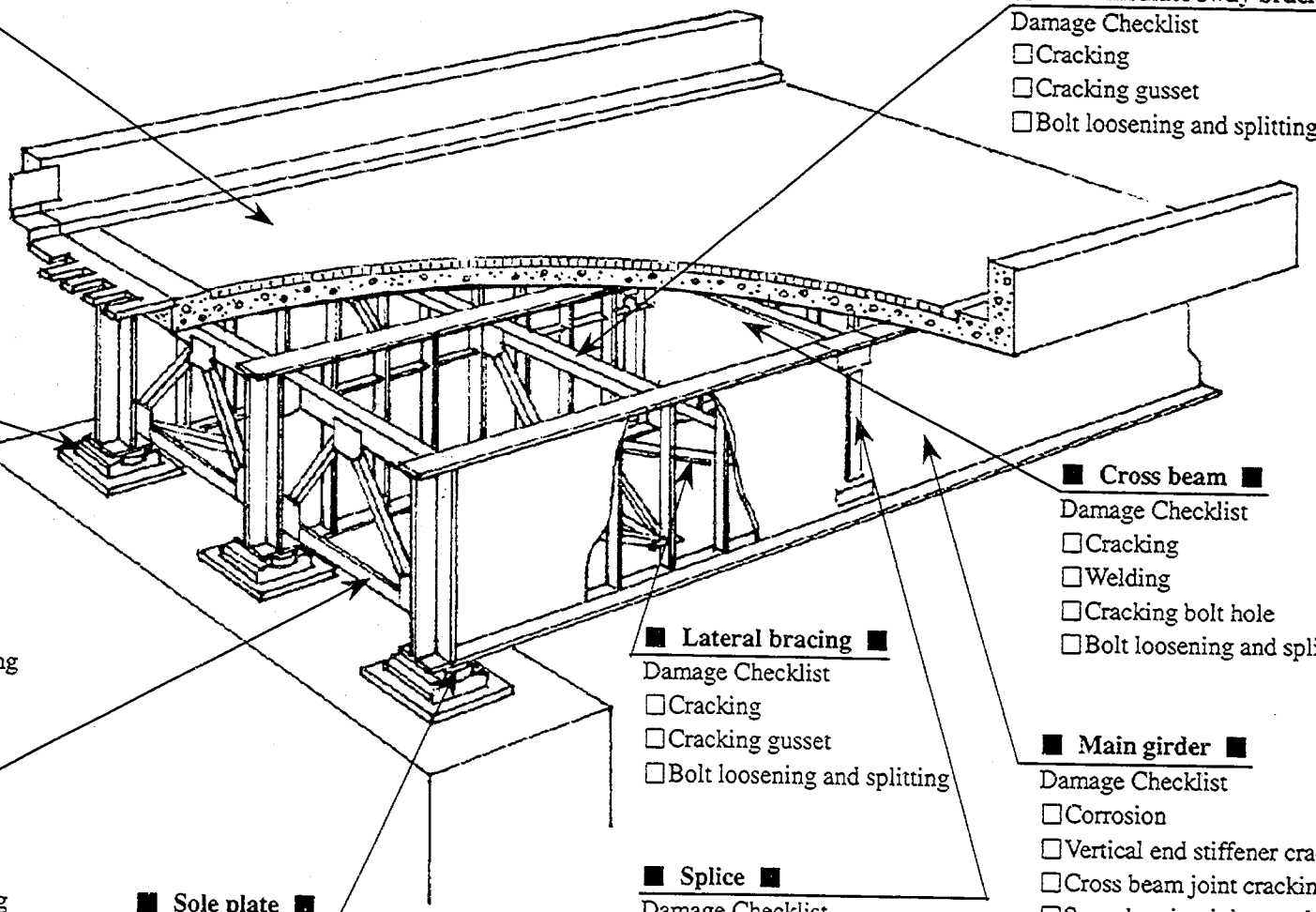
1-2 Flow of Inspection

The following flowchart, about bridge maintenance, shows the execution point which leads you to get to the way of repair and reinforcement from the inspection. The record of bridge diagnosis is made at every maintenance business, and they are collected and managed.



(Fig.1) Flow of inspection

Steel girder maintenance list



■ deck slab ■
Damage Checklist
Above deck slab
☐Pavement cracking
☐Curb cracking
☐Road surface sinking
Below deck slab
☐Cracking
☐Leaking
☐Concrete flaking
☐Steel reinforcing exposure

■ Bearing ■
Damage Checklist
☐Corrosion
☐Cracking and splitting
☐Loosening set bolts
☐Splitting set bolts
☐Loosening anchor bolts
☐Deforming anchor bolts
☐Bearing foundation cracking

■ End sway bracing ■
Damage Checklist
☐Corrosion
☐Cracking
☐Bolt loosening and splitting

■ Sole plate ■
Damage Checklist
☐Cracking
☐Splitting

■ Intermediate sway bracing ■
Damage Checklist
☐Cracking
☐Cracking gusset
☐Bolt loosening and splitting

■ Lateral bracing ■
Damage Checklist
☐Cracking
☐Cracking gusset
☐Bolt loosening and splitting

■ Splice ■
Damage Checklist
☐Corrosion
☐Loosening bolts
☐Splitting bolts

■ Cross beam ■
Damage Checklist
☐Cracking
☐Welding
☐Cracking bolt hole
☐Bolt loosening and splitting

■ Main girder ■
Damage Checklist
☐Corrosion
☐Vertical end stiffener cracking
☐Cross beam joint cracking
☐Sway bracing joint cracking
☐Main girder top edge cracking
☐Gerber hinge cracking

1-3 Inspection

The following are general inspection and examination guidelines

1. Inspection
   1) General Inspection ; Bi-annual, Conducted by general road inspectors on foot.
   2) Regular Inspection ; Every 2 years using scaffolding.
   3) Specified Inspection ; Continued inspections after repairing.
   4) Inspection details ; Site measurements for repair procedure and identification and cause of fault.

2. Inspector Requirement

   1) Specialized engineer
      All inspections and results to be certified by a qualified (Consulting engineer) or person with suitable field experience.

   2) Inspector
      · Minimum 5 years experience for university graduates.
      · Minimum 8 years experience for technical college graduates.
      · Minimum 11 years experience for high school graduates.

   3) Assistants, Traffic inspector (Flagman)

1-4 Bridge Inspection

Before examining the inspection technique of bridge, we studied the damage that is easy to cause in the bridge member and factors of damage, and we collected information in past cases. The result of the study helps us to define the view of facing the attention point in the inspection, the investigation of what causes the damage, the repair and the reinforcement. We have made several 'Inspection List' based on the view for inspector's reference each correspond each type of bridges. The example of 'Inspection List' for steel girder is shown in the next page.

1-5 The Judgement for the Result of Inspection

It is possible that bridge is maintained under the wholesome original condition for dealing with damage while they are slight, thus it is important to take action neatly not to be too late. That is to say, we should consider that an enormous countermeasure such as reconstruction or re-erection of the floor slab becomes necessary when damage is left and go for the worse though it is possible to maintain and repair for saving time and cost while damage is slight. The fundamental vision for judging damage in these guidelines for operation is shown in the following.

1. As for the damage, which directly influences the bearing capacity of bridge, traffic restriction is enforced, and it should be repaired and reinforced urgently.

- crack and deformation in the weld of the main member.
- The settlement of support.
- The cave-in of the deck slab. Etc.

2. The damage which is afraid to be traffic hindrance and to cause incidental disaster should be repaired after being administered the emergency measure, and it does not directly influence the bearing capacity of bridge.
- Deforming or breaking of the protection fence.
- Breaking of some bolts.

3. The stress of the bridge should be measured when the floor slab of the composite girder must be repaired. If there is no problem in the composite behavior between the floor slab and the main girder, there is no necessity of an enormous repair such as reconstruct, and examines a slight repair.

4. Recently, calcium chloride, and so on, is sprayed as an anti-freezing admixture of the road surface during winter. From now on, it is quite likely to increase the damage due to salt damage that can be thought about the influence of theirs. When the damage due to salt damage causes, it is recognized that restoration to the original bearing capacity is difficult, we cannot say that serious damage must not be given to structure, thus the damage must be taken account in particular.

5. The following item must be taken into consideration when an urgent degree for repair or reinforcement is judged.

   1). The bridge located in crowding the area of population.
   2). When there is no detour.
   3). When mixing the rate of heavy traffic is high.
   4). In the case of over-bridge.
   5). The specified the critical line.

1-5 Ending

This guideline for maintenance was made to be the effective materials to carry out repair and reinforcement efficiently and effectively and to get the early detection of damage by the bridge inspection.

From now on, this execution point will be improved with accumulation of inspection information so that maintenance may become more rational and efficient.

Moreover, we will progress the project of constructing the comprehensive bridge management system (BMS) with using this inspection information effectively and taking account of studies of "Bridge Health Measuring System" and "Bearing Capacity Verifying System".

2. The Steel Reinforcing Sandwich Method by the Steel Composite Sandwich

2-1 Introduction

The reinforced deck slab is loaded with unit load per travel wheel, and is the member which damage is easy to cause in most by the influence of storm sewage, freezing and thawing, and so on. Then it has been repaired and reinforced in many bridges until now. The main process of repair and reinforcement until now was the Steel Plate Adhering Method, CFRP, the Top Surface Thickening Method, and so on. When damage is remarkable, complete reconstruction is done. However, the working period of Deck Slab Reconstructing Method is too long. Necessarily there are some case of that floor slab is difficult to be scrapped, so that Deck Slab Reconstructing Method can't be adopted with a railroad viaduct and so on.

We devised "Steel Composite Sandwich" which aimed at the effective use of the damaged existing deck slab in place of Deck Slab Reconstructing Method. This part will introduce the result of experiments.

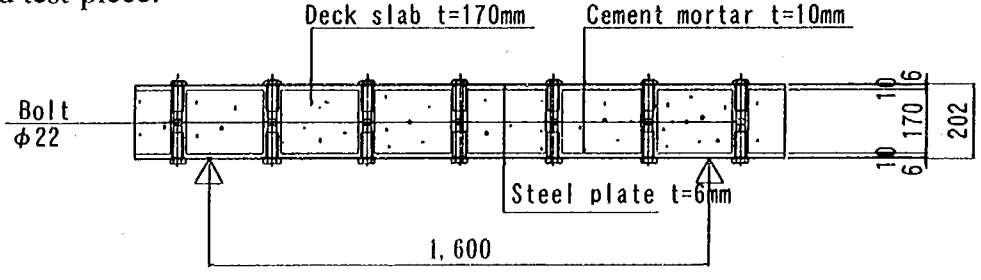
2-2 Abstract of Experiment

2-2-1 Objective of Experiment

As for the steel plate sandwich panel which filled inside with the concrete, steel plate is arranged in top and bottom and is connected by the bolt or the stud bolt, many experiments are carried out, and results of theirs confirm that the panel is excellent in the bearing capacity and toughness. However, there is no instance that sorely damaged existing reinforced floor slab was reinforced by the steel sandwich. For this reason an experiment was carried out for the purpose of verifying whether the Steel Composite Sandwich Floor Slab could be applied to the damaged floor slab.

2-2-2 How to make test-piece

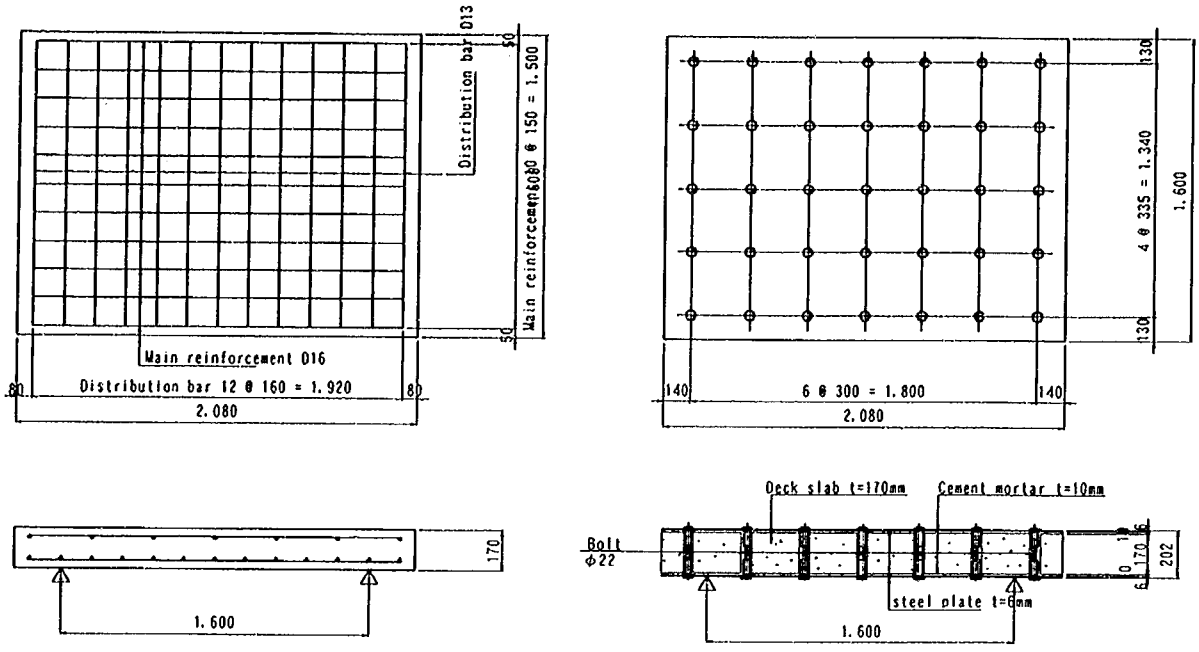
The basement of test-piece, which was the sorely damaged piece of existing the deck slab, was brought down, and steel plates (t= 6mm) were installed in its top and bottom securing the clearance of 10mm. Next, bolts in the spacing of the length and breadth fastened it about 300 mm. Finally non-contraction mortar was poured into the clearance of 10 mm. A test-piece which has the same thickness, arrangement of reinforcing bar and concrete strength as the sorely damaged existing deck slab was made to compare with the reinforced test-piece.



(Fig.2) Steel Composite Sandwich Deck Slab

2-2-3 Experiment methods

Each test-piece was carried out the load test by using an oil pressure jack and load cell, and the deformation and the strain of reinforcement due to the loading were measured. The effective span for floor slab is 1.6m, the loading point is placed to the center of the test-piece (loading plate 20× 20cm), and oil pressure jack used for this experiment has capacity of 2000kN.



Test-piece 1: non-reinforced

Test-piece 2: reinforced

(fig.3) Diagram of test-pieces

2-3 Result of Experiment and Consideration

1. In the case of test-piece No.1 (non-reinforced), the main reinforcement yielded when the load reached 200kN, and the test-piece was destroyed in the figure of punching shear when the load reached 350kN.

2. In the case of test-piece No.2 (reinforced), the stripping of the steel plate and the non-contract mortar appeared when the load reached near 350kN, and steel plate yielded when the load reached 840kN. Displacement increased in connection with the increase of the load after the yield. The yielding of the steel plate expand to overall width when the load reached 1250kN, and displacement increased with tapering load.

   The result corresponds to the yield moment (1210kN) asked by the design of section of the armored concrete which substituted reinforcing bar for the steel plate overall width (1.6m). Moreover, by the FEM solution, the yield load of the steel plate is 760kN, displacement is 9.6mm, and it almost corresponds to the result of the experiment.

3. The load of test-piece No.2 is about 950kN when the displacement is 17 mm, and the

value corresponds to test-piece No.1 (at the time of the shearing destruction, P=350kN).

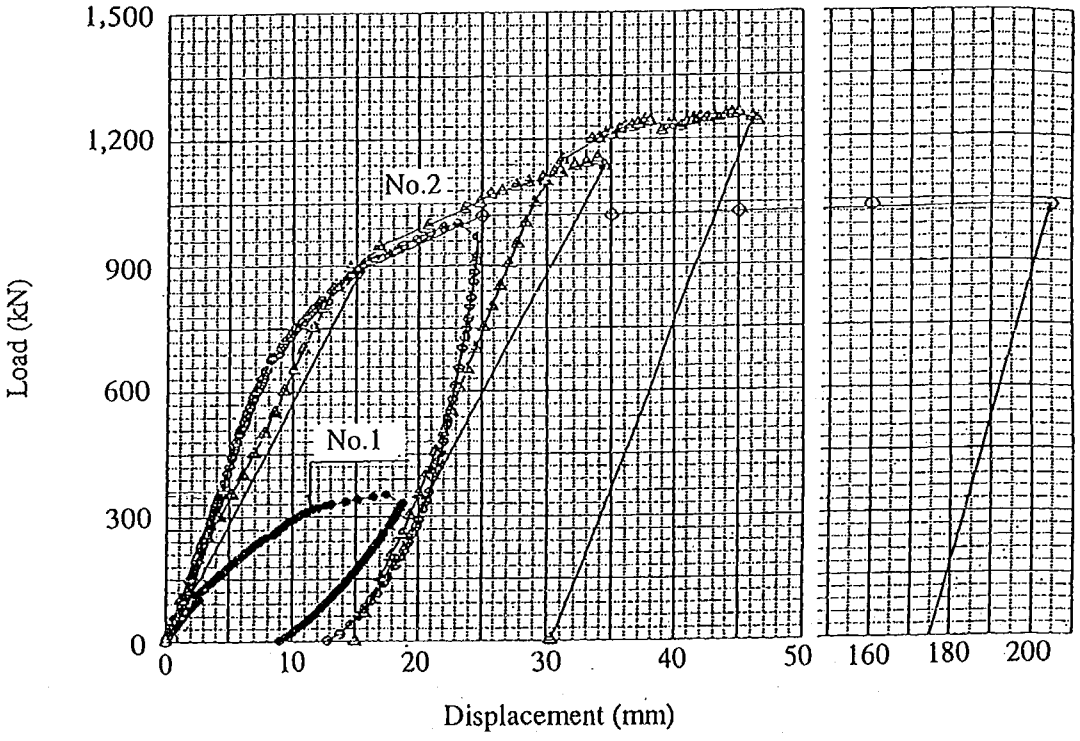
4. Remaining displacement was 4.5mm when it was unloaded because displacement only increased from about the load is 1250kN. Displacement increased holding the load of 1030kN～1050kN when more loaded, then experiment was finished at displacement reached 200 mm.

   It confirmed that the yield strength has been kept about 1000kN although the displacement has been increased even if the steel plate is under complete yielding condition.

5. As for the destruction condition of test-piece No.2, cracks in the vertical direction appeared near the center of the effective span, and cracks in a slant or a level direction appeared with increasing displacement.

6. As a result that top surface steel plate buckled, concrete around loading plate was destroyed by the pressure.

7. Break of bolts did not appear.



(flg.4) Load - Displacement curve

2-4 Summary

When the damaged existing reinforced deck slab is reinforced by the steel sandwich, we can anticipate three times and more of the bearing capacity compared with the non-reinforced floor slab, and smaller displacement under the load of usual, too.

In addition, it confirmed that the bearing capacity of the reinforced slab keeps high value even after the yielding of the steel plate.

3. Application of Steel Composite Sandwich Deck Slab to the Actual Bridge

3-1 Introduction

It confirmed that bearing capacity should be increased by using the reinforcement of The Steel Composite Sandwich to the damaged existing deck slab due to the experiment. This part will introduce the bridge that reinforced by The Steel Composition Sandwich in this part.

3-2 Applicable Bridge

The bridge that reinforced by this method is prestrssed concrete T-Girder Bridge. This bridge decayed sorely, and there are many penetration cracks from the top surface. The information about particular investigation made clear that the decline of the bearing capacity of the deck slab was remarkable. Therefore, the desk slab was reinforced with the aim of the improvement of the bearing capacity of the deck slab in Steel Composition Sandwich Method.

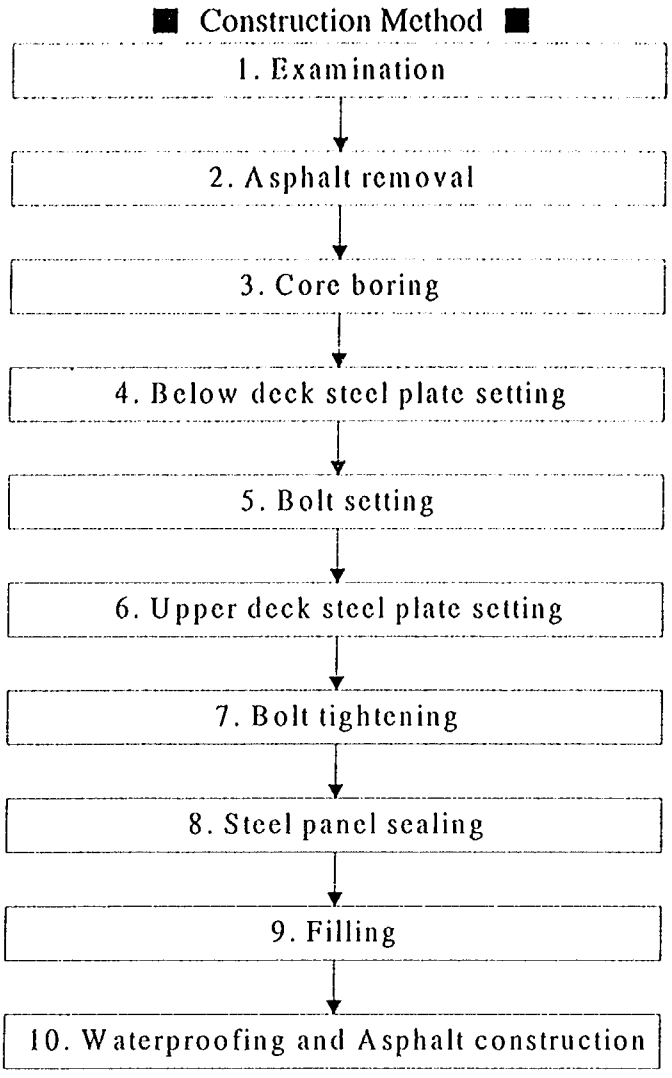
3-3 Design

Thickness of reinforcing the steel plate decided 6 mm allowing for the fatigue and the corrosion of the slab, an accidental deformation at work and marketability. The high tensile bolt M22 was chosen as a connection bolt for fastening both steel plates on top and bottom with installing axial load, and spacing was arranged by less than 300-350mm, in view of result of experiment. It is likely that there is no problem even if bolt spacing is enlarged in practical use when the load which influences the pavement through the deformation of the steel plate on the top surface and the bearing capacity of the deck slab are taken account for. There should be examine about it.

The result of the experiment, described in part 2, shows that the stress which occurred when loaded corresponded with the result of design of section of the armored concrete which substituted a reinforcement for the bottom floor slab. Therefore, stress was calculated in the armored concrete section.

3-4 The Abstract of Work

The abstract of the work is shown in the following.

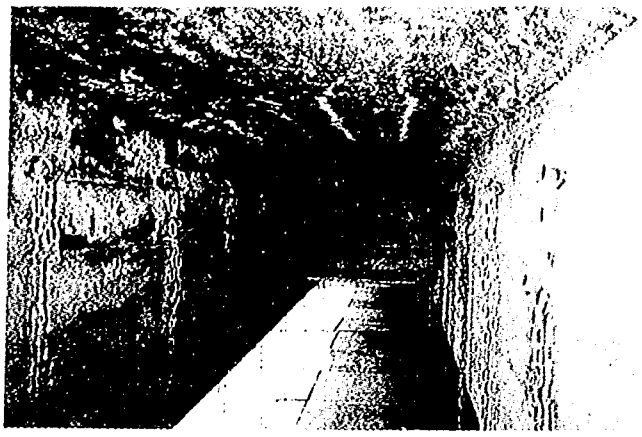


3-5 Ending

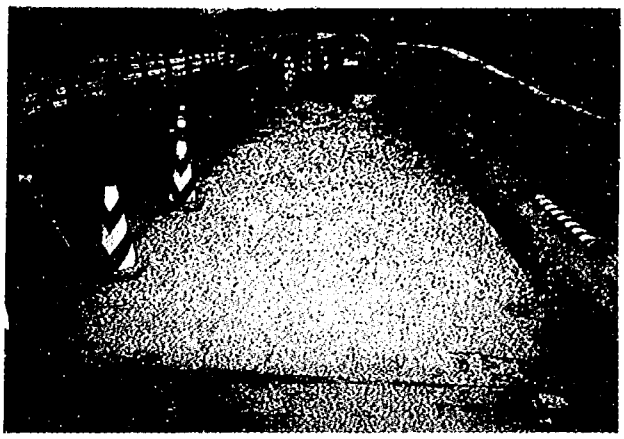
This report has introduced the construction steps in performing The Steel Reinforcing Sandwich Method to increase the load capacity of a damaged deck slab without need of removal. The highlighted bridge was an actual bridge example where the above construction methods were performed. Compared to the standard technique of removing the deck, this new technique reduces the construction time and longevity of materials.

In the future, we plan to advance the installation technique to further reduce the construction period as well as continue out inspection program.

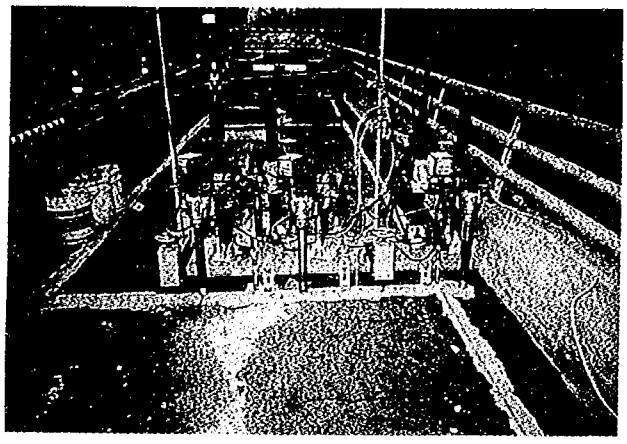
■ Below deck slab (Pre construction) ■



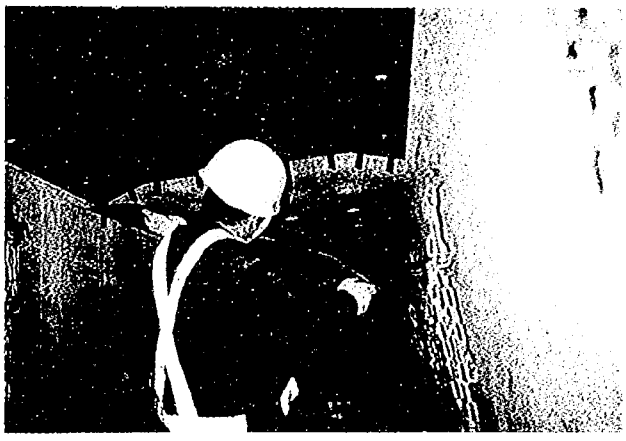
■ Above deck slab (Pre construction. Final asphlt removal) ■



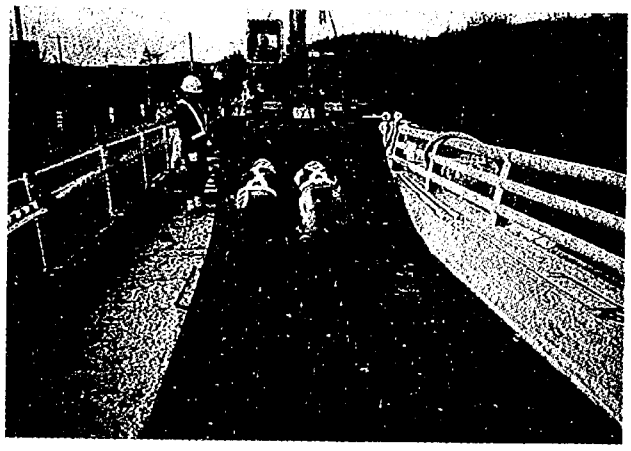
■ Core boring ■



■ Below deck steel plate setting ■



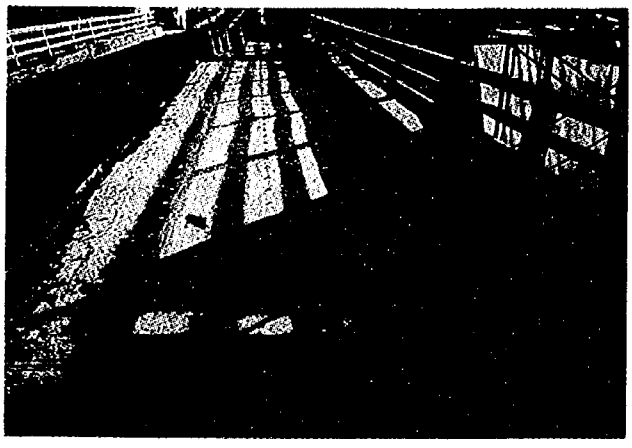
■ Upper deck steel plate setting ■



■ Bolt tightening ■



■ Above deck slab (Final construction) ■



■ Below deck slab (Final construction) ■



SESSION 11: CLOSING SESSION

SESSION 11: CLOSING SESSION

Remarks: James D.Cooper (Chairman for the U.S. side)

Closing Remarks: Kazuhiro Nishikawa (Chairman for the Japan side)

Workshop Program

PROGRAM SCHEDULE

15th U.S.-JAPAN

BRIDGE ENGINEERING WORKSHOP

November 9 and 10, 1999
Tsukuba City, Japan

Public Works Research Institute

15th U.S.-JAPAN BRIDGE ENGINEERING WORKSHOP
PROGRAM SCHEDULE

November 9 and 10, 1999
Tsukuba City, Japan

Tuesday, November 9, 1999 Place: Conference Room (8F) PWRI

SESSION 1: OPENING SESSION 9:00 - 9:15

(Co-Chairmen: Kazuhiro Nishikawa, James D. Cooper)

Welcome Remarks: Tomomitsu Fujii (Director General, PWRI)
Remarks: James D.Cooper (Chairman for the U.S. Side)
Remarks: Kazuhiro Nishikawa (Chairman for the Japan Side)

SESSION 2: EARTHQUAKE REPORTS 9:15 - 11:30

(Co-Chairmen: Masahiko Yasuda, Manos Maragakis)

(1) James D. Cooper, Hamid Ghasemi, Phillip Yen, Roy Imbsen, Saad El-Azazy(9:15 - 9:27)
"The Kocaeli Earthquake Investigation Summary"

(2) Michio Okahara (9:27 - 9:39)
"Turkey Earthquake" (presentation only)

(3) Roy A. Imbsen
"Damage to Transportation Facilities in the Recent August 17, 1999 Kocaeli Earthquake in Turkey"

(4) John B. Mander (9:39 - 9:51)
"The Turkey Earthquake – August 17,1999 Damage to the Transportation Infrastructure"

(5) Shigeki Unjoh (9:51 - 10:11)
"Taiwan Earthquake" (presentation only)

(6) Ian Buckle and Jenn-Shin Hwang (10:11 - 10:31)
"Bridge Performance in the 921 Earthquake, CHI-CHI, TAIWAN"

DISCUSSION (10:31 - 11:30)

PHOTOGRAPH *(Entrance of PWRI Main Building)* 11:30 - 11:45

LUNCH *(Conference Room, 1F)* 11:45 - 12:45

SESSION 3: SEISMIC ISSUES (1) 12:45 - 14:00

(Co-Chairmen: Junichi Hoshikuma, Phil Yen)

(1) Anastasios G. Vlassis, Emmanuel Manos Maragakis and Mehdi Saiid Saiidi (12:45 - 12:57)
"An Update on Analytical and Experimental Research on Bridge Restrainers"

(2) Motoaki Tanaka, Yuji Sato and Hideaki Kasabou (12:57 - 13:09)
"A Static Three Dimensional Elastic-Plastic Analysis of Steel Frame Bridge Piers"

(3) Michel Bruneau and Julia Marson (13:09 - 13:21)
"Cyclic Testing of Composite Concrete-Filled Circular Tubes and Foundation Detail"

(4) Tatsumasa Takaku, Yuhshi Fukumoto, Tetsuhiko Aoki, Takashi Okamoto, Tatsuo Kurokawa and Hiromitsu Morishita (13:21 - 13:33)
"Experimental Study on Strength and Ductility of One-Story and Two-Story Rigid Frame Steel Piers of Highway Bridges"

(5) Cris D. Subrizi (13:33 - 13:45)
"Seismic Resistant Design of the Rio Tempisque Bridge"

DISCUSSION (13:45 - 14:00)

COFFEE BREAK 14:00 - 14:15

SESSION 4: SEISMIC ISSUES (2) 14:15 - 15:45

(Co-Chairmen: Jiro Fukui, David Beal)

(1) Sabanayagam Thevanayagam (14:15 - 14:27)
"Liquefaction and Shear Wave Velocity Characteristics of Silty/Gravely Soils - Implications for Bridge Foundations"

(2) Yan Xiao, J.B. Mander, H.Wu and G. Martin (14:27 - 14:39)
"Experimental Study on Seismic Behavior of Bridge Pile-to-Pile Cap Connections"

(3) Kenji Ikeda, Hiroshi Mitamura, Norimitsu Kishi and Noriyoshi Murakami (14:39 - 14:51)

"A Proposal of Aseismic Strengthening of Wall-type RC Bridge Pier, with Minimum Impact on Its Foundation"

(4) Jamshid Ghaboussi (14:51 - 15:03)
"Advanced Computational Methods in Bridge Engineering"

(5) Susumu Fukunaga (15:03 - 15:15)
"Study on the Stability of the Akashi Kaikyo Bridge for Residual Displacement of Tower Foundation by Large-Scale Earthquake"

(6) James H. Long, Thomas E. Hunt and Boris W. Leoro (15:15 - 15:27)
"Micropiles for Seismic Retrofits"

DISCUSSION (15:27 - 15:45)

COFFEE BREAK 15:45 - 16:00

SESSION 5: SEISMIC ISSUES (3) 16:00 - 17:30

(Co-Chairmen: Yukio Adachi, Yan Xiao)

(1) Martha Sartain, Richard Groff, Craig Shike and Mark Hirota (16:00 - 16:12)
"Assessing Oregon's Seismic Risk"

(2) Keiichi Tamura, Yoshihiro Nakao and Shojiro Kataoka (16:12 - 16:24)
"Developing Seismic Design Ground Motions for Super Long-Span Bridges"

(3) Gokhan Pekcan, W. Phillip Yen and Ian M. Friedland (16:24 - 16:36)
"Seismic Vulnerability Study of Highway Systems: TEA-21 Research Project"

(4) Kiyoshi Miyawaki, Taiichi Kagayama and Fuminobu Okunishi (16:36 - 16:48)
"The System of Real-time Earthquake Damage Estimation in Hanshin Expressway"

(5) H. Ghasemi (Presented by W. Phillip Yen) (16:48 - 17:00)
"The Newly Developed AASHTO Guide Specifications for Seismic Isolation Design"

(6) Michael A. Riley, Fahim Sadek and Bijan Mohraz (17:00 - 17:12)
"Guidelines for Testing Passive Energy Dissipation Devices"

DISCUSSION (17:12 - 17:30)

RECEPTION AT GRAND SHINONOME 19:00 - 21:00
(HOSTED BY JAPAN SIDE)

Wednesday, November 10, 1999

Place: Conference Room (8F) PWRI

SESSION 6: CONCRETE

9:00 - 10:15

(Co-Chairmen: Hirotaka Kawano, Wayne Klaiber)

(1) Yoshiki Tanaka, Hirotaka Kawano, Hiroshi Watanabe and Masahiro Suzuki (9:00 - 9:12)
"Bending Behavior of Prestressed Concrete Girders Damaged by Salt Attack"

(2) Khalid M. Mosalam, Svetlana Khaykina and Clay Naito (9:12 - 9:24)
"Performance of Reinforced Concrete Bridge Joints Subjected to Bi-Directional Loading"

(3) Masaru Terada and Seishi Meiarashi (9:24 - 9:36)
"Development of Electric Anticorrosion Methods for Newly Constructed Concrete Structures"

(4) Yash Paul Virmani (9:36 - 9:48)
"Corrosion Control of Concrete Bridges"

(5) Naoshige Nomura, Yoshihiro Tanaka and Takeyuki Yokooka (9:48 - 10:00)
"Durability and Structural Safety Evaluation of RC Gerber's Bridge Servicing for More Than 60 Years"

DISCUSSION (10:00 - 10:15)

COFFEE BREAK 10:15 - 10:30

SESSION 7: SEISMIC ISSUES (4)

10:30 - 12:00

(Co-Chairmen: Keiichi Tamura, Hamid Ghasemi)

(1) Shigeki Unjoh, Toru Terayama and Junichi Hoshikuma (10:30 - 10:42)
"Draft Manual of Seismic Retrofit Design for Single-Type Reinforced Concrete Columns Using Carbon Fiber Sheets"

(2) David H. Sanders, M. Saiidi Saiidi, Faramarz Gordaninejad, Frank Martinovic and Brett McElhaney (10:42 - 10:54)
"FRP Composites for Seismic Retrofitting of Non-Prismatic Reinforced Concrete Bridge Columns"

(3) Koji Osada, Yoshinori Igase, Takahiro Yamaguchi and Shoji Ikeda (10:54 - 11:06)
"Size Effect in Shear Behavior of Reinforced Concrete Piers Strengthened with Carbon Fiber Sheets"

(4) Yukio Adachi, Shigeki Unjoh and Kazuhiro Nagaya (11:06 - 11:18)
"Seismic Retrofit Methods of Cap Beam of Two-Column Bents"

(5) Thomas E. Sardo (11:18 - 11:30)
"Application of Fiber Reinforced Polymers (FRP) for Seismic Retrofit of California Bridges"

(6) Jun-ichi Hoshikuma and M. J. Nigel Priestley (11:30 - 11:42)
"Seismic Behavior of Circular Hollow Columns without Inside Reinforcement"

DISCUSSION (11:42 - 12:00)

LUNCH *(Conference Room, 1F)* 12:00 - 13:00

SESSION 8: ADVANCED MATERIALS 13:00 - 14:00

(Co-Chairmen: Shigeki Unjoh, David Sanders)

(1) Itaru Nishizaki, Takeshi Kishima and Seishi Meiarashi (13:00 - 13:12)
"Safety Factor and Calculation Method of FRP for Structural Material of Bridge"

(2) Issam E. Harik and P. Alagusundaramoorthy (13:12 - 13:24)
"Development, Testing and Deployment of FRP Structures"

(3) Kenji Suzukawa, Akeo Hattori, Akira Kobayashi and Tokitaro Hoshijima (13:24 - 13:36)
"The Effect of Reinforcement for Bridge Superstructures with Carbon Fiber Sheets"

(4) John B. Scalzi (13:36 - 13:48)
"FRP Composites for Bridge Engineering"

DISCUSSION (13:48 - 14:00)

COFFEE BREAK 14:00 - 14:15

SESSION 9: WIND AND VIBRATION 14:15 - 15:15

(Co-Chairmen: Hiroshi Sato, Roy Imbsen)

(1) Hiroshi Sato, Shigeki Kusuhara and Nobuaki Furuya (14:15 - 14:27)
"Flutter Characteristics of a Super Long-Span Bridge"

(2) Kensaku Hata, Masahiro Koike and Takumi Uno (14:27 - 14:39)
"Aerodynamic Stability of the Cable Stayed Bridge with New Type of Twin Girder "

(3) Kazunori Yamaguchi (14:39 - 14:51)
"Vibration Test of the Tatara Bridge"

(4) Shinichi Yamanobe, Yuji Niihara and Tesuo Takeda
"Damping Characteristics of Prestressed Concrete Cable-Stayed Bridges Based on Measured Data"

(5) Yozo Fujino, Masato Abe, Hajime Shibuya, Masato Yanagihara and Masashi Sato (14:51 - 15:03)
"Monitoring of Hakucho Suspension Bridge using Ambient Vibration"

DISCUSSION (15:03 - 15:15)

COFFEE BREAK 15:15 - 15:30

SESSION 10: CURRENT BRIDGE R&D 15:30 - 17:00

(Co-Chairmen: Jiro Fukui, Paul Virmani)

(1) David B. Beal (15:30 - 15:42)
"AASHTO's Bridge Research Program"

(2) Tadaaki Maruyama, Yukio Kawamura, Masao Yubisui, and Hiroshi Tanaka (15:42 - 15:54)
"Design Concept of a Floating Swing Bridge in Osaka"

(3) David H. Densmore (15:54 - 16:06)
"International Scanning Tours Related to Bridge Technology"

(4) Manabu Fujita, Keiji Umezu, Hideo Arai and Tamon Ueda (16:06 - 16:18)
"Fretting Fatigue Characteristics in the Curved Layout of Large-Capacity Prestressing Strands"

(5) F.W. Klaiber and T. J. Wipf (16:18 - 16:30)
"Use of an Alternate Shear Connector in a Beam-in-Slab Bridge System"

(6) Hiroshi Mitamura, Shizuo Kato, Shigeharu Onsen and Shigeyuki Matsui (16:30 - 16:42)
"Maintenance of Bridge and Reinforcement of Existing Deck Slabs"

DISCUSSION (16:42 - 17:00)

SESSION 11: CLOSING SESSION 17:00 - 17:15

(Co-Chairmen: Kazuhiro Nishikawa, James D. Cooper)

Remarks: James D.Cooper (Chairman for the U.S. side)
Closing Remarks: Kazuhiro Nishikawa (Chairman for the Japan side)

List of Participants

LIST OF PARTICIPANTS

15th U.S. – JAPAN BRIDGE WORKSHOP
(Workshop on Bridge Engineering)

November 9 and 10, 1999

Tsukuba City, Japan

- U.S. SIDE -

Mr. David B. Beal
Senior Program Officer
National Cooperative Highway Research Program
2001 Wisconsin Avenue
Washington, DC 20418
Phone: (202) 334-3228
Fax: (202) 334-2006
E-mail: dbeal@nas.edu

Dr. Michel Bruneau
Professor, Department of Civil, Structural and Environmental Engineering
Deputy Director, Multidisciplinary Center for Earthquake Engineering Research
State University of New York at Buffalo, Buffalo, NY14261
105 Red Jacket Quadrangle
Buffalo, New York 14261-0025
Phone: (716) 645-3391 ext. 104
Fax: (716) 645-3399
E-mail: bruneau@acsu.buffalo.edu

Dr. Ian G. Buckle
Professor of Civil Engineering
Director, Civil Engineering Earthquake Research Center
University of Nevada – Reno
Department of Civil Engineering, Mail Stop 258
University of Nevada, Reno, NV 89557
Phone : (775)784-1519
Fax : (775)784-1390
E-mail : igbuckle@unr.edu

Mr. James D. Cooper
Technical Director
Bridge Research and Development
Federal Highway Administration
Office of Infrastructure Research and Development
McLean, VA 22101-2296
Phone: (202) 493-3023
Fax: (202)-493-3442
E-mail: Jim.Cooper@ms.fhwa.dot.gov

Mr. David H. Densmore
Director of Bridge Technology, HIBT
Office of Infrastructure
Federal Highway Administration
400 7th Street, S.W., Room 3203
Washington, D.C. 20590
Phone: (202) 366-4589
Fax: (202) 366-3077
E-mail: David.Densmore@fhwa.dot.gov

Dr. Jamshid Ghaboussi
Professor of Civil Engineering
University of Illinois
3118 Newmark Civil Engineering Laboratory
MC-250, 205 N Mathews Ave.
University of Illinois at Urbana-Champaign
Urbana, Illinois 61801-2397
Phone: (217) 333-6939
Fax: (217) 265-8039
E-mail: jghabous@uiuc.edu

Dr. Issam E. Harik
Professor of Civil Engineering
Head, Structures Section, Kentucky Transportation Center
Department of Civil Engineering
University of Kentucky
Lexington, KY 40506-0281
Phone : (606) 257-3116
Fax : (606) 257-1815
E-mail: iharik@engr.uky.edu

Mr. Mark E. Hirota
State Bridge Engineer
Oregon Department of Transportation
355 Capitol St. NE, Salem OR 97301-3871
Salem, OR 97301-3871
Phone: (503) 986-3344
Fax: (503) 986-3407
E-mail: Mark.E.Hirota@odot.state.or.us

Dr. F. Wayne Klaiber
Professor of Civil Engineering
Anson Marston Distinguished
Professor of Engineering
Iowa State University
Department of Civil & Construction Engineering
422 Town Engineering Building
Ames, IA 50011
Phone: (515) 294-8763
Fax: (515) 294-8216
E-mail: klaiber@iastate.edu

Dr. James Howard Long
Associate Professor of Civil Engineering
University of Illinois
Department of Civil Engineering
205 N. Mathews
Urbana, IL 61801
Phone: (217) 333-2543
Fax: (217) 333-9464
E-mail: j-long@uiuc.edu

Dr. John B. Mander
Associate Professor
Department of Civil, Structural and Environmental Engineering
University at Buffalo, SUNY
Buffalo, NY 14260-4300
Phone: (716) 645-2114 ext 2418
Fax: (716) 645-3733
E-mail: jmander@acsu.buffalo.edu

Dr. Emmanuel A. Maragakis
Professor and Chair, Civil Engineering
University of Nevada, Reno
Reno, NV 89557
Phone : (775) 784-6937
Fax: (775) 784-1390
E-mail: maragaki@unr.edu

Dr. Khalid M. Mosalam
Assistant Professor of Civil Engineering
712 Davis Hall
University of California, Berkeley, CA 94720-1710
Phone : (510) 643-4805
Fax: (510) 643-8928
E-mail: mosalam@cc.berkeley.edu

Dr. Michael A. Riley
Research Structural Engineer
National Institute of Standards and Technology
Building and Fire Research Laboratory
100 Bureau Dr., Stop 8611
Gaithersburg, MD 20899-8611
Phone : (301) 975-6065
Fax: (301) 869-6275
E-mail: michael.riley@nist.gov

Dr. David Howard Sanders
Associate Professor of Civil Engineering
University of Nevada, Reno
Department of Civil Engineering Mail Stop 258
Reno, Nevada 89557-0152
Phone : (702) 784-4288
Fax: (702) 784-1390
E-mail: sanders@unr.edu

Mr. Thomas E. Sardo
Bridge Engineer
California Department of Transportation
Office of Earthquake Engineering – MS 9
1801 30th Street, Sacramento, CA 95816
Phone : (916) 227-8328
Fax: (916) 227-8898
E-mail: Tom_Sardo@dot.ca.gov

Dr. John B. Scalzi
Program Director
Civil and Mechanical Systems
National Science Foundation
4201 Wilson Blvd.- Rm 545
Arlington, VA 22230
Phone : (703) 306-1361
Fax: (703) 306-0291
E-mail: jscalzi@nsf.gov

Mr. Cristoforo Daniele Subrizi
Lead Engineer
Major Bridge Service Center
Parsons Brinckerhoff Quade & Douglas, Inc.
303 Second Street, Suite 700 N
San Francisco, CA 94107
Phone : (415) 243-4718
Fax: (415) 243-9501
E-mail: subrizi@pbworld.com

Dr. Sabanayagam Thevanayagam
Associate Professor
Dept. of Civil, Struct. & Env. Engineering
212 Ketter Hall, University at Buffalo,
State Univ. of New York,
Buffalo, NY 14260
Phone : (716) 645-2114 ext 2430
Fax: (716) 645-3733
E-mail: theva@eng.buffalo.edu

Dr. Y. Paul Virmani
Program Manager, Office of Infrastructure, Research and Development
Turner-Fairbank Highway Research Center
Federal Highway Administration
6300 Georgetown Pike, McLean, VA 22101
Phone : (703) 285-2439
Fax: (703) 285-2766
E-mail: paul.virmani@fhwa.dot.gov

Dr. W. Phillip Yen
Research Structural Engineer, Office of Infrastructure, Research and Development
Turner-Fairbank Highway Research Center
Federal Highway Administration
6300 Georgetown Pike, McLean, VA 22101
Phone : (703) 285-2315
Fax: (703) 285-2766
E-mail: wen-huei.yen@fhwa.dot.gov

Dr. Yan Xiao
Assistant Professor of Civil Engineering
Department of Civil Engineering
University of Southern California
Los Angeles, CA 90089-2531
Phone : (213) 740-6130
Fax: (213) 744-1426
E-mail: yanxiao@usc.edu

- Japan Side -

(Public Works Research Institute)
Address: 1 Asahi, Tsukuba-shi Ibaraki-ken 305-0804
TEL: +81-298-64-2211
FAX: +81-298-64-2840

Tomomitsu Fujii
Position: Director-General

Syunsoku Kyosai
Position: Deputy Director-General

Tsuneo Uesaka
Position: Assistant Director-General

Takeo Nakajima
Position: Director, Planning and Research Administration Department

Makoto Nakamura
Position: Director, Road Department

Michio Okahara
Position: Director, Structure and Bridge Department

Masahiko Yasuda
Position: Director, Earthquake Disaster Prevention Research Center

Akira Moriyama
Position: Advisory Engineer for Bridge
Planning and Research Administration Department

Seishi Meiarashi
Position: Head, Chemistry Division
Materials and Construction Department

Hirotaka Kawano
Position: Head, Concrete Division, Materials and Construction Department

Hiroshi Watanabe
Position: Senior Research Engineer, Concrete Division
Materials and Construction Department

Yoshiki Tanaka
Position: Research Engineer, Concrete Division
Materials and Construction Department

Jiro Fukui
Position: Head, Foundation Engineering Division
Structure and Bridge Department

Masahiro Nisitani
Position: Senior Research Engineer, Foundation Engineering Division
Structure and Bridge Department

Hiroshi Sato
Position: Head, Structure Division
Structure and Bridge Department

Shigeki Kusuhara
Position: Senior Research Engineer
Structure and Bridge Department

Kenichi Ohgi
Position: Research Engineer
Structure and Bridge Department

Kazuhiro Nishikawa
Position: Head, Bridge Division
Structure and Bridge Department

Arata Hiromatsu
Position: Research Engineer, Bridge Division
Structure and Bridge Department

Keiichi Tamura
Position: Head, Ground Vibration Division
Earthquake Disaster Prevention Research Center

Yoshihiro Nakao
Position: Research Engineer, Ground Vibration Division
Earthquake Disaster Prevention Research Center

Shigeki Unjoh
Position: Head, Earthquake Engineering Division
Earthquake Disaster Prevention Research Center

Yukio Adachi
Position: Senior Research Engineer, Earthquake Engineering Division
Earthquake Disaster Prevention Research Center

Jun-ichi Hoshikuma
Position: Senior Research Engineer, Earthquake Engineering Division
Earthquake Disaster Prevention Research Center

Michio Ohsumi

Position: Research Engineer, Earthquake Engineering Division
Earthquake Disaster Prevention Research Center

(University of Tokyo)

Yozo Fujino

Position: Professor, Department of Civil Engineering
Address: Department of Civil Engineering
University of Tokyo
7-3-1 Hongo, Bunkyo-ku, Tokyo 113-8656
Phone: +81-3-5841-6095
Fax: +81-3-5841-7454
E-mail: fujino@bridge.t.u-tokyo.ac.jp

(Yokohama National University)

Takahiro Yamaguchi

Position: Research Associate, Department of Civil Engineering
Address: 79-5, Tokiwadai, Hodogaya-ku, Yokohama City,
Kanagawa, 240-8501, Japan
Phone: +81-45-339-4045
Fax: +81-45-331-1707

(Hokkaido Development Bureau)

Kenji Ikeda

Position: Structures Division, Structures Dept, Civil Engineering Research Institute
Address: Hiragishi 1-3, Toyohira-ku, Sapporo 062-8602
Phone: +81-11-841-1111 (ext. 300)
Fax: +81-11-820-2714

Hiroshi Mitamura

Position: Structures Division, Structures Dept, Civil Engineering Research Institute
Address: Hiragishi 1-3, Toyohira-ku, Sapporo 062-8602
Phone: +81-11-841-1111 (ext. 303)
Fax: +81-11-820-2714

Shizuo Kato

Position: Senior Engineer of Bridge Engineering Department
Hokkaido Engineering Consultants Co., Ltd.(HEC)
Address: 4-1,1 jo 5 chome Atsubetsu-chuo, Atsubetu-ku, Sapporo 004-8585
Phone: +81-11-801-1540
Fax: +81-11-801-1541
E-mail sk724@mb.docon.co.jp

Noriyosi Murakami

Position: Technical Planner, Bridge Design Consultant Chodai Co. Ltd.
Address: North 1 East 2, 5-3, chuo-ku, Sapporo 060-0031
Phone: +81-11-271-2357
Fax: +81-11-271-6039

(Osaka Municipal Government)

Masao Yubisui

Position: Chief Engineer of Bridge Section
Address: 1-2-2-500, Umeda, Kita-ku, Osaka 530-0001
Phone: +81-6-6208-9650
Fax: +81-6-6348-0580

(Japan Highway Public Corporation)

Yoshinori Igase

Position: Deputy Director of Bridge Division, Expressway Research Institute
Address: 4-1.1Chome, Tadao, Machida-shi, Tokyo 194-8508
Phone: +81-42-791-1621
Fax: +81-42-791-2380
E-mail: igase@jhri.japan-highway.go.jp

Koji Osada

Position: Engineer of Bridge Division, Expressway Research Institute
Address: 4-1.1Chome, Tadao, Machida-shi, Tokyo 194-8508
Phone: +81-42-791-1621
Fax: +81-42-791-2380
E-mail: osada@jhri.japan-highway.go.jp

(Hanshin Expressway Public Corporation)

Kensaku Hata

Position: Deputy Manager, Design Division, Engineering Department
Address: 4-1-3 Kyutaro- Machi, Chuo-ku, Osaka 541-0056
Phone: +81-6-6252-8121
Fax: +81-6-6252-4583
E-mail: hatakenhepc@okym.enjoy.ne.jp

Kiyoshi Miyawaki

Position: Chief of Maintenance Design Division
Maintenance and Facility Design Department
Address: 4-1-3 Kyutaro- Machi, Chuo-ku, Osaka 541-0056
Phone: +81-6-6252-8121
Fax: +81-6-6252-8433

Fuminobu Okunishi

Position: Engineer of Maintenance Design Division
Maintenance and Facility Design Department
Address: 4-1-3 Kyutaro- Machi, Chuo-ku, Osaka 541-0056
Phone: +81-6-6252-8121
Fax: +81-6-6252-8433
E-mail: okunishi@ops.dti.ne.jp

Takumi Uno

Position: Engineer of Survey Division, Second Kobe Construction Department
Address: 22th floor Kobe Harbor Land Center Building
1-3-3 Higashi Kawasaki, Chuo-ku, Kobe 650-0044
Phone: +81-78-260-8129
Fax: +81-78-360-8158
E-mail: unotakumi@msa.biglobe.ne.jp

(Honsyu-Shikoku Bridge Authority)

Susumu Fukunaga

Position: Deputy Manager, Engineering Information Division
Long-Span Bridge Engineering Center
Address: Urban Ace Sannomiya Bldg.
4-1-22 Onoedori, Chuo-ku, Kobe 651-0088
Phone: +81-78-291-1075
Fax: +81-78-291-1362
E-mail: fukunaga@hsba.go.jp

Kazunori Yamaguchi

Position: Deputy Manager of Construction Division
Mukaishima Operation Office, 3rd Operation Bureau
Address: 6904 Mukaishima, Mitsugi, Hirosima 722-0073
Phone: +81-848-44-3700
Fax: +81-848-44-7609
E-mail: yamagukz@hsba.go.jp

(Road Management Technology Center)

Naoshige Nomura

Takeyuki Yokooka

Yoshihiro Tanaka

(Japan Association of Steel Bridge Construction)

Tatsumasa Takaku

Ryu Okamoto

Nobuhide Nakamura

Motoaki Tanaka

Tatsuo Kurokawa

Shigeru Echigo

Fumitaka Machida

(Japan Prestressed Concrete Contractors Association)

Hiroyuki Aburano

Shigeharu Takano

Mitsuru Inokawa

Yuji Tsuji

Takuya Mori

Manabu Fujita

Hijiri Tanaka

Thirugnanasuntharan Aravinthan

Kiyokazu Shinagawa

Takashi Yamane

(Japan Civil Engineering Consultants Association)

Toshio Iwasaki

Kenji Matsui

(Carbon Fiber Repair & Reinforcement Research Association)

Tokitaro Hoshijima

Akeo Hattori

Akira Kobayasi

Photos of Study Tour


明石海峡大橋



